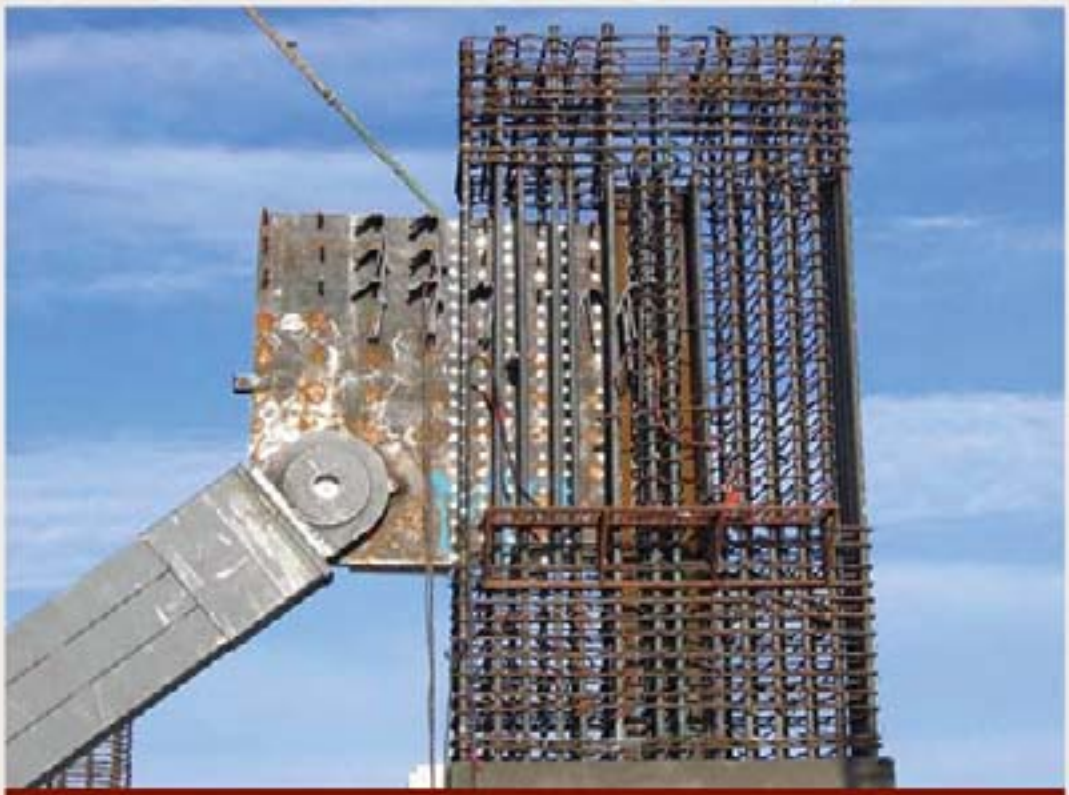
Composite Construction in Steel and Concrete VI



Proceedings of the
2008 Composite Construction
in Steel and Concrete Conference VI

Edited by
Roberto T. Leon
Tiziano Perea
Gian Andrea Rassati
Jörg Lange

ASCE

SEI
ASCE
STRUCTURAL
ENGINEERING
INSTITUTE

Composite Construction in Steel and Concrete VI

PROCEEDINGS OF THE 2008 CONFERENCE

July 20–24, 2008
Devil's Thumb Ranch, Tabernash, Colorado

SPONSORED BY

Engineering Conferences International

The Structural Engineering Institute (SEI)
of the American Society of Civil Engineers

EDITED BY
Roberto T. Leon
Tiziano Perea
Gian Andrea Rassati
Jörg Lange

Published by the American Society of Civil Engineers

Cataloging-in-Publication Data on file with the Library of Congress.

American Society of Civil Engineers
1801 Alexander Bell Drive
Reston, Virginia, 20191-4400

www.pubs.asce.org

Any statements expressed in these materials are those of the individual authors and do not necessarily represent the views of ASCE, which takes no responsibility for any statement made herein. No reference made in this publication to any specific method, product, process, or service constitutes or implies an endorsement, recommendation, or warranty thereof by ASCE. The materials are for general information only and do not represent a standard of ASCE, nor are they intended as a reference in purchase specifications, contracts, regulations, statutes, or any other legal document. ASCE makes no representation or warranty of any kind, whether express or implied, concerning the accuracy, completeness, suitability, or utility of any information, apparatus, product, or process discussed in this publication, and assumes no liability therefore. This information should not be used without first securing competent advice with respect to its suitability for any general or specific application. Anyone utilizing this information assumes all liability arising from such use, including but not limited to infringement of any patent or patents.

ASCE and American Society of Civil Engineers—Registered in U.S. Patent and Trademark Office.

Photocopies and permissions. Permission to photocopy or reproduce material from ASCE publications can be obtained by sending an e-mail to permissions@asce.org or by locating a title in ASCE's online database (http://cedb.asce.org) and using the "Permission to Reuse" link. *Bulk reprints.* Information regarding reprints of 100 or more copies is available at http://www.asce.org/reprints.

Copyright © 2011 by the American Society of Civil Engineers.
All Rights Reserved.
ISBN 978-0-7844-1142-1
Manufactured in the United States of America.

Dedication

Ivan M. Viest



These proceedings are dedicated to Dr. Ivan M. Viest, whose pioneering efforts in research led to the extensive utilization of composite structures in the USA and whose initiative led to the development of this series of conferences.

Dr. Ivan M. Viest was born in Bratislava (now in Slovakia) in 1922. He graduated from the Slovak Technical University with the degree of Inžinier (engineer) in 1946. After participating in several resistance movements against the German invasion during WWII and a short engineering career in Slovakia, he came to the USA in 1947, and enrolled at Georgia Tech, where he earned an MS degree. He transferred to the University of Illinois in 1948, and began his work on composite construction under the mentorship of Dr. Nathan Newmark. Dr. Viest's doctoral work, completed in 1951, contained pioneering experimental and analytical work on shear connectors and composite beams. After graduation, he remained as a faculty member, working in the areas of concrete columns and shear in reinforced concrete. In 1953, he began investigating the use of shear studs in bridges, work that he continued when he took over the AASHO Road Test studies in 1957. His numerous publications from his work in the 1950's led to the development of composite construction design provisions for both buildings and bridges at the end of that decade. Dr. Viest then joined Bethlehem Steel Corp. in 1961 where he worked to promote and improve the use of steel both through his technical expertise and service in national technical committees. Amongst his many contributions are his leadership of AISC TC5 – Composite Construction and his work on the development of the LRFD specification. Dr. Viest retired in 1982 and continues to enjoy his retirement. More details on Dr. Viest can be found in his autobiography: *An Immigrant's Story* (http://www.Xlibris.com)



Conference Participants

Preface

These proceedings summarize the state-of-the-art in composite construction worldwide, as presented at the an international conference on Composite Construction in Steel and Concrete held at the Devil's Thumb Ranch in Tabernash, Colorado (USA) in July 2008. This is the sixth in a series of conferences on this topic organized by the United Engineering Foundation (and now Engineering Conferences International) aimed at assessing and synthesizing the most recent advances in research and practice in the area of composite steel-concrete construction. This conference was preceded by those held in Henniker, New Hampshire, USA (1987), Potosi, Missouri, USA (1992), Irsee, Germany (1996), Banff, Canada (2000), and Kruger National Park, South Africa (2008).

The papers contained in this volume cover a wide variety of topics, including composite bridges, composite slabs, shear connectors, composite columns, innovative composite structural systems, fire and seismic resistance of composite structural systems and practical applications. Seventy-six participants from seventeen countries participated in four days of presentations, panel and informal discussions dealing with all aspects of composite construction. The conference was organized and chaired by Dr. Roberto Leon, Georgia Institute of Technology, U.S.A. and Dr. Jörg Lange, Technische Universität Darmstadt, Germany, with the assistance of Dr. Gian Andrea Rassati (University of Cincinnati), Dr. Jerome Hajjar (Northeastern University), and Dr. W. Samuel Easterling (Virginia Tech). The conference was generously supported by the AISC and NUCOR Corporation.

The papers in the proceedings were peer reviewed as per the guidelines used for the *Journal of Structural Engineering*, ASCE and are eligible for all ASCE awards and are open for discussion in the *Journal of Structural Engineering*, ASCE. The review process was administered by the proceeding editors, who would like to thank all the reviewers for their prompt and useful responses. The publication of the proceedings was supported by the Technical Activities Division of the Structural Engineering Institute, ASCE.

The editors will like to thank the staff of Engineering Conferences International, and particularly Ms. Antoinette L. Chartier, for all their help in organizing and coordinating the conference.

The financial support of the American Institute of Steel Construction and the Vulcraft Division of NUCOR Corporation is also gratefully acknowledged. This conference would not have been possible without that funding.

Finally, the senior editor will like to thank Mr. Tiziano Perea for all his work in preparing the final draft of the proceedings. Without his contributions these proceedings would not have been possible.

Roberto T. Leon, Tiziano Perea, Jörg Lange, and Gian Andrea Rassati
Atlanta, July 2010

Acknowledgments

Organizing Committee

Chairs:
Dr. Roberto T. Leon, Georgia Institute of Technology, Atlanta, GA, USA
Dr. Jörg Lange, Technische Universität Darmstadt, Darmstadt, Germany

Co-Chairs:
Dr. W. Samuel Easterling, Virginia Tech, Blacksburg, VA, USA
Dr. Gian Andrea Rassati, University of Cincinnati, Cincinnati, OH, USA
Dr. Jerome F. Hajjar, Northeastern University, Boston, MA, USA

Scientific Committee

Dr. Ulrike Kuhlmann, University of Stuttgart, Stuttgart, Germany
Dr. K. C. Tsai, NCREE, Taipei, Taiwan
Dr. Brian Uy, University of Western Sydney, Australia
Dr. James Harris, J. R. Harris & Co., Denver, CO, USA
Dr. Toko Hitaka, University of Kyoto, Kyoto, Japan
Mr. Lawrence A. Griffis, W. P. Moore & Assoc., Austin, TX, USA
Dr. Kent Harries, University of Pittsburgh, Pittsburgh, PA, USA
Dr. Yan Xiao, University of Southern California, Los Angeles, CA, USA
Dr. Oreste Bursi, University of Trento, Trento, Italy
Dr. Mario Fontana, ETH, Zürich, Switzerland
Dr. Wolfgang Kurz, University of Kaiserslautern, Kaiserslautern, Germany
Dr. Dennis Lam, University of Leeds, Leeds, UK
Dr. Robert Tremblay, Ecole Polytechnique, Montreal, Canada

Financial Support





Contents

Shear Connection

Prediction of Shear Resistance of Headed Studs in Troughs of Profiled Sheeting 1
Roger P. Johnson

Lifetime Oriented Design Concepts of Steel-Concrete Composite Structures Subjected to Fatigue Loading 14
Gerhard Hanswille and Markus Porsch

Headed Studs Close to the Concrete Surface—Fatigue Behaviour and Application 26
Ulrike Kuhlmann and Jochen Raichle

Fatigue Behavior of Shear Connectors in High Performance Concrete 39
Markus Feldmann, Oliver Hechler, Josef Hegger, and Sabine Rauscher

Cyclic Performances of Shear Connectors..... 52
Adrian Liviu Ciutina and Aurel Stratan

New Steel-Concrete Shear Connection for Composite Bridges..... 65
Jean-Paul Lebet

Continuous Shear Connectors in Bridge Construction 78
Oliver Hechler, Jaques Berthellemy, Wojciech Lorenc, Günter Seidl, and Eva Viefhues

Effects of Group Arrangement on the Ultimate Strength of Stud Shear Connection 92
Chang-Su Shim, Pil-Goo Lee, Dong-Wook Kim, and Chul-Hun Chung

Slab Systems

Innovative Shear Connectors for a New Prestressed Composite Slab System for Buildings with Multiple HVACR Installations 102
Marcin Abramski, Thomas Friedrich, Wolfgang Kurz, and Juergen Schnell

Composite Slab with Integrated Installation Floor Using Cellular Beams.....112
Andrea Frangi, Markus Knobloch, Elio Raveglia, Mario Fontana, Martin Mensinger, and Karl Schwindl

Steel Fibre Reinforced Continuous Composite Slabs..... 125
Florian P. Ackermann and Jürgen Schnell

Elemental Bending Test and Modeling of Shear Bond in Composite Slabs 138
Redzuan Abdullah and W. Samuel Easterling

Composite Beams

Ductility of Composite Beams with Trapezoidal Composite Slabs 151
Mark A. Bradford, Yong-Lin Pi, and Brian Uy

Effect of Strain Profiles on the Behavior of Shear Connectors for Composite Steel-Concrete Beams **160**
O. Mirza and B. Uy

Design Model for Continuous Composite Beams with Web Openings **173**
Torsten Weil, Juergen Schnell, and Wolfgang Kurz

Efficient Design for the Calculation of the Deflection and the Shear Force Capacity of Slim-Floor Girder **185**
Ulrike Kuhlmann and Gunter Hauf

The Multi-Storey Car Park for the "Neue Landesmesse" in Stuttgart over Highway A8, Germany **199**
Roland Friede, Jörg Lange, and Ralf Steinmann

Design and Testing of Two Composite Underspanned Beams **212**
Michel Crisinel and Gabriele Guscetti

Composite Columns

Flexural Behaviour of Concrete-Filled Thin-Walled Steel Tubes with Longitudinal Reinforcement **225**
Andrew Wheeler and Russell Bridge

Behavior of Composite CFT Beam-Columns Based on Nonlinear Fiber Element Analysis **237**
Tiziano Perea and Roberto Leon

Structural Design of Concrete Filled Steel Elliptical Hollow Sections **252**
Dennis Lam and Nicola Testo

Seismic Performance of Composite EWECS Columns in New Hybrid Structural System **263**
Fauzan and Hiroshi Kuramoto

Design of Composite Columns—Steel, Concrete, or Composite Approach? **276**
Russell Q. Bridge

Strength of Concrete Filled Steel Tubes under High-Strain Rate Loading **291**
Yan Xiao, Qiu Zheng, Jingsi Huo, Jianhua Shan, and Baisheng Chen

Strength of Concrete Filled Historic Cast-Iron Columns **304**
Stefan Heyde and Karsten Geißler

Concrete-Filled Steel Tube Columns—Tests Compared with Eurocode 4 ..... **317**
C. Douglas Goode and Dennis Lam

Design of Composite Columns Made of Concrete Filled Tubes with Inner Massive Core Profiles and High Strength Materials **326**
G. Hanswille and M. Lippes

Foundations and Column Bases

Design of Anchor Plates Based on the Component Method **338**
Ulrike Kuhlmann and Markus Rybinski

An Economical and Efficient Foundation Connection for Concrete Filled Steel Tube Piers and Columns **351**
Charles W. Roeder and Dawn E. Lehman

Using Steel Fiber Reinforced Cementitious Composite (SFRCC) in Shallow Embedded Column Base **364**
Yao Cui, Masayoshi Nakashima, and Toko Hitaka

Codes and Structures

Composite Buildings in Germany **377**
Jörg Lange and Wolfgang Kurz

Composite Bridges in Germany Designed According to Eurocode 4-2 ..... **391**
Gerhard Hanswille

Where Structural Steel and Concrete Meet **406**
J. W. B. Stark

Harmonization of Design Rules in Europe **419**
Fernando González and Jörg Lange

Review and Comparison of Encased Composite Steel-Concrete Column Detailing Requirements **427**
William P. Jacobs V and Arvind V. Goverdhan

Seismic Performance of Members and Connections

Composite Joints in Robust Building Frames **442**
Jean-Pierre Jaspart and Jean-François Demonceau

Behavior of Columns in Composite CES Structural System **455**
Hiroshi Kuramoto

Cyclic Tests on RC-Steel Shear Plate Composite Wall System Applicable in Beam Spans with Large Openings **466**
Toko Hitaka and Andres Jacobsen

Performance Evaluation of Innovative Hybrid Coupled Core Wall Systems **479**
Gian A. Rassati, Patrick J. Fortney, Bahram M. Shahrooz, and Paul W. Johnson III

Seismic-Induced Fire Analysis of Steel-Concrete Composite Beam-to-Column Joints: Bolted Solutions **493**
Oreste S. Bursi, Fabio Ferrario, Raffaele Pucinotti, and Riccardo Zandonini

Seismic-Induced Fire Analysis of Steel-Concrete Composite Beam-to-Column Joints: Welded Solutions **506**
Oreste S. Bursi, Fabio Ferrario, and Raffaele Pucinotti

Seismic Behavior of Connections to Gangue-Filled CFT Columns with Ring Stiffeners **519**
Guochang Li, Wei Sun, and Roberto T. Leon

Strengthening of Composite Beam-to-Column Joints: Static and Seismic Behaviour **529**
G. Loho, A. Lachal, and J. M. Aribert

Numerical Models for Beams and Joints

Numerical Modelling of Composite Beam-to-Beam Joints—Innovative Solutions **542**
Samy Guezouli, Hugues Somja, Sao Serey Kaing, and Alain Lachal

Numerical Modeling of Composite Castellated Beams **554**
Marian A. Gizejowski and Wael A. Salah

A Class of Finite Elements for Nonlinear Analysis of Composite Beams **566**
Quang Huy Nguyen, Mohammed Hjiaj, Brian Uy, and Samy Guezouli

Numerical Calculation of the Deflections of Composite Girders **578**
Frank Böhme and Jörg Lange

A Mixed-Finite Element Approach for Performance-Based Design of Rectangular Concrete-Filled Steel Tube (RCFT) Frames **591**
Cenk Tort and Jerome F. Hajjar

Macro-Elements for Composite Beam-Column Connections **604**
Uwe E. Dorka and Saenboon Amorntipsakul

Generic Finite Element Model for Mechanically Consistent Scaling of Composite Beam-Column Joint with Welded Connection **611**
Saenboon Amorntipsakul and Uwe E. Dorka

Fire Design

Geometric Non-Linear Modelling of Partial Interaction in Composite T-Beams in Fire **619**
Amin Heidarpour and Mark A. Bradford

Where Steel and Concrete Meet in the Heat **628**
Rob Stark

Predicting the Standard Fire Behavior of Composite Steel Beams **642**
Guillermo A. Cedeno, Amit H. Varma, and Jay Gore

Innovations

New Results of Material Analysis Regarding the Bauschinger-Effect on the Deflection of Composite Beams **657**
Jörg Lange and Hauke Grages

Evaluation of Adhesive Bonding between Steel and Concrete **669**
Wolfgang Kurz, Christopher Kessler, Paul Ludwig Geiss, and Sarunas Turcinskas

Ultimate Flexural Strength of Hybrid Composite Girders Using High-Performance Steel of HSB600 at Sagging Bending **680**
Seok-Goo Youn, Doobyong Bae, and Young-Jin Kim

Modern Composite Structures Made of High Performance Materials **691**
Sabine Rauscher and Josef Hegger

Steel-FRP Composite Structural Systems **703**
Kent A. Harries and Sherif El-Tawil

Bridges

Towards a Better Understanding of Behaviour of Bridges with Integral Abutments **717**
Martin Nilsson, Jörgen Eriksen, and Milan Veljkovic

Developing Composite Action in Existing Non-Composite Steel Girder Bridges **728**
Gunup Kwon, Michael D. Engelhardt, and Richard E. Klingner

Experimental Investigations of the Shear Connection Behaviour in Joints of Composite Bridges **741**
Alain Lachal, Oliver Hechler, Sao Serey Kaing, and Jean-Marie Aribert

Inelastic Strength Behavior of Horizontally Curved Composite I-Girder Bridge Structural Systems: Fixed-End Bridge FEA Study **754**
Se-Kwon Jung and Donald W. White

Efficient Erection Method of Cantilever Bridge Deck Using Ribbed Steel Form Bolted to Girder **766**
Youn-Ju Jeong, Hyun-Bon Koo, and Hyeong-Yeol Kim

Indexes

Attendee List **779**

Author Index **787**

Subject Index **789**

This page intentionally left blank

PREDICTION OF SHEAR RESISTANCE OF HEADED STUDS IN TROUGHS OF PROFILED SHEETING

Roger P. Johnson
Emeritus Professor, School of Engineering, University of Warwick
Coventry, U.K.
r.p.johnson@warwick.ac.uk

ABSTRACT

Where a composite floor slab is supported on a composite beam of steel and concrete, shear connection is provided by studs in troughs of the sheeting. The resistance of these studs to longitudinal shear depends on over 20 parameters, of which 15 appear in the mechanical models for shear resistance of Johnson and Yuan [1998]. These models have been revised. The mean of over 200 ratios of test/predicted shear resistance is now 1.03. Their mean is higher and their variation is much less than for ratios predicted using the design method of ANSI/AISC 360-05 (2005).

Ratios of test to predicted shear resistances to the relevant British standard and the Eurocode have been studied elsewhere. Summaries of these results are given. All the comparisons show that methods that are both accurate and simple will not be found unless the number of variables is reduced by further standardization.

INTRODUCTION

Trapezoidal profiled sheeting is widely used in composite floor slabs. Stud shear connectors are normally welded through the sheeting to the top flange of each supporting composite beam. Many modern profiles have stiffening ribs, as shown at A and B in Figure 1. The rib in the trough, at A, causes the studs to be placed off centre, in locations that have an unfavourable (U) or favourable (F) effect on the resistance P of a stud to a longitudinal shear force F.

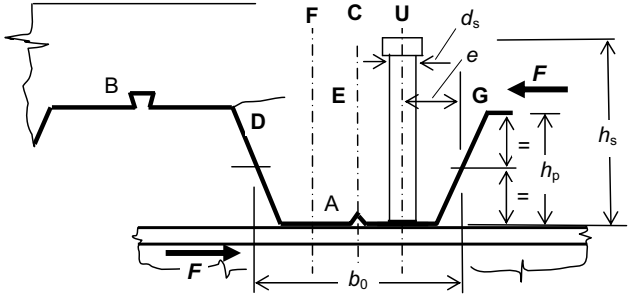


Fig. 1 - Cross-section of a trough of profiled sheeting, with a stud in the 'U' location

Mesh reinforcement should be placed as far as possible below the heads of the studs, to improve the ductility ('slip capacity') of the connection. If the mesh is too high to influence failure by anticlockwise rotation of the trough, with cracking at D and shearing across DEG, then the ductility depends on the behaviour of unreinforced concrete in tension, because the relevant resistance of thin sheeting is very low. Where there is a top rib at B, its height should be added to the required minimum length of the stud, to maintain overlap with mesh laid on the sheeting.

Where this is done and the rib is small, the net or shoulder height of the profile, h_p in Figure 1, can be used for the prediction of shear resistance, rather than the overall height.

PREDICTION OF SHEAR RESISTANCE

Testing has shown that shear resistance may be influenced by the properties of the four materials (concrete, reinforcement, sheeting, and stud), by the geometry of the slab, the reinforcing mesh, the stud and the trough, and by the many possible layouts of studs in a trough – more than 20 parameters. Important ones omitted from most design rules in codes are the thickness t_p and yield strength f_{yp} of the sheeting, the details of reinforcement, the layout of the studs and their required projection above the reinforcement.

It is difficult to deduce properties of studs from tests on beams, so codes have relied on the 'push test'. The well-known version specified in Eurocode 4 for solid slabs has slabs of minimum width 600 mm, and so is relevant for studs in a beam with concrete flanges that project at least 300 mm on each side of the web. For composite slabs, the Eurocode says (clause B.2.2(3)) that the slabs and reinforcement should be 'suitably dimensioned…'. Testing not in accordance with this vague rule is either excluded here, or commented on.

A set of mechanical models and methods of predicting the shear resistance P_r of studs was published [Johnson and Yuan, 1998] based on a study of over 300 push tests. They are referred to here as J-Y methods. The work took no account of top ribs or reinforcement and was based on sheeting of nominal yield strength 280 N/mm^2, typical of practice at the time. The usual strength in the U.K. is now 350 and may soon be 450 N/mm^2. Tests with sheets of measured strength 677 N/mm^2 have been reported [Bradford et al., 2006]. These changes have led to minor revisions of the methods. There is space here only for an outline of the current models for the three modes of shear failure, for normal-density concrete and single studs. A full account is available [Johnson, 2008]. In models (2) and (3), the work done by the loading is equated to the dissipation in the materials, for which rigid-plastic behaviour is assumed.

MODELS FOR THE PREDICTION OF SHEAR FAILURE OF A STUD IN A TROUGH

(1) *Stud shear* is assumed to occur when the predicted shear resistance exceeds the solid-slab resistance P_{rs}. It is rare in sheetings and is not considered further. The mean solid-slab resistance is found from clause 6.6.3.1 of Eurocode 4, with the safety margins removed, and the specified cylinder strength f_{ck} replaced by the measured strength f_{cm}. It is the lower of

$$P_{rs,conc} = 0.37\, A_s\, (f_{cm} E_{cm})^{1/2} \qquad (1)$$

and $$P_{rs,stud} = 0.8\, A_s\, f_u \quad (2)$$

where A_s is the cross-sectional area of the stud and f_u is its tensile strength. Measured values of the mean elastic modulus of the concrete, E_{cm} can be unreliable, and are rarely given, so it has in all cases been calculated from the formula in the concrete Eurocode, which is, in N/mm^2 units:

$$E_{cm} = 11\,026\, f_{cm}^{0.3} \quad (3)$$

(2*) Concrete pull-out* (CP) is the usual mode for studs in 'F' locations. An unknown length of the trough is assumed to rotate through an angle θ, with a torsional plastic hinge on each side of the connection, Figure 2(a). The ultimate torsional shear stress is taken as 0.89 $(f_{cm})^{1/2}$ in N/mm^2 units, for reasons explained elsewhere [Johnson, 2008]. The plastic torsional resistance T_u, found by the sand-heap analogy, is taken as that of a rectangular cross-section b_0 by H, where

$$H = 0.2\, h_p + 0.6\, h_s, \text{ with } H \le 1.4\, h_p \quad (4)$$

with notation as in Figure 2(b). Each stud, of yield strength in tension T_y, is assumed to lengthen by δ_3 at tension force T ($\le 1.1\ T_y$), and the work done in bending it is neglected. The external shear at failure is $n_r P$, so the work equation is

$$n_r P\delta_1 = 2\, T_u\theta + n_r\, T\, \delta_3 \quad (5)$$

where P ($\le 1.1\ P_{rs}$) is the shear resisted by each of the n_r studs in the mechanism.

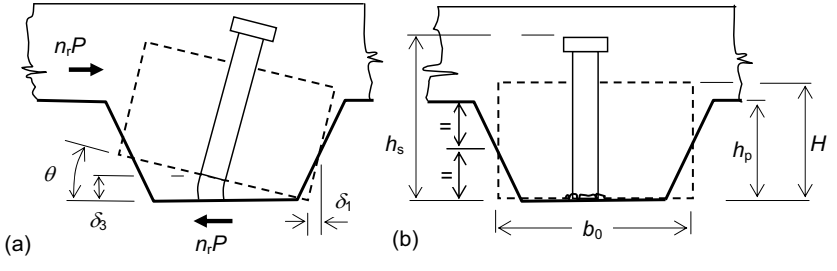


Fig. 2 - Cross-sections of a trough. (a) Geometry of rotation (b) Definition of H

The von Mises-type yield condition for the stud includes an allowance for strain-hardening, and is:

$$(P/P_{rs})^2 + (T/T_y)^2 = (1.1)^2 \quad (6)$$

As T_u, T_y and P_{rs} are known and δ_1, δ_3 and θ are inter-related, these equations can be solved for P. The shear resistance per stud in concrete pull-out mode is taken as

$$P_{cp} = 1.1\, P, \quad \le P_{rs} \quad (7)$$

This model is used also for the mode known as rib shear. For studs near a free edge, as in an L-beam, there is only one surface of torsional failure, so the 2 in eq. (5) is deleted.

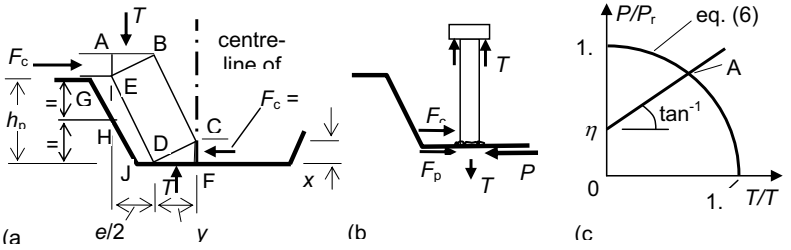


Fig. 3 - Rib punching failure. (a) Forces in the concrete (b) Forces on the stud (c) Influence of parameters η and λ on the shear resistance of a stud

(3) *Rib punching failure* (RP) is the normal mode for 'U' locations. The shear force P, Figure 3(b), is the sum of forces F_c transmitted from the slab via the concrete strut BCDE, Figure 3(a), of width b_c along the trough, and force F_p from the yielding of a length b_p of the sheeting at the base of the stud. The concrete prisms ABE and CDF each resist bi-axial compressive stress σ_c, so

$$F_c = b_c\, \sigma_c\, x \qquad \text{and} \qquad F_p = b_p\, t_p\, f_{yp} \tag{8}$$

Anchorage of the head of the stud in the slab creates tension T in its shank, Figure 3(b), which provides the forces T on surfaces AB and DF in Figure 3(a), where

$$T = b_c\, \sigma_c\, y \tag{9}$$

Depth x is a maximum when $y = e/2$, and from the geometry of Figure 3(a),

$$e^2 = 4\, h_p\, x$$

From the preceding equations, $T = b_c\, \sigma_c\, e/2$, and so

$$P = F_c + F_p = (2T / e)\, (e^2 / 4h_p) + b_p\, t_p\, f_{yp} \tag{10}$$

Equation (6) for the interaction between P and T in the shank of the stud enables T to be eliminated, leaving one unknown, the width b_p. It is chosen by calibration against the test data as

$$b_p = 1.6\, (e + h_s - h_p) \tag{11}$$

Thus, P is found, and the resistance to rib punching is taken as

$$P_{rp} = 1.1\, P, \quad \le P_{rs} \tag{12}$$

Predictions from this model are unchanged if the side GHJ of the trough is rotated about H, until either G reaches E (a rectangular trough) or J reaches D (an uncommonly shallow trough). The model is a little more conservative than one with point E located at corner G, and needs one fewer parameter, the slope of side GJ.

It is shown below that the resistance P_{rp} is strongly influenced by the product $t_p f_{yp}$ in eq. (8). Many publications fail to report one or both of the sheet thickness t_p and its yield strength. Where f_{yp} is not reported, it has been taken here as 300 N/mm^2 for early tests and 350 N/mm^2 for some recent work. Tests with unknown sheet

thickness have been omitted, except where it has been found that mode RP does not govern for any thickness in the range 0.75 mm to 1.2 mm.

The final predicted resistance P_r is the lower of P_{cp} and P_{rp}, which also gives the predicted failure mode. If the prediction equals the solid slab value, the predicted mode is stud shear.

These models have been further developed [Johnson, 2008] to predict resistance of pairs of studs in series, parallel and diagonal layouts, taking limited account of the spacing of the studs.

It is assumed in the CP and RP models that the tensile and shear resistances of the top surface of the trough are overcome before failure by rotation of the trough or rib punching, that any reinforcement that intersects this surface is neglected, and that uplift is not prevented. The models cannot predict slip capacity.

Few of the published accounts of push tests with sheeting define the reinforcement in detail. In early work, with narrow slabs, it may not have been fully anchored. Where the bars in a 200-mm mesh are level with the heads of the studs and may be almost 100 mm from them, their contribution to shear resistance is negligible.

Influence of key parameters. Equation (10) can be written:

$$P/P_{rs} = \eta + \lambda\,(T/T_y)$$

This line and eq. (6) are plotted in Figure 3(c), which shows how the result P, at point A, is influenced by the values of η and λ. For mode RP,

$$\eta_{rp} = b_p t_p f_{yp}/P_{rs} \qquad \text{and} \qquad \lambda_{rp} = eT_y / (2\, h_p P_{rs})$$

For a given stud, P_{rs} and T_y are known. It is evident from Figure 3(c) that for small edge distances (e) and deep troughs (h_p), the shear resistance P increases strongly with both sheeting properties t_p and f_{yp}. The increase becomes smaller as λ_{rp} increases.

For mode CP, η_{cp} is proportional to the torsional resistance of the trough, T_u, and

$$\lambda_{cp} = eT_y / (h_p P_{rs})$$

Again, P increases with e. Increase of depth of trough h_p reduces λ_{cp} but increases η_{cp}, and the net effect on P depends on the other parameters. For both models, the influence of width of trough, b_0, appears in the restriction $e \le b_0/2$, because e in Figure 1 is taken as the lesser edge distance.

These inferences are all as expected, and show that studs should be placed centrally in the troughs.

Comparison of predictions with the results of push tests

Tests with any of the following properties have been omitted: re-entrant profiles; sheeting not transverse to the beam; studs welded through holes in the sheeting (which are weaker); profiles with shoulder depth exceeding 85 mm (the limit in Eurocode 4); specimens weakened by flexural failure of a slab ('back-breaking'); three studs per trough; studs of diameter d_s less than 18.5 mm; and the many reports that give insufficient information to enable J-Y predictions to be made. There are very few tests with lightweight-aggregate concrete. There remain 255 tests from

15 sources, for each of which the ratio of P_e (test) to P_r (prediction) has been calculated.

Information on 42 tests which have been excluded from the main statistical analyses is available [Johnson, 2008]. Briefly, they are:

- twenty tests by Bradford et al [2006] with sheeting with f_{yp} = 677 MPa,
- ten tests with ratios P_e/P_r outside the range 0.75 to 1.35
- one test with three studs per trough, which is outside the scope of Eurocode 4;
- eleven tests at the University of Western Sydney, which gave very low slip capacities.

Table 1 - Test data and results – push tests with transverse trapezoidal sheeting

First Author and year	No. of tests, by layout of studs in troughs							No. of tests			Net depth of sheetings,mm	Note No.
	F	C	U	2F	2C	S	D	Total	t_p<1.0 mm	with top rib		
Robinson, 1988	3	6		3	3			15	0	0	51, 76	1
Lloyd, 1989	9	30						39	0	9	50	2,3
Mottram, 1990		2	11			4	3	20	0	6	46, 50, 60, 76	
Bode, 1991		3						3	3	0	40	
Lyons, 1994	18		9	11			19	57	54	0	51, 76	4
Hicks, 1996	3						10	13	0	13	50	
van der Sanden, 1996	1	19	1				16	21	3	0	50, 75, 77	3, 5
Johnson, 1998	2	2	4			4		12	6	8	55, 60, 80	
Jayas, 1998	1			1				2	?	0	76	1,6
Rambo-Rodden-berry, 2002	7		7	2					16	0	51	4,7
Hicks, 2003	3		6					9	7	9	55, 60, 80	
S.C.I., 2004	6							6	2	6	60	
Total No.	53	62	38	17	3	8	32	**213**	91 ?	51		

Notes:

1) Sheet thickness not known, assumed to be 1.2 mm; edge-beam and U layout tests omitted; slabs 1.22 m wide
2) Widths of slabs ranged from 0.45 m to 1.35 m
3) Sheeting without embossments or indentations
4) Transverse compressive force, 10% of shear force, applied across interface
5) Single slab of area 0.6 × 1.0 m, with single stud, tested horizontally with in-plane bending
6) Sheet thickness not known, assumed to be 1.0 mm. U layout tests omitted.
7) Large slabs, 914 mm square. Defective stud welding in five tests, omitted.

The other 213 tests are listed in date order in Table 1. Most of them were reported over ten years ago. The breakdown by layout in the troughs, and the text here, use initial letters to denote layouts, as follows: Favorable, Central and Unfavorable for single studs; 2F and 2C for pairs in parallel (2U pairs are very weak); S denotes two studs in Series, replaced by D for Diagonal if they are not in line. The Table shows that most of the tests on sheeting less than 1 mm thick (t_p) are from one laboratory and that there are 51 tests on sheeting with top ribs. It also gives the shoulder depths of the sheetings used, and notes on any atypical details. The ratios P_e/P_r found for these tests are summarized in columns 2 to 4 of Table 3.

ANSI/AISC 360-05, 'SPECIFICATION FOR STRUCTURAL STEEL BUILDINGS'

This summary of the LFRD rules for 'nominal shear strength', Q_n, of welded studs is taken from Section I3.2 of this recent code from the USA. The shear strength per stud in a solid slab is the lesser of

$$Q_{n,conc} = 0.5\, A_s\, (f_c' E_c)^{1/2} \quad \text{and} \quad Q_{n,stud} = A_s\, f_u \qquad (13)$$

with $E_c = 0.043\, w^{1.5}\, (f_c')^{1/2}$ N/mm^2

with density w in kg/m^3 units and cylinder strength f_c' in N/mm^2. These values for E for concrete are about 88% of the mean values E_{cm} in EN 1992, eq. (3). Allowing for this, the mean of the ratios of $Q_{n,conc}/P_{rs,conc}$ (from eqs (1) and (13)) for the tests studied here is 1.27. The mean of ratios $Q_{n,stud}/P_{rs,stud}$ is 1/0.8 = 1.25. The partial factors are 1/0.9 (USA) and 1.25 (Eurocode 4) so the design (factored) resistances of a stud in a solid slab given by the AISC code is about 40% higher than the Eurocode value, irrespective of which material governs. Assuming that a 'nominal' value is equivalent to a 'characteristic' value in a Eurocode, these differences are remarkably wide.

For studs in a trough of transverse trapezoidal sheeting, the strength $Q_{n,stud}$ is reduced in the AISC code by a factor R_gR_p, where R_g depends on the number of studs in a trough, n_r, and R_p on the side distance $e - d_s/2$, as shown in Figure 1, with a reduction for distances below 51 mm. The effect of R_p is that the lower value applies for studs in U locations and to one of the two studs in a D or S layout. The values of R_gR_p are given by layout in Table 2, and

$$Q_n = R_gR_pQ_{n,stud} \qquad (14)$$

Table 2 - Values of R_gR_p, from ANSI/AISC 360-05

Layout of studs	No. of studs per trough	$e - d_s/2$	
		≥51 mm	< 51 mm
F, C, U	1	0.75	0.60
2F, 2C	2	0.637	0.51
D, S	2	0.574	0.574

The detailing rules in the AISC code exclude some of the 213 test specimens from its scope. Summaries of these rules and the numbers of tests excluded follow. Some tests fail two rules, which reduces the total to 26, leaving 213 – 26 = 187 tests, as shown in Table 3.

- Nominal rib height, $h_p \leq 3$ in, taken as 77 mm — 10 tests excluded
- Stud height $\geq h_p + 38$ mm — 17 tests excluded
- Stud spacing $\geq 4\, d_s$ where $n_r = 2$ — 8 tests excluded.

RESULTS

The test results P_e are compared with the AISC predictions Q_n and the J-Y predictions P_r in the histograms in Figure 4. Values of the mean and coefficient of variation for the tests with each of the seven layouts, and for all the tests as a group are given in Table 3. In calculating statistical properties, each individual ratio was rounded to the nearer multiple of 0.025.

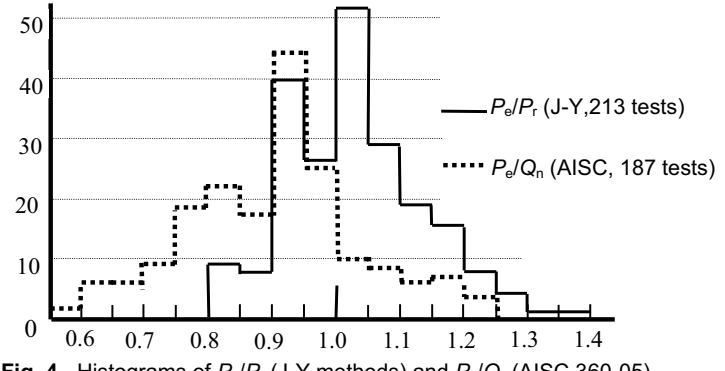


Fig. 4 - Histograms of P_e/P_r (J-Y methods) and P_e/Q_n (AISC 360-05)

The AISC rules are clearly unconservative compared with the tests. The use of $Q_{n,stud}$ in eq. (14) is an important difference from EN 1994-1-1, for the Eurocode factors apply to the lower of $P_{rs,conc}$ and $P_{rs,stud}$, resistances that can in practice differ by more than 30%, with $P_{rs,conc}$ usually the lower. Tests show that the concrete is responsible for most failures in troughs, so it appears that the AISC method could be improved by replacing eq. (14) by

$$P_n = R_g R_p Q_n \qquad (15)$$

where Q_n is the solid-slab strength from the lesser of results from eqs (13).

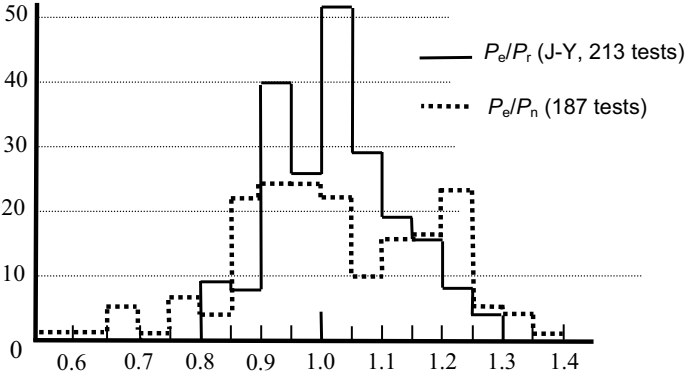


Fig. 5 - Histograms of P_e/P_r (J-Y method) and P_e/P_n (revised AISC method)

Table 3 - Comparisons of predictions with results of tests

Layout of studs	No. of tests	P_e/P_r (J-Y method)		No. of tests	P_e/Q_n (AISC)		P_e/P_n	
		Mean	C of V,%		Mean	C of V,%	Mean	C of V,%
Favorable	53	1.05	10	42	0.95	12	1.00	10
Unfavorable	38	1.09	11	31	0.84	16	1.05	16
Central	62	0.98	8	61	0.87	14	0.92	14
2F	17	1.06	10	17	0.92	12	1.08	14
2C	3	(1.025)	-	3	(1.22)	-	(1.22)	-
Series	8	1.025	10	2	(0.98)	-	(1.32)	-
Diagonal	32	1.005	9	31	0.93	10	1.16	9
All	**213**	**1.03**	**10.4**	**187**	**0.90**	**15.2**	**1.02**	**15.6**

Resistances P_n have been calculated. The results are compared with those for Q_n in Table 3 and with the J-Y predictions in Figure 5.

These results are not statistical properties of a single population. Although diverse, they are all relevant to this study of the AISC design method. The bottom row of Table 3 is influenced by the relative numbers of tests with each layout of studs. Mean values are shown in parentheses for layouts 2C and S because there are so few tests. For each layout, there are wide variations in the shape and properties of the sheeting and the layout of reinforcement in the slabs, as noted below Table 1. Some strengths of the steel for studs and sheeting are nominal rather than measured values.

DISCUSSION

Overall, the modified AISC method appears to give good agreement with tests, as the mean ratio P_e/P_n is 1.02; but where is allowance made for the quite high coefficient of variation ?

In the Eurocodes, a characteristic resistance is defined as the 5% lower fractile. Assuming that this applies to the LRFD method, then from 187 tests, no more than 9 results should give ratios P_e/Q_n less than 1.0. Details of the 14 lowest ratios P_e/Q_n for the unmodified method are given in Table 4. The 9th lowest is 0.655, and the nine lowest include C, U and 2F layouts. For the modified method, column 9, the 9th lowest is 0.752. Similar results are obtained if the cut-off is taken as 1.64 standard deviations below the mean. On this basis, the LRFD method is 'unsafe' by 34%, and the revised method by 25%.

Table 4 - Specimens with low ratios P_e/Q_n

# of tests	P_e/Q_n	Layout	h_p mm	$Q_{n,stud}$ kN	$Q_{n,conc}$ kN	f_c' MPa	Comments	P_e/P_n
1	0.567	2F	76	128	111	24	deep troughs with two studs	0.653
1	0.595	C	75	146	147	36	thin sheet, deep troughs	0.595
3	0.613	C	77	134	109	24	deep troughs	0.752
3	0.653	U	51	131	91	19	weak concrete, U layout, thin sheet (0.775 mm)	0.937
1	0.655	U	51	131	91	19	weak concrete, U layout	0.940
1	0.660	C	75	146	137	32	deep troughs	0.703
3	0.664	C	75	146	146	36	deep troughs	0.666
1	0.689	U	51	129	129	49	U layout, 0.9 mm sheeting	0.689

Exceptionally low ratios P_e/Q_n. Where the number of tests in column 1 of Table 4 exceeds one, the entries are means from a set of nominally-identical specimens that gave consistent results. The predictions of the AISC method appear to be most unconservative for specimens with sheeting of depth h_p at least 75 mm and these further features:

- weak concrete: the method takes no account of strength of concrete
- unfavourable layouts: the failure involves the concrete and the sheeting, not the stud
- thin sheeting: low resistance to rib punching and local deformation.

The extent to which the modified AISC method improves the prediction depends entirely on the relative values of $Q_{n,stud}$ and $Q_{n,conc}$ (columns 5 and 6). The predictions

for the eight specimens with C layouts remain very low. The reason may be that all of these tests are from Lloyd and Wright [1990], on sheeting without embossments or indentations. For more typical sheetings, the two lowest ratios in column 9 are 0.65 and 0.69.

Results for particular layouts. The increases in the mean values given by the revised AISC method (columns 6 and 8 of Table 3) range from 0.05 to 0.23, excluding the small samples. These increases depend entirely on the relative strengths of the concrete and the stud material used in the tests, because the change in predicted resistance depends on the ratio $Q_{n,stud}/Q_{n,conc}$, given by eqs (13). For the test specimens, these ratios range from 0.66 to 1.47. It was found that mean results for all five layouts are related by

$$\text{Mean (revised AISC)} - \text{Mean (AISC)} \approx 0.19\ (Q_{n,stud}/Q_{n,conc})$$

Hence, the results do not reveal any relationship between layout and the change in the AISC method.

In the 187 tests, the cylinder strengths of the concrete ranged from 18 to 49 N/mm^2 (except for one at 61 N/mm^2). The strengths f_u of the studs ranged from 415 to 559 N/mm^2. These well represent the ranges used in practice. For both Q_n and P_n, layout has little influence on the coefficients of variation (columns 7 and 9 of Table 3).

Comparison with the J-Y predictions. The J-Y methods predict mean values, not 5% lower fractiles. The final mean in Table 3, 1.03, is close to 1.0 because some of these 213 tests were used to calibrate the methods. The significant results are that the means for all seven layouts are within 6% of the overall mean and that the six coefficients of variation are consistent and do not exceed 11%. The distribution of the J-Y ratios is close to Gaussian, with its 5% lower fractile at $P_e/P_r \approx 0.86$. Notes on the tests that were excluded are given above.

Push tests and beam tests. Tests on beams [Hicks, 2007; Bradford, 2005] have shown better slip capacities than in related push tests; and in many cases, shear resistance of studs was found to be higher. This suggests that although the AISC method is clearly optimistic (unsafe ?), it does not need to be modified by as much as the 34% found earlier. The standard push test is intended to provide values that can safely be used in all situations within the scope of the relevant code. Situations in practice can be more adverse than those in the beam tests referred to, in respect of continuity at supports, lateral distance to a free edge of the slab, use of more than two studs in a trough, off-centre point loads, transverse bending and shear, etc.

The target relationship between design predictions and push-test results thus remains unclear, and an appropriate deficit for embossed sheeting may be less than that found for the modified AISC method. That modification, which follows Eurocode procedure, is strongly recommended as a first step. Further suggestions, based on Table 4, would be to reduce its scope to sheetings of depth not exceeding, say, 60 mm and thickness not less than 0.9 mm and to reduce the factor R_p for studs in U locations.

The 213 push tests have also been compared [Johnson, 2008] with other predictions. For Eurocode EN 1994-1-1, the overall mean of the ratios P_e/P_{EC4} is 1.045, with coefficient of variation 17%. For the current British code, BS 5950-3-1, the mean of the ratios P_e/P_{BS} is 0.88, with coefficient of variation 17%.

CONCLUSIONS

The revised Johnson-Yuan models for the prediction of the mean shear resistance of a stud in transverse sheeting in a push test are explained and compared with results of 213 tests. They are believed to be the best models available. They enhance understanding of the effects on shear resistance of changes in properties and profiles of sheeting and layouts of studs.

Predictions by the method of ANSI/AISC 360-05 for 187 tests are compared with the tests and are found to be unconservative in many situations. A simple modification of that method is proposed which gives lower predictions, but not as low as the test results. Reductions in the scope of the AISC method are suggested. It is explained why a decision on whether the new predictions are safe enough is essentially a matter for judgement.

REFERENCES

ANSI/AISC 360-05, Specification for structural steel buildings. Amer. Inst. Steel Construction, 2005.

Bode, H. and Künzel, R. Zur Anwendung der Durchschweisstechnik im Verbundbau, Forschungsbericht 1/1991, Universität Kaiserslautern, 1991.

Bradford M.A. Ductility and strength of composite T-beams with trapezoidal slabs. *Proceedings, Int. Symposium, Advances in Steel and Composite Structures,* ed. Chung K.F., Hong Kong Institute of Steel Construction, 1-17, Dec. 2005.

Bradford M.A., Filonov A., Hogan T.J., Ranzi G. and Uy B. Strength and ductility of shear connection in composite T-beams. *Proceedings of the 8th International Conference, Steel, Space and Composite Structures, Kuala Lumpur*, pp. 15-26, 2006.

Hicks S.J. and McConnell, R.E. The shear resistance of headed studs used with profiled steel sheeting. Composite Construction in Steel and Concrete III, ed. Buckner C.D. and Shahrooz B.M., 325-338, Amer. Soc. Civ. Engrs, 1997.

Hicks S.J. Strength and ductility of headed stud connectors welded in modern profiled steel sheeting. *The Structural Engineer,* **85**, No. 22, 32-38, 2007.

Hicks S.J. Resistance and ductility of shear connection: full-scale beam and push tests. *Proceedings of the 6th International Conference, Steel and Aluminium Structures*, ed. Beale R.G., Oxford Brookes University, pp. 613-620, 2007.

Jayas, B.S. and Hosain, M.U. Behaviour of headed studs in composite beams: push-out tests. *Canad. J. Civ. Eng.,* **15**, 240-253, 1988.

Johnson R.P. and Yuan, H. Existing rules and new tests for stud shear connectors in troughs of profiled sheeting. *Proc. Instn Civ. Engrs Structs & Bldgs*, **128**, 244-51, Aug. 1998.

Johnson R.P. and Yuan, H. Models and design rules for stud shear connectors in troughs of profiled sheeting. *Proc. Instn Civ. Engrs Structs & Bldgs*, **128**, 252-63, Aug. 1998.

Johnson R.P. Calibration of resistance of stud shear connectors in troughs of profiled sheeting. To be published, *Proc. Instn Civ. Engrs Structs & Bldgs*, 2008.

Lloyd, R.M. and Wright, H.D. Shear connection between composite slabs and steel beams. *J. Constr. Steel Research*, **15,** 255-85, 1990.

Lyons J.C., Easterling, W.S. and Murray, T.M. Strength of welded shear studs, Vols I and II. Report CE/VPI-St 94/07, pp. 130, 496. Virginia Polytechnic Institute, Dec. 1994.

Mottram, J.T. and Johnson R.P. Push tests on studs welded through profiled steel sheeting. *The Structural Engineer*, **68**, 10, 187-93, 15 May 1990.

Rambo-Roddenberry M., Easterling W.S. and Murray T.M. *Behavior and strength of welded stud shear connectors*. Virginia Polytechnic Institute, Reports CE/VPI-ST02/04 and /05, pp. 266, 513, 2002.

Robinson, H. Multiple stud shear connection in deep ribbed metal deck. *Canad. J. Civ. Eng.*, **15**, 553-569, 1988.

Steel Construction Institute, Ascot, U.K. Private communication, 2005.

van der Sanden, P.G.F.J. The behaviour of a headed stud connection in a 'new' push test including a ribbed slab. BKO-reports 95-15 and 95-16, Technical University Eindhoven, March 1996.

LIFETIME ORIENTED DESIGN CONCEPTS OF STEEL-CONCRETE COMPOSITE STRUCTURES SUBJECTED TO FATIGUE LOADING

Univ.-Prof. Dr.-Ing. Gerhard Hanswille
Institute for Steel and Composite Structures, University of Wuppertal
42285 Wuppertal, Germany
stahlbau@uni-wuppertal.de

Dipl.-Ing. Markus Porsch
Institute for Steel and Composite Structures, University of Wuppertal
42285 Wuppertal, Germany
stahlbau@uni-wuppertal.de

ABSTRACT:
In current national and international standards for composite structures of steel and concrete the determination of the ultimate load capacity and the fatigue life of headed shear studs takes place with separate and independent verifications at the ultimate limit state, serviceability limit state and fatigue limit state. The fatigue resistance is verified in accordance with the design concepts for steel structures, based on nominal stress ranges and linear damage accumulation according to Palmgren and Miner. The effect of pre-damage due to fatigue loading on both the ultimate and the serviceability limit state is not considered. Because cyclic loading of headed shear studs leads to a decrease of static strength of stud connectors, the assumptions for independent limit states are not given and the reliability index of steel-concrete composite structures subjected to fatigue loading may fall below the target values in codes. This paper is dealing with the results of a comprehensive programme of experimental work with more than 90 standard EC4-push-out test specimens and two full scale-beam tests which consider the crack propagation through the stud foot and the local damage of concrete surrounding the studs resulting from high cycle loading. Based on the results of the push-out tests, new design concepts were developed to predict the fatigue life and the residual strength of headed shear studs after high cycle loading. Considering the interaction between the local damage and the behaviour of the global structure, these research results were taken as the basis to simulate the cyclic behaviour of composite beams by means of a new damage accumulation rule.

1 INTRODUCTION

As a result of the benefits of combining the advantages of steel and concrete, steel-concrete composite beams are today widely used for bridges and industrial buildings. The transfer of longitudinal shear forces at the interface between both components is mostly realized by headed shear studs. Especially in bridges due to the current enormous increase in traffic loads these shear studs are subjected to a steadily rising number of high-cycle loadings, which may result in fatigue failure during the lifetime of the structure. In current national [DIN Fachbericht 104] and international [EN 1994-1-1, EN 1994-2] standards the determination of the ultimate load capacity and the fatigue life of headed shear studs take place with separate and independent verifications at the ultimate limit state, serviceability limit state and

fatigue limit state. The fatigue resistance is verified comparably to steel structures, based on a concept with nominal stress ranges and the linear damage accumulation rule according to Palmgren-Miner where effects of pre-damage due to high-cycle loading are neglected. From the investigations by Oehlers [Oehlers 1990] it is known, that cyclic loading of headed shear studs leads to a decrease of static strength, so that the assumptions for independent limit states are not given. Because the design life of cyclic loaded headed shear studs is characterized by a significant change in deformation behaviour and deterioration in strength the reliability index of steel-concrete composite structures subjected to fatigue loading may fall below the target values in codes. On this background a comprehensive programme of more than 90 standard EC4-push-out test specimens and two full-scale beam tests were developed, considering the crack propagation through the stud foot and the local damage of the concrete surrounding the studs as relevant consequences of high-cycle loading.

2 LOCAL BEHAVIOUR OF CYCLIC LOADED HEADED SHEAR STUDS

2.1 TEST SPECIMEN

The test specimen used in the push-out tests complies with the standard push-out specimen according to Eurocode 4. After cutting each steel beam into two halves the headed studs were welded and the steel flanges were greased. The slabs were cast horizontally and two halves of a common specimen were welded again. To ensure the same loading condition as in slabs of composite beams additional lateral restraints at the bottom of each concrete slab were applied. These restraints avoid additional tensile forces especially in the lower row of the studs resulting from the moment of eccentricity. Details of the push-out specimen are given in Figure 1.

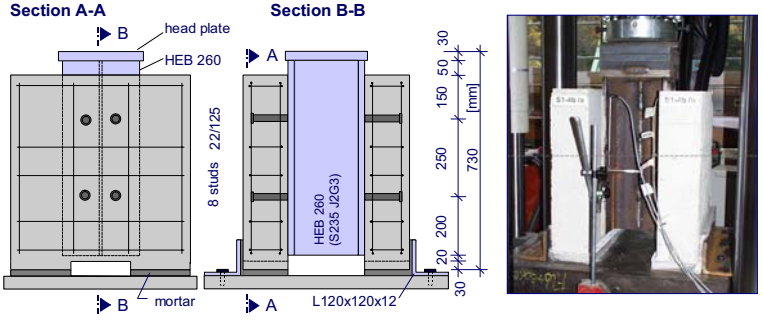


Figure 1 - Test specimen

2.2 EFFECT OF HIGH CYCLE LOADING ON STATIC STRENGTH

In order to investigate systematically the effect of high-cycle loading on the static strength and on the fatigue life five series (S1-S4, S5E) with 54 push-out test specimens were performed with varying loading parameters peak load P_{max} and loading range ΔP. Except for the series S5E, each series consisted of three short time displacement controlled static tests and nine force controlled unidirectional cyclic tests. After performing the static tests to determine the mean value of the ultimate static load $\overline{P}_{u,0}$, taken as a reference value for the cyclic loading parameters, three fatigue tests were carried out to obtain the number of cycles N_f, when the static

strength is reduced to the value of the peak load. Subsequently six cyclic tests were conducted for approximately 30 and 75 % of the average fatigue life $\overline{N}_f$. After reaching the corresponding number of cycles each of these six test specimens was statically loaded under displacement control to obtain the residual strength. During these static tests the necessary information about the ductility behaviour were gathered. All cyclic tests were stopped after specific numbers of cycles and the specimens were released and reloaded in order to collect data about the stiffness and plastic deformation.

The effect of high cycle preloading becomes evident, when the static strengths are plotted versus number of load cycles. This is shown in Figure 2, where the results are related to the mean static strength and the mean fatigue life of each series respectively, completed by five tests from Sweden [Veljkovic 2004] with the same geometry of the test specimens and same supporting conditions. Due to an early crack initiation at each stud foot, followed by a long phase of crack propagation up to a critical crack length, in all test series the static strength decreases already after 10-30 % of each average life time. Between 30 and 80% of the lifetime the reduction is nearly linear. Especially in test series S1, S3 and S5E with low peak loads, leading to very high fatigue lives $\overline{N}_f$, the decrease of static strength within the first 30% of the fatigue life is disproportionately high.

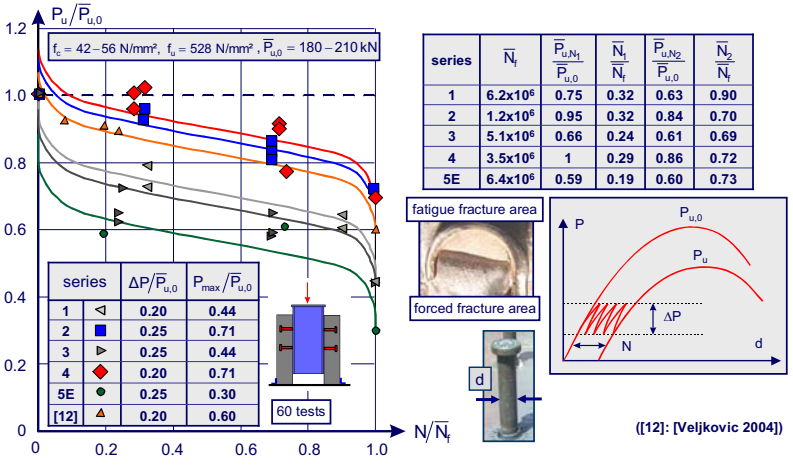


Figure 2 - Test parameter – Decrease of static strength versus life time due to high cycle loading

The sigmoidal shape of the failure envelopes can be described by Equation (1). Because the tests cover only a small relative load range between 0.20 and 0.25, the regression analysis should be repeated, if further tests with additional values could be taken into account.

$$\frac{P_{u,N}}{P_{u,0}} = 0.74\,\frac{P_{max}}{P_{u,0}}\left(1-\frac{\Delta P}{P_{max}}\right) + 0.54 - 0.04\,\ln\left(\frac{1}{1\text{-}N/N_f}\text{-}1\right) \quad \begin{cases} \le 1 \\ \ge \dfrac{P_{max}}{P_{u,0}} \end{cases} \qquad (1)$$

The results of the static tests are in good agreement with the prediction of the theoretical model of Eurocode 4, given by Equation (2). It describes the shear resistance in the case of "failure of the concrete" ($P_{tc,m}$) and "shank failure of the stud" ($P_{ts,m}$) respectively. This model is based on the assumption, that in case of low concrete strength the shear resistance is determined only by the failure of concrete in the lower part of the shank. In case of high concrete strength it is assumed, that the shear resistance is determined by the shear resistance of the stud shank.

$$P_{u,0} = \min\left(P_{tc,m}\,;\,P_{ts,m}\right) = \min\left(0.374\ d^2\sqrt{f_c \cdot E_{cm}}\ ;\ \frac{\pi d^2}{4} f_u\right) \quad , \tag{2}$$

where f_c and E_{cm} are the cylinder compressive strength and the secant modulus of elasticity of the concrete, respectively, in accordance with EC2 [EN 1992-1-1] and d and f_u represent the diameter of the shank and the tensile strength of the shear stud.

2.3 DETERMINATION OF THE LIFE TIME

The fatigue limit state is given, when the reduced static strength has reached the value of the peak load. Thus the fatigue life of headed studs in push-out specimens is affected not only by the load range ΔP but also by the peak load P_{max} and the static resistance $P_{u,0}$. To consider these effects national and international fatigue tests were reanalysed [Hanswille 2006, 2007a, 2007b]. To avoid incomparable results only tests with test specimens meeting the requirements of Eurocode 4 were taken into account.

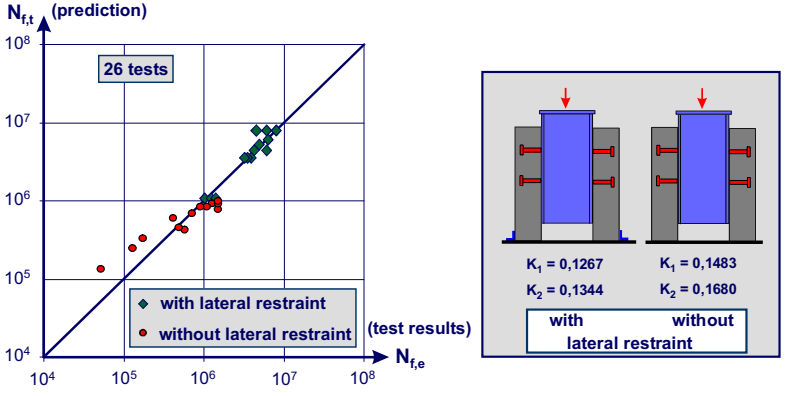


Figure 3 - Test parameter – Relationship between theoretical and experimental fatigue life – Parameters K_1 and K_2

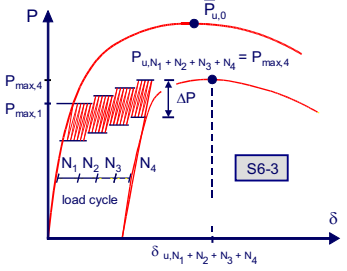
A linear regression, based on 26 tests fulfilling the before mentioned selection criterion, led to the Equation (3).

$$\log N_f = \frac{1-\frac{P_{max}}{P_{u,0}}}{K_1 - K_2 \frac{P_{max} - \Delta P/2}{P_{u,0}}} \tag{3}$$

Regarding the supporting condition of the concrete slabs, the analysis revealed that it is necessary to determine the parameter K_1 and K_2, given in Figure 3, in dependence of the cases "with lateral restraint" and "without lateral restraint". In numerical simulations of cyclic loaded beams the values for the case "with lateral restraint" should be used. Again this model should be used carefully outside investigated parameter ranges.

2.4 LOAD SEQUENCE EFFECTS

Because of nonlinear effects caused by crack propagation through the stud feet and local crushing of the surrounding concrete the linear damage rule of Palmgren-Miner, on which the present design codes are based, cannot be adopted on headed shear studs embedded in normal weight concrete. In order to develop an advanced damage accumulation rule, tests with two and four blocks of loading were performed in test series S5 and S6. As shown in Figure 4 in both series the load range was held constant and the peak load was increased as well as decreased within the range of the loading parameters of the constant amplitude tests. More detailed information about the test results are given in [Hanswille 2006, 2007a, 2007b].



			$P_{max,i} / \overline{P}_{u,0}$			
series	**number of tests**	**$\Delta P / \overline{P}_{u,0}$**	**block 1**	**block 2**	**block 3**	**block 4**
S5-2	3	0.25	0.71	0.44	-	-
S5-3	1		0.44	0.71	-	-
S5-4	4		0.44	0.30	-	-
S5-6	4		0.30	0.44	-	-
S6-3	3	0.20	0.44	0.54	0.64	0.74
S6-4	3		0.74	0.64	0.54	0.44

Figure 4 - Test procedure and parameters in tests with multiple blocks of loading

An improvement of the damage accumulation model according to Palmgren-Miner can be achieved by introducing an additional damage term $\Delta n_{f,i}$, as given in Equation (4).

$$D = \sum_{i=1}^{m} \frac{N_i}{N_{f,i}} + \sum_{i=1}^{m-1} \Delta n_{f,i} \leq 1 \qquad (4)$$

Figure 5 explains the method by means of a cyclic test with two blocks of loading, where the peak load of the first block is raised in the second block while the load range is held constant. After applying N_1 numbers of cycles the static strength reduces to the value $P_{u,N1}$ on curve 1, represented by point B. According to the Palmgren-Miner rule the accumulated damage can be expressed by the ratio $N_1/N_{f,1}$. After increasing the peak load to the higher load level $P_{max,2}$ / $P_{u,0}$ the further reduction of static strength continues from the corresponding point C on curve 2, characterized by the same reduced static strength for the loading parameters of the second block. The offset $\Delta n_{f,1}$ between the damage equivalent points B and C can be interpreted as a loss of lifetime and is additionally introduced to the damage sum. Finally failure occurs, when the relative static strength is decreased to the value of the peak load of block 2 $P_{max,2}$ / $P_{u,0}$ (point D) and the remaining lifetime is governed by the value of $N_2/N_{f,2}$.

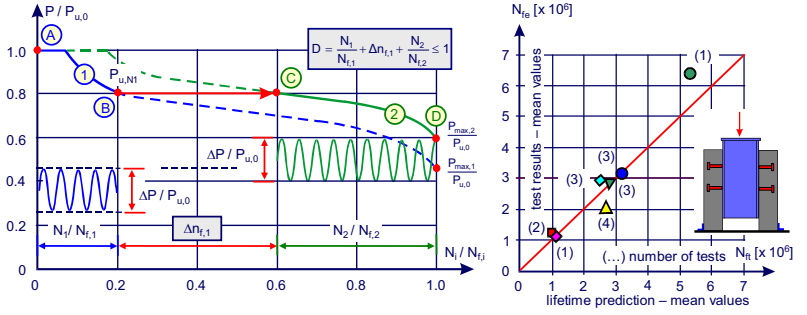


Figure 5 - Damage accumulation model considering the effects of pre-damage due to high cycle loading and comparison of the test results with the new improved damage accumulation model

2.5 DUCTILITY AND CRACK FORMATION

High initial stiffness and high ductility are main advantages of headed studs embedded in normal weight concrete. From the static tests carried out after cyclic preloading it could be found, that the load deflection behaviour is significantly affected by the crack formation, which itself is closely correlated to the peak load level.

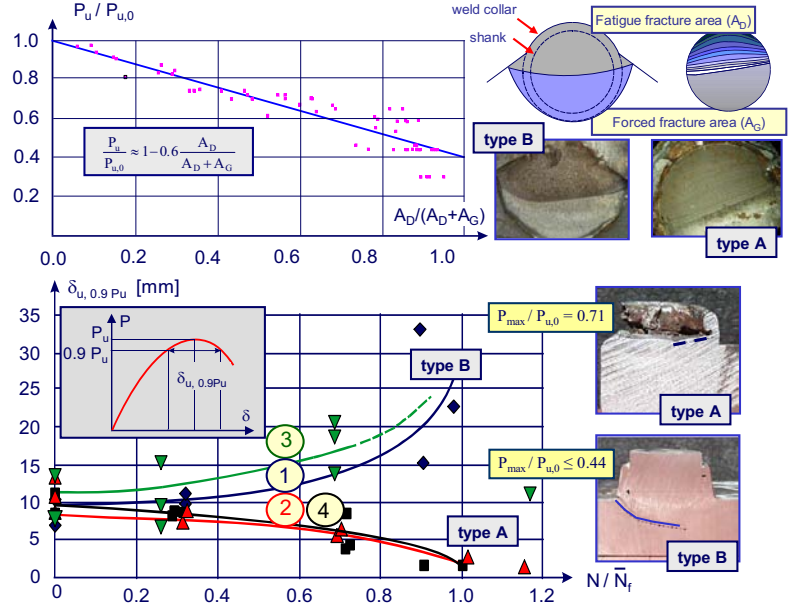


Figure 6 - Relationship between fatigue fracture area and reduced static strength - Ductility after high cycle loading

Very high peak loads cause horizontal cracks through the stud foot like crack type A shown in Figure 6. This formation results in a gradual decrease of ductility during lifetime and the values may fall below the target values of the codes. In case of lower peak loads the cracks propagate into the flange like crack type B and ductility increases. Although different failure modes (A and B) are possible the evaluation of all test results shows a nearly linear correlation between the reduced static strength and the size of the fatigue cracking zone.

2.6 COMPARISON OF TEST RESULTS WITH FINITE ELEMENT CALCULATIONS

In order to simulate the load-deflection behaviour of headed shear studs embedded in solid slabs and to verify the relationship between the fatigue fracture area and the reduced static strength, shown in Figure 6, a comprehensive three-dimensional FE-Model – using the finite element programme ANSYS - of a statically loaded push-out test specimen according to Figure 2 has been built up. Because no detailed information about the material properties of the steel in the heated affected zones, in the weld collar and in the melted zone were available, the material properties of the steel beam and of the studs were taken as the basis of the material properties of the steel affected by the welding process. Microscopic examinations of the steel structure at the stud feet were performed in order to consider sufficiently the weld formations. The von-Mises criterion was used to model metal plasticity behaviour. The concrete behaviour was modelled elastic / perfectly plastic taking into account a yielding surface according to Drucker-Prager (DP) with an associated flow rule. The two parameters of the DP-yield surface were adjusted to the uniaxial (1.0 f_c) and to the biaxial compressive strength – taken as 1.2 f_c - of the concrete, obtained from concrete cylinders stored in the same way as the test specimens.

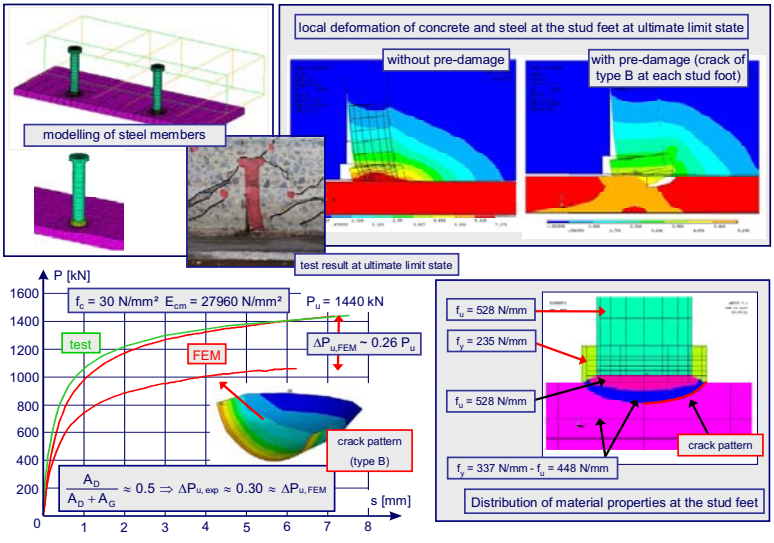
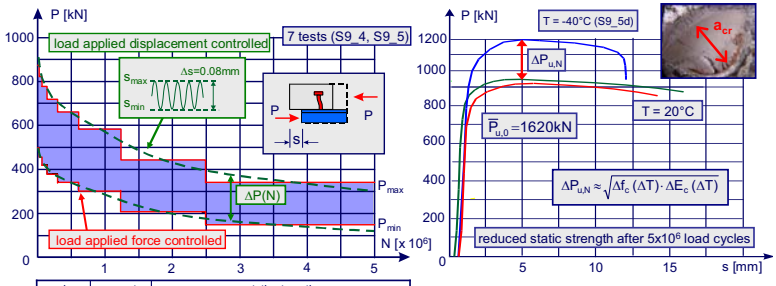


Figure 7 - Comparison between test results and finite element calculations of statically loaded push-out test specimens

Figure 7 shows the result of a numerical simulation of a push-out test, considering concrete strength properties f_c = 30 N/mm² and E_{cm} = 27960 N/mm² (air cured) and a coefficient of friction of 0.2 in the interface between steel and concrete. The calculated load deflection curve as well as the ultimate static strength and the deformation of the studs are in good agreement with the experimental results gained from test series S1 to S9. Based on this model cracks of type B (ratio $A_D/(A_D+A_G)$ ~ 0.5) were implemented at the stud feet and the numerical simulation was repeated. For the given ratio of 0.5 and a reduced coefficient of friction of 0.1, taking into account the sliding in the interface due to cyclic preloading, the calculation confirms the relationship between the fatigue fracture area and the reduced static strength shown in Figure 6.

2.7 EFFECT OF THE CONTROL MODE – EFFECT OF LOW TEMPERATURE

Regarding the simulation of the cyclic behaviour of composite beams by means of the results gained from force controlled push-out tests, in series S9 nine tests were performed in which the influence of the control mode was investigated (Fig. 8).



specimen	parameter	static strength							
S9_1 b-c	$\bar{P}_{u,0}$	T = 20°C							
-	-	cyclic loading - N = 5x 10⁶							
S9_4 c–e	Δs [mm]	0.08 (initial load ~ 0.65 $\bar{P}_{u,0}$) (displacement control)							
S9_5 a–d	block	1	2	3	4	5	6	7	8
	$\bar{P}_{max}/\bar{P}_{u,0}$	0.54	0.51	0.48	0.44	0.41	0.36	0.27	0.21
	$\Delta\bar{P}/\bar{P}_{u,0}$	0.23	0.23	0.22	0.21	0.20	0.17	0.15	0.12
	load cycles	N_1 = 19608	2 N_1	2 N_2	2 N_3	2 N_4	2 N_5	2 N_6	~2 N_7
-	-	reduced static strength							
S9_4 c–e S9_5 a–c	$\bar{P}_{u,N}$	T = 20°C							
S9_5 d	$\bar{P}_{u,N}$	T = -40°C							

Figure 8 - Test series S9 – Effect of control mode – Effect of low temperature on reduced static strength

After experimental determination of the mean static strength $\bar{P}_{u,0}$ three cyclic displacement controlled push-out tests with constant values of the maximum slip s_{max} and the slip range Δs (initial peak load approximately 0.65 $\bar{P}_{u,0}$) were performed. The resulting loading history of the varying peak load P_{max} (N) and the load range $\Delta P(N)$ were classified in seven blocks with constant loading parameters and subsequently taken as input values for four additional cyclic force controlled push-out tests. As

shown in Figure 8 after $5x10^6$ load cycles the load-slip behaviour and the mean values of the reduced static strength $\overline{P}_{u,N}$ were coincident, as well as the crack length a_{cr} through the stud feet. Thus it appears that displacement controlled behaviour of headed studs can also be simulated by results of force controlled push-out tests with multiple blocks of loading, taking into account an appropriate damage accumulation hypothesis, e.g. like given in Equation 4.

Notched-bar impact tests carried out with test specimens taken from welded joints of headed shear studs show that the notched-bar impact values significantly fall below commonly accepted values of steel structures. In order to investigate the interaction between the pre-damage and the toughness the reduced static strength of test specimen S9-5d was tested after cooling down to T = -40°C. In comparison with the before mentioned tests the reduced static strength increases in accordance with the increase of the relevant material properties (f_c, E_{cm}) of the concrete at lower temperatures and the ductility remains sufficiently high (Fig. 8).

3 EFFECTS OF LOCAL FATIGUE DAMAGE ON THE GLOBAL BEHAVIOUR

Considering the interaction between the local damage of headed shear studs and the behaviour of the global structure, the research results based on the push-out tests were taken as the basis for numerical simulations of the static behaviour (with and without any pre-damage effects) and the cyclic behaviour of steel-composite beams subjected to fatigue loads. For calculations the finite element programme ANSYS was improved by implementing an advanced material model for concrete behaviour (CONCRETE) under static loading. As shown in Figure 9 this model used in combination with a flow rule of a von-Mises type in order to simulate both cracking and plastic deformation. This leads to good predictions of the load-deflection behaviour and the load bearing capacity of typical composite beams.

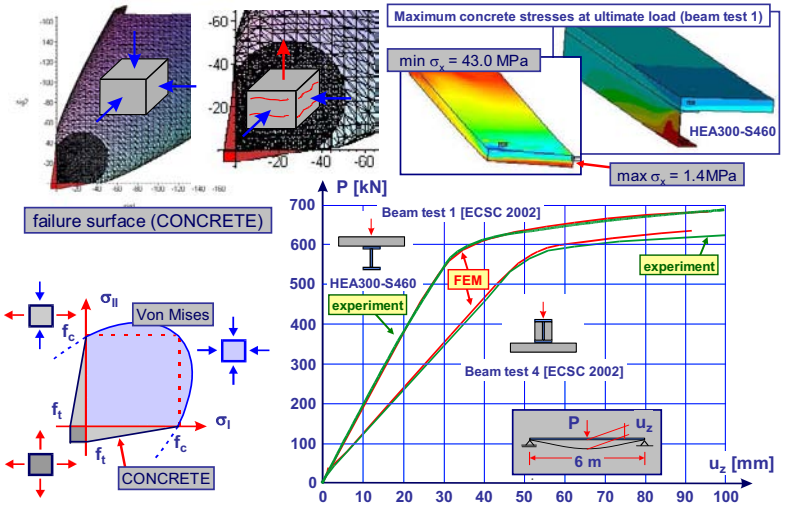


Figure 9 – Results with the modified material model CONCRETE

The calculations of the cyclic loaded beams were based on three-dimensional FE models using discrete non-linear spring elements for the headed studs, taking into account the analytical expressions developed from the push-out tests. In order to verify the theoretical models two additional full-scale beam tests (VT1 and VT2) were performed similar to the concept explained in section 2.2. In case of test specimen VT1 the residual static strength of the beam was determined after subjecting 1.37×10^6 loadings.

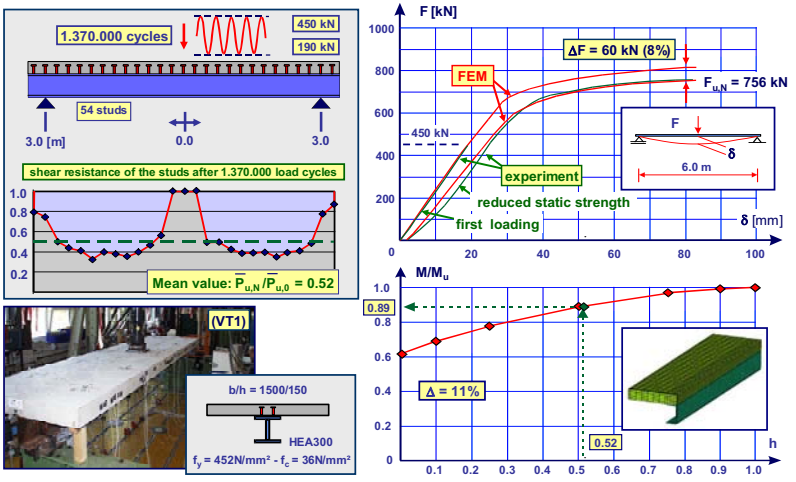


Figure 10 - Test beam VT1 – Effect of high cycle loading on load bearing capacity

As shown in Figure 10 due to crack growth through the stud feet during the cycling loading the static strengths of the studs were partly decreased by up to 65% of its original value. Numerical investigations considering the change of the deformation behaviour of the studs due to cyclic preloading indicate that the reduction of the strength of the interface between steel and concrete causes a loss of the load bearing capacity of the beam of nearly 8%. This result is in good agreement with the result obtained by applying partial-interaction theory taking into account a smeared damage along the interface.

For the simulation of the cyclic behaviour the damage accumulation method acc. to Fig. 5 was used. The total number of load cycles N_k was split in 20 increments and after each FE-analysis, representing an increase of N_k / 20 numbers of load cycles, the relevant mechanical properties of each headed shear stud (plastic slip, elastic stiffness and reduced static strength) were updated, taking into account the modified damage accumulation rule acc. Fig. 5. In each increment it is assumed that the loading parameters of each stud remain unchanged and thus the stud behaviour during the increment can directly be taken from appropriate force-controlled push-out test results. As shown in Figure 11 the results of the numerical simulations are in good agreement with the results of the beam test.

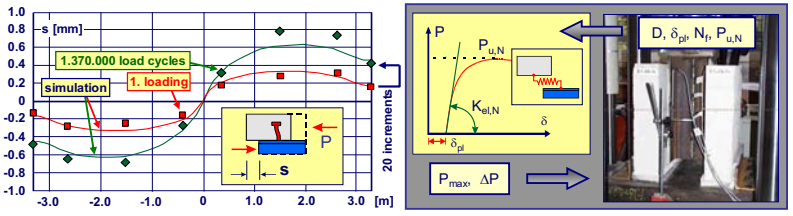


Figure 11 - Cyclic behaviour of test beam VT1 - Verification of the concept

The occurrence of cracks at the stud feet and the early crack initiation has to be assessed a in different way, if a flange is in compression or in tension. For this purpose beam test VT2 in hogging bending was subjected to 2.1 million load cycles. In flanges under compression the cracks typically grow horizontal leading to a deterioration of the properties of the interface between steel and concrete. In tension flanges the direction is additionally influenced by the tensile stresses in the steel flange and the cracks can propagate nearly vertical through the flange. In this case not only the properties of the interface are affected, but also the load bearing capacity of the cross sections.

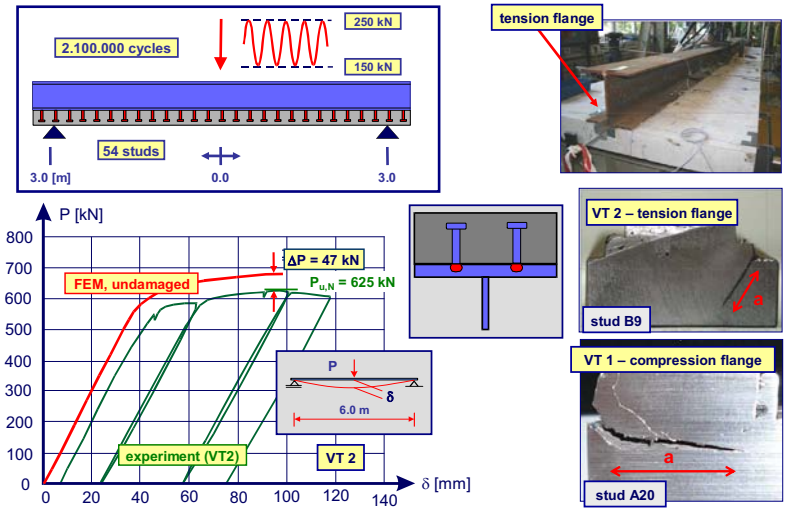


Figure 12 - Effect of cyclic loading on beams with tension flanges (test beam VT2)

The test shows that also in hogging bending the significant local damage causes only a small global reduction of the ultimate load. With regard to fatigue cracks growing in vertical direction through the top flange of the steel girder further research is needed.

4 ACKNOWLEDGEMENTS

The research work is financed by the German Research Foundation (DFG) within the scope of Collaborative Research Centre 398.

5 REFERENCES

DIN-Fachbericht 104, Verbundbrücken, Beuth Verlag, Berlin, 2003

EN 1994-1-1: Eurocode 4, Design of composite steel and concrete structures, Part 1-1: General rules and rules for buildings, Brussels: CEN, 2004

EN 1994-2: Eurocode 4, Design of composite steel and concrete structures, Part 2: General rules and rules for bridges, Brussels: CEN, 2004

EN 1992-1-1: Eurocode 2, Design of concrete structures, Part 1-1: General rules and rules for buildings, Brussels: CEN, 2004

ECSC Research Report 2002. Use of high strength steel S460 – Chapter 5: Composite beams made of high strength steel and normal strength concrete, Final report

Hanswille, G., Porsch, M., Ustundag, C. 2006 (April). Neue Untersuchungen zum Ermüdungsverhalten von Kopfbolzendübeln, Stahlbau, Volume 75 Issue 4

Hanswille, G., Porsch, M., Ustundag, C. 2007a (April). Resistance of headed studs subjected to fatigue loading, Part I: Experimental study , Journal of Constructional Steel Research, Volume 63, Issue 4, Pages 475-484

Hanswille, G., Porsch, M., Ustundag, C. 2007b (April). Resistance of headed studs subjected to fatigue loading, Part II: Analytical study, Journal of Constructional Steel Research, Volume 63, Issue 4, Pages 485-493

Oehlers, D.J. 1990. Deterioration in strength of stud connectors in composite bridge beams, Journal of Structural Engineering; 116(12):3417-3431

Porsch, M. 2007. Modellierung von Schädigungsmechanismen zur Beurteilung der Lebensdauer von Verbundkonstruktionen aus Stahl und Beton, University of Wuppertal, 2008 (Dissertation)

Ustundag, C. 2007 (July). Beitrag zur Bemessung von Verbundträgern unter ermüdungswirksamen Beanspruchungen, University of Wuppertal (Dissertation)

Veljkovic, M. & Johannson, B. 2004 (July). Residual static resistance of welded stud shear connectors, Composite Construction V, South Africa – Berg-en-Dal, Mpumalanga

HEADED STUDS CLOSE TO THE CONCRETE SURFACE - FATIGUE BEHAVIOUR AND APPLICATION

Prof. Dr.-Ing. Ulrike Kuhlmann
Institute of Structural Design, University of Stuttgart
Stuttgart, Germany
sekretariat@ke.uni-stuttgart.de

Dipl.-Ing. Jochen Raichle
Institute of Structural Design, University of Stuttgart
Stuttgart, Germany
jochen.raichle@ke.uni-stuttgart.de

ABSTRACT

Headed studs arranged close to the concrete edge, especially loaded in direction to the free edge, show a lower static resistance and partly a different behaviour than studs further away from the concrete edge. Whereas the static resistance for both load directions and the fatigue strength for a loading parallel to the free edge are well investigated in earlier research works, there is no design rule for the fatigue strength for the load direction orthogonal to the free edge.

Based on push-out tests this paper gives information about the fatigue strength for a loading orthogonal to the concrete edge subjected to the edge distance. Another focus is the residual static resistance after a cyclic preloading.

An interesting development is the application of corrugated steel webs in composite girders. Omitting the steel flange and welding the headed studs close to the surface as shear connectors leads to a favourable application. Due to the corrugation there are tension stresses in the studs limiting the resistance on one hand, however, the corrugation itself acts as connector in the concrete increasing thus the overall connection strength on the other hand.

INTRODUCTION

Independent of a vertical or a horizontal arrangement, see Figure 1, so called horizontally lying shear studs feature a small edge distance a_r of the headed stud to the concrete surface. They allow for new interesting cross sections and applications. For bridges some examples are given in Figure 2.

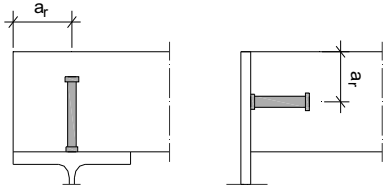
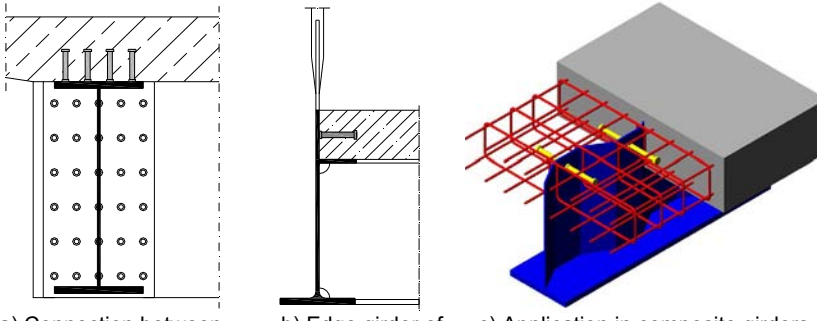


Figure 1 Vertical or horizontal arrangement of headed shear studs with edge influence.



a) Connection between longitudinal steel girder and concrete cross girder

b) Edge girder of an arch bridge

c) Application in composite girders with corrugated steel webs

Figure 2 Some examples for horizontally lying shear studs in bridges

Depending on the load direction parallel or orthogonal to the free concrete edge the behaviour and resistance differ. Shear in longitudinal direction parallel to the edge occurs in general due to beam action and shear in transverse direction orthogonal to the concrete surface may arise due to self weight and direct loading e. g. by the wheel of a vehicle. Substantial fatigue loads in vertical direction may derive from concentrated traffic loads like wheel loads.

STATE OF THE ART

Numerous experimental and numerical investigations [Kuhlmann and Breuninger 2000] [Kuhlmann and Kürschner 2006] lead to design rules for static resistance for both load directions and furthermore for fatigue resistance under longitudinal shear which meanwhile have been implemented in [EN 1994-2 2005] and [DIN 18800-5 2007].

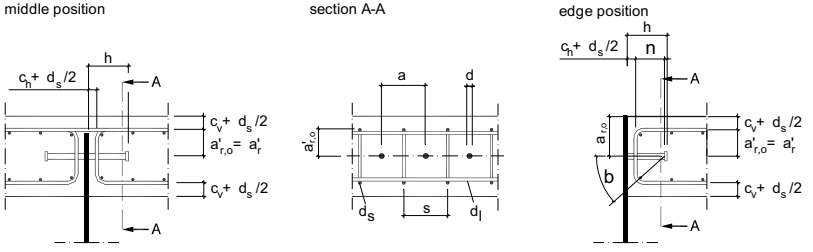


Figure 3 Geometrical parameters of shear connections with horizontally lying shear studs

The resistance is influenced by the reinforcement. Therefore, beside the load direction the resistance is specified depending on the effective edge distance a_r', which is the clearance between the headed stud and the outer reinforcement layer, see Figure 3. While the effective edge distance a_r' for longitudinal shear is interesting on both sides of the studs the edge distance for transverse shear is mainly important on the side of the loading point. With decreasing of the effective edge distance cracking of the concrete gets more important and stud failure is dominated by the concrete cracking. An arrangement in middle position leads to a higher resistance than in the edge position.

As a result of a research project [Kuhlmann and Kürschner 2002] provide a design rule for horizontally lying headed studs under longitudinal shear and cyclic loading:

(1) $$(\Delta P_{R,L})^m \cdot N_R = (\Delta P_{c,L})^m \cdot N_c$$

with $\Delta P_{R,L}$ Fatigue shear strength based on the range of shear force per stud in longitudinal direction [kN]

$\Delta P_{c,L}$ Reference value at $N_c = 2 \cdot 10^6$ cycles depending on the effective edge distance a_r'

a_r' [mm]	50	≥ 100
$\Delta P_{c,L}$ [kN]	24.9	35.6

For $50 < a_r' < 100$ mm $\Delta P_{c,L}$ should be determined by linear interpolation.

m Slope of the fatigue strength curve with the value m = 8

N_R Number of force range cycles

The area of the stud shank was not identified as an influencing factor. Therefore, in contrast to the design rule for headed studs without an edge influence, the design rule deals with forces and not with shear stresses. Similarly to headed studs without an edge influence the fatigue behaviour of studs close to the edge surface under longitudinal cyclic loading features a two stage failure mechanism. Due to an early initiation of concrete crushing close to the weld-collar and concrete splitting, the stud is subjected to bending at an early stage of fatigue loading. Forced by a splitting action, however, for horizontally lying studs the degree of concrete damage is higher, which leads to a slightly reduced fatigue strength compared with studs without edge influence. With increasing edge distance, the influence of splitting action decreases and the fatigue strength life aligns to that of studs without edge influence.

The design codes EN 1994-2 and DIN 18800-5 give rules to determine the static resistance of headed studs independently from the fatigue strength. This implies the assumption that the entire static resistance is valid over the whole life time. The design rules are derived from push-out tests which use shearing of the studs as failure mode [Roik and Hanswille 1990]. However, already [Mensinger 2000] and [Leffer 2003] concluded that a crack usually appears early in life time and that the life time consists mostly of crack propagation. This leads to the assumption that a separate determination of the static resistance and fatigue strength may lead to unsafe results.

A reduced static resistance after a cyclic preloading was already observed in 1967 by [Mainstone and Menzies 1967]. First systematical investigations for the residual static resistance P_{res} for headed studs were made by [Oehlers 1990]. He established a linear correlation between the number of cycles and the residual static strength. When reaching the life time, the residual static strength meets the applied maximum load. This relation is confirmed by the test results of [Veljkovic and Johansson 2006]. Until today [Hanswille and Porsch and Üstündag 2007] carried out the most comprehensive test program concerning this topic. They distinguished four phases, see Figure 4. After a negligible reduction of the residual static strength at the beginning (I), a strong reduction occurs (II). Afterwards, there is a steady-going reduction (III). Again, the final phase shows an increasing reduction (IV).

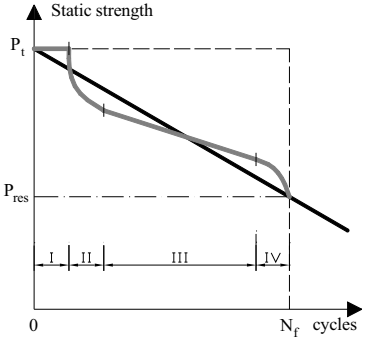


Figure 4 Reduction of the residual static strength of studs without edge influence: Linear: By Oehlers as well as Veljkovic & Johansson; different phases: Hanswille & Porsch & Üstündag

INVESTIGATION ON THE FATIGUE STRENGTH UNDER TRANSVERSE LOADING

Two test series on push-out specimens were performed to investigate the influence of the effective edge distance $a_{r,o}´$. One test series had an effective edge distance $a_{r,o}´$ of 100 mm – test series QE1 – and the other one 50 mm – test series QE2. The distances to the concrete edge a_r were 150 mm respectively 100 mm, see Figure 5. The diameter of studs was 22 mm.

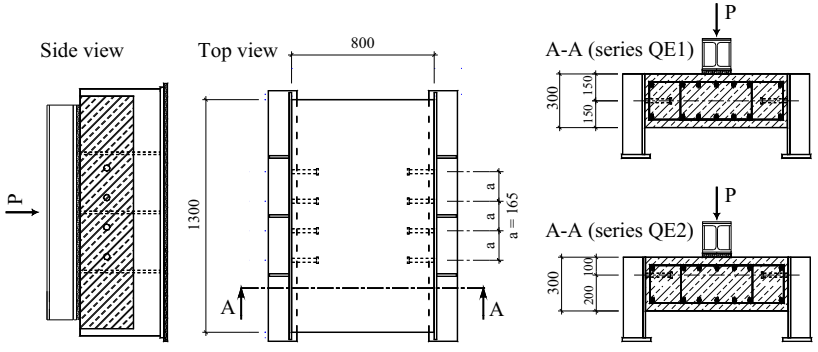
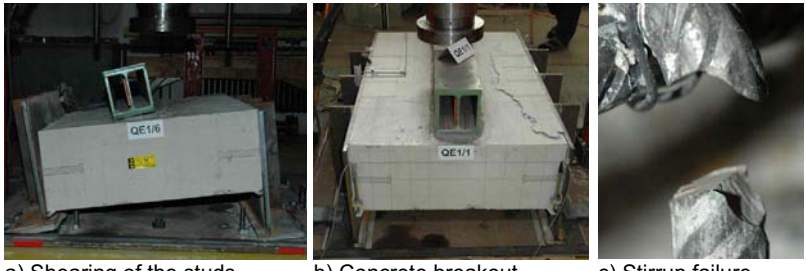


Figure 5 Geometry of the push-out specimens

The specimens were loaded in sinusoidal load cycles at similar maximum load levels and different load ranges. As alternating loaded specimens in comparison to pulsating loaded specimens [Roik and Hanswille 1990], all specimens were loaded in compression only. Except of two test specimens the maximum load level was at least 52% of the theoretical medium static resistance P_t or rather 86% of the design resistance P_{Rd}. The other two specimens were performed on a lower maximum force level. Thereby, the known influence of the stress level of headed studs without edge proximity could be confirmed.

The existing experiences concerning the fatigue behaviour of headed studs only show shearing of the studs as stop criterion. Contrarily, in these tests three different failure modes occurred. Some specimens failed by shearing of the studs, too. But most specimens failed by concrete breakout. Two specimens showed a fatigue failure of the reinforcement. In both cases one stirrup failed in the upper bending, see Figure 6.



a) Shearing of the studs b) Concrete breakout c) Stirrup failure

Figure 6 Failure modes of the test specimens

Contrary to headed studs without an edge influence only a slight concrete crushing at the weld collar could be observed. Concrete cracking at an early stage is essential for the fatigue behaviour. The resulting increasing slip causes bending in the stud shank.

A statistical evaluation comes to S-N curves on the mean level and for the 95%-fractile, see Figure 7. The effective edge distance $a_{r,o}'$ obviously has a significant effect on the fatigue strength.

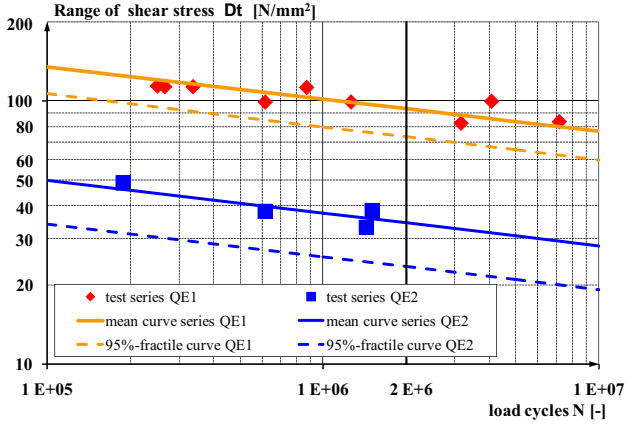


Figure 7 Test values of the fatigue strength depending on the effective edge distance

Based on the test results and the experiences on the fatigue behaviour of horizontally lying headed studs under longitudinal loading as well as headed studs without an edge influence the fatigue strength for headed studs with edge influence under transverse loading has been derived in [Kuhlmann and Raichle 2007] as follows:

(2) $$(\Delta P_{R,V})^m \cdot N_R = (\Delta P_{c,V})^m \cdot N_c$$

with $\Delta P_{R,V}$ Fatigue shear strength based on the range of shear force per stud in transverse direction [kN]

$\Delta P_{c,V}$ Reference value at $N_c = 2 \cdot 10^6$ cycles depending on the effective edge distance $a_{r,o}'$

$a_{r,o}'$ [mm]	50	≥ 100
$\Delta P_{c,V}$ [kN]	8.9	27.7

For $50 < a_{r,o}' < 100$ mm $\Delta P_{c,V}$ should be determined by linear interpolation.

m Slope of the fatigue strength curve with the value m = 8

N_R Number of force range cycles

P_{Rd} Design value of the resistance of horizontally lying shear studs under vertical shear

$P_{V,OL} \leq 0{,}6 \cdot P_{Rd}$ Peak load per stud in vertical direction

$a_{r,o}' \geq 50$ mm	Effective edge distance; $a_{r,o}' = a_{r,o} - c_v - d_s/2$ [mm]
$d_s \geq 12$ mm	Diameter of the stirrups
$d_l \geq 10$ mm	Diameter of the longitudinal reinforcement
$d \geq 22$ mm	Diameter of the shank of the studs
$f_{ck} \geq 30$ N/mm^2	Characteristic cylinder strength of the concrete

For the static resistance the diameter of the stirrups in EN 1994-2 and DIN 18800-5 when using horizontally lying studs is specified as at the least 8 mm. For the fatigue strength the minimum diameter has to be increased to 12 mm due to the two fatigue fractures of the stirrups. Based on the tested specimens the diameter of the shank of the studs is limited to at least 22 mm. Due to the force based design rule the result is on the safe side for headed studs with a shank diameter of 25 mm. For studs with 19 mm further considerations have to be done [Raichle 2010].

The fatigue strength was investigated for an edge position. It can be used for a middle position, also, because these are more favourite conditions.

Depending on the effective edge distance $a_{r,o}'$ the result of the investigations is shown in Figure 8. For evaluation the results Figure 9 shows a comparison with the fatigue strength of horizontally lying headed studs under longitudinal shear and studs without an edge influence. For horizontally lying headed studs under vertical shear and an effective edge distance $a_{r,o}'$ of 100 mm the fatigue strength is lower than for studs without an edge influence. Therefore, there has to be a reduction also for an effective edge distance greater than 100 mm. Before further considerations have been done, it is recommended to use the value for 100 mm also for greater edge distances than 100 mm.

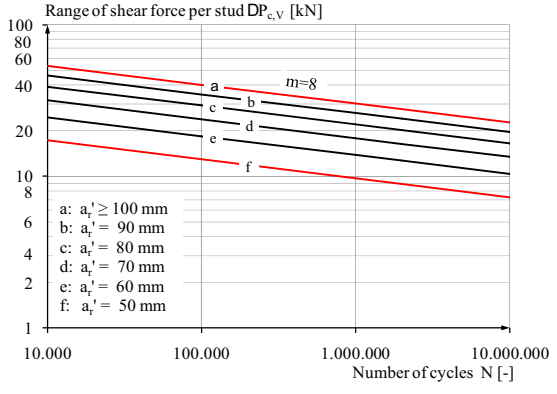


Figure 8 Characteristic fatigue strength curves of horizontally lying shear studs subjected to vertical shear

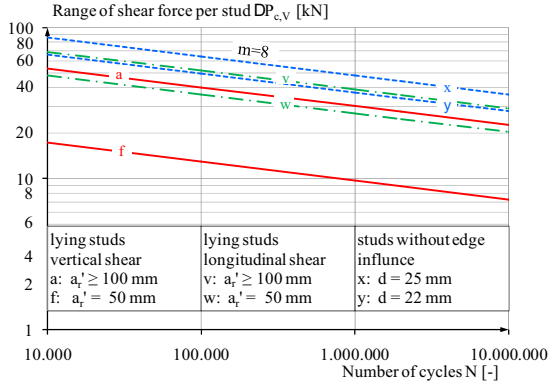


Figure 9 Comparison of the fatigue strength of horizontally lying studs under vertical and longitudinal loading as well as headed studs without edge influence

INVESTIGATION ON THE RESIDUAL STATIC RESISTANCE

To investigate the residual static resistance after a high cycle preloading, a further test series QE3 has been performed. After a variable range of load cycles, the different test specimens were tested statically in a deformation controlled manner. The geometry was equal to series QE1 with an effective edge distance $a_{r,o}$´ of 100 mm. This allows the use of the S-N curve of series QE1. Furthermore, the greatest shear force range of series QE1 was used. One test specimen of each series QE1 and QE3 was tested exclusively under static loading. The number of applied cycles N_i was in the range of 42% to 76% of the number of cycles to failure N_f, calculated as ratio of applied to expected load cycles.

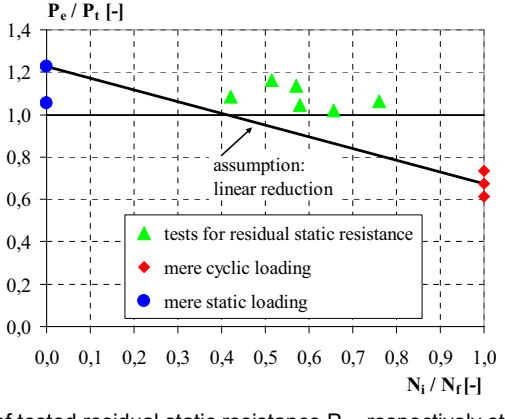


Figure 10 Ratio of tested residual static resistance P_{res} respectively static resistance P_e to expected value P_t dependant on the degree of damage N_i/N_f

Figure 10 shows that all tests for the residual static strength exceed the expected static resistance on mean level P_t. One of the tested specimens under mere static loading exceeded the expected static resistance P_t clearly. Even an assumption of a linear reduction of the residual static resistance over the lifetime according to Oehlers theory based on the reached static strength using this extreme test result comes to lower residual static resistances than tested, see Figure 10. Despite the great residual static resistance the headed studs showed remarkable fatigue cracks.

Four tests were performed with a variable lower cyclic load per stud. This procedure generated lines of rest in the fatigue crack. An evaluation of the lines of rest gives information about the point in time of initial cracking. As only visible lines of rest were counted it is merely possible to give information about the point when a crack appeared at the latest. In the different studs with cracks the crack appeared in a range of not later than 6% to 54% of the expected lifetime.

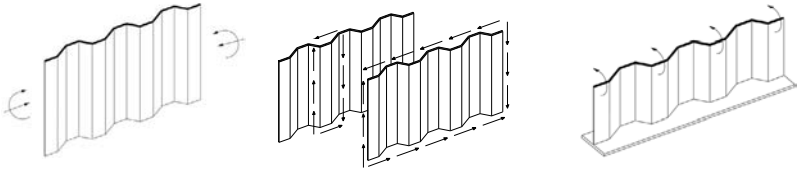
The high residual static strength after a high cycle preloading may be explained with the low resistance of the concrete for a mere static loading. As for horizontally lying headed studs under vertical shear concrete failure limits the static loading decisively, the utilisation of the partially cracked stud sections under cyclic loading is not very high and allows for a higher residual strength compared to normal studs. Therefore, it is not necessary to give a reduction in static resistance to account for the residual static resistance in this case. As the rate of utilisation between concrete and stud failure increases with decreasing effective edge distance, this conclusion is also valid for lower effective edge distances than the tested 100 mm.

APPLICATION OF HEADED STUDS CLOSE TO THE SURFACE WITH CORRUGATED STEEL WEBS

An interesting development is the application of corrugated steel webs in composite girders. Omitting the steel flange and welding the headed studs close to the surface as shear connectors to the webs leads to a favourable application. Due to the corrugation, there are tension stresses in the studs limiting the resistance on one hand, however, the corrugation itself acts as connector in the concrete increasing thus the overall connection strength on the other hand.

Due to the features of the corrugation, see Figure 11, the corrugated steel webs lead to several advantages in comparison to normal composite constructions. The web has a small stiffness in longitudinal direction, so that in case of longitudinal prestressing of the concrete chord no relaxation of the prestressing force from the concrete to the steel occurs. The local and global buckling resistance is increased, so that no longitudinal stiffeners are necessary. In comparison to plane webs, there is a high bending stiffness in transverse direction which allows reducing the number of cross frames in box girder bridges.

The development of bridges with corrugated steel web started in France. Nowadays, most bridges are built in Japan. Until now, only one bridge pilot project has been built in Germany, see Figure 12.



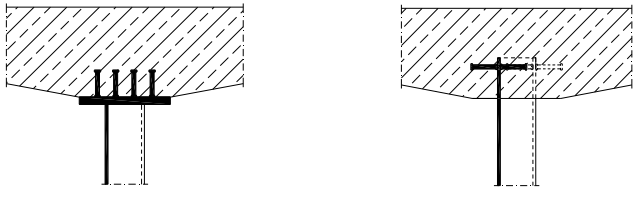
a) Longitudinal direction b) Shear c) Transverse direction

Figure 11 Load bearing in dependence on load direction



Figure 12 Valley bridge Altwipfergrund

An important detail for functionality and cost effectiveness is the composite joint. As the most spread common solution, shear forces are transferred by vertical studs welded to a top steel flange. As an alternative, an embedded steel web in the concrete chord carrying shear connectors has been developed, see Figure 13.



a) Steel flange b) Embedded steel web

Figure 13 Fundamental detailing of the composite joint

Omitting the steel flange leads to further advantages: The corrugation is activated as additional shear connector. By omitting the steel flange the number of welds and therefore the fatigue critical details are reduced. In case of a steel flange with vertical shear connectors, a transverse bending moment induces high tension forces so that extra tension devices are necessary.

In contrast to that, the embedded joint is loaded mainly by shear in longitudinal and transverse direction. Tests under longitudinal shear and transverse bending moment have been carried out, see Figure 14 and Figure 15 [Novák and Kuhlmann et al. 2008]. Besides headed studs concrete dowels have been investigated as additional shear connectors.

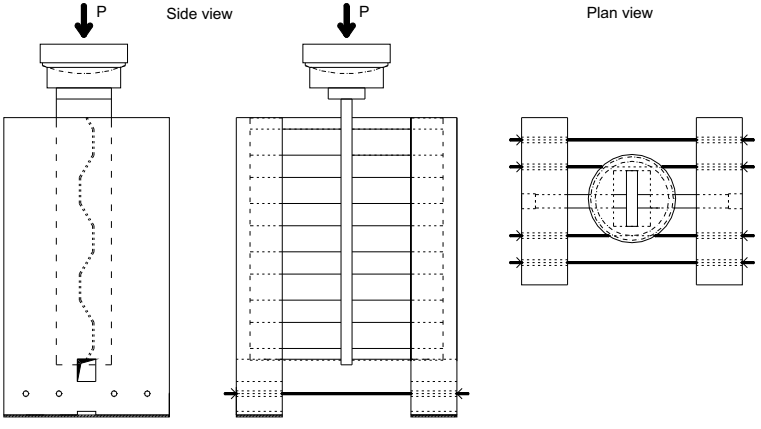


Figure 14 Specimen for longitudinal shear

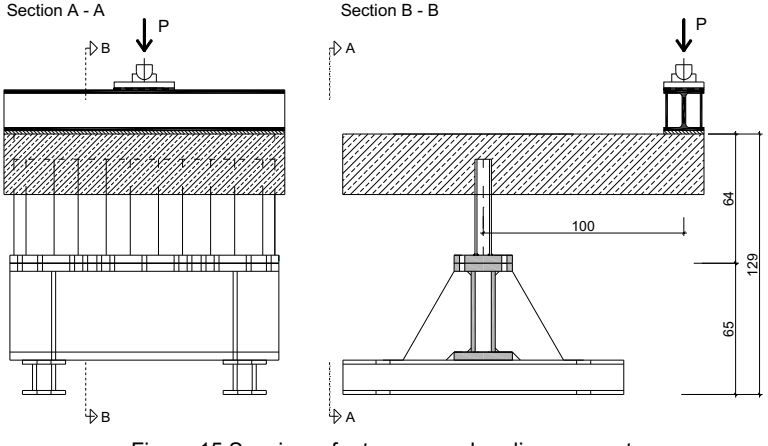


Figure 15 Specimen for transverse bending moment

The tests show the ability to carry considerable forces only by the corrugated web. Additional headed studs or concrete dowels are able to increase the resistances. The embedment depth of the corrugated web features a big influence on the resistance. In general the tests showed a high ductility. Only the tests under longitudinal shear force without shear connectors in addition to the “connector” formed by the steel corrugation showed a sudden slip before reaching the maximum load. That is why the application of additional shear connectors is recommended in any case. For the transverse bending moment the transfer from the steel web by shear connectors into the concrete has been proven by a concrete strut- and- tie-model so that now the innovative structure may also be used in normal design practice.

CONCLUSIONS

The fatigue strength is influenced strongly by the effective edge distance $a_{r,o}´$. The concrete plays the major role for the fatigue behaviour. The reinforcement, especially the stirrups are decisive and have to be chosen with care. The fatigue strength under vertical loading is lower than for longitudinal loading and for the case of headed studs without an edge influence.

There is a high residual static resistance for the tested specimens with an effective edge distance of 100 mm. This refers to the low level of utilisation of the studs in contrast to studs without edge influence.

Considering the existing investigations to horizontally lying headed studs under static shear loading in longitudinal and vertical directions as well as the fatigue strength under longitudinal loading the presented investigations on the fatigue loading in vertical direction allow a design for both static and fatigue loading in longitudinal and vertical direction and the development and application of interesting new composite sections.

In comparison to plane webs the use of corrugated steel webs offers an additional resistance. Especially the embedded steel web may be activated very efficiently also for the transfer of transverse bending.

ACKNOWLEDGEMENT

Parts of this paper are based on the research project FE-Nr. 15.0407/2004/CRB on behalf of the Bundesministerium für Verkehr, Bau und Stadtentwicklung, represented by the Bundesanstalt für Straßenwesen. The authors of this paper are responsible for the content exclusively. The authors gratefully acknowledge the financial support of the research project by the Bundesministerium für Verkehr, Bau und Stadtentwicklung (BMVBS) and the technical and scientific steering of the Bundesanstalt für Straßenwesen (bast).

In the same manner the authors are much obliged to the Forschungsvereinigung Stahlanwendung e. V. (FOSTA). The companies AG der Dillinger Hüttenwerke, Köster & Co GmbH, Max Bögl Bauservice GmbH & Co. KG and voestalpine AG are acknowledged for providing material and fabrication of specimens. Special thanks go to the Otto-Graf-Institut of the Materialprüfungsanstalt Universität Stuttgart (MPA Stuttgart) for carrying out the tests and their practical support as well as cooperation.

REFERENCES

DIN 18800-5 2007: Stahlbauten – Teil 5: Verbundtragwerke aus Stahl und Beton – Bemessung und Konstruktion

EN 1994-2 2005: Eurocode 4: Design of composite steel and concrete structures – Part 2: General rules and rules for bridges

Hanswille and Porsch and Üstündag 2007: Resistance of headed studs subjected to fatigue loading, Part I: Experimental study, Part II: Analytical study. In: Journal of Constructional Steel Research 63, p. 475-484 and p. 485-493, DOI 10.1016/j.jcsr.2006.06.035 and 10.1016/j.jcsr.2006.06.036

Kuhlmann and Breuninger 2000: Behaviour of lying studs with longitudinal shear force. In: Composite construction in steel and concrete IV, Mai 28 - June 2, Banff, Canada, United Engineering Foundation (UEF)

Kuhlmann and Kürschner 2002: Bemessungsregeln für ermüdungsbeanspruchte liegende Kopfbolzendübel unter Längsschub im Brückenbau, Institute of Structural Design, University of Stuttgart. – Research report, project FE 15.326/2000/CRB, Ed. Bundesministerium für Verkehr, Bau- und Wohnungswesen, issue 834, 2002. – ISBN 3-934458-92-0

Kuhlmann and Kürschner 2006: Structural behaviour of horizontally lying shear studs. In: Leon, R. T.; Lange, J.: Composite construction in steel and concrete V, July 18-23, 2004, Kruger National Park, South Africa, American Society of Civil Engineers (ASCE), p. 534-543 – ISBN 0-7844-0826-2

Kuhlmann and Raichle 2007: Ermüdungsverhalten liegender Kopfbolzendübel infolge Querschub, Institute of Structural Design, University of Stuttgart. – Research report, project FE 15.407/2004/CRB, Ed. Bundesministerium für Verkehr, Bau- und Stadtentwicklung

Leffer, A. 2003: Zum Ermüdungsverhalten einbetonierter Kopfbolzendübel unter realitätsnaher Beanspruchung im Brückenbau, phd-thesis, University of Kaiserslautern, Stuttgart: ibidem-Verlag, 2003. – ISBN 3-89821-268-8

Mainstone and Menzies 1967: Shear connectors in steel-concrete composite beams for bridges. 1: Static and fatigue tests on push-out specimen. In: Concrete 1 (9), p. 291-302

Mensinger 2000: Zum Ermüdungsverhalten von Kopfbolzendübeln im Verbundbau, phd-thesis, University of Kaiserslautern, Aachen: Mainz Verlag, 2000. – ISBN 3-89653-679-6

Novák and Kuhlmann et al. 2008: Entwicklung geeigneter Berechnungs- und Konstruktionsgrundlagen für die Anwendung sandwichähnlicher Verbundträger mit Trapezblechstegen, research report, Forschungsvereinigung Stahlanwendung e. V. (FOSTA), P645

Oehlers 1990: Deterioration in strength of stud shear connectors in composite bridge beams. In: Journal of structural engineering 116, No. 12, p. 3417-3431

Raichle 2010: Liegende Kopfbolzendübel im Brückenbau, phd-thesis, Institute of Structural Design, University of Stuttgart, in preparation

Roik and Hanswille 1990: Hintergrundbericht zu Eurocode 4, Nachweis des Grenzzustandes der Betriebsfestigkeit für Kopfbolzendübel, report EC4/11/90, Harmonisierung der europäischen Baubestimmungen, Minister für Raumordnung, Bauwesen und Städtebau, Nr. RS II 2-674102-88, Bochum

Veljkovic and Johansson 2006: Residual static resistance of welded stud shear connectors. In: Leon, R. T.; Lange, J.: Composite construction in steel and concrete V, July 18-23, 2004, Kruger National Park, South Africa, American Society of Civil Engineers (ASCE), p. 524-533. – ISBN 0-7844-0826-2

FATIGUE BEHAVIOR OF SHEAR CONNECTORS IN HIGH PERFORMANCE CONCRETE

Prof. Dr.-Ing. Markus Feldmann
Institute of Steel Construction, RWTH Aachen University
Aachen, Germany
feldmann@stb.rwth-aachen.de

Dipl.-Ing. Oliver Hechler
Commercial Sections, Arcelor Mittal
Luxembourg
oliver.hechler@arcelor.com

Prof. Dr.-Ing. Josef Hegger
Dipl.-Ing. Sabine Rauscher
Institute of Structural Concrete, RWTH Aachen University
Aachen, Germany
rauscher@imb.rwth-aachen.de

ABSTRACT

The paper deals with the fatigue behavior of headed studs and continuous shear connectors in high strength concrete. For both types of shear connectors cyclic push-out tests as well as large-scale beam tests under cyclic loading were carried out. The headed studs failed after a mean lifetime of $2.3 \cdot 10^6$ applying 40% to 50% of the static resistance as a maximum amplitude and R = 0.45 and 0.65, respectively. The residual strength after $1.0 \cdot 10^6$ load cycles was reduced by about 25% in comparison to the static push-out strength. The continuous shear connector, which is called “puzzle strip”, did not fail in the fatigue tests with up to $2.0 \cdot 10^6$ load cycles, and there was no reduction in residual strength at all. The cyclic beam tests with headed studs show that the prediction of the fatigue failure according to the current standards is not satisfactory. A good prediction of the crack propagation (thus fatigue) can rather be accomplished by using an approach based on the crack-slip relationship. For the continuous puzzle strip the fatigue behavior depends on the state of the cutting-induced heat treatment of the surface material and on the surface roughness. For these connectors a threshold value for the crack propagation could be determined.

INTRODUCTION

It is obvious that using high strength materials in composite construction leads to an increased load carrying capacity and slender structures. For the application of high strength steel and concrete to composite beams the specific ductility properties and its load carrying capacities are of particular interest, as well as the fatigue behavior. Within a research project at RWTH Aachen University [Feldmann et al. 2007] the lifetime and residual strength of shear connectors have been investigated. Thereby, two different kinds of shear connectors were compared – headed studs with a diameter of 22 mm and the continuous so-called “puzzle strip”, which consists of a tooth and a recess with equal dimensions (figure 1). The shape was chosen under economic considerations as two strips can be fabricated with only one single cut.

RESEARCH SIGNIFICANCE

In composite construction headed studs are the predominant shear connectors. Lately, continuous shear connectors are becoming more and more popular due to their high load carrying capacity and ductility [Feldmann et al. 2007]. Especially in high strength concrete their performance becomes evident since the shear strength of the headed studs is governed by steel failure. A comparison of their static behavior is given in [Hegger et al. 2006]. However, e.g. for bridges, not only the static behavior but also the fatigue behavior plays an important role. According to the latest research projects [Feldmann et al. 2007] the current design models for fatigue, which are usually based on S/N-curves, are not satisfactory. In many cases the prediction according to the current standards and literature differs fundamentally from the results of beam tests conducted under laboratory conditions. The fatigue of shear studs is dominated by crack propagation rather than by crack initiation [Feldmann et al. 2005]. Furthermore, the stresses in the composite joint are displacement-controlled rather than force-controlled. However, the question is the proportion of load to displacement control, which depends on various parameters such as the amount of studs and the cross section. After all, the fatigue limit state in the shear gap has to be considered under the residual strength of damaged (cracked) studs and the redistribution of the stresses in the studs [Hanswille et al. 2006]. With regard to the enhanced material properties of high strength steel and high strength concrete, which lead to increased service loads, it is evident that the fatigue limit state becomes more important compared to usual strength materials, especially since the fatigue behavior of high strength materials can only be increased to a smaller extend than the ultimate load under static conditions. Thus, the aim of the current paper is to determine the fatigue behavior of different shear connectors and to evaluate the present prediction models for the application of high strength materials.

TEST PROGRAM - CYCLIC PUSH-OUT TESTS

Push-Out tests were performed to investigate the lifetime behavior and to determine the residual strength after a certain amount of load cycles. The test set-up, which is based on the test specimen according to EC 4 [EC4 2004], is presented in figure 1.

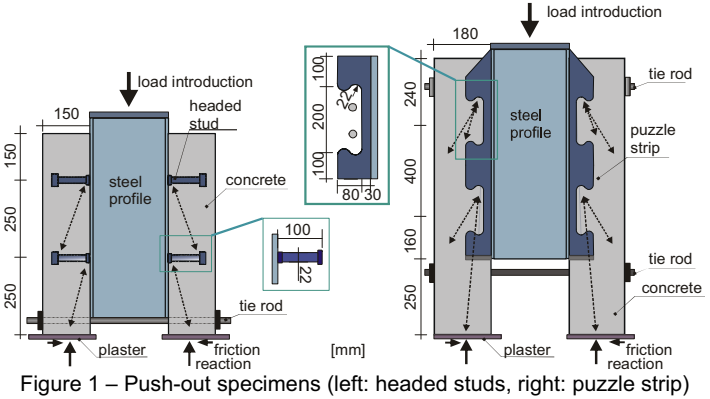


Figure 1 – Push-out specimens (left: headed studs, right: puzzle strip)

Headed studs with a diameter of 22 mm and the puzzle strip cut from a 10 mm thick plate of high strength steel S460 were tested in high strength concrete C80/95 ($f_{c,cube150}$ = 95 N/mm²). Tie rods were arranged to fix the concrete slabs and to

minimize the tensile forces in the shear connectors. With headed studs, the main uplift forces occur in the lower part of the specimen, thus the tie rods were installed at the bottom of the specimens. For the puzzle strip the tie rods were arranged at the top and bottom of the test specimen as uplift forces occur at both levels due to its specific geometry. To determine the forces in the tie rods, strain gauges were applied.

All tests were performed force controlled with a frequency of 4.5 Hz. The maximum static load $P_{u,0}$, the upper load level of the cyclic load P_{max} as well as the load range ΔP between the upper and lower level of the cyclic load are given in table 1. In addition, the load range for each shear connector ΔP_{con} and the stress range $\Delta\tau$ are listed in addition.

Table 1 – Testing parameters

Shear connector	Number of tests		$P_{u,0}$	P_{max}	$P_{max}/P_{u,0}$	ΔP	$\Delta P/P_{u,0}$	ΔP_{con}	$\Delta\tau$
	Lifetime	Residual strength							
[-]	[-]	[-]	[kN]	[kN]	[-]	[kN]	[-]	[kN]	[N/mm²]
Headed stud	3	3	1990	1000	0.50	550	0.28	70	181
Puzzle strip	3*	1 + 2*	2811	1200	0.43	550	0.20	138	73

* tests were stopped without any signs of damage; two specimens were used to investigate the residual strength and one was opened and inspected

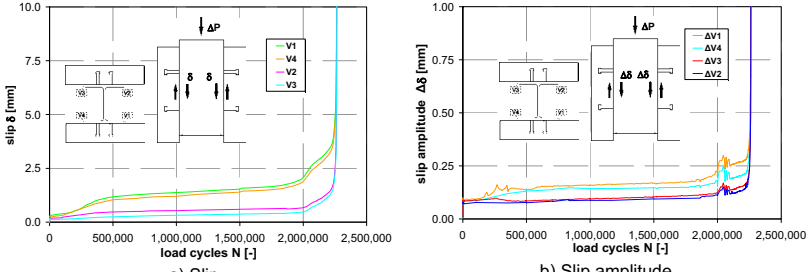
TEST RESULTS – HEADED STUDS

The test results on headed studs are summarized in table 2. For all tests the mean concrete strength of a 150 mm cube $f_{c,cube150}$ and the mean elastic modulus of the concrete E_{cm} were evaluated. The mean value of the lifetime is $2.29 \cdot 10^6$ load cycles.

Table 2 – Test results of the cyclic tests with headed studs

Test	$f_{c,cube150}$	E_{cm}	Load cycles until failure	Mean value	Deviation
-	[N/mm²]	[N/mm²]	-	-	-
HS-lt-1	112	44100	2,113,520	2,294,824	- 8 %
HS-lt-2	112	44300	2,265,273		+ 2 %
HS-lt-3	111	44600	2,505,680		+ 9%

Basically, all three tests showed the same behavior. There is little variation around the mean values. The development of the slip and the slip amplitude depending on the number of load cycles is presented in figure 2 for one of the three push-out tests with headed studs (HS-lt-2). After the initial loading the slip increase is higher for one of the concrete slabs (displacement sensor V1 and V4). At approximately 20% of the lifetime the slip development slows down and merges into a steady phase with only slight slip increase. After approximately $1.9 \cdot 10^6$ load cycles the slip increases extremely at all sensors until failure of the shear connectors at $2.265 \cdot 10^6$ load cycles. The development of the slip amplitude complies with the slip development.



a) Slip b) Slip amplitude

Figure 2 – Test results lifetime - headed studs

After testing the crack surfaces were evaluated and assigned to the crack modes according to [Hanswille 1990]. Most headed studs failed according to crack mode A and B (figure 3a and b), however, also combinations and multiple cracks appeared (figure 3c). The concrete in front of the welded collar was damaged. The stud was stressed by bending moments, which led to crack formation in the lower part of the stud. A second crack developed outside the welded collar, which separated the collar from the base.



a) Crack mode A b) Crack mode B with plane crack c) Combined (multiple) crack formation

Figure 3 – Comparison of crack modes

The failure mode depends on the size of the damaged concrete area. In comparison to normal strength concrete the extent of the damaged concrete area is smaller for high strength concrete. For equal slip the bending stresses on the backside of the stud increase leading to the observed multiple cracks, which are not common in normal strength concrete. The results of the force-controlled fatigue tests indicate an increase in fatigue behavior for high strength materials, which already has been reported in [Roik and Hanswille 1987]. In table 3 the experimental results are compared to the theoretical lifetime according to [EC 4 2004] and [Hanswille et al. 2006]. The approach according to [Hanswille et al. 2006] derived for normal strength materials complies with the experimental lifetime and, therefore, may be applicable for high strength materials. However, for the transfer of the results on the rather slip-controlled composite joint beam tests are essential. The results of the performed beam tests are presented at the end of the paper.

Table 3 – Comparison of theoretical and experimental fatigue life

$N_{f,exp}$ =2,294,824	Equation	Input parameter	$N_{f,theo}$	$N_{f,theo}/N_{f,exp}$
[EC 4 2004]	$(\Delta\tau_f)^m \cdot N_f = (\Delta\tau_c)^m \cdot N_c$ (1)	$\Delta\tau_f$ = 181 N/mm² $\Delta\tau_c$ = 90 N/mm² m = 8	7,520	0.3
[Hanswille et al. 2006]	$\log N_f = \frac{1 - P_{max}/P_{u,0}}{K_1 - K_2 \cdot (P_{max} - 0.5 \cdot \Delta P) \cdot 1/P_{u,0}}$ (2)	$P_{u,0}$ = 249 kN P_{max} = 125 kN Δ P = 70 kN K_1 = 0.1267 K_2 = 0.1344	2,508,239	109.3

The residual strength was determined after 34 - 44 % of the mean fatigue lifetime. In this range the slip as well as the slip range remained constant (figure 2). In figure 4 the load-slip curves are compared to the static reference test (reference). The material properties $f_{c,cube150}$ and E_{cm}, the number of load cycles N_i after the static test is performed, the characteristic load achieved in the reference test $P_{0,Rk}$ as well as the static residual strength $P_{N,Ri}$ are also summarized. Due to the cyclic loading a reduction up to 29% compared to the static load without fatigue damage and a slightly reduced initial stiffness is recorded.

HS ∅22 mm		RS-1	RS-2	RS-3
$f_{c,cube150}$	[N/mm²]	109	107	109
E_{cm}	[N/mm²]	46900	46300	46500
N_i	[-]	$1.0 \cdot 10^6$	$0.75 \cdot 10^6$	$0.75 \cdot 10^6$
$P_{0,Rk}$	[kN]	1918		
$P_{N,Ri}$	[kN]	1417	1567	1363
$P_{0,Rk}/P_{N,Ri}$	[-]	0.74	0.82	0.71

All results for 1 push-out specimen with 8 headed studs

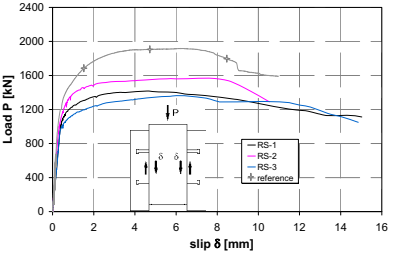


Figure 4 – Static residual strength – headed studs

The experimental residual strength is compared to the theoretical approaches according to [Oehlers 1995] (Eq.3) and [Hanswille et al. 2006] (Eq.4) for the mean lifetime achieved in the tests. The prediction according to Hanswille complies well with the test results (figure 5).

HS ∅22 mm			RS-1	RS-2	RS-3
Test	$P_{N,Ri}$	[kN]	177	196	170
Eq. 3	$P_{N,Ri}$	[kN]	195	208	208
	Deviation	[-]	+10	+6	+22
Eq. 4	$P_{N,Ri}$	[kN]	179	183	183
	Deviation	[kN]	+1	-6	-7

$$\frac{P_{N,Ri}}{P_{0,Rk}} = 1 - \frac{N_i}{N_f} \quad (3)$$

$$\frac{P_{N,Ri}}{P_{0,Rk}} = 0{,}74 \cdot \frac{P_{max} - \Delta P}{P_{u,0}} + 0{,}54 - 0{,}04 \cdot \ln\left(\frac{1}{1 - N_i / N_f} - 1\right) \quad (4)$$

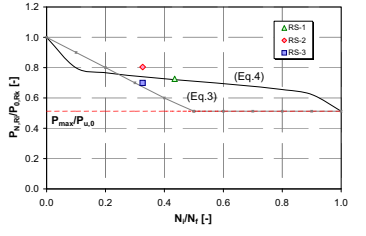


Figure 5 – Comparison of test results with literature – headed studs

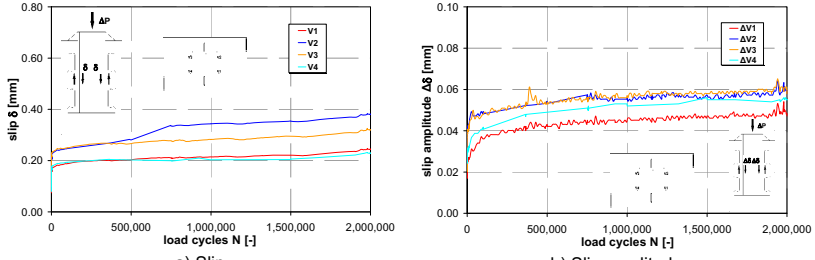
TEST RESULTS – PUZZLE STRIP

Three tests were performed to investigate the fatigue life of the puzzle-strip. After $2.0 \cdot 10^6$ load cycles no indication of damage was identified and the tests were stopped for inspection and determination of residual strength, respectively. The concrete strength $f_{c,cube150}$ and the mean elastic modulus of the concrete E_{cm} were evaluated. During the test, the maximum slip δ_{max} and slip amplitude $\Delta\delta_{max}$ were recorded. In addition, the maximum uplift u_{max} between the steel profile and the concrete slab and the uplift forces F_u measured in the tie rods were measured. The test results are summarized in table 4.

Table 4 – Test results of the cyclic tests with puzzle-strip

Test	$f_{c,cube150}$	E_{cm}	δ_{max}	$\Delta\delta_{max}$	u_{max}	F_u	Remark
-	[N/mm²]	[N/mm²]	[mm]	[mm]	[mm]	[kN]	-
PS-lt-1	117	46200	0.41	0.063	0.130	2.06	No failure – slab removed after testing
PS-lt-2	115	48400	0.29	0.059	0.04	1.44	No failure – residual strength
PS-lt-3	114	47300	0.33	0.031-0.05	0.183	1.44	No failure – residual strength

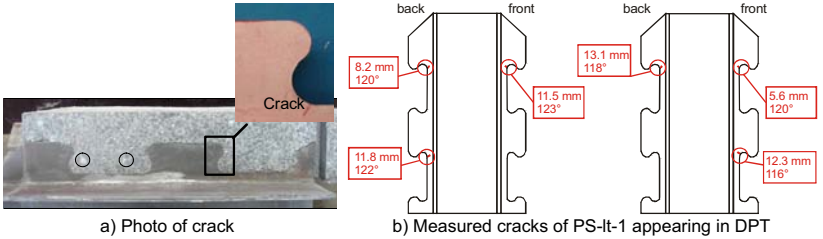
For all tests the measured mean slip is different for the two concrete slabs (see figure 6a for PS-lt-1). The maximum slip after approximately 25 load cycles was in accordance with the slip measured in the static reference test. During testing a negligible increase in slip was measured. The slip increase results from the compression of the concrete matrix directly in front of the shear connector. After approximately 250,000 load cycles a quasi-hydrostatic stress state develops in the concrete and the slip remains nearly constant. The course of the slip amplitude (figure 6b) matches the development of the slip. It increases until approximately 750,000 load cycles; there were no significant changes during testing afterwards. After unloading a residual slip of 0.09 mm (V4) to 0.21 mm (V2) was recorded.



a) Slip b) Slip amplitude

Figure 6 – Test results lifetime – puzzle strip

To investigate the condition of the shear connection the concrete slabs were removed after testing and the puzzle strip was checked by the dye penetration test (DPT) (figure 7a). Three cracks were identified. The inclination and the length of the cracks were determined in the puzzles (figure 7b).



a) Photo of crack b) Measured cracks of PS-lt-1 appearing in DPT

Figure 7 – Cracks in specimen PS-lt-1

The fatigue behavior of the specimens PS-lt-2 and PS-lt-3 is comparable to PS-lt-1. However, the lower values for the slip and slip amplitude indicate a smaller damage of the shear connection. These tests were chosen for the determination of the residual strength, now labeled RS-4 and RS-5. One additional test was performed after $1.0 \cdot 10^6$ load cycles (RS-6). In figure 8 the residual strength of the test specimens is compared to the static reference test. The residual strength of the tests is independent of the cycles performed prior to the tests and there is no difference compared to the static reference test.

Puzzle strip		RS-4	RS-5	RS-6
$f_{c,cube150}$	[N/mm²]	114	115	112
E_{cm}	[N/mm²]	47700	48300	48700
N_i	[-]	$2.0 \cdot 10^6$	$2.0 \cdot 10^6$	$1.0 \cdot 10^6$
$P_{0,Rk}$	[kN]	3226		
$P_{N,Ri}$	[kN]	3228	3110	3254
$P_{0,Rk}/P_{N,Ri}$	[-]	1.0	0.96	1.01

All results for 1 push-out specimen with 4 puzzle recesses

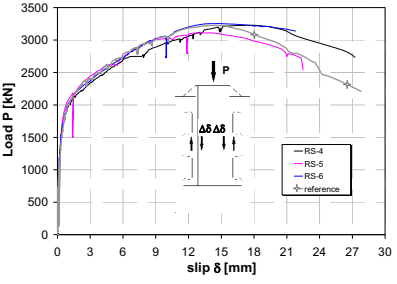
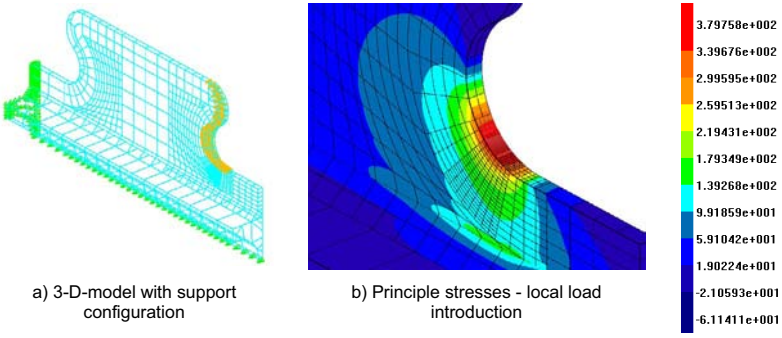


Figure 8 – Static residual strength – puzzle strip

To evaluate the behavior of the puzzle strip subjected to cyclic loading the method of fracture mechanics was applied. Therefore, the software BEASY was used, based on the boundary element method (BEM). With this program the notch stresses in the linear-elastic load range were calculated. If the effective stress intensity factor ΔK_{eff} (calculated with a defined load and a defined initial crack) is smaller than the threshold ΔK_{th}, no crack propagation will occur and therefore, no fatigue damage will be observed. For the calculation a simplified 3-D-model of the puzzle strip has been generated (figure 9a). The van-Mises stresses were checked with a constant area loading of 187.5 N/mm² (150 kN/puzzle) resulting in a maximum van-Mises stress of 440 N/mm² at the lower radius of the puzzle. This is in the elastic range of the puzzle material S460 and in accordance with additional performed FEM-calculations. Furthermore, the principle stresses were calculated (figure 9b). The maximum stresses occurred at the edge of the puzzle strip at a distance of 13 mm from the start of the radius.



a) 3-D-model with support configuration

b) Principle stresses - local load introduction

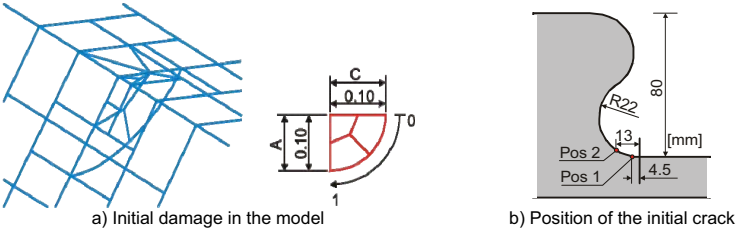
Figure 9 – Modeling the crack behavior using fracture mechanics

The effective stress intensity factor was derived taking into account the stress intensity factors corresponding to each mode (Eq. 5).

$$K_{eff} = \sqrt{(K_I + |K_{III}|)^2 + 2 \cdot K_{II}{}^2} \qquad (5)$$

with: K_{eff} Effective stress intensity factor
K_i Stress intensity factors for each single mode

The initial damage defined for the calculation was a boundary crack with a length of 0.1 mm, (figure 10a). Two positions of the crack were investigated; the first at the base of the radius where the crack initiation was identified in the tests (Pos1) and the second at the location of the maximum principle stresses (Pos2 in figure 10b). With the software the crack growth and the related stress intensity factors K_i were automatically calculated for each specified load.



a) Initial damage in the model

b) Position of the initial crack

Figure 10 – Initial crack shape and crack position

In a next step the threshold value ΔK_{th} was determined. For the evaluation the equations according to [Hobbacher 1996] (Eq. 6) and [Gourney 1979] (Eq. 7) have been investigated. Here, equation (7) is more conservative.

$$\Delta K_{th} = 190 - 144 \cdot R \quad \text{but not smaller than 62 [N/mm}^{-3/2}\text{]} \tag{6}$$

resp.: $$\Delta K_{th} = 240 - 173 \cdot R \quad [\text{N/mm}^{-3/2}] \tag{7}$$

with: R Range

$$R = \frac{K_{min}}{K_{max}} = \frac{\sigma_{min}}{\sigma_{max}} \tag{8}$$

and K_{min} Stress intensity factor for lower boundary

K_{max} Stress intensity factor for upper boundary

σ_{min} Principle stress for lower boundary

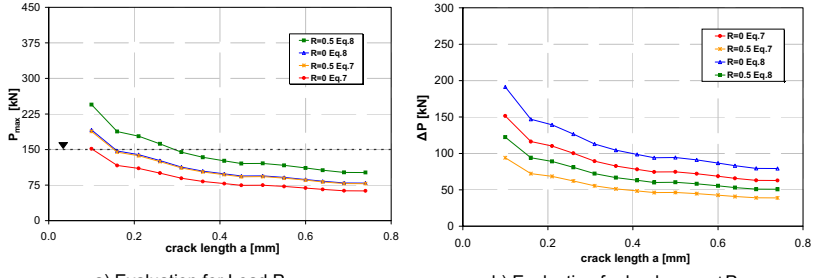
σ_{max} Principle stress for upper boundary

Subsequently, the effective stress intensity factor range for the puzzle strip was calculated.

$$\Delta K_{eff} = K_{eff} \cdot (1 - R) \tag{9}$$

Due to the relation of the stress intensity factor to the maximum load applied P_{max} it is possible to elaborate design diagrams for the maximum load and the load range ΔP for a specific crack configuration with a defined initial edge crack with the length a. Here, position 2 was chosen for presentation, as this position is considered to be significant for the design. It should be noted that, due to definition of linear elastic fracture mechanics, the diagrams are limited to elastic stresses and thus the validity results to maximum loads $P_{max} < 150$kN for the investigated puzzle geometry (figure 11a).

In addition the crack growth has been determined. The results show, that the angularity of the crack growth direction as well as the crack lengths are in accordance with the test results. The calculation indicates an influence of the puzzle shape and the thickness of the used steel strip. Furthermore, the initial damage and the used values of ΔK_{th} influence the fatigue behavior, which depend significantly on the cut quality of the edge of the steel strip.



a) Evaluation for Load P_{max} b) Evaluation for load range ΔP

Figure 11 – Evaluation for crack position 2 depending on crack length and loading range

BEAM TESTS

The question is whether the load carrying behavior of shear connectors obtained from push-out tests can be transferred to real composite beams. In the push-out tests, the shear force acts directly as a shear load onto the shear connector, in composite beams, the horizontal shear force results from a moment gradient produced by a vertical load and lever arm. Furthermore, in a force-controlled cyclic push-out test, the loading has a constant maximum value and range whereas in composite beams the loading is redistributed in the shear joint with increasing damage of the connectors. Therefore, two beam tests with partial shear connection were performed to investigate the slip behavior in the composite joint (further information see [Hegger et al. 2006]). The shear connection was established by headed studs ∅22 mm and the 10 mm thick puzzle strip with a degree of partial shear strength of 31% and 29%, respectively. In order to achieve the partial shear capacity for the beam with the puzzle-strip some recesses were deactivated by means of wooden panels (dark areas in figure 12). To prevent friction forces at the interface between the concrete slab und the upper flange of the steel girder, a two-layer PE-foil was attached. Along the interface between steel profile and concrete slab several displacement transducers were attached to measure the slip. At midspan strain gauges were fixed across the section to investigate the strain distribution.

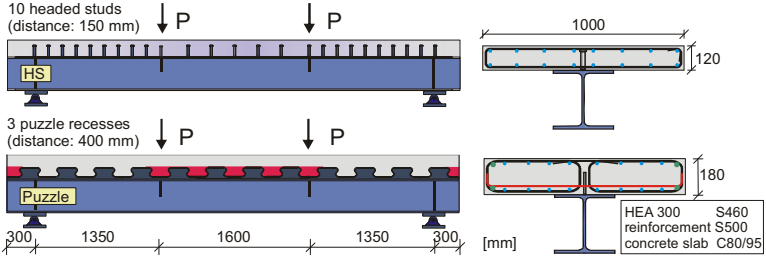


Figure 12 – Test set-up for beam tests

The load range ΔP was chosen 100 kN for both beams with an upper peak load of P_{max} = 230 kN. The tests were carried out with a frequency f = 3.0 Hz. The theoretical shear force range in the interface was 40 kN for one headed stud (appr. 17% of the resistance achieved from push-out test, $P_{Push\text{-}Out}$) and 150 kN for each puzzle tooth (appr. 21% of $P_{Push\text{-}Out}$). After $2.0 \cdot 10^6$ load cycles none of the shear connectors failed.

The slip distribution along the composite joint of the tested beams indicated a linear increase in slip during the testing period (figure 13). For the beam with headed studs the slip range $\Delta\delta$ grew linearly until 0.14 mm per load cycle. For the puzzle-strip a maximum slip amplitude of 0.18 mm was observed. The absolute slip value also grew steadily with increasing load cycles. However, the slip range decreased, which can be explained by the crushed concrete in front of the puzzle tooth.

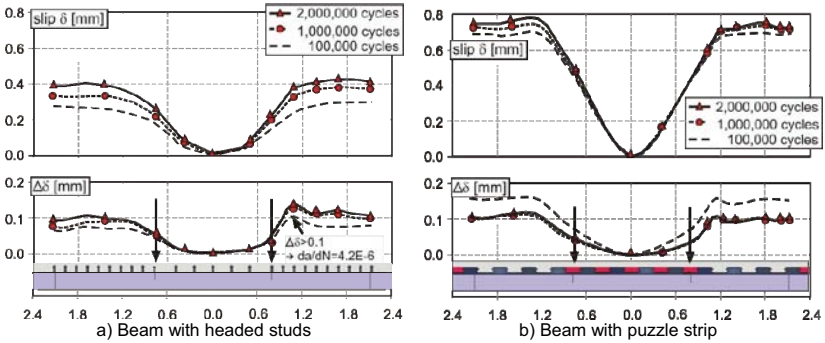


Figure 13 – slip distribution

At both tests, no specimen showed any major failure, however, after removing the concrete slab, cracks were identified in the headed studs as well as in the puzzle-strip (figure 14).



a) Headed stud b) Puzzle strip

Figure 14 – Failure modes in the shear connectors

The maximum crack width of 10 mm at the stud's base where the maximum slip range occurred agrees with the crack propagation law introduced in [Feldmann and Gesella 2005]. The fatigue lifetime of headed studs in composite beams can be determined depending on the slip range $\Delta\delta$. For slip ranges exceeding 0.1 mm a continuous crack propagation is observed (Eq. 10).

$$\Delta\delta \geq 0{,}10mm: \quad \frac{da}{dN} = \left[-1{,}4047 \cdot 10^{-5} + 1{,}4142 \cdot 10^{-4} \cdot \Delta\delta_t\right] \cdot \alpha_{t,da/dN} \tag{10}$$

$$R_\delta < 0 : \alpha_{t,da/dN} = \left(\frac{\left|\frac{1}{R_\delta}\right|}{1 + \left|\frac{1}{R_\delta}\right|} \right)^{-3,4} \quad ; \; R_\delta \geq 0 : \alpha_t = 1 \tag{11}$$

with da/dN Crack propagation rate

α_t ,$\alpha_{t,da/dN}$ Coefficient taking into account the slip amplitude [-]

R_δ Slip ratio of lower slip level $\Delta\delta_l$ and upper slip level $\Delta\delta_u$

For the composite beam with headed stud shear connection an average crack width of 10.2 mm is predicted, which complies with the test results. However, as already shown by the push-out tests, the prediction by means of S/N-diagrams according to [EC 4 2004] is not suitable.

CONCLUSIONS

Even though the load carrying behavior of the composite joint is mostly deformation controlled, which determines the damage and crack- propagation, force controlled push-out tests are capable of determining the fatigue behavior of shear connectors in high performance concrete in contrast to normal strength materials. The lifetime and residual strength of headed studs embedded in high strength concrete have been evaluated according to the damage models described by [Hanswille 2006]. A comparison with tests performed on headed studs in normal strength concrete indicates an enhanced fatigue behavior of headed studs in high strength concrete. The puzzle strip is a promising continuous shear connector. The crack phenomena as well as the theoretical crack growth and threshold values could be calculated using BEM simulations. The quality of the fatigue prediction depends on the surface finish of the cut strip. The cyclic beam tests with headed studs show, that their fatigue behavior in high strength concrete is in good accordance with the model according to [Feldmann and Gesella 2005], which predicts the slip-and-crack-development for displacement controlled loading of the studs. However, the tests also indicate that there is crack development underneath the proposed minimum level of slip amplitude. Further investigations are required to examine the region of low slip amplitudes and compare the differences between normal and high strength materials.

REFERENCES

prEN 1994-1-1: Design of composite steel and concrete structures Part 1.1 – General rules and rules for buildings, Brussels, Dec. 2004.

prEN 1994-2: Design of composite steel and concrete structures Part 1.1 – General rules and rules for bridges, Brussels, Dec. 2004.

Feldmann, M.; Hechler, O.; Hegger, J.; Rauscher, S.: Untersuchungen zum Trag- und Verformungsverhalten von Verbundmitteln unter ruhender und nicht ruhender Belastung bei Verwendung hochfester Werkstoffe. FOSTA-Abschlussbericht zum AiF-Vorhaben AiF 13867, Aachen 2007 (in German).

Feldmann, M.; Hechler, O.; Hegger, J.; Rauscher, S.: Shear Connectors in High Performance Concrete under static and fatigue loading, 2nd Symposium on Connections between Steel and Concrete, 2007, pp. 1017-1026.

Feldmann, M.; Gesella, H.: Zur Vorhersage des Rissfortschritts bei einbetonierten Kopfbolzendübeln in Verbundträgern unter nicht ruhender Belasting. Stahlbau 74, 2005, pp. 767-779 (in German).

Gurney, T.R.: Fatigue of welded structures; Cambridge, University Press, 1979.

Hanswille G., Porsch M., Üstündag C.: Resistance of headed studs supjected to fatigue loading, Part I Experimental study, Part II: Analytical study, Journal of Constructural Steel Research, 2006

Hegger, J.; Feldmann, M.; Rauscher, S.; Hechler, O.: Load-Deformation Behavior of Shear Connectors in High Strength Concrete subjected to Static and Fatigue Loading, IABSE Symposium 2006, Budapest/Hungary, Sept 13-15, pp 438-43.

Hobbacher, A.: Empfehlungen zur Schwingfestigkeit geschweißter Verbindungen und Bauteile; IIW-Doc. XIII-1539-96/XV-845-96, International Institute of Welding, 1996.

Oehlers, D.J.: Design and assessment of shear connectors in composite bridge beams. Journal of Structural Engineering 121, 1995, pp. 214-224.

Roik, K.; Hanswille, Zur Dauerfestigkeit von Kopfbolzendübeln bei Verbundträgern. Bauingenieur 62, 1987, pp. 273-285 (in German).

Roik, E.H., Hanswille, G.: Background Report on EUROCODE 4, Limit state of fatigue for headed studs, 1990.

NOTATION

$f_{c,cube}$	concrete strength	$P_{u,0}$	static load	P_{max}	upper load level
ΔP	load range	$\Delta\tau$	stress range	E_{cm}	elastic modulus
N_f	fatigue lifetime	P_N	residual strength	δ	slip
$\Delta\delta$	slip range	u	uplift	F	force in tie rod
σ	stress	K	stress intensity factor		

CYCLIC PERFORMANCES OF SHEAR CONNECTORS

Adrian Liviu CIUTINA
Lecturer, "Politehnica" University of Timişoara, Faculty of Civil Engineering
Department of Steel Structures and Structural Mechanics
Timişoara, Romania
adrian.ciutina@ct.upt.ro

Aurel STRATAN
Lecturer, "Politehnica" University of Timişoara, Faculty of Civil Engineering
Department of Steel Structures and Structural Mechanics
Timişoara, Romania
aurel.stratan@ct.upt.ro

ABSTRACT

Natural cyclic loads such as strong winds and earthquakes can cause changes in bending moment signs in composite structural elements. Consequently, the connectors will be subjected to alternate shear forces. For this reason, the cyclic behavior of shear connectors is particularly important in these loading conditions.

The research described in this paper refers to a set of 10 experimental tests on five different types of connectors (angle profiles, Φ16mm and Φ22mm shear connectors, perfobond connectors and reinforcement hooks), subjected to cyclic and monotonic loading, through push-out and respectively push-pull tests. The experimental results are discussed in terms of resistance, ductility and stiffness, and compared to analytical formulae used for strength determination.

INTRODUCTION

The transfer of internal forces between steel and concrete components represents the mechanism that renders the composite action feasible (Oehler and Bradford 1995). Although there are several forms to realize the transfer of shear longitudinal forces between steel and concrete (by chemical adhesion or chemical bond, interface friction, mechanical interlocking etc), in the case of the transfer of heavy shear forces, suitable mechanical connectors are usually considered (Bursi et al. 1999). In this situation, the shear transfer is done by mechanical deformation of a steel dowel embedded in concrete which transfers the loads from the steel profile and vice versa. The behavior of the mechanical dowel depends upon various parameters that govern the shear transfer.

Mechanical connectors could be considered in different shapes and arrangements and for this reason sometimes it is difficult to predict their final behavior. The most common way to asses the dowel behavior is by standard push-out testing. However, for the composite elements in which the bending moment changes from hogging to sagging (such as main beams or large composite columns subjected to important earthquake or wind loads), the mechanical connectors will be naturally subjected to alternate shear. Consequently, in this situation the push-out testing procedure

becomes unsafe with regard to the loading type, the characteristic loading type being of the push-pull type.

The investigations using the latter procedure can make the difference between the cyclic and monotonic loading for the mechanical connectors. In fact, this issue represents the main scope of the study. Results are used in expressing the limitations and safety conditions for use of connectors in composite elements subjected to cyclic loading.

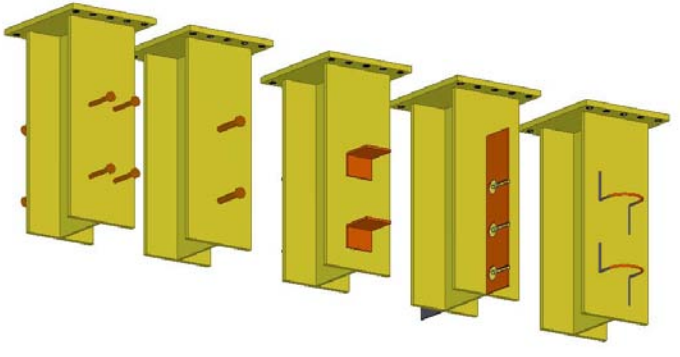
SPECIMENS AND TESTING SET-UP

The test specimens were conceived according to the paragraph B 2.2 from the Annex B of Eurocode 4 (CEN, 2004) regarding the standard push-out tests. For all specimens, the dimensions of concrete slabs (150x600x650mm) and steel profile (HEB 260) were kept constant for all tests, as well as the configuration and diameter of the reinforcing bars (Φ 10mm) according to Figure B.1 of Eurocode 4. Table 1 offers the names and characteristics of the experimental specimens.

Table 1 – Summary of the test program.

Specimen	Type of connectors	Height [mm]	No. of connectors
PT-16/I-M	8Φ16 (2 rows)	120	8
PT-16/I-C	8Φ16 (2 rows)	120	8
PT-22-M	4Φ22 (1 row)	120	4
PT-22-C	4Φ22 (1 row)	120	4
PT-A-M	Reinf. hooks (Φ 10mm)	120	4
PT-A-C	Reinf. hooks (Φ 10mm)	120	4
PT-II-M	Perforated steel plate	125	2
PT-II-C	Perforated steel plate	125	2
PT-LS/II-M	L120x80x8	120	4
PT-LS/I-C	L120x80x8	120	4

The choice of connecting devices was done in such a way to cover the main types of connectors used and not for having comparable design resistance. Five different arrangements of mechanical connectors have been considered, as shown in Figure 1. In fact, there have been considered four types of connectors, all of them encased in concrete slab and welded on the steel flange: Φ16 KOCO headed studs placed on two rows (120mm height), Φ22KOCO headed studs placed on one row (120mm height), LL120x80x8 angle profile, pre-perforated steel plate (perfobond connectors) and reinforcement anchor hooks 10mm in diameter (hooks of 150mm in diameter). The details of the perfobond connectors are shown in Figure 2. Two specimens corresponding to each arrangement of connectors were manufactured, one being tested under monotonic loading, the other under cyclic loading.



PT-16/I PT-22 PT-LS/II PT-II PT-A

Fig. 1 – Arrangement of connectors on steel profiles.

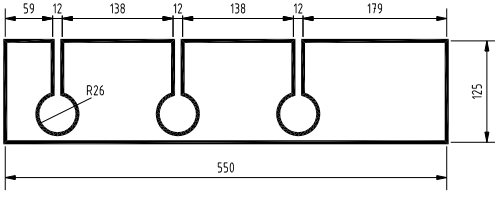


Fig. 2 – Details of the perfobond strip connectors.

The test set-up consists mainly in a loading actuator (displacement controlled), the test specimen and the reaction table as support. In the case of push-pull (cyclic) procedure, a tension support was added in order to resist the traction forces (see Figure 3a).

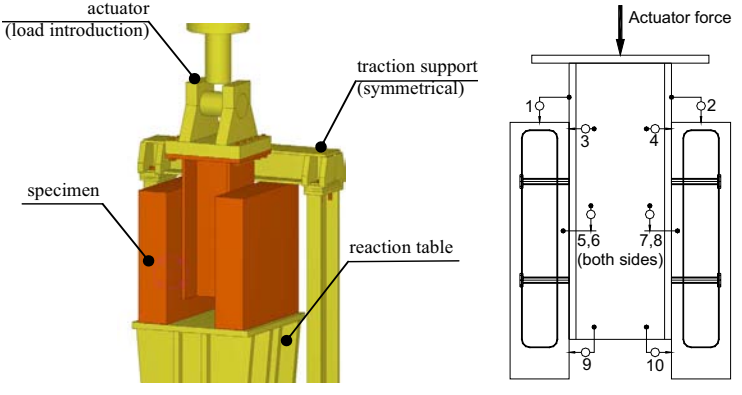


Fig. 3 – a) Testing set-up; b) Measuring arrangement

In the case of monotonic loading (push-out tests), the load was first applied in increments up to 40% of the expected failure load and then cycled 25 times between 5% and 40% of this load, according to the Eurocode 4 provisions. Subsequently, load increments were imposed up to failure. In the case of cyclic loading, the ECCS (ECCS 1986) procedure used for low-cycle fatigue phenomena was applied, with the yielding characteristics computed on the results obtained from the monotonic tests.

Displacement transducers (see Figure 3b) have been used in order to measure the relative slip between the concrete slabs and steel profile, but also the separation between the two elements. A total of 10 displacement transducers have been used for each test - 6 of them for measuring the relative longitudinal slip (transducers 1,2,5,6,7 and 8) and 4 for measuring the top and bottom separation of the concrete slab from the steel profile (transducers 3,4,9 and 10). The F-δ curves presented in this paper were derived from the force of the actuator and the mean value of the relative slip measured by the transducers 1 and 2, located on top of concrete slabs.

The following basic interpretation of the results was adopted: The connector shear capacity $P_{R,k}$ represents the maximum load capacity reduced by 10% and divided to the number of shear connectors; the connector's slip capacity δ_u is taken from the load-slip deformation curve, as the slip displacement corresponding to the shear capacity $P_{R,k}$ on the softening branch of the F-δ curve (see Figure 4).

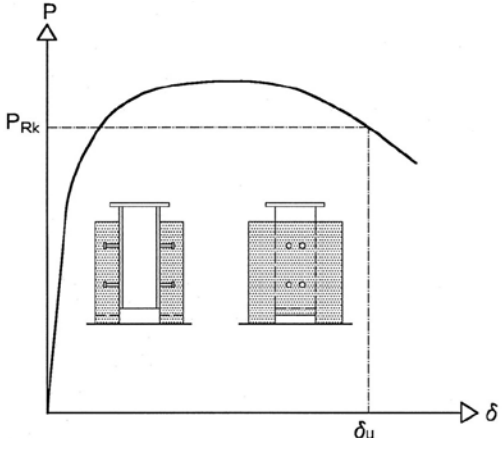


Fig. 4 – Determination of shear ($P_{R,k}$) and slip capacity (δ_u) according to Eurocode 4.

EXPERIMENTAL RESULTS

Table 2 shows the values of the main characteristics that resulted from the interpretation of the experimental tests. These characteristics have been computed on the F-δ curves in the case of monotonic curves, and on the envelopes of the cyclic tests. The notations used in the table have the following significations:

- F_y represents the yielding force, computed according to ECCS (1986) recommendations as the force corresponding to the intersection of the initial stiffness

line and a tangent to the force-displacement curve having a slope of 10% of the initial stiffness;
- δ_y is the corresponding yielding displacement;
- $S_{j,ini}$ is the initial stiffness of the F-δ curve;
- F_{max} is the maximum recorded force during testing;
- δ_u is the slip capacity of the connectors;
- $P_{R,k}$ is the connector's shear capacity.

Table 2 – Main results of the characteristic F-δ curves.

Specimen	F_y [kN]	δ_y [mm]	$S_{j,ini}$ [kN/mm]	F_{max} [kN]	δ_u [mm]	$P_{R,k}$/conn. [kN]
PT-16/I-M	396.0	0.20	983.4	801.1	4.91	90,1
PT-16/I-C	430.0	0.29	1454.0	579.0	2.33	65,1
PT-22-M	405.8	0.35	1093.5	737.6	14.43	166,0
PT-22-C	407.0	0.44	871.0	474.0	2.11	106,7
PT-A-M	396.0	0.20	1813.0	590.6	7.84	132,9
PT-A-C	339.0	0.08	4361	544.3	1.98	122,5
PT-II-M	557.5	0.13	3701.4	1033.0	21.46	464,9
PT-II-C	403.0	0.09	3939	586	0.60	263,7
PT-LS/II-M	586.8	0.21	2677.1	794.4	2.36	178,7
PT-LS/I-C	650.0	0.27	2274.0	774.3	0.98	174,2

Results of monotonic tests

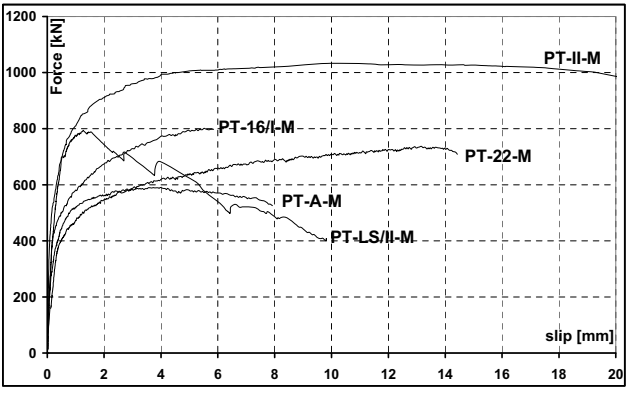


Fig. 5 – Comparison of monotonic curves.

Figure 5 presents the curves resulted from the interpretation of the monotonic tests of push-out type, in addition to the numerical results presented in Table 2. The specimen that shows the best performance in terms of resistance and ductility is by far the perfobond specimen (PT-II-M) with a slip capacity of almost 22mm, generally

more than double than the one recorded for other types of connectors. It is to be underlined however the fact that this ductility practically represents the ability of the slab reinforcement to bend around the cuts of the connector, and not the ductility of the connector itself.

It is very interesting to note the fact that in the case of stud connectors, the maximum loading value was almost the same (as the shear area for the connectors is about the same), but the slip for the maximum force was more than double in favor of the specimen with 22mm studs. However, the headed stud connectors showed an expected behavior, by a rather good ductility and a resistance according to their classic design. As expected, the lowest performance in terms of resistance was reached by the anchor connectors (PT-A specimen), as they had in fact the smallest shear area.

The initial stiffness (computed between the points of 0.1 and 0.4 times the maximum force F_{max}) has the highest values for the LL and II specimens, considered a priori as rigid connectors. A relatively high rigidity was obtained for the case of specimen anchor hooks (PT-A-M), value double than the one recorded for stud specimens. However, the initial stiffness is a value that is very sensitive to the method adopted for its computation and considering the fact that the values of displacement used for the calculation of rigidity are very small and generally vary from 0.05 to 0.2mm.

Results of cyclic tests

The cyclic tests were conducted according to the ECCS loading procedure, applying the loading in displacement control by 3 cycles for each even multiple of the δ_y value resulting from the corresponding monotonic test.

Figure 6 displays the behavior of the cyclic specimens. In Figure 7 it is shown the comparison between the envelope curves of the semi-cycles in compression with the monotonic curves of similar specimens. The monotonic yielding displacement is also represented. As a general trend, all the cyclic specimens have shown a reduction both in strength and ductility capacity. For example, for the specimen PT-16 with 16 mm headed studs, the P_{Rk} resistance reduction is about 40%, while the slip capacity is reduced by more than 50%, as compared to the monotonic tests. The same conclusion could be stated for the PT-22 specimens, but with a higher degree of reduction in ductility.

Generally, the main reason for resistance decrease in cyclic loading is represented by local crushing of concrete and/or low-cycle fatigue of steel connectors. It should be mentioned that the ECCS loading procedure is particularly severe, and could have contributed to very poor cyclic performance of specimens.

A particular attention should be payed to the perfobond connectors under cyclic loading. As proved by the experimental tests this represents the most dangerous situation for users. Although the monotonic test has proved a quite good behavior, leading to the best ductility and resistance among the monotonic tests, the cyclic test has proved a very poor behavior. This is proven by 40% reduction in resistance and a very small ultimate slip displacement δ_u (0.6mm). The problem in this case appears due to the loss of the shear connection between the steel connector and the concrete in the very first cycles due to the “knife” effect of the perfobond connector.

In the following cycles, the strip connector practically slides freely on the concrete slab. Consequently, there takes place a rapid decrease of its resistance and practically there is no energy dissipation during the cycles.

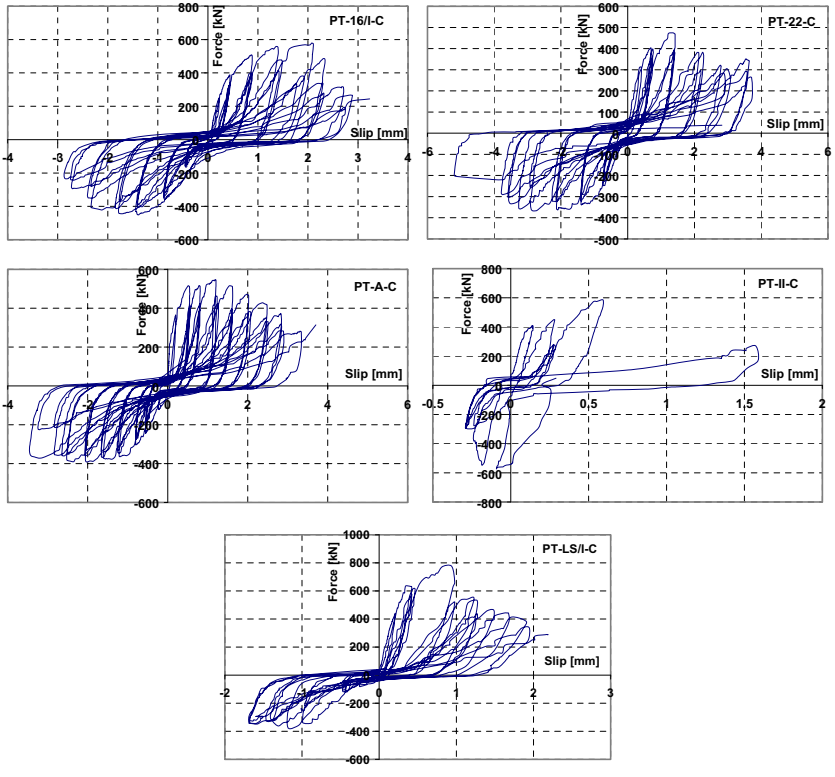


Fig. 6 – Force-slip curves for cyclic specimens.

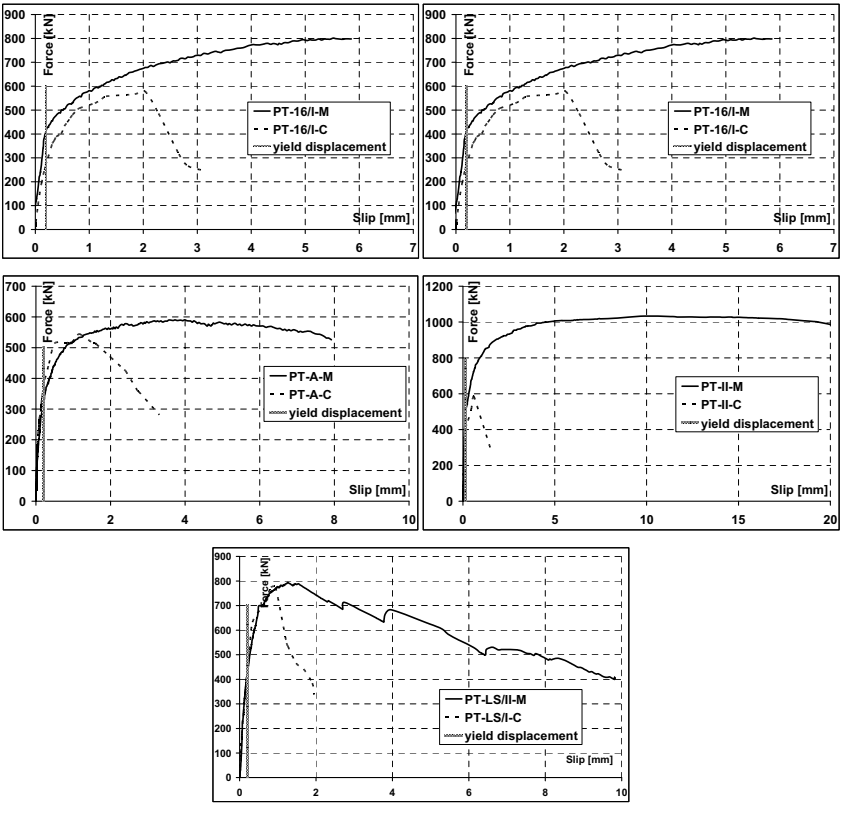


Fig. 7 – Differences in monotonic and cyclic envelopes.

However, another interesting situation appears in the case of LL (PT-LS) and anchor hook (PT-A) specimens, where, despite the important reduction in ductility (δ_u < 2mm for both cyclic specimens), the resistance capacity reduction is under 10%, as compared to the one of monotonic tests. This fact is due to the failure mode which is more linked to the steel elements than to concrete crushing.

As a general idea, it has to be stressed out that in all cyclic cases, the slip capacities do not pass the ductility criterion of 6 mm stipulated in Eurocode 4-1, 6.6.1.1.

Although a limited study, cyclic tests clearly show that monotonic response do not necessarily lead to the same cyclic performance and consequently the use of shear connectors for the structural zones in which reversal of bending moments is possible should be reconsidered.

ANALYSIS OF THE FAILURE MODES

Figures 8 and 9 show the typical failure modes for different types of connectors considered within the study. With the exception of the perfobond strip specimens, all series of tests have proven the same failure under monotonic respectively cyclic loading.

In the case of the shear stud specimens (Figure 8 a), although the global behavior can be characterized as ductile, the failure was brittle in nature, by the shearing of the headed studs located on one side of the specimen. It is to be added that there is no evidence of concrete crushing, with the exception of the concrete located at the base of the shear stud.


a)

b)

Fig. 8 – Failure modes (by shear) for headed studs and reinforcement hooks.

The failure mode of specimens with anchor hooks (Figure 8 b) was by shear of the reinforcement hooks at the steel profile-concrete interface. No crushing of concrete was recorded. This type of failure was considered to be ductile, due to the fact that not all the shear fractures were at the same time.

For LL specimens failure occurred by bending of the shear profiles (Figure 9), but without a real fracture of the steel material. In these cases, the flange embedded in concrete was pulled out very rapidly from the concrete after reaching the maximum load. Other researchers have proven that the use of reinforcing bars through the embedded flange could postpone the failure and improve the resistance and ductility performances.



Fig. 9 – Failure modes by bending for LL profiles.

The CP-II-M specimen represents a special case, due to the fact that the failure was not related to the steel connector, but to the concrete slab and reinforcement. Practically, it acted as a „knife“ into the body of the concrete slab. The first signs of failure were by longitudinal cracks of the concrete slabs in the middle of the slabs, and continued by the crushing of concrete at the bottom of the slab. After the crushing of the destroyed concrete, there was found that the transversal reinforcing bars were bent by the perforated steel plates. In fact, this type of connection led to a ductile behavior for the monotonic specimen, but also to a rapid loss of concrete-to-connector adherence in the case of cyclic specimen.

COMPARISON OF ANALYTICAL AND NUMERICAL RESULTS

In order to have a correct evaluation of the experimental results, it is very instructive to have a comparison with the analytical values, usually used in the design or evaluation of the characteristic resistance.

Analytical evaluation of the shear strength ($P_{R,k}$)

In the case of shear stud connectors, the evaluation of the shear resistance for a single connector is done by the classical formula, also provided in the Eurocode 4 (paragraph 6.6.3.1):

$$P_{R,k} = \min\left(\frac{0,8 f_u \pi d^2}{4\gamma_V}; \frac{0,29\alpha d^2 \sqrt{f_{ck} E_{cm}}}{\gamma_V}\right) \quad (1)$$

where:

- f_u is the ultimate resistance of the steel connector;
- d is the diameter of the shank;
- γ_V is the partial safety factor for connectors (taken here 1,0);
- α is the shape coefficient (α=1,0 for the geometry used in these tests);
- f_{ck} is the compressive resistance of concrete, according to Eurocode;
- E_{cm} is the Young modulus for concrete.

The shear resistance of an angle profile is given by the following formula, not mentioned in the latest edition of Eurocode 4, but present in some older versions of the same code:

$$P_{R,k} = \frac{10 b h^{3/4} f_{ck}^{2/3}}{\gamma_V} \quad (2)$$

where (only notations different from above):

- h is the height of the free flange (embedded in concrete);
- b is the length of the angle connector.

For the hook shear connectors, considering their shape and the fact that the concrete was not practically affected during testing, the shear resistance was computed on the principle of shearing of the steel anchors, as follows:

$$P_{R,k} = 1.15 \frac{f_u A_a}{\gamma_V} \quad (3)$$

where (only notations different from above):

- A_a is the area of the connector bar (diameter is of 10mm);
- f_u is the ultimate resistance of the reinforcing bar.

The analytical evaluation of the perfobond connectors is practically very difficult to obtain due to the fact that these types of connectors are relatively new on one hand, and on the other they can have various forms and shapes, according to the designer's will. Therefore, the following formula was adopted, based on the research done by Chromiak and Studnicka on similar connectors.

$$P_{R,k} = 273 + 14.1 f_{ck,cyl} + 313 A_{st} \tag{5}$$

where (notations different from above):

- A_{st} is the transversal reinforcement [mm^2/mm].

It is to be mentioned however, that the above formula was found by an analytical regression on a series of tests with the height of 100mm (120mm was used for the perfobond connectors in the case of PT specimens) and using circular cuts for the passage of reinforcement.

Comparison with experimental results

The following table presents the analytical and experimental values of shear resistances for a single connector, The last column of the table presents the difference in percents between the two values, positive values being in the safe side.

For the stud connectors, the analytical evaluation is on the safe side only for the monotonic tests. The same values prove that although there is a certain reserve in analytical evaluation, it is not sufficient to cover the loss of strength resulted from cyclic regime. Therefore, the resistance reduction to 75% in the case of connectors present on composite dissipative members, stipulated in Eurocode 8-1 7.6.2 (CEN, 2004) is fully justified in the case of headed stud connectors.

The results for anchor hooks connectors clearly show that both experimental strengths (monotonic and cyclic) are much greater than the analytical ones. This demonstrates that the failure mechanism is not by pure shear of the reinforcement, but more precisely by pulling of the reinforcement. The latter leads to an analytical value $P_{R,k}$ of 102 kN, closer to the experimental values. It is to be noticed the small loss of resistance in the case of cyclic loading, which can lead to the conclusion that a good monotonic design (with a small reserve in strength) can also lead to a safe design in cyclic loading.

The analytical strength evaluation of perfobond connectors as chosen for our case represents an unsafe solution with regard to the results of the monotonic test, and in this case an adequate formula should be used. The problem becomes quite dangerous when used in cyclic loading, due to the fact that the loss of strength is almost 50% in cyclic loading, as shown in the description of the tests. In the authors' opinion, this is a matter of further investigation, but mainly in monotonic loading, the cyclic use of such connectors being not adequate in composite members under cyclic loading.

Table 3 – Analytical and experimental comparison of shear strengths.

Specimen	$P_{R,k}$ – Analytical evaluation [kN]	$P_{R,k}$ – Experimental evaluation [kN]	*Difference [%]*
PT-16/I-M	78,9	90,1	*+12,4*
PT-16/I-C	78,9	65,1	*-21,2*
PT-22-M	149,2	166,0	*+10,1*
PT-22-C	149,2	106,7	*-40,8*
PT-A-M	59,1	132,9	*+55,5*
PT-A-C	59,1	122,5	*+51,8*
PT-II-M	631,5	464,9	*-26,4*
PT-II-C	631,5	263,7	*-139,0*
PT-LS/II-M	199,3	178,7	*-11,5*
PT-LS/I-C	201,4	174,2	*-15,6*

For angle connectors (PT-L specimens), the analytical values are unsafe with respect to the experimental results both in monotonic and cyclic loading. As shown by other researchers, the use of longitudinal reinforcement bars that pass through the free flange of the angle will lead to a proper anchoring of connectors in concrete and to a better behavior and increased resistance.

CONCLUSIONS

Although a limited study, the experimental tests and their analytical evaluation of the shear resistance lead to the following conclusions:

- in monotonic response, the global behavior of connectors (judged in terms of Force-Slip curve) depends mainly on the type of connectors chosen. The ductility under monotonic loading could be characterized as satisfactory (according to Eurocode 4). However, cyclic loading in inelastic range drastically diminished the slip capacities in all the cases considered. Further investigations are necessary to determine if the 2 mm slip capacity - obtained in several cyclic tests – is sufficient in order to maintain the connection of a composite member subjected to cyclic loading;

- cyclic loading introduces an important reduction in the characteristic shear resistance P_{Rk}, ranging from 10 to 40% as compared to the corresponding monotonic ones. Consequently, the 25% reduction in the connector's resistance (as requested by Eurocode 8-1 chapter 7) is justified for headed stud connectors, but in other cases this reduction is insufficient;

- the use of perfobond connectors should be avoided in composite elements that may undergo cyclic loading, their behavior being completely inefficient in cases of reversal loadings.

In the author's opinion, there are two alternatives to correct the poor performance of shear connectors under inelastic cyclic loading:

(i) the first one is to ensure, through capacity design principles, an elastic response of the shear connectors, avoiding inelastic deformations. Regarding this subject,

the author's opinion is that the 0.25 reduction in the resistance of connectors under cyclic conditions should be reconsidered and analyzed from case to case;

(ii) the second alternative is to consider in design connectors with adequate strength and ductility to sustain inelastic deformations. For this purpose further analyses are necessary at structural level, in order to identify the required ductility in case of reversal loading.

ACKNOWLEDGEMENT

This work was carried out in the CEMSIG Laboratory of the Department of Steel Structures from the Politehnica University of Timişoara. The financial support from the Romanian Ministry of Education and Research (CEEX-ET grant no. 3153/13.10.2005) is gratefully acknowledged.

REFERENCES

Bursi, O. (editor): *Seismic qualification of Cast-in Channels and Shear Connector Devices between Steel and Concrete*, Report No. 4, CASCADE Project Task 6: Enhancement of Standards for Dynamic Qualification, 2004.

CEN EUROCODE 4 - Part 1.1 (EN): *Design of composite steel and concrete structures* Section 1: *General Rules and Rules for Buildings,* Brussels, September 2004.

CEN EUROCODE 8 (EN): *Design of structures for earthquake resistance* – Part 1: *General rules, seismic actions and rules for buildings,* Brussels, December 2004.

ECCS: *Recommended Testing Procedures for Assessing the Behaviour of Structural Elements under Cyclic Loads*, TC 1, TWG 1.3 – Seismic Design, n° 45, 1986 .

Oehlers, D.J. & Bradford, M.A.: *Composite Steel and Concrete Structural Members*, ISBN 008041919 Pergamon, 1995.

Chromiak, P., Studnicka, J.: *Computer Model for Perfobond Connector*, Proceedings of the International Colloquium on Stability and Ductility of Steel Structures – SDSS 2006, Lisbon, 06-08 September 2006 IST Press, Lisbon ISBN 972-8469-61-6.

NEW STEEL-CONCRETE SHEAR CONNECTION FOR COMPOSITE BRIDGES

Jean-Paul Lebet
Swiss Federal Institute of Technology Lausanne, EPFL
Steel Structures Laboratory, ICOM
1015 Lausanne, Switzerland
Jean-paul.lebet@epfl.ch

ABSTRACT

This paper presents experimental and analytical research that was conducted on new connections “by adherence” for steel-concrete composite bridges. Their resistance is achieved by the frictional shear resistance of different interfaces positioned in a judicious manner. These connections make it possible to erect the structure quickly with full-depth precast concrete slabs, while the concreting works on site are limited as much as possible. Experimental results show that these connections exhibit a high resistance to horizontal shear forces and are very rigid compared to traditional connectors (headed studs). However, their ductility is limited. Based on the experimental results, a calculation model was developed and was used in a parametric study. Some results of the parametric study are presented and discussed in this paper. A simplified method for determining the resistance of these connections, design rules and recommendations for construction are proposed.

INTRODUCTION

Nowadays, the steel-concrete connections used in composite bridges with precast slabs (i.e., groups of headed studs connected to the slab when concreting the pockets in the slab on site) are not helping to achieve a short construction duration. Indeed, this kind of connection tends to slow down the assembly work because of the numerous small quantities of concrete that need to be poured on site to fill the pockets. Moreover, cracks may develop in the corners of the pockets, which tend to increase the risk of degradation by corrosion of the slab reinforcement.

The duration of on-site work has a significant influence when building new bridge structures, or widening or replacing existing bridges, not only on the costs, but also on the potentially harmful effects of the construction work. The generated noise, pollution, traffic jams, and deviations [Collin and Johansson 1999] are detrimental to people. Thus, it is of interest to design structures in such a way that the construction time is minimum. Steel-concrete composite bridges are ideal for this purpose [Tadros and Baishya 1998, Lebet and Meystre 2006] as the steel beams may be welded and the concrete slab precast in the factory, leaving only the erection and assembly work to be performed on site. Consequently, on site, the connection between the precast slabs and the steel structures must be realized in a as fast and effective way. This requirement leads to the need for developing new types of connections. Connections by adherence [Dauner 2002], whose resistance is due to friction between the various interfaces, constitute a very promising solution to this problem. Figure 1 illustrates an example of a connection by adherence. An embossed steel plate is first welded longitudinally on the upper flange of the steel

beam. The upper flange may then be coated with a bonding layer which consists of an epoxy resin and coarse sand. The concrete deck elements are precast in the factory with a longitudinal rib in the lower face. The concrete surface of this U-shaped rib is roughened by the use of a mechanical (water-jetting, sandblasting) or chemical (retarder) technique. On site, the precast deck elements are laid on the steel girders and the transverse joints of the slab are glued together. The deck is then longitudinally prestressed (for discussion on prestressing see [Dauner 2002]). The gap between the steel girder and the concrete deck elements is finally injected with a cement paste from one end of the bridge, in a manner similar to that of a post-tensioning duct. The injection procedure was successfully tested on a 50 m long connection ([Dauner 2005]). When hardening, the cement paste makes the static link between the slab (rough concrete) and the beam (embossed steel plate, bonding layer).

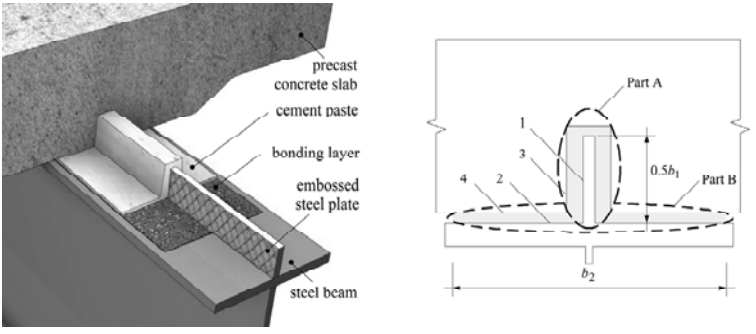


Figure 1 – Connection by adherence and definition of interfaces 1 to 4

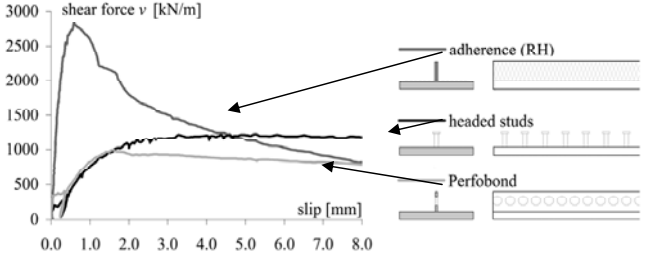


Figure 2 – Comparison between different connection types

Many push-out tests on connections by adherence and on other types of connections have been conducted [Dauner 2005, Thomann 2005]. All the tested specimens were made of two precast concrete elements that are connected to the steel connectors with an injection of cement paste of strength f_c = 80 MPa. Some of the results are illustrated in Figure 2. The connection with headed studs was made

of 9, 22 mm diameter studs, per meter. The Perfobond connection [Leonhardt et al. 1987] is made of a steel plate with 14 holes, 50 mm diameter, per meter. There is no transverse reinforcement through the holes. It can be seen that the connections by adherence exhibit very high shear resistance and stiffness compared to headed studs and Perfobond. The ductility of the connection by adherence is however limited compared to that of headed studs. Among the various types of connections by adherence tested, those with an embossed steel plate welded perpendicularly to the steel beam's upper flange were the most promising. These connections may be used with a bonding layer on the beam's upper flange (RH connections) or without a bonding layer (R connections). Research on these two kinds of connections by adherence and their application on composite beams are considered in this paper.

CONNECTION BEHAVIOUR

When loaded in shear, the deformation of the connection creates compressive stresses on the sheared interfaces (Figure 3). When a slip, s, is longitudinally applied between the steel beam's upper flange and the concrete slab, uplifts, u_i, (subscript i applies for the interfaces according to Figure 1, i = 1…4) occur perpendicular to the interfaces. These uplifts are due to the roughness of the interfaces, as illustrated in Figure 4 (right). Figure 3a illustrates the uplift, u_1, that occurs between the embossed steel plate and the cement paste (interface 1). Uplift, u_1, is partially prevented both by the concrete slab around the embossed plate and by the interfaces of part B positioned perpendicularly to the embossed plate-cement paste interface. Thus a normal force, N, develops in the lower reinforcement of the concrete slab, while shear stresses, $\tau_{imp,2}$, develop in the bonding layer-cement paste interface (interface 2). Normal compressive stresses, $\sigma_{conf,1}$, (subscript "conf" applies for "confining effects") develop from equilibrium on the embossed steel plate-cement paste interface (interface 1). Equation (1) expresses this equilibrium. ($\sigma > 0$ is defined in compression).

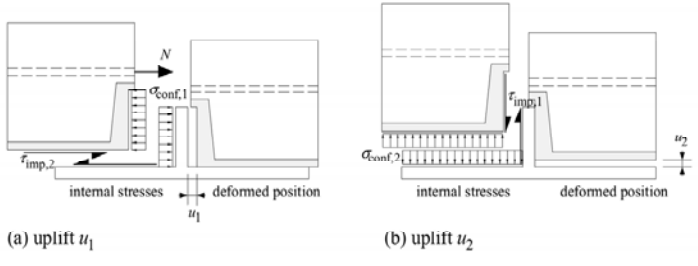


Figure 3 – Deformed position and associated internal stresses and forces

Figure 3b illustrates the uplift, u_2, that occurs between the bonding layer and the cement paste (interface 2). The same considerations apply as for uplift u_1, except that the slab does not restrain uplift u_2. Normal compressive stresses, $\sigma_{conf,2}$, develop by equilibrium on the bonding layer-cement paste interface. Equation (2) expresses this equilibrium. k_{slab} is the stiffness of the slab around part A of the connection. The results of a study by [Thomann and Lebet 2007] were used to propose the simplified

analytical relationship (3) between k_{slab} and the relevant parameters: E_c is the Young's modulus of concrete, h is the depth of the precast concrete slab, $h_1 = b_1/2$, h_2 and h_3 are the position of the lower and upper layers of reinforcement above the U-shape of the slab, respectively

$$\sigma_{conf,1}(s) = \sigma_{conf,3}(s) = k_{slab}(u_1+u_3)+\tau_{imp,2}\frac{b_2}{b_1} \quad (1)$$

$$\sigma_{conf,2}(s) = \sigma_{conf,4}(s) = \tau_{imp,1}\frac{b_1}{b_2} \quad (2)$$

$$k_{slab} = \frac{E_c h_3}{33 h h_1}\left(\frac{h_2+h_3}{h_2}\right)^{0.3} \quad (3)$$

According to the failure criteria for the interfaces (see Figure 5a below), the shear resistance, τ_{Ri}, in the interfaces increases with $\sigma_{conf,i}$. Although not illustrated in Figure 3, uplifts, u_i, occur in the other interfaces also (u_3 in interface 3 and u_4 in interface 4, Figure 1). These uplifts increase $\sigma_{conf,i}$ and consequently cause τ_{Ri} to increase also. The shear resistance due to u_3 and u_4 can be explained in the same way as the one due to u_1 and u_2.

Moreover, external normal stresses may also act on the interfaces and consequently increase the shear resistance of the connection. These normal stresses may be caused by a transverse prestressing or by the transverse bending of the slab, for example. These stresses, $\sigma_{ext,i}$, should be added to the normal compressive stresses due to confining effects, $\sigma_{conf,i}$,, according to Equation (4). Of course, depending on the eccentricity of the transverse prestressing cables, the normal stresses due to prestressing may act in tension. The eccentricity should however be chosen so that the stresses under long-term actions (prestressing, self-weight of the slab) always act in compression on the connection.

$$\sigma_i(s) = \sigma_{conf,i}(s) + \sigma_{ext,i} \quad (4)$$

Thus, the main parameters that influence the shear resistance of the connection are the interface behaviour (slip, s, - uplift, u, relationships, failure criteria and slip, s, - shear stress, τ, relationships), the confining effect of the slab around part A of the connection, the geometry (b_1, b_2) and the external stresses, σ_{ext}, acting on the interfaces.

INTERFACES BEHAVIOUR

The interfaces behaviour was studied experimentally by means of direct shear tests. The experimental setup was similar to the one used by [Matsumura 1990]; a block of cement paste was casted between two plates (embossed steel or rough concrete or steel with bonding layer) as illustrated in Figure 4.

These tests are described in detail in [Thomann 2005]. The interfaces are loaded in compression and shear. There is no mechanical connection, only the natural adherence and roughness between surfaces which resists shear. The normal stress, σ, is kept constant during one test, while slip is increased until failure and then until the residual shear stress is stabilized to a constant value. Thirty-six specimens were tested. The parameters studied were the normal stress, σ, the type of interface

(embossed steel plate-cement paste, rough concrete-cement paste, bonding layer-cement paste) and the cement paste compressive strength, f_c.

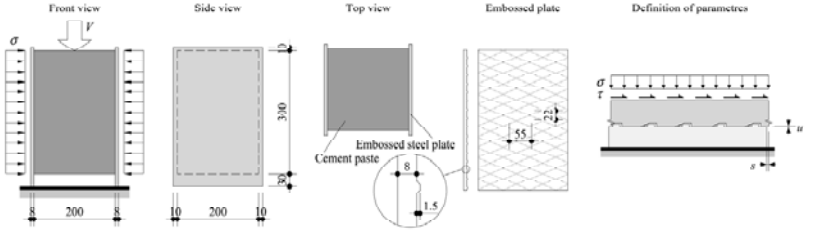


Figure 4 – Direct shear tests setup and definition of parameters

Figure 5 illustrates some of the most important results of the direct shear tests. Figure 5a illustrates the failure criteria between normal stress, σ, and shear stress at failure, τ_{max}, for different interfaces. It can be observed that this relationship is linear, except for the bonding layer-cement paste interface. In that case, the maximal shear stress is governed by loosening (debonding) of the epoxy resin from the steel plate at about 5.5 MPa, corresponding to a normal stress of about 1.8 MPa. Figure 5b illustrates the constitutive laws between slip, s, and shear stress, τ, for two different values of σ. In this figure the ductility seems to increase with decreasing values of σ. However, this observation was not confirmed by other tests: it was rather shown [Thomann 2005, Thomann and Lebet 2007] that the post-failure average slope in a τ-s diagram is independent of the normal stress, σ. Figure 5c illustrates the kinematical laws between slip, s, and uplift, u, where the asymptotic behaviour and the dependency with σ can be observed.

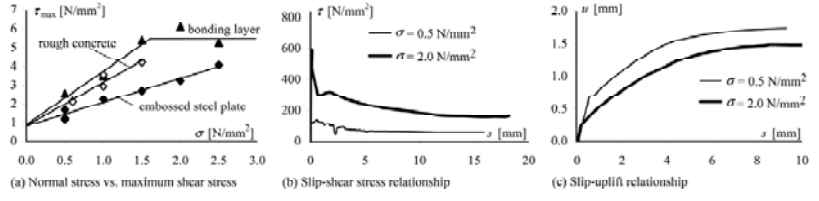


Figure 5 – Typical results from direct shear tests

These three different kinds of laws were modeled and calibrated using the test results [Thomann 2005]: a linear failure criterion between τ_{max} and σ (Equation (5)); a trilinear constitutive law between τ and s with a maximal value $\tau_{max}(\sigma)$ (Equation (6), and an exponential kinematical law between s and u (Equation (7)), which also depends on the value of σ (Figure 6). These laws take into account the cement paste strength, the normal stress acting on the interface and the roughness of the interface (embossments geometry, concrete roughness, etc.). The coefficients c, d, e, s_α, $u_{max,0}$, r and $k(s)$ in Equations (5) to (7) are experimentally based coefficients and can be found in [Thomann 2005, Thomann and Lebet 2007].

$$\tau_{max} = c + d\sigma \leq e \tag{5}$$

$$\tau = k(s) \cdot s \tag{6}$$

$$u = u_{max}(1 - e^{-s/s_\alpha}); \quad u_{max} = u_{max,0} - \frac{r\sigma}{f_c} \tag{7}$$

The constitutive and kinematical laws are strongly dependant on the normal stress, σ. However, as shown in Equation (4), the normal stress acting on the interfaces in a connection by adherence is not constant but increases with increasing slip. To take a varying normal stress into account, an incremental calculation method was developed [Thomann 2005], in which the value of s_{ij}, u_{ij}, τ_{ij} and σ_{ij} were calculated for each step j. For a given interface i, these values are simplified as s_j, u_j, τ_j and σ_j.

Figure 6 illustrates this method for a linear boundary condition: the confinement is a linear relationship of slope $\Delta\sigma/\Delta u$, starting at (first step, j = 1) $\sigma = \sigma_1$ when $s_1 = 0$ and $\tau_1 = 0$. When a slip $s_2 = s_1 + \Delta s$ is applied (step 2, j = 2), the corresponding shear stress τ_2 can be calculated from Equation (6) for $\sigma = \sigma_1$. Uplift, u_2, can be determined with Equation (7). Once u_2 is known, the new normal stress, σ_2, corresponding to the slip, s_2, can be calculated according to the boundary condition. If σ_2 is much larger than σ_1, an iterative calculation must be done with the corresponding constitutive and kinematical laws. If σ_2 and σ_1 are close to each other, the error remains small and no iteration is needed. A new calculation step (step 3, j = 3) can start by increasing slip to $s_3 = s_2 + \Delta s$ with the laws corresponding to $\sigma = \sigma_2$. This calculation process continues until failure ($\tau = \tau_{max}$), which occurs when the loading path (thick dotted line in Figure 6) reaches the failure criterion (Equation (5)). The calculation can even go further if the laws are also defined for the post-failure domain.

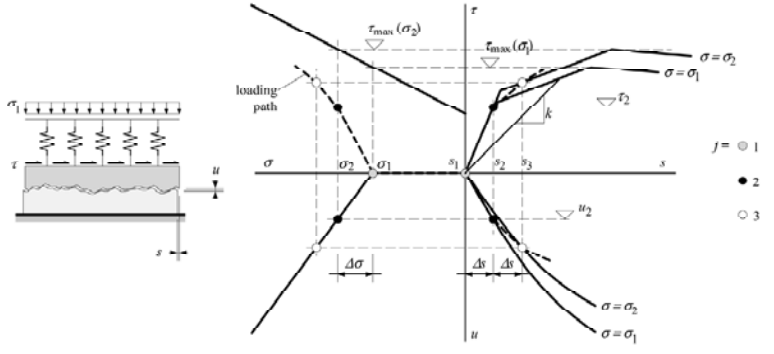


Figure 6 – Calculation method for a confined interface

MECHANICAL MODEL OF THE CONNECTION

To calculate the shear resistance, v_R, of the connection by adherence, a mechanical model was developed [Thomann 2005]. This model is based on the kinematics described in Figure 3, on the behaviour of the interfaces (Equations (5) to (7)) and on the slab's stiffness around the connector (Equation (3)). The boundary conditions

are considered in the model as external normal stresses acting on the interfaces. Figure 7 illustrates the comparison between the push-out test results and the corresponding simulations of the mechanical model for the different connection types (R and RH connections). It can be observed that the model provides very accurate results for both the pre- and the post-failure domains. The prediction of the maximal resistance is also excellent. Although not illustrated here, the model was also checked with results from push-out tests on other types of connections by adherence (for example using different geometries and interfaces) [Thomann 2005]. The mechanical model was consequently used for a parametric study. In this study, the effect of different geometries (b_1, b_2, Figure 1), and the effect of external stresses, σ_{ext}, was closely investigated. The results were used to develop a simplified calculation method for the connection.

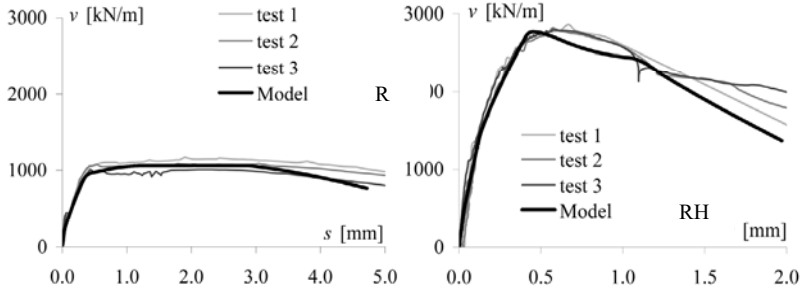


Figure 7 – Comparison between test results and mechanical model

SIMPLIFIED CALCULATION METHOD FOR THE CONNECTION

The general design of a connection by adherence is illustrated in Figure 1. The bonding layer on the upper flange provides additional shear resistance but makes the post-failure behaviour more brittle (Figure 7). Consequently, an RH connection with bonding layer should be used only when statically needed. Otherwise the more ductile R connection without bonding layer should be used.

The design must obey certain hypotheses of the mechanical model:

1- In case where a bonding layer is used, its width, b_2, must be larger than b_1 (double height of the connector).

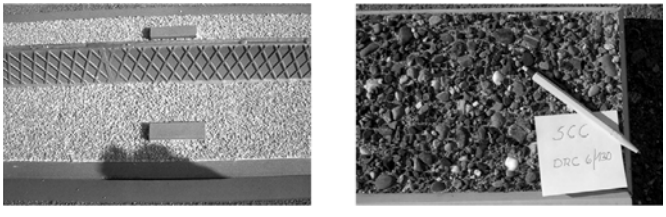
2- A transverse reinforcement must be placed as low as possible in the concrete slab, that is, as close as possible from the top of the connector (i.e. from the top of the U-shaped rib in the slab). This has a very favorable effect on the stiffness of the slab.

3- Stirrups must be placed around the rib in the concrete slab. This prevents the failure surface to propagate inside the concrete slab instead of following the interfaces. The stirrups can be placed directly against the formwork without a concrete cover.

4- The design of possible transverse prestressing cables and the amount of prestressing should be chosen so that the lower layer of the concrete slab

remains compressed under long-term loads which are applied after the connection has been injected.

The materials must meet the following requirements. The cement paste used for the injection must have a compressive strength, f_c, of at least 80 MPa. The connector must be made of two embossed steel plates BRI 8/10 S235 welded back to back and continuously welded on the upper flange of the steel beam. The embossments should be oriented as illustrated on Figure 8a, i.e. perpendicular to the shear force. The concrete surface in contact with the cement paste must be roughened by the use of a chemical retarder, for example. The depth of the roughness must be of at least 6 mm, as shown on Figure 8b. Where a bonding layer is used, the steel flange must be sandblasted (SA 2½) immediately before the epoxy resin is applied. No other corrosion protection should be applied to the upper face of the flange. The sand must be of diameter 2-3.2 mm and applied directly on the fresh epoxy resin. An example of the bonding layer is given in Figure 8a. Finally, the injection of the cement paste must be controlled by using control pipes and manometers, for example. More information about dimensioning, pre-design, detailing and execution of connection by adherence can be found in [Dauner 2002, Thomann 2005].



(a) Embossed plate and bonding layer (b) Rough concrete

Figure 8 – Surfaces prior to injection

If the pre-design is carried out according to the aforementioned instructions, the calculation of the shear resistance, v_{Rd}, can be carried out according to the following nine points:

1- Choose the design of the connection, the slab and the transverse reinforcement. If transverse prestressing is used, choose the force, P and the eccentricity.

2- Calculate the neutral axis position, x_c. As shown in Figure 9, x_c is the height of the neutral axis corresponding to bending and normal force in the slab. To calculate x_c, consider only the long-term actions applied after the connection has been injected.

3- If $x_c < h_1$ (height of the connector), then set $h_{1,\text{eff}} = x_c$ and $b_1 = 2h_{1,\text{eff}}$. This means that the height of a connector that is above the neutral axis will not be considered in the shear resistance. Thus, it is useless to design a connection with $h_1 > x_c$.

4- Calculate the external normal stresses, $\sigma_{\text{ext},1}$ (and $\sigma_{\text{ext},2}$ in case of an RH connection), acting on the connection. Consider only the long-term actions applied after the connection has been injected. Traffic loads should not be

considered, unless it can be proved that these loads necessarily act in the same section as the one where the shear force will be maximal. Limit (cut off) the compressive normal stresses to $\sigma_{ext,1} \leq 3.0$ MPa and $\sigma_{ext,2} \leq 1.0$ MPa. This condition is necessary to respect the stress range for which the laws of behaviour for the interfaces were validated. In case the external stress is in tension, the shear resistance must be locally set to zero.

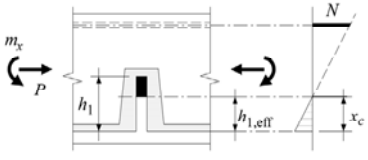


Figure 9 – Neutral axis x_c and height $h_{1,eff}$

5- Calculate the slab's stiffness, k_{slab}, according to Equation (3).

6- For the RH connection, ensure that the failure surface will not be located between the bonding layer and the steel surface; this would lead to a very brittle failure. This can be checked with Equation (8) and Figure 10.

$$\bar{\sigma}_{ext,2} = \sigma_{ext,2} + \frac{\sigma_{ext,1}}{9.2} \tag{8}$$

7- Determine the value of u_{conn} from Figure 10. If the connection is of type RH, calculate also the coefficient χ using Equation (9).

$$\chi = 1.0 + 5\frac{b_1}{b_{tot}} \leq 2.0 \tag{9}$$

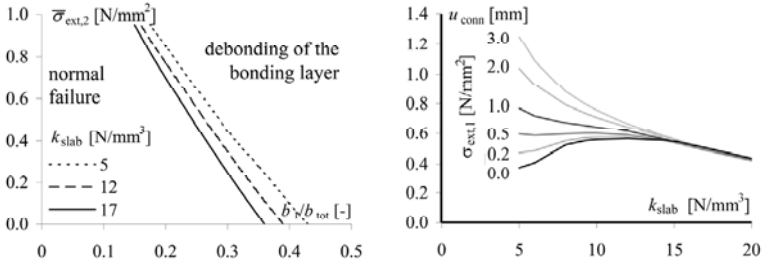


Figure 10 – Criterion to control position of failure surface and coefficient u_{conn}

8- Calculate v_{Rk} with Equation (10) for R connections and with Equations (10) to (12) for RH connections.

$$v_{Rk,1} = 0.8b_1(0.93 + 0.8(\sigma_{ext,1} + k_{slab}u_{conn})) \tag{10}$$

$$v_{Rk,2} = 0.8b_2(0.94 + 0.4\sigma_{ext,2}) \tag{11}$$

$$v_{Rk} = \chi(v_{Rk,1} + v_{Rk,2}) \tag{12}$$

9- Calculate v_{Rd} with Equation (13).

$$v_{Rd} = v_{Rk} / \gamma_v \,, \qquad \gamma_v = 1.25 \text{ according to [Eurocode 4 part 2, 2005]} \tag{13}$$

COMPOSITE BEAMS

Because of the reduced ductility of the connections by adherence, it is of interest to know whether a steel-concrete composite beam with such a connection can reach the full plastic bending moment or not. Because the slip capacity is much smaller than the 6 mm required by European standards [Eurocode 4 part 2, 2005], it is clear that an elastic calculation of the longitudinal shear flow must be performed. Thus, a calculation method for the elastic distribution of the shear flow when the bending moment reaches the plastic resistance is needed.

Six steel-concrete composite beams spanning 4 to 8 meters and connected by adherence were tested to study the failure mechanism and the distribution of shear flow in the steel-concrete interface [Thomann 2005]. These beams were also numerically simulated with an ANSYS macro developed by [Bärtschi 2004]. The test setup is shown on Figure 11. Typical test results are shown in Figure 12 for three of the six tested beams. This Figure shows a diagram with deflection, w, at mid-span vs. applied load, F_{test}, on the beam (normalized by the calculated load, $F_{Mpl,b}$, that creates a plastic hinge at mid-span taking into account the actual material properties of steel and concrete). It can be seen that the full plastic bending resistance can be reached with connections by adherence, $F_{test}/F_{Mpl,b} > 1.0$, provided that the connection is designed with sufficient shear resistance. Failure was attained by the crushing of concrete in compression. Beam B3 was tested with a negative bending moment (concrete in tension). The full plastic bending resistance was also reached with this beam. The shear resistance of the connection with concrete in tension was the same as with concrete in compression, which shows that the design method described above may be used both in negative and positive bending moment regions.

However, a large peak was measured in the slip distribution where the bending moment exceeds the elastic bending resistance. This peak corresponds to a peak in the shear flow. It must remain strictly smaller than the shear resistance in the connection because no plastic redistribution of the shear flow can occur due to the limited ductility of the connection. If the shear flow exceeds the shear resistance, even locally, a brittle failure may propagate quickly along the beam's longitudinal axis (zip-flyer effect, [Leskelä 2006]). To calculate this peak, a calculation method based on the non-linear relationship between moment and normal force in the slab was developed. This method is described in [Thomann 2005, Thomann and Lebet 2007].

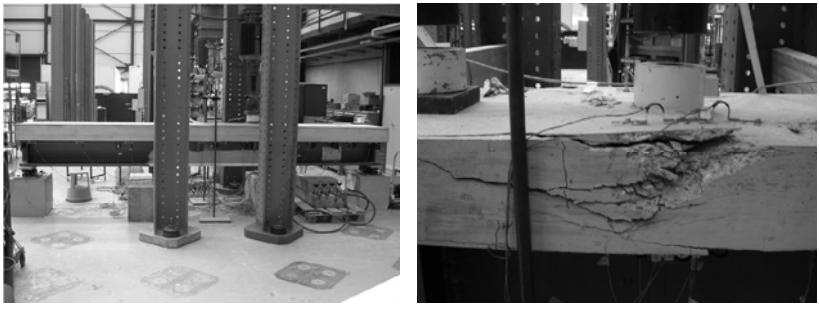


Figure 11 – Composite beam test setup and plastic hinge at mid span of beam B2

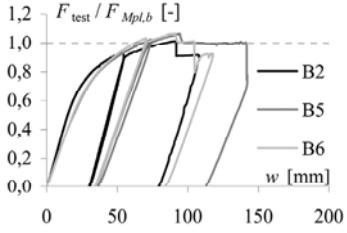


Figure 12 – Test results on three steel-concrete composite beams

CONCLUSiONS

Connections by adherence, whose resistance is due to friction between various interfaces, constitute a very promising solution for the fast erection of steel-concrete composite bridges with full-depth precast decks. The study presented in this paper provides tools for the design of these connections. These connections meet the specified requirements of economy (shorter construction duration) robustness and reliability (confirmed with the fatigue tests actually performed in our laboratory). Their high longitudinal shear resistance and stiffness ensure excellent static behaviour, both under service and ultimate loads. A mechanical model has been developed. It is based on the laws governing the behaviour of confined interfaces loaded in shear. This model takes into account the geometry of the connection (b_1, b_2) and the stiffness of the concrete slab around the connection. Important conclusions are drawn from this work:

- A simplified calculation method for the shear resistance as well as practical recommendations for the pre-design and the detailing are described. The minimal surface roughness for the different materials (embossed steel, concrete, bonding layer) is defined.
- The behaviour of composite beams with connections by adherence has been studied. It has been shown that despite the low ductility of the connection, full

plastic bending resistance can be reached both in positive and negative bending. This is however true only if the shear resistance of the connection is higher than the shear flow at every point. This shear flow must be calculated elastically and thus takes into account the effects of the plastification of the cross-section.

Further research on connections by adherence should investigate in more detail the fatigue and long-term behaviour of the connections. A simpler but still economic and safe calculation method for the ultimate shear resistance of connections by adherence should also be found.

NOTATIONS

b_1, b_2 : width of the interfaces according to Figure 1; $b_{tot} = b_1 + b_2$
E_c : Young's modulus of concrete
f_c : compressive strength of concrete (cylinder)
h, h_1, h_2, h_3: h is the depth of the precast concrete slab, $h_1 = b_1/2$, h_2 and h_3 are the position of the lower, resp. upper, layer of reinforcement above the U-shape of the slab
$h_{1,eff}$: height of the connector for the calculation of the shear resistance, see Figure 9
i : numbering of the interfaces, i = 1…4
j : numbering of the calculation step for the mechanical model
k_{slab} : stiffness of the slab, see Equations (3)
s : slip
u : uplift
u_{conn} : equivalent uplift on the connector for the calculation of the shear resistance
v : shear flow or shear resistance [kN/m]
x_c : position of neutral axis in the transverse direction of the slab, see Figure 9
χ : coefficient to take the confining effect into account
γ_v : resistance factor for ultimate limit state of the connection, γ_v = 1.25
σ : normal stress on an interface
$\bar{\sigma}_{ext,2}$: equivalent external normal stress on interface 2 (for loosening of the bonding layer)
τ : shear stress in an interface

Subscripts

1….4 : refers to interfaces 1 to 4, see Figure 1
conf : due to confining effects in the connection
ext : due to external loads (prestressing, dead weight,…)
imp : due to an imposed displacement
k : characteristic value
R : resistance

REFERENCES

Bärtschi R. (2004). *A nonlinear numerical analysis model for composite beams*, Proceedings of the PhD Symposium, Delft University.

Collin P, Johansson B. (1999). *Wettbewerbsfähige Brücken in Verbundbauweise*. Stahlbau, 68:908 – 18.

Dauner H-G. (2002). *Techniken zum Bau der Fahrbahnplatte bei Verbundbrücken*, Stahlbau, 71:625 – 31.

Dauner H-G. (2005). *Neue Verbindungstechnik im Verbundbrückenbau*, ASTRA Report No. 583. Bern: Swiss Federal Roads Authority.

Eurocode 4, (2005). Final Draft: *Design of composite steel and concrete structures* Part 2: General rules and rules for bridges. European Committee for Standardisation, Brussels.

Lebet J-P, Meystre T. (2006). *Remplacement de ponts sous traffic*, ICOM Report, Steel structures laboratory ICOM, Ecole polytechnique fédérale de Lausanne.

Leonhardt F, Andrä W, Andrä H-P, Harre W. (1987). *Neues, vorteilhaftes Verbundmittel für Stahlverbund-Tragwerke mit hoher Dauerfestigkeit. Beton- und Stahlbetonbau,* 12:325 – 31.

Leskelä MV. (2006). *Accounting for the effects of non-ductile shear connections in composite beams*, In: Leon RT, Lange J, editors. Composite Construction in Steel and Concrete V, Proceedings. American Society of Civil Engineers, Reston (VA), 293 – 303.

Matsumura H. (1990). *Concrete-filled Rectangular Hollow Sections with Inner Ribs*, IABSE Symposium, Construction mixte acier, béton et nouveaux matériaux, Brussels, 119 – 24.

Tadros MK, Baishya MC. (1998). *Rapid Replacement of Bridge Decks*, NCHRP report 407, Transportation research Board, National Research Council, Washington D.C.

Thomann M. (2005). *Connexions par adherence*, ICOM Report No. 535, Steel structures laboratory ICOM, Ecole polytechnique fédérale de Lausanne.

Thomann M. (2005). *Connexions par adhérence pour les ponts mixtes acier-béton*, EPFL Thesis No. 3381, Ecole polytechnique fédérale de Lausanne.

Thomann M, Lebet JP. (2007). *The modelling of an embossed steel-to-cement paste confined interface loaded in shear*, Journal of Constructional Steel Research, 63:693 – 46.

Thomann M, Lebet J-P. (2007). *Design method for connections by adherence for steel-concrete composite bridges*, Structural Engineering International, 16(1):86 – 93.

CONTINUOUS SHEAR CONNECTORS IN BRIDGE CONSTRUCTION

Oliver Hechler
ArcelorMittal, Commercial Sections, Technical Advisory
Esch-sur-Alzette, Luxembourg
Oliver.Hechler@arcelormittal.com

Jacques Berthellemy
Sétra, French National Agency for Road Technology
Bagneux, France
Jacques.Berthellemy@developpement-durable.gouv.fr

Wojciech Lorenc
Wroclaw University of Technology, Faculty of Civil Engineering
Wroclaw, Poland
Wojciech.Lorenc@pwr.wroc.pl

Günter Seidl, Eva Viefhues
SSF Ingenieure GmbH
Munich, Germany
gseidl@ssf-ing.de, eviefhues@ssf-ing.de,

ABSTRACT

Continuous shear connectors offer an upcoming solution for composite beams. They are characterized by a high initial stiffness, bearing capacity and ductility. With their use new and economic construction methods have been invented, e.g. the PreCoBeams (**Pre**fabricated **Co**mposite **Beam**).

PreCoBeams are composite beams associating T-sections acting as tension member with a concrete top chord acting as compression member. Steel parts are generally obtained from rolled steel profiles that are longitudinally cut, with a special shape, in two T-sections. The shape of the cut allows for shear transmission between steel and reinforced concrete, which is continuous regarding the steel.

In general, prefabricated composite bridge elements are produced, consisting of the steel T-section with a precast first phase concrete flange. The second phase concrete layer is then completed in-situ after placing of the bridge elements on the abutments. These PreCoBeam bridges are very economic in design and construction, though the main market drawback for PreCoBeams is the missing design approach for the shear connection.

This paper introduces the static and fatigue design of continuous shear connections used for PreCoBeams derived from recent research activities; however the focus is on the steel design.

INTRODUCTION

Prefabricated composite bridges are commonly built in Germany since 7 years and are now established as a standard solution [Schmitt and Seidl 2001]. This bridging method is based on a prefabricated composite girder (VFT®-girder) as main bearing element of the superstructure. It consists of a steel beam with a precast concrete flange under compression, see figure 1.

A partially prefabricated concrete flange has many advantages. The concrete flange stabilizes the girder during transportation and in the construction stages. Braces are not longer needed for concreting the residual in-situ plate. Scaffolding for the concrete plate is unnecessary. Stiffeners are usually not required because of the high neutral axis of the sections.

Partially prefabricated composite bridges fulfill the demands of modern construction with the well planned and economic use of steel and concrete materials. However the key issues for the success of this method on the German market was achieved by the high degree of prefabrication and the design of new structural systems. Due to the high degree of prefabrication the finishes on site by the steel contractor became superfluous. All elements are manufactured under good conditions in the workshop, so that the quality of the structure increases substantially. The completely assembled girders are delivered on site and can be lifted and placed with a light-weight crane (compared to the heavy weight of pre-stressed concrete girders) as e.g. carried out for the Horlofftal bridge (D), see figure 2. From the beginning, the concrete flange is connected to the steel girder. Consequently the composite action is already present during erection, while the risk of lateral buckling of the beam is reduced. Continuous beam systems and frames can simply be realised by connecting the elements with studs and specially designed reinforcements to control the cracking of the concrete. These new structural systems, especially the frames, may lead to a considerable increase in slenderness. Even 1-bay frames may substitute 2-bays continuous beams of the same total span with disposition of the medium support [Schmitt et. al. 2005].

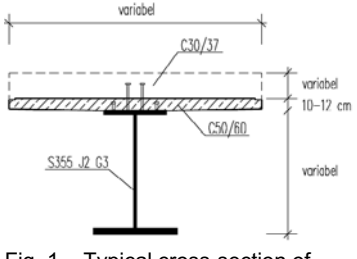


Fig. 1 – Typical cross-section of VFT®



Fig. 2 – VFT®-solution with rolled steel beam

® VFT is a registered trademark of SSF Ingenieure

In addition investigations in continuous shear connectors fabricated by a single cut have been carried out since 1997 (e.g. [Wurzer 1997], [P486 2000], [P612 2007]. These investigations have been based on welding a profiled steel strip on the top flange of a steel beam to achieve a shear transfer in the joint between the steel beam and the concrete chord of a composite beam. The shear bearing mechanism is equivalent to a concrete dowel.

Continues shear connectors are hence defined as continuous steel connecting elements in longitudinal direction. Complete continuous shear connection regarding the concrete side can also be achieved by additionally activating friction e.g. by transverse pre-stressing through the recesses of the dowels [Berthellemy 2009]. This method improves the durability of the concrete decks as it was demonstrated by several highway bridges built in France since 1966.

Consequently the potential of combining the use of this continuous shear connectors and the VFT®-construction technique has been identified and a new, innovative and economic construction method has been invented, the PreCoBeam method **(Pre**fabricated **Co**mposite **Beam**) [Schmitt et. al. 2004].

This prefabrication method uses longitudinally cut-half rolled steel beams. A concrete top chord is then added to each element: this first layer is cast in the workshop. A second phase layer is finally cast in-situ to complete the cross section. This flexible method offers a large choice of cross section possibilities responding to many types of design requirements, see figure 3.

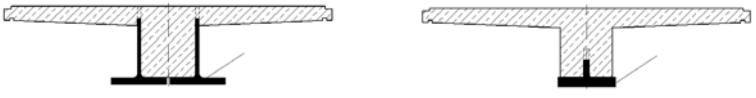


Fig. 3 – Potential cross-sections for PreCoBeams for bridges with concrete dowels

The cutting line of the rolled beam has a special shape and creates concrete dowels identically to continuous shear connectors mentioned before. In figure 4 cut beams already assembled to pairs are shown during appliance of the corrosion protection. In the next step reinforcement bars are placed through the cutting shape (figure 5) and a concrete top chord is concreted to produce a prefabricated bridge element in the workshop. The shape of the cut hereby allows for the shear transmission in the shear joint already in the construction stage similar to VFT®-constructions. Subsequently the prefabricated bridge elements are transported to the site (figure 6), placed on the abutments (figure 7) and, finally, the residual top-layer of the concrete chord is added [Schmitt et. al. 2004].



Fig. 4 – Rolled girders after cutting and coating in the shop



Fig. 5 – Reinforcement for prefabricated concrete plate



Fig. 6 – Transport of the PreCoBeams from the concrete plant to the construction site



Fig. 7 – Placing of the PreCoBeams with 32.50m length

As a result PreCoBeams, with the use of the state of art concerning the concrete dowels technology and integrating the advantages of VFT®-constructions, meet the following targets for competitive and sustainable construction:

- High safety standard for vehicle impact, especially for bridges with only two girders (shock);
- Reduction of coating surface;
- Shear connection that can be designed for fatigue by choosing the web thickness, and using the CL shape if necessary;
- Elementary steel construction nearly without any welding;
- Sparse maintenance and easy monitoring.

Though, the main market drawback for PreCoBeams is the missing design approach for the continuous shear connectors. In the following details of experimental investigations and design concept for PreCoBeams and concrete dowels, especially on the steel part of the concrete dowels, are presented to close this lack of knowledge.

FAILURE CRITERIA OF CONCRETE DOWELS

The bearing capacity of a concrete dowels is limited by steel or concrete failure. In a good design both failures are balanced up to the ultimate load.

Steel failure is limited in the ultimate limit state by a) the shear resistance, b) yielding due to bending of the dowel and in the fatigue limit state by c) fatigue cracks due to dynamic loading, see figure 8. Interaction of shear and bending is also to be considered.



a) b) c)

Fig. 8 – Failure modes for steel

Concrete failure is characterized by several failure modes. Which mode finally occurs depends on the boundary conditions like geometry, concrete grade, reinforcement design, adding of fibers etc. For further information on concrete failure and design reference is given to [PreCo-Beam].

OPTIMISATION OF THE CONCRETE DOWEL BY EXPERIMENTAL INVESTIGATIONS

Static as well as cyclic tests on various shapes of continuous shear connectors using the concrete dowel approach have been performed in the last years. First, tests have been conducted on the Perfobond strip, characterized by cut-outs in a steel strip used for shear connection, leading to a general national approval in Germany [DIBT 1991]. Later, tests focusing on concrete dowels especially designed for the application in PreCoBeams have been carried out [Schmitt et. al. 2004]. The Push-out Standard Tests (POST) according to EC4 (figure 9) and beam tests have been performed. In the tests concrete failure as well as steel failure has been observed. It has been concluded, that the ULS resistance of the steel is almost independent from the shape of the dowel. Also fatigue cracks according to figure 8 c) have been observed in the POST after 2 million load cycles [P612 2007]; they have been caused by a very high level of stress amplitude in the tests. The fatigue cracks observed have a limited propagation due to the fact that the steel part is compressed in the POST (equivalent to negative bending moment region); thus a subsequent ULS-test resulted in no significant decrease of the residual strength.

It has been concluded, that the ultimate limit state design seems not to be so important for the shear connection in PreCoBeam bridges compared to the fatigue limit state.

Consequently an additional test program has been set up in the scope of [PreCo-Beam] to investigate in the following:

- Influence of the shape of dowel on the pressure profile coming from concrete to steel dowel to estimate the loading on each dowel;
- Dependency of the ultimate bearing resistance and the fatigue resistance of the steel on the shape of the dowel with regard to derive mechanical models and equations for design;
- Influence of the dowel shape, reinforcing and geometry of the composite element on the concrete failure at ultimate limit state.

One crucial aspect, especially for the fatigue verification of the steel dowels, is the superposition of stresses resulting from shear in the composite joint and global bending of the beam (normal stresses in the web). In case of a concrete dowel located in a tension zone of the web, fatigue cracks would propagate through the web and possibly into the flange which causes not only failure of the shear connection but collapse of the composite beam. Hence new POST specimens (NPOT) had to be developed to simulate the behavior of a shear connector located in the tension zone [PreCo-Beam], see figure 10, and fatigue tests have been conducted on three different shapes of shear connectors, see table 1.

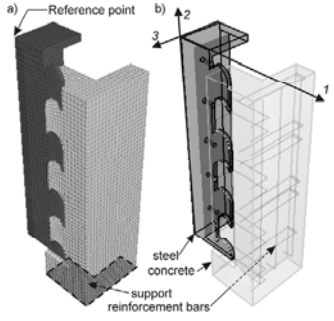


Fig. 9 – POST

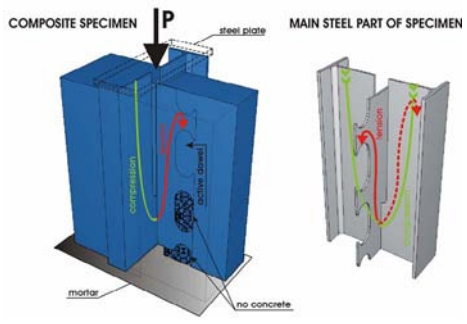
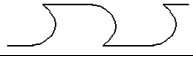
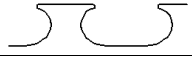


Fig. 10 – NPOT

As expected, one crack in the PZ shape could be produced with the NPOT fatigue tests according to figure 8 c). It occurred at 350000 load cycles due to a stress range reaching locally about $\Delta\sigma$ = 280MPa. This fatigue crack initiation is coherent with the fatigue design [Berthellemy, Hechler, Lorenc et. al. 2009]. According to the expectations, the crack propagated through the entire web. However, only one of the specimens exhibited a fatigue failure.

Table 1 – Shapes of continuous shear connectors for PreCoBeams [PreCo-Beam]

	PZ	SA	CL
Shape			

As conclusion of the test series the puzzle shape (PZ) has been chosen to be the most promising shape considering of fabrication aspects, bearing capacity and fatigue. For structures highly subjected to fatigue the clothoidal shape (CL) is recommended.

ANALYSIS OF LOADING ON THE STEEL DOWEL

In addition to the fatigue test a static NPOT on the CL shape connector has been carried out with a large number of strain gauges at the steel dowel for analyzing the stresses and for the calibration of FE analyses, carried out simultaneously with the tests. The results of the test have been in accordance with the numeric results and the numerical model has been modified for the PZ shape reference is given to in this paper, see Figure 11.

On this basis, as first step, an analytic model for the local behavior of a shear connector has been derived. In this paper the puzzle geometry is been focused. However it is possible to transfer the approach to any geometry for each inventor of a new shape.

The local approach is based on the load introduction in a single tooth. Hereby S represents the center of the projection area A_p in shearing direction; h_s is the distance from the center to the base of the shear connector. The projection area is defined as the area constricting a concrete block on front of the dowel, shown e.g. for the PZ shape in figure 11.

The loading on each steel tooth is composed by the shear force in the composite joint P_τ and the stress distribution due to the global loading depending on the geometry of the composite cross section; P_{up} for the uplifting forces due to the location of the shear joint in respect to the neutral axis of the cross section and σ_{en} for the notching effect from the nominal stress of the steel section, see figure 12.

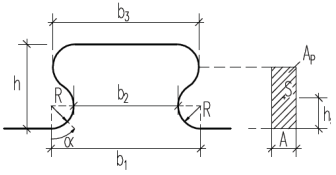


Fig. 11 – Geometry of puzzle tooth (PZ)

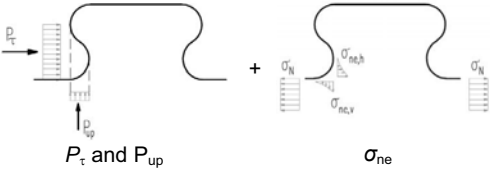


Fig. 12 – Forces on the steel dowel (PZ shape)

To determine P_τ it is conservatively assumed that the load distribution along the height of the dowel is constant. For non-reinforced tooth P_τ is located at h_s. For reinforced tooth (transversal reinforcement between the steel tooth) P_τ is located in the reinforcement bar and h_s is to be modified to be the distance of the center of reinforcement bar to the base of the shear connector.

The uplifting force P_{up}, resulting from the eccentricity h' of the shear joint to the centre of the composite compression chord, see figure 13, is in general taken over by stirrups located in the recesses of the dowels and the eccentricity is assumed to become h' = 0mm. Without stirrups, the trajectory generates an uplifting force on the steel dowel which must be considered in design and prevented with the undercut in the shape of the steel dowel. Hence the undercut of the steel dowel implements two functions; first, it generates the 3D stress state for the kernel of the concrete dowel and second, it locks the shear connection against uplift in vertical direction.

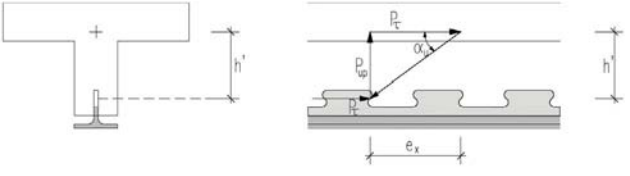


Fig. 13 – Uplifting force due to eccentricity of the shear joint to the neutral axis at support

The determination of the uplifting force is based on h'_i depending on the stress distribution of the composite section, see figure 14. In the following full shear connection is assumed. It is required to differentiate between the ULS and the SLS respectively the fatigue design. Further, construction stages have to be considered.

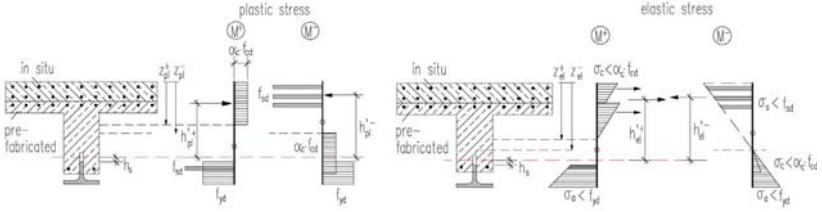


Fig. 14 – Determination of h'_i for ULS and SLS

Generalised P_{up} is therefore calculated for structures without stirrups according to figure 13 as:

$$P_{up} = P_{\tau} \cdot \frac{h'}{e_x} \quad \text{[kN]} \qquad \text{Eq. 1}$$

with $h' < e_x$ else $P_{up} = P_{\tau}$.

The σ_{ne} is the notching effect on the normal stresses in the web of the steel girder due to the shape of dowel. The increase in stress hereby depends on the geometry of the dowel.

On the basis of an FEA (figure 15) it has been concluded, that σ_{ne} depends directly on the ratio of the connector length to the radius of the cut out (b_1 / R), but not on length and radius separately. For realistic ratios, the height h of the dowel is not significant for the notching effect.

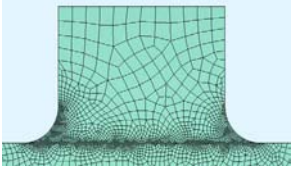


Fig. 15 – FE model for analysis

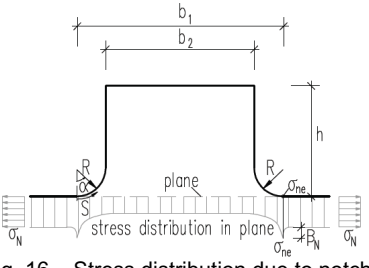


Fig. 16 – Stress distribution due to notch effects

On the basis of an parametric study using FEA the notching stresses have been derived to

$$\sigma_{ne} = \beta_N \cdot \sigma_N \quad \text{[MPa]} \qquad \text{Eq. 2}$$

with the notch factor

$$\beta_N = \left[1.192 + 0.1029 \cdot \left(b_1 / R\right) - 0.0022 \cdot \left(b_1 / R\right)^2\right] \cdot f(\alpha) \quad \text{[-]} \qquad \text{Eq. 3}$$

where $f(\alpha)$ expresses the decrease of the amplitude along the cut out

$$f(\alpha) = 0{,}9077 + 0{,}0104\ \alpha - 0{,}0005\ \alpha^2 \qquad [\text{-}] \qquad \text{Eq. 4}$$

The higher the ratio b_1 / R of the tooth, the higher is the notching effect expressed by the factor β_N. Thus, not only the sharpness of the notch itself but also the increase in stiffness depending on the length of the dowel is influencing the notch effect, which is in accordance to the effect of longitudinal stiffeners.

STRESS ANALYSIS ON THE STEEL DOWEL

For the validation of the loading on a steel dowel and the resulting stresses the modified FE-analysis to the PZ shape has been consulted. For the local effects due to longitudinal shear, the model presented in [PreCo-Beam] was modified to model (M3) according to [Lorenc et. al. 2007] – hereby the shear force is induced into the steel part over the concrete via contact interactions. The stresses due to the notching effect of the nominal stresses in the web and the uplift forces have been calculated considering only the steel part in model (M2) as concrete part is neglectable for those actions. The geometric properties of the dowel have been chosen to b_2 = 125mm, h = 100mm and t_w = 10.2mm web thickness of the steel beam.

Hereafter the influence of each loading on the stresses of a single puzzle tooth has been evaluated along the cut. For this purpose, separate calculations have been conducted for P_τ = 50kN (Load L), P_{Up} = 50kN (Load U) and the global stresses in the web σ_N = 50MPa (Load G). In Fig 17 the resulting principle stresses at the critical region of stress concentration are presented, both as stress plots and as diagram in dependency of the location along the edge of the cut-out. On this basis an analytic model has been derived for the ULS and fatigue design of a steel dowel.

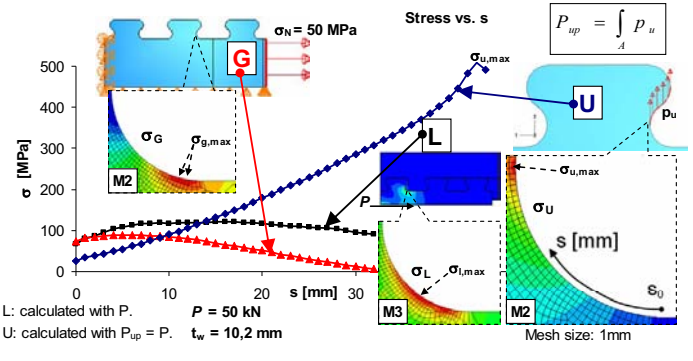


Fig. 17 – Principal stresses distribution in steel dowel along arc length from specific actions: σ_{ne} (σ_g, G), P_τ (L) and P_{up} (U)

ULTIMATE LIMIT STATE DESIGN OF THE STEEL DOWEL

In [P621 2007] continuous shear connectors have been experimentally investigated. Hereby cracks in the steel strip have been observed whereas the concrete matrix

has not significantly been damaged (figure 18). In reference to this failure mode a steel failure criterion has been derived.

For its application for PreCoBeam bridges this formula has to be extended to cover the additional uplifting forces from the global geometry of the cross sections, see figure 19. However the overall assumption, that the resulting maximum equivalent Von Mises stresses do not exceed the yield strength is kept as basis of design.

Consequently the bearing resistance of a single steel tooth P_{Rd} is determined in dependency of the loading specified and in accordance with [P621 2007]. Hereby influence of the increase of the nominal stresses of the steel section due to the dowel geometry has been neglected as it is insignificant in the plastic design.



Fig. 18 – ULS-failure [P621 2007]

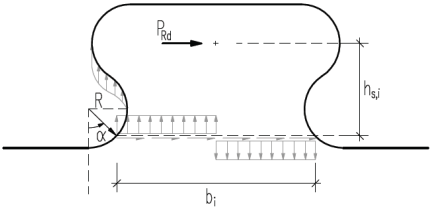


Fig. 19 – Forces and stresses in a critical section at ULS

Thus, the following design criterion is derived:

$$P_{Rk} = \frac{f_y \cdot t_w \cdot b_i^2}{\sqrt{\left(4 \cdot h_{s,i} + \frac{h'_i \,(b_2 + b_3)}{e_x}\right)^2 + 3 \cdot b_i^2}} \quad \text{[kN]} \qquad \text{Eq. 5}$$

with f_y Yield strength steel [MPa],

t_w Plate thickness of web [mm],

$h_{s,i}$ Distance of centre of gravity to critical section

$= h_s - (1 - \cos\alpha) \cdot R$ [mm],

b_i Width at critical section

$= b_1 - 2 \cdot \sin\alpha \cdot R$ [mm],

h'_i $= h' - (1 - \cos\alpha) \cdot R$ [mm],

e_x distance between connectors [mm], fig. 13.

α angle along cutting edge [°], fig. 11,

For the puzzle shape the maximum equivalent stresses derived from equation 5 has been located to be at α = 70° for the POST which is in accordance to the tests, see figure 18.

FATIGUE RESISTANCE OF A GAS CUT EDGE

The fatigue design of the steel part is divided into two parts. One part is dedicated to the fatigue design of the web taking the increase in stress due to the notching effect of the steel tooth into account. The second part treats the estimation of the fatigue

stresses along the gas cut edge of the dowel itself, considering the effect of the shear stresses as well as the nominal stresses in the steel section and their verification.

However at first, the fatigue resistance of a gas cut edge has to be specified. According to the Eurocode [EC3-1-9] the fatigue category of a gas cut edge is 140 when subsequent dressing is applied. Hereby all visible signs of edge discontinuities have to be removed. The cut areas are to be machined or ground and all burrs to be removed. Any machinery scratches, for example from grinding operations, can only be parallel to the stresses. If the cut has shallow and regular drag lines with cut quality II according to EN 1090 (for railway bridges cut quality I [DIN FB 103]) the fatigue category is reduced to 125. For both categories repair by weld refill is not allowed. Re-entrant corners are to be improved by grinding appropriate stress concentration factors.

Therefore the roughness and cutting tolerances from the oxy-cutting process have been measured in dependency to the cutting speed. The results are shown in table 2. The deviation is small and all cutting surfaces are class I.

Table 2 – Roughness in dependency of the cutting speed

Cutting speed *v*	Medium surface roughness Rz	Tolerances of rectangularity and inclination
350 [mm/min]	43 – 63 [µm]	0.10 [mm]
500 [mm/min]	20 – 74 [µm]	0.40 [mm]
650 [mm/min]	40 – 62 [µm]	0.25 [mm]

In addition knowledge on the fatigue resistance is found in the research project [P185]. In this project the influence of the cutting quality on the fatigue design made from fine-grain steels (according of today's EN10025-4) has been investigated. It has been noted, that the initial crack occurs from the blasted surface in the heat affected zone (HAZ) from cutting. However it has been noticed that short stopping of the flame cutter decreases the fatigue strength to 60%. This results from the change of the failure initiation to the cut edge. Further it has been observed that hammering (an effect which may occur due to hammering of the continuous shear connector in gaps from which plastified concrete may have disappeared), cutting speed, warming before cutting and material strength have hardly an influence on the fatigue strength.

Therefore crack initiation occurs in the HAZ along the cut. The design value is therefore conservatively derived to $\Delta\sigma_C$ = 125MPa. If stopping of the flame cutter can not be avoided it should take place at an irrelevant location in terms of fatigue.

FATIGUE DESIGN OF THE STEEL WEB

Due to the notch effect of the steel tooth the stresses of the web along the cut edge are increased. The reduction due to the geometry is comparable to the effect by longitudinal stiffeners, however only the geometrical effect has to be considered as the material notch due to welding is inexistent. Therefore the fatigue verification has

to be performed with the fatigue category of gas cut edges $\Delta\sigma_C$ = 125MPa according to [EC3-1-9] and:

$$\Delta\sigma_{E,2} = \Delta\sigma_{N,w} \cdot \beta_N \quad \text{[MPa]} \qquad \text{Eq. 6}$$

with: $\Delta\sigma_{N,w}$ relevant longitudinal stresses in web along bottom line of the connector [MPa],

β_N according to equation 3.

FATIGUE DESIGN OF THE STEEL CONNECTOR

Fatigue crack initiation and propagation depend on the principle stresses along the cutting edge. To derive an analytic design model for fatigue verification the principle stresses have consequently to be considered, which are supposed perpendicular to the radius (figure 20).

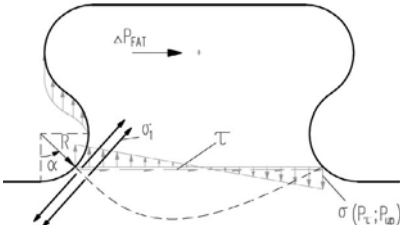


Fig. 20 – Analytic model for principle stresses (in dependency of the angular *α*)

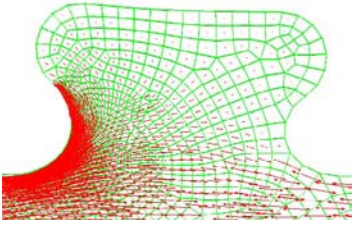


Fig. 21 – Principal stress trajectories in dowel (P_{Rd} and $P_{up} \neq 0$ and σ_N influence)

With the loading defined previously and in dependency of *α*, the following fatigue load resistance has been derived:

$$\Delta P_{FAT} = \left(\Delta\sigma_C - \beta_N \cdot \Delta\sigma_{N,w}\right) \cdot \frac{t_w \cdot b_r^2}{b_r \cdot \cos\alpha + \left(6h_{s,i} + \frac{3h'_i\,(b_2 + b_3)}{2 \cdot e_x}\right) \cdot \sin\alpha} \quad \text{[kN]} \qquad \text{Eq. 7}$$

with $\Delta\sigma_C$ Fatigue strength of gas cut edge [MPa],

$h_{s,i}$, t_w , h'_i , e_x , α see equation 5,

$\Delta\sigma_{N,w}$, β_N see equation 6,

b_r arc length at critical section

$$= \frac{\pi(90-\alpha)\left(\frac{1}{2}b_1 - \sin\alpha \cdot R\right)}{90 \cdot \cos\alpha}$$

[mm].

For the puzzle geometry investigated the maximum principle stresses along the cut edge have been derive at an angle *α* = 20°.

SUMMARY

In this paper, the PreCoBeam construction technique and their advantages are presented. Further the main problems for this construction in design have been identified based on experimental results from the previous years and own test results. Especially the fatigue design of the continuous shear connectors are here to be mentioned.

Consequently a design concept for the steel part of continuous shear connectors applied in PreCoBeam constructions has been derived. Main focus has been laid on the analytic approach for hand calculation and its validation by experimental results and FEA.

Alternatively to the approach presented in this paper it is possible to calculate the Von Mises and the principle stresses resulting from the local loading by FEA and to derive shape functions for each connector [PreCo-Beam]. Also for information on concrete failure and design reference is given to [PreCo-Beam].

The authors wish to express their deep gratitude to the RFCS (Research Fund for Coal and Steel of the European Community) for its financial support of [PreCo-Beam] and to the representatives of the partners Université de Liège, Ramböll Sverige and Universität der Bundeswehr Munich for their inspiring cooperation.

REFERENCES

Deutsches Institut für Bautechnik (DIBT): Zulassungsbescheid Perfobondleiste, Zulassungsnummer Z-26.1-23, Berlin 22.07.1991

DIN-Fachbericht 103: Stahlbrücken. Deutsches Institut für Normung e.V. (DIN). 2003

Döinghaus, P., Hegger, J., Trumpf, H., Sedlacek, G.: Untersuchungen zur Duktilität der Verbundmittel bei Anwendung von hochfestem Stahl und hochfestem Beton. P486/25/99 / AiF-Nr. 12124 N. Arbeitsgemeinschaft industrieller Forschungsvereinigungen e.V., Studiengesellschaft Stahlanwendung e.V., 2000

EN 1090: Execution of steel structures. European Committee for Standardization (CEN). 2004

EN 10025-4: Hot rolled products of structural steels - Part 4: Technical delivery conditions for thermomechanical rolled weldable fine grain structural steels. European Committee for Standardization (CEN). 2004

Eurocode 3: Design of steel structures - Part 1-9: Fatigue. European Committee for Standardization (CEN). 2005

Eurocode 4 (EC4): Design of composite steel and concrete structures - Part 1-1: General rules and rules for buildings. European Committee for Standardization (CEN). 2004

Feldmann M., Hegger J., Hechler O., Rauscher S.: Untersuchungen zum Trag- und Verformungsverhalten von Verbundmitteln unter ruhender und nicht ruhender Belastung bei Verwendung hochfester Werkstoffe. AiF-Forschungsvorhaben P621, AiF-Nr. 13867, Arbeitsgemeinschaft industrieller Forschungsvereinigungen e.V., FOSTA, 2007

Lorenc W., Ignatowicz R., Kubica E., Seidl G.: Numerical model of shear connection by concrete dowels. Recent Developments in Structural Engineering Mechanics and Computation, Millpress 2007, Rotterdam, Netherlands.

PreCo-Beam: Prefabricated enduring composite beams based on innovative shear transmission. Technical Report No 2. Research Fund for Coal and Steel, Contract N° RFSR-CT-2006-00030. 01/07/2006 – 30/06/2009.

Schmitt V., Seidl G.: Verbundfertigteil-Bauweise im Brückenbau. Beton- und Stahlbetonbau 70, Heft 8, 2001

Schmitt V., Seidl G., Hever M., Zapfe C.: Verbundbrücke Pöcking – Innovative VFT-Träger mit Betondübeln. Stahlbau 73, Heft 6, 2004

Schmitt V., Seidl G., Vogel C., Schülke B., Koch E.: Untersuchungen zum verstärkten Einsatz von Stahlverbundkonstruktionen bei Brücken kleiner und mittlerer Spannweiten. Final Report, Forschungsvorhaben P 629, Forschungsvereinigung Stahlanwendung e.V., 2005

Wurzer O.: Zur Tragfähigkeit von Betondübel, Dissertation am Institut für Konstruktiven Ingenieurbau, Universität der Bundeswehr, München, Juni 1997

Berthellemy J.: French bridges experiences from prefabricated deck elements. ELEM-Workshop, Stockholm, 2009

Berthellemy J., Hechler, O., Lorenc W., Seidl, G., Viefhues, E.: Premiers résultats du projet de recherche européen Precobeam de connexion par découpe d'une tôle, CTICM Revue 2009.

EFFECTS OF GROUP ARRANGEMENT ON THE ULTIMATE STRENGTH OF STUD SHEAR CONNECTION

Chang-Su Shim
Department of Civil Engineering, Chung-Ang University
Ansungsi, Korea
E-mail: csshim@cau.ac.kr

Pil-Goo Lee
Civil Engineering Research Department, RIST
Hwasung, Korea
E-mail: pg289@rist.re.kr

Dong-Wook Kim
Department of Civil Engineering, Chung-Ang University
Ansungsi, Korea
E-mail: clearup7@nate.com

Chul-Hun Chung
Department of Civil Engineering, Dankook University
Yonginsi, Korea
E-mail: chchung5@dankook.ac.kr

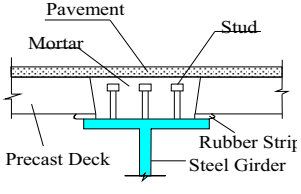
ABSTRACT

For the design of shear connection for region of highly concentrated shear force in steel-concrete composite bridges, connection details are the most important design issues. Failure modes of the shear connection govern the ultimate strength for the design and governing design parameters can be changed. Instead of rigid shear connectors, this paper deals with the group stud shear connection for the precast decks. Shear pockets for stud connectors arise difficulty in the details of precast decks. Push-out tests were conducted to evaluate the ultimate strength according to the expected failure modes. Main parameters of the test were stud spacing, reinforcement details and stud diameter. Test results showed that current design provisions for the stud connectors can be used for the design of group stud shear connection when the design requirements on the minimum spacing of studs are satisfied and the splitting failure of concrete slab is prevented. An empirical equation was proposed to consider the effect of stud spacing when the spacing is less than the minimum requirement. Fatigue tests showed that the group stud connectors with spacing of more than three times of diameter has similar fatigue life with current design codes. Based on the test results, design recommendations for shear connection in a precast deck bridge were derived.

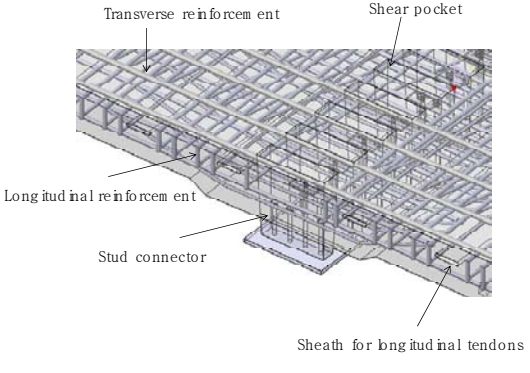
INTRODUCTION

There are various short and medium span composite bridges varying in section, connection details and method of construction. For these steel-concrete composite or hybrid girders, proper shear connection details are required. Connectors are embedded in a concrete medium and impart highly concentrated forces onto the

concrete element. This concentrated load can cause the concrete to fail in tension by embedment cracking, ripping, shear and splitting resulting in the decrease of ultimate strength of shear connection. Failure modes of the shear connection can be guided according to the ratio of the shear strength of mechanical connectors and concrete strength. Stud shear connectors are the most common type of mechanical connector used and need to be arranged according to the design provisions on minimum and maximum spacing requirements. Due to the constraints, rigid connection such as perfobond connectors is frequently used for the high shear regions with small area for the connectors. Rigid connectors such as perfobond connectors showed that the failure mechanisms were associated with the failure of the concrete slabs, with little or no deformation of the perfobond rib (Valente and Cruz, 2004). The failure occurred with longitudinal cracks and the concrete smashing under the perfobond rib. It is difficult to utilize the rigid connector for the shear connection of precast decks and composite truss joints because reinforcement details cannot be easily accommodated in the pocket area or in the narrow joint area as shown in Figure 1. Furthermore, the strength of the connection is usually governed by the strength of the concrete slab. In order to resolve these limitations, group stud shear connection with relatively large studs is proposed and details for the connection have been investigated (Shim et al., 2004). Figure 1 shows the typical examples of the shear connection details dealt in this paper.



(a) shear connection



(b) details of precast deck

Fig 1- Shear connection for precast deck

Stud shear connectors are influenced by several parameters according to previous researchers, with major factors categorized into shank diameter, height and tensile strength of studs, compressive strength and elastic modulus of concrete, and direction of concrete casting. In addition for shear connection in precast deck bridges, material properties of filling material and bedding height must also be considered for the evaluation of structural performance of stud shear connection (Shim, 2000; Shim, 2001). Large studs up to 31.8mm diameter were experimentally investigated and availability of the current design provisions on stud shear connectors was verified based on the test results (Badie et al., 2002, Shim et al., 2004). Hanswille et al. (2007) examined the effects of the loading sequence and damage accumulation on the fatigue life and showed early reduction of the static strength from the damage. The failure modes of shear connection can be categorized according to relative strength of surrounding concrete and stud connectors. Mode-1 is defined as stud failure without considerable concrete damage. Mode-3 means the concrete failure without stud failure. When the connectors are failed after considerable concrete damage, it can be categorized as Mode-2.

In this paper, two series of group arrangement of stud connectors were dealt with. One is the shear connection with 25mm studs in relatively stronger concrete slab resulting in stud failure. The other is the group stud connection for precast decks including internal and external reinforcements to increase the bearing strength and the splitting strength of the concrete slab, respectively. Based on the failure modes, three design equations from current design codes were verified and proper adjustment factors were suggested. General design guidelines for the group stud connectors were discussed.

EXPERIMENTAL PROGRAM

In order to evaluate the effect of stud spacing on the static and fatigue strength of shear connection, push-out specimens with group arrangement were fabricated. Nine 25mm and 22mm studs were welded at each flange with different stud spacings, such as $5d_s$, $4d_s$ and $3d_s$. Current minimum spacing of stud connectors is five times of the stud shank diamter. In order to strengthen the shear strength of the concrete slab, additional reinforcements were placed inside and outside of the shear pockets. Table 1 summarizes the test specimens for static tests. Compressive strength of concrete was designed to have 35MPa.

Figure 2 shows the push-out specimen for precast decks and CIP slab. Precast decks with 250mm thickness were prefabricated and were combined with steel beam by filling non-shrink mortar in shear pockets. Nine studs were arranged at each face by a stud welding gun. External reinforcements were placed before casting concrete of the precast decks. Internal reinforcements were put in the shear pockets after placing the slab on the steel beam. Figure 3 presents the reinforcing details. Dimensions of the shear pocket were the same for all the specimens. The stud spacing cannot be less than $3d_s$ because of workability of a welding gun.

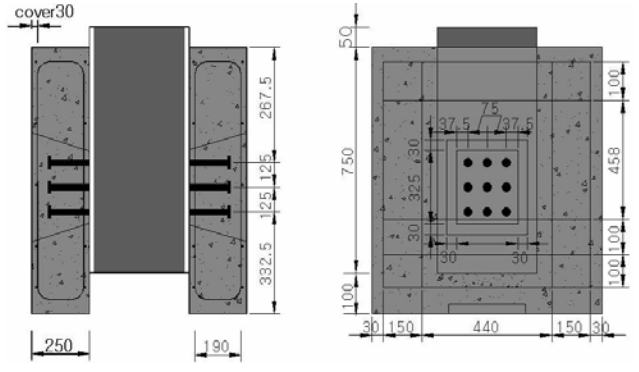
Two additional test results were used from the previous tests on shear connection in precast decks [Shim, 2000] and six specimens on shear connection in cast-in-place concrete slab were referred [Shim, 2004]. According to the failure modes of shear connection, a proper design equation needs to be used. The effect of stud spacing

on the static strength can be expected when the surrounding concrete has some damage under relatively low shear load. Therefore, the stud failure after concrete crushing was intended for some specimens in order to estimate the effect of stud spacing.

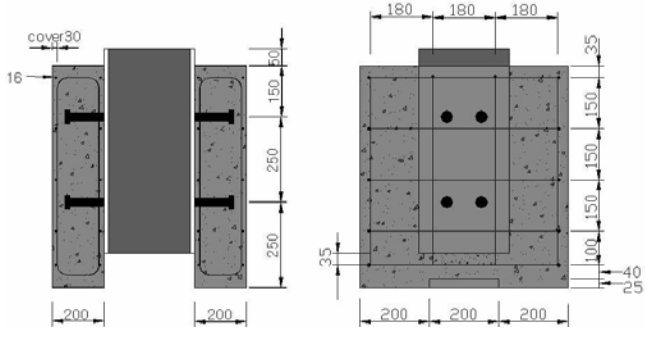
Generally, stud spacing is decided from fatigue design. Four specimens were fabricated to evaluate the effect of group arrangement on the fatigue endurance and were compared with previous test results [Shim, 2000 & Shim, 2004]. The stud spacing was smaller than the current minimum requirement in design codes [Eurocode-4, 1997]. Fatigue endurance of group stud shear connectors should be verified for the enhanced details of shear connection for precast decks. In relatively low stress level, the effect of group arrangement is expected to have little effect. Therefore, the stress level was decided to have low cycle fatigue judging from the previous test results. This assumption can provide more severe condition to the shear connection with group arrangement. The fatigue endurance of group stud shear connection was compared with that of previous tests. Table 2 summarizes the specimens.

Table 1- Static test specimen for precast decks

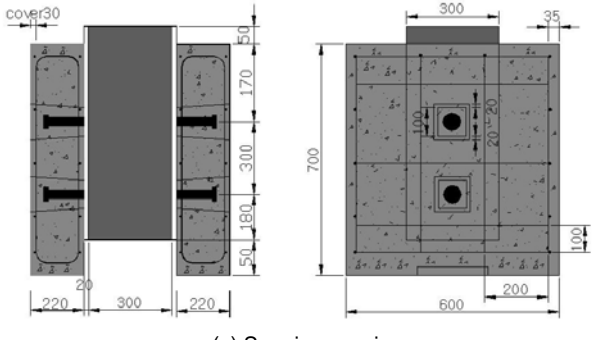
Specimen	Shank diameter (mm)	Compressive strength of mortar (N/mm^2)	Compressive Strength of concrete (N/mm^2)	Bedding height (mm)	Stud spacing (mm)	Reinforcement
G25NS	25	49.5	32.6	20	$5d_s$	No additional r.f.
G25OS	25	49.5	32.6	20		External r.f.(D16)
G25IS	25	49.5	32.6	20		Internal r.f.(D10)
G25OS-1	25	49.5	32.6	20	$4d_s$	External r.f.(D16)
G25NS-2	25	49.5	32.6	20	$3d_s$	No additional r.f.
G25OS-2	25	49.5	32.6	20		External r.f.(D16)
G25IS-2	25	49.5	32.6	20		Internal r.f.(D10)
G22OS	22	49.5	32.6	20	$4d_s$	External r.f.(D16)
G22IS	22	49.5	32.6	20		Internal r.f.(D10)
G22OS-1	22	49.5	32.6	20	$3d_s$	External r.f.(D16)
G22IS-1	22	49.5	32.6	20		Internal r.f.(D10)
CIP25A1	25		35.3		$10d_s$	No additional r.f.
CIP25A2	25		35.3		$10d_s$	No additional r.f.
CIP25A3	25		35.3		$10d_s$	No additional r.f.
CIP25B1	25		49.4		$10d_s$	No additional r.f.
CIP25B2	25		49.4		$10d_s$	No additional r.f.
CIP25B3	25		49.4		$10d_s$	No additional r.f.
S22A	22	61.09	35.8	20	$13d_s$	No additional r.f.
S22B	22	61.09	35.8	20	$13d_s$	No additional r.f.



(a) G-series specimen



(b) CIP series specimen



(c) S series specimen

Fig. 2- Test Specimen

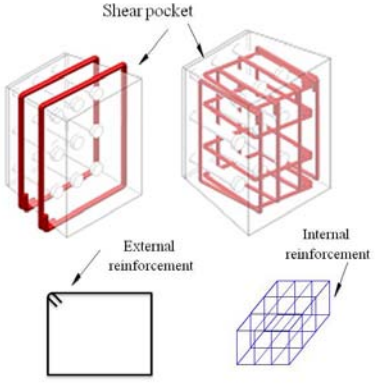


Fig. 3- Reinforcing details

Table 2- Fatigue tests for shear connection

Specimen	Compressive strength of mortar(MPa)	Compressive strength of concrete (MPa)	Stud spacing	Stress range (MPa)
FG25OS-1	49.5	32.8	$4\,d_s$	130
FG25OS-2	49.5	32.8	$4\,d_s$	150
FG25OS-3	49.5	32.8	$3\,d_s$	130
FG25OS-4	49.5	32.8	$3\,d_s$	150
F150A	54.88	35.8	$13\,d_s$	125.2
F170A	54.88	35.8	$13\,d_s$	142.5
F130B	61.09	35.8	$13\,d_s$	107.9
F150B	61.09	35.8	$13\,d_s$	125.2
F180B	61.09	35.8	$13\,d_s$	151.1
F130C	71.38	35.8	$13\,d_s$	107.9
F150C	71.38	35.8	$13\,d_s$	125.2
F180C	71.38	35.8	$13\,d_s$	151.1
F130C	71.38	35.8	$13\,d_s$	151.1

STATIC STRENGTH OF GROUP STUD SHEAR CONNECTION

Test specimens showed different failure modes according to relative strength ratio between concrete slab and stud connectors. Figure 4 shows typical load-slip curves of the shear connection according to strengthening details. For group stud connection of precast decks, closer spacing reduced the shear strength up to 30% when the failure mode is stud failure after concrete cracking of the slab. External

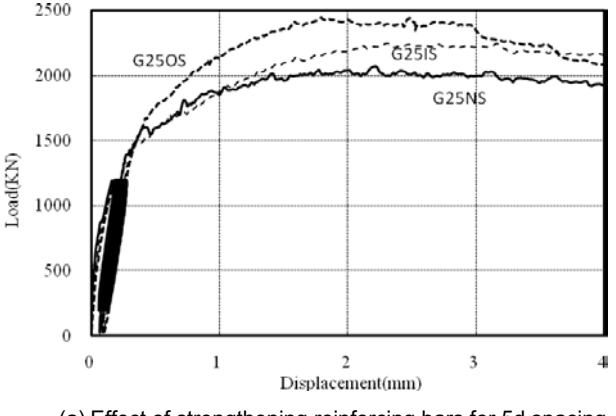
reinforcements increased post-cracking strength of the concrete slab while internal reinforcement increased bearing strength a little. Therefore, it is important to strengthen the concrete slab when group stud connectors are used. When the failure mode is splitting failure of the concrete slab without stud failure, current design provisions on shear strength of concrete slab are appropriate to evaluate the strength of the connection.

In order to allow the particular design situation of closer stud spacing than the design requirement, it is necessary to provide an empirical equation for the shear connection in precast decks. Based on test results including the previous research [Shim et. al 2000, 2001], an empirical equation (1) for the reduction factor of stud spacing is proposed by linear regression analysis as in Figure 5. When the stud spacing is smaller than three times of stud diameter, the ultimate strength of the shear connection can be evaluated using the equation. The equation considers stud failure after concrete cracking. Although this equation needs improvement by more tests, it showed clear view on the effect of stud spacing. In the equation, the d_s can be used as 5 when the stud spacing is greater than five times of shank diameter of stud.

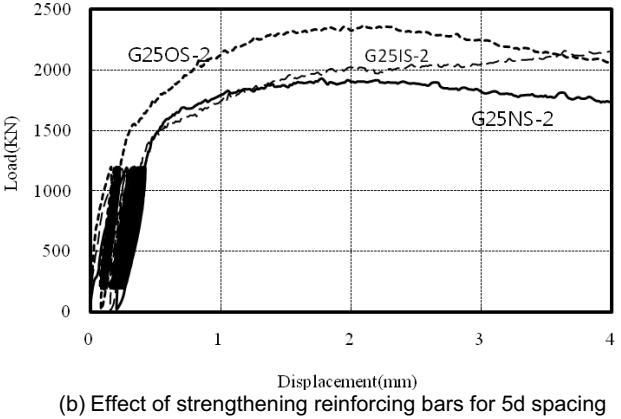
$$\begin{cases} \beta_s = 0.174 d_s + 0.13 & for\ 3 \le d_s \le 5 \\ \beta_s = 1 & for\quad d_s > 5 \end{cases} \tag{1}$$

where, d_s is the stud spacing multiplier to stud diameter.

When the failure mode of the shear connection is the concrete slab failure, the ultimate strength of the shear connection should be the shear strength of the concrete slab. Local strengthening reinforcements need to be considered in the evaluation of the shear strength of concrete slab. For the group arrangement of stud connectors, it is necessary to estimate the shear strength of shear connection and concrete slab. For the shear connection in precast decks, the internal strengthening is less effective than the external strengthening.



(a) Effect of strengthening reinforcing bars for 5d spacing



(b) Effect of strengthening reinforcing bars for 5d spacing

Fig. 4 – Load-slip curves

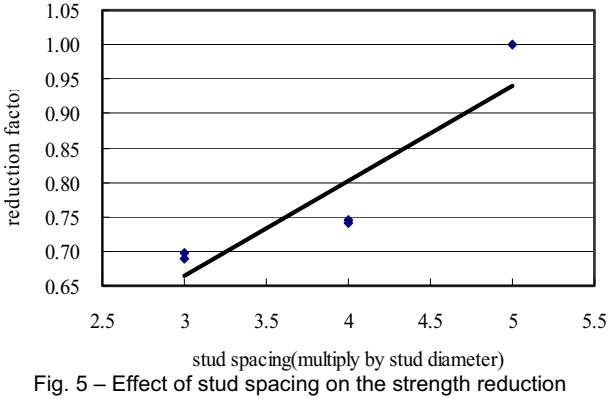


Fig. 5 – Effect of stud spacing on the strength reduction

FATIGUE STRENGTH OF GROUP STUD SHEAR CONNECTION

Normally, the stud spacing is determined from the fatigue design. In order to enhance the connection details, it is necessary to prove that there is no significant reduction in fatigue strength due to damage overlapping of each connector and its surrounding medium. When local crushing of bearing regions is overlapped, the fatigue strength can be reduced and it should be considered in the design.

When the static failure mode of the shear connection is stud failure with negligible damage of concrete slab, fatigue endurance of the shear connection with group arrangement was greater than the design value. Figure 6 shows the S-N curves of the shear connection and Figure 7 illustrates the failure patterns.

For the shear connection in precast decks which showed stud failure with shear cracking of concrete slab, fatigue endurance is similar with the design value from Eurocode-4 and also with previous test results of the shear connection for precast

decks without group arrangement. From this result, the group arrangement of stud connectors in high shear region can be adopted effectively. Even though the ultimate strength of the shear connection is reduced, the fatigue endurance will be similar with current design value.

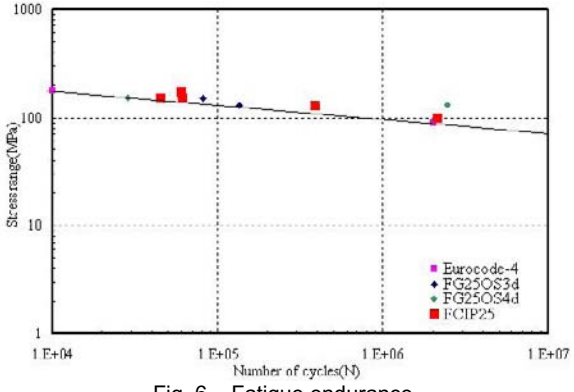
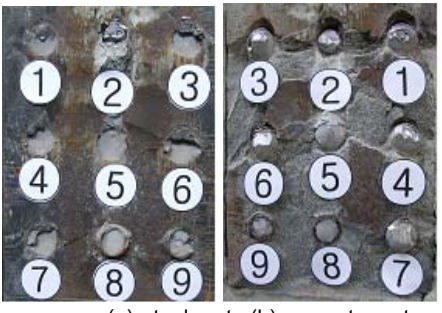


Fig. 6 – Fatigue endurance



(a) steel part (b) concrete part

Fig. 7- Fatigue failure mode

CONCLUSION

In high shear region, we need stronger shear connection. Group stud shear connection is dealt with in this paper in terms of static strength and fatigue endurance. Push-out tests were conducted for the shear connection in precast decks.

For the specimens of precast deck bridges, the effects of the stud spacing and confining reinforcements were clearly observed. Decreasing the stud spacing resulted in lower ultimate strength of the shear connection. The confining reinforcements inside and outside of the shear pocket can enhance the shear strength of the shear connection. The requirement of the minimum spacing for the stud connectors needs to be revised for precast decks. However, the shear connection with smaller spacing should have adequate reinforcement details to prevent premature failure of concrete slab. In this paper, the empirical equation was

proposed and fatigue endurance of the shear connection with group arrangement was verified.

Based on experimental results, design of precast decks for steel-concrete composite bridges can be enhanced. In a shear pocket, stud connectors with group arrangement can be placed to reduce the number of pockets in a precast deck. This enhacement provides better details of precast decks near supports where the horizontal shear is high.

REFERENCES

Badie, S.S. Tadros, M.K. Kakish, H.F. Splittgerber, D.L. Baishya M.C. 2002, Large Shear Studs for Composite Action in Steel Bridge Girders, J. of Bridge Engineering, Vol. 7, No. 3, May, pp. 195-203

Eurocode 4, 1997, Design of composite steel and concrete structures, Part 2 : composite bridges (ENV 1994-2), CEN

Hanswille, G. Porsch, M. Ustundag, C. 2007. Resistance of headed studs subjected to fatigue loading Part I: Experimental study, Journal of Constructional Steel Research, 63, pp. 475-484.

Minami, H. Yamamura, M. Taira, Y. Furuichi, K. 2004, Design of the KINOKAWA Viaduct Composite Truss Bridge, Proceedings 1st Congress, Composite Structures, pp. 371-380.

Oehlers, D.J. Bradford, M.A. 1995. Composite Steel & Concrete Structural Members; Fundamental Be-havior, PERGAMON.

Shim, C.-S. Lee, P.-G. Yoon, T.-Y. 2004. Static behavior of large stud shear connectors, Engineering Structures, 26(12), pp. 1853-1860.

Shim, C.S. Kim, Chung, C.H. and Chang, S.P. 2000. The Behavior of Shear Connection in Composite Beam with Full-Depth Precast Slab, Structures and Buildings, The Institution of Civil Engineers, Jan., Vol. 140, pp. 101-110.

Shim, C.S. Chang, S.P. Lee P.G. 2001. Design of Shear Connection in Composite Steel and Concrete Bridges with Precast Decks," Journal of Constructional Steel Research, 57 pp. 203-219.

Shim, C.S. Park, J.S. Jeon, S.M. Kim, D.W. 2007. Experimental Study on Group Stud Shear Connection, Proceeding of 5th International Conference on Advances in Steel Structures, pp. 932-937.

Tsujimura, T. Shoji, A. Noro, T. Muroi, S. 2000. Experimental Study on a Joint in Prestressed Concrete Bridge with Steel Truss Web, Proceedings 1st Congress, Composite Structures, pp. 347-352.

Valente, I., Cruz, Paulo J.S. 2004. Experimental analysis of Perfobond shear connection between steel and lightweight concrete, Journal of Constructional Steel Research, 60, pp. 465-479.

INNOVATIVE SHEAR CONNECTORS FOR A NEW PRESTRESSED COMPOSITE SLAB SYSTEM FOR BUILDINGS WITH MUTIPLE HVACR INSTALLATIONS

Marcin Abramski
Kaiserslautern University of Technology
Kaiserslautern, Germany
mabramski@rhrk.uni-kl.de

Thomas Friedrich
Domostatik GmbH
Bernkastel-Kues, Germany
th.friedrich@domostatik.com

Wolfgang Kurz
Kaiserslautern University of Technology
Kaiserslautern, Germany
wkurz@rhrk.uni-kl.de

Juergen Schnell
Kaiserslautern University of Technology
Kaiserslautern, Germany
jschnell@rhrk.uni-kl.de

ABSTRACT

In modern buildings various installation systems for HVACR, electricity and communication have to be installed. An innovative approach to this requirement is to include the necessary space in the slab construction. Using this approach a new composite slab system has been developed. It consists of two concrete slab layers on top and bottom side of the construction that are connected with vertical steel webs. Precast slab elements with pre-assembled HVACR equipment are installed at site. For improvement of performance in SLS and ULS the system is prestressed without bonding. To optimize the economics the shear connection between concrete and steel shall be realized with concrete dowels. Due to the installation of pipes and ducts various web openings have to be incorporated in the design of the slab system. Secondary bending moments cause considerable additional loads to the steel web and especially to the concrete dowels connecting steel and concrete. Therefore new types of dowels shall be developed to improve load capacity and ductility both for vertical and horizontal shear forces. Results of the new development on concrete dowel's geometry will be presented. Also a short overview of the first application of this slab system in a multi-story building will be given.

1 INTRODUCTION

The concrete dowels are specially designed openings through the steel section, so that the dowel action appears between the steel web and the concrete slab.

The concrete dowel is an alternative method of the shear connection for composite structures. The traditional method of designing a shear connection for the composite

structures loaded in flexure is to employ mechanical connectors; normally headed steel studs on top of the steel section.

The concrete dowels are known, developed and researched since the 80's of the last century [1]. Up to now development concentrated mainly on concrete dowels of regular round forms. Recent research papers describe also concrete dowels of jigsaw puzzle forms [3, 4, 5].

2 APPLICATIONS OF CONCRETE DOWELS

One of the first applications of the concrete dowels in form of jigsaw puzzle, which was described in the specialist literature, was viaduct over the railway in Pöcking next to Starnberg (Germany). The viaduct, built in 2003, consists of two spans of length 16,6 m each. The structure of the 10.35 m wide viaduct includes 3 so-called VFT-girders (fig. 1), in which steel webs are connected with concrete slab with the use of jigsaw puzzle – formed concrete dowels.



Fig. 1: Concrete dowels in Pöcking bridge [5].

Direct inspiration to this research subject described in this paper was an innovative composite floor system consisting of steel web and upper and lower concrete slabs. This system is at this point in time applied in a multi-storey building of Hypothekenbank in Düsseldorf (fig. 2). Various web openings for ducts and pipes have to be incorporated. Precast floor elements with pre-assembled HVAC equipment are installed at site.

The civil engineering designers applied in this project headed steel studs welded in the horizontal position to the webs. The current development in steel structures manufacturing allows cutting out even complicated shapes of steel webs with the use of laser. This solution may reduce costs of welding numerous headed steel studs. Therefore new types of dowels should be developed to improve load capacity and ductility both for vertical and horizontal shear forces.




Fig. 2: Manufacturing of precast floor elements with pre-assembled HVAC equipment.

3 STATE OF RESEARCH DEDICATED TO CONCRETE DOWELS

There were two extensive research programmes undertaken at Bundeswehr University in Munich, which were dedicated especially to concrete dowels. The results of this research were described in the doctoral thesis [6], [7] and in [4]. According to the above-mentioned publications there are four mechanisms of the concrete dowels fracture:

1) Local pressure in concrete – load-carrying capacity denoted below as P_{Rk1}
2) Cutting out of the steel web from concrete (visible in concrete in form similar to cones) - P_{Rk2}
3) Cutting-off in concrete - P_{Rk3}
4) Yielding and cutting-off in steel - P_{Rk4}

The following equations taken from [4] are valid for the above mentioned fracture modes:

(1) $$P_{Rk1} = 72{,}7 \cdot \sqrt{f_{cm}} \cdot h_d \cdot t_w \quad ,$$

(2) $$P_{Rk2} = 25{,}6 \cdot h_{tc}^{\,2} \cdot f_{ctm} \cdot \rho_i \quad ,$$

(3) $$P_{Rk3} = 23{,}4 \cdot A_d \cdot f_{ctm} \cdot \rho_i \cdot f_h \quad ,$$

(4) $$\text{where } f_h = \left(1{,}2 - \frac{h_d}{180}\right) \le 1{,}00$$

f_{cm} - mean compressive strength of the concrete
f_{ctm} - mean tensile strength of the concrete
h_d - height of the recess in the steel web
t_w - thickness of the steel web
h_{tc} - height of the breach cone (equal to the distance between the centre of gravity of the recess in the steel web and the lower edge of the concrete slab)
ρ_i - reinforcement ratio of the concrete dowel
A_d - area of the recess in the steel web

4 PROGRAM OF EXPERIMENTAL TESTS

Six specimens for push-out tests have been manufactured. The aim of the experiments was to determine the load-carrying capacity and the horizontal deformation capacity of the developed novel concrete dowels. The vertical deformation capacity was not investigated yet.

Previously an optimization of the form of concrete dowels has been made. The basis of this optimization was the research presented in [4], [6] and [7] and described above in paragraph 3.

The theoretical load-carrying capacity based on the steel fracture criterion (P_{Rk4}) was determined working on the assumption, that the critical cross-section of the steel web is loaded simultaneously by bending moment and shearing force. Reduced stresses (Huber-Hencky-Mises hypothesis) were taken into account.

The steel S355 ($f_{y,k} = 355\,MPa$) and the concrete C35/45 ($f_{cm} = 43{,}0\,MPa$, $f_{ctm} = 3{,}2\,MPa$) were used to manufacture the specimens. The following geometrical parameters were obtained as the results of the optimization (symbols see in paragraph 3): $h_d = 50\,mm$, $t_w = 8\,mm$, $h_{tc} = 42{,}3\,mm$, $A_d = 50{,}0\,cm^2$. There was no reinforcement used in the concrete dowels ($\rho_i = 1{,}00$).

The analytically derived load-carrying capacities of concrete dowels designed on this basis are presented in Table 1.

Table 1: Results of theoretical calculation of load-carrying capacity, based on the nominal values of steel and concrete characteristics listed above. The table presents results obtained for the single concrete dowels as well as for the whole push-out specimens, consisting of four concrete dowels.

Fracture criterion			Theoretical load-carrying capacity [kN] for:	
			single concrete dowel	push-out specimen
1	Concrete	Local pressure in concrete	190,7	762,8
2		Cutting out of steel web	146,6	586,3
3		Parting-off in concrete	345,3	1381,1
4	Steel	Steel yielding and its parting-off	177,3	709,2
Minimal load capacity:				586,3

The specimens for push-out test are presented in figures 3 and 4. In case of three specimens (No. 4, 5 and 6) spiral reinforcement was used (see fig. 4a and 4b). A specific number of spirals were placed between two adjacent puzzle elements (see Table 2). The carrying capacities corresponding to the local pressure of concrete and to cutting out of steel web from the composite section, were expected to be increased with the use of this reinforcement. The spirals were made of normal steel, diameter was equal to 5mm. The diameter of spiral was 50 mm.

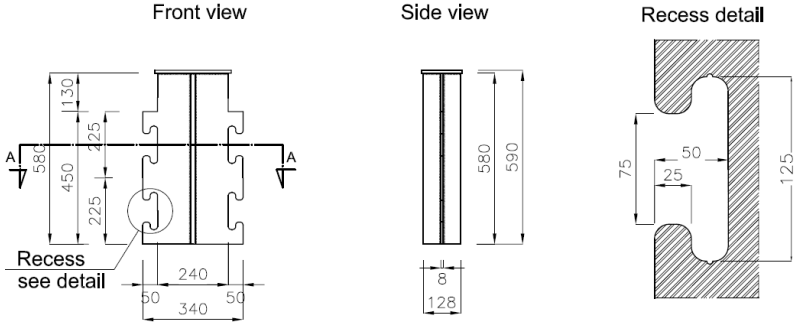


Fig. 3: Geometry of steel web used in experimental investigation, obtained as a result of the optimization.

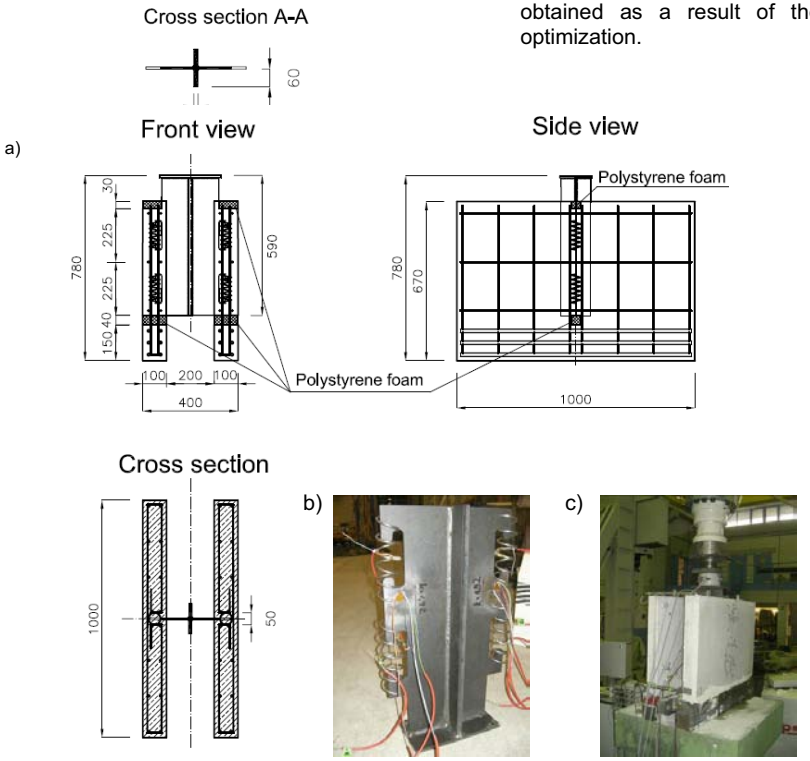


Fig. 4: Test specimens: a) drawings, b) picture of the manufacturing the steel web (see confining reinforcement and installed strain gauges), c) picture made by the testing (see horizontal upper and lower displacement transducers).

Table 2: Spiral reinforcement used by manufacturing of Push-out specimens.

Specimen	Number of spirals placed between two adjacent puzzle elements	Distance between two adjacent spirals [mm]
1	0	-
2	0	-
3	0	-
4	4	41,7
5	5	31,3
6	6	25,0

5 EXPERIMENTAL TESTS

The loading process has been carried out strictly according to the regulations of Eurocode 4 [2]. The initial 25 loading cycles between the load levels of 5% and 40% of theoretical loading capacity were made. The aim of this pre-loading is – according to Eurocode 4 – to eliminate the adhesion between steel and concrete. These loading cycles were controlled by displacement and were carried out at a deformation rate of 4 mm/min. Then the final test was carried out. It was also controlled by displacement. The rate was 0,25 mm/min. It lasted about 0,5 hour until the maximal load was reached. Next the loading with the same rate of displacement was continued until the load fell by 20 per cent. That was the moment of finishing the push-out test. It lasted altogether about 2 hours.

During the tests vertical displacement between steel web and the both concrete slabs was measured. This measuring was carried out with the use of two vertically assembled inductive displacement transducers. Moreover the distance between the both concrete slabs was measured in order to check whether a horizontal force component developing as a result of a complicated, rounded shape of the steel web, leads to lifting effect of the slab. This distance was measured with the use of two horizontally assembled inductive displacement transducers. Taking of these measurements is obligatory for Push-out tests (see Eurocode 4 [2], Annexe B). The lifting effect is a result of a substitutive moment, which develops in the composite structure due to the shearing force. The relationship between lifting deformation and shearing deformation is a measure of the stiffness of concrete dowels against such an effort.

a) b)

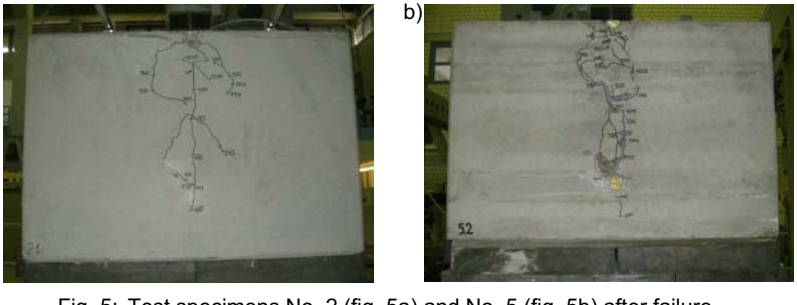


Fig. 5: Test specimens No. 2 (fig. 5a) and No. 5 (fig. 5b) after failure

The crack propagation on the both slabs was marked (only outsides) at specific load stages and recorded by photographs. Typical crack pattern, as well as view of a specimen after its failure, is presented in fig. 5.

6 RESULTS OF EXPERIMENTAL TESTS

The experimental concrete strength of slabs f_{cm}=56,9 MPa (see Table 3) was 32% higher than expected f_{cm}=43,0 MPa (see Table 3).

Table 3: Concrete strength of the push-out specimens

Specimen No.	Concrete strength [MPa]		
	left slab	right slab	mean for both slabs
1	69,9	60,5	65,2
2	69,5	56,7	63,1
3	65,8	61,3	63,6
4	70,1	62,1	66,1
5	70,6	61,4	66,0
6	69,9	66,7	68,3
mean for cube specimen:	69,3	61,5	65,4
mean for cylinder specimen:	60,3	53,4	56,9

Therefore theoretical load-carrying capacities for the whole push-out specimen for three failure mechanisms P_{Rk1} to P_{Rk3} were also higher than expected. (see Table 4). The load-carrying capacity P_{Rk4} calculated for the steel fracture criterion was always minimal and thus decisive.

Table 4: Theoretically obtained load-carrying capacities of the whole push-out specimen, re-calculated from the results presented in Table 1 for the actual compressive strength of concrete

P_{Rk1}	P_{Rk2}	P_{Rk3}	P_{Rk4}	$\min P_{Rk}$
877,6 kN	732,8 kN	1726,4	709,2	709,2

The load-carrying capacities obtained from the experiments are presented in Table 5 and in fig. 6. The mean of experimental load-carrying capacities of specimen No. 1, 2 and 3 P_{Rk_mean} = 548,3 kN is lower than the above mentioned theoretical value $\min P_{Rk}$ =709,2 kN. Therefore the equations: (1), (2) and (3) are not conservative. All the specimens with spiral reinforcement were of higher load-carrying capacity than the specimens without them. The difference of mean values was equal to ca. 20 %.

There were observed two fracture mechanisms of the concrete dowel. In the specimens No. 1, 2 and 3 the fracture in concrete due to cutting out of the steel web was decisive. This type of fracture is presented in figs. 5a and 7. The steel web has not been destroyed in those cases. In the specimens No. 4, 5 and 6 confining reinforcement influenced positively the carrying capacity of the concrete dowels. Final fracture occurred in the steel web (see figs. 5b and 8). The upper element of the web, which had only half the length in comparison to a regular one, parted off. Therefore the real growth of the carrying capacity of concrete dowels due to confining reinforcement cannot be determined in these tests.

Table 5: Main results obtained from the experiments (see also fig. 6) and comparison to the theoretically obtained results

Specimen No.	Failure mode	Load-carrying capacity			Vertical displacement
		$P_{max,exp}$	$P_{max,calc}$	$P_{max,exp}$ / $P_{max,calc}$	δ (P_{max})
		[kN]	[kN]	[-]	[mm]
1	Cutting out of steel web + Local pressure in concrete	505,4	709,2	0,71	4,57
2		552,8	709,2	0,78	7,62
3		586,7	709,2	0,83	5,38
4	Steel yielding and its parting-off + Local pressure in concrete	629,2	709,2	0,89	6,19
5		657,8	709,2	0,93	7,72
6		709,2	709,2	1,00	8,65
mean 1 to 3 (without spirals)		548,3	709,2	0,77	5,86
mean 4 to 6 (with spirals)		665,4	709,2	0,94	7,52

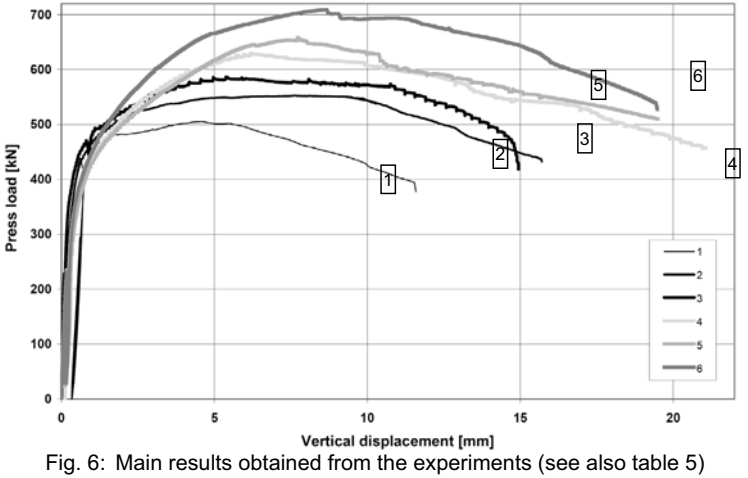


Fig. 6: Main results obtained from the experiments (see also table 5)

According to Eurocode [2] relation between horizontal and vertical displacement of the specimen must not be greater than 0,5. In the experimental tests this condition was fulfilled in 4 of 6 cases (fig. 9, Table 6).



Fig. 7: Specimen No. 2 after cutting off

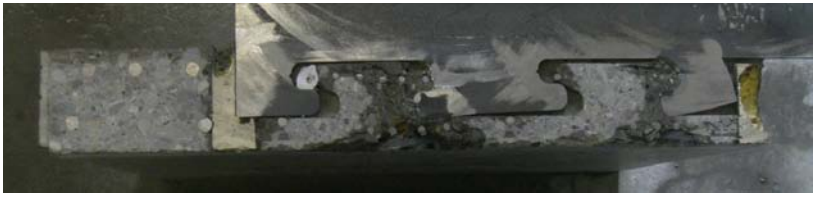


Fig. 8: Specimen No. 6 after cutting off

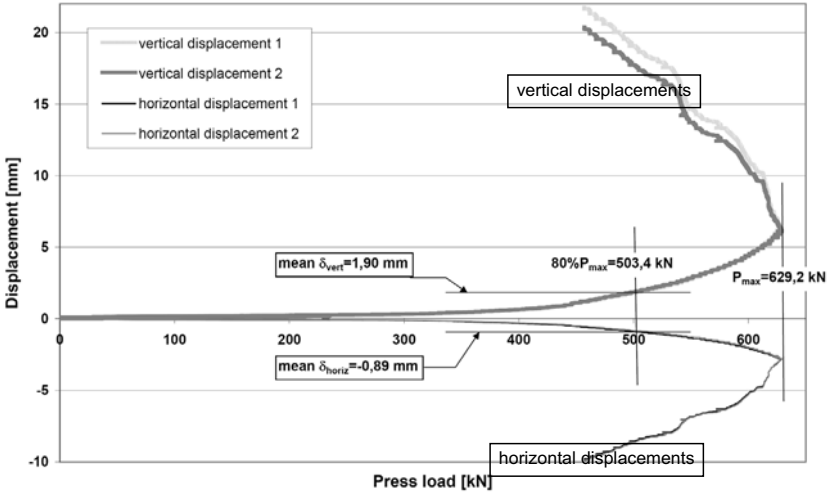


Fig. 9: Effect of lifting of the slab as a result of shearing force, on example of the specimen No. 4

Table 6: Relation vertical / horizontal displacement (see also fig. 9)

Specimen No.	Press load		Displacement at 80% P_{max}			Condition vert./horiz. displac.
	P_{max}	80% P_{max}	vertical	50% vertical	horizontal	
	[kN]	[kN]	[mm]	[mm]	[mm]	
1	505,4	404,3	0,77	0,39	-0,45	not met
2	552,8	442,2	0,71	0,36	-0,32	OK.
3	586,7	469,3	0,95	0,47	0,08	OK.
4	629,2	503,4	1,90	0,95	-0,89	OK.
5	657,8	526,3	2,52	1,26	-1,61	not met
6	709,2	567,3	2,49	1,25	-1,24	OK.

7 CONCLUSIONS

The equations derived in [4], [6], [7] for the load-carrying capacity of the concrete dowels were not conservative in the carried out experiments in case of three specimens without confining reinforcement.. In case of three other specimens with confining reinforcement steel fracture was a decisive criterion. In the experimental tests deformation capacity of concrete dowels was equal to about 6 mm. Application of spiral reinforcement can improve the load-carrying capacity, as well as the ductility of concrete dowels. The condition of relation between horizontal and vertical displacement in push-out test was fulfilled in 4 of 6 cases. The further experimental investigations need to be carried out in order to confirm these conclusions. In order to avoid steel yielding and the parting off of the upper element of the steel web, it should be manufactured as long as the medium one.

8 ACKNOWLEDGEMENT

The tests are part of comprehensive research project aiming at novel type of composite floor consisting of steel web and upper and lower concrete slabs. The space between the slabs is intended for placing HVAC installations. The authors would like to thank the Arbeitsgemeinschaft industrieller Forschungsvereinigungen (AiF) for financial support within the framework of KF 0440201ES6.

REFERENCES

[1] Andrä H.-P., “Novel connector for securing in-situ concrete slabs to steel girders”, *Beton- und Stahlbetonbau,* Vol. 80, No. 12, Dezember 1985, pp. 325-328 (in German).

[2] DIN EN 1994-1-1. Eurocode 4: *Design of composite steel and concrete structures* – Part 1.1: *General rules and rules for buildings;* German version EN 1994-1-1:2004. Edition July 2006 (in German).

[3] Hechler O., Feldmann M., Rauscher S., Hegger J., “Continuous shear connectors in high performance concrete”, Proceedings of the International Conference on *Connections between Steel and Concrete,* September 4-7, 2007, Stuttgart, Germany, pp.1017-1026.

[4] Mangerig I., Zapfe C., Burger S., “Concrete dowels in composite structures”, *Stahlbau Kalender*, Vol. 7, 2005, pp. 535-598 (in German).

[5] Schmitt V., Seidl G., Hever M., Zapfe C., „Composite bridge Pöcking – innovative girders VFT with concrete dowels“, *Stahlbau*, Vol. 73, No. 6, June 2004, pp. 387-393 (in German).

[6] Wurzer O., *Loading capacity of concrete dowels,* PhD dissertation, University of Bundeswehr, Munich, 1997, 237 pp. (in German).

[7] Zapfe C., *Loading capacity and behaviour under load of composite girders with concrete dowels as longitudinal shear connectors,* PhD dissertation, University of Bundeswehr, Munich, 2001, 200 pp. (in German)

COMPOSITE SLAB WITH INTEGRATED INSTALLATION FLOOR USING CELLULAR BEAMS

Andrea Frangi, Markus Knobloch, Elio Raveglia, Mario Fontana
Institute of Structural Engineering, ETH Zurich
8093 Zurich, Switzerland
frangi@ibk.baug.ethz.ch, knobloch@ibk.baug.ethz.ch
raveglia@ibk.baug.ethz.ch, fontana@ibk.baug.ethz.ch

Martin Mensinger, Karl Schwindl
Chair of Metal Construction, Technische Universität München
80333 Munich, Germany
m.mensinger@bv.tum.de, k.schwindl@bv.tum.de

ABSTRACT

The paper presents a new composite floor system using cellular beams. A major benefit of the novel system is the integrated installation floor, adding additional value to the floor without extra costs. The system is based on half cellular beams made of existing hot-rolled sections. The openings in the cellular beams allow placing all kind of installations in all directions, thus providing excellent flexibility to the user when changing installations. First the paper presents the general design and details of the construction of the novel floor system. Then the paper experimentally analyses the load-carrying and dynamic behaviour of two floor elements with a span of 7.2 m. The results are compared to common calculation models for composite slabs.

INTRODUCTION

A large variety of composite floor systems are widely used for buildings throughout the world. They allow fast erection and are light weight [Johnson 2004]. However in central Europe they are mostly not cost efficient in comparison to cast-in-place concrete slabs and have therefore a small market share. Floor systems for new modern buildings shall satisfy high requirements with regard to structural behaviour (stiffness, strength and vibration), sound insulation and fire safety. Further, especially office buildings require flexibility for installations that during use need to be regularly controlled, repaired, changed or replaced. Under this aspect the possibility to integrate installations in common concrete flat slabs is quite limited. The installations can be partially cast into the concrete slab (see Figure 1 left), however after concrete pouring modifications are not more possible and the reparation of damaged installations becomes difficult. For office buildings a raised installation floor is therefore frequently required (see Figure 1 right).

The Institute of Structural Engineering IBK of ETH Zurich in collaboration with the Chair of Metal Construction of the Technische Universität München is currently developing and testing a new composite slab with integrated installation floor using cellular beams. The paper first presents the general design and details of the construction of the novel floor system. Then the results of tests on the dynamic behaviour and the load-carrying capacity of two floor elements with a span of 7.2 m are presented and compared to common calculation models for composite slabs.

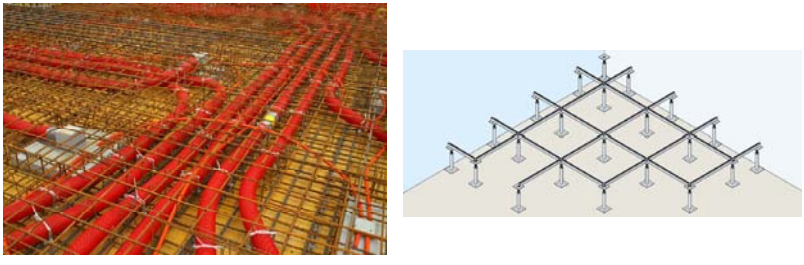


Figure 1 – Left: Installations placed in the concrete slab before concrete pouring; Right: typical raised installation floor using pedestals attached to the structural slab

NEW COMPOSITE FLOOR SYSTEM

The new composite floor system is based on half cellular steel beams made of hot-rolled sections cut by torch cutting. The cellular steel beams are cast into the concrete as shown in figure 2. The composite action between cellular beam and concrete slab is provided by reinforcing steel welded to the cellular beam.

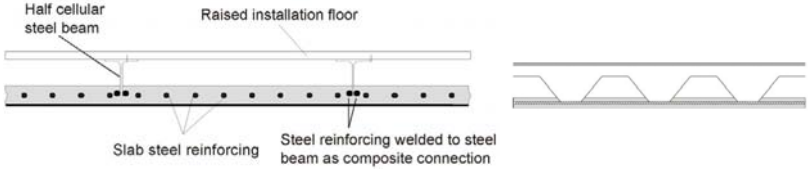


Figure 2 – New composite slab with integrated installation floor using cellular beams: the concrete slab is placed on the bottom

The composite floor elements are produced in the factory, transported from the factory directly to the site and then joined with bolted connections (see Figure 3). The size and form of the prefabricated elements are limited mainly by production, transportation and erection possibilities: cross-sections with two steel beams and with max. width of 2.5 m are favorable for production and transportation; T-cross-sections are also possible. Size of the cellular steel beams and diameter of the reinforcing steel result from static calculations. The thickness of the concrete slab varies between 8 and 10 cm depending on requirements on fire safety and sound insulation. Based on preliminary analysis the production cost of the new composite floor system is in the range of CHF 200.-/m^2 and thus comparable to cast-in-place concrete slabs.

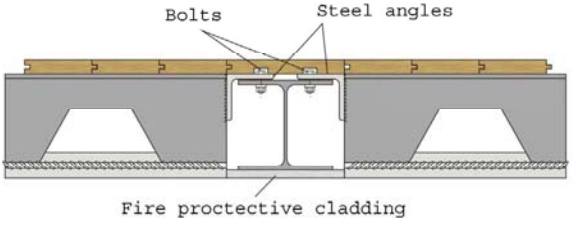


Figure 3 – Possible connection of cellular steel beams with the primary steel members

The concrete slab on the bottom of the beam seams to be on the wrong site as the concrete is in tension. However, for slabs in bending other aspects than bending resistance can become dominant. The main advantage of the new composite floor system is the integration of the raised installation floor into the slab without additional costs. The openings in the cellular beams allow placing installations in the transverse direction, thus providing excellent flexibility to the designers during construction and to the user especially during use when changing installations. Further, the concrete slab improves the fire resistance at no extra cost with respect to conventional composite floor systems. In the most cases the steel beams may remain unprotected as the fire load due to installations is small. According to the Swiss fire regulations no fire resistance is required if the fire load due to installations is less than 50 MJ/m^2. The composite action is provided by common reinforcing steel, welded headed studs or other kinds of shear connectors are not required. The steel beams are embedded in the concrete slab and create a frame action permitting to stabilize the compressive flange of the steel beams against lateral-torsional buckling.

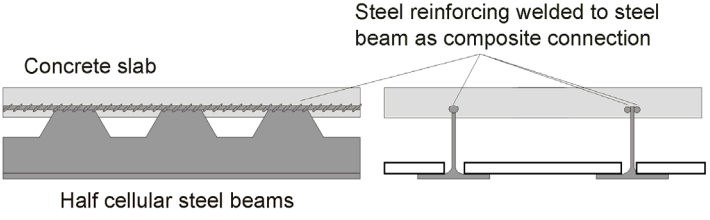


Figure 4 – New composite slab with integrated installation floor using cellular beams: the concrete slab is placed on top

When sagging bending resistance is a dominant requirement, the new composite floor system can also be used in a classical way, i.e. with the concrete slab on top (see Figure 4). In this case prefabricated panels can be placed between the steel beams forming a suspended ceiling. Thus, the composite floor system with the concrete slab on top can be implemented in lieu of conventional floor systems with suspended ceiling.

TEST SPECIMENS

The dynamic and load-carrying behaviour of the novel composite floor system was experimentally analysed using two test specimens. The composite floor elements with a total length of 7.4 m were manufactured as T-beams by the industrial partner H. Wetter AG, 5608 Stetten Switzerland, and transported to the ETH testing laboratory. The composite floor elements consisted of half cellular steel beams WPE360 (beam height = 270 mm) with steel quality S235 according to EN 10025-1 (2004). One element (called "beam I") was tested with the concrete slab on top (see Figure 5), the other beam (called "beam II") with the concrete slab on the bottom (see Figure 6). As shear connectors for beam I two rebars with diameter of 16 mm were welded to the steel beam, for beam II two rebars with diameter of 20 mm were used. The 80 mm thick concrete slab was reinforced with a steel mesh with diameter of 10 mm and spacing of 150 mm for both directions. For beam II additional reinforcing rebars with ø=10 mm were placed through the cavities of the cellular steel beam (3 rebars through each cavity). Normal concrete C25/30 according to the EN 1992-1-1 (2004) and common reinforcing steel with steel quality B500 according to the Swiss Standard SIA 262 (2003) were used. Stiffeners with thickness of 15 mm were welded on both side of the steel beam for the supports and the concentrated vertical test loads. Figures 5 and 6 show longitudinal and cross-section of the composite beams.

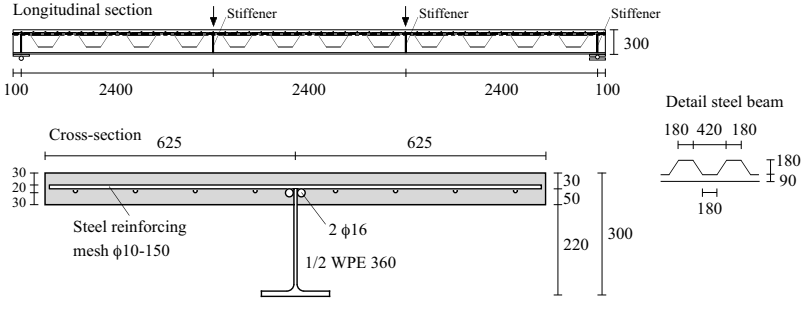


Figure 5 – Steel-concrete composite beam with concrete slab on top ("beam I")

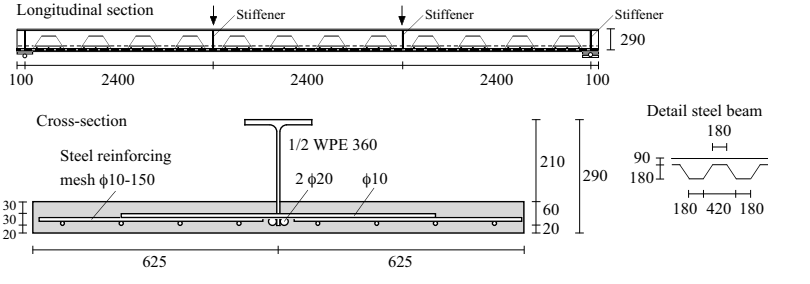


Figure 6 – Steel-concrete composite beam with concrete slab on bottom ("beam II")

The concrete compressive strength of each composite beam was tested using 3 cubes with dimensions of 150 mm according to EN 12390-3 (2001). The yield and

tensile strength of the steel beam II and the reinforcing steel used were tested with a series of tensile tests according to EN 10002-1 (2001). Table 1 summarizes the concrete cube compressive strength for both beams. Table 2 summarizes the yield and tensile strength of the steel beam II and reinforcing steel.

Table 1 – Concrete compressive strength for the composite beams

Beam	Date of beam production	Date of bending test	Date of concrete strength test	Mean strength f_c [N/mm^2]	Mean density ρ [kg/m^3]
Beam I	12.9.2007	1.11.2007	2.11.2007	39.5	2320
Beam II	14.9.2007	5.11.2007	2.11.2007	38.0	2320

Table 2 – Yield strength f_y and ultimate tensile strength f_u of beam II and reinforcing steel

	Steel beam II		Reinforcing steel ø10 mm		Reinforcing steel ø20 mm	
	Test 1	Test 2	Test 1	Test 2	Test 1	Test 2
f_y [N/mm^2]	314	304	481	475	545	544
f_u [N/mm^2]	428	430	617	618	649	647

TEST SET-UP AND TEST PROCEDURE

The vibration and bending tests were performed in the IBK testing laboratory of ETH Zurich. The bending tests were performed as four point tests with a span between the supports of 7.2 m. The distance from the support to the point load was 2.4 m (see Figure 7).

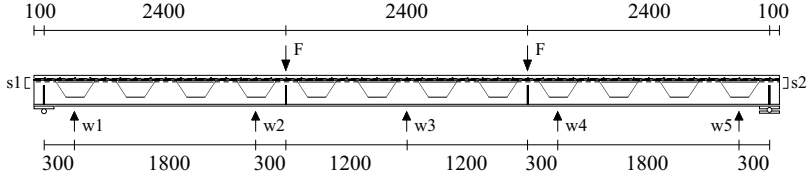


Figure 7 – Static system and position of LVDTs for the bending tests with steel-concrete composite beams (“beam I” is shown, for “beam II” same test arrangement)

Figure 8 shows an overview of the test arrangement in the IBK testing laboratory and a detail of the point load. Details of the fixed and sliding support are shown in Figure 9. The steel plates at the supports were 200 mm long. The beams were braced in order to prevent lateral-torsional buckling (see Figure 8).



Figure 8 – Overview of the test arrangement for the bending tests (left) and detail of the point load (right)

During the tests the vertical deformation of the beam was measured close to the supports and the point loads as well as at mid-span using linear voltage displacement transducers (LVDTs). Further the end slip deformation between concrete slab and steel beam was measured at both supports using LVDTs (see Figure 9). Figure 7 shows the position of all LVDTs used for the bending tests (w1-w6: vertical deformation; s1-s2: end slip deformation). The load level was directly measured from the pressure of the hydraulic jacks.

Before the bending test was carried out the dynamic behaviour of both beams was experimentally studied with a series of vibration tests. Sandbag and heel drop tests were used to measure the vibration response to a sudden impact. The sandbag test was performed using a sandbag of 25 kg that was dropped from about 1 m height at mid-span of the beam. The heel drop test was performed by a person of average weight (75 kg), standing at mid-span of the beam, rising onto the balls of his feet and then dropping down on his heels. For both tests the resulting acceleration as well the vertical deformation were measured by accelerometers and LVDTs placed at mid-span of the beam. The analysis of the response spectrum permitted the evaluation of the frequency of the beams.

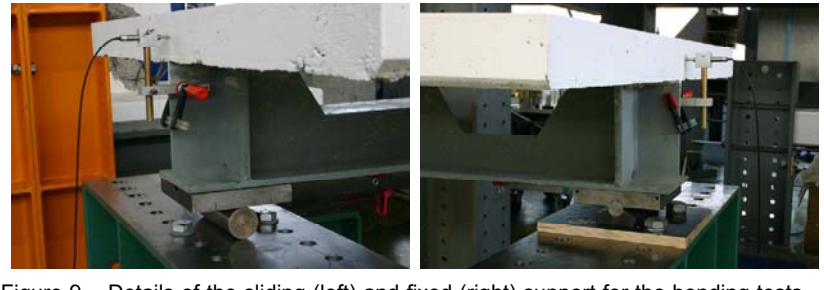


Figure 9 – Details of the sliding (left) and fixed (right) support for the bending tests. Figure shows also the LVDTs used to measure the end slip between concrete slab and steel beam

RESULTS OF BENDING TESTS

Beam I with the concrete slab on top (see Figure 5) was first subjected to seven loading cycles. The maximum value of the loading cycles was 5, 10, 15, 20, 30, 40 and 60 kN. Then the beam was loaded to failure at a rate of approximately 10 kN per minute.

Figure 10 shows the measured load per jack-vertical deflection curves for the bending test with beam I. Figure 10 left shows the vertical deflection at mid-span. The deflection measured with the other LVDTs is shown in figure 10 right. No end slip deformation between concrete slab and steel beam was measured. The beam showed linear-elastic behaviour until approximately 70 kN. At higher load levels a non-linear plastic behaviour was observed. The steel beam started yielding at about 92 kN leading to a large increase of the vertical deflections. The load level remained constant during yielding of the steel beam until the test was concluded when the deflection at mid-span reached about 230 mm (see Figure 11 left). During the test no significant cracks in the concrete slab were observed, except a longitudinal crack on the top of the concrete slab observed during yielding of the steel beam (see figure 11 right). Possible reason for the crack are splitting forces (i.e. tensile stresses) in the concrete slab perpendicular to the steel beam direction.

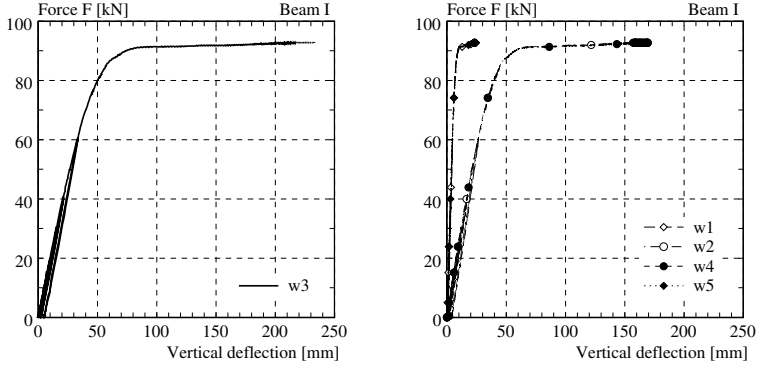


Figure 10 – Measured load per jack-vertical deflection curves for the bending test with beam I



Figure 11 – Bending test with composite beam I (left) and cracking of the concrete slab observed during yielding of the steel beam (right)

Beam II with the concrete slab on the bottom (see Figure 6) was first subjected to six loading cycles. The maximum value of the loading cycles was 5, 8, 10, 15, 20 and 30 kN. Then the beam was loaded to failure at a rate of approximately 10 kN per minute. Figure 12 shows the measured vertical deflection curves for the bending test. No end slip deformation between concrete slab and steel beam was measured. The beam showed linear-elastic behaviour until about 8 kN, when the first cracks occurred in the concrete slab. When the load was increased further additional cracks were observed that successively reduced the stiffness of the composite beam and thus led to a non-linear increase of the vertical deflections. The development of the last cracks was observed at about 45 kN. The reinforcing steel started yielding at about 66 kN leading to a large increase of the vertical deflections. The load level remained fairly constant during yielding until the test was concluded when the deflection at mid-span reached about 200 mm (see figure 13). Based on visual observations after the bending test it can be assumed that the upper flange of the steel beam reached the yield strength during yielding of the reinforcing steel.

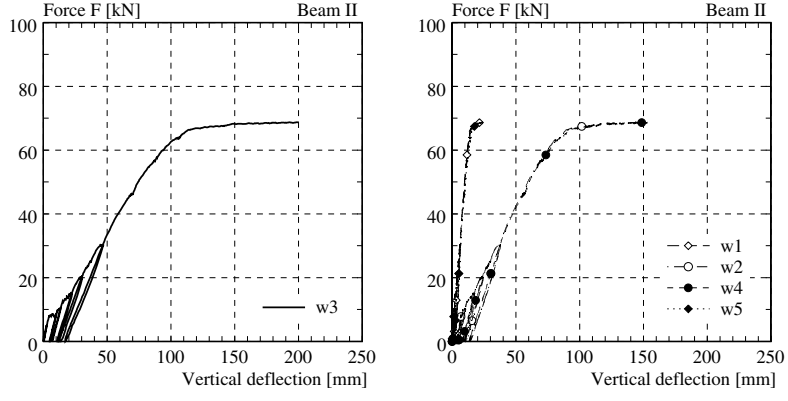
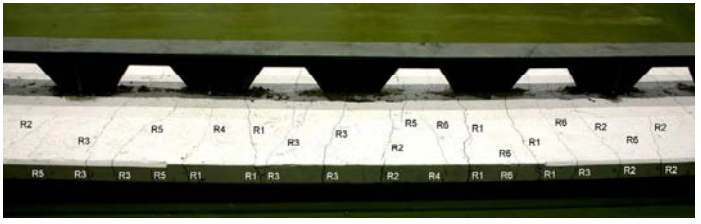


Figure 12 – Measured load per jack-vertical deflection curves for the bending test with beam II



Figure 13 – Bending test with composite beam II

Figure 14 shows the cracks observed on the concrete slab in the middle part of the beam between the hydraulic jacks. Further Figure 14 shows at which load level the different cracks marked with R1 to R6 occurred during the bending test. The cracks were equally distributed with a spacing of about 150mm.



Load level
R1: 8 kN
R2: 10 kN
R3: 15 kN
R4: 20 kN
R5: 30 kN
R6: 45 kN

Figure 14 – Observed cracks on the concrete slab

BASIC ANALYTICAL MODELS

The results of the bending tests were compared to results based on simple analytical models. The bending tests showed that the reinforcing steel welded to the steel beam was able to guarantee a rigid full composite action between steel beam and concrete slab. Thus, the load-carrying behaviour of the tested beams was calculated using conventional principles of the structural analysis for steel-concrete composite beams (see for example EN 1994-1-1 2004 and Johnson et al. 2007). The plastic resistance moment M_{pl} of the composite beams was calculated based on the rigid-plastic theory.

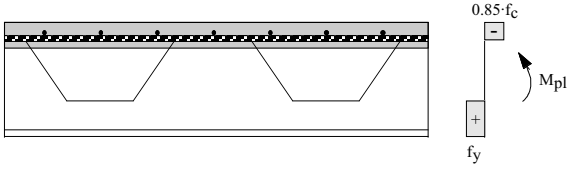


Figure 15 – Model for the calculation of the plastic resistance moment M_{pl} of the composite beam I with concrete slab on top

For beam I with the concrete slab subjected to compression and the steel beam mainly subjected to tension it was assumed that the flange and the lower part of the web of the steel beam was stressed to its yield strength f_y and the concrete slab resisted a compressive stress of $0.85*f_c$, constant over the whole depth between the plastic neutral axis and the most compressed fibre of the concrete (see Figure 15). For the calculation of M_{pl} the effective measured values of yield strength f_y and compressive strength f_c according to Table 1 and 2 were considered. Further, the reinforcement in the concrete slab was neglected. The elastic behaviour of the composite beam was calculated assuming the uncracked flexural stiffness, i.e. assuming that the whole thickness of the concrete slab was uncracked. The following moduli of elasticity were assumed for the calculation: E_a = 210 kN/m^2 for steel and E_c = 35 kN/m^2 for concrete. Figure 16 left compares the calculated load-carrying behaviour of the composite beam I with the measured load-deflection curve. The simple analytical model led to adequate results for the stiffness and the ultimate resistance compared to the test results.

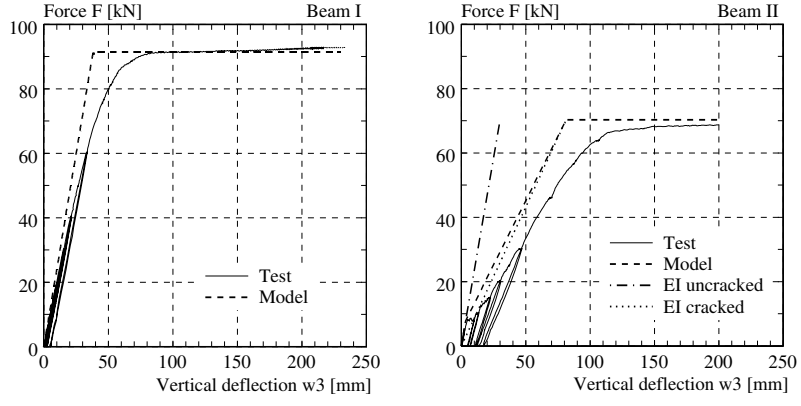


Figure 16 – Comparison between test results and simple calculation models

For beam II with the concrete slab subjected to tension and the steel beam mainly subjected to compression it was assumed that the reinforcing steel (2ø20 + 8ø10, see Figure 6) were stressed to their yield strength f_y, while the flange of the steel beam partially reached its yield strength f_y (see Figure 17).

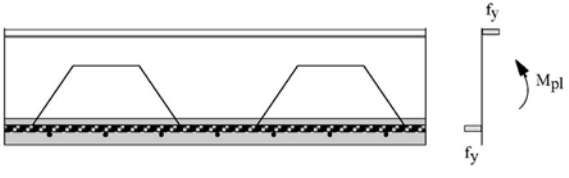


Figure 17 – Model for the calculation of the plastic resistance moment M_{pl} of the composite beam II with concrete slab on the bottom

The elastic behaviour of the composite beam was calculated assuming the uncracked flexural stiffness as well as the cracked flexural stiffness. The uncracked flexural stiffness was calculated assuming that the concrete slab in tension was uncracked. The cracked flexural stiffness was calculated neglecting the concrete slab in tension but including the reinforcing steel. The cracking moment of the concrete slab was calculated assuming a concrete tensile strength of 3.0 MPa based on the compressive strength measured. For the moduli of elasticity of concrete and steel the same values as for beam I were assumed. Table 3 compares the calculated and measured values for the composite beam II. It can be seen that the calculated cracking moment $M_{cracking}$, the plastic resistance moment M_{pl} as well as the uncracked and cracked flexural stiffness of the composite beam well agreed with the measured values. Figure 16 right compares the calculated load-carrying behaviour of the composite beam II with the measured load-deflection curve. Under service loads the model predicted the deflection measured fairly well. By increasing load level the measured deflection was underestimated by the calculation model due to the strong influence of concrete cracking.

Table 3 – Comparison between calculated and measured values for beam II

	$EI_{uncracked}$ [kN/mm^2]	$EI_{cracked}$ [kN/mm^2]	$M_{Cracking}$ [kNm]	M_{pl} [kNm]
Test	$2.823 \cdot 10^{10}$	$1.004 \cdot 10^{10}$	19.2	158
Model	$3.097 \cdot 10^{10}$	$1.145 \cdot 10^{10}$	20.1	168
Test/Model	0.91	0.88	0.95	0.94

RESULTS OF VIBRATION TESTS

Before the bending test was performed the dynamic behaviour of the composite beam was experimentally analysed with a series of vibration tests. Table 4 and 5 shows the results of the vibration tests for beam I with the concrete slab on top (see Figure 5) and beam II with the concrete slab on the bottom (see Figure 6). The tests were performed first with sliding supports on both sides and then with the same supports as for the bending test (i.e. fixed on one side and sliding on the other side). For beam II the vibration tests were repeated after the composite beam was loaded up to 20 kN, i.e. after the concrete slab was mostly completely cracked. This allowed the analysis of the influence of concrete cracking on the natural frequency of the composite beam.

Table 4 – Results of the vibrations tests with beam I

Test	Support	Frequency [Hz]	Max. vertical deformation [mm]
Sandbag	Sliding on both sides	9.5	1.20
Heel drop	Sliding on both sides	9.5	0.40
Heel drop	Sliding on both sides	9.5	0.47
Sandbag	Fixed and sliding	9.5	1.16
Sandbag	Fixed and sliding	9.5	1.22
Heel drop	Fixed and sliding	9.7	0.50
Heel drop	Fixed and sliding	9.7	0.65

The measured natural frequency of beam I was about 9.5 Hz for both tests (sandbag and heel drop) and both supports tested. For beam II with the uncracked concrete slab the measured natural frequency varied between 9.1 and 9.3 Hz for both tests (sandbag and heel drop) and both supports tested and was fairly the same as for beam I. For beam II with the cracked concrete slab the measured natural frequency varied between 7.2 and 7.4 Hz. The observed reduction of the natural frequency for beam II was due to the reduction of the stiffness of the composite beam after cracking of the concrete slab.

Table 5 – Results of the vibrations tests with beam II

Test	Support	Concrete slab	Frequency [Hz]	Max. vertical deformation [mm]
Sandbag	Sliding on both sides	Uncracked	9.1	1.40
Sandbag	Sliding on both sides	Uncracked	9.1	1.35
Heel drop	Sliding on both sides	Uncracked	9.3	0.42
Heel drop	Sliding on both sides	Uncracked	9.3	0.31
Sandbag	Fixed and sliding	Uncracked	9.2	1.39
Sandbag	Fixed and sliding	Uncracked	9.2	1.37
Heel drop	Fixed and sliding	Uncracked	9.3	0.88
Heel drop	Fixed and sliding	Uncracked	9.2	0.85
Sandbag	Fixed and sliding	Cracked	7.3	1.80
Sandbag	Fixed and sliding	Cracked	7.3	1.87
Sandbag	Fixed and sliding	Cracked	7.2	1.91
Heel drop	Fixed and sliding	Cracked	7.4	0.68
Heel drop	Fixed and sliding	Cracked	7.2	0.44

The requirements on building floor systems with regard to vibration depend on the expected use of the building [CEB Bulletin 2001]. For example the Swiss Standard SIA 260 (2003) recommends for dance and concert halls that the natural frequency should be higher than 7.0 Hz, for gymnasiums and sport halls higher than 8.0 Hz. Office buildings are less subjected to man-induced vibrations and the natural frequency should be higher than 5.0 Hz [Bachmann et al. 1997]. Thus, the natural frequency measured for beam I can be evaluated as not critical with regard to vibrations. The vibration tests with beam II with the cracked concrete slab showed that this beam may be susceptible to vibration problems.

CONCLUSIONS

The paper presented a new composite floor system with integrated installation floor, adding additional value to the floor without extra costs. The system is based on half cellular beams made of hot-rolled sections with the web of the steel beam cast into the concrete. The openings in the cellular beams allow placing all kinds of installations in all directions, thus providing excellent flexibility to the designers during construction and to the user especially during use when changing installations. Further, the concrete slab placed on the bottom of the steel beams improves the fire resistance of the composite floor with respect to conventional composite floor systems with the concrete slab placed on top of the steel beams. The composite action between cellular beam and concrete slab is provided by common reinforcing steel welded to the cellular beams. Welded headed studs or other kinds of shear connectors are not required.

Two bending tests were performed with composite beams with a span of 7.2 m, one with the concrete slab on top subjected to compression, the other one with the concrete slab on the bottom. For both tests, the reinforcing steel welded to the steel beam was able to guarantee a rigid full composite action between steel beam and concrete slab. The composite beam with the concrete slab on top showed typical elasto-plastic behaviour. For the composite beam with the concrete slab on the bottom a non-linear behaviour was observed due to cracking of the concrete slab.

For both tests large deflections were observed due to yielding of the steel beam and steel reinforcing. The load-carrying behaviour of the composite beams was calculated with simple analytical model considering plastic bending moment distribution and cracking of concrete. For both tests, the simple model led to adequate results for the stiffness and the ultimate resistance compared to the test results. The measured natural frequency of the composite beam with the concrete slab on top was about 9.5 Hz, for the composite beam with the concrete slab on the bottom the measured natural frequency varied between 9.1 and 9.3 Hz before concrete cracking and 7.2 and 7.4 Hz after concrete cracking. Further research and investigations are planned to study in detail the dynamic behaviour of the composite floors with the concrete slab on the bottom.

REFERENCES

Bachmann, H. et al. (1997), "Vibration problems in structures – Practical Guidelines", 2nd Edition, Birkhäuser Editor, Basel, Boston, Berlin.

CEB Bulletin No. 209, Vibration problems in structures, Practical Guidelines, CEB - Comite Euro-International du Beton, 1991.

EN 1992-1-1 (2004), Eurocode 2: Design of concrete structures - Part 1-1: General rules and rules for buildings.

EN 1994-1-1 (2004), Eurocode 4: Design of composite steel and concrete structures - Part 1-1: General rules and rules for buildings.

EN 10002-1 (2001), Metallic materials - Tensile testing - Part 1: Method of testing at ambient temperature.

EN 10025-1 (2004), Hot rolled products of structural steels - Part 1: General technical delivery conditions.

EN 12390-3 (2001), Testing hardened concrete - Part 3: Compressive strength of test specimens.

Johnson, R.P., "Composite structures of steel and concrete: beams, slabs, columns, and frames for buildings, LinkMalden, MA: Blackwell Publishing, 2004.

Johnson, R.P. and Anderson, D., "Designers' guide to EN 1994-1-1: Eurocode 4: design of composite steel and concrete structures", Thomas Telford, London, 2007.

SIA 260 (2003), Basis of structural design, Swiss Association for Standardization.

SIA 262 (2003), Concrete Structures, Swiss Association for Standardization.

STEEL FIBRE REINFORCED CONTINUOUS COMPOSITE SLABS

Florian P. Ackermann
Kaiserslautern University of Technology
Institute of Concrete Structures and Structural Design
Kaiserslautern, Germany
Florian.Ackermann@rhrk.uni-kl.de

Jürgen Schnell
Kaiserslautern University of Technology
Institute of Concrete Structures and Structural Design
Kaiserslautern, Germany
jschnell@rhrk.uni-kl.de

ABSTRACT

The paper deals with composite slabs using steel fibre reinforced concrete as topping. The aim of a research project of the Kaiserslautern University of Technology is the evaluation of design recommendations for steel fibre reinforced composite slabs. The constructive as well as the structural conventional reinforcement are substituted completely by the use of steel fibres. The main focus of a first test series was to research the load-bearing behaviour and the possible rotation capacity of steel fibre reinforced composite slabs in the region of negative bending. In a second test series, four full scale tests on continuous composite slabs were accomplished.

INTRODUCTION

Nowadays, the use of steel composite floors in buildings is common practice. Conventional steel composite floors have proved themselves as an extremely cost-effective floor system for domestic, commercial or industrial buildings. Significant advantages arise from the low construction costs and especially from the benefit of saving time during the building process. Researches in composite slabs with steel fibre reinforced concrete topping are in progress at the Kaiserslautern University of Technology. Different types of slabs with varied geometries are selected for the tests. Special attention should be paid to the redistribution of bending moments from the support to the field. The conventional reinforcement is completely substituted by the steel fibres. Thus, for continuous composite floors an even more efficient and more economic slab system can be achieved.

Steel composite slabs are load bearing members, which consist of steel sheeting and a concrete topping. In the construction process, the steel sheeting will be placed by hands. After fixing, it is available as a working platform that provides a safety screen at the same time. During the concreting, the sheeting acts as a shuttering. Thus, a quick and a space-saving progress of construction work can be achieved. Figure 1 displays the layout of a conventional composite slab (left) and a steel fibre reinforced one (right).

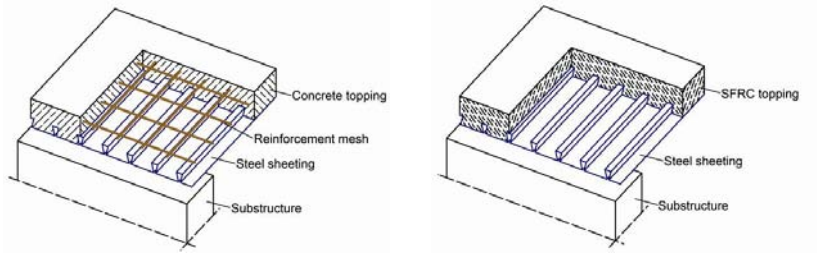


Fig. 1 – layout of a conventional composite slab (left) and a steel fibre reinforced one (right)

In composite building construction the application of steel sheets as long as possible and therewith the utilization of continuously working composite floor slabs has been proved to be an outstanding productive construction method [Bode 1998].

In Germany, the design of steel decking and composite slabs is regulated by DIN 18800-5:2007 [DIN 18800-5 2007], in Europe by Eurocode 4 [DIN EN 1994-1-1 2006]. According to these guidelines the concrete topping has always to be proved with a nominal reinforcement of 0.8 cm²/m in both directions. This reinforcement may be imputed to the calculated reinforcement which is required for structural bending. Usually, the steel sheets are installed over several spans. No joints are arranged in the concrete topping and therefore the floor behaves as a continuous slab system and negative bending will occur over the inner supports. Hence, for all composite slabs an additional reinforcement has to be built in (see Figure 1 left). The aim of the research project is to substitute the constructive as well as the structural reinforcement by the use of steel fibre reinforced concrete.

STEEL FIBRE REINFORCED CONCRETE

The application of fibres as an additive in order to advance the ductility of the concrete has got its origins in the ancient times. Animal hairs and straw fibres were used in order to enhance the material properties of adobes. The idea to improve the material properties of concrete by fibre admixture doesn't reach back so far. The first patent for the application of steel fibres was granted in 1874. However, the researches in the field of steel fibre reinforced concrete have been started substantially later (since 1960).

In Germany, no standard for the design of steel fibre reinforced concrete exist until now. Its appliance is regulated by technical approvals or by approval in individual cases only. The German Society for Concrete and Construction Technology (DBV) has published a technical bulletin concerning the design of steel fibre reinforced concrete [DBV 2001], which does not provide an officially codified standard yet. According to this bulletin, steel fibre reinforced concrete is defined as a concrete corresponding to the German concrete standard [DIN 1045-1 2008] which is provided with steel fibres in order to achieve specific attributes. In order to resolve the drawback that no codified standard exists to regulate the steel fibre reinforced material, the German Committee for Structural Concrete (DAfStb) has decided to issue a new guideline [DAfStb 2008]. This document corresponds to the regular German concrete standard [DIN 1045-1 2008] and supplements it with the additional

regulations for steel fibre reinforced concrete. But at present the guideline is not complete yet (it is located in the final draft). The decision of its transfer to the approval procedure is running at present.

Until now, industrial ground floor slabs constitute the main field of application of the steel fibre reinforced concrete. In Germany, 25 percent of the manufactured ground floor slabs are made of this material [Falkner and Teutsch 2006]. In the past years, this material shows a favourable trend, what is reflected in the application for domestic construction, too. Here, floor slabs and cellar walls represent the main field of the application. Primary, the substitution of the constructive reinforcement is the main focus. A large number of tests have shown that a complete substitution of the structurally required reinforcement is impossible. The addition of fibres with volume ratios that are common in practice does not increase the resistance capacity significantly. Solely the manipulation of the post fracture behaviour and as a result the improvement of the ductility stands to the fore.

The vision of some planners that steel fibre reinforced concrete will substitute the normal concrete totally has to be invalidated. It will never be likely to displace the normal concrete. Quite the contrary, steel fibre reinforced concrete can be integrated between the reinforced concrete and the unreinforced one. In the uncracked state the fibres do not effect a significant modification of the resistance capacity, because their volume ratio constitutes only a small part of the entire volume. The addition of steel fibres effects only a marginal enhancement of the compression strength. Solely, the behaviour after crushing shows an appreciable changing. With increasing fibre ratio, the ductility is progressing. In tension, the behaviour depends on the fibre ratio. The more fibres are admixed, the merrier is the load bearing behaviour after cracking. If the fibre ratio is conforming to the critical fibre volume V_{crit}, the full load can be carried by the cracked cross section. Is the volume higher than the critical volume, the actual load can be increased after cracking.

For members the design of which is in accordance with [DBV 2001] or [DAfStb 2008], a firm condition of equilibrium has to be reached after cracking of the cross section. In statically determinated systems, this demand is not possible with fibre volumes that are common in practice. It becomes apparent that pure steel fibre reinforced concrete can substitute the conventional reinforcement only in statically indeterminated systems or in statically determinated systems with a permanent normal compressive force as a result of an extraneous cause. Within the research project on steel fibre reinforced continuous composite floors, the application of steel fibre reinforced concrete as a load bearing element is possible, because the possibility of a redistribution of the stress resultants after cracking is given. The ductile behaviour of steel fibre reinforced concrete affected by a multiple crack pattern allows a large rotation and thus the precondition of redistribution.

The use of steel fibre reinforced concrete as a load bearing element call for considerations concerning a raised security level. The investigated composite slab systems possess an adequate redundancy. In case of bad workmanship (e.g. undersized fibre content – or worst case – no fibre content over the intermediate support) a series of simply supported beams emerges and the steel sheeting keeps the slab in position.

STEEL FIBRE REINFORCED COMPOSITE SLABS

Based on researches described in [Sauerborn 1995], [Droese and Riese 1996] and [Riese 2006] steel fibre reinforced continuous composite slabs are investigated at Kaiserslautern University of Technology. Aim of the research project is the evaluation of design recommendations for steel fibre reinforced composite slabs. No conventional steel reinforcement (bars or mesh) have been built in: the hogging bending moment is only carried by the steel fibre reinforced concrete. This innovative slab system comprises an enormous potential for savings. Its outstanding beneficial characteristics are:

- Profile sheeting acts as stay-in-place formwork and constitutes bottom reinforcement for the slab; furthermore it offers an immediate working platform
- Labour intensive steel fixing, reinforcement drawings and the reinforcement acceptance procedure can be omitted
- Enormous time saving in building process
- Due to its low weight the sheets can be placed by hand without using any crane
- Lower stock requirements needed
- Less deflection due to the continuous bending effect will occur
- For the complete system savings in the range of 10 percent of the total costs are predicted [Gossla and Pepin 2004]

In the area of negative bending moments, the structural analysis is carried out in analogy to a normal concrete slab. The upper face of the slab is tensioned and at the bottom side the compression zone is located, which has a more or less comb-shaped form as a result of the geometry of sheeting. The steel sheet section may account for the structural analysis, if it runs continuously over the intermediate support. In case of a joint or an overlapping, the resistance of the steel sheet section may not be taken into account. This effect was found by Stark and Brekelmans during their researches, too [Stark and Brekelmans 1996]. Particularly in case of a poor reinforcement ratio of the hogging area – what is common in case of plain steel fibre reinforced concrete – or in case of a larger sheet thickness, the load bearing capacity of the sheet is respectable. In the area of negative bending, the depth of the compression zone as a result of the humble reinforcement ratio is very small. The plastic neutral axis is located very deep in the sheeting, which therefore is related with a small compressive force only. Correspondingly, the forces that have to be carried over the composite joint are small, too. Already sheets with a very bad composite behaviour achieve a full dowelling ratio at the support.

According to [DIN 18800-5 2007] or [DIN EN 1994-1-1 2006] the moment resistance of a continuous composite slab at the support can be analysed with a perfect plastic stress distribution. This proposed distribution was modified for the analysis of steel fibre reinforced composite slabs. The tensile resistance of the steel fibre reinforced concrete is also considered by a stress block. For the determination of the tensile properties, material tests on steel fibre reinforced concrete beams according to [DBV 2001] were carried out and evaluated (determination of $f_{eq,ct,II}$). Figure 2 displays the miscellaneous bearing ratios, which are accounted for the evaluation of the plastic moment resistance. According to [DBV 2001] a scale factor α_{sys} (values between 1.0 and 0.8, subject to the slab height) and a factor for the long term behaviour of the concrete α_c (value 0.85) are also taken into account for the calculation. Due to the use of a stress block in the compression zone, the compressive strength of the

concrete is reduced by a factor k_c of 0.8 according to [DASt 1994] (national annex of Eurocode 4).

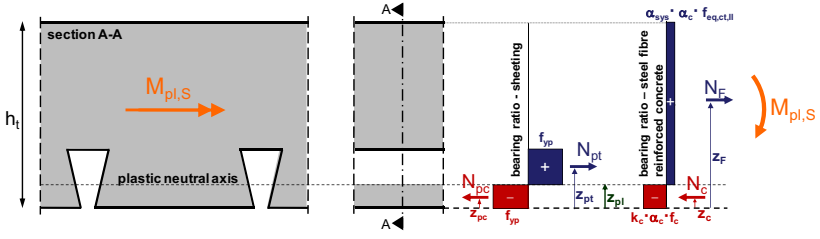


Fig. 2 – determination of the full plastic moment resistance for negative bending

with: N_{pc}: compression force in the sheeting
N_{pt}: tensile force in the sheeting
N_c: compression force in the steel fibre reinforced concrete
(the value of the stress block is calculated by $k_c \cdot \alpha_c \cdot f_c$)
N_F: tensile force in the steel fibre reinforced concrete
(the value of the stress block is calculated by $\alpha_c \cdot \alpha_{sys} \cdot f_{eq,ct,II}$)

The location of the plastic neutral axis has to be estimated by an iterative procedure as long as the equilibrium condition (1) is fulfilled.

$$-(N_c + N_{pc}) + N_{pt} + N_F = 0 \quad (1)$$

Then the full plastic moment resistance is calculated according to equation (2).

$$M_{pl} = N_{pt} \cdot z_{pt} + N_F \cdot z_F - N_{pc} \cdot z_{pc} - N_c \cdot z_c \quad (2)$$

TEST PROGRAM

Steel fibre reinforced concrete (SFRC) properties of the used mixtures

For the first two series, different steel fibre reinforced concrete mixtures were used. In series #1, concrete with a fibre content of 100 kg per cubic meter (or 1.27 Vol. %) was mixed. The corrugated ARCELOR-TABIX fibre with a length of 50 mm and a diameter of 1.3 mm was employed. In order to get the material properties of the concrete, different material tests were accomplished before starting the slab tests. The compressive strength $f_{cm,cyl}$, the modulus of elasticity E_{cm}, the flexural strength and - outcoming from this - the equivalent tensile strength $f_{eq,ctm,I/II}$ were determined (see Table 1). The evaluation of the SFRC-properties was carried out according to SFRC-bulletin [DBV 2001]. In a further step, the concrete mixture should be optimised. The main focus of these optimisations was to reduce the fibre volume, while keeping up the good concrete properties of the 100 kg/m³ mixture. For an additional test specimen of series #1, a new high strength fibre of ARCELOR (type: HE+) was used. The straight fibre with hooked ends has a length of 60 mm and a diameter of 1 mm. Its tensile strength averages 1450 MPa. The fibre content was reduced to 60 kg per cubic meter (or 0.76 Vol. %). Although the fibre ratio was scaled down, the behaviour of this optimised mixture shows a better load carrying capacity, especially in the range of higher displacements (see Figure 3).

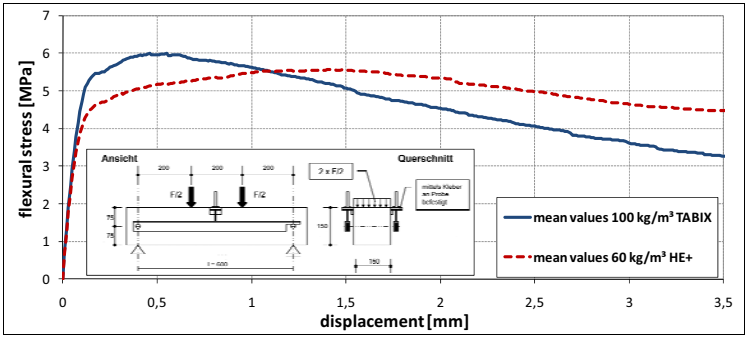


Fig. 3 – Stress-displacement curves for the SFRC concrete mixtures of series #1 and #2

specimen	fibre content	$f_{cm,cyl}$ [N/mm²]	E_{cm} [N/mm²]	$f_{eq,ctm,I}$ [N/mm²]	$f_{eq,ctm,II}$ [N/mm²]	$f_{eq,ctm,II,25‰}$ [N/mm²]	age [d]
S1_SHR_51_V1	100 kg/m³ TABIX 1.3/50	61,72	34790	2,49	1,63	1,30	42
S1_SHR_51_V2		63,71	33950	2,34	1,43	1,13	66
S1_HODY_V1		61,72	34790	2,49	1,63	1,30	42
S1_HODY_V2		57,56	36190	2,46	1,61	1,27	64
S1_SHR_51_V3	60 kg/m³ HE+ 1.0/60	59,60	38619	2,22	1,81	1,44	45
S2_SHR_51_V1		46,97	35197	2,41	2,01	1,59	34
S2_SHR_51_V2		41,01	30702	1,69	1,27	1,03	36
S2_HODY_V1		41,49	31207	2,44	2,01	1,59	32
S2_HODY_V2		43,99	29678	2,15	1,70	1,35	35

Table 1 – SFRC material properties series #1 and #2

with:

$f_{cm,cyl}$: mean value of cylindrical compressive strength

E_{cm}: mean value of modulus of elasticity

$f_{eq,ctm,I}$: mean value of equivalent tensile strength, deformation range I

$f_{eq,ctm,II}$: mean value of equivalent tensile strength, deformation range II

$f_{eq,ctm,II,25‰}$: mean value of equivalent tensile strength, deformation range II, evaluation at 25 ‰

Test series and specimen

Until now, two different test series were carried out. In the first tests series, the possible rotation at the middle support of a two-span composite slab was investigated. Therefore, only the area of the hogging moment was simulated and tested. In the second test series, four full scale tests on continuous composite slabs were carried out. For all tests of the first two series, two different cross sections were used (see Figure 4).

In the meantime, several different types of steel sheeting exist for the construction purposes. According to their geometry they can be separated into two main categories: the re-entrant (dovetail) profiles with or without indentations and the trapezoidal profiles with web indentations or embossments.

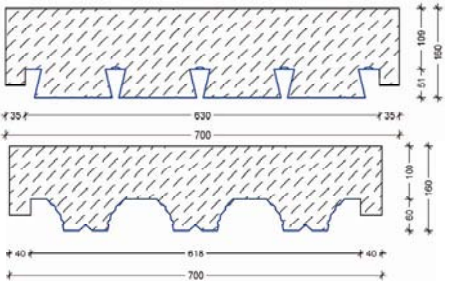


Fig. 4 – cross sections of the test specimens (left: HOLORIB SHR51 sheet, right: HODY sheet)

A sufficient composite action between the sheet and the concrete topping has to be guaranteed. For testing sheets of both categories were used. As a typical representative for the re-entrant geometry the SUPERHOLORIB SHR 51 sheet was used (see. Figure 4 left), as typical representative for the trapezoidal geometry the HODY sheet was built in (see Figure 4 right). All specimens were fully supported during casting. This is the most unfavourable case for the composite joint, because it has to cope with the dead loads as well. Both lateral edges of the sheeting were enclosed with concrete flanges in order to avoid a separating of the sheeting and the concrete topping. So, the full participation on the load bearing of the sheeting can be guaranteed over the entire width. Table 2 gives an overview over the specimens and dimensions of the first and second test series.

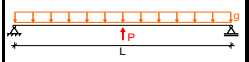
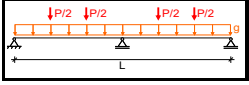
specimen		system	length L [mm]	width [mm]	height [mm]
	S1_SHR_51_V1	single-span	2000	700	160
	S1_SHR_51_V2		2000	700	160
	S1_HODY_V1		2000	700	160
	S1_HODY_V2		2000	700	160
	S1_SHR_51_V3		2000	700	160
	S2_SHR_51_V1	two-span	6000	700	160
	S2_SHR_51_V2		6000	700	160
	S2_HODY_V1		6000	700	160
	S2_HODY_V2		6000	700	160

Table 2 – test specimens of series #1 and #2

Series #1

The test setup of series #1 is shown in Figure 5. The span of the slab averages 2.00 meters, the width 70 centimetres and the slab depth 16 centimetres (sections see

Figure 4). In the middle of the span, the load was linearly set up by a hydraulic jack. It was increased by imposing small load steps up to the failure load. The tests were carried out with displacement control so that as much information as possible could be recorded on the support behaviour. The loads at the crossheads were measured with load cells. The displacements and the end-slip were recorded with displacement transducers. In the middle and in the quarters of the span, strain gauges were applied to the top and the bottom of the steel sheeting. The strain at the surface of the concrete slab was recorded with strain-measuring points. Further information and details about series #1 can be gleaned from [Ackermann 2007].

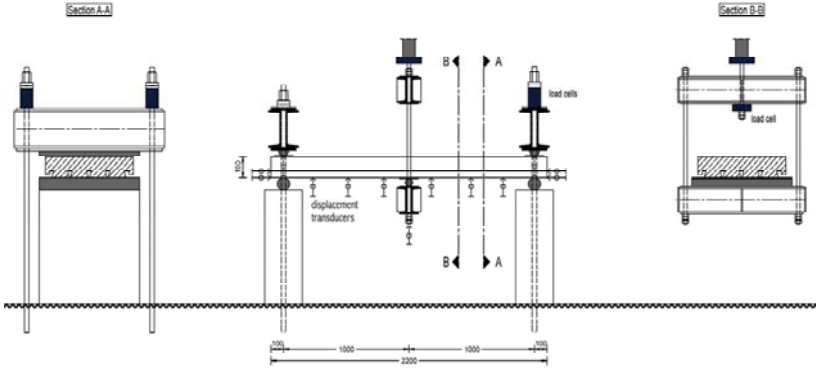


Fig. 5 – test setup - series #1 (dimensions in mm)

Series #2

In a second test series, four tests on continuous composite slabs were carried out. The setup is shown in Figure 6. Both spans of the slab are 3.00 meters, the width 70 centimetres and the slab depth 16 centimetres (sections see Figure 4). In the third points of the span, the load was linearly set up by hydraulic jacks. It was increased in small load steps up to the failure load. The loads at the crossheads were measured with load cells. Under the middle support, the reactions were recorded with two load cells.

The slab was built up as a simple span slab. Afterwards, the crossheads and the load introduction construction were arranged. In a first step, the middle support was lifted up by spindles until the hogging moment has a value of a hogging moment produced of dead load and superstructural parts. Then, the test was started. The displacements and the end-slip were recorded with displacement transducers. At the middle support and at the load introduction points, strain gauges were applied to the top and the bottom of the steel sheeting. The strain at the surface and on the side of the concrete slab was recorded with strain-measuring points. In order to achieve a predefined shear introduction length, crack inducers were built in under the outmost load introduction points.

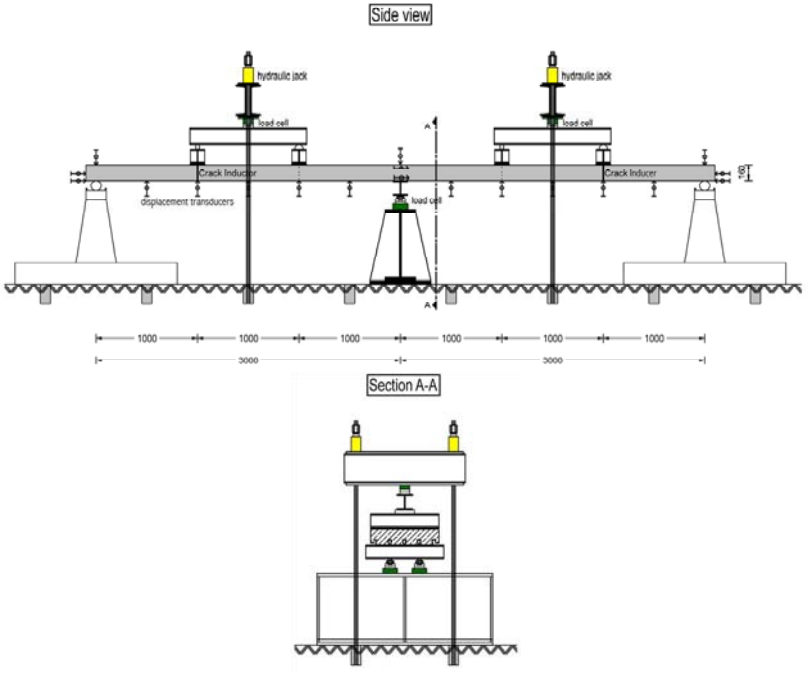


Fig. 6 – test setup - series #2 (dimensions in mm)

TEST RESULTS

The first series was carried out in order to determine the load-bearing behaviour and the possible rotation of steel fibre reinforced composite slabs in the regions of negative bending. The plastic rotation was evaluated in the post-crack region at a value of 95% of the maximum load. In the tests, values between 20 and 25 mrad were reached. Even after reaching the maximum value the hogging moment could be kept approximately constant further on (see Figure 7). An abrupt decrease of the moment resistance with increased rotation could not be observed. The last specimen of series #1 (S1_SHR51_V3) having been provided with the optimised concrete mixture shows as good results as the other ones although the fibre ratio was reduced to 60 kg per cubic meter. No end-slip was measured during the tests of series #1 run; full shear connection between steel sheeting and concrete could be realised. Following the good results with the optimised concrete mixture one has decided to use this mixture for the test on continuous slabs (series #2), too.

In series #2, the good rotation behaviour of series #1 could be confirmed. Figure 8 displays the load bearing behaviour of the steel fibre reinforced continuous slab system exemplarily for the test S2_SHR51_V2. The other tests of series #2 show an identical behaviour.

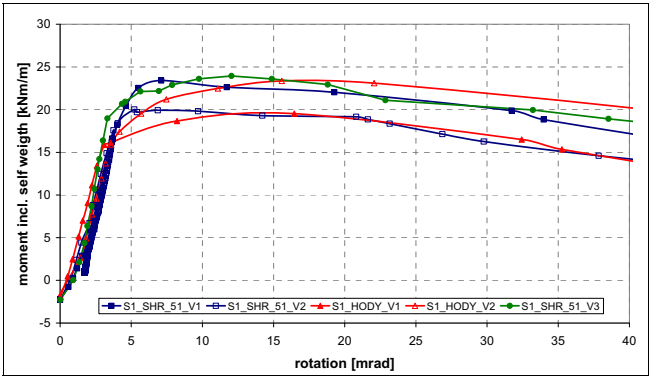


Fig. 7 – Moment-rotation diagram of series #1

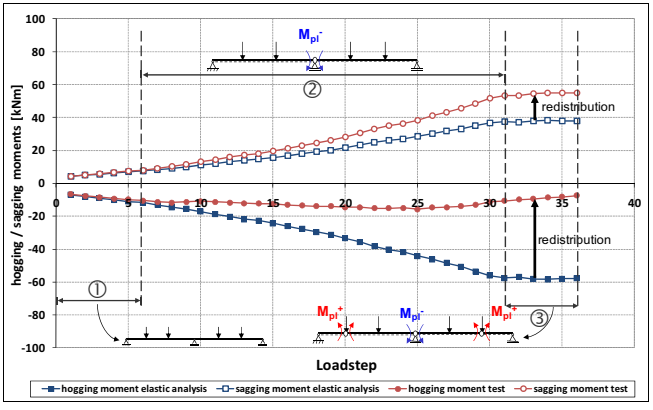


Fig. 8 – load bearing behaviour – exemplarily for test S2_SHR_51_V2

The load could be increased until the tensile strength of the concrete is reached (range ①). After cracking, a plastic hinge (M_{pl}^-) with good rotation ability is formed at the middle support (range ②). The hogging moment could be kept approximately constant up to the failure of the slab, whereas the sagging moments are increased while raising the load. The hogging moments are redistributed to the span till the sagging plastic moment resistance (M_{pl}^+) is reached (range ③). Then the system bearing capacity is exhausted. The value of the plastic moment resistance in the span depends on the composite behaviour of the sheeting. The higher is the dowelling ratio of the sheet the higher is the plastic moment resistance, too. Contrary to series #1, all continuous slabs of series #2 show end-slip failure. The sagging plastic moment resistance (M_{pl}^+) is limited by the partial interaction. Concerning to its better dowelling ratio, the re-entrant HOLORIB profile has a better load bearing behaviour as the trapezoidal HODY sheet. The hogging and sagging moments of series #2 tests are displayed in Figure 9. The whole test series #2 as well as the respective sheeting among each other show a good correlation.

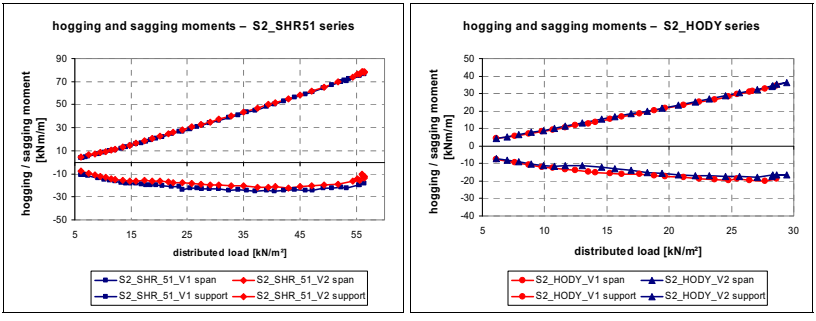


Fig. 9 – hogging and sagging moments – series #2

Figure 10 shows the crack widths subject to the distributed load. In the serviceability limit state range no cracks could be discovered yet. The crack widths do not rise suddenly during the load increase. Figure 11 displays the test setup of series #2.

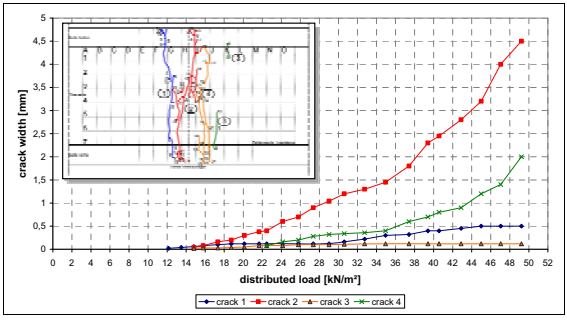


Fig. 10 – crack widths – exemplarily for test S2_SHR_51_V2



Fig. 11 – Test setup – series #2 specimen

The hogging moment resistance of the tests was calculated with the stress distribution which is displayed in Figure 2. Table 3 displays both, the measured maximum hogging moment values and the calculated plastic moments. The calculated values correspond relatively well with the reached test values. Here, the bearing capacity of the sheet was taking into account.

specimen	$M_{test,u}$ [kNm/m]	$M_{pl,calc.}$ [kNm/m]
S1_SHR_51_V1	-23,4	-23,3
S1_SHR_51_V2	-20,0	-21,5
S1_HODY_V1	-19,5	-19,9
S1_HODY_V2	-23,4	-19,6
S1_SHR_51_V3	-23,9	-24,8
S2_SHR_51_V1	-25,3	-26,5
S2_SHR_51_V2	-22,4	-20,6
S2_HODY_V1	-20,4	-21,8
S2_HODY_V2	-17,7	-19,8

Table 3 – hogging moment – test results and calculated values

CONCLUSIONS

Two different test series on composite slabs consisting of steel fibre reinforced concrete topping and steel sheeting were carried out.

In both test series, the efficiency of the steel fibre reinforced slab system becomes already apparent. The test results demonstrate that – due to the favourable crack-distribution ability of the steel fibre reinforced concrete – the slabs achieve a good rotation capacity in the hogging area. After cracking, the moment could be kept approximately constant over a large range of rotation. The tests on continuous composite slabs indicate that large moment redistributions are possible. After the first plastic hinge arises at the middle support, the load could be increased further on until the system bearing resistance is reached as soon as the second plastic hinge emerges in the span. Pertaining to the ability of moment redistribution, steel fibre reinforced continuous composite slabs constitute an efficient and economical slab system.

A further test series on steel fibre reinforced composite slabs with various slab depths is in progress at this time. Here the influence on the load bearing behaviour of slabs with various thicknesses should be determined. Furthermore, a test series on continuous slabs using steel sheeting with a lower depth (only 16 millimetres) is provided. For the structural analysis design diagrams and tables are being developed.

In order to determine the fibre distribution and orientation researches using the computer tomography for analysing fibre structures are in progress, too. The results of these researches are considered in order to draw conclusions concerning the fibre distribution in the area of negative bending. Further information can be gathered from [Schnell 2008].

ACKNOWLEDGEMENTS

This research was supported by BBR (Bundesamt für Bauwesen und Raumordnung), Arcelor Mittal, Dyckerhoff AG, Holorib GmbH, SAFA GmbH, Spillner Spezialbaustoffe GmbH and Woermann Degussa.

REFERENCES

[Ackermann 2007] Ackermann, F. P.; Schnell, J.: Innovative steel fibre reinforced composite slabs. fib-Congress: Innovative Materials and Technologies for Concrete Structures. Proceedings of the 3rd Central European Congress on Concrete Engineering, September 2007, Visegrád, Hungary, pp. 251-256.

[Bode 1998] Euro-Verbundbau, Konstruktion und Berechnung. 2. Auflage. Werner-Verlag, 1998.

[DAfStb 2008] Deutscher Ausschuss für Stahlbeton (DAfStb): Richtlinie „Stahlfaserbeton“, Schlussentwurf Juli 2008. Ergänzung zu DIN 1045, Teile 1 bis 4 (08/2008), Juli 2008.

[DASt 1994] Deutscher Ausschuss für Stahlbau (DASt): DASt-Richtlinie 104: Richtlinie zur Anwendung von Eurocode 4, Februar 1994.

[DBV 2001] Deutscher Beton- und Bautechnikverein e.V. (DBV): Merkblatt „Stahlfaserbeton“, Oktober 2001.

[DIN 1045-1 2008] DIN 1045-1: Tragwerke aus Beton, Stahlbeton und Spannbeton. Teil 1: Bemessung und Konstruktion. August 2008.

[DIN 18800-5 2007] DIN 18800 Part 5: Verbundtragwerke aus Stahl und Beton, Bemessung und Konstruktion. März 2007.

[DIN EN 1994-1-1 2006] DIN EN 1994-1-1 – Eurocode 4: Bemessung und Konstruktion von Verbundtragwerken aus Stahl und Beton – Teil 1-1: Allgemeine Bemessungsregeln und Anwendungsregeln für den Hochbau, Deutsche Fassung EN 1994-1-1:2004, 2006.

[Droese and Riese 1996] Droese, S; Riese, A.: Belastungsversuche an zwei Durchlauf-Plattenstreifen aus Elementplatten mit Aufbeton aus Stahlfaserbeton. Heft 123, IBMB Braunschweig, 1996.

[Falkner and Teutsch 2006] Falkner, H.; Teutsch, M.: Stahlfaserbeton – Anwendungen und Richtlinie, Betonkalender 2006, Ernst & Sohn, 2006.

[Gossla and Pepin 2004] Gossla, U.; Pepin, R.: Decken aus selbstverdichtendem Stahlfaserbeton. Braunschweiger Bauseminar, 2004.

[Riese 2006] Riese, A.: Decken aus Elementplatten mit Stahlfaserbetonergänzung. Dissertation, TU Braunschweig, 2006.

[Sauerborn 1995] Sauerborn, I.: Zur Grenztragfähigkeit von durchlaufenden Verbunddecken. Dissertation TU Kaiserslautern, 1995.

[Schnell 2008] Schnell, J.; Ackermann, F. P.; Rösch, R.; Sych, T.: Statistical analysis of fibre distribution in ultra high performance concrete using computer tomography. 2nd International Symposium on Ultra High Performance Concrete, March 2008, Kassel, Germany. pp. 145-152.

[Stark and Brekelmans 1996] Stark, J.W.B.; Brekelmans, J.W.P.M.: Plastic design of continuous composite slabs, Structural Engineering International, Vol. 6, No. 1, February 1996, pp. 47-53.

ELEMENTAL BENDING TEST AND MODELING OF SHEAR BOND IN COMPOSITE SLABS

Redzuan Abdullah
Faculty of Civil Engineering
Universiti Teknologi Malaysia
Skudai, Johor, Malaysia
Redzuan@utm.my

W. Samuel Easterling
The Via Department of Civil and Environmental Engineering
Virginia Polytechnic Institute and State University
Blacksburg, Virginia
seaster@vt.edu

ABSTRACT

This paper discusses a new experimental bending test and shear bond modeling of steel deck reinforced concrete (composite) slabs. The objective of experimental work is to develop a new elemental bending test method for evaluating the performance and behavior of composite slabs, and also for determining the shear interaction property for use in numerical analysis. The analytical study is conducted to determine whether data from the small scale tests can be used in the present shear bond (*m-k*) and Partial Shear Connection (PSC) methods, to predict the strength of the actual slabs, to use the same test data for input in numerical analysis, and to improve the existing PSC design procedure. The results of the study demonstrate that the elemental bending test of composite slab using trapezoidal shape steel deck is feasible as a replacement for the full-size test utilizing the same steel deck. Data from the elemental bending test can be used not only in the existing analytical methods but also in the numerical analysis, thus eliminating the need for separate push off type tests. The improved PSC design procedure is found to be comparable with the *m-k* method.

INTRODUCTION

A composite slab comprised of structural concrete cast on cold-formed steel deck is the most popular type of floor system used in steel framed buildings. The system is well accepted by the construction industry due to the many advantages over other types of floor systems. Designers typically work with design aids generated and published by deck manufacturers. The manufacturers rely on a combination of experimental programs and semi empirical calculation procedures to generate design load tables. A typical test configuration consists of a single, simple span that utilizes one or two deck sheets, thus the specimen generally varies in width from 610 to 1,830 mm. Among the well established calculation procedures are the shear bond method known as the *m-k* method (ASCE, 1992, Eurocode 2004), the Partial Shear Connection method (PSC) (Eurocode 4, 1994 and 2004) and the Multi Linear Regression method (CSSBI, 1996). These methods however, rely on the parameters obtained from a series of full scale bending tests. Because many full scale tests are involved, the design process is expensive and time consuming.

As an alternative, non-linear finite element (FE) modeling and analysis can be conducted to mimic the test behavior. The non-linear FE method requires data from elemental tests as an input to the model. The data, which is the interaction property between the steel deck and the concrete in the form of shear bond force versus relative end slip, is typically obtained from elemental direct shear tests (push off or pull out tests) (Veljkovic, 1995 and 1996a; Patrick and Poh, 1990, An, 1993; Daniels and Crisinel, 1993a and 1993b) . Because of the nature of the direct shear test configurations, the effect of curvature due to slab bending and shear span to depth ratio, herein referred to as the *slenderness*, could not be considered in the interaction property. As a result the accuracy of the non-linear FE analysis of composite slab with different slenderness is still questionable (Daniels and Crisinel, 1993a and 1993b; An, 1993). Hence the FE procedure is typically only used as a research tool and not for design.

The *m-k* method, represented in Eq 1 and Figure 1, was originally developed by Schuster (1970) and adopted in ASCE (1992) and Eurocode 4 (2004) and is the most reliable tool for predicting composite slab strengths. Many researchers have used this method as a basis for comparison with procedures they developed. The *m-k* method however is a semi-empirical method that offers no mechanical model, but rather uses statistical evaluation of tests to determine the *m* and *k* parameters. Thus, the values of *m* and *k* are applicable to specific deck/slab configurations. Because of that, researchers in Europe developed the Partial Shear Connection (PSC) method. The method is based on a clear mechanical model, which can be extended to different design situations such as end anchorage, additional reinforcement, frictional effect, etc. (Bode et. al. 1996 and Bode and Dauwel, 1999).

$$\frac{V}{bd} = m\frac{A_p}{bL_s} + k \qquad \textbf{(1)}$$

The PSC method, which is adopted in Eurocode 4 (2004), does not properly address the effect of slab slenderness (L_s/d) when the degree of interaction, η is determined from a test, as is illustrated in Figure 2. It is known that the moment obtained from the test, which relates directly to η, depends on the load position (i.e. shear span length) and concrete thickness. Slender slabs (i.e. large L_s/d) yield low ultimate moment and compact slabs (i.e. small L_s/d) yield high ultimate moment. As a result, a variable degree of interaction and subsequently variable shear bond strengths, τ_u, as indicated in Eq 2, exists for the same slab.

$$\tau_u = \frac{\eta N_{cf}}{b(L_s + L_o)} \qquad \textbf{(2)}$$

This indicates that if the shear strength obtained from tests of compact slabs was used to design a slender slab, an unsafe design is produced. On the other hand, if the compact slab was designed based on the shear strength obtained from tests of slender slabs, an overly conservative design may be produced. Eurocode 4 Annex B (Cl. B.3.2 (7)) specifies that the test specimens to be used for determining the design value of longitudinal shear strength, τ_u should be as long as possible (most slender) while still providing failure in longitudinal shear. This means that slender slab tests should be in region A of Figure 1. As a result the evaluation of a compact slab by the PSC method is always conservative and potentially uneconomical.

Objective

The objective of this paper is to present composite slab research results from studies carried out at Virginia Tech. The purpose of the experimental work was to develop a new method for conducting elemental bending tests of composite slabs. The test is multipurpose in that it can be used for product (deck profile) development, for producing design tables, for generating shear bond properties for use in numerical modeling, and for replacement of full scale bending tests. Because the elemental specimen is narrow in size, the test is more economical and easier to perform than the full scale tests. A procedure called the Force Equilibrium method, which considers the effect of slab slenderness, was developed to generate shear bond properties from the elemental bending test. Using the procedure, the accuracy of the finite element analysis of variable slenderness composite slabs was improved. A new procedure for evaluating the shear bond strength that is used in the PSC method was developed. The procedure was obtained by modification of the m-k equation and it takes into account the effect of slab slenderness.

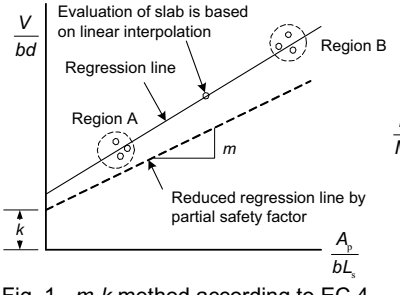


Fig. 1 - *m-k* method according to EC 4

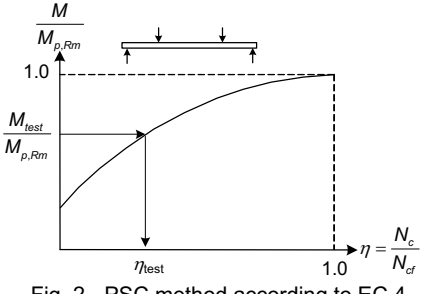


Fig. 2 - PSC method according to EC 4

Experimental Investigation

The experimental program was conducted in three series: One series for full-size bending tests and two series for elemental tests. The full-size series consisted of twenty-four specimens with twelve different parameters (Test #1 - #12). All specimens were built using trapezoidal deck profiles. Two depths of deck and three thicknesses of steel sheeting were used. The depths were 50 and 76 mm and thicknesses were 0.9, 1.2 and 1.5 mm. The full-size specimens were 1,830 mm wide and constructed in a three-span configuration with the end details and temperature and shrinkage reinforcements similar to actual construction practice. One-way bending tests were conducted and therefore the transverse bending was neglected. The full-size tests were part of an earlier program (Abdullah and Easterling, 2003.). Results from these full-size tests were used to verify the performance of a new elemental bending test method developed in this research.

Elemental bending tests

Two series of elemental bending tests were conducted. Series 1 consisted of 16 specimens (Test #13 - #20). Series 1 specimen used the same deck profile (75mm) and sheeting thickness (1.5 mm) but three concrete thicknesses (125 mm, 165 mm and 190 mm) and three shear span lengths (560 mm, 660 mm and 760 mm). The tests were conducted to study the effect of web curling, which is illustrated in Figure 3.

Results of Series 1 provided the basis for detailing of Series 2. The tests in Series 2 consisted of 32 specimens (Test #21 - #36). The variables for Series 2 tests were similar to the full-size specimens, which included deck depths, sheeting thickness, span length, concrete thickness, and shear span length. The details of the elemental specimens are depicted in Figures 4 and 5. Two specimens with pin and roller supports as shown in Figure 5(b) were built to determine the effect of end constraint. Support details as shown in Figure 5(c) were used for other specimens in Series 2 and these were similar to the end details of full-size specimens. Because of space limitation, the specimens were built in two batches, hence two concrete strengths resulted. However, concrete strength was not considered a test variable. Series 2 tests were conducted to study the behavior of the elemental specimen due to different support details, and ultimately to compare them with the full-size results.

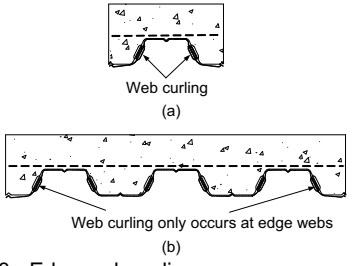


Fig. 3 - Edge web curling

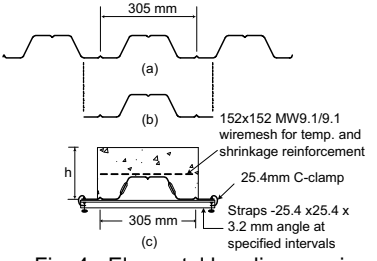
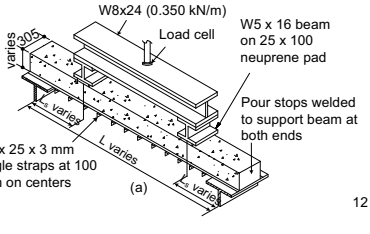


Fig. 4 - Elemental bending specimen



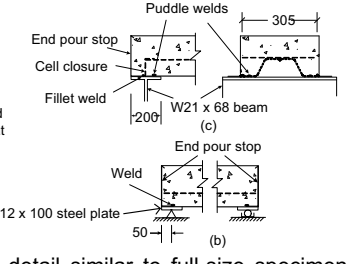


Fig. 5 (a) Series 2 test setup; (b) Support detail similar to full-size specimen; (c) Simple support

Test results and discussion (Series 1)

Web curling occurs in the edge webs as shown in Figure 3. It occurs due to overriding of concrete against the embossments on the web surface when concrete slips under bending. This results in reduced horizontal shear resistance especially in the elemental specimen. Wider specimens exhibit web curling to a lesser degree than the elemental specimen. In Series 1 tests, the web curling effect was reduced by using straps fixed to the bottom flanges of steel decks as shown in Figure 4.

Figure 6 shows a typical result of the effect of strapping to restrain the web from curling. The average increase of the ultimate load due to strapping for all tests ranges from 30 to 40%. The results also indicated that lower slab strengths and larger vertical separation was produced by specimens with larger strap spacing. From Series 1 results, it was decided that the strap spacing to be used in Series 2 specimens was 100 mm.

Test results and discussion (Series 2)

The effect of providing different end constraint details at the support is illustrated in Figure 7. Figures 8 and 9 depict the comparison of load-deflection curves and load-end slip curves between elemental and full-size specimens with compatible details for compact and slender specimens. It can be seen that, provided sufficient strapping and similar end details are constructed in the elemental specimen, the strength and behavior of the elemental specimens are comparable with the full-size specimens. The failure modes were also equal between the elemental and the full-size specimens. In general, the elemental specimens failed at slightly lower deflections than the full-size specimens. Detailed results and discussions of this investigation can be found in Abdullah and Easterling (2007) and Abdullah (2004.)

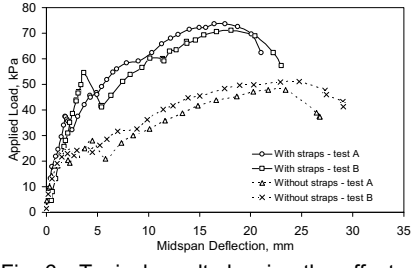


Fig. 6 - Typical result showing the effect of strapping in the elemental specimen

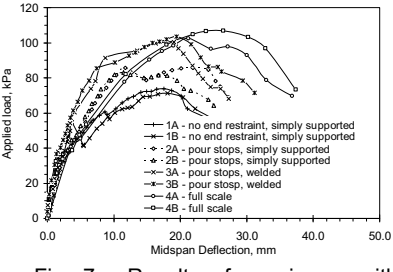
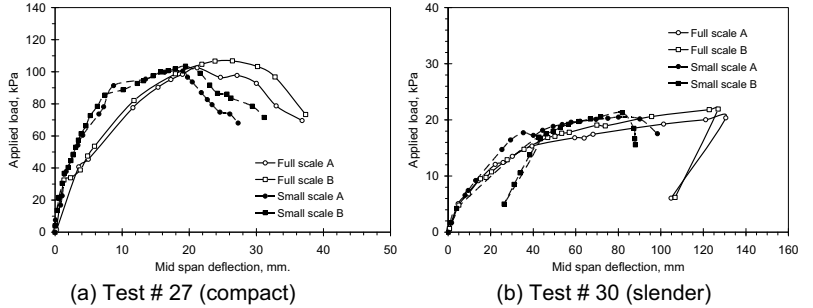
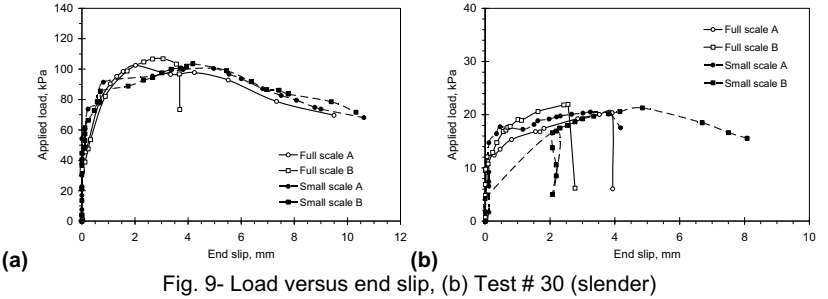


Fig. 7 - Results of specimens with straps but of different end constraints



(a) Test # 27 (compact) (b) Test # 30 (slender)

Fig. 8 - Load versus mid span deflection



(a) **(b)**

Fig. 9- Load versus end slip, (b) Test # 30 (slender)

Shear bond modeling from bending test data

As mentioned in the Introduction section, the shear bond properties used in many FE studies of composite slabs were obtained from direct shear tests, such as elemental push off or pull out type tests. Because of the nature of the direct shear test configurations, the effect of curvature due to slab bending, shear span length, and concrete thickness could not be incorporated. Therefore, it is proposed here that the shear bond properties be obtained from the elemental bending test, which accounts for these parameters.

An Equilibrium Force method was developed to derive the shear bond property curve from elemental bending test data. The method was derived based on the following assumptions, which were in part made based on the observation from bending tests as discussed above and from classical bending theory:

- The relative slip is uniform along the shear span hence the distribution of horizontal shear stress is also uniform along the shear span.
- Composite section neutral axis is above the deck and moves up as the crack and end slip increase. Thus, the compressive force in the concrete moves upward accordingly.
- Slip occurs at the failing end, while at the non-failing end, slip is small and negligible.
- The difference of curvatures between the concrete and the steel deck after the slip has occurred is small and hence are assumed equal.
- Due to slip, two neutral axes exist and therefore the steel deck is always taking a fraction of load by bending about its own neutral axis.
- Steel deck behaves elastically and remains fully effective up to the maximum load.
- Plane sections remain plane and normal to neutral axis.
- Concrete stress in tension is neglected.
- Small displacement theory is valid.

A free body diagram of a composite slab section tested with two-point loads is shown in Figure 10(a). The corresponding strain and internal force distributions at the critical sections are depicted in Figures 10(b) and 10(c). At any point, *i,* during the test, the horizontal shear force F_i is equal to the axial force, T_i, in the steel deck. At the partial interaction phase, the steel deck can also take a fraction of the applied load by bending about its own neutral axis. The remaining bending resistance in the steel deck is denoted by M_{ri}. Neglecting the concrete self weight, the horizontal shear force, F_i can be calculated by taking moment about the compression force, C;

$$F_i = T_i = \frac{\left(\frac{P_i}{2} L_s - M_{ri}\right)}{z_i} \quad \textbf{(3)}$$

where P_i = total applied load, L_s = shear span length, and z_i = moment arm between tension and compression force.

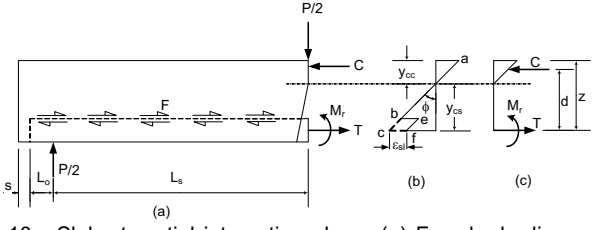


Fig. 10 - Slab at partial interaction phase (a) Free body diagram of the critical section, (b) Strain distribution diagram, (c) Stress and internal force diagram

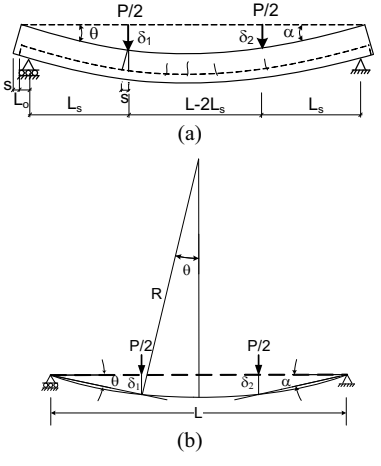


Fig. 11 - Slab under bending, (a) At cracking mode, (b) Deflection and curvature of the deck

From the moment-curvature relationship, M_{ri} in Eq 3 can be determined from:

$$M_{ri} = \frac{\delta_{1i} + \delta_{2i}}{L_s\left(L - 2L_s\right)} E_s I_s \qquad \textbf{(4)}$$

where δ_{1i} and δ_{2i} = measured deflections at load point 1 and 2 (Figure 11), E_s Modulus of elasticity, and I_s = moment of inertia of the steel deck.

Moment arm, z_i in Eq 3 is an unknown parameter to be determined approximately from test data. Its value depends on the location of the composite section neutral axis, which at partial interaction, moves upward as the load increased. The first location of the composite neutral axis, y_{cc}, is at the tip of the first crack in the concrete. It then moves upward as the end slip and vertical deflection increase while the load is added. The value off y_{cc} at first cracking is calculated based on cracked section analysis of full interaction as indicated by line abc of Figure 10(b). The calculation can be taken from Eq. B-1 of ASCE (1992) as:

$$y_{cc} = d\left\{\left[2\rho n + (\rho n)^2\right]^{\frac{1}{2}} - \rho n\right\} \quad \textbf{(5)}$$

where d = effective depth of slab section, ρ = ratio of steel area to effective concrete area = $A_s/(bd)$, and n = modular ratio = E_s / E_c

Thereafter, y_{cc} reduces or the composite neutral axis moves upward as the crack length, y_{cs} increases. From geometry as shown in Figure 11(a), the crack length at i, is estimated by:

$$y_{csi} = \frac{s_i L_s}{(\delta_{1i} + \delta_{2i})} \quad \textbf{(6)}$$

where s_i = measured end slip.

Therefore; $y_{cci} = d - y_{csi}$; $0 \le y_{cci} \le h_c$ **(7)**

where h_c = concrete cover above deck top flange.

The moment arm is therefore; $z_i = d - \frac{1}{3} y_{cci}$ **(8)**

Each test data point, i was applied to Equation (3) through (8) to obtain the horizontal shear bond force, F_i. The values were then divided by the deck surface areas along the shear spans to obtain the average shear bond stresses. The values were plotted against the corresponding end slips that were measured in the tests. A typical relationship between shear bond stress and end slips obtained by this procedure is shown in Figure 12. Figure 13 shows the simplified shear bond properties calculated from elemental bending test that were used in the FE analysis. The properties were for specimens using the same deck but of different slenderness (Different shear span length and concrete thickness). To validate the proposed calculation method, the maximum shear bond stress obtained from the graphs for all test data were compared with the maximum values calculated using the PSC method available in Eurocode 4 (2004). The mean of the ratio of the maximum shear bond stress calculated by the PSC method to that by the proposed Force Equilibrium method was 1.02 and standard deviation was 0.12.

Finite Element analysis

The property curves as presented in Figure 13 were used to model the interaction behavior between the steel deck and the concrete in the FE analyses. Each curve was assigned to its respective model. The results are shown in Figure 14 (The specimen of Figure 14 was used as the basis for model development) and Curves A in Figure 15. It can be seen that the load-deflection curves of the tests could be traced accurately by the FE results. When the property curve #27 was used to model other specimens of different slenderness, the results were overestimated for more compact slabs (specimen #25) and underestimated for more slender slabs (specimens #28, #29 and #30). This is shown by Curve B in Figure 15. The FE results clearly show that in order to obtain the correct analysis, the shear bond property must be changed according to the slenderness of the slab. The use of single property curve, as usually obtained from push off tests may yield good result for one slab geometry, but inaccurate results for other geometries. More detailed results of the FE analysis and discussions of the modeling method are presented in Abdullah and Easterling (2008) and Abdullah (2004.)

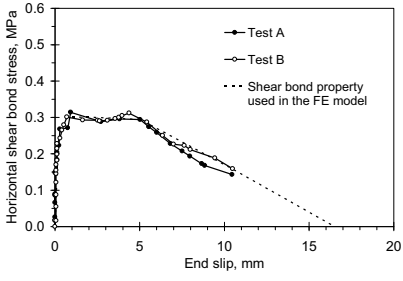


Fig. 12 – Typical shear bond response

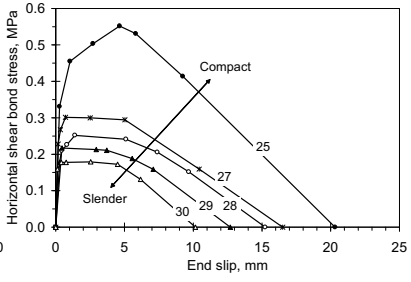


Fig. 13 – Horizontal shear bond response for a range of slenderness specimens

Improvement of the PSC method

In the free body diagram in Figure 10(a), $P/2$ is the reaction force and is equal to the vertical shear, V in the m-k equation. By taking moments about the compressive force, C and considering that the moment arm differs very slightly from the slab effective depth, the moment equilibrium equation can be estimated as:

$$VL_s = Td + M_r \quad \textbf{(9)}$$

Substituting T with $\tau(L_s+L_o)b$, Eq 9 becomes;

$$VL_s = \tau\left(L_s + L_o\right)bd + M_r \quad \textbf{(10)}$$

where V = reaction or vertical shear force, L_s = shear span length, L_o = overhanging length, τ = shear bond stress, b = slab width, d = effective depth, M_r = remaining moment strength in the deck.

Equation 10 is approximate because the lever arm is always less than the effective depth. Nevertheless, for composite slabs the difference is insignificant because after shear slip has taken place, the crack tip grows up bringing the composite neutral axis close to the top fiber.

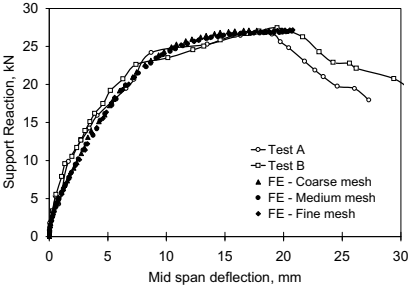


Fig. 14 – FE and test results for specimen #27

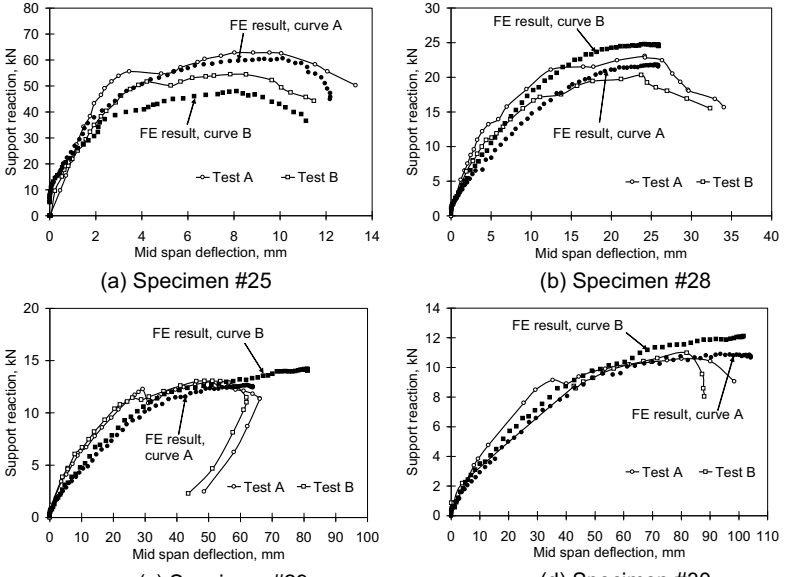


Fig. 15 – Results of FE analysis. Note-The specimen # follows Abdullah and Easterling (2007)

Solving Eq 10 for V and substituting into the PSC Eq 1, a new equation relating shear bond stress to the slab geometry is obtained, as given by Eq 11.

$$\tau d = m\frac{A_p}{b}\frac{d}{(L_s + L_o)} + \left(\frac{kbdL_s - M_r}{b(L_s + L_o)}\right) \qquad \textbf{(11)}$$

If b is taken as the length of the steel sheeting over its width, then A_p/b is equal to the thickness, t of the sheeting.

When deriving the original *m-k* equation, Schuster 1970 neglected the contribution of the remaining moment strength, M_r in the steel deck and so did Patrick and Bridge (1994), Veljkovic (1996b) and Widjaja and Easterling (1996) for their modified PSC methods. For deck profiles with re-entrant shape, which is popular in Europe and Australia and used to a limited degree in the United States, the contribution of M_r is negligible, because the deck depth is usually small and the moment capacity of such profiles is low. For trapezoidal profiles which are popular in the United States, the United Kingdom and other parts of the Europe, the contribution of M_r can be significant, especially near the ultimate load. The behavior beyond ultimate load is also influenced by M_r. In this study however, the last term in Eq 11 was found to be constant and therefore a determination of the M_r term here is not needed. Equation 11 can be simplified to:

$$\tau d = m\frac{td}{(L_s + L_o)} + k \qquad \textbf{(12)}$$

The overhanging length, L_o is usually short. It is assumed here that L_o is not a determining factor for the slab behavior and therefore it can be ignored. However its contribution to the horizontal shear resistance cannot be neglected and it should be included when τ is calculated either using the PSC method or using the Force Equilibrium method as discussed earlier.

To differentiate between the constants m and k from the m-k method, p and s are used here instead, so that the equation relates the shear bond term, τd to the inverse of slenderness parameter, d/L_s. The sheeting thickness, t is also included as part of the strength parameter. Therefore Eq 12 can be simplified to:

$$\tau d = p\frac{td}{L_s} + s \qquad \textbf{(13)}$$

Maximum shear stresses, τ, were calculated from all elemental bending specimens using the Force Equilibrium method as discussed earlier. The results are applied to Eq 13 and plotted in Figures 16 and 17. The graphs show that all results fall along straight lines, with slope p and intersection value s. This confirms that the shear bond strength of composite slab is a linear function of the inverse of slab slenderness. The incorporation of sheeting thickness, t in Eq 13 enables the comparison between slabs built using different sheeting thickness. A comprehensive discussion of Eq 13 is given by Abdullah (2004).

Summary and Conclusions

A new method for testing composite slabs in bending in an elemental (narrow) configuration has been developed. If the same end details are utilized in both elemental and full-size specimens, the elemental tests can produce comparable results with the full-size specimens.

Edge web curling, end anchorage details, and type of support have significant influence on the slab specimen strength and behavior. Angle straps can provide sufficient restraint to the edge web, thus enabling elemental specimens to behave in a manner similar to full-size specimens. The use of angle straps at a spacing of 100 mm and end conditions that are comparable to a given full-size specimen enable the use of the elemental specimen developed in this experimental study to be used as an alternative to the full-size specimen.

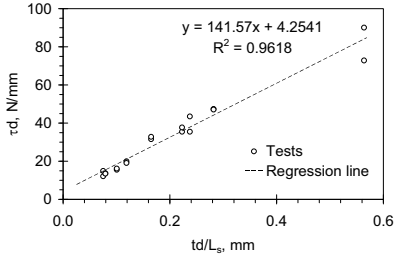


Fig. 16 - τd vs td/L_s for 76mm specimens

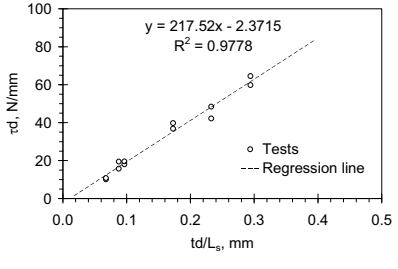


Fig. 17- τd vs td/L_s for 50 mm specimens

The elemental tests developed in this investigation are simple and easy to construct. The side formwork, angle straps and C-clamps are reusable, which make the testing more economical. Four elemental specimens can be set up in the same space needed for one full-size specimen that is 1,830 mm wide, with almost an equal amount of material.

Because the elemental test is conducted in bending, where the span length and the concrete thickness similar to a traditional full-size test can be used, the data from the elemental tests can be applied directly to the present design specifications, namely the m-k and the PSC methods in the ASCE (1992) and Eurocode 4 (2004).

The study also addresses the shear bond modeling issue in composite slabs. The accuracy of the shear bond property depends on the slenderness of the slab. Because slenderness effects can not be replicated in the elemental push off or pull out test, bending test data has been used in the study. The Force Equilibrium method was derived for calculating the shear bond property from bending tests. The accuracy of the method was validated by comparing the results with the established PSC method. The resulting properties were applied to FE models. The results of FE analysis have shown that the slab behavior and load capacity can be predicted accurately for slabs with variable slenderness provided the shear bond properties used in the models are obtained from the tests whose geometries are similar to the models. If the shear bond properties are not altered, the model may be accurate for a particular geometry slab but underestimates the more compact slabs and overestimates the more slender slabs.

Other parameters that contribute to the shear bond property such as sheeting strain, support friction, vertical separation, natural clamping and curvature have already been included implicitly in the shear bond property obtained from bending tests, hence they can be ignored in the FE model. Thus the small scale test developed here is more favorable than the push off type tests for shear bond data gathering.

A shear bond-slenderness equation with constants p-s was successfully derived to express the relationship between the shear bond stress and slenderness parameter. Using this equation, the PSC method can be improved significantly, especially for estimating the shear bond strength of slabs of variable dimensions, thus enabling the PSC method to be compared vis-à-vis with the m-k method.

Because the shear bond stress varies linearly with the slab compactness, only two regions of small scale tests are required to provide adequate data for design with the improved PSC method. This is similar to test requirement for the m-k method and therefore data from the same test can be used for both methods. As such the same number of specimens and test procedure as prescribed in the present specifications for conducting full scale tests can be followed.

Acknowledgement

The authors thank the Ministry of Higher Education (MOHE), Malaysia; Universiti Teknologi Malaysia (UTM), Malaysia; and Virginia Tech for providing financial assistance in conducting the study.

References

Abdullah, R. and Easterling, W. S. (2003), Structural Evaluation of a new composite deck profile: Phase II." Rep. No. CEE/VPI-ST03/01, VPI&SU, Blacksburg, VA.

Abdullah, R. (2004). "Experimental Evaluation and Analytical Modeling of Shear Bond in Composite Slab", Ph.D. dissertation, VPI&SU, Blacksburg, VA.

Abdullah, R. and Easterling, W. S. (2007), "Determination of Composite Slab Strength Using a New Elemental Test Method", *Journal of Structural Engineering*, 113(9), 1268-1277

Abdullah, R. and Easterling, W. S. (2008), "A New Method for Modeling the Horizontal Shear Bond in Composite Slabs", Submitted to The Journal of Constructional Steel Research.

An, L. (1993). "Load Bearing Capacity and Behaviour of Composite Slabs with Profiled Steel Sheet," Phd Dissertation, Chalmers University of Technology, Sweden.

ASCE. (1992). *Standard for the Structural Design of Composite Slabs. ANSI/AASCE 3-91*, American Society of Civil Engineers, New York.

Bode, H., and Dauwel, T. (1999). "Steel-Concrete Composite Slabs - Design Based on Partial Connection." *Proceedings of the International Conference on Steel and Composite Structures*, Delft, The Netherlands, 2.1-2.10.

Bode, H., Minas, F., and Sauerborn, I. (1996). "Partial Connection Design of Composite Slabs." *Structural Engineering International* (1(Jan.)), 53-56.

CSSBI. (1996). *Standard for Composite Steel Deck, CSSBI 12M - 96*, Canadian Sheet Steel Building Institute.

Daniels, B. J., and Crisinel, M. (1993a). "Composite Slab Behavior and Strength Analysis. Part I: Calculation Procedure." *Journal of Structural Engineering,* 119(1-4), 16-35.

Daniels, B. J.. and Crisinel, M. (1993b). "Composite Slab Behavior and Strength Analysis. Part II: Comparisons With Test Results And Parametric Analysis." *Journal of Structural Engineering,* 119(1-4), 36-49.

Eurocode 4. (1994). *Design of Composite Steel and Concrete Structures, Part 1.1, General Rules and Rules for Buildings. ENV 1994-1-1:1992*, European Committee for Standardization, Brussels.

Eurocode 4. (2004). *Design of Composite Steel and Concrete Structures - Part 1.1: General Rule and Rules for Buildings, BS EN 1994-1.1:2004,* European Committee for Standardization, Brussels.

Patrick, M., and Poh, K. W. (1990). "Controlled Test for Composite Slab Design Parameters." *IABSE Symposium, Brussels, Belgium - Mixed Structures, Including New Materials*, Zurich, Switzerland, 227-231.

Patrick, M., and Bridge, R. Q. (1994). "Partial Shear Connection Design of Composite Slabs." *Engineering Structures*, 16(5), 348-362.

Schuster, R. M. (1970). "Strength and Behavior of Cold-Rolled Steel-Deck-Reinforced Concrete Floor Slabs," Phd Dissertation, Iowa State University, Ames, Iowa.

Veljkovic, M. (1995). "Longitudinal Shear Capacity of Composite Slabs." *Nordic Steel Construction Conference '95*, Malmo, Sweden.

Veljkovic, M. (1996a). "Behaviour and Resistance of Composite Slabs," Phd Thesis, Lulea University of Technology, Lulea, Sweden.

Veljkovic, M. (1996b). "An Improved Partial Connection Method for Composite Slab Design." *Proceedings of an Engineering Foundation Conference in Composite construction in steel and concrete III,* American Society of Civil Engineers, 644-659.

Widjaja, B. R., and Easterling, W. S. (1996). "Strength and Stiffness Calculation Procedures for Composite Slabs." *Proceedings of the 13th International Specialty Conference on Cold-Formed Steel Structures*, St. Louis Missouri, 389-401.

DUCTILITY OF COMPOSITE BEAMS WITH TRAPEZOIDAL COMPOSITE SLABS

Mark A Bradford
Centre for Infrastructure Engineering and Safety, The University of New South Wales
Sydney, NSW, Australia
m.bradford@unsw.edu.au

Yong-Lin Pi
Centre for Infrastructure Engineering and Safety, The University of New South Wales
Sydney, NSW, Australia
y.pi@unsw.edu.au

Brian Uy
School of Engineering, University of Western Sydney
Sydney, NSW, Australia
b.uy@uws.edu.au

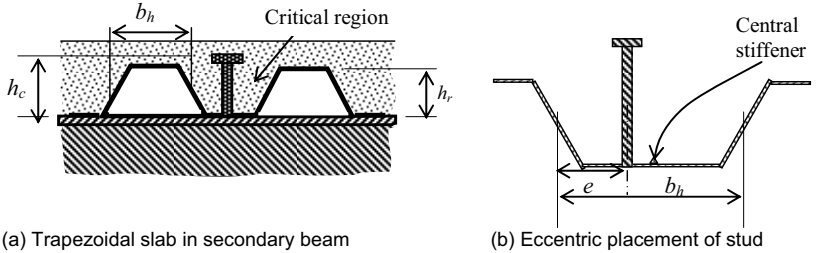
ABSTRACT

Deep trapezoidal slabs supported compositely on steel I-beams by headed mechanical stud shear connectors provide a popular and economical structural solution for flooring in steel building frames, and they are used widely. When the ribs in the sheeting are oriented orthogonal to the steel beams so that longitudinal stresses traverse the voids, predicting their structural response is difficult, and full-scale testing is very costly. Because of this, an inexpensive and accurate means of analysis that incorporates the non-linear response of the shear connection is much needed. This paper presents such a finite element technique, which incorporates non-linearity in the concrete, steel joist, reinforcement and the shear connection; the latter being derived from specialised push test data embodying the complex interactions in the trough region of the slab. The procedure is used to analyse two full-scale beams for which relevant push test data is available, and the agreement is shown to be very good.

INTRODUCTION

Composite beams, which comprise of concrete slabs cast on profiled trapezoidal steel decking and which are supported by steel I-section joists with headed stud shear connectors, are used frequently in contemporary steel and composite building frames. These deep trapezoidal profiles allow for large spans between supporting beams with or without propping, and therefore they provide a very economical structural system. Because of the location of the voids in the profiled deck when the ribs are orthogonal to the steel beam (Figure 1), the stud shear connectors need to be placed in the troughs and usually eccentrically, with the concrete region that surrounds the studs being limited by the geometry of the deck profile (Figure 1(b)). This situation clearly differs from a conventional T-beam with a flat slab soffit or a re-entrant deck profile [Oehlers and Bradford 1995], and the presence of the large

voids has ramifications on the mode of failure of the composite beam, in which the shear connection may not be as robust as for flat soffit or re-entrant profiles and models for the failure modes have been proposed [Johnson and Yuan 1998a,b]. The usual procedure for predicting the strength of the shear connection is based on a reduction factor k_r to be applied to the (empirical) formula for a solid slab, but research such as that by [Johnson 2005, Bradford *et al.* 2006a,b, Hicks 2007] has suggested that the formulae for k_r in the British BS5950 and American LRFD specifications are unconservative. Because of both the increased use of trapezoidal profiles and the introduction of thin-walled deep decks with high strength steel, increased vigour in research has occurred in recent years in order to allay concerns regarding strength predictions and ductility of these composite beams, particularly when the deck ribs are orthogonal to the steel joist as occurs in "secondary beams" in a steel flooring grid (Figure 1).



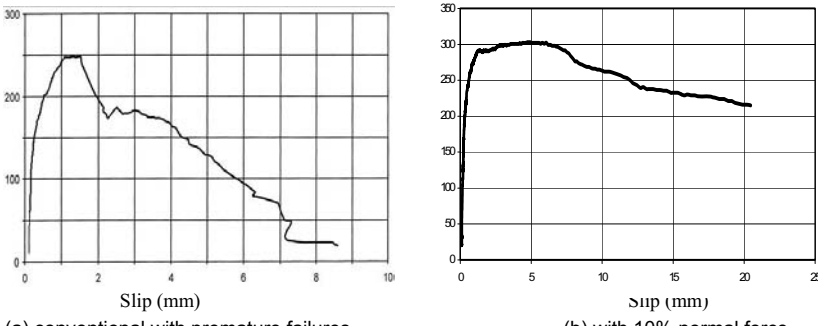
(a) Trapezoidal slab in secondary beam (b) Eccentric placement of stud

Fig. 1 - Secondary beam with ribs orthogonal to steel beam

The main concern with predicting the strength of composite beams with trapezoidal slabs used in practice is that conventional push testing [Oehlers and Bradford 1995] creates a force transfer regime which is different to that which occurs in full-scale beams and consequently produces premature failures. In particular, the so-called rib shear failure reported by [Patrick and Bridge 2002] which is the same as the 'concrete pull-out' failure identified by [Johnson and Yuan 1998a,b] occurs in push test specimens, resulting in brittle failure and low strengths depending on the configuration of the studs in the trough. [Bradford *et al.* 2006a,b] reported similar behaviour in conventional push tests, as well as back-breaking modes, and concluded that the conventional push test set-up is inadequate. As a result, they proposed a modified push-test methodology [Bradford *et al.* 2006a,b] in which a normal force is applied based on results reported by [Rambo-Roddenberry *et al.* 2002] and elsewhere, which better replicates the flexural behaviour in full-scale beams. Figure 2 shows the results of a push test without a normal force (Figure 2a), and with a normal force of 10% of the horizontal force (Figure 2b).

Despite the conclusions of [Ernst *et al.* 2006], recent full-scale test results of typical secondary beams with trapezoidal decks conducted at The University of Cambridge by [Hicks 2007] and at The University of Sydney by [Ranzi *et al.* 2008] have achieved extensive ductility with significant slip at the slab-joist interface. Figure 3 shows the deformation of one of the two Sydney beams; the other Sydney beam and the Cambridge beams behaved similarly. The beams tested at Sydney were chosen to correspond to companion push tests using the modification of incorporating a normal force [Bradford *et al.* 2006a,b], and the bending capacities of the two beams tested at Sydney (which had low degrees of shear connection) [Ranzi *et al.* 2008] were very close to those predicted using the shear connection strengths obtained

from the modified push tests based on partial interaction rigid plastic theory [Oehlers and Bradford 1995]. Clearly, some means of confidently predicting the strength of the shear connection is needed in lieu of highly expensive full-scale testing.



(a) conventional with premature failures (b) with 10% normal force

Fig. 2 - Push testing results

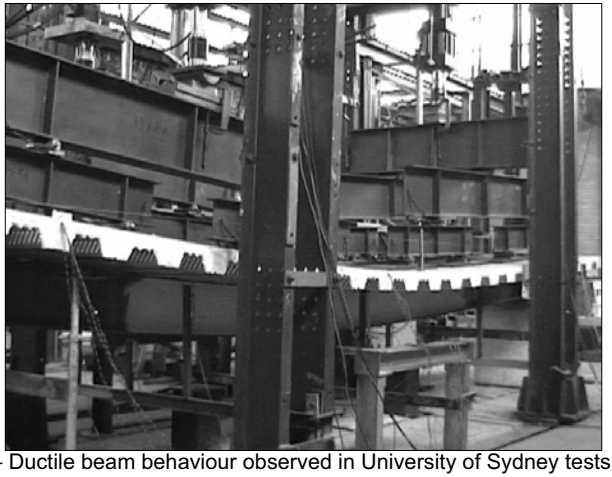


Fig. 3 – Ductile beam behaviour observed in University of Sydney tests (CB1)

Finite element modelling of shear connection in composite beams is not new [Kim *et al.* 1999], [Sebastian and McConnel 2000], but studies using contemporary software packages are far from comprehensive or conclusive. Rather than using a fine plane stress meshing as seems typical, the technique presented herein is based on a line element for geometric and material non-linear analysis of composite beams developed by [Pi *et al.* 2006a,b]. This finite element modelling is applied to analyse the full-scale beams studied by [Ranzi *et al.* 2008], using as its input the companion load-slip characteristics of the push test results which have premature failure modes removed [Bradford *et al.* 2006a,b]. It is concluded that the finite element results

using the companion load-slip characteristics for the shear connection agree closely with the full-scale tests.

NON-LINEAR FINITE ELEMENT FORMULATION

Kinematics

A sophisticated modelling of composite steel-concrete members has been presented by [Pi *et al.* 2006a,b], which allows for not only geometric non-linearity, but also for the material non-linear response of the shear connection, steel joist, concrete slab, slab reinforcement and profiled sheeting. In this formulation, the stress and strain measures used in the total Lagrangian formulation are the second Piola-Kirchhoff stress tensor and the Green-Lagrange strain tensor. Under the assumption of small strains, these tensors have a physical significance close to that of the conventional stress and strain measures. Since elasto-plastic constitutive models for steel and concrete are usually developed using engineering stress and strain measures, they are directly applicable in the total Lagrangian formulation. This formulation also conveniently enables the inclusion of the slip, since this is usually referred to an undeformed configuration, and expressed in a way that is equivalent to engineering stress and strain measures by virtue of its load-slip characteristics.

The line-element herein is developed by considering the deformation of a point with position vector $\mathbf{a}_0$ in a fixed Cartesian reference system as

$$\mathbf{a}_0 = \mathbf{r}_0 + y\mathbf{p}_y\,, \tag{1}$$

in which $\mathbf{r}_0$ is the position vector of the centroid of the beam, $\mathbf{p}_y$ is a basis vector in the plane of the web through its cross-section and y the coordinate of this point along $\mathbf{p}_y$. The deformation can be considered using the Frenet-Serret formulae for curvature transformations, for which $\mathbf{a}_0$ is mapped to its deformed position with a position vector $\mathbf{a}$ relative to the fixed Cartesian reference axes. This deformed position vector is

$$\mathbf{a} = \mathbf{r} + y\mathbf{q}_y + \Omega\mathbf{q}_z\,, \tag{2}$$

in which $\mathbf{r}$ is the position vector of the centroid after the deformation, $\mathbf{q}_y$ and $\mathbf{q}_z$ are body-attached basis vectors along the locus of the deformed cross-section, and the function Ω is

$$\Omega = w_{sp}\begin{cases} -1 & \text{concrete slab} \\ 1 & \text{steel joist} \end{cases} \tag{3}$$

and $w_{sp}(z)$ is the slip at the slab/joist interface. Defining the gradient tensors by

$$\mathbf{F}_0 = \left[\partial\mathbf{a}_0/\partial y \quad \partial\mathbf{a}_0/\partial z\right] \quad \text{and} \quad \mathbf{F} = \left[\partial\mathbf{a}/\partial y \quad \partial\mathbf{a}/\partial z\right] \tag{4}$$

allows the strain tensor to be expressed as [Love 1944]

$$\begin{bmatrix} \varepsilon_{yy} & \frac{1}{2}\gamma_{yz} \\ \frac{1}{2}\gamma_{zy} & \varepsilon_{zz} \end{bmatrix} = \tfrac{1}{2}\left\{\mathbf{F}^{\mathrm{T}}\mathbf{F} - \mathbf{F}_0^{\mathrm{T}}\mathbf{F}_0\right\} = \tfrac{1}{2}\left\{\mathbf{F}^{\mathrm{T}}\mathbf{F} - \mathbf{I}\right\} \tag{5}$$

and which leads to the normal strains at a point in the section being

$$\varepsilon_{yy} = 0\,, \tag{6}$$

$$\varepsilon_{zz} \approx w' + \Omega' + \tfrac{1}{2}v'^2 + \tfrac{1}{2}w'^2 + \tfrac{1}{2}\Omega'^2 - y\left[v''(1+w') - v'w''\right] + yv''\Omega'\,, \tag{7}$$

and to the shear strains being

$$\gamma_{zy} = \gamma_{yz} \approx -\Omega v'' \tag{8}$$

when third and higher order terms have been neglected. The non-linearities in Eq. (7) also occur in restrained composite beams in fire [Heidarpour and Bradford 2008], relating to the axial force.

Constitutive modelling

For the *steel joist*, the von Mises yield criterion can be written in terms of the stress vector $\boldsymbol{\sigma}$ as

$$F(\boldsymbol{\sigma}, \lambda) = \sigma_e - \sigma_y = 0 \tag{9}$$

in which σ_y is the uniaxial yield stress determined from a suitable hardening parameter H'_s and σ_e = $\sqrt{(\sigma_{zz}^2 + 3\tau_{zy}^2)}$ is the effective stress. Based on the associated flow and isotropic hardening theory, the relationship between the stress and total (elastic and plastic) strain increments is

$$\mathrm{d}\boldsymbol{\sigma} = \mathbf{E}^{ep}\,\mathrm{d}\boldsymbol{\varepsilon} \tag{10}$$

where $\mathbf{E}^{ep}$ is the standard tangent modulus material matrix [Pi *et al.* 2006].

For *concrete in tension*, the concrete is assumed to be elastic with a crack detection surface being represented as

$$F_t(\boldsymbol{\sigma}, \lambda_t) = \sigma_e^t - \left[3 - b_0\left(\sigma_t / \sigma_t^u\right)\right]\, p^t - \left[2 - (b_0/3)\left(\sigma_t / \sigma_t^u\right)\right]\, \sigma^t = 0 \tag{11}$$

where σ^t_e is the von Mises equivalent deviatoric stress (the same as for the steel), p^t the effective tensile stress, $\sigma_t(\lambda_t)$ the hardening parameter, σ^u_t the ultimate stress in uniaxial tension and b_0 a constant [Menetrey and Willam 1995]. After cracking, tensile stresses are generated in the cracked slab as a result of transfer, via shear and bond, of the stresses from the reinforcement and the steel component. The constitutive model therefore includes tension stiffening [Gilbert and Warner 1978], which is incorporated into the tangent material matrix $\mathbf{E}^{cr}$ in $\mathrm{d}\boldsymbol{\sigma} = \mathbf{E}^{cr}\mathrm{d}\boldsymbol{\varepsilon}$.

For *concrete in compression*, the compression yield surface is represented by

$$F_c(\boldsymbol{\sigma}, \lambda) = \sigma_e^c - \sqrt{3}a_0 p^c - \left(1 - a_0/\sqrt{3}\right)\sigma_c = 0 \tag{12}$$

where $p^c = -\sigma_{zz}/2$, σ^c_e is the von Mises equivalent deviatoric stress (the same as for the steel), $\sigma_c(\lambda)$ the hardening parameter and a_0 a constant [Menetrey and Willam 1995]. The associated flow rule generally over-predicts the inelastic volume strain. However, for computational efficiency and simplicity in the line element, the associated flow and isotropic hardening rules are also used for the concrete component when compression is dominant.

For the *shear connection*, it is assumed herein that the force/slip relationship can be obtained from a curve of the type depicted in Figure 2(b), which is obtained empirically from push testing data. The line element herein derives its computational efficacy by an empirical formulation for the shear connection; this behaviour comprising of the behaviour of the stud connectors in the trapezoidal profiles together with the surrounding concrete, reinforcement and profiled sheeting. The behaviour of the shear connection zone, which is assumed to be smeared along the beam element, is characterised by the curve in Figure 2(a), which can include the material non-linearity and softening depicted in the figure.

Non-Linear Equilibrium

The non-linear equations of equilibrium for a beam element can be derived from the principle of virtual displacements, which requires that

$$\int_{vol} \delta\boldsymbol{\varepsilon}^{\mathrm{T}}\boldsymbol{\sigma}\,\mathrm{d}(vol) + \int_{\ell} \delta w_{sp} q_{sh}\,\mathrm{d}z - \int_{\ell} \delta\mathbf{u}^{\mathrm{T}}\mathbf{q}\,\mathrm{d}z - \sum\nolimits_{k} \delta\mathbf{u}_k^{\mathrm{T}}\mathbf{Q}_k = 0 \qquad (13)$$

for all kinematically admissible virtual displacements δv, δw, δw_{sp}, and where $\boldsymbol{\sigma} = \{\sigma_{zz},\ \tau_{zy}\}^{\mathrm{T}}$, $\delta\boldsymbol{\varepsilon} = \{\delta\varepsilon_{zz},\ \delta\gamma_{zy}\}^{\mathrm{T}}$, q_{sh} and δw_{sp} are the shear flow force and conjugate virtual slip at the slab-joist interface, $\mathbf{q}$, $\mathbf{Q}_k$ and $\delta\mathbf{u}$ are vectors of the external distributed and concentrated loads and the vector of conjugate virtual displacements. The efficient method herein is reliant on the principle of consistent linearization of the principle of virtual displacements, which plays a key role in the numerical implementation employing an incremental-iterative solution procedure. The full description of the technique in a generic framework for composite beams has been described by [Pi *et al.* 2006a,b], and it is able to produce efficacious solutions for composite members.

PUSH TESTS

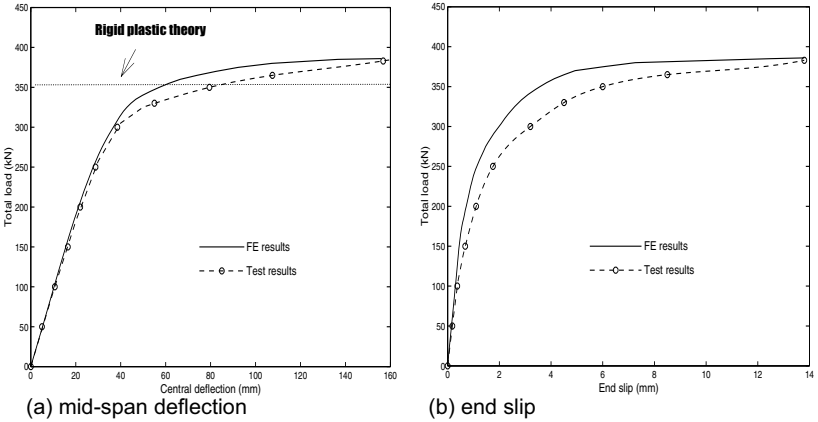
The rationale for the efficient numerical procedure proposed herein is to encapsulate the behaviour of the shear connection region in a trapezoidal slab from rational (empirical) push tests into a load-slip curve of the type shown in Figure 2b; this curve is intended to represent the stiffness and ductility of the shear connection in a curve which can be described in the numerical model as being piecewise linear. As noted previously, the difficulty in using conventional methodologies in composite beam design for deep trapezoidal profiles is extrapolating conventional push test results to full-scale beam behaviour, and so a sufficient degree of confidence is needed to allow push test data to be used for flexural beams in frame structures.

Conventional push tests as structurally analysed by [Oehlers and Bradford 1995] have shortcomings when extrapolated to full-scale specimens, and in order to replicate the full-scale tests theoretically from push tests, it is hypothesised that the push testing methodology incorporating a normal force can be used to provide empirical data for the finite element modelling.

ANALYSIS OF FULL-SCALE TEST RESULTS

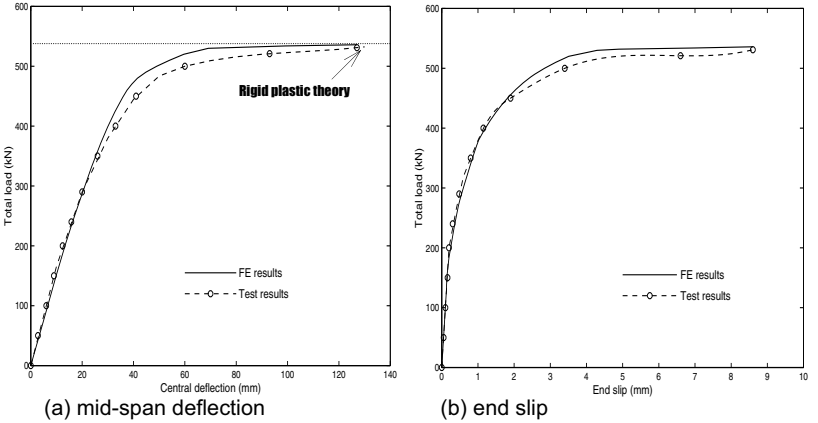
The finite element modelling has been applied to the two full-scale beam tests at The University of Sydney reported by [Ranzi *et al.* 2008] using the companion non-linear push test data for these beams given by [Bradford *et al.* 2006a,b]. For this modelling, the additional properties assumed were steel yield strengths of 310.5 MPa for beam CB1 and 332.3 MPa for CB2, concrete compressive strengths of f_c = 26.4 MPa for CB1 and 28.3 MPa for CB2, a concrete elastic modulus of $E_c = 0.043\times\rho^{1.5}\sqrt{f_c}$ with a

density ρ = 2400 kg/m^3 and, for simplicity, the slab was modelled as being a void for 78 mm above the top of the steel joist and as solid of width 2000 mm width and 52 mm depth above this.



(a) mid-span deflection (b) end slip

Fig. 4 - Comparison of full-scale tests and non-linear finite element results for CB1



(a) mid-span deflection (b) end slip

Fig. 5 - Comparison of full-scale tests and non-linear finite element results for CB

The finite element results for beams CB1 and CB2 are compared with the test results in Figures 4 and 5 respectively, in terms of both load versus mid-span and load versus end slip deflections. It can be seen that there is very good agreement between the numerical and test results, notwithstanding representing the shear connection as being smeared uniformly along the beam. Importantly, the figures show that the ductile load-slip curve derived empirically from the modified push tests is manifested in the ductile beam behaviour in the finite element solutions. This simplified technique allows the influence of the thin-walled high strength profiled

decks to be incorporated in the empirical load-slip curve from the push tests with a normal force.

Using rigid plastic partial interaction analysis, based on a stud strength from the push tests of 49 kN for beam CB1, it can be shown that the degree of partial interaction is η = 0.31 and that the mid-span flexural capacity is M_{push} = 364 kNm; this value is shown in Figure 4(a) and is about 5% conservative in predicting the strength of the beam. Based on a stud strength from the push tests of 39 kN for bean CB2, η = 0.38 and M_{push} = 545 kNm, which is about 1% unconservative in predicting the beam strength (Figure 5(a)).

CONCLUSIONS

This paper has described the application of an advanced line-type finite element analysis, which considers material and geometric non-linearity, for predicting the behaviour of composite beams with deep trapezoidal decks orthogonal to the steel joist. These beams are known to possess unique shear connection properties depending on many variables (such as the number of studs in a trough and their orientation, location of reinforcing mesh, stud height, slab depth, sheeting geometry and thickness), and the methodology adopted includes this behaviour by making recourse to the load-slip response of the shear connection derived from push testing in which unrepresentative premature failure modes have been prevented.

The numerical model was used to investigate two full-scale 8 m long beams which were tested at The University of Sydney, and for which companion push test data was available. The agreement between test and theory was excellent, being represented by the load versus mid-span deflection and load versus end slip curves. The theory also predicted the highly ductile response observed in the tests. Because of the expense of full-scale testing, it is impossible to quantify the influence of all governing parameters on the behaviour of a full-scale beam from full-scale tests, and this method provides a convenient means of translating the non-linear load-slip behaviour of a modified push testing procedure which includes implicitly the interaction of variables and relevant modes of failure into models for realistic flexural beam behaviour.

ACKNOWLEDGEMENT

The work in this paper was supported by the Australian Research Council through Discovery and Linkage Projects awarded to the authors.

REFERENCES

Bradford MA, Filonov A, Hogan TJ (2006) Push testing procedure for composite beams with deep trapezoidal slabs. *Eleventh International Conference on Metal Structures*, Rzeszow, Poland.

Bradford MA, Filonov A, Hogan TJ, Uy B, Ranzi G (2006) Strength and ductility of shear connection in composite T-beams with trapezoidal steel decking. *Eighth International Conference on Steel, Space and Composite Structures*, Kuala Lumpur, Malaysia; 15-26.

Ernst S, Bridge RQ, Patrick M (2006) Behaviour of the longitudinal shear connection in secondary composite beams incorporating trapezoidal steel decking. *Nineteenth Australasian Conference on Mechanics of Structures and Materials*, Christchurch, New Zealand; 49-56.

Gilbert RI, Warner RF (1978) Tension stiffening in reinforced concrete slabs. *Journal of the Structural Division, ASCE* 104: 1885-1900.

Heidarpour A, Bradford MA (2008) Geometric non-linear modelling of partial interaction in composite T-beams in fire. *Composite Construction in Steel and Concrete VI*, Devils Thumb Ranch, Colorado.

Hicks S (2007) Strength and ductility of headed stud connectors welded in modern profiled steel sheeting. *The Structural Engineer* 85: 32-38.

Johnson RP (2005) Shear connection in beams that support composite slabs – BS 5950 and EN 1994-1-1. *The Structural Engineer* 83: 21-24.

Johnson RP, Yuan H (1998a) Existing rules and new tests for stud shear connectors in troughs of profiled sheeting. *Proceedings of the Institution of Civil Engineers Structures and Buildings* 128: 244-251.

Johnson RP, Yuan H (1998b) Models and design rules for stud shear connectors in troughs of profiled sheeting. *Proceedings of the Institution of Civil Engineers Structures and Buildings* 128: 252-263.

Kim B, Wright HD, Cairns R, Bradford MA (1999) The numerical simulation of shear connection. *Sixteenth Australasian Conference on the Mechanics of Structures and Materials*, Sydney, Australia; 341-346.

Love AEH (1944) *A Treatise on the Mathematical Theory of Elasticity*. 4th Edn., Dover Publishers, New York.

Menetrey P, Willam KJ (1995) Triaxial failure criterion for concrete and its generalization. *ACI* Structural Journal 92: 311-318.

Oehlers DJ, Bradford MA *Steel and Concrete Composite Structural Members: Fundamental Behaviour*. Pergamon Press, Oxford, UK.

Patrick M, Bridge RQ (2002) Shear connection in composite beams incorporating open through-profile decks. *Third International Conference on Advances in Steel Structures*, Hong Kong; 519-526.

Pi Y-L, Bradford MA, Uy B (2006a) Second order nonlinear analysis of steel-concrete members. I: Theory. *Journal of Structural Engineering, ASCE* 132:751-761.

Pi Y-L, Bradford MA, Uy B (2006b) Second order nonlinear analysis of steel-concrete members. II: Applications. *Journal of Structural Engineering, ASCE* 132:762-771

Rambo-Roddenberry M, Easterling WS, Murray TM (2002) Behavior and strength of welded stud shear connectors. *Reports CE/VPI STO/04* and *CE/VPI STO/05*, Virginia Polytechnic Institute and State University, Blacksburg, Virginia.

Ranzi G, Bradford MA, Ansourian P, Filonov A, Rasmussen KJR, Hogan TJ, Uy B (2008) Full-scale tests on composite steel-concrete beams with steel trapezoidal decking. Submitted for publication.

Sebastian WM, McConnel RE (2000) Nonlinear FE analysis of steel-concrete composite structures. *Journal of Structural Engineering, ASCE* 126: 662-674.

EFFECT OF STRAIN PROFILES ON THE BEHAVIOR OF SHEAR CONNECTORS FOR COMPOSITE STEEL-CONCRETE BEAMS

O.Mirza
School of Engineering, University of Western Sydney
Penrith, New South Wales, Australia
o.mirza@uws.edu.au

B.Uy
School of Engineering, University of Western Sydney
Penrith, New South Wales, Australia
b.uy@uws.edu.au

ABSTRACT

In composite steel-concrete construction applications, the behavior of the shear connectors is paramount to the overall system performance. The most common method for evaluating shear connector strength and its behavior is through the use of a push test. Push tests have been used as early as the 1960's to predict the strength and behavior of shear studs in solid slabs. The performance of steel-concrete composite structures is greatly dependent on the load-slip characteristics of shear connectors. Significant research work has been performed on composite beams in regard to their stiffness and ductility of the shear connectors for both solid and profiled slabs. This paper describes the strength and ductility of the shear connectors in composite beams with both the solid and profiled steel sheeting slabs when different strain regimes were implemented in the concrete element. An accurate non-linear finite element model using ABAQUS is developed herein to study the behavior of shear connectors for both solid and profiled steel sheeting slabs. The reason for employing different strain regimes in push tests is to properly simulate the behavior of shear connectors in composite beams where trapezoidal slabs are used. The pertinent results obtained from the finite element analysis were verified against experimental results from other researchers. Based on the finite element analysis and experimental results, it has been determined that the strength and the load-slip behavior of composite steel-concrete beams is greatly influenced by the strain regimes existent in the concrete element.

INTRODUCTION

When a push test is undertaken, the shear connectors are subjected to pure shear, however shear connectors in a composite steel-concrete beam are subjected to both bending and shear deformations. For a simplified explanation, consider the push test with a horizontal axis of symmetry, shown in Figure 1. A horizontal line of the cross-section is shown at the interface of the concrete slab and structural steel beam which will be referred to as the neutral axis of the composite steel-concrete beam. Next consider a typical element of composite beam between two planes perpendicular to the beam's neutral axis. From the elevation, the element is denoted as *aabb*. When the structure is subjected to loading in the web of the structural steel beam, shown in Figure1a, it will be pushed as shown in this figure and section *aabb* will remain

undeformed. Therefore, the shear stud is in pure shear where critical loading conditions are applied to the shear connectors in composite steel-concrete beams. In this case, the strain will remain constant along the section, as shown in Figure 1c.

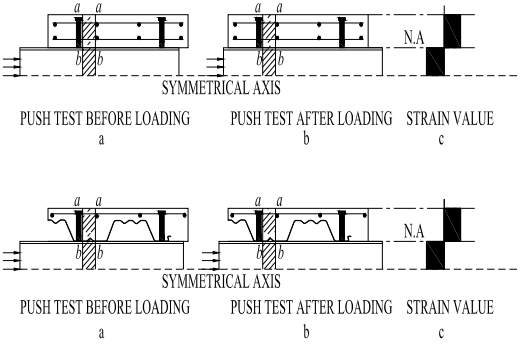


Fig. 1 - Behavior of composite steel-concrete push test in pure shear

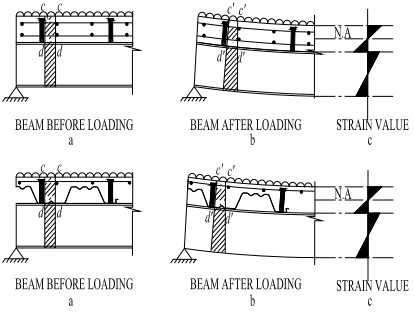


Fig. 2 - Behavior of composite steel-concrete beams in pure bending

When a composite steel-concrete beam is subjected to bending moments, consider the beam with a vertical axis of symmetry given in Figure 2. The horizontal line of the cross-section is similar to the push test explained above. When the structure is subjected to loading on the concrete slab shown in Fig. 2a, the structure will bend as illustrated in Fig. 2b, and then the section *ccdd* deforms to become *c'c'd'd'*. Thus, the cross-section is said to be in bending. For this case, the strain gradually changes throughout the depth of the section as shown in Fig. 2c.

A linear variation in strain is schematically shown in Figure 3, and the value of strain is represented using a parameter defined as α. When the structure is subjected to pure shear, the strain distribution is represented by Figure 3a where $\alpha = 1$. For the case when the structure is subjected to pure bending, the strain distribution is represented by Figure 3e where $\alpha = -1$. Figures 3b, 3c and 3e illustrate the different variations of strain which represents the different locations of the neutral axis.

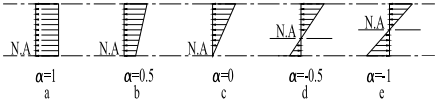


Fig. 3 - The value of α and location of neutral axis for the concrete element

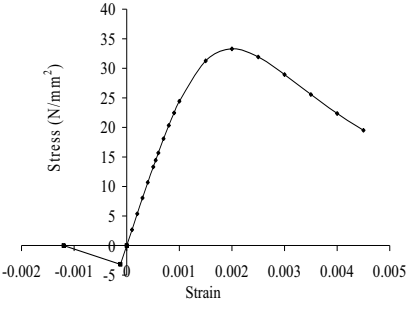


Fig. 4 - Stress and strain relationship for concrete, [Carreira and Chu 1985]

MECHANICAL BEHAVIOR OF THE CONSTITUENT MATERIALS

Constitutive laws are used to define the stress-strain characteristics of the material. The accuracy of the analysis is dependent on the constitutive laws used to define the mechanical behavior. In materials such as the concrete, structural steel and reinforcing steel, profiled steel sheeting and shear connectors, the constitutive laws are represented by the stress-strain relationships of the materials.

Concrete properties

Plain concrete was recommended by [Carreira and Chu 1985], where the stress in compression is assumed to be linear up to a stress of $0.4f'_c$. Beyond this point, the stress is represented as a function of strain according to Eq. (1).

$$\sigma_c = \frac{f'_c \gamma(\varepsilon_c / \varepsilon'_c)}{\gamma - 1 + (\varepsilon_c / \varepsilon'_c)^{\gamma}} \tag{1}$$

where

$$\gamma = \left| \frac{f'_c}{32.4} \right|^3 + 1.55 \text{ and } \varepsilon'_c = 0.002$$

For concrete in tension, the tensile stress is assumed to increase linearly relative to strain until the concrete cracks. After the concrete cracks, the tensile stress decreases linearly to zero. The value of strain at zero stress is usually taken to be ten times the strain at failure, which is shown in Figure 4.

Structural steel, reinforcing steel, shear connectors and profiled steel sheeting properties

The stress-strain characteristics of reinforcing steel, shear connectors and profiled steel sheeting are essentially similar to structural steel. Their behavior is initially elastic after which yielding and strain hardening develop. A piecewise linear approach was found to be sufficiently accurate to represent the stress-strain

relationships. Moreover, these curves are utilized in the model when the stress-strain data is not available.

According to [Loh et al. 2003], the stress-strain relationship for structural steel can be represented as a simple elastic-plastic model with strain hardening. The mechanical behavior for both compression and tension is assumed to be similar. Figure 5 represents the stress-strain relationship for steel and Table 1 indicates the different values of stress and strain for each material.

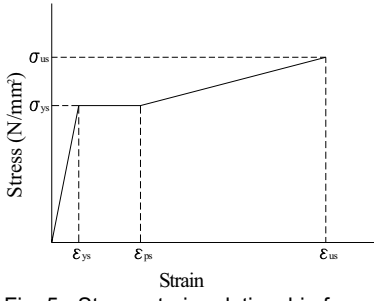


Fig. 5 - Stress-strain relationship for structural steel [Loh et al. 2003]

Table 1 - Stress-strain values for structural steel beam, shear connectors, profiled steel sheeting and steel reinforcing

Element	σ_{us}	ε_{ps}	ε_{us}
Steel beam	$1.28\sigma_{ys}$	$10\varepsilon_{ys}$	$30\varepsilon_{ys}$
Steel Reinforcing	$1.28\sigma_{ys}$	$9\varepsilon_{ys}$	$40\varepsilon_{ys}$
Profiled Sheeting	-	$20\varepsilon_{ys}$	-
Shear Connectors	-	$25\varepsilon_{ys}$	-

PUSH TEST FINITE ELEMENT ANALYSIS

Experimental investigation of push tests.

The push tests performed by [Lam and El-Lobody 2005] considered shear connection of both solid and profiled slabs. The authors have modified Lam's solid slab to consider a profiled slab To evaluate the differences between the solid and profiled slabs. The authors also used the experiments conducted by [Hicks 2007] for both push and beam tests as a comparison with the finite element analysis for the profiled slabs.

Parametric studies for push tests.

Parametric studies were undertaken by the authors to look at different types of profiled steel sheeting and their effects on the shear connector behavior when different strain regimes were considered. Three different types of profiled steel sheeting were considered, and they include G1, G2 and G3 profiled decks. The dimensions and profiled steel sheeting details are provided in Table 2 and shown in Figure 6.

Finite element type and mesh

Three dimensional solid elements were used to model the push off test specimens in order to achieve an accurate result from the finite element analysis using the finite element program known as ABAQUS [Karlsson and Sonrensen 2006a], [Karlsson and Sonrensen 2006b] and [Karlsson and Sonrensen 2006c]. For both the concrete slab and the structural steel beam, a three-dimensional eight node element (C3D8R) was used. A three dimensional thirty-node quadratic brick element (C3D20R) for the shear connectors, a four-node doubly curved thin shell element (S4R) for the profiled

steel sheeting and a two-node linear three dimensional truss element (T3D2) for the steel reinforcing were used.

Table 2 - Dimensions and profiled steel sheeting details of parametric study

Group	Specimen	Dimensions							Strain Profiles
		Profiled Sheeting			Stud		Slab		
		b_0 (mm)	h_p (mm)	t (mm)	d (mm)	h (mm)	B (mm)	D (mm)	α
G1	G1-1	145	78	0.9	19	100	806	405	1
	G1-2	145	78	0.9	19	100	806	405	0.5
	G1-3	145	78	0.9	19	100	806	405	0
	G1-4	145	78	0.9	19	100	806	405	-0.5
	G1-5	145	78	0.9	19	100	806	405	-1
G2	G2-1	136	55	0.9	19	100	806	405	1
	G2-2	136	55	0.9	19	100	806	405	0.5
	G2-3	136	55	0.9	19	100	806	405	0
	G2-4	136	55	0.9	19	100	806	405	-0.5
	G2-5	136	55	0.9	19	100	806	405	-1
G3	G3-1	144	60.9	0.9	19	100	806	405	1
	G3-2	144	60.9	0.9	19	100	806	405	0.5
	G3-3	144	60.9	0.9	19	100	806	405	0
	G3-4	144	60.9	0.9	19	100	806	405	-0.5
	G3-5	144	60.9	0.9	19	100	806	405	-1

*The value of α and location of neutral axis for concrete element is shown in Figure 3

For the experiments of [Lam and El-Lobody 2005], the finite element model was used to represent half of a stud of the push test, due to symmetrical boundary conditions for both the solid and modified profiled slabs which are shown in Figures 7 and 8 respectively. Whilst for [Hicks 2007] experiments, the finite element model used to represent half of the push test models is shown in Figure 9. The reason the authors used half a stud for Lam's experiment while half a model for Hick's experiment was to reduce the simulation cost.

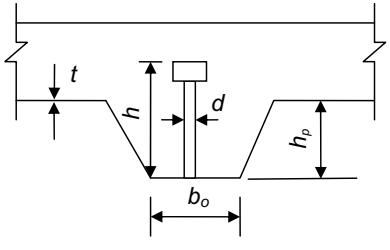


Fig. 6 – Dimensions of profiled steel sheeting

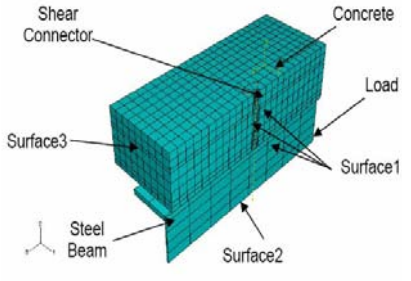


Fig. 7 - Finite element mesh and boundary condition of [Lam and El-Lobody 2005] solid slab model

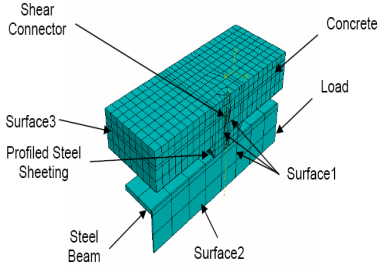


Fig. 8 - Finite element mesh and boundary condition of the Lam's modified profiled slab model

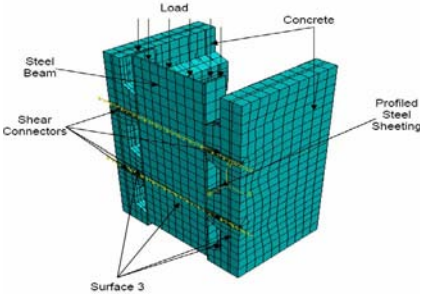


Fig. 9 - Finite element mesh and boundary condition of the [Hicks 2007] trapezoidal profiled steel sheeting slab model

Boundary conditions and load application

In Figures 7 and 8, the nodes that lie on the other symmetrical surface (Surface 1) for concrete, shear connectors, structural steel beam, steel reinforcing and profiled steel sheeting are restricted from moving in the *x*-direction. All the nodes in the middle of the structural steel beam web, which are designated as Surface 2, are restricted to move in the *y*-direction. All the nodes of the concrete and the profiled steel sheeting, which are designated Surface 3, are restricted to move in the *z*-direction. Whilst in Figure 9, Surface 3 which consists of a concrete slab, structural steel beam, steel reinforcing and profiled steel sheeting are restricted to move in the *z*-direction.

For the application of load, a static concentrated load was applied to the centre of the web for [Lam and El-Lobody 2005] model and a uniformly distributed load was applied to the web surface of the structural steel for the Hick's model. The modified RIKS method was employed to the load in order for the load to be obtained through a series of iterations for each increment for a non-linear structure.

RESULTS AND DISCUSSION

[Lam and El-Lobody 2005] experiments

The first series of analyses considered was compared with the experimental investigations undertaken by [Lam and El-Lobody 2005] for solid slabs. The authors then modified the solid slab to simulate a profiled slab to consider the differences in the results. It can be observed in Figure 10 that the stiffness is similar for both the experiments and the finite element analyses within the elastic region. The experimental study showed that the maximum shear connector capacity was 118 kN whilst the finite element result obtained was 119 kN. This shows that the finite element model accurately analyzed the experiments with a discrepancy of 0.7 %. When the model is subjected to bending where α = -1, after the elastic region, the finite element analysis had a higher shear connector capacity when compared with the model subjected to pure shear where α = 1.

From the finite element model, the authors also had shown that when the composite steel-concrete beam is subjected to pure shear, the structure is subjected to the most detrimental loading case. This can be verified from Figure 10 where the model is subjected to bending, the shear connector capacity increased by 2.2 % to 121 kN. Even though the loading behavior of the push test changed, 2.2 % of increment in the shear connector capacity is not significant.

Figure 10 established that the different strain regimes in solid slabs is not critical where increments in 0, 0.7 and 1.3 % for α = 0.5, α = 0 and α = -0.5 respectively. Therefore, it is illustrated that the push test to determine the shear connector capacity for composite steel-concrete solid slabs is reliable and accurate. It is observed that the failure mode changes when the value of α changes. When α = 1, the failure mode is governed by shear stud fracture. In the finite element model, the yielding of the stud element was discerned near the shear connector collar followed by the attainment of the maximum compressive stress being reached by the concrete elements around the shear connector. When α = 0.5, 0, -0.5 and -1, the failure mode is governed by concrete failure where the concrete starts to crack surrounding the shear connector due to the addition of load when the value of α changes.

Figure 11 illustrates that the stiffness is similar for the finite element analyses within the elastic region. The finite element analysis showed that the maximum shear connector capacity was 68 kN when α = 1 for the push test under pure shear, however when the model is subjected to the bending condition where α = -1, the maximum shear connector capacity was 92 kN. This shows a significant increment of 27 %. This result is expected when the push test changes from pure shear to pure bending due to the loading condition for the worst case scenario when compared with pure bending. Figure 11 illustrates that the different strain regimes in the profiled slab are crucial where an increment in 7, 13 and 19 % for α = 0.5, α = 0 and α = -0.5 respectively. Therefore, it is illustrated that the push test to determine the shear connector capacity for composite steel-concrete profiled slabs with trapezoidal ribs is unreliable. From Figure 11, it can be seen that the failure mode changes when the value of α changes. When α = 1 and 0.5, the failure mode is governed by concrete failure where the concrete cracks through the middle of the trough. This is shown by concrete element reaching its maximum tensile stress. When α = 0, -0.5 and -1, the failure mode is dominated by stud failure where the shear connectors started to shear off the concrete, causing the concrete to crack surrounding the shear connector. This is shown by the stud element reaching its maximum stress then followed by the concrete element reaching its maximum stress.

Hicks 2007 experiment

The second analysis considered was these associated with the experiments conducted by [Hicks 2007] for both push tests and beam tests. Figure 12 shows the comparison between the experimental tests undertaken by Hicks and the finite element model performed by the authors. The results are as stated by [Hicks 2007], the initial similarity is the stiffness for both the push test and the beam test. However, the maximum shear connector capacity and slip measured in the push test is well below the level attained in the beam test. Figure 12 verifies the accuracy of the finite element analysis. For the push tests, the experimental study showed a maximum shear capacity of 84 kN and the finite element analysis showed the value of 89 kN with a discrepancy of 6 %. As for the beam tests, the experimental study and finite element analysis illustrated that the maximum shear capacities were 124 kN and 128

kN respectively, with a discrepancy of 3 %. Furthermore, from the experimental studies and finite element analyses, the failure governed the push tests was concrete failure at the trough rather than stud failure. When the beam test is taken into account, the failure is caused by stud failure. The behavior of the shear connectors in the push test provides a conservative result and they do not replicate the strength and ductility that can be achieved in a beam test. Therefore, the standard push test to determine the shear connector capacity for the profiled slab is questionable.

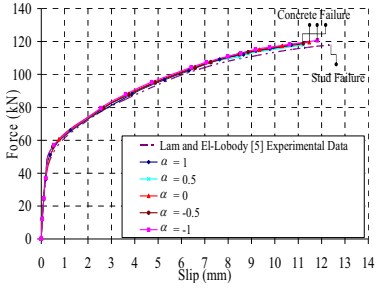


Fig. 10 - [Lam and El-Lobody 2005] experiment compared with different strain regimes

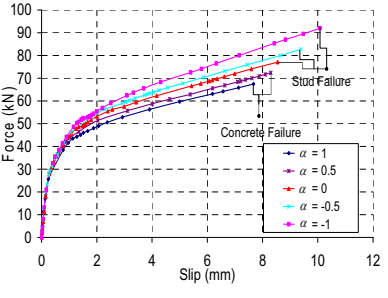


Fig. 11 - Lam and El-Lobody's modified push test with different strain regimes

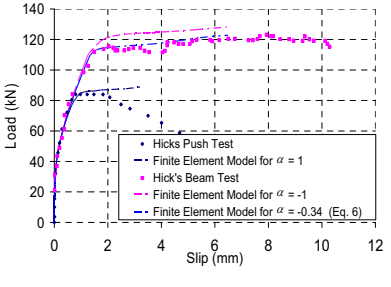


Fig. 12 - Comparison of experimental data and finite element result for [Hicks 2007]

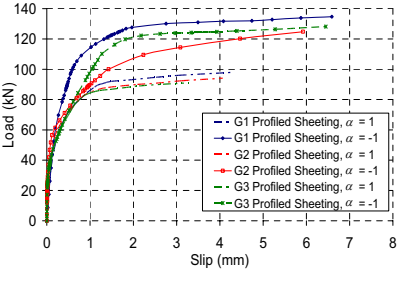


Fig. 13 - Comparison of force slip relationship for different types of profiled steel sheeting

Parametric studies

A total of fifteen push tests were investigated in the parametric study. The push tests were divided into three major groups. These are G1, G2 and G3. Each group

included five different push tests having different α values with the same type of profiled steel sheeting, as described in Figure 3. The dimensions of the profiled steel sheeting and details of the parametric study are explained in Table 2. Figure 13 illustrates the force-slip relationship for G1, G2 and G3 profiled steel sheetings. It can be seen that between the three profiled steel sheeting types, G1 profiled steel sheeting can withstand higher forces when compared with the other two sheetings. Therefore, G1 has a higher strength capacity and is more ductile. Figure 13 reveals a maximum shear connector capacity of 135 kN, 125 kN and 128 kN for G1, G2 and G3 profiled steel sheeting respectively. G1 illustrates that it has a shear connector capacity 5 % higher than that of the G3 trapezoidal profiled steel sheeting and 7 % higher than that of the G2 profiled steel sheeting. Figure 13 also shows that the shear strength capacity of composite steel-concrete profiled slabs is greatly dependent on the width and depth of the ribs of the profiled steel sheeting.

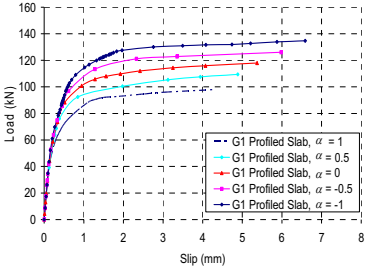


Fig. 14 - Force slip relationship for G1 profiled steel sheeting with variation of α value

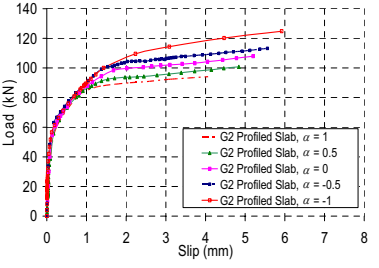


Fig. 15 - Force slip relationship for G2 profiled steel sheeting with variation of α value

The first group of parametric studies, the authors varied the strain regimes from α = 1, 0.5, 0, -0.5 and -1 for the G1 profiled steel sheeting. Figure 14 depicts the force-slip relationship of the G1 profiled steel sheeting with the variation of α value. It can be observed that the composite steel concrete beam increases the shear strength and ductility when the structure is varied from pure shear to pure bending. When the structure is subjected to pure shear, the maximum shear connector capacity of 98 kN is achieved. However, when it is subjected to pure bending, the maximum shear capacity increases to 135 kN, which is a 27 % shear capacity increment.

The second group of parametric studies, the authors varied the strain regimes which included α = 1, 0.5, 0, -0.5 and -1 for G2 profiled steel sheeting. Figure 15 shows the force-slip relationship of G2 profiled steel sheeting with a variation of α value. When the structure is subjected to pure shear and pure bending, the maximum shear connector capacity is 94 kN and 125 kN respectively, which is a 25 % shear capacity increment.

The third group of parametric studies, G3 is used to verify [Hicks 2007] trapezoidal profiled steel sheeting. Figure 16 illustrates the force-slip relationship of G3 trapezoidal profiled steel sheeting with a variation of α value. When the structure is exposed to pure shear and pure bending, the maximum shear connector capacity is 91 kN and 128 kN respectively which is a 29 % increase in shear capacity.

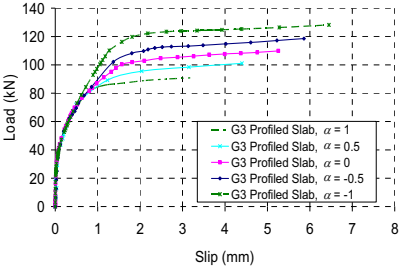


Fig. 16 - Force slip relationship for G3 profiled steel sheeting with variation of α

To include the α value into the force-slip relationship, the [Aribert and Labib 1982] force-slip relationship was used and shown in Eq. (2). Due to Q_u, c_1 and c_2 are the changing parameters in the equation, the relationship of these values with respect to α can be determined and is shown in Eqs. (3) to (5) for G1, G2 and G3 profiled steel sheeting.

$$Q = f_1(\alpha)\left(1 - e^{-f_2(\alpha).d}\right)^{f_3(\alpha)} \tag{2}$$

$$Q_u = f_1(\alpha) = -17.94\alpha + 117.2 \ , \ -1 \le \alpha \le 1 \ \text{ for G1} \tag{3a}$$

$$Q_u = f_1(\alpha) = 13.3\alpha^3 - 1.5\alpha^2 - 28.6\alpha + 111.5 \ , \ -1 \le \alpha \le 1 \ \text{for G2} \tag{3b}$$

$$Q_u = f_1(\alpha) = -18.36\alpha + 109.74 \ , \ -1 \le \alpha \le 1 \ \text{for G3} \tag{3c}$$

$$c_1 = f_2(\alpha) = -0.06\alpha^3 + 0.13\alpha^2 + 0.12\alpha + 1.2 \ , \ -1 \le \alpha \le 1 \ \text{for G1} \tag{4a}$$

$$c_1 = f_2(\alpha) = 0.15\alpha^3 + 0.15\alpha^2 + 0.35\alpha + 0.96 \ , \ -1 \le \alpha \le 1 \ \text{for G2} \tag{4b}$$

$$c_1 = f_2(\alpha) = 0.67\alpha^4 + 0.2\alpha^3 - 0.27\alpha^2 + 0.3\alpha + 1.05 \ , \ -1 \le \alpha \le 1 \ \text{for G3} \tag{4c}$$

$$c_2 = f_3(\alpha) = -0.07\alpha^4 - 0.0313\alpha^3 + 0.17\alpha^2 + 0.03\alpha + 0.4 \ , \ -1 \le \alpha \le 1 \ \text{for G1} \tag{5a}$$

$$c_2 = f_3(\alpha) = 0.02\alpha^4 - 0.07\alpha^3 - 0.03\alpha^2 + 0.07\alpha + 0.4 \ , \ -1 \le \alpha \le 1 \ \text{for G2} \tag{5b}$$

$$c_2 = f_3(\alpha) = -0.07\alpha^4 - 0.03\alpha^3 + 0.17\alpha^2 + 0.03\alpha + 0.4 \ , \ -1 \le \alpha \le 1 \ \text{for G3} \tag{5c}$$

where Q is the force of the shear connector, Q_u is the ultimate force, c_1 and c_2 are the parameters of the model and d is the slip capacity of the shear connector.

From the above equations, the Q_u, c_1 and c_2 for [Hicks 2007] can be determined and the force-slip relationship is derived as shown in Eq. (6).

$$Q = 115.98\left(1 - e^{-0.92.d}\right)^{0.41} \tag{6}$$

Eq.(6) is plotted in Figure 12, and from Figure 12, it is verified that when the correct α value of -0.34 is determined, the discrepancy of the result is only 0.3 % when compared with the initial assumption of α = -1 where the discrepancy is 4 %.

Table 3 - Comparison of ultimate load for shear connector between experimental results, finite element models and international standards

Concrete Properties, f'_c = 35 MPa										
Profiled Type	FEM Result	Australian Standard		Eurocode		AISC		FEM/Standard		
		SF	CF	SF	CF	SF	CF			
	(kN)							AS	EC	AISC
G1	98.2 (CF)	116.1	110.7	80.5	72	125.0	117.6	0.85	1.22	0.80
G2	94.1 (CF)	116.1	110.7	113.5	101.6	145.1	136.4	0.81	0.83	0.66
G3	91.1 (CF)	116.1	110.7	85.2	76.2	132.4	124.5	0.78	1.07	0.70

*S.F denotes stud failure and C.F concrete failure

Profiled slabs compared with existing standards

A comparison was made to evaluate the finite element models undertaken by authors with three existing international standards. They included the Australian Standard [AS 2327.1 2003], [British Standards Institute 2004] and American Standard [AISC 2005]. A summary of the ultimate loads for the shear connector, *P* which is calculated using the Australian Standard, Eurocode and American Standard is given in Table 3.

For G1 profiled slabs, the finite element result showed the ultimate load of 98 kN. The ultimate loads for the Australian Standard and American Standards are 116 kN and 122 kN, respectively. Therefore, ultimate load values for Australian and American Standards are 15% and 19% higher, respectively, when compared against the finite element models. This verified that the finite element model is more conservative. On the contrary, the Eurocode seems to be very conservative, with an ultimate load of 80 kN which is 21% lower than the finite element predicted value.

For G2 profiled slabs, when compared with the finite element models, all the standards demonstrated that the ultimate loads for shear connectors were higher. The finite element models showed the ultimate load of 94 kN, whilst the Australian Standard, Eurocode and American Standard were 116 kN, 114 kN and 172 kN, respectively. The Australian Standard, Eurocode and American Standard showed a higher ultimate load of 19%, 17% and 45%, respectively, when compared with finite element models. This indicated that the finite element models were more conservative.

G3 profiled slabs presented similar results to those observed in G1 profiled slabs where both American and Australian standards had higher ultimate load values whilst the Eurocode has a lower ultimate load value when compared with the finite element results. The finite element result showed the ultimate load of 91 kN. The ultimate loads calculated according to the Australian and American provisions are 116 kN and 129 kN, respectively. This proved that the ultimate load values for the Australian and American Standards are 21% and 29% higher, respectively, than those obtained by finite element analysis. The Eurocode showed the ultimate load of 85 kN, and it was 7% lower than the finite element solution.

CONCLUSIONS

Shear connection nonlinearity always results in significant changes in the strength and ductility of composite steel-concrete beams. To highlight such phenomena, a non-linear finite element procedure with varying strain regimes implemented in the concrete element has been presented to account for both the shear connection strength and ductility.

A comparison with experimental results allows the validation of such a procedure with reference to both solid slabs and profiled slabs for both push tests and beam tests. The finite element analysis that has been undertaken in this paper demonstrated that the push test to determine the shear connection capacity for solid slabs is reliable and accurate. However this is not the case for slabs with profiled steel sheeting.

An extensive parametric study of fifteen push test specimens with different profiled steel sheeting geometries was performed using the established finite element models. The comparison of shear connector capacities obtained from the finite element models proved that they depend significantly on the width and rib types of profiled steel sheeting.

The introduction of the parameters such as α, Q_U, c_1 and c_2 are the key characteristics of the proposed method because they account for the behavior of the shear connection nonlinearity effects. When accurate parameter values were applied to the force-slip relationship equations, it seems to suggest that the proposed method has less discrepancy when compared with the experimental study, and it is also useful for design engineers using these profiles in industry.

When the American, Eurocode and Australian Standards are compared with finite element results, the Australian Standards and American Standards proved to be less conservative whilst Eurocode appeared to be very conservative. The ultimate load for shear connectors is proven to be higher than finite element models for Australian and American Standards. However, the Eurocode seems to be very conservative where lower ultimate loads were observed when compared with the finite element model.

ACKNOWLEDGEMENTS

The authors would like to thank the Australian Research Council and BlueScope Lysaght Sydney for providing funding for this project and the University of Western Sydney for providing a conducive environment for the authors to prepare this paper described herein.

REFERENCES

AISC. 2005; Specification for structural steel building. American Institute of Steel Construction.

Aribert, J. and Labib, A. 1982; Modèle calcul èlasto-plastique de pustres mixtes a connexion partielle. Journal of Construct Metallique 4:3-51.

AS 2327.1, A. S. 2003; Composite structures, Part 1: Simply supported beams. Standard Australia International AS 2327.1-2003.

British Standards Institute. 2004; Design of composite steel and concrete structures, Part 1.1 General rules and rules for buildings, British Standard Institute, London.

Carreira, D. and Chu, K. 1985; Stress-strain relationship for plain concrete in compression. Journal of ACI Structural 82(11):797-804.

Hicks, S. J. 2007. Resistance and ductility of shear connection: Full-scale beam and push tests. 6th International Conference on Steel & Aluminium Structures, St. Catherine College, University of Oxford, England.

Karlsson and Sonrensen. 2006a; ABAQUS, Theory manual version 6.5. Pawtucket, Rhode Island, Hibbitt Publication.

Karlsson and Sonrensen. 2006b; ABAQUS User's manual version 6.5. Pawtucket, Rhode Island, Hibbitt Publication

Karlsson and Sonrensen. 2006c; ABAQUS Analysis user's manual version 6.5. Pawtucket, Rhode Island, Hibbitt Publication

Lam, D. and El-Lobody, E. 2005; Behaviour of headed stud shear connectors in composite beam. Journal of Structural Engineering-ASCE 131(1):96-107.

Loh, H. Y., Uy, B. and Bradford, M. A. 2003; The effects of partial shear connection in the hogging moment region of composite beams Part II - analytical study. Journal of Constructional Steel Research 60:921-962.

DESIGN MODEL FOR CONTINUOUS COMPOSITE BEAMS WITH WEB OPENINGS

Torsten Weil
Ed. Zueblin AG
Stuttgart, Germany
torsten.weil@zueblin.de

Juergen Schnell
Kaiserslautern University of Technology
Concrete Structures and Structural Design
Kaiserslautern, Germany
jschnell@rhrk.uni-kl.de

Wolfgang Kurz
Kaiserslautern University of Technology
Steel Structures
Kaiserslautern, Germany
wkurz@rhrk.uni-kl.de

ABSTRACT

Continuous composite beams can be designed according to the plastic hinge theory. In that case in a statically indeterminate system plastic hinges are formed one after the other until a kinematic mechanism is generated (ultimate limit state). In the case of continuous beams with web openings, areas of plastic deformation can be generated in the area near the opening itself. This means that under certain circumstances local plastic moment hinges are formed in the corners of the opening. All these local hinges together result in a global plastic hinge for shear forces. Up to now the structural and deformation behaviour of such a hinge was not clarified if it acts as a global mechanism with one degree of freedom. The necessary conditions to generate such a plastic hinge for shear forces were also not clear.

At Kaiserslautern a research project, that examined such beams, has been completed. Its results and a design model are described in this paper.

1 INTRODUCTION

Continuous composite beams can be designed according to the plastic hinge theory. According to this theory in a statically indeterminate system plastic hinges are formed one after another until a kinematic mechanism is generated at the ultimate limit state. Then the load maximum is reached. The use of the plastic hinge method depends on the plastic structural behaviour of the static system, the cross-sections and its capacities of rotation. A plastic moment hinge is generated, as soon as the plastic bearing capacity [7] of the cross section is accomplished at one location. In case plastic rotation is possible at this location, the bending moment operates at the plastic moment level; an increase of this moment is no longer possible. The potential rotation at the location of the first plastic hinge enables the system to redistribute internal forces so that the overall load can be increased beyond this loading state. The load is transferred to other system areas. In this case other plastic hinges are

generated. After occurring of the last plastic hinge the system becomes kinematic; the ultimate limit state is accomplished.

At continuous beams without openings plastic moment hinges are normally formed above the middle support and in the area of maximum sagging moment. At continuous beams with large web openings plastic ranges can be generated in the area near the opening. This means that under certain circumstances local plastic moment hinges are formed in the four corners of the opening. These local plastic hinges together result in a global plastic hinge for shear forces.

The basic differences in the design according to the plastic hinge theory between continuous composite beams with and without web openings are described by [6]. Zhou shows the influence, which is caused by the opening, on the arrangement of stress resultants ([9] and [10]). In [6] several questions in this context are determined and the results of six large-scaled tests are presented. A design model which was also developed within this work is shown in this paper.

2 GENERAL DESIGN FUNDAMENTALS

The conditions which must be fulfilled basically for the plastic hinge theory are given in German standard [4]. For continuous beams with large web openings it has to be considered particularly, that in the area of plastic hinges the cross section has to comply to class 1. In addition, only rolled steel girders are allowed. Furthermore two neighbouring spans of the beam should not differ more than 50%, based on the smaller span. Also the end span may not be greater than 115% of the neighbouring span. For construction steel the material requirements must be fulfilled according to German standard [4].

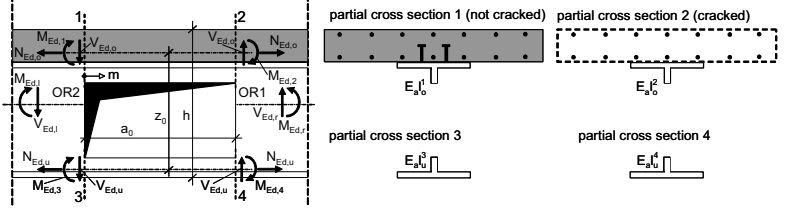


Figure 1 – Stress resultants and cross sections at the area of the opening

For the calculation the cross sections and the static system must be identified. Then for the used cross sections the values (centre of gravity, stiffness) have to be calculated - like e.g, shown in. [1] - for the cracked and the uncracked area without opening. The calculation of those values for the partial cross sections (shown in fig. 1) in the area of the opening corners occurs in a similar way. However, for both upper partial cross sections the effective width b_l by [5] has to be taken into account. If the distance between a partial cross section and a support or a single load under which a global plastic hinge of moments is possible, is smaller than the total height h of the cross section, so b_{eff} of the unweakened system according to [4] has to be used instead of b_l. For the static system the position of the opening has to be determined exactly. The distance m, defining the position of the global plastic hinge

for shear forces, starting at the left edge of the opening (OR2, cf. Figure 1) is calculated with the use of the stiffness:

$$m = \frac{E_a I_o^1 + E_a I_u^3}{E_a I_o^1 + E_a I_o^2 + E_a I_u^3 + E_a I_u^4} \cdot a_0$$

The presented calculation model can be applied for continuous beams with one opening per field. For the applicability on beams with more than one opening per field, the minimum distance between two openings has to comply with the greater opening length (cf. Figure 2).

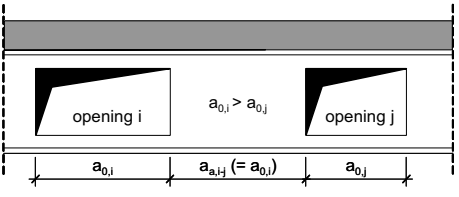


Figure 2 – Minimum distance between two openings

3 LOCAL CALCULATION OF THE OPENING

The calculation of continuous composite beams without an opening according to the plastic hinge theory results in a failure mechanism consisting of moment hinges above the middle support and in the field. The accomplished investigations [6] have shown that these plastic hinge mechanisms can not be expected on beams with large web openings. To implement the calculation of the opening into the plastic hinge theory, a local treatment - as described in the following - must be arranged first. The opening can be transferred schematically into the static system as a frame according to Figure 3.

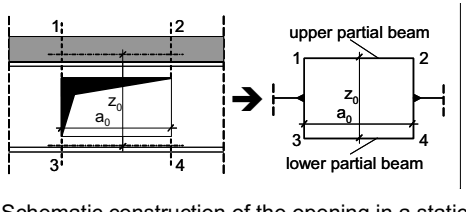


Figure 3 – Schematic construction of the opening in a static system

Every opening at a continuous beam can be embedded by this local calculation into the possible hinge mechanism of the complete system as a global part. The global behaviour in the area of the opening is described by three different failure models: Pure plastic hinge for shear forces (I), pure plastic moment hinge (II) and combined failure in the area of the opening (III). In the following three chapters the calculation of the bearing capacity of each model is described.

3.1 PURE PLASTIC HINGE FOR SHEAR FORCES (I) AT THE AREA OF THE OPENING

The pure plastic hinge for shear forces (I) is generated, when local plastic moment hinges are formed in all four corners of the frame modelling the web opening. This model is shown in Figure 4.

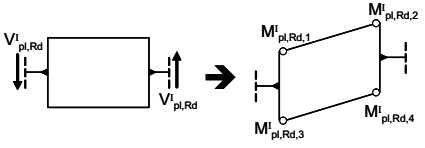


Figure 4 – Model of the pure plastic hinge for shear forces (I)

For the plastic hinge theory the global shear bearing capacity of the area at the opening must be calculated with the plastic moment capacity of the four partial cross sections. The calculation of the moment capacity in those partial cross sections results from the so-called basic functions established by Zhou ([8] and [10]). Due to the extensive correlation with global forces the exact calculation would have to be done in an iterative way. To simplify this, it is assumed that no global bending moment operates at the area of the opening. This simplification can be done because a possible moment at the area of the opening has either no influence or is covered by one of the other local mechanisms ((II) or (III)). Therefore no axial force is taken into account in the upper and in the lower flange. If the pure plastic hinge for shear forces (I) is set in the system, it can be supposed that the active shear force uses the remaining web completely. Indeed, due to the disregard of the web the maximum secondary bending moments would be calculated without the consideration of the influence caused by opening height. Calculations in [6] have shown that a reduction of the web thickness with the coefficient $\sqrt{0{,}02}$ is a good estimate. This coefficient results from the assumption that the shear force in the web reaches 98% of the plastic shear force. The position of the zero line in the upper partial beam is expected to be in the concrete slab. For the lower partial beam it is assumed in the flange. With the reduction of the web in the calculation no other position of the zero line will occur.

With these assumptions the plastic secondary bending moments in the partial cross sections can be calculated with the basic functions. For the partial cross section 1 the plastic moment results as follows:

$$M^{I}_{pl,Rd,1} = -\frac{1}{2}\cdot b_l \cdot f_{cd} \cdot y_{12}^2 + \frac{1}{2}\cdot b_l \cdot f_{cd} \cdot z_s^2 + b_{f,o} \cdot t_{f,o} \cdot f_{yd} \cdot \left(\frac{t_{f,o}}{2} + \bar{y}_c\right) + \sqrt{0{,}02} \cdot t_w \cdot h_{w,o} \cdot f_{yd} \cdot \left(\frac{h_{w,o}}{2} + t_{f,o} + \bar{y}_c\right)$$

For the partial cross section 2:

$$M^{I}_{pl,Rd,2} = \frac{1}{2}\cdot b_l \cdot f_{cd} \cdot \left(y_{24}\right)^2 - b_l \cdot f_{cd} \cdot \frac{z_s^2 + \bar{y}_c^2 - (z_s - y_{23})^2}{2} - b_{f,o} \cdot f_{yd} \cdot \frac{(\bar{y}_c + t_{f,o})^2 - \bar{y}_c^2}{2}$$
$$- \sqrt{0{,}02} \cdot t_w \cdot h_{w,o} \cdot f_{yd} \cdot \left(\frac{h_{w,o}}{2} + t_{f,o} + \bar{y}_c\right)$$

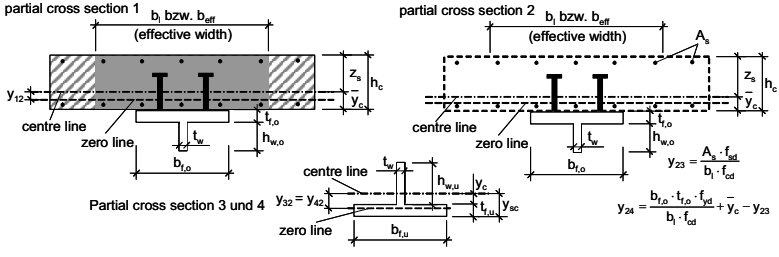
For the partial cross section 3:

$$M^{I}_{pl,Rd,3} = -b_{f,u} \cdot f_{yd} \cdot \left(y_{32}\right)^2 + b_{f,u} \cdot f_{yd} \cdot \frac{y_c^2 + y_{sc}^2}{2} + \sqrt{0{,}02} \cdot t_w \cdot f_{yd} \cdot \frac{(h_{w,u} - y_c)^2 - y_c^2}{2}$$

For the partial cross section 4:

$$M^{I}_{pl,Rd,4} = b_{f,u} \cdot f_{yd} \cdot \left(y_{42}\right)^2 - b_{f,u} \cdot f_{yd} \cdot \frac{y_c^2 + y_{sc}^2}{2} + \sqrt{0{,}02} \cdot t_w \cdot f_{yd} \cdot \frac{(h_{w,u} - y_c)^2 - y_c^2}{2}$$

The definitions of the symbols are summarised in Figure 5.



secondary bending moments using the basic functions from [8] and [10]

After the evaluation of the plastic secondary moments, the shear forces can be calculated in the upper and the lower partial beam:

$$V^{I}_{pl,Rd,o} = \frac{\left|M^{I}_{pl,Rd,1}\right| + \left|M^{I}_{pl,Rd,2}\right|}{a_0} \quad \text{and} \quad V^{I}_{pl,Rd,u} = \frac{\left|M^{I}_{pl,Rd,3}\right| + \left|M^{I}_{pl,Rd,4}\right|}{a_0}$$

Then the global plastic shear capacity of the pure plastic hinge for shear forces that is necessary for the calculation of the possible plastic hinge mechanism results to:

$$V^{I}_{pl,Rd} = V^{I}_{pl,Rd,o} + V^{I}_{pl,Rd,u}$$

3.2 PURE PLASTIC MOMENT HINGE (II) AT THE AREA OF THE OPENING

From the local point of view the pure plastic moment hinge is composed of two plastic hinges for axial forces which are generated in the upper and the lower flange. The used model of this hinge is shown in Figure 6.

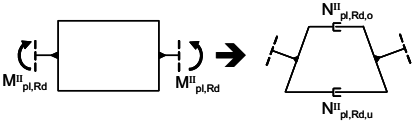


Figure 6 – Model of the global pure moment plastic hinge (II) at the area of the opening

When the pure plastic moment hinge occurs, in reality there are also local moments, shear and axial forces which operate at the area of the opening. The calculation of this interaction would be very complicated and could be solved only in an iterative way. The shear force can be neglected because it has either no influence or is covered by one of other failure mechanisms at the opening ((I) or (III)). So the calculation of the global bearing capacity for plastic moments is done with the assumption that no secondary moments operate in the flanges. So for the calculation

in the flanges there are no stress resultants except the axial forces. The plastic axial forces are calculated in the following way:

$$N^{II}_{pl,Rd,o} = A_{a,o} \cdot f_{yd} + A_{c,eff} \cdot f_{cd} \quad \text{and} \quad N^{II}_{pl,Rd,u} = A_{a,u} \cdot f_{yd}$$

with: $A_{a,o;\ Aa,u}$ area of the upper respectively the lower steel cross section
$A_{c,eff}$ area of the concrete slab inside of the effective width

Both axial forces have to be balanced. Because of that the smaller value calculated above has to be used. In normal case this is the axial force in the lower partial cross section. The interior moment arm z_0 is known by the values of the partial cross sections. Then the global plastic moment capacity of the pure plastic moment hinge can be calculated for the area of the opening:

$$M^{II}_{pl,Rd} = N^{II}_{pl,Rd} \cdot z_0$$

3.3 COMBINED FAILURE AT THE AREA OF THE OPENING (III)

This criterion of local failure shows no plastic hinge, it is a kind of exclusion criterion for the calculation. If this failure is decisive, no kinematic mechanism is generated at ultimate limit state. The bearing capacity is limited by a shear crack in the concrete slab as it is shown by the experimental investigations [6]. For the plastic-plastic calculation the model which is shown in Figure 7 can be applied.

The shown pattern is based on the shear crack. This sudden failure of the concrete slab leads to the fact that in the upper partial beam no more shear force can be transferred. In fig. 7 this is shown by a symbol of a hinge for shear forces. In addition, the open crack in the concrete slab also avoids the transfer of axial force in the upper partial cross section. By that reason no global moment can occur at the area of the opening. Due to that it is supposed for the analytical model that the plastic axial force reaches the ultimate limit in both the upper and the lower rest of the steel beam. In Figure 7 this is marked with two hinges for axial forces in both remaining cross sections.

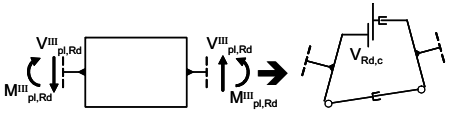


Figure 7 – Model of the combined failure (III) at the area of the opening

Because of the sudden failure of shear force transfer in the upper partial beam the whole shear force would have to be transferred by the lower partial beam. Therefore the global failure mode of the opening is completed by two local moment hinges in the lower partial cross section.

The model for the combined failure is fixed by the shear capacity of the concrete slab above the opening and the global moment capacity of the steel beam. The shear capacity of the concrete slab according to [5] is calculated as follows:

$$V_{Rd,c,o} = V_{Rd,1} + V_{Rd,ct,2}$$

The lower value of the following two equations is used for the shear capacity $V_{Rd,1}$ of the concrete slab in zone 1 (cf. chapter 6.6 in [5]):

$$V_{Rd,max,1} = \frac{b_{w1} \cdot h_{ef} \cdot 0{,}75 \cdot f_{cd}}{\cot\theta + \tan\theta} \quad \text{and} \quad V_{Rd,sy,1} = \frac{A_{sw1}}{e_L} \cdot f_{sd} \cdot h_{ef} \cdot \cot\theta$$

with: θ angle of traction strut (cf. [5] and [2])
b_{w1} width of the zone 1 (distance to the edge of the shear stud including stud heads in transverse direction)
h_{ef} effective height of shear studs (clearance between stud head and flange)
A_{sw1} cross section area of the shear stud
e_L distance between axles of the shear studs in longitudinal direction
$A_{c,eff}$ area of the concrete slab within the effective width

The shear capacity $V_{Rd,ct,2}$ of the concrete slab in zone 2 (cf. chapter 6.6 in [5]) is calculated as follows:

$$V_{Rd,ct,2} = \left[0{,}1 \cdot \kappa \cdot \left(100 \cdot \rho_l \cdot f_{ck}\right)^{1/3} - 0{,}12 \cdot \sigma_{cd}\right] \cdot b_{w2} \cdot d$$

with: κ scale factor (cf. [5] and [2])
ρ_l level of reinforcement in longitudinal direction (cf. [5])
b_{w2} width of the zone 2 (effective width of the concrete slab minus bw1)
d effective depth

For the calculation of the shear capacity it has to be considered that the required axial force cannot be calculated exactly. An iterative calculation would be necessary. So the axial stress is neglected, by equating σ_{cd} to zero.

For the calculation of the angle of the traction strut θ the shear force $V_{Ed,c,o}$ is required. However, this force is not known. But in case of full utilisation, this operating shear force has to be equal to the shear force resistance $V_{Rd,c,o}$. Therefore the calculation has to be done in an iterative way. At the end of the iteration is considered:

$$V_{Rd,c,o} = V_{Ed,c,o}$$

The pull out of the shear studs is calculated:

$$V_{Rd,c,e} = V_{Rd,1} + V_{Rd,ct,2,2}$$

$V_{Rd,1}$ minimal value of $V_{Rd,max,1}$ and $V_{Rd,sy,1}$ (see above)

$$V_{Rd,ct,2,2} = \frac{\nu_{Rd,ct,2,2} \cdot u_2}{1{,}4} \quad \text{with} \quad u_2 = \pi \cdot 1{,}5 \cdot (h_{ef} - (h_c - d)) \quad \text{and}$$

$$\nu_{Rd,ct,2,2} = \nu_{Rd,ct,2,1} = \left[0{,}14 \cdot \kappa \cdot \left(100 \cdot \rho_l \cdot f_{ck}\right)^{1/3}\right] \cdot d$$

The resistance against punching is calculated as follows:

$$V_{Rd,c,a} = V_{Rd,1} + V_{Rd,ct,2,1} \quad \text{with} \quad V_{Rd,ct,2,1} = \frac{\nu_{Rd,ct,2,1} \cdot u_1}{1{,}4} \quad \text{and} \quad u_1 = \pi \cdot 1{,}5 \cdot d + (b_{f,o} - b_{w1})$$

The minimal value of the calculated resistances is decisive:

$$V_{Rd,c,o} = \min \begin{cases} V_{Rd,c,o} \\ V_{Rd,c,e} \\ V_{Rd,c,a} \end{cases}$$

If the shear capacity of the concrete slab is known, the shear force which operates in the upper partial beam can be calculated by means of the stiffness $EI_{c,o}$ for the concrete slab and $EI_{a,o}$ for the remaining upper steel beam:

$$V_{Rd,o} = V_{Rd,c,o} \cdot \frac{EI_{c,o} + EI_{a,o}}{EI_{c,o}}$$

The global plastic shear capacity for the combined failure at the area of the opening is calculated by the stiffness of the upper and lower partial beam (EI_o, EI_u):

$$V_{pl,Rd}^{III} = V_{Rd,o} \cdot \frac{EI_o + EI_u}{EI_o}$$

For the calculation according to the plastic hinge theory the moment capacity of the steel beam at the area of the opening is required. This is done in a similar way than for the pure plastic moment hinge. However, shear forces are taken into consideration in the way that the complete remaining steel web sections and the concrete slab are only loaded by shear forces. Therefore, the plastic axial force has to be calculated with the area of the upper and the lower steel flange section ($A_{a,f,o}$, $A_{a,f,u}$) only:

$$N_{pl,Rd}^{III} = \min \begin{cases} N_{pl,Rd,o}^{III} = A_{a,f,o} \cdot f_{yd} \\ N_{pl,Rd,u}^{III} = A_{a,f,u} \cdot f_{yd} \end{cases}$$

Then the plastic moment capacity for the steel beam is calculated as follows:

$$M_{pl,Rd}^{III} = N_{pl,Rd}^{III} \cdot z_{0,a}$$

$z_{0,a}$ lever arm between upper and lower cross section of the remaining steel beam

4 APPLICATION OF THE PLASTIC HINGE THEORY

4.1 KINEMATIC MECHANISM OF PLASTIC HINGES

To identify the kinematic mechanism of hinges which is decisive, all possible plastic hinges and their position are required. For continuous composite beams with web openings the plastic hinges "plastic moment hinge in the span", " plastic moment hinge above the support", "pure plastic hinge for shear forces at the area of the opening (I)", "pure plastic moment hinge at the area of the opening (II)" and the "combined failure at the area of the opening (III)" are possible.

For the plastic hinges for sagging moments in the field and over the support the plastic moment bearing capacity has to be calculated in the standard sections (example is shown in [1]). The plastic bearing capacity of the possible plastic hinges at the area of the opening is calculated as shown in chapter 3.

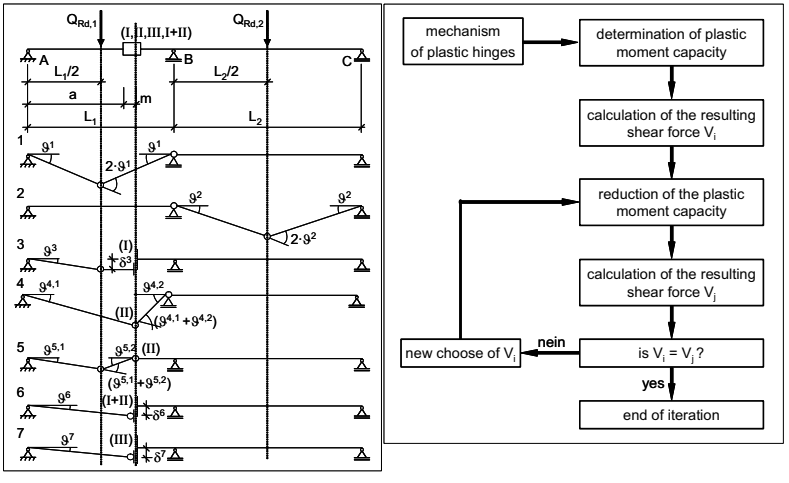


Figure 8 – Independent kinematic mechanism of a two-span beam with a web opening (left) and Iterative determination of the reduced plastic bearing capacity for bending moments (right)

When the plastic hinges are identified, the possible independent kinematic mechanisms have to be calculated. In Figure 8 (left) the possible basic mechanisms for a two-span beam with a concentrated load and one web opening are shown. The mechanism 7 in Figure 8 cannot be considered as a real mechanism of plastic hinges. This is a model which is based on the shear failure of the concrete slab. In chapter 3.3 this exclusion criterion is already explained. For continuous beams with more than two fields nearly the same independent mechanisms are generated. A system with three or more fields is also getting kinematic, if two plastic hinges are in one field. Mechanisms, where the plastic hinges are not in one field, are added. For such a case more than two hinges are necessary.

After the possible mechanisms are arranged, the reduction of the moment capacity caused by the operating shear force has to be calculated. However, the calculation of the stress resultants according to the plastic hinge theory depends on the value of the bearing capacity for bending moments. So for each mechanism the reduction has to be calculated in an iterative way. The schematic principle for the calculation is shown in Figure 8. No iterative calculation of the moment reduction is necessary for the mechanisms where the value of the shear force is defined by a plastic hinge for shear forces.

If the opening is located in an area influenced by a concentrated load where a plastic moment hinge is possible, the area for shear stress A_V – which is required for the calculation – has to be reduced. Therefore the position of the opening must be checked. The schematic area affected by a concentrated load with the considered opening and the necessary calculation is shown in Figure 9.

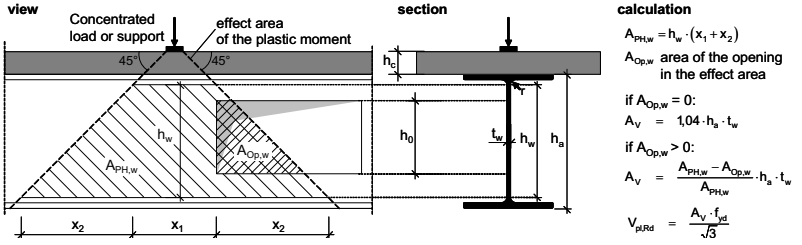


Figure 9 – Area of influence for a concentrated load taking the opening for calculating the plastic shear bearing capacity into account

The possible independent mechanisms of plastic hinges shown in Figure 8 are complemented with combinations of these mechanisms. Practically only the independent mechanisms which lead to a logical combination of mechanisms are combined. In most cases the smallest ultimate load is reached by one of the basic mechanisms. Only in special cases combinations of mechanisms lead to the lowest ultimate load for continuous beams. In Figure 10 every possible independent mechanism for the example which is shown in Figure 8 is indicated.

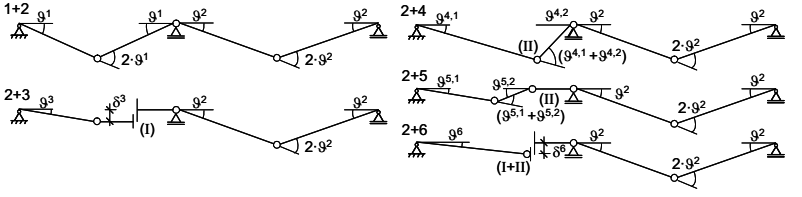


Figure 10 – Possible combinations of kinematic mechanism for a two-span beam with opening

4.2 CALCULATION OF THE ULTIMATE LIMIT STATE

The controlling mechanism of plastic hinges is calculated by means of the energy theorem. The internal work W_i and the external work W_a of the particular mechanism or combination is required. The external work is calculated by the external effects:

$$W^a = \sum Q_{Rd,j} \cdot \delta_j$$

with: $Q_{Rd,j}$ possible loads (external forces)
δ_j displacement of the corresponding force

The internal work is done at the hinges:

$$W^i = \sum (M_{pl,j} \cdot \vartheta_j) + \sum (V_{pl,j} \cdot \delta_j)$$

with: $M_{pl,j}$; $V_{pl,j}$ plastic marginal values of the plastic hinges
ϑ_j rotation of the corresponding moment hinge
δ_j shear sliding of the corresponding plastic hinge for shear forces

To calculate the ultimate load, the equilibrium must be satisfied:

$$W^a + W^i = 0$$

For example, the external and the internal work for the mechanism 3 is calculated as follows:

$$W^{a,3} = Q_{Rd,1} \cdot \delta^3 \quad \text{and} \quad W^{i,3} = -M_{pl,Rd,Feld1} \cdot \frac{\delta^3}{L_1/2} - V^{l}_{pl,Rd} \cdot \delta^3 = -\left(\frac{2 \cdot M_{pl,Rd,Feld1}}{L_1} + V^{l}_{pl,Rd} \right) \cdot \delta^3$$

By the equilibrium the ultimate load is calculated for the mechanism 3 in the following way:

$$W^{a,3} + W^{i,3} = 0 \quad \rightarrow \quad Q_{Rd,1} \cdot \delta^3 = \left(\frac{2 \cdot M_{pl,Rd,Feld1}}{L_1} + V^{l}_{pl,Rd} \right) \cdot \delta^3 \quad \rightarrow \quad Q_{Rd,1} = \frac{2 \cdot M_{pl,Rd,Feld1}}{L_1} + V^{l}_{pl,Rd}$$

According to this method the ultimate load can be calculated for all possible mechanisms. The smallest ultimate load is decisive. Then the operating loads which have to be calculated according to [3] can be verified:

$$Q_{Ed,j} \leq Q_{Rd,j}$$

If the controlling mechanism is known, the stress resultants of the system can be calculated. The stress resultant at a plastic hinge is given by the corresponding plastic limit value. With these values the distribution of the stress resultants can be calculated.

After global calculation of the beam, the detailed verifications for the composite beam as required by the code [4], can be accomplished. In addition, the steel beam has to be calculated at the opening edges (shown in [5]).

5 SUMMARY OF THE CALCULATION MODEL

The introduced calculation method for the appliance of the plastic hinge theory on continuous composite beams with big web openings is summarized as a flowchart in Figure 11.

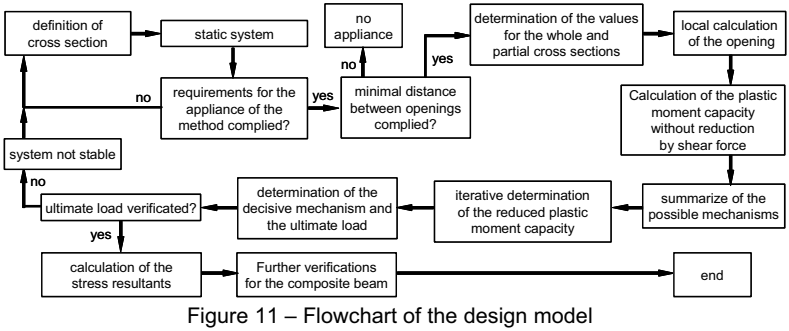


Figure 11 – Flowchart of the design model

The presented model was calibrated with the results of the experimental test shown in [6]. These test results correspond to the recalculation with the model but a statistical evaluation was not possible because of the small number of tests. So the calculation model must be calibrated by further experimental investigations for a verified use which is statistically significant.

6 REFERENCES

[1]
Bode, H.: Euro-Verbundbau, Konstruktion und Berechnung. 2. Auflage. Werner-Verlag 1998.

[2]
DIN 1045-1: Tragwerke aus Beton, Stahlbeton und Spannbeton. Teil 1: Bemessung und Konstruktion. Juli 2001

[3]
DIN 1055: Einwirkungen auf Tragwerke.

[4]
DIN 18800 Teil 1: Stahlbauten, Bemessung und Konstruktion. November 1990.
DIN V 18800 Teil 5: Verbundtragwerke aus Stahl und Beton, Bemessung und Konstruktion. Entwurf, November 2004.

[5]
Ramm, W., Kohlmeyer, C.: Schubtragverhalten des Stahlbetongurtes von Verbundträgern im Bereich von großen Stegöffnungen. Forschungsbericht zum DFG-Forschungsprojekt RA 353/7-1 und RA 353/7-2. Technische Universität Kaiserslautern, Oktober 2006.

[6]
Schnell, J.; Weil, T.: Anwendung der Fließgelenktheorie auf durchlaufende Verbundträger mit großen Stegöffnungen. Forschungsbericht zum DFG-Forschungsprojekt SCHN 771/1-1 und SCHN 771/1-2. Technische Universität Kaiserslautern, Juni 2007.

[7]
Weil, T.; Schnell, J.: Continuous Composite Beams with large Web Openings. Third International Conference on Steel and Composite Structures (ICSCS07). Manchester, Great Britain, 30. July until 1. August 2007.

[8]
Zhou, D.: Ein Rechenverfahren für Verbundträger mit Stegöffnungen. Stahlbau 72 (2003).

[9]
Zhou, D.: Besonderheiten von Durchlaufverbundträgern mit Stegöffnungen. Stahlbau 73 (2004).

[10]
Zhou, D.: Beitrag zum Tragverhalten und zur Entwicklung der Rechenmodelle von Verbundträgern mit Stegöffnungen. Dissertation. Universität Kaiserslautern. Kaiserslautern 1998.

EFFICIENT DESIGN FOR THE CALCULATION OF THE DEFLECTION AND THE SHEAR FORCE CAPACITY OF SLIM-FLOOR GIRDER

Prof. Dr.-Ing. Ulrike Kuhlmann
Institute of Structural Design, Universität Stuttgart
Stuttgart, Germany
sekretariat@ke.uni-stuttgart.de

Dipl.-Ing. Gunter Hauf
Institute of Structural Design, Universität Stuttgart
Stuttgart, Germany
Gunter.Hauf@ke.uni-stuttgart.de

ABSTRACT

Composite slim-floor girders form an attractive alternative to usual reinforced concrete beams. However, their effective design suffers from assumptions concerning the effective width of the concrete chord that are not reflecting the real deflection behaviour. This paper reports on the investigations already executed concerning the deformation of single span slim-floor girders as well as analytical and numerical evaluations of the effective width. Ongoing research work now deals with the effective width at the support area of multi span girders. Considering the restraint moment at support the calculated deflection that often limits the utilization of slim-floor girders may be reduced. First analytical conclusions are shown.

Aside of the bending restraint at support the limited shear capacity of the slim-floor girders may be decisive. Usually, the contribution of the concrete chord of a composite girder is not considered for the shear force capacity. Only the steel web is adopted to verify sufficient shear capacity. However, tests with slim-floor girders showed that the shear capacity of the concrete chord was up to 80% of the total shear force, underlining the importance of the concrete chord for the shear capacity.

INTRODUCTION

Slim-floor girders being integrated into wide spanned concrete slab systems form an attractive alternative to normal reinforced concrete beams and slabs. In comparison to common reinforced concrete slabs and beams they show significant advantages:

- high load resistance and flexural stiffness
- easy and quick erection
- better exploitation of the building height due to reduced overall construction depth

  resulting e. g. in extra floors.

STRUCTURAL BEHAVIOUR AND DEFLECTIONS BEHAVIOUR

Among others, there are three main reasons for the differences between the structural behaviour of slim-floor girders (Figure 1) on the one side and normal composite girders on the other [Kuhlmann and Fries 2001], [Fries 2001]:

- The concrete of slim-floor girders is already in cracked condition under service loads also in regions of sagging moments (Figure 2).
- For slim-floor girders the contribution of the concrete chord to the effective moment of inertia $I_{i,0}$ of the composite cross section is not negligible ($I_{c,0}$ ~ 30% - 60% $I_{i,0}$).
- The bending moment M_c of the concrete chord plays an important role for the resistance of slim-floor girders.

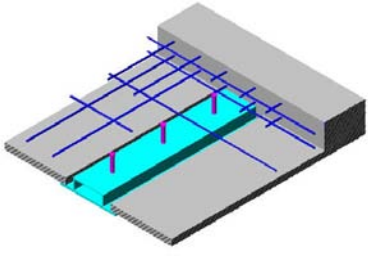


Figure 1: Slim-floor girder (hat-profile)

However, the common design rules for the effective width of composite girders have been derived for composite girders with a large height [Brendel 1960]. They are based on the assumptions that the concrete chord is in an uncracked pure membrane state and that the bending stiffness of the concrete is negligible. Thus, the effective width and the stiffness of slim-floor girders are underestimated [Kuhlmann and Rieg 2004a], [Kuhlmann and Hauf 2006].

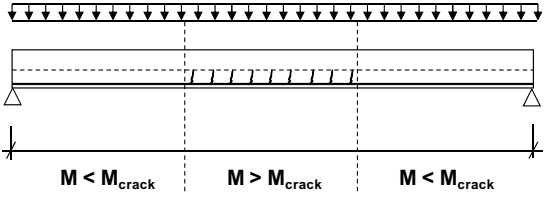


Figure 2: Single-span girder – concrete cracking of slim-floor girders due to sagging moment

As a consequence, for slim-floor girders the calculated deflections are usually overestimated resulting in an inefficient design where the verification of the serviceability limit state (SLS) decides on the sectional dimensions. Clarifications of the real deformation behaviour are therefore needed for an efficient design.

EFFECTIVE WIDTH OF COMPOSITE GIRDERS

Whereas the influence of the effective width on the ultimate bending moment is not very decisive, it is of high importance on the calculative stiffness of composite cross sections in the serviceability limit state. For slim-floor girders the check of the deflections in SLS in most cases leads to a larger cross section than necessary for the ultimate limit state (ULS). Therefore the effective width forms an essential parameter for calculation of the deformation and the efficiency of these girders. In addition, in order to give reasonable information for cambering and brittle partition walls, a realistic calculation of the deflections is of interest, but unknown due to the calculative stiffness based on incorrect assumptions.
Figure 3 shows that the effective width of composite girders according to different international codes varies in a wide range. All these codes have in common that they neglect the influence of the load level on the effective width. With exception of the German rules of Heft 240 [Grasser and Thielen 1991] the influence of the ratio d/d_0 of the slab thickness to the overall girder height on the effective width is ignored.

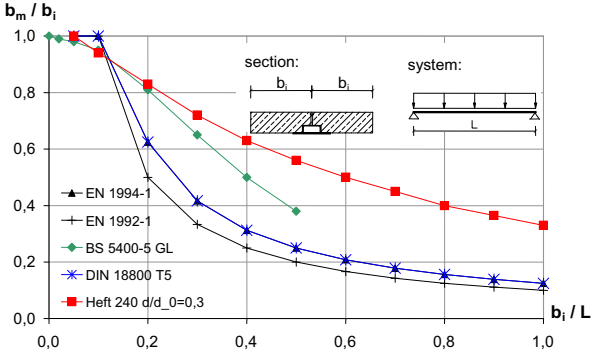


Figure 3 - Rules for the effective width b_m according to different codes

EXPERIMENTAL INVESTIGATIONS FOR EFFECTIVE WIDTH

The experimental investigations were part of the research project [Kuhlmann and Hauf 2006]. They have been performed in 2006 at the Otto-Graf-Institute, Research and Testing Establishment for Building and Construction (MPA) of the University of Stuttgart.

The aim of this test program of slim-floor girders was to verify the analytical models concerning the effective width, to study the deflection behaviour and the stiffness of these composite girder systems, see Figure 4 and Table 1. For more details see [Kuhlmann et al 2006] and [Kuhlmann and Hauf 2007].

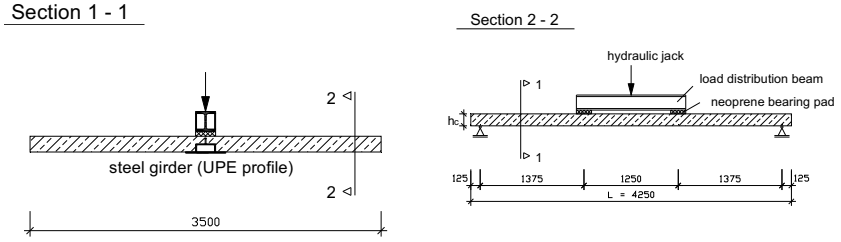


Figure 4 – Experimental tests with slim-floor girders

Table 1 shows the chosen parameters for the single-span girder tests. The girder thickness was varied, also the load position (centric/eccentric) and the degree of partial shear connection.

specimen	concrete grade	L [m]	B [m]	h_c [cm]	η* [-]	e*** [m]
VT 1 SF	C 20/25	4.25	3.50	22	1.0	0.0
VT 2 SF	C 20/25	4.25	3.50	**30**	1.0	0.0
VT 3 SF	C 20/25	4.25	3.50	22	1.0	**0.75**
VT 4 SF	C 20/25	4.25	3.50	22	1.0	**1.25**
VT 5 SF	C 20/25	4.25	3.50	22	**0.5**	0.0
VT 6 SF	C 20/25	**4.25** **	3.50	22	1.0	0.0

* degree of partial shear connection
** additional cantilever with 0.75 m span
*** eccentric load position in transverse direction (transverse bending)

Table 1 – Experimental test parameters

Figure 5 shows a comparison of measured deformation curve to the calculated deformation curve in midspan. The effective stiffness observed in the tests is by far larger (+43%) than proposed by the current codes and as concluded from elastic calculations but also less than considering the complete width of the girder.

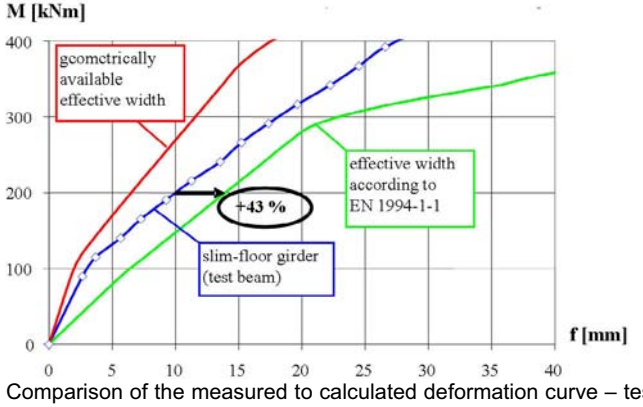


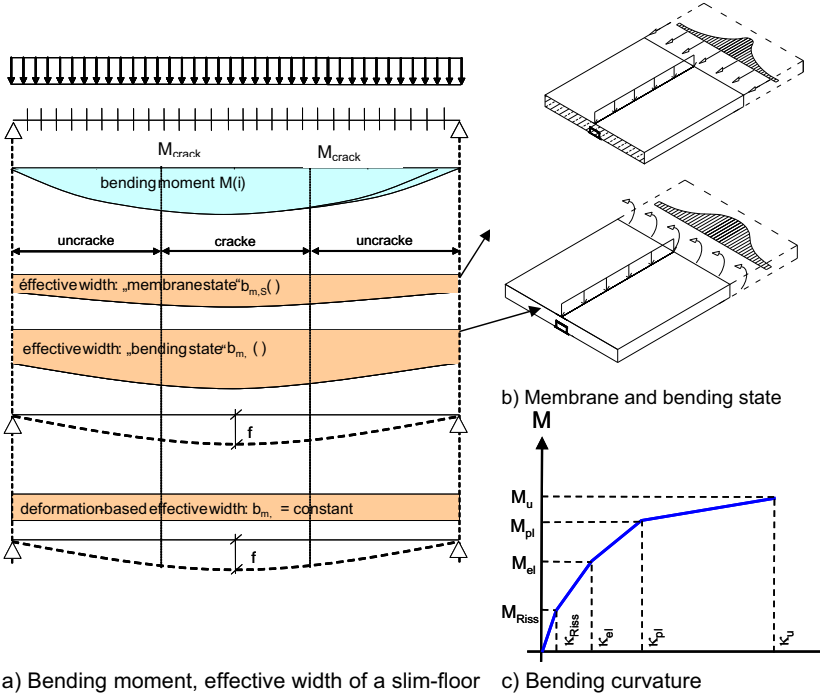
Figure 5 - Comparison of the measured to calculated deformation curve – test girder VT 1 SF

THEORETICAL INVESTIGATION OF DEFLECTIONS

In principle the structural behaviour of a concrete chord is composed of a pure membrane state and a pure bending state (Figure 6). In the membrane state the concrete chord acts as a shear panel resulting from the compression force N_c in the concrete and neglecting its bending stiffness I_c. In the bending state the concrete chord acts as a plate, as a consequence of the bending stiffness I_c resulting in a concrete moment M_c. For thin chords e. g. a steel flange the exclusive consideration of the pure membrane state is adequate. But for slim-floor girders the bending state should not be neglected [Rieg 2006].

Most of the rules for the effective width in current codes are based on the pure elastic membrane state of the concrete chord. For linear-elastic material behaviour the membrane and bending state of the concrete chord can be separated from each other according to the principle of superposition:

b_{mS} - refers to the compression force N_c of the concrete chord and therefore is valid for the cross sectional area A_c of the concrete.
b_{mB} - refers to the bending moment M_c and the bending stiffness I_c.



a) Bending moment, effective width of a slim-floor single span girder c) Bending curvature

Figure 6 – Calculation of deflection of a slim-floor single span girder

On the basis of these different effective width values the effective stiffness $I_{i,0}$ of the composite cross section may be determined [Rieg 2004], [Kuhlmann and Rieg 2004b]. As a result the calculative stiffness is considerably higher compared to the values of current codes.

The stiffness given in the following equation (1) is based on purely elastic behaviour. Normally as shown in Figure 6 the non-linear material behaviour has to be considered for bending moments $M > M_{crack}$.

(1)
$$I_{i,o} = I_a + I_{c,0} + S_{i,0} \cdot a_{St} = I_a + \frac{b_{mB} \cdot h_c^3}{12 \cdot n_0} + \frac{\frac{b_{mS} \cdot h_c}{n_0} \cdot A_a}{\frac{b_{mS} \cdot h_c}{n_0} + A_a} \cdot a_{St}^2$$

with $I_{i,0}$, I_a moment of inertia of the composite and steel cross section

$I_{c,0} = \frac{b_{mB} \cdot h_c^3}{12 \cdot n_0}$ reduced moment of inertia of the concrete cross section

$S_{i,0} = A_{c,0} \cdot z_{i,0}$

$A_{c,0} = b_{mS} \cdot h_c / n_0$ reduced cross sectional area of the concrete section

A_a cross sectional area of the steel cross section

$z_{i,0} = \frac{A_a}{A_a + A_{c,0}} \cdot a_{St}$

$n_0 = E_a / E_{cm}$ relation of Young's modulus of steel and concrete respectively

b_{mS}, b_{mB} effective width for the pure membrane and the pure bending state

h_c thickness of concrete slab

a_{St} distance between the centers of gravity of the concrete and steel section

In [Kuhlmann and Rieg 2004a] and [Kuhlmann and Hauf 2006] an analytical model has been developed which takes into account the cracking of the concrete by calculating for each of the single elements of the composite girder the actual M-κ relationship, see Figure 6c. Based on this the deformation of the girder in midspan is derived. This model has been verified against the test results.

NEW DEFINITION OF "DEFORMATION" BASED EFFECTIVE WIDTH

To allow a more easy calculation of the deformation in [Rieg 2006] and [Kuhlmann and Hauf 2006] a new definition of the effective width has been developed: an effective width referring to the deformation of a girder and not to the stress distribution. The "deformation-based" effective width is derived from a comparison between the real deformation (f_M) calculated by a sophisticated model as explained before and the midspan deflection of an equivalent composite (f_{EG}) beam with

constant section and plate width constant along the length of the beam, see Figure 7.

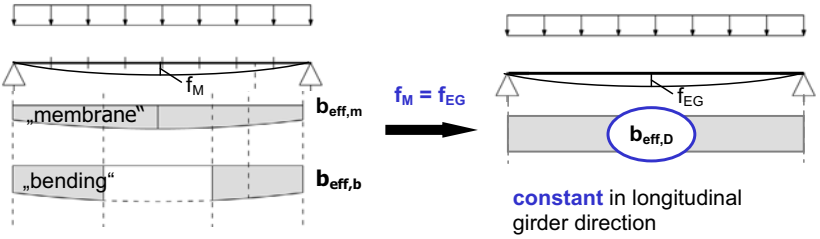


Figure 7 - Deformation-based effective – equivalent girder with a constant effective width $b_{eff,D}$

So whereas the usual stress-based effective width varies along the beam and differs according to the local M-κ relationship, the deformation-based effective width is one integral value for the whole beam. Extensive parameter studies in [Kuhlmann and Hauf 2006] with the sophisticated analytical model described above have led to a simplified relationship between the value of the deformation-based effective width value $b_{m,V}$ and the local load level.

(2) $$b_{eff,D} = b_{eff,m} + (b_{eff,D,0} - b_{eff,m}) \cdot \beta_{eff,D}$$

with
$b_{eff,D}$ deformation-based effective width
$b_{eff,m}$ effective width (membrane state)
$b_{eff,D,0}$ elastic value for deformation-based effective width
$\beta_{eff,D}$ reduction factor for deformation-based effective width, considering material and geometrical parameters:

(3) $$\beta_{eff,D} = 0{,}80 \cdot (1 - k_M)^{1{,}54} \cdot \left(\frac{f_{ct}}{f_{ct,0}}\right)^{0{,}28} \cdot \left(\frac{h_a}{h_c}\right)^{-0{,}15} \cdot \left(\frac{f_y}{f_{y,0}}\right)^{0{,}18} \cdot \left(\frac{A_{ges}}{h_a^2}\right)^{-0{,}57} \leq 1$$

As shown in Figure 8 the value of the deformation-based effective width decreases when the midspan moment M has passed the crack moment M_{crack}. When reaching the ultimate Moment M_u the deformation-based effective width is assumed of the order of the pure elastic membrane value of the stress based effective width. Due to plastification of the steel girder the tests show a rising value near $M = M_u$, which is neglected in (2) or (3). However, for SLS a reduced load level is relevant which clearly shows an advantage for the design.

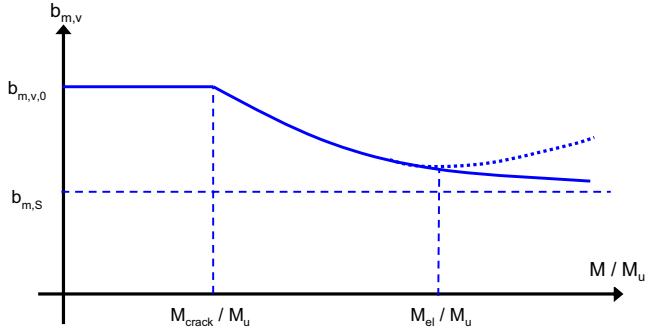


Figure 8 - Deformation-based effective width of a slim-floor girder (single span)

CONTINUOUS GIRDER – CALCULATION OF THE DEFLECTION

The calculation of a continuous girder is dominated by the effect of cracking of the concrete plate of the slim-floor girder in the sagging and hogging moment areas, see Figure 9.

Similar to single-span girder the concrete chord develops cracks on the bottom side in mid of the girder due to the sagging moments, but also at the mid support. The cracking of the concrete leads to a loss of the girder stiffness.
For static indeterminate systems, the bending moment gradient depends on the distribution of the stiffness of girder section (moment of inertia). And therefore the calculation of the deflection strongly depends on the cracking of the concrete and the reinforcement influencing the girder stiffness along the girder.
Thus the calculation of the deflection strongly depends on the cracking of the concrete and the reinforcement influencing the girder stiffness along the girder.

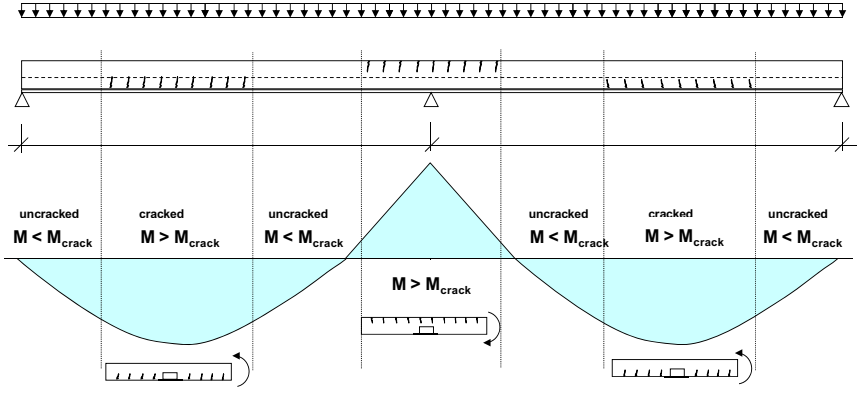


Figure 9 - Cracking of slim-floor girders due to sagging and hogging moments

In addition to the calculation of a single-span girder the bending-curvature has been calculated for each element of continuous 2-span girder for sagging and hogging moments (Figure 9). The results of the calculation of the deflection for a single and two-span girder are shown in the following Figure 10.

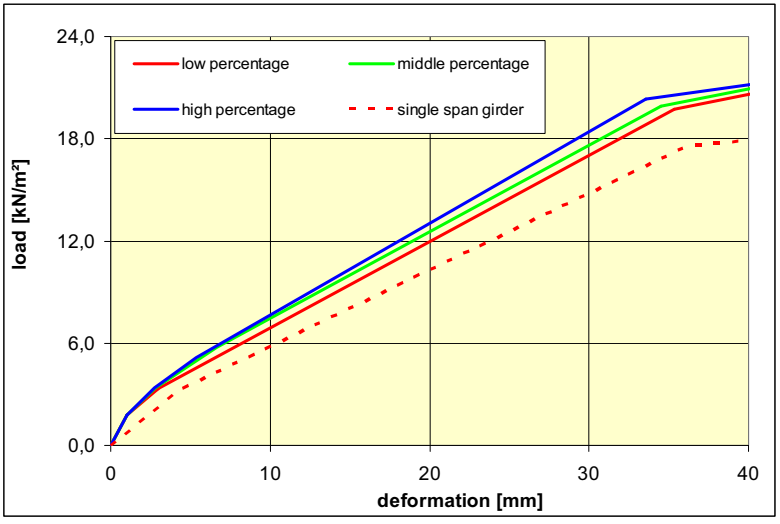


Figure 10 - Influence of support reinforcement to deformation (1- and 2- span girder), slim-floor girder: $L_{1,2}$ = 6.0 m, b = 3.0 m, h_c = 0.2 m, reinforcement between 5-15 cm²/m (upper layer)

The figure shows clearly that the deflection curves of the single span und 2-span girder have nearly the same gradient. For the 2-span girder the deflection gradient is slightly higher due to the constraint by the hogging moment. Hence, the deflection of course decreases. In this figure only the service limit state is shown.

SHEAR FORCE CAPACITY OF SLIM-FLOOR GIRDERS

Usually the contribution of the shear force capacity of the concrete chord of a composite girder is not considered. Only the steel web of the steel section is considered to verify sufficient shear capacity.
However, first tests [Fries 2001] with slim-floor girders with a hat profile (see Figure 1) showed that the shear capacity of the concrete chord was up to 80% of the total shear force. This indicates that the concrete chord might participate significantly to the shear capacity.

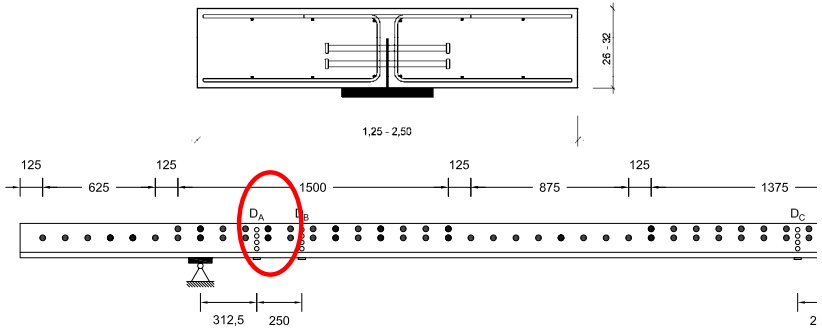


Figure 11 – Slim floor girder for shear capacity test

For the verification five additional slim-floor girders were experimentally tested [Kuhlmann et al 2007], see Figure 11. The aim of these tests was to get the realistic distribution of the shear force between the steel and concrete sections.
The results showed that the shear force lies between 60% and 80% of the total shear force of the girder, see Figure 13. With increasing test load (from about 20% to 60% of the ultimate load) the shear force in the concrete chord decreased due to the cracking of the concrete chord. From 60% up to the maximum bearing load the ratio of the concrete shear force increased due to the plastic behaviour of the steel web.

The failure of the all test girders occurred near the support and showed a typical shear cracking of the concrete, see Figure 12.



Figure 12 – Shear failure of slim-floor girder at the support

This might be critical, if the existing shear stress has in reality to be superposed with the shear stress of a single load at the concrete slab or with shear stress induced from transverse supporting direction. So, further investigations to quantify the shear capacity of the concrete chord are necessary. For that reason, the results from the five tested slim-floor girders form a good basis.

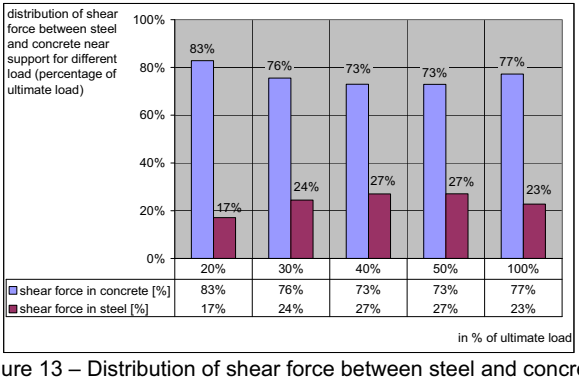


Figure 13 – Distribution of shear force between steel and concrete

In a subsequent research program the aim will be to determine the real shear force distribution for slim-floor girders and to define an own value of the effective width of the concrete chord for transverse shear. A new analytical approach will lead to a more efficient design of these structures by considering the shear force capacity of the concrete chord.

CONCLUSIONS

Slim-floor girders show a different structural behaviour than normal composite beams. Thus, the common composite design rules for the effective width are not applicable. In order to investigate the influences on the effective width and its value experimental, analytical and numerical investigations have been carried out. These investigations show that the effective width is considerably larger than given by current codes. A new definition of a deformation based effective width is introduced. For single-span girders a new and more realistic design approach for the effective width has been derived.

The tests on two-span girders (Figure 13) have just been finished. For the serviceability the constraint behaviour of the mid support appeared clearly, further detailed results will be shown after a precisely analysis of the tests [Kuhlmann, Hauf 2009a].

The calculation of the deflection for multi span girders is dominated by the cracking of the concrete chord in hogging and sagging bending moment areas, as the first analytical calculations and tests showed. Due to the restraint effect at support area the deflection for two span girders are quite lower than for single span girders at serviceability, as it can be seen in Figure 14 with two tested girders, one as a single span girder (L= 4.0m) and one as a two span girder (L= 2 x 4.0m) with the same concrete section, reinforcement and steel section.

Indeed, though the concrete chord nearly cracks over its total height, due to the reinforcement of the chord at the support the girders offer a certain bending restraint. As the effective width has a high influence on the calculative stiffness and deflection of composite girders, a realistic design value for the effective width will lead to more economical dimensions.

All girders showed the same failure behaviour. The girders failed due to punching at the mid support area.

For the shear force capacity slim-floor girders also show a different behaviour than normal composite beams. First experimental tests showed that the shear force in the concrete is much larger than in steel. Within a research program investigations about the shear force capacity came up with ratios of 80% of the total shear [Kuhlmann et al 2007], [Kuhlmann, Hauf 2009b].



Figure 14 – Test specimen of a two-span slim-floor girder

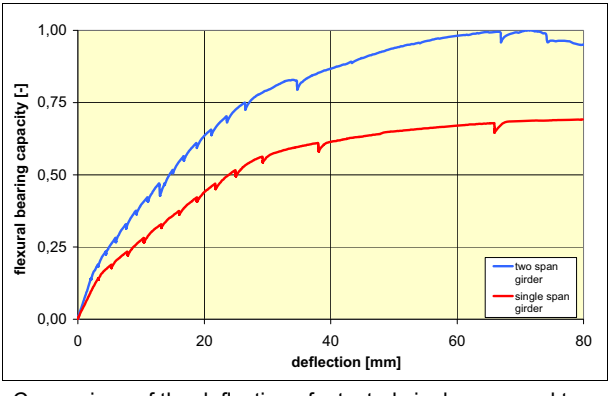


Figure 15 – Comparison of the deflection of a tested single span and two-span girder

OUTLOOK

The first studies and analytical calculations for two-span girders will be continued. With the help of experimental studies the effective width of a continuous girder, especially at the support area, should be investigated as well as the main influence parameters for the degree of constraint and the deflection of the slim-floor girder.
The final aim is a simplified approach for the effective with of multi-span girders and the deflection calculation leading to a more efficient calculation and use of slim-floor girders. As for the support area the interaction of bending moment and shear is decisive, also the investigation concerning the shear resistance will be continued aiming a realistic approach for the design of slim-floor girder systems.
As it is shown in the beginning the service limit state often is decisive for the use of slim-floor girders, with the planned new approach the design of slim-floor girders will be more efficient.

REFERENCES

[Brendel 1960] Brendel, G., Die mitwirkende Plattenbreite nach Theorie und Versuch, Beton- und Stahlbetonbau 55 (1960), pp. 177-185, Germany.

[DIBt 2005] DIBt (Deutsches Institut für Bautechnik), Slim-Floor Träger mit UPE-Profilen, Allgemeine bauaufsichtliche Zulassung Nr.Z-26.2-48 (Approval), Berlin, Germany, 2005.

[DIN 1045-1] DIN 1045-1: Tragwerke aus Beton, Stahlbeton und Spannbeton, Teil 1: Bemessung und Konstruktion (inkl. Berichtigung 2 – June 2005). Berlin: Beuth Verlag, July 2001.

[DIN 18800-5] DIN 18800-5: Stahlbauten – Teil 5: Verbundtragwerke aus Stahl und Beton – Bemessung und Konstruktion, Berlin: Beuth Verlag, March 2007.

[Fries 2001] Fries, J., Tragverhalten von Flachdecken mit Hutprofil, Dissertation, Number 2001-1, Institute of Structural Design, Universität Stuttgart, Germany, 2001.

[Grasser and Thielen 1991] Grasser, E., Thielen, G., “Hilfsmittel zur Berechnung der Schnittgrößen und Formänderungen von Stahlbetontragwerken, Deutscher Ausschuss für Stahlbeton, Heft 240, 3. Auflage, Beuth Verlag, Berlin, 1991.

[Kuhlmann and Fries 2001] Kuhlmann, U., Fries, J., Optimierung der Bemessung von deckengleichen Verbundträgern in Hutform, AiF research project, Number 12017, Studiengesellschaft Stahlanwendung, Düsseldorf, Germany, 2001.

[Kuhlmann and Hauf 2006] Kuhlmann, U., Hauf, G., Rieg, A., Effiziente Dimensionierung niedriger Verbundträger, SIF-Forschungsvorhaben Nr. S 668, Final report, Stiftung Industrieforschung, Köln, Germany, October 2006.

[Kuhlmann and Hauf 2007] Kuhlmann, U., Hauf, G.: Innovative slab systems with slim-floor girders, In: Eligehausen et al.: Proceedings, 2nd Symposium on Connections between Steel and Concrete, Stuttgart, ibidem-Verlag, p. 1245-1254, 2007.

[Kuhlmann and Hauf Kuhlmann, U., Hauf, G.: Effiziente Verbundflachdeckenträgersysteme im Hochbau – Ganzheitliche

2009a] Optimierung für Montage und Nutzung, research project FOSTA/AiF no. 15675N/1, Stuttgart, Germany, in preparation.

[Kuhlmann and Hauf 2009b] Kuhlmann, U., Hauf, G.: Querkrafttragfähigkeit von Slim-Floor Trägern, research project DASt/AiF no. 15639N, Stuttgart, Germany, in preparation.

[Kuhlmann and Rieg 2004a] Kuhlmann, U., Rieg, A., Mittragende Betongurtbreite niedriger Verbundträger, AiF research project No. 13460 N/1, DASt report 3/2005, Deutscher Ausschuss für Stahlbau DASt, Düsseldorf Germany, 2004.

[Kuhlmann and Rieg 2004b] Kuhlmann, U.; Rieg, A.: Deflection Behaviour of Composite Girders with Reduced Height. Composite Construction V, Krueger National Park, South Africa, July 18-23, 2004.

[Kuhlmann et al 2006] Kuhlmann, U.; Rieg, A.; Hauf, G.: Effective Width Of Composite Girders With Reduced Height, A forecast of the future for steel and composite steel-concrete structures - Professor Jean-Marie Aribert, Retirement Symposium, Editors HJIAJ & UY, 3-5 July 2006, Institut National des Sciences Appliquées (Rennes), ISBN 978-2-912095-01-5, France, July 2006.

[Kuhlmann et al 2007] Kuhlmann, U.; Hauf, G., Konrad, M.; Raichle, J., Schubtragfähigkeit von Verbundflachdecken, DIBt Forschungsvorhaben ZP 52-5-17.12-1109/04, Berlin, 2007.

[Rieg 2004] Rieg, A., Effective Width of Composite Girders with Reduced Height, in: Walraven, J., Blaauwendraad, J, Scarpas, T., Snijder, B. (Eds.), Proceedings of the 5th International PhD Symposium in Civil Engineering, 16-19 June 2004, Delft, The Netherlands, 2004.

[Rieg 2006] Rieg, A., Verformungsbezogene mittragende Breite niedriger Verbundträger, Dissertation, Mitteilung No. 2006-2, Institute of Structural Design, Universität Stuttgart, Germany, November 2006.

ACKNOWLEDGEMENTS

The authors gratefully acknowledge the financial support of the research project by *Stiftung Industrieforschung*, research project number no. S 668, as well as Fa. Salzgitter AG and Haller Stahlbau GmbH for sponsoring the steel girders. We also gratefully acknowledge the financial support of the SIF research project by Leonhardt, Andrä und Partner GmbH, Ingenieurbüro Kuhlmann-Gerold-Kraus-Eisele, Spannverbund GmbH, Harrer Ingenieure GmbH, Haller Industriebau GmbH, Ingenieurgruppe Bauen, Stahl + Verbundbau GmbH, Fa. Köster & Co. GmbH, Germany. We also want to thank the Materialprüfanstalt (MPA) Stuttgart of the Universität Stuttgart for the execution of our test programs.

The project about the shear capacity of slim-floor girders was financed by the *DIBt, Deutsches Institut für Bautechnik*, Berlin, research project number ZP 52-5-17.12-1109/04, the authors thank for that support.

The two current projects on the effective width (AiF no. 15675) and the shear force capacity (AiF no. 15639) are financed by the *Industriellen Gemeinschaftsförderung (IGF)* of the *Bundesministerium für Wirtschaft und Technologie*.

The multi-storey car park for the “Neue Landesmesse” in Stuttgart over the highway A8, Germany

Dipl.-Ing. Roland Friede
Technische Universität Darmstadt,
Darmstadt, Germany
Friede@stahlbau.tu-darmstadt.de

Prof. Dr.-Ing. Jörg Lange
Technische Universität Darmstadt,
Darmstadt, Germany
lange@stahlbau.tu-darmstadt.de

Dr.-Ing. Ralf Steinmann
Donges Stahlbau International Engineering & Construction GmbH
Darmstadt, Germany
Ralf.Steinmann@donges.de

ABSTRACT

From 2000 till 2007 a complete new fairground was developed nearby the Stuttgart-Airport. Within this project arose 7 exhibition halls with 75.000 m², one high hall with 25.000 m², one convention centre and a multi-storey car park with 4.000 lots. Additional planning of the traffic flow was necessary. At that time it was the biggest construction site in Germany with an investment volume of 800 million Euros. More than 65.000 to of steel structure were erected. 13.500 to for the multi-storey car park across the highway A8. The car park is an eye-catching landmark for the new fairground in Stuttgart. This paper concentrates on the planning and the erection of the multi-storey car park.

PART I: THE DESIGN

INTRODUCTION

In springtime of the year 2000 the planning process for the new trade fair center in Stuttgart nearby the airport started. In an architectural competition the sketch of the architecture office “Wulf und Partner” won the first price. Part of the sketch was the crossover of the busy highway A8 and the new railroad trek for the ICE (Germanys high speed train) with a multi-storey car park with 4.000 parking lots (figure 1). The office “Leonhardt, Andrä und Partner” was responsible for the structural planning of the car park and the planning of the so called outer traffic site development.



Fig. 1- Car park as a landscape bridge

Despite the architectural-, structural- and traffic planning, one of the challenges was the extraordinary situation for the authority approvals with the crossover of the car park over public traffic routes. The concept of the traffic development for the new fairground had to include the main transport systems: the highway A8, the through road B27 and the new railroad track for the ICE. The keynote of the development was that the driveway to and from the car park would not intersect the highway. The solution: The car park itself became a part of the development (figure 2).

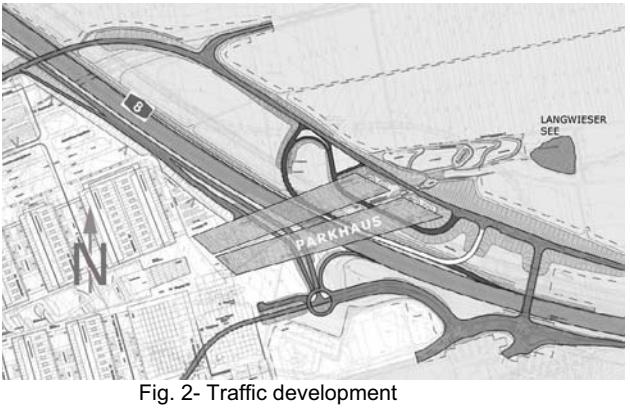


Fig. 2- Traffic development

ARCHITECTONICAL CONCEPT

The easy access to the car park from the highway and the through road is one reason for the success of this sketch. The architectonical concept included two aspects: (1) The car park builds one line with the main route of the fair trade, though it had to cross the highway. (2) On the other hand the car park links as a natural bridge the fairground with the natural surrounding of the Filderraum. Due to that the car park has got a rolling shaped top with natural plantings (figure 1).

The building itself can be divided into two parts. In the floor plan those two parts look like two V-shaped fingers. Due to that they were called the “fingers” (figure 3). The fingers contain the parking decks and are linked with a deck, called the intermediate zone (figure 4). The intermediate zone is the main entrance for the visitors to the fairground.

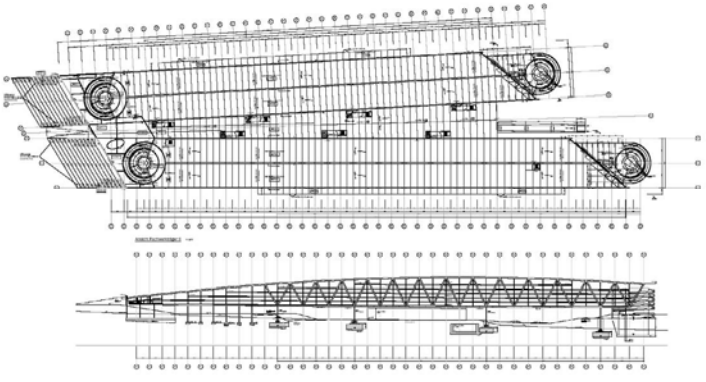


Fig. 3- Parking garage levels and newel ramp

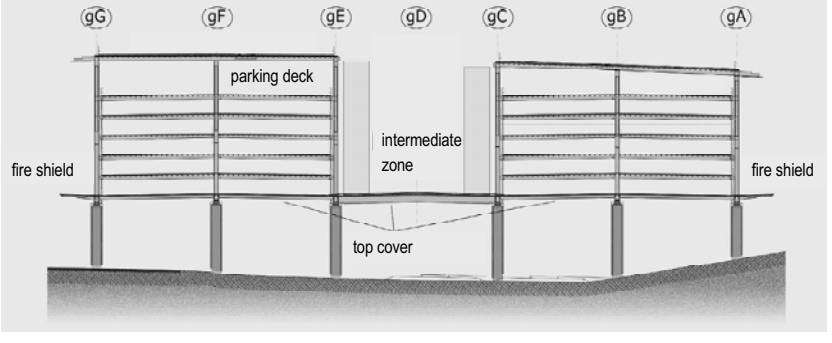


Fig. 4: Cross section

FIRE PROTECTION

On the first view the car park over the highway A8 and the railroad track is an open grand-garage. In this case the German regulations only require inflammable materials.

But because of the bridge-like placement over public transport and a railroad track it was necessary to make sure that during a fire under the bridge, e.g. caused by an accident, the construction would not collapse. Due to that the lowest level of the two fingers, the intermediate zone and a 5 m fire shield at the sides formed a so called highway top cover. This top cover had a fire resistance of 90 minutes and shields the car park against the heat. The columns below the top cover were built with a fire resistance of 120 minutes. All parts above had a resistance period of 30 minutes.

STEEL AND COMPOSITE STRUCTURE

Due to the wide span over the traffic it is necessary to improve the basic structure of a common multi-storey car park. The result is the effective integration of the main structure in the construction of the car park.

Framework

The main structures of the car park fingers are three parallel frameworks. Each of those frameworks is a continuous beam with three parts and a total span of about 250 meters. The three frameworks have got a distance of 17,30 m in between and a maximum height of more than 20 m. The frameworks passing over the highway and the railroad track are dominating the appearance.

Because of the acute angel between the highway and the building, the frameworks are shifted in the ground plan. The structure between the frameworks is always rectangular. The flanges of the framework are box girders with a cross section of 800 x 600 mm.

The forces of the parking decks are implemented always in the nodes of the framework. That is possible with vertical bars, differing tensile bars and pressure props. Those bars are part of the portal frames running in cross direction.

Portal frame

In the cross section the vertical bars of the framework are jointed bending stiff with the floor joists. Together they build a multi-storey double portal frame. The joints of the vertical bars and the framework are shown in figure 5. Those portal frames are parts of a common multi-storey car park. But with the bending stiff joints and the combination of a framework they build a unit similar to a chassis of a car.

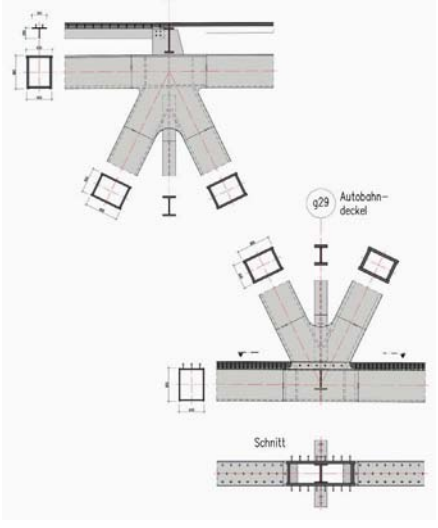


Fig. 5- Main truss nodal point

Parking decks, top floor and highway top cover

The parking deck is a regular system out of 17,30 m long composite beams with a pattern of 5,00 m. The composite beams are part of a thin concrete slab. The intermediate zone is built in a similar way. The span expands to a maximum of 25 m. Together with the intermediate zone the lowest floor build the so called highway top cover. Despite the highway top cover the decks consist of “Hoesch-Additiv-Decken” (figure 6), slim composite slabs. The top cover is built by precast concrete elements with in-situ concrete.

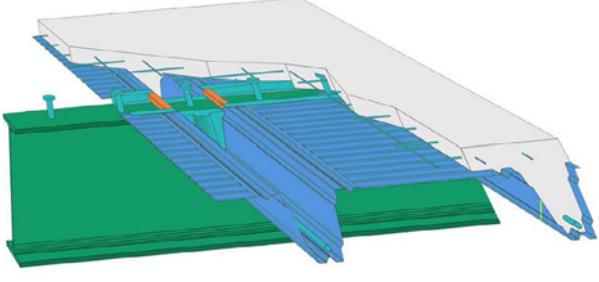


Fig. 6 - Slim composite slabs: „Hoesch-Additiv-Decken“

Main columns

The framework structure founds onto columns. The length of those main columns varies between 11,00 and 17,00 m. The cross section of the columns is 1.500 x 600 mm. Lengthwise the columns are very slender to reduce the forces resulting from deformation. To amplify that effect the columns are placed into inspection chambers to elongate the effective length. Those chambers are up to 10 m deep. The bearing on top of the columns is over articulated bearings. Because of the heavy loads it was not possible to use common elastomer or calotte bearings.

Bracing

The fixed-point of the building is the thrust bearing on the side of the trade fair. On the other side the bearing is lengthwise movable. In cross direction it is held by a rod. The rod links the parking decks with the spindle. Due to that the bearing situation of the building is similar to a bearing of a bridge. The aim is to reduce the forces resulting out of displacement. The main part of the horizontal bracing is the highway top cover.

PART II ERECTION OF THE MULTI-STOREY CAR PARK

INTRODUCTION

The very short time for the structural work from March 2005 to August 2006 and the requirement to minimize the influence on the traffic on the highway A8 were the biggest challenges for the erection. Part of a first concept was the usage of a safety scaffold above the highway. During the bidding phase several different ideas to optimize the erection process were discussed. The launching concept developed from the “Donges Stahlbau GmbH” turned out to be the most workable and the cheapest possibility. Due to that the steel building company Donges took over the responsibility for the structural planning and the whole steel and composite construction. The incremental launching method is well-known as an erection method for bridges but rarely used for frameworks of car parks over busy highways.

THE CONCEPT

The two fingers of the car park were erected separately and finally linked with the composite beams of the intermediate zone. Each finger was divided in six parts (figure 7). Three parts were launched over the highway beneath running traffic. Each of these parts consisted of three main framework trusses, the complete highway top cover and the portal frame bars necessary for the bracing. The highway top cover took the part of a safety scaffold for the highway. Due to that it was possible to continue the erection over the running traffic later on without extra scaffolding. To reduce the structural weight during the launching only the necessary parts were assembled. The length and weights during the launching are listed in table 1.

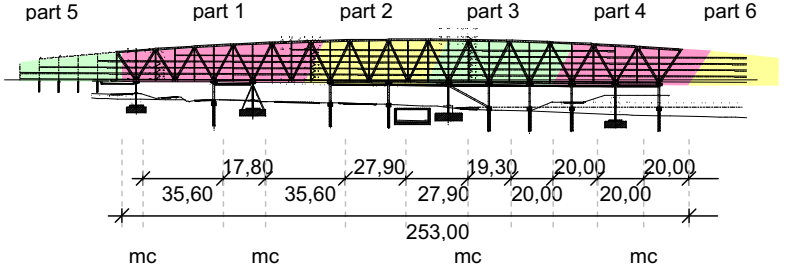


Fig. 7 - Partition of the main truss (axis G), position of the main columns (mc)

For the erection and launching process additionally columns where placed in each of the six axis (three for each finger of the car park). Seven extra columns supported the four main columns. Therefore the maximum span was reduced to 35,60 m. Due to that it was possible to launch the structure right over the lower flange of the framework. Additional launching tracks were not needed.

Launching	Launching distance [m]	Steel weight [to]	Total launching weight [to]
Part 1 southern	75,1	1.837	1.837
Part 1 northern	77,8	1.747	1.747
Part 2 southern	58,0	2.545	3.840
Part 2 northern	54,9	2.428	3.712
Part 3 southern	39,0	3.932	5.524
Part 3 northern	36,4	3.765	5.369

Table 1: Distance and weights during the launching process

The parts four to six could be erected in the final position. For the erection of highway top cover of the intermediate zone including the beams and the semi-finished slabs the highway A8 had to be closed for three night-time operations only.

ERECTION

Due to a very short time-schedule and confined space each step had to be planned precisely: Columns had to be removed and replaced to outlay the framework on site. The position of some mobile cranes where appointed with a tolerance of a centimeter to account interfering edges. The progress can be divided into 3 parts:

(1) Launching process: The parts 1 to 4 contain the main framework. The framework is laid out on the Plieninger side. They were welded together, straightened up with cranes and placed on top of the columns in 11m height. For the bracing additional trusses were needed. The highway top cover was paved. Parts 1 to 3 were launched over the highway. The two fingers were erected separately with a time gap of two weeks. The parts 5 and 6 could be erected with single components in the final position (picture 7).

(2) Completion of the structural work: After the launching the columns were unloaded and the launching compensators were replaced by the final articulate bearings. The sheets of the additive slabs were arranged and filled with concrete. The stairways were erected. Due to the top cover the affection of the traffic could be minimized.

(3) Cladding, guardrails and finishes: After completion of the structural work the finishes work started.

PLANNING OF THE ERECTION OF THE STEEL CONSTRUCTION

Bracing during the erection

The three main-frameworks of each finger build lengthwise, together with the portal frames in cross direction, one fully braced unit. The launching system placed under each framework made sure that the movement went on synchronously. Due to that the interference between the three axes was minimized. The horizontal together with the vertical loads are led from the lower flange over the heads of the columns into the substructure.

On each head of the columns two launching compensators were installed directly under the webs of the box girders of the lower flange. The horizontal loads in cross direction were taken over by a horizontal track (picture 8).

In the final state the top cover as a slab is a major part of the bracing system. During the erection it was not possible to use that slab. Due to that the columns had to be braced separately in both horizontal directions. In cross direction the columns of the middle axis were clamped in the foundation. The columns were built as a truss with a base of two meters. The main columns are clamped in cross section anyway. The columns of the outer axis are built as a box girder and are simply supported, carrying only vertical loads. The horizontal tracks on the head are necessary to embrace the column over the main construction together with the columns in the middle axis. In picture 9 ones see the static system of the bracing in cross direction.

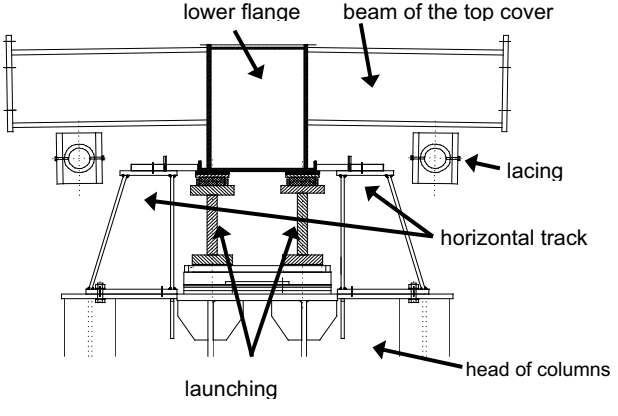


Fig. 8: Launching compensator with horizontal track

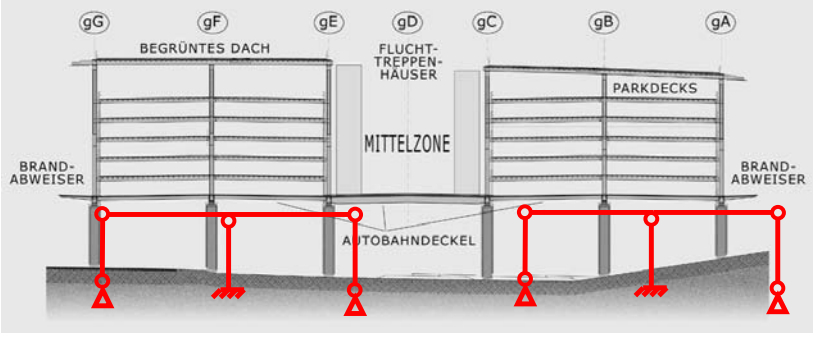


Fig. 9: Bracing system in cross direction

Lengthwise, which is the direction of the launching, all columns where connected at the head or held with separate bracings. In this direction the main forces result out of the launching process. The substructure can be divided in three parts (picture 10). Part one was linked with a compression strut to the parking spindle. In part two the main column was braced with two trusses. The other columns were linked with compression struts. In part three all heads were linked with horizontal trusses. With these trusses the horizontal forces due to the launching were shortened. The bracing was realized with a diagonal truss.

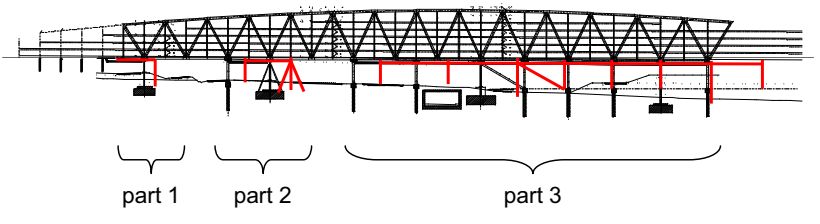


Fig. 10: System for longitudinal bracing of the columns

On head of main columns the launching jacks were installed. The lacings were stretched to each back of the last part. The decline of the launching was with 0.5 % positive. Due to that there was no need to hold the superstructure but with the laces. In between the launching process, the superstructure was fixed with an additional joint bar.

Modeling of the launching process

The frameworks are planned with a lengthwise offset of two framework units. The length of the units vary from 8.90 m, 9.30 m and 10 m. Due to the geometrical situation the nodes of the framework do not obligatory run over a column at the same moment. Due to that the launching process was simulated in steps of 75 cm. Together with the launching distance from over 170 meter for each finger, 450 models had to be generated and analyzed.

Part of the analyzing was the diagram of the bearing force. Picture 11 shows the development of the bearing force of one column over the launching distance. After 40 m the superstructure hits the launching compensator. The force rises continuously to the maximum and goes down. Within constant distances high and small intermediate peaks alternate.

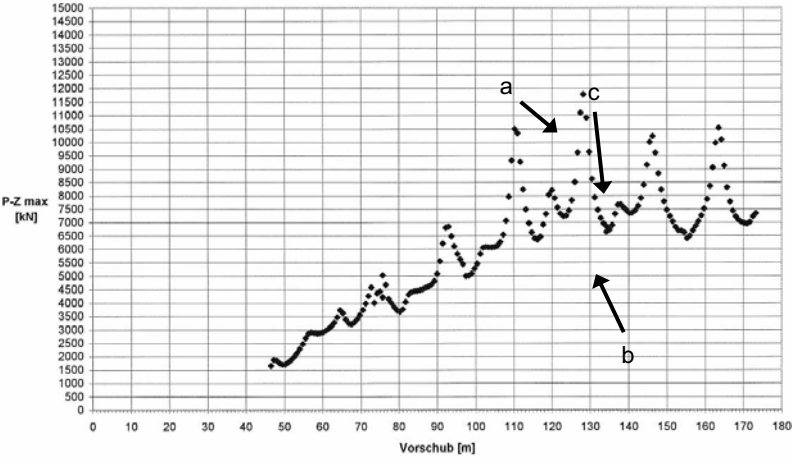


Figure 11: Vertical reaction load at a column vs. the way of launching

The alternating bearing force results of the different stiffness of the framework. The peaks represent the stiff nodes of the framework running over the launching compensators (figure 12 a). The intermediate peaks show the situation when the less stiff portal frame stud runs over the column (figure 12 c). In between the peaks the more flexible lower flange runs over the column (figure 12 b). Figure 12 shows the three situations together with the deformation of the framework. The geometrical complexity and the immense differences of the bearing forces made the immense effort for the modeling necessary.

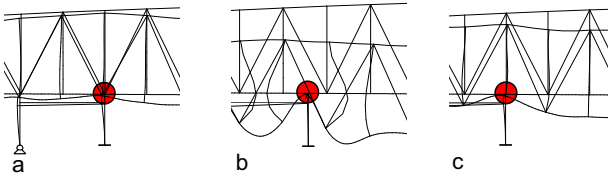


Fig. 12: Deformation of the truss in specific constellations

Another situation shows the impact of the immense stiffness of the framework (length / height < 2 during the erection). During the modeling the load case “10 mm settlement of the columns” was analyzed. In some launching situations the small settlements of only 10 mm made the stiff framework lift of a column. This shows the possibility of heavy load relocation during the launching process. To minimize these relocations the required tolerances during the fabrication and on the site had to be very high.

For the lower flange of the framework the launching process was the most critical situation. Because of the bending and the local buckling under the pressure of the launching compensators the box girders had to be enforced.

ERECTION

Assembly of the steel structure

The assembly of the parts 1-4 (main framework) of both fingers was the same procedure. As an example the assembly of part one of the southern fingers is described with great detail.



Fig. 13: Erection of the truss

During fabrication the entire framework was already assembled, measured and temporary linked true to size. On the site the framework was welded after a detailed welding plan. The possible shrinking of the weld seams was included into the concept. The raising of the framework with a maximum weight of 340 to and 80 m long parts was conducted with four cranes. Two heavy cranes for 800 to, a 60 m telescope pylon and 160 to of ballast were used. The heavy cranes were placed in the middle and lifted by displacement. The two outer cranes with a maximum weight of 200 supported, running by force. For the last 10 degrees of the lifting winches were used to protect the framework against knock over. Picture 13 shows the framework with the four cranes. The weights of the different parts are shown in table 2. After the raising the framework was braced with trusses.

	Framework in axis E		Framework in axis F		Framework in axis G	
	length [m]	weight [to]	length [m]	weight [to]	length [m]	weight [to]
Part 1	80,10	300	80,10	364	80,10	288
Part 2	55,00	220	54,20	265	53,40	197
Part 3	57,90	283	56,50	310	55,80	213
Part 4	60,00	162	60,00	207	59,30	179

Table 2: Weights and measures of the parts of the south finger

Launching

Every two weeks a launching took place with a change of the northern and southern finger. Without a closing of the highway the fingers were launched over the columns in 11 m height. With an average speed of 6 m per hour the four 140 to jacks pulled each finger with 14 lacings each. Each lacing had a diameter of 140 mm^2. For the heavier axis in the middle two jacks were installed on the outer side is only one jack.

The lower flange, a box girder, runs over the launching compensators (figure 14). Together with sheets of elastomer the compensators on articulated bearings made it possible to induce the force constantly. For the demounting of the launching compensators or to adjust the framework during the launching positions for jacks were planned.

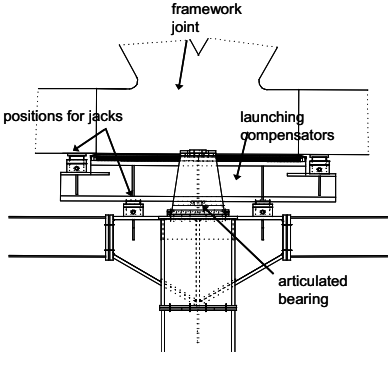


Fig. 14 - Launching system

Each supporting point was staffed with one person for each launching compensator. During the third launching 24 points had to be staffed. Due to that more than 70 persons were necessary. Because of the highway the three sites (Plieninger side, side of the fair trade and median strip) were separated. For each site material, jacks, aggregates, tools and persons had to be foreseen. The coordination was running with the help of radio units.

PART III ABSTRACT AND PERSPECTIVE

The coordination and planning for the car park and the main constructions for the traffic development were concentrated in one contractor. Due to that the development of an integrated concept was possible. The integration of the car park in the traffic development concept is an innovating solution. The planning was delivered to two engineering bureaus with an expert-knowledge for many years: “Bung Ingenieure” and “Leonhardt, Andrä und Partner”.

The key to success was detailed planning among an integrated team. The construction was done by a consortium of the companies “Donges Stahlbau GmbH”, “Wayss und Freytag” and “Baresel”. The concept for the erection together with the revision was done by Donges. Because of the experience for many years in the field of bridges and wide span buildings is was possible to invent an excellent solution for the difficult site conditions. Only an integrated concept made a competitive solution for the erection possible.

Since 2007 the car park is open to public (figure 15).



Figure 15: Picture of the car park in 2007

In September 2007 Donges Stahlbau GmbH received the European award for steel structures 2007 for the ‚multi-storey car park of the new trade fair centre Stuttgart' by the European Convention for Constructional Steelwork ECCS.

References

[1] V. Angelmaier, R. Friede, R. Steinmann "Das Parkhaus für die Neue Landesmesse in Stuttgart über der Autobahn A8", Bauingenieur (81) 2006

DESIGN AND TESTING OF TWO COMPOSITE UNDERSPANNED BEAMS

Michel CRISINEL
Steel Structures Lab ICOM, Swiss Federal Institute of Technology EPFL
CH-1015 Lausanne, Switzerland
michel.crisinel@epfl.ch

Gabriele GUSCETTI
Guscetti & Tournier SA Ingénierie civile
CH-1227 Carouge, Switzerland
guscetti@gti.ch

ABSTRACT

This paper presents the results of the laboratory testing conducted at serviceability and ultimate limit-states on two full size composite underspanned beams and comparisons with the previous *in situ* measurements, as well as with finite element calculations. The comparisons have shown very good correlations in terms of static behavior under point loads (simulation of an heavy forklift truck), of the composite behavior (embedment of the steel beam in the concrete slim-floor, introduction of the tensile force of the tie bar in the top chord, relative slippage between steel and concrete) and of the dynamic behavior (natural frequencies, damping rates). These results confirm the very good structural behavior of the floor under service loads as well as the capability of the underspanned system to withstand asymmetrical loads

INTRODUCTION

In the framework of the construction of a new multi-story industrial factory, a innovative structural system, which makes significant use of prefabrication methods both in concrete and steel, was developed [Crisinel et al 2006]. The system is composed of steel underspanned beams, prefabricated concrete elements and a layer of cast-in-place concrete. A prototype building was erected, the objectives being the verification of the main parameters of the project (modularity, need for large spaces free of columns, high dynamic service loads and density of the technical installations) as well as the comparison of the hypotheses related to the structural behavior (resistance, rigidity, cracking and vibrations) with *in situ* measurements. Two underspanned composite beams – 12.5m long and 2.5m wide – were taken from this prototype building and tested in the laboratory [Nissille et al 2007].

The conclusions of the first part of this research [Crisinel et al 2006] are the following: During this project, a particular structural solution was developed which integrates a significant number of constraints and requirements. The composite underspanned beam system brings many advantages to the construction and exploitation of the watch production factory. Thanks to the technical analysis, a certain number of hypotheses were put forward and verified by tests on a prototype and on the completed construction. These tests made it possible to validate the overall behavior of the structure. Many points of detail remain to be analyzed at the level of the transfer of forces and constraints (the connection between the integrated

beam and concrete slab, the effect of the asymmetrical and concentrated loads, the transverse distribution between beams). It is believed that this type of structure offers an interesting potential for wider application. Research at the academic level would facilitate a better understanding of its behavior and thus the exploitation of its true potential.

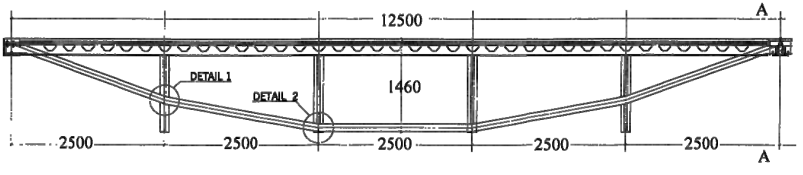
In the present paper, emphasis will be given to the results of the laboratory testing conducted at serviceability and ultimate limit-states on two full size composite underspanned beams and comparisons with the previous *in situ* measurements, as well as with finite element calculations.

TESTED BEAMS

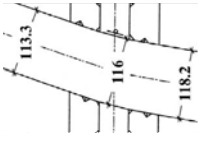
Two underspanned beams (named beam 1 and beam 2 in this paper) were taken from the prototype building when demolished, and were tested in the Steel Structures Laboratory of the Ecole polytechnique fédérale de Lausanne, Switzerland [Nissille et al 2007].

Description

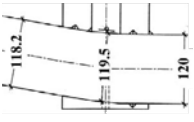
The total length of the beams is 12.5 m; the top chord is composed of a triangular welded section embedded in the thickness of the reinforced concrete slab (slim floor), 2.5 m wide. The tie-bar is connected to the lower flange of the top chord with vertical members at 2.5 m distance. The maximum free distance between lower and top chord is 1.09 m. At each end, the sloping tie-bar joins the upper chord and is welded to transverse steel sections. Figure 1 shows the elevation and cross-section of the beam as well as two connection details.



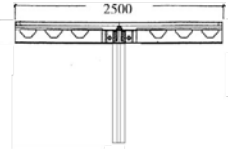
a) Beam elevation



b) Detail 1



c) Detail 2



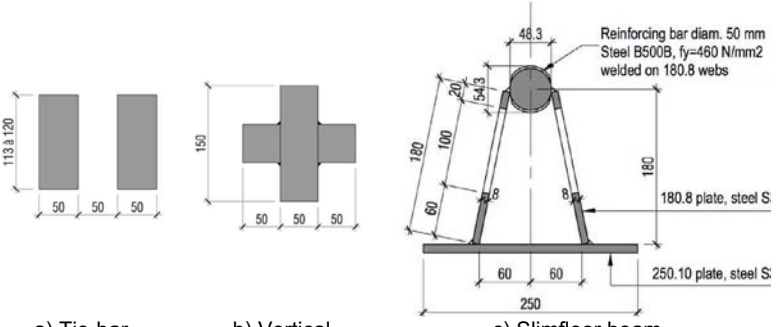
d) Cross-Section A-A

Fig. 1 : Beam geometry.

Steel sections

The tie-bar is composed of two rectangular massive sections 50 mm x 113-120 mm cut out of heavy S235 steel plates (Fig. 2a). The vertical members, also made of S235 steel, are cruciform, composed of a 50 x 150 mm section with two welded 50 x 50 mm sections (fig. 2b).

The lower flange of the integrated steel beam is a flat plate 250 x 10 mm made of S355 steel. The two sloping webs, steel S355, are flat plates 180 x 8 mm with openings. A concrete reinforcement steel bar B500, 50 mm in diameter, constitutes the upper part of this slimfloor beam (fig. 2c).



a) Tie-bar b) Vertical member c) Slimfloor beam

Fig. 2 – Steel element cross-sections of the composite underspanned beam (dim. in mm).

Slimfloor slab

The reinforced concrete slab is composed of prefabricated prestressed elements seated on the lower flanges of the steel beams and cast-in-place concrete (fig. 3). The total depth of the slab is 250 mm (190 mm where sound absorption take place).

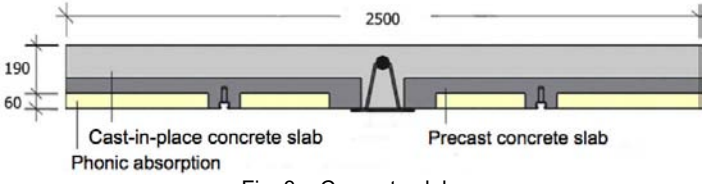


Fig. 3 – Concrete slab.

Material properties

The standard characteristics according to EN Standards as well as tension test results were used in the calculation models.

LABORATORY TESTS

Test set-up

The test set-up is composed of steel frames on which jacks are attached according to the different load cases (from one to four 1000 kN hydraulic jacks, 100 mm maximum stroke). The beams were seated at each end on half-round bars allowing for free rotation of the beams.

Test plan

The two beams were submitted to three types of tests: static, dynamic and failure tests.

Static tests were conducted to study:

- The serviceability limit-state, the beams being submitted to a concentrated load of 200 kN placed at different positions along the beam,
- The composite behavior of the slimfloor beam, the jack being placed between two vertical bars,
- How the tension force in the tie-bar is introduced in the slimfloor beam slab,
- What is the distribution of this force between the steel beam and the concrete slab.

Consequently, the beams were equipped with multiples strain gauges and displacement transducers and submitted to several load cases (Fig. 4).

Dynamic tests (vibrations tests) were conducted to determine:

- The natural frequencies corresponding to the different vibration modes of the beams,
- The damping rate of the beams.

Figure 5 illustrates the different load cases, the positions of the measuring points and mass introduction (150 kg falling from an height of 0.5 m), and the three vibration modes.

Failure tests were conducted to study the behavior of the beams under an asymmetric force applied up to the failure of the beams, the shape of the tie-bar being designed for an optimum distribution of the internal forces in the elements under symmetric distributed or concentrated loads. Figure 6 illustrates the positioning of the jacks (placed above the vertical bars on transverse HEB 300 sections).

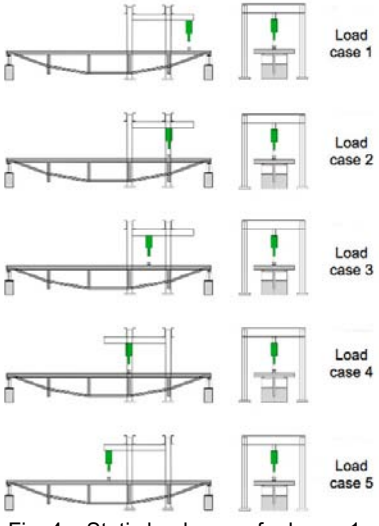


Fig. 4 – Static load cases for beam 1.

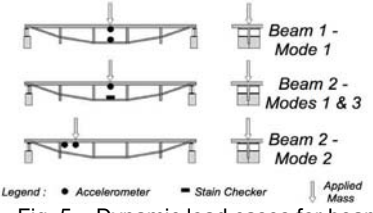


Fig. 5 – Dynamic load cases for bean 1 and 2.

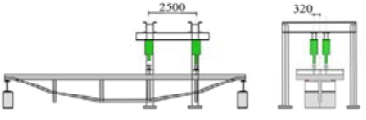


Fig. 6 – Position of the four jacks for failure tests.

Instrumentation

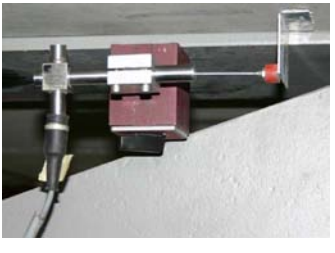
The instruments used for the measurement of the deformation and vibration of the beams are shown on figure 7 (displacement transducers) and figure 8 (*Omega* gauges, *Strain checkers* [Ojio et al 2006] and accelerometers).



Vertical displacement transducer



Beam 1 underneath view with displacement transducers

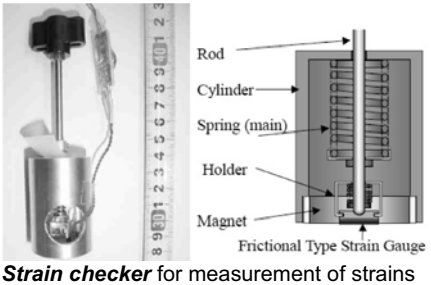


Displacement transducer measuring slip

Fig. 7 – Displacement transducers for deflections and steel-concrete slips.



Omega gauges for measurement of concrete strains in mm/100 mm



Strain checker for measurement of strains by pressing the gauge on the steel surface with a spring inside a steel cylinder with magnet [Ojio et al 2006]



Accelerometer for measurement of the accelerations of the beams

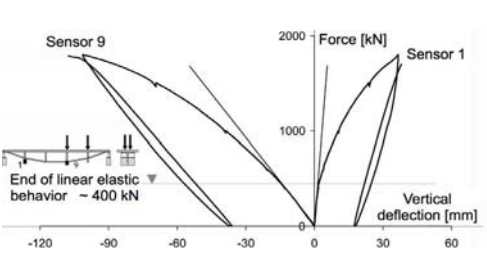
Fig. 9 – Omega gauge, strain checker and accelerometer.

TEST RESULTS AND COMPARISONS

Failure tests

Failure of beam 1

The maximum force applied on beam 1 at failure was 1786 kN, without forewarning (Fig. 10 left). The rupture occurred near the support close to the force introduction (Fig. 10 right bottom), the transverse integrated beam rotating with an angle of about 30°. In order to determine the origin of this brittle failure, the concrete around the connection of the tie-bar to the transverse steel section was removed. It appears that the weld connecting the tie-bar to the massive steel section (replacing the integrated beam, Fig. 10 right top) failed. It must be mentioned that this type of failure cannot occur in the real construction because of the continuity of the integrated beam.



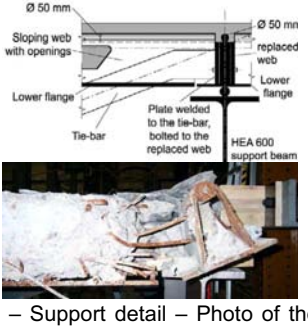


Fig. 10 – Beam 1 failure test: Force vs. deflection – Support detail – Photo of the rupture.

Failure of beam 2

Following this unexpected failure of beam 1, the support system of beam 2 was changed (Fig. 11 left). The failure of beam 2 was never realised, because the vertical displacements were larger than the stroke of the hydraulic jacks. The maximum recorded force was 2'128 kN.

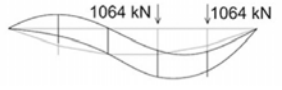
SERVICEABILITY LIMIT-STATE TESTS

Bases of comparisons

The test results [Nissille et al 2007] are presented in this chapter together with their comparisons with in situ measurements [Crisinel et al 2006] and the results of a finite element analysis. These comparisons are given in term of vertical deflections, internal forces, strains on the concrete surface and vibration phenomena (natural frequencies and damping rates). Consequently, the comparisons are made for laboratory test load cases close to the serviceability limit-state and similar to *in situ* load cases. The software used for the FE analysis was AXIS VM 7.0 for bars, beams, plates and shells. The geometry of the model was similar to the dimensions of the tested beams (fig. 12).



Bearing system of beam 2



Beam 2 deformation
(max. deflection 128 mm)



Fig. 11 – Failure test of beam 2 (right: deformation under of total force of approx. 2 x 1'000 kN).

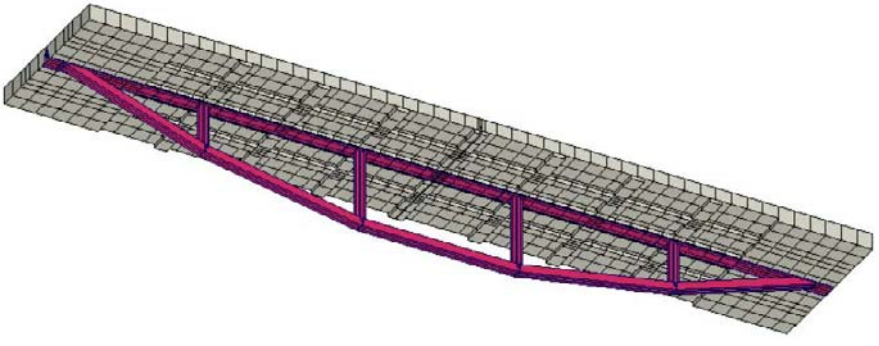


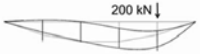
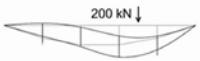
Fig. 12 – Finite Element Modelling.

Vertical displacements

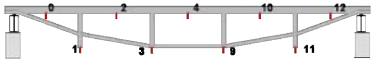
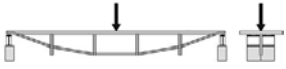
Table 1 shows the deflections measured during the static tests. The vertical displacements were measured using 9 transducers (Fig. 9). Thanks to these measured values, it was possible to draw the global beam deformations for the different load cases.

The first comparison (Fig. 13) is made between the *in situ* "Checkerboard" load case and load case 5 of beam 1 test (laboratory test and FE modeling). "Checkerboard" load case correspond to a total force of 78 kN on a 12.5 m by 2.5 m slab, this value was considered for load case 5. By substracting the right end support deflection (0.7 mm), deflection values are very similar, particularly at the two center vertical members (see table 2).

Tabl. 1 – Beam 1 deformation under 5 load cases.

Load case	Max deflection	Beam deformation	Load case	Max deflection	Beam deformation
1	4.7 mm		4	6.9 mm	
2	7.6 mm		5	7.1 mm	
3	8.1 mm				

Tabl. 2 – Measured vertical deflections [mm] under maximum service forces and FEM values.

Position of transducers										
Transducer number		Under the concrete slab					On the steel tie bar			
		0	2	4	10	12	1	3	9	11
 *Applied maximum force: 200 kN*	Lab test	0.9	3.3	7.1	3.1	0.8	1.7	5.1	5.1	1.5
	FE M	0.9	3.6	7.2	3.6	0.9	1.9	5.6	5.6	1.9
Difference FEM – Lab test		0	0.3	0.1	0.5	0.1	0.2	0.5	0.5	0.4

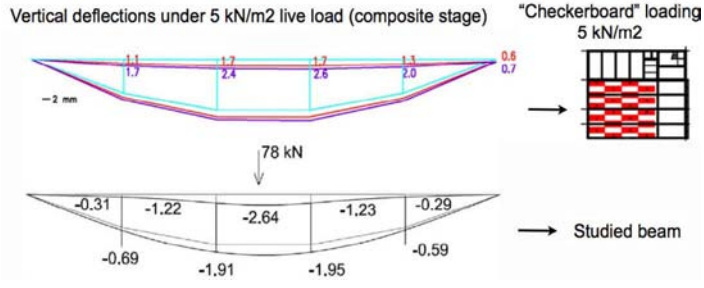


Fig. 13 – Comparison between in situ measurements ("Checkerboard" 5 kN/m2) and load case 5 results (concentrated force of 78 kN). *In situ* measurements: top numbers are FE calculations, bottom numbers are measured values.

The second comparison (fig. 14) is made between the *in situ* "point loading" (2 x 75 kN placed between two underspanned beams) and load case 1 of beam 1 (one 150 kN force centrically on the steel beam). The laboratory test deflections are greater in the beam center (*in situ*: 2.1 mm, lab: 3.3 mm). An uplift of the beam takes place in the lab test, but not in the in situ loading. This is due to the continuity of the *in situ* floor and to center position of the jack in the laboratory test.

For static tests of beam 1, the correspondence between FEM results and laboratory test results is satisfactory. Maximum differences occur near the point of application of the force.

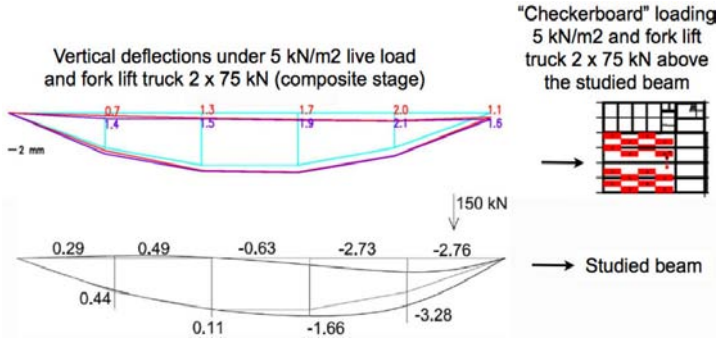


Fig. 14 – Comparison between *in situ* measurements (2 x 75 kN) and load case 1 results (concentrated force of 150 kN).

Internal forces

The results of FEM calculations and static load tests are close. Greatest differences (load cases 1 and 4) are situated at point III and V (fig. 15) due to residual stresses in steel elements.

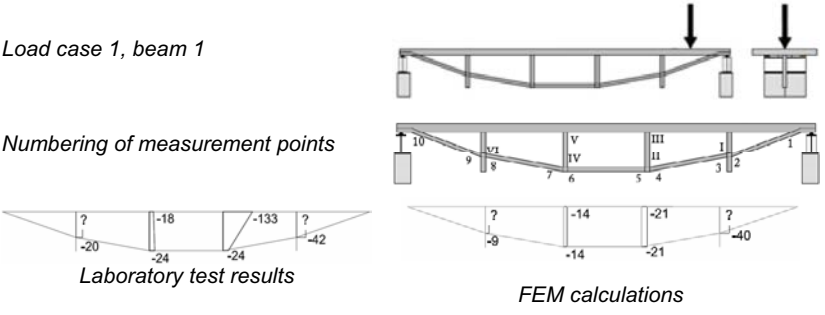
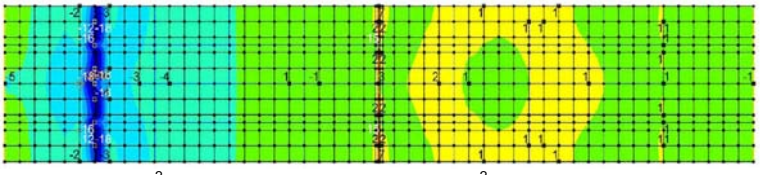


Fig. 15 – Axial forces in vertical members [kN].

Stresses at the top surface of the concrete slab

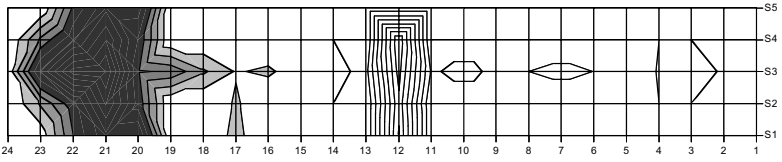
The graphical representation of the results (fig. 16) show a good correlation between FEM calculations and laboratory measurements, as well at the introduction of the tension force of the tie bar in the slimfloor slab, under the applied force or in the zones with few compression. Tension and compression stresses are situated in the same areas and the numerical values are very similar.

FEM calculations



- 18 N/mm^2 + 22 N/mm^2

Laboratory test



- 17 N/mm^2 cracked concrete

Fig. 16 – Stresses on the top surface of the concrete slab (load case 1, beam 1, see fig. 14).

Vibrations

The *in situ* dynamic measurements allowed the determination of natural frequencies at several stages of the construction of the prototype building [Crisinel et al 2006]. The *in situ* load case comparable to one of the laboratory tests is the composite beam subjected to its own weight only: first mode natural frequency = 11.8 Hz. Laboratory test results presented natural frequences of 10.2 Hz (beam 1) and 11.4 Hz (beam 2). Deviations between *in situ* and lab results are certainly due to differences in the measurement modes.

CONCLUSIONS

The structural solution developed in the framework of this building integrates an important number of constraints and requirements. The composite underspanned beam system brings many advantages to the construction and exploitation of the watch production factory. The objective of the laboratory testing conducted at serviceability and ultimate limit-states on two full size composite underspanned beams was the validation of the local and global behaviors of the structure, particularly regarding asymmetric and concentrated loads. Many points of detail were analyzed (the connection between the integrated beam and the concrete slab, the position of the asymmetrical and concentrated loads, concrete cracking, vibration behavior, failure mechanisms).

The interaction between the elements of the structural system (reinforced concrete slab, integrated steel beam, tie-bar, vertical members) is complex. The behavior is different according to the loading types, symmetric or asymmetric, the internal forces changing from essentially axial to flexional/axial. This is the reason why the beams were subjected to different load cases from serviceability limit-state (most probable

in the real structure) to ultimate limit-state (failure load case with asymmetrical concentrated forces).

The main conclusions to be drawn from the laboratory test results are the following:

Serviceability limit-state

The maximum service load corresponds to the axle load of a forklift truck represented by a concentrated force of 200 kN placed in different positions along the axis of the beams.

- Over all, the results are satisfactory. Deflections of 7 to 8 mm were measured, corresponding to 1/1000 of the length between two points of zero deflection.
- There is a good correlation between the linear-elastic FEM results and measured values, for deformations as well as for forces and stresses.
- At this loading level, the introduction of the tie-bar force in the composite slimfloor beam do not induce any concrete cracking problem at the top surface of the slab; the general level of concrete slab cracking is low.
- The general behavior of the underspanned beam stays linear-elastic until a force of about 450 kN. The FEM simulating the global composite behavior (tie-bar/integrated beam – slimfloor slab) can be considered as representative of the real behavior up to this limit.
- The dynamic laboratory tests confirm the value of the natural frequency f = 11 Hz, very close to the FEM calculated and the *in-situ* measured values. If a supplementary uniform load of 500 kg/m^2 according to the design requirements, the natural frequency should decrease to 8 Hz. The mean measured damping rate ζ = 0.056 is usual for this type of construction.

Ultimate limit-state

Several asymmetric load cases were tested to evaluate the ultimate load bearing capacity of different failure mechanisms. The tests concentrated essentially on the composite slab behavior (integrated beam).

- Above a load of about 500 kN, the beam behavior is no more linear-elastic. The rigidity of the composite sections decreases according to the increase of the concrete cracking. Furthermore, plastic zones appear near the steel connections of the underspanned beam. This is due to the Vierendeel effect of these rigid connections.
- The composite behavior of the slimfloor beam is ductile. No sign of brittleness was detected in the adherence connection between this top chord and the concrete slab.
- The first critical load case is obtained when the concentrated force is placed between two vertical members of the underspanned beam (local yielding of the steel beam under a maximum measured force of 500 kN). The calculated maximum load is higher than the measured one, because of the residual stresses present in the real welded structure.

- When the force is applied directly above a vertical member, the load bearing capacity of the underspanned beam is increased 3 to 4 times (ultimate force greater than 2'000 kN). The rupture is still situated in the slimfloor beam.
- At a load above 1'000 kN, a main longitudinal crack occurs along the axis of the top chord in the zone of introduction of the tie-bar force. This crack, 2.3 m long, is induced by the transverse tension stresses due to the diffusion of the tie-bar force.

Over all, the laboratory tests allow for a better knowledge of the behavior of an underspanned composite beam. It will be possible for the user of the industrial building to evaluate quickly and precisely the positioning of heavy finishing machines on the floors. For instance, concentrated masses up to 300 kN (in addition to the uniform load of 5 kN/m^2) will be acceptable if they are placed along the axis of the underspanned beams.

The structural system composed of a 12.5 m span slimfloor beam underspanned by a tie-bar is high performance when lightness, transparency (in term of technical installations) and rigidity are looked for. The laboratory tests have shown the high performance of the tie-bar in case of concentrated asymmetric loads. This practical, theoretical and experimental study have shown that this type of composite structure could be applied for other industrial projects in which the concepts of flexibility and adaptability are of high importance for the development of the production activities.

REFERENCES

[Crisinel et al 2006] Crisinel, M., Sautier, F., Guscetti, G., Kalix, F., Perregaux, N. and Walgenwitz, M. "Development of a new type of composite underspanned beam". In: Proceedings "Composite Construction V" Engineering Conference International, Kruger National Park, South Africa, July 18-23, 2004. ASCE, 2006, pp. 325-335.

[Nissille et al 2007] Nissille, R. and Crisinel, M. "Essais de charge de deux poutres mixtes à sous-tirant", Report ICOM 523, Ecole polytechnique fédérale de Lausanne, EPFL, Steel Structures Laboratory ICOM, 2007.

[Ojio et al 2006] Ojio, T., Yamada, K., Saito, Y. and Shiina, S. "Strain Checker: stethoscope for bridge engineers", Proceedings of IABMAS 06, Third International Conference on Bridge Maintenance, Safety and management, Porto, July 2006.

[Kalix et al 2007] Kalix, F., and Nissille, R.. "Une structure sous tension", Tracés, Lausanne, 2007, pp. 7-13.

[Bachmann et al 1995] Bachmann, H. et al. "Vibration Problems in Structures – Practical guidelines", Birkhäuser Verlag, Basel, 1995.

FLEXURAL BEHAVIOUR OF CONRETE-FILLED THIN-WALLED STEEL TUBES WITH LONGITUDINAL REINFORCEMENT

Dr. Andrew Wheeler
School of Engineering, University of Western Sydney
Locked Bag 1797 Penrith South DC
NSW 1797 Australia
a.wheeler@uws.edu.au

Prof. Russell Bridge
School of Engineering, University of Western Sydney
Locked Bag 1797 Penrith South DC
NSW 1797 Australia

ABSTRACT

Concrete filled steel tubes (CFTs) are efficient members in structural applications including bridges, buildings and piled foundations and their use in the building industry is increasing. To date their primary use has been in axial applications, with the design methodology based on theory and tests of columns under loads applied axially or at relatively small eccentricities. Limited in to research into the behaviour of CFTs subjected to large eccentricities or loading in pure flexure have been conducted, with preliminary experimental investigation suggesting that stiffness of composite members tending towards that of the tube at relative low loads. An ongoing research program on the flexural behaviour of CFTs is being undertaken at the University of Western Sydney with a particular emphasis on thin-walled steel tubes that can provide an economical form of construction.

In this paper, the results from additional experimental work will be presented with a particular emphasis on the stiffness of the members when subjected to flexural loading. The experimental work to date has demonstrated that even in composite specimens where there is negligible end slip; the stiffness of the specimens under pure flexure tends to the stiffness of the bare steel tube. A numerical model will also be presented that can accurately generate the bond/slip relationship of the concrete within the steel tubes and consequently the behaviour of the specimens modelled. From the experimental results and the numerical model some guidelines for the design of concrete filled tubes subjected to primarily flexural loading will be presented.

Introduction

The use of concrete filled steel tubes in the construction industry continues to increase, and methods for the design of such elements are continually being developed. The most common form of use for these members is as structural columns, where the compressive strength of the concrete is used effectively with the exterior steel tube providing the tensile capacity for bending and acting as a confining member and occasionally as supporting member during construction. As this type of construction is most effective for axially loaded columns, the resulting research has primarily focused on concrete filled tubes (Gourley and Hajjar 1993; O'Shea and Bridge 2000; UY 2000). With the existing experimental studies looking

at both circular tubes and square/box tubes with axial loads concentrically loaded and with small eccentricities.

For effective design of the concrete filled tubes, the understanding of how these members behave under flexural loading is necessary. The use of concrete filled tubes in pure bending has been studied to some degree with recent tests involving flexural loading of concrete filled rectangular tubes being presented by a number of authors (Lu and Kennedy 1994; Prion and Boehme 1994; Elchalakani, Zhao et al. 2001; Nakamura, Momiyana et al. 2002; Han 2003; Wheeler and Bridge 2003; Han, Lu et al. 2006; Shawkat, Fahmy et al. 2008), with the majority of these tests have been on small diameter tubes (<300 mm). The tests carried out by Nakamura *et al.* (Nakamura, Momiyana et al. 2002) were on a small number of 600mm diameter tubes for verification for use as flexural members in a composite bridge. Wheeler and Bridge carried out a small number of tests flexural members with tubes from 406 mm to 456 mm in diameter.

The prediction of the flexural strength of composite tubes has been well documented with the majority of studies carried out presenting methods to obtain a better prediction (Bergmann, Matsui et al. 1995; Elchalakani, Zhao et al. 2000; Han 2003; Han, Lu et al. 2006). Prion and Boehme (1994) carried out a study on tubes filled with high strength concrete concluding that the strengths predicted using plastic section analysis methods available gave conservative results. These conclusions were echoed by Han (2003, 2006), with the inclusion of a model to predict the flexural stiffness at various levels of load based on a calibrated numerical model.

In the tests carried out at the University of Western Sydney (Wheeler and Bridge 2003), the flexural stiffness of the tubes was measured. The experimental work detailed that at relatively low loads the flexural behaviour of the composite member under pure flexure tended towards the theoretical stiffness of the steel tube. Han (Han, Lu et al. 2006) also observed a change in flexural behaviour and modified the design method appropriately. However, this change in stiffness was not as significant as observed by Wheeler and Bridge (2003). Furthermore, looking closer at the experimental work the relative change in flexural stiffness deteriorates with an increase in the diameter. In the experimental work conducted by Shawkat et al. (Shawkat, Fahmy et al. 2008) for the concrete filled tubes that had large depth to span ratios (i.e. flexural members) there was significant cracking on the tension side of the specimen with multiple cracks at close centres. This effect was also noted by Wheeler and Bridge (Wheeler and Bridge 2003). Both these issues further the argument that there is a size effect on the flexural behaviour of concrete filled tubular members.

Another application of concrete filled tubes is in the field of foundation engineering, with piles consisting of a large diameter tubes that are filled in-situ with a reinforced concrete infill. To date the design method for such members has typically ignored the external sleeve on the assumption that in the typical corrosive environments of the ground will render the unprotected steel ineffective in the long-term. The use of these types of piles is common in large bridge structures where in the serviceability state the piles are normally subjected to axial loading. However, during construction these piles or pile groups may be subjected to significant flexural loads that are not realised once the structure becomes serviceable. Thus the contribution of the steel tube in bending during the construction stage would be advantageous. In this

situation the concrete filled tubes would contain a measure of longitudinal reinforcement that may influence the flexural behaviour. The work by Shawkat et al. (2008) looked at both steel tubes and fibre reinforced polymers tubes. While the major focus of the study was the FRP tubes, comparative tests on tubes with and without longitudinal reinforcement were conducted. It was noted that significant differences in the ultimate strength but more importantly in the stiffness of the sections was observed when the longitudinal reinforcement was included.

In this paper the additional results from the experimental work conducted at the University of Western Sydney will be presented with a particular emphasis on the flexural rigidity of concrete filled circular tubes at discrete points and as a flexural member. To further the study of the flexural behaviour of concrete filled tubes, a preliminary finite element study into the inclusion of longitudinal reinforcement is also presented looking at the effect of the additional reinforcement on the stiffness of the cross-section, in an endeavour to develop a testing program.

Experimental Results

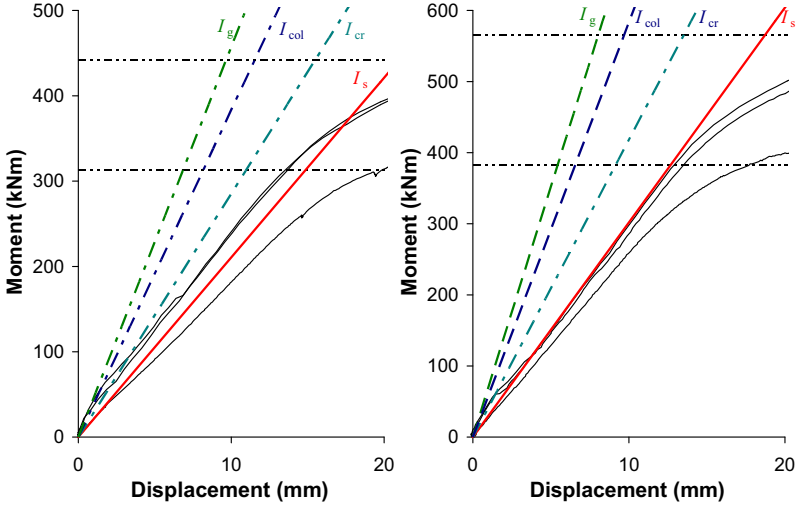
The full details of the test program conducted at the University of Western Sydney have been published in Wheeler and Bridge (2003). In this publication the focus was on the behaviour under flexural conditions focusing on the strength and looking superficially at the flexural stiffness. In this paper a more detail analysis of the flexural behaviour looking at both the moment displacement and moment curvature relationships is conducted.

In Figure 1 the moment - mid-span deflection relationship for the experimental work is presented, up to the onset of plasticity in the tubular section. To obtain an understanding into the relative stiffness, the theoretical moment displacement relationships assuming various cross-section states are also shown. These include the elastic bare steel tube stiffness (I_s); the cracked composite section stiffness (I_{cr}), which is determined using the elastic properties of the materials and the assumption that plane sections remain plane. Next the nominally assumed column stiffness (I_{col}) which is commonly used for axially loaded members, based on the assumption that the steel tube is fully effective with 70 percent of the concrete being effective ($I_{cr} = I_s + E_c/E_s\ 0.7\ I_c$). Finally, the gross cross sectional stiffness with both the concrete and steel being fully effective.

In Figure 1 it is evident that the concrete filled tube has an initial stiffness that closely resembles the uncracked composite section stiffness. As the load increases at relatively small loads (less than 50 kNm) there is a marked reduction in stiffness, this level of load corresponds to the cracking moment of the concrete. As the load increased the stiffness continues to decreases until the stiffness appears to be similar to the theoretical stiffness of the bare steel tube (I_s).

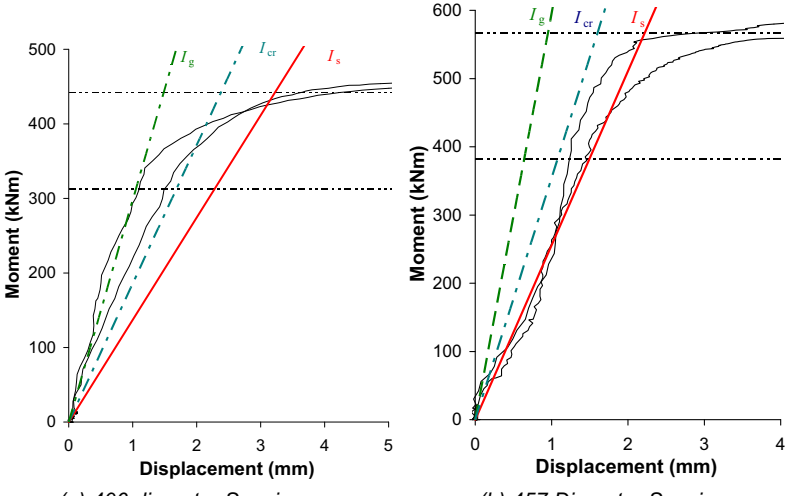
While it was assumed in the development of the test program that sufficient length was selected to have a fully bonded cross section, thus resulting in full composite behaviour, it was recognised that this might not be the case and the regions with a moment gradient may not be fully bonded. Consequently the load deflection behaviour for the constant moment region, (between the load points) was derived from the experimental work. These relationships are presented in Figure 2. While the measured displacements are significantly smaller the general trends of the curves

are similar to the overall deflection and the curvature, after an initial stiff portion of the concrete cracks and considerable softening occurs. For the 406 specimens the general trend for the curvature is towards the cracked stiffness, while for the 456 specimens the trend is below the crack stiffness and tending towards the sectional stiffness.



(a) 406 diameter Specimens *(b) 457 Diameter Specimens*

Figure 1 – Moment – Mid-span Displacement Relationship

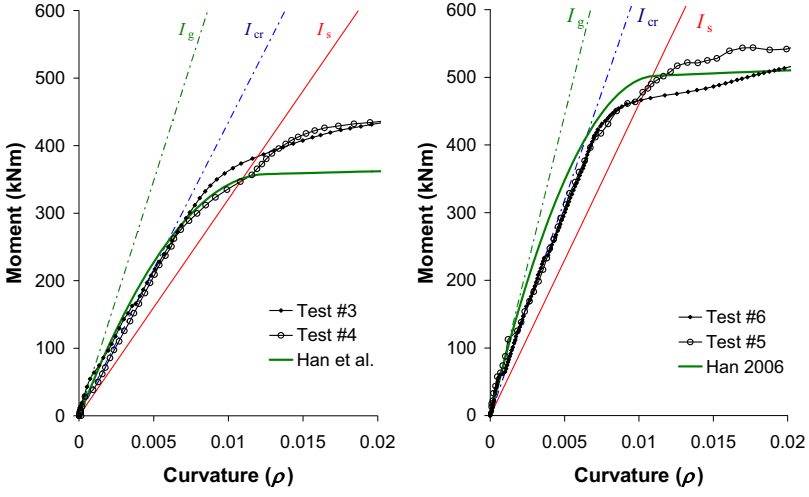


(a) 406 diameter Specimens *(b) 457 Diameter Specimens*

Figure 2 – Moment Curvature Relationship

Additional to the deflection measurements, the strains on external surface of the specimen member were also measured. These strains located at mid-span, were measured on the top and bottom of the specimen and third points around the specimen. From these results the moment curvature of the specimen at discrete point (mid-span) were determined and presented in Figure 3. Also presented in the figure are the relative curves for the assumed section behaviour as in Figure 1. The figure again demonstrates that initially the behaviour is similar to the gross cross section, with the onset of cracking the stiffness falls to a level that is similar to but in general below that expected for a cracked cross section. Unlike moment displacement relationship shown in Figure 1 2, where the stiffness is averages out over the constant moment region, the moment curvature presented in Figure 3 is the curvature at a given cross-section, and is dependent on the location of the cracks within the cross-section. For example if a crack is not present at the location of the strain gauge then the gross-section stiffness may be measured, and the presence of an adjacent crack will provide a much lower stiffness.

The moment curvature relationship using the method presented by Han (2006) is also shown in Figure 3. For the smaller tube (405mm) the prediction of the stiffness could be considered good, while for the larger cross-section (456mm) the predicted stiffness is higher than the measured stiffness.



(a) 406 diameter Specimens *(b) 457 Diameter Specimens*

Figure 3 – Moment Curvature Relationship

Elastic cross-section analysis reveals that the moment to cause cracking in the extreme tensile fibre in these specimens is less than 10 kNm. This fact is born out in the displacement and curvature results with the loss of stiffness at relatively small loads. In test specimen #3 and #5 the curvature curves (Figure 3) suggests that cracking does not occur until approximately 50 kNm and 100 kNm respectively, while the displacements curves (Figure 1) demonstrate an early deviation form the full

composite behaviour. This variation is attributed to the positioning of the cracks, as the deflection curves are a function of the behaviour of the loaded section of the tube, any cracking in the concrete along this length with be observed in the measured results. However, for the curvature results a crack away from the measured cross-section will not be observed in the results, but as loading increases and additional cracks form in the measured cross-section then the change in stiffness is observed.

The difference between the calculated curvature using the strains and the measured curvature suggests that the assumption that plane sections remain plane may not hold. Generally, this phenomenon is observed in end slip between the concrete and steel sections. The slip at the ends of the specimens between the steel tube and the concrete in-fill was also measure in the tests. This slip was measured at top and bottom of the section were independently, and were found to be identical. The typical load slip relationships for all the concrete filled tubes are presented in Figure 4. The end slip in all specimens were minimal, with negligible amounts measured until the specimens entered the plastic region and even at this stage did not exceed 0.5 mm.

After testing the tube was removed from portions of the specimens to observe the failure patterns in the encased concrete. It was observed that on the tensile face of the concrete there numerous closely spaced cracks, a similar cracking pattern was also observed in the work by Shawkat et al. (2006). The formation of the cracks and the spacing is thought to be the result of the confinement of the tube, as the tube bends for continuity the concrete must also take a similar profile thus inducing numerous closely spaced cracks. The spacing of these cracks was approximately 20 mm which corresponded to the maximum aggregate size specified for the concrete mix.

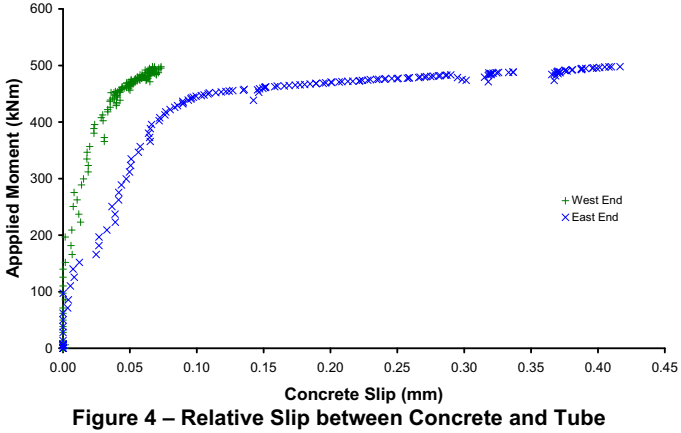


Figure 4 – Relative Slip between Concrete and Tube

Based on the experimental work and the comparisons with the theoretical values, the assumption that there was sufficient length in the tubular sections to ensure full composite interaction between the concrete and the steel mat not have been correct. While two section depths were tested the length of the shear gradient was not scaled proportionally and remained the same for both size specimens. In the test program the measured average end slip in the larger cross-section was not noticeably

different to that observed in the smaller section, but there were considerable variations between the measured curvatures and displacements against the theoretical values. The authors consider that while the end slip may have had an effect on the behaviour, this is not conclusive and for future testing measures will be taken to ensure that no end slip occurs.

Another factor that may be contributing to the reduction in the flexibility is the number and spacing of the cracks in the concrete infill. Fine cracking will cause a reduction in the tension stiffening effect on the member as a whole thus reducing its flexural rigidity. With this in mind will the inclusion of longitudinal reinforcement into the concrete infill have an effect on the flexural stiffness of the members? It is recognised that the inclusion of the additional reinforcement will increase the gross and elastic second moments of area. But when a reinforced concrete member is considered and assessed for flexural rigidity, a value between the gross and cracked is considered due to the tension stiffening effects. With the placement of reinforcement within the tube a have a similar effect or this effect already realised by the presence of the steel tube.

Design Methods

A number of models have been developed to predict the behaviour of the composite beams systems ranging from simple beam theory that assumes full shear connection, to finite element modelling with either partial or full shear connectivity between the steel and concrete members. When concrete filled tubes are considered the general assumption that plane sections remain plane, thus assuming that full shear connection exists between the concrete infill and the tube.

The existing models for the determination of ultimate strength of the concrete filled tubes are either based on an elastic analysis or a cross-sectional analysis that considers the non-linear material properties. Again the simplified methods generally assume that full composite action between the steel and the concrete exist. These methods typically predict accurate estimates of the ultimate strength that tend to be on the conservative and are thus considered appropriate to predict the ultimate capacity.
For the determination of the flexural stiffness of concrete filled tubes the current methods used in international design standards vary significantly. In general the effective stiffness of a column is a determined for the material and geometric properties as expressed by

$$K_e = E_s \times I_s + \alpha \times E_c \times I_c$$

where I_c, E_c and I_s , E_s are the second moments of area and Modules of Elasticity for the concrete and steel respectively. □is the concrete ratio, and is code dependent and varies from 0.2 in the AIJ (AIJ 1997) to 1 in the BS5400 (BSI 1997).

To overcome the crudeness of the methods Han has recently looked in some detail into the flexural behaviour of concrete filled tubes considering both the ultimate strength and the flexural stiffness (Han 2004; Han, Lu et al. 2006). In this work, a model has been developed using a numerical model which in turn was then compared with the experimental results for eighteen circular tubes and thirty four square or rectangular tubes. Variables that are included in this model include the shape of the cross-section, the strength of the materials and the confinement of the

concrete. The method looks at both the strength and the stiffness, and has been refined to have a three stage relationship. The first stage is an initial linear stiffness up to 20% of the ultimate load, followed by a stiffness which is a function based on an arbitrary curvature to a strength of 60% of the ultimate capacity. A third function is used to define the post serviceability loads. In this model there is no allowance for the inclusion of longitudinal reinforcement with in the concrete infill. All specimens detailed in Han's work had specimen depths equal to or less than 200 mm.

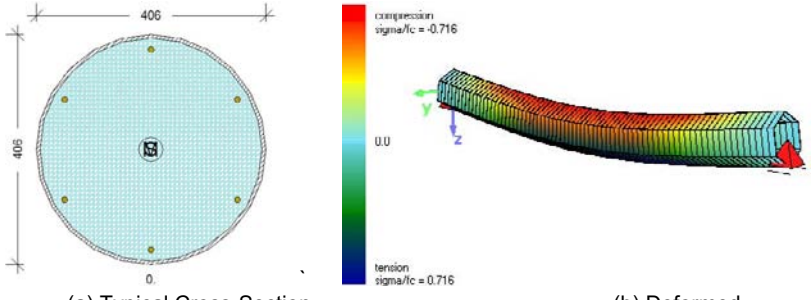
While experimental work is critical in determining the behaviour of composite members, the cost associated with this type of work are high, and the testing of realistic section sizes limited due to handling and loading issues. Conversely, the modelling of the behaviour with numerical methods is relatively cheap, but prone to error as unexpected behaviour may not be modelled so a reliable model to predict the behaviour is required. The experimental work carried out at the University of Western Sydney has also been supported with an extensive numerical study as outlined in (Wheeler and Pircher 2002; Wheeler and Pircher 2002; Wheeler and Pircher 2003).

The focus of the current study is to look at the effect of internal reinforcement on the flexural stiffness of concrete filled tubes. The preliminary part of the study is to conduct a numerical study on sections with and without reinforcement, to study the effect of the additional reinforcement of the stiffness of the members. This study was conducted using the SOFiSTiK FEA package, using beam element with the inclusion of nonlinear materials for the tubes and reinforcement as well as cracked concrete. When using beam elements the assumption that plane sections remain plane is always made, thus there is no interface slip between the concrete and the steel tube.

The numerical analyses was conducted on the composite cross section shown in Figure 1(a), the assumption in using this particular cross-section is that there full bond between the steel tube, the reinforcing bar and the concrete infill. The modelling was set up to duplicate the test program, consisting of a single span with two point loads applied at given distances from the supports. This method of testing provides a constant moment region for a portion on the section at mid span. The model with typical stresses and deflections is shown in Figure 1(b).

This study is to quantify the effect of reinforcement on the stiffness of the member. As shown in Figure 5 the reinforcement is placed at discrete locations around the cross section at a given distance from the tube as shown. The reinforcement location for this study remains constant, with the variable being the amount of reinforcement at these locations. The material properties used in the numerical analysis are shown in Figure 6. The tube material had a yield strength of 350 MPa with a strain hardening region as shown. The concrete as shown is a nonlinear function with an ultimate strength of 42.5 MPa.

In Figure 7 the effect of varying the reinforcement on the theoretical stiffness is demonstrated. In this figure as the ratio of the reinforcement is increased the stiffness increases also increases. The increases are inline with those determined using linear elastic analysis and would be considered relatively small changes and difficult to ascertain experimentally. The ultimate capacity of the member is increased and can be calculated using elastic methods.



(a) Typical Cross-Section (b) Deformed Model

Figure 5 – FEA Modelling

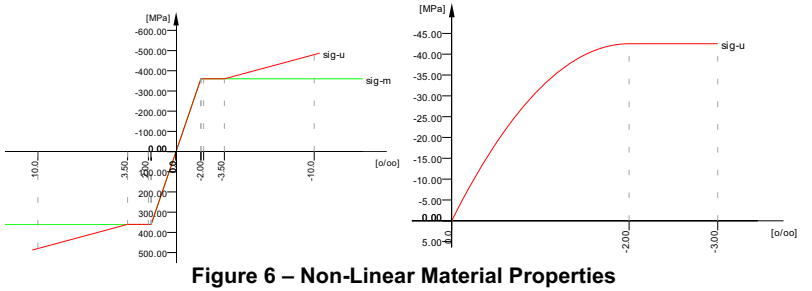


Figure 6 – Non-Linear Material Properties

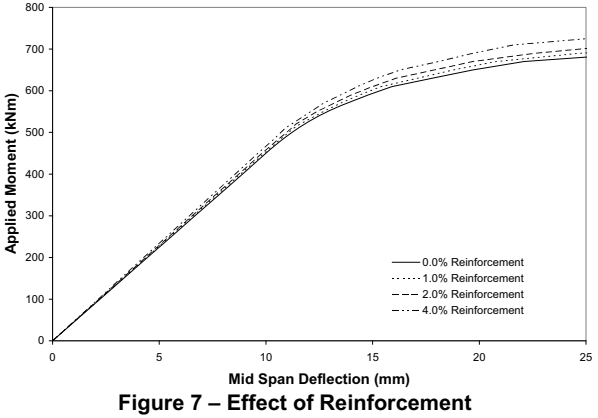


Figure 7 – Effect of Reinforcement

This type of behaviour is expected with the additional reinforcement, but it should be noted that the numerical analysis shown here always predicts an initial linear portion of the curve which could be attributed to the fact that the FEA beams sections consider a smeared approach for the concrete cracking. What varies significantly from the experimental results is the initial high stiffness due to whole cross section being considered prior to the concrete cracking. In an endeavour to model the behaviour more accurately the numerical analysis was then repeated using a concrete with a tensile capacity. For this case it was assumed that the concrete have a tensile capacity equal to sixty percent of the square of the concrete strength. The effect of the tensile capacity is demonstrated in Figure 7.

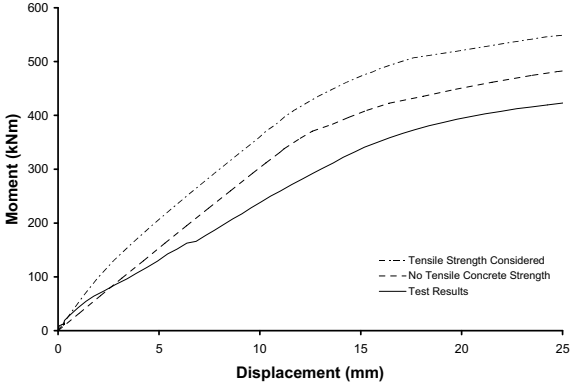


Figure 8 – Effect of Tensile Strength of Concrete

In this figure a high initial stiffness is observed with the stiffness reverting to a similar stiffness to that observed in the models with no concrete tensile strength. The load displacement curve for the test results is also presented in Figure 7, while the inclusion of the concrete tensile strength moves the initial stiffness of the cross-section resemble the stiffness of the experimental work. The overall stiffness of the experimental work in considerably less than the stiffness derived from the numerical analysis. While care should be taken in comparing the numerical and experimental results due the fact some end slip was measured this was comparatively negligible. Consequently, analysis is suggesting the beam elements are appropriate for load loads where the assumption that plane sections remain plane is correct, but as multiple closely spaced cracks form is this assumption still correct.

Conclusions

An ongoing investigation into the Flexural behaviour of concrete filled tubes is being conducted at the University of Western Sydney. The focus has been on the behaviour of tubes with moderate D/t ratios with diameters greater than 400 mm. The focus has been on both experimental and numerical work in an effort to fully understand the flexural behaviour and develop a model to predict both the flexural rigidity and the ultimate strength.

A detail analysis concentrating on the flexural rigidity of a number of tests on concrete filled tube has demonstrated that for this test series there is some irregularities between the measured moment curvature behaviour of a cross section (measured at a single point), and the measured moment deflection behaviour of the same specimen over a constant moment span. The trend was that the larger the cross section the further the deviation from the expected results. This difference may be the result of either loss of bond between the tube and the concrete thus rendering the assumption that plane section remain plane or is it the result of the combination of fine cracking limiting the contribution of the concrete to the stiffness of the member.

For a number of applications longitudinal reinforcement is placed in the composite sections and a current test program is looking at the effect of this longitudinal reinforcement of the flexural stiffness. The experimental analysis detailed suggested that insufficient bond length of the concrete infill in the concrete tube could have contributed to the reduction in the member stiffness, thus in the test program restraints against this will be included to ensure that there is no end slip.

A basic model was developed that demonstrated the need to model the tensile capacity on the section to accurately predict the initial stiffness of the cross-section. The results presented in this paper suggest that the use of beam elements, even with non-linear properties, is limited and that a model where the concrete cracking and the interface between the concrete and steel is considered. Other issues that need to be included in the model include concrete restraint and the effect of longitudinal reinforcements and concrete aggregates size.

REFERENCES

AIJ (1997). Recomendations for the design and construction of concrete filled tubular structures. AIJ.

Bergmann, R., C. Matsui, et al. (1995). Design Guide for concrete filled hollow section columns under static and seismic loading, Verlag TUV Rheinland.

`British Standards Institution. **BS8110:Part 1:1997**.

Elchalakani, M., X. L. Zhao, et al. (2000). "Bending tests to determine slenderness limits for cold-formed circular hollow sections." Journal of Constructional Steel Research.

Elchalakani, M., X. L. Zhao, et al. (2001). "Concrete-filled circular steel tubes subjected to pure bending " Journal of Constructional Steel Research **57**(11): pp. 1141-1168

Gourley, B. C. and J. F. Hajjar (1993). A Synopsis of studies of the Monotonic and Cyclic Behaviour of Concrete-Filled Steel Tube Beam Columns, Dept. of Civil Engineering, University of Minnesota, Minneapolis, USA,.

Han, L.-H. (2003). "Felxural behaviour of concrete filled steel tubes." Journal of Constructional Steel Research **60**: pp. 313-337.

Han, L.-H. (2004). "Flexural behaviour of concrete filled steel tubes." Journal of Constructional Steel Research **60**(2): pp. 313-337.

Han, L.-H., H. Lu, et al. (2006). "Further study on the flexural behaviour of concrete filled steel tubes." Journal of Constructional Steel Research **62**: 554-565.

Lu, Y. and D. Kennedy (1994). "Flexural Behaviour of Concrete filled Hollow Structural Sections." Canadian Journal of Civil Engineering **21**(1): pp. 11-130.

Nakamura, S., Y. Momiyana, et al. (2002). "New technologies of steel/concrete composite bridges." Journal of Constructional Steel Research **58**(1): pp. 99-130.

O'Shea, M. D. and R. Bridge (2000). "Design of Thin-walled Concrete Filled Tubes." Journal of the Structural Division, ASCE **126**(11): pp. 1295-1303.

Prion, H. G. L. and J. Boehme (1994). "Beam Column Behaviour of Steel Tubes Filled with High strength Concrete." Canadian Journal of Civil Engineering **21**(pp 207-218).

Shawkat, W., W. Fahmy, et al. (2008). "Cracking patterns and strength of CFT beams under different moment gradients." Composite Structures **84**: 159-166.

UY, B. (2000). "Strength of concrete filled steel Box columns incorportating local buckling." Journal of Structural Engineering **126**(3): 341-352.

Wheeler, A. and R. Bridge (2003). Thin-walled steel tubes filled with high strength concrete in beanding. Engineering Foundation Conference, Composite Construction V, Kruger, South Africa.

Wheeler, A. and M. Pircher (2002). The Influence of Material Properties on the Local Buckling of Concrete filled Steel Tubes. Advances in Building Technology (ABT 2002) Hong Kong, China.

Wheeler, A. and M. Pircher (2002). Measured Imperfections in Six Cold-Formed Thin Walled Steel Tubes. Research Report CCTR001. Sydney Australia, Centre For construction Technology and Research, The University of Western Sydney.

Wheeler A., Pircher M. (2003) Buckling Behaviour of Thin-Walled Steel Tubes Subjected to Flexure, *Proceedings: ICMS 2003*, Miskolc, Hungary, pp 129-136

BEHAVIOR OF COMPOSITE CFT BEAM-COLUMNS BASED ON NONLINEAR FIBER ELEMENT ANALYSIS

Tiziano Perea
Georgia Institute of Technology
Atlanta, GA 30332-0355
Email: tperea@gatech.edu

Roberto Leon
Georgia Institute of Technology
Atlanta, GA 30332-0355
Email: roberto.leon@ce.gatech.edu

Abstract

The results obtained from nonlinear fiber element analyses for concrete filled tubes (CFT) are discussed. The studies were aimed at assessing primarily the overall behavior and stability effects on these structural elements as a prelude to a large full-scale testing program. The study focuses on ultimate strength analyses for CFT composite columns with different stress-strain models for both concrete and steel. Fiber analyses using OpenSees are used to assess the impact on the ultimate strength based on the assumed stress-strain material curves, member slenderness, initial imperfections, and both material and geometric nonlinearities. Fiber analysis results are also compared with those obtained from AISC (2005). Fiber-based results show a compatible correlation with the expected element behavior, which is also captured in the current AISC (2005) Specifications.

Introduction

The use of composite columns in moment-resistance frame systems is increasing worldwide. Composite columns not only provide many advantages in construction speed and economy, but also result in a substantial improvement of mechanical properties of the member when compared to either steel or reinforced concrete columns. However, there still exist some knowledge gaps in their behavior in areas such as the effective stiffness under lateral forces, instability effects in slender beam-columns, and the secondary effects due to the steel-concrete contact interaction. Nonlinear fiber element analyses provide a very useful analytical tool to investigate some of these behavioral aspects of composite elements. Fiber elements offer an efficient approach as they can incorporate directly into the model flexural buckling, initial imperfection, geometric and material nonlinearity, and hardening effects.

Fiber element analysis have been widely used to understand and predict the behavior of steel (i.e. White, 1986; Liew and Chen 2004; etc.), reinforced concrete (i.e. Taucer et al., 1991; Izzudin et al., 1993; Spacone and Filippou, 1995; etc.) and composite steel-concrete elements. Table 1 summarizes briefly a number of analytical studies that have looked at fiber analysis of composite elements; this table is not meant to be comprehensive, however it gives an idea of the maturity and breath of the approach.

Table 1. Summary of analytical studies with fiber analysis in composite elements

Reference	Applied to:	Brief comments
Tomii and Sakino (1979)	CCFT and RCFT cross-sections	Calibrated fiber M-ϕ results with experimental results adjusting σ-ε curve in concrete, keeping steel as elastic-perfectly-plastic.
Elnashai and Elghazouli (1993)	SRC beam-columns	Developed a non-linear model for SRC frame structures subjected to cyclic and dynamic loads, accounting for geometric nonlinearities, material inelasticity, confinement effects in concrete, and local buckling and cyclic degradation in the steel. The model is calibrated and compared with experimental data.
Ricles and Paboojian (1994)	SRC beam-columns	Analyzed SRC beam-columns with fiber analysis, which accounted for strain compatibility, material nonlinearity, and confinement effects using the Mander model.
Hajjar and Gourley (1996)	RCFT cross-sections	Developed a polynomial expression to represent a 3D axial-bending interaction equation for square CFT cross-sections. This polynomial equation was fitted based on results from nonlinear fiber element analysis.
El-Tawil and Dierlein (1999)	SRC cross-sections	Compared experimental and fiber-based results of monotonic M-ϕ curves. From the fiber-based model, interaction curves were obtained for 3 SRC cross-sections with different steel ratios, which were compared with the ACI and AISC strength.
Lakshimi and Shanmugan (2000)	CFT beam-columns	Used fiber models to predict behavior of biaxially-loaded CFT beam-columns and axially-loaded slender CFT columns.
Uy (2000)	CFT columns	Used fiber models in CFT columns with thin-walled steel tubes. Buckling and post-buckling behavior were incorporated through a finite strip method and an effective width approach.
Aval et al. (2002)	CCFT and RCFT beam-columns	Developed a fiber element accounting for bond/slip interaction between concrete and steel (due to the difference between axial elongation and curvatures). The effect of semi- and perfect bond is investigated and compared with experiments.
Fujimoto et al. (2004)	RCFT cross-sections	Used the empirical σ-ε curves developed by Nakahara-Sakino-Inai in fiber analysis to predict monotonic M-ϕ curves.
Inai et al. (2004)	RCFT cross-sections	Used the empirical σ-ε curves developed by Nakahara-Sakino-Inai in fiber analysis to predict cyclic M-ϕ curves.
Varma et al. (2004)	RCFT beam-columns	Adapted and implemented σ-ε curves for both high strength steel and concrete to predict the response of square CFT elements. These curves were adapted from results of 3D finite element analyses, which implicitly accounts for local buckling of the steel tube, transverse interaction between steel and concrete infill, and confinement of the concrete infill.
Lu et al. (2006)	RCFT cross-sections	Obtained M-ϕ curves and interaction P-M_u diagrams, which accounted for residual stresses in the steel and confinement effects in concrete, as well as the material nonlinearity.
Choi et al. (2006)	RCFT cross-sections	Developed a parametric study to determine the P-M interaction diagram varying with the b/t and fc'/Fy ratios.
Kim and Kim (2006)	RCFT beam-columns	Compared fiber-based cyclic M-ϕ and force-displacement (F-Δ) curves with those obtained experimentally.
Liang (2008)	RCFT cross-sections	Determined P-M interaction diagrams for short CFT beam-columns assuming material nonlinearity. Fiber element results are compared with experimental data and existing solutions. Evaluated the influence of steel ratios, fc' and Fy.

The results shown in this paper were aimed at assessing primarily the overall behavior and stability effects on composite CFT structural elements as a prelude to a large full-scale testing program. Fiber analysis results were obtained with the software OpenSees (Makena and Fenves, 1999), which confinement effects, local buckling, member slenderness and instability effects are being predicted.

An overview of nonlinear fiber element analysis

Fiber element analysis is a numerical technique which models a structural element by dividing it into a number of two-end frame elements, and by linking each boundary to a discrete cross-section with a grid of fibers (Figure 1). The material stress-strain response in each fiber is integrated to get stress-resultant forces and rigidity terms, and from these, forces and rigidities over the length are obtained through finite element interpolation functions which must satisfy equilibrium and compatibility conditions.

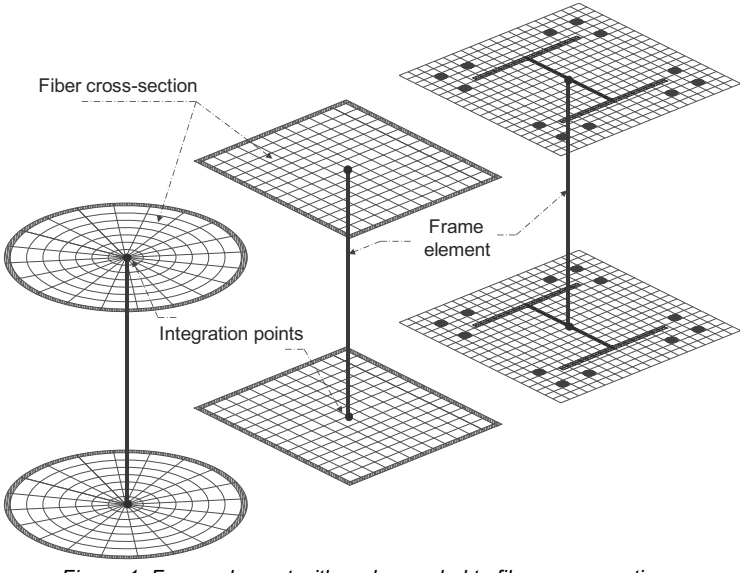


Figure 1. Frame element with ends coupled to fiber cross-sections

There are several advantages which justify the use of fiber analysis. Some of these advantages include but are not limited to their ability to handle:

- Complex cross-sections. A fiber cross-section can have any general geometric configuration formed by subregions of simpler shapes; geometric properties of the more complex section are calculated through the numerical integration.
- Tapered elements. Since the length of the fiber is not considered, the cross-section defined at each of the two ends can be different, and therefore, the response can be roughly estimated. Precision can be increased with more integration points.
- Complex strength-strain behavior. Since each fiber can have any stress-strain response, this technique allows modeling nonlinear behavior in steel members (steel σ–ε and residual stresses), reinforced concrete members (unconfined and confined concrete σ–ε, and steel reinforced σ–ε), and composite members.
- Accuracy and efficiency. Since each fiber is associated to a given uniaxial stress-strain (σ–ε) material response, higher accuracy and more realistic behavior effects can be captured in a fiber-based model than in a frame-based model, and at less computing time than for a 3D finite-based model.

As described previously, the uniaxial σ–ε curve can directly account for the material nonlinearity in monotonic or cyclic loads or displacements, and the residual stresses in the structural steel members. However, some researchers have calibrated, based on experimental or analytical 3D finite-based results (i.e. Varma et al., 2004; Tort and Hajjar, 2007), the uniaxial σ–ε to account for additional behavior effects like:

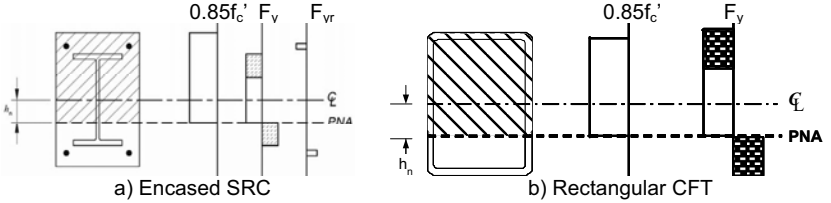
- Confinement effects in the concrete due to either steel reinforcement (as in RC or SRC cross-sections) or a steel tube (as in CFT cross-sections). Concrete confinement in CFT elements remain meanwhile the steel-concrete contact is hold.
- Local buckling in steel tubes through a degradation of the compressive σ–ε beyond the corresponding strain (ε_{lb}) when local buckling take place. Local buckling in CFT elements can be reached when the steel is highly stressed and the steel-concrete contact is lost.

Stability effects through geometric nonlinearity and initial imperfections can be captured directly with the frame-based analysis. In turn, slip between concrete and steel have been modeled in the frame-based formulation by adding degrees-of-freedom (i.e. Hajjar et al., 1998, Aval et al., 2002; Tort and Hajjar, 2007).

Stress-strain modeling

Fiber analyses are obviously sensitive to the assumptions in the stress-strain curves. Consequently, several research studies have been conducted on this topic to predict more "realistic" responses.

The current AISC (2005) specification allows the use of strain compatibility and fully-plastic stress distribution methods to calculate the cross-section strength. The plastic distribution method (Roik and Bergmann, 1992) basically assumes that each component in cross-section has reached the maximum plastic stress (Figure 2).



a) Encased SRC b) Rectangular CFT

Figure 2. Fully-plastic stress distribution in composite cross-sections

While very useful and accurate for design purposes, the plastic distribution approach can only match the ultimate strength of the cross-section. When the entire moment-curvature (or load-deformation) behavior is of interests, more complex uniaxial stress-strain curves are needed. These include strain compatibility approaches to model reinforced concrete (i.e. Kent and Park, 1971; Mander et. al., 1988), steel (i.e. Menegotto and Pinto, 1973), CFT (i.e. Collins and Mitchell, 1990; Sakino and Sun, 1994; Chang and Mander, 1994; Nakahara and Sakino, 1998; Susantha et al., 2001), and SRC members (similar to those used for RC and steel).

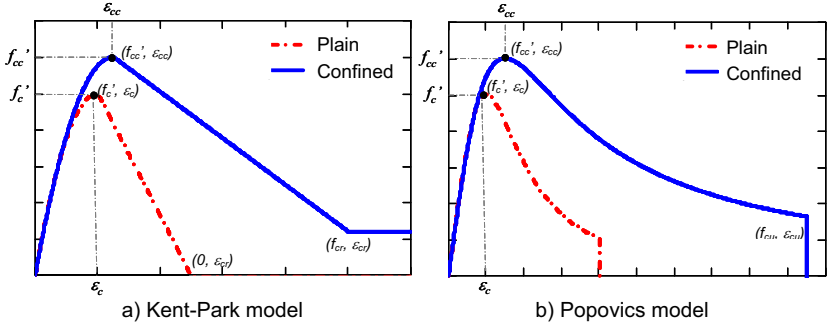
The concrete model proposed by Kent and Park (1971) is defined by a curve up to the peak strength (Equation 1) followed by a descending line and finally constant beyond

some residual stress (f_{cr}) and strain (ε_{cr}); the values f_c' and $\varepsilon_c=2f_c'/E_c$ used in this equation for plain concrete are replaced by f_{cc}' and ε_{cc} in confined concrete (Figure 3.a).

$$\sigma(\varepsilon)=f_c'\left(\frac{2\varepsilon}{\varepsilon_c}-\left(\frac{\varepsilon}{\varepsilon_c}\right)^2\right) \tag{1}$$

The concrete model proposed by Popovics (1973) is a continuous σ–ε curve in terms of the peak strength and a empirical coefficient $n=E_c/(E_c-f_c/\varepsilon_c)$. Based on this equation, Mander *et al.* (1988) proposed an approach to estimate the confinement parameters f_{cc}', ε_{cc}, ε_{cu} that best fit the σ–ε response of rectangular and circular reinforced concreted columns confined by stirrups and spirals (Equation 2, Figure 3.b).

$$\sigma(\varepsilon)=f_{cc}'\left(\frac{\varepsilon}{\varepsilon_{cc}}\right)\left(\frac{n}{n-1+(\varepsilon/\varepsilon_{cc})^n}\right)$$
$$\varepsilon_{cc}=\varepsilon_c\left[1+5\left(\frac{f_{cc}'}{f_c'}-1\right)\right] \tag{2}$$



a) Kent-Park model b) Popovics model

Figure 3. σ–ε curves in plain and confined concrete

Based on empirical data and its calibration with an analytical study, Sakino and Sun (1994) proposed uniaxial σ–ε models for both concrete (Equation 3, Figure 4) and steel (Figure 5) for circular and rectangular CFT elements that account for confinement, local buckling and biaxial stresses. Equation 3 describes the σ–ε curve for concrete proposed by Sakino and Sun (1994), which is in terms of the effective hoop stresses (σ_{re}) and the peak concrete strength.

$$\sigma(\varepsilon)=f_{cc}'\left(\frac{V(\varepsilon/\varepsilon_{cc})+(W-1)(\varepsilon/\varepsilon_{cc})^2}{1+(V-2)(\varepsilon/\varepsilon_{cc})+W(\varepsilon/\varepsilon_{cc})^2}\right) \tag{3}$$

Where: $V=\dfrac{E_c\varepsilon_{cc}}{f_{cc}'}$ $W=1.5-0.0171f_c'(MPa)+2.39\sqrt{\sigma_{re}(MPa)}$ (3.a)

And the effective hoop stresses (σ_{re}) and the peak strength values are defined by:

For circular CFTs:

$$\sigma_{re} = \frac{0.0677 F_y}{D/t - 2}$$

$$f_{cc}' = f_c' + \frac{1.558 F_y}{D/t - 2}$$

$$\varepsilon_{cc} = \begin{cases} \varepsilon_c \left[1 + 4.7 \left(\frac{f_{cc}'}{f_c'} - 1 \right) \right] & if \quad f_{cc}' < 1.5 f_c' \\ \varepsilon_c \left[3.35 + 20 \left(\frac{f_{cc}'}{f_c'} - 1.5 \right) \right] & if \quad f_{cc}' \geq 1.5 f_c' \end{cases}$$

For rectangular CFTs:

$$\sigma_{re} = \frac{2(b/t - 1) F_y}{(b/t - 2)^3}$$

$$f_{cc}' = f_c' \qquad (3.b)$$

$$\varepsilon_{cc} = \varepsilon_c = 0.94 x 10^{-3} \left(f_c'(MPa) \right)^{0.25}$$

Figure 4 shows σ–ε curves obtained with the Sakino and Sun model in a 5 ksi strength concrete that is confined by circular and rectangular steel tubes with 50 and 100 width-to-thickness ratios (D/t, b/t). As shown in this figure, confinement improves strength and ductility in circular CFTs and just ductility in rectangular CFTs.

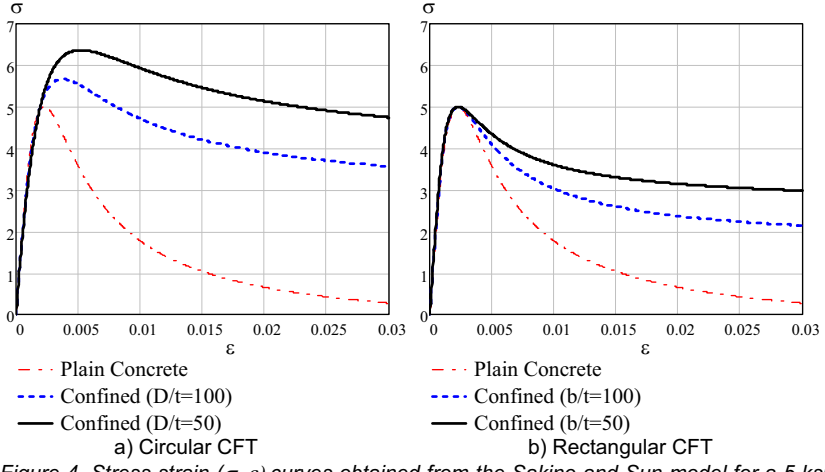
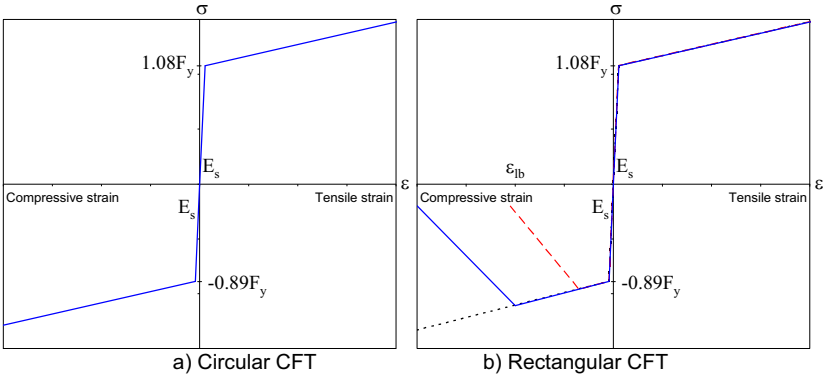


Figure 4. Stress-strain (σ–ε) curves obtained from the Sakino and Sun model for a 5 ksi strength concrete confined by a steel tube with different width-to-thickness ratios.

Conversely, steel tubes can be modeled through an unsymmetrical σ–ε curve to satisfy the Von Misses yield criteria with biaxial stresses. Depending on the b/t ratio, local buckling in rectangular tubes can be handled by a descending branch of the σ–ε curve at a critical strain (ε_{lb}). A careful calibration of the experimental data is needed to obtain the strain ε_{lb} when local buckling takes place. This model postulates that ε_{lb} in circular tubes is reached at high values of strain, and therefore, local buckling effects can be neglected; this approach is tied to the Japanese design requirements for b/t ratios which basically preclude this failure mode.



a) Circular CFT b) Rectangular CFT

Figure 5. Stress-strain (σ–ε) for the steel tubes used with the Sakino and Sun's model

Fiber analysis

As originally described, this study intends to obtain the best prediction in the strength and ductility of a set of large full-scale circular and rectangular CFT beam-columns. The results shown in this section correspond to the following specimens.

1) CCFT20x0.25-5ksi, which is a circular CFT cross section integrated by an HSS20x0.25 steel tube (A500 Gr. B, R_y=1.4, F_y=42ksi, R_u=1.3, F_u=58ksi) filled with 5 ksi strength concrete. The D/t ratio of this section is 86.0, which is approaching the limit permitted for design in the 2005 AISC specification and 2005 AISC seismic provisions ($D/t=0.15E_s/F_y$=103.6), and well beyond that proposed for the 2010 AISC seismic provisions ($D/t=0.075E_s/F_y$=51.8).

2) RCFT20x12x0.3125-5ksi, which is a rectangular CFT cross section integrated by an HSS20x12x0.3125 steel tube (A500 Gr. B, R_y=1.4, F_y=46ksi, R_u=1.3, F_u=58ksi) filled with 5 ksi strength concrete. Similarly, the section b/t ratio is 65.7, which is higher than the limits in the 2005 AISC specification ($b/t=2.26\sqrt{(E_s/F_y)}$=56.7) and the one proposed for the 2005 AISC seismic provisions ($b/t=\sqrt{(2E_s/F_y)}$=35.5).

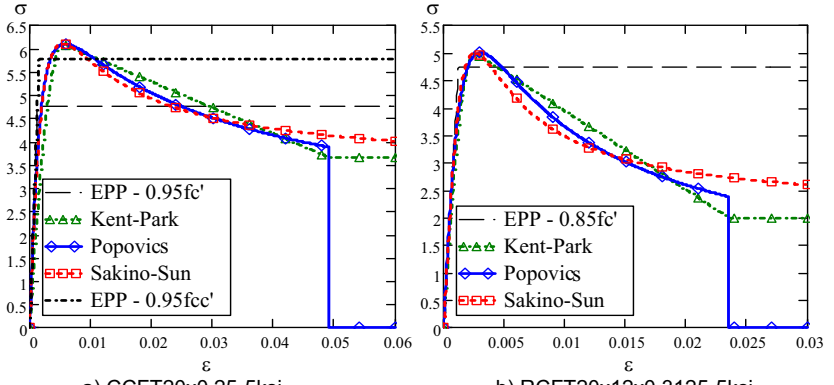
The uniaxial σ–ε models used for concrete in the fiber analysis technique are show in the Figure 6 and summarized in the Table 2 and Table 3. The confined concrete strength (f_{cc}') provided by the tubes were obtained with the equation stated in 3.b.

Table 2. Concrete parameters used in the CCFT20x0.25-5ksi specimen

	Peak strength		Ultimate strength	
Model	Stress	Strain	Stress	Strain
EPP-0.95f_c'	0.95f_c'=4.75 ksi	0.95f_c'/E_c=0.0012	0.95f_c'=4.75 ksi	NA
Kent-Park	f_{cc}'=6.1 ksi	ε_{cc}=0.0054	f_{cr}=0.6f_{cc}'=3.6 ksi	ε_{cr}=9ε_{cc}=0.049
Popovics	f_{cc}'=6.1 ksi	ε_{cc}=0.0054	NA	ε_{cu}=9ε_{cc}=0.049
Sakino-Sun	f_{cc}'=6.1 ksi	ε_{cc}=0.0053	NA	NA
EPP-0.95f_{cc}'	0.95f_{cc}'=5.78 ksi	0.95f_{cc}'/E_c=0.0015	0.95f_{cc}'=5.78 ksi	NA

Table 3. Concrete parameters used in the RCFT20x12x0.3125-5ksi specimen

	Peak strength		Ultimate strength	
Model	Stress	Strain	Stress	Strain
EPP-0.85f_c'	0.85f_c'=4.25 ksi	0.85f_c'/E_c=0.0011	0.85f_c'=4.25 ksi	NA
Kent-Park	f_c'=5.0 ksi	ε_c=2f_c'/E_c=0.0026	f_{cr}=0.4f_{cc}'=2.0 ksi	ε_{cr}=9ε_c=0.0234
Popovics	f_c'=5.0 ksi	ε_c=2f_c'/E_c=0.0026	NA	ε_{cu}=9ε_c=0.0234
Sakino-Sun	f_c'=5.0 ksi	ε_c=2f_c'/E_c=0.0026	NA	NA



a) CCFT20x0.25-5ksi b) RCFT20x12x0.3125-5ksi

Figure 6. Uniaxial σ–ε models used in the concrete fibers

On the other hand, the steel was modeled with an unsymmetrical elastoplastic σ–ε with hardening effects (EPH) as described in Figure 5, except when the concrete was assumed elastic-perfectly-plastic (EPP) in which the steel was assumed as well symmetric EPP (Table 4). The overstrength ratios of the nominal yield stress (R_y=1.4) and ultimate stress (R_u=1.3) were adopted from the AISC seismic provisions (2005). Note that in the elastoplastic with hardening model (EPH) for the RCFTs, a local buckling strain (ε_{lb}) was assumed equal to 25 times de compressive yielding strain (ε_{yc}); this assumption will be validated and calibrated experimentally in the future.

Table 4. Steel parameters used in the fiber analysis

Specimen →	CCFT20x0.25-5ksi		RCFT20x12x0.3125-5ksi	
Model →	EPP	EPH	EPP	EPH
Tensile ultimate σ_u	R_uF_u=75.4 ksi	1.08R_uF_u=81.4 ksi	R_uF_u=75.4 ksi	1.08R_uF_u=81.4 ksi
Tensile ultimate ε_u	100ε_y=0.20	100ε_y=0.22	100ε_y=0.22	100ε_y=0.24
Tensile yield σ_y	R_yF_y=58.8 ksi	1.08R_yF_y=63.5 ksi	R_yF_y=64.4 ksi	1.08R_yF_y=69.6 ksi
Tensile yield ε_y	R_yF_y/E_s=0.002	1.08R_yF_y/E_s=0.0022	R_yF_y/E_s=0.0022	1.08R_yF_y/E_s=0.0024
Comp. yield σ_{yc}	R_yF_y=-58.8ksi	0.89R_yF_y=-52.3 ksi	R_yF_y=-64.4 ksi	0.89R_yF_y=-57.3 ksi
Comp. yield ε_{yc}	R_yF_y/E_s=-0.002	0.89R_yF_y/E_s=-0.0018	R_yF_y/E_s=-0.0022	0.89R_yF_y/E_s=-0.002
Local buckling strain	NA	NA	NA	ε_{lb}=80ε_{yc}=-0.16
Comp. ultimate σ_{uc}	R_uF_u=-75.4 ksi	0.89R_uF_u=-67.1 ksi	R_uF_u=-75.4 ksi	NA
Comp. ultimate ε_{uc}	100ε_{yc}=-0.20	100ε_y=-0.18	100ε_y=-0.22	NA

Moment-curvature of the cross-section

Figure 7 shows, for the postulated uniaxial $\sigma-\varepsilon$ models, the monotonic and cyclic moment-curvature (M/M_o vs. ϕ) results obtained for the circular CFT cross-section with an initial compression $P=0.2P_o$. In this figure, M_o is the pure bending strength (point B in AISC-05), and P_o is the pure compression strength (point A in AISC-05); As observed, there are low differences regarding the moment strength (EPP $M_{max}=1.24M_o$ vs. others $M_{max}=1.34M_o$), but very different curvature ductility and both strength and stiffness degradation. Monotonic and envelope cyclic differences at high curvatures are caused by the degradation model proposed by Karsan and Jirsa (Makena and Fenves, 1999) that is implemented in the OpenSees software when unloading and reloading cyclically.

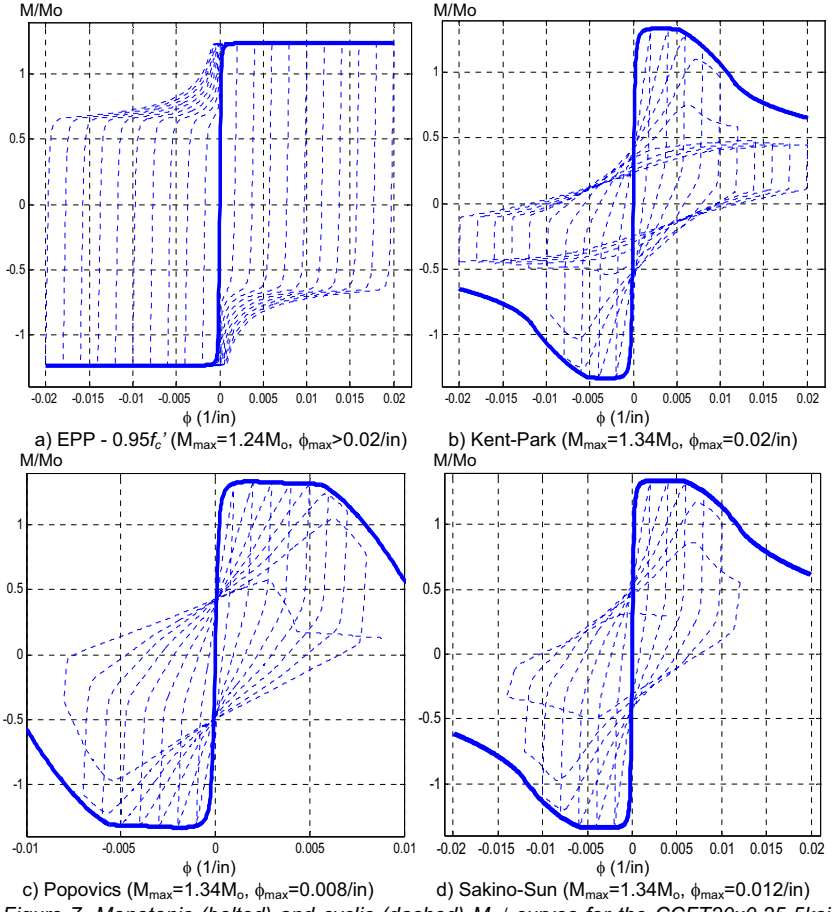
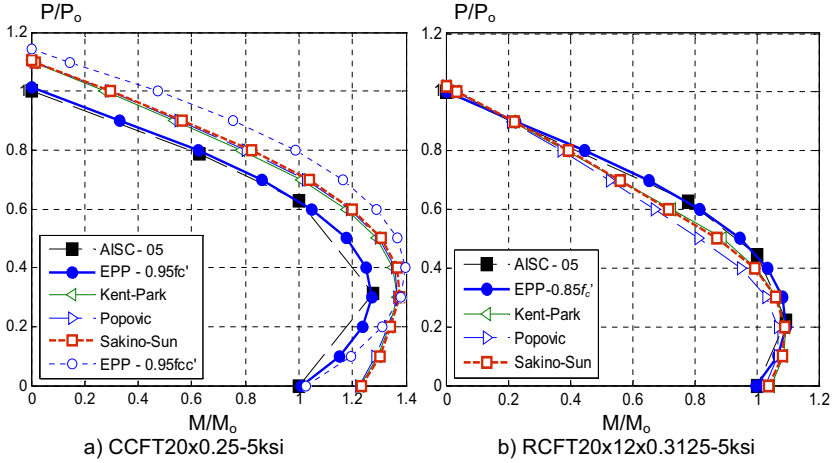


Figure 7. Monotonic (bolted) and cyclic (dashed) M-ϕ curves for the CCFT20x0.25-5ksi cross-section with constant compression force $P=0.2P_o$.

P-M interaction diagrams of the cross-section

The P-M interaction diagram is, by definition, the curve or surface outlined by the axial load and bending moment associated to a desired target (strain, curvature, maximum strength, etc.). In reinforced concrete members, this target is generally defined in terms of the maximum concrete compressive strain, which is usually taken as ε_c=0.003 for unconfined concrete. This target intends in reality to capture the maximum cross-section strength, which can also be directly taken from the M-ϕ curves.

Based on a maximum strength target from M-ϕ curves, Figure 9 shows the P-M interaction surfaces for both proposed CFT cross-sections. The strength obtained with the fully-plastic stress distribution equations (as stated in the AISC Design Examples, 2005, points A to E), is also illustrated in this figure. As noticed in this figure, AISC equations (which are based on the fully-plastic stress distribution) have a good prediction of what is expected based on the strain distribution approach with complex uniaxial σ–ε models.

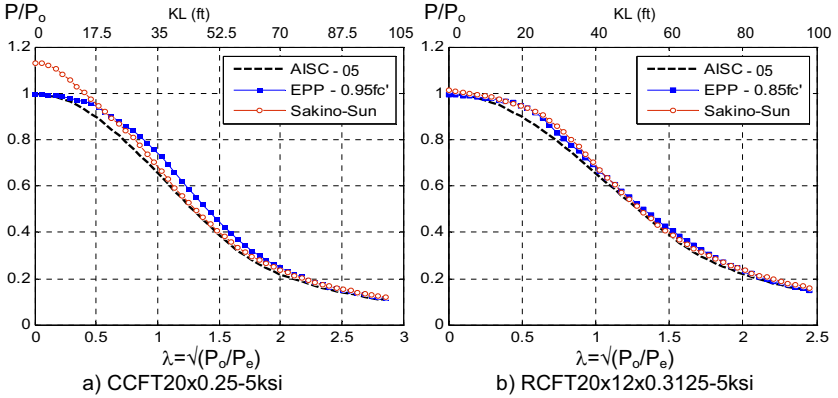


a) CCFT20x0.25-5ksi b) RCFT20x12x0.3125-5ksi

Figure 8. P-M interaction diagrams for the CFT cross-sections with different σ–ε models.

Column curves

Stability effects can be only captured modeling the length, initial imperfections, and a good discretization of the frame elements such that more integration points allow that both P-Δ and p-δ second order effects are considered. Figure 9 shows the results for columns with both circular and rectangular CFT cross-sections, and obtained from the fiber analyses and AISC-05. These curves highlight the benefits of composite columns, with an inelastic buckling range (λ<1.5) that includes columns with effective lengths (KL) up to 52.5 ft in the CCFT and 60 ft in the RCFT. Besides, note that fiber analysis results predicted Euler behavior (λ>1.5), which is reduced by a 0.877 factor in the AISC specifications to account for geometric imperfection effects. Small differences between AISC and fiber analysis with EPP are due to residual stresses in the structural steel, which are implicitly in AISC but neglected in the fiber-based results.

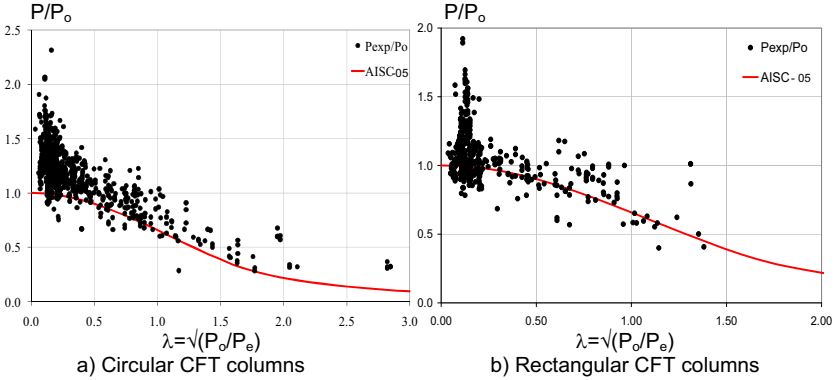


a) CCFT20x0.25-5ksi b) RCFT20x12x0.3125-5ksi

Figure 9. Column curves obtained with AISC (2005) and fiber analysis.

According with the CCFT results, Sakino-Sun model exhibits (due to the f_{cc}' parameter in CCFTs only) a higher strength for short columns (about λ<0.5, KL=17.5 ft, KL/D=10.5), which concurred somehow with the European EC-4-2004 (λ=0.5) and Japanese AIJ-2001 (KL/D=12) code limits regarding the allowed overstrength due to confinement effects in circular CFT columns; AISC-05 uses the 0.95 factor in the concrete strength ($0.95f_c'$) to account for this confinement effects.

This overstrength is as well exhibited in experimental results. Figure 10 illustrates the maximum compression strength obtained experimentally (P_{exp}) in composite CFT columns, which is normalized with the pure compression strength (P_o) and plotted vs. the slender parameter (λ) as specified in the 2005 AISC specification; The AISC-05 column curve is also plotted in this figure. These empirical results were obtained from databases collected by Aho and Leon (1997), Kim and Leon (2005), and Goode (2007). As observed in this figure, the overstrength is highly impacting short columns mainly in both circular and rectangular CFT columns, with high dispersion though.

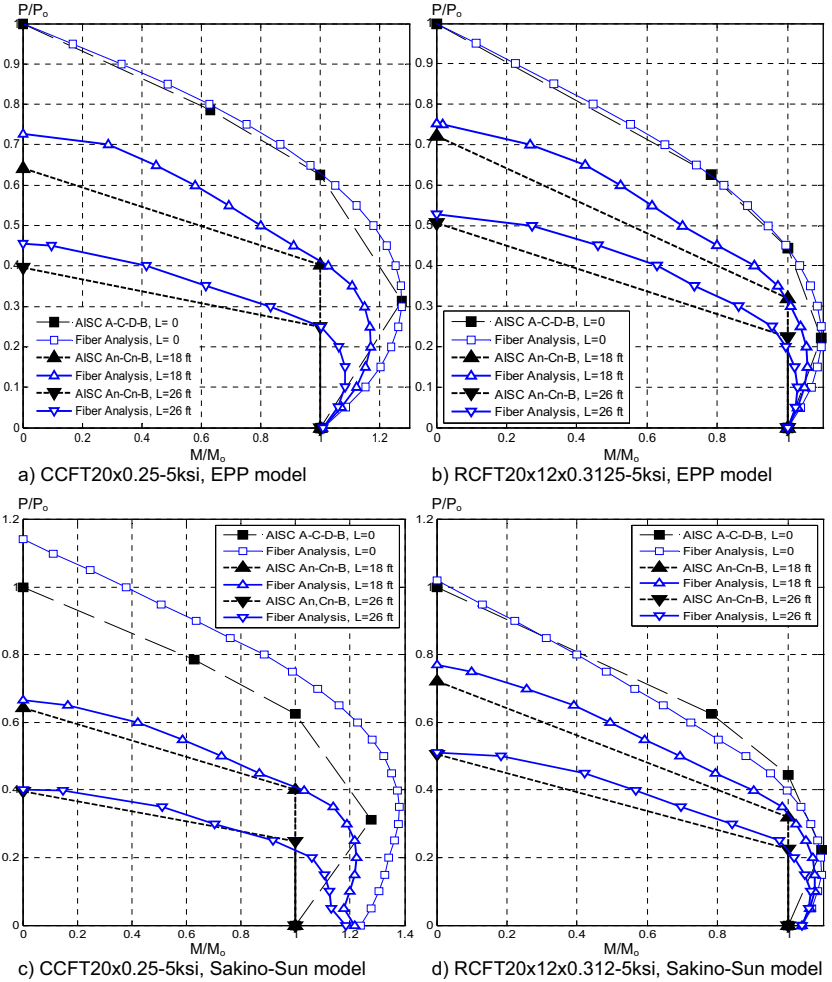


a) Circular CFT columns b) Rectangular CFT columns

Figure 10. Comparison between the AISC column curve and experimental results

P-M interaction diagrams of the beam-column elements

Figure 11 illustrates the beam-column P-M interaction diagrams obtained with fiber analysis for the EPP and Sakino-Sun models. The postulated beam columns have the previously described circular and rectangular CFT cross sections, lengths of L=18 ft and L=26 ft, fixed-free boundary conditions (K=2), and L/500 initial out of plumbness. The corresponding AISC simplified bilinear P-M diagram (AISC A_n-C_n-B) proposed for slender beam-columns, as well as the cross-section strength based on fiber analysis and the 2005 AISC specification (AISC A-C-D-B) are also compared in this figure.



a) CCFT20x0.25-5ksi, EPP model

b) RCFT20x12x0.3125-5ksi, EPP model

c) CCFT20x0.25-5ksi, Sakino-Sun model

d) RCFT20x12x0.312-5ksi, Sakino-Sun model

Figure 11. P-M interaction diagrams for the composite CFT beam columns

According to these results, AISC simplified bilinear interaction surface is a conservative lower bound of the maximum expected flexural-compressive strength. Note again that confinement induces higher compressive and flexural strength at the cross-section level and short beam-columns (λ<0.5), but such compressive overstrength vanished for intermediate beam-columns (0.5<λ<1.5) and long beam-columns (λ>1.5).

Lateral force-displacement curves

Expected lateral force (F) vs. the lateral drift (Δ/L) obtained from the fiber analysis using Sakino-Sun model on the postulated CFT beam-columns are shown in Figure 12; these beam-columns have an initial L/500 out-of-plumbness, $0.2P_o$ constant axial compression force, and then they are subjected to cyclic lateral displacement (Δ) with a 1% drift (Δ/L) increment. As a consequence of the local buckling degradation beyond the strain ε_{lb} modeled in the RCFT tubes, the displacement ductility is lower than that obtained in the CCFT beam-columns. However, as mentioned before, the definition of the strain at local buckling was assumed without an experimental calibration and, since this parameter is very sensitive in the final ductility, this variable may change accordingly.

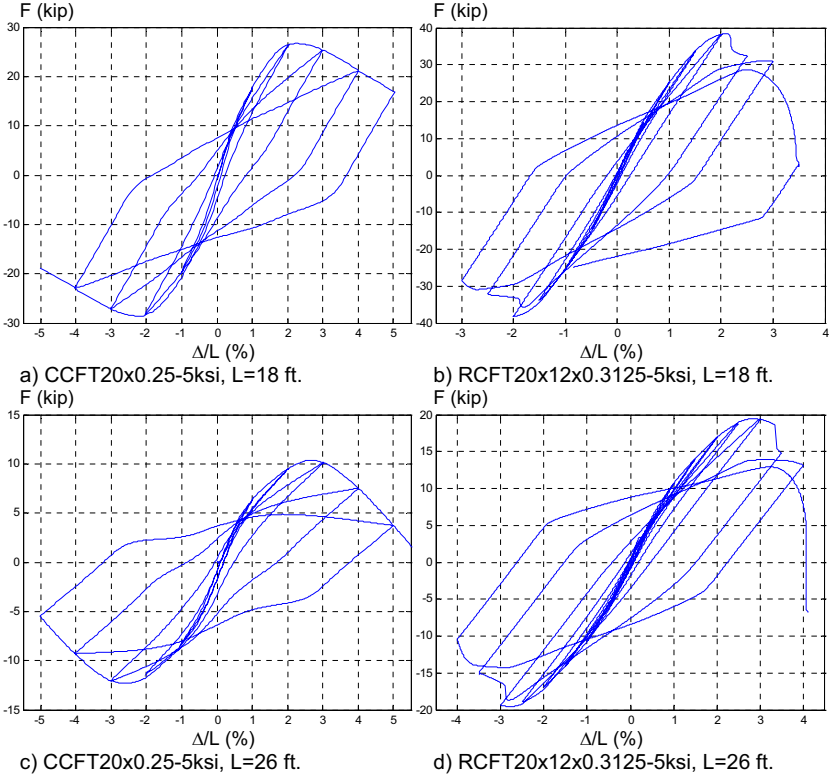


Figure 12. Expected lateral force (F) vs. the lateral drift (Δ/L) using Sakino-Sun model

Conclusions

The benefits on the fiber element analysis technique were briefly described. Based on this technique, some results were obtained and shown emphasizing some issues in the structural behavior of composite cross-sections and composite beam-column elements, such as the effects due to the compressive force, material nonlinearity (stress-strain model), concrete confinement, steel local buckling, triaxial stresses, initial imperfection and geometric nonlinearity effects. Fiber-based analytical results were also compared with those obtained with the AISC (2005) Specification.

As described previously, fiber analysis is a very useful technique to predict the overall behavior of composite beam-column elements. However, the accuracy on the results is highly dependable on the stress-strain model coupled to the fiber cross-section. Simple stress-strain models predict reasonably the ultimate strength; however, more complex material models should be assumed to predict ductility and high displacements such that damage is considered. On the other hand, most of the nonlinearity sources (like strength/stiffness degradation, confinement, local buckling and triaxial stresses effects) have to be calibrated with experimental results and/or more complex analytical techniques in order to incorporate them later on in the uniaxial stress-strain used in the fiber-based model.

More complex techniques, like 3D finite element analysis, can deal with these sources in a straightforward manner. Definition of contact surfaces between concrete and steel can consider a more realistic interaction within these materials; therefore, confinement, local buckling and triaxial stresses can be directly integrated in the behavior (with no influence on the material model). More computing resources and time will be required though.

References

Aho, M. and Leon, R. (1997), “A database for encased and concrete-filled columns”, Master Thesis, School of Civil and Environmental Engineering, Georgia Institute of Technology, Atlanta, Georgia.

AISC (2005), “Specifications for structural steel buildings”. ANSI/AISC 360-05. Chicago, IL, USA.

AISC Commentary (2005), “Commentary on the specifications for structural steel buildings”. AISC. Chicago, IL, USA.

AISC Design Examples (2005), “Design examples. Version 13.0”, CD-ROM included in the Steel Construction AISC Manual. AISC. Chicago, IL, USA.

AISC Seismic Manual (2005), “Seismic Provisions for structural steel buildings”. ANSI/AISC 341-05. Chicago, IL, USA.

Aval, S. Saadeghvaziri, M. and Golafshani, A. (2002). “Comprehensive composite inelastic fiber element for cyclic analysis of concrete-filled steel tube columns”. Journal of Engineering Mechanics, Vol. 128, No. 4, ASCE, ISSN 0733-9399. pp. 428-437.

Choi, Y. Foutch, D. LaFave, J. (2006). “New approach to AISC P–M interaction curve for square concrete filled tube (CFT) beam–columns”. Journal of Engineering Structures. Vol. 28. pp. 1586–1598.

Elnashai, A. and Elghazouli, A. (1993). “Performance of composite steel/concrete members under earthquake loading. Part I: analytical model”. Journal of Earthquake Engineering and Structural Dynamics. Vol. 22, pp. 315-345.

El-Tawil, S. and Deierlein, G. (1999). “Strength and ductility of concrete encased composite columns”. Journal of Structural Engineering, Vol. 125, No. 9, September, 1999. ASCE, ISSN 0733-9445/99/1009–1019. Paper No. 19768.

Goode C. (2007), “ASCCS database of concrete-filled steel tube columns”. ASCCS, http://web.ukonline.co.uk/asccs2/

Hajjar, J. and Gourley, B. (1996). “Representation of concrete-filled steel tube cross-section strength”. Journal of Structural Engineering. Vol. 122, No. 11. pp. 1327–36.

Hajjar, J. Schiller, P. and Molodan, A. (1998). ‘‘A distributed plasticity model for concrete-filled steel tube beam-columns with interlayer slip’’ J. of Engineering Structures, Vol. 20, No. 8, pp. 663–676.

Izzuddin, B. Karayannis, C. and Elnashai, A. (1993). “Advanced nonlinear formulation for reinforced concrete beam-columns”. Journal of Structural Engineering. ASCE. Vol. 120. No. 10. pp. 2913-2934.

Kim, D. and Leon, R. (2005), “A database for composite columns”, Master Thesis, School of Civil and Environmental Engineering, Georgia Institute of Technology, Atlanta, Georgia.

Kim, J. and Kim, T. (2006). “Seismic performance of in-filled steel-concrete composite columns using fiber analysis method”. Journal of Key Engineering Materials. Vol. 326-328. pp 1821-1824.

Liang, Q. (2008). “Nonlinear analysis of short concrete-filled steel tubular beam–columns under axial load and biaxial bending’. Journal of Constructional Steel Research. Vol. 64. pp. 295–304.

Liew, R. and Chen, H. (2004). “Explosion and Fire Analysis of Steel Frames Using Fiber Element Approach”. J. of Structural Engineering, Vol. 130, No. 7, ASCE, ISSN 0733-9445. pp. 991-1000.

Lu, F.W. Li, S.P. and Sun, G. (2006). “A study on the behavior of eccentrically compressed square concrete-filled steel tube columns”. Journal of Constructional Steel Research.

McKenna, F. and Fenves, G. (1999) “Open system for earthquake engineering simulation: OpenSees version 1.7.0”. Pacific Earthquake Engineering Research Center. University of California, Berkeley.

Nishiyama, I. Morino, S. Sakino, K. Nakahara, H. Fujimoto, T. Mukai, A. Inai, E. Kai, M. Tokinoya, H. Fukumoto, T. Mori, K. Yoshioka, K. Mori, O. Yonezawa, K. Uchikoshi, M. and Hayashi, Y. (2002), “Summary of research on concrete-filled structural tube column system carried out under the US-Japan cooperative research program on composite and hybrid structures”. Building Research Institute (BRI), Report No. 147. ISSN 0453-4972.

Park, R. and Pauley, T. (1975). “Reinforced concrete structures”. Wiley-Interscience. ISBN 0-471-65917-7. pp. 11-47. USA.

Ricles, J. and Paboojian, S. (1994). “Seismic performance of steel-encased composite columns”. J. of Structural Engineering, Vol. 120, No. 8, ISSN 0733-9445. Paper No. 6828. pp. 2474-2494.

Roik, K. and Bergmann, R. (1992), “Composite columns”. Constructional steel design. Dowling, P. Harding, J. and Bjorhovde, R. (eds.). Elsevier Sc. Publ. ISBN 1-85166-895-0. New York. pp. 443–470.

Spacone, E. and Filippou, F. (1995). “A fiber beam element for nonlinear dynamic analysis of reinforced concrete structures”. Proceedings of the 10th Conference, Engineering Mechanics, University of Colorado at Boulder, Colorado, pp. 818-821.

Taucer, F. Spacone, E. and Filippou, F. (1991). “A fiber beam-column element for seismic response analysis of reinforced concrete structures”. Report No. UCB/EERC-91/17, College of Engineering, University of California at Berkeley.

Tomii, M. and Sakino, K. (1979). “Elastoplastic behavior of concrete filled square steel tubular beam–columns”. Architectural Institute of Japan. Vol. 280. pp. 111–20.

Tort, C. and Hajjar, J. (2007). “Reliability-based performance-based design of rectangular concrete-filled steel tube (RCFT) members and frames”. Structural Engineering Report No. ST-07-1. University of Minnesota. Department of Civil Engineering. Minneapolis, MN.

Varma, A. Ricles, J. Sauce, R. and Wu Lu, L. (2004), “Seismic behavior and design of high-strength square concrete-filled steel tube beam columns”. J. of Structural Engin. Vol. 130, No. 2, pp. 169-179.

White, D. (1986). “Material and geometric nonlinear analysis of local planar behavior in steel frames using interactive computer graphics”. Report No. 86-4. Cornell University, Dep. of Struct. Engineering.

STRUCTURAL DESIGN OF CONCRETE FILLED STEEL ELLIPTICAL HOLLOW SECTIONS

Dr Dennis Lam
School of Civil Engineering
University of Leeds, LS2 9JT, UK
e-mail: d.lam@leeds.ac.uk

Miss Nicola Testo
School of Civil Engineering
University of Leeds, LS2 9JT, UK
e-mail: n.testo@leeds.ac.uk

ABSTRACT

This paper presents the behaviour and design of axially loaded elliptical steel hollow sections filled with normal and high strength concrete. The experimental investigation was conducted with three nominal wall thickness (4mm, 5mm and 6.3mm) and different infill concrete cube strengths varied from 30 to 100 MPa. The effect of steel tube thickness, concrete strength, and confinement were discussed together with column strengths and load-axial shortening curves were evaluated. The study is limited to cross-section capacity and has not been validated at member level. Comparisons of the tests results together with other available results from the literature have been made with current design method used for the design of composite circular steel sections in Eurocode 4 and AISC codes. It was found that existing design guidance for concrete filled circular hollow sections may generally be safely applied to concrete filled elliptical steel tubes.

INTRODUCTION

Concrete filled steel tube (CFST) columns are becoming increasingly popular due to the advantages they offered. They are not only considered aesthetically pleasing but can also offer significant improvement in axial capacity without increases in cross-sectional area being required. Elliptical steel hollow sections represent a recent and rare addition to the range of cross-sections available to structural engineers, however, despite widespread interest in their application, a lack of verified design guidance is inhibiting uptake. The use of elliptical steel hollow section (EHS) with concrete infill is new and innovative, not only provides the advantage mentioned above, but also on the basis of both architectural appeal and structural efficiency. The role of the concrete core is not only to resist compressive forces but also to reduce the potential failure of local buckling by the steel sections. Although local buckling of the steel sections is reduced by the presence of the concrete core, local buckling will still occur to some extent. The concrete core will prevent the steel sections buckling inwards and therefore buckling will generally occur by the outwards buckling of the steel tube. In turn, the steel section reinforced the concrete to resist any tensile forces, bending moments and shear forces and provides confinement to the concrete core. Composite members are of significant interest not only for this reason alone but also for their design suitability in seismic zones [Hajjar, 2000] and their inherent fire resistance [Han et al., 2003]. Existing research on EHS

are mainly focused on its behaviour in compression and bending [Gardner and Chan 2007, Chan and Gardner 2007, Zhu and Wilkinson 2006] and also in welded connections [Choo et al 2003, Pietrapertosa and Jaspart 2003, Willibald et al 2006]. Previous research into the structural behaviour and design of concrete filled elliptical hollow sections has been rather limited, with the only reported studies to date by [Zhao et al., 2007]. The results from this study are analysed in this paper.

EXPERIMENTAL STUDY

In order to investigate the behaviour of the elliptical CFSTs, 12 specimens were tested. 150 × 75 mm hot-finished elliptical hollow section (EHS) with 4.0mm, 5.0mm and 6.3mm wall thickness and three nominal concrete strength – C30, C60 and C100 were used for the tests. All specimens were 300mm in length to reduce end effects and to ensure that the specimens behaved as stub columns with little effect from column slenderness. The properties for all the specimens are listed in Table 1.

Table 1: Measured geometric properties of the specimens

Reference	Major axis, outer diameter, 2a (mm)	Minor axis, outer diameter, 2b (mm)	Wall thickness, t (mm)	Steel area, A_s (mm^2)	Concrete area, A_c (mm^2)
150×75×4	150.40	75.60	4.18	1471.5	-
150×75×4-C30	150.40	75.60	4.18	1471.5	7458.6
150×75×4-C60	150.57	75.52	4.19	1475.8	7455.0
150×75×4-	150.39	75.67	4.18	1471.8	7466.0
150×75×5	150.23	75.74	5.08	1773.8	-
150×75×5-C30	150.12	75.65	5.12	1785.5	7133.9
150×75×5-C60	150.23	75.74	5.08	1773.8	7162.8
150×75×5-	150.28	75.67	5.09	1777.1	7154.2
150×75×6.3	148.78	75.45	6.32	2164.1	-
150×75×6.3-	148.78	75.45	6.32	2164.1	6652.3
150×75×6.3-	148.92	75.56	6.43	2202.1	6635.5
150×75×6.3-	149.53	75.35	6.25	2149.1	6700.0

Testing of the composite columns was carried out using a 3000kN capacity ToniPACT testing machine and the experimental set up is shown in Figure 1. Both ends of the specimens were milled flat and capped with rigid steel plate in order to distribute the applied load uniformly over both the concrete and steel section for the composite loaded columns. The specimens were loaded at 50kN intervals at the beginning of the test (i.e. in the elastic region) and at a loading rate of 10kN intervals after the column began to yield, in order to have sufficient data points to delineate the “knee” of the stress-strain curve. A linear variable differential transducer (LVDT) was used to monitor the vertical deformation. All of the operation and the change of loading rate were operated manually and all the readings were recorded when both load and strain had been stabilized. After the immediate drop of the load due to local

buckling, the test continued until excessive deformation of the column was observed. After the test, the specimens were removed, photographed and carefully examined.



Figure 1: Test arrangement and instrumentations

Concrete Properties

Three nominal concrete strengths – C30, C60 and C100 were studied. The concrete was produced using commercially available materials with normal mixing and curing techniques; the three mix designs are shown in Table 2 together with the cube and cylinder strength at test day. The strength development of the concrete was monitored over a duration of 28 days by conducting periodic cube and cylinder tests – the results of the cube tests are illustrated in Figure 2. Additionally, at the time of each series of stub column tests, two further standard cube tests and two standard cylinder tests were performed.

Table 2: Concrete mix proportions (% by weight) and the compressive strength (test day)

Grade	Cement	Fines	Coarse	w/c ratio	Silica fume	Super-plasticiser	f_{cu} (N/mm^2)	f_{ck} (N/mm^2)
C30	1.0	2.5	3.5	0.65	0	0	36.9	30.5
C60	1.0	2.0	3.3	0.40	0	0	59.8	55.3
C100	1.0	1.5	2.5	0.30	0.1	0.03	98.4	102.2

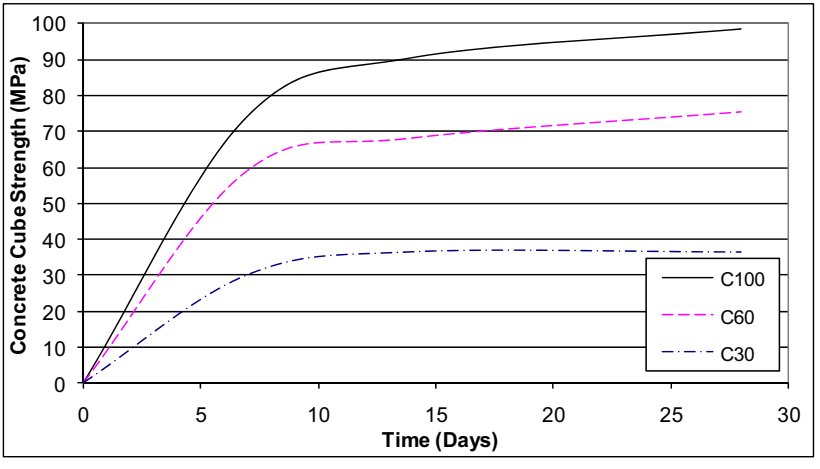


Figure 2: Concrete development strength

Steel Properties

Coupons were cut from the EHS and tested to [EN10002-1 2001] to determine the tensile strength. The coupons were cut form the in the region of maximum radius of curvature (i.e. the flattest portion of the section) and milled to specification. Some flattening of the ends occurred while gripping the specimen but this was well away from the 'neck' of the sample. The results from the coupon tests are summarized in Table 3.

Table 3: Steel properties of the EHS

Specimens	Young's modulus E (N/mm^2)	Yield stress f_y (N/mm^2)	Ultimate strength f_u (N/mm^2)
150×75×4	217500	376.5	513
150×75×5	217100	369.0	505
150×75×6.3	216500	400.5	512

TEST RESULTS

All the specimens were tested under axial compression until failure. The typical failure modes of the composite specimens are shown in Figure 3. For the unfilled EHS, both inward and outward local buckling was observed in the deformed specimen while for the filled tubes, although inward buckling was prevented by the concrete core, outward local buckling is clearly evident in the deformed specimens.



Figure 3: Typical failure mode of the composite EHS

The load vs. end shortening curves from the EHS stub column tests are shown in Figures 4 to 6. The results show the clear advantage of composite EHS columns over their bare (unfilled) EHS counterparts. Overall, it may be observed from Figures 4 to 6 that the stockier EHS tubes with lower concrete strengths have more ductility, though enhancements in load carrying capacity beyond that of the bare steel sections due to concrete filling are more significant for slender sections with higher concrete strengths. The ultimate loads from the stub columns tests $N_{u,Test}$ are presented in Tables 4 with the composite factor, ϕ. The level of strength enhancement (beyond that of the unfilled tubes) can be represented by the composite factor, ϕ, the definition of which is given by Eq. (1). This index provides a quantitative measure of the benefit arising from concrete-filling.

$$\phi = \frac{N_{u,filled}}{N_{u,unilled}} \tag{1}$$

Where,

$N_{u,filled}$ is the ultimate resistance of the concrete-filled elliptical test specimens;
$N_{u,\ unfilled}$ is the ultimate test resistance of the corresponding empty EHS.

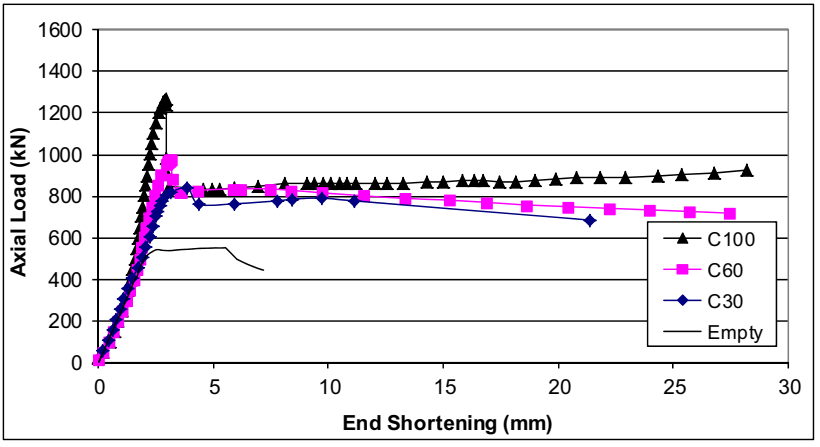


Figure 4: Axial load vs. end shortening curves for 150×75×4 EHS composite columns

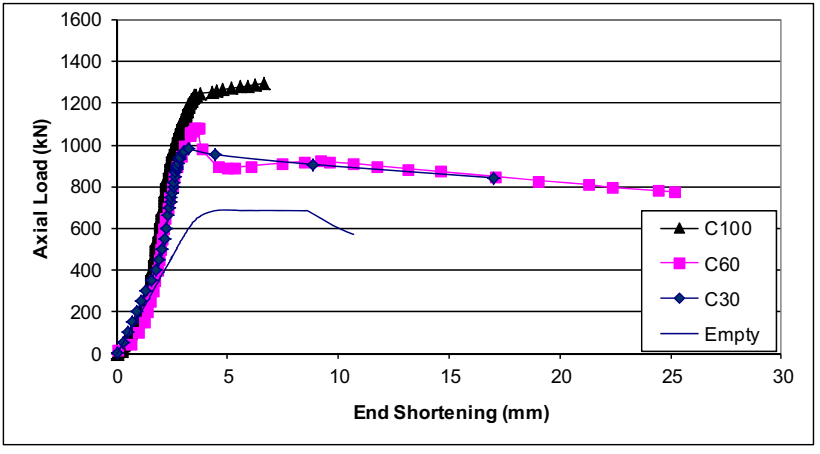


Figure 5: Axial load vs. end shortening curves for 150×75×5 EHS composite columns

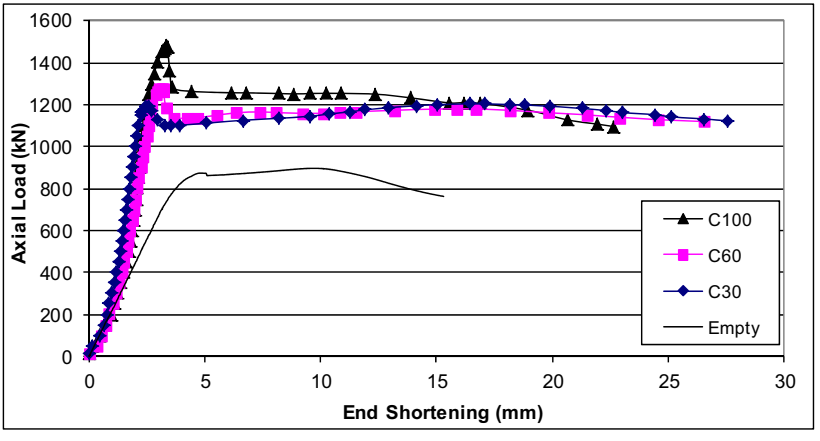


Figure 6: Axial load vs. end shortening curves for 150×75×6.3 EHS composite columns

Table 4: Summary of test results and composite factor, ϕ

Reference	$N_{u, Test}$	Composite factor, ϕ
150×75×4	550.0	1.00
150×75×4-C30	838.6	1.52
150×75×4-C60	974.2	1.77
150×75×4-C100	1264.6	2.30
150×75×5	688.9	1.00
150×75×5-C30	981.4	1.42
150×75×5-C60	1084.1	1.57
150×75×5-C100	1296.0	1.88
150×75×6.3	871.8	1.00
150×75×6.3-C30	1202.9	1.38
150×75×6.3-C60	1280.1	1.47
150×75×6.3-C100	1483.2	1.70

Figure 7 shows the relationship between the composite factor, ϕ and the cube strength of the concrete f_{cu} for the three different tube thicknesses. The results show that, as expected, the concrete contribution ratio increases for the higher concrete strengths, and that the level of enhancement is more significant for the thinner tubes; the 4mm elliptical tube shows a doubling in capacity with the C100 concrete infill.

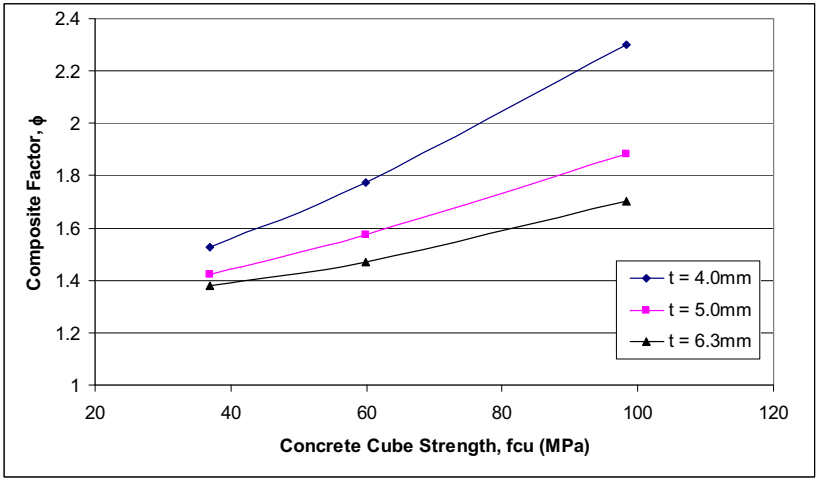


Figure 7: Composite factor vs. concrete cube strength curves

DESIGN CODE

Concrete-filled elliptical hollow sections are not explicitly covered by current design codes. The test results obtained in the present study have been combined with those reported by [Zhao et al., 2007] and compared with existing design guidance for the circular concrete-filled tubes. The codes considered are [EN 1994-1-1 2004] and [AISC 360-05 2005] respectively abbreviated to EC4, and AISC in this paper. The principal differences between the codes relate to the factors that are applied to the individual steel and concrete contributions to the composite resistance. Following the comparisons, design recommendations are made for concrete-filled elliptical hollow sections.

EC4 covers concrete encased and partially encased steel sections and concrete-filled tubes with and without reinforcement. The compressive resistance $N_{u,EC4}$ of concrete-filled steel tubes is given by Eq. (2). This is the latest design code that takes into account increases in concrete capacity due to confinement by the steel sections.

$$N_{u,EC4} = \eta_a A_a f_{yd} + A_c f_{cd}\left(1 + \eta_c \frac{t}{d}\frac{f_y}{f_{ck}}\right) \quad (2)$$

Where,

$N_{u,EC4}$	Ultimate axial capacity of the composite column
f_{cd}	Design compressive strength of the concrete
f_{ck}	Cylinder strength of concrete
f_y	Yield strength of the steel tube
f_{yd}	Design strength of the steel tube

d	Larger diameter of the elliptical steel section
t	Thickness of steel tube
η_c	Coefficient of concrete confinement
η_a	Coefficient of steel confinement

In the AISC code, the compressive resistance of concrete-filled circular hollow sections $N_{u,AISC}$ is given by Eq. (3). The 0.95 factor on the concrete contribution in Eq. (3) reflects the superior performance of concrete-filled CHS over their rectangular counterparts.

$$N_{u,\mathrm{AISC}} = A_s f_y + 0.95 A_c f_{ck} \tag{3}$$

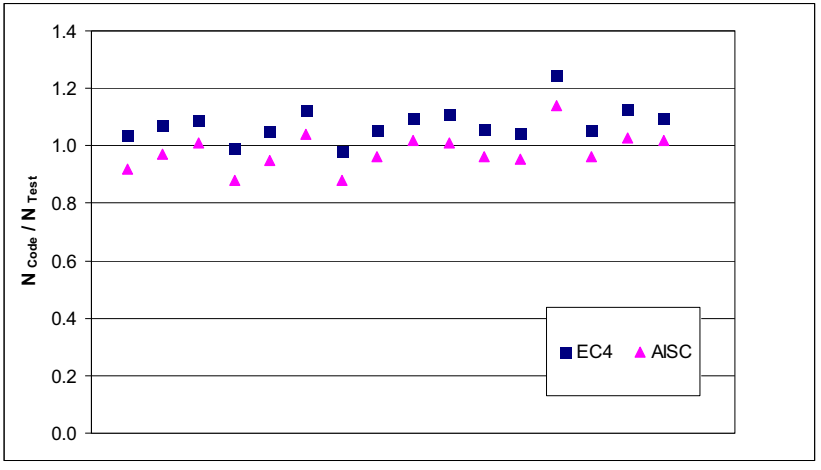


Figure 8: Comparison of code prediction

All the test results presented in this paper have been combined with those reported by [Zhao et al. 2007] and compared with the predictions from the aforementioned design codes. The comparisons, shown in Figure 8 and Table 5 reveal that the ultimate test loads from the 16 concrete-filled EHS specimens are generally over-predicted by the EC4 formulations for concrete-filled CHS by 8% and underestimated by 2% by the corresponding AISC concrete-filled CHS formulations. On the basis of the comparisons, it is recommended that the AISC expression for concrete-filled CHS (Eq. (3)) is most suitable for predicting the resistance of concrete-filled EHS. However, it is clear that the level of confinement and hence the resistance of concrete-filled EHS are related to the aspect ratio of the section and further research to investigate this feature is ongoing.

Table 5: Comparison between test results and codes prediction

Reference	$N_{u,\,Test}$ (kN)	$N_{u,\,EC4}$ (kN)	$\frac{N_{u,EC4}}{N_{u,Test}}$	$N_{u,AISC}$ (kN)	$\frac{N_{u,AISC}}{N_{u,Test}}$
150×75×4-C30	838.6	871.7	1.04	770.1	0.92
150×75×4-C60	974.2	1046.6	1.07	947.3	0.97
150×75×4-C100	1264.6	1379.1	1.09	1279.0	1.01
150×75×5-C30	981.4	977.8	1.00	865.6	0.88
150×75×5-C60	1084.1	1140.7	1.05	1030.8	0.95
150×75×5-C100	1296.0	1459.2	1.13	1350.4	1.04
150×75×6.3-C30	1202.9	1184.6	0.98	1059.5	0.88
150×75×6.3-C60	1280.1	1354.2	1.06	1230.5	0.96
150×75×6.3-C100	1483.2	1630.1	1.10	1511.2	1.02
150×75×4-C60*	1075	1193.1	1.11	1087.9	1.01
150×75×5-C60*	1163	1229.5	1.06	1118.4	0.96
150×75×6.3-C60*	1310	1370.3	1.05	1247.8	0.95
200×100×5-C60*	1598	1991.3	1.25	1819.4	1.14
200×100×6.3-C60*	2068	2181.4	1.05	1989.5	0.96
200×100×8-C60*	2133	2404.7	1.13	2193.3	1.03
200×100×10-C60*	2290	2514.9	1.10	2331.2	1.02
*Test reported by [Zhao et al.,		Mean	1.08	Mean	0.98
		SD	0.061	SD	0.064

CONCLUSIONS

A total of 12 tests – 9 compositely loaded and 3 unfilled elliptical hollow sections have been performed to investigate the compressive behaviour of concrete-filled elliptical hollow sections. The compressive response was found to be sensitive to both steel tube thickness and concrete strength, with higher tube thickness resulting in higher load-carrying capacity and enhanced ductility, and higher concrete strengths improving load-carrying capacity but reducing ductility. The experimental results from the present study were combined with an additional 7 experimental results from literature, and compared with existing code provisions for circular hollow sections. From the comparisons, it may be concluded that existing design rules for concrete-filled CHS may be safely applied to EHS, and that the AISC design expression for CHS provide an accurate prediction of composite EHS behaviour.

ACKNOWLEDGEMENTS

The authors would like to thank Dr Leroy Gardner of Imperial College for his time and help with the research work and Corus for providing the steel specimens used in

this research project. The skilled assistance provided by the technical staff in the School of Civil Engineering at Leeds University is also appreciated.

REFERENCES

AISC 360-05 (2005), Specification for structural steel buildings, American Institute of Steel Construction.

Chan, T. M. and Gardner, L (2008), Compressive resistance of hot-rolled elliptical hollow sections, Engineering Structures, 30, pp. 522 – 532.

Choo, Y.S., Liang, J.X. and Lim, L.V. (2003), Static strength of elliptical hollow section X-joint under brace compression, 10th. Int. Symposium on Tubular Structures, Madrid, Spain, pp. 253 – 258.

EN 10002-1 (2001). Metallic materials – Tensile testing – Part 1: Method of test at ambient temperature, British Standard Institute.

EN 1994-1-1 (2004), Eurocode 4: Design of composite steel and concrete structures - Part-1-1: General rules and rules for buildings, British Standard Institute.

Gardner, L. and Chan, T. M. (2007), Cross-section classification of elliptical hollow sections, Journal of Steel and Composite Structures, 7(3), pp. 185 – 200.

Hajjar, J.F. (2000), Concrete filled steel tube columns under earthquake loads, Progress in Structural Engineering and Materials, 3(1), pp. 72 – 81.

Han, L.H., Yang, Y.E. and Xu, L. (2003), An experimental study and calculation on the fire resistance of concrete-filled SHS and RHS columns, Journal of Constructional Steel Research, 59(4), pp. 427 – 452.

Pietrapertosa, C. and Jaspart, J.-P. (2003), Study of the behaviour of welded joints composed of elliptical hollow sections, 10th. Int. Symposium on Tubular Structures, Madrid, Spain, pp. 601 – 608.

Willibald, S., Packer, J.A. and Martinez-Saucedo, G. (2006), Behaviour of gusset plate connections to ends of round and elliptical hollow structural section members, Canadian Journal of Civil Engineering, 33, pp.373 – 383.

Zhao, X. L., Lu, H. and Galteri, S. (2007). Tests of Elliptical Sections Filled with SCC (Self-Compacting Concrete). Proceedings of the 5th International Conference on Advances in Steel Structures. Singapore, pp. 950 – 955.

Zhu, Y. and Wilkinson, T. (2006), Finite element analysis of structural steel elliptical hollow sections in pure compression, 11th. Int. Symposium on Tubular Structures, Québec City, Canada, pp. 179 – 186.

SEISMIC PERFORMANCE OF COMPOSITE *EWECS* COLUMNS IN NEW HYBRID STRUCTURAL SYSTEM

Fauzan
Department of Civil Engineering
Andalas University
Padang, Indonesia
fauzan@ft.unand.co.id

Hiroshi Kuramoto
Department of Architectural Engineering, Graduate School of Engineering
Osaka University
Suita, Japan
kuramoto@arch.eng.osaka-u.ac.jp

ABSTRACT

This paper presents the results of experimental and analytical studies on Engineering Wood Encased Concrete-Steel (EWECS) composite columns. A total of four specimens with the scale of about two-fifth were tested under combined constant axial load and lateral load reversals. Variables investigated include the type of woody shell connection between column and loading stub and the presence of shear studs. The test results indicated that EWECS columns had excellent hysteretic behavior without severe damage even at large story drift of 0.04 radian. The results also showed that EWECS columns with the type of column-stub connection consisting of woody shell and wood panel attached to stub showed high performance in both capacity and damage limit. In addition, the presence of shear studs on EWECS columns improved the deformation capacity of the column and reduced the damage of woody shell. An analytical study was also performed using fiber section analysis to simulate the behavior of the composite columns.

INTRODUCTION

A new type of hybrid structural system called engineering wood encased concrete-steel (EWECS) structural system has been developed by the authors to solve a problem on the limitation of story number for unfireproof wooden structures that is limited to not more than three stories based on the Building Standard Law of Japan. The proposed structural system consists of EWECS columns and engineering wood encased steel (EWES) beams, as shown in Figure 1. For the first stage of the research program, composite EWECS columns were investigated. The composite column consists of concrete encased steel (CES) core with an exterior woody shell (Figure 1).

Both economical and structural benefits are realized from this type of composite column due to the use of woody shell as column cover. During construction, the woody shell acts as forming for the composite column, decreasing the labor and materials required for construction and, consequently, reducing the construction cost and time. From the structural point of view, the shell improves the structural behavior of the column through its action to provide core confinement and resistance to

bending moment, shear force and column buckling. These advantages make EWECS columns possible as an alternative to SRC columns, which have weaknesses due to difficulty in constructing both steel and reinforced concrete (RC) (Kuramoto et al. 2000, Kuramoto et al. 2002).

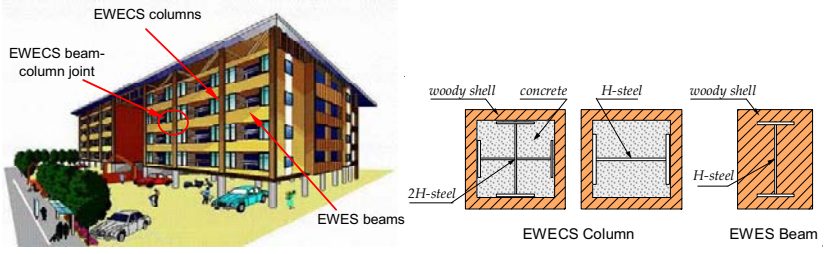


Figure 1 – Schematic view of EWECS structures

In our previous studies (Fauzan et al. 2004, Kuramoto and Fauzan 2005), the structural behavior of an EWECS column using double H-section steel had been investigated to apply to columns subjected to bending moments and shear forces in two directions, such as those in the frame structures. It was found that the EWECS column had a stable spindle-shaped hysteresis characteristic without degradation of load-carrying capacity until the maximum story drift angle, R of 0.05 radian. The results also showed that the presence of woody shell on EWECS columns contributed to flexural capacity by around 12 % in maximum. Furthermore, EWECS columns using single H-section steel, shown in Figure 2, are being developed to apply to columns in one-way moment frame connected with shear wall in the orthogonal directions.

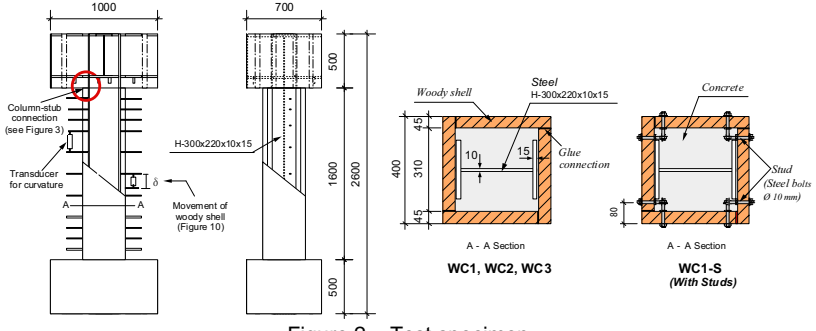


Figure 2 – Test specimen

This paper presents the results of a feasibility study on the structural behavior of EWECS composite columns using single H-section steel subjected to combined constant axial load and lateral load reversals that simulated earthquake loading. The performance of the columns was evaluated in terms of hysteresis loops, failure mode, and curvature. An analytical study was also conducted using fiber section analysis in order to compare with the experimental data.

EXPERIMENTAL PROGRAM

Specimens and materials used

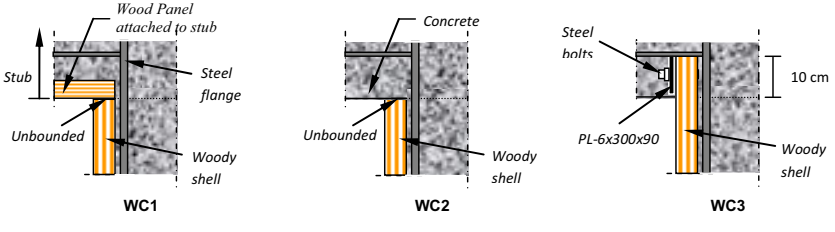
A total of four composite column specimens of which the scale is about two-fifth, were tested in this study. The main test parameters were the type of woody shell connection between column and loading stub and the presence of shear studs. The dimensions and details of the specimens are shown in Figure 2 and Table 1. For the first parameter, three types of woody shell connection at column-stub joints were constructed, as shown in Figure 3:

- Connection between woody shell and wood panel attached to stub (Specimen WC1)
- Connection between woody shell and concrete stub (Specimen WC2)
- Continuous woody shell connected with steel plates in the stub using bolts (Specimen WC3)

Table 1 – Test program

Specimen		WC1	WC2	WC3	WC1-S
Column -stub connections		Woody shell and wood panel attached to stub	Woody shell and concrete stub	Continuous woody shell into stub	Woody shell and wood panel attached to stub
Woody Shell - core connection		----			With studs
Woody Shell Thickness (mm)		45			
Concrete strength (MPa)		35			27
Built-in steel (mm)		H-300 x 220 x 10 x 15			
Column Height: h (mm)		1600			
Cross section : b x D (mm)		400 x 400			
Axial Compression	N (kN)	1031			
	N/Ntot	0.16			0.18
Calculated Ultimate flexural strength: Qmcal (kN)		712			703

N_{tot} = Total axial compressive strength of the column (b_c .D_c .σ_B + b_w .D_w .σ_w), where bc .Dc .σB: the width, depth and compressive strength of concrete core, and bw .Dw .σw: the width, depth and compressive strength of woody shell.



(Connection between woody shell and (Connection between woody (Continuous woody shell

Figure 3 – Types of woody shell connection between column and stub

For the second parameter, shear studs made from steel bolts were attached from the woody shell to CES core along the column height for Specimen WC1-S, as shown in Figures 2 and 4. The purpose of the shear studs is to enhance the bond between the CES core and the woody shell, thereby increasing the composite action of the column. The effect of shear studs on the behavior of EWECS columns can be examined by comparing Specimens WC1 and WC1-S. Both specimens have the same column dimensions and configurations, and the main difference is only the presence of the studs.

All specimens had a column with 1,600 mm height and 400 mm square section. The thickness of the woody shell was 45 mm and the steel encased in each column had a single H-section steel of 300x220x10x15 mm. The mechanical properties of the steel and the woody shell are listed in Tables 2 and 3, respectively. Normal concrete of 35 MPa was used for Specimens WC1, WC2 and WC3, while for Specimen WC1-S the concrete strength was 27 MPa due to different period of concrete placement.

Table 2 – Mechanical properties of steel

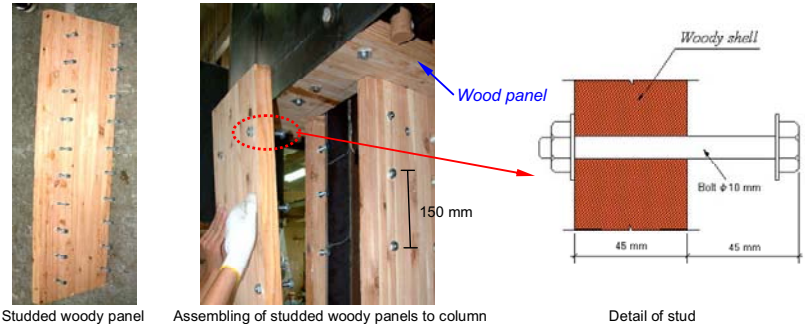
Steel	Yield Stress σy (Mpa)	Max. Stress σs (MPa)	Notes
H-300x	284	450.5	Flange
220x10x15	295.5	454.9	Web

Table 3 – Mechanical properties of woody shell

Woody Shell panel (mm)	Wood type	*Comp. Strength σw (MPa)	Elastic Modulus Es (GPa)
40x160x4.5	Glue laminated pine wood	45	11.5

* the direction is parallel to axis of grain

In manufacturing the specimens, the steel sections were accurately cut to size of the column and stub first. Then the woody shell panels were assembled to the column by using wood glue. For Specimen WC1-S, the studs were installed to the woody panels before assembling the panels to the column (Figure 4). Finally, the concrete was cast into the column without additional formwork because the woody shell also serves as mold forms for concrete placement.



Studded woody panel **(a)** Assembling of studded woody panels to column **(b)** Detail of stud **(c)**

Figure 4 – Fabrication of Specimen WC1-S

Test setup and loading procedures

The specimens were loaded lateral cyclic shear forces by a horizontal hydraulic jack and a constant axial compression of 1031 kN by two vertical hydraulics jacks, as shown in Figure 5. Considering the cross-section of the woody shell, the applied axial force ratio, N/N_{tot}, for Specimens WC1, WC2 and WC3 were 0.16, while for Specimen WC1-S the ratio was 0.18 (see Table 1).

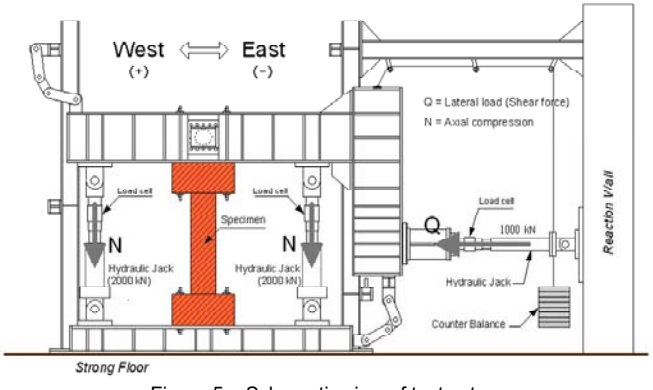


Figure 5 – Schematic view of test setup

The loads were applied through a steel frame attached to the top of a column that was fixed to the base. The incremental loading cycles were controlled by story drift angles, R, defined as the ratio of lateral displacements to the column height, δ/h. The lateral load sequence consisted of two cycles to each story drift angle, R of 0.005, 0.01, 0.015, 0.02, 0.03 and 0.04 radians followed by half cycle to R of 0.05 rad. For Specimen WC1-S, the test was continued until story drift, R of 0.067 rad., because the specimen was still capable to resist the applied force after R of 0.05 rad.

EXPERIMENTAL RESULTS AND DISCUSSIONS

Hysteresis characteristics and failure modes

Shear versus story drift angle relationships of all specimens are given in Figure 6. In this figure, the predicted flexural capacities calculated by flexural analysis with superposition method (AIJ 2001) are shown by the dotted lines. The yield and maximum strengths and the corresponding story drift angles for each specimen are listed in Table 4. The yielding of each specimen was assumed when the first yielding of steel flange at the top and/or bottom of the columns was observed, which corresponds to a triangle mark on the shear versus story drift angle response (see Figure 6). Crack modes of all specimens at final stage are presented in Figure 7.

Table 4 – Measured strength

Specimen	at Yielding		at the Max. Capacity	
	Qy (kN)	Ry (rad.)	Qmax (kN)	Rmax (rad.)
WC1	422.5	0.00571	706.5	0.05
WC2	570	0.01002	690	0.04
WC3	-498	-0.00768	725	0.05
WC1-S	427.6	0.007	705.2	0.067

From Figure 6, it can be seen that all four specimens showed ductile and stable spindle-shaped hysteresis loops without degradation of load-carrying capacity until story drift, R of 0.04 radian. The measured maximum flexural strengths fairly agreed with the calculated flexural strengths.

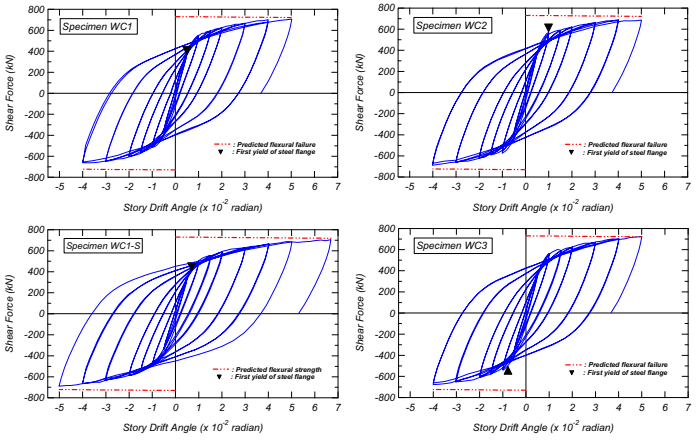


Figure 6 – Shear force - story drift angle relationships

In Specimen WC1 with column-stub connection consisting of woody shell and wood panel attached to stub, the first cracks in the woody shell occurred at around 30 cm away from the top of the column at story drift, R of about 0.032 rad. With an increase of the story drift, the cracks propagated along the column faces. Sink and uplift were observed significantly after R of 0.02 rad. at two opposite sides of both the top and bottom of the column due to different grain directions between the woody shell and the wood panel attached to stub. The hysteresis loops of this specimen showed excellent behavior without strength degradation until the last cycle. The maximum capacity of 706.5 kN was reached at story drift, R of 0.05 rad.

For Specimen WC2 with column-stub connection consisting of woody shell and concrete stub, the hysteresis curve showed a stable behavior with a little strength degradation after attaining the maximum capacity at R of 0.04 rad. The maximum capacity of this specimen was less than that of Specimen WC1.

Specimen WC3 with continuous woody shell into stub showed high performance, with the highest maximum capacity compared to the other 2 above specimens. However, the brittle failure of the woody shell and severe damage of the concrete stub around the column-stub joints were observed significantly in this specimen after R of 0.03 rad.

By comparing among these three specimens with different woody shell connections between column and stub, it is revealed that all the specimens had excellent hysteretic behavior with almost the same maximum capacity. However, the test specimens showed different cracking patterns at the column faces, as shown in Figure 7. Up to story drift, R of 0.03 rad., no damage was observed in Specimen WC1 and little crack occurred in Specimens WC2 and WC3. However, the damage situations of the columns were different at the last story drift, R of 0.05 rad. At this stage, the most damage of the woody shell was observed in Specimen WC2, while Specimen WC1 showed better performance in damage limit than the other two specimens.

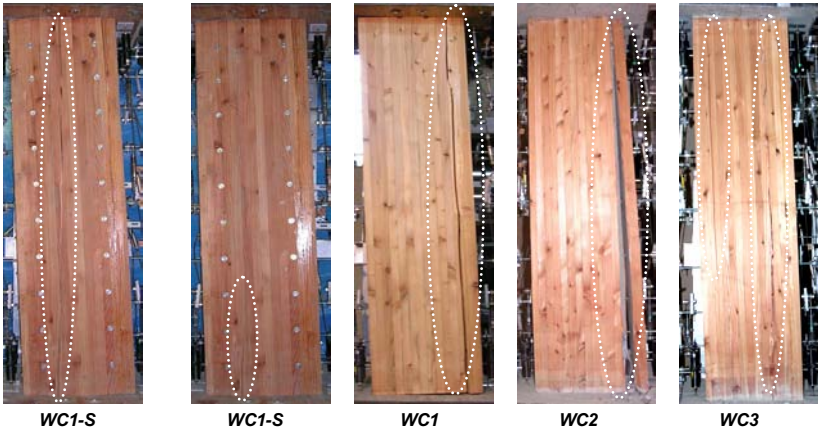


Figure 7 – Crack modes of specimens after loading

The different failure modes at critical joint regions between column and stubs were also observed among these 3 specimens. Sink and uplift occurred in Specimens WC1 and WC2, while slip between woody shell and concrete stub (slip displacement) was observed in Specimen WC3, as shown in Figure 8. Specimen WC1 had little damage at the column-stub joints due to the effect of sink and uplift that occurred at the joint regions. Meanwhile, the most damage of the woody shell at the joint region was observed in Specimen WC2 due to the higher stiffness of concrete than woody shell. For Specimen WC3, the slip between woody shell and concrete stub at the joints caused the crush of concrete stub around the joint regions.

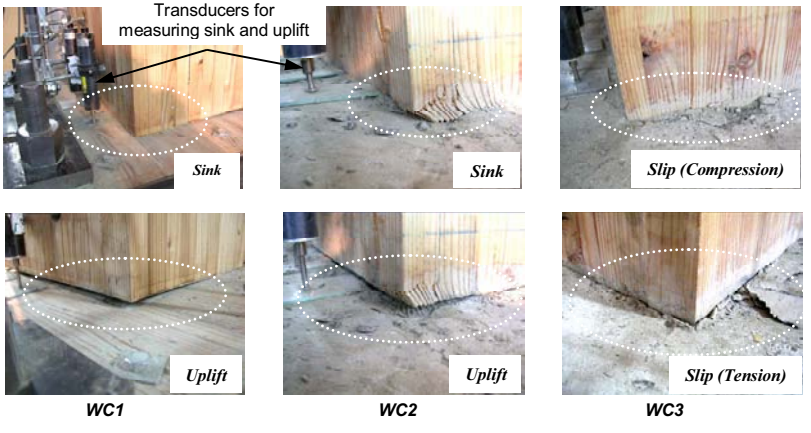


Figure 8 – Failure patterns of specimens at column-stub joint after loading

For the column with shear studs (Specimen WC1-S), the hysteresis loops also showed a stable behavior, as shown in Figure 6. Up to a story drift, R of 0.04 rad., no damage was observed on the column faces. Then a little crack occured at column faces at R of 0.05 rad. For this reason, the test of this specimen was continued until R of 0.067 rad. Also, the brittle failure of this specimen was not significant during testing. The first yielding of steel flange occurred at R of 0.007 rad. and a shear force of 427.6 kN, and the maximum strength of 705.2 kN was reached at R of 0.067 rad.

Compared with Specimen WC1, Specimen WC1-S resulted in increase of ductility due to the presence of shear studs, as shown in Figure 6. Although the higher displacement was applied to this specimen, the damage of the column was less than that of Specimen WC1 (Figure 7) due to the enhancement of bond between woody shell and CES core by the shear studs. In addition, both specimens had almost the same maximum capacity, which means that there is not much effect of the shear studs on the capacity of EWECS columns.

Figure 9 shows the comparison of sink, uplift and slip displacements of the woody shell at each story drift angle for all specimens. The values were obtained by measuring the vertical displacement at the connections between column woody shell and stub using transducers (see Figure 9). A comparison of the 3 specimens with different column-stub connections revealed that Specimen WC1 had the highest value of sink and uplift displacements compared with the other two specimens. For this specimen, the maximum sink of 7.4 mm and uplift of 10.5 mm were reached at R of 0.04 rad. The highest sink and uplift values of this specimen confirmed the less damage of the column woody shell, especially at the column-stub connections. From Figure 9, it can also be seen that there was not much influence of shear studs on sink behavior of the column in which the values of sink displacement for Specimen WC1-S had almost similar with that for Specimen WC1 until R of 0.04 rad. However, the uplift of Specimen WC1-S was smaller due to the presence of the studs.

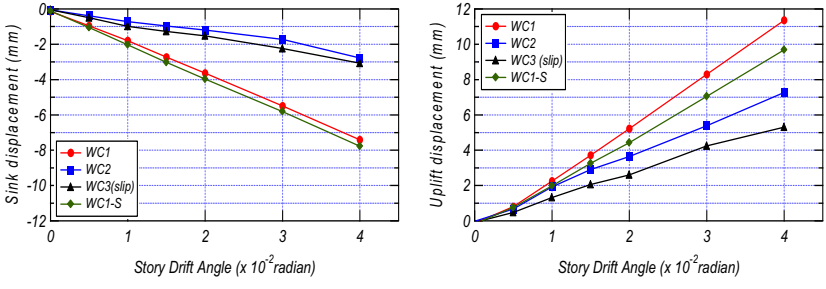


Figure 9 – Sink and uplift displacements of woody shell at column-stub joint

Figure 10 compares the movement of the woody shell from the CES core at top and middle of the column until the story drift, R of 0.03 rad. for all specimens. The values were obtained by measuring the displacement between the CES core and the woody shell using vertical transducers installed at the encased steel and the woody shell at the top, middle and bottom of the column (see Figure 2). As shown in Figure 10, the movement of the woody shell from the CES core at the top and middle of the columns was relatively small for all specimens. Comparing among 3 specimens with different column-stub connection, the smallest movement of the woody shell was

observed in Specimen WC1 due to the effect of sink and uplift at column-stub joints. In Specimen WC2, on the other hand, the highest movement occurred at the middle of the column, possibly due to the deterioration of the woody shell at the column-stub joints after R of 0.01 rad. Moreover, the effect of shear studs on the woody shell movement can also be seen in Figure 10. Compared with Specimen WC1, Specimen WC1-S had the smaller movement of the woody shell due to the enhancement of bond between the CES core and the woody shell by the shear studs.

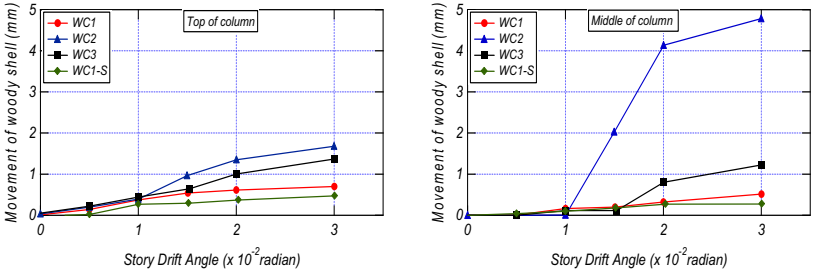


Figure 10 – Movement of woody shell from CES core

From this study, it was also observed that the woody shell contributed to flexural strength until large story drift, R of 0.05 rad. for Specimens WC1 and WC3 and until R of 0.067 rad. for Specimen WC1-S, although the cracks appeared along the column faces after R of 0.03 rad. (see Figures 6 and 7). By extracting the woody shell after testing, it was observed for all specimens that the in-filled concrete had crushed in flexure at both the top and bottom of the column and there was no local buckling occurred at the encased steel.

Curvature Distribution

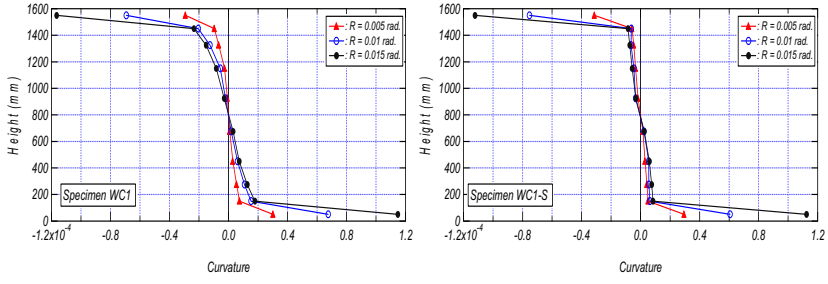


Figure 11 – Curvature distribution

Figure 11 shows the curvature distributions along the column height at R of 0.005, 0.01 and 0.015 radians for Specimens WC1 and WC1-S. The curvature distributions of the other two specimens (WC2 and WC3) were not presented in this paper because they had almost similar behavior with that of Specimen WC1. The values of curvature were obtained from transducers installed on the two opposite sides along the column height, as shown in Figure 2. As seen in Figure 11, the distribution of curvature was almost identical at each story drift angle for both specimens in which

the highest curvature occurred at both the top and bottom of the column. However, the curvature distribution slopes of Specimen WC1-S were smaller than that of Specimen WC1 due to the increase of composite action by the shear studs.

ANALYTICAL INVESTIGATIONS

Summary of analytical study

Fiber section analysis method was used to construct moment-curvature relationships of critical section. In the method, the cross section is discretized into a number of small areas or filaments, as shown in Figure 12. Each fiber is assumed to be uniaxially stressed and to behave according to assumed hysteresis stress-strain characteristic of its constituting materials, as explained below. In this study, the cross section of column was divided into 40 elements. This method assumes that the plane sections to remain plane, thus implying full compatibility between the steel, concrete and woody shell components of a composite cross section.

The analysis is controlled through a series of small steps by curvature or displacement history in terms of X-axis. With the axial strain at the center of the cross section, $\Delta\varepsilon_0$ and the curvatures along in terms of X-axis, $\Delta\phi_x$, the axial strain at the fiber element of i, $\Delta\varepsilon_i$ is found according to

$$\Delta\varepsilon_i = \Delta\varepsilon_0 + y_i \Delta\phi_x \quad (1)$$

where y_i is the distance from the X-axis to the i th fiber element on the section.
Considering the equilibrium of the section, axial force ΔN and bending moment ΔM are written as follows, using stiffness matrix [K];

$$\{\Delta N, \Delta M\}^T = [K] \{\Delta\varepsilon_0, \Delta\phi_x\}^T \quad (2)$$

In this analysis, ΔN, ΔM and $\Delta\varepsilon_0$ were calculated by satisfying Eqs. (1) and (2), and considering the mechanical properties of steel, concrete and woody shell, as $\Delta\phi_x$ was the input data. Load-displacement relations for the columns were obtained assuming an antisymmetric distribution of bending moments along the column height, with the inflection point at midheight. Considering the experimental results for curvature distribution along the column height (Figure 11), the relation between curvature and displacement rotation angles, R was assumed as ϕ = 2.3 R/L and ϕ = 2.2 R/L for Specimens WC1 and WC1-S, respectively, although in elastic assumption the relation is defined as ϕ = 6 R/L, where L is the column height.

The hysteretic model used for the steel was the trilinear model proposed by Shibata (1982), as shown in Figure 13. Yield strengths in both compression and tension were assumed to be equal. The hysteretic model of confined concrete adopted was the divided linear model (Kuramoto et al. 1995), as shown in Figure 14. In this model, a magnification factor of concrete strength K for confined core concrete was considered as 1.15 and the compressive strain at the stress peak, ε_0 was taken as 0.0036. The hysteretic model of woody shell used was almost similar to the concrete model that is divided linear model, as shown in Figure 15. The compressive strain at the stress peak, ε_0 was taken as 0.004.

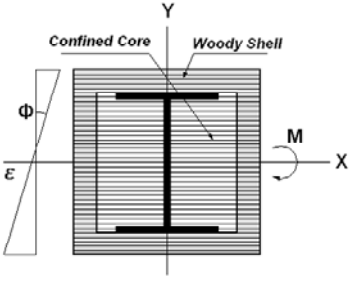


Figure 12 – Fiber model

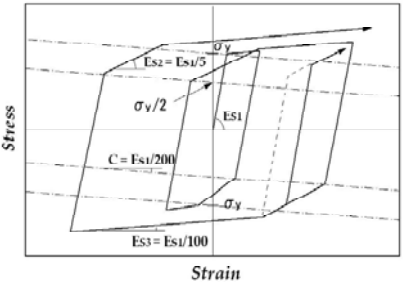


Figure 13 – Stress-strain model of steel

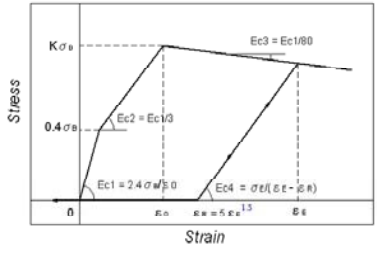


Figure 14 – Stress-strain model of confined concrete

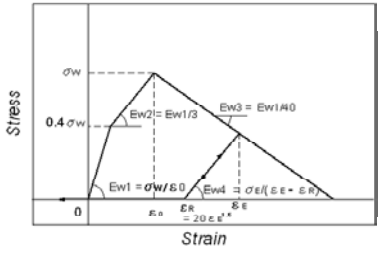


Figure 15 – Stress-strain model of woody shell

Analytical results

Fiber section analysis results were compared to the experimental data for Specimens WC1 and WC1-S, as shown in Figure 16. From this figure, it can be seen that the analytical results for shear force versus story drift relationships of each specimen showed a good agreement with the test results. The analytical models adequately simulated the behavior of the test specimens. These comparative good results confirmed the accuracy of the proposed numerical analysis to predict the ultimate flexural strength and behavior of EWECS columns under constant axial load and lateral load reversals.

The contributions of each material component to shear force and axial load were also examined from this analysis, which confirmed the test data of Specimen WC1-S for the contributions of woody shell to shear force and axial load until R of 0.067 rad.

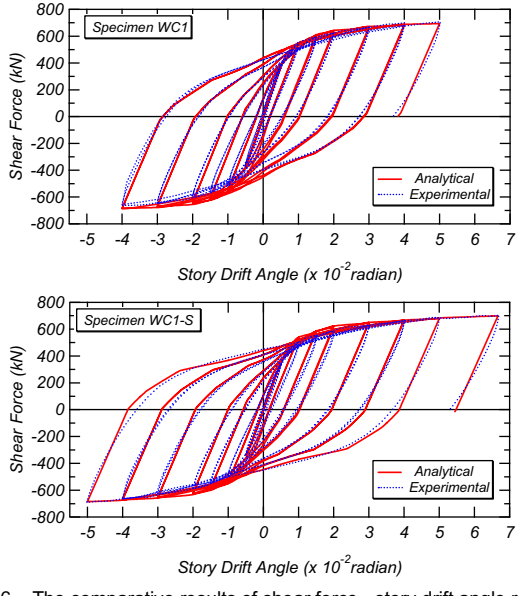


Figure 16 – The comparative results of shear force - story drift angle relationships

CONCLUSIONS

Based on the experimental and analytical studies presented here, the following conclusions can be drawn:

(1) EWECS columns using single H-section steel had excellent structural performance without severe damage, even at large story drift, R of 0.04 rad.

(2) EWECS column with column-stub connection consisting of woody shell and wood panel attached to stub showed excellent performance in both capacity and damage limit of the composite column due to the effect of sink and uplift of the woody shell that occurred at the joint regions.

(3) The presence of shear studs on EWECS columns improved the ductilty of the column and reduced the damage of woody shell., but there was not much influence on maximum flexural strength of the column.

(4) With shear studs, the woody shell contributed to flexural capacity until large story drift angle, R of 0.067 rad., although cracks appeared at the column faces after R of 0.04 rad.

(5) The calculated hysteresis loops using fiber analysis showed a good agreement with the experimental results, indicating that the analytical method can be used to predict accurately the ultimate strength and behavior of EWECS columns.

REFERENCES

Architectural Institute of Japan (AIJ). (2001). "AIJ Standard for Structural Calculation of Steel Reinforced Concrete Structures." Tokyo, Japan.

Fauzan, Kuramoto H., Shibayama Y. and Yamamoto T. (2004). "Structural Behavior of Engineering Wood Encased Concrete-Steel Composite Columns." *Proceedings of the Japan Concrete Institute (JCI)*, Vol. 26, No.2, pp. 295-300.

Kuramoto, H., Takahashi, H. and Maeda, M. (2000). "Feasibility Study on Structural Performance of Concrete Encased Steel Columns using High Performance Fiber Reinforced Cementitious Composites." *Summaries of Technical Papers of Annual Meeting*, AIJ, Vol.C-1, pp. 1085–1088 (in Japanese).

Kuramoto, H., Adachi, T. and Kawasaki, K. (2002). "Behavior of Concrete Encased Steel Composite Columns Using FRC." *Proceedings of Workshop on Smart Structural Systems Organized for US-Japan Cooperative Research Programs on Smart Structural Systems (Auto-Adaptive Media) and Urban Earthquake Disaster Mitigation*, Tsukuba, Japan, pp. 13-26.

Kuramoto H and Fauzan. (2005). "Feasibility Study on Engineering Wood Encased Concrete-Steel Composite Columns." *Proceedings of the Eleventh International Colloquium on Structural and Geotechnical Engineering (11th ICSGE)*, Ain Shams University, Cairo, Egypt, CD-ROM Paper Code-F05ST20.

Shibata M. (1982)," Analysis of Elastic-Plastic Behavior of Steel Brace Subjected to Repeated Axial force." *International Journal of Solids and Structures*, Vol. 8, No. 3, pp. 217-228.

Kuramoto H., Kabeyasawa T. and Shen F-H. (1995)." Influence of axial deformation on ductility of high-strength reinforced concrete columns under varying triaxial forces." *ACI Structural Journal, Vol.* 92, No. 5, pp. 610-618.

DESIGN OF COMPOSITE COLUMNS – STEEL, CONCRETE OR COMPOSITE APPROACH?

Russell Q. Bridge
Construction Technology Research Group
University of Western Sydney
Penrith, New South Wales, Australia
rq.bridge@uws.edu.au

ABSTRACT

Composite columns are a combination of two traditional structural forms: structural steel and structural concrete. As composite columns were generally developed after steel columns and reinforced concrete columns, their design approach could have been based on either steel or concrete design methods. However, steel column design methods have differed from concrete design methods in a number of fundamental ways. Despite this, either design approach can be used as the basis for developing a design method for composite columns and this can be seen in the different methods currently used in Europe and the USA for composite columns. While the design approaches appear fundamentally different, the end results can be surprisingly similar. By understanding the design philosophies, designers can take full advantage of each approach for the effective use and economy of composite columns.

1 INTRODUCTION

Steel column design methods have differed from concrete design methods in a number of fundamental ways. For example, steel column design typically accounts for slenderness effects by utilizing a column curve based on the stability of a pin-ended column with initial imperfections and residual stresses whereas concrete column design typically accounts for slenderness indirectly by utilizing a minimum applied end eccentricity and moment magnification. Steel column design typically utilises load-moment interaction through interaction equations that separate out the load and moment contribution to the strength whereas concrete column design utilises load-moment interaction through a combined load-moment strength interaction curve.

In all current design provisions for reinforced concrete, steel and composite columns, the design action effects (the axial force N^* and the maximum moment M^*) resulting from the application of the design loads can be determined from a first-order elastic analysis, but second-order effects must be accounted for by the use of a moment magnifier. Alternatively, the second-order effects can be determined directly from a second-order elastic analysis of the structure. In design, the member of a structure is proportioned so that its design strength is not less than the corresponding design action effect.

In Australia, the design of reinforced concrete columns is determined in accordance with the provisions of AS 3600 which are similar to those of BS 8110, ACI 318-05 and Eurocode 2. Similarly, the design of steel columns is determined in accordance with the provisions of AS 4100 which are similar to those in BS 5950, ANSI/AISC 360-05 and Eurocode 3. There is no current Australian Standard for the design of composite steel-concrete columns, but Eurocode 4 (and more recently ANSI/AISC

360-05) contains design provisions which are being considered for possible inclusion in a new Australian Standard for Composite Construction. Therefore, in this paper, the material design approaches of AS 3600, AS 4100 and Eurocode 4 are compared in order to highlight the many similarities and to discuss some of the fundamental differences thereby clarifying a number of issues that confront structural engineers who design columns in all three methods of construction.

2 SECTION STRENGTH

Section strength is defined as the load and moment capacity of a cross-section i.e. a short column without any overall member instability. The pure moment capacity (zero axial load) is denoted by M_{uo} and the pure axial compressive load capacity (zero moment) is denoted by $N_{uo.}$

2.1 Reinforced Concrete

2.1.1 Strength

The section strength can be calculated on the basis of equilibrium and strain-compatibility considerations. This requires knowledge of the geometry of the cross-section and the stress-strain relationships for both the concrete and the reinforcement. Most codes allow simplified rectangular stress blocks to be used for the concrete stress distribution. For a range of practical cross-sections, load-moment interaction curves have been calculated and provided in design handbooks (eg. CCAA HB71-2002). A typical reinforced concrete curve is shown in Figure 1.

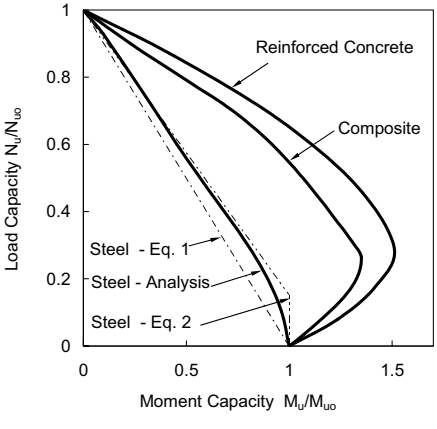


Fig. 1 Load-moment interaction curves

2.1.2 Local Buckling

Local buckling of the reinforcement is restrained by the concrete surrounding the reinforcement. Tests by Hudson (1966) on reinforced concrete columns with or without ties showed that the concrete alone apparently provided sufficient restraint against reinforcement buckling such that the absence of ties seemingly had no effect on the maximum load capacity of the columns. However, ties and maximum tie

spacing are stipulated by AS 3600 to provide restraint, ensuring a more ductile performance in the post-ultimate region, i.e. provision against brittle failure.

2.2 Steel

2.2.1 Strength

The strength of a bare steel cross-section can also be determined by analysis on the basis of equilibrium and strain-compatibility considerations. The results are shown by the curve marked analysis in Figure 1 for a typical Universal Beam section bent about its major axis. However, as the moment capacity is not enhanced with the application of low levels of axial compressive load, as it is for cross-sections containing concrete where the axial load reduces cracking, it has been traditional in steel standards such as AS 4100 to use a simple linear expression of the form

$$\frac{M_u}{M_{uo}} = 1 - \frac{N_u}{N_{uo}} \tag{1}$$

to represent the load-moment interaction curve in a conservative manner as shown in Figure 1. For doubly symmetric compact I-sections bent about the major-axis, a closer approximation to the analytical result is permitted by AS 4100 where

$$\frac{M_u}{M_{uo}} = 1.18\left[1 - \frac{N_u}{N_{uo}}\right] \le 1.0 \tag{2}$$

The corresponding equations in ANSI/AISC 360-05 are even closer to the analytical solution.

2.2.2 Local Buckling

The strength can be reduced by local buckling of the steel plate elements forming the cross-section. This is a function of the slenderness λ_e of the plate elements defined in AS 4100 as $\lambda_e = b/t\sqrt{(f_y/250)}$ for flat plate elements, and $\lambda_e = d_o/t(f_y/250)$ for circular hollow sections. When λ_e exceeds the plate element yield slenderness limit λ_{ey}, the actual width b is replaced by a reduced effective width b_e which can carry the yield stress where

$$b_e = b\frac{\lambda_{ey}}{\lambda_e} \le b \tag{3}$$

This process is similar to other steel codes (ANSI/AISC 360-05, BS 5950 and Eurocode 3).

2.3 Composite

2.3.1 Strength

As for reinforced concrete, the strength of a composite cross-section, as defined by its load-moment interaction curve, can be calculated on the basis of equilibrium and strain-compatibility considerations in conjunction with appropriate material stress-strain relationships (Eurocode 4, ANSI/AISC 360-05). This process is a little more complex than for a reinforced concrete as the steel section in the composite member has its own inherent stiffness without the concrete. Calculations are best done using

a computer program (Wheeler and Bridge 1993). A typical curve is shown in Figure 1 for an I-section encased in concrete and bent about its major axis. For simple cross-sections such as concrete filled tubes and encased I-sections, both Eurocode 4 and ANSI/AISC 360-05 provide simplified plastic calculations resulting in an approximation using four straight lines. Studies done by Bridge, O'Shea and Zhang (1997) have found that the simplifications can lead to erroneous results for concrete filled circular tubes with very thin-walled steel tubes and/or high strength concretes.

For circular concrete filled tubes, Eurocode 4 allows for an additional increase in strength of the concrete due confinement by the steel tube provided the eccentricity of loading e does not exceed $d_o/10$ and the non-dimensional column slenderness λ does not exceed 0.5 where λ is defined as

$$\lambda = \sqrt{N_{uo}/N_{cr}} \tag{4}$$

and N_{cr} is the elastic critical buckling load calculated using an "effective" flexural stiffness and the effective length of the column (see Equation 10). The effect of concrete confinement on the strength is shown in Figure 2. It is interesting to note that the cross-section strength is influenced by the column slenderness!

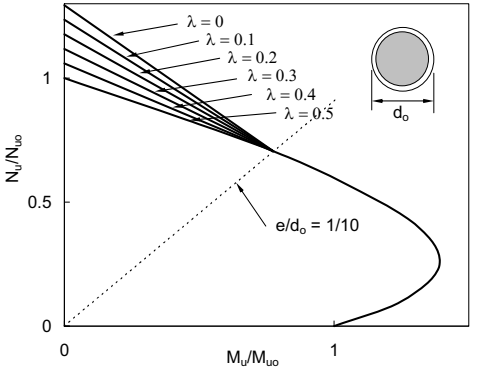


Fig. 2 Effect of concrete confinement - Eurocode 4

The increase in strength due to confinement depends on the diameter to thickness ratio d_o/t of the steel tube, thicker tubes obviously giving a greater increase. However, studies by O'Shea and Bridge (1999b, 2000) using circular tubes (d_o/t values ranging from 60 to 200) with very high strength concrete infill (in the range 110 MPa) have shown that the increase in strength due to confinement is negligible. The confinement provisions in Eurocode 4 have been developed for normal concrete with strengths up to 50 MPa. It is recommended that the confinement provisions should not be extrapolated to higher strength concrete unless verified by tests.

2.3.2 Local Buckling

For fully encased steel sections, Eurocode 4 allows the effects of local buckling to be neglected provided that: the cover is not less than 40 mm nor less than one-sixth of the width b of the flange; longitudinal reinforcement with an area not less than 0.3%

of the concrete cross-section is provided; and ties are provided to Eurocode 2 which has similar provisions to AS 3600.

For concrete filled tubes and partially encased I-sections, local buckling effects can be neglected if the slenderness of the plate elements is less than yield slenderness limits set in Table 6.3 of Eurocode 4. These limits are slightly higher than the values in AS 4100 for bare steel sections indicating that some allowance has been made for restraint by the concrete. If the limits are exceeded, "the influence of local buckling shall be considered" (Eurocode 4) but no direct guidance is given.

Tests by Bridge and O'Shea (1998) on thin-walled square steel tubes with unbonded concrete infill show that the local buckling strength of the steel tube is increased by the concrete infill which changes the buckling mode such that only outwards buckles can form rather than both inwards and outwards buckles which would normally occur in bare steel tubes. This can be accounted for in AS 4100 by a modified effective width b_e given by

$$b_e = b\frac{\lambda_{ey}}{\lambda_e}\sqrt{\frac{k_b}{k_{bo}}} \le b \tag{5}$$

where k_b is the actual elastic buckling coefficient for the plate element determined by a rational buckling analysis of the whole member as a flat plate assemblage taking into account the internal restraint provided by the concrete, and k_{bo} is the buckling coefficient implied in the code for long plates with standard support conditions along the plate edges (eg. k_{bo} = 4 for a flat plate with simply supported edges as for a bare steel square tube).

For thin-walled circular tubes in axial compression, the pattern of local buckling is mainly an outwards buckle around the circumference of the tube, usually at one end ("elephant's foot" buckle). In this case, the presence of concrete infill would be expected to have little influence on the strength of the steel tube. This has been verified in tests by O'Shea and Bridge (1999a,c).

3 MEMBER STRENGTH - AXIAL LOAD

3.1 Reinforced Concrete

Reinforced concrete design standards traditionally do not make use of a column curve which accounts for the effects of geometric and material imperfections. Instead, axially loaded members are treated as beam-columns with the load being applied at a minimum eccentricity of 0.05D (AS 3600) or 0.03D + 15mm (ACI 318-05). Using this minimum eccentricity applied at both ends of a pin-ended column, an equivalent column curve can be generated for reinforced columns using a non-linear column analysis (Bridge and Roderick 1978) for a range of column slenderness. The results of the analysis for a typical rectangular reinforced column are shown in Figure 3 and are compared with the column curves for steel members in AS 4100. It can be seen from Figure 3 that even for a column of zero slenderness (i.e. a cross-section), the axial column strength N_c is less than the pure axial compressive load capacity N_{uo} for reinforced concrete columns as a result of using the value of 0.05D for the minimum eccentricity of load.

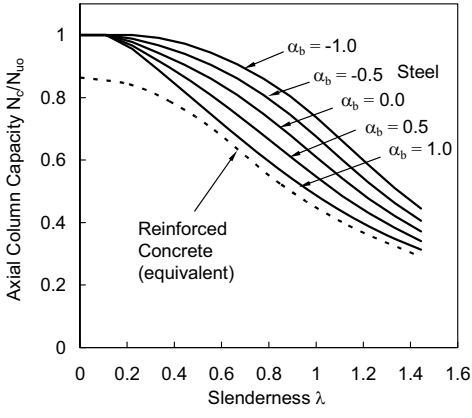


Fig. 3 Column curves for steel and reinforced concrete

3.2 Steel

The axial load capacity N_c for steel columns is determined in AS 4100 from a series of five column curves as shown in Figure 3. Each curve is defined by a member section constant α_b which reflects the method of manufacture of the column section which in turn influences the degree of out-of-straightness of the member and the level of residual stress, factors which affect the column capacity. For example, rectangular and circular hollows steel sections are relatively straight with low membrane residual stresses and are therefore designed to the upper curve with α_b = -1.0. Multiple column curves are also used in Eurocode 3 and BS 5950 whereas ANSI/AISC 360-05 continues to use a single column curve.

3.3 Composite

In Eurocode 4, the axial load capacity of composite steel and concrete columns can be determined from the column curves in Eurocode 3 for the design of steel structures using the slenderness λ as defined in Equation 4 in which the buckling load N_{cr} is calculated using an effective stiffness. The appropriate column curve depends on the method of manufacture of the steel section used in the composite column, similar to the procedure used for steel columns in AS 4100. In fact, the column curves in Eurocode 3 are very similar to those in AS 4100 which are shown in Figures 3 and 4. A similar design approach to Eurocode 4 is used in ANSI/AISC 360-05 which uses only a single column curve.

The non-linear analysis column analysis by Bridge and Roderick (1978) was used to calculate the axial strength of two typical composite sections: an encased universal column UC section; and a concrete filled square hollow SHS section. An out-of-straightness of L/1000 was used which is the fabrication tolerance specified in AS 4100. Typical residual stresses were used for the steel sections. Shrinkage stresses induced in the steel and concrete of the encased section were also included assuming a free concrete shrinkage of 600 micro-strain. The members were analysed as pin-ended columns for a range of different slenderness. The results are

shown in Figure 4 and are compared with the steel column curves in AS 4100. Eurocode 4 also allows the use of such a direct analytical approach for the strength of axially loaded members and specifies the equivalent member imperfection to be used in the second-order analysis.

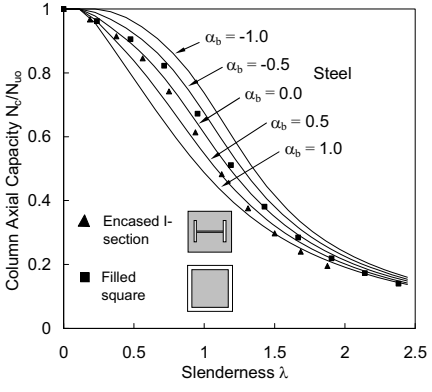


Fig. 4 Column curves for steel and composite columns

It can be seen from Figure 4 that the column curves in AS 4100 could be adapted for composite columns although it is likely, as a result of this preliminary study, that a lower column curve than that based purely on the method of manufacture of the steel section would have to be selected.

4 DESIGN ACTION EFFECTS

In modern codes for reinforced concrete, steel, and composite structures, the direct design for structural stability and strength is allowed provided that second-order effects are taken into account including geometrical imperfections, material non-linearity, creep and shrinkage, concrete cracking, tension stiffening, three dimensional effects and construction sequence. This is called “rigorous structural analysis” in AS 3600, “advanced structural analysis” in AS 4100 and “general method of design” in Eurocode 4. These approaches can be quite complex and, in general, simpler methods are used for a wide range of regular structures with uniform members in which the axial force N^* and the maximum end moment M_2^* for end-loaded braced members, resulting from the application of the design loads, can be determined from a first-order elastic global analysis. Second-order effects within the member are accounted for by the use of a moment magnifier δ_b whereby the maximum moment M^* in the column is given by

$$M^* = \delta_b M_2^* \tag{6}$$

where
$$\delta_b = C_m/(1 - N^*/N_{cr}) \geq 1 \tag{7}$$

and
$$C_m = 0.6 - 0.4\beta \geq 0.4 \quad \text{(AS 3600)}$$

$$C_m = 0.6 - 0.4\beta \quad \text{(AS 4100)}$$

$$C_m = 0.66 - 0.44\beta \geq 0.44 \qquad \text{(Eurocode 4)} \qquad (8)$$

and
$$\beta = M_1^*/M_2^* \qquad (9)$$

where β is ratio of the smaller to the larger end moments and is positive when the member is bent in double curvature.

Also
$$N_{cr} = \pi^2 EI/\ell^2 \qquad (10)$$

where ℓ is the effective length of the column. However, the three codes differ in their determination of the flexural rigidity EI as follows.

4.1 Reinforced concrete

In the AS 3600, the flexural rigidity EI is given by

$$EI = 200 M_{ub} d/(1 + \beta_d) \qquad (11)$$

where EI is the secant flexural stiffness corresponding to the "balanced" moment capacity M_{ub} of the cross-section taken to occur when the neutral axis is at a value of $0.6d$ (where d is the depth to the outermost layer of tensile steel) and the extreme concrete fibre strain in compression is 0.003 (Bridge 1986). Values of M_{ub} are also given in charts in handbooks (CCAA HB71-2002).

4.2 Steel

In AS 4100, the flexural rigidity EI is given by

$$EI = E_s I_s \qquad (12)$$

where I_s is the second moment of area of the steel section and E_s is the elastic modulus.

4.3 Composite

In Eurocode 4, the flexural rigidity EI is given by

$$EI = 0.9(E_s I_s + 0.5 E_c I_c/(1 + \varphi_t \beta_d)) \qquad (13)$$

where I_s and I_c are the second moments of area of the steel and concrete, E_s is the steel elastic modulus, E_c is the concrete secant modulus, φ_t is the creep coefficient (Eurocode 2) and β_d is the ratio of permanent loading to the total loading to account for creep effects using a reduced modulus approach. For the short term loading used in laboratory strength tests, $\beta_d = 0$.

An alternative (Bridge et al 1986) to Equation 13 is a modification to Equation 11 where

$$EI = 167 M_{ub} D/(1 + \varphi_t \beta_d) \qquad (14)$$

and EI is the secant flexural stiffness of the cross-section corresponding to the "balanced" moment capacity M_{ub} of the cross-section taken to occur (Rotter 1982) when the neutral axis is at mid-depth $D/2$ of the composite section and the extreme concrete fibre strain in compression is 0.003 (Bridge 1990). The advantage of Equation 14 is that the value of M_{ub} takes into account the particular material and

geometric configuration of the cross-section and hence obviates the need for the calibration and correction factors used in Equation 13.

5 MEMBER STRENGTH – COMBINED AXIAL COMPRESSION AND BENDING MOMENT

In this section, only the in-plane strength of beam-columns is considered as reinforced concrete and composite steel-concrete columns are usually of such a shape that out-of-plane effects are not significant. This may not be the case for steel columns bent about their strong axis.

The applied axial force N^* and larger end moment M_2^* for end-loaded braced members can be determined from a global first-order elastic analysis. The maximum design bending moment M^* within the column, magnified for second-order effects, is then determined from Equation 6.

5.1 Reinforced Concrete

Using the provisions AS 3600, the in-plane strength of a member in combined bending and axial compression is best described with reference to the load-moment interaction curve in Figure 5.

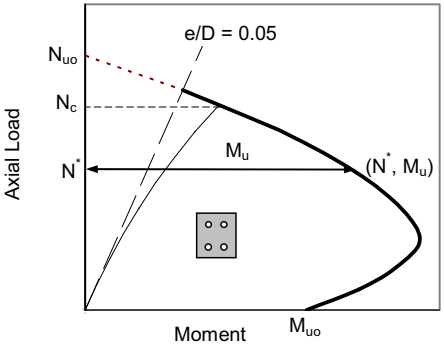


Fig. 5 Interaction curve for reinforced concrete

Where the larger end eccentricity $e_2 = M_2^*/N^*$ is less than the minimum eccentricity of $0.05D$, the end moment M_2^* (and M_1^* assuming symmetrical single curvature) is taken as

$$M_2^* = N^*(0.05D) = M_1^* \tag{15}$$

Using moment magnification, this results in the curved dashed line in Figure 5 which intersects the solid line for cross-section strength at a value of load N_c which can be considered the strength N_c in axial compression. It should be noted that the minimum eccentricity of $0.05D$ is not in addition to any end eccentricities resulting from the applied loads and end moments.

At the level of the design axial force N^*, AS 3600 assumes that the nominal bending strength available to resist the maximum design bending moment M^* (magnified for second-order effects as in Equation 6) is M_u. This is obtained directly from the load-

moment interaction curve as shown in Figure 5. The strength is considered sufficient if

$$M^* \le M_u \tag{16}$$

ignoring the capacity reduction factor ϕ, otherwise $M^* \le \phi M_u$. The factor ϕ can be taken as unity for laboratory tests where material properties and member geometry are accurately known.

5.2 Steel

Using the provisions AS 4100, the in-plane strength of a member in combined bending and axial compression is considered sufficient if

$$M^* \le M_i \tag{17}$$

where M_i is the in-plane moment capacity given by

$$M_i = \left(1 - \frac{N^*}{N_c}\right) M_{uo} \tag{18}$$

and N_c is the capacity in axial compression determined from the column curve appropriate to the column cross-section. Column curves for steel members are shown in Figures 3 and 4.

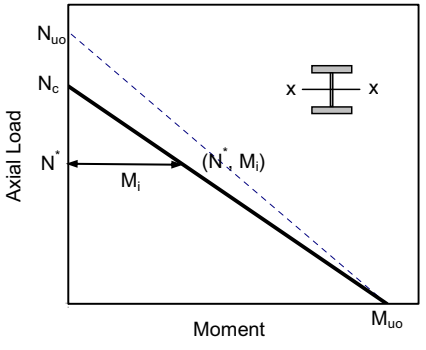


Fig. 6 Interaction curve for steel members

This procedure can also be described in terms of a load-moment interaction diagram and is shown in Figure 6 for comparison with concrete and composite interaction diagrams. The full section strength is denoted by the dashed line and it can be seen that the section moment strength corresponding to the applied axial load N^* is not utilised (difference between the solid and dashed lines at N^*). As member imperfections are not explicitly included in AS 4100 for the analysis of the design moment M^*, this difference in the lines accounts for the additional moments arising from member imperfections. It is particularly conservative for members bent in

double curvature where imperfections can have little or no effect on the design moment *M**.

5.3 Composite

Using the provisions of Eurocode 4, the in-plane strength of a member in combined bending and compression is best described with reference to the load-moment interaction curve in Figure 7.

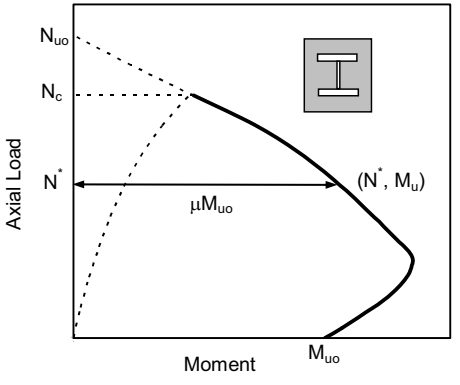


Fig. 7 Interaction curve for composite members

The curved dashed line in Figure 7 is the locus of axial load and the second-order moments arising from axial load acting on an imperfect column with only an initial bow imperfection as prescribed in Table 6.5 of Eurocode 4. This equivalent bow imperfection is larger than actual member out-of-straightness to account for residual stresses and other member imperfections. The column strength N_c in axial compression is where this dashed line intersects the cross-section strength defined by the solid line. Alternatively, N_c is obtained with the use of the appropriate column curve in Eurocode 3 for the steel section using the slenderness λ of the equivalent pin-ended column (see Section 3.3 above). At the level of the design axial force N^*, the remaining bending strength available to resist the maximum design bending M^* (magnified for second-order effects as in Equation 6 and including imperfections) is μM_{uo}. The strength is considered sufficient if

$$M^* \le \mu M_{uo} \tag{19}$$

If the simplified plastic stress distribution procedures of Eurocode 4 are used to determine the load-moment interaction equation, then the strength is considered sufficient if

$$M^* \le \alpha_m \mu M_{uo} \tag{20}$$

where α_m is 0.9 for lower steel grades 235 to 355 and 0.8 for higher steel grades 420 and 460. The reduction factor α_m accounts for the unconservatism in the strength calculations using full plastic stress blocks for the steel and concrete which ignore considerations of strain.

6 DISCUSSION

In examining the current design provisions for reinforced concrete, steel, and composite steel-concrete columns, there are more similarities in the methods than is first apparent. All use cross-section load-moment strength interaction determined using either simple plastic methods (with correction factors where appropriate) or strain compatibility in conjunction with material stress-strain relationships. All require the determination of second-order effects, either directly by analysis or by the use of moment magnification of first order end moments. The major difference between the methods is the manner in which stability and the geometric and material imperfections are taken into account.

For reinforced concrete columns to AS 3600, a minimum eccentricity of load (and hence minimum moment) is required which, in conjunction with moment magnification, can be used to effectively establish the axial load capacity N_c (and hence define a column curve). However, this minimum moment is ignored when the moments resulting from the application of load, as determined by global analysis of the structure, exceed this value. Member imperfections are not accounted for explicitly. The effective stiffness used in second-order analysis is based on a secant stiffness derived for each particular cross-section geometry and material properties.

For steel columns to AS 4100, a column curve accounts for the imperfections, the effect of which is assumed, conservatively, to decrease linearly with decreasing axial force through the use of a linear load-moment interaction equation. Member imperfections are not accounted for explicitly. The effective stiffness used in second-order analysis is the elastic stiffness.

For composite columns, the approach in Eurocode 4 is similar to that for reinforced columns in AS 3600 (compare Figures 5 and 7) except that the minimum eccentricity in AS 3600 is replaced by an explicit equivalent member imperfection which, in conjunction with moment magnification (second-order effects), can be used to effectively establish the axial load capacity N_c (and hence define a column curve). Alternatively, N_c can be determined using a relative slenderness λ together with an appropriate steel column curve from Eurocode 3 (similar to AS 4100). Although member imperfections are to be included explicitly in accounting for second-order effects (moment magnification), it is not entirely clear how this is done for members with end moments. For an imperfect member with no end moments (axially loaded), the moment factor C_m = 1.0 and hence the first-order imperfection moment at the centre of the column will be magnified (Equation 7) as expected. For an imperfect member with first-order end moments, it could be construed that the distribution of first-order imperfection moments along the column is added to the linear moment distribution from the end moments and if the maximum first-order moment is within the length of the column rather than at the end, then a value of the moment factor C_m = 1.0 should be used in Equation 7. However, it is known (Trahair and Bradford 1998) that the moment factor C_m in Equation 8 was derived using an elastic second-order analysis of columns of varying length with a member imperfection proportional to their lengths. Using the Eurocode 4 expression for C_m, its value is 1.1 for a column with equal end moments bent in symmetrical single curvature. This implies that the moment resulting from the imperfection is 10% of the end moment. This needs clarification. The effective stiffness used in second-order analysis is an elastic stiffness modified by correction and calibration factors.

7 ACKNOWLEDGMENTS

The composite tube research has been supported by an ARC Collaborative Grant with BHP Steel and Connell Wagner. The experimental work for the composite columns was carried out in the School of Civil Engineering at the University of Sydney. The analytical studies were carried out in the School of Engineering at the University of Western Sydney.

8 NOTATION

α_b = a constant that reflects the method of manufacture of steel section

α_m = reduction factor used in plastic stress distribution calculations

β = ratio of smaller to larger applied end moments (M_1^*/M_2^*)

β_d = ratio of permanent loading to total loading on a column

δ_b = moment magnification factor for an end-loaded braced column

λ = non-dimensional column slenderness ($\lambda=\sqrt{N_{uo}/N_{cr}}$)

λ_e = plate element slenderness normalised for yield stress ($\lambda_e=b/t\sqrt{(f_y/250)}$)

λ_{ey} = plate element slenderness limit (AS4100) beyond which elements do not yield

ϕ = capacity (strength) reduction factor

φ_t = concrete creep coefficient (Eurocode 2)

μ = ratio of M_u to M_{uo} at the level the design applied axial force N^*

b = width of a plate element in a cross-section

b_e = effective width of a plate element in a cross-section which can reach yield

C_m = factor to convert a column with unequal end moments to one with equal moments

d = effective depth of a reinforced concrete cross-section

d_o = outside diameter of a circular tube

D = overall depth of a cross-section

e = eccentricity of loading at a column end

E_c ,E_s= elastic modulus of concrete section and steel section respectively

EI = flexural stiffness of a section used in moment magnification calculations

f_y = yield stress of steel

I_c, I_s = second moment of area of concrete section and steel section respectively

k_b = elastic plate buckling coefficient determined by rational buckling analysis

k_{bo} = elastic plate buckling coefficient for plates with standard edge support conditions

ℓ = "effective" buckling length of a column

M_i = in-plane moment capacity of a steel column subjected to design axial force N^*

M_u = moment capacity of a section subjected to applied axial force N_u

M_{ub} = "balanced" moment capacity of a reinforced concrete section (AS 4100)

M_{uo} = moment capacity of a section in the absence of axial compressive load

M^* = maximum moment within the length column subjected to design axial force N^*

M_1^* = smaller end moment at an end of a column subjected to design axial force N^*

M_2^* = larger end moment at an end of a column subjected to design axial force N^*

N^* = axial force in a column subjected to design applied loads

N_{cr} = buckling load of column based on flexural stiffness used in moment magnification

N_u = axial compressive capacity of a section subjected to applied moment M_u

N_{uo} = axial compressive capacity of a section in the absence of bending moment

t = thickness of a plate element within a cross-section

9 REFERENCES

ACI 318-05 (2005), "*Building Code Requirements for Structural Concrete*", ACI, Detroit.

ANSI/AISC 360-05 (2005), "*Specification for Structural Steel Buildings*", AISC, Chicago.

AS 3600-2001, "*Australian Standard - Concrete Structures*", Standards Australia, Sydney.

AS 4100-1998, "*Australian Standard - Steel Structures*", Standards Australia, Sydney.

Bridge, R.Q. (1986), "Design of Reinforced Concrete", *Short Course Notes*, School of Civil Engineering, University of New South Wales and Unisearch Ltd, May, pp. 8.1 - 8.36.

Bridge, R.Q. (1990), "Design of Composite Columns", *Postgraduate Course Notes*, School of Civil and Mining Engineering, University of Sydney, pp. 63-86.

Bridge, R.Q. and O'Shea, M.D. (1998), "Behaviour of Thin-walled Steel Box Sections With or Without Internal Restraint", *Journal of Constructional Steel Research,* Vol. 47, No. 1/2, July-August, pp. 73 - 91.

Bridge, R.Q., Pham, L. and Rotter, J.M. (1986), "Composite Steel and Concrete Columns - Design and Reliability", *Proceedings*, 10th Australasian Conference on the Mechanics of Structures and Materials, Adelaide, Aug, 1986, pp. 33-38.

Bridge, R.Q. and Roderick, J.W. (1978), "The Behaviour of Built-up Composite Columns", *Journal of the Structural Division*, ASCE, Vol. 104, No. ST7, July, pp. 1141-1155.

Bridge, R.Q., O'Shea, M.D. and Zhang, J.Q. (1997), "Load-Moment Interaction Curves for Concrete Filled Tubes", *Proceedings*, 15th Australasian Conference on the Mechanics of Structures and Materials, Melbourne, 8-10 Dec., pp. 141-146.

BS 5950-1:2000, "*Structural Use of Steelwork in Buildings*", BSI, London.

BS 8110-1:1997, "*Structural Use of Concrete*", BSI, London

CCAA HB71-2002, "*Reinforced Concrete Design in Accordance with AS 3600-2001*", Cement, Concrete and Aggregates Australia, 4th edition, 2002, Sydney.

Eurocode 2 (2004), EN 1992-1-1:2004 "*Design of Concrete Structures*", CEN, Brussels.

Eurocode 3 (2005), EN 1993-1-1:2005 "*Design of Steel Structures*", CEN, Brussels.

Eurocode 4 (2003), EN 1994-1-1:2003 "*Design of Composite Steel and Concrete Structures*", CEN, Brussels.

Hudson, F.M. (1966), "Reinforced Concrete Columns: Effects of Lateral Tie Spacing on Ultimate Strength*", American Concrete Institute, Special Publication,* No. 13, 1966, pp. 235-244.

O'Shea, M.D. and Bridge, R.Q. (1999a), "Tests on Circular Thin-walled Steel Tubes with Medium and High Strength Concrete", *Australian Civil Engineering Transactions*, Vol. CE40, 1998, IEAust, pp. 15-27.

O'Shea, M.D. and Bridge, R.Q. (1999b), "Behaviour of Circular Thin-Walled Steel Tubes Filled with Very High Strength Concrete", *Australian Journal of Structural Engineering*, IEAust, Vol. SE2, No. 1, pp. 19-30.

O'Shea, M.D. and Bridge, R.Q. (1999c), "Local Buckling and Confinement in Axially Loaded Steel Tubes filled with Normal and High Strength Concrete", *Australian Journal of Structural Engineering*, IEAust, Vol. SE2, Nos. 2 & 3, 1999, pp. 123-133.

O'Shea, M.D. and Bridge, R.Q. (2000), "Design of Circular Thin-Walled Concrete Filled Steel Tubes", *Journal of Structural Engineering*, ASCE, Vol.126, No. 11, Nov., pp. 1295-1303.

Rotter, J.M. (1982), "Composite Columns- Lectures 3 and 7", *Postgraduate Course Notes*, School of Civil and Mining Engineering, The University of Sydney.

Trahair, N.S. and Bradford, M.A. (1998), "*The Behaviour and Design of Steel Structures to AS 4100*", 3rd Australian edition, E & FN Spon, London.

Wheeler, A.T. and Bridge, R.Q. (1993), "Analysis of Cross-Sections in Composite Materials", *Proceedings*, 13th Australasian Conference on the Mechanics of Structures and Materials, Vol. 2, Wollongong, July, pp. 929-936.

STRENGTH OF CONCRETE FILLED STEEL TUBES UNDER HIGH-STRAIN RATE LOADING

Xiao, Yan
Director, MOE Key Laboratory of Building Safety and Efficiency,
Hunan University, China
Professor, University of Southern California, Los Angeles, USA
cipres@hnu.cn, yanxiao@usc.edu

Zheng, Qiu; Huo, Jingsi; Shan, Jianhua; and Chen, Baisheng
MOE Key Laboratory of Building Safety and Efficiency, Hunan University, China
cipres@hnu.cn

ABSTRACT

A Split Hopkinson Pressure Bar (SHPB) equipment was used to perform the high-strain rate compressive tests on concrete filled steel tubes (CFT) under both room and elevated temperatures. This paper reports the results of load-deformation relationships, the dynamic compressive strength corresponding to different strain rates and temperatures. The results reveal the existence of a steel tube and concrete core interaction mechanism. Although the dynamic yielding strength of CFT specimens under elevated temperatures decreases somewhat with the increasing of temperature, the dynamic ultimate strength decreases little with the elevated temperature. A calculation of the dynamic compression strength for CFT columns under both room and elevated temperatures using the simple additive equations without considering confinement was attempted and shown to yield reasonable underestimation to the test results.

INTRODUCTION

Concrete filled steel tubular columns (CFT) have become widely applied in the civil and military constructions, due to their excellent mechanical behavior and other merits. In a CFT column, the steel tube not only carries axial load, flexural moment and shear, but also provides transverse reinforcement for the concrete core. The concrete core shares the load and prevents or delays overall and local buckling of the steel tube. Furthermore, in a structural system with CFT columns, the steel tube can serve as formwork and provide shoring during construction, thus reducing construction costs.

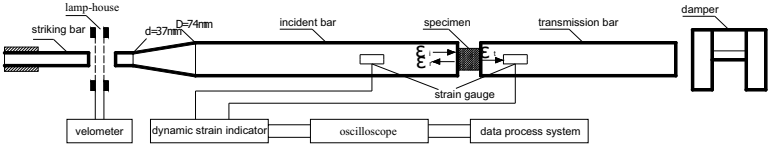
Studies on mechanical behavior of CFT under static and seismic load can be found in a reasonably wide range of existing literature [for example, Viest et al. 1997; Xiao and Mahin 2000]. Several design codes are also established to guide the design and construction practice of CFT column structures [AISC, EC4]. However, structures, either in civil projects or in military constructions, not only bear conventional loading conditions, but could also subject to extreme dynamic load such as strong impact and explosion. Needless to say, structures under blast induced high-strain rate loading become increasingly concerned for civil structures in recent years. CFT columns could provide potential merits in developing blast or impact resistant structures. However, study related to CFT columns under high-strain rate loading is

rare. Chen used hydraulic pressure test machine to carry impact tests on CFT specimens [Chen et al. 1980]. Prichart and Perry performed CFT impact experiment using the drop hammer apparatus [2000]. Recently, the authors applied the light gas gun to study the mechanical behavior of CFT under high-speed impact load [Xiao et al. 2005; Shan et al. 2007]. All these existing studies showed some merits of CFT in resisting dynamic loads compared with conventional reinforced or plain concrete.

Split Hopkinson pressure bar (SHPB) is frequently used as a high-strain rate dynamic loading apparatus with the advantages of convenience, efficient control of strain rate and low operation cost [Ross et al. 1989; Ross and Kuennen 1995]. In this study, a newly manufactured 74 mm-diameter variable cross section SHPB and 36mm-diameter SHPB at the Center for Integrated Protection Research of Engineering Structures (CIPRES) of the Hunan University was respectively used to perform dynamic compressive test of CFT under room and elevated temperature to provide fundamental studies on behavior of CFT under high-strain rate dynamic effects.

SHPB APPARATUS AND TESTING PROGRAM

The dynamic compressive test of CFT was performed using the 74 mm-diameter variable cross section SHPB apparatus shown in Figure 1. The SHPB apparatus consists of two long slender bars that sandwich a short cylindrical specimen between them. The specimen is snugly clamped between the two bars with the surface frictions holding it from dropping under gravity.



(a)



(b)

Fig.1 – SHPB with maximum 74 mm-diameter cross section: (a) conceptual details; (b) apparatus setup.

By striking the end of the incident bar, an incident impulse, εi, is generated and immediately begins to traverse towards the specimen. When the elastic wave

reaches the interface between the incident bar and the specimen, due to the impedance mismatch between the sample and the bar a fraction of the wave is reflected back into the incident bar to form a reflected impulse, εr. The remainder of the wave travels through the specimen and reaches the interface between the specimen and the transmission bar to become a transmission impulse εt, as shown in Figure 1(a). These impulses can be recorded with the strain gauges attached in the surface of the incident and transmission bar. Based on two fundamentals: one-dimension stress wave in the pressure bar and the uniform stress in the sandwiched specimen along its axial direction, the following well known equations can be derived to calculate the stress, strain and strain rate of specimen according to the one-dimension stress wave theory:

$$f_{\mathrm{a}} = E\frac{A}{A_0}\left(\varepsilon_{\mathrm{i}} + \varepsilon_{\mathrm{t}}\right) \tag{1a}$$

$$f_{\mathrm{b}} = E\frac{A}{A_0}\left(\varepsilon_{\mathrm{t}}\right) \tag{1b}$$

$$f_{\mathrm{s}} = \frac{f_{\mathrm{a}} + f_{\mathrm{b}}}{2} = E\frac{A}{2A_{\mathrm{s}}}\left(\varepsilon_{\mathrm{i}} + \varepsilon_{\mathrm{r}} + \varepsilon_{\mathrm{t}}\right) \tag{2}$$

$$\varepsilon_{\mathrm{s}} = \frac{c_0}{l_0}\int_0^{\mathrm{t}}(\varepsilon_{\mathrm{i}} - \varepsilon_{\mathrm{r}} - \varepsilon_{\mathrm{t}})dt \tag{3}$$

$$\dot{\varepsilon}_{\mathrm{s}} = \frac{c_0}{l_0}(\varepsilon_{\mathrm{i}} - \varepsilon_{\mathrm{r}} - \varepsilon_{\mathrm{t}}) \tag{4}$$

where, f_{a} is the stress in the interface between the sample and the incident bar; f_{b} is the stress in the interface between the sample and the transmission bar; f_{s} and ε_{s} are the average specimen stress and strain, respectively; c_0 is the elastic wave velocity of the pressure bar; l_0 is the initial length of specimen; E is the elastic modulus of the pressure bar; A is the cross section area of the specimen.

Small-scale models of CFT segment were made for the testing. In SHPB testing, a longer specimen has negative effect on stress uniformity of the specimen. However, too short length is also inappropriate for possible disturbance to the test result due to the boundary effect. The length to diameter ratio was taken as 0.5 with the specimen length being 25 mm corresponding to a diameter of 50 mm. Such length to diameter ratio is quite common in testing concrete and rock using SHPB in literature [for examples, Bischoff and Perry 1991]. Table 1 shows the detail mixture proportion of concrete infill in steel tube for room and elevated temperature separately, and Table 2 lists the dimension of specimens and the strength of material.

Table 1 - Mixture proportions per cubic meter concrete

	Water (Kg)	Cement (Kg)	Coarse aggregates (Kg)	Fine aggregates (Kg)	HWRA (Kg)
For room temperature	200	500	1010	625	2.5
For elevated temperature	200	444	1217	539	

Table 2 - The dimension of specimens and the strength of material

Specimens	Diameter (mm)× Length (mm)	Thickness of steel tube (mm)	Yield strength of steel tube (MPa)	Strength of concrete infill (MPa)
For room temperature	50×25	1	337	39
For elevated temperature	32×16	1	313	35.9

The two end surfaces of the specimens were carefully ground smoothly. Strain gauges were also affixed on the steel tube surface to measure the axial and circumferential strains for the experiment under room temperature. Proper alignment of the pressure bars with the specimen ensures a uniaxial state of stress while the thin layer of grease applied to the specimen promotes homogeneous deformation in the specimen. All the test cylindrical specimens are coated with a thin layer of grease and placed between two cylindrical bars.

The main purpose of the experiment under room temperature was to test CFT specimens under different strain rates. For the convenience of testing control, three sets of air pressure, 0.5 MPa, 0.8 MPa and 1.2 MPa, were selected as control loading air pressures to propel the striker bar. Table 3 also shows the average maximum input loading forces and strain rates corresponding to the loading pressures based on the measured strain of incident bar.

For the experiment under elevated temperature, After heating the specimen to the pre-determined temperature and keeping it constant for 15 minutes to make the temperatures in the section of the specimen equal to the pre-determined temperature, then, fired the striker bar, and record the result of this test. The velocity of the striker bar is 10 m/s. It should be mentioned that although the heating system can be used to heat the specimen up to 600^{o}C, the maximal testing temperature was only 400 ^{o}C in order to guarantee the reliability of the impact test under high temperature because the bar are also heated together with the specimen.

SHPB EXPERIMENT UNDER ROOM TEMPERATURE

Table 3 shows the parameters and main room temperature testing results of CFT specimens under different stain rates.

The average stress strain relationship curves of CFT shown in Figure 2 illustrate its elastic-plasticity characteristic. Note that compression is taken as positive in this paper. In the early loading stage the stress increased almost linearly with the strain. After achieving the peak value the stress began to decrease to a certain level and maintained the stress approximately at same level, which means that the CFT specimen has a rather high residual strength after impact. The area enclosed by the stress strain curve of a CFT specimen is large, indicating the superior energy dissipation capacity of CFT. Under the same loading pressure, CFT stress strain curves of different specimens are quite similar in the rising stage while the curves are disturbed significantly in the later stages of loading. This was considered due to oscillation caused by the wave dispersion in the large-dimension pressure bar across a relatively long loading duration.

Table 3 - Testing parameters and main test result

Specimen No.	Loading Force (kN)	Strain rate (s^{-1})	Average Strain rate (s^{-1})	Diameter increase * (%)	Length decrease (%)	Compression strength (MPa)	Peak strain	Secant stiffness (GPa)
CFT-1	431.9	81	84	0.88	0.94	132.4	0.008676	15.3
CFT-2	433.5	82		1.38	1.04	145.2	0.007341	19.8
CFT-3	428.4	89		1.61	1.37	157.0	0.007269	21.6
CFT-4	553.6	138	135	3.41	2.66	163.1	0.008365	19.5
CFT-5	553.9	132		4.03	2.46	146.5	0.008334	17.6
CFT-6	559.3	135		1.64	2.19	146.5	0.008098	18.1
CFT-7	693.7	194	191	-	-	162.3	0.008017	20.2
CFT-8	687.0	182		5.68	3.92	154.0	0.008680	17.7
CFT-9	686.1	196		6.46	2.00	173.9	0.008926	19.5

Notes: * The diameters of CFT-8 and CFT-9 were measured as the maximum diameters due to their excessive local buckling while the average diameter is adopted for other specimens. Specimen CFT-7 were damaged by second impact during one test, thus, the dimension change was discarded.

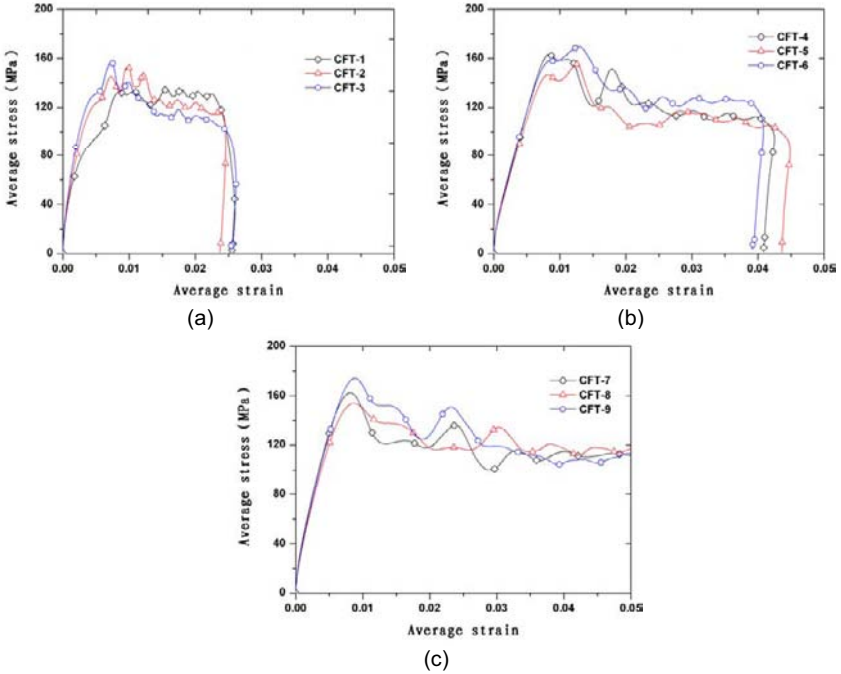


Fig.2 - Stress strain curve of CFT under different strain rates: (a) 84 s^{-1}; (b) 135 s^{-1}; (c) 191 s^{-1}.

DYNAMIC COMPRESSIVE STRENGTH

Behaviors of materials and structures are strain rate-dependant at high strain rate. The most evident exhibition is the increase of strength at higher strain rate, which is

described as the so-called dynamic increase factor (DIF), or the ratio of dynamic strength to static strength.

Static compression test of CFT specimen was conducted for comparison with SHPB test in this study. The specimens in both static and dynamic tests had the same cross section. The length to diameter ratio was the standard value of 2.0 for the static test, whereas 0.5 in SHPB test. The static axial load carrying capacity of CFT specimen was 173kN and the average compression strength was 88 MPa.

Based on Bischoff and Perry [1991], when the strain rate reached a certain value, the stress increase of plain concrete becomes so quickly that time is not enough for the center part of specimen to expand and lateral inertia confinement is formed to the center part. The lateral inertia confinement contributes partially to the strength increase of plain concrete at high strain rate due to its sensitivity to lateral confinement. However, the lateral inertial confinement to concrete core of CFT has less contribution to strength increase due to the existing confinement from the steel tube which is much greater than the lateral inertia confinement. In addition, the capacity of a CFT specimen is shared by both concrete and steel, and the DIF of steel materials are generally smaller than the brittle material concrete [Malvar 1998].

In this study, the simple superposition of dynamic strength of concrete and steel tube is used to estimate the dynamic strength of CFT specimens. Many existing literatures present the DIF of plain concrete and some empirical formulations are concluded to calculate the DIF of concrete at different strain rates. The following empirical equation is recommended by CEB [1988],

$$\frac{f_c}{f_{cs}} = \left(\frac{\dot{\varepsilon}}{\dot{\varepsilon}_s}\right)^{1.026\alpha}, \qquad \text{for } \dot{\varepsilon} \le 30\,\text{s}^{-1} \tag{5a}$$

$$\frac{f_c}{f_{cs}} = \gamma\left(\frac{\dot{\varepsilon}}{\dot{\varepsilon}_s}\right)^{\frac{1}{3}}, \qquad \text{for } \dot{\varepsilon} > 30\,\text{s}^{-1} \tag{5b}$$

where, the empirical parameter is taken as $\alpha = (5 + 3f_{cu}/4)^{-1}$, and $\log\gamma = 6.156\alpha - 2$.

On the other hand, the following DIF equation for reinforcing steel proposed by Marlvar [1998] can be assumed here for the axial stress behavior of steel tube, if the interaction between concrete and steel is neglected.

$$f_{yd} / f_y = (\dot{\varepsilon}/10^{-4})^{(0.074 - f_y/414)} \tag{6}$$

where, f_{yd} and f_y are dynamic strength and static yield strength of steel, respectively; and $\dot{\varepsilon}$ is strain rate.

Based on the assumption of simple superposition of the axial strengths of concrete infill and the steel tube neglecting their interaction, the following equation can be expressed to calculate the dynamic compression strength of CFT:

$$N^d_{CFT} = f_{cd}A_c + f_{yd}A_s \tag{7}$$

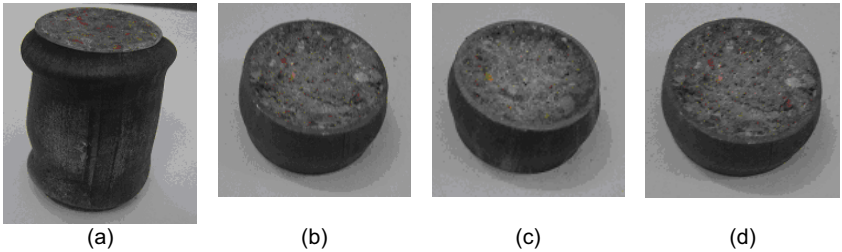
where, A_c and A_s are the cross sectional areas of concrete infill and the steel tube, respectively. The calculated results of the N^d_{CFT} of the CFT specimens are compared with the test results in Table 4. As demonstrated in Table 4, the simple analysis predicts the N^d_{CFT} of CFT specimens reasonably well, however the analysis underestimates the test results for about 30%. Neglecting the interaction mechanisms between the concrete infill and the steel tube is considered to be one of the main reasons for the underestimation.

Table 4 - Dynamic compression strength of the specimens under room temperature

Specimen No.	Strain rate (s^{-1})	Compression strength (kN)	Calculated strength (kN)
CFT-1	81	260.0	176.7
CFT-2	82	285.1	177.2
CFT-3	89	308.3	181.0
CFT-4	138	320.2	203.4
CFT-5	132	287.7	201.0
CFT-6	135	287.7	202.2
CFT-7	194	318.7	223.2
CFT-8	182	302.4	219.3
CFT-9	196	341.5	223.8

SHPB TESTS UNDER ELEVATED TEMPERATURE

Testing parameters and main results for CFT specimens under elevated temperature are shown in Table 5. The static test of concrete-filled steel tube was carried out using a testing machine. The recorded strength at the steel tube yielding point is about 41kN. The failure mode of specimen C00 as shown in Figure 3-a) demonstrates that the failure mechanism of Specimen C00 was local buckling of the outer steel tube (outward folding). The failure modes of the impact-loaded specimens are shown in Figure 3, and the deformations of the specimens are shown in Table 5. The middle part of the specimens after impact was plumped up so that the specimens look like drum. The concrete surface at the end of the specimen was impacted broken off to some degree and comes into being concave pit. There is no obvious difference between the failures modes of different specimens at different high temperature. The surface of the specimens tested at 400°C became black. It can be concluded from the failure modes and deformation of all the specimens that concrete-filled steel tube has an excellent deformation resistance at elevated temperatures. The enhanced structural behavior of the members can be attributed to "composite action" between the steel tube and the concrete core.



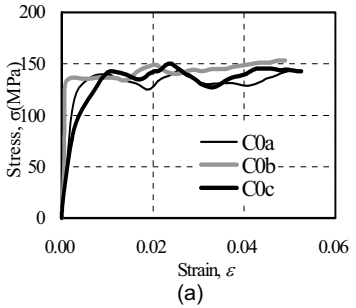
(a) (b) (c) (d)

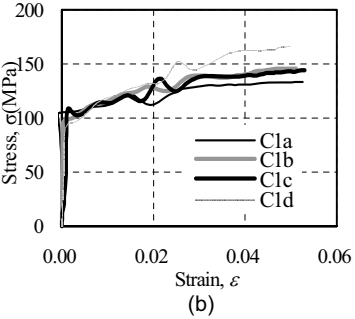
Fig.3 - Specimen failure patterns: (a) static test (C00); (b) C1a; (c) C0b; (d) C4d

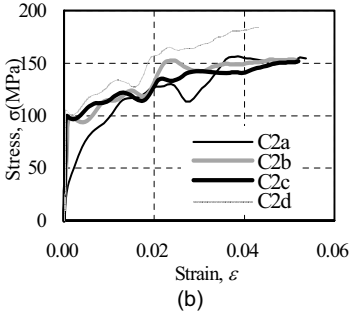
Table 5 - Summary of test result of specimens under elevated temperature

Specimen number	Temperature (℃)	Impact velocity (m/s)	Strain rate (s^{-1})	Yield strength （kN）	Diameter increase* (%)	Length decrease (%)
C00	10	0	Static	40.9	20.1	18.9
C0a	10	10	254	73.3	10.0	8.7
C0b			245	109.4	9.4	7.8
C0c			263	56.4	9.4	8.2
C1a	100		265	85.0	10.5	8.1
C1b			260	80.0	9.7	9.1
C1c			265	86.5	9.8	8.8
C1d			256	76.8	10.1	8.8
C2a	200		270	36.5	8.7	7.5
C2b			265	79.7	9.1	8.1
C2c			263	78.1	7.6	3.7
C2d			217	81.0	9.4	7.5
C4a	400		258	66.5	8.8	8.0
C4b			275	45.6	9.3	6.5
C4c			288	28.3	9.4	7.4
C4d			241	67.9	8.5	7.0

NOTE: The diameters were measured as the maximum diameters after tested.







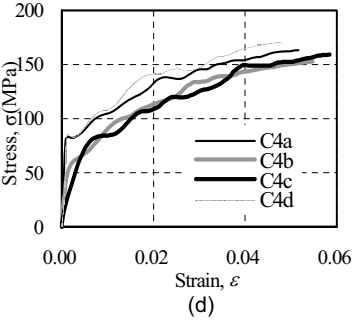


Fig.4 - Stress - strain relationships of CFT at elevated temperatures: (a) 10□(room temperature); (b) 100°C; (c) 200 °C; (d) 400 °C

The average strain rate of the impact test range from 240 to 288 s-1. Figure 4 shows the recorded load versus axial deformation relation curves of concrete-filled steel tubes at elevated temperatures. The load increased with strain linearly by and large before the steel tube yielded. There was no obvious increase in load for the specimens at room temperature after the steel tube yielded, while for the specimens at high temperatures there was remarkable increase in load almost up to the values of the specimens at room temperature.

Figure 5 compares the typical load versus axial deformation relation curves of CFT at elevated temperatures with those of CFT at room temperature and that of CFT under static compression. It can be shown from Figures 4 and 5 that the strength of the specimen being exposed to high temperature decrease to some extent compared to that of the specimen at ambient temperature, however, the after-strength would still increase under great axial deformation. Therefore, the load versus axial deformation relations demonstrates that CFT has an excellent impact resistance under high temperatures.

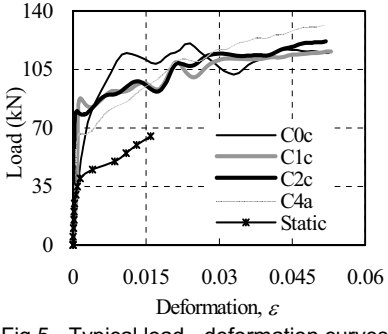


Fig.5 - Typical load - deformation curves

INFLUENCE OF HIGH TEMPERATURE ON YIELD STRENGTH

At present, there is no basis found to be used to determine the strength index of concrete-filled steel tube under impact load. The yielding strength is taken as the measured load corresponding to the steel yielding strain in the load versus deformation curve in the paper. The yielding strain of steel at ambient temperature is 0.0019, and the yielding strain of steel at high temperature is determined according to the following models (Equations 8-9) described by ECCS [1983].

$$\frac{f_y(T)}{f_y} = \begin{cases} 1 + \dfrac{T}{767 \ln \dfrac{T}{1750}} & 0 \le T \le 600°\text{C} \\ \dfrac{108\left(1 - \dfrac{T}{1000}\right)}{T - 440} & 600°\text{C} \le T \le 1000°\text{C} \end{cases} \tag{8}$$

$$\frac{E(T)}{E} = -17.2\times10^{-12}T^4 + 11.8\times10^{-9}T^3 - 34.5\times10^{-7}T^2 + 15.9\times10^{-5}T + 1,$$

for, $0 \le T \le 600°\text{C}$ (9)

where, f_y is the yield strength of steel tube at room temperature, $f_y(T)$ and $E(T)$ are the yield strength and modulus of elasticity of steel tube at high temperature T respectively.

The yielding strength values of the specimens are shown in Table 5. Figure 6 shows the changing of the yielding strength with the increasing of temperature. it demonstrates that although the test data is much discrete, the yielding values of the specimens decrease with the increasing of temperature evidently. The yielding values of the specimens at 400℃ fall by 39.4%.

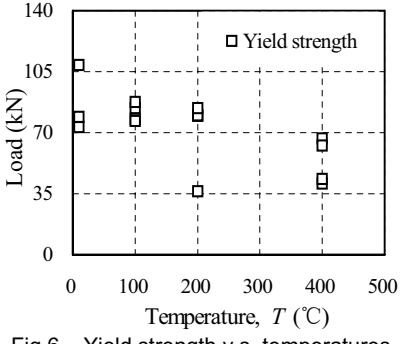


Fig.6 – Yield strength v.s. temperatures

DYNAMIC COMPRESSION STRENGTH OF CFT UNDER ELEVATED TEMPERATURE

In order to determine theoretically the dynamic strength of CFT under high temperatures, the dynamic increase factors of steel and concrete at ambient conditions are used because there are no reliable research on the dynamic increase factors of steel and concrete under high temperatures. Furthermore, the degeneration of strengths of steel and concrete under high temperatures should be considered.

The concrete compressive strength at elevated temperatures can be determined according to the following Eq.10, which was described by Lie [1995[.

$$\frac{f_c(T)}{f_c} = \begin{cases} 1 & 0°\text{C} < T < 450°\text{C} \\ 2.011 - 2.353\left(\dfrac{T-20}{1000}\right) & 450°\text{C} \le T \le 874°\text{C} \\ 0 & T > 874°\text{C} \end{cases} \quad (10)$$

where, f_c is the concrete cylinder strength at room temperature. The yield strength of steel tube at elevated temperatures can be determined according to Eq.8.

On the assumption that the core concrete were loaded to the ultimate compressive strength when the steel tube yielded under impact loading, the ultimate strength of CFT, $N^{\mathrm{d}}_{\mathrm{CFT}}$ would be the summation of the dynamic strength of steel tube $N^{\mathrm{d}}_{\mathrm{steel}}$, and that of concrete, $N^{\mathrm{d}}_{\mathrm{concrete}}$, as follows,

$$N^{\mathrm{d}}_{\mathrm{CFT}} = N^{\mathrm{d}}_{\mathrm{concrete}} + N^{\mathrm{d}}_{\mathrm{steel}} \tag{11}$$

Based Eqs.5-6 and Eqs.8-11, the following equation to determine the ultimate strength of CFT can be obtained.

$$N^{\mathrm{d}}_{\mathrm{CFT}} = DIF_{\mathrm{steel}} \cdot \frac{f_{\mathrm{y}}(T)}{f_{\mathrm{ys}}} \cdot f_{\mathrm{ys}} A_{\mathrm{s}} + DIF_{\mathrm{concrete}} \cdot \frac{f_{\mathrm{c}}(T)}{f_{\mathrm{cs}}} f_{\mathrm{cs}} A_{\mathrm{c}} \tag{12}$$

Figure 7 shows the comparisons of the predicted ultimate dynamic strengths of CFT under elevated temperature with the tested results. It can be concluded that from Figure 10 that the predicted strength is generally smaller than the tested result because the confinement effect of steel tube on core concrete was neglected.

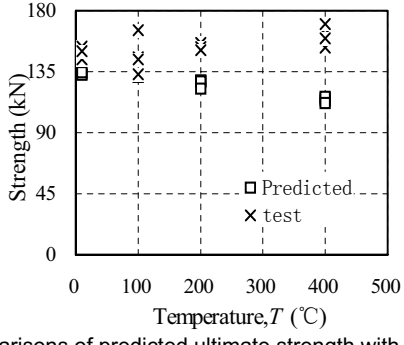


Fig.7 - Comparisons of predicted ultimate strength with tested results

CONCLUSION

Split Hopkinson Pressure Bar (SHPB) was used to perform the high-strain rate dynamic compression tests of concrete filled steel tube (CFT) under both room and elevated temperatures. The following conclusions can be drawn:

1. Strain measurements of the CFT specimens under room temperatures indicate that a significant amount of circumferential strain was developed in the steel tube, hinting the existence of a steel tube and concrete interaction mechanism.

2. Although the dynamic yielding strength of CFT specimens under elevated temperatures decrease somewhat with the increasing of temperature, the dynamic ultimate strength don't decrease with the elevated temperature.

3. A calculation of the dynamic compression strength for CFT columns under both room and elevated temperatures using the simple additive equations without considering confinement was attempted and shown to yield reasonable underestimation to the test results.

4. The specimens behaved well under impact loads and high temperatures, concrete-filled steel tube has an excellent impact resistance and after-strength at elevated temperatures, and it's suitable for CFT to carry impacting and blasting loads.

ACKNOWLEDGEMENTS

The research described in this paper was conducted at the Ministry of Education Key Laboratory of Building Safety and Efficiency of the Hunan University, under the support of the Program for Changjiang Scholars and Innovative Research Team Project (Project No. IRT0619). Partial support for the first author was provided by the University of Southern California.

REFERENCE

Bischoff, P.H. and Perry, S.H. (1991), "Compressive behavior of concrete at high strain rates," Materials and Structures/Materiaux et Constructions, 1991, 24(144): 425 – 450.

CEB (1988), "Concrete structures under impact and impulsive loading," Synthesis Report, Bulletin d'Information, No.187.

Chen Z.Y., Luo, J.Q. and Pan, X.W. (1986), "The performance of reinforced concrete structures subjected impact load (in Chinese)," Qinghua University Press, Beijing, 1986.

ECCS (1983) European recommendations for the fire safety of steel structure, Elsevier, Amsterdam.

Lie T.T., Irwin R.J. (1995) Fire resistance of rectangular steel columns filled with bar-reinforced concrete. Journal of Structural Engineering, 121(5): 797-805

Malvar, L.J. (1998), "Review of static and dynamic properties of steel reinforcing bars," ACI Materials Journal, 95(5): 609-616.

Prichard, S.J. and Perry, S.H. (2000), "The impact behaviour of sleeved concrete cylinders," Structural Engineering, September, 78(17): 23－27.

Ross, C.A., Thompson, P.Y. and Tedesco, J.W. (1989), "Split-Hopkinson Pressure-Bar Tests on Concrete and Mortar in Tension and Compression," ACI Materials Journal, Vol. 86, No. 5, September-October, pp. 475-481.

Ross, C.A., Tedesco, J.W. and Kuennen, S.T. (1995), "Effects of Strain Rate on Concrete Strength," ACI Materials Journal, Vol. 92, No. 1, January-February, pp. 37-47.

Shan, J.H., Chen, R., Zhang, W.X., Xiao, Y. and Lu, F.Y. (2007), "Behavior of concrete filled tubes and confined concrete filled tubes under high speed impact," International Journal of Advances in Structural Engineering, A Multi-Science Publication, UK, 10(2): 209-218.

Viest, I.M., Colaco, J.P., Furlong, R.W., Griffis, L.G., Leon, R.T. and Wyllie, Jr.L.A., editors (1997), "Composite construction design for buildings," ASCE and McGraw-Hill.

Xiao, Y. and Mahin, S. edited, (2000) "Composite and Hybrid Structures,'' Vol.1 and 2, Proceedings of 6th ASCCS International Conference, Los Angeles, March 22-24, 2000, 1220p.

Xiao Y., Zhang W.X., Shan J.H., Chen, R., Yi, W.J., Lu, F.Y. (2005), “Impact tests of concrete filled tubes and confined concrete steel tubes,” Proceedings of 6th Asia-Pacific Conference on Shock and Impact loads on Structures. Perth, December 7-9, 2005: 657-664.

STRENGTH OF CONCRETE FILLED HISTORIC CAST-IRON COLUMNS

Stefan Heyde, Dr.-Ing.
Technical University of Berlin, Department of Steel structures
Berlin, Germany
stefan.heyde@tu-berlin.de

Karsten Geißler, Prof. Dr.-Ing.
Technical University of Berlin, Department of Steel structures
Berlin, Germany
ek-stahlbau@tu-berlin.de

ABSTRACT

Cast-iron columns were used in many industrial and public buildings erected from about 1800 until the early 1900s. During renovation of these old buildings the load carrying capacity has to be checked again and if it fails following the higher load it's obvious to fill the mainly hollow columns with concrete to increase the ultimate load capacity. Because of the special material properties of structural cast-iron it is not possible to determine the capacity of these columns with simple design rules based on present design codes for composite structures e.g. DIN EN 1994-1-1 or the German code DIN 18800-5. As part of a general investigation on historic cast-iron columns a number of tests and numerical calculations have been carried out to clarify the special behaviour of concrete-filled cast-iron columns. Additionally, the bond strength between concrete and the inner surface of the columns was determined by push-out tests.

1 INTRODUCTION

Cast-iron has been extensively used in the construction of buildings throughout the 19th century. Because of its availability and fairly good compressive strength, it was the most economical material for columns until the early 1900s. During renovation, the preservation of these historic columns is a current tendency of public authorities and also of economic interest. Often the loads change due to floor replacement. In these cases it is required to assess the structural design of the cast-iron columns with the current loads again. If the design check fails according to the higher load it is obvious to fill the mainly hollow columns with concrete to increase the ultimate load capacity.

Because of the material properties of structural cast-iron the strength of these columns concerning stability effects cannot be estimated with simple design rules based on present design codes for composite structures e.g. DIN EN 1994-1-1 [DIN EN 1994-1-1 2004] or the German code DIN 18800-5 [DIN 18800-5 2007].

As part of a general investigation on historic cast-iron columns tests and numerical calculations were carried out to clarify the special behaviour of concrete-filled cast-iron columns. To determine the bond characteristic between concrete and the inner surface of the column twelve push-out tests with different diameter to length ratio and four full scale ultimate load tests with eccentrically loaded hollow and concrete-

filled cast iron columns were carried out. As concrete infill self-compacting concrete was taken. The experimental results have been used to calibrate a FE model taking into account the geometrical and physical nonlinearity (ANSYS 10, three dimensional elements). Based on this FE model the influence of important parameters as the stress-strain curve of the cast-iron, the non-dimensional slenderness and the concrete grade were studied.

2 CHARACTERISTIC OF HISTORIC CAST-IRON COLUMNS

2.1 GEOMETRICAL CHARACTERISTICS AND IMPERFECTIONS

The fabrication technique of historic cast-iron columns was mainly a manual one and generally the columns were cast in a horizontal position. Therefore the cross sections often show inner eccentricities resulting from lifting forces on the casting core during this process. A typical hollow cast-iron section is shown in Figure 1. The hole is eccentric to the outer circle and therefore the section has an irregular wall thickness. This leads to a bending moment even in the case of a centrically loaded column.

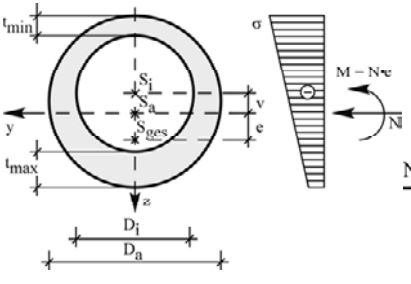


Fig. 1 – Cross-section with eccentricity

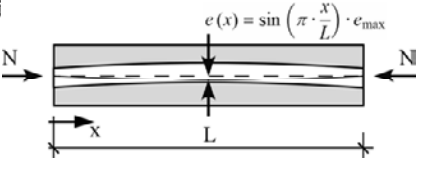


Fig. 2 – Typical cut through a cast-iron column with inner eccentricity *e*

The properties of the eccentric section can be derived from the following equations.

(1) $$e = \frac{-v \cdot \frac{D_i^2 \cdot \pi}{4}}{A}$$

(2) $$k = \frac{D_a^2 + D_i^2}{8 \cdot D_a}$$

(3) $$m = \frac{e}{k}$$

(4) $$\overline{\lambda} = \frac{\lambda}{\pi}\sqrt{\frac{R_d}{E_0}}$$

where

D_a, D_i	External and internal diameter	v	Displacement of the hole
m	Non-dimensional parameter for the inner eccentricity	e	Eccentricity of the cross section
t_m	$=(t_{max}+t_{min})/2$, Average thickness	$\overline{\lambda}$	Non-dimensional slenderness considering the eccentrically section

Different measurements using ultrasonic e.g. by *Käpplein* [Käpplein 1991], *König* [König 1995] and at TU Berlin [Lindner and Heyde 2007], [Heyde 2008] have shown, that the eccentricity e can be idealized by a sinusoidal curvature along the column with a maximum e_{max} in the middle of the span length (see Equation (1)). This assumption is shown in Figure 2 and leads to a non-dimensional inner eccentricity m which may be expressed by Equation (3). For most of the measured columns the value for m lies between 0.0 and 0.5 and the average thickness normally can be obtained with a value of $t_m = 0.1 \times D_a$.

It is very difficult to achieve reliable information about geometrical imperfections of cast-iron columns. Like all steel columns, originally they are not straight. At the early 20th century *Salmon* [Salmon 1921] collected data for wrought and cast-iron columns with different section shapes (rectangular and circular, hollow and solid) and as a result he proposed an initial imperfection of v_0 = L/750. Although not all measurements were made for cast-iron columns they are characteristic for the fabrication tolerances in the 19th century. Except for a few specimens this value gives an upper limit of many measurements and is slightly higher than the commonly used initial deflection for actual steel structures with v_0 = L/1000 [ECCS 1976]. More recent investigations for geometrical imperfections are not available due to the difficulties caused by the irregular shape of cast-iron columns. Calculations conducted from the author in [Heyde 2008] have been shown, that mostly the inner eccentricity m governs the geometrical non-linear behaviour and an assumption for the geometrical imperfection of v_0 = L/1000 is a save estimate for cast-iron columns.

2.2 MATERIAL BEHAVIOUR

Grey cast-iron is characterized by a high compressive strength R_d and a remarkable reduced tensile strength R_m caused by the relative high carbon content. The behaviour can be described as ductile in compression and brittle in tension. Some typical stress-strain curves for cast-iron resulting from tests performed by various authors are shown in Figure 3. The curves are obtained by compression and tension tests on small cylindrical test specimen. It can also be observed that the ultimate compressive strength corresponds with a relatively high strain. For these reasons a full plastic moment does not exist. Only a short range in compression and tension with nearly elastic behaviour can be described by the initial elastic modulus E_0. The differences between different materials concerning the shape of the nonlinear curves and the ultimate compressive strength are remarkable.

It is very difficult to find a good mathematical formulation for these nonlinear curves which covers all the different shapes. Several methods have been presented by *Käpplein* [Käpplein 1991], *König* [König 1995] and *Rondal* and *Rasmussen* [Rondal

and Rasmussen 2003] but the parameters have widely varying values so that a general formulation doesn't exist until yet.

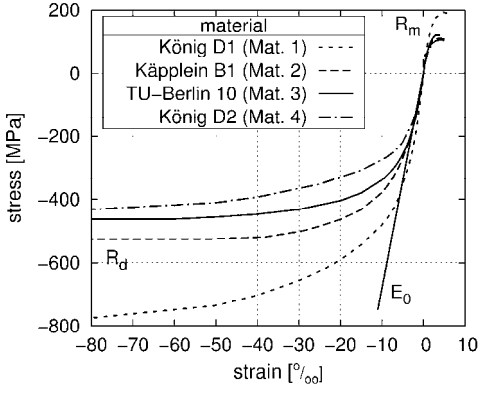


Fig. 3 – Typical stress-strain curves for cast-iron

3 PUSH-OUT TESTS

3.1 TEST SPECIMEN

To determine the bond strength between concrete and the inner surface of the columns twelve push-out tests with different diameter to length ratio were carried out according to standard push-out tests on concrete filled steel tubes (see [Shakir-Khalil 1993],[Virdi and Dowling 1980]). Considering the real situation on a building site where a mechanical compaction isn't possible for a subsequent concreted cast-iron column a self-compacting concrete was used. Additionally, this concrete has a higher flowability than usual concrete. This has the advantage that only small holes to concrete the columns are needed. As concrete grade a common C 30/37 was chosen.

The cast-iron tubes were cut from two old cast-iron columns from a building that was built round 1900. The ends of the tubes were machined to ensure that the ends were parallel to each other and rectangular to the sides. The inner surface was treated with a wire brush to remove rust and loose scale. Some tubes were brushed with a hand brush only to study the influence of this parameter. During the cleaning it could be seen that the inner surface was very rough and in places some unevenness were to find. Figure 4 shows the inner surface of specimen A2 with a remarkable roughness and an obvious local surface unevenness.

After filling the tubes with concrete up to the last 40 mm without any mechanical compaction the specimens were cured for four weeks covered with a plastic film (see Figure 5). The characteristic strength of concrete was tested by six cubes cast and cured in similar conditions and was between 44 MPa and 51 MPa. In Table 1 the properties and the treatment for all specimens are given.

3.2 TEST PROCEDURE

The tests were made with a 3000 kN testing machine (ToniTechnik) using a circular loading pad with a thickness of 30 mm to move the concrete core with respect to the

cast-iron tube. That means that the maximum slip was limited to the plate thickness which corresponded to the air gap. The loading pad was approximately 15 mm smaller than the internal diameter of the cast-iron tube. During the tests the load was increased with 0.25 mm/min. The load-deflection curves were taken from the machine and continuously recorded. In most cases the loading was continued without interruption until the load-slip curves got a parallel slope (frictional movement). Some specimens failed at an earlier stage by a crack in the cast-iron tube due to high local stresses. However, also in these cases a higher slip has already occurred. At the test with specimen A2 the concrete core ran out of the maximum slip of 30 mm without failure. For three specimens of series B (B1, B2 and B4) the load was unloaded and repeated loaded in different stages of the load-slip curve.



Fig. 4 – Cast-iron tube with local unevenness (Nr. A2)

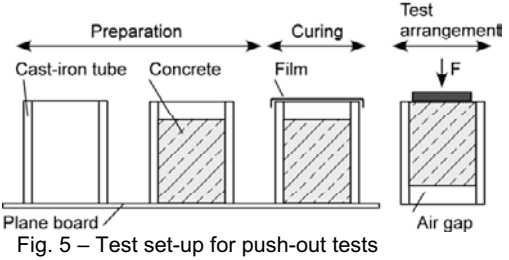


Fig. 5 – Test set-up for push-out tests

Table 1 – Properties for all push-out tests

Test Nr.	L [mm]	D_a [mm]	D_i [mm]	t_m [mm]	L_c [mm]	Air gap [mm]	L_c/D_i	Treatment
A1	347.0	230.0	182.0	24.3	307.0	40.0	1.69	Brushed
A2	343.0	230.0	182.0	24.3	303.0	40.0	1.66	Wire brushed
A3	230.0	231.0	182.5	24.3	190.0	40.0	1.04	Brushed
A4	264.0	231.5	184.0	24.3	224.0	40.0	1.22	Brushed
A5	262.0	231.0	184.0	23.8	222.0	40.0	1.21	Wire brushed
A6	262.0	230.0	182.5	23.8	222.0	40.0	1.22	Brushed
B1	258.0	278.5	218.5	30.3	218.0	40.0	1.00	Brushed
B2	250.0	280.0	216.5	31.8	210.0	40.0	0.97	Wire brushed
B3	307.0	279.5	215.5	31.8	267.0	40.0	1.24	Brushed
B4	307.0	278.0	215.5	31.3	267.0	40.0	1.24	Wire brushed
B5	308.0	278.0	218.0	30.5	268.0	40.0	1.23	Brushed
B6	307.0	279.0	215.0	32.0	267.0	40.0	1.24	Wire brushed

3.3 TEST RESULTS

The results in form of load-deflection curves are shown in Figures 6 and 7. The curves show a nearly uniform shape and can be divided into three stages. In the first stage very high bond strength can be considered with a linear load-deflection relationship. In the last stage the curves tend to a parallel slope but not all. Between these stages a more or less distinct change can be seen. According to the results of *Virdi* and *Dowling* [Virdi and Dowling 1980] the first stage with the high initial stiffness can be related to the interlock between concrete and the rough inner surface of

cast-iron (*microlocking*). The last stage can be attributed to the variation of the shape of the cross section of the cast-iron tube along the x-axis (*macrolocking*). In this stage the frictional resistance interfered with local effects determines the slip resistance. These influences are well known from push-out tests with concrete filled steel tubes, see [Shakir-Khalil 1993], [Virdi and Dowling 1980]. A third influence from local effects, like unevenness and inclusions which are typical for cast-iron columns and related to the fabrication, influences both stages and leads to the high bond resistance. Figure 8 shows these different effects.

The curves for the tests with unloading plotted in Figure 7 show that the deflections after unloading and repeated loading are slightly higher than before at the same load level. The slopes for unloading and loading are nearly parallel. But it can also be assumed that the frictional resistance remains unaffected by unloading. Also the influence of the preparation of the inner surface of the cast-iron tube is negligible.

To get comparable results the load-slip curves were transformed into bond strength–slip curves given in Figure 9. The ultimate bond strength was defined on the basis of a critical bond strain related to the typical critical strain of concrete with $\varepsilon_u = 0.35\%$.

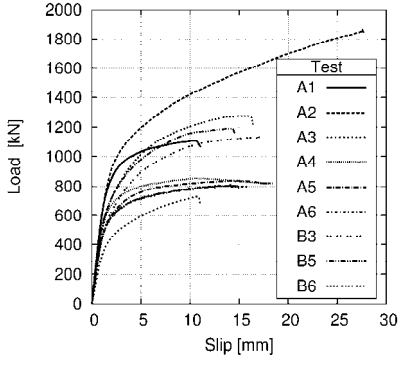


Fig. 6 – Load-deflection curves for the tests without unloading

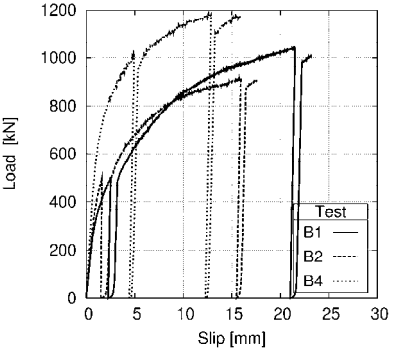


Fig. 7 – Load-deflection curves for the tests with unloading and repeated loading

The critical strain was reached by all specimens with a slip lower than 3 mm and therefore it lies in the first stage of the strain-slip curve with the high initial stiffness. Besides, this approach has the advantage that the frictional resistance does not need to be determined. The results for the ultimate load and the ultimate bond strength are shown in Table 2.

A statistical evaluation shows that the ultimate bond strength $\tau_{0,35}$ has a coefficient of variation of 22% attributed to the individual condition and roughness of the inner surface of the cast-iron tubes. The characteristic strength usual can be obtained by equation (5). For the presented tests the result of the statistical evaluation is figured out in the last row of Table 2.

(5) $$x_k = \mu - 1{,}64 \times \sigma$$

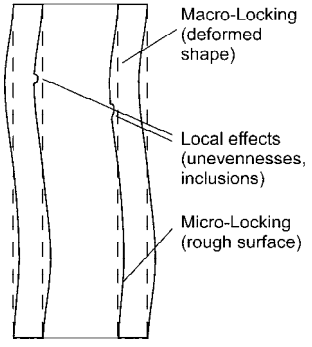


Fig. 8 – Effects on the bond strength

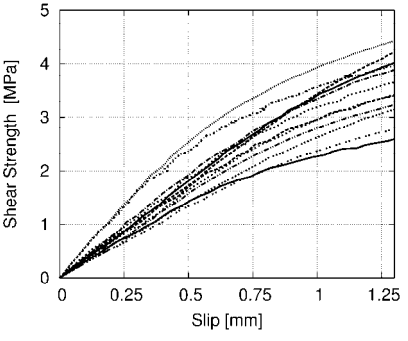


Fig. 9 – Bond strength-deflection curves for all test specimens, first stage

Table 2 – Results for all push-out tests

Test Nr.	$Load_{ultimate}$ [kN]	$Load_{0,35}$ [kN]	Deflection [mm]	max. τ [MPa]	max. $\tau_{0,35}$ [MPa]
A1	1113.3	625.7	1.083	6.29	3.54
A2*	1865.4	611.4	1.053	10.85	3.55
A3	734.7	224.7	0.662	6.78	2.07
A4	857.2	455.5	0.797	6.51	3.46
A5	842.3	363.5	0.781	6.53	2.82
A6	807.8	393.2	0.777	6.35	3.09
B1	1040.1	265.4	0.735	7.21	1.84
B2	914.2	280.2	0.677	6.95	2.13
B3	1135.0	410.4	0.936	6.27	2.27
B4	1184.3	544.8	0.932	6.57	3.02
B5	1193.1	494.6	0.942	6.48	2.69
B6	1284.3	456.8	0.946	7.04	2.50
	Mean μ			6.633	2.748
	Stand deviation σ			0.317	0.598
	μ - 1,64 σ			6.11	1.77

* excluded for max. τ

Taking into consideration that parameters like concrete grade, length of concrete and steel interface, the diameter of the tube and the thickness of the tube have only a small influence on the bond strength (see [Virdi and Dowling 1980]) with the given results a characteristic value for the ultimate bond strength of $\tau_{u,k}$ =1.77 MPa can be recommended for use in design. Although this is strictly valid only for comparable

columns, it can be assumed that generally the typical rough inner surface leads to values in this range.

4 CAST-IRON COMPOSITE COLUMNS

4.1 TESTS PROCEDERE

For centrically loaded cast-iron columns full scale ultimate load tests were carried out by *Käpp-lein* [Käpplein 1991] and *König* [König 1995]. For clarification the behavior of these columns in case of eccentricities at both ends and to determine the influence of concrete filling two tests without and two tests with a concrete filling were performed at TU Berlin. For the tests columns from an old railway bridge with a length of L = 3200 mm were available. The columns were cleaned by sandblasting and an overall measurement by using an ultrasonic pulse-echo instrument was carried out to determine the thickness and the inner eccentricity over the length of the specimen. For the concrete filling a self-compacting concrete C 20/30 was used. An eccentricity of 30 mm at both ends was committed according to the capacity of the test machine. During the ultimate load tests the deflection at five points along the length as well as the strain was measured. After the tests the material properties were determined using cylindrical test specimen cut off from the columns. The results are shown in Table 3.

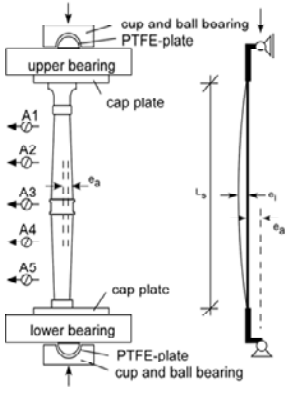


Fig. 10 – Test set-up

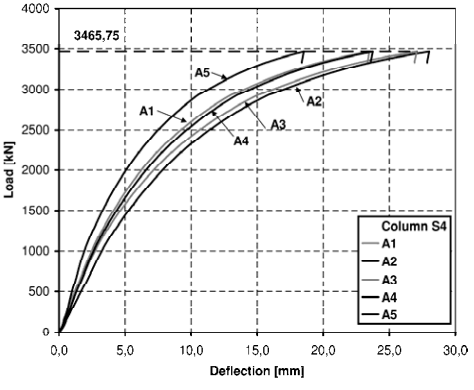


Fig. 11 – Load-deflection curves for test S4

Table 3 – Test results and material properties for the full-scale tests

Column	L_S [mm]	Concrete C 20/30	F_u [kN]	v_{max} [mm]	R_d [MPa]	R_m [MPa]	E_0 [MPa]
S1	3200		2994.0	37	462.0	125.0	95836

S2	3200		2900.0	42	448.0	111.0	111100
S3	3200	x	3477.0	32	450.0	113.0	98060
S4	3200	x	3466.0	28	434.0	108.0	94349

4.2 ULTIMATE LOAD CALCULATIONS

For the ultimate load calculations a three-dimensional FE model was used (ANSYS 10, SOLID 185, MPC 184) [ANSYS 2005] taking into account geometrical and physical nonlinearities. Due to the high bond strength, as described before, and to simplify the calculations the elements for the cast-iron tube and the elements for the concrete infill were coupled directly without interface elements. For loading and support constraint elements were used. The FE model in comparison to the original column is shown in Figure 12 and a detail of the FE model in Figure 13. The stress-strain curves for cast-iron as well as for concrete were included as multilinear curves in the FE model. The concrete strength was taken into account with different values for f_{cm} considering the scatter of this parameter. Also the initial imperfection v_0 was varied. The results of the ultimate load calculations for all specimens are shown in Table 4. As expected the concrete infill increases the ultimate load of the columns notable. For the given examples the increase is approximately 25-30 % related to the ultimate load calculation for the cast-iron column with a geometrical imperfection of v_0 = L/1000.

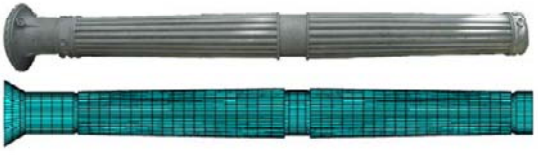


Fig. 12 – Original column and FE model

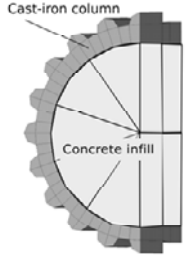


Fig. 13 – FE model, detail

The influence of the geometrical imperfection is rather small since the geometrical nonlinear calculation is governed by the eccentricity e of the cross section. Figure 14 provides a comparison of the load-deflection behaviour for the test and the calculations for specimen S4. The differences between the results of the tests and the ultimate load calculations are quite small. Thus a very good correspondence between calculations and test result concerning the deformation behavior and the ultimate load can be stated. It can be concluded that the FE model and the chosen method represent the load carrying behaviour of these columns correctly.

Table 4 – Results for the FE calculations

Column	$F_{u,\,Test}$ [kN]	e_{max} [mm]	v_0 [mm]	f_{cm} [MPa]	$F_{u,\,FE}$ [kN]	$F_{u,\,FE}$ / $F_{u,Test}$	$F_{u,\,FE,\,L/1000}$ / $F_{u,\,FE}$
S1	2994.0	6.8	0	–	2981	1.00	1.02

			L/1000	–	2935	0.98	1.00
S2	2900.0	6.5	0	–	2888	0.99	1.02
			L/1000	–	2842	0.98	1.00
S3	3477.0	9.1	0	–	2662	0.77	1.01
			L/1000	–	2638	0.76	1.00
			L/1000	38.0	3304	0.95	1.25
			L/1000	43.0	3370	0.97	1.28
S4	3466.0	6.4	0	–	2726	0.79	1.02
			L/1000	–	2668	0.77	1.00
			L/1000	38.0	3380	0.97	1.27
			L/1000	43.0	3472	1.00	1.30

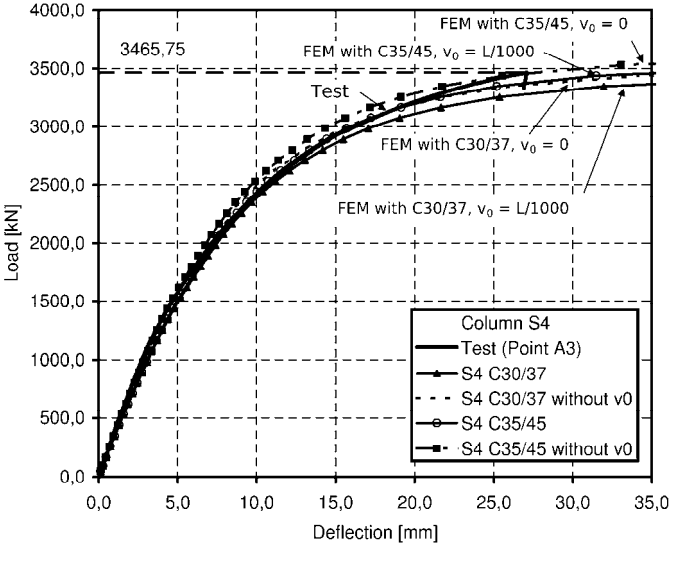


Fig. 14 – Results for the ultimate load calculation for column S4

5 RESULTS OF PARAMETRIC STUDIES

A parametric study, which considered the influence of the cast-iron strength, the concrete strength and the non-dimensional slenderness, was conducted for centrically loaded columns. The cross-section size was chosen circular with a typical external diameter of D_a = 200 mm and a ratio t_m/D_a = 0.1. However, common concrete grades C 30/37 and C 35/45 were chosen as a parameter for the infill, for the cast-

iron the different stress-strain curves are given in Figure 3. As explained before a geometrical imperfection of $v_0 = L/1000$ was estimated.

The effect of the concrete infill on the ultimate load capacity is shown in Figure 15. It can be noted that the ultimate load increases over the whole range of non-dimensional slenderness. The increase depends on different parameters as the compressive strength of cast-iron, the strength of concrete, the non-dimensional slenderness and the non-dimensional inner eccentricity *m*. Related on the ultimate load of the hollow cast-iron column the effect of the concrete infill is more comparable. This is plotted in Figure 16 for cast-iron materials with different compressive strength. The load factor *f* in this figure is defined by equation (6) as ratio of the ultimate load of a concrete filled column $F_{u,\,cast}$ and the hollow cast-iron column $F_{u,cast}$.

(6) $$f = \frac{F_{u,composite}}{F_{u,cast}}$$

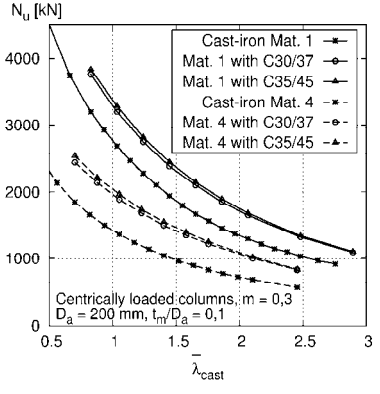


Fig. 15 – Results for the ultimate load calculation for centrically loaded concrete filled cast-iron columns, *m* = 0,3 (see equation (3)) and different concrete grades

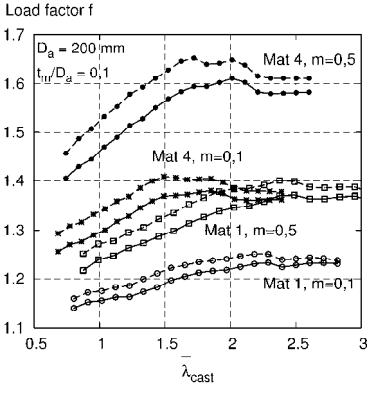


Fig. 16 – Load factor *f* for centrically loaded concrete filled cast-iron columns, dashed line: C 35/45, solid line: C 30/37

For slender columns with a high inner eccentricity *m* and a small compressive strength R_d the gain in capacity is higher than for stubby columns. In the same way a higher concrete grade leads to a higher ultimate load capacity.

6 CONCLUSIONS

A short survey on the design and the characteristic of concrete filled historic cast-iron columns has been presented. As a result of push-out tests a characteristic value for the ultimate bond strength of 1.77 MPa can be recommended for use in design.

Parametric studies have shown that a considerable higher ultimate load can be reached by concreting hollow cast-iron columns with self-compacting concrete. But it also became clear that a treatment of theses composite columns according to simplified interaction formulae from actual design codes is not possible. Due to the many parameters the load carrying capacity depends on, an estimation of the ultimate strength concerning the stability behaviour has to be assessed taking into account physical and geometrical nonlinearities and the actual geometry of the column.

Recently, this method has been applied very successfully during renovation of an old braced multi-storey office building with approximately 270 cast-iron columns in Berlin. Because of the higher live load for a lot of these old columns the stability check had to be assessed again. Only by concreting some of the highly loaded cast-iron columns it was possible to preserve the existing structure which was of enormous benefit for the client to keep this building project economically (see [Geißler and Heyde 2007]).

7 ACKNOWLEDGEMENTS

The authors express their thanks to em. Prof. Dr.-Ing. J. Lindner who also was involved in this research project, to „Deutsche Forschungsgemeinschaft (DFG)“ for partly funding the experimental work, to Dipl.-Ing. Wilke and Dipl.-Ing. Diercksen for experimental work within their diploma thesis and Dipl.-Ing. R. Klüsener for his work within the DFG-project.

8 REFERENCES

[ANSYS 2005] ANSYS 10: Release documentation for ANSYS 10.0. www.ansys.com, 2004.

[DIN EN 1994-1-1 2004] Eurocode 4: Design of composite steel and concrete structures – Part 1-1: General – Common rules and rules for buildings. CEN, 2004.

[DIN 18800-5 2007] Steel structures – Part 5: Composite structures of steel and concrete – Design and construction. Beuth-Verlag Berlin, 2007.

[ECCS 1976] ECCS–CECEM–EKS: MANUAL ON STABILITY OF STEEL STRUCTURES, Report 22. Brüssel, 1976.

[Geißler and Heyde 2007] Geißler, K., Heyde, S.: Gutachten zur Tragfähigkeit der historischen Gussstützen im Gebäude Rosenthaler Hof, Berlin-Mitte. Expert's report 07-02, unpublished, TU Berlin, Department of Steel structures, 2007.

[Heyde 2008] Heyde, S.: Nachweisverfahren für historische Stützen aus Grauguss. Dissertation, TU Berlin, 2008.

[Käpplein 1991] Käpplein, R.: Zur Beurteilung des Tragverhaltens alter gußeiserner Hohlsäulen. In: Berichte der Versuchsanstalt für Stahl, Holz und Steine der Universität Fridericiana in Karlsruhe. 4. Folge, Heft 23, Karlsruhe 1991.

[König 1995] König, B. Historische gusseiserne Stützen – ein zerstörungsfreies Beurteilungsverfahren für die Belastung bei Normaltemperatur und im Brandfall. Dissertation, Bergische Universität Wuppertal, 1995.

[Lindner and Heyde 2007] Lindner, J., Heyde, S.: Traglastuntersuchungen an historischen gusseisernen Stützen. DFG–Abschlussbericht (VR 2148). TU Berlin, FG Metall– und Leichtbau, 2007.

[Rondal and Rasmussen 2003] Rondal, J., Rasmussen, K.J.R.: On the Strength of Cast Iron Columns. Report R829, University of Sydney, Department of Civil Engineering, 2003.

[Salmon 1921] Salmon, E.H.: Columns. A treatise on the strength and design of compression members. Oxford Technical Publications, London, H. Frowde and Hodder & Stoughton, 1921.

[Shakir-Khalil 1993] Shakir-Khalil, H.: Resistance of concrete-filled steel hollow tubes to push-out forces. The Structural Engineering, 71(13), p. 234–243 and Pushout strength of concrete-filled steel hollow section. The Structural Engineering, 71(13), p. 230–233. 1993

[Virdi and Dowling 1980] Virdi, K.S. and Dowling, P.J.: Bond strength in concrete filled steel tubes. IABSE Periodica 3/1980, p. 125-139, Zürich, 1980.

CONCRETE - FILLED STEEL TUBE COLUMNS - TESTS COMPARED WITH EUROCODE 4

C. Douglas Goode
University of Manchester (retired)
Draughton, Skipton, BD23 6DY, England
e-mail: cdgoode@mypostoffice.co.uk

Dennis Lam
School of Civil Engineering
University of Leeds, LS2 9JT, England
e-mail: d.lam@leeds.ac.uk

ABSTRACT

This paper summarises the data from 1819 tests on concrete-filled steel tube columns and compares their failure load with the prediction of Eurocode 4. The full data is given on the website http://web.ukonline.co.uk/asccs2 . The comparison with Eurocode 4 is discussed and shows that Eurocode 4 can be used with confidence and generally gives good agreement with test results, the average Test/EC4 ratio for all tests being 1.11. The Eurocode 4 limitations on concrete strength could be safely extended to concrete with a cylinder strength of 75 N/mm^2 for circular sections and 60 N/mm^2 for rectangular sections.

INTRODUCTION

The properties (D (or h & b), t, f_y, E_s, f_{cyl}, E_c, L, e) and the failure load in the test (N_u) are given for all 1819 tests on the website http://web.ukonline.co.uk/asccs2 [Goode 2007] together with the Eurocode 4 [BSI 2005] calculation of ultimate load capacity (N_{uEC4}) for each test with the material partial safety factor (γ_m) as unity. The website also contains graphs of all the tests compared with Eurocode 4 and a list of 109 references to the papers from where the data has been obtained. The data is divided into circular section and rectangular section columns, with and without moment, and whether the columns are short (L/D or L/b ≤ 4) or long (L/D or L/b > 4) with separate groups for hollow sections and those with preload on the steel or which were subject to a sustained load. Eleven rectangular columns that were subjected to biaxial bending are also included in the database. Table 1 summarises these results for each type of column and gives the average ratio of Test/EC4 prediction (N_u/N_{uEC4}) and the standard deviation of this ratio for each set. The database website is more comprehensive and gives this information for each author's data.

Composite columns and composite compression members are covered in Section 6.7 of Eurocode 4 and a detailed discussion of these clauses is given in [Goode & Narayanan 1997]. The principal limitations and conditions as far as CFST columns are concerned are that the steel grade should be S235 to S460 (yield strength 235 to 460 N/mm^2) and normal weight concrete of strength classes C20/25 to C50/60 (concrete cylinder strength 20 to 50 N/mm^2, cube strength 25 to 60 N/mm^2) (Clause 6.7.1(2)P). The Code also states that local buckling of the steel tube can be neglected for circular section columns if $t > D/(90*(235/f_y))$ and for rectangular columns if $t > h/(52*\sqrt{(235/f_y)})$, f_y in N/mm^2 (Clause 6.7.1(9)). Tests which were outside these limits have not been excluded from the comparison.

For circular CFST columns enhancement factors ('eta' (η) factors, Clause 6.7.3.2(6)) can be applied to allow for the increase in concrete strength caused by the confining effect of the steel tube which produces a triaxial compressive stress state in the concrete thus increasing its failure load [Hobbs et al 1977]. For rectangular section CFST columns the Code takes the failure stress in the concrete as the cylinder strength, without the 0.85 factor that is applied in unrestrained concrete to relate the concrete's cylinder strength to its uniaxial strength.

Overall buckling is allowed for in the Code by introducing a buckling factor (χ) related to the relative slenderness, $\bar{\lambda}$, by the buckling curve (Clause 6.7.3.5(2)). When there is a moment on the column two methods of analysis are permitted. A 'simplified' method in which the second-order effects (P-Δ effect and member imperfections) are allowed for by multiplying the first-order applied moments by a factor 'k' (greater than unity) and a more exact method where the second-order effect, the lateral deflection due to the end moment, is analysed and allowed for. When comparing with the tests the member imperfections have been assumed to be zero and both the 'simplified' and 'second-order' methods have been used to analyse long columns with an end moment and the results are included in the database and summarised in Table 1 of this paper. In the simplified method the calculated strength has been divided by the 'k' factor to compare with the test result (rather than factoring the test result by 'k') and the failure load predicted by the code is compared with the test result at the same axial load/moment ratio as was used in the test.

DISCUSSION AND COMPARISON WITH EUROCODE 4

General

It can be seen from Table 1 that the average failure load in the test divided by the Eurocode 4 prediction (Test/EC4) value for each type of column is greater than unity indicating that Eurocode 4 predicts a lower value than the test and thus a 'safe' result.

However, individual tests and test series by some investigators occasionally gave unsafe results (see website for details). Excluding the eleven biaxial bending tests (which gave very safe results) the average Test/EC4 ratio for the 1808 tests analysed in this paper was 1.11 with a standard deviation of 0.108 using the 'k' factor method, and 1.12 with SD of 0.112 when second order analysis is used for the long columns with moment. If the hollow, preload, sustained load and biaxial tests are omitted the average for the remaining 1658 tests is also 1.11. Of these 1658 tests 970 (59%) satisfied all the Code conditions (strength not greater than 50 N/mm^2 or less than 20 N/mm^2 and local buckling criterion satisfied) and the average Test/EC4 for these was 1.15; 173 (18%) of these failed before the Code strength was attained, ie Test/EC4 < 1, the average for these being 0.93, that is 7% below the predicted strength.

Table 1 – Summary of results for each type of column.

Type of Column		Number of Tests	Average Test/EC4	St Dev of Test/EC4
Short Circular No Moment		368	**1.06**	0.091
Long Circular No Moment		369	**1.17**	0.148
Long (and a few short) Circular with Moment	'k' factor method	254	**1.15**	0.111
	2^{nd} order analysis	254	**1.15**	0.119
Short Rectangular No Moment		330	**1.09**	0.096
Long Rectangular No Moment		212	**1.06**	0.097
Short rectangular with Moment		29	**1.01**	0.108
Long Rectangular with Moment	'k' factor method	96	**1.10**	0.097
	2^{nd} order analysis	96	**1.20**	0.148
Short Hollow Circular No Moment		76	**1.22**	0.095
Circular with Moment and Preload on steel		23	**1.15**	0.123
Rectangular with Moment and Preload on steel		19	**1.03**	0.099
Long Rectangular No Moment and Sustained Load		8	**1.25**	0.051
Square, 8-sided, 16-sided Hollow No Moment		24	**1.16**	0.108
Totals (excluding Biaxial Bending, 'k' factor analysis)		**1808**	**1.11**	0.108
Rectangular with Biaxial Bending	Code straight line interaction	11	**1.52**	0.058
	Elliptical interaction, $\alpha_M = 1$	11	**1.20**	0.041

Concrete strength

The use of concrete with a cylinder strength greater than 50 N/mm^2 was the main reason the tests did not satisfy the Eurocode 4 criteria. Figure 1 shows all the circular section columns plotted against the cylinder strength (except for 5 tests by Salani, who used mortar as the filling, which gave a very high result Test/EC4 > 2.5; these were omitted to reduce the 'y' axis scale and thus make the graph more readable). The numbers in brackets ( ) indicate the number of tests in each set of results. 21% of tests failed below the Eurocode 4 prediction, points below the line, however there were not significantly more 'unsafe' results when the concrete strength was outside the 20 – 50 N/mm^2 cylinder strength permitted by the Code than when it was within this range. Thus the authors suggest that the Code limitation on concrete strength could be safely extended to a cylinder strength of 75 N/mm^2; and possibly even to 110 N/mm^2 though more tests are required with concrete greater than 100 N/mm^2 to justify this.

Figure 2 shows the ratio for all the rectangular section columns plotted against cylinder strength. For rectangular columns a decrease in this ratio when high strength concrete was used is evident. However, the authors suggest that the Code limitation on concrete strength could, for square and rectangular sections, be safely extended to concrete with a strength of 60 N/mm^2. This is also illustrated in Table 2, showing a slight increase in the average Test/EC4 (Av.) values when only columns containing concrete with a cylinder strength less than 60 N/mm^2 are considered and unsafe results for short columns with concrete greater than 60 N/mm^2. The last column in Table 2 shows that safe results are achieved for these rectangular columns when f_{cyl} is replaced by 0.85 f_{cyl}; thus the 0.85 factor, which the Code says can be omitted for concrete filled sections (Clause 6.7.3.2(1)), should be included for rectangular columns when concrete with a cylinder strength greater than 60 N/mm^2 (cube strength 75 N/mm^2) is used.

Table 2 – Use of 0.85 factor for rectangular section columns when $f_{cyl} > 60$ N/mm^2

Type of Rectangular Section Column	All Columns		fcyl ≤ 60 N/mm^2		fcyl > 60 N/mm^2		
	No.	Av.	No.	Av.	No.	fcyl Av.	$0.85f_{cyl}$ Av.
Short no Moment	330	1.09	277	1.12	53	0.97	1.06
Long no Moment	212	1.06	169	1.06	43	1.09	1.19
Short with Moment	29	1.01	25	1.02	4	0.93	1.01
Long with Moment 'k'	96	1.10	64	1.10	32	1.11	1.25
Long with Moment 2nd order	96	1.17	64	1.17	32	1.18	1.29
Overall Average ('k' factor)	667	1.08	535	1.09	132	1.04	1.15

Note: No. is the number of tests, Av. is the average for each set of tests of the ratio Test/EC4

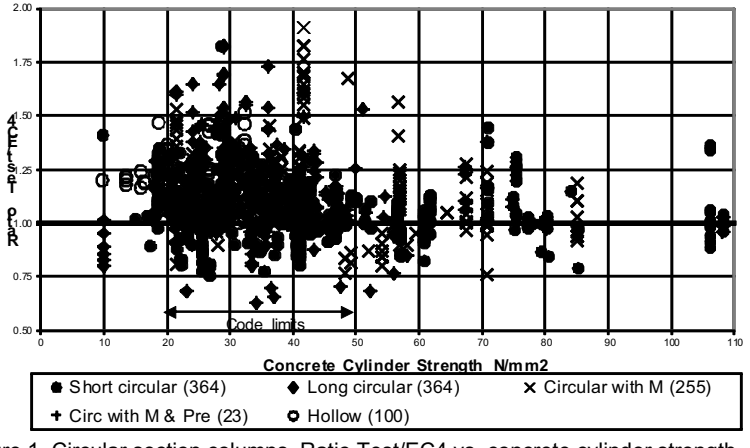


Figure 1. Circular section columns. Ratio Test/EC4 vs. concrete cylinder strength

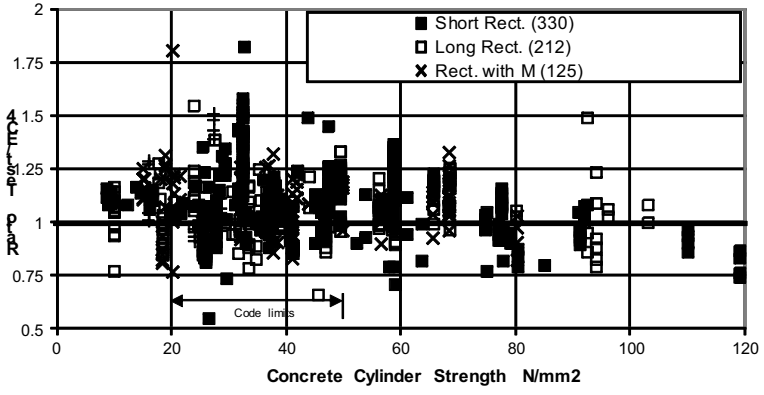


Figure 2. Rectangular columns. Ratio Test/EC4 against concrete cylinder strength

Because of the number of tests involved the separate groups cannot be distinguished in the more densely tested zones in these black and white figures. However, the general trend is clear; the individual tests can be distinguished in the coloured graphs on the website.

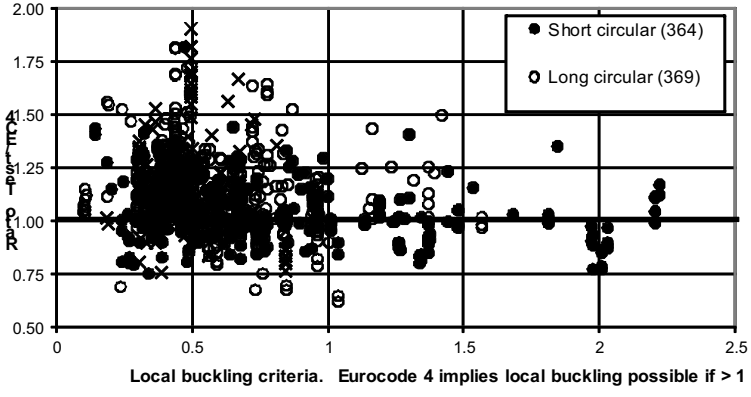


Figure 3. Circular columns. Ratio Test/EC4 against Eurocode 4 local buckling criteria

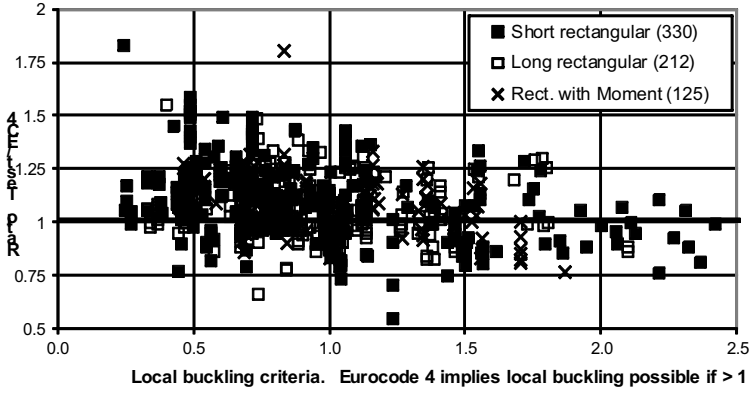


Figure 4. Rectangular Columns. Ratio Test/EC4 against local buckling criteria

Local buckling

The Test/EC4 ratio plotted against the local buckling criteria is shown in Figure 3 for the circular section columns and in Figure 4 for the rectangular section columns. There is a general downward trend in the results for both circular and rectangular section columns when the local buckling criteria is exceeded (> 1.0) so it is probably desirable to keep the existing limits. In some tests the steel would have had to be over twice as thick to satisfy the Code criteria; however, in all cases where the Code condition is exceeded, if a 0.75 factor were applied to the Eurocode 4 prediction the tests would be safe.

Slenderness

Figure 5 (short columns without moment), Figure 6 (long columns without moment) and Figure 7 (columns with an end moment) show the ratio Test/EC4 against slenderness. They all show that the Code method of allowing for slenderness is satisfactory. Indeed, as Figure 6 shows, for circular columns without moment there is a slight upward trend in the ratio as the columns become more slender; this could be because the buckling factor (χ) used in the code is conservative when the columns are slender. However, it would be prudent for no changes to be made to the Eurocode 4 buckling factor unless further tests confirm this trend.

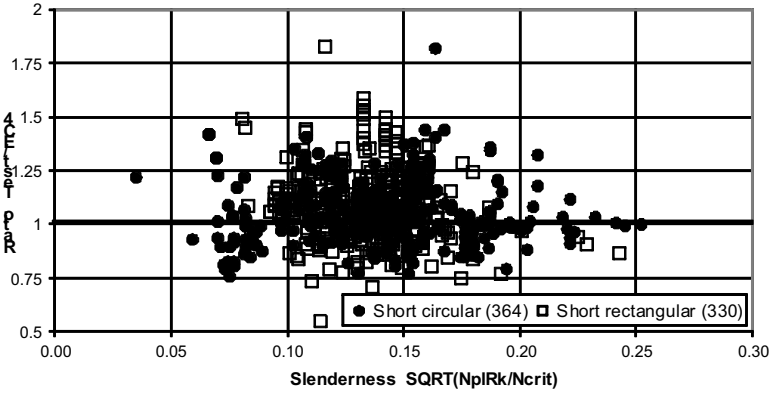


Figure 5. Short columns without moment. Ratio Test/EC4 against Slenderness

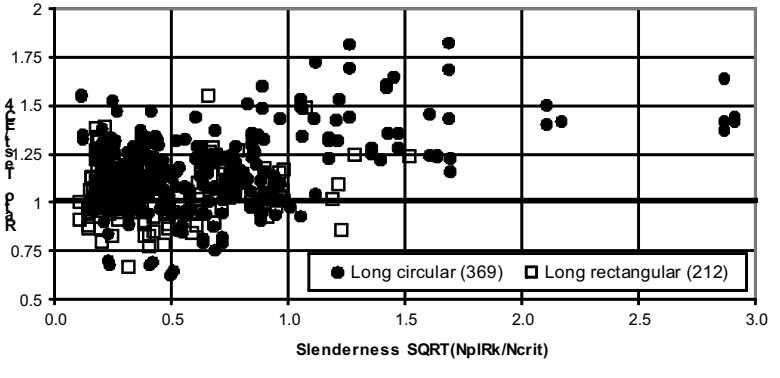


Figure 6. Long columns without moment. Ratio Test/EC4 against Slenderness

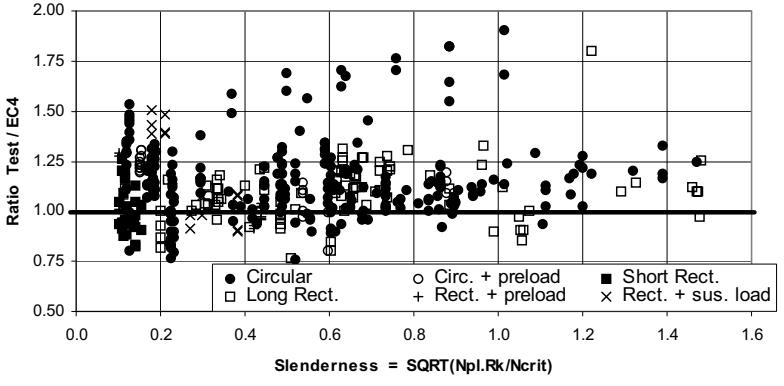


Figure 7. Columns with moment. Ratio Test/EC4 against Slenderness

Hollow sections (rows 10 and 14 in Table 1)
Hollow sections were formed by spinning the steel tube with some concrete in it so that centrifugal force leaves a hole in the concrete. All the hollow sections used low strength concrete, none greater than 40 N/mm^2, and gave column strengths about 20% greater than predicted. This may be due to the difficulty of measuring the true strength of the spun concrete which might be higher than the measured cylinder strength. However, it appears that hollow sections can be designed safely using Eurocode 4 if the hole is allowed for.

Preload and sustained load (rows 11, 12, 13 in Table 1)
Pre-load (up to 60% of the capacity of the steel) on the steel tube before filling with concrete seems to have had no effect on the strength; the average Test/EC4 for the 23 circular columns (11 short and 12 long) being 1.15 (SD 0.123) and for the 19 rectangular columns (10 short and 12 long) being 1.03 (SD 0.099). The eight tests which sustained an average load of between 53% and 63% of their capacity for 120 or 180 days before being loaded to failure carried a slightly higher load before failing (average Test/EC4 = 1.25) than their six comparison tests without sustained load (average Test/EC4 = 1.08); these six companion tests are included in the 212 tests of row 6 of Table 1.

Biaxial bending
Only eleven tests on rectangular columns with biaxial bending are reported and these all failed at much higher loads than predicted by Eurocode 4, average Test/EC4 was 1.52. The Code uses a straight line interaction for the bending resistance between the two axes with an additional safety factor α_M, (with α_M as 0.9 for steel grades S235 to S355 and 0.8 for steel grades S420 and S460, Clause 6.7.3.7). Using an elliptical interaction between the moments about the two axes and omitting this additional safety factor, ie. $\alpha_M = 1$, gives much closer agreement with the test failure load, an average Test/Prediction of 1.20 for these eleven tests; see the last two rows of Table 1.

CONCLUSIONS

a) Eurocode 4 can be used with confidence for the design of concrete filled steel tube columns. The average Test/EC4 ratio from 1808 tests being 1.11.

b) For circular section columns the Code limitation on concrete cylinder strength could be safely extended to 75 N/mm^2 (cube 94 N/mm^2). Even columns with cylinder strengths above 100 N/mm^2 (cube 125 N/mm^2) were safe, though more tests with such high strength concrete are desirable to justify using the Code with such high strength concrete.

c) For rectangular section columns the concrete strength limitation could be safely extended to 60 N/mm^2. When higher strength concrete is used its cylinder strength should be factored by 0.85, equivalent to assuming no enhancement of concrete strength due to containment.

d) Sections, both circular and rectangular, which have a wall thickness thinner than permitted by the local buckling Clause 6.7.1(9) could be used if a factor of 0.75 was applied to the strength predicted by Eurocode 4.

e) Hollow sections can be designed using Eurocode 4 provided allowance is made for the hole.

f) Neither preload on the steel tube nor sustained load on the filled column had any significant effect on the failure strength of the column.

g) More testing of rectangular columns under biaxial bending is needed. The eleven tests reported show the straight line interaction used in Eurocode 4 to be very safe (Test/EC4 = 1.52) and an elliptical interaction might be preferable (Test/Prediction = 1.20).

REFERENCES

BSI 2005. British Standards Institution. *Eurocode 4: Design of composite steel and concrete structures – Part 1-1: General rules and rules for buildings. BS EN 1994-1-1:2004.* Milton Keynes, BSI, 2005.

Goode 2007. Website with database of all 1819 tests and 109 references to this data: http://website.ukonline.co.uk/asccs2 (also available for £5 as a CD with all data, supplementary calculations and analysis from Douglas Goode, e-mail: cdgoode@mypostoffice.co.uk)

Goode & Narayanan 1997. Goode C. D. and Narayanan R. 'Design of concrete filled steel tubes to EC4', *International Conference on Composite Construction – Conventional and Innovative, Seminar by ASCCS on Concrete Filled Steel Tubes,* Innsbruck, 18 September 1997, p 1-25.

Hobbs et al 1977. Hobbs D. W., Pomeroy C. D. & Newman J. B. 'Design stresses for concrete structures subject to multi-axial stresses', *The Structural Engineer,* **55**/4, 1977, p 151-164.

NOTATION

D	outer diameter of the circular steel tube
h	larger dimension of the rectangular steel tube
b	smaller dimension of the rectangular steel tube
t	thickness of the steel tube
f_y	yield stress of the steel
E_s	modulus of elasticity of the steel (E_a in EC4) = 200 N/mm^2 if not given by the tester
f_{cyl}	cylinder strength of the concrete = $0.8f_{cu}$ if cube strength given by the tester
f_{cu}	cube strength of the concrete
E_c	secant modulus of elasticity of the concrete to $0.4f_{cyl}$ = $22*((f_{cyl} + 8)/10)^{0.3}$ if E_c was not given by the tester
L	length of the column
e	eccentricity of load on the end of the column, causing end moment
N_{uEC4}	ultimate load capacity of the column as calculated using Eurocode 4
N_u	axial load at failure in the test
χ	buckling factor = $1/(\varphi + \sqrt{(\varphi^2 - \bar{\lambda})})$ where $\varphi = 0.5*(1 + 0.21*(\bar{\lambda} - 0.2) + \bar{\lambda}^2)$
$\bar{\lambda}$	slenderness ratio = $\sqrt{(N_{plRk}/N_{cr})}$
N_{plRk}	plastic resistance of the composite section
N_{cr}	elastic critical load = $\pi^2(EI)_{eff}/L^2$
$(EI)_{eff}$	effective flexural stiffness of the composite section = $E_aI_a + 0.6*E_cI_c$
k	factor to take account of second order effects in the simplified analysis, which, for columns with equal end moment, = $1/(1 - N_u/N_{cr,eff})$ where $N_{cr,eff}$ uses $(EI)_{eff,II} = 0.9*(E_aI_a + 0.5*E_cI_c)$ to obtain the elastic critical load

DESIGN OF COMPOSITE COLUMNS MADE OF CONCRETE FILLED TUBES WITH INNER MASSIVE CORE PROFILES AND HIGH STRENGTH MATERIALS

Univ.-Prof. Dr.-Ing. G. Hanswille
Institute for Steel and Composite Structures, University of Wuppertal
Wuppertal, Germany
stahlbau@uni-wuppertal.de

Dipl.-Ing. M. Lippes
Gevelsberg, Germany
lippes@email.de

ABSTRACT

This paper deals with the design of composite columns made of concrete filled tubes with inner massive core profiles as well as high strength steel and high strength concrete. New research work regarding the effect of residual stresses in inner core profiles resulting from the cooling process during fabrication is presented. Based on Finite Element studies new models are presented for the determination of the distribution of residual stresses in solid round steel bars, taking into account the steel grade, the dimensions of the core profiles and the cooling conditions during fabrication. Additional theoretical investigations are presented to estimate the effects of creep and shrinkage under long term loading. Finally recommendations are given for the design of this type of composite column based on the methods given in Eurocode 4-1-1 [1].

1 INTRODUCTION

The use of composite columns made of high-strength steel and high strength concrete is beneficial to realise a high resistance in combination with small dimensions of cross section. At present the design of composite columns according to Eurocode 4 Part 1-1 [1] is applicable only for steel grades up to S460 and concrete strengths up to C50/60, because no sufficient test data are available. In the following new test results and analytical investigations are presented to open the scope in Eurocode 4-1-1 especially for high strength concrete. To fulfil the demand for more slender columns, the use of concrete filled tubes with additional massive inner core profiles is very effective. Due to limited information about the effects of residual stresses in massive core profiles which develop during production, the use of massive round steel cores is also not yet covered by the standards in general. Therefore numerical investigations for the determination of residual stresses in massive round steel bars had been made in order to widen the scope in EN 1994-1-1 [1] for this type of column.

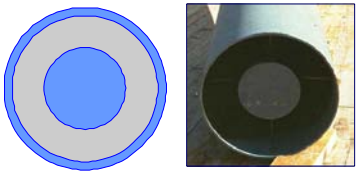


Fig. 1- Composite column with inner massive core profile

2 NEW TESTS AND EXPERIMENTAL SETUP

The test program comprises 6 columns with concrete filled tubes (series C1) and further 6 columns with additional massive inner core profiles with a diameter of 70 mm (series C2). Columns in axial compression and with uniaxial bending due to end eccentricity e_o of 5 mm, 20 mm and 60 mm were performed. Information about the test specimen and the test program is given in Figure 2 and Table 1. The concrete cylinder strength was 95 N/mm^2, the yield strength of the tubes 333 N/mm^2 and the yield strength of the massive bars was 411 N/mm^2 in the centre of the profile and 447 N/mm^2 at the surface.

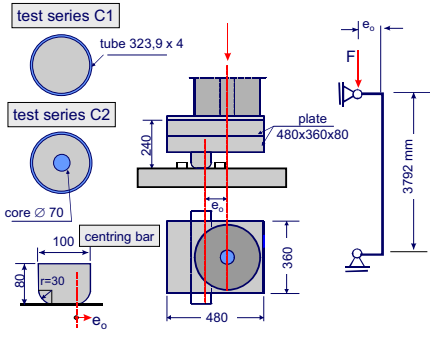


Fig. 2 – Test setup

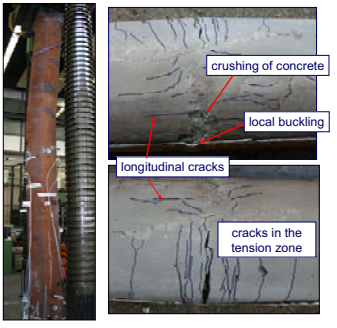


Fig. 3 – typical failure mode

According to EC4-1-1 appendix B [1] the columns were preloaded. At first the load was applied in increments up to approximately 50% of the expected failure load and then cycled 150 times between 25% and 50% of the expected failure load. During the cyclic loading the load was applied force controlled. After this procedure the load was increased and applied displacement controlled up to the failure load. Each test was held at specific load levels for more than 15 minutes to get information about relaxation. In this manner the ultimate static load considering relaxation effects could be determined. In nearly all tests a reduction up to 4% of the ultimate short time static load could be observed. When reaching the ultimate load all tests failed in the middle third of the column by crushing of concrete and local buckling of the steel tube (Figure 3).

Two columns did not reach the expected failure load. The unexpected failure was caused by airlocks due to an inefficient compaction of the concrete in the middle of the column and under the end plates. The concrete had been filled from the top. Based on the results it can be stated that this method and a rapid settling of the concrete leads to the risk of an insufficient compaction of the concrete especially when using high strength concrete. Because of the unexpected results these columns were excluded from further analyses. The horizontal deflection under maximum loads and the strains measured in the middle of the columns were used to determine the internal forces and the effective load eccentricity at failure load. Using the experimental stress-strain curves, the bending moment in the middle of the column was calculated with the assumption that the cross section remains plain. The evaluation of the tangential strains in the tubes indicated that the confinement effect of the tube on the compressive strength of concrete can be neglected.

The evaluation of the internal forces showed that the effective eccentricity e_x for the recalculation of the columns depends on the load level and is given by $e_x = e_o + \Delta e_x$ according to Figure 4. At the beginning of loading the effective eccentricity was approximately equal to the distance between the axis of the load introduction and the centre line of the centring bar. By increasing the load and also the rotation at the bearing of the column the eccentricity moved to the edge of the centring bar. The evaluation showed that the effective eccentricity converges to a value $\Delta e_{x,u}$ with increasing loading, so that the load eccentricity at failure could be exactly determined (Figure 4).

Table 1 – Experimental and calculated ultimate loads and corresponding horizontal deformations

	test series C1					test series C2				
test	1	3	4	5	6	1	2	3	4	6
experimental values										
e_0 [mm]	20	60	60	5	5	20	20	60	60	5
F_u [kN]	5439	3192	2986	5980	5903	5560	5322	3392	3277	7359
$\Delta e_{x,u}$ [mm]	10	14	15	13	15	10	17	10	11	7
$u_x(F_u)$ [mm]	12,4	20,2	19,6	15,1	11,6	16,0	16,1	23,8	23,2	15,0
$e_{x,u}=e_o+\Delta e_x+u_x$	42,4	94,2	94,6	33,1	30,6	46,0	53,1	93,8	94,2	27,0
results of the recalculation with the FE - model										
$e_{o,cal}$ [mm]	30	74	75	18	20	30	37	70	71	12
F_u [kN]	4981	3247	3188	6182	5938	5493	5094	3401	3409	6969
$u_x(F_u)$ [mm]	17,5	26,5	25,4	17,4	17,9	20,5	22,2	28,4	29,6	14,3
$e_{x,u}=e_{o,cal}+u_x$	47,5	100,5	100,4	35,4	37,9	50,5	59,2	98,4	100,6	26,3

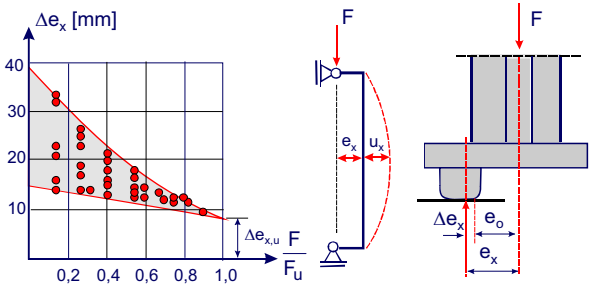


Fig. 4 – Relation between the effective eccentricity and the load level

3 NUMERICAL INVESTIGATIONS AND EVALUATION OF TEST RESULTS

For the recalculation of the columns a 3-dimensional model with cuboid elements of the FE-program Ansys was used. The mechanical properties of steel were represented by a multi-linear elastic-plastic stress-strain relationship on the basis of the von Mises yield criterion. For the mechanical properties of concrete an additional condition described by Porsch in [3] was used to take into account the low resistance against tension stresses more accurately. In order to take into account the bond behaviour between steel and concrete, in the interfaces between steel and concrete contact elements were used with a friction coefficient $\mu = 0.5$. The model allows considering initial bow imperfections and additional eccentric positions of the massive inner steel core. A typical relation between the normal force and the bending moment at midspan is shown in Figure 6. The measured and calculated strains in Figure 6 demonstrate that for design it can be assumed that the cross section remains plain.

In order to check the safety level in comparison with the simplified design methods in Eurocode 4 the general design method in Eurocode 4 has to be used. Regarding the safety concept in case of non linear finite element analysis the Eurocodes for composite structures give no clear guidance. Therefore the method developed by Hanswille and Bergmann in [4, 5] was used, whereas for the resistance an overall safety γ_R has to be determined which depends on the relation between the acting normal force and the acting bending moment. The safety factor γ_R can be determined using the full plastic cross-section interaction curve of the section. As shown in Figure 5, the interaction curves using the mean values (measured values in case of tests) for the material strength as well as the curve using the design values according to Eurocode 4 have to be calculated. For the determination of the interaction curve based on design values, the partial factor 1.5 for concrete, 1.1 for structural steel and 1.15 for reinforcement have to be used. For a given combination of internal forces N_{Ed} and M_{Ed} the safety factor γ_R is given by the ratio of the vectors $R_{pl,m}$ and $R_{pl,d}$. The incremental finite element analysis has to be performed using an initial geometrical bow imperfection and considering residual stresses in the massive inner core profile. It has to be verified, that the load amplification factor λ_u is greater than the overall safety factor γ_R for the resistance.

The test results were evaluated based on the statistical method given in EN 1990, app. D [2] in order to determine characteristic and design values. This method is based on a comparison of the experimental $F_{u,exp}$ and theoretical $F_{u,cal}$ values of the ultimate load, where the theoretical values result from a mechanical model. For the columns the theoretical values $F_{u,cal}$ were determined by the aid of a finite element analysis taking into account the measured stress strain relations from the tests and considering residual stress in the core profiles determined according to the following section 4. For the calculation of the ultimate Load F_{um} in addition to the end eccentricities acc. to Table 1 geometrical bow imperfections with a parabolic shape and a maximum value L/1000 were assumed. The results of the statistical evaluation of the test results acc. to EN 1990 are shown in Figure 7. The characteristic values are given by $F_{R,k} = 0{,}9\ F_{u,m}$ and the appropriate design value result to $F_{R,d} = 0{,}79\ F_{u,m}$. For comparison in Figure 7 also the design values resulting from the general design method in Eurocode 4-1-1 are shown. These values were calculated with the partial factors acc. to Eurocode 4-1-1 and the safety concept shown in Figure 5. It can be seen that the general design method in Eurocode 4-1-1 leads to safe results also in case of high strength materials.

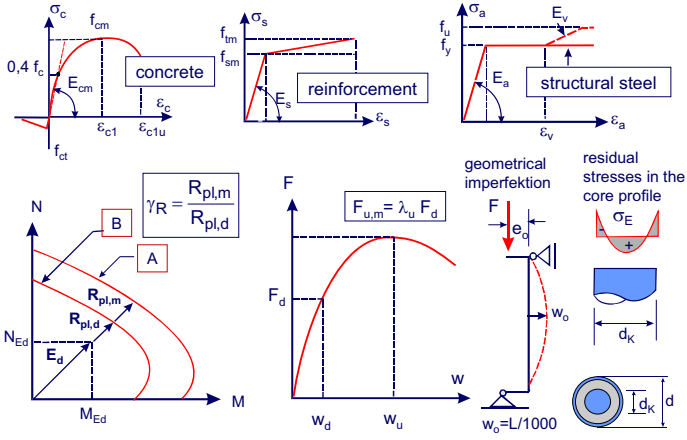


Fig. 5 – Safety concept in case of non linear design of composite columns [4, 5]

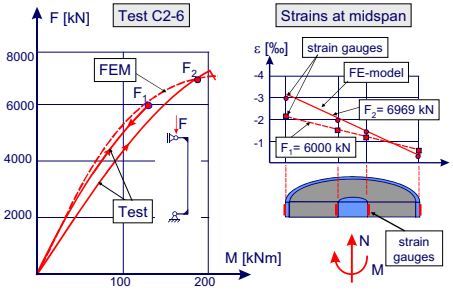


Fig. 6 - Relation between the normal force and the bending moment at midspan and strain distribution

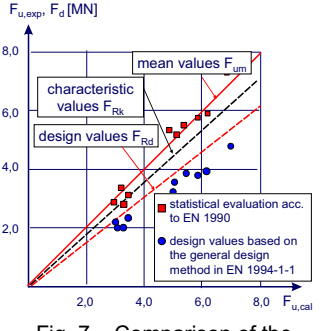


Fig. 7 – Comparison of the experimental and theoretical ultimate loads and test evaluation acc. to. EN 1990

4 RESIDUAL STRESSES IN MASSIVE ROUND STEEL BARS

As mentioned before, structural and geometrical imperfections must be taken into account for the determination of ultimate loads of columns. For composite columns with inner massive core profiles especially the residual stresses in the steel cores have to be considered.

Residual stresses arise during production due to the uneven temperature distribution while the steel bar is cooling of. The surface areas are cooling down and hardening

faster with ongoing cooling. The later cooling of the inner parts causes then compression in the already hardened part near the surface and tension stresses in the inner parts of the cross section. In composite columns these residual stresses cause a reduction of flexural stiffness and a reduction of the ultimate load due to earlier yielding of structural steel and increasing yielding zones in the structural steel section.

The simplified design method in Eurocode 4-1-1 covers the influence of residual stresses by equivalent initial bow imperfections, where the distribution of residual stresses in structural steel sections are taken into account by different buckling curves. For columns with round inner core profiles until now no information is given in Eurocode 4-1-1 regarding the relevant buckling curve and the corresponding member imperfections. Up to now only a few experimental investigations are known which give information about the distribution of residual stresses in massive round steel bars (Roik, Schaumann [6]).

To obtain more detailed information about the stress distribution and the maximum stresses, the cooling process was simulated using the FE-program ANSYS. The residual stresses were calculated for different diameters and steel grades. The temperature dependent material-properties were taken from DIN EN 1993-1-2 [7]. Furthermore it was assumed, that there is no subsequent treatment to diminish the residual stresses.

First of all the time-dependent temperature distribution was determined. The calculations were performed for the period of cooling after the final rolling of the steel. Acc. to [7] a maximum temperature for the rolled steel of 1200°C was assumed. At higher temperatures, it can be assumed that the steel has no mechanical stiffness. A temperature gradient in this range has no effect on the development of residual stresses. Thereby the convective and radiative heat transmission coefficients and the initial temperature of the massive profile were the most important parameters which influence the distribution and values of the residual stresses. The simulations were performed with two different cooling conditions. Additional to normal cooling conditions unfavourable environmental conditions were examined. To achieve this, the convective heat transfer coefficient was determined for different continuous air flow. For the normal cooling conditions an air flow rate of w=1 m/s was assumed. With an air flow rate of w=5 m/s extremely unfavourable cooling conditions were taken into account. This extreme cooling condition was used to get information about the relation between the residual stresses and the different cooling conditions. The interaction between convection and radiation was not considered because this leads to a more slowly cooling and therefore to smaller residual stresses. Considering the interval of cooling from the initial state down to 100 °C the environmental conditions lead to cooling durations as shown in Figure 8. Figure 9 shows the development of the temperature in the centre and at the surface for a solid bar with a diameter of 200 mm.

With the temperature dependent stress-strain relationships according to [7] the distributions of the residual stresses can be determined from the calculated time-dependent temperature distributions. Different environmental conditions affect the residual stresses significantly. For normal cooling conditions the distribution is characterised by nearly constant tensile stresses in the inner part of the cross section. When the cooling speed is increased the stress distribution can be approximated by a parabolic function. The area with constant tensile stresses in the centre becomes more distinctive for higher steel grades (Figure 10).

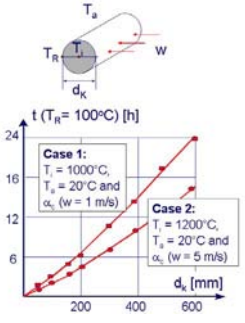


Fig. 8 – Duration of cooling down to a temperature T_R =100°C at the surface of the solid profile

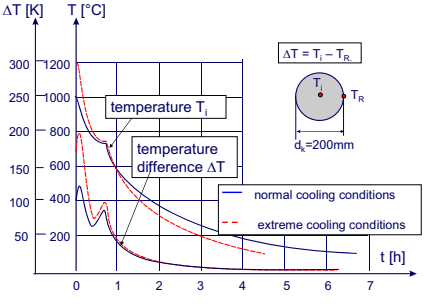


Fig. 9 – Time dependent development of the temperature and the temperature difference for a solid bar with a diameter d_k= 200 mm

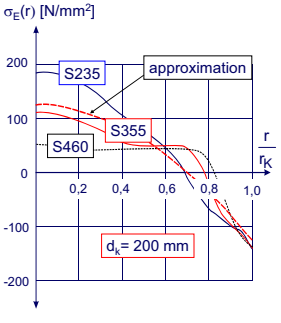


Fig. 10 – Influence of the steel grade on the distribution of residual stresses in solid round bars

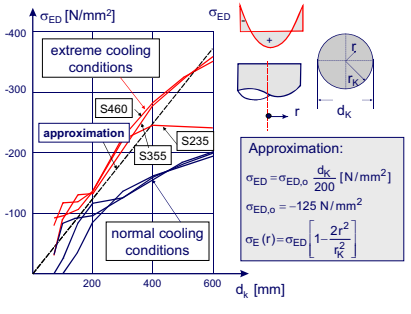


Fig. 11 – Maximum compressive residual stresses at the surface of the cross section as a function of the steel grade and the diameter d_k

Figure 11 shows that the approximation for maximum residual compressive stress at the surface of solid bars and the distribution of the residual stresses are in good agreement with the more accurate values. Because the residual stresses near the surface are mainly responsible for the reduction of the ultimate loads for the recalculation of the tests the approximation was used.

5 INFLUENCES OF CREEP AND SHRINKAGE

Under permanent loads creep and shrinkage of concrete cause in composite members a redistribution of the sectional internal forces from the concrete section to the structural steel section. In case of further loading this can lead to an earlier yielding in the steel section, to larger yielding zones and therefore to a significant reduction of the flexural stiffness at ultimate limit states. For columns in compression and bending the decrease of the flexural stiffness causes increasing horizontal deformations and additional second order effects. Eurocode 4-1-1 [1] takes into account these effects by a reduction of the flexural stiffness of the column. The tests

were subjected to short-term loading only. To obtain information about the influence of creep and shrinkage more exact calculations were done, where the creep function for high strength concrete according to Eurocode 2 -1 [8] and the test results of Ichinose, Watanabe and Nakai [9] were used. The tests with concrete filled hollow sections in [9] show that for concrete filled tubes a reduced creep coefficient can be assumed, which is in the range of 25% of the value for a cross section with its surface fully exposed to the ambient environmental conditions. In a first step, the redistribution of sectional forces and the horizontal deformations were determined for permanent loads by an incremental analysis, taking into account second order effects. In a second step, the ultimate loads were determined by a non-linear calculation taking into account the redistribution of internal forces and the additional deformations caused by creep and shrinkage due to permanent loads and the effects of residual stresses, geometrical imperfections and non linear material behaviour. The calculations were carried out for a nominally pinned column in axial compression with a representative cross-section with a concrete filled steel tube 406.4 x 8.8, steel grade S355 and concrete strengths of 60 N/mm² and 100 N/mm². Table 2 shows the results of four columns with a related slenderness of 1.0 and 2.0 where $F_{Rd,c+s}$ is the design value of the ultimate load taking into account creep and shrinkage and F_{Rd} is the ultimate load without creep and shrinkage effects. It can be seen that in case concrete filled tubes with high strength concrete the effects of creep and shrinkage lead to a reduction of the ultimate load less than 5%, even if the column has a high related slenderness. Comparative results can be achieved by using the simplified design method given in EC4-1-1.

Table 2 –Effects of creep and shrinkage and comparison with the simplified design method in EN 1994-1-1

compressive cylinder strength f_c	related slender-ness $\bar{\lambda}_k$	creep coefficient $\varphi(t_\infty,t_0)$	Exact non-linear calculation		Simplified method acc. to Eurocode 4-1-1 with equivalent imperfections w_o acc. to section 6		
			F_{Rd} [kN]	$\frac{F_{Rd,c+s}}{F_{Rd}}$	L/w_o	F_{Rd} [kN]	$\frac{F_{Rd,c+s}}{F_{Rd}}$
f_c= 60 N/mm²	1.0	0	5912	0,97	360	5679	0,98
		0,25x 1,34	5722			5555	
f_c= 60 N/mm²	2.0	0	2112	0,98	440	2037	0,95
		0,25x 1,34	2077			1941	
f_c= 100 N/mm²	1.0	0	7425	0,97	360	7437	0,98
		0,25x 0,873	7224			7324	
f_c= 100 N/mm²	2.0	0	2869	0,98	440	2842	0,96
		0,25x 0,873	2844			2724	

6 PROPOSALS FOR A SIMPLIFIED DESIGN METHOD BASED ON EUROCODE 4

The use of the general design method in Eurocode 4 based on a geometric and physical nonlinear calculation can not be recommended for practical design because of an enormous calculation effort. In the following a simplified method is presented which is based on the simplified design method in Eurocode 4-1-1 and shown in Figure 12. Internal forces have to be determined by second order linear elastic

analysis with an effective flexural stiffness $(EI)_{eff,II}$. This stiffness accounts for the cracking of concrete and the yield zones in the structural steel section (factors K_o and $K_{e,II}$ in Fig. 12). The influence of geometrical and structural imperfections is taken into account by equivalent geometrical bow imperfections, which depend on the type of cross-section. In case of axial compression and bending it has to be verified that in the critical cross-section the design value of the second order bending moment M_{Ed} does not exceed the design value of bending resistance M_{Rd} of the cross-section. The bending resistance results from the plastic M-N interaction curve of the cross-section and an additional correction factor α_M which takes into account the difference between the plastic and the non-linear bending resistance with strain limitations.

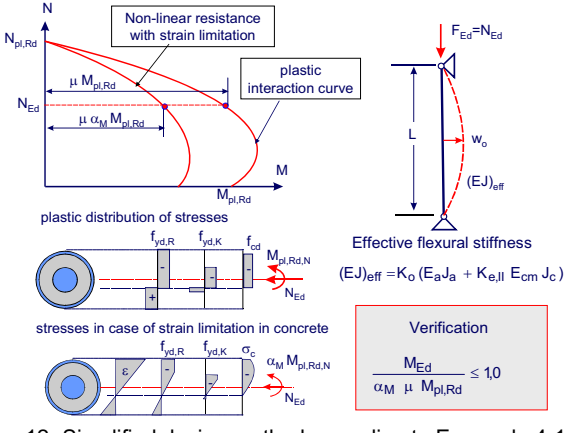


Fig. 12- Simplified design method according to Eurocode 4-1-1

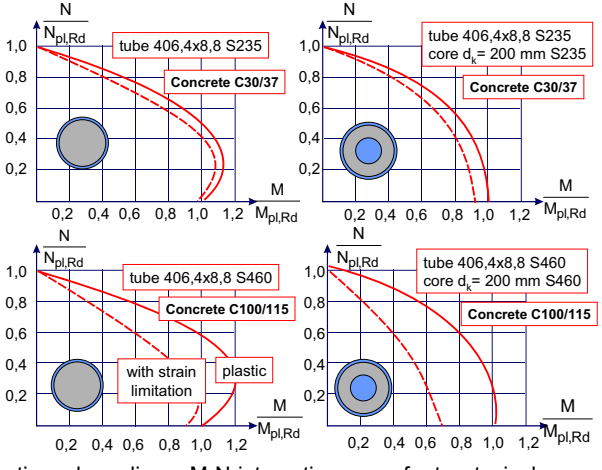


Fig.13 –Plastic and non-linear M-N-interaction curve for two typical cross sections

For high strength materials and concrete filled steel tubes with additional inner massive steel cores the interaction curve depends strongly on the strength of the used materials. The proportion between the plastic interaction curve and the interaction curve with strain limitation for the concrete can differ significantly. Figure 13 shows this for typical cross-sections. Therefore the constant values for the correction factor α_M in Eurocode 4 can not be used for columns with high strength concrete. The analysis of various cross-sections led to the following approximation for the correction factor α_M

$$\alpha_M = \alpha_{Mo} - \alpha_N \frac{N_{Ed}}{N_{pl,Rd}} \quad (1)$$

where the values α_{Mo} and α_N are given in table 3 and N_{Ed} is the design value of the normal force and $N_{pl,Rd}$ the plastic resistance to compression. Intermediate values can be determined by linear interpolation.

Table 3 – values α_{Mo} and α_N

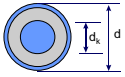
steel grade of the core section	$f_{yd,core}$ [N/mm²]	concrete grade	f_{cd} [N/mm²]	d_k/d= 0		d_k/d= 0,75	
				α_{Mo}	α_N	α_{M0}	α_N
S235	218	C30/37	20	0,90	0,10	0,85	0,15
		C 60/75	40	0,90	0,25	0,80	0,15
		C100/115	60	0,90	0,40	0,75	0,15
S460	418	C30/37	20	0,85	0,25	0,70	0,20
		C 60/75	40	0,85	0,35	0,60	0,20
		C100/115	60	0,85	0,45	0,50	0,20

Based on the correction factor α_M, the equivalent bow imperfection can be determined by comparison of the ultimate loads of the simplified method with the ultimate loads determined by an exact non-linear calculation taking into account a geometrical imperfection of L/1000 and structural imperfections according to Section 4. The equivalent imperfections depend on the cross section geometry and on the slenderness as well as on the effective flexural stiffness [4, 5]. The analysis of several columns that cover different material strengths, buckling lengths, eccentricities and cross-sections gave the following equation (2) for the maximum value of equivalent bow imperfection w_o, where the factors k_i are given in Table 4. The factor k_1 takes into account the influence of the steel grade, the factor k_2 the influence of the diameter d_k of the inner core cross-section and the factor k_3 the influence of the related slenderness.

$$\frac{L}{w_0} = 400 \cdot k_1 \cdot k_2 \cdot k_3 \quad (2)$$

For two typical columns Figure 9 shows a comparison of ultimate loads determined with the general design method according to Eurocode 4-1-1 and the ultimate loads determined with the simplified design method according to Eurocode 4-1-1 but using the correction factor α_M according to equation (1) and the equivalent bow imperfection acc. to equation (2). The comparison demonstrates that the proposed design method gives an excellent agreement with the exact general design method.

Table 4 – Geometrical bow imperfection for concrete filled tubes with additional inner core profiles

	steel grade	S355	$k_1 = 1$
		S460	$k_1 = 1{,}25$
	diameter d_k of core	≤ 200 mm	$k_2 = 1 + \frac{d_K\,[mm]}{400}$
		> 200 mm	$k_2 = 2 - \frac{d_K\,[mm]}{400}$
$\bar{\lambda}_K = \sqrt{\frac{N_{pl,k}}{N_{cr}}}$	related slenderness	$\bar{\lambda}_K \le 0{,}5$	$k_3 = 0{,}8$
		$\bar{\lambda}_K > 0{,}5$	$k_3 = 0{,}7 + 0{,}2\,\bar{\lambda}_K$

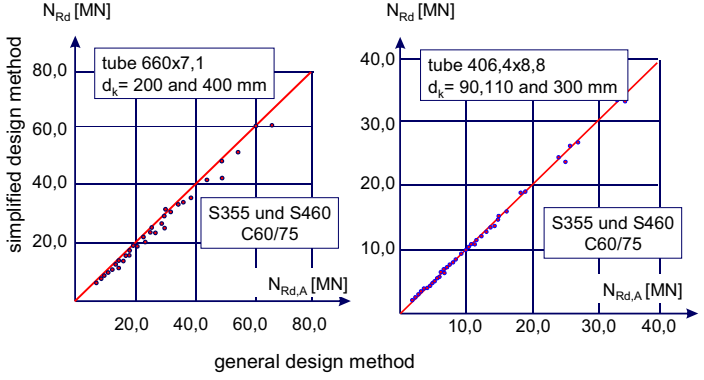


Fig. 9 – Comparison of the ultimate loads determined with the general design method and the simplified design method acc. to Eurocode 4-1-1

7 REFERENCES

[1] EN 1994-1-1: Eurocode 4: Design of composite steel and concrete structures Part 1-1: General rules and rules for buildings (2004)

[2] EN 1990: Eurocode - Basis of structural design (2002)

[3] Porsch, M: Modellierung von Schädigungsmechanismen zur Beurteilung der Lebensdauer von Verbundkonstruktionen aus Stahl und Beton, Dissertation, Fachbereich Bauingenieurwesen, Institut für Konstruktiven Ingenieurbau, Lehrstuhl für Stahlbau- und Verbundkonstruktionen, Bergische Universität Wuppertal (2008)

[4] Hanswille G.: Die Bemessung von Stahlverbundstützen nach nationalen und EU-Regeln, Der Prüfingenieur 22, (2003)

[5] Bergmann, R., Hanswille, G.: New design method for composite columns including High strength steel, ASCE, Proceedings of the 5th international conference Composite Construction in Steel and Concrete V, South Africa, 2004

[6] Roik, K., Schaumann, P.: Tragverhalten von Vollprofilstützen – Fließgrenzenverteilung an Vollprofilquerschnitten, Institut für Konstruktiven Ingenieurbau, Ruhr-Universität Bochum, Juli 1980

[7] EN 1993-1-2:2005: Eurocode 3: Design of steel structures, Part 1-2: General rules, Structural fire design (2005)

[8] EN 1992 -1-1: Eurocode 2: Design of concrete structures, Part 1-1: General rules and rules for Buildings (2004)

[9] Ichinose, L.H., Watanabe, E, Nakai, H.: An experimental study on creep of concrete filled steel pipes, Journal of Constructional Steel Research 57 (2001), S. 453 – 466

Design of anchor plates based on the component method

Prof. Dr.-Ing. Ulrike Kuhlmann
Institute of Structural Design
Universität Stuttgart
Stuttgart, Germany
u.kuhlmann@ke.uni-stuttgart.de

Markus Rybinski
Institute of Structural Design
Universität Stuttgart
Stuttgart, Germany
markus.rybinski@ke.uni-stuttgart.de

ABSTRACT

Steel or composite joints can be designed and optimised by the component method according to Eurocodes [EN 1993-1-8:2005] and [EN 1994-1-1:2004]. The structural behaviour (strength, stiffness, ductility) of these joints is defined by assembled components. Their individual behaviour is described by a mechanical spring model. For the extension of the component method to anchor plates, which are used to transfer loads between steel and concrete structures, a mechanical model has been developed. The model is based on several test series with anchor plates carried out by the Institute of Structural Design (Universität Stuttgart) and describes the load-carrying capacity of anchor plates. In some tests supplementary reinforcement has been taken into account influencing the load capacity and ductility of these steel-to-concrete joints. Additional tests have been performed to study the influence of a flexible anchor plate on the structural behaviour of the joint. Altogether, the component model shows transparency of load distribution and may easily be transferred to alternative situations.

APPLICATION OF ANCHOR PLATES

In mixed buildings various steel or composite elements like girders, columns or bracing ties have to be connected to concrete members like staircases and fire protection walls, columns, strip foundations or foundation slabs. An effective solution for the load transfer between these structural steel and concrete elements is the application of anchor plates allowing for a quick and easy connection.

In Figure 1a-c different solutions for a pinned joint with anchor plates and welded headed studs are shown. The steel or composite elements are connected by a butt strap or a connection with welded bolts developed by the steelwork and engineering companies. These fastening solutions meet basic demands like an economical and easy fabrication and a quick and easy erection also allowing for the adjustment of tolerances. By using post-installed anchors, these joints can also be used to connect steel members to existing concrete structures. Also rigid or semi-rigid joint solutions for steel members may be realized by taking into account the moment resistance, stiffness and ductility of the joint. The joints of composite joints may be enhanced by assigning shear and compression loads to the anchor plate and using the slab reinforcement for tension load transfer. So there is a variety of possibilities for the use of anchor plates as joints between steel / composite and concrete elements.

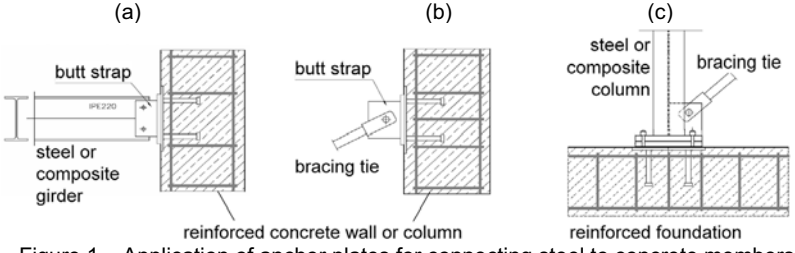


Figure 1 – Application of anchor plates for connecting steel to concrete members

But typically problems occur where steel and concrete meet, due to a gap between the rules of fastening design in concrete and steel design. There are different design methods for anchor plates as shown in the following section with different limitations in applicability and calculated load capacity. Therefore, new experimental and numerical investigations have been conducted to aim for an integrative solution of steel and concrete design rules based on the component method which is already used for steel and composite joints.

EXISTING DESIGN METHODS FOR ANCHOR PLATES

At present, in European countries anchor plates are designed according to technical approvals [EOTA 2006]. The load distribution on anchors is calculated by elastic theory as shown in Figure 2. For example, the anchor forces of an anchor plate loaded by a moment can be determined by taking into account the stiffness of the anchors with positive elongation and the stiffness of the concrete under compression. The stiffness is proportional to the stressed cross-section and the modulus of elasticity. The stiffness of anchors under compression is neglected. The calculation is based on the assumption of a stiff anchor plate with full contact to the base, where the anchor plate remains plane and stays in the elastic range. The yielding of the anchor plate has to be avoided and the anchor displacements are normally insignificant.

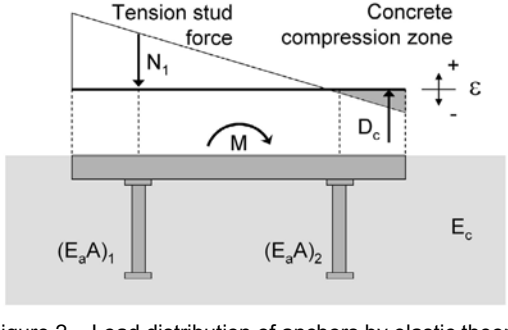


Figure 2 – Load distribution of anchors by elastic theory

The ultimate resistance of the anchors is calculated by the Concrete Capacity-Method [EOTA 2006], [Eligehausen and Mallée and Silva 2006] which describes very well the load capacity of anchors in plain concrete. If necessary, the influence of edge distances of the anchors has to be taken into account. The possibilities to consider supplementary reinforcement are limited and if both shear and tension forces occur, a conservative interaction relation has to be verified. Also in some cases, supplementary reinforcement may even not be considered for anchors with small edge distances.

The final draft of the Technical Specification [prCEN/TS 1992-4-2:2007] considers hanger reinforcement for anchors loaded by tension forces by a strut and tie model, see Figure 3a. The tension forces of the studs are anchored by stirrups. The resistance of the stirrups is calculated with the effective anchor length l_1, and the concrete bond strength in the concrete breakout cone follows [EN 1992-1-1:2004]. In addition, for surface reinforcement acting rectangular to the edges another strut and tie model is applied to take up shear forces, see Figure 3b. Thus, the actual situation to consider reinforcement for the transfer of shear/tension forces has strongly improved.

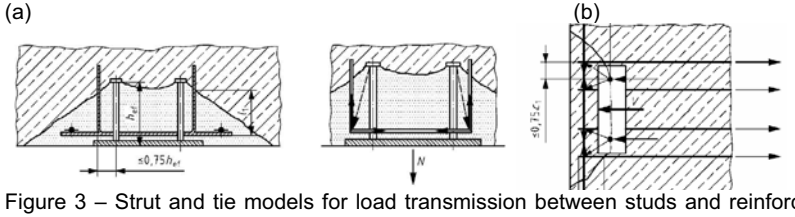


Figure 3 – Strut and tie models for load transmission between studs and reinforcement [prCEN/TS 1992-4-2:2007]

The design of anchor plates with elastic theory often leads to thick, uneconomic steel plates. Therefore, an optimization of the joint may be achieved by a plastic design approach.

In [prCEN/TS 1992-4-2:2007] rules for flexible, thin anchor plates are given. Focus is given to a maximum utilization of the fasteners, so no yielding of the base plate on the tension side is allowed whereas yielding of the base plate on the compression side is possible. However, in dependence of the stiffness of the anchor plate, a reduced inner lever arm of the resultant concrete compression force and the tension stud force has to be taken into account. Thus, a certain optimization of the construction of the joint may be realized but this plastic design approach does not include any regulations for the design of the joint stiffness and ductility what is necessary for a complete plastic design approach.

Hence the application of the component method offers the possibility to determine the structural joint behaviour like strength, stiffness and ductility. But up to now the implementation of this method for the design of column bases in [EN 1993-1-8:2005] shows some limitations and weaknesses [Stark 2007]. For example, the types of fasteners are restricted to anchor bolts with sufficient anchorage length of the anchor bolts to avoid a concrete failure mode, other types are not sufficiently described or included. Also a very conservative position of the concrete compression force directly under the compression flange of the column has to be considered.

A combination of the introduced design methods with consideration of the needs of steel and fastenings designer on basis of the component method will help to realize an economic and safe design of the mentioned steel-to-concrete joints. Different experimental und numerical investigations have been started to verify and improve the component method for anchor plates.

INVESTIGATIONS ON ANCHOR PLATES WITHOUT INFLUENCE OF EDGE DISTANCES

Within the first experimental investigations [Kuhlmann and Imminger 2004] main focus was given to the load capacity of stiff anchor plates with headed studs without influence of edge distances in dependence of different joint parameters like the effective stud length h_{ef}, the distance s between the stud axis, the number n of stirrups in the concrete breakout cone, the surface reinforcement $a_{s\perp}$ and $a_{s\parallel}$, the concrete grade and the load eccentricity e (related to the concrete surface), see Figure 4a. The anchor plate was installed flush with the concrete surface. Due to an installed soft strip at the edges of the anchor plate shear loads were only transmitted by mechanical shear elements and friction. The tests were performed deformation-controlled to examine the joint ductility, the load capacity and the structural behaviour after failure. The test setup for pure shear loading (α=0°) is shown in Figure 4b.

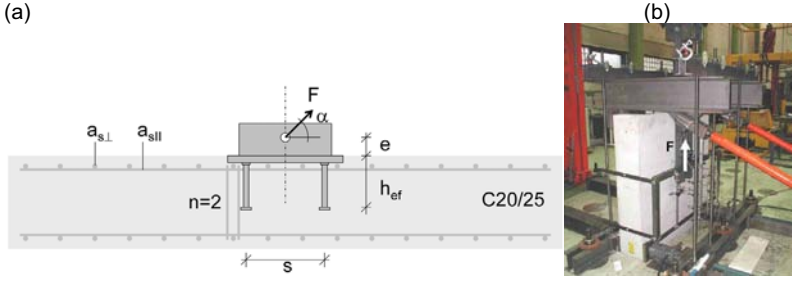


Figure 4 – Tests without edge distances: (a) varied parameters and (b) test set-up for shear loading

Due to the variation of only one parameter within a test row, the influence of each parameter could be identified. The most effective way to increase the joint load capacity was to extend the effective stud length h_{ef}, as shown in Figure 5a. Besides the increasing load-carrying capacity of the concrete breakout cone, an increased transmission length between headed studs and stirrups enhances the load capacity of the whole joint.

The influence of the number n of stirrups within the concrete breakout cone is shown in Figure 5b. The load capacity increases by 30 percent when using an additional stirrup within the concrete breakout cone and can be increased up to 45 percent by using several stirrups.

Also the ductility of these steel-to-concrete joints is increased clearly due to the ductile behaviour of the supplementary reinforcement instead of a brittle failure of the concrete cone.

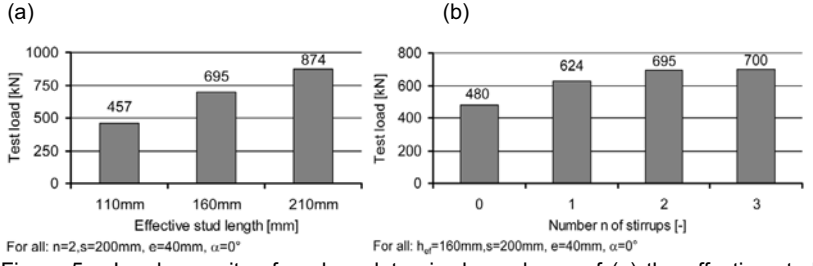


Figure 5 – Load capacity of anchor plates in dependence of (a) the effective stud length h_{ef} and (b) the number of stirrups within the concrete breakout cone

The experimental investigations were accompanied by numerical investigations with the program MASA© developed for non-linear calculations of fastenings in concrete at the Institute of Construction Materials, Universität Stuttgart. The numerical model showed satisfying correlation between test and calculated load capacity of the anchor plates with supplementary reinforcement. So the numerical model was used for further parameter studies to identify the decisive parameters for the mechanical model.

As an example, for an anchor plate loaded by a shear force V the inner load distribution may be described as follows: due to the eccentricity of the shear force a tension stud force N on the non-loaded side of this configuration appears, see Figure 6a. The integrated normal stress of the other studs sums up to nearly 0, so that these studs have no tension forces which have to be considered for the design of the inner moment resistance. In Figure 6a and 6b sketches of the normal stresses σ_z and σ_y calculated for the anchor plate at maximum load are shown. The shear force V is transmitted into the concrete specimen mostly by the shear studs V_2 on the loaded side as well as by the shear studs V_1 and friction V_f between anchor pate and concrete surface.

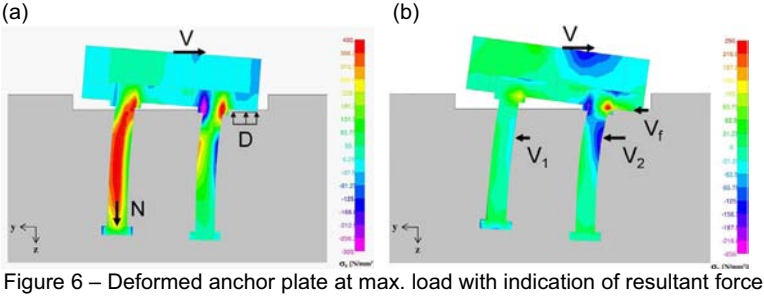


Figure 6 – Deformed anchor plate at max. load with indication of resultant forces and normal stress distribution: (a) normal stresses σ_z and (b) normal stresses σ_y

INVESTIGATIONS ON ANCHOR PLATES CLOSE TO THE EDGE

Anchor plates with studs in short edge distances like strip foundations, see Figure 7a, or concrete columns are often designed by technical approvals [EOTA 2006]. Here, consideration of supplementary reinforcement like stirrups is not included sufficiently. Therefore some experimental and numerical studies have started [Kuhlmann and Rybinski 2007] to take into account the influence of stirrups on the load-capacity for longitudinal shear loading, see Figure 7b.

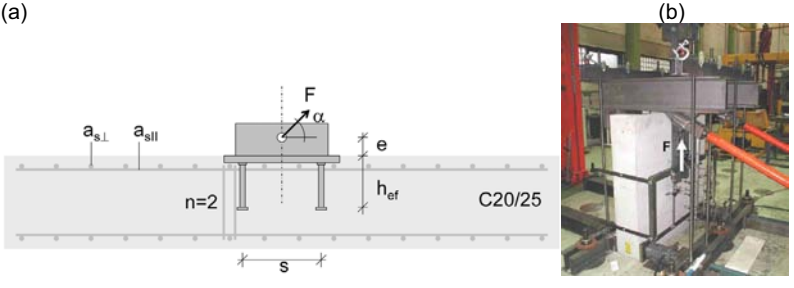


Figure 4 – Tests without edge distances: (a) varied parameters and (b) test set-up for shear loading

The test specimens were loaded by shear forces with an eccentricity e=45 mm, combined tension / shear forces or tension forces. Besides variation of the concrete grade, the main focus was given to the variation of the hanger reinforcement. The tests were performed with a minimal configuration (stirrups ∅6/150mm), a basic configuration (stirrups ∅8/150mm) and an advanced configuration (stirrups ∅10/150mm and additional stirrups beside stud rows).

In Figure 8a the load-displacement curve for the basic configuration is shown. When first cracks appeared, the tension load of the stud row 1 was transferred to the nearby stirrups with increasing loading, see Figure 8b. Due to the application of stirrups in the concrete breakout cone, a ductile joint failure could be observed. However, for this configuration the measured strains in the stirrups remained in the elastic range.

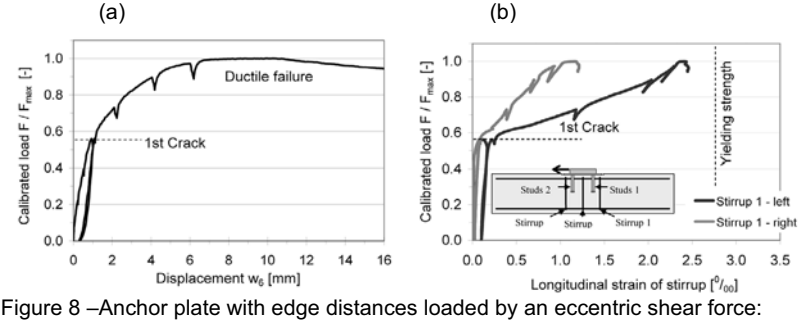


Figure 8 –Anchor plate with edge distances loaded by an eccentric shear force: (a) load-displacement curve and (b) load-strain curve of stirrups

In Figure 9 the influence of the different stirrup configurations on the load capacity is shown. For the minimal configuration a pure concrete failure mode is decisive whereas the configuration with stirrups ∅8/150mm is about the borderline between stirrup and concrete failure. An increased load-capacity can be achieved by the configuration with more stirrups. However, for the studs in short edge distances the most effective way to increase the load-capacity is a higher concrete grade.

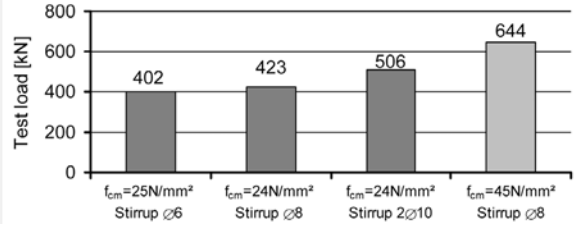


Figure 9 – Test loads under shear loading

For anchor plates close to the edges more failure modes like concrete edge failure have to be considered than for fastenings in continuous slabs. The calculative consideration in the component model is possible by existing design rules for the fastenings [prCEN/TS 1992-4-2:2007], [EN 1994-2:2005].

MECHANICAL MODEL FOR DESIGN OF ANCHOR PLATES

Based on the component method, a first mechanical model for stiff anchor plates was developed and verified by the accomplished tests [Kuhlmann and Imminger 2004], [Kuhlmann and Rybinski 2007] where the calculated load capacity slightly underestimates the test results. The design model may be used for anchor plates under shear, tension or combined forces independent of the kind of fastener and with consideration of supplementary reinforcement.

Within the scope of this first model only the maximum strength was considered. The stiffness and the ductility of the components as also of the joint were not been taken into account, due to a clear inner load distribution, e.g. as there is only one type of fastener for tension load transfer. If shear forces are transmitted by several rows of fastener or different fasteners, the stiffness of the fastener has to be considered in order to calculate the inner distribution of the shear force. If, in addition, the connection device is designed according to plastic resistance, the ductility of the fastener has to be considered as well. However, for the examined anchor plates the stiffness and ductility of the components may be neglected.

For each configuration of anchor plates three different component groups are identified in dependence on the component loading: tension, shear and compression. The component group "tension" may be modeled as several springs in a row. Each failure mode of the component group can be understood as a single spring and the load capacity of the component group is defined by the weakest spring. The component group "shear" may be understood as spring model with springs in parallel. Each shear component is defined as a single spring. Thus, a failure of one component does not cause a complete failure of the whole joint. The load capacity of the component group "shear" can be determined as the sum of the shear components.

The maximum resistance of anchor plates loaded by shear forces may be calculated following the calculation scheme in Figure 10. The scheme may be adopted for other types of loading.

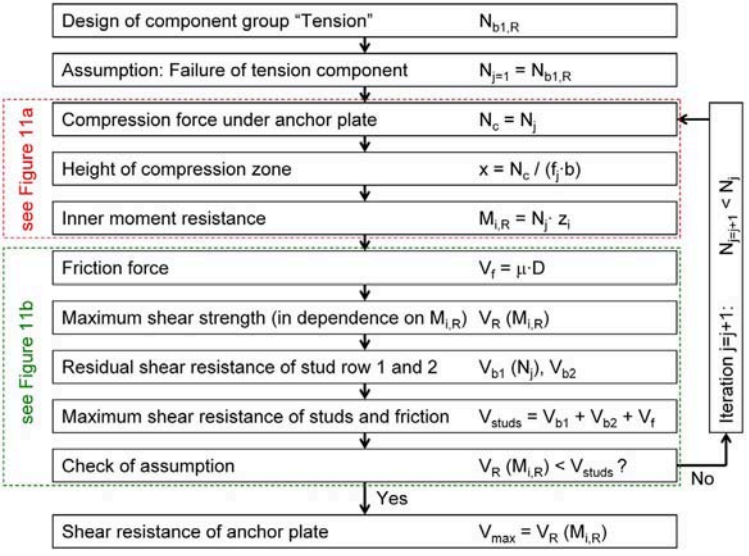


Figure 10 – Calculation scheme for anchor plates with shear loading

So in the first step the maximum strength of the component group "tension" $N_{b1,R}$ has to be calculated taking into account the different failure modes like steel failure $N_{R,s}$, pull-out failure $N_{R,p}$, blow-out failure $N_{R,cb}$ and concrete cone failure with or without reinforcement $N_{R,c}$ or $N_{R,re}$ according to [prCEN/TS 1992-4-2:2007], see Equation (1). Figure 3a shows the strut and tie model [prCEN/TS 1992-4-2:2007] for determining the transferable load of the reinforcement. The load of the reinforcement is limited by steel and anchorage failure [EN 1992-1-1:2004].

(1) $$N_{b1,R} = min\left[N_{R,s}; N_{R,p}; N_{R,cb}; max\left(N_{R,c}; N_{R,re}\right)\right]$$

Then the assumption is made that the component group "tension" is decisive for joint failure $N_j=N_{b1,R}$. Figure 11a shows the equilibrium of forces acting rectangular to the concrete surface, where the concrete compression force N_c has to be equal to the tension force of stud row $N_{b1,R}$. The height of the compression zone x can be determined by the allowable stress f_j according [EN 1993-1-8:2005] and [EN 1992-1-1:2004]. Thus the inner lever arm and the inner moment resistance of the anchor plate can be determined, see Equation (2).

(2) $$M_{i,R} = N_c \cdot \left(d - 0.5 \cdot x\right) = N_c \cdot z_i$$

In Figure 11b the shear forces acting parallel to the concrete surface are identified. The friction force V_f may be calculated with the coefficient of friction μ between steel and concrete and the compression force N_c. The maximum shear strength $V_R(M_{i,R})$ in dependence on the calculated inner moment resistance $M_{i,R}$ of the anchor plate may

be calculated by the equilibrium of moment in the point of application of the resultant shear force V_{b2} of the studs whereas it is assumed that inner lever arm e_{b1} is approximately equal to e_{b2}. The inner lever arm can be estimated in dependence of the stud diameter d_{stud}, the concrete grade and the degree of utilisation of the stud. In the component model the inner lever arm was set equal to 0.5-1.0 d_{stud}.

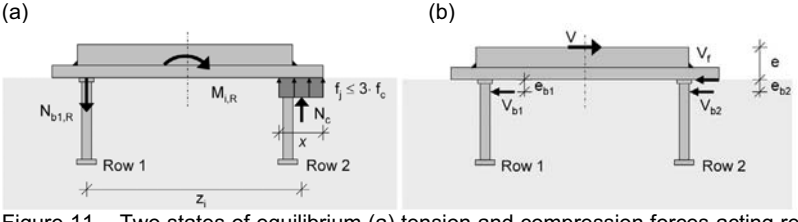


Figure 11 – Two states of equilibrium (a) tension and compression forces acting rectangular to the concrete surface and (b) shear forces acting parallel to the concrete surface

The maximum shear strength of the component group "shear" consists of the friction force V_f, the shear resistance of stud row $V_{b2,R}$ and the residual shear resistance $V_{b1,R}(N_j)$ considering the interaction relation between shear and tension forces of the studs. The maximum shear resistance of the studs has to be calculated taking into account the different failure modes like local concrete failure $V_{R,cl}=P_{Rd,2}$ [EN 1994-2-1:2004], steel failure $V_{R,s}$, concrete pry-out failure $V_{R,cp}$ or concrete edge failure $V_{R,c}$. If the concrete edge failure becomes decisive, the stirrups can be taken into account to strengthen the component load capacity as shown in Figure 12. They take up the rectangular acting splitting forces comparable to the design model for horizontally lying shear studs in concrete slabs of composite girders [EN 1994-2:2005]. The factor $\psi_{a,c}$ takes into account the orientation of the shear loading V_{bi} and position of the stirrups [Kuhlmann and Rybinski 2007].

In the last step the assumption of a tension failure mode has to be checked. If the calculated strength $V_R(M_{i,R})$ exceeds the calculated shear resistance of the stud rows $V_{b1,R}$ and $V_{b2,R}$ and the friction force V_f, the assumption of a tension failure mode is not fulfilled and the load capacity of the anchor plate has to be recalculated iteratively with a reduced tension stud force $N_{j+1} < N_j$ unless the assumption is fulfilled and the maximum shear resistance is determined as $V_R(M_{i,R})$.

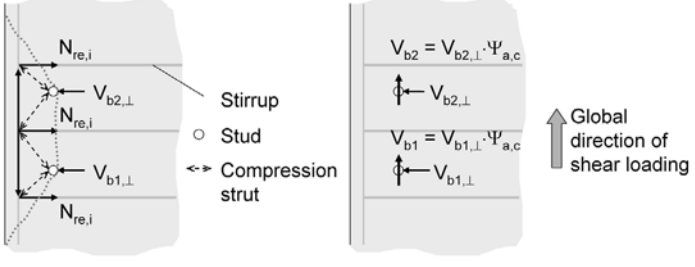


Figure 12 – Strut and tie model for concrete edge failure

The introduced model is valid for stiff anchor plates in pure or reinforced concrete members with or without influence of edges and if the loading of the anchor plate is in longitudinal orientation of the concrete member. The load transfer inside of the concrete member is assumed on both sides of the anchor plate as shown in the simplified strut and tie model for tension and shear loading in Figure 13. First studies of anchor plates in a cantilever have started, but need more general investigations for validation.

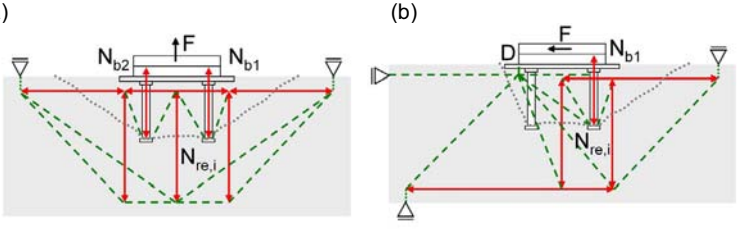


Figure 13 – Simplified strut and tie model for an anchor plate in a reinforced concrete member (a) loaded by a tension force and (b) loaded by an eccentric shear force

SEMI-RIGID COLUMN BASES FOR PLASTIC DESIGN

Steel and composite structures like mixed buildings or steel frames shown in Figure 14a are often designed using plastic design methods. Besides the load capacity also the stiffness and ductility of the joints have to be taken into account because they determine the inner forces, the frame displacements and the joint loading.

Especially the design of steel structures like sway frames as shown in Figure 14b is very sensitive to the joint stiffness. The usual assumption of a rigid or pinned connection for column bases often does not comply with the real behaviour of the steel-to-concrete joints. Therefore, an appropriate design model for steel-to-concrete joints is needed, determining the realistic structural behaviour of column bases under normal and shear forces and bending moments.

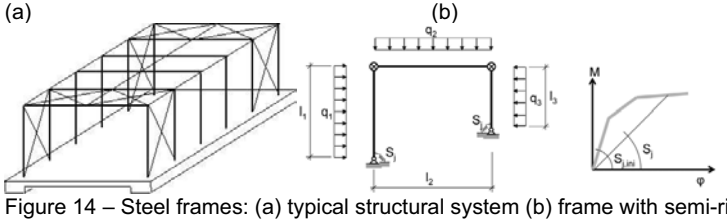


Figure 14 – Steel frames: (a) typical structural system (b) frame with semi-rigid joints

An interdisciplinary research collaboration [Kuhlmann et al 2008] of the Institute of Structural Design and the Institute of Construction Materials has been started where several tests on column bases have been conducted examining the structural behaviour of semi-rigid steel-to-concrete joints. The project aims at a design model determining a realistic structural behaviour of column bases under combined loading (shear and normal forces, bending moment) considering the different methods for steel and fastenings design.

INVESTIGATIONS FOR FLEXIBLE ANCHOR PLATES

Within the experimental investigations in the frame of the interdisciplinary research project [Kuhlmann et al 2008] different parameters were varied like the thickness and stiffness of the anchor plate, the eccentricity of the applied shear force (e=50/1000mm, see Figure 15a), the type of fastener (headed studs and undercut anchors with mortal layer), the diameter and effective length h_{ef} of the studs as also the normal force in the column. The measurements also considered the influence of friction coefficient between the anchor plate and concrete element/mortal layer. So different failure modes like concrete cone failure, concrete pry-out failure, steel failure of the studs in tension or shear and yielding of the anchor plate could be observed and used for verification of the adapted component model. Altogether, the test program included 12 tests with headed studs and 8 tests with undercut anchors and mortal layer without edge distances and without supplementary reinforcement. By application of strain gauges and conductors the tension forces in the studs as also the deformations of the anchor plate in the compression and tension zone were monitored during loading and are basis for followed numerical examinations.

The component model was adapted by considering the stiffness of the anchor plate on the tension and compression zone. The non-linear behaviour of the anchor plate was defined in comparison to the equivalent T-stub model [EN 1993-1-8:2005]. The basic calculation principle of two equilibriums of forces was retained unchanged, see Figure 15b. In the first step the anchor plate was calculated for a M-N-interaction, where the stiffness of the flexible anchor plate ($K_{a,T}$ and $K_{a,C}$), the stiffness of the studs, considering the elongation of the studs $K_{b1,1}$ and the displacement at the head of the studs $K_{b1,2}$, and the concrete compression zone K_c, simulated by several non-linear concrete springs, were considered. The evaluated approaches for the prediction of the component ductility are listed in [Kuhlmann et al 2008]. In the second step the shear resistance of the anchor plate is checked considering the stiffness of the different stud rows $K_{b1,V}$ and $K_{b2,V}$ and the friction forces in the concrete compression zone. The interaction effects of the two states were considered by interaction of the structural behaviour of the studs.

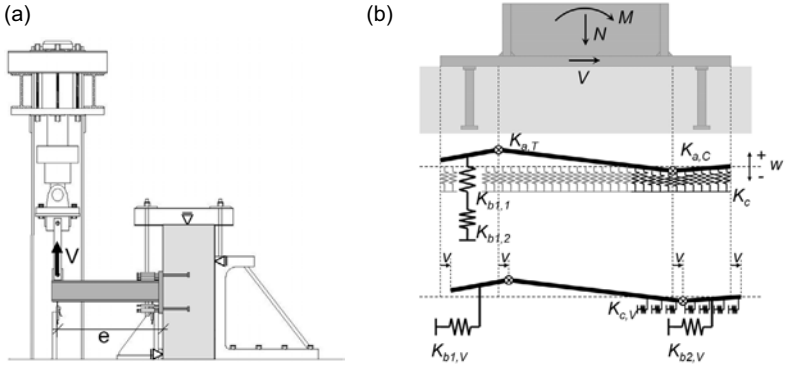


Figure 15 – (a) Test-set-up for large load eccentricity and (b) adapted component model for column bases with stiff or flexible anchor plates

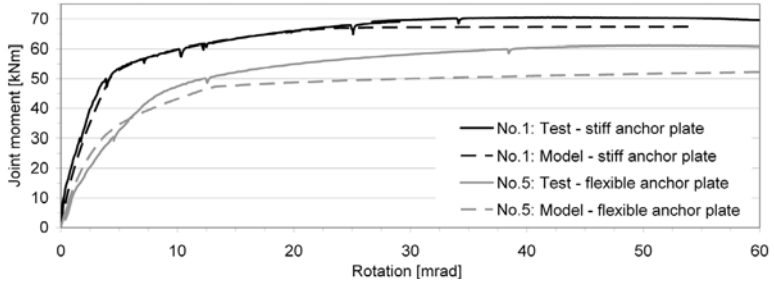


Figure 16 – Measured and calculated M-φ-curves for ductile steel failure

Altogether, the component model slightly underestimates the load-capacity of the anchor plates for flexible anchor plates in particular. The moment-rotation-curves for a ductile steel failure of the fastener are shown in Figure 16, whereas Figure 17 shows a non-ductile concrete breakout failure each for a stiff and a flexible anchor plate. The calculated failure modes and the load-displacement curves were sufficiently described compared to the test results, so that the component model shows good correlation to the performed tests.

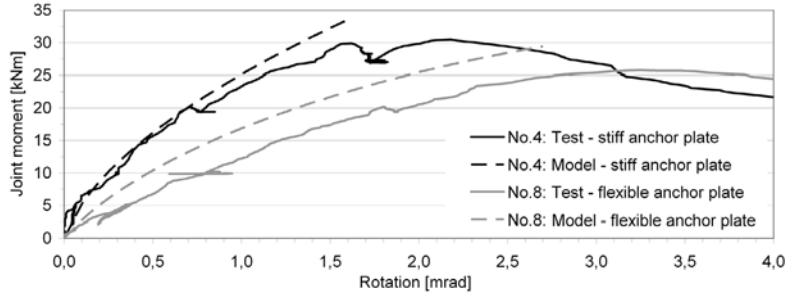


Figure 17 –Measured and calculated M-φ-curves for non-ductile concrete failure

CONCLUSION

The developed component model for the design of anchor plates considers the different possible failure modes of the studs, of the concrete member, of the supplementary reinforcement and of the anchor plate. The structural behaviour of the components is described on basis of existing European Codes [EN 1993-1-8:2005], [EN 1992-1-1:2004] and Technical Specifications [prCEN/TS 1992-4-2:2007]. The structural behaviour of the whole joint like load-capacity, stiffness and ductility is determined quite well, but still needs more investigations and verification to achieve a better acceptance of the component model for steel-to-concrete joints.

ACKNOWLEDGEMENT

Acknowledgement is given to the research funding associations "Deutsche Forschungsgemeinschaft (DFG)", "Forschungsvereinigung Stahlanwendung e.V." as also to the companies Goldbeck West GmbH and Köster &Co. GmbH for their financial support of the research projects carried out. The authors also want to thank the staff members of the testing laboratories of the Institute of Construction Materials and the Otto-Graf-Institute (FMPA) at Universität Stuttgart.

REFERENCES

EN 1992-1-1:2004: Eurocode 2: Design of concrete structures – Part 1-1: General rules and rules for buildings, European Committee for Standardization, 2004.

EN 1993-1-1:2005: Eurocode 3: Design of steel structures – Part 1-1: General rules and rules for buildings, European Committee for Standardization, Brussels, 2005.

EN 1993-1-8:2005: Eurocode 3: Design of steel structures – Part 1-8: Design of joints, European Committee for Standardization, 2005.

EN 1994-1-1:2004: Eurocode 4: Design of composite steel and concrete structures – Part 1-1: General rules and rules for buildings, European Committee for Standardization, 2004.

EN 1994-2:2005: Eurocode 4: Design of composite steel and concrete structures – Part 2: General rules and rules for bridges, European Committee for Standardization, 2005.

Eligehausen and Mallée and Silva 2006: Anchorage in Concrete Construction, Berlin, Ernst & Sohn Verlag, 2006.

EOTA 2006: Guideline for European Technical Approval of Metal Anchors for Use in Concrete, Annex C, EOTA, Brussels, 2006.

Kuhlmann and Eligehausen and Rybinski and Fichtner 2008: Modellierung biegeweicher Stützenfüße im Stahl- und Verbundbau als integriertes System von Tragwerk und Fundament, Report, Deutsche Forschungsgemeinschaft (DFG), 2008.

Kuhlmann and Imminger 2004: Ankerplatten und Anschlussdetails zur Kraftüberleitung im Stahlbau, Report 1/2004, Deutscher Ausschuss für Stahlbau DASt, Düsseldorf, Germany, 2004.

Kuhlmann and Rybinski 2007: Tragfähigkeit von Ankerplatten mit Kopfbolzendübeln in stabförmigen Bauteilen. Forschung für die Praxis P 722, FOSTA, Verlag und Vertriebsgesellschaft, Düsseldorf, Germany, 2007.

prCEN/TS 1992-4-2:2007: Design of Fastenings for Use in Concrete – Part 2: Headed Fasteners, Final Draft, 2007.

Stark 2007: Design of Connections between Steel and Concrete in Eurocodes, In: Eligehausen and Fuchs and Genesio and Grosser (Edt.): Second Symposium "Connections between Steel and Concrete", Volume 1, ibidem-Verlag, 2007.

An Economical and Efficient Foundation Connection for Concrete Filled Steel Tube Piers and Columns

Charles W. Roeder
Dept. of Civil Engineering, University of Washington
233B More Hall, Seattle, WA 98195-2700)
croeder@u.washington.edu

Dawn E. Lehman
Dept. of Civil Engineering, University of Washington
233B More Hall, Seattle, WA 98195-2700)
delehman@u.washington.edu

ABSTRACT

Concrete filled steel tubes (CFT) are economical and result in rapid construction. The steel tube serves as formwork and reinforcement to the concrete fill, and the fill increases the compressive strength and stiffness of the tube. The fill delays and restrains local buckling, and enhances ductility and resistance if composite action is achieved. Circular CFT provides better performance because the circular tube provides greater confinement of the concrete and composite interaction between the two materials. However, circular CFT is more difficult to connect to other structural elements, and recent research has provided a simple and economical connection to connect circular CFT piers or columns to reinforced concrete foundations, beams and pier caps. The connection does not require any reinforcement or dowels connecting the tube to the footing. A second variation of this connection permits sequencing of steel and concrete construction trades and connecting to precast concrete elements. A series of experiments have been completed to evaluate the inelastic seismic performance and establish design criteria for the connection. This work shows that the connection can develop the full capacity of the composite column, and provide great ductility and inelastic deformation capacity under seismic loading.

INTRODUCTION

Concrete filled steel tubes (CFT) permit economical structures that result in rapid construction. The steel tube serves as formwork and reinforcement to the concrete fill, and the fill provides increased compressive strength and stiffness to the steel tube. The fill delays and restrains local buckling, and enhances ductility and resistance if composite action is achieved. Both circular and rectangular CFT have been employed in construction. In general. circular CFT provides better performance than rectangular CFT, because the circular tube provides (Roeder, Lehman, and Thody, 2008):

- greater confinement of the concrete,
- increased bond stress and composite interaction between the two materials, and
- reduced susceptibility to local buckling

However, rectangular CFT is sometimes used, because it is much easier to connect to other structural elements. As a result, recent research at the University of Washington has focused on development of improved and economical connections for circular CFT connections to capitalize on the full benefits of the CFT construction method.

CFT is stiff and strong in axial compression with substantial bending resistance, and this makes them appropriate for bridge piers and columns in braced frames and multi-story buildings. CFT piers and columns also result in rapid and economical construction. Rapid construction is beneficial for bridge construction, because a large portion of the construction is accomplished in the presence of heavy existing traffic, and this poses severe safety risks and huge social and economic costs. Therefore, rapid construction has obvious benefits for bridge construction. In buildings, rapid construction is beneficial, because it leads to rapid collection of rents and amortization of the construction costs. Rapid construction is achieved with CFT construction, because the tube is prefabricated, placed quickly and may be filled with self-consolidating concrete. No time or materials are required for formwork, reinforcing cages, vibration of concrete or shoring supports. The steel tube provides reinforcing at the optimal location, and no reinforcing bars or shear connectors are needed inside the steel tube. The resulting pier or column requires significantly smaller diameter and less material to achieve a given resistance level than reinforced concrete members as shown in Figure 1. Hence, CFT may result in lighter structures and smaller seismic design forces. For example, the CFT pier shown in Figure 1 will have comparable resistance to a larger reinforced concrete pier, but will have 27% lighter weight, correspondingly less material, and smaller mass. This occurs because CFT places the reinforcement at the optimum location, and the concrete is better confined to reduce damage due to concrete spalling.

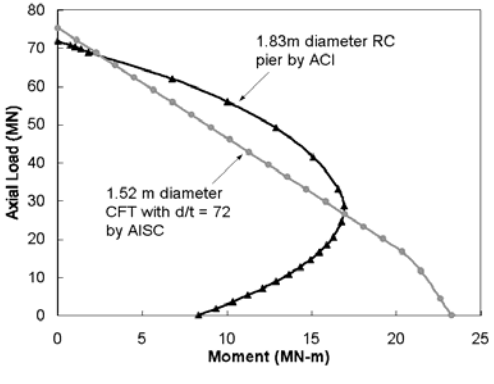


Fig. 1 - Comparison of design resistance of CFT with a larger reinforced concrete element

Circular CFT offers excellent strength, stiffness and ductility and improved inelastic performance. However, as noted earlier, circular CFT is more difficult to connect to other structural elements. As a result, a simple and economical CFT cast-in-place column-to-footing connection that permits rapid construction has been developed.

THE PROPOSED CONNECTION

Figure 2 shows 4 categories of CFT column base connections, which were developed to achieve the flexural strength of the composite CFT pier or column sections. Embedded column connections such as shown in Figure 2a have been investigated and are common in Japan (Hsu and Lin, 2003; Hitaka, Suita, and Kato, 2004). In some cases, building a pedestal around the column base rather than totally recessing the column into the foundation achieves the embedment. CFT columns with embedment depths equal to 0.5, 1.0, and 1.5 times the column diameter, D, with D/t ratios of 50 have been studied. A full rectangular plate was used to provide anchorage at the base of the CFT column. The embedment depth of 1.0D achieved the theoretical flexural strength of the column and large inelastic column deformations with minimal damage to the foundation. Little improvement in the behavior was achieved with increased embedment depth. The Architectural Institute of Japan (AIJ) recommends that CFT columns be embedded to a depth such that bearing of the embedded column on the concrete resists column forces. Embedment depths of 2D are generally sufficient to achieve this AIJ recommendation.

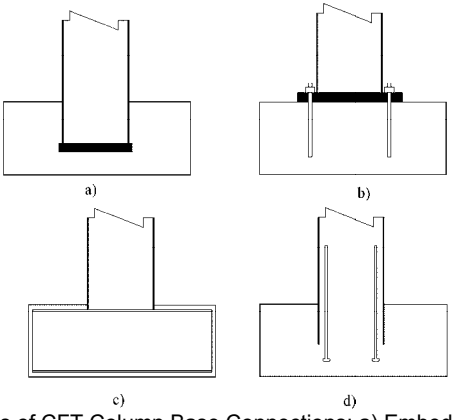


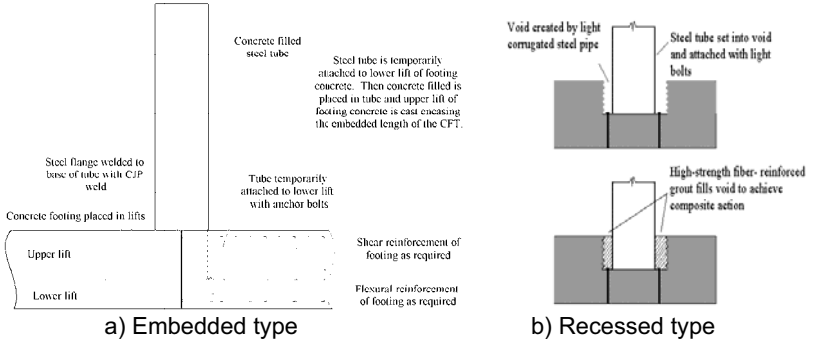
Fig. 2 - Categories of CFT Column Base Connections; a) Embedded, b) Base Plate, c) Embedded Structural Steel, d) Reinforcing Steel Transfer

Variations on the steel base plate connection (Figure 2b) have been used in practice, and research has also been performed (Hitaka, Suita, and Kato 2004). It is difficult to achieve the full moment capacity of the CFT member with this connection, and the base plate may sustain significant damage when the transferred moment becomes large. Figure 2c illustrates another variation of embedded connection. With this connection, the steel tube is welded to a pair of channels and the channels are embedded into the footing or foundation (Marson and Bruneau, 2004). The connections behaved well in experimental research, but the channels must be proportional to the column size. As a result, this is practical only for smaller column diameters, and is increasingly expensive for most practical applications. Figure 2d illustrates a dowel connection, which relies on reinforcing bars within the tube to transfer forces and bending moments to the foundation (Kadoya, Kawaguchi, and Morino 2005, Morino et al. 2003). Variations of the dowel connection are also used to connect prestressed concrete piles to wharf decks. Dowel connections can

achieve significant resistance and inelastic deformation capacity, but they may sustain significant deterioration of stiffness and resistance at larger deformation levels (Roeder et al., 2005). Dowel connections are relatively costly and time consuming for construction.

Figure 3 illustrates another CFT column-to-foundation connection that was recently developed (Kingsley et al. 2005). It is a hybrid or a combination of the embedded and base plate connections. It employs a welded flange or annular ring, which is welded to the base of the steel tube with a complete joint penetration (CJP) weld. The plate is a hollow ring rather than a closed end plate. The open hole in the flange offers continuity of the concrete fill of the CFT pier with the foundation and economy and efficiency not afforded by full plate connections. The ring or flange projects out from the tube to interlock the CFT column with the foundation. It also penetrates slightly into the tube to provide blocking and binding to the concrete fill. The flange serves as a temporary attachment for the tube, while concrete is being placed. There are no dowels penetrating from the tube into the foundation, nor is there any reinforcement within the tube. The embedded tube and annular ring are solely responsible for the connection force and moment transfer. The footing is reinforced as required by the foundation design.

The construction procedure is accomplished in one of two ways as depicted in Figure 3. First, the connection can be constructed by placing the concrete in two lifts as illustrated in Figure 3a. The lower lift is cast, and the tube is then temporarily attached to the lower lift by anchor bolts. The remainder of the footing and concrete fill of the tube are cast in a second lift. The footing is reinforced with normal shear and flexural reinforcement as required for the foundation design. The second variation of the connection is illustrated in Figure 3b. With this second option, the footing or pile cap is cast to its full depth with a recess formed for later placement of the tube. The recess has an inside diameter that is slightly larger than the outside diameter of the flange or annular ring. The recess is economically formed by using a light gauge corrugated metal pipe such as commonly used for culverts and drainage. The tube is placed in the recess after the foundation is cast, and the recess between the tube and the corrugated pipe is filled with high strength fiber reinforced grout. The steel tube is filled with low shrinkage self consolidating concrete to complete the CFT application and connection.



a) Embedded type b) Recessed type

Figure 3 - Proposed CFT foundation connection

EXPERIMENTAL TEST PROGRAM

A series of large-scale specimens were tested to evaluate the feasibility and effectiveness of the connections (Kingsley 2005, Williams 2007, and Chronister 2008). The tests evaluated the connection under axial compression and cyclic lateral load, and several variations in connection design and loading were considered. A specialized self-reacting test frame, shown in Figure 4, was constructed under a 10.7MN Baldwin Universal Testing Machine, which applied a constant vertical gravity load to the specimen. Most specimens were subjected to a compressive load of 1,824 kN, which is approximately 10% of the gross cross capacity of the CFT members, but larger loads were applied on other tests as shown in Table 1. The compressive load is applied through a dimpled, lubricated Polytetrafluoroethylene (PTFE) sliding surface on a spherical bearing and a #8 mirror finish stainless steel mating surface. Therefore, P-δ effects are directly simulated in the test, and the friction has a miniscule effect on specimen performance. A 979-kN horizontal actuator was used to apply cyclic lateral loading. The columns were cantilevers, with the point of loading 1.86m above the surface of the footing. The displacement history, shown in Figure 5, was based on ATC-24 protocol (ATC 1992). However, Specimen X was tested with a near fault variation of this deformation history. Nonlinear analyses were used to estimate the yield drift as required for development of the drift history.

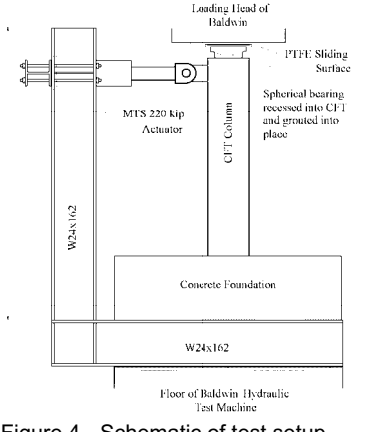


Figure 4 - Schematic of test setup

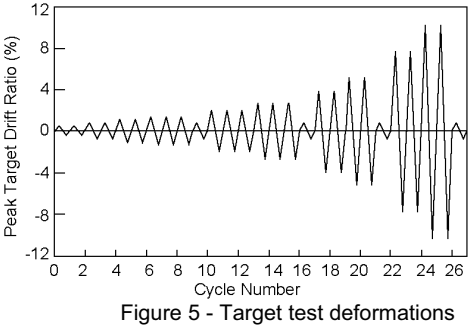


Figure 5 - Target test deformations

To date 12 tests have been completed. The specimens all approximately simulate a full-scale building column or a half-scale bridge pier. The steel tubes were identical for all specimens and were 508 mm in outside diameter with a 6.4-mm wall thickness. This results in a diameter-to-thickness ratio, D/t, of 80, which exceeds limiting ratio of 62.5 recommended by AISC 2005 provisions for a specified yield strength, F_y, of 490 MPa. The welded flange annular ring was 160-mm wide and 6.4-mm thick, and it projected 102 mm beyond the outside of the tube and 51 mm inside of the tube. The flange was welded to the tube with a CJP weld of matching metal with weld process meeting in AISC demand critical weld criteria. The embedment depth of the tube varied from specimen to specimen as shown in Table

1. The shallowest embedment was chosen to evaluate the adequacy of smaller embedment depths on connection performance, and the larger embedment depth was selected to achieve the full load capacity and displacement ductility of the CFT element.

Table 1. Experimental Parameters and Material Properties

	EMBED DEPTH l_e/D	SPECIFIC GOALS	F'C (MPA)	MAX. DRIFT	MAX. LOAD (KN)	FAILURE MODE
I	0.6	SHALLOW EMBEDDED W/LIGHT SHEAR AND TRANSVERSE REINFORCEMENT	75.8	8.5%	581	CONE PULLOUT
II	0.6	SHALLOW EMBEDDED	75.8	9.5%	599	CONE PULLOUT
III	0.9	0.9D EMBEDDED	69.2	8.0%	735	DUCTILE TEARING OF TUBE
IV	0.6	SHALLOW RECESSED	69.2	7.8%	618	CONE PULLOUT
V	0.9	0.9D EMBEDDED	77.8	9.0%	749	DUCTILE TEARING
VI	0.75	0.75D RECESSED	82.0	9.6%	770	DUCTILE TEARING
VII	0.75	0.75D RECESSED PUNCHING TEST	63.9	NA	3413	PUNCHING SHEAR W/225MM DEPTH
VIII	0.75	0.75D RECESSED CYCLIC PUNCHING TEST	64.6	NA	3044	CYCLIC PUNCHING W/225MM DEPTH
IX	0.9	RECESSED - GALVANIZED	68.9	8.5%	770	DUCTILE TEARING
X	0.9	RECESSED - GALVANIZED W/NEAR FAULT CYCLIC DEFORMATION	67.4	10.5%	797	DUCTILE TEARING
XI	0.9	RECESSED - INCREASED AXIAL LOAD (2737 KN)	63.9	10.4%	743	DUCTILE TEARING
XII	0.9	RECESSED - INCREASED AXIAL LOAD (3649 KN)	68.8	9.5%	788	DUCTILE TEARING

Figure 6 shows the geometry and foundation reinforcement for all test specimens. The dimensions of the footing were 1.93m x 1.73m in plan as shown. The depth of the footing was 610mm or 1.2 times the diameter of the CFT member as shown in figure. The footing dimensions and reinforcement were selected to permit full

transfer of the column forces and to minimize the effect of the footing size on the behavior or mode of failure of the connection. In addition, the footing reinforcement was scaled to that typically used in bridge foundation footings For all specimens, the horizontal reinforcement in the longitudinal plane of bending at the top and the bottom of the footing consisted of #6 (19-mm diameter) bars spaced at 102 mm on center. The reinforcement in shear and in the transverse flexural direction varied somewhat from specimen to specimen as shown in Table 1. Specimens 1 and 2 had no additional supplemental shear ties, and the transverse flexural reinforcement consisted of lighter bars at greater spacing (#4 bars and 228.6mm) as shown in the figure. All remaining specimens had transverse flexural reinforcement consisting of #6 bars at 102 mm and #3 vertical shear ties detailed with standard seismic hooks. To ensure development of the longitudinal reinforcement over the relatively short length of the base, the longitudinal bars were bent as shown in Figure 6.

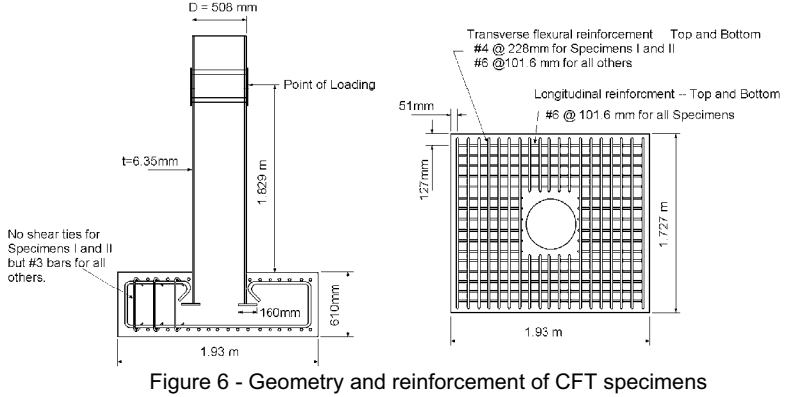


Figure 6 - Geometry and reinforcement of CFT specimens

EXPERIMENTAL RESULTS

Table 1 provides a brief summary of the experimental results. It is not possible to provide a detailed description of the test program in this paper, but the results of 3 separate tests will be discussed in detail to provide an overview of the research results.

Specimen I was a normal embedded connection designed with a shallow embedment depth (.6D). At less than 0.3% drift, a crack formed at the column-footing interface and cracking spread from the column base, parallel and perpendicular to the direction of loading with increasing deformation. The widths of the cracks increased with subsequent cycles at the same drift level and at increasing drift levels. The maximum horizontal load of 580.5 kN was reached at 2.4% drift. Resistance deteriorated increasingly at larger drifts as depicted in Figure 8. This resistance approximates the theoretical yield force of the tube, but it is smaller than the ultimate plastic capacity of the composite CFT section. At approximately 4% drift, some of the cracks in the footing were more than 5-mm wide. At this drift level, the footing concrete was severely damaged and began to separate from the footing. Loading was terminated at 8% drift. The final damage state is shown in Figure 9.

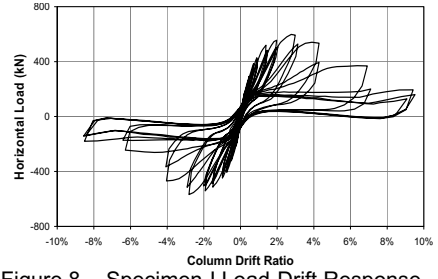


Figure 8 - Specimen-I Load-Drift Response

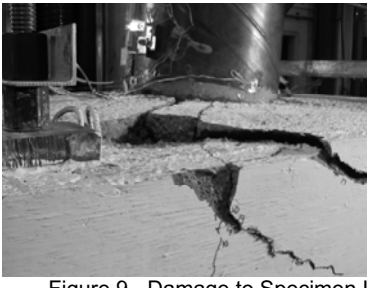


Figure 9 - Damage to Specimen I

Specimen III is also an embedded specimen, but it is embedded to a greater depth (.9D) than Specimen I. At very low drift levels, the response of Specimen III was similar to Specimen I, since a small foundation crack formed at 0.5% drift. However, the foundation cracks remained much smaller and less widely distributed at larger deformations than for Specimen I. At approximately 1.3% drift, tension yielding occurred in the tube of Specimen III at a horizontal load of approximately 597.4 kN. This yield resistance is similar to the maximum resistance noted for Specimen I. Figure 10 shows the measured force-drift response of Specimen III. The maximum horizontal load of 734.5 kN was reached at 2.4% drift. This resistance exceeds the ultimate plastic capacity of the composite CFT member, and it exceeds the maximum capacity of Specimen 1 by 26%. The resistance deteriorates somewhat after 2.4% drift, but the deterioration is significantly smaller than that observed for Specimen I. It should be noted that the deterioration in lateral resistance seen in these plots includes the effect of P-δ moments. Hence, actual material deterioration in resistance at larger deformations is smaller than shown in the figure. At 4% drift local buckling of the tube was visible as shown in Figure 11a. By 6% drift, local buckling had led to initiation of ductile tearing around the circumference of the tube. The concrete fill at the base of the tube had crushed. The test was terminated at 8% drift due to significant tearing around the perimeter of the steel tube at the local buckled region as shown in Figure 11b. The specimen sustained limited damage to the footing as can be seen in Figure 11b, but it had greater resistance, energy dissipation, and drift capacity than Specimen I.

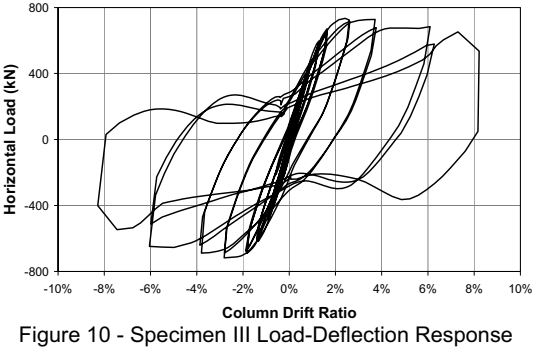
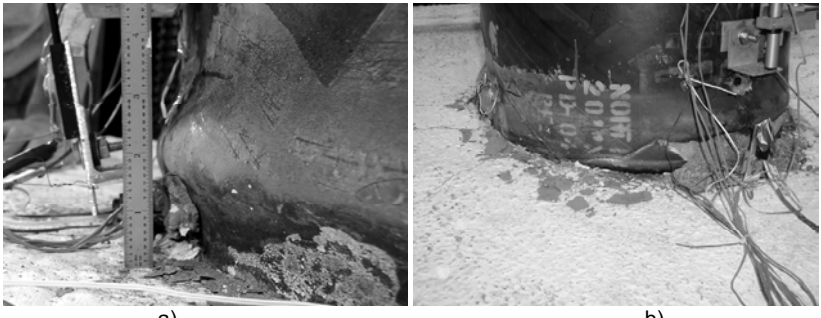


Figure 10 - Specimen III Load-Deflection Response



a) b)

Figure 11 - Damage to Specimen III at high drift levels

Specimen VI is a recessed and grouted specimen, but it is recessed to a 0.75D depth. Its horizontal force-story drift behavior is shown in Fig. 12. At very low drift levels, the response of Specimen VI was similar to Specimens I and III, since a small foundation crack formed at 0.85% drift. However, the foundation cracks remained much smaller and less widely distributed at larger deformations than for Specimen I. The corrugated pipe used to form the recess appeared to retard radial foundation crack growth. Ultimately, foundation cracking was somewhat more severe for Specimen VI than for Specimen III because of the shallower embedment depth, but it was significantly less severe than for Specimen I. At 2.5% drift, the corrugated pipe uplifted approximately 7.5mm. There was little or no increase in this uplift at subsequent cycles of increased amplitude. Yielding of the tube initiated at approximately 1.2% drift at 543 kN, and visible local buckling of the steel tube was observed at 3.1% drift. Initiation of tearing at the highly strained peak of the buckle was noted at 6% drift, and tearing increased with repeated cycles and increasing deformation. The tear effectively encompassed the entire perimeter of the tube by 8.9% drift. The maximum horizontal load on the tube was a 770kN and it occurred at the deformation. This test shows that the recessed, grouted connection will develop the full capacity of the tube with an embedment depth as short as 375 mm or 0.75D.

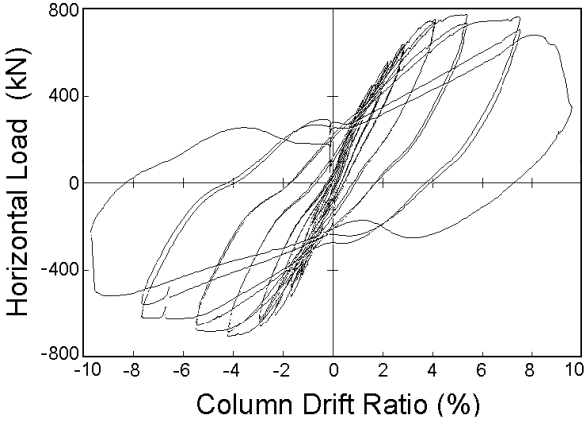


Figure 12. Specimen VI Load Deflection Response

Table 1 shows that a number of additional tests were performed. These tests evaluated:

- punching shear and cone pullout resistance for the given tube and flange connection,
- differences between embedded connections and recessed, grouted connections,
- effect of embedment depth,
- effect of galvanization as a corrosion control measure,
- effect of increased axial load on the connection resistance and deformation capacity, and
- differences in behavior caused by changes in the seismic deformation history.

It is not practical to discuss all of these issues within the length limits of this short paper. However, it can be seen the both connection options develop substantial inelastic deformation capacity and the full ultimate resistance of the composite section if the connection is embedded to an adequate depth. For the given steel tube of high strength steel, the required embedment depth is in the range of 0.75D to 0.9D. This depth would appear to be economical and practical for many applications. The tube and connection permits very rapid construction. The columns may be significantly smaller and lighter than reinforced concrete columns with the same required resistance, and the inelastic deformation capacity of the CFT foundation connections suggests significantly less deterioration in resistance and improved inelastic deformation capacity over that achieved with reinforced concrete columns or piers of the same resistance level.

CONCLUSIONS AND FUTURE WORK

CFT construction represents a practical, efficient, and effective construction method for various structural applications, and the connection of piers and columns to the foundation is critical in ensuring good system performance. Circular CFT is advantageous, because it provides better confinement of the concrete fill and greater bond stress and composite action between the steel tube and fill. However, in the US, relatively few economical and reliable connections are available for circular CFT. A research program was initiated to investigate a simple CFT column-to-foundation connection. The connection consists of an annular ring (or flange) welded to the base of the tube and embedded directly into the foundation. The tube may be directly embedded or a recessed, grouted connection detail, which permits placement of the tube after the concrete footing is cast. This connection is a variation on the traditional embedded connection in that a ring, rather than a full plate, was used, and rather shallow embedment is required. In this research, a slender (D/t = 80) spiral welded tube manufactured using a high-strength (480 MPa yield), vanadium-alloy steel was used, and the tube was filled with a low-shrinkage, self-consolidating, high-strength (65 MPa) concrete. The tube slenderness and yield strength are larger than currently permitted by the AISC design provisions.

To date, 12 connections have been tested for a range of different connection design details and loading conditions. The specimens simulated full-scale building or half-scale bridge columns. Embedment depths of 0.6D to 0.9D were tested. Three of

these tests are described in somewhat greater detail. Specimen with the short (0.6D) embedment depths had significant foundation damage with cone pullout fractures. Shear reinforcement was varied in these shallow embedded tests, but the specimen without any shear reinforcement and lighter flexural reinforcement had similar failure modes and deformation capacity and only slightly smaller resistance than the specimen with significant amounts of vertical shear reinforcement.

Specimens with more significant embedment depth 0.75D to 0.9D developed the full composite resistance of the CFT member and attained large inelastic deformations prior to connection failure. Local buckling of the thin wall tubes was typically visible at drift levels of 3% to 4%. The maximum lateral resistance of the connection (included reduction for P-δ effects) occurred at drift levels slightly smaller that the level where buckling was observed. However, the degradation in resistance was insignificant until a deformation level of approximately 6% drift. After multiple cycles of severe buckling deformation tears initiated in the peak of the buckle, and this tear initiation normally occurred at drift levels larger than 6%. The tear grew around the perimeter of the buckled tube with multiple cycles of increasing deformation, and ultimate failure of the tube was noted at drift levels between 8 and 10.5%. These drift levels at failure are significantly larger than those observed from similar size reinforced concrete pier and column base connections.

Each of the specimens with larger embedment depth was able to achieve the nominal moment capacity of the column (determined using the strain compatibility method), despite exceeding the AISC D/t ratio limit. This suggests that composite action was present in the column and connection. There are clear benefits to using stocky tubes in CFT construction, but this research also suggests that there are also benefits to using more slender tubes, since the reinforcement ratio in the CFT column is directly related to the tube slenderness. It may be easier to develop the full capacity of these slender tubes with a shorter embedment depth.

Two types of connection - a true embedded connection and a recessed and grouted connection where the tube and flange are set into a foundation recess and grouted into the footing - where tested, and both performed well. The test results indicate that the proposed annular-ring embedded connection is effective and practical. Specimens with the longer embedment depth are capable of achieving drift capacities far in excess of the maximum seismic design drifts without degradation of the system and minimal damage to the footing. Therefore, this connection is an appropriate detail for high seismic zones and other extreme loading conditions. Although termed the “longer” embedment depth, this recommended length is shorter than the current recommendation of 1.5D to 2D (Morino et al., 2003, Hitaka, Suita, and Kato, 2004). Analysis of the experimental results indicates that the CFT construction method and tested connections are a promising improvement for future structural engineering applications, including resistance to extreme loads with significant ductility demands. The detail permits rapid construction with reduced labor requirements for formwork and tieing and placing reinforcement.

The current test series represent a limited study regarding the relationship between the D/t ratio, the steel strength (F_y) and the required embedment depth ratio, l_e/D. Because these parameters determine the tension force demand, which in part determines the embedment length requirements, additional study is required. Further, the axial load ratio and the deformation of the footing can influence the force transfer mechanism and resulting damage pattern. Experimental and analytical

research also is needed to develop design expressions for CFT columns and their foundation connections.

ACKNOWLEDGMENTS

Research was sponsored by the Army Research Laboratory and was accomplished under Cooperative Agreement Number DAAD19-03-2-0036. The views and conclusions contained in this document are those of the authors and should not be interpreted as representing the official policies, either expressed or implied, of the Army Research Laboratory or the U.S. Government. The U.S. Government is authorized to reproduce and distribute reprints for Government purposes notwithstanding any copyright notation heron. The authors gratefully acknowledge the financial support of the Army Research Laboratory, and the advice and assistance provided by Mr. Jon Tirpak, the Advanced Technology Institute and the Vanadium Technology Partnership.

REFERENCES

AISC (2005). "Specification for Structural Steel Buildings," American Institute of Steel Construction, Chicago, Illinois.

ATC-24 (1992). "Guidelines for Testing Steel Components," Applied Technology Council, Redwood City CA, 1992, 57 pp.

Azizinamini, A. and Schneider, S. (2004). “Moment Connections to Circular Concrete-Filled Steel Tube Columns”. Journal of Structural Engineering, Volume 130, Issue 2, pp. 213-222.

Chronister, Andrew (2008). " ," a thesis submitted in partial fulfillment of the degree of Master of Science in Civil Engineering, University of Washington, Seattle, WA.

Hitaka, T., Suita, K., and Kato, M. (2003) “CFT Column Base Design and Practice in Japan,” Proceedings of the International Workshop on Steel and Concrete Composite Construction (IWSCCC-2003), Report No. NCREE-0.-0.26, pp. 291-290. National Center for Research in Earthquake Engineering, Taipei, Taiwan.

Hsu, H. and Lin, H. (2003) “Performance of Concrete-Filled Tube Base Connections Under Repeated Loading,” Proceedings of the International Workshop on Steel and Concrete Composite Construction (IWSCCC-2003), Report No. NCREE-0.-0.26, pp. 291-299. National Center for Research in Earthquake Engineering, Taipei, Taiwan.

Kadoya, H., Kawaguchi, J., and Morino, S. (2005) “Experimental Study on Strength and Stiffness of Bare Type CFT Column Base with Central Reinforcing Bars”, Composite Construction in Steel and Concrete V Ed. Roberto Leon and Jörg Lange, United Engineering Foundation, Inc.

Kingsley, Angela (2005) "Experimental and Analytical Investigation of Embedded Column Base Connections for Concrete Filled High Strength Steel Tubes," a thesis submitted in partial fulfillment of the degree of Master of Science in Civil Engineering, University of Washington, Seattle, WA.

Marson, J. and Bruneau, M. (2004) “Cyclic Testing of Concrete-Filled Circular Steel Bridge Piers Having Encased Fixed-Base Detail”, ASCE Journal of Bridge Engineering, Vol.9, No.1, pp.14-23.

Morino, S., Kawaguchi, J., Tsuji, A., and Kadoya, H. (2003) “Strength and Stiffness of CFT Semi-Embedded Type Column Base,” Proceedings of ASSCCA 2003, Sydney, Australia, A. A. Balkema, Sydney, Australia.

Roeder, C. W., Cameron, B., Brown, C. (1999). “Composite action in concrete filled tubes,” ASCE Journal of Structural Engineering, Vol. 125, no. 5, pp. 477-484.

Roeder, C.W., Graff, R., Soderstrom, J. and Yoo, J.H. (2005) "Seismic Performance of Pile-Wharf Connections," ASCE, *Structural Engineering Journal,* Vol. 132, No. 3, March, 2005, pgs 428-37.

Roeder, C.W., Lehman, D.E., and Thody, R., (2008) "Composite Action in CFT Components and Connections," submitted for publication review to AISC, *Engineering Journal*, Chicago, IL.

Williams, Travis (2007) "Experimental Investigation of High Strength Concrete Filled Steel Tubes in Embedded Column Base Foundation Connections," a thesis submitted in partial fulfillment of the degree of Master of Science in Civil Engineering, University of Washington, Seattle, WA.

Using Steel Fiber Reinforced Cementitious Composite (SFRCC) in Shallow Embedded Column Base

Yao Cui
Graduate Student, Department of Architecture Engineering, Kyoto University
Kyoto, Japan
snoopy.cy@steel.mbox.media.kyoto-u.ac.jp

Masayoshi Nakashima
Professor, Disaster Prevention Research Institute, Kyoto University
Kyoto, Japan
nakashima@archi.kyoto-u.ac.jp

Toko Hitaka
Associate Prof., Disaster Prevention Research Institute,
Kyoto University
Kyoto, Japan
toko.h@ay2.ecs.kyoto-u.ac.jp

ABSTRACT

Exposed column bases in Japan are commonly covered with lightly reinforced concrete (RC) slab, whose effect is neglected in seismic design so far. However, many experimental investigations showed that the strength, stiffness and energy dissipation are increased by the contribution of the RC slab. In this study, steel fiber reinforced cementitious composites (SFRCC) is employed for the covered slab to further improve the behavior of exposed column base. Here, 0.4 mmx12.0 mm and 6% volume fraction straight steel fibers were adopted for SFRCC. Eight specimens, one exposed, three concrete and four SFRCC specimens, are tested. The test parameters included slab material and reinforcement ratio (size and strength of steel bars).

INTRODUCTION

Column bases are important structural components, which have significant effect on the structural performance of steel frames. The column base connections can

be classified into two types: “pinned” supports and “fixed” supports. Exposed column bases, classified as “pinned” supports, have been particularly popular for low- and medium- rise buildings In exposed column bases, axial compression is transferred through a steel base plate welded to the end of the column; axial tension and shear force are transferred through anchor rods to the foundation. Due to the advantage of constructability and cost, the exposed column base is common in low and medium rise buildings. However, strength of exposed column bases is usually smaller than that of columns. The hysteretic behavior of the exposed column base is pinched.

If a column base is embedded directly in a reinforced concrete foundation beam with the suggested depth, the column base connection is classified as “fixed” support. For steel tube box columns, the suggested embedded length is larger than 2D, where D is the lateral dimension of the column cross section in the plane of bending (Nakashima and Igarashi, 1986); for wide-flange columns, it is D~2D (Pertold et al., 2000a, 2000b). The hysteresis of this column base is defined by that of the column. Therefore from the viewpoint of hysteretic behavior, the exposed column base is perceived less desirable than the embedded column base, where a hinge forms in the lower end of the column, not in the column base.

On the other hand, in real building designs, there always is a floor slab to cover exposed column bases for architecture view. The contribution of such slab to the seismic behavior is ignored in provisions, because of the relatively small embedment length. A Shallow Embedded Column Base, proposed in this study, is an exposed column base embedded in a floor slab. The thickness of the slab (or the embedment depth) of the column base is less than D. In this column base system, the advantages of exposed and fixed column base are combined.

Moreover, application of steel fiber reinforced cementitious composite (SFRCC) to the slab is proposed. With a densified material structure, SFRCC has good bond performance, as well as high compressive and tensile strength compared with normal concrete. Performance of the column base will be improved by simply changing the material of the slab from concrete to SFRCC. By utilizing SFRCC with reinforcing bars in a large amount unfeasible with normal concrete, the column base’s performance will be greatly improved. This benefit is remarkable, because in structural connections, reinforcing bars are typically congested.

In the following, material and kinematic characteristics of SFRCC are briefly presented and the results of tests on shallow embedded column bases with conventional concrete and SFRCC are described. In the subsequent sections, the contribution of plain/reinforced SFRCC slab are investigated and compared to conventional plain/reinforced concrete slab. The evaluation of composite performance focuses on elastic stiffness, maximum strength, ductility, and energy dissipation as well as other indices, such as extent of damage, and matrix/reinforcement interaction.

SFRCC CHARACTERISTICS

SFRCC is a special type of fiber reinforced concrete with a considerably large amount of steel fibers (at least 6% vol.), compared to the traditional fiber reinforced concrete, which has at most of 2% vol. steel fibers. SFRCC with such a large amount of fiber and an acceptable workability can be manufactured using a large content of water reducing agent in the matrix. However, the matrix of SFRCC has a very large content of microsilica and water/binder ratios, e.g. 0.2 or lower. Because of the large content of steel fibers the matrix is very ductile and that makes it possible to utilize reinforcing bars much more effectively without having large cracks under service conditions. Because relatively small size of the fibers and fine aggregate are used, the distance between reinforcing bars and the cover layer to the reinforcement generally is around 15mm. Moreover, compared to conventional concrete, SFRCC has remarkably large compressive strength and better tensile behavior in terms of the tension strength and the ductility, as shown in Figure 1. The ductility and tensile strain capacity are achieved by using the relatively high steel fibers content.

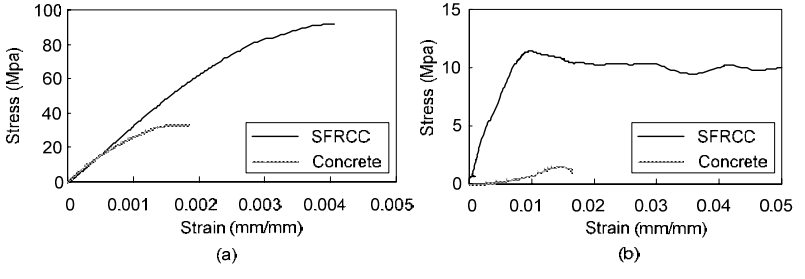


Fig. 1 Stress-strain behavior of concrete and SFRCC: (a) in compression; (b) in tension.

The SFRCC matrix used in this particular study utilized 6% volume steel straight fiber (diameter of 0.4mm, length of 12.0mm, tensile strength of 1350MPa), high early strength Portland cement, silica fume, fine aggregates (maximum grain size 0.25 mm), water, a high-range water-reducing admixture(Flowric SF200S, amino sulfonic acid system compound). Compositions for per m^3 were summarized in Table 1.

Table 1 Compositions for 1 m^3 SFRCC

High early strength Portland cement	801 kg
Silica fume	164kg
Fine aggregate	1235 kg
Steel fiber	471 kg
Water	190 kg
High-range water-reducing agent	32 kg

EXPERIMENTAL PROGRAM

Test Specimens

An interior exposed column base, following the standard design practice, was chosen as the base-line specimen. Besides the base-line specimen, seven shallow embedded specimens with a 100 mm (0.5D) thick flat slab: three with concrete slab and four with SFRCC slab, were fabricated. They were approximately 2/3 scaled, with all specimens having the global dimensions shown in Figure.2. To investigate the modes of failure in the column base, the specimens were designed so as to isolate failure within the region of the base plate connections. A relatively strong column was used to ensure that the base plate connection and/or the covered slab would initiate the development of damage during cyclic loading before significant deformation or damage was developed in the column. The foundation beam was designed strong enough so that an anchor-bolt failure would precede and a cone-like failure of concrete would not occur. The normal strength concrete was used for the foundation beams. High-strength non-shrinkage mortar was adopted to fill in the gap between the base plate and foundation beam. All specimens comprised a cold-formed, square-tube cross section column (200 mm in the width, with thickness of 9 or 12

mm) with a shop-welded hot-rolled, square base plate (300 mm and 25 mm in the width and thickness), twelve machined anchor bolts, and a reinforced concrete foundation beam. Concrete or SFRCC floor slab was placed on top of the foundation beam. Table 2 summarizes the test variables of the eight specimens.

The seven shallow embedded column base specimens are divided into two groups, namely specimens with unreinofrced slab and those with reinforced slab. In the first group, specimens 'CS' and 'SS', specimens with plain concrete and SFRCC slab were designed to investigate the direct effect of conrete and SFRCC, respectively. In the second group, 'CR13' and 'SR13' are the specimens arranged with 13 mm diameter normal reinforcing bars, commonly used in Japan, while specimens 'CR785' and 'SR785' are the specimens with 13 mm diameter high strength reinforcing bars. The rebar with 19 mm diamters were only adopted for SFRCC Specimen 'SR19', since the rebar cover, 17mm, is smaller than the limitation of covering thickness for the concrete specimen. Deformed reinforcing bars are placed to both prevent the rotation of the base plate and delay the slab failure. As shown in Figure 3, the bent part of the reinforcing bar is set perpendicular to the failure surface in the concrete slab. All reinforcing bars are set around the column upon the base plate, two pieces at each column side and in each direction. The 13 mm diameter steel bars with different strengths were adopted to investigate the effect of reinforcement in the concrete and SFRCC slab. The 19 mm diameter normal strength reinforcing bar was adopted for SFRCC slab to investigate the interaction between matrix and rebars.

Table 2 Summary of test specimens

Specimen	Slab material	Rebar diameter (mm)	Rebar material	Column thickness (mm)
Exposed	--	--	--	9
CS	Concrete	--	--	9
CR13	Concrete	13	SD295	9
CR785	Concrete	13	KW785	12
SS	SFRCC	--	--	12
SR13	SFRCC	13	SD295	12
SR19	SFRCC	19	SD295	12
SR785	SFRCC	13	KW785	12

Table 3 Material properties (concrete and steel)

		Yield strength σ_y (N/mm^2)	Tensile strength σ_u (N/mm^2)
Column	□-200×12, SM490A	353	512
Column Base	Anchor bolt,SS400	317	450
	Base plate, SM490A	322	510
Reinforcement	D13,SD295	325	461
	D19,SD295	332	514
	KW785	716	970

		Compressive strength f_c' (N/mm^2)	Splite strength f_{sp}' (N/mm^2)
Slab	SFRCC	93.2	11.5
	Concrete	34.5	1.6
Foundation Beam	Filled mortar	66.7	--
	Concrete	34.5	--

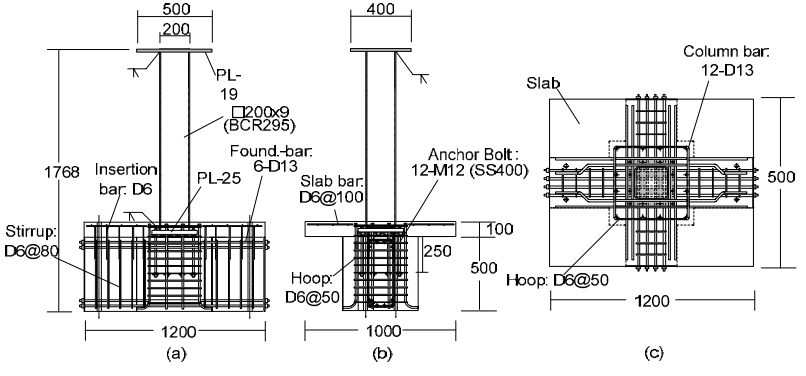


Fig. 2 Test specimen: (a) front elevation; (b) side elevation; and (c) plane view (unit: mm)

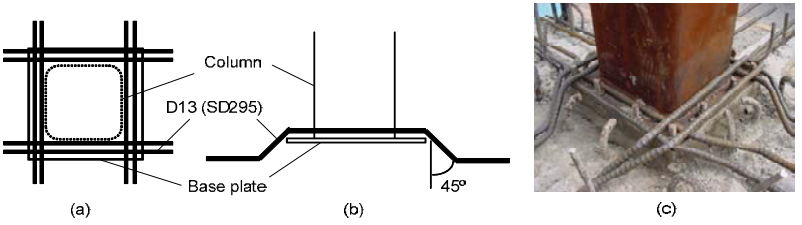


Fig. 3 Configuration of reinforcing bars: (a) plan view; (b) elevation; and (c) arrangement of reinforcing bars

The material properties of the steel, SFRCC and concrete used for the specimens are obtained from the associated material tests are summarized in Table 3.

Test Setup and Loading Program

The test specimen was placed in the loading frame as shown in Figure 5. The foundation beam was clamped on the reaction floor. The column top was clamped to two oil jacks in the horizontal and vertical directions, respectively. The specimen was subjected to a constant vertical force of 511 kN, which equals to 0.2 times the calculated yield axial load of specimen 'Exposed', throughout the test. A displacement-controlled cyclic load was applied quasi-statically in horizontal direction. Figure 4 shows the loading history adopted. The displacement was expressed in terms of the overall drift angle, defined as the horizontal displacement at the loading point relative to the height of the column (1238mm). Overall drift angles of 0.005, 0.015, 0.0225, 0.03, 0.04, 0.06, 0.08, and 0.1 rad were adopted. The test was terminated when the drift angle reached 0.1 rad or ten of the twelve anchor bolts fractured which was regarded as complete failure of the specimen.

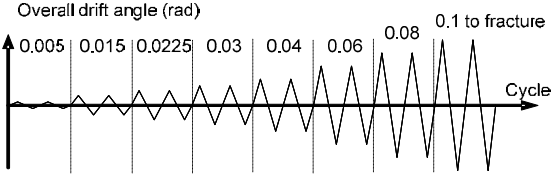


Fig. 4 Loading history

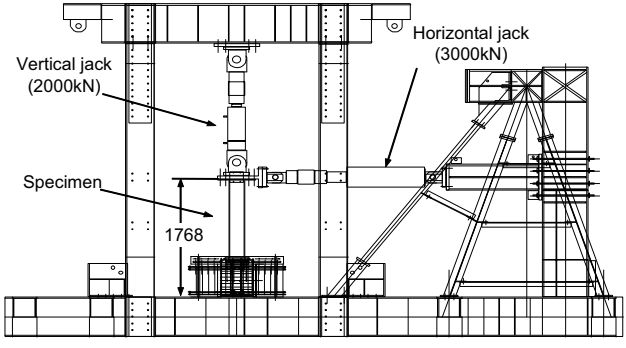


Fig. 5 Elevation of the loading system (unit: mm)

TEST RESULT

Experimental Observation

All of the shallow embedded column base specimens failed by punching shear in the slab.

Failure of all specimens with floor slab was similar, regardless of the differences in slab material or reinforcement detailing. Cracking patterns of shallow embedded column base specimens are shown in Figure 6. All the specimens failed by punching shear in the slab. The concrete slab was uplifted by the rotation of the base plate, and the punching shear failure occurred on the uplifted side. All cracks were connected to each other and formed a cone-like crack during the cycles of 0.03 rad for the concrete specimens and 0.04 to 0.06 rad for the SFRCC specimens, when the specimen reached the maximum strength. As the column rotation increased, part of the concrete slab around the base plate was forced to be separated. Such separation caused the strength deterioration. At the end of the loading, a cone with failure surface radiating from the top of base plate to the surface of concrete slab at a slope angle of about 45° was observed in all specimens. Buckling of rebars was observed in the conrete specimens, whereas rupture of rebars was observed in the the SFRCC specimens (Figure 7). The portion failed in punching was separated entirely from the concrete slab, all the while the punching part remained partially connected to each other for the SFRCC specimens, because of the presence of steel fibers. A large punching crack circle was formed in concrete slab, as shown in Figure 6, while smaller punching region and more cracks was formed in SFRCC slab.

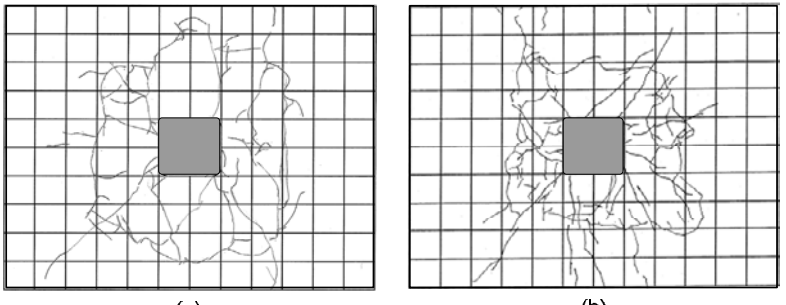


Fig. 6 Cracking patterns of slab: (a) concrete slab; (b) SFRCC slab.

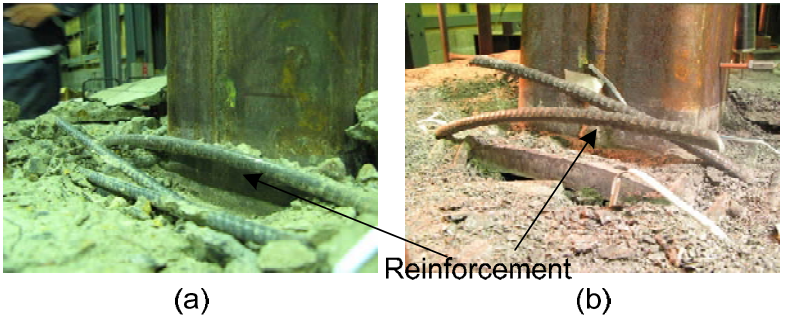


Fig. 7 Deformation of reinforcement: (a) buckling; (b) rupture

Moment-Rotation Relationships

Figure 8 shows the force-deformation relationships for specimens in terms of the end-moment (M) versus overall drift angle (θ). Here the relations of 'CR785' and 'SR785', those with high-strength reinforcing bars, are not presented in that their behavior was nearly identical to the corresponding specimens with normal strength reinforcing bars. Note that the end moment includes that induced by the P-Δ effect. The dashed line represents the initial stiffness of the specimen. To highlight notable differences in behavior during different deformation ranges, Figure 8 uses two different scales for the abscissa: one scaled to 0.03 rad and the

other to 0.12 rad. The value of 0.03 rad was chosen as the maximum rotation that column bases of steel moment resisting frames may experience in contemporary seismic design. Behavior with rotations greater than 0.03 rad was examined for the seismic capacity of the column base to failure.

In view of the moment-rotation relationships up to the rotation of 0.03 rad, the following observations are notable. The initial stiffness and maximum strength are improved by the concrete slab, and further improved by using SFRCC, because of the larger young's Modules and compressive and tensile strength for SFRCC as compared with conventional concrete. Furthermore, the hysteresis loops of reinforced SFRCC specimens were fattest. In the contrary, hysteresis loops observed in the exposed specimen and reinforced concrete specimen, which showed slip behavior. According to the test results, the initial stiffness increased by 16% and 46% for the concrete and SFRCC specimens, respectively. For the maximum strength (up to 0.03 rad), the improvement of plain concrete and SFRCC slab was 1% and 71%, respectively. The improvement of the specimens with 13 mm steel bars was 24% and 97% for the concrete and SFRCC specimens, respectively. The maximum strength of 'SR19', the one with reinforcing bars with a larger diameter, was improved 124%.

The following observations are notable from the moment-rotation relationship up to the rotation of 0.1 rad. The specimens without reinforcement, i.e., 'CS' and 'SS', exhibited slip behavior similar to that observed in the exposed column base, 'Exposed'. All the concrete specimens arrived at the maximum strength at around 0.03 rad. The strength of specimens with unreinforced slabs descended sharply after this point. The strength deterioration was due to the punching shear failure of the concrete slab, and the strength eventually dropped at a level of 'Exposed'. Strength deterioration of reinforced specimens (CR13 and CR785) was reduced significantly. For the SFRCC specimens, slip behavior and pinching of the hysteresis curves was less notable when they were reinforced. 'SS' exhibited serious strength deterioration by 50% up to 0.8 rad drift angle, because of the lack of reinforcing bars, while all other SFRCC specimens those with reinforcement, showed more stable behavior, with the strength deterioration of at most 15%. This is most significant for 'SR19', the one with the largest reinforcing bars, which the strength did not deteriorate up to the drift angle of 0.8 rad.

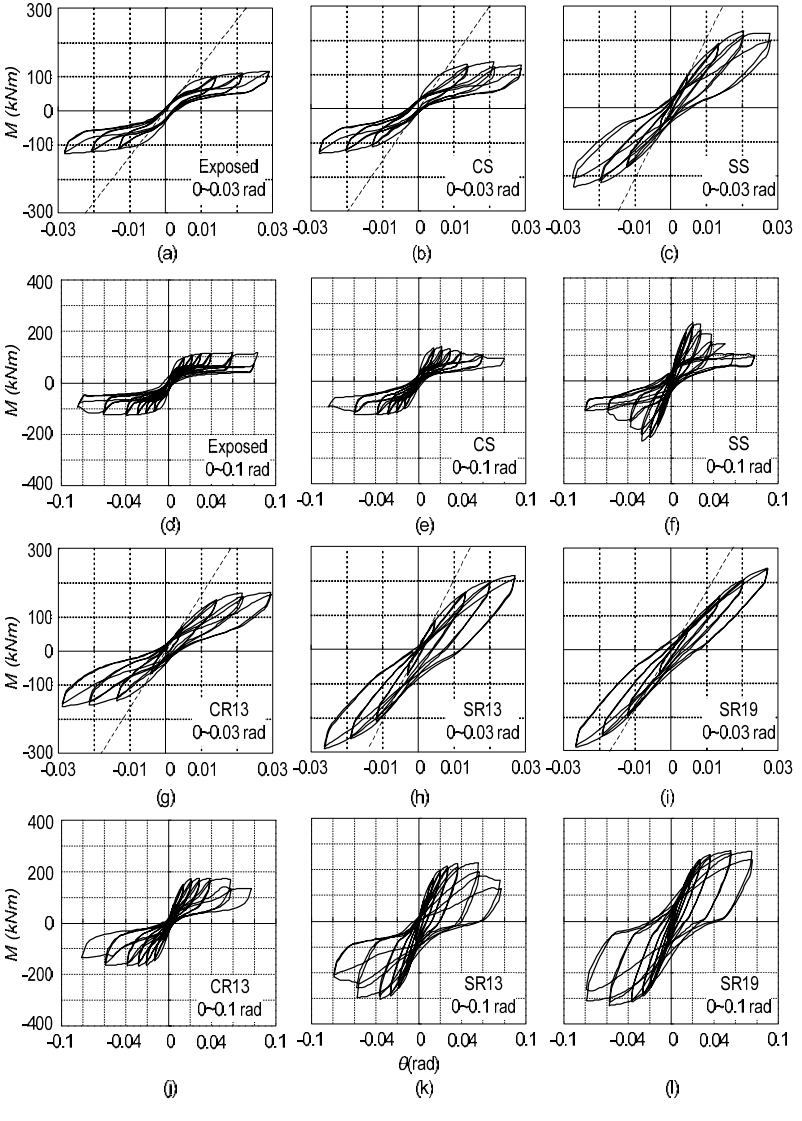


Fig.8 Moment versus rotation relationships: (a) Exposed to 0.03 rad; (b) CS to 0.03 rad; (c) SS to 0.03 rad; (d) Exposed to 0.1 rad; (e) CS to 0.1 rad; (f) SS to 0.1 rad; (g) CR13 to 0.03 rad; (h) SR13 to 0.03 rad; (i) SR19 to 0.03 rad; (j) CR13 to 0.1 rad; (k) SR13 to 0.1 rad; and (l) SR19 to 0.1 rad.

Energy dissipation

To evaluate the effect of SFRCC on the energy dissipation capacity, the cumulative dissipated energy was estimated. The cumulative dissipated energy (Figure 9) was identical at drift levels prior to 2.25% drift. The concrete specimens have little energy dissipation capacity beyond the maximum strength level (2.25%) due to the rapid strength degradation. On the other hand, SFRCC shows steadily increasing cumulative energy dissipation until the failure by rupture of steel reinforcement.
From observation, the large energy dissipation in SFRCC specimens appears to be attributed to the good bond property and the steel fiber in SFRCC. As mentioned earlier, small but many cracks are formed in SFRCC. These are formed primarily due to the bridging effect of the steel fibers, i.e. the fibers connect two concrete chunks separated by a crack and prevent the crack to develop. These fibers, on the other hand, will sustain some plastic deformation. The element that absorbs energy is deemed to be the fibers.

As noted earlier, the specimens with high strength reinforcing bars ('CR785' and 'SR785') showed similar moment-rotation curves as the corresponding specimens with normal strength steel bars. As shown in Figure 9, the cumulative energy dissipation was nearly identical before the drift angle of 0.06 rad at which the maximum strength was attained. In fact, the high strength steel bars remained elastic at this drift level. In addition, the strain data collected through gages on the steel bars suggest that the stress level in the high strength bars were almost the same as the yield stress of normal reinforcing bars.

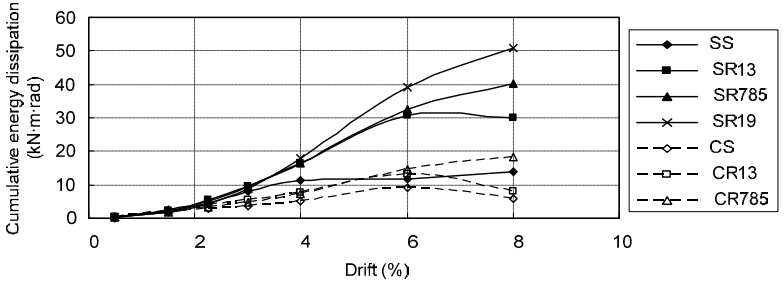


Fig. 9 Cumulative energy dissipation of Specimens

CONCLUSIONS

1. The tests confirmed the improvement of the elastic stiffness, maximum strength and energy dissipation by floor slabs of normal concrete. Increase of these values was enhanced further by using SFRCC instead of the conventional concrete for shallow embedded column bases. Moreover, the punching failed region in slab was reduced by using SFRCC.
2. By using reinforcement, the strength deterioration is mitigated. Due to the good bond properties of SFRCC, the energy dissipation of reinforced SFRCC specimen was significantly improved. Furthermore, the limitation of rebar cover was reduced.
3. The contribution to the maximum strength from high strength bars is limited, since high strength bar still worked in elastic region when the maximum strength was reached. Therefore, for shallow embedded column base, it is more effective to use larger size conventional rebar.

This study provided fundamental information on the behavior of shallow embedded column bases featured with SFRCC floor slab. A separate study in which FEM analysis is employed is underway to quantify the effects of various parameters such as the column size on the strength and energy dissipation. The results together with design method will be reported later.

REFERCENCES

[1] Nakashima, S. and Igarashi, S., 1986. “Behavior of Steel Square Tubular Column Bases for Interior Columns Embedded in Concrete Footing Under Bending Moment and Shearing Force, Part 1, Test Program and Load-displacement Relationships.” *J. Struct. Constr. Eng.*, 366, 106-118. (in Japanese).

[2] Pertold, J., Xiao, R. Y., and Wald, F. (2000a). “Embedded Steel Column-Base – I. Experiments and Numerical Simulation,” Journal of Constructional Steel Research, 56, 253-270.

[3] Beche, H. H., 1981. Desified Cement/Ultrafine Particle-Based Materials, Presented at Second International Conference on Superplasticizers in Concrete, Ottawa, Canada.

[4] Kaneko. Y. et al. 2000. Mechanical Properties and Application of Steel Fiber Reinforced Cementitious Composite. Cement Science and Concrete Technology, 54,723-730.

Composite Buildings in Germany

Prof. Dr.-Ing. Jörg Lange
Technische Universität Darmstadt
Darmstadt, Germany
lange@stahlbau.tu-darmstadt.de

Prof. Dr.-Ing. Wolfgang Kurz
Technische Universität Kaiserslautern
Kaiserslautern, Germany
wkurz@rhrk.uni-kl.de

ABSTRACT

Starting in the early 1950s the use of composite members in buildings increased significantly in Germany. High-rise office buildings and since the 1980s multi-storey industrial buildings were built with composite decks, beams, and columns. Basic research and the development of design procedures on fire-resistant composite members supported this development. The paper presents some of the most important composite buildings that were built in Germany recently.

HISTORY

From 1950 to 1980 many important high-rise office buildings were built using steel and composite members. Starting with the 16 storey building for the Continental Gummiwerke in Hannover in 1952 followed by the Thyssen building in Düsseldorf (28 storeys, built in 1960), the office building for the delegates of the national assembly in Bonn (31 storeys, 1969, [1], Fig. 1a) to the Deutsche Welle in Köln (33 storeys, 1979, [2], Fig. 1b).

Based on the research on fire-safe steel and composite structures that started in the late 1970s new industrial buildings were designed often using partly encased composite beams and columns that have great advantages for the users. These are:

- easy retrofitting and refurbishment
- fast erection
- good fire resistance

Starting 1982 with the new motorcycle production facilities in Berlin ([3], Fig. 2a), the new paint shop for a car fabrication line in Eisenach (1992, [4]) and the combined office-, fabrication- , and storage-building in Berlin (1993, [5], Fig. 2b) many large multi-storey industrial buildings have been built.

Within the last 10 years the focus shifted towards high-rise office buildings. Due to the national legislation that asks for outside view from normal workplaces, the standard floor plan of an office building in Germany is usually not wider that 12 to 14 m. This is the depth of two office bays and the central corridor.





Fig. 1a) Office building for members of the national assembly, Bonn b) Deutsche Welle, Köln





Fig. 2a) Motorcycle production facilities, Berlin b) Office-, fabrication- and storage-building, Berlin

Starting with the Düsseldorfer Stadttor (20 storeys, 1997, [6], Fig. 3a) and the Commerzbank-Building in Frankfurt (63 storeys 1997 [7], Fig. 3b) architects and structural engineers developed staggered floor plans. By connecting two or three independent towers structural engineers built a frame that can resist horizontal loads much better than a single tower. In the Stadttor this was done by building three 3-storey trusses on top of the 16th floor. This truss-area houses office space and a large, glas-covered atrium. In the Commerzbank-Building Vierendeel-trusses holding 8 floors of office space are connected to the cores that are located in the corners. Between these trusses four floors are kept open for large “sky”-gardens.





Fig. 3a) Düsseldorfer Stadttor b) Commerzbank-Building, Frankfurt

HIGHLIGHT MUNICH BUSINESS TOWERS

The design of these two high-rise buildings follows the idea of maximum. Therefore architect and structural engineer decided to use a flat concrete slab, circular columns with minimized diameters and to avoid solid walls for the bracing of the towers.

Both towers have a width of 13.5 m and a length of about 80 m with three lines of composite columns. The slab has spans of approx. 7 m and 5 m between the column lines and short outriggers with a small concrete edge beam. The thickness of the slab is 28 cm. It is connected to the columns in a way that allows transmitting bending moments from the slab to the columns. The typical column grid is 8.10 m in towers longitudinal direction, fig. 4. The height of the towers is 133 m and 113 m respectively.

All columns outside the bracing systems were made of steel tubes filled with an I-section. They were filled with concrete after erection. The diameter of the tubes varies from 813 mm at the bottom floors to 324 mm at the top floors of the tower. Also the I-sections were varied in order to adopt the column capacities to varying loads in the different floors. All columns were designed as hinged columns with the height of one story. The maximum ultimate loads were about 29 MN.

Both towers are independent buildings with independent bracings. Due to flexibility demands the bridges between the buildings can be dismantled or other new bridges can be added. The elevator shafts are designed as tree-dimensional steel frames and are located outside the towers between the buildings. Those shafts are connected to the concrete slabs of the floors. They do not brace the buildings.

Bracing is realized with two U-shaped truss structures at each tower, Fig. 4. The bracing consists of composite columns, composite diagonals, and composite beams. The columns are realized with thin steel tubes outside, I-sections, and concrete between steel core and the tube. This construction uses the thermal insulation effects of the concrete for the steel cores and reaches the required fire resistance without additional fire protection. Due to the very high loads up to 94 MN in compression the columns have diameters up to 1016 mm and very huge steel cores that are made of several steel lamellas, Fig. 5. Because of the small dead load on the truss columns also very high tensile loads up to 29 MN do appear. Those tensile loads are transmitted by bolted or welded connections of the steel lamellas of the core profile, fig. 5.

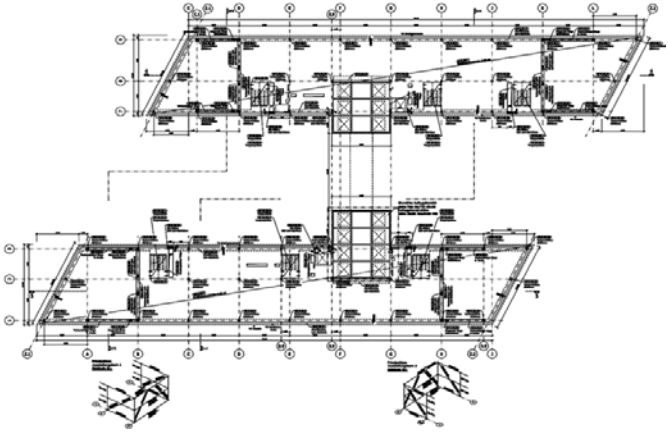


Fig. 4: Grid and bracing of the towers

The trusses are connected to every other floor of the towers. The floor slabs in between are connected to the truss columns and transfer their horizontal loads by bending moments into the bracing.

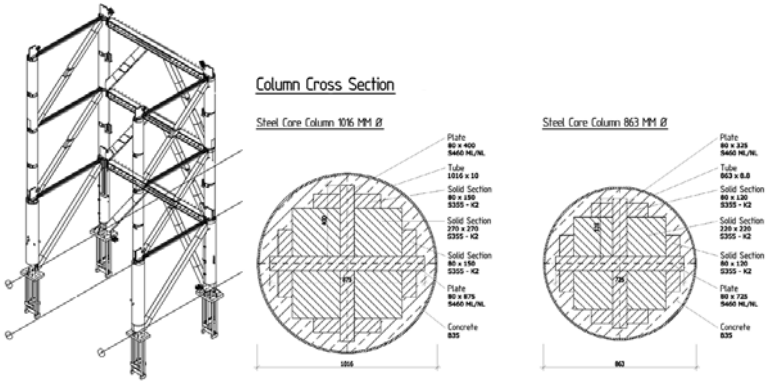


Fig. 5: Truss system and cross section of truss columns

By the use of high performance composite structures the idea of transparency in the office towers could be realized.




Fig. 6: Inside view of tower floor with bracing and view of tower and elevator shaft

Further information about the structure, the engineering approach and the erection can be found in [8] and [9].

WESTEND DUO, FRANKFURT

This office building was finished in 2006. It has 26 storeys and a height of 96 m. Architects were „KSP Engel und Zimmermann“, structural engineer „Weischede + Partner”. The special feature of it is the innovative floor system. The maximum height was given due to zoning laws. Based on a floor plan with a central corridor and offices at the windows a girder was developed that spans approx. 14 m. In the office area the deck rests on the lower flanges of the girder. The false floor is on the level of the top flange giving the girder’s depth for installation (HVAC, electricity, and telecommunication). This leads to the large web openings producing a Vierendeel-truss, fig. 8.




Fig. 7a) Outside view of a regular storey b) Inside view of a regular storey

In the corridor the deck rests on the top flanges giving space for HVAC and lighting of the corridor. The depth of the whole girder including concrete slab and fire protection is 45 cm. The girders rest on primary beams, mainly made of concrete due to the curvature of the façade, and composite columns.

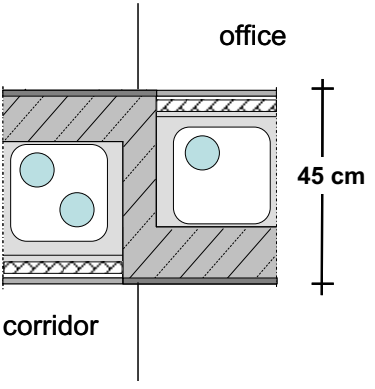


Fig. 8: Staggered floor

JUNGHOF, FRANKFURT

In the centre of Frankfurt the office building “Junghof” had to be refurbished to make it attractive for modern use. When it was built in the 1950s five storeys were located around a central court. The new concept developed by the Frankfurt-based architects “Schneider + Schumacher” added two storeys. Structural designers were “Lange + Ewald”.



Fig. 9a) Outside view



b) inside view

Only the four corners of the building are able to carry the additional loads. Therefore a structure was designed that resembles an arch bridge (Fig. 9a). These arches are made of circular steel sections (diameter: 355.6 mm, wall thickness: 12 to 20 mm).

The tension element tying the arches horizontal bearing forces is made of an I-beam. The need for a light structure combined with the architects design aim to produce a transparent, open office space led to the use of composite slabs (depth = 16 cm, spanning nearly 2 m without erection support) on composite beams spanning from outside wall to outside wall (maximum span = 7.5 m) without any interior columns (Fig. 9b). This led to a common design of the 7th floor slab but to very odd shapes of the roof-beams on account of the shell-like roof. A re-entrant composite profile (h = 51 mm), was used for the slab. More information on this project is given in [10].



Fig. 10: Roof seen from below

MAIN RAILWAY STATION BERLIN

The Main Railway Station in Berlin is located in direct neighbourhood to the German government and Parliament and connects two high-speed-Railway sections to the center of the German capital. The railway tracks in north-south direction are located below the ground in a tunnel. They are made visible by two buildings at both sides of the track, the so-called “Bügelbauten”. The railway track running in east-west direction is located on bridges above the ground level. It passes trough the two buildings marking the North-South track. This architectural concept made it necessary to have a building structure that bridges above the railway tracks with a span of about 87 m, a view of which is given in figure 11.

Each building consists of two towers with twelve stories and a four-story bridge in between that connects both towers. The towers are braced by concrete cores with shear walls. The composite columns are located outside the facade. Composite beams connect the columns with the core wall and support the concrete slab with a thickness of 20 cm. The slabs are restrained in the core walls to activate some frame effects to maximize the stiffness of the towers. Steel beams outside the façade also connect the columns. They are only installed for architectural purposes, fig. 11.

The bridges are truss structures with a height of about 20.6 m, a width of 20.5 m and a span of 87 m. They are supported by four columns in the edges of the bridges, the so-called pylons. In order to minimize restrain forces the slabs are not directly connected to the slabs of the towers. Only transverse horizontal loads can be transmitted to the tower slabs. The bridge slabs were concreted with lightweight aggregate concrete to minimize the dead load of the structure. Loads are transferred by two trusses from the bridge floors to the supporting columns. Those trusses are also located outside the façade and visible, fig. 11.

The columns of the towers were welded square steel boxes with a width of 500 mm. Inside there was a reinforcement mesh with a high amount of longitudinal reinforcement. The reinforcement was built into the steel sections in the steel fabrication shop. After erection the columns were filled with concrete by pumping the concrete from the bottom upwards. The composite girders had a height and a width of 280 mm. Due to the fact that there was no composite action at the outer ends flange thickness reached values up to 50 mm.



Fig. 11: Building with load carrying composite structure outside of the façades

The pylons are rectangular steel boxes with a second steel box inside the column and additional reinforcement. The cross section is 1200 mm high and 800 mm wide and steel plates have thicknesses of up to 50 mm. These columns were also filled with concrete by pumping from the bottom upwards. The girders of the trusses are also steel boxes with concrete filling. The lower chord has additional vertical and horizontal steel plates inside the box with plate thicknesses up to 60 mm. The upper chord is filled with reinforcement and only vertical additional steel plate. All vertical members of the truss are steel boxes with reinforcement and concrete. The diagonals are thin steel tubes with thick steel lamellas as core profile and concrete filling. Typical cross sections can be seen in fig. 12.

A special challenge was the erection of the bridge structures over the east-west railway track. This track was under operation during erection so there were only three weekends available to close down the traffic and to erect both bridges. The bridges were erected in a vertical position in two halves and then tilted over by 90 degrees into a horizontal position. After lowering the two halves were connected in the middle over the railway track so that the truss could act as a single span beam before the railway track was opened to traffic again. Fig. 13 shows the system minutes before the end of this procedure.

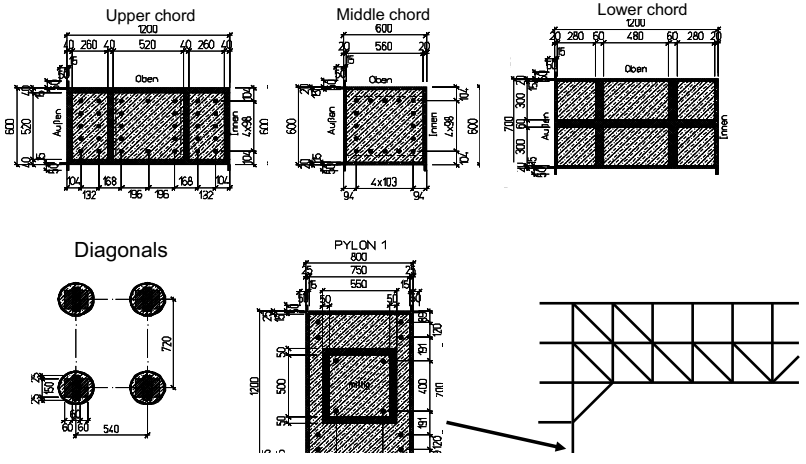


Fig. 12: Typical cross sections of the bridge structure



Fig. 13: Final positioning of bridge halves by using strand jacks

Fig. 14 shows the hinge in the pylon columns and a detail of the connection of steel box girders with reinforcement inside.

Further information about the structural details, construction process, and erection can be found in [11, 12, 13].



Fig. 14: Connection detail in bridge truss girder and hinge construction in the pylon column

TRANSPARENT MANUFACTURE DRESDEN

The Transparent Manufacture Dresden is a multi-story production building for the assembly of luxury cars. The overall dimensions are 140 m x 140 m. In the basement level there are storage facilities, preassembly lines for chassis and drive line and a car park. In the first upper level there is an event area of 80 m x 80 m with a 40 m high cylindrical steel structure that is used for storage and presentation of finished cars. The L-shaped rest of this floor is used for an assembly line and test facilities. The second upper level is also used for production with two assembly lines, fig. 15.



Fig. 15a) Building site with L-shaped assembly b) Section with composite beams

The construction of the event area was a conventional steel composite structure with hinged columns composite beams and a 25 cm thick concrete slab. In the assembly area there was a central atrium. Around this atrium there were 16 m wide areas where the assembly line was supported by a composite structure. The column grid was 16 m x 8 m. Slab was supported each 4 m by a composite beam, fig. 15b.

All columns were realized as steel tubes with concrete filling. In the event area those columns had an additional reinforcement. In the assembly area steel core profiles were used. All columns in the event area had a diameter of 700 mm, all columns in the assembly area of 406 mm. The design idea was that the construction height

visible at the facades should be as small as possible. Therefore the beams along the façade had a height of only 35 cm plus the concrete slab that is 25 cm thick. The assembly should not be visible from outside. This was realized by folding the composite beams supporting the slab. The assembly line is located in the lowered area of the slab. All beams are designed as single span composite members.

Another design specification was that there should be no visible connections between columns and beams. To realise this, a new connection between columns and beams was developed. The load from the columns of the upper floors was transmitted by vertical steel plates between the bottom plate of upper column and top plate of lower column. For this system the load concentration in the steel core profile was helpful to minimize thickness of the column end plates, Fig 16. The webs of the composite girders connected to the column were directly placed on top of the lower columns end plate. Therefore the girder flanges had to be cut in order to avoid collisions between the girders, Fig. 16.

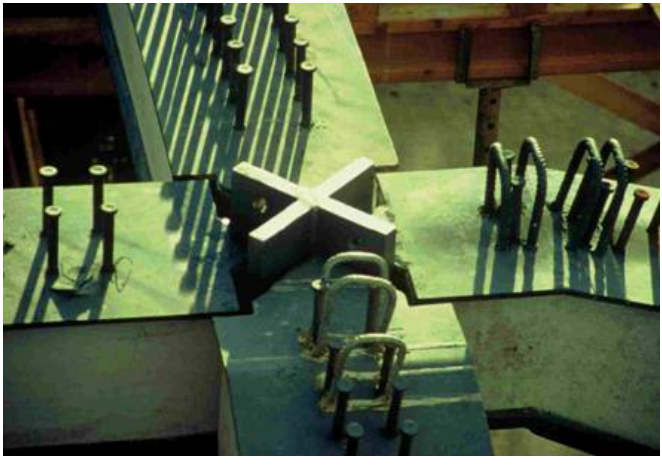


Fig. 16: Connection between Columns and girder and transfer of loads in column line

Another new type of connection was developed for the load transfer between the composite beams supporting the slab and the small main girder along the façade. This connection is shown in Fig. 17. Here the top flange of the main girder is slotted and also the concrete encasement of this beam is slotted. The steel web of the secondary beam is therefore shaped in a way that it will fill the slot in the primary beam and also use a part of the concrete slab thickness to provide a high steel plate for transfer of shear loads from secondary beam to primary beam.

The new developed solutions for connections between beams to girders and beams to columns had also some more advantages. First advantage is a very economic erection because no bolting or welding is necessary. After placing the girders at the right position erection is finished. After pouring of slab concrete connections are fixed. Second advantage is the fire resistance. All connections and also all composite members had a fire resistance of 90 minutes without any additional fire protection.





Fig. 17: End support of secondary beam and erection in slots in primary beams

More information and details about this building is given in [14].

FIRE ENGINEERING

The improvement of fire design was a driving force behind the development of new composite elements and structures. Starting with the tests that were performed to support the fire design of the motorcycle production facilities in Berlin (Fig. 18a, [3]) and the tests of the Demo-Bau in Stuttgart (1985, Fig 18b, [15]) and not ending with the fire design of the whole structure of the Junghof (Fig. 19, [10]) many important small steps were taken.





Fig. 18a) Fire tests on connections b) Full scale fire tests in Stuttgart

For the Junghof conventional fire protection (boards and cementitious spray) was used for most steel and composite members. Some members stayed unprotected due to the architect's goal to achieve great transparency. For the load case "fire" the whole structure was modeled without these unprotected members. The good composite action of the composite members gave the residual structure enough strength to hold all loads.

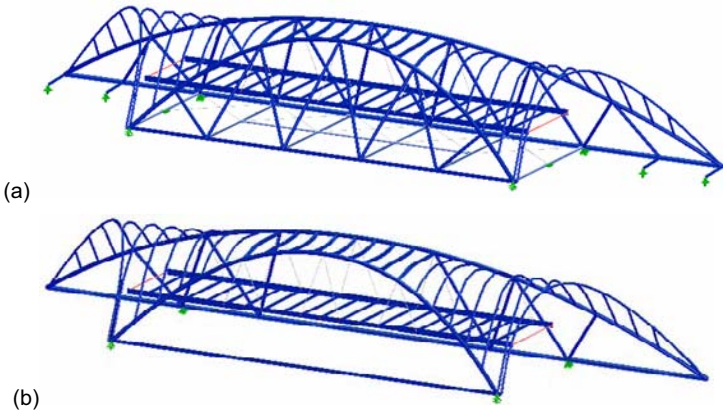


Fig. 19 Structural system (a) before and, (b) during a fire

Currently new rules are developed and used to exploit the catenary action that can occur due to large deflections in a fire. Plank (Fig. 20, [16]) gives a good overview of this method. At first the thermal expansion leads to compressive arching against the adjacent structure and finally buckling of the plate. Then the catenary tension support reacts against the adjacent structure.

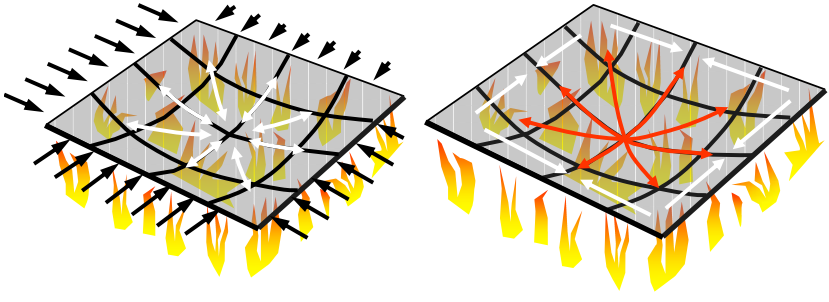


Fig. 20 a) Buckling due to thermal expansion; b) Catenary tension support

REFERENCES

[1] E. Werner “Das Hochhaus für den Bundestag“, Stahlbau (39), Ernst & Sohn, 1970

[2] D. Hirsch, K. Reimers “Hochhäuser für die Deutsche Welle in Köln“, Bauingenieur (53), Springer Verlag, 1978

[3] H. Muess, W. Schaub “Neubau einer zweigeschossigen Fertigungshalle mit neuartigem Brandschutzkonzept“, Stahlbau (51), Ernst & Sohn, Berlin, 1982

[4] E. Jöst, G. Hanswille, R. Heddrich, H. Muess, D.A. Williams “Die neue Opel-Lackiererei in Eisenach in feuerbeständiger Verbundbauweise“, Stahlbau (61), Ernst & Sohn, Berlin, 1992

[5] H. Eichhorn, B. Kühn, H. Muess “Der Neubau der Siemens AG Verkehrstechnik in Berlin-Treptow“, Stahlbau (65), Ernst & Sohn, Berlin, 1996

[6] J. Lange, K. Ewald “Das Düsseldorfer Stadttor - ein 19-geschossiges Hochhaus in Stahlverbundbauweise“, Stahlbau (67), Ernst & Sohn, Berlin, 1998

[7] W. Ladberg “Commerzbank-Hochhaus Frankfurt/Main. Planung, Fertigung und Montage der Stahlkonstruktion“, Stahlbau (65), Ernst & Sohn, Berlin, 1996

[8] W. Sobek, M. Duder, Th. Winterstetter, N. Rehle, St. Hagenmayer “Das Hochhausensemble am Münchner Tor“, Stahlbau (73), Ernst & Sohn, Berlin, 2004

[9] N. Sauerborn “Verbundstützen im Hochhausbau“, Bautechnik (83), Ernst & Sohn, Berlin, 2006

[10] J. Lange, K. Ewald “Office Building Junghof - Visible Steel for a Fire Safe Structure”, Structural Engineering International, IABSE, Zürich, 1/2007

[11] B. Naujoks, T. Nicolay, J. Gugeler “Die Stahlverbundkonstruktion der Bügelbauten des Lehrter Bahnhofs”, Stahlbau (75), Ernst & Sohn, Berlin, 2006

[12] L. Petersen, B. Naujoks “Verbundstützen der Bügelbauten über dem Berliner Hauptbahnhof”, Beton- und Stahlbetonbau (101), Ernst & Sohn, Berlin, 2006

[13] B. Naujoks “Tragwerk und Montage der Bügelgebäude des Berliner Hauptbahnhofs”, Bauingenieur (81), Springer – VDI, Düsseldorf, 2006

[14] W. Haumer, T. Thiele, R. Laudahn, K.-J. Jentzsch, W. Kurz, J. Schmitt, J. Opolka “Gläserne Manufaktur Dresden – Eine Idee wird Wirklichkeit”, Bautechnik (78), Ernst & Sohn, Berlin, 2001

[15] R. Lehmann “Brandschutz-Technologien für Stahl- und Verbundkonstruktionen im Stuttgarter Demonstrationsbauvorhaben”, Bautechnik, Ernst & Sohn, Berlin, 1986

[16] R. Plank “Fire Design in UK”, Conference “Brandsicher bauen mit sichtbarem Stahl”, Institut für Stahlbau und Werkstoffmechanik, TU Darmstadt, June 2008

COMPOSITE BRIDGES IN GERMANY DESIGNED ACCORDING TO EUROCODE 4-2

Univ.-Prof. Dr.-Ing. Gerhard Hanswille
Institute for Steel and Composite Structures, University of Wuppertal,
Wuppertal, Germany
stahlbau@uni-wuppertal.de

ABSTRACT

The Eurocodes for the design of steel, concrete and composite bridges have been introduced in Germany since 2003. The development and the implementation of the new generation of design codes in combination with the construction of several new freeways in the eastern part of Germany after the German Reunification initiated new types of composite bridges. This paper gives an overview about new developments in composite bridge design and about the experience and the consequences resulting from the new generation of European design codes.

1 INTRODUCTION

The number of composite bridges has significantly increased in Germany within the last 15 years. The main reason for this development is the high durability and robustness of this type of bridge structures and the development of new types of cross-sections and erection methods for bridges with small and medium spans as well as for superstructures. Further reasons for the increasing number of composite bridges are:

- Concrete and structural steel are used in a way that the high tensile strength of structural steel and the high compressive strength of concrete are used in an optimal combination.
- This combination allows very slender and aesthetic bridges, especially when high strength materials are used;
- Composite bridges have advantages with regard to the foundation and settlements of supports, because the dead weight of composite bridges is significantly lower than the weight of comparable concrete bridges;
- In comparison with steel bridges composite bridges have a better behaviour with regard to freezing in winter;
- In case of restrictive crack width limitation in combination with a sufficient depth of the concrete slabs the decks have a high durability and fatigue strength;
- Because of innovative erection methods and the use of partially prefabricated composite girders composite bridges are often used for passing over existent rail- and highways without any restriction for the traffic during erection;
- Where existing freeways with two lanes in each traffic direction are widened, the short erection time of composite bridges avoids longer restrictions for the traffic;
- Introduction of new design codes /1, 2/.

In the following some typical examples for new and innovative types of composite bridges are presented. After the reunification of Germany especially in the eastern part of Germany several new freeways were built. The advantages explained above are the main reasons why more than 50% of bridges for these freeways are composite structures.

2 COMPOSITE BRIDGES FOR FREEWAYS

For freeways with two or three traffic lanes in each direction, a particular requirement of the German Federal Ministry of Transport relates to two separate superstructures for each traffic direction. By this separation traffic lanes 2+2 can be moved on one superstructure only if the other superstructure needs to be closed for repair and maintenance reasons. Furthermore in Germany the design specifications recommend that for composite bridges prestressing of concrete slabs by bonded tendons should be avoided. In order to get a high durability of the concrete deck, minimum slab thickness in combination with special detailing of reinforcement is given in the design specifications and the crack width has to be limited to 0.2 mm for bridges with normal open sections and box girders, and to 0.1-0.15 mm for concrete tension members in composite bowstring arches. In order to fulfil these requirements only special types of cross-sections can be used.

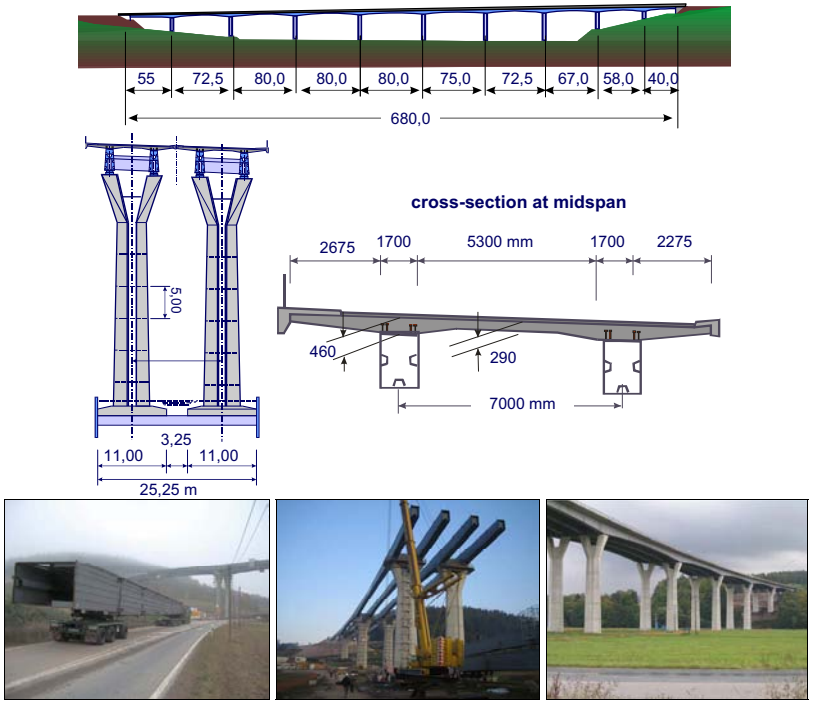


Fig. 1 - Freeway bridge “Schleusetal” with two separate superstructures

In the last years especially the cross-section with two airtight box girders became very popular (Figure 1), because with this type very big box girder elements with a total length equal to the span length of the bridge can be prefabricated in the shop and then transported to site. For bridges with a pier height up to 40 m the steel elements can be built in easily by cranes. The torsional restraint of the concrete slab by the steel boxes allows normal reinforced concrete slabs for bridge decks with a total width up to 17 m. Diaphragms are used only at the internal supports. At the abutments normally concrete end cross girders are used. This type of bridge structure is very economical and allows a very short construction time. A typical example for this type of bridge is the bridge “Schleusetal” shown in Figure 1.

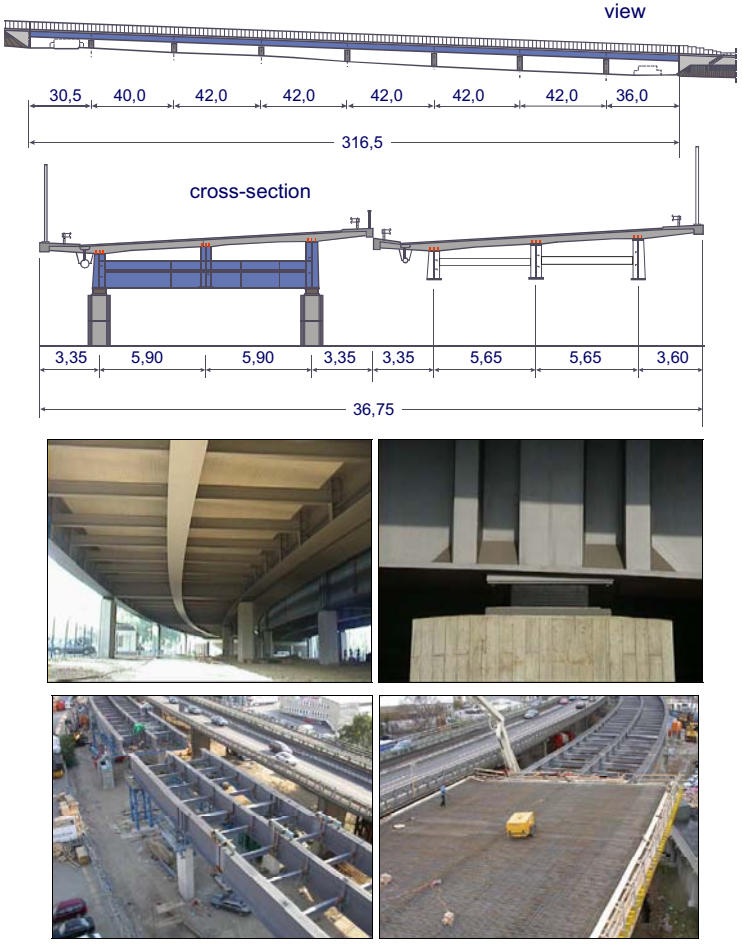


Fig. 2 - Freeway bridge “Langerfeld” in the course of the freeway A1

A typical example for a composite bridge with an open cross-section and multiple main girders is the bridge “Langerfeld” in the course of the freeway A1 (Fig. 2). This type of cross-section allows also concrete decks without prestressing by tendons. The freeway A1 currently has two traffic lanes in each direction which do not provide sufficient capacity. In order to ease the situation the freeway is widened to three lanes in each traffic direction by supplementing most of the old prestressed concrete bridges by modern composite bridges.

3 COMPOSITE BOX GIRDERS WITH WIDE CONCRETE DECKS

In the eastern part of Germany after the German reunification several new highways were built. Across the mountain range of the Thuringian Forrest - a typical holiday area - many aspects during the planning process regarding environmental requirements and especially aesthetics had to be considered. This is the reason why for these particular bridges composite box girders with wide concrete decks are used instead of traditional separate bridge decks and piers for each traffic direction. A typical cross-section is shown in Figure 3.

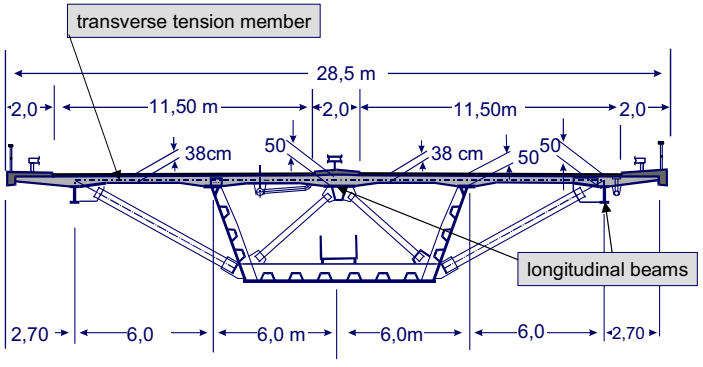


Fig. 3 - Typical cross-section of a box girder with wide concrete decks

The cross-section consists of the main steel box with a width between 9 and 12 m and an additional central and two external secondary longitudinal composite beams. The concrete deck has a total width between 28 and 30 m and is supported in transverse direction by the webs of the box girder and additional longitudinal beams. The cross-section is braced with transverse diaphragms with 5-6 m spacing, which are performed with inside and outside diagonals and with a transverse composite tension member integrated in the concrete slab. With this type of cross-section several superstructures were erected in the last 15 years in the course of construction of new freeways in the eastern part of Germany /3-5/. Figure 4 shows some typical examples. Composite bridges with wide cantilevering concrete decks are very economical solutions. The average weight of structural steel is in range between 220 to 260 kg/m^2 of the bridge deck. For the design of the concrete deck three main effects have to be considered:

- the deck is subjected to bending due to local traffic loads, with local bending moments acting mainly in transverse direction;
- the deck is acting in longitudinal direction as a compression or tension flange of the composite box girder and the additional longitudinal beams;
- the concrete deck is acting as a composite tension member in transverse direction as a part of the diaphragms.



Bridge Albrechtsgraben



Bridge Reichenbachtal /4/



Bridge Wilde Gera /3/



Bridge Oehde /5/

Fig. 4 - Typical examples for composite box girders with wide concrete decks

For the bridges shown in Figure 4 different solutions for the transverse composite tension members were used (see Figure 5). The solutions A and B have the advantage of simple and economical connections with the top flanges of the main box and the longitudinal secondary girders but the disadvantage of high stresses due to local wheel loads, especially with regard to the fatigue resistance. The solutions C and D avoid high stresses due to local wheel loads. Therefore quiet complicate connections are necessary caused by the eccentricity between the tension member and top flanges of the box girder.

As mentioned above, normally it is a general requirement in Germany to have separate bridges for each traffic direction in order to be able to divert the full traffic on the remaining bridge in case of major maintenance work on the other. The concrete deck is the most vulnerable part of a bridge. With regard to the expected intensive increase of road traffic and local wheel loads in future, the concrete deck must be considered as a wearing part in contrast to the steel structure with implication of different lifetimes of the concrete deck and the steel structure.

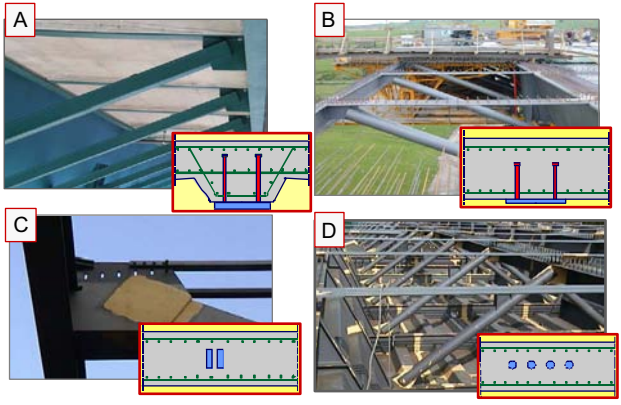


Fig. 5 - Different solutions for the detailing of the joints of transverse tension members

Therefore in design it was considered that parts of the concrete decks can be exchanged and the flow of traffic can be maintained in both directions just on one half of the bridge during a future replacement of the bridge deck. For this procedure the bridge deck will be partially cut out with high-pressure water method and will be replaced by a new bridge deck. During this procedure significant additional stresses result in the superstructure, which were taken into account in design and construction.

For the partial exchange of the bridge deck the methods shown in Fig. 6 can be used. The problem of the partial replacement of the concrete slab is caused by the unsymmetrical loading and the torsional and distorsional deformations. The method depends mainly on the span of the bridge. Method *A* is possible for bridges with small spans only. The bridge deck will be removed in one half of the total section over a total length of 12 to 15 m in longitudinal direction. Variation *B* in Fig. 6 shows the partial exchange of the concrete deck in two steps. During the first step the outer and afterwards the inner quarters will be removed and replaced. Another possibility to avoid an open cross section in the area of the exchange of the deck is to build temporary horizontal bracings (method *C*). In order to reduce the torsional and distorsional effects all methods can be combined with additional ballast. Figure 6 shows for the different methods the stresses in the concrete slab and in the steel section due to dead weight of the concrete slab related to the values of the cross-section with the closed box section. It can be seen that especially method *A* leads to a significant increase of the stresses.

For the casting of concrete movable formwork units are used (Fig. 8). The formwork inside the box and between the box and the external longitudinal beams consists of formwork tables supported by temporary brackets and is liftable by wedges. Two possible solutions for the formwork exist for the external cantilevering parts of the concrete deck. The formwork carriage runs on the top of the concrete slab and is supported by the webs of the box girder or the external longitudinal beams with particular elements which are left in the concrete slab (Fig. 7A). The suspension of

the formwork needs penetration through the concrete deck which makes it difficult to pour the concrete and in addition it is disadvantageous for the quality of the concrete surface. A better solution is shown in Figure 7 B where the formwork carriage is underneath the concrete deck.

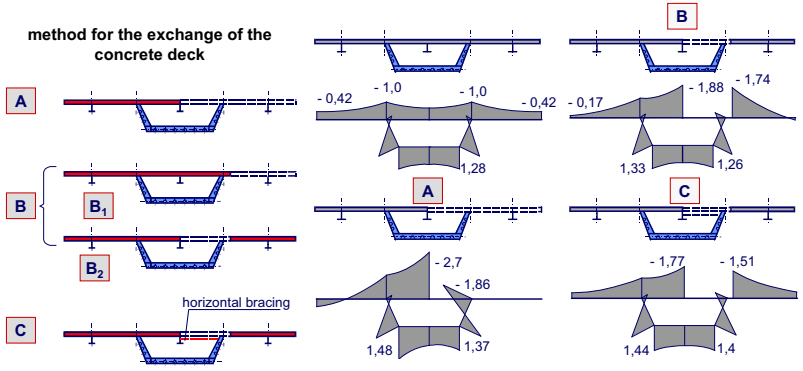


Fig. 6 - Different methods for the exchange of the concrete decks and distribution of normal forces in the concrete deck due to exchange of the concrete deck

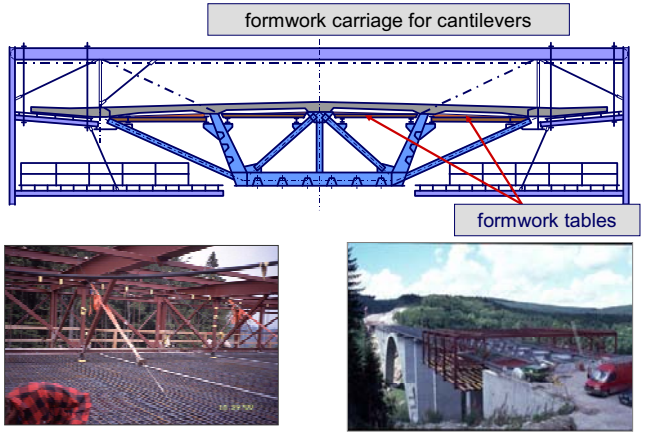
4 COMPOSITE BOW STRING ARCHES

Composite bowstring arches with concrete decks are an often used system for composite bridges where the construction depth is limited for example for bridges over canals and rivers. In the past either the concrete deck was separated from the main system or connected with the steel structure and additionally prestressed by tendons in the longitudinal direction. During the last years several bridges were erected, where the reinforced concrete deck is connected to the steel structure by horizontal bracings at the end of the bridge, and where the concrete deck acts as a tension member in the tie of the main system.

In the last years in the north of Germany several canals were widened in order to increase the capacity of the canals for container ships. Hundreds of new bridges were necessary and most of them were erected as composite bowstring arches. The bridge Ladbergen in the course of the freeway A1 and the other bridges shown in Figure 8 are only some typical examples for this type of bridge construction.

Where a reinforced concrete deck acts as a part of the tie, cracking of concrete and the effects of tension stiffening of concrete between cracks influence the distribution of internal forces significantly. The first design rules were developed for the design of the Bridge Dömitz. Meantime the German design codes and also Eurocode 4 Part 2 give simplified design rules for the design of the concrete tension member. For this type of bridge the crack width in the concrete deck is normally limited to 0.1 to 0.15 mm. Another important issue is the transfer of local vertical shear forces across cracks. The results of new research work were implemented in Eurocode 4-2 /1/.

A - Formwork carriage running on the top of the deck



B - Formwork underneath the concrete deck

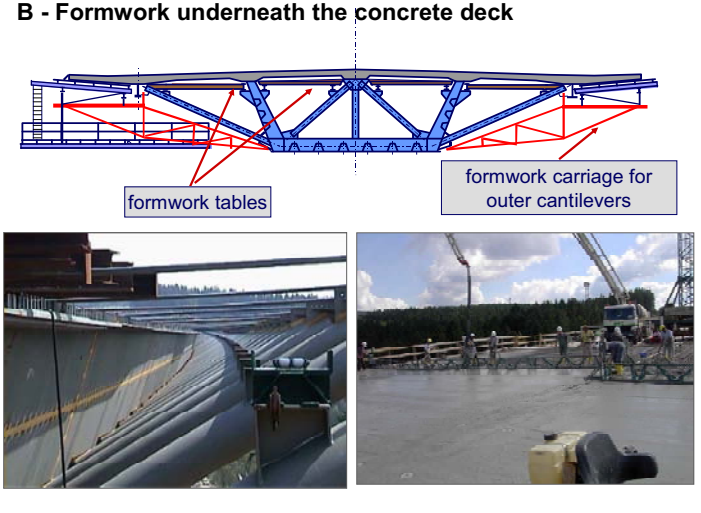
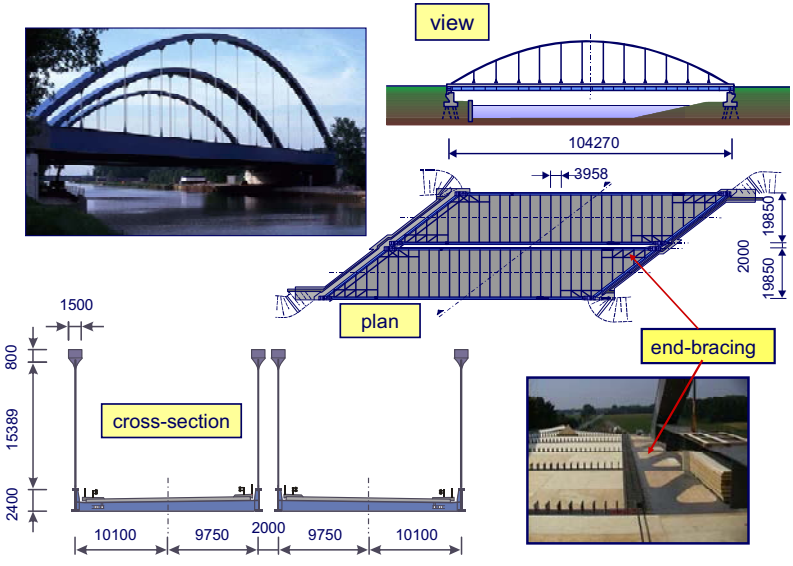


Fig. 7 – Different solutions for the formwork of box girders with wide flanges



Bridge Ladbergen in the course of the freeway A1



Bridge across the river Saale, Besedau /6/



Composite bow string Arch near Rheine

Fig. 8 – Examples for composite bow string arches

5 COMPOSITE TRUSSES FOR ROAD BRIDGES

The first composite trusses were built for the new German high speed railway lines several years ago. The most well-known example for this type of bridge is the railway bridge Nantenbach /7/. In the last years some new road bridges using steel trusses with hollow sections and cast iron nodes were erected. A typical example is shown in Figure 9 /8/. The cross-section with a triangular shape has a high torsional rigidity. Shear connection is provided by headed stud shear connectors and the concrete deck is prestressed by unbonded tendons in longitudinal direction.

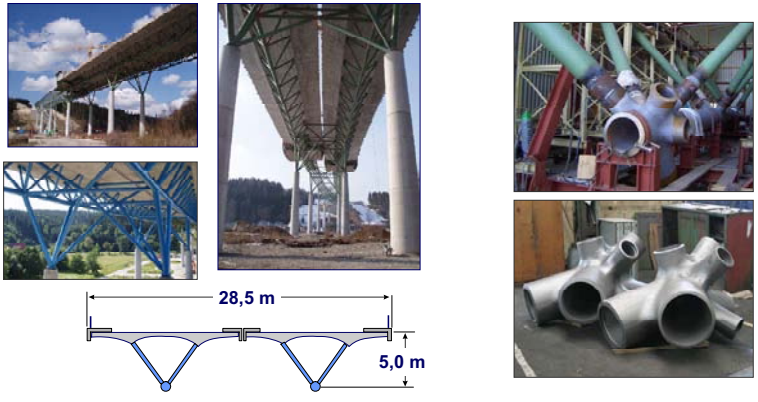


Fig. 9 - Bridge St. Kilian /8/

6 COMPOSITE BRIDGES FOR SMALL AND MEDIUM SPANS

About 75 % of all bridges in Germany have spans below 35 m and most of them are normal reinforced and prestressed concrete structures. In the last years there is a tendency to use composite bridges especially for overpass structures crossing over high-, free- and railways. In this special cases restrictions for the traffic have to be avoided as far as possible. This can be achieved by composite bridges, because with prefabricated or partially prefabricated composite members and simple erection methods extremely short construction times without any temporary supports or formwork are possible. Typical examples for this type of bridge construction are shown in Fig. 10. The main girders are welded or rolled steel cross-sections completely prefabricated in the shop. The normal reinforced concrete deck consists of partially prefabricated elements and additional insitu concrete. Only cross girders at supports are used and these girders are normal reinforced concrete members. This solution allows a simple erection without significant welding on side.



Fig. 10 - Typical bridges for small and medium spans with rolled and welded steel sections

In the German design specification and codes /2/ special rules for the cross girders and the minimum dimensions are given. At internal supports the width of the concrete girder should not be less than 60 cm in case of direct support of the main girders by bearings and not less than 80 cm for indirect support conditions. The detailing of the prefabricated concrete elements is shown in Fig. 12. The depth of the concrete above the prefabricated elements h_c should be not less than 20 cm within the traffic lanes. In other regions h_c should not be less than 15 cm. For the partially prefabricated concrete elements elastomeric support strips with a thickness of 2 cm and a width of 3 cm are used. The minimum value of pressing should be 3-5 mm and the maximum value should not exceed 10 mm (see Fig. 11).

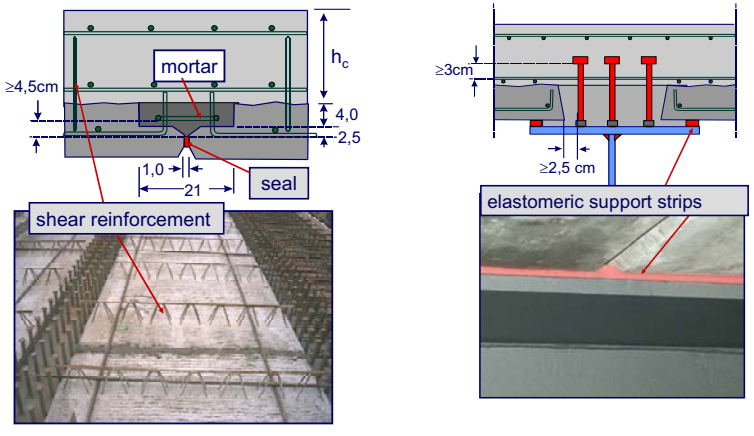


Fig.11 - Detailing of partially prefabricated concrete slabs

In order to reduce the erection time the so called VFT – girders were developed /9 - 11/. In this case a partially prefabricated composite member consisting of welded steel girders and a partially prefabricated concrete flange is produced in the shop and then transported to site (Figure 12). A new trend and further development of this type of bridge construction is the VFT-Filler Beam shown in Figure 13.

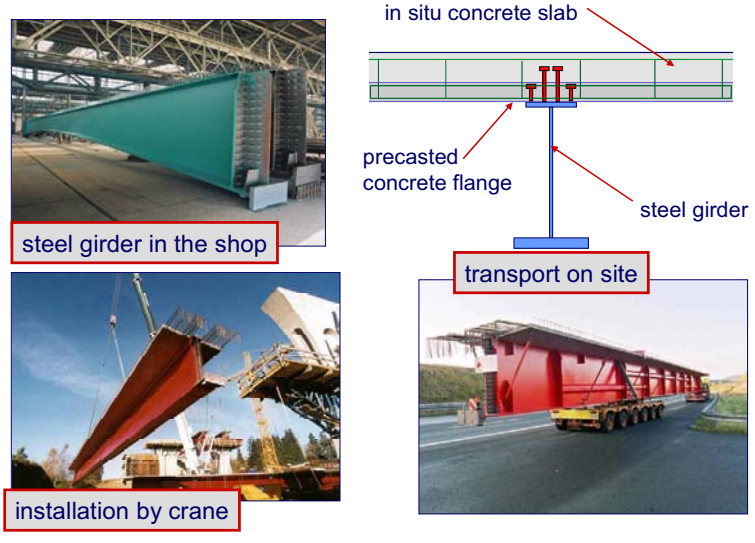


Figure 12 –Prefabricated composite girders VFT-Bridge

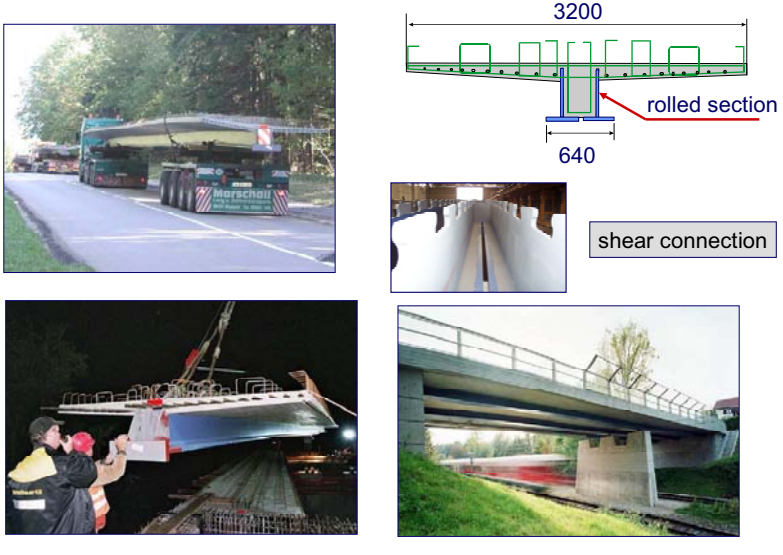


Fig. 13 - Prefabricated composite girders –VFT-Filler beam

7 CABLE-STAYED BRIDGES

At present two big cable stayed bridges are under construction in Germany. The first one is the Strelasund bridge in the north-east of Germany /12/. The second one is the new cable stayed bridge Wesel over the river Rhine in north-west of Germany (Fig. 14).

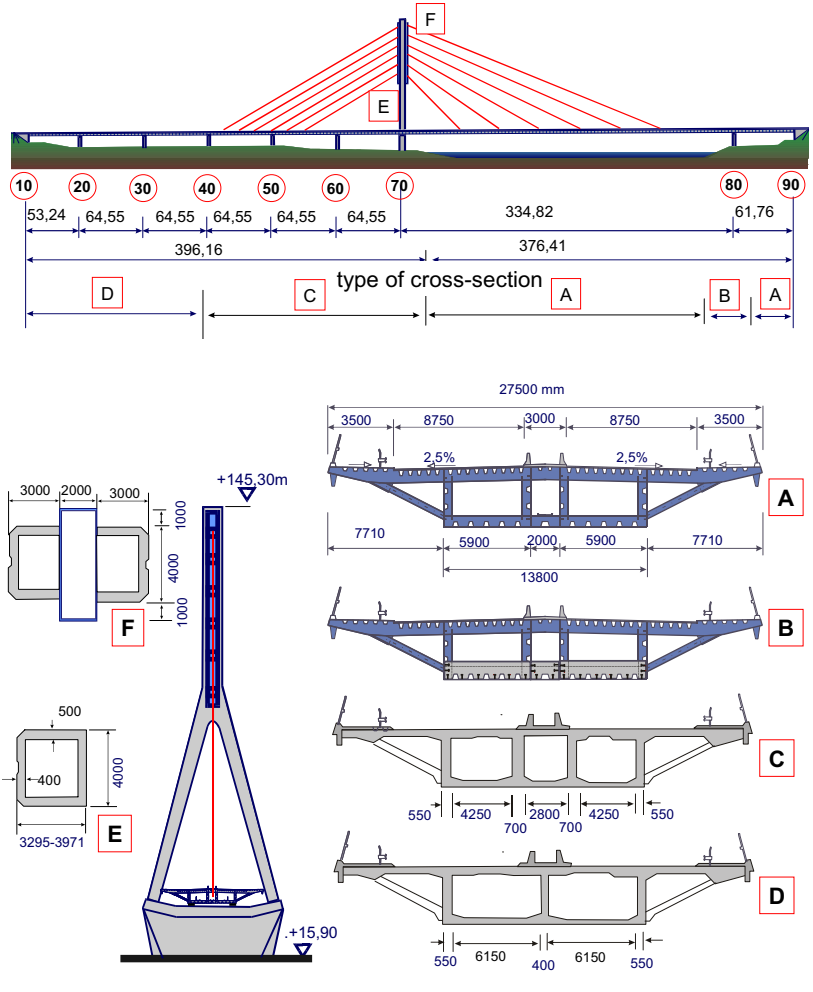


Fig. 14 - Cable-stayed bridge Wesel, view and cross-sections

For cable-stayed bridges normally hybrid structures are used in Germany. The pylon of the bridge Wesel is made of high strength concrete and has a concrete section in the bottom part of the two legs and a composite section at the top where the cables are anchored. The bridge deck has between the axes 10 and 40 a two cell and between the axes 40 to 90 a three cell boxed section. Between the axes 10 to 70 prestressed concrete with external tendons and in the main span over the river a steel-section with an orthotropic deck is used.

In the region of the axis 80 due to extreme high hogging bending moments a composite section with a composite bottom flange is used. The end cross-girder in axis 90 is a heavyly reinforced concrete member in order to prevent lifting up of the bearings. The depth of the cross-section is 3670 mm. The Strelasund Bridge and the Bridge Wesel are the first cable-stayed bridges in Germany with parallel strand cables instead of the traditionally used fully locked coil ropes. The tensile elements consist of galvanized, waxed and PE-coated strands /13/.

For the erection of the bridge Wesel it was the first time in Germany that the prestressed concrete bridge between the axes 10 and 70 was launched by using the first two units of the steel bridge as launching girders. Parallel to the launching of the concrete bridge the steel structure between the axes 80 and 90 was erected by cranes. The erection of the pylon was finished in March of 2008. The erection of the main span is going on as cantilever erection.



Fig. 15 - Bridge Wesel

8 REFERENCES

[1] EN 1994-2 Eurocode 4: Design of composite steel and concrete structures, Part 2: General rules and rules for bridges (2005)

[2] DIN Fachbericht 104 Verbundbrücken, 2003

[3] Denzer, G., Gräßlin, W., Hanswille, G., Schmidtmann, W.: Die Talbrücke über die Wilde Gera – Erfahrungen bei der Planung und Ausführung von Talbrücken mit einteiligen Verbundquerschnitten. Stahlbau 69 (2000), H.11, S. 842-850.

[4] Denzer, G., Schmackpfeffer, H.: Entwicklungen im Stahlverbundbrückenbau – Autobahnbrücken mit einteiligen Verbundquerschnitten. Stahlbau 74, H. 9, (2005),

[5] Marzahn, G., Hamme, M., Prehn, W., Swadlo, J.: Wupper River Valley Bridge: A State of the Art Composite Bridge, Structural Engineering International, Volume 17, No. 1, 2007

[6] Glitsch, W.: Bridge across the river Saale, Besedau, Germany, Structural Enginneering International, Volume 12, No. 4, 2002

[7] Haensel J.: Recent trends in composite bridge design and construction in Germany, Composite Construction in Steel and Concrete III, ASCE, 1997

[8] Denzer, G., Weyer, U., Diekmann, C.: Die Talbrücke St. Kilian-Entwurf und Ausführung, Stahlbau 75, H. 2 (2006)

[9] Schmitt, V., Frenzel, J., Schiefer, S., Seidl, G., Weber, J.: Innovation im Verbundbrückenbau, Talbrücke Oberhartsmansreuth, Stahlbau 69, 2000

[10] Seidl, G., Braun, A., Weizenegger, M.: Rahmentragwerke im Brückenbau, Beton- und Stahlbetonbau 03/2006

[11] Schmitt, V., Seidl, G., Hever, M., Zapfe, C.: Verbundbrücke Pöcking – Innovative VFT-Träger mit Betondübeln, Stahlbau 73, H.06 (2004)

[12] Kleinhans, K., Saul, R.: The second Strelasund Crossing – a modern cable-stayed bridge in close vicinity to the cultural heritage of Stralsund, Germany, Structural Engineering International, Volume 17, No.1, 2007

[13] Gläser, Ch., Scheibe, M., Zilch, K.: Die zweite Strelasundquerung - Erste deutsche Anwendung von Parallellitzenseilen, Bauingenieur, 4-2007

Where structural steel and concrete meet

Prof. J.W.B. Stark
Delft University of Technology / Stark Partners
Delft, The Netherlands
janstark@planet.nl

ABSTRACT

Traditionally "steel structures" and "concrete structures" formed more or less two different worlds in structural engineering. Fortunately this situation is changing rapidly. It is now recognised that each of the two materials have advantages and disadvantages and that often an optimal solution is found by combining both materials. This may be a combination of steel and concrete in an element as is the case in "Composite steel-concrete construction" or the combined use of concrete elements and steel elements in "Mixed construction". For the design of composite steel-concrete elements specific design standards have been developed. However for “Mixed construction” a combined use of steel design standards and concrete design standards is necessary. It is important that the design rules for the two materials are consistent, especially for those components connecting both materials. However, in the past the design standards and recommendations for concrete and steel have been developed separately. So evidently, at this moment there are considerable differences in design assumptions and treatment of various aspects. In the paper design methods for connections between structural steel and concrete will be discussed. The methods will be illustrated for column bases, being the most frequently used type of connection between steel and concrete, though the information can also be used for related types of connections.

INTRODUCTION

In the past, for the design of a building the choice was normally between a concrete structure and a steel structure. Looking at recent practice there is an evident tendency that designers also consider the combined use of concrete and steel in the form of composite or mixed structures as a serious alternative. Use of **composite elements** in the form of composite beams, composite columns and composite slabs is already common practice in many countries. Applications are supported by accepted Standards or Recommendations as for example the European Standard: EN 1994 - Eurocode 4. However, this supporting material is not available for **mixed constructions** where (reinforced or prestressed) concrete elements and structural steel elements are used in combination. The elements itself are covered by the respective design standards for concrete and steel. But in many cases the joints where the elements meet form a black spot as far as Design Standards and information is concerned. So the designer has to develop design models based on a creative interpretation of methods and rules in use for concrete and steel. It is of course a complication when these design methods for the different materials are not consistent. In the past, the Design Standards and Recommendations for concrete and steel have been developed separately. So evidently at this moment there are still considerable differences in design assumptions and treatment of various aspects. Some examples of these differences will be illustrated in this paper.

TYPOLOGY

Many different details exist depending on the type of members to be connected, the actions to be transferred and the performance requirements. An exhaustive treatment of all possible details is not possible in the context of this paper. Just to give an idea two categories are discussed.

Column bases

This is one of the most commonly used details. The steel column is connected to a base plate, which is attached to the concrete foundation by some form of so-called "holding down" assembly. A typical detail is shown in Figure 1. The system of column, base plate and holding down assembly is known as a column base. The holding down assembly comprises two, but more commonly four (or more) holding down bolts (anchors). These may be cast-in-place, or post-installed to the completed foundation. Cast-in-place bolts sometimes have some form of tubular or conical sleeve, so that the top of the bolts are free to move laterally, to allow the base plate to be accurately located.



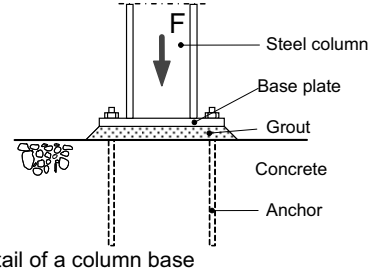


Fig. 1 - Typical detail of a column base

Base plates for cast-in assemblies are usually provided with oversized holes and thick washer plates to permit translation of the column base. Anchor plates or similar embedded arrangements can be attached to the embedded end of the anchor assembly to resist pull-out. Post-installed anchors may be used, being positioned accurately in the hardened concrete. Post-installed assemblies include, for instance, torque-controlled expansion anchors, under-cut anchors and bonded anchors.

Connections of steel beams to concrete walls or columns

A stiff concrete core often provides the stability of a multi-storey steel frame. The steel beams of the floors are connected to the wall of the concrete core (see Figure 2a). To provide sufficient fire resistance sometimes (prefabricated) concrete columns are used instead of steel columns with fire protection. In Figure 2b a connection is shown as used in a refurbishment project where new steel floor beams are connected to existing concrete columns by means of an extended end plate connection.

A great number of different forms of connection details are possible for these types of connection.

a  b 

Fig. 2 - Connection composite beam-concrete core (a); steel beam-concrete column (b)

A treatment of all possible details is not possible in the context of this paper. Therefore the treatment is restricted to column bases. This is one of the most commonly used types of connection. Another reason to focus on column bases is that this type of connection is explicitly covered by the recently completed Eurocodes.

STANDARDS AND RECOMMENDATIONS

As the author is most familiar with the situation in Europe, the treatment in this paper will focus on the design methods as covered by European standards and in particular by the Eurocodes.
The column base connection is a typical detail where steel and concrete meet. But in addition to steel and concrete there is in effect a third element and that is the connecting element in the form of anchors or fasteners. Each of these three composing elements is covered by Eurocodes. But unfortunately the development of these Eurocodes was not fully coordinated so that inconsistencies still exist in the various design approaches as will be illustrated in this paper. The situation is as follows:

Steel

In EN1993-Eurocode 3 all the design rules for joints have been collected in a separate part of Eurocode 3: EN1993-1-8 [3]. In this part the design of column bases is not treated separately but is integrated in the so-called “component-approach”. The advantage is that the rules are fully consistent with the design approach for steel-steel connections. However, this way of presentation makes the rules not easy accessible for users. The rules are based on the results of a project carried out within the framework of the European Project COST C1 (Semi-rigid behavior of civil engineering structural connections) and the Technical Committee 10 of ECCS (European convention for constructional steelwork). For background information refer to a recent special issue of Heron [13].

Concrete

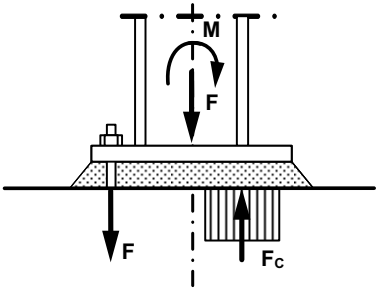
For concrete aspects reference is made to EN1992-1-1 [3] but this code does not give specific rules in all cases as will be demonstrated later. Furthermore the rules are only applicable if the anchorage has sufficient deformation capacity. This is often not the case for short anchors.

Anchors

Recently CEN issued a series of drafts for an addition to EN1992-Eurocode 2 covering design rules for connections with short anchors [5] – [9]. The content is based on an existing CEB-Design Guide [10] and EOTA (European Organisation for Technical Approvals) Guideline [11].

COMPARISON OF DESIGN APPROACHES

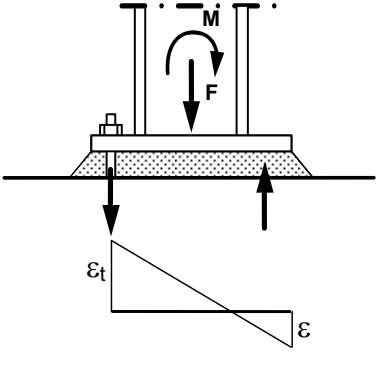
The design approaches in Eurocode 3 ("steel world") and CEB-Guide/Eurocode2-PT4 ("fastener world") are essentially different. This is illustrated in Figure 3 where the load distribution is shown for a column base subjected to compression and bending.



EN1994-1-8: Eurocode 3

Ultimate limit state
- Plastic design
- Only equilibrium conditions
- Component method
- Base plate assumed to be flexible
- Compression concentrated under footprint

Serviceability limit state
- Rules for stiffness
- Classification for stiffness



CEB / EN1992-4

Ultimate limit state
- Elastic design
- Compatibility conditions
- Consideration of complete connection
- Base plate assumed to be rigid
- Linear distribution of strains (forces?)

Serviceability limit state
- Not covered

Fig. 3 – Design approaches "steel world" versus "fastener world"

The following comments apply for the "CEB" method:
- The stiffness of the base plate required for the assumption of a rigid plate is expressed in a maximum stress criterion and not a deformation criterion. Tests and inspection of demolished structures has shown that the compression always concentrates under stiff parts of the column section (flanges and web).

– In case of a fully rigid end plate the distribution of the displacements will be linear. But this does not imply that also the strain distribution is linear. Strain = displacement/length , and the length of concrete in compression and anchor in tension is not the same.
– The calculation is more complicated than for the “Eurocode 3” method.
– Unnecessary thick base plates or even stiffeners are required.
– Serviceability limit state is not covered.

COMPONENT METHOD

The component method consists of the following issues: identification, characterization, assembly, classification and modeling. The identification is the process of decomposing a joint in different components. Figure 4 shows the components of a column base. In the characterization of each component, the relevant mechanical properties are determined: the resistance, the stiffness and the deformation capacity. In the assembly, the mechanical properties of the components are combined in order to determine the resistance, the stiffness and the rotational capacity of the joint. The joints may be classified in terms of the resistance, the deformation capacity or the stiffness. The purpose of the classification is simplification of the joint behavior for the frame analysis, for instance by classifying for stiffness as rigid. Modeling is required to determine how the (non-linear) mechanical properties of the joint are taken into account in the frame analysis.

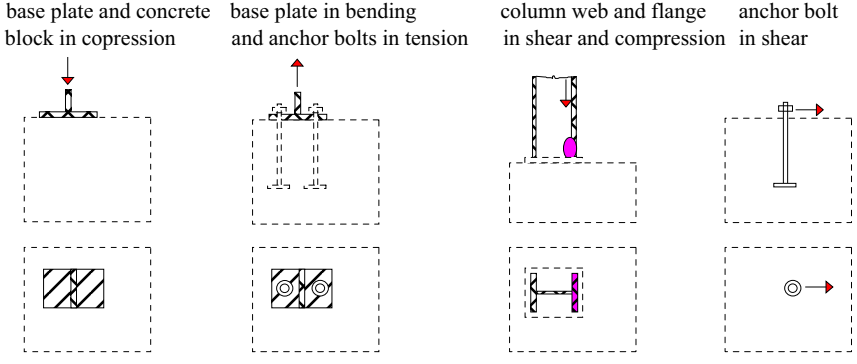


Fig. 4 – The major components of a column base

BASE PLATE AND CONCRETE BLOCK IN COMPRESSION

The resistance is determined by an equivalent rigid plate concept. In Figure 5 is shown how an equivalent rigid plate is defined to replace a flexible plate in case the base plate connection is loaded by axial force only. This rigid plate follows the footprint of the column.

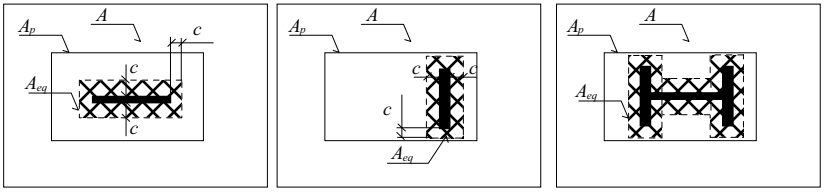


Fig. 5 - Flexible base plate modeled as a rigid plate of equivalent area.

The resistance is now determined by two parameters: the bearing strength of the concrete and the dimensions of the equivalent rigid plate.

Dimensions of the equivalent rigid plate

The flexible base plate, with area A_p, is replaced by an equivalent rigid plate with area A_{eq}, see Figure 5. This rigid plate area A_{eq} is composed of one T-stub under the column web and two T-stubs under the column flanges.

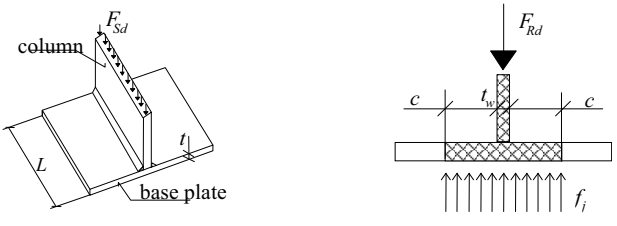


Fig. 6 - T stub in compression

The additional bearing width c of the T-stub, see Figure 6, is determined on the basis of the following assumptions:

– No plastic deformations occur in the flange of the T-stub, so that the flange remains relatively flat. Therefore, the resistance per unit length of the T-stub flange is taken as the elastic resistance.

$$M_{bp} = t^2 f_y / 6 \quad (1)$$

– It is assumed that the T-stub is loaded by a uniform stress distribution. The bending moment per unit length on the base plate acting as a cantilever of span c is:

$$M_{bp} = f_{jd}\, c^2 / 2 \quad (2)$$

The equivalent width c can be resolved by combining equations (1) and (2):

$$c = t \left[f_y / (3 f_{jd}) \right]^{0,5} \quad (3)$$

Bearing strength of the concrete

The bearing strength of the concrete under the plate is dependent on the size of the concrete block. EN1992-1-8 refers to EN1992-1-1;6.7 “Partially loaded concrete” as follows:

The design bearing strength of the joint f_{jd} should be determined from:

$$f_{jd} = \beta_j F_{Rdu} / (b_{eff} l_{eff}) \quad (4)$$

where:

β_j is the foundation joint material coefficient, based on observations that the grout layer in practice often shows imperfections and/or air bubbles. The value in EN1993-1-8 is 2/3 provided that the characteristic strength of the grout is not less than 0,2 times the characteristic strength of the concrete foundation and the thickness of the grout is not greater than 0,2 times the smallest width of the steel base plate. In cases where the thickness of the grout is more than 50 mm, the characteristic strength of the grout should be at least the same as that of the concrete foundation.

F_{Rdu} is the concentrated design resistance force given in EN 1992, where A_{c0} is to be taken as ($b_{eff}l_{eff}$) (see Figure 7).

$$F_{Rdu} = A_{c0} f_{cd} (A_{c1}/ A_{c0})^{0,5} \leq 3{,}0\, f_{cd} A_{c0} \quad (5)$$

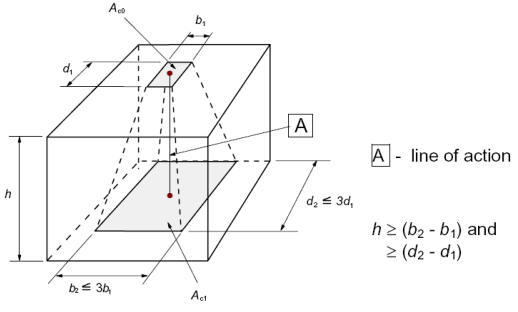


Fig. 7 – Design distribution for partially loaded areas

Open questions

- The limit for the characteristic strength of the grout given in EN1993-1-8 is very low. The value is based on tests. Question is whether these tests cover the most unfavourable cases. For example high compression stresses at edges of short base plates.
- The high local stresses in the concrete foundation will cause splitting stresses transverse to the direction of loading. Rules for the verification for splitting failure and requirements for transverse reinforcement are missing.
- The influence of packing or washers under the plate used for erection are not covered. These elements are normally kept in place after erection and will influence the stress distribution. Washers may cause compression in the anchors.

BASE PLATE IN BENDING AND ANCHOR BOLTS IN TENSION

If the column base is subjected to an axial force plus a relatively large bending moment one side will be in compression and the other side in bending (see Figure 8). The behaviour of the tension side is determined by two components:

– Base plate in bending (EN1993-1-8;table 6.1 – component 5)
– Anchor bolt in tension (EN1993-1-8;table 6.1 – component 16)

Base plate in bending

In Figure 8 is illustrated that the configuration of the tension side of a base plate is similar to the tension region of an end-plated beam-to column connection. In EN1993-1-8 both are treated as an equivalent T-stub flange. However because of the larger elongation of cast in place anchor rods compared to bolts in beam to column connections it is stated that prying forces should not be taken in consideration. This is a conservative assumption for the verification of the base plate but may lead to an unsafe estimation of the load on the anchors.

Anchor bolts in tension

The traditional way of anchoring is with cast in place long anchors. They are provided with a hook, a washer plate or some other load distributing member as for example a grillage beam. Although not explicitely stated the rules in EN1993-1-8 are derived for this type of anchorage.
The design resistance of the anchor bolts is the smaller of:

– The design tension resistance of the anchor bolt, reference is made to the rules for bolts.
– The design bond resistance of the concrete on the anchor bolt according to EN 1992-1-1.

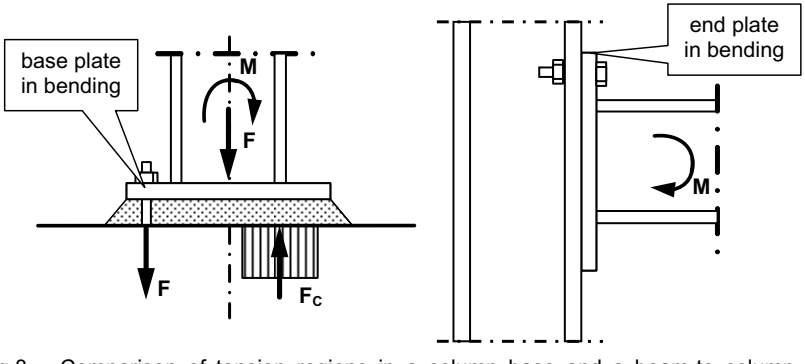


Fig.8 – Comparison of tension regions in a column base and a beam-to column connection

The use of hooked anchors is restricted to material with yield strength ≤ 300 N/mm^2. When the anchor bolts are provided with a washer plate or other load distributing member, no account should be taken of the contribution of bond.

As an alternative to the cast in place long anchors according to the "*reinforced concrete technique"* also post installed short anchors according to the "fastener technique" are used. These anchors show other governing failure modes as illustrated in Figure 9.

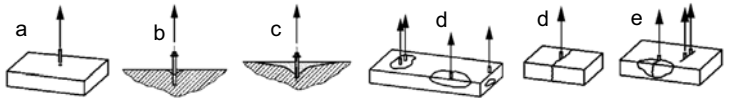


Fig. 9 – Possible failure modes of short anchors

Key to figure 9:

a. Steel failure
b. Pull-out failure
c. Concrete cone failure
d. Splitting failure
e. Concrete blow out failure

Rules for the design resistance based on the CEB-Design Guide [10] are given in prCEN/TS1992-4 [5]-[9]. In this document also rules are given for the load distribution and the design of the base plate, which are not consistent with EN1993-1-8 (see Figure 3).

Open questions

– Is it necessary to consider prying forces for the design of the anchors?
– Is it possible to extend the application of hooked anchors for yield strength > 300 N/mm^2?
– Threaded rods are often used as anchor. The bond strength of these anchors is not covered.
– EN1992-1-1 does not give explicit rules for the resistance of load distributing devices as washer plates.
– More specific rules are needed for the required reinforcement to avoid splitting and blow out if long anchors are placed near edges of the concrete foundation.
– Harmonisation of the rules in EN1993-1-8 and EN1992-4 is required.

SHEAR RESISTANCE

According the CEB Design Guide for base plates with a grout layer thicker than 3 mm plastic design is not allowed, friction forces underneath the base plate should be neglected and the shear capacity has to be calculated for the mechanism "*shear load with lever arm*". For column bases usually a grout layer with a thickness greater than 3 mm is used. Though it is realised that there may be uncertainties about the strength and quality of the grout layer, the CEB method will be very conservative in many practical cases. This was confirmed by COST/WG2 [13] that compared design values with test results for column bases loaded in shear and with a varying thickness of the grout layer. In particular in case of low strength bolts and a thick grout layer (60 mm) the experimentally obtained maximum shear load was many times (between 10 and 25 !!) greater than the calculated characteristic shear strength of the connection.

According EN1993-1-8;6.2.8.1 one of the following methods may be used to resist shear force:

– *Friction*

The design friction resistance $F_{f,Rd}$ is to be derived as follows:

$$F_{f,Rd} = C_{f,d}\, N_{c,Ed} \quad (6)$$

where:

$C_{f,d}$ is the coefficient of friction. The following values may be used:

– for sand-cement mortar $C_{f,d} = 0{,}20$
– for other types of grout the coefficient of friction $C_{f,d}$ should be determined by testing

$N_{c,Ed}$ is the design value of the normal compressive force in the column.

– *Shear resistance of the anchor bolts*

The design shear resistance of an anchor bolt $F_{vb,Rd}$ is the smaller of $F_{1,vb,Rd}$ and $F_{2,vb,Rd}$ where:

$F_{1,vb,Rd}$ is the bearing resistance of the anchor bolt calculated as for a normal bolt

$$F_{2,vb,Rd} = \alpha_b\, f_{ub} A_s / \gamma_{Mb} \quad (7)$$

where:

$\alpha_b = 0{,}44 - 0{,}0003\, f_{yb}$

f_{yb} is the yield strength of the anchor bolt, where $235\ \text{N/mm}^2 \le f_{yb} \le 640\ \text{N/mm}^2$

– *Shear resistance of special elements such as block or bar shear connectors*

For the design bearing resistance of a block or bar shear connector EN1993-1-8 refers to EN 1992. But this is not explicitly covered in that document.

– *Shear resistance of the surrounding part of the foundation*



The design method in EN1993-1-8 is based on the results of a research project, carried out at TU-Delft [12].

Due to the horizontal displacement, not only shear and bending in the bolts will occur, but also the tensile force in the bolts will be increased due to second order effects. The horizontal component of the increasing tensile force gives an extra contribution to the shear resistance. The increasing vertical component gives an extra contribution to the transfer of load by friction.

Fig. 10 - Test specimen loaded by shear force and tensile force (Stevin, 1989).

Open questions

– In EN1993-1-8 is given that the design shear resistance may be based on the summation:

$$F_{v,Rd} = F_{f,Rd} + n\, F_{vb,Rd} \quad (8)$$

However summation seems to be in contradiction with 6.2.2(5) and 6.2.8.1(5)

– The shear resistance by friction is based on the normal compressive force in the column $N_{c,Ed}$ (see formula 6) . However it is expected that the normal force caused by bending will also contribute to the friction resistance.

– The rules in EN1993-1-8 are based on tests on column bases with cast-in-place long anchors. The applicability to short anchors should be investigated.
– The implications of use of oversized or slotted holes should be defined.
– More specific rules are needed for the required reinforcement in case of anchors placed near edges of the concrete foundation.

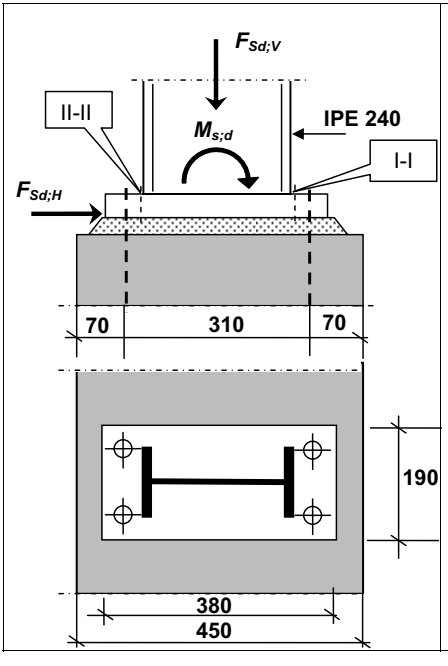
STIFFNESS OF COLUMN BASES

Fitting within the design concept of EN1993-1-8 also design rules are provided to determine the rotational stiffness of column bases. This is covered in EN1993-1-8;6.3.4 and the stiffness coefficients are included in table 6.11. The restricted space in this paper does not allow discussing this in detail.
In EN1993;5.2.2.5(2) also the classification boundary for rigid column bases is given.

REFERENCES

1. Stark, J., Hordijk, D., Where structural steel and concrete meet, Proc. Int. Symp. Connections between Steel and Concrete, Stuttgart, 2001, Rilem Pro21
2. Stark, J., Design of connections between steel and concrete to Eurocodes, Proc. Int. Symp. Connections between Steel and Concrete, Stuttgart, 2007, Rilem Pro21
3. EN 1993-1-8:2002, Eurocode 3 : Design of steel structures; Part 1.8: Design of joints.
4. EN 1992-1-1, Eurocode 2 : Design of concrete structures - Part 1-1: General rules and rules for buildings.
5. prCEN/TS 1992-4-1:XXX, Design of Fastenings for Use in Concrete - Final Draft - Part 1: General. CEN/TC 250/SC 2 N 677, 2008 (*Document for formal vote*).
6. prCEN/TS 1992-4-2:XXX, Design of Fastenings for Use in Concrete - Final Draft - Part 2: Headed Fasteners. CEN/TC 250/SC 2 N 678, 2008 (*Document for formal vote*).
7. prCEN/TS 1992-4-3:XXX, Design of Fastenings for Use in Concrete - Final Draft - Part 3: Anchor channels. CEN/TC 250/SC 2 N 679, 2008 (*Document for formal vote*).
8. prCEN/TS 1992-4-4:XXX, Design of Fastenings for Use in Concrete - Final Draft - Part 4: Post-installed fasteners - mechanical systems. CEN/TC 250/SC 2 N 680, 2008 (*Document for formal vote*).
9. prCEN/TS 1992-4-5:XXX, Design of Fastenings for Use in Concrete - Final Draft - Part 5: Post-installed fasteners – chemical systems. CEN/TC 250/SC 2 N 680, 2008 (*Document for formal vote*).
10. Comité Euro-International du Béton: Design of fastenings in concrete. Design Guide. Parts 1 to 3. Thomas Telford, CEB-Bulletin 233, januari 1997.
11. European Organisation for Technical Approvals: Guideline for European Technical Approval of Metal Anchors for Use in Concrete. Part 1: Anchors in general; Part 2: Torque-controlled Expansion anchors; Part 3: Undercut anchors, Issue-1997. (Part 5: Bonded Anchors,Issue-March2002).
12. Bouwman, L.P., Gresnigt A.M., Romeijn, Research into the connection of steel base plates to concrete foundations (*in Dutch*), Stevin Laboratory report 25.6.89.05/c6, Delft.
13. Heron, Special issue: “Steel column bases”, Volume 53 (2008), issue 1/2, Delft.

WORKED EXAMPLE FOR COLUMN BASE IN COMPRESSION, BENDING AND SHEAR



Column section IPE 240

Steelgrade, base plate S235

Baseplate: b_p = 190 mm
h_p = 380 mm
t_p = 35 mm

Concrete grade C20/25

Concrete foundation
B = 450 mm
H = 800 mm

Anchors M24; 8.8
rolled thread
Spacing anchors: h_a = 410 mm
b_a = 120 mm
Edge distance: e = 35 mm

Loads:
$F_{Sd;V}$ = 85,5 kN
$F_{Sd;H}$ = 37,5 kN
$M_{S;d}$ = 75 kNm

Detail calculation	**Clause**
Distribution of internal forces $z.F_{T,l,E} + ½ (h_a - t_f).N_{Ed} - M_{Ed} = 0$ $270.F_{T,l,E} + ½ (240 - 9{,}8).\ 85{,}5.10^3 - 75.\ 10^6 = 0$ $F_{T,l,E}$ = 241,3 kN $F_{C,r,E} = F_{T,l,E} + N_{Ed}$ = 241,3 + 85,5 = 326,8 kN	EN1993-1-8 6.2.8.1 Fig. 6.18d
Design bearing strength C20/25 $\rightarrow f_{cd} = \alpha_{cc} f_{ck}/\gamma_C$ = 1,0. 20/1,5 = 13,33 N/mm^2 $F_{Rdu} = A_{c0}.f_{cd}.\sqrt{(A_{c1}/A_{c0})} \leq 3{,}0.f_{cd}\ A_{c0}$ Assume c = 70 mm $b_1 = b_{eff} = t_f + 2c$=9,8 + 2.70= 149,8 ; $d_1 = b_p$ = 190 b_2 = 149,8 + 2.35 = 219,8 ; d_2 = 3.190 = 570 A_{c0} = 149,8.190 = 28462 ; A_{c1} = 219,8.570 = 125286 $\sqrt{(A_{c1}/A_{c0})} = \sqrt{(125286/28462)} = 2{,}10$ F_{Rdu} = 28462. 13,33. 2,10 .10^{-3} = 797 kN (6.6): $f_{jd} = \beta_j F_{Rdu} / A_{c0}$ = (2/3)(797000/28462) f_{jd} = 18,7 N/mm^2	EN1992-1-1 3.1.6 EN1992-1-1 6.7 (Fig. 6.29) EN1993-1-8 6.2.5

Detail calculation – Cont.	**Clause**
Additional bearing width	
(6.5): $c = t\,[f_y / (3\,f_{jd}\,\gamma_{M0})]^{0,5}$ c = 35 [235 / (3 18,7.1,0)]^{0,5} = 71,6 mm > 70 (Short projection)	EN1993-1-8 6.2.5
Design compression resistance of T-stub (6.4): $F_{C,Rd} = f_{jd}\,b_{eff}\,l_{eff}$ b_{eff} = 70 + 9,8 + 71,6 = 151,4; l_{eff} = b_p = 190 $F_{C,pl,Rd}$ = 18,7. 151,4. 190 = 538 kN > $F_{C,r,E}$ = 326,8 kN	EN1993-1-8 6.2.6.9 Fig.6.4a
Verification plate cross-section II-II (1) Reference to 6.2.6.5 (2) Prying force to be neglected. Table 6.2: $F_{T,l,Rd} = M_{pl,i,Rd} / m$ (half T-stub) $M_{pl,i,Rd}$ = 0,25 $l_{eff}\,t^2\,f_y\,/\gamma_{M0}$ = 0,25.190. 35^2. 235 / 1,0 $M_{pl,i,Rd}$ = 13,674. 10^6 m = ($h_a - h$)/2 = (310 – 240)/2 = 35 mm $F_{T,l,Rd}$ = 13,674.10^6. 10^{-3} / 35 = 390 kN > $F_{T,l,E}$ = 241,3 kN *Note: shear stresses in base plate neglected in this example*	EN1993-1-8 6.2.6.11 6.2.6.5 6.2.4
Anchors $F_{T,l,E}$ = 241,3 kN → per anchor $F_{t;E}$ = 241,3/2 = 120,7 kN Table 3.4: $F_{t,Rd} = k_2\,f_{ub}\,A_s\,/\gamma_{M2}$ $F_{t,Rd}$ = 0,9. 800. 353. 10^{-3} /1,25 $F_{t,Rd}$ = 203,4 kN > $F_{t;E}$ = 120,7 kN 6.2.6.12(5): Use of hook not permitted for grade 8.8 Use washer plate, see fig. 6.14b 6.2.6.12(6): When washer plates are used no account may be taken of the contribution of bond.	EN1993-1-8 6.2.6.12 3.6
Shear Frictional design resistance: (6.1): Design friction resistance $F_{f,Rd} = C_{f,d}\,N_{c,Ed}$ Fors and-cement mortar : $C_{f,d}$ = 0,20 $F_{f,Rd}$ = 0,20 . 326,8 = 65 kN > $F_{Sd;H}$ = 37,5 kN Design shear resistance of the anchor bolts: By the 2 anchors in compression region: $F_{vb,Rd} = \alpha_b\,f_{ub}\,A_s\,/\gamma_{Mb}$ α_b = 0,44 – 0,0003 f_{yb} = 0,44 – 0,0003. 640 = 0,248 γ_{Mb} is not referred. Assume $\gamma_{Mb} = \gamma_{M2}$ = 1,25 $F_{vb,Rd}$ = 0,248 .800. 353. 10^{-3} /1,25 = 70 kN 2 anchors: $F_{v,Rd}$ = 140 kN > $F_{Sd;H}$ = 37,5 kN Both resistances by friction and shear resistance of anchors are separately sufficient. Summation allowed by 6.2.2(8) form (6.3) is not required.	EN1993-1-8 6.2.2

Harmonization of Design Rules in Europe

Dipl.-Ing. Fernando González
Technische Universität Darmstadt,
Department of Civil Engineering and Geodesy
Darmstadt, Germany
gonzalez@stahlbau.tu-darmstadt.de

Prof. Dr.-Ing. Jörg Lange
Technische Universität Darmstadt,
Department of Civil Engineering and Geodesy
Darmstadt, Germany
lange@stahlbau.tu-darmstadt.de

ABSTRACT

In the last decades the Eurocodes have been developed in order to harmonize the technical rules for the structural design in Europe. Since the beginning in 1975 the aim was the elimination of technical obstacles in trades throughout Europe. Today most of the Eurocodes are published. The ECs are no rigid technical rules; they keep room for national differences. The National Annex which is valid in conjunction with the relevant Eurocode contains information on those parameters which are left open for national choice. Due to the fact that the Eurocodes are still not mandatory in Europe and not even used by some of the European Countries, it is necessary to make the engineers sensitive to the Eurocodes and to train the use.

The European Union launched in 1995 the Leonardo Da Vinci Programme with the objective of improving the provision of vocational education and training across Europe. The paper will describe the current Leonardo Project named “Eur-Ing” and show some results.

INTRODUCTION

The Eurocodes 1, 3 and 4 [1] [2] [3] will soon become mandatory in Europe. The creation of the National Annexes (NA) which are valid in conjunction with the EC is partly finalized. The Annexes include factors which have been left open in the EC for national choice. This information together with the relevant Eurocode is used as the national standard. It has to be noted that structural design will not be standardized. The design depends also on the national practice and tradition including specific national features, legislations etc. Local engineers normally are aware of the national practice and know how to merge it into the design. Problems arise when engineers are required to produce designs in other European countries, either for their own national company or as individuals working in the free market. Designers in this position will have to familiarize themselves quickly with the country-specific national annexes and the national practice. The knowledge of the national practice is very important and the influence on the design can be huge. In the UK for example a multi-storey framed building would generally be designed as pin-jointed with a composite floor. In Greece by contrast the frame is designed using rigid connections. The difference can be explained by the seismic activity in this region. This information is fundamental for the development of a design. Further examples

concerning the importance of the national practice are described in the following chapters. The vision of real mobility across Europe which is inspired by the Eurocode can only be realized, giving engineers the required information about the design processes in the county they are working in. Due to this the material developed in this project will be simultaneously helpful for designers who are learning how to design according to the Eurocodes in their own country and if necessary in other European countries.

THE "Eur-Ing" PROJECT

The "Eur-Ing" project is a 2 year pilot project part-funded by the European Commission under the second phase of the Leonardo da Vinci program. The project started in October 2006 and runs untill October 2008. Its full title is "Development of ICT (Information and Communications Technology) supported, flexible training to enable designers to apply Eurocodes in accordance with the national regulations of different member states". The aim of "Eur-Ing" is therefore to enable designers from any European country to produce easily a steel building design in their own and in other European countries. In order to achieve this aim a real steel-framed multi-storey building was redesigned by each country involved (see Table 2) using the Eurocode in conjunction with the corresponding national annex. Each partner prepared in addition a technical description of the building to give a more precise view on the static system and on the chosen design approach. A further document named "national context" has been prepared showing e.g. national differences in legislation, practice etc. Most of the documents (see Table 1) have been translated into the language of each partner country. It is intended that all information produced will be hosted on the project website. This will include the facility to compare procurement and design approaches and national annexes in different countries. In order to ensure that the material produced in this project is appropriate and in a suitable format for designers and companies, each country has an advisory (steering) committee which provides valuable feedback at key stages of the project. The steering committees comprise large and small design companies, steel fabricators, contracting organizations and trainers.

A complete building design for each country involved in the project incorporating the national annex
A Technical Description explaining the design approach in each country. This was translated into all partner country languages
An explanation of the national practice issues which need to be taken into account when procuring and designing a building in a particular country. This will include links to useful documents including legislative. This document has also be translated into all partner languages
A comparative list of the major differences between the national annex clauses for EC3 and EC4 in each country

Table 1 - Overview of the project results

UK - University of Sheffield., The Steel Construction Institute, Epistemics Ltd
Germany – Fachgebiet Stahlbau TU Darmstadt
Belgium - Centre Information Acier
Greece - Technical Chamber of Greece and IEKEM
Spain - Fundación Universidad de Oviedo
Hungary - University of PECS
Slovakia – Slovak University of Technology Bratislava

Table 2 – Project Partners

THE STRUCTURAL DESIGN

The Bioincubator (see Figure 1 and 2) is a scientific research centre located in the centre of Sheffield. The building has five storeys each measuring approximately 20 m x 29 m on plan, resulting in a total floor area of 2800 m². A plant room is housed on the roof. The height from ground to first floor is 3.975m; the remaining floor to floor heights are 3.875m. The Bioincubator is a typical steel frame building designed in the UK according to the British Standard.



Fig. 1 - South (front) of Bioincubator



Fig. 2 - North West corner

The redesign was made on basis of the Eurocodes 3 and 4 and may enable engineers all over Europe to use the EC and the corresponding NA accordingly. Furthermore it will be possible for engineers to compare the differences in the design approach of the single countries, due to the fact that the national practice might lead to varying results. In order not to have too much variation between the various designs it was decided by the partners to fix some key points so that the outcome remains comparable. The following points were used as the basic parameters for the structural design of the building. All partners assumed these points as fixed.

- Building geometry: bay sizes, grid, height
- Composite floor slab
- Dead Loads (finishes 0,6 kN/m²; partitions 1 kN/m²)
- Bracing location
- Occupancy (office)
- Plant room loads (5 kN/m²)
- Wall finish (cassette) – non brittle

Based on these parameters the structural engineer was free to choose e.g. the material grades, slab thicknesses, connection types etc. Even though it is very interesting to see that there are still a lot of differences between the partner countries. The determination of the climatic loads is of course different due to e.g. varying wind speeds, snow heights, earthquake loads etc. But also the non climatic loads can be slightly different. Most of the partners applied a live load of 3.0 kN/m² as it is usual for office buildings. In the UK by contrast it is very common to use a live load of 4.0 kN/m², due to the fact that most of the owners prefer to be flexible with reference to the occupancy. The steel grade used depends on the delivery possibilities of the suppliers. In some regions S235 is not available and therefore S275 is used or vice versa. In Slovakia the normal steel grade is a S355. The concrete grade varies in a usual margin depending on the designing engineer. The connections for the steel framed building are normally pinned, but in Greece, Hungary or Spain it is thoroughly common to use rigid or semi-rigid connections for the horizontal load transfer. A big difference is visible concerning the assumed fire resistance. In Germany, UK and Spain the normal fire resistance for these kinds of buildings is 90 minutes. In Belgium and Hungary 60 minutes by contrast is normal. In Greece a fire resistance of 30 minutes is sufficient using e.g. sprinkler and other protection systems. The steel element protection was achieved by an encasement with plaster boards or by an intumescent coating. It has to be mentioned that the painting is due to the high costs not common. In Germany the columns are often executed as composite elements having nearly automatically the required fire resistance.

NATIONAL PRACTICE - NATIONAL CONTEXT

A very useful role of the steering committees was their input into capturing the different approaches to procurement and design of steel buildings in each country. A questionnaire was developed and sent to the national steering committees. This questionnaire covered five main areas:

• Initiation of a new project

• Finalizing a design

• Direct issues relating to the design of a building

• How the process of design takes place

• Further issues that can affect engineers designing steel buildings

In these areas various degrees of differences between the partner countries were found.

Initiation of a new project

In most building projects whether public or private sector, the client appoints his design team which is usually led by an architect. The quantity surveyor is a typical design team member in the UK. He is responsible for handling the expenses, a task that is executed by the architect in most other countries. Tendering for professional services is common only in the public sector except for Belgium, but in recent years an increasing number of private clients are adopting the tendering process to procure the design. In Spain the architect is generally responsible for the whole project design even if his involvement is minimal. Fire Engineers are uncommon but some countries (UK, Germany) have positive experiences with this discipline mainly in high rise buildings. Although the traditional form of contractual arrangement is found in all countries many new formats are used too. In the traditional form where the client appoints his design team to develop tender documents, the design team retains responsibility for the design throughout the project. Design-and-build-contracts can be found in increasing numbers throughout Europe. Especially in Hungary and Greece they are used for large scale public sector projects. In these projects the client's design team is only responsible for the performance specifications and the outline design. The design team might be retained by the client to help him checking the quality of the contractors. Contractual arrangements such as "Management Contracts", "Turn Key", "Construction Management" and with increasing number "Build-Operate-Transfer" are common throughout Europe. In the UK an arrangement called "Novation" is often used in these types of contract. Here the design team will be employed by the client to produce scheme designs but will move into the contractors team once he is appointed. Mainly cost consultants will be retained throughout the project by this scheme.

Finalizing a design

Even though the harmonization of design rules led to a reduction of barriers in the common market many traditions and local regulations have still to be taken into account by designers. For example local fire fighting regulations lead to minor differences in design rules that have to be considered. The critical height of a building is in Belgium 25 m (middle height building, out of the classes "high", "middle high", "low"). Designers would generally avoid exceeding a 25 m building height as this would involve more complex regulations. In Germany 22 m is an important value. Up to this we have a class 5 building (out of 5 classes). A building exceeding 22 m falls into the "nonstandard group" with many additional restrictions. These are sometimes state or even local regulations making the design vulnerable for legal specialties. The limitation of building width follows a tradition with regard to light and outside view for example in Germany and Belgium. This is uncommon in the UK. Another important influence on cost and speed is the design of connections. In all partner countries it is common practice for the steel fabricator to design the connections. However, recent developments show that an increasing number of design consultants are producing connection designs as well as the member design. This is appropriate if the connections form an important part of the architectural expression but it could lead to increased cost if the designer is not aware of the abilities of the contractors. It might also reduce competition because some companies might be very good in fabricating one sort of connection but might be excluded from the tender due to early and unnecessary restrictions. The proof engineer who works on behalf of the civil service is common practice in Germany. Belgium has a central insurance (SECO) to check the good execution of works. In Greece final designs are approved by local government officials, as part of issuing a building permit. In some cases the client appoints also an independent checker. In

Spain, the OCTs offices are responsible for quality control process for the full process from design to execution of the building's structure. In the UK most designs are subjected to building regulations which involve an independent check by the local authority.

Direct issues relating to the design of a building

The most important direct issue relating to the design of a building is the fire safety. In Spain the structural fire safety is checked following the main structural design. This check could be carried out by the same engineer who produced the main structural design. In Germany the fire safety of the structure is part of the proof engineers checking process. A common problem in all partner countries is the area of tolerances. As the steelwork contractor will rarely be fully aware of the overall design it is essential that the other designers appreciate the tolerances to which steelwork can be fabricated and erected. The need for any tolerances outside the codes should be clearly communicated to the contractor during the tender process. These problems occur mainly at the gap between steelwork and modern glass façades.

How the process of design takes place

Stiff connections are commonly used in Spain and Greece, there mainly to improve the earthquake resistance. Hungary, UK, and Germany usually use pinned connections in buildings, nevertheless continuous beams might be used to improve deflection or robustness. The account for second order effects is sometimes neglected in the UK, a fact that has to be regarded by non-UK designers.

Further issues that can affect engineers designing steel buildings

In all participating countries excepting the UK, design engineers and architects tend to produce building designs in concrete because they usually have more experience with this material. Consultant engineers with good knowledge and experience in steel are usually working in the design of industrial buildings not office buildings.

THE WEB-BASED COURSE

The portal developed for Eur-Ing uses the public domain Drupal [4], an open source software (http://drupal.org). Drupal was chosen for its wealth of features that include:

- Content Management System
- Blogs
- Forums
- Project Resources
- Multi-lingual support
- Translation Workflow

Based on past experience of the problems associated with multi-lingual content the ability for partners to translate and correct their own content on-line in a controlled workflow is probably the single most important feature of the Drupal domain. It is hoped that the extensibility of Drupal will allow more languages to be added as required and that the forums will provide a self-sustaining community of practice that will support engineers throughout Europe. n-AKTive Structural Steel Design e-Learning web page [5] (Figure 3 and 4) is the portal that has been designed for the Eur-Ing project. This portal was designed to provide access to knowledge about the

design of steel and composite structures, particularly with regard to the new European Union Eurocode standards (EC3 and EC4).

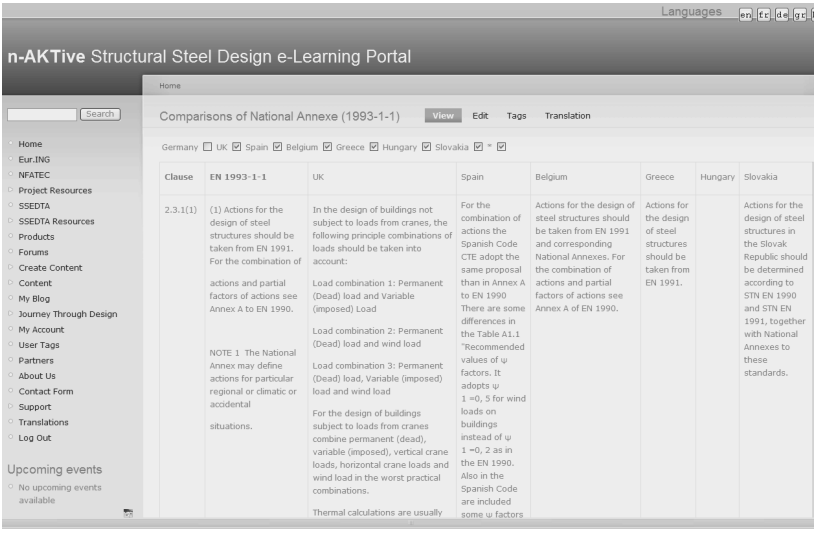


Fig. 3 - The n-AKTive portal. Comparisons of National Annexes

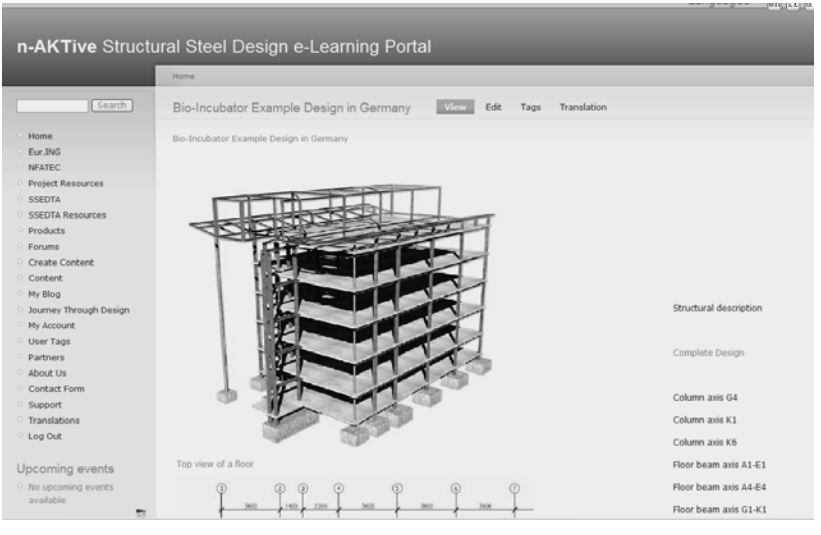


Fig. 4 - Bio-Incubator example design in Germany

n-AKTive provides access to e-Learning materials developed by leading industrial and academic experts within the EU. It also provides a forum for discussion and collaboration. This website covers:

• The National Context Documents which were developed by the national steering committees identifying the national practice affecting the building design such as planning, procurement, building regulation, health and safety, fire safety and environmental issues.

• Bio-Incubator example designs. Complete National designs of the Bio-Incubator, a real building in Sheffield which has already been constructed. These designs were produced by all partner countries, including full design calculations, drawings and sketches, in accordance with their version of the Eurocodes, national annexes and national practice permitting a reasonable comparison between the national designs. Fig. 4 shows the Bio-Incubator example design for Germany.

• The comparison of National Annexes. A comprehensive comparison of the national annexes in each country related to the respective Eurocode clauses has been produced. It allows the user to compare directly the clauses with the seven national annexes considered by means of a grid that highlights the main differences. Fig. 3 shows a sample of the grid. The project website incorporates facilities for course presentation, forums, blogs, and commercialization and on line translation. It was launched 2008 and can be visited using the following web-address: “www.n-aktive.co.uk”.

SUMMARY

The main innovative process in the Eur-Ing project is the production of a multi-national approach to the design of one real building. Worked examples in this field do exist, but are country-specific and do not describe how national annexes and local applications and regulations affect the design process in different countries, resulting usually in different solutions. By working in a trans-national way it has been discovered that, not only differences in codes and annexes but also variations in design and construction practice, planning procedures, procurement routes and other factors contribute to very diverse national design approaches. It is expected that the availability of such innovative reference and learning material in seven European languages will facilitate the mobility of designers and the ability of organizations to operate under the regulations and traditions of other countries by increasing confidence.

REFERENCES

[1] CEN, EN 1991 Eurocode 1: Actions on structures, Parts 1-1and 1-2, 2002.

[2] CEN, EN 1993 Eurocode 3: Design of steel structures, Parts 1-1, 1-2, 1-8, 2005.

[3] CEN, EN 1994 Eurocode 4: Design of composite structures, Parts 1-1, 1-2, 2005

[4] The official website of Drupal Association, http://drupal.org/

[5] n-AKTive Structural Steel Design e-Learning web page, http://www.n-aktive.co.uk/, 2008.

REVIEW AND COMPARISON OF ENCASED COMPOSITE STEEL-CONCRETE COLUMN DETAILING REQUIREMENTS

William P. Jacobs, V
SDL Structural Engineers
Atlanta, Georgia, USA
wjacobs@sdlal.com

Arvind V. Goverdhan
SDL Structural Engineers
Atlanta, Georgia, USA
agoverdhan@sdlal.com

ABSTRACT

While there is a wealth of literature regarding strength models used to determine the capacities of encased composite columns, there is little information devoted to the equally important topic of detailing provisions with respect to these columns. The goal of this paper is to fill this gap by summarizing and comparing detailing provisions within three different model standards. Several areas where broad differences exist between the standards reviewed are highlighted, and recommendations for harmonizing these provisions are made.

INTRODUCTION

The purpose of this paper is to identify, present, and compare the encased composite steel-concrete column detailing provisions of ANSI/AISC 360-05 (AISC 2005) by the American Institute of Steel Construction, ACI 318-08 (ACI 2008) by the American Concrete Institute, and EN 1994-1-1:2004 (CEN 2004b), commonly known as Eurocode 4. Hereafter, these standards will be referred to as AISC, ACI, and EC4, respectively. The primary goal is to collect detailing provisions from these standards into a single reference for comparison and to provide comment and recommendations for the harmonization of these provisions.

Similarities exist when comparing the method of presentation for detailing provisions between the AISC and ACI standards with those of the Eurocodes. EC4 contains a majority of the detailing provisions required for composite design; however, it relies on EN 1992-1-1:2004 (CEN 2004a), commonly known as Eurocode 2, and hereafter referred to as EC2, for many of the concrete and mild reinforcement provisions. Similarly, AISC has traditionally relied on the provisions of ACI for detailing requirements pertaining to concrete and mild steel reinforcement while providing explicit provisions related to the steel core. The main discrepancies between the standards arise because the Eurocodes are developed by a single entity with the expressed intent of functioning as a unit, while AISC and ACI are developed by separate entities and often contain conflicting and overlapping provisions. It is, therefore, a secondary goal of this paper to examine the conflicts between AISC and ACI and to provide recommendations to aid in their resolution.

DETAILING CRITERIA - DISCUSSION

The detailing criteria reviewed in this paper are as follows: concrete material properties, steel core requirements, transverse reinforcement requirements, longitudinal reinforcement requirements, and shear transfer provisions. Detailed discussion on each topic is provided in this section followed by a section on recommendations for achieving consensus among the standards. An extensive table summarizing the provisions for each of these topics, including the applicable code references, is provided in the Appendix. It is important to note that the detailing criteria provided herein for EC4 and EC2 may be overridden by the National Annex of the country under consideration.

Concrete Material Properties

Minimum compressive concrete strength limits for normal weight concrete are similar among the three standards. AISC requires 3.0 ksi (21 MPa), ACI requires 2.5 ksi (17 MPa), and EC4 requires 2.9 ksi (20 MPa). Maximum compressive strength limits of 10 ksi (70 MPa) and 7.3 ksi (50 MPa) are provided by AISC and EC4 respectively, although AISC allows higher values to be used for stiffness calculations. According to the AISC Commentary, these limits provide a lower bound for good quality concrete and an upper bound based on available test data. Similar reasoning for the concrete limits in EC4 is given by Johnson and Anderson (2004), who state limited knowledge exists for “composite members with weak or very strong concrete.”

EC4 composite column provisions do not address lightweight concrete, while AISC imposes a limit of 6.0 ksi (42 MPa). In the United States, composite columns are typically constructed of normal weight concrete, and they are primarily used for increased flexural stiffness and axial load capacity for highly loaded members (Viest et al. 1997). It is doubtful that minimum limits on concrete strength or limits for lightweight concrete are restrictive in practice. The maximum concrete strength limitation for normal weight concrete could become a factor for high-rise construction. AISC addresses this limitation by explicitly allowing higher strengths where “justified by testing or analysis.”

Steel Core Requirements

AISC sets the lower limit for the cross-sectional area of the steel core to 1% of the gross cross-sectional area of the composite section. Since the typical range of steel core ratios for economic construction is considerably higher (Leon and Hajjar 2008), this limit is of minimal practical concern. ACI has no such limit, while EC4 is unique in that it provides a strength-based classification system that examines the contribution of the steel core to the plastic axial strength of the composite section. This system requires the steel core to provide between 20 and 90% of the section strength for the column to be considered composite. For core ratios below 20%, the member should be designed as a reinforced concrete column. For core ratios above 90%, the member should be designed as a steel column. This classification system is the most rational method among the three standards; however, it is cumbersome in that it requires strength calculations to be performed prior to determining core ratio acceptability.

The maximum specified yield stress of the structural steel core is similar between AISC and EC4, while ACI provides a more restrictive limit. AISC allows the use of 75 ksi steel (525 MPa) based on the upper limit of 72.7 ksi (500 MPa) represented within the test database for encased composite columns used to calibrate the column strength equations (Leon et al. 2007). EC4 provides an upper limit of 67 ksi (460 MPa) which is also based on test data limits. EC4 also imposes an additional limitation on strength calculations for composite columns that contain steel cores with yield stresses exceeding 61 ksi (420 MPa). This limit is in the form of an interaction check that must be performed under combined axial load and bending. The interaction ratio should typically be less than 0.9, but the use of high strength core steel decreases the maximum limit to 0.8. The reduced limit accounts for adverse effects due to increased strains within the concrete present at yielding of higher strength steel (Johnson and Anderson 2004). ACI attempts to justify a more conservative limit of 50 ksi (345 MPa) by stating that this stress corresponds to a maximum concrete strain of approximately 0.0018, below which concrete is unlikely to spall. This justification does not appear to take into account the confining effect provided by the transverse reinforcement present in these columns. The amount of transverse steel required to provide adequate confinement to prevent spalling of the core concrete is further addressed in the following section on transverse reinforcement. It is of interest that both ACI and EC4 address limitations on high strength steels in some manner (by disallowing them or setting further strength limits respectively), while AISC offers no additional provisions.

Although not a direct requirement for the actual core, a related consideration is the amount of concrete cover that must be provided to the steel core. Of the three standards, only EC4 provides explicit direction for determining this cover requirement. EC4 stipulates both a maximum (for calculations) and a minimum concrete cover requirement to the steel core. Traditionally, minimum cover requirements to mild reinforcement, such as those presented in ACI, are derived from environmental exposure and fire rating concerns. It is presumed that these same requirements would also apply to the steel core. The literature indicates two additional reasons for core cover requirements in EC4. First, the applicability of the simplified design procedure was validated within this range of steel core covers (Johnson 2004). Second, the concrete encasement provides restraint against local steel column buckling (ECCS 2000). Although they do not have explicit cover requirements for the steel core, ACI and AISC provide a minimum concrete cover limit of 1.5 in. (38 mm) to the transverse reinforcement. With a No. 4 tie, even in the unlikely condition that no space is provided between the core and tie, this provision would result in an absolute minimum of 2 in. (51 mm) of cover to the core. This amount is within the general range of EC4 provisions for the majority of core sizes.

Transverse Reinforcement Requirements

The primary purpose of transverse reinforcement in concrete-encased composite columns is to provide concrete confinement to prevent spalling around the structural steel core and to properly support longitudinal reinforcement to prevent buckling of the bars (Viest et al. 1997). Transverse reinforcement can also provide additional shear capacity. All three standards require some form of continuous transverse reinforcement (ties or spirals) within composite columns.

ACI limits the maximum tie spacing to 16 times the longitudinal bar diameter, 48 times the tie diameter, or one-half of the least column width. AISC specifies the

same limits as ACI, with the notable exception of a minimum tie diameter limit which will be reviewed further in a following discussion. EC4 requires ties to be spaced at a maximum of 20 times the longitudinal bar diameter, the least column dimension, or 15.75 in. (400 mm).

The allowable transverse reinforcement limits have been plotted for the three standards over a range of square column widths and longitudinal bar sizes in Figures 1, 2, and 3. These figures indicate the maximum permissible spacing of transverse reinforcement when No. 3, No. 4, and No. 5 tie bars are utilized. The figures are plotted based on a range of standard reinforcing bar sizes found in typical column construction in the United States.

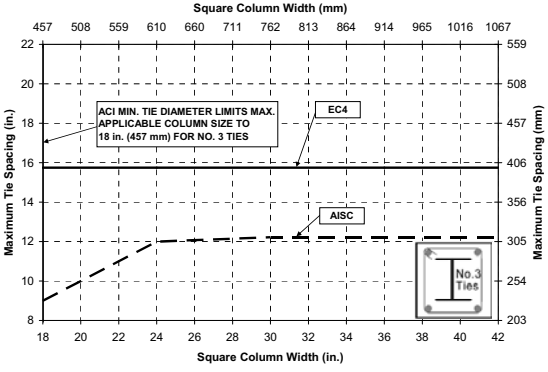


Figure 1 – Maximum transverse reinforcement spacing (No. 3 ties)

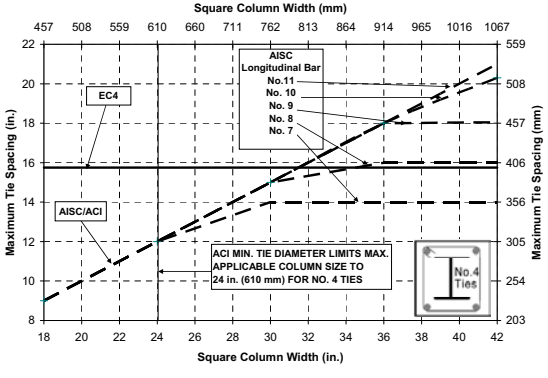


Figure 2 – Maximum transverse reinforcement spacing (No. 4 ties)

Several observations can be made through the examination of Figures 1, 2, and 3. First, the largest discrepancy between the three standards arises in the requirements for minimum tie diameters, where ACI is significantly more restrictive. ACI composite provisions result in the requirement of No. 4 ties for columns larger than 18 in. (457 mm) and No. 5 ties for columns larger than 24 in. (610 mm). Second, AISC does not have explicit provisions for tie diameters; however, it does limit the

minimum area of the tie to 0.009 in.^{2} per in. (6 mm^2 per mm) of tie spacing. A similar limit can be traced back to the seminal composite column work by SSRC Task Group 20 (1979). If interpreted correctly, the limit has the effect of controlling vertical tie spacing to a maximum of approximately 12 in. (300 mm.) for No. 3 bars and 22 in. (560 mm.) for No. 4 bars. However, this limit is quite confusing to apply in its current form. Typically, concrete reinforcement limits are based on cross-sectional areas, not areas per unit of reinforcement spacing. Also, this limit leaves itself open to interpretation as to how many legs of the transverse reinforcement are to be used in its calculation. Third, for column sizes exceeding 36 in. (914 mm), AISC provisions yield significantly larger tie spacing for No. 4 ties when compared to the other two standards. Finally, the 15.75 in. (400 mm) limit of EC4 tends to control throughout the range of most composite column sizes including all configurations depicted in Figures 1, 2, and 3.

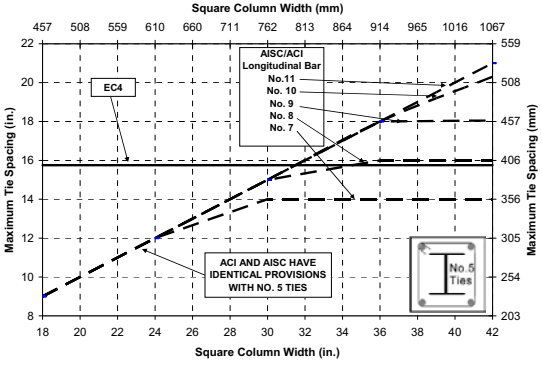


Figure 3 – Maximum transverse reinforcement spacing (No. 5 ties)

In addition to tie reinforcement provisions, ACI provides explicit provisions for spiral (helical) reinforcement. Both AISC and EC4 indicate that spiral reinforcement may be used, but neither provides specific provisions governing its use beyond those previously discussed for lateral ties.

A secondary topic in the discussion on transverse reinforcement is the requirement for intermediate ties for the support of longitudinal reinforcement located away from the column corners. EC4 provisions require longitudinal reinforcement in compression zones to be located within approximately 6 in. (150 mm) of a restrained bar. ACI has separate provisions for typical reinforced concrete columns and for composite columns. For reinforced concrete (non-composite) columns, ACI contains similar provisions in Section 7.10.5.3 that require every alternate longitudinal bar meeting certain limitations be laterally supported by intermediate ties. Additionally, no longitudinal bar can be located more than 6 in. (150 mm) away from a restrained bar. ACI is ambiguous as to whether the compression member provisions of Chapter 7 extend to composite members, although it seems reasonable to assume that they do. AISC does not provide specific intermediate tie requirements, although the general provisions provide a blanket statement referencing the building code and/or ACI for detailing of concrete and steel reinforcement. AISC Design Guide 6

provides further guidance on the detailing of intermediate ties including the use of "carry bars" adjacent to the steel core (Griffis 1992).

As mentioned in the preceding discussion on steel core requirements, the use of high strength steel (F_y > 50 ksi (345 MPa)) for the core raises the question of how much transverse reinforcement is required to prevent spalling at the high strain levels associated with core yielding. To the authors' knowledge, there are no experimental studies that focus specifically on the effect of transverse reinforcement on composite column performance, regardless of the core yield strength. The current code requirements appear to be based on provisions for non-composite reinforced concrete columns. There are provisions in place for seismic design, such as those in ACI Section 21.6.4.4, which are known to provide adequate levels of concrete confinement for highly loaded columns. A history of the seismic provisions can be found in Saka and Shaikh (1989), and further discussion can be found in Paulay and Priestley (1992), Park and Paulay (1975), and Viest et al. (1997). Until experimental testing focusing on transverse reinforcement effects for encased composite beam-columns with high strength steel cores becomes available, the reader is cautioned to pay careful attention to tie detailing and to consider the use of seismic tie provisions for such columns.

Longitudinal Reinforcement Requirements

With respect to minimum longitudinal reinforcement requirements, ACI notably differs from EC4 and AISC by requiring the same percentage reinforcement for composite columns as that required for non-composite columns (1% of the concrete cross-sectional area). AISC and EC4 permit 0.4% of the gross column cross-sectional area and 0.3% of the net concrete cross-sectional area, respectively. According to the ACI Commentary, the 1% minimum limit for non-composite columns is based upon the phenomenon of stress transfer from the concrete to the reinforcement due to creep and shrinkage under service load levels. However, the inclusion of an encased structural steel section mitigates this effect and should consequently allow a smaller ratio of longitudinal reinforcement to concrete area.

Maximum longitudinal reinforcement percentages are generally based on construction considerations to limit congestion. ACI caps this overall percentage at 8%. Since this is the maximum limit within a splice region, typical reinforcing bar layouts yield considerably less reinforcement percentages through the remainder of the column length. An exception occurs where mechanical splices are used, thus permitting the full reinforcement percentage to be utilized throughout the column length. AISC does not provide a specific limit but defaults to ACI by general reference. EC4 allows up to 6% longitudinal reinforcement in non-lap regions to be used in calculations, which is more liberal than the 4% recommended by EC2 for non-composite concrete columns (Johnson and Anderson 2004). It is unlikely that steel reinforcement ratios exceeding 3% will be utilized, and these limits will, therefore, not be encountered in practice often.

Provisions for the required number of longitudinal reinforcing bars for composite columns are present within all three standards. EC4 states that longitudinal bars must be provided within each corner of the column. AISC is more specific and requires at least four continuous bars. AISC assumes that the bars are to be placed in column corners; however, this is not specifically stated, nor is the AISC provision applicable to irregular column geometries. ACI is unclear as to the minimum number

of longitudinal bars required in a composite cross section. Section 10.13.8.6 states that "a longitudinal bar shall be located at every corner of a rectangular cross section, with other longitudinal bars spaced not farther apart that one-half the least side dimension of the composite column." This statement can be interpreted to require a minimum of eight longitudinal bars, although it is the authors' opinion that this is not the intent and that a minimum of four bars is sufficient. For circular columns, ACI and EC4 require a minimum of four longitudinal bars, with ACI requiring six bars for columns with spiral reinforcement.

Other considerations for longitudinal reinforcement are the minimum spacing allowed between reinforcing bars as well as between reinforcing bars and the steel core. ACI requires a minimum clear distance between longitudinal bars of 1.5 times the bar diameter or 1.5 in. (38 mm) whichever is greater. EC4 has a similar limit. AISC does not address this topic directly, and a general statement that steel reinforcement detailing shall be governed by ACI applies. EC4 is the only standard that directly addresses the clear distance required between longitudinal reinforcement and steel core. EC4 allows the reinforcement to be placed immediately adjacent to the core provided that the bond surface used to calculate development lengths is reduced. ACI provisions for increased development lengths for bundled bars are based on similar principles and could also be applied to this situation. Alternately, the same provisions used for minimum spacing between longitudinal bars could be used to the steel core.

Finally, it should be noted that development lengths, splice lengths, and anchorage provisions for longitudinal and other mild reinforcement are provided in Chapter 12 of ACI and by implicit reference to EC2 in EC4. AISC refers to ACI for general reinforcement detailing requirements within the general provisions of the composite member specification.

Shear Transfer (Load Introduction)

The method of load introduction is a significant topic for encased composite columns and one in which the three standards differ significantly. ACI is minimalistic, stating that "any axial load strength assigned to concrete of a composite member shall be transferred to the concrete by members or brackets in direct bearing on the composite member concrete." EC4, on the other hand, devotes four pages to the topic.

As an overview, EC4 splits composite columns into two regions: the introduction length, and the remainder of the column length. The introduction length is defined as the smaller of twice the minimum column width or one-third of the column length. Load introduced to the column must be transferred between the steel core and concrete encasement within the introduction length to attain force equilibrium of the cross section. The amount of longitudinal shear to be transferred is allowed to be determined by either elastic or plastic theory. EC4 is unique among the three standards in that it allows the use of bond for force transfer in encased columns. EC4 provides a design bond strength of 43.5 psi (0.30 MPa) for unpainted sections to be used for this purpose. If the bond strength is exceeded, mechanical connection (stud connectors) must be provided unless loads are introduced to both materials concurrently by endplates. Outside of the area of load introduction, no stud connectors are required unless additional longitudinal shears are created by transverse loads or end moments. EC4 does not provide a direct method for

calculating the shear to be resisted due to these loads and simply states that elastic analysis considering creep and shrinkage of concrete may be used.

AISC requires the use of mechanical anchorage to transfer load. Although not specifically stated, the equations provided for the determination of the required shear force to be transferred are based on a plastic resistance model and are actually the same as those provided in ECCS (2000) for fulfillment of the more generic EC4 provisions. AISC provisions are somewhat confusing in that the differentiation between transfer mechanisms for load application to the column and load transfer within the column are not well defined. These provisions should be clarified to direct the designer to break the loading process down into two stages. First, force should be transferred to the composite column using direct connection to the steel (either through shear connection or direct bearing on the steel), direct bearing onto the concrete, or a combination of the two. Second, the amount of force required within the steel core and concrete encasement for cross-sectional equilibrium should be calculated using the plastic resistance equations provided in the standard. The difference in forces between what is applied and what is required for cross-sectional equilibrium is the longitudinal shear that must be transferred between the two materials using shear connectors or internal bearing plates.

AISC contains what is believed by the authors to be an error in the detailing requirements for load introduction. For composite construction, it is generally advisable to achieve composite action expeditiously to ensure that the full capacity of the composite section may be used for force resistance. AISC requires that "shear connectors shall be distributed along the length of the member at least a distance of 2.5 times the depth of the encased composite column above and below the load transfer region." This provision requires a *minimum* load transfer length. It is the authors' belief that the intent was to require that the shear connectors be distributed *within* a distance of 2.5 times the depth of the encased composite column. This revision would result in a *maximum* introduction length similar to that specified in EC4, which would allow the steel core to become composite with the concrete encasement within a compact distance.

AISC sets a limit on maximum spacing between shear connectors of 16 in. (406 mm), and provides no guidance for resisting longitudinal shear due to flexure.

DETAILING CRITERIA – HARMONIZATION

Through comparison of the provisions within AISC, ACI, and EC4, it is apparent that further work is needed to move toward a more complete and consistent set of composite detailing provisions. The discordance between ACI and AISC when compared to the tight integration of EC2 and EC4 is of particular importance. The overlapping and often conflicting provisions between ACI and AISC serve to create confusion within the design community. Also, although it is recognized that EC4 is based on alternate sets of test data and is sometimes aimed towards construction techniques that might not be common within the United States, there are several areas in which the American and European standards can benefit from the careful consideration of each other's provisions.

The following list is a summary of recommendations aimed at both improving the harmonization of detailing provisions among the three standards and filling perceived gaps within the standards themselves.

- *General Coordination Between ACI and AISC:* In order to improve integration between the steel (AISC) and concrete (ACI) standards in use within the United States, it is recommended that one of two options be explored.

  The first option is a revision of ACI composite column provisions to include only concrete and mild reinforcement detailing criteria and to reference AISC for strength design and other steel core related criteria. As current ACI composite provisions have not undergone a significant update in many years, the detailing provisions would also need to be revised to incorporate more recent research. Additional revision would be necessary to eliminate ambiguities regarding the required number of longitudinal reinforcing bars and intermediate tie requirements. AISC could then remove concrete and mild reinforcement detailing information and incorporate ACI's provisions for these items by reference. This option would eliminate overlapping and conflicting provisions while maintaining the traditional symbiotic relationship between ACI for concrete design and AISC for structural steel design.

  The second, and perhaps more practical short-term option, is for AISC to explicitly exclude the composite-column-specific provisions of ACI and refer to the remainder of the non-composite provisions within ACI for the majority of mild reinforcement detailing needs. Additional limits and detailing provisions could then be provided within AISC for criteria specific to composite columns. Option 2 is not as clean as option 1; however, given the time and coordination effort that option 1 would require, option 2 is a viable one to provide designers with a comprehensive set of composite column design criteria that minimizes contradictory provisions.

- *Material Strengths:* It is recommended that EC4 allow the use of higher strength concretes where justified by testing or analysis as permitted by AISC.

- *Steel Core Requirements:* Although the process of determining the minimum steel core ratio is more rational in EC4, the requirement of strength calculations to determine this ratio is cumbersome for practical designs compared to the 1% limit of AISC.

- *Transverse Reinforcement Requirements:* ACI tie diameter provisions need to be re-evaluated due to their conservatism when compared to the other two standards. It is recommended that AISC rewrite their tie provisions to make them clearer. Requiring the use of a No. 3 bar at 12 in. (305 mm) and a No. 4 or greater bar at 16 in. (406 mm) would meet AISC's intent for No. 3 bars and impose a more conservative upper spacing limit for larger tie bars consistent with EC4. The proposed maximum spacing would also coincide with the maximum shear stud spacing currently allowed in AISC.

  Both AISC and EC4 need to provide more explicit treatment of spiral (helical) ties.

  AISC and ACI need to clarify that additional intermediate ties are required for the support of longitudinal bars not placed at the corners of the cross section.

  Determining the amount of transverse reinforcement required to prevent concrete spalling and promote structural integrity when high strength (F_y > 50 ksi (345 MPa)) steel is used in the core is a topic that warrants further research. Until such research can be performed, it is recommended that highly loaded encased columns that make use of high strength steel cores utilize transverse reinforcement based on the seismic design provisions of ACI Section 21.6.4.4.

- *Longitudinal Reinforcement Requirements:* For practical designs, the maximum and minimum limits for longitudinal reinforcement are generally not of concern. The ACI minimum limit is extremely conservative compared to the other standards, and consideration should be given to its revision.

  ACI and AISC provisions for the required minimum number of longitudinal bars need to be clarified. ACI's provisions can be interpreted as requiring eight bars, and AISC's provisions are too specific to apply to general non-rectangular sections.

  ACI and AISC should address minimum spacing requirements between longitudinal steel and the steel core. It is recommended that a minimum spacing similar to that used in ACI between longitudinal bars be imposed. Alternately, a development length extension factor similar to that used for bundled bars could be utilized.

- *Shear Transfer (Load Introduction):* ACI's provisions for load introduction are inadequate and need to be revisited. Alternately, reference to another document should be made.

  EC4's axial load introduction provisions are extensive and provide detailing requirements and provisions beyond the level of information typical of American standards. Shear transfer due to flexure is one topic where guidance is lacking.

  AISC's shear transfer provisions are incomplete and, at times, confusing. It is recommended that they be re-written to clarify the distinction between load application to the column and load transfer for equilibrium within the column. It is the authors' opinion that an error exists within the load transfer length provisions that needs to be revised to allow for composite action to be attained more quickly. The use of bond and the allowance of alternate methods for the determination of transfer forces should be investigated as is allowed by EC4. Finally, as recommended for EC4, provisions for shear transfer due to flexure should be provided.

APPENDIX: TABULAR SUMMARY OF DETAILING REQUIREMENTS

The following table contains the provisions for each topic covered within the preceding discussion. The first column contains an overall subject, the second "requirement" column indicates a specific topic, and the following three columns provide related provisions from the three standards. A reference to the standard section from which this information is taken is provided in italics at the bottom of each provision. For EC4 provisions, references are provided to EC4 unless specifically denoted as being from EC2.

	REQUIREMENT	AISC	ACI	EC4
Material Properties	Concrete compressive strength (normal weight)	Min. f'_c = 3.0 ksi (21 MPa) Max. f'_c = 10.0 ksi (70 MPa) *[I1.2(1)]*	Min. f'_c = 2.5 ksi (17 MPa) *[1.1.1]*	Min. f_{ck} = 2.9 ksi (20 MPa) Max. f_{ck} = 7.3 ksi (50 MPa) *[3.1(2), 6.7.1(2)]*
	Concrete compressive strength (lightweight)	Min. f'_c = 3.0 ksi (21 MPa) Max. f'_c = 6.0 ksi (42 MPa) *[I1.2(1)]*	Min. f'_c = 2.5 ksi (17 MPa) *[1.1.1]*	Not permitted. *[6.7.1(2)]*
Steel Core	Steel core limitations	The cross-sectional area of the steel core shall comprise at least 1% of the total composite section. *[I2.1a(1)]*	No requirement.	Limitations are based upon a minimum and maximum "steel contribution ratio" which measures the portion of plastic bending resistance of the composite section provided by the steel core. To be considered composite, this ratio can not be less than 20%, or more than 90%. *[6.7.1(4), 6.7.3.3(1)]*
	Concrete cover for encased steel member	No requirement.	No requirement.	Min. of 1.6 in. (40 mm) or one-sixth times steel core flange width, whichever is greater. *[6.7.5.1(2)]* A max. of 0.4 times the composite column width in the strong direction or 0.3 times the composite column depth in the weak direction may be used for calculations. *[6.7.3.1(2)]*
	Steel core yield strength	Max. F_y = 75 ksi (525 MPa) *[I1.2(2)]*	Max. F_y = 50 ksi (345 MPa) *[10.13.7.1, 10.13.8.1]*	Max. F_y = 67 ksi (460 MPa) with more restrictive strength limits for $F_y \geq 61$ ksi (420 MPa) *[3.3(2), 6.7.3.6(1)]*
Transverse Reinforcement	General transverse reinforcement requirements	Concrete encasement of the steel core shall be reinforced with continuous longitudinal bars and lateral ties or spirals. *[I2.1a(2)]*	Lateral ties shall extend completely around the steel core. *[10.13.8.2]*	Every longitudinal bar or bundle of bars placed in a corner should be held by transverse reinforcement. *[6.7.5.2(2), EC2 9.5.3(6)]*
	Transverse reinforcement area/diameter	Min. tie area shall be at least 0.009 in^2 per in. (6 mm^2 per mm) of tie spacing. *[I2.1a(2)]*	Min. tie diameter = 0.02 times greatest column dimension. Bars must not be less than a No. 3, or more than a No. 5 bar. *[10.13.8.3]*	Min. tie diameter shall be no less than 0.25 times the longitudinal bar diameter or 0.24 in. (6 mm), whichever is greater. *[6.7.5.2(2), EC2 9.5.3(1)]*

	REQUIREMENT	AISC	ACI	EC4
Transverse Reinforcement Cont.	Intermediate transverse reinforcement requirements	General reference made to ACI. *[I1]*	No specific requirement for composite members. General rules for compression members require that every corner and alternate longitudinal bar shall have lateral support. Additionally, no longitudinal bar shall be farther than 6 in. (150 mm) clear from a laterally supported bar. *[7.10.5.3]*	No bar within a compression zone shall be located further than 6.0 in. (150 mm) from a restrained bar. *[6.7.5.2(2), EC2 9.5.3(6)]*
	Transverse reinforcement spacing	Max. spacing of lateral ties is the least of $16d_b$, $48d_{stirrup}$, or 0.5 times the least column dimension. *[I2.1f]*	Max. spacing of lateral ties is the least of $16d_b$, $48d_{stirrup}$, or 0.5 times the least column dimension. *[10.13.8.4]*	Max. spacing of lateral ties is the least of $20d_b$, the least column dimension, or 15.75 in. (400 mm). At beam-column intersections and lapped joints, spacing is limited to 60% of the above requirement. *[6.7.5.2(2), EC2 9.5.3(3,4)]*
	Spiral transverse reinforcement requirements	General reference made to ACI. *[I1]*	Volumetric spiral reinforcement ratio (ρ_s) shall not be less than: $\rho_s = 0.45\left(\frac{A_g}{A_{ch}} - 1\right)\frac{f_c'}{f_{yt}}$ *[10.13.7.2, 10.9.3]*	No specific requirement.
Longitudinal Reinforcement	Longitudinal reinforcement ratio	$0.004A_g \le A_{sr}$ *[I2.1a(3)]*	$0.01A_c \le A_{sr} \le 0.08A_c$ *[10.13.7.3, 13.13.8.5]*	$0.003A_c \le A_{sr} \le 0.06A_c$ *[6.7.5.2(1),6.7.3.1(3)]*
	Concrete cover for longitudinal reinforcement	Min. reinforcement clear cover = 1.5 in. (38 mm) *[I2.1f]*	Min. reinforcement clear cover = 1.5 in. (38 mm), or more for special conditions. *[7.7.1]*	Min. reinforcement cover ranges from 0.4 in. (10 mm) to 2.2 in. (55 mm). with a minimum of one bar diameter based on exposure condition, bond, and fire resistance. *[6.7.5.1(1), EC2 4.4.1]*
	Min. diameter of longitudinal reinforcement	No requirement.	No requirement.	Min. dia. =0.3 in. (8 mm) *[6.7.5.2(2), EC2 9.5.2(1)]*
	Location and number of longitudinal reinforcement bars	At least four continuous bars shall be used in encased composite columns (presumably at corners, although not specifically stated). *[I2.1f]*	Vertical bars must be located at each member corner, with other longitudinal bars spaced not farther apart than one-half the least side dimension of the composite member. 4 bar min. for circular ties, 6 bar min. for spirals. *[10.13.8.6, 10.9.2]*	Min. of one bar per corner for any column shape, and four bars for a circular shape. *[6.7.5.2(2), EC2 9.5.2(4)]*

	REQUIREMENT	AISC	ACI	EC4
Longitudinal Reinforcement Cont.	Longitudinal reinforcement spacing	General reference made to ACI. *[I1]*	Min. clear distance is $1.5d_b$, or 1.5 in. (38 mm), whichever is greater. *[7.6.3]*	Min. spacing is the longitudinal bar diameter, the diameter of aggregate + 0.2 in (5 mm), or 0.8 in. (20 mm), whichever is greater. However, rebar may be directly attached to the steel shape provided the bond surface is reduced by 1/2 or 3/4, depending upon the location of the reinforcement with respect to the embedded steel shape. *[EC2 8.2(2), 6.7.5.2(3)]*
Shear Transfer (Load Introduction)	Load transfer between concrete encasement and steel core	Shear connectors must be placed symmetrically on at least two sides of the steel core. Shear connectors must be distributed above and below the load transfer region for a distance equal to at least 2.5 times the column depth. Max. connector spacing may not exceed 16 in. (406 mm). *[I2.1f]*	Any axial load strength assigned to concrete of a composite member shall be transferred to the concrete by members or brackets in direct bearing on the composite member concrete. *[10.13.3]*	Need not be used if the design bond/friction strength is sufficient. If required, must be distributed in the region equal to 2 times the min. transverse column dimension (or diameter for circular columns) or 1/3 of the column length, whichever is greater. Concrete confinement effects may be considered in computation of shear resistance for members with studs connected to the web. *[6.7.4.2]*
General Reinforcement	Development length	General reference made to ACI. *[I1]*	Various requirements are contained in ACI Chapter 12. *[12.2-12.13]*	No specific requirement in EC4; implicit reference made to EC2 which contains various reqs in Clause 8. *[1.2.2, EC2 8.4,8.8,8.9]*
	Lap splices	General reference made to ACI. *[I1]*	Requirements for tension lap splices, compression lap splices, and general provisions are contained in ACI Chapter 12. *[12.14-12.17]*	No specific requirement in EC4; implicit reference made to EC2 which contains various reqs in Clause 8. *[1.2.2, EC2 8.7-8.9]*
Miscellaneous	Connection of multiple encased shapes	When 2 or more steel shapes are encased, they must be interconnected with lacing, tie plates, batten plates, or otherwise, to avoid individual shape buckling prior to concrete hardening. [*I2.1f]*	No requirement.	No requirement.

NOTATION

A_c = cross-sectional area of concrete, in.^{2} (mm^2)
A_{ch} = cross-sectional area of a column measured to the outside edges of transverse reinforcement, in.^{2} (mm^2)
A_g = gross cross-sectional area of the column section, in.^{2} (mm^2)
A_{sr} = area of continuous longitudinal reinforcing bars, in.^{2} (mm^2)
d_b = diameter of longitudinal reinforcement, in. (mm)
$d_{stirrup}$ = diameter of transverse reinforcement, in. (mm)
f'_c = specified minimum concrete compressive strength, ksi (AISC/ACI)
f_{ck} = characteristic compressive cylinder strength of concrete at 28 days, MPa (EC2/EC4)
F_y = specified minimum steel yield stress, ksi (MPa)
f_{yt} = specified minimum yield stress of transverse reinforcement, ksi (MPa)
ρ_s = ratio of volume of spiral reinforcement to volume of core confined by the spiral (measured out-to-out of spirals)

REFERENCES

ACI (2008), *Building Code Requirements for Structural Concrete*, ACI 318-08, American Concrete Institute, Farmington Hills, MI.

AISC (2005), *Specification for Structural Steel Buildings*, ANSI/AISC 360-05, American Institute of Steel Construction, Inc., Chicago, IL.

CEN (2004a), *Eurocode 2: Design of Concrete Structures - Part 1-1: General Rules and Rules for Buildings*, EN 1992-1-1:2004, CEN, Brussels, Belgium.

CEN (2004b), *Eurocode 4: Design of Composite Steel and Concrete Structures - Part 1-1: General Rules and Rules for Buildings*, EN 1994-1-1:2004, CEN, Brussels, Belgium.

ECCS (2000), *Design Handbook for Braced Composite Steel-Concrete Buildings According to Eurocode 4,* Technical Publication n^0 96, ECCS, Brussels, Belgium.

Griffis, L.G. (1992), *Load and Resistance Factor Design of W-Shapes Encased in Concrete*, Steel Design Guide Series No. 6, American Institute of Steel Construction, Inc., Chicago, IL.

Johnson, R.P. (2004), *Composite Structures of Steel and Concrete: Beams, Slabs, Columns, and Frames for Buildings,* Third Edition, Blackwell Publishing, Oxford.

Johnson, R.P., and Anderson, D. (2004), *Designers' Guide to EN 1994-1-1: Eurocode 4*, Thomas Telford Publishing, London, England.

Leon, R.T., Kim, D.K., and Hajjar, J.F. (2007), "Limit State Response of Composite Columns and Beam Columns Part I: Formulation of Design Provisions for the 2005 AISC Specification," *Engineering Journal,* AISC, Vol. 44, No. 4, 4th Quarter, pp. 341-358.

Leon, R.T., and Hajjar, J.F. (2008), "Limit State Response of Composite Columns and Beam Columns Part II: Application of Design Provisions for the 2005 AISC Specification," *Engineering Journal,* AISC, Vol. 45, No. 1, 1st Quarter, pp. 21-46.

Park, R., and Paulay, T. (1975), *Reinforced Concrete Structures,* Wiley-Inter-Science, New York, NY.

Paulay, T., and Priestley, M.J.N. (1992), *Seismic Design of Reinforced Concrete and Masonry Buildings,* John Wiley & Sons, New York, NY.

Sakai, K., and Sheikh, S.A. (1989), "What Do We Know About Confinement in Reinforced Concrete Columns? (A Critical Review of Previous Work and Code Provisions)," *ACI Structural Journal,* Vol. 86, No. 2, Mar.-Apr., pp. 192-207.

SSRC Task Group 20 (1979), "A Specification for the Design of Steel-Concrete Composite Columns," *Engineering Journal,* AISC, Vol. 16, No. 4, 4th Quarter, pp. 101-115.

Viest, I.M., Colaco, J.P., Furlong, R.W., Griffis, L.G., Leon, R.T., and Wyllie, L.A., Jr. (1997), *Composite Construction: Design for Buildings,* McGraw-Hill, New York, NY.

COMPOSITE JOINTS IN ROBUST BUILDING FRAMES

Jaspart Jean-Pierre
University of Liège, ArGEnCo Department
Liège, Belgium
Jean-Pierre.Jaspart@ulg.ac.be

Demonceau Jean-François
University of Liège, ArGEnCo Department
Liège, Belgium
jfdemonceau@ulg.ac.be

ABSTRACT

Recent events such as natural catastrophes or terrorism attacks have highlighted the necessity to ensure the structural integrity of buildings under exceptional actions. Accordingly, a European RFCS project entitled “Robust structures by joint ductility” has been set up in 2004, for three years, with the aim to provide requirements and practical guidelines for the design of steel and composite structures under exceptional actions. In this project, the importance of the structural joints has been shown; as a particular case, these ones experience additional high tying forces after the loss of a column, as a result of the development of membrane forces in the beams located just above the damaged column. Moreover a reversal of moments occurs in some joints. In this paper design models for the evaluation of the mechanical properties of joints in such extreme situations are presented. References are made to recent tests on joints in isolation and joints in frames recently achieved at Stuttgart and at Liège University in the framework of the above-mentioned RFCS project.

INTRODUCTION

A structure should be designed to behave properly under service loads (at SLS) and to resist design factored loads (at ULS). The type and the intensity of the loads to be considered in the design process may depend on different factors such as: the intended use of the structure (type of variable loads…), the location (wind action, level of seismic risk…) and even the risk of accidental loading (explosion, impact, flood…). In practice, these individual loads are combined so as to finally derive the relevant load combination cases. In this process, the risk of an exceptional (and therefore totally unexpected) event leading to other accidental loads than those already taken into consideration in the design process in itself is not at all covered. This is a quite critical situation in which the structural integrity should be ensured, i.e. the global structure should remain globally stable even if one part of it is destroyed by the exceptional event (explosion, impact, fire as a consequence of an earthquake …). In conclusion, the structural integrity will be required when the structure is subjected to exceptional actions not explicitly considered in the definition of the design loads and load combination cases.

According to Eurocodes ([prEN 1991-1-7 2004], [ENV 1991-2-7 1998]) and some different other national design codes ([BS 5950-1:2000 2001], [UFC 4-023-03 2005]), the structural integrity of civil engineering structures should be ensured through appropriate measures but, in most of the cases, no precise practical guidelines on how to achieve this goal are provided. Even basic requirements to fulfil are generally not clearly expressed. Different strategies may therefore be contemplated:

- Integrate all possible exceptional loads in the design process in itself; for sure this will lead to uneconomical structures and, by definition, the probability to predict all the possible exceptional events, the intensity of the resulting actions and the part of the structure which would be affected is seen to be "exceptionally" low.
- Derive requirements that a structure should fulfil in addition to those directly resulting from the normal design process and which would provide robustness to the structure, i.e. an ability to resist locally the exceptional loads and ensure a structural integrity to the structure, at least for the time needed to safe lives and protect the direct environment. Obviously the objective could never be to resist to any exceptional event, whatever the intensity of the resultant actions and the importance of the structural part directly affected.

In the spirit of the second strategy, a European RFCS project entitled "Robust structures by joint ductility – RFS-CR-04046" has been set up in 2004, for three years, with the aim to provide requirements and practical guidelines allowing to ensure the structural integrity of steel and composite structures under exceptional events through an appropriate robustness. Within the project, Liège University was mainly concerned by the exceptional loading "loss of a column further to an impact" in steel and composite buildings. At this occasion, the importance of the structural joints has been shown; indeed, these ones are initially designed to transfer shear forces and hogging bending moments, but experience additional high tying forces after the loss of a column, as a result of the development of membrane forces in the beams located just above the damaged or destroyed column. Moreover a reversal of moments occurs in the joints located just above the damaged column. In this paper design models for the evaluation of the mechanical properties of joints in such extremes situations [Demonceau 2008] are presented, as a part of a more global study carried out at Liège University and aimed at deriving design requirements for robust composite building frames. References are first made to recent experimental tests on joints in isolation and joints in frames recently achieved at Stuttgart University and at Liège University in the framework of the above-mentioned RFCS project. Then, the design models developed within the project are presented.

PERFORMED EXPERIMENTAL TESTS

Introduction

During the previously mentioned European project, an experimental test campaign was foreseen, as illustrated in Figure 1. In a first step, an experimental test on a substructure simulating the loss of a column in a composite building frame had to be performed at Liège University; the objective of this test was to observe the

development of membrane forces within the beams and their effects on the joint response. Then, in a second step, the composite joint configuration used in the substructure test had to be tested in isolation at Stuttgart University with the objective to derive its response under combined bending moments and tensile forces. Finally, in a third step, all the components activated in the joints studied as part of the substructure in Liège and in isolation in Stuttgart had to be tested at Trento University. In order to reach a full adequacy between the experimental results, all the steel elements used for the tested specimens had to come from the same producer and from the same production. In the next paragraphs, the substructure test and the joint tests in isolation are presented.

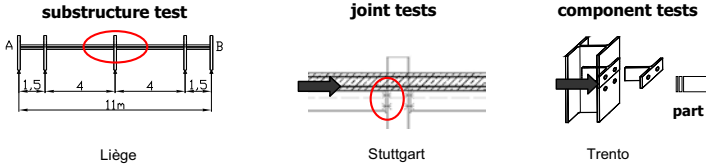


Fig. 1 – Test campaign within the RFCS project “Robust structures by joint ductility”

Substructure test

As mentioned previously, the substructure experimental test has been performed at Liège University. To define the substructure, an “actual” composite building has first be designed according to Eurocode 4 [EN 1994-1-1 2004], under “conventional” loading conditions (i.e. loads recommended in Eurocode 1 for office buildings [EN 1991-1-1 2002]); the aim was to get realistic dimensions for the structure to be tested. In particular, the composite joints were designed so as to exhibit a ductile behaviour at collapse, under M-N (moment - axial force) combined loading [Demonceau 2008]. The details of the selected joints are shown later in Figure 7.

As it was not possible to test a full 2-D actual composite frame within the project, a substructure was then extracted from the actual building as presented in Figure 2; the extracted substructure was defined so as to respect the dimensions of the testing slab but also to exhibit a similar behaviour as the one which would be observed in the actual frame. In particular, by extracting the substructure from the actual building frame, a key parameter influencing significantly the development of the membrane forces was considered: the lateral restraint “K” emanating from the part of the structure not directly affected by the column loss. So, to simulate this lateral restraint, two horizontal jacks were placed each side of the tested specimen and were calibrated so as to exhibit a lateral restraint at the substructure extremities as close as possible to the one exhibited by the actual frame (numerically determined). The so-defined symmetrical substructure is illustrated in Figure 3. The following load sequence was followed during the test :

- The substructure is first subjected to an uniformly distributed load on the internal beams (Beam B in Figure 3); during this loading phase, two jacks placed below column C are locked so as to simulate the presence of the central column.
- In a second step, the support under the central column C is progressively removed by unlocking the jacks; when the latter may be removed, the free deflection of the system is observed. Finally, a vertical force is applied until collapse through a jack located above column C (as seen in Figure 3).

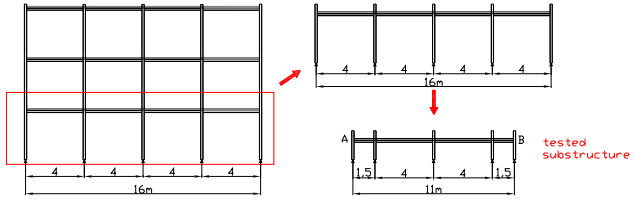


Fig. 2 – From the actual composite building frame to the tested substructure

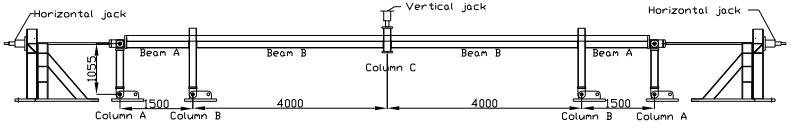


Fig. 3 – Tested substructure with lateral restraints

The evolution of transverse deflection of the beams at the middle of the tested substructure according to the load applied in the jacks is presented in Figure 4. The vertical reaction in the central column which is associated to the uniformly distributed load and to the self-weight of the substructure is equal to 33,5kN as seen in Figure 4 (value of the load at point “O”). After the application of the uniform load, the jacks are unlocked and progressively removed. The system is completely released when a deflection of 29mm is reached. At this stage, first cracks at the vicinity of the external joints are observed and first yielding appears in the column web panel of the internal composite joints (close to column C). This loading step corresponds to part “OA” of the curve presented in Figure 4; from the latter, it can be seen that the structure is still in its elastic range of behaviour when “A” is reached. Then, a vertical load is progressively applied until collapse of the tested specimen. During this stage, two “unloading-reloading” cycles are performed. From point “A” to “B”, yielding progresses until finally a beam plastic mechanism forms at point “B” (plastic hinges in the joints under sagging and hogging moments). During this stage, the cracks in the vicinity of the external composite joints are more pronounced and yielding of some steel joint components is observed (column web and beam flange in compression); also, for the internal composite joint, a separation of the end-plate and the column flange is seen under sagging moment. From point “B” to “C”, a yield plateau develops; the concrete cracks in the vicinity of the external composite joints continue to enlarge and yielding spreads in the steel components. Another important phenomenon to be mentioned is the crushing of the concrete in the internal composite joints. At point “C”, significant membrane forces start to develop in the composite beams as confirmed by the shape of the curve “CD” in Figure 4. When the point “D” is reached, the longitudinal rebars in the external composite joints fail in tension and the concrete at the internal joint is fully crushed; at this moment, the joints work as steel ones (Figure 5) and further plasticity develops in the different components of the internal and external composite joints. At point “D”, a loss of stiffness is observed which is linked to the loss of the longitudinal rebars in the vicinity of the external joints; indeed, when these rebars are lost, the tensile stiffness of the external joints decreases, phenomenon which affects the development of the

membrane forces. At the end of the test (point “E”), a maximum vertical displacement of 775mm is reached for an applied vertical load of 114kN; the associated deformation of the specimen is shown in Figure 4. The maximum horizontal displacement at each side of the structure is equal to 45mm for a horizontal load of 147kN. The test was stopped when cracks occurred in the welds connecting the IPE140 profile to the end-plate in the internal composite joints.

The rotations measured in the joints versus the applied load at the middle of the substructure are reported in Figure 6. The maximum joint rotations reached at the end of the test are equal to 11° (192 mrad) and to 9,5° (166 mrad) for the internal and external composite joints respectively. It can be observed in Figure 6 that:

- the beam plastic mechanism in the substructure develops with formation of plastic hinges in the joints;
- the internal and external composite joints exhibit a similar behaviour;
- the joint rotations are mainly associated to the rotation of the connections.

From the maximum rotation values observed at the end of the test, it may be concluded that the joints exhibited a very ductile behaviour (very high rotation capacity), as expected.

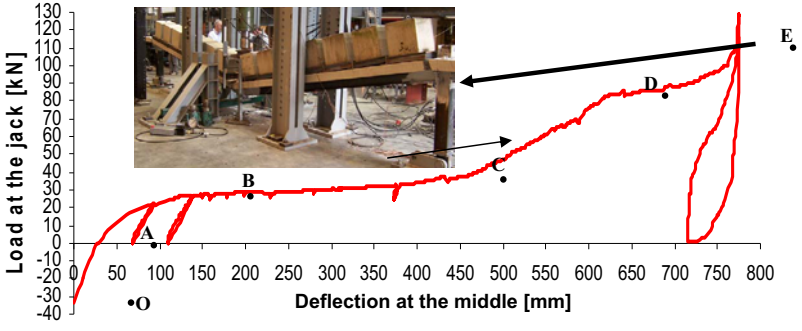


Fig. 4 – Vertical applied load vs. deflection at the middle of the substructure curve

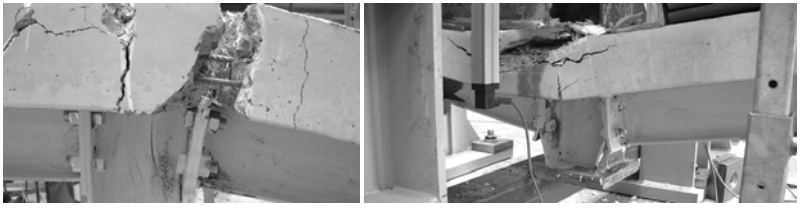


Fig. 5 – Internal and external composite joints at point “D” of Figure 6

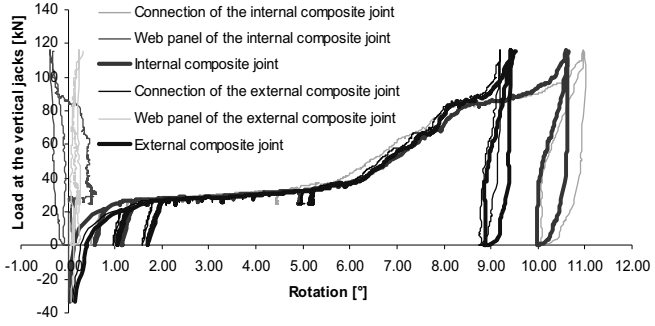


Fig. 6 – Joint rotations vs. applied load at the middle of the substructure

Experimental tests on the substructure composite joint in isolation

The test campaign at Stuttgart University was performed in close collaboration with Liège University. The tested joint configuration (coming from the substructure) is presented in Figure 7. S355 steel was used for the profiles and the end-plates, ductile S450C steel for the rebars and C25/30 for the concrete.

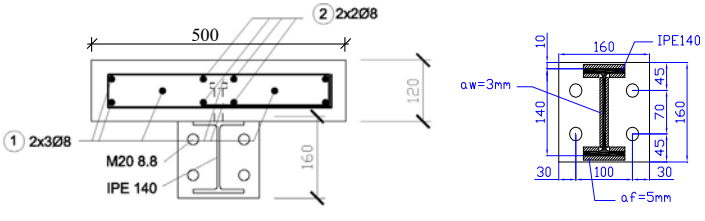


Fig. 7 – Joint configuration tested at Stuttgart University

In total, five tests on this joint configuration have been performed. The objective of these tests was to derive the full M-N resistance interaction curve of the tested joints (in the tensile zone), as illustrated in Figure 8. The joints differ by the loading sequences followed during the tests, as described here after.

Three tests were first performed under hogging moments and axial force:

- one test where the joint is first subjected to hogging moments, until the ultimate resistance in bending is almost reached; in a second step, further to a slight reduction of the applied bending moment, the joint is then subjected to tension forces, until the collapse of the joint (TEST 1);
- two tests with a rather similar loading sequence but in which the bending moments applied in the first step are kept lower than the ultimate bending resistance of the joint (TEST 2 & TEST 3).

Two tests were then performed under sagging moments and axial force; the loading sequences applied were similar to the ones described above, for TEST 4 and TEST 5 respectively.

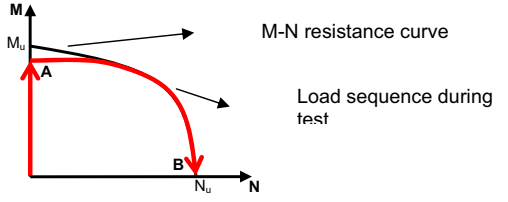


Fig. 8 – M-N resistance curve of the joint to be characterised through the tests

TEST 1 and TEST 4 were initially performed to characterise the behaviour of the tested joint under hogging and sagging moments. The "bending moment vs. joint rotation" curves are presented in Figure 9 while the M-N interaction curves are shown in Figure 10. During the tests, the collapse of the rebars in tension was observed at point A of Figure 10 during TEST 1 and at point A' during the other tests. After the collapse of the rebars, the tested joints may be considered as steel ones. It is observed that, after the resistance loss, the remaining steel components are able to sustain additional tension loads. To pass from the "pure bending moment" loading to the "maximum tensile force" one, only ductile components such as the end-plate and the column flange in bending or the rebars in tension were activated, as expected through the joint design. All the observations made during the experimental tests are presented with more details in [Stuttgart University 2008]. In the next section, the so-obtained experimental results are used to validate the analytical models developed at Liège University.

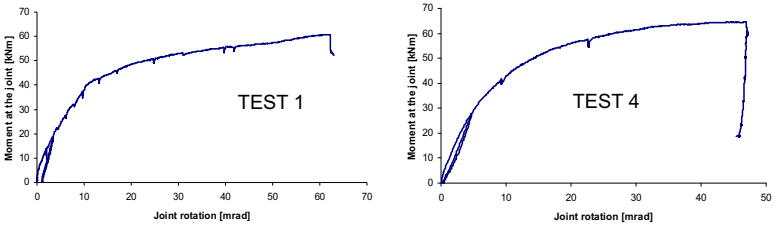


Fig. 9 – Bending moment vs. joint rotation curve obtained through TESTS 1 and 4

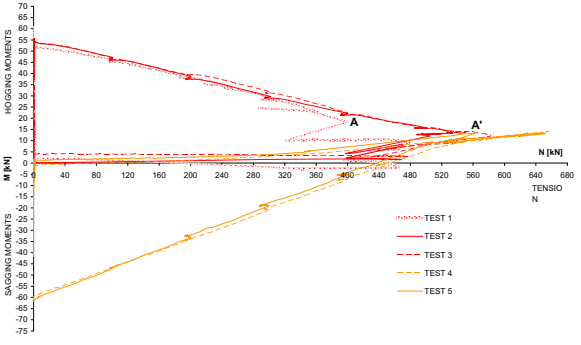


Fig. 10 – Experimental M-N interaction curves

DESIGN MODELS FOR COMPOSITE JOINTS SUBJECTED TO SAGGING MOMENTS AND TO COMBINED BENDING MOMENTS AND AXIAL FORCES

Design model for composite joints subjected to sagging bending moments

In the Eurocodes, the analytical method recommended for the joint design is the "component method". Insufficient information is provided there to predict the behaviour of composite joints subjected to sagging moments. Indeed, no method is available to characterise one of the activated components under such loading: the concrete slab in compression. In recent researches, methods to characterise this component in term of « resistance » have been proposed. Their aim is to define a rectangular cross section of concrete participating to the joint resistance.

The procedure which is proposed in this section combines results of two methods suggested by Ferrario [Ferrario 2004] and Liew [Liew et al 2004] respectively. The combination of these two methods permits to reflect in a more appropriate way how the concrete resists to the applied load in the vicinity of the joint. Also, a formula for the characterisation of this component in term of "stiffness" is proposed.

In the PhD thesis of [Ferrario 2004], a formula is proposed to compute the width of the concrete $b_{eff,conn}$ which has to be taken into account for the joint component "concrete slab in compression":

$$b_{eff,conn} = b_c + 0,7h_c \leq b_{eff}$$

where b_c is the width of the column profile flange, h_c the height of the column cross-section and b_{eff}, the effective width of the concrete/composite slab to be considered in the vicinity of the joint; b_c represents the contribution of the concrete directly in contact with the column flange while $0,7.h_c$ the contribution of the concrete struts which develop in a "strut-and-tie" system (see Figure 11).

In the article of Liew et al, the width of the concrete is taken as equal to the width of the column flange ($b_{eff,conn} = b_c$) and the effect of the concrete struts is neglected.

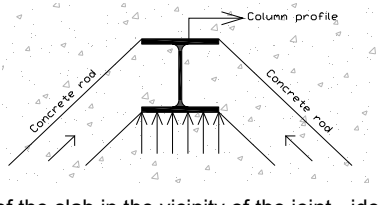


Fig. 11 – Plane view of the slab in the vicinity of the joint - identification of concrete struts in compression under sagging moment

The definition of the width given in [Ferrario 2004] is here preferred as it reflects in a more appropriate way the mechanism which actually develops in the concrete slab, according to the observations reported during experimental tests ([Ferrario 2004] and [Demonceau 2008]).

Another difference between the two methods is linked to the definition of the height of concrete to be considered and to the position of the centre of compression within the joint. In [Ferrario 2004], the centre of compression is assumed to be at mid-

height of the concrete slab while in [Liew et al 2004], the following procedure is given to compute the position of this point:

- the characterisation of the components in tension and eventually in shear is performed according to the rules recommended in the Eurocodes;
- then, the height of the concrete/composite slab contributing to the joint behaviour is computed by expressing the equilibrium of the load developing in the concrete/composite slab in compression with the components in tension or in shear and assuming a rectangular stress distribution in the concrete (equal to $0,85\ f_{ck}/\gamma_c$ in a design). For instance, in the example illustrated in Figure 12, the concrete height to be considered is equal to:

$$z = \frac{F_{Rd,1} + F_{Rd,2} + F_{Rd,3}}{b_{eff,conn}.(0,85.f_{ck}\ /\ \gamma_c)} \le h_{concrete}$$

  where $h_{concrete}$ is the total height of the concrete slab (in case of a composite slab, $h_{concrete}$ is equal to the concrete above the ribs);
- finally, the characterisation of the joint is performed assuming that the centre of compression is situated at the middle of the height of the contributing part of the concrete slab (z).

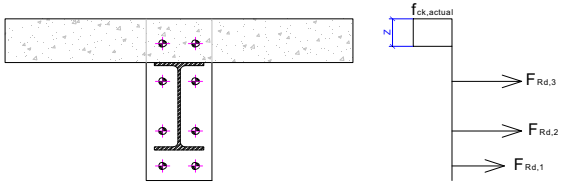


Fig. 12 – Height of concrete to be considered in characterisation of new component

The Liew procedure is selected in the proposed method as it seems to reflect better the observations made during experimental tests [Demonceau, 2008].

So, the resistance of the component "concrete slab in compression" can be computed through the following formula:

$$F_{Rd,CSC} = b_{eff,conn}.z.(0,85.f_{ck}/\gamma_c)$$

The two previously mentioned references only deal with the characterisation of the component "concrete slab in compression" in terms of resistance but no formulae are proposed for stiffness; however, the latter is requested in order to be able to predict the initial stiffness of the joint (and to derive the moment-rotation curve).

If reference is made to [Weynand 1999], a formula is proposed to predict the stiffness of a concrete block against a rigid plate. In the present case, the steel column encased in the concrete slab can be considered as a rigid plate; so, the formula proposed in [Weynand, 1999] is extended for the computation of the stiffness of the component under consideration:

$$k_{csc} = \frac{E_c.\sqrt{b_{eff,conn}.z}}{1,275.E_a}$$

where E_C is the secant Young modulus for the concrete, E_a, the elastic Young modulus for the steel and k_{CSC}, the stiffness of the component "concrete slab in compression" to be considered in the component method.

With the so-defined procedure for the characterisation of the component "concrete slab in compression", the composite joint tested at Stuttgart University under sagging moments (i.e. TEST 4) has been characterised through the component method and the so-obtained moment-rotation curve has been compared to the experimental (Figure 13).

For the analytical computations, the actual material properties (without safety factors) are used. The resistant bending moment M_{Rd} and the initial stiffness $S_{j,ini}$ are computed in full agreement with the component method recommended in the Eurocodes while the ultimate moment M_u, the post-limit stiffness $S_{j,post\text{-}limit}$ and the rotation capacity ϕ_u are computed according to the method proposed in the PhD thesis of Jaspart [Jaspart 1991] (which is in full agreement with the component method), as no specific procedure to compute these properties is proposed in the Eurocodes.

In Figure 13, two analytical curves are reported; they differ by the shape of the non-linear part of the curves. In fact, the non-linear part of the curves is computed according to the rule recommended in the Eurocodes and is a function of a shape factor called Ψ. The proposed value for joints with bolted end-plates is equal to 2.7. If this value is used, it can be observed in Figure 13 that the comparison with the experimental test result is not very satisfactory. Indeed, the initial stiffness and the resistant and ultimate bending moments are in good agreement, but the post-elastic stiffness is under-estimated. The difference is associated to the development of membrane forces in the "column flange in bending" and "end-plate in bending" components, as a result of the significant deformations appearing in the latter when high tensile forces are applied to the joint; this phenomenon is not yet included in the component method as it is actually presented in the Eurocodes. If – just as a trick – the value of the shape factor called Ψ is modified to take implicitly into account this phenomenon (for instance, Ψ equal to 1), it can be observed that a very good agreement is obtained between the analytical prediction and the experimental result. In reality, this is not the right way to proceed and for sure further developments aimed at integrating membrane effects into the resistance model for "column flange in bending" and "end-plate in bending" components are requested; such works have already been initiated at Liège University.

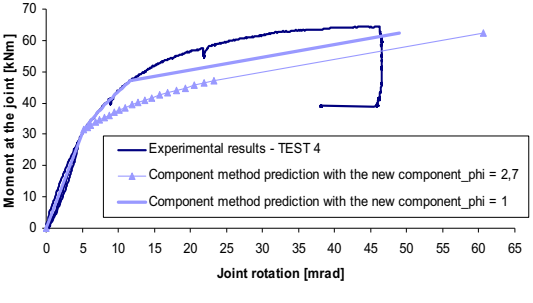


Fig. 13 – Comparisons between analytical and experimental result (TEST 4)

The proposed analytical model has also been validated through comparisons with other available experimental results in [Demonceau 2008].

Design model for composite joints subjected to combined bending moments and axial loads

The presence of axial forces in the beams has an influence on the rotational stiffness, the moment resistance and the rotation capacity of the joints. The component method is presently, in the Eurocodes, limited to the characterisation of joints subjected to small bending moments: the axial force N_{Ed} acting in the joint should remain lower than *5 %* of the axial design resistance of the beam cross-section $N_{pl,Rd}$:

$$\left|\frac{N_{Ed}}{N_{pl,Rd}}\right| \leq 0{,}05$$

This limitation is a fully arbitrary one and is not at all scientifically justified. For instance, this criterion refers to the axial design resistance of the beam cross-section $N_{pl,Rd}$ and not to the design resistance of the joint, what looks quite surprising! If this criterion is not satisfied, the Eurocodes suggest a M-N interaction resistance diagram defined by a polygon joining the four points corresponding respectively to the hogging and sagging bending resistances of the joint in absence of axial force and to the tension and compression axial resistances of the joint in absence of bending.

In a previous study [Cerfontaine 2003], it was shown that the proposed method is quite questionable. So, in [Cerfontaine 2003], an improved design procedure, based on the component method concept, has been developed to predict the response of steel joints subjected to combined axial loads and bending moments. In [Demonceau 2008], the design procedure of Cerfontaine is extended to composite joints and validated through comparisons with the experimental test results obtained at Stuttgart University (Figure 14).

The computation details to obtain the analytical M-N resistance interaction curve are presented in [Demonceau 2008]. In Figure 14, two analytical curves are reported: one named “plastic resistance curve” which is based on the plastic resistance of the joint components, and one named “ultimate resistance curve” which refers to the ultimate strength of the latter.

In Figure 14, the computed analytical curves are in very good agreement with the experimental results. Indeed, the experimental curves are between the plastic and ultimate analytical resistant curves what is in line with the loading sequence followed during the tests. It is also seen in Figure 14 that the maximum tensile load which can be supported by the joint is underestimated by the analytical procedure. This difference can be justified by the fact that the proposed analytical procedure does not take into account the appearance of membrane forces in the components "column flange in bending" and "end-plate in bending", as a result of the large deformation of these components when high tensile loads are applied to the joint. This phenomenon has already been previously identified when studying the response of the joints subjected to sagging moments.

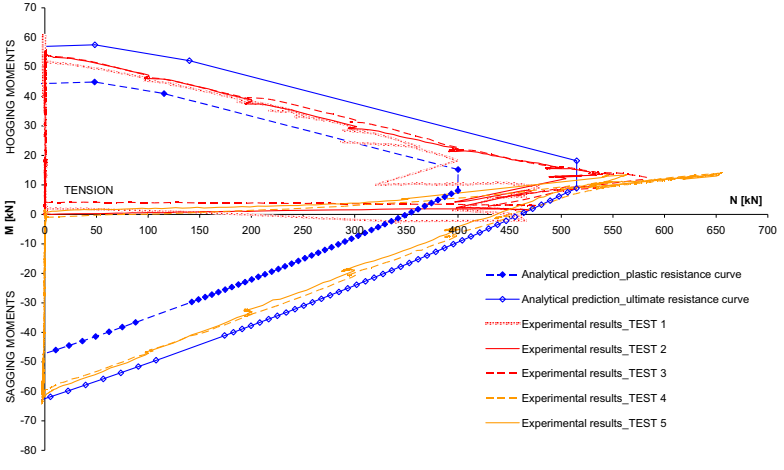


Fig. 14 – Comparison of the resistance interaction curves

CONCLUSIONS

In the present paper, experimental and analytical investigations conducted at Liège University and related to the response of composite joints have been presented. A specific attention has been devoted to the behaviour of the joints located in beams in which significant membrane forces developed further to the loss of a column in the building, as a result of an exceptional event (impact, explosion …). In particular, two analytical models dedicated to the prediction of the response of composite joints subjected to sagging moments and to combined bending moments and axial forces, situations not actually covered by the actual codes, have been briefly described and their validity has been demonstrated through comparisons with experimental test results.

REFERENCES

BS 5950-1:2000 (2001), “Structural use of steelwork in building – Part 1: Code of practice for design – Rolled and welded sections”.

Cerfontaine, F. (2003), Study of the interaction between bending moment and axial force in bolted joints (in French). PhD thesis presented at Liège University.

Demonceau, J.-F. (2008), “Steel and composite building frames: sway response under conventional loading and development of membranar effects in beams further to an exceptional action”, PhD thesis presented at Liège University.

EN 1991-1-1 (2002). “Eurocode 1: Actions on structures – Part 1-1: General actions – Densities, self-weight, imposed loads for buildings”. European committee for standardization, April 2002.

EN 1994-1-1 (2004), “Eurocode 4: Design of composite steel and concrete structures – Part 1-1: General rules and rules for buildings”. European committee for standardization, December 2004.

ENV 1991-2-7 (1998), “Eurocode 1: Basis of design and action on structures – Part 2-7 : Accidental actions due to impact and explosions”, final draft, June 1998.

Ferrario F., 2004, “Analysis and modelling of the seismic behaviour of high ductility steel-concrete composite structures”, PhD thesis presented at Trento University.

Jaspart J.P. (1991), “Study of the semi-rigidity of beam-to-column joints and its influence on the resistance and stability of steel buildings”, PhD thesis, Liège University, in French.

Liew R.J.Y., Teo T.H. and Shanmugam N.E., 2004, “Composite joints subject to reversal of loading – Part 2: analytical assessments”, Journal of Constructional Steel Research, pp. 247-268.

prEN 1991-1-7 (2004), “Eurocode 1 – Action on structures – Part 1-7: General actions – Accidental actions”, final project team draft (stage 34), 9 July 2004.

Stuttgart University (2008), “Robust structures by joint ductility - Final report of the RFCS project N° RFS-CR-04046”, to be published.

UFC 4-023-03 (2005), “Unified Facilities Criteria (UFC) - Design of buildings to resist progressive collapse”, Department of Defence, USA. 25 January 2005.

Weynand K. (1999), “Column bases in steel building frames. COST C1 – Semi-rigid behaviour of civil engineering structural connections”, Luxembourg.

Behavior of Columns in Composite *CES* Structural System

Hiroshi Kuramoto
Department of Architectural Engineering, Graduate School of Engineering
Osaka University
Suita, Japan
kuramoto@arch.eng.osaka-u.ac.jp

ABSTRACT

New composite structural systems consisting of only steel and concrete, the concrete encased steel (CES) structures, have been proposed by the author in order to realize simplification and cost reduction in construction works for SRC structures. Experimental studies on CES columns using fiber reinforced concrete (FRC) have been carried out to investigate the seismic performance, in which the main test parameters were the section shape of encased steels, the type and content of fibers used for FRC and the applied axial load levels. The experimental results showed that CES columns had excellent seismic performance with a stable spindle-shape hysteresis characteristic and less damage. This paper introduces the summary of the experimental studies carried out in past about eight years with the advantage of CES structure.

INTRODUCTION

Reinforced concrete encased steel structures referred to as SRC structures are typical composite structural systems consisting of steel and reinforced concrete (RC) and possess an excellent earthquake resistance with high capacities and deformability. However, SRC structures have a weak point in the construction due to complex works of both steel and RC. In order to realize simplification and cost reduction in construction works for SRC structures, concrete encased steel structures consisting of only steel and concrete (see Figure 1), hereafter referred to as CES structures, have been proposed by the author (Kuramoto et al. 2000). In the feasibility study to examine the structural performance of CES columns, it was conformed that damages of the columns with an increase of lateral deformation such as cracking and crushing in concrete can be reduced by using high performance fiber reinforced cementitious composites (HPFRCC) instead of normal concrete. Moreover, the hysteretic characteristics of the CES columns were almost the same as those of SRC columns. However, significant reduction of the initial stiffness in the shear versus story drift responses and the development of drying shrinkage in the cover concrete were observed in the CES columns due to use of HPFRCC without aggregates. In addition, the production and casting of HPFRCC were very difficult due to less workability.

In order to solve these problems in the columns using HPFRCC, use of fiber reinforced concrete (FRC) for CES members have been proposed, and the structural performance of the columns (Kuramoto et al. 2002, Adachi et al. 2003, Taguchi et al. 2006) and the beam-column joints (Matsui and Kuramoto 2007, Kuramoto et al. 2008) have been investigated.

The experimental studies on CES columns using FRC are introduced with the advantage of CES structures in this paper.

ADVANTAGE OF CES STRUCTURES

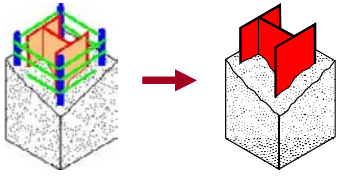
CES structure using FRC is a simple composite structural system consisting of only steel and FRC, as shown in Figure 1. This "simple structure" has excellent seismic performance and can make construction cost and time reduced. In addition, CES structure is widely used for several purposes, from low to high-rise or from small-scale to large-scale buildings, and the pre-cast design and construction of CES structure will be easier than those of SRC structure.

The structural advantage of CES structure can be illustrated using a simple example shown in Figure 2. The figure shows the cross-section of a column in 1st story of 13-story SRC building and the cross-sections of RC and CES columns which have the same flexural strengths as the SRC column. SRC column has a cross section of 900 mm square (Fc36), 2-H-600×300×16×28 (SN490), 12-D29 (SD390). If it is compared with RC column using the same concrete strength, 24+8-D38 (SD490) reinforcing bars are needed and the column section should be 900 mm square. For CES column, on the other hand, if built-in steel 2-H-700×450×16×28 (SN490) is used, the cross section will be 800 mm square (Fc36) which is smaller than that of SRC column.

Thus, CES column can be designed with smaller section in comparison with the SRC column having the main reinforcement in the four corners. If the reinforcing bars in SRC column are eliminated, the concrete cover will be smaller while the size of the steel will be larger in order to keep the same flexural strength of the column. Also, it is possible to use the wider steel flange for this purpose. Therefore, the effective utilization of steel is one main advantage of CES structural system.

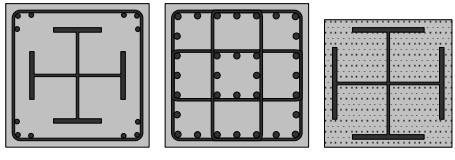
Another advantage of CES structure is that the structure can be applied for various construction types, as shown in Figure 3. Basically, CES structural system consists of CES columns and CES beams (see Figure 3(a)). In addition, the CES structural members can be designed easily with other types of structural members such as CES columns with steel-concrete composite (SC) beams or steel beams, as shown in Figure 3(b). Also, it is possible to use RC and SRC beams if it is considered the method to fix the main reinforcement of beams with CES columns. Furthermore, it is also possible to use CES beams in steel structures, SRC structures and CFT structures (see Figure 3(c)).

In real structure, CES structure can be applied not only for the whole building but also for a part of building (see Figure 3(d)). In addition, not only the pure CES frame can be constructed, but many types of earthquake-proof elements can be also installed easily to CES structure such as steel brace, shear wall, damper, etc, as shown in Figure 3(e).



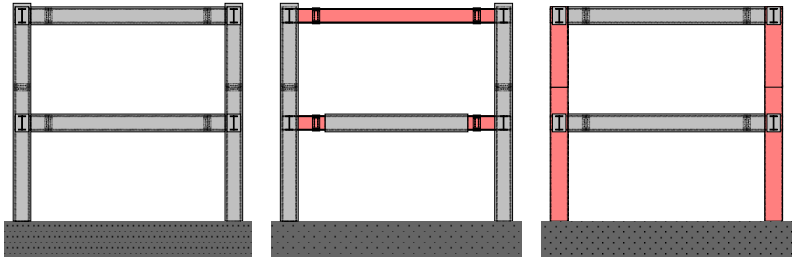
SRC CES

Figure 1 –Concrete Encased Steel

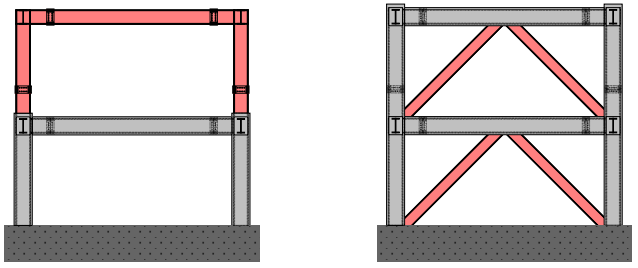


(a) SRC (b) RC (c) CES

Figure 2 – Comparison of column section



(a) CES Column＋CES Beam (b) CES Col.＋SC or S Beam (c) SRC or CFT Col.＋CES Beam



(d) Lower CES Structure＋Upper S Structure (e) CES Structure＋Braces, etc.

Figure 3 – Examples of construction with CES structural members

STRUCURAL CHARACTERISTICS OF CES COLUMNS

Experimental Program

(1) Specimens and material used

A total of nine composite columns including seven CES columns using FRC, one CES column using normal concrete and one SRC column were tested to investigate the structural performance of the columns (Kuramoto et al. 2000, Kuramoto et al. 2002, Adachi et al. 2003, Taguchi et al. 2006). The dimension and detail of specimens are shown in Figure 4 and Table 1.

The tests are divided into three phases. The first phase test was for Specimens SRC, SC, VF1, VF2 and SF2 in which the behavior of CES columns using normal concrete and FRC with different fiber was compared with that of SRC column. The second phase test was conducted to investigate the effect of applied axial force using Specimens VF2N3, VF2N5 and VF2NV. The third phase was to investigate the behavior of CES column using single H-section steel for Specimen CESU.

In the first phase test, Specimens SC, VF1, VF2 and SF2 which are CES columns had the same dimension and steel details. The different was only the concrete used. For Specimen SC, a normal concrete was used while FRC with Poly-vinyl Alcohol fiber (PVA fiber: RF4000) of 1.0% and 2.0% in the volume content ratios were used for Specimens VF1 and VF2, respectively. For Specimens SF2, on the other hand, FRC with stainless steel fiber (SS fiber: F430D) of 2.0% was used. All specimens

had columns with a 400mm square section and 1,600mm height, and the height-depth ratio was 4.0. Steels encased in each column had a cross shape section combining two H-section steels (i.e., double-H section steel) of 300x150x6.5x9 mm. In Specimen SRC, the cross section was similar with the other 4 above specimens, however, the smaller size of H-section steel, 250×125×6×9 mm, was used due to the present of reinforcing bars.

Specimens VF2N3, VF2N5 and VF2NV which were used in the second phase test had the same cross section, while axial forces with different loading pattern were applied. Due to less axial loading capacity of the loading apparatus used, the cross section of these three specimens had become smaller, 330mm square, compared with previous specimens with a 400 mm square section. The column height of 1,320

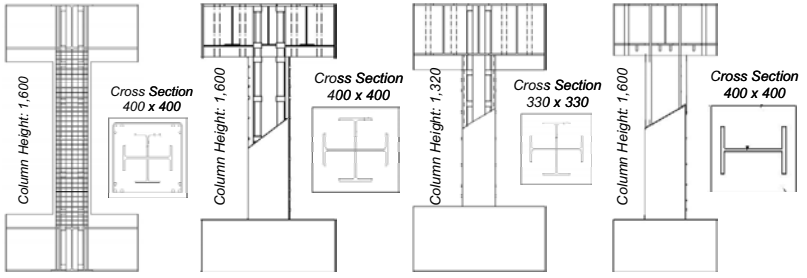


Figure 4 – Test specimens

Table 1 – Test program

Specimen			SRC	SC	VF1	VF2	SF2	VF2N3	VF2N5	VF2NV		CESU
Reinforcement fiber		Type	-		PVA fiber (RF4000)		SS fiber (F430D)	PVA fiber (RF4000)				
		Volume content	-		1.00%	2.00%	2.00%	2.00%				1.50%
Column Section	Width	b(mm)	400					330				400
	Depth	D(mm)	400					330				400
Concrete	Comp. Strength	σ_B(MPa)	35.5	37.3	52.3	55.5	65.3	46	38			33.5
	Young Modulus	E_c(GPa)	24.1	26.1	26.2	26.3	26.5	29.8	27.4			-
Column height		h(mm)	1600					1320				1600
Shear-span ratio		a/D	2									
Built-in Steel	Shape		Double H section (+ shaped)									H section
	Section size		250×125 ×6×9	300×150×6.5×9				250×125×6×9				300×220 ×10×15
	Flange Yield Strength	σ_{fy}(MPa)	300	323	337			335				289
	Web Yield Strength	σ_{wy}(MPa)	347	412	364			393				299
Applied Axial Force		Loading	Constant							Varying		Constant
		N(kN)	1100					1500	2380	2380	-910	1600
Axial yield		$bD\sigma_B$(kN)	5680	5968	8368	8880	10448	5009	4138			5360
		N_o(kN)*	7186	8125	9994	10414	11699	6670	5959			6906
Axial force ratio		$N/bD\sigma_B$	0.19	0.18	0.13	0.12	0.11	0.30	0.58	0.58	-0.22	0.30
		N/N_o	0.15	0.14	0.11	0.11	0.09	0.22	0.40	0.40	-0.15	0.17

* : $N_o = {}_cN_{cu} + {}_sN_{cu} = {}_cr_u \cdot \sigma_B \cdot {}_cA + {}_s\sigma_y \cdot {}_sA$

mm was planned to be the height-depth ratio of 4.0. FRC with PVA fiber of 2.0% in the volume content ratios and double-H section steel of 250×125×6×9 mm were used for all specimens.

On the other hand, Specimen CESU in the third phase test had the same cross section and column height as specimens in the first phase test, while FRC with PVA fiber of 1.5% and single H-section steel of 300×220×10×15 mm were used.

All CES specimens don't have shear connector on the encased steel to enhance stress transferring capacity between FRC and steel.

(2) Test set-up and loading procedures

In the first phase test, the specimens were loaded lateral cyclic shear forces by using two horizontal hydraulic jacks, which were installed in parallel each other for one direction, and a constant axial compression of 1,100kN by using four vertical actuators, as shown in Photo 1. The axial compression ratios, $N/(b \cdot D \cdot \sigma_B)$, were 0.19 for Specimen SRC, 0.18 for Specimen SC, 0.13 for Specimen VF1, 0.12 for Specimen VF2 and 0.11 for Specimen SF2, respectively. The loads were applied through a steel frame attached at the top of a column that was fixed to the base. The four vertical actuators to apply the constant axial compression were also used to keep the column top beam parallel to the bottom beam, so that the column would be subjected to anti-symmetric moments.

In the second phase test, the loading apparatus used was the same as in the first phase test. Specimens VF2N3 and VF2N5 were subjected to constant axial load of 1,500 kN and 2,380 kN ($N/(b \cdot D \cdot \sigma_B)$=0.3 and 0.58), respectively. On the other hand, Specimen VF2NV was subjected to varying axial load of ranging from -910 kN to 2,380 kN ($N/(b \cdot D \cdot \sigma_B)$=-0.22 to 0.58). This specimen represented an external column in the lower story of 20-story frame building. The applied varying axial force was given by $N = 0.1 \cdot N_i \pm Q$, where N_i = Initial axial force and Q = applied shear force.

Specimens CESU in the third phase test was tested by using new loading apparatus shown in Photo 2, which was almost the same function and performance as the apparatus used in the first and second phases. Constant axial load of 1,600 kN ($N/(b \cdot D \cdot \sigma_B)$=0.3) was applied to the specimen.



Photo 1 – Test set-up for Phases 1 and 2



Photo 2 – Test set-up for Phase 3

The same loading pattern was employed in all tests. The incremental loading cycles were controlled by drift angles, R, defined as the ratio of lateral displacements to column height, δ/*h*. The lateral loading sequence consisted of two cycle to *R* =0.005, 0.01, 0.015, 0.02, 0.03, 0.04 rad. and half cycle to R=0.05 rad., then the test was terminated.

STRUCTURAL PERFORMANCE OF CES COLUMNS USING FRC

Failure Mode and Shear-Drift Response

The yield and maximum strengths and the corresponding drift angles in the positive loadings for each specimen are listed in Table 2. The yielding of each specimen was assumed when the first yielding of steel flange was observed. The shear versus drift angle responses and crack patterns after loadings for each specimen were compared in Figure 5 and Photo 3, respectively. In the Figure 5, dotted lines express the flexural strengths, Q_{fcal}, calculated by the strength superposition method (AIJ 2001) in which the flexural strengths contributed by FRC and steel are cumulatively increased. The dotted lines are drawn by considering the P-δ effect due to the loading system employed.

In the first phase test, Specimen SRC showed relatively stable behavior with spindle shaped hysteresis loops which is a marked characteristic of composite column although a little deterioration in load carrying capacity after attaining to the maximum strength was observed. Bucking of reinforcing bars at the both column ends was also observed in the loading cycle of R of 0.04 rad. due to spalling of cover concrete caused by compressive failure in critical hinge regions, as shown in Photo 3.

Table 2 – Yield and maximum strengths and the corresponding drift angles in positive loading

Specimen		SRC	SC	VF1	VF2	SF2	VF2N3	VF2N5	VF2NV	CESU
at Yielding	R_y (rad./100)	1.3	1.0	1.1	1.0	1.1	1.0	1.0	1.4	0.6
	Q_y (kN)	620	527	612	608	643	425	415	448	592
at Max. Capacity	R_{max} (rad./100)	1.5	1.0	1.5	1.5	2.0	1.5	1.2	1.5	1.3
	Q_{max} (kN)	638	527	689	703	738	481	439	454	734



SRC SC VF1 VF2 SF2 VF2N3 VF2N5 VF2NV CESU

Photo 3 – Crack modes of specimens after loading

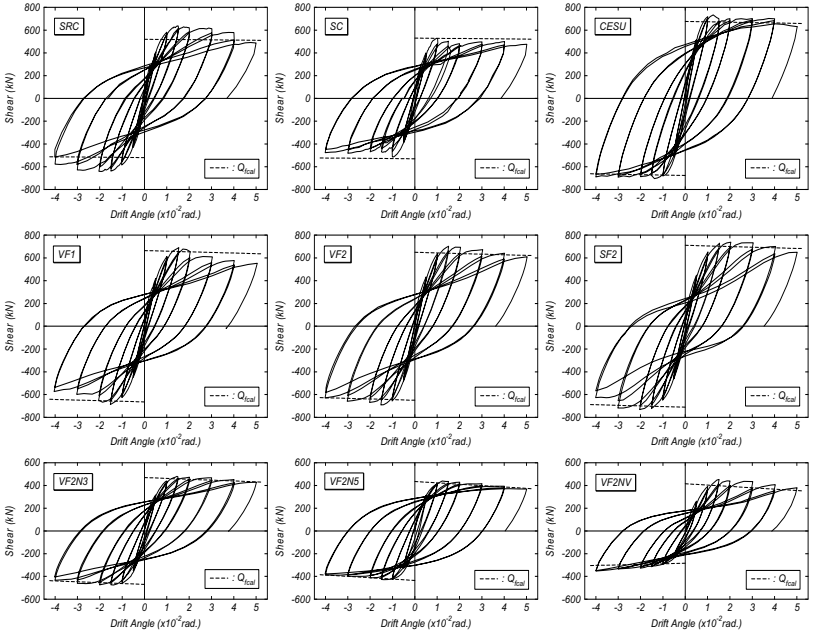


Figure 5 – Shear versus drift angle responses

In Specimen SC which is a CES column with normal concrete, shear cracks occurred in the central part of the column at an early stage, R of 0.005 rad., due to no transverse reinforcement. Then, after attaining to the maximum strength with yielding of steel flange in the both end of the column at R of 0.01 rad., significant propagation of the shear cracks, the spalling of cover concrete and a little deterioration in load carrying capacity were observed with an increase of drift angles. As shown in Figure 5, however, the column showed relatively stable behavior with spindle shaped hysteresis loops as well as Specimen SRC although the maximum strengths in both positive and negative loadings were somewhat less than the calculated flexural strength.

In CES column specimens with FRC, on the other hand, crack modes of concrete were quite different from those in Specimens SRC and SC.

In Specimen VF1 with PVA fiber of 1.0% in the volume content ratio, flexural cracks occurred first at R of about 0.003 rad. at both top and bottom of the column. With an increase of drift angles, the flexural cracks propagated and thin shear cracks dispersed all over the column. The specimen showed stable and spindle shaped hysteresis loops with a little deterioration in load carrying capacity after attaining to the maximum capacity at *R* of 0.015 rad. Specimen VF2 with PVA fiber of 2.0% showed slightly better hysteresis loops without distinct deterioration in load carrying capacity than those of Specimen VF1. Specimen VF2 also showed better propagation of cracks in cover concrete that means better performance in the damage limitation than Specimen VF1. Specimen SF2 with SS fiber of 2.0% showed

high structural performance with the highest maximum capacity among the tested specimens. As shown in Photo 3, the spalling of cover concrete due to the propagation of cracks, crushing in concrete and so on was not observed until *R* of 0.05 rad. in these three specimens.

In the second phase test, the compressive failure and fall down of concrete cover did not occurred for all specimens, Specimens VF2N3, VF2N5 and VF2NV, as seen in Photo 3. In all specimens, moreover, there was concrete unfilled part near the bottom of the column after concrete casting which was repaired by concrete mortar, and it is observed that most of flexural deformation concentrated with the development of significant flexural cracks on the repaired part. In Specimen VF2N5 subjected to high constant axial force, the significant vertical cracks, which are compressive cracks, occurred. On the other hand, for Specimen VF2NV which is subjected to varying axial force, many small shear cracks dispersedly occurred.

Specimen VF2N3 had the highest maximum strength compared with other two specimens. It is considered as one of the reasons that the concrete strength of this specimen was higher than that of other two specimens, even though the lowest axial force ratio ($N/(b \cdot D \cdot \sigma_B)$ =0.32) was applied among these 3 specimens. In this specimen, the maximum strength of 481kN was reached at R of 0.015 rad. After attaining to the maximum strength, the load carrying capacity decreased slightly. However, if the P-δ effect due to the behavior of the loading apparatus is considered, it is seen that there is almost no decrease of the strength. After R of 0.03 rad. at the second cycle, the shape of hysteresis curve was changed to be the pinching shape gradually.

Specimen VF2N5 showed larger spindle shaped hysteresis loops than those of Specimen VF2N3. In this specimen, the maximum strength of 439 kN was reached at R of 0.012 rad. Also, if the P-δ effect due to the loading system, there was little strength degradation after attaining to the maximum strength, which is almost similar with Specimen VF2N3 showing a stable behavior. However, the axial deformation reached to 10mm at R of 0.04 rad. The elastic behavior of axial deformation was observed until R of 0.01 rad., then, the compression deformation increased rapidly. It was observed that the development of axial deformation in this specimen was the highest among these three specimens tested.

In Specimen VF2NV which is subjected to varying axial force, the column had the maximum strength of 453.5kN at R of 0.0151rad. When tensile axial force was applied, moreover, the maximum strength of 349 kN was reached at R of -0.04rad. On tensile axial force side, the spindle shaped hysteresis loops was observed, while the curves showed a pinching shape on compressive axial force side. For axial deformation, tensile deformation increased with the increase of drift angles on tensile axial force side, but, on compressive axial force side, the peak axial deformation of 1.3 mm was reached at R of 0.015rad. and then, the deformations tended to be constant. The axial deformation versus drift angle response of Specimen VF2NV is shown in Figure 9(b) with the analytical results.

As mentioned earlier, there was a repaired part near the bottom of the column for each specimen where the flexural-shear and axial deformations were intensive in this portion. However, the shear versus drift angle responses showed a stable behavior.

In Specimen CES-U, cracks occurred in the connections between the column and loading stubs at R of 0.005 rad. in the tension side of the top and bottom of the

column, and simultaneously flexural cracks occurred in the tensile region of the top and bottom of the column due to bending moments. These flexural cracks propagated and then, shear cracks appeared on the top and bottom of the column at R of 0.01rad. Cracks due to compression were also observed in this stage. Moreover, flexural and shear cracks increased with an increase of drift angles, and the increase of compression cracks was observed significantly. The specimen showed almost elastic behavior until the yielding of steel at R of 0.013 rad. in positive loading and -0.014 rad. in negative loading. After attaining to the maximum strength, little deterioration in load carrying capacity was observed until R of ±0.04 rad. At R of 0.05 rad., however, the strength degradation was somewhat observed.

Simulating Behavior of CES Column

The analytical method used for simulating the behavior of CES columns is a common fiber idealization that explicitly models the column by dividing its cross section into a number of small areas or filaments, as shown in Figure 6. Each fiber is assumed to be uniaxially stressed and to behave according to assumed hysteresis stress-strain characteristics of its constituting materials, as explained below. For this analysis, the cross section of column was divided into 40 elements to obtain a higher accuracy. This method assumes that the plane sections to remain plane, thus implying full compatibility between the steel and FRC components of a composite cross section.

The analysis is controlled through a series of small steps by curvature or displacement history in terms of X-axis. With the axial strain at the center of the cross section, $\Delta\varepsilon_0$ and the curvatures along in terms of X-axis, $\Delta\phi_x$, the axial strain at the fiber element of i, $\Delta\varepsilon_i$ is found according to $\Delta\varepsilon_i = \Delta\varepsilon_0 + y_i \Delta\phi_x$, where y_i is the distance from the X-axis to the i-th fiber element on the section. Considering the equilibrium of the section, axial force ΔN and bending moment ΔM are written as $\{\Delta N, \Delta M\}^T = [K] \{\Delta\varepsilon_0, \Delta\phi_x\}^T$, where [K] is stiffness matrix. In this analysis, ΔN, ΔM and $\Delta\varepsilon_0$ were calculated by considering the mechanical properties of steel and FRC, as $\Delta\phi_x$ was the input data.

In this section, analytical results for Specimen VF2NV subjected to varying axial forces are shown as an example.

The hysteretic model used for the steel was the tri-linear model proposed by Shibata (1982), as shown in Figure 7. Yield strengths in both compression and tension are assumed to be equal. Post yield stiffness E_{S3} and reduced stiffness due to the Bauschinger effect E_{S2} are taken as 1/200 and 1/5 of the elastic stiffness E_{S1}, respectively. The incline of stiffness changing line C is taken as -1/200 of E_{S1}.

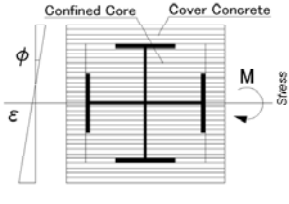


Figure 6 – Fiber model

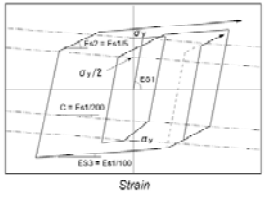


Figure 7 – Steel model

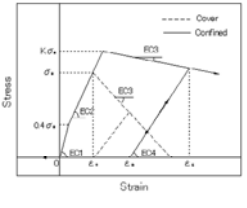


Figure 8 – Concrete model

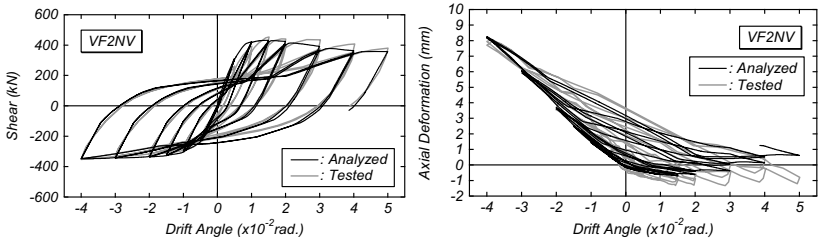


Figure 9 – Comparison between analytical and experimental results for Specimen VF2NV

The hysteretic models of concrete adopted were the divided linear models shown in Figure 8 for both cover and core concrete. For cover concrete, an initial linear stiffness up to 40 percent of concrete strength E_{C1}, a reduced linear stiffness until peak stress has reached E_{C2}, and the slope of failing linear branch E_{C3}, were given as $1.6\sigma_B/\varepsilon_{c0}$, $E_{C1}/3$ and $E_{C1}/5$, respectively, according to the results of concrete cylinder tests, where σ_B is the concrete cylinder strength and ε_{c0} is the compressive strain at the stress peak, which was taken as -0.003. For core concrete, on the other hand, the same values of E_{C1} and E_{C2} were adopted as the cover concrete although E_{C3} was taken as $E_{C1}/80$ for Specimens VF2NV. Furthermore, a magnification factor of concrete strength K for confined core concrete was considered as 1.25 for the specimen. Liner stiffness at unloading E_{C4} for both cover and core concrete was taken as $\sigma_E/(\varepsilon_E-\varepsilon_R)$, where σ_E and ε_E were the stress and strain at an unloading point on the envelope curve, and ε_R was the residual strain ($\varepsilon_R=5\varepsilon_E^{1.5}$ and $|\varepsilon_R| \leq 4|\varepsilon_E|/5$).

The shear versus drift response for the columns were obtained assuming an antisymmetric distribution of bending moments along the column height, with the inflection point at mid-height. Considering the experimental results for curvature distribution along the column height, the relation between curvature and drift angles, ϕ and R, was assumed as ϕ = 3.3 R/L for Specimens VF2NV, although in elastic assumption the relation is defined as ϕ = 6 R/L, where L is the column height. Moreover, the axial deformation, δ_v, was calculated by assuming as $\delta_v = \varepsilon_0 * L/2$.

Figure 9 shows the analytical results of the shear versus drift angles response and the axial deformation versus drift angle response. As can be seen in both responses, the analytical results showed a satisfactory agreement with the experimental results. Thus, the hysteresis behavior of CES columns can be simulated precisely by a common fiber analysis because the columns are simple composite structural members consisting of only steel and FRC.

CONCLUSIONS

Experimental studies on CES columns using FRC conducted by the authors in past about eight years were introduced with the advantage of CES structures. The principle conclusions obtained from the studies can be drawn as follows.

1) CES structure is a simple composite structural system consisting of only steel and FRC, which can make construction cost and time reduced. CES structure can be widely used for various scaled buildings from low to high-rise or from small to large-scale. And also the pre-cast design and construction of CES structure will be easier than those of SRC structure.

2) CES structural system can be applied for not only CES frame buildings but also various mixed building types such as consisting of CES columns with other structural type of beams, CFT columns with CES beams, CES frame with braces or shear walls, etc.

3) CES columns using FRC have almost the same structural performance as SRC columns which possess an excellent earthquake resistance with high capacities and deformability.

4) Use of FRC makes the easy restoration of CES columns possible because the damages in cover concrete of the columns due to flexural and shear cracks are relatively light even at the large story drifts.

5) The hysteresis behavior of CES columns can be simulated precisely by a common fiber analysis because the columns are simple composite structural members consisting of only steel and FRC.

REFERENCES

Adachi. T., Kuramoto, H., Kawasaki, K. and Shibayama, Y. (2003). "Study on Structural Performance of Composite CES Columns Using FRC Subjected to High Axial Compression", *Proceedings of Japan Concrete Institute*, Vol. 25, No. 2, pp. 289-294. (in Japanese)

AIJ (2001). "*Standard for Structural Calculation of Steel Reinforced Concrete Structures",* Architectural Institute of Japan.

Kuramoto H., Kabeyasawa T. and Shen F-H. (1995)." Influence of axial deformation on ductility of high-strength reinforced concrete columns under varying triaxial forces." *ACI Structural Journal, Vol.* 92, No. 5, pp. 610-618.

Kuramoto, H., Takahashi H. and Maeda M. (2000), "Feasibility Study on Structural Performance of Concrete Encased Steel Columns using High Performance Fiber Reinforced Cementitious Composites". *Summaries of Technical Papers of Annual Meeting, AIJ*, Vol. C-1, pp.1085-1088. (in Japanese)

Kuramoto, H., Adachi, T. and Kawasaki, K. (2002). "Behavior of Concrete Encased Steel Composite Columns Using FRC." *Proceedings of Workshop on Smart Structural Systems Organized for US-Japan Cooperative Research Programs on Smart Structural Systems (Auto-Adaptive Media) and Urban Earthquake Disaster Mitigation*, Tsukuba, Japan, pp.13-26.

Kuramoto, H., Matsui, M., Nagata, S. and Fujimoto, T. (2008). "Structural Performance of Exterior Beam-Column Joints for Composite CES Structural Systems", *Journal of Structural and Construction Engineering (Trans. of AIJ)*, No.624, pp.235-242. (in Japanese)

Matsui, T. and Kuramoto, H. (2007), "Three Dimensional Non-Linear FEM Analysis of CES Beam-Column Joints", *Proceedings of 8th Pacific Conference on Earthquake Engineering*, Singapore, Paper No. 4A127 (CD-ROM).

Shibata M. (1982)," Analysis of Elastic-Plastic Behavior of Steel Brace Subjected to Repeated Axial force." *International Journal of Solids and Structures*, Vol. 8, No. 3, pp. 217-228.

Taguch. T., Nagata, S., Matsui, T. and Kuramoto, H. (2006). "Structural Performance of CES Columns Using Single H-shaped Steel", *Proceedings of Japan Concrete Institute*, Vol. 28, No. 2, pp.1273-1278. (in Japanese)

CYCLIC TESTS ON RC- STEEL SHEAR PLATE COMPOSITE WALL SYSTEM APPLICABLE IN BEAM SPANS WITH LARGE OPENINGS

Toko Hitaka
Disaster Prevention Research Institute, Kyoto University
Kyoto, Japan
toko.h@ay2.ecs.kyoto-u.ac.jp

Andres Jacobsen
Department of Architecture Engineering, Faculty of Engineering, Kyoto University
Kyoto, Japan
andres.jacobsen@kt5.ecs.kyoto-u.ac.jp

ABSTRACT

A new hysteretic damper system utilizing slit steel shear plates and out-of-plane restraining wood panels is proposed. In this system, the upper half of the damper is a slit shear plate, whereas the lower half is a base wall. The slit shear plate and the wooden restraining panels are attached through bolts designed to prevent shear force transfer to the wood panels. Cyclic loading tests were performed to investigate seismic performance of the proposed system. The restrained specimens mostly behaved in stable manner. While the local out of plane deformation around the slit ends were not restrained, the wood panels were effective to restrain global out-of-plane deformation of shear plates.

INTRODUCTION

Application of hysteretic dampers to buildings is popular in Japanese structural designs nowadays. The topic of this research is the development of a hysteretic damper system utilizing slit steel shear plates stiffened by a set of wood panels.

Use of panels for stiffening shear plates is effective, because the panels restrain the entire plate's transverse movement, unlike stiffeners. This method has been applied for stiffening of steel braces, where precast concrete panels were used (Inoue et al., 1992, 1993). The panel stiffening approach has also been applied for slit shear plates (Hitaka, et al. 2003), where the panel-stiffening method proved to

be effective. However the panels were heavy and fabrication of bolt holes in the mortar panels required special caution. In addition, cracking of the panels occurred at relatively small drift levels due to limited deformation capacity of the mortar. These problems may be solved by changing the material from mortar to wood.

In the research presented in this paper, a total of eight specimens for the proposed damper (referred to as Slit Wall Damper, hereafter) was tested under cyclic loading. In the following, behavior of slit shear plates is briefly explained. Then the design of the Slit Wall Dampers is explained. Lastly, the hysteretic behavior of the specimens and the effect of stiffening are investigated.

BEHAVIOR OF SLIT SHEAR PLATES

The slit shear plates (Hitaka, et al. 2003, 2007), as shown in Figure 1, are made of a steel plate with a series of slits. When subjected to seismic input, the steel plate between the slits behaves as a series of flexural links, which undergo large flexural deformations relative to their shear deformation. Neglecting the slit width, the elastic stiffness (K_{wt}) and the ultimate strength (Q_{wtu}) of the slitted shear plate are calculated using the following equations:

$$K_{wt} = \frac{1}{\frac{\kappa h}{GBt} + \frac{(l+b)^3}{Etb^3} \cdot \frac{m}{n}} = \frac{1}{1 + \frac{G}{\kappa E} \cdot \frac{(1+\alpha)^3}{\alpha} \cdot \beta} \cdot K_{wo} \tag{1}$$

$$Q_{wtu} = \alpha^2 \left(1 - \cos\frac{\sqrt{3}}{\alpha}\right) \cdot Q_{wty} = \alpha^2 \left(1 - \cos\frac{\sqrt{3}}{\alpha}\right) \cdot \frac{\sqrt{3}}{2\alpha} \cdot Q_{wo} \tag{2}$$

where E is the Young's modulus, G is the shear modulus, κ is the shear deformation shape factor for rectangular section (=1.2), α is the shear span aspect ratio (=l/b where l is the length and b is the width of flexural links), and β is the ratio of total link length in the vertical direction to the wall height (=ml/h), K_{wo} and Q_{wo} are the shear stiffness and shear yield strength of the steel plate without slits ($K_{wo} = \kappa$ h/GBt and $Q_{wo} = \sigma_y Bt/\sqrt{3}$), and Q_{wty} is the yield strength of the slit shear plate ($Q_{wty} = ntb^2\sigma_y/2l$) .Other geometric notations are defined in Figure 1. In addition, the ultimate strength point (displacement at which the resisting force of a slitted shear plate reaches Q_{wtu}) is calculated by the following equation,

$$\delta_{wtu} = \frac{Q_{wtu} \cdot h}{GBt} + \frac{88}{9} \cdot (\alpha + 1)^2 \cdot b\varepsilon_y \tag{3}$$

where ε_y is the yield strain of the steel plate. To ensure that the steel plate works as an effective damper device, it is necessary that yielding initiates at small lateral deformations. From this viewpoint, slit designs that achieve small Q_{wty} / K_{wt} is desirable. Equations 1-2 suggest that reducing the value of β is the most effective way to achieve this goal.

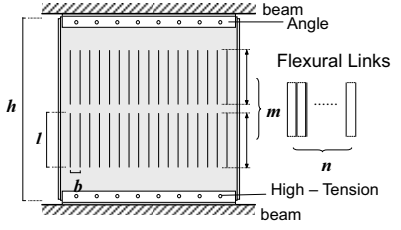


Fig. 1 – Slit Shear Plate.

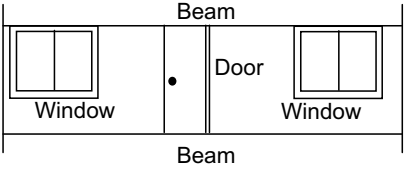


Fig. 2 – Design of a Wall of the Prototype Building

DESIGN OF SLITTED SHEAR WALLS

In Japanese design practice, hysteretic dampers are designed such that the dampers, after yielding at small drift levels, e.g. less than 0.4%, behave in a stable manner to more than 2% drift. In addition, the dampers are typically designed to resist about 10-20% of the building's base shear. In the proposed system, the slit shear plates are designed to reach these goals for a 12 story building.

Moreover, the damper was designed for a wall adjacent to window and door openings, as shown in Figure 2, typically seen in a frame facing isles. In these walls under seismic excitation, the base walls beneath the window restrain the in-plane deformation of the lower portion of the walls, hence shear deformation is concentrated in the upper portion of the walls. In the Slit Wall Damper, the slit shear plate is applied only in the upper portion of the Wall Damper. In such a design, β in Equations 1 is reduced, and large initial stiffness and small yield drift can be achieved. However, for dampers installed in the mid beam span to yield at 0.4% story drift level, the dampers must yield when the shear deformation angle within the damper reaches about at about 0.2% drift, because the damper will rotate as the connected beams bend. The dampers were designed considering this effect.

The test specimens were fabricated in a 1/2 scale, with a total height and width of 1100mm and 800mm, respectively. The upper 600mm portion is the slit shear plate made of a 2.3mm thick Japanese standard SS400 steel plate. The slits, i.e. m, b, l in Figure 2, were designed as shown in Figure 3. Two series of tests (Series SP and DW) were conducted with a total of 8 specimens, as summarized in Table 1.

The specimens for Series SP are 800mm tall slit shear plates, with 100mm bolt connection portion at both upper and lower ends. These specimens, which do not include base walls, were planned for investigating the effect of wood panel stiffening. In contrast, DW series specimens are 1100mm tall in total, with a 600 mm tall slit shear plate and a 500mm tall base wall with two types of base wall design.

Test parameters for SP series specimen are thickness of wood panels (0, 12, 24mm) and steel plate thickness (the standard thickness, 2.3mm, and 1.2mm). Nineteen SS400 8mm diameter steel bolts are used to attach the wood panels to the steel plates in each specimen. The bolts are passed through perforations in the steel plates. These perforations are oversized with respect to the bolt diameter in order to avoid transference of the lateral force to the wood panel during loading.

Damper wall specimens comprise a 2.3mm thick slit shear plate attached to 24mm thick wood panels, and a base wall. In one specimen, DW-CP, the steel plate extends through the base wall to the lower beam, and the plate is embedded in a reinforced concrete (RC) wall with the plate's lower end fillet welded to the beam through a fin plate. Configuration of the RC wall is similar to that of base walls in RC and SRC condominiums. The reinforcement ratio of the specimen's base wall (0.2%) is approximately two times of that of condominiums'. In another specimen, DW-WP, the slit shear plate is connected to a 6mm thick steel plate through intermittent fillet weld, which extends to the lower beam. The entire plate is covered with approximately 24mm thick wood panels. A steel plate thicker than the slit shear plate was used for the plate in the base wall, to minimize shear deformation in the base wall and overall out of plane deformation.

Mechanical characteristics of the steel used for the walls are shown in Table 2. Considering the relatively small punching strength of the plywood panels, 2.3 mm thick, 30mm long square washers were used for the bolts. Wood panels are made of 5-12 layers thick plywood. Flexural stiffness (EI_w) and yield moment (M_{max}), normalized with respect to width, are shown in Table 3. These values were

calculated based on the relation between the load (P) and the vertical displacement at the loading point (δ) obtained experimentally with the setup shown in Figure 4. The P-δ relation for wood panels was linear elastic until M_{max} was reached. At this point the plywood layers separated and the moment decreased.

LOADING AND MEASUREMENT

Loading conditions are shown in Figures 5(c) and 5(d). The drift was increased by 3mm after completing two cycles of loading until 24mm of story drift was achieved.

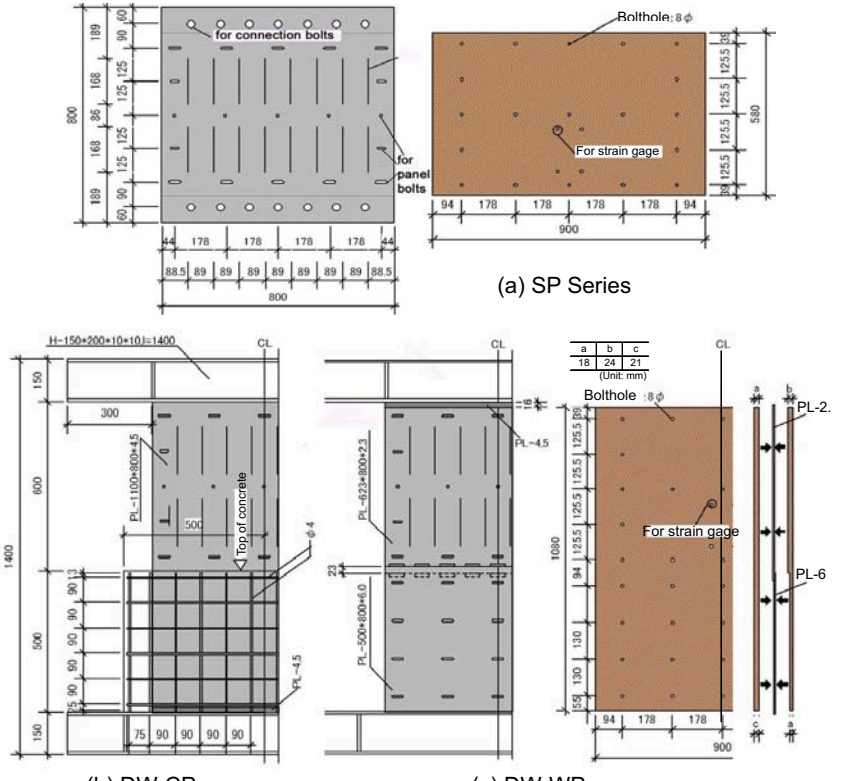


Fig. 3 – Specimens.

Table 1 – Specimens

Specimen	Steel plate thickness	Wood panel thickness	Calculated strength Q_{wtu}	Measured strength (kN)	Calculated stiffness K_{wt}	Measured stiffness (kN/mm)
SP23-NST	2.3	-	115	42	56	67
SP12-WP12	1.2	12	71	81	32	37
SP12-WP21	1.2	21	71	76	32	28
SP23-WP18	2.3	18	123	131	60	76
SP23-WP24	2.3	24	123	118	60	58
DW-WP	2.3	18	123	113	48	61
DW-CP	2.3	18	123	132	60	75

Table 2 – Material Properties.

Steel Plate	σ_y (N/mm^2)	σ_u (N/mm^2)	Eelongation(%)
PL-1.2	297	370	32.2
PL-2.3	278	359	40.0

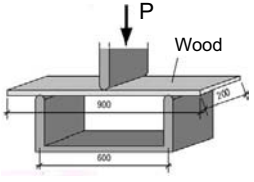
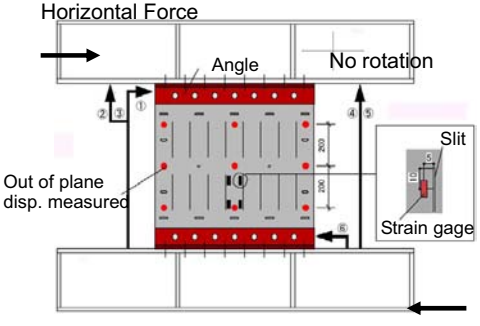


Fig. 4 – Measurement of Flexural Properties.

Table 3 – Flexural Properties of Wood Panel

Wood Panel	EI_w	M_{max}
WP12	0.31	0.18
WP18	1.4	0.21
WP21	2.9	0.23
WP24	4.1	0.91



(a) SP Series (b) DW Series

Fig. 5 – Measurement.

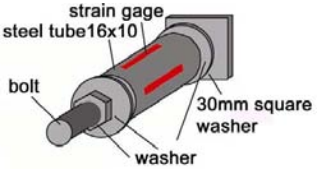


Fig. 6 – Load Cell for Measuring Bolt Tension.

Lateral and vertical displacements were measured using transducers as shown in Figure 5. Out of plane displacement was measured for all the specimens in 9 different locations, also shown in Figure 5. In addition, axial force in the bolts was measured by the load cell shown in Figure 6.

EXPERIMENTAL RESULTS

Behavior of Slit Shear Plate specimens

The horizontal force – drift relations for each specimen are shown in Figure 7. In Figure 7, the horizontal dashed line shows the ultimate force Q_{wtu} calculated with Equation 2; the vertical dashed line shows the drift angle corresponding to δ_{wtu} calculated with Equation 3. In addition, Table 1 shows Q_{wtu} and the initial stiffness K_{wt} calculated with Equations 1 - 2. Also, Figures 8 –10 shows pictures of different element specimens after the conclusion of the experiment.

In the specimen without out of plane restraining, the initial stiffness is almost the same as (K_{wt}), although after the drift (Δ) reached 2mm, shear buckling occurred as shown in Figure 8(a), and the strength decreased. In contrast, specimens with out-of-plane restraining behaved in a stable manner up to Δ=24mm. These specimens sustained similar behavior and deformation (Figure 8(b)), independent of the thickness of the steel plate and wood panel. Plastic behavior initiated at a drift of 2mm and Q_{wtu} was closely related to δ_{wtu}. After yielding, further hysteretic loops were of stable slip type with small strength deterioration and out of plane deformation.

The slip behavior of the specimens is likely to have been induced by out of plane buckling of the steel plate in the vicinity of the end of the slits, as shown in Figure 9(a). This type of out of plane deformation is called local out of plane deformation hereafter, as opposed to the global transverse deformation observed for the non-stiffened specimen. In a slit shear plate, yielding occurs in the vicinity of slit ends, and the buckling wavelength occurred inside this plastic zone, because the steel plates are thin (less than 2.3mm). The data, measured from strain gages attached to both faces of the steel plate at the end of the slits, suggest that such local buckling initiated at the same time as the slip behavior began.

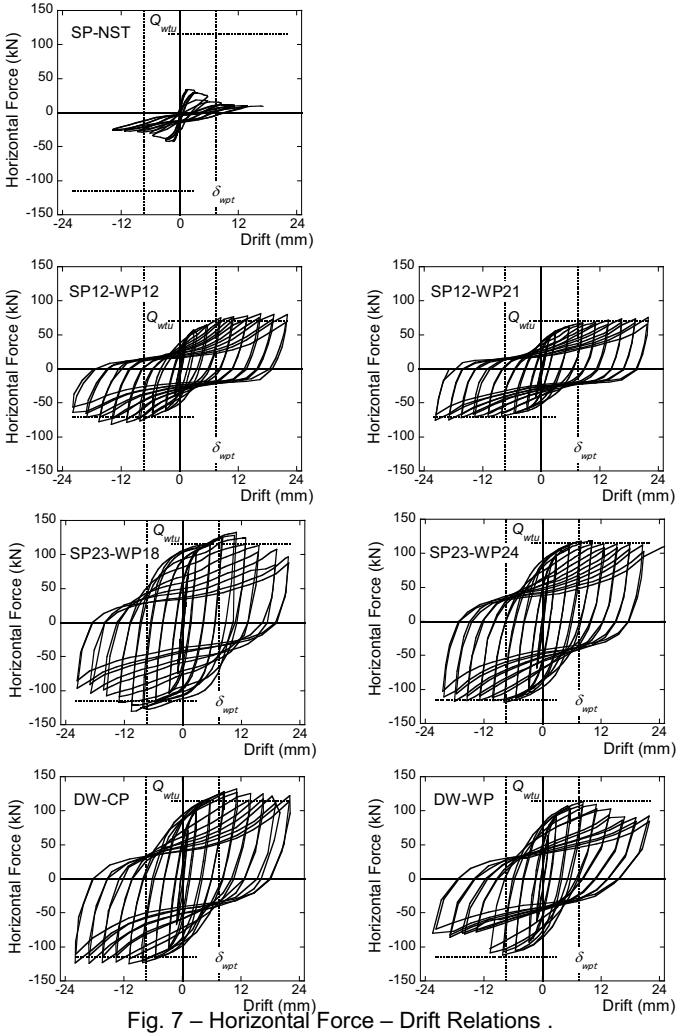
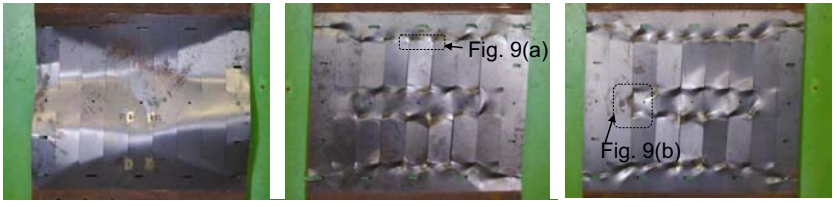


Fig. 7 – Horizontal Force – Drift Relations .

Apart from this observation, cracks initiating from the slit ends as shown in Figure 9(b) and fractures initiating at the bolt perforation advancing to the side of the steel plate, as shown in Figure 10(b) were found after the tests in almost all specimens. However, there was almost no strength deterioration caused by these events, presumably because the wood panels remained undamaged and provided sufficient transverse stiffening to restrain global out of plane deformation.

The behavior of specimens SP23-WP18 and SP12-WP12 differed from the other specimens in some aspects. In specimen SP23-WP18 the hysteresis loop was fat until Δ=12mm, but at Δ=16mm, the strength noticeablly deteriorated. Also, as shown in Figure 9(b), cracks developed at mid-height between the end of the slits on both upper and lower ends. In specimen SP12-WP12, when loading in the negative direction to a drift larger than 16mm, the strength also deteriorated slightly. In this specimen, the wood panels, whose thickness (12mm) is the smallest of all specimens, sustained damage in the vicinity of the corner bolts as shown in Figure 10(a) at Δ=9mm. In this region of the steel plate, large compression forces are induced by the bending moment on both upper and lower ends of the wall. Out of plane deformation of these portions of the plate led to the damage in the surrounding wood panels.



(a) SP23-NST (b) SP23-WP24 (c) SP23-WP18

Fig. 8 – Slit Shear Plates of SP Series Specimens after Testing.



(a) Local out of plane deformation (b) Fracture and cracks SP23-WP18 (left) and DP-WP (right)

Fig. 9 – Deformation, Fracture and Cracks around Slit Ends.

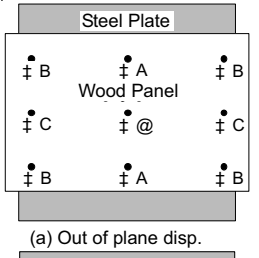


(a) SP12-WP12 (b) Steel around edge bolts (c) DP-WP

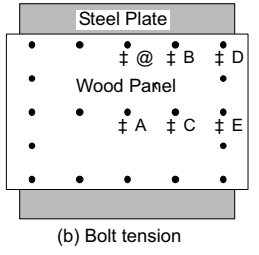
Fig. 10 – Deformation Concentration.

Behavior of Damper Wall specimens

The behavior observed for specimen DW-CP was similar to the one observed for SP23-WP24. In the base wall, cracking mainly occurred on the sides of the steel plate. On the other hand, for DW-WP specimen, strength at δ_{wtu} is 9% less than Q_{wtu} . In this specimen, a larger out of plane displacement occurred as explained in the next section, and local out of plane deformation was observed only in the uppermost links after testing (Figure 10(c)). Figure 9(c) shows crack initiation at the end of the slits for specimen DW-WP, where extensive local out of plane deformation was observed, crack length was around twice as long as for specimen E-WS-WP. The strength of this specimen probably degraded as cracks advanced.



(a) Out of plane disp.



(b) Bolt tension

Fig. 11 – Meas. Locations.

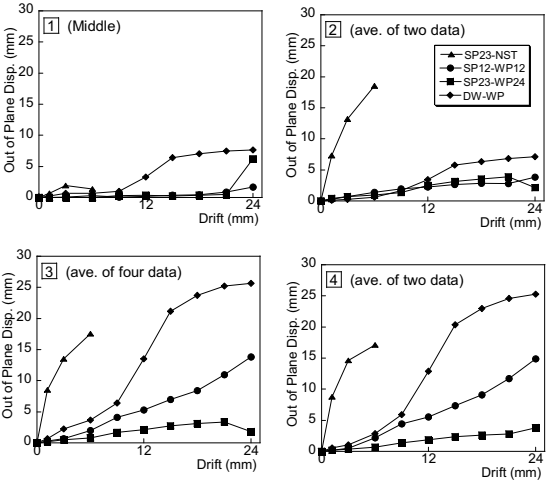


Fig. 12 – Out of Plane Displacements.

Out-of-plane deformation

Figure 12 shows out of plane deformation plots for each cycle of specimens SP23-NST, SP12-WP12, SP23-WP24 and DW-WP. Of the out of plane deformations of the wood panel, measured in 9 points shown in Figures 5, classification was done according to equivalence of the locations where displacements were measured, e.g. (1) – (4) shown in Figure 11(a). The displacements shown in Figure 12 are the average of the displacements at peak of the first cycle within each group.

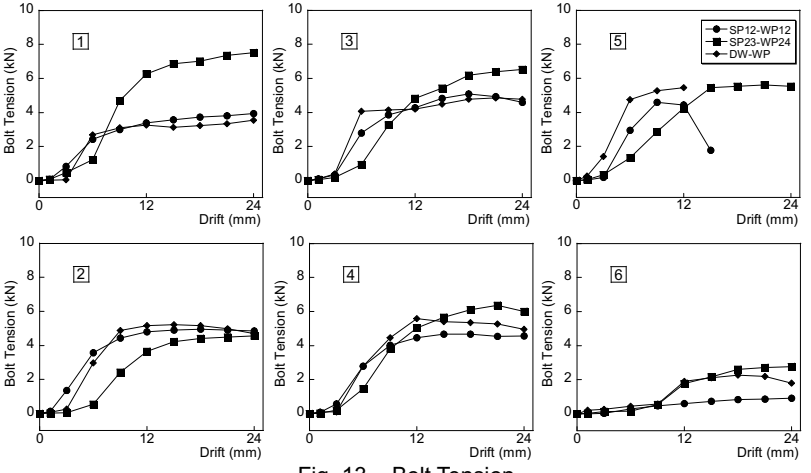


Fig. 13 – Bolt Tension.

In specimen SP23-NST (no restraining), out of plane deformation of all points but the center (1), is remarkably larger than that in the other specimens. This phenomenon was observed as soon as out of plane deformation initiated. Already at Δ=6mm, out of plane deformation of SP23-NST is 10 mm larger than those of the other specimens. For stiffened specimens, the out of plane deformation is small until Δ=12mm; for specimen SP12-WP12, which exhibits the largest out of plane deformation, deformation at Δ=12mm is less than 5 mm. For SP12-WP12, the damage in the wood panel caused a deformation increase at locations 2 and 4. However out of plane deformation at the remaining locations, as well as for specimen SP23-WP24, is less than 3 mm. The out of plane deformations of specimens SP12-WP21, SP23-WP18 and E-SW-WP, not shown in Figure 12, was similar to specimen SP23-WP24.

Unlike the rest of the specimens, out of plane deformation of specimen DW-WP is not evenly distributed in the horizontal direction, but the progression is similar, as is shown in Figure 12. Out of plane deformation of specimen DW-WP is larger than the corresponding deformation of the other specimens, specially for $\Delta \geq$ 12mm. Out of plane deformations in the left and right edges of the shear wall (3 and 4) are particularly large.

Bolt tension

Figure 13 shows the maximum force in the bolts for each deformation level for specimen SP12-WP12, SP23-WP24 and DW-WP. Bolt forces are measured at all 19 points, and Figure 11(b) shows the location of the six bolts presented. Bolt tensions of other specimens showed behavior similar to that of SP23-WP24.

As shown in Figure 13, the bolt forces increase after $\Delta \geq 3$mm and the increment stalls around Δ =12mm. In specimens SP12-WP12 and SP23-WP24, bolts labeled 1 and 4 (center) and 5 (four corners) show large forces, in bolt 6 forces are approximately a 30% smaller. Out of plane deformation of specimens SP12-WP21 and SP23-WP18 was similar to specimen SP23-WP24, indicating no relation between the bolts' tension and steel plate or wood panel thickness.

On the contrary, in specimen DW-WP, bolt 5 shows large forces from the early stages of loading, but the forces of the other bolts are the same or less when compared to other specimens. In the plots, horizontal dashed line indicates maximum forc of the bolts except 1 and 6, but those forces are particularly small compared to 1 and 6. As mentioned in the previous section, out-of-plane deformation of specimen DW-WP was concentrated in the upper side shear links. The residual local out of plane deformation was larger in this specimen than the others. Thus, the bolt tensions at the same drift level were larger in DW-WP.

CONCLUSIONS

1. Slit steel plates yield at small drift (2mm) and the behavior does not present major strength deterioration until the drift exceeds 21mm. The deterioration is slight unless fracture or large cracks are formed close to slit ends.
2. Out-of-plane restraining by wood panels provides sufficient stiffening to restrain global (shear) buckling for the proposed application. However, it is difficult to restrain local out of plane deformation in the plastic zone around the slit ends. This local deformation caused slip after the ultimate strength is reached (0.6 - 0.7%).
3. The hysteretic behavior of the bolts is independent of the thickness of the steel plate and wood panel and is smaller in the midsection of the specimen. Particularly large forces are observed in the bolts near the edge of the shear links where out-of-plane deformation is most significant.

REFERCENCES

[1] Inoue, K., et al. 1992. “Bracing Design Criteria of the Reinforced Concrete Panel Including Unbonded Steel Diagonal Braces.” *J. Struct. Constr. Eng.*, 432, 41-49. (in Japanese).

[2] Inoue, K., et al. 1993. “Stiffening Design at the Edge of the Reinforced Concrete Panel Including Unbonded Steel Diagonal Braces.” *J. Struct. Constr. Eng.*, 443, 137-146. (in Japanese).

[3] Hitaka. T. and Matsui C. 2003. “Experimental Study on Steel Shear Wall with Slits.” *J. Struct. Eng.*, 129, 586-595.

[4] Hitaka. T. and Matsui C. 2007. “Cyclic Tests on Steel and Concrete-filled Tube frames with Slit Walls.” *Earthquake Engineering and Structural Dynamics.*, 36. 6, 707-727.

PERFORMANCE EVALUATION OF INNOVATIVE HYBRID COUPLED CORE WALL SYSTEMS

Gian A. Rassati
Department of Civil and Environmental Engineering – University of Cincinnati
Cincinnati, OH 45221-0071 USA
gian.rassati@uc.edu

Patrick J. Fortney
Cives Engineering Corporation – Cives Steel Co.
Roswell,, GA USA
pfortney@cives.com

Bahram M. Shahrooz
Department of Civil and Environmental Engineering – University of Cincinnati
Cincinnati, OH 45221-0071 USA
bahram.shahrooz@uc.edu

Paul W. Johnson, III
Department of Civil Engineering – Clemson University
Clemson, SC 29634 USA
pwjohns@clemson.edu

ABSTRACT

The paper presents an ongoing investigation of the cyclic performance of steel coupling beams in hybrid coupled core wall systems. Coupled core wall systems offer remarkable lateral strength and stiffness, and taking advantage of the favorable cyclic behavior of steel coupling beams makes the best use of all materials employed. Moreover, the inherent characteristics of the systems considered are ideal for an application of performance-based design approaches. Preliminary results are discussed from the standpoint of seismic performance, demonstrating the advantages of steel coupling beams and innovative details of coupling beams, conceived with reparability in mind, are presented. The design of a prototype structure is discussed, and a two-phase experimental campaign is described. It is anticipated that a hybrid, pseudo-dynamic analysis of the coupled core wall systems considered will show that the use of steel coupling beams in a performance-based design framework can deliver economical and safe structures with remarkable strength, stiffness, and ductility.

INTRODUCTION

Coupled core wall systems are used with increasing frequency in mid- to high-rise residential, office, and hotel structures, combining concrete flat plate floor systems with reinforced concrete wall lateral force resisting systems, with coupling beams connecting the individual wall piers, creating a frame-like lateral force resisting system. This structural system has the advantage of limiting floor-to-floor heights,

and of providing larger lateral stiffness and resistance than what would be achieved by using isolated wall piers. The presence of properly detailed coupling beams, that traditionally are diagonally-reinforced concrete beams, causes the overturning moment resisting mechanism to change from flexural action of the wall piers alone to a combination of flexural action and the action of a tension/compression couple developing in the wall piers. As a result, a coupled core wall system provides the structure with exceptional lateral stiffness, and can be detailed so that strength and ductility can be also maximized. As a consequence of this overturning moment resisting mechanism, the wall piers are subject to large axial forces that result from the beam shears developing due to the rotational restraints at the beam-wall interface. This behavior is further complicated by structural irregularities and in situations where the contribution of higher modal responses is important. For optimum performance, coupling beams must be adequately strong and stiff, behave in a ductile manner, and exhibit significant energy absorbing characteristics. Additionally, wall piers need to be designed to ensure plastic hinge formation in most of the coupling beams over the height of the structure, followed by plasticization of the base of each wall pier. Limitations of the current design codes [Fortney et al. 2007a] and lack of a sufficient knowledge base for cases most commonly encountered in practice effectively limit a more widespread use of coupled wall systems despite their structural and architectural advantages.

Hybrid coupled core wall systems are an attractive alternative to traditional reinforced-concrete coupled core wall systems, which offer enhanced lateral stiffness, with the added advantages of more stable hysteretic behavior, larger ductility, and the potential for ease of reparability. The use of a steel coupling beam to transfer forces between wall piers has been investigated in the past [Fortney et al. 2007a,b; Harries et al. 1992 and 1997; Shahrooz at al. 1992 and 1993; Shahrooz and Gong 1998]. Large-scale experiments have shown that a properly detailed steel coupling beam will offer a higher peak-to-peak stiffness, and a larger amount of dissipated energy when compared to traditional diagonally-reinforced concrete coupling beams [Fortney et al. 2007a]. The expected post-elastic behavior of a hybrid coupled core wall system is similar to that of traditionally reinforced-concrete coupled core wall systems: plastic hinges, in shear or flexure, are supposed to form along the height of the building, followed by yielding of the base of each of the wall piers.

One aspect that has been mostly overlooked in the development of traditional coupling beam codes and detailing rules is the post-event reparability of the structure, which has a considerable impact on owner's costs, both in terms of insurance and of potential loss of revenue. Hybrid coupled core wall systems are the ideal structural typology for developing reparable, damage tolerant lateral resisting structures, which can be successfully employed in mid- to high-rise buildings in seismic areas.

This paper presents an ongoing study focused on the development of steel coupling beams to be used in hybrid coupled core wall systems, which offer superior stiffness, strength, ductility, and energy absorbing characteristics, and are additionally easily reparable. The experimental and analytical program planned for this study is described first, followed by a description of the test specimens, with an in-depth discussion of the design philosophy envisioned for these innovative coupling beams. Some conclusions are drawn, and the future direction of research is briefly discussed.

PRELIMINARY WORK

The following discussion presents recommendations and experimental data resulting from work conducted at the University of Cincinnati [Fortney et al. 2007a, b].

DESIGN PHILOSOPHY OF STEEL AND FUSE COUPLING BEAMS

Shear and Moment Capacity of SCB and Main Sections of FCB: The steel coupling beam is designed per the ANSI/AISC 341-05 and ANSI/AISC 360-05 provisions [ANSI/AISC 2005a,b] The beam is sized based on the factored moment and factored shear expected from the applied load to the beam.

The relationship between moment and shear is according to ANSI/AISC 341-05, Sect. 15.3, and is given in Equation (1), where, l is the clear span of the beam, M_P is the plastic moment capacity of the beam and, V_P is the plastic shear capacity of the beam. This relationship is based on the provisions for the spacing of intermediate web stiffeners based on maximum expected beam rotations. Equation (1) is applicable for rotations smaller or equal to 0.08 radians.

$$l \le \frac{1.6M_P}{V_P} \tag{1}$$

The required plastic section modulus, Z_x, is determined both for the plastic moment and for the relationship given above. The beam is then sized to ensure that the provided plastic section modulus was equal to or greater than the largest required plastic section modulus.

Shear Capacity: The thickness of the web is checked to ensure that the thickness satisfies both the required plastic section modulus and the required plastic shear capacity. Web Stiffeners are designed according to Sect. 15.3 of ANSI/AISC 341-05.

Embedment Length: The length of embedment of the beam into the shear wall is established based on laboratory tests conducted by Harries, Gong, and Shahrooz [2001a, b]. The embedment length is determined by Equation (2):

$$V_U = 0.9 f_b \beta_1 b_f L_E \left[\frac{(0.58 - 0.22\beta_1)}{(0.88 + \left(\frac{a}{L_E} \right))} \right] \tag{2}$$

where, V_U is taken as $1.5V_P$ and, L_E is the embedment length into the shear wall.

Fuse Link: The fuse is designed to have the same overall dimensions as that of the main section. Web shear yielding is the desired failure mechanism for the fuse. To assure web shear yielding in the fuse, the plastic moment capacity of the fuse is set to be greater than or equal to the plastic moment capacity of the main beam. The fuse is detailed so as to govern the design of the entire system. The main beam sections are detailed to have a plastic shear capacity 40% larger than that of the fuse. This is done to assure that yielding occurs in the fuse in shear without damaging the components of the main beams, or their connection to the fuse. The maximum length of the fuse is controlled by the required size of the splice plates. The fuse must be long enough to accept the splice plates and also allow for a web area between two stiffener plates with an aspect ratio less than or equal to 4.0. Figure 1 illustrates the required length of the fuse.

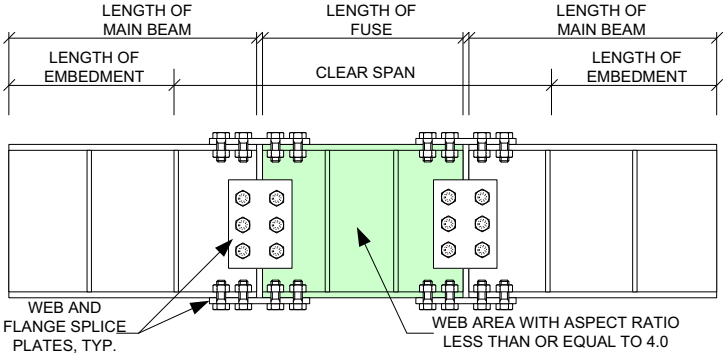


Fig. 1. Elevation of a steel coupling beam with a fuse link.

Flange and Web Splice Plates: The flange and web splice plates are sized to assure that the moment of inertia of the splice is greater than or equal to the moment of inertia of the main beam. The connection of the main beam to the fuse is designed to be a slip critical connection. The size, spacing, and required pretension force of the bolts at the flange and web splices are determined per the AISC Specifications. The SCB and FCB coupling beams are designed based on past recommendations as discussed in the Introduction to this paper.

Test results of a SCB specimen are then compared and contrasted to the results of a steel coupling beam fitted with a central fuse (FCB). To evaluate the feasibility of fuse replacement, two different fuses were tested. The first fuse coupling beam (FCB-2) utilized a fuse with a shear capacity of 50% of that of the main sections (see Figure 1). The test protocol of FCB-2 was to load up to a point where the fuse sufficiently yielded while the main sections remained elastic. At this point, the loading was stopped, and the damaged fuse was replaced with a new fuse (FCB-1) which had a shear capacity of 70% of the main sections. Upon replacing the fuse, testing recommenced from the beginning and continued until failure.

The target beam shear for both specimens was taken as 534*kN* which corresponds to the maximum design shear for the prototype building chosen as representative of a practical CCW system. Since the shear capacities of the FCB-2 fuse and the FCB-1 fuse was taken as 50% and 70%, respectively of the outer sections, the target shear capacities of the FCB-2 and FCB-1 fuses were 267*kN* and 374*kN* , respectively. The beams had a clear span equal to 914*mm*, a flange width of 127*mm*, and a depth of 356*mm*. The reinforcement used in the wall piers was the same for both specimens. The specified material strengths used for design of the specimens was also the same for all specimens. Grade 60 steel (F_y=414*MPa*) was used for all reinforcing bars, the specified strength of the concrete was 35*MPa*, and the steel plate material used to fabricate the built-up I-shape coupling beams was A36 steel (F_y=248*MPa*).

Steel Coupling Beam (SCB) Design: The SCB specimen was designed and detailed following the design methodology as described in [Fortney et al. 2007a]. Since rolled I-shapes rarely have the required cross-sectional properties needed, a built-up I-shape was designed using A36 steel plate material (F_y=248*MPa*) with the following dimensions: t_f=25.4*mm*, b_f=127*mm*, t_w=12*mm* and an overall height, d=356*mm*. The

calculated shear capacity, V_p, of the SCB, using measured material strengths, is 578*kN*. The embedment length was determined based on recommendations by [Gong and Shahrooz 2001a]. Taking V_u to be equal to the calculated probable shear strength of 578*kN*, the required embedment length was determined to be 775*mm*. As recommended by past research [Gong and Shahrooz 2001a,b], face-bearing plates and auxiliary transfer bars were incorporated along the embedded regions of the beam. Further details of the SCB specimen can be found in [Fortney 2005].

Fuse Coupling Beam (FCB) Design: The main sections of the FCB and their embedment length into the wall piers were designed similarly to those of the SCB. Thus, the main sections are the same as the section designed for the SCB and so is the embedment length into the wall piers. The main-fuse connection is designed as slip-critical, and the web and flange splice connections are designed to transfer the shear and moment calculated at the location of the splice.

The design procedure for the fuse section is relatively straightforward. The top and bottom flanges are designed to be the same size as that of the main sections. Thus, the flanges of both fuses had b_f=127*mm* and t_f=25.4*mm*. The overall height of the beam was the same (h=256*mm*). The only section dimension needed is the value of t_w. Since h=256*mm* and t_f=25.4*mm* are the same for all the sections, the web thickness of the fuse, t_w, is simply proportional to the percentage of the design shear strength of the main section. Hence, t_w=(0.5)(12*mm*)=6*mm* for the 50% fuse and t_w=(0.7)(12*mm*)=8.4*mm* for the 70% fuse. The final step involves the design of the slip-critical main/fuse connections. To simplify the design of the flange and web splice plates, the flange splice plates were assumed be the same size as the flanges of the main section. Hence, t_{fsp}=25.4*mm* and b_{fsp}=127*mm*. To ensure that the splice connection can transfer at least a shear force equal to the shear capacity of the main section (V_p=692*kN*), the web splice plates (one on each side of the web) were assumed to have the same thickness as the main section web thickness, and the height of the web splice plates was sized to ensure clearance of the weld root. Clearances between the top and bottom edges of the web splice plate and the flanges of the beam were taken as 25*mm*. Hence, t_{wsp}=12*mm* and h_{wsp}=d-25*mm*=305*mm*-50*mm*=255*mm*. A check was then performed to ensure that $I_{sp} \geq I_{main\ section}$. Further details of the SCB specimen can be found in [Fortney 2005].

The design shear for the connection is 534*kN* and each bolt is in double shear. The design was based on 25.4*mm* diameter A490X bolts. In order to minimize the number of required bolts, a mean slip coefficient equal to 0.33 was assumed. The design moment at the end of the beam is 244*kN-m*. The same size bolts used for the web splice plates were used to transfer the total flange force developed at the location of the flange splice plates. Assuming that two rows of bolts are required and that the length of the fuse must be at least 356*mm* long to allow room for the splice plates, the splice was located 191*mm* from the point of zero moment (at midspan of the beam). The flange splice bolts were in single shear and therefore have a capacity equal to half of that calculated for the web splice plate bolts (the same size bolts are assumed).

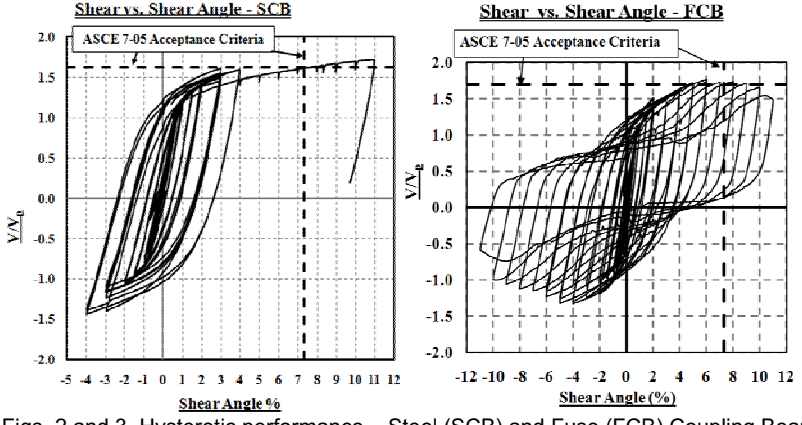
The spacing of the bolts is determined based on minimum distances required for entering and tightening. Bolt bearing and block shear were not considered. This decision is considered to be reasonable considering that for bolt bearing or block shear to occur, the connection must slip. If slipping occurs, the intended behavior of the beam will not be achieved. Furthermore, connection slip would have to occur at

a majority of the floor levels before significant changes in global response are seen; that is to say that there is appreciable redundancy built in to the system.

Additionally, allowances are made for filler plates at the web splices between the web of the fuse and the web splice plate to make up for the difference in the web thicknesses of the main and fuse sections. The same connections are used for both of the fuse beam tests. However, due to the difference in the web thicknesses between the 50% and 70% fuses, the thickness of the filler plates are different.

HYSTERESIS - PERFORMANCE EVALUATION

ASCE/SEI 7-05 [ASCE/SEI 2005] §16.2.4.2 prescribes limits of acceptability for strength degradation and total deformation: specifically, it is stated that member deformations shall not exceed either 2/3 of the deformation that results in loss of ability to carry dead loads, or 2/3 of the deformation corresponding to deterioration of member strength to less than 2/3 of its peak value. The hysteretic responses of the two steel beams were experimentally-measured and then evaluated against the ASCE/SEI 7-05 acceptance criteria. Figures 2 and 3 show the hysteretic performance of the SCB and FCB, respectively; the acceptable limits are shown in the figures as dashed lines. Beam SCB is still above 67% of the peak force at 11% chord rotation. Therefore, the acceptance criteria is measured based on deformation capacity. As can be seen in Figure 2, an acceptable rotational demand, based on ASCE 7-05, is 7.33% chord rotation. Similarly, the acceptable chord rotation demand for the FCB, as seen in Figure 3, is 7.33%. From a performance perspective, although their hysteretic behaviors appear qualitatively different, both the SCB and FCB beam types provide a similar deformation capacity, and it is reasonably concluded that providing a fuse segment in a steel coupling beam has no negative effect on deformation capacity, and has the added advantage of ease of repair.



Figs. 2 and 3. Hysteretic performance – Steel (SCB) and Fuse (FCB) Coupling Beam

RESEARCH PROGRAM AND TEST SETUP

The primary objectives of the experimental program are (a) to generate the fundamental data needed for developing novel coupling beam details, (b) to compare and evaluate the performance of several promising concepts, (c) to develop *in situ* assessment techniques of post-event reparability of coupled walls with innovative coupling beams, and (d) to identify the most promising detail that will be further examined through hybrid testing, allowing realistic loading histories, as well as addressing higher mode effects, outrigger action of out-of-plane members, and other 3D effects. The research program consists of experimental and analytical endeavors that will culminate into the hybrid testing of a realistic prototype structure. The experimental sub-assemblages will be extracted from the prototype structure, in which coupled walls are the sole lateral force resisting system.

PROTOTYPE STRUCTURE

The prototype structure designed is a 20-story building with 2.75 m (9 ft) interstory height, a 30.5m x 30.5m (100x100ft), 18cm (7 in.) thick post-tensioned floor plate. The core wall system consists of a 61cm (24 in.) thick reinforced concrete wall, and steel coupling beams, with I-shaped cross section, designed using the equivalent lateral force (ELF) procedure. The design parameters for the prototype structure are: a short period spectral ordinate of 1.5g, a 1-second period spectral ordinate of 0.6g, corresponding to design values of 1.0g and 0.65g, respectively, per ASCE/SEI 7-05 [ASCE/SEI 2005]. The soil category chosen is D, corresponding to a stiff soil with intermediate S-wave velocity, and the occupancy category of the building is II. The category of lateral force resisting system chosen is *Special Composite Reinforced Concrete Shear Wall with Steel Elements*, corresponding to a reduction factor $R = 6.0$, a deflection amplification factor $C_d = 5.0$, and an overstrength factor $\Omega_o = 2.5$.

The steel coupling beams used in the prototype structure are designed for a degree of coupling of 76% (including effects of accidental torsion) and of 71% (excluding effects of accidental torsion). The degree of coupling is defined as the ratio between the total overturning moment resisted by frame action and the total overturning moment [Harries et al. 2006]: The distribution of design shear demand and capacity is provided in Figure 4. Note that the design shear demand distribution excluding the effects of torsion is provided to illustrate the demand distribution used to compute the wall overstrength factor. The wall piers were designed including a wall overstrength factor, in order to ensure yielding of the coupling beams preliminary to the formation of plastic hinges at the base of the wall piers. Refer to [Fortney et al. 2007a,b] and [Harries and McNeice 2006] for further information regarding wall overstrength factors.

The experimental substructures are hypothetically extracted from the prototype structure at any of the floors from 5 to 8, corresponding to the largest predicted beam shear demand. The substructures consist of ¾ scale specimens, which include an interstory length of each of the wall piers and one coupling beam, with span-to-depth ratio between 2.5 and 3.

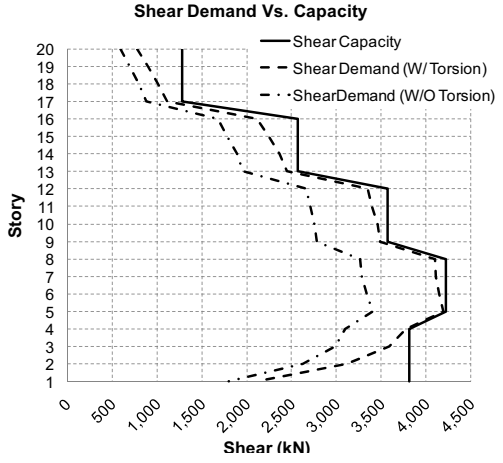


Fig. 4. Beam shear demand vs. capacity of the prototype structure (1 kip = 4.448 kN)

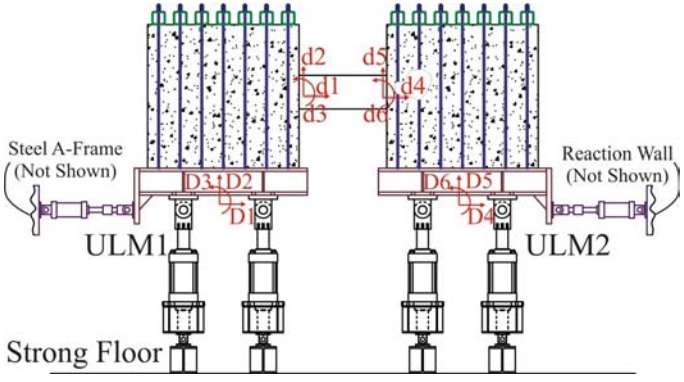


Fig. 5. Experimental test setup with installed substructure

The experimental testing configuration is shown in Figure 5, as installed on the testing rig. Each of the wall piers is allowed three in-plane degrees of freedom (horizontal and vertical displacement and in-plane rotation) that are independent of the degrees of freedom of the other wall pier. This configuration allows for the most general situations to be simulated, including different rotations of the two wall piers (due to differences in flexural stiffness induced by the presence of tensile/compressive axial forces), axial restraint, or lack thereof. The experimental substructures will be subject in a first series of tests to a quasi-static cyclic reversal relative vertical displacement history, as obtained from Appendix S of the AISC Seismic Provisions [ANSI/AISC 2005a]. Three different configurations of the test specimens will be considered, designed with the common goals of (a) providing adequate strength, stiffness, ductility, and energy absorption capacity to perform during a seismic event according to the pre-set performance objectives, (b)

minimizing costly post-event repairs by allowing replacement of damaged coupling beams without the need for expensive wall pier repair, and (c) reducing construction difficulties associated with traditional diagonally reinforced concrete coupling beams.

Type 1 coupling beam: Figure 6 shows a detail of Type 1 fuse steel beam, similar to specimens FCB-1 and -2 tested in the preliminary phase. The main built-up steel beam is embedded into the wall piers, as per the design procedure discussed above, and a built-up fuse section is bolted near the midspan, using slip-critical details and filler plates. Stiffener plates are employed in a similar way to FCB-1 and -2 specimens, as discussed above. The main detailing differences involve the weld detail of the built-up section of the fuse, which is specified as a demand-critical [ANSI/AISC 2005a] complete joint penetration weld, as opposed to the fillet welds used in the FCB specimens. The fuse employed in Type 1 coupling beams is in fact subject to very large strain demands, because the entire plastic deformations to attain the chord rotation required of the coupling beam are to be concentrated within the length of the fuse section. These demands subject the welds between web and flanges of the fuse to very large combined shear and flexural stresses that ultimately caused failure of the FCB-1 and -2 specimens. A properly detailed weld, with attention to the welding procedure and the choice of electrodes, is expected to be able to withstand these demands, thereby allowing the fuse to develop its full capacity, both in terms of strength and ductility. A potential issue with this detail, which was not observed in FCB-1 and -2 tests due to the premature failure of the welds, is the damaging of the connection area of the steel beam sections that are connected to the fuse. While this does not preclude a safe and satisfactory response of the coupling beam, it may create difficulties during the replacement of the fuse section, thereby invalidating the fundamental idea of ease of repair. In order to prevent this issue, two more details have been devised, that are described in the following. Note that the extra holes shown in the detail drawing for Type 1 coupling beam are not part of the currently described detail, but will be used for Type 2 details.

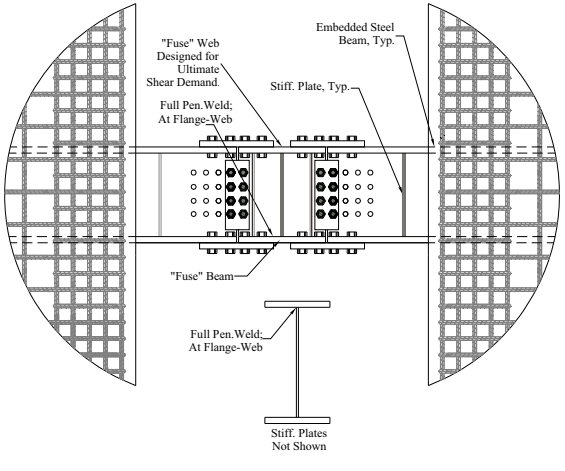


Fig. 6. Fuse Steel Beam Type 1

Type 2 coupling beam: this detail employs two back-to-back stiffened channel profiles that are bolted to the steel beams embedded in the wall piers (Figure 7). The mechanical properties of the channels are chosen so that flexural continuity is maintained along the length of the coupling beam, while shear capacity is decreased according to the desired yielding level and performance of the fuse. The connections are detailed as slip critical, and only take place on the webs of the profiles involved. In this detail, there are no flange connections between fuse and embedded sections. If on one hand this renders maintaining flexural continuity slightly more challenging, it limits the localized demands on the flanges of the embedded beams, thereby reducing the risk of undesired damage outside of the fuse elements. Also, the midspan area of the beam is characterized by lower levels of bending moment, reducing the transfer demands. Moreover, the slip critical connection on the web, which virtually doubles the thickness of the web in the connection area, eliminates the need for stiffeners, thereby reducing the fabrication costs. As for the case of Type 1 connection, bearing and tear-out are not a consideration, because slip is to be considered an ultimate limit state, not a service limit state. The back-to-back channels are laced together at midspan, so as to force the two profiles to behave as one in terms of local and lateral stability: notice that the lacing plates are bolted to the channels, instead of the more common welding approach. This is due to the ultimate goal of ease of repair for these details: a bolted connection allows for an easy replacement of any of the damaged components.

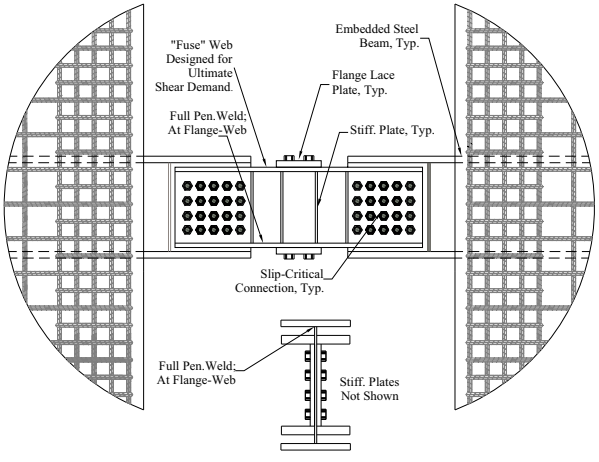


Fig. 7. Fuse Steel Beam Type 2

Type 3 coupling beam: A third set of details, pictured in Figure 8, and dubbed Type 3 was devised, with the flexural continuity of the coupling beam in mind, and building on the vast number of applications in literature of extended end plate beam-to-column connections. In this case, the bolted connections are not located directly on either the fuse or the embedded sections, but rather they connect complete joint penetration-welded extended plates at the end of the sections. The main difference from the previous two details is in this case that all fasteners are acting in tension, as opposed to shear. This takes advantage of the higher capacity and better reliability of fasteners in tension [Moore 2007] and allows for a more straightforward

installation process. The extended part of the end plates above the coupling beam is considered to be inconsequential with respect to construction issues, since it would be embedded in a concrete floor slab, if needed. The part under the beam does not create any conflict. The detail in Figure 8 does not include stiffening haunches of the end plates, due to the lower amounts of bending moment in the fuse region, but they could be provided with some additional fabrication cost. One remark that needs be heeded is that the extending plate below the bottom flange of the coupling beam might create a conflict with elevator systems and other hardware in the case of low floor-to-floor height.

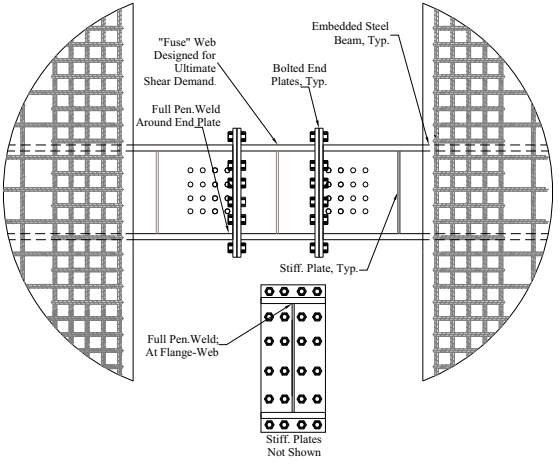


Fig. 8. Fuse Steel Beam Type 3

As anticipated, these three designs have been devised based on the preliminary results, giving for granted satisfactory strength, stiffness, and ductility characteristics, and focusing on the reparability of the structure. This would also imply that little to no damage is to be suffered by the wall piers, thereby assuring an elastic rebound of the structure to its original undeformed configuration once the damaged fuses are removed from the system.

Two sets of tests will be performed on these specimens. A first series of tests will serve as a proof-of-concept, will demonstrate the strength, stiffness, and ductility behavior of the sub-assemblages, and will help in identifying the most promising configuration for the second phase of testing, which will involve a hybrid, pseudo-dynamic analysis [Takanashi 1975; Takanashi and Nakashima 1987; Mahin et al. 1989; Shing et al. 1994; Shing et al. 1996; Mosqueda et al. 2004] of the prototype structure subject to a reference earthquake. Hybrid testing consists of a real-time exchange of information between an experimental substructure and a numerical substructure, integrated together by a pseudo-dynamic engine.

The numerical substructure will simulate the wall pier behavior, all masses in the system, the response and contribution of the gravity and outrigger frames, both in plane and out of plane. Considering the distribution of demands in the coupling beams shown in Figure 4, the experimental substructure will account for the behavior of coupling beams in floors 5 through 8, while all other less stressed

coupling beams will be simulated analytically. The interface between the numerical and experimental substructures is represented by six degrees of freedom at the two ends of the coupling beam. Through a transformation matrix ([T]), the deformations ({D}) applied by the two Universal Loading Modules (ULMs) will be related to the coupling beam deformation requests computed by the analytical engine ({d}). As part of this process, the transformation matrix will also correct for similitude ratios between the approximately ¾-scale experimental substructures and the actual prototype structure simulated in the analytical engine. The forces measured by the ULMs are related to the restoring forces at the ends of the coupling beam through another transformation matrix. Using substructuring techniques, these forces will be combined with restoring forces from the analytical substructure of the remaining portion of the coupled wall structure. As a result, the target displacements for each successive time increment will be determined, and the testing protocol will incorporate displacements that are expected in a full-scale structure subjected to a suite of realistic ground motions. It should be noted that the wall pier segments in the test specimens are intended only to provide proper boundary conditions for state of stress, rebar anchorage, etc. The measured restoring forces will include the effects of connection flexibility around the beam-wall connection, and these effects will not have to be simulated in the analytical engine.

This arrangement eliminates one of the main shortcomings of previous tests, i.e., coupling beams were subjected only to double curvature with the inflection point fixed at the midspan. Using a 3-D analytical substructure, another shortcoming of previous tests, namely omission of the 3-D effects, will also be addressed. For instance, it will be possible to incorporate the effects of variations in the wall piers axial forces due to frame action and outrigger action of the out-of-plane frames and/or walls in the displacement request to the experimental coupling even though the test specimen is 2-D. The 3-D modeling will also allow a more refined simulation of the floor diaphragms, the stiffness of which can affect the amount of axial force in the coupling beams. The difference between the two phases of testing is important, because in the first phase the coupling beam is always in double curvature, subject to a near-constant shear force along its length, paired with a linear distribution of bending moment, having zero value near the midspan of the beam. In the second phase, on the other hand, the test setup, paired with the results coming from an analytical engine in real time, will allow for realistic demands to be applied at the ends of the coupling beam, corresponding to combinations of relative vertical, horizontal, and rotational displacements, which have not been applied in the past in the laboratory to a coupling beam subassemblage.

CONCLUSIONS AND FUTURE RESEARCH

This paper discusses innovative applications of steel coupling beams for hybrid coupled core wall systems. Results in literature prove that steel coupling beams provide excellent strength, stiffness, and ductility response characteristics, when properly detailed. Based on experimental results obtained at the University of Cincinnati, it is concluded that, from a performance standpoint, there are no differences between the overall response of a traditional steel coupling beam and that of a steel coupling beam in which a fuse member has been installed, in order to focus all inelastic phenomena in a replaceable member. Although the hysteretic

responses of the two typologies are qualitatively quite different, it is maintained that the strength, stiffness, and ductility performances are satisfactory in both cases.

Furthermore, this paper presents and discusses a set of three different innovative details for the application of the fuse concept to steel coupling beams, in the framework of an ongoing experimental and analytical research project. The main goal of this project is to obtain data as to the actual behavior of coupling beams when subject to realistic deformation demands, as part of a 20-story prototype structure. It is expected that the replaceable fuse details presented will perform satisfactorily under standardized cyclic reversal loading histories, as well as when subjected to a suite of earthquake records as part of a three-dimensional structure, accounting for realistic deformation demands.

REFERENCES

ANSI/AISC, 2005a. *ANSI/AISC 341-05. Seismic Provisions for Structural Steel Buildings*. AISC, Chicago, IL

ANSI/AISC, 2005b. *ANSI/AISC 360-05. Specification for Structural Steel Buildings*, AISC, Chicago, IL

ASCE/SEI, 2005. *ASCE/SEI 7-05. Minimum Design Loads for Buildings and Other Structures,* ASCE, Reston, VA.

Fortney, P.J., 2005. *Next Generation of Coupling Beams*, PhD Dissertation, University of Cincinnati.

Fortney P.J., Shahrooz B.M., Rassati G.A., 2007a. "Seismic Performance Evaluation of Coupled Core Walls with Concrete and Steel Coupling Beams", *Steel and Composite Structures Journal*. Vol. 7(4):279-301

Fortney P.J., Shahrooz B.M., Rassati G.A., 2007b. "Large-Scale Testing of a Replaceable Steel Coupling Beam", *ASCE Journal of Structural Engineering*, 133(12):1801-1807

Gong B. and Shahrooz B.M., 2001a. "Concrete-Steel Composite Coupling Beams-Part I: Component Testing", *ASCE Journal of Structural Engineering*, 127(6):625-631.

Gong B. and Shahrooz B.M., 2001b. "Concrete-Steel Composite Coupling Beams-Part II: Subassembly Testing and Design Verification", *ASCE Journal of Structural Engineering*, 127(6):632-638.

Harries, K.A., Mitchell, D., Cook, W.D., Redwood, R.G., 1992. "Seismic response of steel beams coupling reinforced concrete walls", *ASCE Journal of the Structural Division*, 119(12):3611-3629.

Harries, K.A., Mitchell, D., Redwood, R.G., Cook, W. D., 1997. "Seismic Design of Coupling Beams – A Case for Mixed Construction", *Canadian Journal of Civil Engineering*, Vol. 24, No. 3, pp 448-459.

Harries K.A., Shahrooz B.M., Brienen P., Fortney P.J., Rassati G.A., 2006. " Performance-Based Design of Coupled Wall Systems", in Leon R.T. and Lange J. *Composite Construction in Steel and Concrete V,* ASCE, Reston, VA

Harries, K.A. and McNeice, D.S., 2006. “Performance-Based Design of High-Rise Coupled Wall Systems”, *The Structural Design of Tall and Special Buildings*, Vol. 15(3):289-306.

Mahin S.A., Shing P.B., Thewalt C.R., Hanson R.D., 1989. “Pseudodynamic Test Method – Current Status and Future Direction.” *ASCE Journal of Structural Engineering*, 115(8):2113-2128.

Moore A.M., 2007. *Evaluation of the Current Resistance Factors for High Strength Bolts*, MS Thesis, Department of Civil and Environmental Engineering, University of Cincinnati.

Mosqueda G., Stojadinovic B., Mahin S., 2004. “Geographically distributed continuous hybrid Simulation”. *Proceedings of the 13th World Conference on Earthquake Engineering*, August 2004.

Shahrooz B.M., Remmetter M.A., Qin F., 1992. “Seismic Response of Composite Coupled Walls”, in Composite Construction in Steel and Concrete II, ASCE, pp 429-441.

Shahrooz B.M., Remmetter M.A., Qin F., 1993. “Seismic Design and Performance of Composite Coupled Walls”, *ASCE Journal of the Structural Division*, Vol. 119, No. 11, pp 3291-3309.

Shahrooz B.M., Gong, B., 1998. “Steel-Concrete Coupling Beams: A Critical Overview of Design Guidelines”, *Structural Engineers World Wide*, paper T186-3.

Shing P.B., Vannan M.T., Carter, E., 1991. “Implicit Time Integration for Pseudodynamic Tests”, *Earthquake Engineering and Structural Dynamics*, Vol. 28.

Shing P.B., Nakashima M. Bursi, O.S., 1996. “Application of Pseudodynamic Test Method to Structural Research”, *EERI Earthquake Spectra*, 12(1):29-54

Takanashi K., 1975. *Non-Linear Earthquake Response Analysis of Structures by a Computer-Actuator On-line System*.

Takanashi K., Nakashima M.,1987. “Japanese activities on on-line testing”, *ASCE Journal of Engineering Mechanics*, 113(7):1014-1032.

SEISMIC-INDUCED FIRE ANALYSIS OF STEEL-CONCRETE COMPOSITE BEAM-TO-COLUMN JOINTS: BOLTED SOLUTIONS

Oreste S. Bursi
Department of Mechanical and Structural Engineering, University of Trento
Trento, Italy
oreste.bursi@ing.unitn.it

Fabio Ferrario
Department of Mechanical and Structural Engineering, University of Trento
Trento, Italy
fabio.ferrario@ing.unitn.it

Raffaele Pucinotti
Department of Mechanics and Materials, Mediterranean University of Reggio Calabria
Reggio Calabria, Italy
raffaele.pucinotti@unirc.it

Riccardo Zandonini
Department of Mechanical and Structural Engineering, University of Trento
Trento, Italy
riccardo.zandonini@ing.unitn.it

ABSTRACT

In this paper, a multi-objective advanced design methodology is proposed for steel-concrete composite moment-resisting frames. The research activity mainly focused on the design of beam-to-column joints under seismic-induced fire loading together with the definition of adequate structural details for composite columns. Thermal analyses of cross sections were performed in order to obtain internal temperature distribution; structural analyses were then carried out on the whole frame to assess the global behavior under the combined action of static and fire loadings. Furthermore, results of numerical analyses were used in order to derive information about the mechanical and numerical behavior of joints. In this paper the experimental program carried out on four beam-to-column joint specimens under seismic loading is described and results are presented and discussed together with the outcomes of numerical simulations owing to seismic and fire actions. Experimental tests demonstrated the adequacy of the seismic design. Numerical simulations showed a satisfactory performance of joints under seismic-induced fire loading.

INTRODUCTION

Steel-concrete composite structures are becoming increasingly popular around the world due to the favorable performance regarding stiffness, strength and ductility of composite systems under seismic loading, and also due to the speed and ease of erection. Moreover, such structures exhibit better fire resistance characteristics

compared to bare steel structures. Considering the high probability of a fire after a seismic event, the use of steel–concrete composite structures in seismic areas potentially represents a fairly effective design solution. In fact, the adoption of such a solution is in general more efficient from both a structural and a constructional viewpoint when compared to bare steel structures. The benefits increase, if the probability that an earthquake and a fire can occur in sequence is high. In current Eurocodes for structural design, seismic and fire safety are accounted for separately, and no sequence of seismic and fire loading is taken into account. In reality, the risk of loss of life increases if a fire occurs in a building after an earthquake. In the Kobe Earthquake (1995) many people died due to the collapse of buildings exposed to a fire that followed an earthquake; in fact, large sections of the city burned, greatly contributing to the loss of lives. It is obvious therefore that seismic-induced fire is a design scenario that should be properly addressed in any performance-based seismic design. In this situation the traditional single-objective design is not adequate, and a multi-objective advanced design has to be adopted. This makes it possible to take into account of: (i) seismic safety with regard to accidental actions; (ii) fire safety with regard to accidental actions (iii) seismic-induced fire safety on a structure characterized by stiffness deterioration and strength degradation owing to seismic actions. As a result, the fire design applied to a structure with reduced capacity owing to seismic damage will permit a simultaneous fulfillment of the requirements associated with structural, seismic and fire safety, and with structural fire safety and structural seismic safety, separately, considered as accidental actions. In order to characterize the seismic behaviour of composite joints, a research project were carried out by the University of Trento with the objective of developing a design procedure for composite joints under the *'combined'* action of earthquake and post-earthquake fire. The research activity was mainly concerned with the design of bolted beam-to-column joints with CFT columns with circular hollow steel sections. This solution derives from a parent welded design solution developed in a European project (Bursi et al. 2008) and is aimed at ensuring easiness of assembly and avoiding problems related to on-site welding. The results of the experimental programme devoted to the evaluation of the cyclic behavior of beam-to-column bolted joints are reported in the following. In order to better understand the activation of all the transfer mechanisms proposed in Eurocode 8 (UNI EN 1998-1, 2005), a numerical finite element (FE) model of the slab has been developed, together with FE model of the joint subject to fire.

SEISMIC AND FIRE DESIGN OF REFERENCE FRAMES

A reference composite steel-concrete office building was considered, made up of three five storeys moment resisting frames, placed at a distance of 7.5 m each in the longitudinal direction and braced in the transverse direction. The storey height was equal to 3.5 m. Two moment resisting frames, having the same structural typology but different slab systems, were analyzed: i) a composite steel-concrete slab with structural profiled ribbed steel sheeting; ii) a concrete slab composed of electro-welded lattice girders. Since the two slab systems had different load bearing capacities, a different distance between the secondary beams was adopted for the two solutions. The distance slightly affected the frame geometry. The first solution (steel sheeting slab), is depicted in Figure 1a while the second one, with the slab on prefabricated lattice elements, is shown in Figure 1b. The elevation is shown in Figure 1c (Bursi et. al 2008). Two different types of composite beams were hence

designed according to Eurocode 4 (UNI EN 1994-1-1, 2005); the steel section was maintained in both cases as an IPE400 of steel grade S355 (A615 grade 50). The slab, 150 mm (5.90 in.) deep, was designed in accordance with the relevant specifications of Section 9 of Eurocode 4 [1994-1-1. 2005]; moreover design procedure indicated by the producer of the prefabricated lattice elements was followed in the second case. All connections between the steel beam and the slab were made by Nelson 19 mm stud connectors made of steel with an ultimate tensile strength f_u=450 MPa.

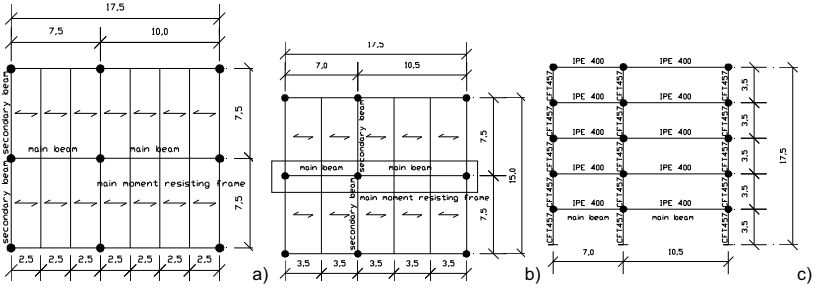


Figure 1 - The configuration of the building and the longitudinal five-storey MR Frame; slab with a) profiled ribbed steel sheeting; b) slab with prefabricated lattice girder; c) elevation

The frames were designed to have a dissipative structural behavior according to Eurocode 8 (UNI EN 1998-1, 2005). In detail two following structural types were considered.

1. *Moment Resisting Frames*: in which dissipative zones were mainly located to the end of the beams, in the vicinity of beam-to-column connections, where plastic hinges could develop (UNI EN 1998-1, 2005, 7.1.2 b);
2. *Concentrically braced frames*: in which the horizontal forces were mainly resisted by members subjected to axial forces with dissipative zones located on the tension diagonals only (UNI EN 1998-1, 2005, 7.1.2 c).

The effective width of the slab in composite beams was determined according to Eurocode 4 (UNI EN 1994-1-1, 2005, 5.4.1.2) for static and fire analyses, and to Eurocode 8 (UNI EN 1998-1, 2005, 7.6.3) for seismic analyses. Beam-to-column connections resulted to be rigid according to Eurocode criterion (UNI EN 1994-1-1, 5.1.2). The design of structural elements were performed considering static and seismic design situations. Moreover, numerical simulations on two-dimensional (2D) frames, were first performed by means of the SAFIR program (Franssen J.-M. 2000), in order to study different fire scenarios acting in the reference buildings and to evaluate the performance of different elements, i.e. composite beams, composite columns, and beam-to-column joints, under fire load for different times of exposure to fire. Five fire scenarios were considered. In the first one (FS1), fire acted only into a span in the first floor as illustrated in Figure 2a.

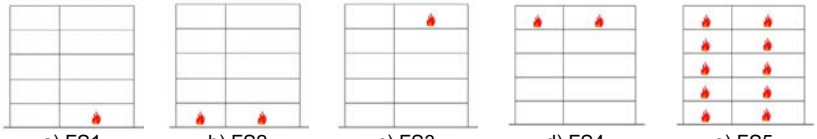


Figure 2 - Fire scenarios considered in thermal analysis

In the second one (FS2), fire acted on the whole first floor; this means that the first level columns and the first level beams were heated. In the third one (FS3), fire acted only into a span on the last floor. In the fourth one (FS4), fire acted on the whole fifth floor. Finally, in the fifth one (FS5) fire acted on the whole frame. The fire load followed the ISO 834 fire law. Figure 3 shows the evolution of the bending moment and of the axial force as a function of time at various locations in the FE model for the case FS1. In detail the bending moment in column C shows an inversion in the sign when axial forces in the beams changes sign too. In fact, the increase in temperature causes first an increment of axial load in the beam (compression) to about 18 min owing to the presence of the column restraint. Afterwards, the reduction of stiffness of the columns subject to fire prevails and the axial force in the beam turns to tension, being similar to a “catenary” structure (with large displacement and deflection). The elongation of the beam due to increase in temperature and the different “restraint” effect offered by the column also causes a reversal of the sign of bending moment at mid-span of the beam which from sagging becomes hogging and then sagging again. The results of the analysis shows that the frame collapses because of the formation of a beam mechanism in the longest span involving the formation of three plastic hinges located at mid-span and at both beam ends near supports. Figure 4 shows column temperature distributions in the fire case FS1; it is possible to notice that the steel tubular section offers a practically negligible protection to internal concrete; therefore temperatures of steel elements directly exposed to fire are equal to that of the external atmosphere.

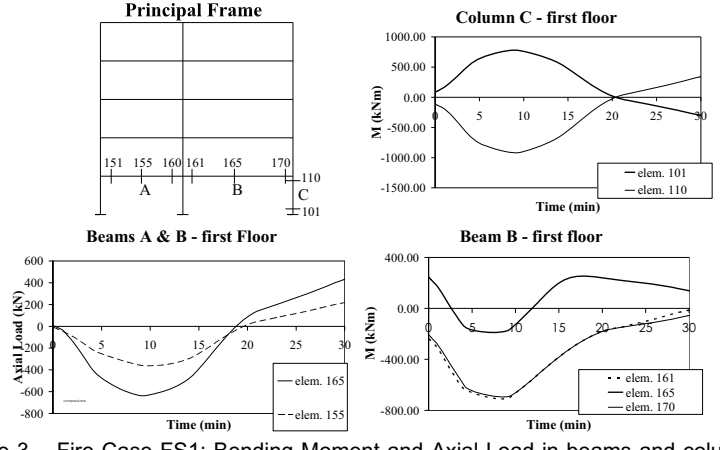


Figure 3 – Fire Case FS1: Bending Moment and Axial Load in beams and columns of the first storey

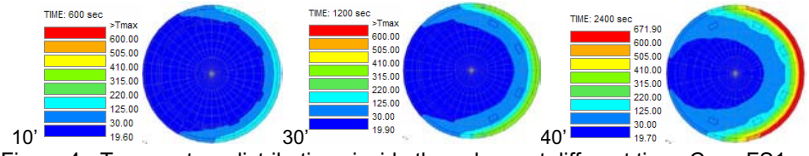


Figure 4 - Temperature distributions inside the column at different time. Case FS1

The thermal distribution, for the composite slab with steel sheeting, evaluated after 10 min, 30 min and 40 min of ISO fire, by means of the thermal FE model created by SAFIR, are presented in Figure 5, while Figure 6 shows the thermal distribution for the case of the composite slab with the prefabricated slab. As expected, the temperature increment was higher in the composite slab with steel sheeting than in the slab with prefabricated R.C. elements. As a result, the moment resistance of the former slab was lower than in the latter owing to the higher reduction in material strength.



Figure 5 – Fire case FS1. Evolution of the temperature distribution inside beam B with a steel sheeting composite slab.

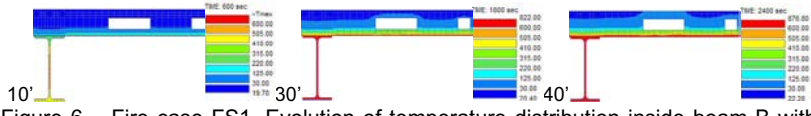


Figure 6 – Fire case FS1. Evolution of temperature distribution inside beam B with prefabricated elements

DESIGN OF BEAM-TO-COLUMN JOINTS

The beam-to-column joint design aimed at ensuring a joint overstrength with respect to the beam. The proposed bolted solution derives from a parent welded design (Bursi et al. 2008) and was conceived to guarantee easiness of assembly and to avoid problems related to welding on site. The joint comprised of two horizontal diaphragm plates and a vertical through-column plate attached to the tube by groove welds as indicated in Figure 7.

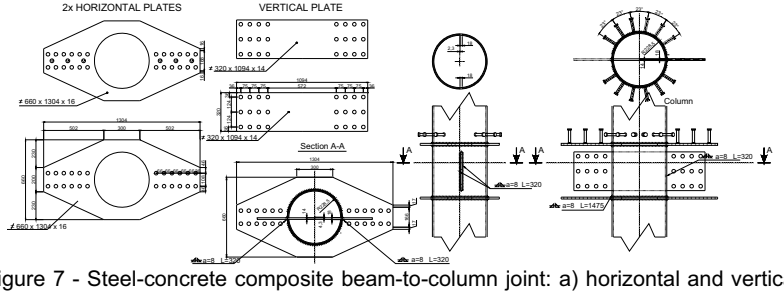


Figure 7 - Steel-concrete composite beam-to-column joint: a) horizontal and vertical plates; b) Nelson studs in columns

The flanges and the web of each beam were connected to the horizontal plates and the vertical plate by two and three rows of bolts M27 10.9 (1-1/8 A490), respectively. Apart from the slab type, also the joints differed due to the presence of strengthening plates with holes required by Eurocode 8 to avoid brittle fracture in the net sections of bolted joints. Thus, specimens JB-P1 and JB-S1, see table 1, where endowed with extra plates; whereas JB-P2 and JB-S2 had no plate being non-dissipative joints. Beam-to-column joint design was developed using the component method. The joint was simulated by a series of different components in agreement with Eurocode 3 par 1-8 and Eurocode 8 (UNI EN 1993-1-8, 2005, UNI EN 1998-1, 2005), achieving the necessary overstrength to the joint with respect to the connected composite beams. Stiffness and strength of complex components, like top and bottom plates or concrete slab in compression, were defined by means of refined Finite Element (FE) models of the joint including friction between the slab and the column. Depending on the level of friction, the distribution of the compression forces in the slab under sagging bending moment was found to be different: it is localized in front of the column for a friction coefficient equal to 0,35 as indicated in Figure 8a while it spreads over a more extended portion of the slab due to increasing values of the friction coefficient. In detail, the diffusion angle becomes greater than 80 degrees for a friction coefficient of about 1. The results show that, in order to activate the transfer mechanisms proposed in Eurocode 8 (UNI EN 1998-1, 2005), i.e. Mechanism 1 front mechanism and Mechanism 2 strut and tie mechanism (see Figure 8b), it is necessary to increase the level of friction between the concrete slab and the composite column. As a result, Nelson 19 mm stud connectors welded around the column were used in the tested specimens as indicated in Figure 7. As a result beam-to-column joints were rigid full-strength joints satisfying the relation:

$$M_{j,Rd} \geq s \cdot \gamma_{ov} \cdot M_{b,pl,Rd} \tag{1}$$

in which $M_{j,Rd}$ is the resisting moment of full-strength beam-to-column joints and $M_{b,pl,Rd}$ is the resisting moment of the composite beam (UNI EN 1998-1, 2005). Moreover, the ductile behaviour of joints was guaranteed by the following relationships:

$$R_{d,bolt} \geq s \cdot \gamma_{ov} \cdot R_{pl,Rd,beam} \tag{2}$$

$$R_{d,bolt} \geq R_{pl,Rd,plates} \tag{3}$$

$$F_{v,Rd} \geq F_{b,Rd} \tag{4}$$

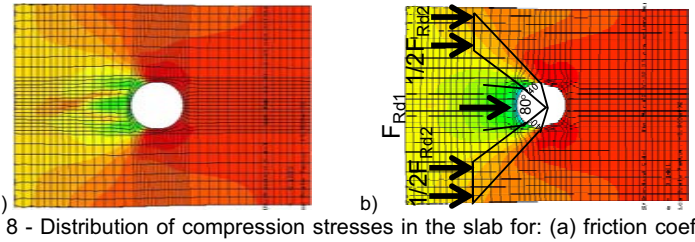


Figure 8 - Distribution of compression stresses in the slab for: (a) friction coefficient equal to 0,35; b) friction coefficient equal to 1

where $s = \min\{f_t / f_y; 1.25\}$, $\gamma_{ov} = 1.1$, $R_{d,bolt}$ is the design strength of bolts, $R_{pl,Rd,beam}$ is the plastic design strength of the beam, $R_{pl,Rd,plates}$ is the plastic design strength of the plates, while $F_{v,Rd}$ and $F_{b,Rd}$ are the design shear strength and design bearing resistance of bolts, respectively. The following conditions were also fulfilled for joints JB-P1 and JB-S1 to avoid brittle fracture in the net sections, i.e.:

$$\frac{0.90 A_{net} f_u}{\gamma_{M2}} \geq \frac{A f_y}{\gamma_{M0}} \text{ and } \frac{0.90 A_{net} f_u}{\gamma_{M2}} \geq \frac{A_f f_y}{\gamma_{M0}} \quad (5)$$

where A_f is the area of the tension flange. Nevertheless, being non-dissipative joints, JB-P2 and JB-S2 did not. A 3D finite element model of the interior joint was implemented in the Abaqus 6.4.1 code (Hibbitt et al. 2000). Then beam-to-column joints subjected to fire load were designed. In particular, the component approach, exclusively applied to the moment-rotation-temperature behaviour, was adopted, in the absence of axial thrust owing to the thermal expansion restraint of the beam. A simplified model was derived, which can predict the moment-rotation-temperature characteristic of the joint. As a result, at high temperatures, the joints were designed to transfer shear forces owing to vertical loads from one beam to the other. Accordingly, vertical through column plate, top horizontal plate together with Nelson stud connectors welded around the column were arranged. In addition, two longitudinal steel rebars were added to the slab to reduce the damage produced by the seismic actions before fire.

EXPERIMENTAL TESTS

The experimental programme consisted of 4 tests under cyclic loading of full-scale substructures representing an interior full-strength bolted beam-to-column joint (Figure 9). Experimental tests were carried out at the Laboratory for Materials and Structures of the University of Trento. Joint specimens were subjected to cyclic loadings up to collapse, according to the ECCS stepwise increasing amplitude loading protocol, modified with the SAC procedure (ECCS 1986, SAC 1997) by using e_y=0.005h=17.5 mm where h represents the storey height.

The slab reinforcement, in the composite steel-concrete beams with steel sheeting, consisted of 3+3ϕ12 (3+3#4) longitudinal steel rebars in order to carry the sagging moment, and of 4+4ϕ12@100 mm (4+4#4@4 in.) and 7+7ϕ16@250 mm (7+7#5@10 in.) transverse steel rebars, in order to enable development of the seismic slab-to-column transfer mechanism as well as the resistance to the shear force. A mesh ϕ6@200x200 mm (ϕ6@8x8 in) is also present as shown in Figure 10a. The concrete class was C30/37 (4350 psi) while the steel grade S450 (A615 Grade 60) was adopted for reinforcing steel bars. In the case of the concrete slab prefabricated R.C. elements, the slab reinforcement was made up of 3+3ϕ12 (3+3#4 in.) longitudinal steel rebars and by 5+5ϕ12@100 mm (5+5#4@4 in.) plus 8+8ϕ16@200 mm (8+8#5@8 in.) transverse steel rebars. The same mesh was adopted as for the composite slab (Figure 10b).

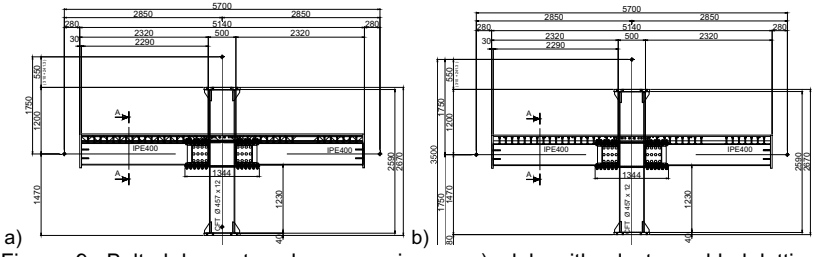


Figure 9: Bolted beam-to-column specimens a) slab with electro-welded lattice girders, b) composite slab with profiled steel sheeting

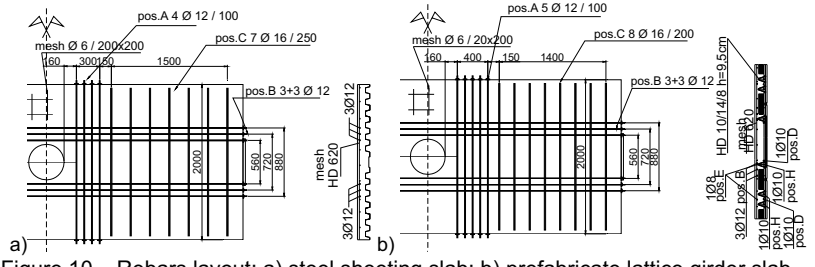


Figure 10 – Rebars layout: a) steel sheeting slab; b) prefabricate lattice girder slab

The columns were concrete-filled columns with a circular hollow steel section with a diameter of 457 mm (18 in.) and a thickness of 12 mm (0.438 in). Steel grade is S355 (A615 Grade 50). The column reinforcement consisted of 8ϕ16 (8#5) longitudinal steel rebars and of stirrups ϕ8@150 mm (ϕ8@6 in.) (Figure 11). The concrete class was C30/37 (4350 psi), while steel grade S450 (A615 Grade 60) was adopted for the reinforcing steel bars. Actual values better than nominal ones can be found in (Bursi et al. 2008). A scheme of the test set-up is shown in Figure 12.

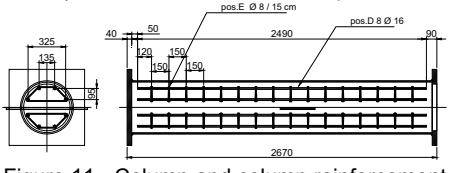


Figure 11 - Column and column reinforcement

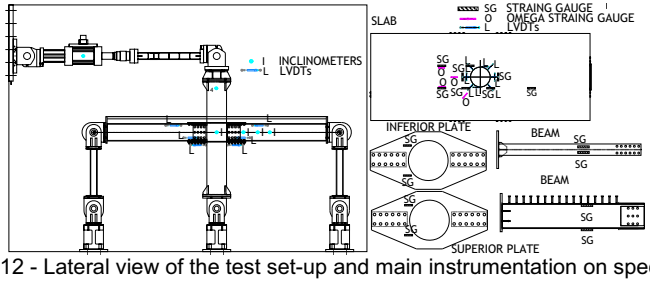


Figure 12 - Lateral view of the test set-up and main instrumentation on specimens

No vertical actuator was imposed on the column in order to be consistent with tests in other labs. In the tests, the following instrumentation was employed as illustrated in Figure 12: a) 5 inclinometers measured the inclinations: of the column at the top and, in the zone adjacent to the joint, and of the beams near the connection; b) 4 LVDTs detected the interface slip between the steel beam and the concrete slab and between the bottom horizontal joint plate and the flange of beam; c) 2 LVDTs were employed in order to measure the bottom horizontal joint plate deformations; d) 10 LVDTs were utilized in order to measure concrete slab deformations in the zone around the column; e) 4 Omega-shaped strain gauges detected the deformations of the concrete slab; f) 8 strain gauges monitored axial deformations of the reinforcing bars to scrutinise the effective breadth of the reinforcing bars at each loading stage; g) 4 strain gauges monitored deformations of top and bottom horizontal plates; h) 4 strain gauges recorded flange strains in order to estimate internal forces in steel beams; i) 2 load cells were set on the top of pendula and were utilized in order to measure the horizontal and vertical components of the forces; l) 1 digital transducer (Heidenhein DT500) was used in order to measure the top column displacement.

RESULTS AND SIMULATIONS

The observed response clearly indicated that all specimens exhibit a good performance in terms of resistance, stiffness, energy dissipation and local ductility. Both the overall force-displacement relationship and the moment-rotation relationships relevant to plastic hinges formed in composite beams exhibited a hysteretic behaviour with large energy dissipation without evident loss of resistance and stiffness, as seen in Figures 13 to 15. Hysteretic loops of moment-rotation relationship are unsymmetrical owing to the different flexural resistance of the composite beam under hogging and sagging moments as can be observed in Figure 15. It was evident that owing to local buckling effects, severe strength degradations appeared to exceed 20 per cent of maximum strength values with rotations of about 40 mrad. The collapse of all specimens was caused by plastic buckling in compression of the bottom beam flange near the horizontal plate as illustrated in Figure 16 or fracture in tension.

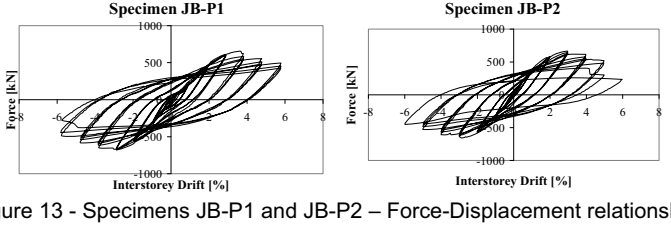


Figure 13 - Specimens JB-P1 and JB-P2 – Force-Displacement relationship

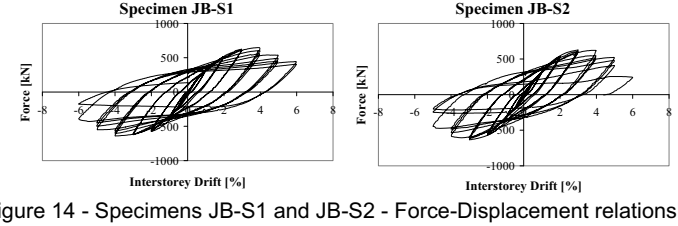


Figure 14 - Specimens JB-S1 and JB-S2 - Force-Displacement relationship

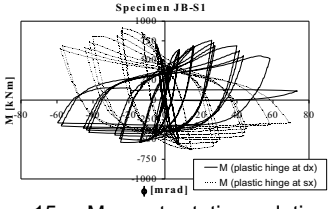


Figure 15 - Moment-rotation relationship of the plastic hinges for the JB-S1



Figure 16 – Specimen JB-S1, plastic hinge in the composite beam

Table 1 reports some key experimental data for each test: maximum applied displacement d, maximum value F of the force, maximum values of both sagging and hogging moments M, total number N_{tot} of cycles performed during the tests. Joint behaviour is essentially symmetric in terms of force, while, for all specimens, sagging moments are about 40 per cent larger than hogging moments. Figure 17 shows a comparison between Force-Interstorey drift curves for the specimens with and without plate strengthening of the horizontal diaphragms in both prefabricated slabs and steel sheeting slabs. These reinforcing plates were introduced in order to satisfy the relationships in (5). In this case, in which dissipative zones were located at the end of the beams, beam-to-column joints were rigid full-strength and the introduced reinforcing plates did not influence the specimen behaviour. Moreover, beam-to-column joints subjected to fire load were analyzed. In particular, the component approach, exclusively applied to the moment-rotation-temperature behaviour, was adopted, in the absence of axial thrust owing to the thermal expansion restraint of the beam. A simplified model was derived, which can predict the moment-rotation-temperature characteristic of the joint.The method is capable of predicting the variation of failure modes owing to change in the joint geometrical and material properties, as well as loading conditions. The temperature distribution into the composite joint subjected to three different time-temperature curves, as depicted in Figure 18, was implemented in ABAQUS 6.4.1 software (Hibbitt et al., 2000) and a 3D FE model of joint was studied. Figure 19 shows the mean temperature distribution on the slab as a function of the time of fire exposure obtained from the application of the three inputs. It is evident that the application of the natural fire curve produces a lower rise in temperature in the concrete slab than the application both of the ISO 834 curve and parametric curve proposed in EC1 (UNI EN 1991-1-2 2004).

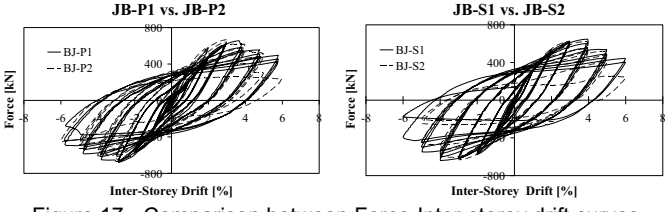


Figure 17 - Comparison between Force-Inter-storey drift curves

Table 1: major experimental data

Name	Test Method	d [mm]	F [kN]	*M [kNm]	N_{tot}	Type of Specimen
JB-P1	Cyclic	210	+655.09 -680.92	+1047.2 -747.75	22	Specimen with electro-welded lattice girders slab and Nelson connectors around the column, with reinforcement plates
JB-P2	Cyclic	210	+666.70 -657.60	+892.60 -760.23	20	Specimen with electro-welded lattice girders slab and Nelson connectors around the column, without reinforcement plates
JB-S1	Cyclic	210	+647.12 -639.66	+760.09 -537.59	20	Specimen with profiled Steel Sheeting slab and Nelson connectors around the column with reinforcement plates
JB-S2	Cyclic	175	+627.19 -634.58	+887.46 -636.37	19	Specimen with profiled Steel Sheeting slab and Nelson connectors around the column, without reinforcement plates

* + Sagging Moment; - Hogging Moment

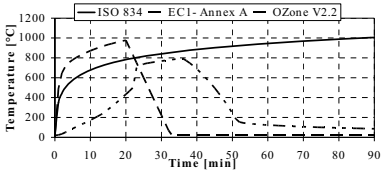


Figure 18 - Different time-temperature curves applied as a function of the time of fire exposure

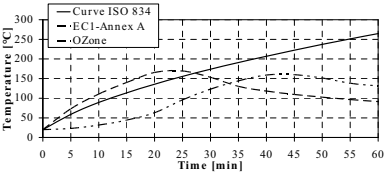


Figure 19 - Mean temperature distribution on the slab as a function of the time of fire exposure

As a result, Figure 20 shows that all the steel parts exposed to fire increase their temperature very fast, reaching a very high temperature after only 15 minutes. Conversely, in the concrete and in the steel component with a concrete cover rebars, as in the horizontal plates and the vertical plate (passing through the column) the temperature does not increase so quickly, remaining near the value of the ambient temperature. On this basis, it was possible to incorporate degradation characteristics of the material into the mechanical component model based on the "Strength Reduction Factor-SRF", which is actually a strength retention factor present in the current European Design codes (CEN, Eurocode 3-1-2, 2003).

This is basically the residual strength of steel and concrete materials at a particular temperature relative to its basic yield strength at room temperature. Figure 21 shows the reduction of the design moment capacity of the joint as a function of the time of fire exposure.

An attentive reader can observe how the hogging moment capacity reduces to approximately 90-95 per cent of its initial value after 15 minutes of exposure. The degradation in resistance and stiffness is observed both for the sagging and the hogging bending moment, respectively; nevertheless these numerical results show

that beam-to-column joints are able to carry the internal action that beams transfer to columns for a time of 15 minutes without any passive fire protection. This period of time is considered enough to evacuate the building after a severe earthquake. Clearly, these simulations need to be confirmed by fire tests; in this respect, the companion full strength beam-to-column welded solution investigated by Bursi et al. (2008), was shown to be successful.

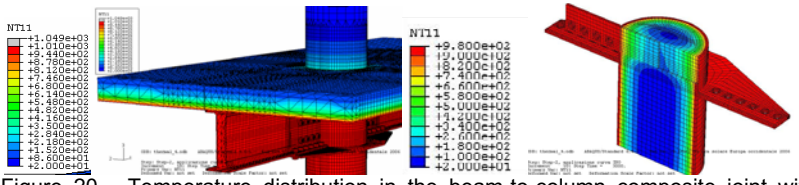


Figure 20 - Temperature distribution in the beam-to-column composite joint with prefabricated slab

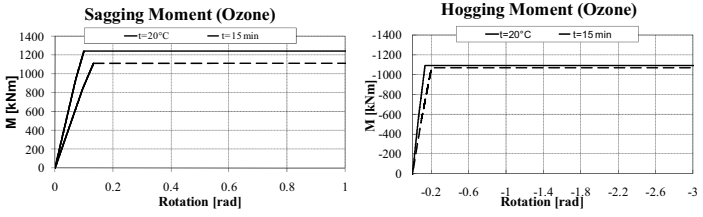


Figure 21 - Moment-rotation relationship of the joint as a function of the time of fire exposition

CONCLUSIONS

The paper presented part of the results of a numerical and experimental study aimed at developing performed-based design methods for beam-to-column joints, by considering their structural performance under seismic-induced fire loading. In particular, the paper discussed the experimental program carried out on steel-concrete composite beam-to-column joints together with numerical simulations regarding their seismic-induced fire behaviour. Experimental and numerical results showed how joint details influence beam-column sub-assemblage responses. All sub-assemblages exhibited rigid behaviour for the designed composite joints and favorable performance in terms of resistance, stiffness, energy dissipation and local ductility; as expected plastic hinges developed in beams as a consequence of the capacity design. Moreover, a behaviour factor of about 4 was observed for the composite frames analysed. As a results, the joint can be used in Ductility Class M structures according to Eurocode 8. Numerical fire simulations have shown that the joint is able to carry the internal action for a maximum time of 15 minutes without any passive fire protection: this period of time is enough to evacuate the building after a severe earthquake. Moreover, joints endowed with prefabricated slab exhibit a better behavior compared to joints endowed with composite slabs.

ACKNOWLEDGEMENTS

The experimental programme was made possible by the grant provided under the RELUIS National programme for seismic engineering: Task n.5 - "Development of innovative approaches on the design of steel and steel-concrete composite structures." The authors express their gratitude to Dr: Marco Molinari and the technicians of the Structural Testing Laboratory of Trento University, who skilfully prepared and followed the tests.

REFERENCES

Bursi O.S., et al. Editors, Final Report PRECIOUS Project Contr. N. RFSCR-03034, 2008. Prefabricated Composite Beam-to-Concrete Filled Tube or Partially Reinforced-Concrete-Encased Column Connections for Severe Seismic and Fire Loadings;

ECCS 1986. Recommended Testing Procedure for Assessing the Behaviour of Structural Steel Elements under Cyclic Loads. ECCS Publication n° 45;

Ferrario F., Pucinotti R., Bursi O. S., Zandonini R. 2007, Steel-Concrete Composite Full Strength Joints with Concrete Filled Tubes. Part II: Experimental and Numerical Results, Proceeding of 21st Conference of Steel Structures C.T.A., Catania, 1-3 October, pp. 397-404, Dario Flaccovio Editor;

Franssen J.-M. 2000. "SAFIR; Non linear software for fire de-sign". Univ. of Liege;

Hibbitt, Karlsson and Sorensen 2000. "ABAQUS User's manuals". 1080 Main Street, Pawtucket, R.I. 02860;

RELUIS Task n.5: "Development of innovative approaches on the design of steel and steel-concrete composite structures. Unità di Ricerca 8 - Buri O.S., Zandonini R.

SAC 1997, Protocol for Fabrication, Inspection, Testing, and Documentation of Beam-Column Connection Tests and Other Experimental Specimens, report n. SAC /BD-97/02;

UNI EN1991-1-2. 2004. "Eurocode 1: Actions on Structures. Part 1-2 : General Actions – Actions on structures exposed to fire";

UNI EN 1992-1-2. 2005. "Eurocode 2: Design of concrete structures. Part 1-2: General rules - Structural fire design;

UNI EN 1993-1-1. 2005. "Eurocode 3: Design of steel Structures. Part 1: General rules and rules for buildings";

UNI EN 1993-1-8. 2005. "Eurocode 3: Design of steel Structures - Part 1-8: Design of joints";

UNI EN 1993-1-2. 2005. "Eurocode 3: Design of steel Structures. Part 1-2: General rules - Structural fire design";

UNI EN 1994-1-1. 2005. "Eurocode 4: Design of composite steel and concrete Structures - Part 1.1: General rules and rules for buildings";

UNI EN 1994-1-2. 2005. "Eurocode 4: Design of composite steel and concrete Structures - Part 1.2: General rules – Structural fire design";

UNI EN 1998-1. 2005. "Eurocode 8: Design of structures for earthquake resistance - Part 1: General rules, seismic actions and rules for buildings".

SEISMIC-INDUCED FIRE ANALYSIS OF STEEL-CONCRETE COMPOSITE BEAM-TO-COLUMN JOINTS: WELDED SOLUTIONS

Oreste S. Bursi
Department of Mechanical and Structural Engineering, University of Trento
Trento, Italy
oreste.bursi@ing.unitn.it

Fabio Ferrario
Department of Mechanical and Structural Engineering, University of Trento
Trento, Italy
fabio.ferrario@ing.unitn.it

Raffaele Pucinotti
Department of Mechanics and Materials, Mediterranean University of Reggio Calabria
Reggio Calabria, Italy
raffaele.pucinotti@unirc.it

ABSTRACT

A multi-objective design methodology dealing with seismic-induced fire on steel-concrete composite moment resisting frames endowed with concrete filled tubes (CFT) full strength joints is presented in this paper. In order to achieve these goals analytical and FE simulations including thermal analyses were carried out to design the proposed joints: this was followed by experimental tests under monotonic and cyclic loadings. Preliminary, seismic and fire analyses provided valuable information on the performance of moment resisting frames endowed with the chosen joint typology. A total of six specimens was designed and subjected to lateral loads. The specimens were subassemblages of interior beam-to-column joints connected by means of welded connections. Relevant experimental results are presented and commented. Furthermore, since the scope of the project was to promote joint typologies able to survive a seismic-induced fire, specimens were damaged by imposing monotonic loads equivalent to damage induced by seismic excitations, before being subjected to fire loadings. Thus, valuable information was obtained about the endurance of the proposed joint typology.

INTRODUCTION

Major earthquakes in urban areas were often followed by significant conflagrations that were difficult to control and resulted in extensive damage to property. For instance in the 1995 Kobe earthquake, more than a few fires occurred in fire-resistant buildings (Kobe City Fire Dept., 1995). Also, various surveys revealed that many fire protection systems, e.g. sprinkler systems, were damaged by earthquakes and lost their function because of mechanical failure and/or deformation by earthquake motion (MFIAJ, 1995). As a result: i) seismic-induced fire risk assessment methods able to evaluate fire risk according to size and type of

buildings, installed fire protection systems and intensity of input earthquake motion have been developed (Yashiro et al., 2000); ii) some studies on the evaluation of the fire resistance rating reduction of perimeter moment-resisting multi-storey frames owing to seismic loading were performed (Della Corte et al., 2003). At the beam-to-column joint level, different studies were carried out to evaluate the performance of steel joints under fire both from a numerical and a design viewpoint (Simoes da Silva et al., 2007, Simoes da Silva et al., 2005, Block et al., 2007). However, research seems to be very limited with respect to the performance of beam-to-column joints under fire loading, even though research is still active in the field of monotonic and cyclic loading (Gil and Bayo, 2007 and 2008, Salvatore et al., 2005). This context of limited information on beam-to-column steel-concrete composite joints under fire and seismic-induced fire, motivated the European Union-financed research project PRECIOUS, devoted to the development of fundamental data, design guidelines and prequalification of two types of fire-resistant composite beam-to-column joints: one endowed with partially reinforced-concrete-encased columns with I-section; one with CFT columns (Bursi et al., 2008). Because fire and earthquake are accidental actions and have been treated most often as independent events (EN Eurocode 1991-1-2, 2004, EN Eurocode 1998-1, 2005), the project fitted in a modern multi-objective performance-based design where fire safety is also considered on a structure characterized by stiffness deterioration and strength degradation owing to seismic actions. In detail: the intensity measures were defined by means of artificial accelerograms and natural fires; engineering indices were defined in terms of joint distortions, interstory drifts and time for fire resistance; damage measures owing to earthquake and fire were considered both at the joint and at the frame level taking into account the interaction between joints and members; decision variables were related to life safety (SEAOC, Vision 2000). The project achieved its objective through a balanced combination of analytical/numerical and experimental work. The present paper only concentrates on Type 2 joints, for which it is presented: i) both frame design and joint design for seismic and fire loadings; ii) the analysis of both mechanical and thermal behavior of this typology by means of experimental tests; iii) results from moment resisting frames endowed with the investigated joint solution under seismic loading.

DESIGN OF REFERENCE FRAMES UNDER EARTHQUAKE AND FIRE

In order to obtain design actions on joints, two moment resisting frames were designed with the same structural typology but different slab systems. In the frame design, particular attention was paid to the layout of structural elements according to economic criteria and to their optimization both for vertical and lateral loads. The reference structures are depicted in Figure 1(a) to 1(c) and are made up of three moment resisting frames placed at the distance of 7.5 m each in the longitudinal direction; while they are braced in the transverse direction with an interstorey height of 3.5 m. Two different slab systems were considered: i) a concrete slab composed of electro-welded lattice girders as shown in Figure 2(a); ii) a composite steel-concrete slab with structural profiled steel sheeting as illustrated in Figure 2(b). All slabs were arranged in parallel to main frames. Steel beams and slabs were fully connected with full interaction by means of Nelson 19 mm (3/4 in.) stud connectors with an ultimate tensile strength f_u=450 MPa. In both cases, composite beams were realized with S355 (A615 Grade 50) IPE400 steel profiles, while composite columns were realized with 457 mm (18 in.) circular steel tubes with 12 mm thickness. The

seismic performance of typical frames was evaluated by means of nonlinear static pushover analysis. Afterwards, the fire design issue was considered and the structural fire performance of the complete frame was evaluated by means of the SAFIR software (Franssen, 2000). In this respect, several simulations were carried out on the frames depicted in Figure 1 to assess the seismic-induced fire performance of the aforementioned moment resisting frames. Along the line of Della Corte et al. (2003), the effect of the seismic loading applied prior to fire loading was taken into account by imposing one loading-unloading cycle through identical horizontal forces applied at each floor. In addition to an initial imperfection, this loading cycle induced some plasticity in each frame. The impact of the earthquake on the fire resistance of the analysed frames appeared to be not so significant because failure occurred when a beam plastic mechanism formed in the long-span heated beams. Moreover, no global instability modes formed under fire loading with a fire exposure lower than 30 minutes in the majority of cases.

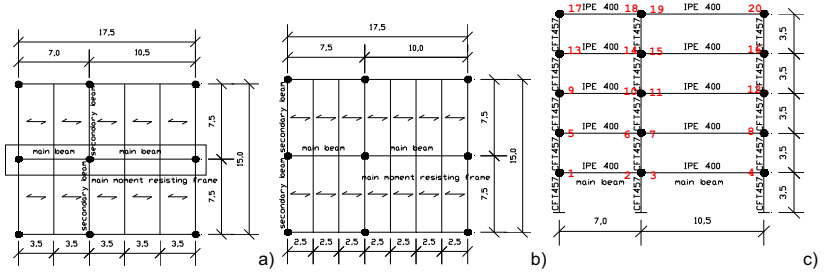


Figure 1 – Geometric layout of reference structures: a) structure with slabs with prefabricated lattice girders; b) structure with slabs with profiled steel sheeting; c) frame elevation

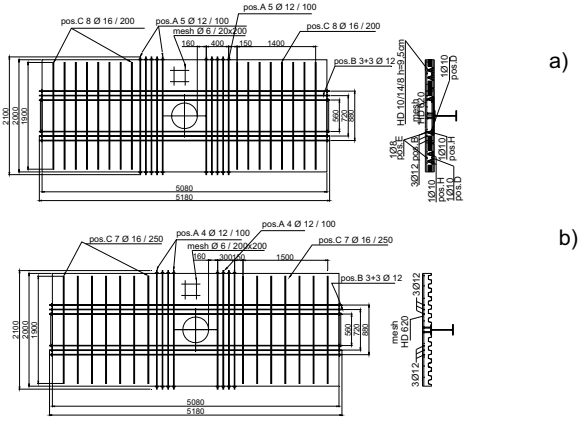


Figure 2 – Schematic view: a) solution with prefabricated lattice girders; b) solution with steel sheeting. (Dimensions in mm)

The slabs composed by prefabricated lattice girders illustrated in Figure 2(a) were endowed with 3+3ϕ12 (3+3#4 in.) longitudinal rebars and 5+5ϕ12@100 mm (5+5#4@4 in.) plus 8+8ϕ16@200 mm (8+8#5@8 in.) transversal steel bars. A mesh ϕ6@200x200 mm (ϕ6@8x8 in.) completed the slab reinforcement. Conversely, the slab with profiled steel sheeting was endowed with 3+3ϕ12 (3+3#4 in.) rebars, 4+4ϕ12@100 mm (4+4#4@4 in.) and 7+7ϕ16@250 mm (7+7#5@10 in.) transversal steel bars as shown in Figure 2(b); a mesh ϕ6@200x200 mm (ϕ6@8x8 in.) was adopted. It should be recalled that longitudinal and transversal rebars are needed to activate strut and tie Mechanism 1 and 2 foreseen in EN Eurocode 1998-1 (2005); one couple of longitudinal rebars was designed to face damage owing to seismic loading. The rebar steel grade was S450B (A615 Grade 60) while the concrete class was C30/37 (4350 psi). Composite beams were of Class 2 (EN 1993-1-1,2005).

The concrete filled tubular (CFT) columns were S355 (A615 Grade 50) endowed with 8ϕ16 (8#5) longitudinal rebars and ϕ8@150 mm (ϕ8@6 in.) stirrups as illustrated in Figure 3. The steel grade was S450B (A615 Grade 60) with concrete class C30/37 (4350 psi). Due to circular CFTs, the seismic design of composite beam-to-column joints was conceived to provide both adequate overstrength and stiffness with respect to connected beams, thus forcing plastic hinges formation in adjacent beams (EN 1998-1, 2005). Basides that: joints were detailed by using the component method as illustrated in Figure 4a (EN 1993-1-8. 2005).

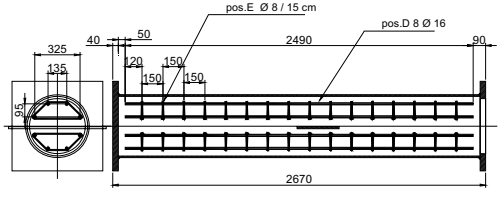
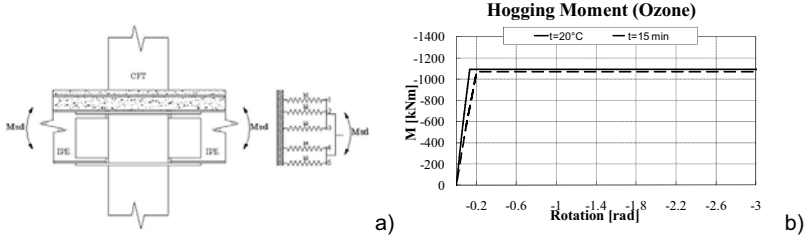


Figure 3 - Column stub and reinforcements capable of hosting a through-column web plate

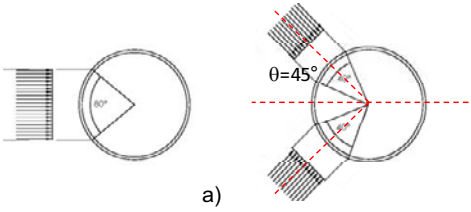


a) b)

Figure 4 – (a) Interior Type 2 joint and mechanical model; (b) Moment-rotation relationship of a joint as a function of the time fire resistance

The following components were considered in the method: concrete slab in compression; upper horizontal plate in compression; vertical plate in bending and lower horizontal plate in tension, for sagging moment; reinforcing bars in tension, upper horizontal plate in tension; vertical plate in bending and lower horizontal plate in compression for hogging moment. Eurocode 3 (EN 1993-1-8, 2005) does not provides formulas for some components, specially for tubes, thus, the concrete slab

in compression and the upper horizontal plate in tension were characterized by means of FE models set with ABAQUS (Hibbitt et al., 2000), as illustrated in Figure 5 and 6, respectively.



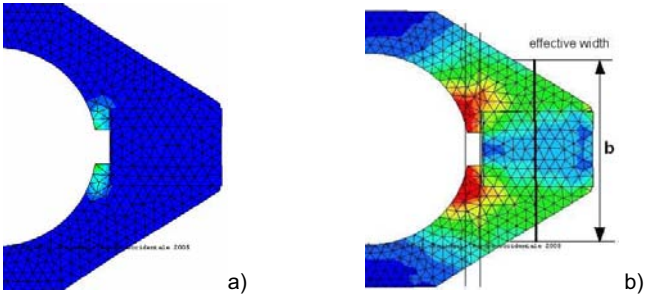
a) b)

Figure 5 – Strut and tie mechanisms assumed in the slab: a) Mechanism 2; b) Mechanism 1

The effective width b of plates was approximately assumed to be half of the total plate width. In the application of the component method the composite column was assumed to be infinitely rigid. Beam-to-column joints were rigid full-strength joints with respect to adjacent beams satisfying the condition that $M_{j,pl,Rd}$ was at least 1.3 $M_{b,pl,Rd}$ (EN 1998-1, 2005). Moreover, full groove and fillet welds were used. In detail, fillet welds satisfied the relationship:

$$R_d \geq 1.1 \cdot \gamma_{ov} \cdot R_{fy} \tag{1}$$

with an overstrength factor $\gamma_{ov} = 1.25$.



a) b)

Figure 6. FE model of a plate in tension: (a) elastic stresses; (b) inelastic stresses and effective width.

The beam-to-column joint is shown in Figure 7. It is composed of two horizontal plates and a vertical through-column plate. Only half of the top plate has to be welded on site. The presence of the vertical through-column plate shown in the top left of Figure 7 and the presence of concrete close to the top plate help the joint to keep a lower temperature of these components, when exposed to fire. Thus the induced-seismic fire resistance objective imposed by design should be achieved. In fact, joints were designed to exhibit a residual load-bearing capacity for 15 minutes without passive or active fire protections.

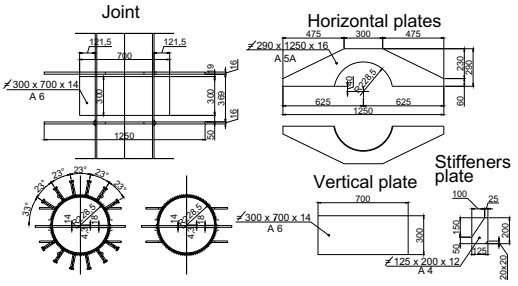


Figure 7 – Details of an interior composite beam-to-column joint. (Dimensions: mm)

In view of fire resistance, thermal analyses of joints were performed to obtain internal temperature distributions. In this respect, a 3D finite element model of an interior joint was implemented in the Abaqus software (Hibbitt et al., 2000) and employed to conduct thermal analyses for different fire exposures, i.e. 15, 30 and 60 min, respectively. The joint endowed with prefabricated slabs exhibited a better performance compared to the joint endowed with steel sheeting, see Figure 8; in fact the concrete slab temperature of the first solution was smaller than the temperature in the second solution. Moreover, FE analyses allowed the component method to be applied to joints at different fire exposures. As an example, Figure 4(b) shows how the hogging moment capacity reduces of about 90-95 per cent of its initial value after 15 minutes of exposure. These numerical results indicate that beam-to-column joints are able to carry this internal action that beams transfer to columns for a time of at least 15 minutes without any additional passive fire protection.

TEST PROGRAM

The experimental programme covered the execution of six seismic tests and six fire tests on full-scale substructures representing interior welded beam-to-column joints. Seismic tests were carried out at the University of Trento, Italy, considering both cyclic and monotonic loadings. Fire tests were conducted at the Building Research Establishment, UK, with asymmetric loading on joints to simulate adjacent primary beams of different lengths.

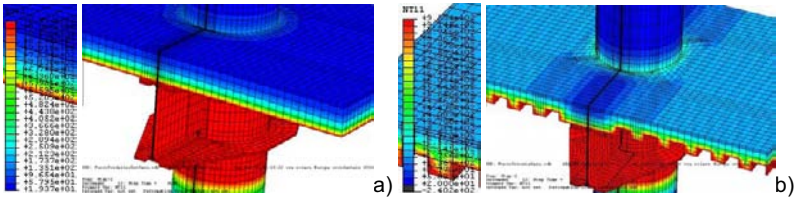


Figure 8 - FE model and temperature distribution for an interior joint endowed with: a) prefabricated lattice girder slabs b) profiled steel sheeting slabs.

Table 1 reports the joint specimens subjected to cyclic and monotonic loading up to collapse. Specimens 2-5 were endowed with horizontal Nelson stud connectors welded around the column, see Figure 7, to increase the friction level between the concrete slab and the composite column, thus favouring the Mechanism 2 idealized

in Figure 5b. Specimen were tested according to the ECCS stepwise increasing amplitude loading protocol, modified with the SAC procedure (ECCS 1986, SAC 1997). In detail, it was imposed a yield displacement e_y= 0.005h = 17.5 mm, where h represents the storey height.

Table 2 reports the test nomenclature of four interior specimens subjected to fire tests. In particular before fire testing, two specimens T21 and T24 were pre-damaged to simulate damage caused by an earthquake, i.e. by means of Type 1 spectrum compatible accelerograms at 0.4g pga (EN 1998-1, 2005). Conversely, Test T22 and T25 were not pre-damaged, to better appreciate seismic damage effects on fire resistance.

Table 1 – Specimens subjected to monotonic and cyclic tests

N.	Label	Test Protocol	Type of Specimen
1	WJ-P1	Cyclic	Specimens with electro-welded lattice girder slabs and no Nelson connectors around the column
2	WJ-P2	Cyclic	Specimens with electro-welded lattice girder slabs and Nelson connectors around the column
3	WJ-PM	Monotonic	Specimens with electro-welded lattice girder slabs and no Nelson connectors around the column
4	WJ-S1	Cyclic	Specimens with profiled steel sheeting slab and no Nelson connectors around the column
5	WJ-S2	Cyclic	Specimens with profiled steel sheeting slab and Nelson connectors around the column
6	WJ-SM	Monotonic	Specimens with profiled Steel Sheeting slab and no Nelson connectors around the column

To accurately simulate damage owing to seismic events, non-linear dynamic time histories were performed by using the IDARC-2D program (Valles et al., 1996). Experimental data of joints were used to define both hysteretic laws in IDARC-2D and damage domains according to the Chai & Romstad criterion (Chai et al., 1995).

Table 2 – Specimens subjected to fire tests

N.	Label	Test Method	Type of Specimen
1	T21	Fire	Pre-damaged Specimen endowed with steel sheeting slabs
2	T22	Fire	Undamaged Specimen endowed with steel sheeting slabs
3	T24	Fire	Pre-damaged Specimen endowed with prefabricated lattice slabs
4	T25	Fire	Undamaged Specimen endowed with prefabricated lattice slabs

The corresponding values of damage in joints provided by IDARC-2D simulations are gathered in Table 3 where average values for joints with prefabricated slab and steel sheeting slab are provided owing to the limited number of experimental data. The trend is evident: the damage in joints was limited and repairable.

Table 3 – Damage index for joints with prefabricated slabs, slabs with steel sheeting

Joint typology	Damage index D
Exterior joint	0.43
Interior joint	0.34

Subsequently, specific deformations were prescribed on joints through monotonic vertical loading to induce the damage identified in Table 3. Hence, specimens were loaded according to the fire load combination (EN 1991-1-2, 2004) and fire tests were undertaken.

Typical beam-to-column joint specimens are illustrated in Figure 9. A welding procedure employed in laboratories was conceived to simulate on site welding, taking into account the Type of electrode employed, i.e. OERLIKON-ETC PH355 ϕ=3.25, with a pre-heating at 80°C.

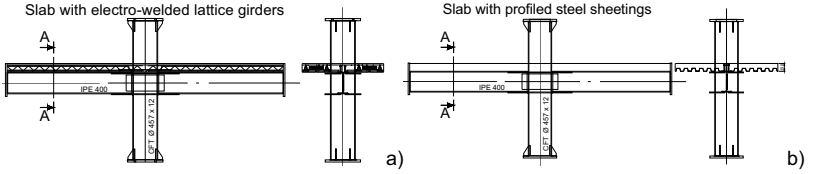


Figure 9 - Beam-to-column joint specimens: a) slab with lattice girders; b) slab with sheetings

The experimental set-up employed for seismic tests is shown in Figure 10. A hydraulic actuator endowed with a capacity of ±1000 kN and a stroke ±250 mm were used. Different sensors were utilized: 5 inclinometers to measure rotations of joint and beams; 4 LVDTs to detect interface slip between steel beam and concrete slab; 2 LVDTs to measure joint deformations; 10 LVDTs and 4 Omega strain gauges to assess concrete slab deformations; 8 strain gauges to monitor axial deformations of rebars; 8 strain gauges to measure top and bottom plate deformations and flange strains; 2 load cell located in trusses to measure horizontal and vertical components of reaction forces; 1 digital transducer DT500 to detect top column displacements.

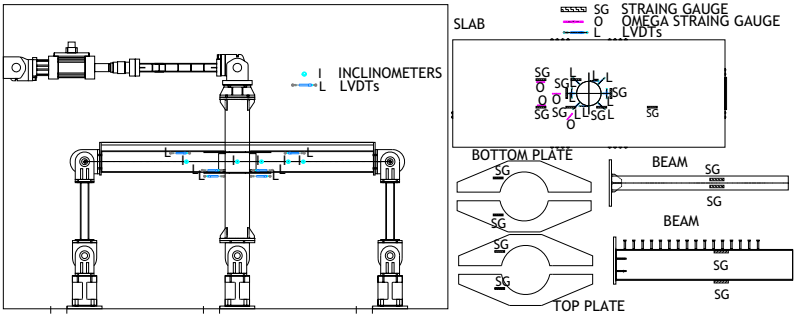


Figure 10 - Lateral view of the test set-up and instrumentation

TEST RESULTS AND ANALYSIS

Seismic test results of beam-to-column joints

Both the force-interstory drift and moment-rotation relationships of WJ-P1 and WJ-P2 specimens with electro-welded lattice slabs and without/with Nelson connectors around the column are illustrated in Figure 11 and 12, respectively. Plastic hinges developed in beams adjacent to joint and progressive deterioration of strength and stiffness was associated with beam flange buckling. Failure was due to beam flange cracking. A reader can observe that specimens exhibited a similar behaviour and beams developed plastic rotations greater than 25 mrad required by Eurocode 8 (EN 1998-1, 2005) for moment resisting frames of Medium ductility class.

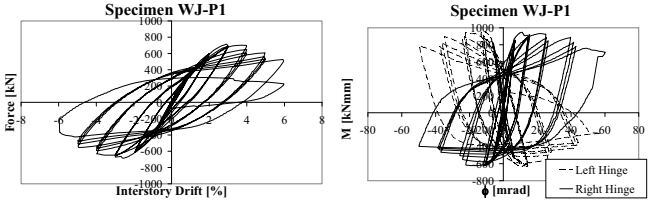


Figure 11 – Specimen WJ-P1: Force-Displacement and Moment-Rotation curves

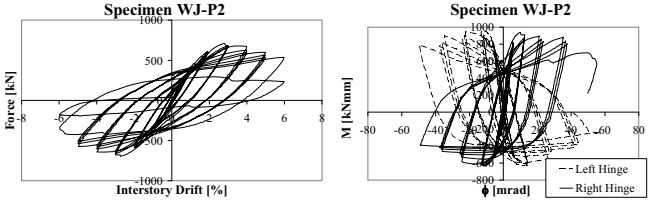


Figure 12 – Specimen WJ-P2: Force-Displacement and Moment-Rotation curves

Similar results were obtained for specimens WJ-S1 and WJ-S2 endowed with slabs with profiled steel sheeting and without/with Nelson connectors around the column, respectively. Experimental results are shown in Figure 13 and Figure 14, respectively. Favourable results can be observed. Nonetheless differently from previous cases, both in beams and joints, the neutral axis was located in the beam web for sagging moment owing to the greater damage imparted by lateral loads to the slabs endowed with steel sheeting.

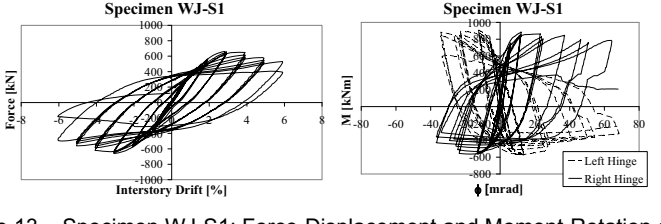


Figure 13 – Specimen WJ-S1: Force-Displacement and Moment-Rotation curves

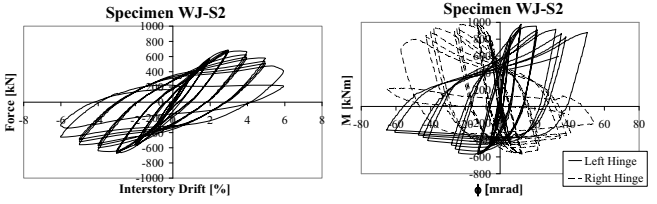


Figure 14 - Specimen WJ-S2: Force-Displacement and Moment-Rotation curves

Monotonic test results for the specimen WJ-PM endowed with prefabricated slabs with electro-welded lattice girders without Nelson connectors welded around the columns are plotted in Figure 15. Similar results were obtained for the specimen WJ-SM slab endowed with slabs with profiled steel sheeting (Bursi et al., 2008). The electro-welded lattice slabs of WJ-PM exhibited less damage owing a most favourable composite action in the plastic hinge beam section.

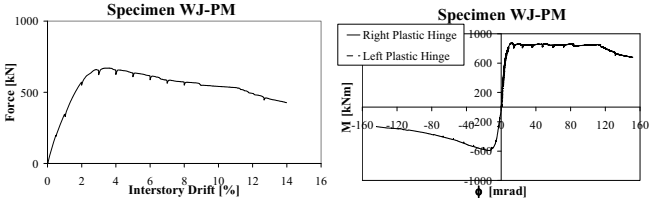
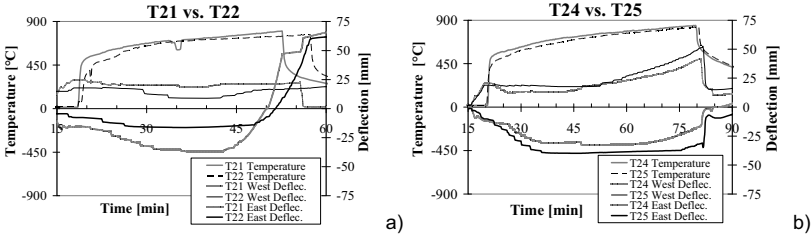


Figure 15 - Specimen WJ-PM: Force-Displacement and Moment-Rotation curves

Fire test results of beam-to-column joints

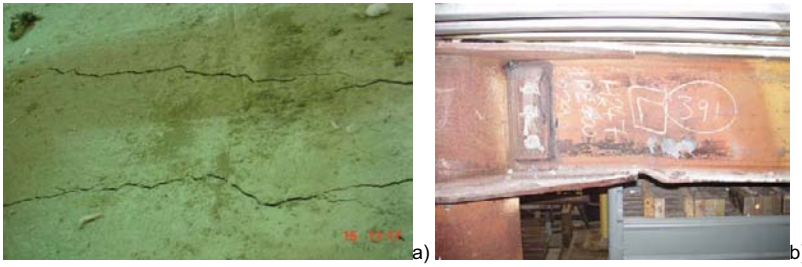
Both pre-damaged and undamaged specimens were subjected to fire loading, see Table 2, and some results are presented herein. The temperature vs. time curve imposed to the specimens T21-T22 and T24-T25 is shown in Figure 16(a) and (b), respectively. Specimens T21 and T22 with profiled steel sheeting slabs exhibited failure owing to an excessive rate of deflection at approximately 40 minutes. The test on specimen T21 terminated after approximately 34 minutes owing to runaway deflection. Following the fire test, the profiled steel sheeting separated from the slab; then the slab cracked both along the surface and through the depth with extensive buckling at one hour both of the lower flange and the web of the adjacent east beam, as shown in Figure 17. T24 and T25 specimens endowed with prefabricated slabs endured one hour of fire; however, in both cases specimens were very close to failure as indicated, in Figure 16b, by an increasing rate of deflections towards the end of the test.

However, at this stage, there was no permanent deformation and no sign of any significant damage from fire tests. Hence, it can be underlined that: i) there was no noticeable difference in the fire performance between pre-damaged and undamaged specimens both with precast and steel sheeting slabs; this result is in agreement with damage values reported in Table 3 and with the inherent safety of composite joints (EN 1998-1, 2005; Bursi et al., 2008); ii) precast slabs performed better also in fire tests than the corresponding specimens with steel sheeting at a fire exposure in excess of the 15 minutes required; iii) all specimens exhibited favourable seismic properties by performing in a ductile manner also under fire loading.



a) b)

Figure 16 – Performance of damaged (T21/T24) and undamaged (T22/T25) specimens.



a) b)

Figure 17 – Specimen T21: a) Surface cracking of the slab; b) Local buckling of east beam

Supplementary moment resisting frame analyses

At the frame level, several simulations were performed to assess both the seismic and fire behaviour of moment resisting frames endowed with the proposed joint both with steel sheeting and prefabricated slabs (Bursi et al., 2008). In detail, specimens subjected to cyclic loadings developed plastic rotations greater than 25 mrad, thus being adequate for moment resisting frames of Medium ductility class (EN 1998-1, 2005). Along the line of the Aribert et al (2006) work, incremental dynamic analyses were performed on the prototype frames depicted in Figure 1, in order to find some correlation between required plastic rotations for high ductility moment frames, i.e. about 35 mrad, interstorey drifts and the demand in p.g.a. It is found that by using artificial accelerograms compatible with Type 1 Eurocode 8 spectrum (EN 1998-1, 2005), interstory drifts between 3.41÷5.80 per cent developed with p.g.a. ranging between 1.40÷1.92g. For brevity, some results provided by these analyses for joints endowed with Nelson studs around the columns are gathered in Table 4 where large p.g.a. values are evident. Moreover, it was shown that energy dissipating mechanisms within frames endowed with the examined joints relied on the formation of plastic hinges at beam ends and that a behaviour factor of about 4 was estimated, thus allowing to adopt the proposed joints for Ductility Class M moment frames.

Table 4 – Seismic demands and drifts for plastic joint rotations from frame analyses

Specimens endowed with electro-welded lattice slabs and with column's Nelson studs				
Time History	pga (g)	Plastic Joint Rotation (mrad)	Location in Fig.1c	Interstorey Drift (%)
Accelerogram 1	1.92	26.1	10	5.80
Accelerogram 2	1.80	26.2	6	4.55
Accelerogram 3	1.50	26.7	2	4.19
Specimens endowed with steel sheeting slabs and with column's Nelson studs				
Time History	pga (g)	Plastic Joint Rotation (mrad)	Location in Fig.1c	Interstorey Drift (%)
Accelerogram 1	1.72	23.0	7	5.36
Accelerogram 2	1.60	29.4	4	3.68
Accelerogram 3	1.40	26.1	1	3.98

CONCLUSIONS

A multi-objective design methodology dealing with seismic-induced fire actions on steel-concrete composite moment resisting frames endowed with full strength joints using concrete filled tubes has been presented in this paper. Instead of a traditional single-objective design, where fire safety and seismic safety are achieved independently and the sequence of seismic and fire loadings are not accounted for, in the proposed multi-objective design developed by means of mechanical resistance of members and joints, it has been guaranteed: i) seismic safety with regard to accidental actions; ii) fire safety with regard to accidental actions; iii) fire safety for at least 15 min fire exposure on a structure characterised by stiffness deterioration and strength degradation owing to an earthquake. As a result, the fire design applied to a structure with reduced capacity owing to seismic actions has provided structural, seismic and fire safety as required, but also structural and fire safety and structural and seismic safety, respectively. These objective were achieved through a balanced combination of analytical/numerical and experimental works.

ACKNOWLEDGMENTS

The writers are grateful to the European Union for financial support under the project PRECIOUS-RFS-CR-03034 and to the partners as well. Nonetheless, conclusions of this paper are those of the authors and not of the sponsor agency.

REFERENCES

Aribert J.M., Ciutina A.L., Dubina D., 2006, “Seismic response of composite structures including actual behaviour of beam-to- column joints”, in Composite construction in steel and concrete V, Leon and Lange ed. South Africa. ASCE, 708-717.

Block F.M., Burgess I.W., Davison J. B., Plank R. J. 2007 The development of a component-based connection element for endplate connections in fire. Fire Safety Journal 42. 498–506.

Bursi O.S., et al. Editors, Final Report PRECIOUS Project Contr. N. RFSCR-03034, 2008. Prefabricated Composite Beam-to-Concrete Filled Tube or Partially Reinforced-Concrete-Encased Column Connections for Severe Seismic and Fire Loadings.

Chai Y.H., Romstad K.M., Bird S.M. 1995, “Energy-based linear damage model for high-intensity seismic loading”, Journal of Structural Engineering, ASCE, 121(5), 857-864.

Della Corte G., Landolfo R., Mazzolani F.M. 2003, “Post-earthquake fire resistance of moment resisting steel frames”, Fire Safety Journal, 38, 593-612.

ECCS. 1986. Recommended Testing Procedure for Assessing the Behaviour of Structural Steel Elements under Cyclic Loads. Publication n° 45;

EN 1991-1-2. 2004. “Eurocode 1: Actions on Structures. Part 1-2 : General Actions – Actions on structures exposed to fire”;

EN 1993-1-1. 2005. “Eurocode 3: Design of steel structures. Part 1-1: General rules and rules for buildings;

EN 1993-1-2. 2005. “Eurocode 3: Design of steel structures. Part 1-2: General rules - Structural fire design”;

EN 1993-1-8. 2005. “Eurocode 3: Design of steel structures - Part 1-8: Design of joints”;

EN 1994-1-2. 2005. “Eurocode 4: Design of composite steel and concrete structures - Part 1.2: General rules – Structural fire design”;

EN 1998-1. 2005. “Eurocode 8: Design of structures for earthquake resistance - Part 1: General rules, seismic actions and rules for buildings”;

Franssen J.-M. 2000. “SAFIR; Non linear software for fire design”. Univ. of Liege;

Gil B., Bayo E. 2008. An alternative design for internal and external semi-rigid composite joints. Part I: Experimental research Engineering Structures 30. 218–231

Gil B., Bayo E. 2008. An alternative design for internal and external semi-rigid composite joints. Part II: Finite element modeling and analytical studies. Engineering Structures 30. 232–246

Hibbitt, Karlsson and Sorensen 2000. “ABAQUS User’s manuals”. 1080 Main Street, Pawtucket, R.I. 02860;

Kobe City Fire Department 1995 Investigation report on damages fire protection systems caused by the Hanshin-Awaji earthquake in Kobe.

SAC 1997, Protocol for Fabrication, Inspection, Testing, and Documentation of Beam-Column Connection Tests and Other Experimental Specimens, report SAC /BD-97/02;

Salvatore W, Bursi OS, Lucchesi D. 2005. Design, testing and analysis of high ductile partial-strength steel–concrete composite beam-to-column joints. Computers & Structures; 83 (28–30):2334–52.

Santiago, A, Simões da Silva L, Vila Real P, Milan Veljkovic. 2007. Numerical study of a steel sub-frame in fire. Computers and Structures. (submitted).

SEAOC - Structural Engineers Association of California. 1995. Performance Based Seismic Engineering of Buildings, Vision 2000 Committee, 2 vols. Sacramento, CA.

Simões da Silva, L., Santiago, A., Moore, D. e Vila Real, P. 2005. Behaviour of steel joints and fire loading. Int. J. of Steel and Composite Structures 5(6), pp. 485-513.

The Marine and Fire Insurance Association of Japan (MFIAJ) 1995. Study report on reliability of fire protection systems at an earthquake, 1995.

Valles R.E., Reinhorn A.M., Kunnath S.K., Li C., Madan A. 1996, IDARC2D Version 4.0: A Program for the Inelastic Damage Analysis of Buildings, Report NCEER-96-0010, 1-8.

Yashiro, Y., Ebihara, M. and Notake, H., 2000, Fire safety Design and Fire Risk Analysis Incorporating Staff Response in Consideration of Fire Progress Stage. 15th meeting of US-Japan Cooperative Program in Natural Resources by Int. Assoc. for Fire Safety Science.

SEISMIC BEHAVIOR OF CONNECTIONS TO GANGUE-FILLED CFT COLUMNS WITH RING STIFFENERS

Guochang Li
School of Civil Eng., Shenyang Jianzhu Univ. , Shenyang 110168, china
liguochang0604@sina.com

Wei Sun
School of Civil Eng., Shenyang Jianzhu Univ. , Shenyang 110168, china
elitesunwei@hotmail.com

Roberto T. Leon
School of Civil and Environmental Eng., Georgia Institute of Technology, Atlanta 30332-0355, USA
rl58@ce.gatech.edu

Abstract

To make full use of the excellent mechanical performance of gangue light-weight concrete, half-size models of joints between steel beams and gangue concrete-filled steel tube columns with ring stiffeners were tested under reversed low cyclic loads. Data collected included extensive strain measurements in key areas of the connection. The data indicates that the behavior of the connection can be adequately predicted by simple mechanical models except in the vicinity of the ring stiffeners. The joints exhibited very robust behavior, with loads increasing until failure was reached due to weld fracture. The cumulative plastic strain resisted by the welds was large, and the gangue lightweight aggregate concrete demonstrated equal or better performance than conventional LW concretes.

1 Introduction

Concrete-filled steel tubes (CFT) are used extensively used in high-rise construction projects because of their high strength, excellent hysteretic behavior and ductility, shorter construction cycles and economy. It is well known that joints are the most important element in the design of moment-resisting frames in seismic zones, and therefore, characterizing the cyclic inelastic behavior of joints is very important to the utilization of concrete-filled steel tubes[1-4], particularly when new materials are being used as aggregates in the concrete.

Gangue is a lightweight, industrial waste, a byproduct of the extraction of many mineral resources. In China, where gangue is mostly the by-product of small coal mines, gangue not only takes up a great deal of usable land but also is a large source

of pollution to the environment. Thus, it is necessary to find alternative uses for this waste material [5]. If gangue is used as aggregate in concrete, it will contribute to a sustainable building industry because it both uses recycled materials and reduces the structure weight. Research on the cyclic inelastic behavior of joints between steel beams and CFTs with lightweight concrete is scant. The research presented herein is intended to both promote the use of joints with lightweight concrete-filled steel tubes and to add fundamental knowledge of the performance of CFT connections with lightweight aggregates [6-7].

2 Experimental Research

To assess the behavior of connections to gangue-filled CFT columns, two half-scale joints between concrete-filled steel tube columns and steel beams were designed and constructed. Member sizes are given in Table 1. One specimen was an interior joint and the other an exterior one. Details of the specimens are given in Figure 1; the exterior specimen was identical to that shown in Fig. 1, except that it was missing the right beam. Both specimens had connections that included through ring stiffeners around the column to facilitate the construction of the connection.

The column was fabricated from a thread-welded tube with a diameter of 325mm and thickness of 6mm. The D/t is 54.2, which corresponds to a moderately stocky section for which little local buckling would be expected. The beam is a welded I shape with stiffeners added 200mm from the ends of the beam to facilitate the force transfer from the actuators [8-10]. The b_f/t_f for the flanges is 7.5 and the h/t_w for the web is 41; both of these ensure that large inelastic strains can be reached. All welds are 6mm fillet welds with electrodes having an ultimate strength greater than 690 Mpa.

Table 1 Member and connection dimensions (all in mm)

Beam				*Column*	*Stiffener Plate/ Weld*		
b_f	t_f	t_w	H	（D×t）	b_s	t_1	h_f
150	10	8	350	Φ325×6	80	10	6

b_f = width of steel beam flange; t_f = thickness of steel beam flange

t_w = width of steel beam web; h = thickness of steel beam

b_s = width of ring stiffener; t_1 = thickness of ring stiffener

D = diameter of steel tube; t = thickness of steel tube shell

h_f = weld size.

The ring stiffeners have the same thickness as that of the beam flanges. All welded sections were made from low-carbon Q235B plate steel. Actual yield (f_y) and ultimate strengths (f_u) and modulus of elasticity (E_s) are shown in Table 2 for the different thicknesses of the Q235B plates used (6mm, 8mm and 10mm respectively). The concrete is nominally a C30 gangue concrete with a density of 1900 kg/m^3. Actual strengths at time of testing were 35.6 MPa for the interior joint specimen and 35.6 MPa for the exterior joint one.

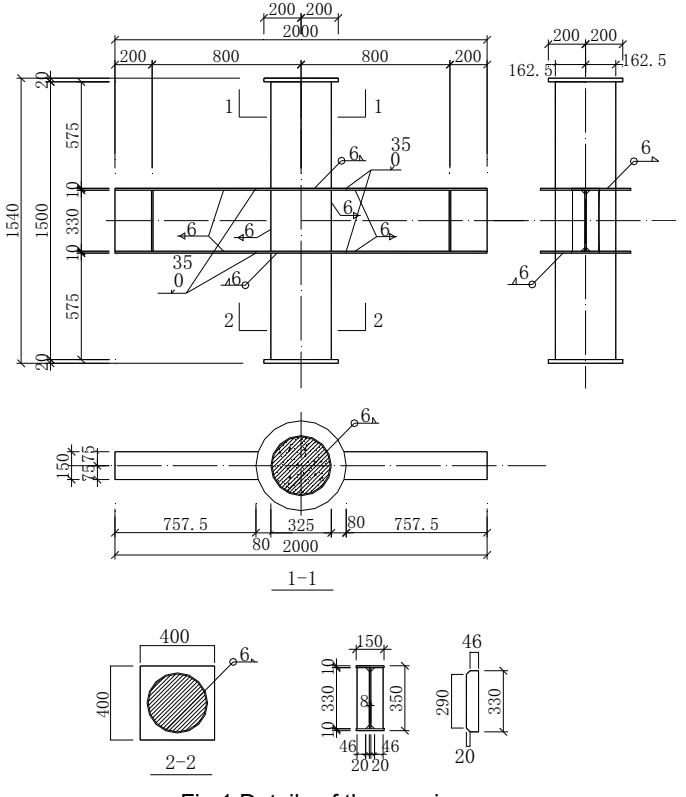


Fig.1 Details of the specimens

Table 2 Average material properties for Q235B steel

Steel type	*f_y/MPa*	*f_u/MPa*	*E_s/GPa*
t_s=6mm	324.8	459.9	197
t_s=8mm	306.4	417.5	202
t_s=10mm	347.1	578.2	204

The tests were carried out on 5000kN reaction frame in the Construction Engineering Laboratory of Shenyang Jianzhu University. Because the intent was to examine the force transfer mechanism in the ring stiffener in detail, the specimens were extensively instrumented with strain gages, as shown in Figs. 2 and 3. Rosette strain gauges were glued to the surface of the ring stiffeners at locations 45º and 90º degrees from the beam axis with the R and H gages aligned radially and tangentially to a line from the center of the column. Similar rosettes were used in the tube and beam web (Fig. 4). Longitudinal gages were used in the beam flanges.

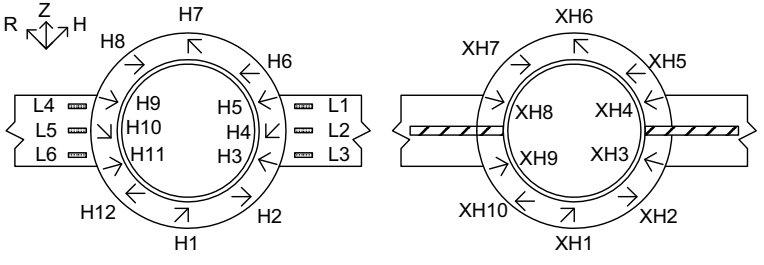


Fig.2 Position of the strain gauges in the beams and ring stiffeners

To start the tests, a 1800kN axial compressive force was applied to the top of the concrete-filled steel tube using a 5000kN jack. This axial load corresponded to about 0.6 of the nominal axial strength of the column and was maintained through the whole experiment[11-13]. Vertical reversed low cyclic loads were then imposed on the steel beams by electro-hydraulic actuators.

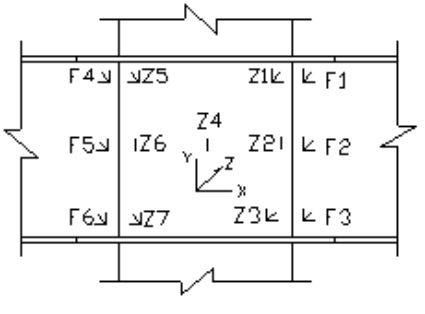


Fig.3 Position of the strain gauge in the joint

For the exterior joint, the initial load was 10kN with 5kN added at each new load level. The specimen was cycled 3 times at each of these load levels until the load reached

160kN; afterwards, the test was controlled by beam end displacements, in increments of 2mm, until the load reached 280kN when the joint failed. For the interior joint, displacement control was used for the whole experiment. The initial displacement was 3mm, and 2mm were added at every displacement increment, which consisted of 3 cycles. After yield was reached, the displacement change was increased to 3mm and only 2 cycles were applied until the load reached 250kN when the joints failed.

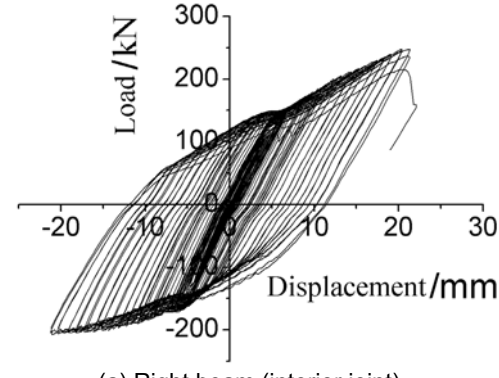
The load vs. beam end displacement curves are shown in Fig.4. Each 10mm of beam end displacement corresponds to about 1.25% interstory drift. It can be seen from Fig.4 that the curves are full, indicating the joints have excellent energy dissipation and hysteretic behavior. The large number of cycles imposed is also obvious from the figures.

After the joints yield (200kN), the two cycles at each deformation level almost coincide and the strength and stiffness decline very gradually. Overall, the joints are characterized by excellent ductility. The right beam for the interior joint showed a somewhat higher strength (250 kN) in the positive, or initial, direction of loading. In general, every 3mm increment resulted in a load increase of about 6.5kN until failure occurred due to fractures of the welds at the beam-ring interface. It should be noted that given the large number of cycles imposed, the total energy dissipated and the summation of the local plastic strains at the welds was large. An assessment of the significance of the weld failure at a relatively low interstory drift (2.5%) needs to take this into account.

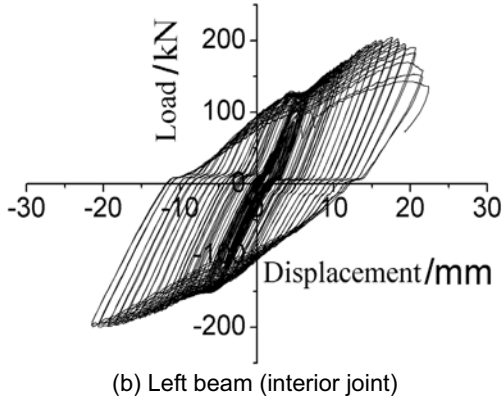
3 Analysis of strain data

Fig. 5 shows the strain profiles across the flanges of the one interior and the exterior beam at three positions (refer Fig. 2 for gage locations). Before the load reached ±100kN, the strain values at the three locations are basically the same in the first direction of loading (positive load). When the load is between ±100kN and ±160kN, strain values at the three locations change differently, particularly in the negative direction of loading, but all maintain a straight line trend. When the load reaches ±160kN, the specimen starts to yield, and the strains increase rapidly as the steel beam enters the elastic-plastic stage. With additional loads beyond ±160kN, the plastification of the specimen is becoming obvious. The strain increment also increases along with until the load reaches ±220kN when the local strain value begins to stabilize, yielding extends, and a full plastic hinge forms.

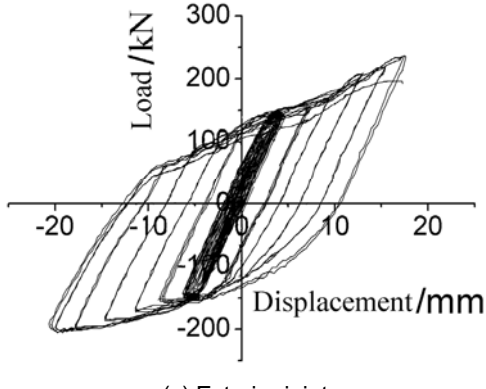
Throughout the test, the longitudinal strains in the steel beam flanges increase gradually and predictably. The strain data indicates a reasonably uniform distribution of strains across the flange and the formation of a full plastic hinge in the positive direction of loading (downwards) but a pronounced asymmetry and lack of yielding in the negative direction. This appears to be due to incipient lateral torsional buckling.



(a) Right beam (interior joint)

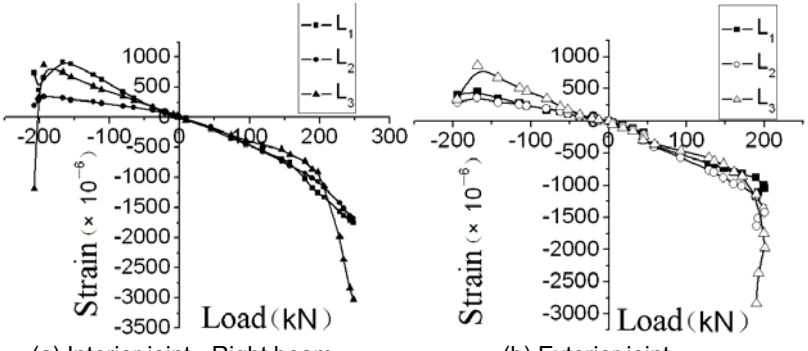


(b) Left beam (interior joint)



(c) Exterior joint

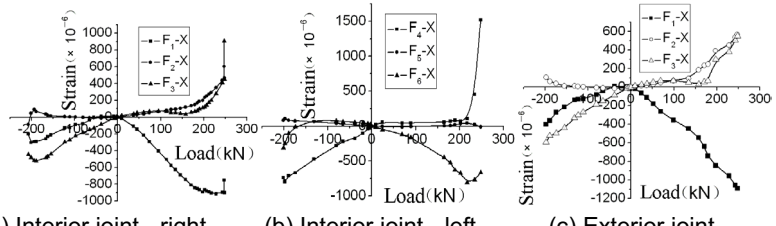
Fig.4 Load-beam end displacement curve



(a) Interior joint - Right beam (b) Exterior joint

Fig.5 Strains in the flanges of the steel beams

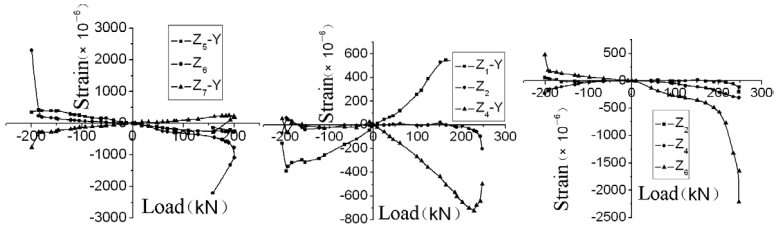
Fig.6 shows the strains in the web of the beam (refer to Fig.3 for strain gauge locations). The shape of the strain distribution for the interior and exterior joints is similar. The magnitude of the maximum strains is also close, and these strains are consistent with those in the steel beam flanges. The change of the strain value at F1-X and F3-X are reasonable and intuitive, while that of F2-X is not.



(a) Interior joint - right (b) Interior joint - left (c) Exterior joint

Fig.6 Strains in beam webs

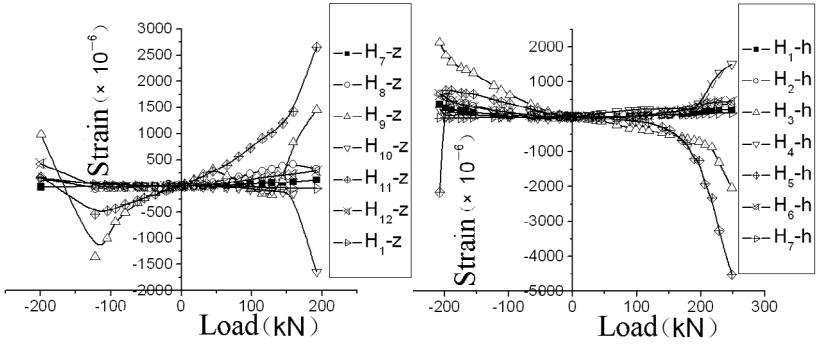
The difference is due to the ring stiffener located close to F1-X and F3-X. The ring stiffener affects the stress distribution of the section and the stress is concentrated in this area. F2-X is far from the ring stiffener. Fig.8 shows the shapes of the strain distribution at the junction of the steel tube and the steel beam. These differ because the weld affects the strain distribution in the steel tube in this area and the geometric centerline and the loading axis of the specimen do not coincide exactly. Therefore, the axial force affects these two measuring points differently and the maximum strain values are also different. Compared with points Z1-Y, Z4-Y, Z5-Y, Z7-Y, points Z2 and Z6 changed little as the load increased. The reason is that the four measure points are close to the ring stiffener and the steel webs, where the welds are concentrated and the joint is weak. When the load reached 160kN, this is the location where the joint begins to yield.



(a) Right connection (S1) (b) Left connection (S1) (c) Centreline

Fig.8 Strains in the steel tube

Point Z4 is in the center of the steel tube, and as it can be seen from Fig.8 (c), the strain changed little and showed no yield phrase. The curve just decreased(?) a little when the load reached to 250kN. This implies that that the loads on the beams have only a small affect on the strain of the center of the steel tube; the main influence is from the axially compressive force. The concrete in the steel tube is also good for the stability of the steel tube. The steel ring stiffeners symmetry was fully considered when the positions of the measurement points were selected. As can be seen from Figs. 9 and 10, the strain of the steel ring stiffeners followed the expected patterns. In Fig.9, for the top ring, gages H9-z, H10-z, H11-z, H3-h, H4-h and H5-h are above the area of the junction of the steel ring stiffener and steel beam flanges. In Fig.10, for the bottom ring, gages XH8-z, XH9-z, XH3-h and XH4-h are below the area of the junction of the steel ring stiffener and steel beam flanges.

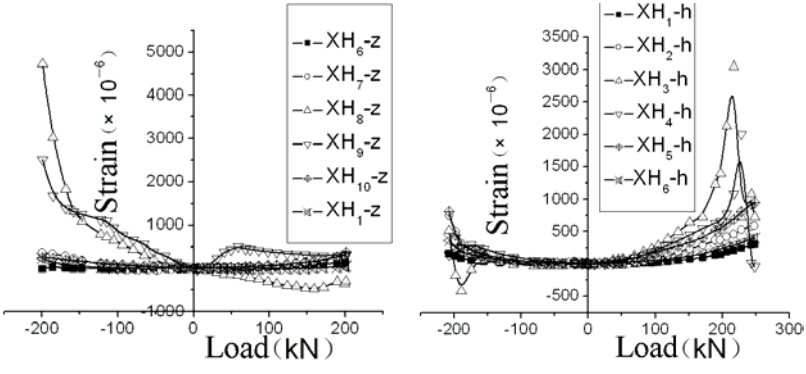


(a) Left steel ring stiffener (b) Right steel ring stiffener

Fig.9 Strain in the top steel ring stiffener

The strains of all these points changed predictably as the load increases. Points H9-z, H11-z, H3-h, H5-h, XH8-z, XH9-z, XH3-h and XH4-h, which are in near the corner of

the steel ring stiffener and steel beam flanges, change rapidly after the yield value is reached. The stress in these areas is concentrated (maximum strain is 4.9×10^{-3}) and is also the position which was damaged first. Points H8-z, H12-z, H2-h, H6-h, XH7-z, H10-z, XH2-h and XH5-h are in the areas of 45° angle of the ring-flat and beam axis. The strain of these measure points also change fast but at a lower rate than the ones in the corner areas. This shows that the areas near 45° are also high stress areas. Points H1-z, H7-z, XH1-z and XH6-z are in the areas of 90° angle of the ring-flat and beam axis and their strain changes little with the load increments. The curves are linear and have no obvious influence from the beam forces. The reason is that these points are far from the center of the joints and are affected only marginally by the shear force coming from the beams.



(a) Left steel ring stiffener (b) Left steel ring stiffener

Fig.10 Strain of the steel ring stiffeners below

4 Conclusions

The examination of the data obtained indicates that:

The force distribution at the center of the joints is complex and not in accord with those of a simple mechanical joint model. The behavior of other parts of the joints coincided with those from the mechanical models.

The areas up to a 45° angle of the ring are high stress areas but less so than the areas around a 0° angle to the beam. It appears that little can be done to reduce the stress concentrations in this region of the connection.

Extrapolation for the measured strains to the location of welds indicates that the strain state in these areas is complex, that high stress concentrations are likely, and that damage to the welds is likely under reversed cyclic loads.

The concrete in the steel tube is good for the stability of the steel tube. The loads on the beams affect the strain of the centre steel tube only marginally; the main effect is the axially compressive force.

Acknowledgements

The article was written while the senior author spent a sabbatical year at Georgia Tech. The support of the PRC government is gratefully acknowledged.

References

[1] ST Zhong. *Concrete-filled steel tube*. Harbin: Heilongjiang Science and Technology Press, 1995.
[2] DX Zhang, SM Zhang. Dynamic behavior of joints between concrete-filled steel tubes and beams. Journal of Harbin Jianzhu Univ., 2001,34(1):21-27.
[3] LH Han. C*oncrete-filled steel tube*. Beijing: Science Press, 2000.
[4] Beutel J., Thambirtnam D., and Perera N. Cyclic behaviour of concrete filled steel tubular column to steel beam connection. Eng. Structures, 2002, 24(11): 29-38.
[5] Li, G.C. and Liu, Z.Y. Self-Stress light-weight Concrete-filled steel tube. Shenyang: Northeastern Univ. Press, 2001.
[6] Li, G.C and Yang, H. Experimental research on the composite material mechanical properties of Self-Stress Light-weight Concrete-filled steel tube. Journal of Nanjing construction engineering college, 2001,(3): 21-25.
[7] Hao, G.Q. Research on the application of the light-weight concrete-filled steel tube. Journal of Building Materials and Application, 1999,(5): 27-32.
[8] Liu, Y.W. *Steel and concrete composite structure by manual calculation*. Beijing: China Construction Industry Press, 2004.
[9] Ge, H.B., Susantha, K.A.S., Satake Y., and Usami, T. Seismic demand predictions for concrete-filled steel box columns. Engineering Structures, 2003, 25:337~345.
[10] Zhong, S.T. *Concrete-filled steel tube in high-rise buildings*. Harbin: Heilongjiang Science and Technology Press, 1999.
[11] Huang, T. Basic research and design method for joints of concrete-filled steel tubes. Guangzhou: CE Department Huanan Polytechnic University, 2000.
[12] Mazzolani, F. *Moment resistant connections of steel frames in seismic areas -Design and reliability,* London: E & FN Spon, 2000.
[13] Li, Z.X.. Theory and Technique of Engineering Structural Testing. Tianjin: Tianjin Univ. Press, 2004.

STRENGTHENING OF COMPOSITE BEAM-TO-COLUMN JOINTS: STATIC AND SEISMIC BEHAVIOUR

G. LOHO
LGCGM - Structural Engineering Research Group, INSA
Rennes, France
Ghandi.Loho@yahoo.fr

A.LACHAL
LGCGM - Structural Engineering Research Group, INSA
Rennes, France
Alain.Lachal@insa-rennes.fr

J.M.ARIBERT
LGCGM - Structural Engineering Research Group, INSA
Rennes, France
jean-marie.aribert @insa-rennes.fr

ABSTRACT

This paper deals with the strengthening of beam-to-column end-plate bolted joints. Two strengthening dispositions have been developed and studied. The first one consists in adding a haunch welded on the beam bottom flange in the vicinity of the column. The second one consists in strengthening the column web panel (in presence or not of haunches) with double steel plates. This strengthening arrangement is studied in this paper from both experimental and numerical approaches. Based on these studies, two new static design models are proposed. The first model deals with the composite haunched joints. The second model provides a design method for the column panel zone strengthened by double steel plates.

INTRODUCTION

End-plate bolted beam-to-column joints are currently used in Europe in steel and composite construction. These joints often are semi-rigid and partial strength. The use of such joints in moment resisting frames in high ductility class (DCH) requires to strengthen them in order to make them rigid and full-strength. Besides EN 1998-3 [CEN, 2005] has specified recommendations, based on the works of [Yu et al. 2000], to strengthen beam-to-column steel connections of existing building by adding haunches.

Moment resisting frames subject to static or seismic lateral loads may develop large unbalanced moments in their beam-to-column joints and consequently high shear deformations in the column panel zone of these joints. In such a situation, the shearing of the panel zone has a significant influence on the moment-rotation behaviour of the joint and consequently should be taken into account in the global analysis of the structure (with regard to story drifts, second-order effects and stability) [Foutch DA 2002]. So, it is important to design properly the panel zone and therefore to control the resistance and the ductility of the joint. For that purpose

doubler plates welded on the web column may be an appropriate solution. EN 1993-1-8 (clause 6.2.6.1) [CEN, 2005] gives some design rules to strengthen the column web panel by adding doubler plates. In order to calculate the shear resistance, this code defines a shear resistance area including parts of the column and the doubler plates cross-section. Nevertheless, EN 1993-1-8 limits the maximum thickness of the doubler plates to the thickness of the column web if the total thickness of the doubler plates exceeds the web thickness. In addition, EN 1993-1-8 assumes uniform distribution of shear stress within the panel zone.

Both approaches used to strengthen beam-to-column joints (doubler plates or/and haunches) are studied in this paper from an experimental program and a three-dimensional finite element modelling. On the basis of the numerical and experimental results, two new static design models are proposed here for each strengthening solution.

EXPERIMENTAL INVESTIGATION

Program of tests

An experimental program was carried out at INSA of Rennes-France to study the general behaviour of beam-to-column composite joints with emphasis on the effect of joint strengthening on its seismic performance. Two strengthening dispositions have been considered. The first one consists in extending the end-plate below the beam and adding adjacent haunches at the corners with the column. The second one consists in strengthening the column web panel (in presence or not of haunches) with double steel plates welded to the root radius of the column section with full penetration butt welds and welded to the column web by fillet welds (Figure 3).

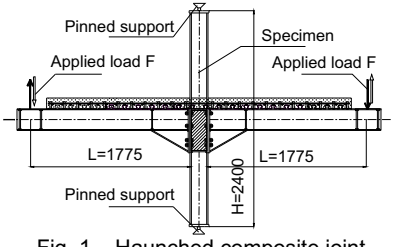


Fig. 1 – Haunched composite joint (Test G23)

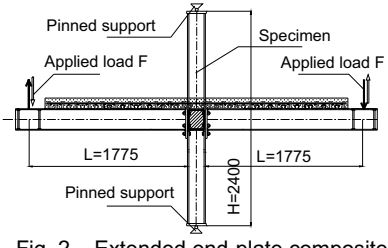


Fig. 2 – Extended end-plate composite joint (Tests G20 and G21)

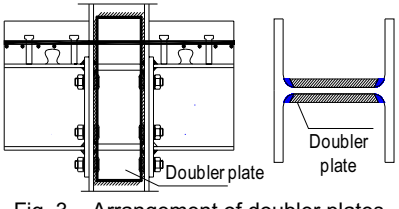


Fig. 3 – Arrangement of doubler plates strengthening the column web panel

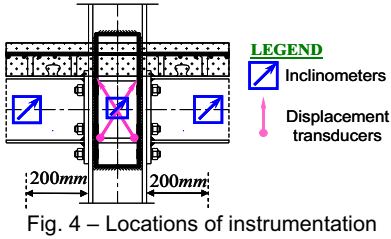


Fig. 4 – Locations of instrumentation

Figures 1 and 2 present the main characteristics of three full-scale beam-to-column joints G20, G21 and G23 (major axis connections) with cruciform arrangement. Common characteristics are a full shear connection for all composite specimens with welded headed studs Φ = 19 mm (h= 80 mm) and a composite slab (cast on a steel sheeting COFRASTRA 40) with a cross-section of dimensions 120×1000 mm. This slab is reinforced by 10 longitudinal rebars Φ10 mm and by transverse rebars Φ10 mm spaced each 10 cm. For all composite specimens, two doubler plates were connected to the column, as explained above, to strengthen the column web panel. Total doubler plate thicknesses are 2x6, 2x10 and 2x12mm in the three specimens G20, G21 and G23, respectively. All columns are HEB 200 steel sections and all steel beams are IPE 240. End-plate thickness is 15mm in the specimen G20 and 20mm in specimens G21 and G23. The joint rotations, column web panel distortion in shear and beam rotation are mainly deduced from inclinometers and linear displacement transducers (Figure 4). Bending moments in different cross-sections are determined from the measured actuator loads F multiplied by the appropriate lever arm L (Figures 1 and 2). In order to simulate the seismic action, the ECCS loading procedure [ECCS 1986] was followed. Two vertical loads were applied at each cantilever beam end on each side of the column by two hydraulic servo controlled actuators working out-of-phase in order to create loads acting in opposite direction.

Experimental results

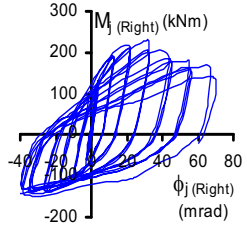
For test G20 (without haunches) and test G23 (with haunches), the moment-rotation curves presented in Figures 5-a to f are only related to the right side of the joints. The bending moment $M_{j\,(Right)}$ is calculated at the load-introduction cross-section of the connection, i.e. the interface between end-plate and column flange. These moment-rotation curves show the respective contributions of the column panel zone ϕ_{Pa} (Figure 5-c and f) and the load-introduction cross-section (connection) $\phi_{li\,(Right)}$ (Figure 5-b and e) to the global joint rotation $\phi_{j\,(Right)}$ (Figure 5-a and d). Also, for test G23 (with haunches), the moment-rotation curve $M_b - \phi_b$ of the right beam (at the haunch tip) is illustrated in Figure 5-g. In Figure 5-h, we give the cyclic moment-rotation $M_{Pa} - \phi_{Pa}$ curve of the column panel zone in test G21 (without haunches). The moment M_{Pa} corresponds to the total moment acting in the joint ($M_{Pa} = M_{j\,(Right)} - M_{j\,(Left)}$). Also, Figure 5-h shows the skeleton curve and the curve obtained from EN 1993-1-8 [CEN, 2005] model. The results presented in Figures 5 to 8 allow to draw the following conclusions.

- Whereas the failure of full-strength joint G23 (with haunches) result from the rupture of the steel beam at the haunch tip (Figure 6) failures of partial-strength joints G20 and G21 (without haunches) occur by rupture in low-cycle fatigue of welds connecting beams to end-plates (Figure 7).
- For the specimen with full-strength joints (with haunches), joint rotations remain low in accordance with the small joint deformations observed during the tests (Figure 5-d); the main part of the rotation comes from the beam (Figure 5-g), providing a rotation capacity generally greater than 35 mrad (here, the rotation

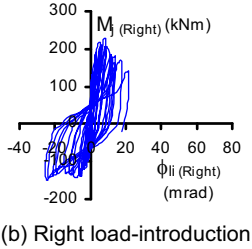
capacity is defined as the maximum rotation for which the resistance moment is 0.8 times the maximum resistance moment). As a reminder, this rotation capacity is required by EN 1998-1 (clause 6.6.4 (3)) [CEN, 2004] in dissipative zones to consider frames in high ductility class (DCH).

– The specimen with full-strength joints (G23), where the flexural yielding mainly occurred in the beam at the haunch tip, exhibits a greater dissipation energy than the specimens with partial-strength joints G20 and G21 (see Figure 8) (here, the dissipation energy is calculated by summing the area of all the cycles until the rotation capacity is reached). This can be explained by the premature rupture of some components (concrete, welds,…).

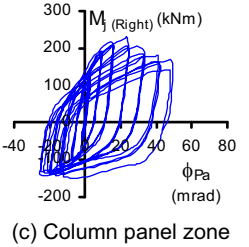
– For test G20 (partial-strength joint) the column panel zone distortion allowed to bring an important contribution to the dissipative capacity of the joint (Figure 8). The connection contribution remained reduced.



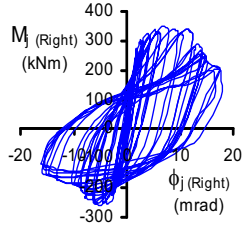
(a) Right joint (Test G20)



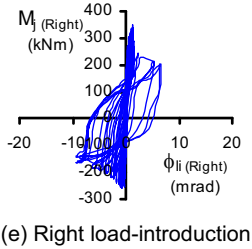
(b) Right load-introduction (Connection) (Test G20)



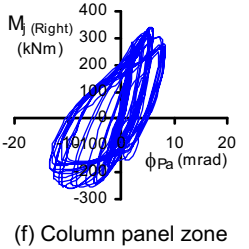
(c) Column panel zone (Test G20)



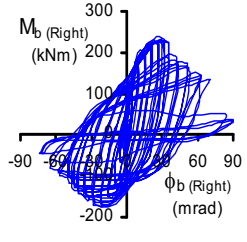
(d) Right Joint (Test G23)



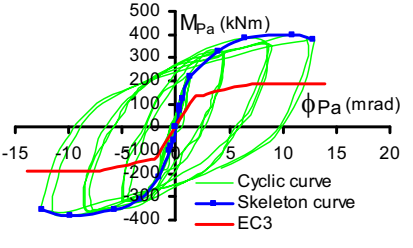
(e) Right load-introduction (Connection) (Test G23)



(f) Column panel zone (Test G23)



(g) Right Beam (Test G23)



(h) Column panel zone (Test G21)

Fig. 5 – Moment-rotation curves

- For both partial-strength joints G20 and G21 the failure occurred, almost at the same level of load, in the connection by rupture in low-cycle fatigue of welds connecting beams to end-plates. So, the additional strengthening of the column panel zone has not increased the joint resistance. However, it has reduced the rotation capacity of the joint and consequently its dissipative capacity (see Figure 8).
- For both stiffness and resistance, the comparison in Figure 5-h between the experimental skeleton moment-rotation curve of the column panel zone and the curve obtained according to EN 1993-1-8 shows that this code is very conservative. This difference can be explained by two reasons. On the one hand, EN 1993-1-8 [CEN, 2005] assumes a uniform shear stress distribution within the column panel zone. As we will see further, the shear stress distribution in the column panel zone is not uniform. On the other hand, this code obviously underestimates the shear area of the column stiffened with doubler plates. An analytical column panel zone model which takes into account the two previous observations is proposed in this paper.



Fig. 6 – Rupture in the beam at the haunch tip (G23)



Fig. 7 – Rupture of welds in heat affected zone (HAZ) (G21)

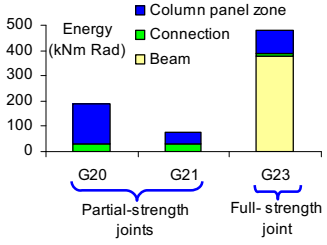


Fig. 8 – Different contributions to energy dissipation

3D FINITE ELEMENT MODEL

The three-dimensional finite element model presented below was created using [CASTEM 2000] software developed at the CEA–DRN/DMT/SEMT (Commissariat à l'Energie Atomique, France).

Description of the model

The studied substructure is an interior composite beam-to-column haunched joint. The three-dimensional finite element model has the configuration and dimensions of the tested specimen G23 shown in Figure 1. Figure 9 gives a view of the mesh of the joint. Most of the substructure elements: column, beam, haunch, end-plates, stiffeners and doubler plates are modelled using 4-node thin shell elements labelled COQ4 with six degrees of freedom per node [CASTEM 2000]. The reference plane of the shell (defined by the shell element nodes) has been made coincident with the mid-plane of each steel plate.The slab is modelled with multi-layered thin shells, making it possible to take into account the flexural behaviour of the slab by the use of one reference plane with which is associated a set of layers in plane stress state. The layer of reinforcing bars has been taken as the reference plane of the multi-layered thin shells used to model the slab. Beam elements are used to model the

longitudinal and transversal reinforcing bars in a discrete manner. Bond slip is neglected and a perfect connection between concrete and reinforcement bars is assumed. Bolts are modelled with bar elements connecting the end-plates and the column flanges. The behaviour of each bar element is characterized on the basis of the stiffness and the plastic resistance of the bolt. Stud shear connectors are modelled with three-dimensional Timoshenko beam elements in order to connect the top flange of the steel beam and the reference plane considered for the slab. Mechanical and geometrical characteristics of the beam element were modified to make them equivalent in both strength and stiffness to the actual shear stud connector in the composite beam. An elastic perfectly plastic shear force-slip law, deduced from theoretical formulae is adopted for the shear connectors. The joint and its loading are symmetrical with respect to the mid-plane of the web of the beam and column (plane xoz). So only one half of the substructure is modelled. A more dense mesh is used in the region of the joint where a stress concentration is expected.

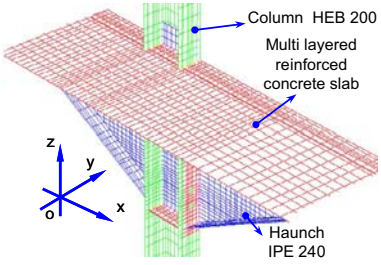


Fig. 9 – 3D FE model of an interior joint

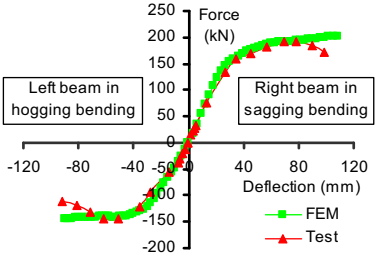


Fig. 10 – Comparison between finite element modelling and experimental results

Behaviour of materials

The steel is modelled as an elasto-plastic material governed by Von Mises yield surface including isotropic strain hardening. This model is calibrated by means of a three-linear stress-strain law assumed symmetrical in tension and compression and deduced from tensile tests. The concrete model combines a Rankine fixed crack model for tension and an elasto-plastic law with Drucker-Präger criteria for compression. In tension, there is cracking when one of the two principal stresses reaches the tension resistance of the concrete. The first crack at one integration point defines a cracking frame of reference and then the only crack being able to appear at this point is assumed perpendicular to the first crack. Cracking involves a strong reduction in the shear strength taken into account using a small shear modulus (practically the uncracked modulus divided by 10). In bi-axial compression, the theory of plasticity is used with associated flow rule and linear hardening rule. The damaged concrete (tension or crushing cracks) is regarded as a continuous medium with strain softening. The softening laws are linear and independent for the two directions of cracking. Compression is not possible as long as the tension cracks are open. A law labelled BILIN_EFFZ [CASTEM 2000] is used for the beam elements employed to model the shear stud connectors. It is an uniaxial elasto-plastic law with linear kinematic stress hardening which associates the shear strain

to the shear force. Finally, a bi-linear stress-strain relationship was adopted for the material behaviour of bolts.

Boundary conditions and loading

According to the tested specimens, the base and the top of the column are pinned. The symmetrical boundary conditions are also applied to the relevant parts of the slab, beam and column. Unilateral conditions of support, characterised by the possibility of separation and contact, are used to model the contact between the slab and the column on the one hand, and between the column flanges and the end-plates on the other hand. Insofar as prestressed bolts are used in the tests, the beam vertical shear forces are transmitted by friction at the interfaces between the end-plates and the column flanges. This mechanism is modelled using unilateral conditions of support, characterised by the preventing of slip at these interfaces. It is assumed that the concrete slab cross-section and the steel beam cross-section have the same curvature and consequently no uplift at the slab-steel beam interface. This assumption is expressed in the model by imposing equality of the rotation (round y axis) at the ends of every connector (modelled by several Timoshenko beam elements). In order to reduce the complexity of the FE analyses conducted with [CASTEM 2000], only monotonic loading regimes are considered hereafter. The substructure is loaded monotonically and subjected simultaneously to sagging and hogging bending (unbalanced moments); the obtained deflection-load curve will be compared to the skeleton curve of the experimental cyclic curve. For the comparison we consider the skeleton curve as an acceptable approximation of the curve that can be obtained under experimental monotonic loading. The loading is carried out by two monotonic vertical imposed displacements applied at each cantilever beam end with opposite directions. Geometrical nonlinearities are not taken into account in the analysis.

Model validation by comparison with experimental results

Figure 10 shows the comparison, in terms of applied force vs. deflection at the end of the right beam in sagging bending and at the end of the left beam in hogging bending, between the experimental and numerical results of the test G23. A good agreement between numerical and experimental curves can be observed until the maximum experimental moment is reached. The difference observed beyond the maximum moment can be explained as follow. To avoid the convergence problems, very slow decreasing softening branches have adopted for the concrete. In addition, as already mentioned, the geometrical nonlinearities are not taken into account in the analysis. So, the model was not able to simulate the decrease of experimental sagging moment due to the concrete failure nor the decrease of experimental hogging moment due to the local buckling observed during the test in the web and the bottom flange of the beam at the haunch tip. Therefore, the numerical curve maintains a positive slope (almost null) whilst the test curve switches to a negative slope when the specimen fails.

Column panel zone behaviour

For a better understanding of the column panel zone behaviour, the elastic shear stress distribution in the column panel zone and doubler plates has been investigated. Figure 11.a shows the shear stress profile along the column axis on the height of the strengthened panel zone. Figure 11.b shows the shear stresses distribution along the depth of the strengthened column cross-section located at a vertical distance of $0.25h_b$ above the level of the centreline of the steel beam.

This corresponds almost to the position of the maximum shear stress in the column web panel. A non-uniform distribution of shear stress within the panel zone can be clearly observed. Based on this result, three sub-panels can be considered; a first sub-panel in contact with the slab, a second sub-panel in contact with the steel beam and a last one in contact with the haunch. Figure 9.a shows that the highest shear stresses are produced in the sub-panel in contact with the steel beam. Curves given in Figure 9 show the same shear stress intensity in the column web and doubler plates. This allows to replace both cross-sections (the column and the doubler plates) by a single cross-section.

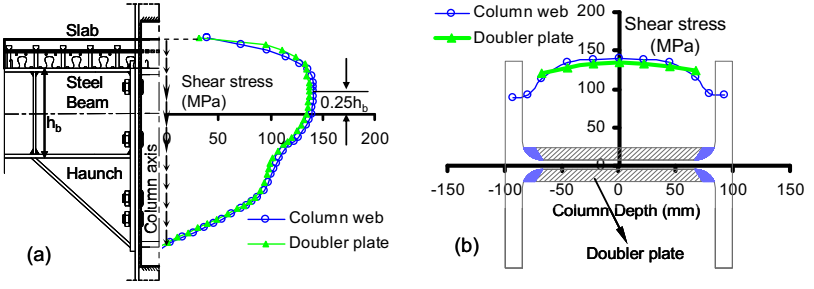


Fig. 11 – Shear stress profiles in the column panel zone

Behaviour of the haunched composite beam

Figure 12 shows the flexural stress contours σ_{xx} (iso-curves) in a segment of the beam including the haunch region and a portion of the beam at the haunch tip. It can be observed that the neutral axis shifts slightly in the haunch region. This shows that this segment (beam + haunch) does not behave as an equivalent beam with a variable second moment of area (according to the expectation of beam theory) but rather as a beam with a constant section supported by the haunch.

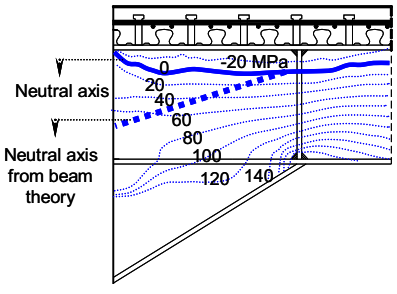


Fig. 12 – Flexural stress contours (iso-curves) and neutral axis location in sagging bending

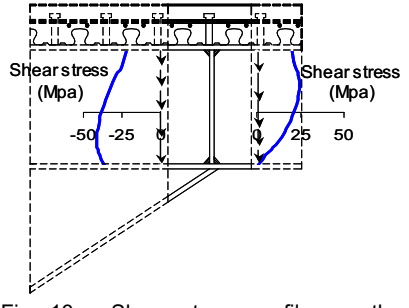


Fig. 13 – Shear stress profiles on the depth of two steel beam cross-sections in hogging bending

ANALYTICAL MODELS BASED ON THE NUMERICAL AND EXPERIMENTAL STUDIES

Analytical static design model of haunch

Following the numerical and experimental investigation of bolted haunched beam-to-column joints, an analytical model with a view of static design has been developed. In this model we consider the interaction (i.e. force equilibrium and deformation compatibility) between the beam and the haunch. The static design of the haunch refers to a situation in which plastic hinges form in the beam at the haunch tip (see Figure 14). In this Figure, $M^{+}_{pl,Rd,be}$ and $M^{-}_{pl,Rd,be}$ are the beam probable plastic moments at the haunch tip in sagging and hogging bending, respectively. They should be calculated taking into account the material overstrength factors, in particular for the structural steel, and the strain hardening of the steel. $V^{+}_{Ed,be}$ and $V^{-}_{Ed,be}$ are the beam shear forces produced by the moments $M^{+}_{pl,Rd,be}$ and $M^{-}_{pl,Rd,be}$ and the gravity loads acting within the beam span L' between the plastic hinges. To determine the interaction forces at the beam-haunch interface, the proposed model considers the haunch flange as a truss element and the haunch web as a three-node triangular plane stress finite element. This approach is similar to the one already adopted in references [Yu et al. 2000] and [Lee and Uang 2001].

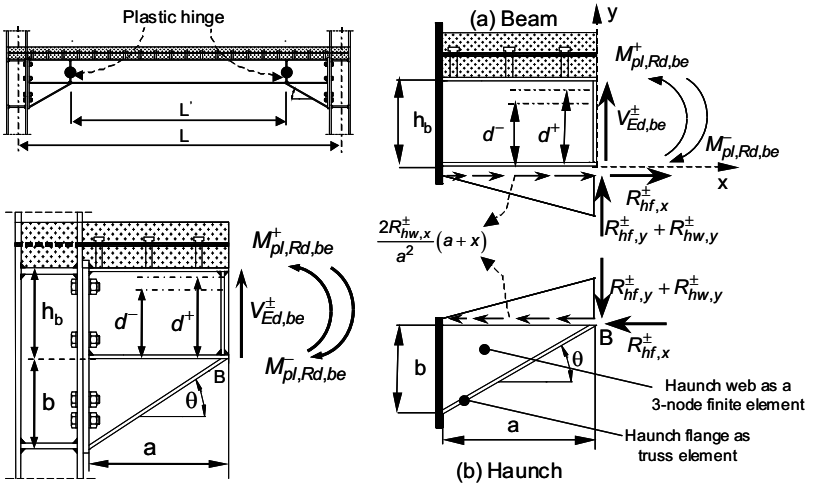


Fig. 14 – Simplified interaction model between the beam and the haunch

To simplify the interaction forces at interface between the beam and the haunch web, the actual shear stress distribution is approximated as triangular and the normal stress distribution is replaced by concentrated force $R^{\pm}_{hw,y}$ acting at the haunch tip. Figure 14 shows this simplified interaction model. In this figure, $R^{\pm}_{hw,y}$ and $R^{\pm}_{hw,x}$ are the resultant forces of the normal and shear stresses along the interface between the haunch web and the steel beam, respectively. $R^{\pm}_{hf,x}$ and $R^{\pm}_{hf,y}$ are the horizontal and vertical components of the haunch flange axial force, respectively [(+) in sagging bending and (-) hogging bending]. h_b is the steel beam depth. a, b and θ are the length, the depth and the angle of the haunch, respectively. d^+ and d^- are the distance from the plastic neutral axis to the external face of the beam bottom flange in sagging and hogging bending, respectively. The forces $R^{\pm}_{hw,y}, R^{\pm}_{hw,x}, R^{\pm}_{hf,y}$ and $R^{\pm}_{hf,x}$ are the unknowns of the problem. To solve them, the compatibility of vertical and horizontal displacements ($v^{\pm}_B$ and $u^{\pm}_B$) at the haunch tip (point B) is considered.

Once the forces $R^{\pm}_{hw,y}, R^{\pm}_{hw,x}, R^{\pm}_{hf,y}$ and $R^{\pm}_{hf,x}$ are obtained, stresses can be easily calculated in the haunch region. Then, the composite beam above the haunch, the haunch elements (flange, web and welds) and the joint can be designed. More details can be found in the references [Lachal et al. 2006] and [Loho 2008].

Analytical model of strengthened column panel zone

Based on the numerical and experimental results presented in this paper, it has been possible to develop a more accurate model which takes into account the non-uniform distribution of shear stress in the column panel zone. We give only here the principal information of this model. More details can be found in the reference [Loho et al. 2008]. The model proposed in this paper is based on a partition of the column panel zone into an equivalent set of three sub-panels (see Figure 15): a first sub-panel in contact with the slab **(SL)**, a second sub-panel in contact with the steel beam **(B)** and a last one in contact with the haunch **(H)**. This model represents the most general configuration for a haunched composite joint. Of course, using appropriate sub-panels, it can be used for other configurations of joints as composite joints without haunches, haunched steel joints or steel joints without haunches.

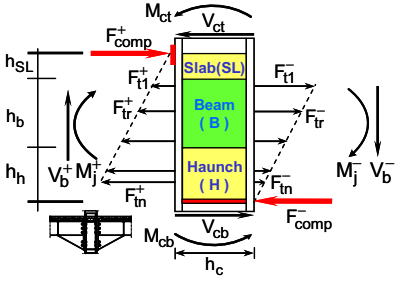


Fig. 15 – Forces acting on interior haunched composite joint, at the periphery of column panel zone

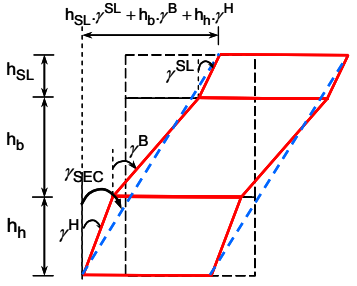


Fig. 16 – Deformation of web panel in shear (Hunched composite joint)

In this way, the whole column panel zone can be treated as a multi-spring serial system in shear, where each spring corresponds to one of the sub-panels previously described (see Figure 16. The main purpose of the proposed approach is to determine the spring characteristics of each sub-panel. Then, the whole column panel zone model is obtained as an equivalent spring. In the proposed model, realistic forces distribution transmitted from the beam, at periphery of the column panel zone, are considered. These forces are the tension forces in bolt-rows $F_{tr}^{+/-}$ and the forces acting in the compression centres $F_{comp}^{+/-}$. Both shear and bending deformation in the elastic and post-elastic phases are taken into account, as well as the contribution of the column flanges to the supplementary resistance of the web panel. A multi-linear relationship has been developed to describe the moment-distortion behaviour of each sub-panel [Loho et al. 2008]. To accurately model the elastic and post-elastic behaviours of the column panel zone, five phases have been considered for each sub-panel. The first phase is elastic and each plastic phase is related to the spread of yielding in the sub-panel. In order to simplify the prostration here, only the case of doubler plates having a yield stress lower than the web panel one is considered, so that the elastic phase ends with the first yielding of the doubler plates. The second phase ranges from the onset of the doubler plates yielding to the first yielding of the column web. The third phase starts from the end of the previous phase and finishes by the entire yielding of the doubler plates and column web. The

fourth phase accounts for the formation of plastic hinges in the flanges of the column at the four corners of the sub-panel. The fifth phase allows for an increase of the resistance due to the strain hardening of the steel web panel. Finally, it is worth mentioning that the shear area adopted in the proposed model considers the total area of doubler plates cross-section.

Comparison with test results (column panel zone model)

Comparisons between experimental results of both specimens G21 (without haunches) and G23 (with haunches) and moment-distortion curves predicted by the proposed model are presented In Figure 17. The curve predicted by the proposed model of this paper appears in good agreement with the experimental skeleton curve deduced from cyclic moment-distortion curves; as well as in the first elastic phase than in post-elastic phases. Compared with test results, the curve obtained from EN 1993-1-8 [CEN, 2005] model shows inability to predict suitably the real behaviour of the column panel zone (see Figure 17).

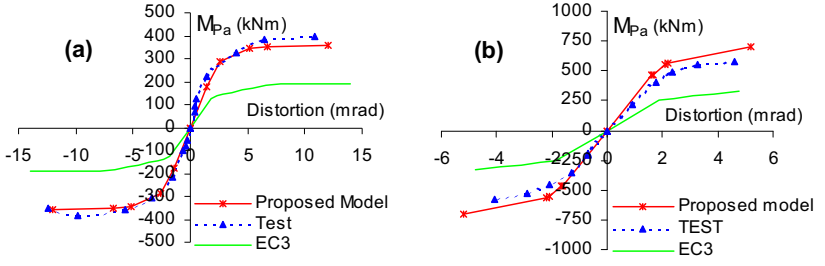


Fig. 17 – Comparison with test results: (a) Specimen G21 (without haunches); (b) Specimen G23 (with haunches).

CONCLUSION

Based on experimental and numerical approaches the strengthening of beam-to-column end-plate bolted joints using haunches and steel doubler plates has been investigated. From experimental results, it seems that adding a haunch improves significantly the cyclic behaviour of the joint. The plastic energy capacity of specimens with full-strength joints is clearly greater than specimens with partial-strength joints, and the rotation capacity can exceed 35mrad without risk of low-cycle fatigue rupture in the welds connecting beam flanges to the end-plates. From numerical results, a non-uniform distribution of shear stress within the panel zone has been observed. It was observed that the shear stress in the haunch region acts in the opposite direction than the corresponding one located outside the haunch region. This result is a direct consequence of the effect of the vertical reaction transmitted by the haunch flange to the beam at the haunch tip.

Two new static design models are proposed in this paper. The first model provides a design method for composite haunched joints. It considers the interaction (i.e. force equilibrium and deformation compatibility) between the beam and the haunch. This model consists in idealizing the haunch flange as a truss element and the haunch web as a three-node triangular plane stress finite element. The second model deals

with the column panel zone strengthened by double steel plates in composite haunched joints. In order to take into account the non-uniform distribution of stress numerically observed, the panel zone has been divided into an equivalent set of three sub-panels. The panel zone model corresponds to the resulting spring serial system in shear where each spring is related to a sub-panel. The behaviour of each sub-panel can be accurately described by a moment-distortion relationship with five phases. After a first elastic phase, four phases describe the post-elastic behaviour as a function of the spread of yielding in the sub-panel. Comparison with experimental results has shown the ability of the proposed model to simulate suitably the moment-distortion panel zone behaviour. On the contrary, EN 1993-1-8 [CEN, 2005] model is very conservative.

ACKNOWLEDGMENT

The authors would like to thank the “French Ministry of Ecology and Sustainable Development” through the DRAST (Research management) managed by Prof. André Colson for the financial support of this research.

REFERENCES

[CASTEM 2000] : Millard A. CASTEM 2000, Guide d’utilisation. Rapport CEA 93/007, *Saclay, France,* 1993.

[CEN, 2004]. EN 1998-1: Design of structures for earthquake resistance Part 1: General rules, seismic actions and rules for building. *December 2004, Brussels.*

[CEN, 2005]. EN 1993-1-8: Design of Steel Structures Part 1-8: Design of joints. *May 2005, Brussels*.

[CEN, 2005]. EN 1998-3: Design of structures for earthquake resistance Part 3: Strengthening and repair of buildings. *June 2005, Brussels.*

[Cheol-Ho Lee1 and Chia-Ming Uang 2001]. Analytical modelling and seismic design of steel moment connections with welded straight haunch. ASCE, *Journal of Structural Engineering* 127(9): 1028–1035.

[ECCS 1986]: Recommended testing procedure for assessing the behaviour of structural steel element under cyclic loads, TC 1, TWG 1.3 – Seismic design n°45.

[Foutch DA, Yun SY 2002]. Modeling of steel moment frames for seismic loads. *Journal of Constructional Steel Research* 2002; 58(5–8):529–64.

[Lachal, A. Aribert, J.M. & Loho, G. 2006]. Analytical and experimental investigation of bolted haunched beam-to-column joints with a view of seismic design. *International Journal of Advanced Steel Construction* n° 2, p.137-160, 2006.

[Loho 2008]: Static and seismic behaviour of steel and steel-concrete composite bolted end-plate beam-to-column joints. PhD thesis, National Institute of Applied Sciences; 2008 [in French].

[Loho G., Lachal A. 2008]. Modelling of strengthened column web panel in bolted end-plate composite joints. *J. of Constructional Steel Research* 64(5): 584–595.

[Yu, Q.-S., Uang, C.-M., & Gross, J. 2000]. Seismic rehabilitation design of steel moment connection with welded haunch, ASCE, *Journal of Structural Engineering* 126(1): 69–78.

NUMERICAL MODELLING OF COMPOSITE BEAM-TO-BEAM JOINTS – INNOVATIVE SOLUTIONS

Samy GUEZOULI
Samy.Guezouli@insa-rennes.fr

Hugues SOMJA
Hugues.Somja@insa-rennes.fr

Sao Serey KAING
ksserey@yahoo.fr

Alain LACHAL
Alain.Lachal@insa-rennes.fr

LGCGM – Structural Engineering Research Group,
INSA Rennes, France

ABSTRACT

This paper deals with a numerical F.E. modelling investigation of new joint typology to connect continuously composite beams in bridges. Different types of joint have been selected, designed and tested under fatigue and monotonic loading. For an accurate interpretation of the test results and a better understanding of some specific behaviours (not accessible to measurement) with complex geometries and with the objective to generalize the study, numerical models have been developed using several Finite Element programs including specific programs for composite beams and 3D models based on standard FEM codes. The main numerical results are presented and compared against experimental ones.

INTRODUCTION

In order to promote new composite techniques for bridges of small and medium spans, innovative solutions have been investigated for the design and the fabrication of beam-to-beam joints. In Europe, several projects have been carried out on this subject the past few years [ECCS, 2000]. In France, taking benefit of a National Research Project, the Laboratory of Structural Mechanics at INSA in Rennes has undertaken research work to find new types of beam-to-beam joint ensuring the continuity of composite beam in bridges. Three new joint solutions presented in Figures 1, 2 and 3 have been selected [Lachal A. et al., 2002]. The main reason why these solutions were selected is the economical interest :

- using, if possible, standardized or ordinary prefabricated elements easily mounted on site by the same builder with a minimum of construction operations and without any sophisticated technology (as outdoor welding for example),

- taking into account usual builder practice in Europe,

- introducing new technologies as direct contact (without end-plate with partial depth as previously used by [Dorka V.E. et al., 2004]), embedding, web shear anchors (stud, transverse rebars, …).

Analytical methods have been developed for these new joints and used to design and fabricate test specimens, approximately at half scale of the actual bridges. Specimens have been tested on the platform of the Laboratory under fatigue and monotonically increasing loading up to the specimen collapse.

For an accurate interpretation of monotonic test results and a better understanding of some specific behaviours numerical models have been created. In addition, these models are also able to give information not accessible to measurement. Several Finite Element programs were used depending on the nature of the investigated phenomena. These include specific beam FE models developed or co-developed (de Ville V., 1988) by the group and 3D models based on CASTEM code. This paper gives a description of these finite element models used for this research. The numerical models have been calibrated against experimental results and adjusted to take into account the contribution of several components in the global behaviour of the joints.

The main result deals with the ability of the numerical models to simulate the flexural behaviour of the joints. Very useful local information are also obtained with the prospects to develop design methods for these joints.

PRESENTATION OF THE SELECTED BEAM-TO-BEAM JOINTS TO BE STUDIED

The joints of the beam-to-beam specimens tested at INSA in Rennes are illustrated in the Figures 1, 2 and 3. For all the joints, steel girders are HEA 500 rolled sections in steel grade S355. The width of the slab is 1600 mm and the thickness is 160 mm. The strength class C45/55 is used for the concrete. The transfer of the tensile forces in the upper part of the joint is allowed by the shear connection and the reinforcement in the slab. In the reinforced zone around the beam-to-beam connection, the longitudinal reinforcement consists of 2 layers of ribbed bars (4100 mm length) of 17Φ16 with high bond action and with steel grade S500 – Category 3, ensuring high ductility (the percentage of longitudinal reinforcement being 2.67%). The slab is connected to the steel flange with 12 welded headed studs per meter (Φ *22* mm and h = 125 mm). Outside the connection zone, the percentage of reinforcement is 1.26% (composed of 2 layers of ribbed bars of 8 Φ16) and the number of connectors is 6 studs/meter. Steel girders were prepared in the factory (ArcelorMittal - Wallerich - Differdange) and equipped with additional plates and welded studs. They were transported to INSA in RENNES where the reinforcement was installed and the continuity of the composite beam was completed by concreting the slab and the joint in a single shot.

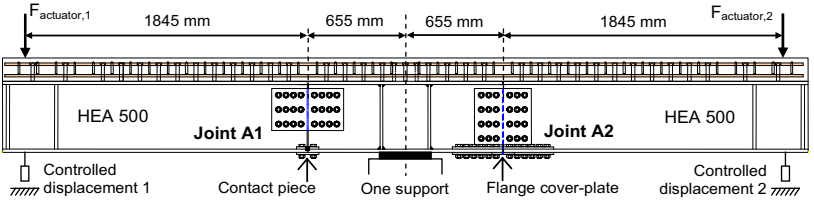


Fig. 1 – Joint with bolted cover-plates (and direct contact)

The first type of joint is presented in Figure 1. Steel girders are connected with cover-plates and high strength bolts. On the upper side, the tensile forces are directly transferred from top flanges to the reinforcement of the slab through the shear connection. A new technology has been developed with a direct contact between compressed bottom flanges (Figure 1) in order to avoid flange cover-plates and so to reduce considerably the number of bolts. Such a type of joint may be located anywhere along the span. In fact, it will be more often located near an intermediate support where the bending moment is low. This type of joint remains easy to build on site and presents the advantage of having no welds subjected to fatigue.

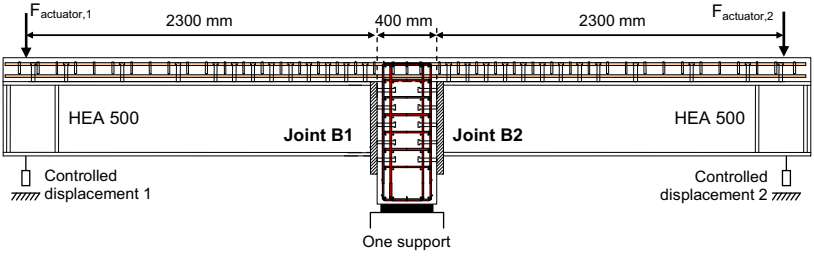


Fig. 2 – Beam-to-beam joint with butt-plates and shear studs connected to a transversal concrete beam.

The second type of joint is presented in Figure 2. Steel girders are equipped with butt-plates welded at their ends. These are connected with shear studs to a transverse deep beam lying on an intermediate pier. This type of joint is necessarily located at intermediate support.

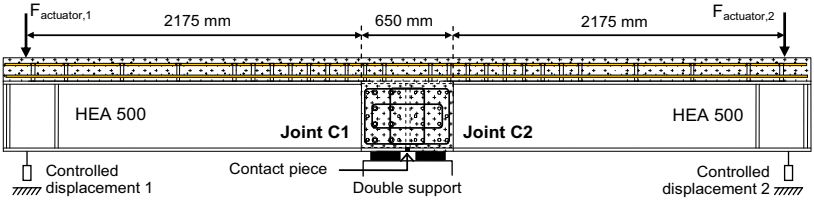


Fig. 3 – Beam-to-beam joint with concrete embedding.

The third type of joint is presented in Figure 3. Both ends of steel girders are embedded in a concrete block resisting over the pier. Each steel girder lies directly over it own support in order to avoid a shear force transfer through the mid-cross-section of the embedding. A direct contact between the ends of the bottom flanges of the girders over the support ensures the transfer of the compression forces in the joint. Shear studs welded on the webs and/or rebars passing through the webs are used to connect the steel girders inside the block.

Most part of analytical mechanical models used to design the joint specimens presented under above are novel in so far as Eurocodes (EN 1994-2) does not give specific provisions to design beam-to-beam joints in continuous composite bridges.

So, some of these joints overall and local behaviour need to be checked against experimental test results and numerical ones in order to be better understood.

Loading and support arrangements used for the tests are indicated in Figures 1, 2 and 3. Main measurement devices during the tests are : inclinometers, linear potentiometric transducers and strain gauges used to measure the joint rotation, deflections, relative displacements (slips) and strains at several parts of the specimen. Crack widths were measured on the top surface of the concrete slab. More information about details and results of this experimental study can be found in a companion paper [Lachal A. et al., 2008].

PRESENTATION OF THE FINITE ELEMENT MODELS DEVELOPPED FOR THIS STUDY AND SOME NUMERICAL RESULTS

Short overview of available finite element techniques

For global analysis of continuous composite bridges, a specific fiber beam element accounting for partial shear interaction was developed (see for instance [XU H. et al., 2000]). These beam elements are able to accurately model the nonlinear shear force-slip behaviour and to give accurate internal force distribution for standard continuous composite beams. For a more detailed analysis, 3D F.E. modeling cannot be avoided. 3D F.E. models of composite beams proposed in the literature often involves shell elements to model both the deck and the girders and beams for the connection [Ahmed B. et al., 1995]. Recently, several authors have been using 3D elements for all the components of the composite beam and joint [Fu F. et al. 2007, Sieffert Y. et al 2006, Chung W. 2006].

In the numerical study presented in this paper, the whole state-of-the-art finite element software has been taken into account and different numerical solutions have been selected according to the specific research objectives for each joint.

Shell and 3D beam finite element model applied to joints A2 with cover-plates

A simplified 3D finite element model is proposed for the joint with cover-plates (test specimen of type A). It is reminded that, the joint is located at a distance of 655 mm from the mid-support axis. In spite of the asymmetry of the specimen with respect to the mid-axis, the present numerical simulation considers only the right side part from the mid-axis (joint A2) with the possibility to replace the flange cover-plates by a simple contact for future numerical simulations. The most important aspects for this joint is the influence of the discontinuity of the girder (especially the one at the top flange) on the joint behaviour (moment-rotation curve) and the slip of the studs along the beam. All material behaviours are elasto-plastic with kinematic hardening (E/10). The Young's modulus E, the yield and the ultimate stresses are given in table 1.

Table 1 – Material mechanical characteristics (MPa).

Material	Steel girder	Stiffeners	Cover-plates	Bars	Studs
Young's modulus	200000	200000	200000	200000	200000
Yield stress	430	430	385	600	350
Ultimate stress	525	525	580	680	660

The F.E. discretization and the main assumptions are summarized below :

- The concrete slab is supposed completely cracked and its strength in tension is neglected.

- The reinforced bars are replaced by an equivalent “plate”. Its width is equal to the flange one, its thickness and its position with respect to the top flange are calculated by imposing a geoemetric and material equivalence with the actual cross-section with rebars. This equivalence concerns the second moment of area and the position of the centroid of the cross-sections. This equivalent “plate” is modeled with shell finite elements.

- The girder, the stiffeners and the cover-plates are meshed with shell finite elements.

- The studs are meshed with 3D beam finite elements (to ensure the displacement compatibility with shell elements). The stud has a common node with the equivalent “plate”. The slip of the stud is defined in figure 4.

- The cover-plates are connected to the girder with high strength preloaded bolts. The connection of the cover-plates has been designed in order to be slip-resistant using 10.9 bolts and a class B or A ($\mu \geq 0.4$) of surface friction. In this case, the cover-plates remain in contact with the girder during the test and the solutions with or without bolts (direct contact between the cover-plates and the girder) appear to be equivalent.

The numerical simulation predicts a higher rotation capacity of the joint than the one calculated from the experimental results (Figure 5). Its seems that, even if the specimen is tested under negative bending moment, the concrete being in different stages of cracking could give an additional stiffness thanks to the tension stiffening effect. Since the concrete in tension is completely neglected, beneficial effect from tension stiffening is not taken into account. Accordingly, we can expect an overestimation of the rotation capacity by the numerical model. On the right side of the discontinuity, the experimental and numerical results of the studs slip (Figure 6) are close together while on the left side, the results appear different. On this side, the transfer of the internal forces from the top of the flange to the reinforcing bars through the studs hides some local phenomena that the present 3D model is not able to reveal.

3D solid finite element model applied to joint B with butt-plates

For the specimen B, the 3D finite element model is more detailed than the previous one. The whole specimen is modeled with cubic solid elements (3 d.o.f. per node) taking into account the concrete as-well-as the real number and position of longitudinal and transverse reinforcing bars in the slab. The single simplification concerns the deep beam resting on the support where the reinforcement is too complex to be modeled with solid elements. Therefore, the reinforced concrete of the deep beam has been replaced by an equivalent homogeneous material. Details are given in Figures 7, 8 and 9. The adherence between (the girder and the slab) and (the concrete joint and the butt-plate) could be either neglected (in this case the interfaces are empty and the connexion is only carried out by the vertical and horizontal studs), or modeled with a material having a very low Young’s modulus. According to the experimental specimen, the percentage of longitudinal reinforcement is reduced at 2050 mm from the middle axis of the joint. During the

cyclic preloading, the slab concrete of the specimen was cracked. To take into account this initial cracking in the numerical model, a reduced elastic concrete modulus of $E_a/100$ = 2000 MPa has been adopted over a length of 600 mm from the butt-plate.

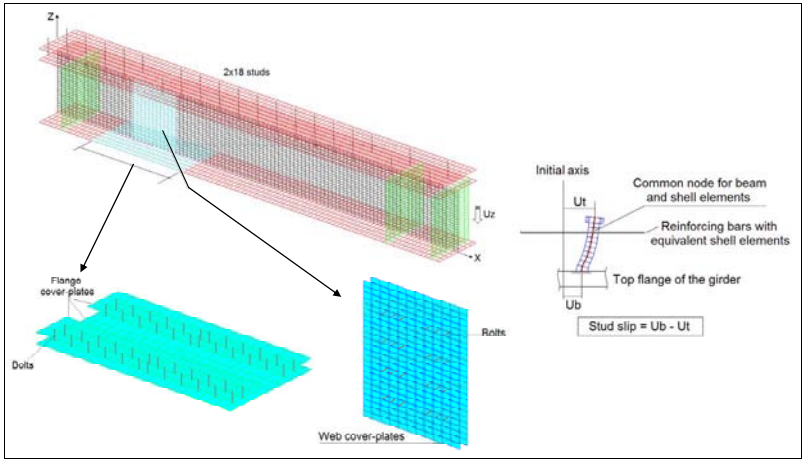


Fig. 4 – Simplified 3D model details.

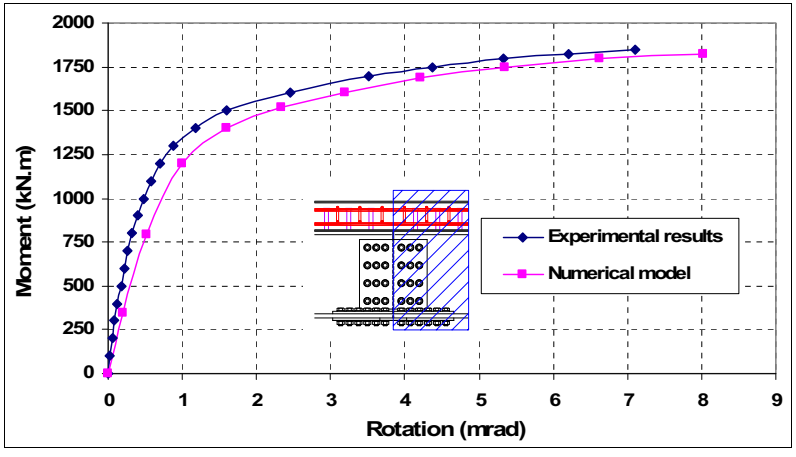


Fig. 5 – Moment-Rotation curve of the joint.

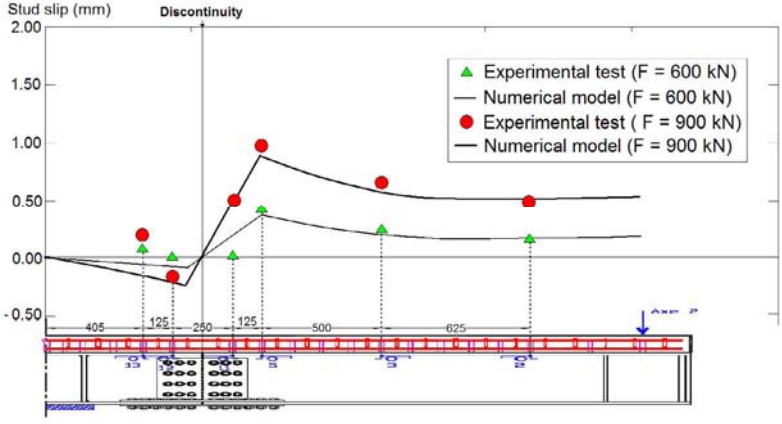


Fig. 6 – Slip of the studs along the specimen.

Except concrete, all material behaviours are elasto-plastic with kinematic hardening (E/10). For concrete, the model proposed by Mazars (elasto-plastic behaviour including damage) is well adapted for monotonic loading. The comparison between experimental and numerical results is shown in figures 10 and 11. This comparison concerns different load levels (200 kN – 600 kN – 900 kN for experimental test) and (220 kN – 610 kN – 920 kN for numerical calculation). These last values are not exactly the same because the numerical model is loaded with imposed displacement and the corresponding load is calculated at the mid-support. The longitudinal displacements of the butt-plate are plotted in figure 10. The comparison seems to be more accurate for low load levels than for high ones, especially at the top of the butt-plate. The curves of the studs slip along the specimen are plotted in figure 11. The decreasing of these curves around 800 mm on X-axis seems to be due to the cracking slab just near the joint as modeled in figure 8. The results could be more accurate if the slab cracking is taken into account continuously from the butt-plate to the end of the specimen but this correction is difficult to estimate.

Beam finite element model applied to joints C1 and C2 with concrete embedding

The geometry of the joint is clearly three-dimensional. It could be expected that a thorough investigation of the stress distribution inside the embedded zone would need a 3D finite element model using solid elements. In fact, such model does not give all guarantees of reliable results due to the complex nonlinear interaction between the steel and the concrete, through the studs and direct contact. So, a first simple and effective investigation has been carried out in order to reproduce a global flexural behaviour. The part of a continuous composite beam located over its supports can be accurately modeled by plane beam finite elements, the slip at the interfaces being taken into account. The initial conception of the specimen tries to ensure the continuity of the beam. Consequently, it appeared rapidly that beam models were still applicable and could give valuable information.

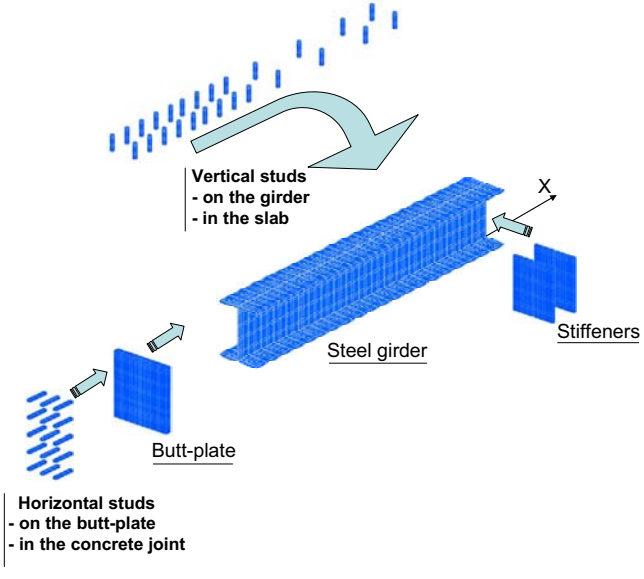


Fig. 7 – 3D model details – Steel girder – Studs – Butt-plate - Stiffeners.

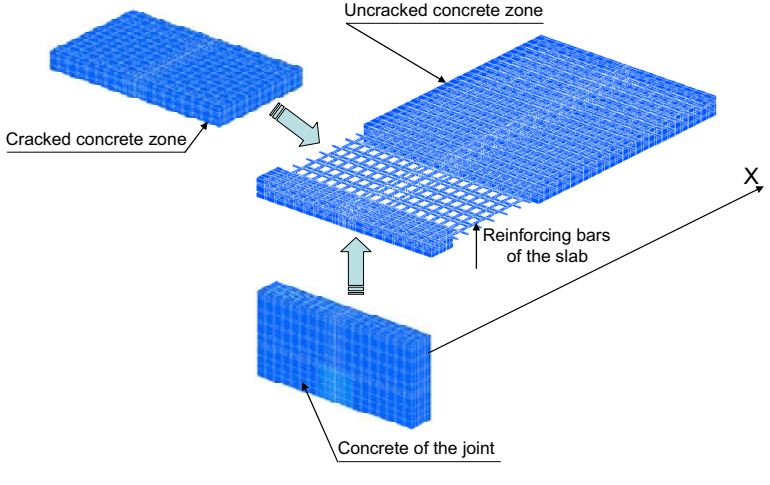


Fig. 8 – 3D model details – Concrete and reinforcing bars.

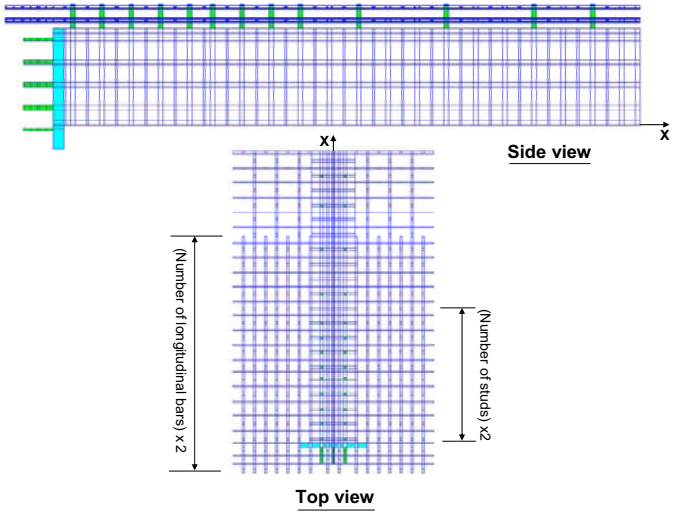


Fig. 9 – 3D model details – Top and side views.

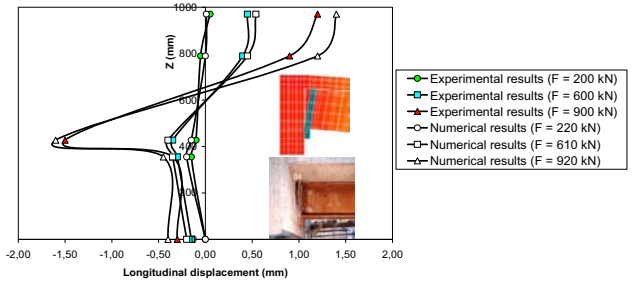


Fig. 10 – Longitudinal displacements U_{xx} of the butt-plate.

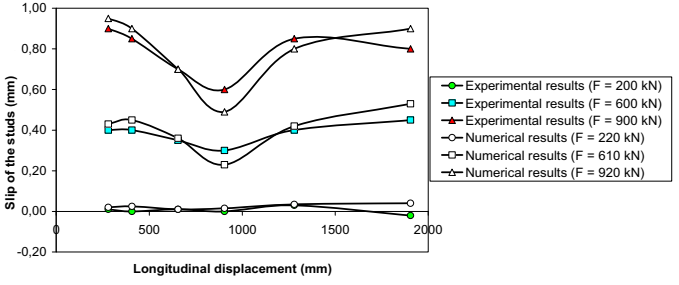


Fig. 11 – Slip of the vertical studs.

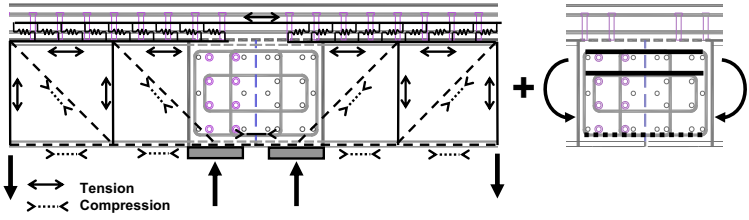


Fig. 13 a and b – Global strut and tie model (a) contribution of the embedding (b)

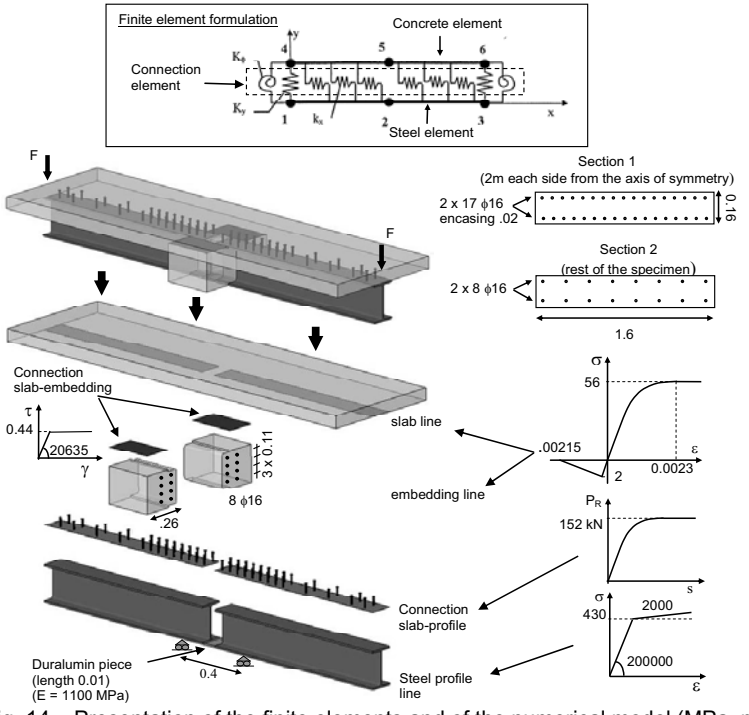


Fig. 14 – Presentation of the finite elements and of the numerical model (MPa, m)

Indeed, considering a strut and tie model (Figure 13.a) and thinking of differences with a classical joint with a continuous steel profile, the discontinuity has no effect on the lower compression strut thanks to the piece of contact. The discontinuity of the upper flange induces a total deviation of the upper tension tie in the slab, but with no real spatial local impact. Considering the web, no shear stress has to cross the joint from one side to the other due to the symmetry of the experimental loading. The bending role of the web is cancelled ; but it is replaced by a transmission through the embedding (Figure 13.b) whose resistance has been set by design equal to 15 % of the total bending capacity which is equivalent to the part of the global moment

supported by the web outside the joint. This embedding flexure is evidently a 3D phenomenon, including a transversal diffusion of the stresses and a complex interaction with the slab and the steel profile. However the small part of the embedding in global flexure lowers the effects of the hypotheses that will have to be set to model it by a plane beam. Consequently, a plane beam modeling has been undertaken using FINELG software [5], developed at the University of Liège and Greisch engineering office. Separated specific finite elements with 3 nodes are used for concrete and steel parts of the structure. They are bounded by a connection element (Fig. 14) with rigid transversal and rotational springs to avoid uplifting and with a uniform distribution of longitudinal springs whose rigidity k_x is obtained from the force-slip relationship of the studs.

An exploded view of the topology of the model is presented in figure 4. Three parallel lines of beam elements are considered. The two main lines, for the steel and the concrete slab, are continuous over the length of the specimen. At the support, the part of concrete not included in the slab is represented by a new concrete line called "embedding". An effective width of 52 cm is considered for this part. In each section all lines are supposed to have the same rotation and vertical displacements, but a longitudinal slip is possible. Longitudinal restraints are only defined between the slab and the steel profile and between the slab and the embedding. Mechanical properties are synthesized in figure 14. Due to the initial cyclic loading, the duralumin piece is damaged and its experimental stiffness is measured equal to 1100 MPa. In figures 15 and 16, experimental vertical displacements at the actuators location and slip along the slab-profile interface are compared against the results from numerical simulation. A relatively good agreement is obtained in both cases. This confirms the hypotheses set from the preliminary design. Further the ability of this simplified 2D model to simulate the behaviour of such a joint allows to consider the future development of an analytical component design approach.

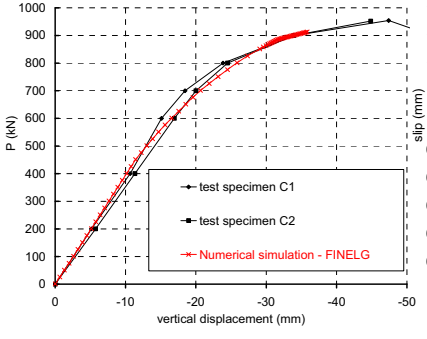


Fig. 15 –Vertical displacements at actuators

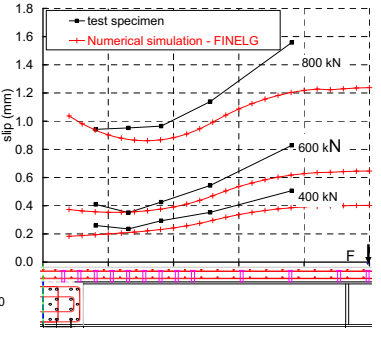


Fig. 16 – Slip deck-profile distribution

CONCLUSION

The choice of a specific F.E. model for beam-to-beam composite joints mostly depends on its complexity and the phenomena we want to analyze. The most important rule is to respect the mechanical scheme of the joint behaviour. The proposed models for the joint solutions under investigation are based on simplifications affecting differently the results as well as the computation time. On

the whole, the comparison between numerical and experimental results appears satisfactory and well-adapted to each type of joint. Even if some improvements could be added to the actual models, they should give at least necessary data for future design methods. With this aim in mind, several numerical simulations are planned to study the influence of some parameters on the design variables. For example:

- For the shell and 3D beam finite element model applied to joints A2 with cover-plates, the influence of a single contact material between the bottom flanges should be investigated as well as the influence of possible slip between the girder and the cover-plates.
- For the 3D solid finite element model applied to joint B with butt-plates, the thickness of the butt-plate and the rebars and studs density in the slab could be varied.
- For the beam finite element model applied to joints C1 and C2 with concrete embedding, the contact material is also of special interest.

ACKNOWLEDGEMENTS

The authors would like to thank IREX, the "French Ministry of Ecology and Sustainable Development", ArcelorMittal-Research and SNCF-Engineering for their financial and technical support through the national project MIKTI.

References

Ahmed B. Numerical modeling of semi-rigid composite joints. Ph.D. thesis. UK: University of Nottingham; 1996.

ARIBERT J.M., XU H. et RAGNEAU E., Theoretical investigation of moment redistribution on composite continuous beams of different classes. ASCE proceedings of COMPOSITE III Conference in Irsee, Germany – June 9-14, 1996 (p. 392-405).

CASTEM 2000, Un code de calcul aux éléments finis, CEA/DMT/LAMS, Sarclay, France.

Chung W., Sotelino E.D. Three-dimensional finite element modeling of composite girder bridges. Engineering Structures 28 (2006) 63-71.

Dorka V.E., Pruss J., Short span modular composite bridges. Proceedings of COMPOSITE V Conference, Kruger National Park, South Africa, July 18 – 23, 2004 (p. 87 – 92).

ECCS STEEL RTD PROGRAMME (CECA), Composite Bridge Design for Small and Medium Spans, RWTH-CTICM-PROFILARBED, Interim Report N°2, 2000.

Fu F., Lam D., Ye JQ. Parametric study of semi-rigid composite connections with 3D finite element approach. Engineering Structures 2006.07.003 (in press).

Lachal A., Aribert J.M., National Research Project MIKTI, Theme 1, Design of outstanding decks in the framework of small spans, Subject 1-B : Innovative techniques to connect continuous beams, specifications. Research report, feb 2002.

Lachal A., Hechler O., Kaing S.S. and Aribert J.M., Experimental investigations of the shear connection behaviour in joints of composite bridges. Composite VI, Devil's Thumb Ranch, Colorado, 20-25 July 2008.

Sieffert Y., Michel G., Ramondenc Ph., Jullien JF. Effects of the diaphragm at mid-span on static and dynamic behaviour of composite railway bridge: A case study. Engineering Structures 28 (2006) 1543-1554.

NUMERICAL MODELING OF COMPOSITE CASTELLATED BEAMS

Marian A. Gizejowski
Warsaw University of Technology, Faculty of Civil Engineering
Department of Building Structures
Warsaw, Poland
m.gizejowski@il.pw.edu.pl

Wael A. Salah
Warsaw University of Technology, Faculty of Civil Engineering
Department of Building Structures
Warsaw, Poland
w.salah@il.pw.edu.pl

ABSTRACT

In modern composite structures, higher steel grades are used for structural steel profiles in order to increase span capacity without an unnecessary increase in the composite floor depth. This tendency results in beams that are more vulnerable to the failure modes that involve either web LSB (local shear buckling) and/or compression flange RDB (restrained distortional buckling). The effects of shear stresses as well as web buckling and post-buckling behavior on the overall beam performance have been investigated both experimentally and numerically in order to resolve the most important behavioral issues of plain-webbed composite beams. Less attention has been paid to investigations of instability effects on the ultimate strength of steel profiles in continuous castellated composite beam systems. In this paper, different finite element techniques are used to investigate the in-plane behavior with use of geometrically linear analysis and the out-of-plane distortional behavior with use of geometrically nonlinear analysis, with both techniques applied to trace the performance of continuous composite beams.

INTRODUCTION

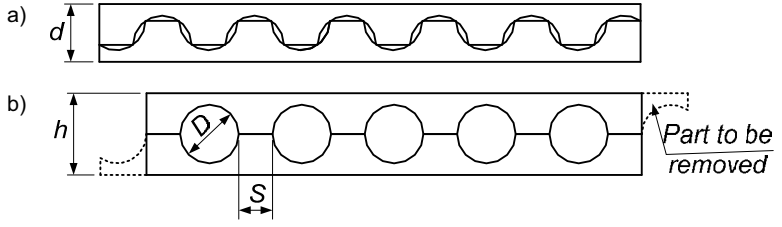
Steel castellated or cellular beams, which are lighter than conventional shapes, have been used in order to create flexible floor plans that are free of interior columns. The renaissance of their application in modern building structures has resulted from the utilization of their composite action in floor constructions. To further economize a floor framing design, asymmetric open-webbed shapes used in composite construction require smaller top flanges in the transformed section, while a larger bottom flange resists tension in sagging moment regions and out-of-plane distortional buckling in hogging moment regions. Modern composite beams of higher-grade structural steel profiles are more vulnerable to failure modes that involve web LSB (local shear buckling) and/or compression flange RDB (restrained distortional buckling). The effects of shear stresses as well as web buckling and post-buckling behavior on the overall beam performance have been investigated in recent years both experimentally and numerically, in order to resolve the most important behavioral issues of simply supported castellated composite beams.

Experimental investigations of bare steel castellated beams were recently carried out in order verify the distortional buckling behavior (Zirakian and Showkati 2006). Six steel castellated beams were tested up to failure. Lateral buckling with section distortion was observed at the failure load for all tested beams. Five castellated composite beams were tested up to failure at the Structural Engineering Laboratory of McGill University (Megharief 1997). The aim of this testing project was to observe the behavior of simply-supported composite castellated beams under sagging moment and different beam lengths, corresponding to different shear-to-moment ratios. Therefore, the tested specimens were divided into two groups, namely short and long spans, to represent shear and flexural specimens, respectively. The beams were fabricated from a bantam beam section. Results obtained experimentally indicated that the ultimate strength of shear composite beams was associated with lateral-torsional buckling of the web-posts, while longer flexural composite beams reached their ultimate strength when most of the studs failed, resulting in lateral-torsional buckling because of a sudden change in the restraining conditions of the I-section compression flange.

Little attention, if any, has been paid to investigations of the strength of continuous castellated composite beam systems where different instability effects start to play an important role, especially in the hogging moment zone (Gizejowski and Salah 2007). A variety of parameters that may affect the failure load of statically indeterminate composite beams was studied, such as negative moment span length, shape of the web openings, opening arrangements at both sides of the beam support, and web opening spacing. Openings of the same opening area but with different shaped and spaced c/c at the same distances, namely rectangular, hexagonal and circular, were investigated. The numerical study conducted indicated that castellated composite beams are more sensitive to different distortional buckling modes in the negative moment zone. Failure modes were associated with shear and bending, and with stress concentration in the area of openings causing early yielding and stiffness degradation effects, especially when openings consist of sharp corners. Circular openings were found to be the most effective in both load transfer and distortional buckling resistance. This type of opening is therefore considered in the numerical investigations of the present study.

MODELING TECHNIQUES USED IN NUMERICAL SIMULATIONS

Numerical simulations are conducted with the use of ABAQUS software (ABAQUS/Standard 2005) in the form of parametrical studies for flanged composite castellated beams in which the web is made of structural steel I-section arranged with circular openings (called hereafter the cellular I-profile), and the flange made of reinforced concrete as a slab of the effective width. Structural steel cellular I-profiles are obtained from standard IPE profiles of the following depths: 200 mm, 300 mm, 400 mm, 500 mm, and 600 mm, cut as shown in Figure 1a) and then shifted longitudinally and welded to form the resultant castellated shape element shown in Figure 1 b). The steel grade of S355, according to the Eurocode 3 specification (EN 1993-1-1 2005), is adopted. The reinforced concrete part of 1000x100 mm is made of the concrete class C50/60 according to the Eurocode 2 specification (EN 1992-1-1 2004). Grade B500 reinforcement is used, and represents 1% of the concrete area. The full composite action is assumed to be developed between the web of the composite beam, i.e., the steel cellular I-profile, and the flange of the composite beam, i.e., the reinforced concrete slab. The properties of structural steel, concrete and reinforcement material are considered at their characteristic values.



h/d=1.4, *D/d*=1.05, *S/D*=0.5

Figure 1 – Castellation process arrangements for: a) cutting, b) welding

The parametric study is performed for a two-span continuous beam static scheme, loaded with a uniformly distributed load, *W*, and for different span-to-cellular-I-profile-depth ratios that are set from approximately 10 (shortest spans) to 30 (longest spans) with an interval of five. The static scheme and the section of composite beam series are shown in Figure 2.

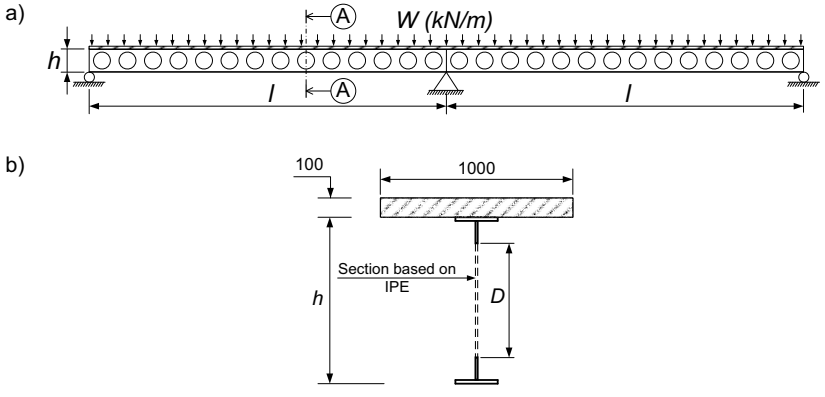


Figure 2 – Two-span cellular composite beam: a) static scheme, b) cross-section (A-A)

Two types of FE models are considered for the purpose of this study, namely:

a) FE-SS: thin four-node shell elements (S4R5) with reduced integration and five degrees of freedom (DOFs) per node are used for modeling the components of the steel cellular I-profile. The reinforced concrete flange is modeled using thick four-node shell elements (S4R) with reduced integration (see Figure 3a). The steel reinforcement in the concrete is provided by means of a rebar layer that is an available option in ABAQUS for modeling concrete reinforcement

b) FE-SB: thin four-node shell elements (S4R5) with reduced integration and five DOFs per node are used for modeling the components of steel cellular I-profile, while 3D two-node beam elements (B31) are used for the reinforced concrete flange as depicted in Figure 3b. The steel reinforcement is modeled using the rebar option provided by ABAQUS for modeling the reinforcing bars within the beam elements

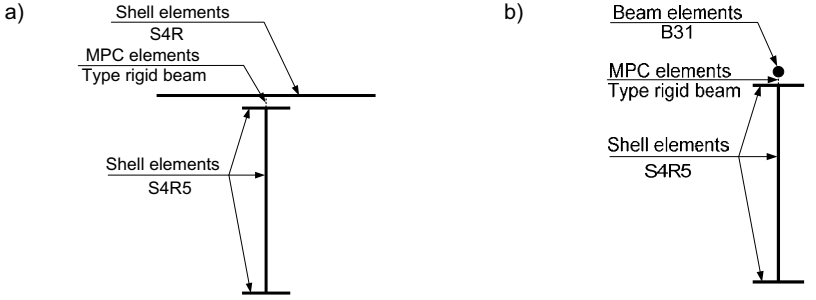


Figure 3 – Finite element modeling techniques: a) FE-SS model, b) FE-SB model

In the FE-SS model, the so-called SC model (smeared crack model) available in ABAQUS is used for concrete material. The stress-strain relationship for concrete is diagrammatically shown in Figure 4. Details of this type of constitutive law used for the reinforced concrete slab modeled with the use of shell elements are given elsewhere (ABAQUS/Standard 2005). In this model, concrete is assumed to be an isotropic material prior to cracking. In tension, concrete is considered a linear elastic material up to the uniaxial tensile strength, and then a linear softening model is used to represent the post-failure behavior in tension. The post-cracking behavior for direct straining across cracks is modeled with a tension stiffening option in ABAQUS. The tension softening option allows for important effects of interaction between the reinforcement and cracked concrete to be accounted for. The shear retention option in ABAQUS is used to consider the linear shear stiffness reduction of open cracks to zero as the crack opening increases.

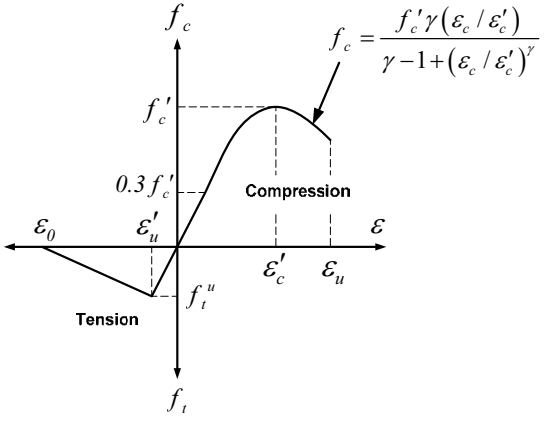


Figure 4 – Stress-strain characteristic of concrete material in SC model

In the FE-SB model, the concrete flange is modeled by using 3D beam elements (B31), and the full steel-concrete composite action is achieved using the MPC option, as shown in Figure 3b. The concrete material is modeled by using the CI model (cast iron model) with different yield stresses for tension and compression. The cast iron compression hardening and cast iron tension hardening options are used to specify the two sets of hardening data in compression and tension, respectively. A typical stress-strain curve used in the cast iron model is shown in Figure 5. For adequate modeling of the limited strength and ductility of concrete in tension, a yield stress in tension of a substantially lower value than that obtained from the standard tests of concrete is adopted.

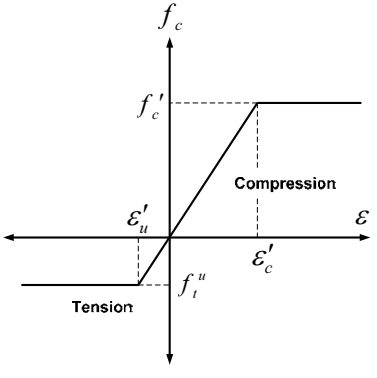


Figure 5 – Stress-strain characteristic of concrete material in CI model

Classic steel plasticity models of elastic-perfectly-plastic type are used for the nonlinear material effects of both structural steel and reinforcement.

CALIBRATION OF CONCRETE MODEL PARAMETERS

The calibration exercise is performed for a simply supported plain-webbed composite beam tested experimentally elsewhere (Nie et al. 2004). As a result of studying the effect of different softening parameters in the SC constitutive model of the FE-SS modeling technique on the behavior and stress redistribution process, zero tension stress in the softening region of concrete deformations is to be attained for the strain across the cracks of 0,1. Results of the computer simulation with use of the above-stated value of the softening phase of concrete in tension proved to represent the best fit to the experimental load deflection behavior of the considered tested composite beam specimen.

A similar exercise is carried out for the FE-SB modeling technique for which the value of 1/10 of the real tension strength of concrete is adopted in the CI constitutive model, while in compression the yield stress is directly equal to the concrete compression strength.

The comparison of load deflection characteristics obtained from computer simulations and that from the test is given in Figure 6. It is observed that both modeling techniques adopted with concrete model parameters are in good agreement with experiments, especially in the elastic region. For inelastic deformations, the SC model of concrete in the FE-SS modeling technique gives the lower bound estimation up to the point of reinforcement rupture, while the CI model in the FE-SB modeling technique creates the upper bound solution. Since an acceptable agreement is found for both modeling techniques and constitutive law parameters of the mentioned above concrete models were used, they are adopted hereafter in numerical studies of the behavior of a series of two-span continuous castellated composite beams.

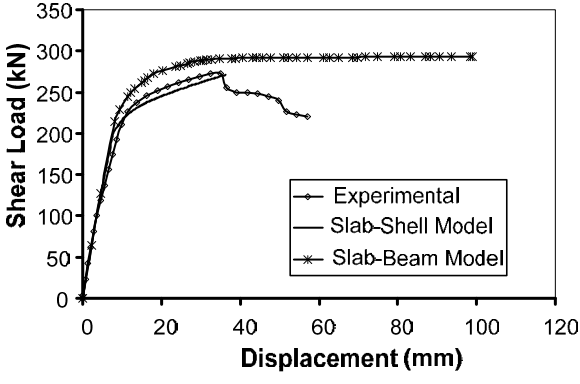


Figure 6 – Numerical and experimental load-deflection characteristics

PARAMETRIC STUDY FOR IN-PLANE BEHAVIOR

The study presented in this section is directly related to the evaluation of the in-plane limit load by methods of computer modeling. Since the behavior of cellular composite beams is more complex than that of the plain-webbed composite ones, the first attempt was to develop a suitable FE-BB model in which all the elements of the composite beam would be modeled by line finite elements behaving in the plane of loading. Investigations were in line with those classical ones carried out for castellated beams, the elastic behavior of which would be represented by the behavior of Vierendeel plane frame systems. A number of different approaches were examined, for which effective section properties of a uniform section of post and chord members of castellated steel I-sections were selected to represent the actual behavior of the whole composite beam system. The concrete was treated as ineffective in tension and removed from the calculation of section properties, while in compression it was treated as fully effective. Numerical results of the limit load evaluated from first order plastic hinge analysis showed that it would not be possible to propose uniform rules for the development of such a simple FE-BB model in the whole range of I-section depths and span lengths. From these investigations, one

can formulate the conclusion that more refined models would be necessary for the development of the behavior of castellated composite beams.

Such refined numerical models of FE-SS and FE-SB types, as described in the previous section, are proposed herein, in which the castellated structural steel is modeled with the use of finite shell elements, while the concrete part is modeled as composed of shell elements in the former, and line elements in the latter. The material properties used in the numerical simulations carried out with use of both above-mentioned models are listed in Table 1.

Table 1 – Basic material properties of considered two-span continuous composite beam

Model	I-section*)	Reinforcing bars*)	Concrete**)		
	f_y [N/mm2]	f_y [N/mm2]	f_c' [N/mm^2]	f_t^u [N/mm^2]	ε_0
FE-SS	355	500	50	4.0	0.1
FE-SB				0.4	-
*) E= 210000 [N/mm2], **) E= 37000 [N/mm2]					

Since the in-plane ultimate strength is looked at, the general static analysis option in ABAQUS is used for the estimation of in-plane failure load. Figures 7, 8, 9, 10 and 11 show the results obtained for the cellular I-section increasing depths *l/h* where the depth of a cellular I-section *h* corresponds to *d* of the depth of original plain-webbed I-section, being equal to 200 mm, 300 mm, 400 mm, 500 mm and 600mm, respectively.

The presented comparison of in-plane failure loads obtained from simulations based on FE-SS and FE-SB models leads to the following:

1. Application of CI concrete constitutive law and modeling of reinforced concrete slab with use of line finite elements is simple and yields generally safe predictions if compared with more advanced modeling of the slab that is based on finite shell elements
2. Differences are more pronounced for beams of shorter span lengths than for beams of longer spans

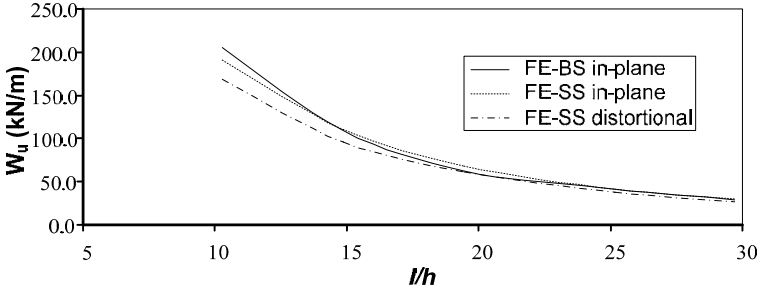


Figure 7 – Ultimate loads for composite beams fabricated from IPE200

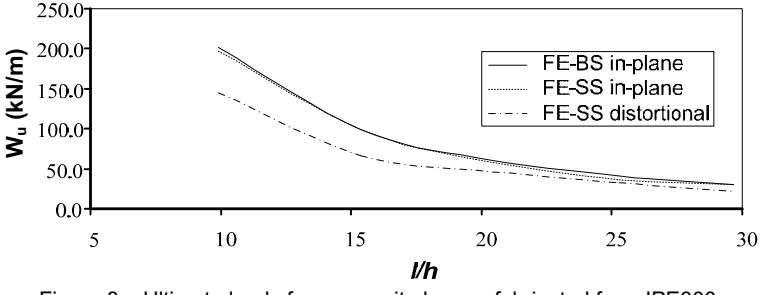


Figure 8 – Ultimate loads for composite beams fabricated from IPE300

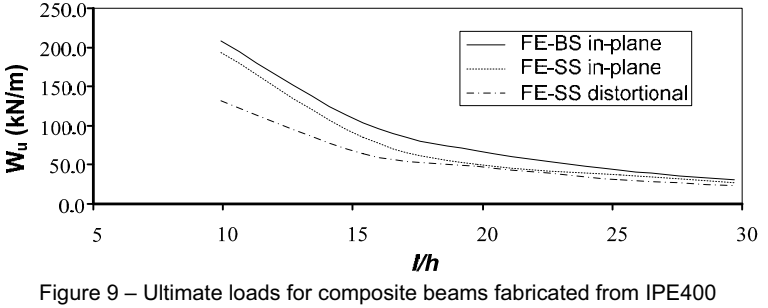


Figure 9 – Ultimate loads for composite beams fabricated from IPE400

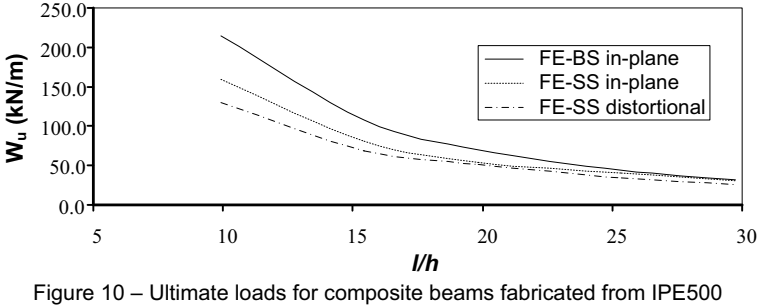


Figure 10 – Ultimate loads for composite beams fabricated from IPE500

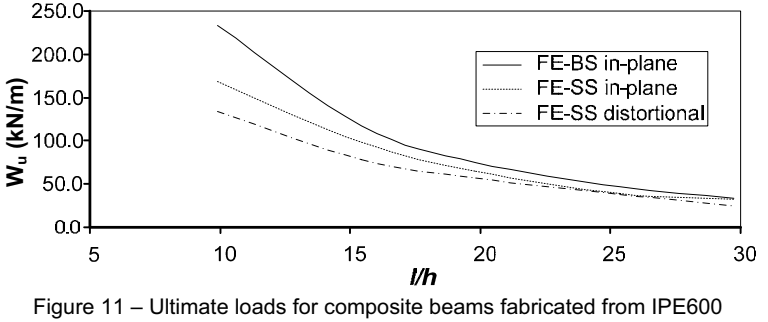
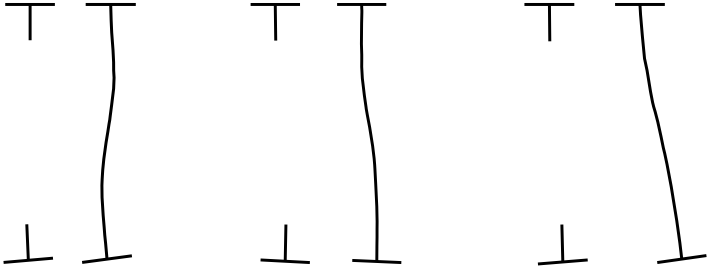


Figure 11 – Ultimate loads for composite beams fabricated from IPE600

PARAMETRIC STUDY FOR DISTORTIONAL OUT-OF-PLANE BEHAVIOR

The proposed FE-SS model is used to determine the RDB failure loads of two-span cellular composite beams, the in-plane failure loads of which are presented in the previous section. The inelastic behavior of composite beam materials and geometric nonlinearity due to large displacements are considered for nonlinear RDB analysis. The first buckling mode shape obtained from the elastic RDB analysis is used to describe an initially imperfect system. A small value of the maximum geometric imperfection equal to half of the thickness of the I-section web is applied. The option of modified Riks method is chosen in ABAQUS to simulate the behavior of composite beams not only prior to the limit point but also in the post-limit range, if applicable (ABAQUS/Standard 2005). The FE models are also able to predict the behavior in the negative moment region where the behavior of the cracked concrete is controlled by using either the tension softening SC model or the ductile CI model of different yield stresses in tension and compression. The Riks nonlinear stability analysis enables the prediction of the beam's ultimate state and its ultimate strength with regard to buckling effects.

The results of nonlinear stability analysis are added to the results of in-plane analyses in Figures 7, 8, 9, 10, and 11 from the previous section in order to directly compare them with the results of general in-plane static analysis. It can be observed that the ultimate strength is always located below that corresponding to the in-plane failure load calculated either by FE-SS or FE-SB modeling techniques. The state of RDB out-of-plane deformations at failure differs for considered beams, and is dependent predominantly on the beam span length. For short-span beams, the mode of buckling is of the torsional-distortional form and changes to almost lateral-distortional mode when the span length increases from the shortest one to the longest one analyzed. As an illustration of this effect, section distortional shapes at the first opening with reference to internal support and along the post of the full-web section following the first opening are presented in Figure 12 for selected cellular beams fabricated from IPE 600 (corresponds to the ultimate loads presented in Figure 11).



a) l/h=10 b) l/h=20 c) l/h=30

Figure 12 – Section distortional shapes for different l/h: a) 10, b) 20, c) 30

ULTIMATE LOADS OF PLAIN-WEBBED COMPOSITE BEAMS

The behavior of cellular composite beams is compared hereafter with that of their plain-webbed counterparts. Another study carried out by the authors (Salah and Gizejowski 2008) presents the results of investigations towards the behavior of plain-webbed composite beams with regard to their behavior in the hogging moment zone. For the same cross-section of the concrete slab, different IPE profiles, namely IPE200, IPE300, IPE400, IPE500 and IPE600, are used as the structural steel part of the analyzed two-span composite beams. The in-plane failure load for these beams is calculated based on the in-plane plastic-hinge mechanism theory. The effect of shear force is accounted for by assuming that only the web of steel I-section carries the shear flow. The out-of-plane distortional buckling load is calculated using ABAQUS code, with the same analysis options as used in the present study. Figures 13, 14, 15, 16 and 17 show a comparison between the in-plane plastic-hinge failure load and the ultimate RDB load evaluated numerically with the use of ABAQUS.

For the lightest section, the in-plane failure load is always smaller than that corresponding to the RDB ultimate strength, and the maximum difference is for the shortest span. This difference diminishes when the beam span length increases (see Figure 13). When IPE cross-sections are heavier, the ultimate strength loads start from a higher value than that of the in-plane failure load for the shortest beam spans, and then the difference decreases constantly with an increase in the beam span length. The ultimate RDB load finally drops below that of the plastic-hinge mechanism one (see Figures 14-17). Finally, for the heaviest I-section, the in-plane plastic-mechanism load and the ultimate RDB load do not cross each other. The ultimate load for all beam span lengths is less than that of the plastic-hinge mechanism.

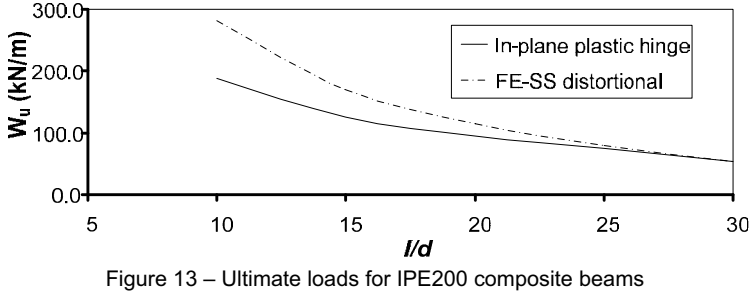


Figure 13 – Ultimate loads for IPE200 composite beams

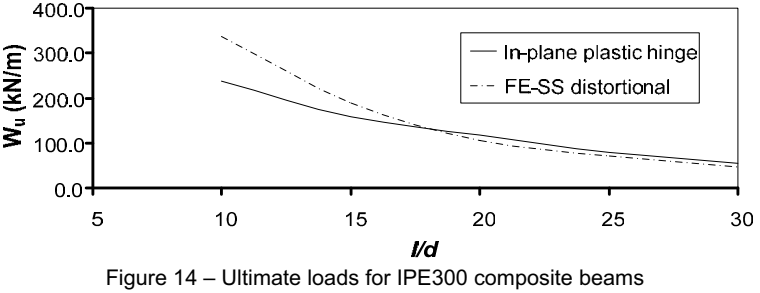


Figure 14 – Ultimate loads for IPE300 composite beams

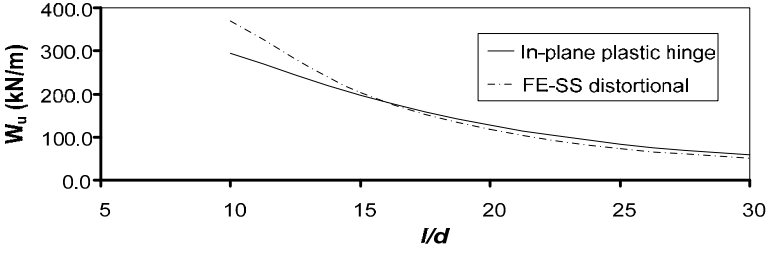


Figure 15 – Ultimate loads for IPE400 composite beams

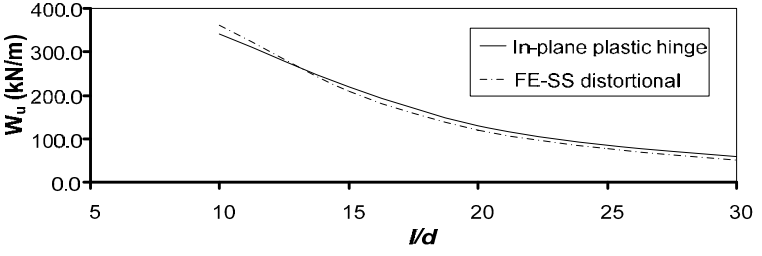


Figure 16 – Ultimate loads for IPE500 composite beams

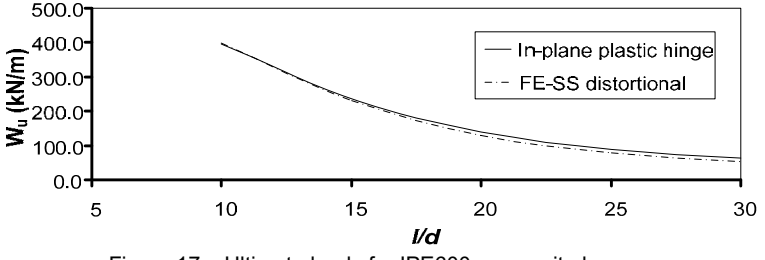


Figure 17 – Ultimate loads for IPE600 composite beams

On the other hand, Figures 13-17 show that in short span plain-webbed beams, where the effect of shear stresses is more important than normal stresses due to bending, the shear force is taken up not only by the web of the I-section, as assumed in the plastic-hinge mechanism theory, but also by the concrete slab. Since the web area in the lighter I-sections is smaller in comparison with the concrete area than that of heavier I-sections, the difference between the plastic-hinge mechanism failure load and the ultimate RDB load is greater for beams with short span lengths. The shear contribution of the concrete slab has also been observed in tests (Liang et al. 2004).

CONCLUSIONS

The behavior of statically indeterminate castellated composite beams is more complex than that of simply supported beams. The complex behavior is associated with different instability effects that the castellated composite beam may be subjected to in negative moment regions where the bottom compression flange of the beam is unrestrained.

Numerical investigations to predict the in-plane behavior with use of two finite element models, namely the shell model FE-SS and the beam-shell model FE-SB, are carried out in this paper. In the former model, the reinforced slab and the steel cellular section are modeled with the use of shell elements, and the material modeling is based on the smeared crack constitutive law for concrete. In the latter model, the reinforced slab is modeled with the use of line elements, and the cast iron constitutive law for concrete is used, while the steel cellular section is modeled as in the shell modeling technique. It is found that the FE-SB modeling technique coincides with that of FE-SS for lighter steel sections where the concrete slab reduces the amount of vertical shear carried out by the chord tee-sections at the opening and the horizontal shear in the post, and also for heavier steel sections and longer beam spans where the effect of bending dominates.

Numerical investigations carried out for out-of-plane distortional behavior prove that instability is the governing failure mode which is more pronounced for shorter beams and all the cellular steel sections analyzed. The RDB buckling mode is a torsional-distortional one for shorter beam spans, while for longer spans the buckling mode changes towards the lateral-distortional one.

The comparison between plain-webbed and cellular composite beams shows that the beam plastic-hinge mechanism theory for in-plane behavior with shear force contribution included only in the steel profile leads to lighter I-sections and lower values than those corresponding to the RDB ultimate load. This behavior is different from that of heavier sections.

REFERENCES

[1] ABAQUS/Standard, User's Manual I-III, version 6.5, Hibbit, Karlsson and Sorenson Inc., Providence, RI, 2005
[2] EN 1992-1-1, Eurocode 2 Part 1-1: Design of concrete structures – Part 1-1: General rules and rules for buildings, CEN, Brussels 2004
[3] EN 1993-1-1, Eurocode 3 Part 1-1: Design of steel structures – Part 1-1: General rules and rules for buildings, CEN, Brussels 2005
[4] Gizejowski M.A., Salah W., Failure modes of composite beams in the hogging moment region of continuous or semi-continuous systems. In: Lightweight Structures in Civil Engineering-Contemporary Problems (ed. J. B. Obrebski). Proceedings: Local Seminar of the Polish Chapter of IASS, 7 December, Micro-Publisher, 114-136, Warsaw 2007
[5] Liang Q.Q., Uy B., Bradford M.A., Ronagh H.R., Ultimate strength of continuous composite beams in combined bending and shear, Journal of Constructional Steel Research, 60, 1109-1128, 2004
[6] Megharief J.D., Behavior of composite castellated beams. MSc thesis, McGill University, Montreal 1997
[7] Nie J., Xiao Y., Chen L., Experimental studies on shear strength of steel–concrete composite beams, Journal of Structural Engineering, 130, 8, 1206-1213, 2004
[8] Salah W., Gizejowski M.A., Restrained distortion buckling of composite beams - FE modelling of the behaviour of steel-concrete beams in the hogging moment region. Proceedings: Eurosteel Conference, 3-5 September 2008, Graz, Austria, submitted.
[9] Zirakian T., Showkati H., Distortional buckling of castellated beams. Journal of Constructional Steel Research, 62, 863-871, 2006.

A CLASS OF FINITE ELEMENTS FOR NONLINEAR ANALYSIS OF COMPOSITE BEAMS

Quang Huy NGUYEN
INSA de Rennes – Structural Engineering Research Group
20 Avenue des Buttes de Coësmes, 35043 Rennes Cedex, France
quang-huy.nguyen@ens.insa-rennes.fr

Mohammed HJIAJ
INSA de Rennes – Structural Engineering Research Group
20 Avenue des Buttes de Coësmes, 35043 Rennes Cedex, France
mohammed.hjiaj@insa-rennes.fr

Brian UY
School of Engineering, University of Western Sydney
Penrith South DC NSW 1797, Australia
b.uy@uws.edu.au

Samy GUEZOULI
INSA de Rennes – Structural Engineering Research Group
20 Avenue des Buttes de Coësmes, 35043 Rennes Cedex, France
samy.guezouli@insa-rennes.fr

ABSTRACT

In this paper, we investigate the performance of three finite element formulations for continuous composite beam analysis. These formulations include displacement-based, force-based and mixed models. Specific attention is devoted on how to take into account discrete connection which seems, in some cases, to be more representative of the actual behavior. The nonlinear behavior of concrete is modeled using a softening plasticity model. The parameters of the models are obtained by matching the uniaxial stress-strain relationship provided by the CEB-FIP 90 model. Tension-stiffening is taken into account as well. A consistent time-integration is performed using the Euler backward scheme. The predictions of the FE models are compared and the study shows good performance of the mixed formulation.

INTRODUCTION

Recent years have seen the development of several formulations for composite beams with partial interaction including displacement-based, force-based and mixed formulations (Daniel and Crisinel 1993), (Aribert, Ragneau et al. 1993), (Salari 1999), (Ayoub 2003). Displacement-based F.E. beam models are derived from the principle of virtual work and provide an approximate solution where the displacement field fulfills strictly the compatibility relations but the equilibrium is satisfied only in a weak sense. For highly nonlinear problems, this formulation requires a large number of elements (Spacone, Filippou et al. 1996). The force-based formulation for the composite beam has become particularly attractive in recent years as this formulation seems to be more accurate than the displacement-based formulation with the same number of elements. In this formulation, the strong form of equilibrium

equations is satisfied along each element regardless of the section behaviour while compatibility is is enforced in a weak form. The little disadvantage of the force-based elements is the relative complexity to implement such elements in a general purpose finite element program (Spacone, Ciampi et al. 1996). A two-field mixed formulation is derived from the Hellinger-Reissner variational principle where both displacements and internal forces are varied separately. In the mixed formulation presented by Ayoub (Ayoub 2001), continuity of the displacement field is enforced.

In this paper, we analyze the performance of these three finite element formulations for continuous composite beams analysis. For all these formulation, the possibility to have discrete shear connection is considered in this paper. Further, the nonlinear behaviour of steel and concrete is modeled using the rigorous framework of the theory of plasticity. The nonlinear discrete governing equations are derived by applying the standard backward Euler scheme. The study highlights the superiority of the force-based and mixed formulations over the displacement formulation.

GOVERNING EQUATIONS OF COMPOSITE BEAMS

In this section we recall the field equations for a composite beam with partial shear interaction in a small displacement setting. The constitutive relations are presented in the next section. All variables subscripted with *c* belong to the concrete slab section and those with *s* belong to the steel beam. Quantities with subscript *sc* are associated with the shear connectors.

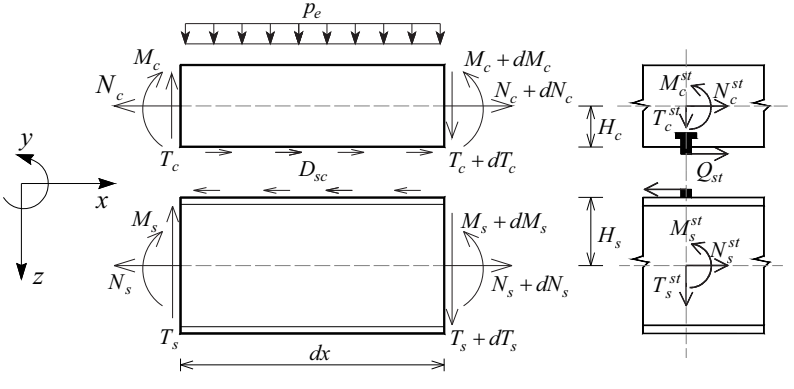


Fig. 1 – Free body diagram of an infinitesimal composite beam segment.

Equilibrium

The equilibrium conditions are derived by considering the infinitesimal beam segment without connector and the connector elements shown in Figure 1. The equilibrium equations can be written as follows:

$$\partial \mathbf{D} - \partial_{sc} D_{sc} - \mathbf{P}_e = 0 \tag{1}$$

$$\mathbf{Q}_{st} - \mathbf{b}_{sc}^T Q_{st} = 0 \tag{2}$$

where $\mathbf{D}(x) = \begin{bmatrix} N_s & N_c & M \end{bmatrix}^T$; $M = M_c + M_s$; $H = H_c + H_s$; $\mathbf{P}_e = \begin{Bmatrix} 0 & 0 & p_e \end{Bmatrix}^T$ and the operator ∂, ∂_{sc} et $\mathbf{b}_{sc}$ are defined as:

$$\partial = \begin{bmatrix} \frac{d}{dx} & 0 & 0 \\ 0 & \frac{d}{dx} & 0 \\ 0 & 0 & -\frac{d^2}{dx^2} \end{bmatrix} \; ; \; \partial_{sc} = \begin{bmatrix} 1 & -1 & H\frac{d}{dx} \end{bmatrix} \text{ and } \mathbf{b}_{sc} = \begin{bmatrix} 1 & -1 & \frac{1}{H} \end{bmatrix}$$

Kinematic relationships

The curvature and the axial deformation at any section are related to the beam displacements through kinematics relations. Under small displacements and neglecting the relative transverse displacement between the concrete slab and the steel beam, these relations are as follows:

$$\partial \mathbf{d} - \mathbf{e} = 0 \tag{3}$$

$$\partial_{sc} \mathbf{d} - d_{sc} = 0 \tag{4}$$

where $\mathbf{d} = \begin{bmatrix} u_s & u_c & v \end{bmatrix}^T$ is the displacement vector; $\mathbf{e} = \begin{bmatrix} \varepsilon_s & \varepsilon_c & \kappa \end{bmatrix}^T$ is the deformation vector, in which u is the longitudinal displacement, v the transversal displacement, ε_c the strain at the concrete section centroid, ε_s the strain at the steel section centroid, κ the curvature and d_{sc} the relative slip between the concrete slab and the steel beam.

Force-deformation relationships

The fiber discretization is used to describe the section behaviour in the proposed model. The force-deformation incremental relationship of the cross section is:

$$\Delta \mathbf{D} = \mathbf{k}\, \Delta \mathbf{e} \text{ or } \Delta \mathbf{e} = \mathbf{f}\, \Delta \mathbf{D} \tag{5}$$

where $\mathbf{k}, \mathbf{f}$ respectively are the tangent stiffness and flexibility matrix of the cross section obtained by integrating over the cross-section the uniaxial discrete constitutive relations for both steel and concrete. Similarly, the connector force is related to the slip at the interface through the following equation:

$$\Delta D_{sc} = k_{sc}\, \Delta d_{sc} \text{ and } \Delta Q_{st} = k_{st}\, \Delta d_{sc} \tag{6}$$

where $k_{sc}(x)$ is the tangent stiffness of the continuous bond (adherence) along the composite beam and $k_{st}(x)$ is the tangent stiffness of discrete bond (shear stud).

DISCRETE CONNECTOR ELEMENT

To establish the stiffness matrix of such element, one uses the principle of virtual work. Considering the virtual displacement $\delta\mathbf{q}_{st} = \begin{bmatrix}\delta u_s & \delta u_c & \delta\theta\end{bmatrix}^T$ of the bond element, the internal and external virtual work is given by:

$$\delta W_i = Q_{st}\delta d_{sc} = Q_{st}\begin{bmatrix}1 & -1 & -H\end{bmatrix}\delta\mathbf{q}_{st} \tag{7}$$

$$\delta W_e = \delta\mathbf{q}_{sc}^T\mathbf{Q}_{st} \tag{8}$$

By substituting (6) into (7) and then setting $\delta W_i = \delta W_e$, one obtains:

$$\mathbf{K}_{st}\Delta\mathbf{q}_{st} = \mathbf{Q}_{st} - \mathbf{b}_{st}Q_{st}^{i-1} \tag{9}$$

where $\mathbf{K}_{st} = \mathbf{b}_{st}^T k_{st}\mathbf{b}_{st}$ is the connector element tangent stiffness matrix.

DISPLACEMENT-BASED FORMULATION

In the displacement-based formulation, the displacements serve as primary variables. The displacement field is assumed to be continuous along the beam:

$$\mathbf{d} = \mathbf{a}\,\mathbf{q} \tag{10}$$

where $\mathbf{a}$ is a matrix of $3 \times n_d$ displacement shape functions with n_d being the total number of displacement degrees of freedom and $\mathbf{q}$ the vector of element nodal displacement. The weighted integral form of the equilibrium equation (1) is derived from the principle of virtual work and takes the form:

$$\int_L \delta\mathbf{d}^T\left(\partial\mathbf{D} - \partial_{sc}D_{sc} - \mathbf{P}_e\right)dx = 0 \tag{11}$$

where $\delta\mathbf{d}^T(x)$ are the displacement fields fulfilling the kinematics conditions. By integrating by parts (11) and substituting (5) and (6) into (11), one obtains:

$$\mathbf{K}_e\Delta\mathbf{q} = \mathbf{Q} + \mathbf{Q}_0 + \mathbf{Q}_R \tag{12}$$

where $\mathbf{K}_e$ is the element stiffness matrix at the last iteration, defined as:

$$\mathbf{K}_e = \int_L \left[\partial^T\mathbf{a}\,k\,\partial\mathbf{a} + \partial^T\mathbf{a}_{sc}\,k_{sc}\,\partial\mathbf{a}_{sc}\right]dx = 0 \tag{13}$$

$\mathbf{Q}_0$, which corresponds to the vector of nodal forces due to the distributed load p_0, is given by:

$$\mathbf{Q}_0 = \int_L \mathbf{a}^T\mathbf{P}_e\,dx \tag{14}$$

and $\mathbf{Q}_R$ is the vector of nodal resisting forces at the last iteration, defined as:

$$\mathbf{Q}_R = \int_L \left[\partial^T\mathbf{a}\,\mathbf{D}^{i-1} + \partial^T\mathbf{a}_{sc}\,D_{sc}^{i-1}\right]dx = 0 \tag{15}$$

FORCE-BASED FORMULATION

In the force-based formulation, the internal forces serve as primary variables. Typically this element has to be developed without rigid-body displacement modes (Figure 2) as the element flexibility matrix need to be eventually inverted to get the element stiffness matrix (Salari 1999). In short, the internal forces $\mathbf{D}$ and the bond force D_{sc} are expressed in terms of the element nodal forces $\mathbf{Q}$ and the bond forces $\mathbf{Q}_{sc}$ using the interpolation functions obtained from the equilibrium conditions. The resulting expression is

$$\mathbf{D} = \mathbf{b}\,\mathbf{Q} + \mathbf{c}\,\mathbf{Q}_{sc} + \mathbf{D}_0 \tag{16}$$

$$D_{sc} = \mathbf{b}_{sc}\,\mathbf{Q} + \mathbf{c}_{sc}\,\mathbf{Q}_{sc} \tag{17}$$

where $\mathbf{b}, \mathbf{c}, \mathbf{b}_{sc}$ and $\mathbf{c}_{sc}$ are the forces interpolation functions.

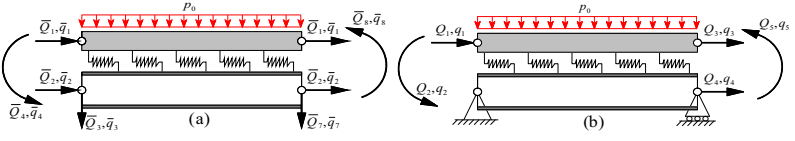


Fig. 2 Composite beam element: (a) without rigid body modes; (b) Rigid body modes

Using the virtual forces $\delta\mathbf{D}$ and δD_{sc}, the compatibility conditions (3) and (4) may be enforced in the integral form as:

$$\int_L \delta\mathbf{D}^T \left(\partial\mathbf{d} - \mathbf{e}\right) dx + \int_L \delta D_{sc} \left(\partial_{sc}\mathbf{d} - d_{sc}\right) dx = 0 \tag{18}$$

By substituting (5), (6), (16) and (17) into (18) and after eliminating the nodal virtual forces using arbitrariness arguments, one obtains:

$$\begin{bmatrix} \mathbf{F}_{bb} & \mathbf{F}_{bc} \\ \mathbf{F}_{bc}^T & \mathbf{F}_{cc} \end{bmatrix} \begin{bmatrix} \Delta\mathbf{Q} \\ \Delta\mathbf{Q}_{sc} \end{bmatrix} = \begin{bmatrix} \mathbf{q} \\ \mathbf{0} \end{bmatrix} - \begin{bmatrix} \mathbf{q}_r \\ \mathbf{q}_{rsc} \end{bmatrix} \tag{19}$$

where

$$\begin{aligned} \mathbf{F}_{bb} &= \int_L \mathbf{b}^T \mathbf{f}\, \mathbf{b}\, dx + \int_L \mathbf{b}_{sc}^T \mathbf{f}_{sc}\, \mathbf{b}_{sc} dx \\ \mathbf{F}_{bc} &= \int_L \mathbf{b}^T \mathbf{f}\, \mathbf{c}\, dx + \int_L \mathbf{b}_{sc}^T \mathbf{f}_{sc}\, \mathbf{c}_{sc} dx \\ \mathbf{F}_{cc} &= \int_L \mathbf{c}^T \mathbf{f}\, \mathbf{c}\, dx + \int_L \mathbf{c}_{sc}^T \mathbf{f}_{sc}\, \mathbf{c}_{sc} dx \end{aligned} \tag{20}$$

$$\mathbf{q}_r = \int_L \mathbf{b}^T \mathbf{e}^{i-1} dx + \int_L \mathbf{b}_{sc}^T d_{sc}^{i-1} dx + \int_L \mathbf{b}^T \mathbf{f}\, \Delta\mathbf{D}_0 dx \tag{21}$$

$$\mathbf{q}_{rsc} = \int_L \mathbf{c}^T \mathbf{e}^{i-1} dx + \int_L \mathbf{c}_{sc}^T d_{sc}^{i-1} dx + \int_L \mathbf{c}^T \mathbf{f}\, \Delta\mathbf{D}_0 dx \tag{22}$$

Solving the second equation of (19) for $\Delta\mathbf{Q}_{xc}$ and substituting the result into the first equation of (19), the governing equation of the element is obtained as:

$$\mathbf{F}_e\, \Delta\mathbf{Q} = \mathbf{q} - \mathbf{q}_R \tag{23}$$

where $\mathbf{F}_e$ is the element flexibility matrix at the last iteration, defined as:

$$\mathbf{F}_e = \mathbf{F}_{bb} \left(\mathbf{F}_{cc}\right)^{-1} \mathbf{F}_{bc}^T \tag{24}$$

$\mathbf{q}_R$ is element nodal displacements due to the lack of compatibility conditions, defined as:

$$\mathbf{q}_R = \mathbf{q}_r + \mathbf{F}_{bb} \left(\mathbf{F}_{cc}\right)^{-1} \mathbf{q}_{rsc} \tag{25}$$

In order to introduce this formulation in a displacement based procedure, the flexibility matrix $\mathbf{F}_e$ must be inverted to obtain the element stiffness matrix. After inversion, the rigid body modes are added using simple transformation matrices.

HELLINGER-REISSNER MIXED FORMULATION

In the Hellinger–Reissner mixed formulation, both the displacement and the internal forces fields along the element are approximated by independent shape functions. More detailed treatment of this mixed formulation can be found in (Zienkiewicz and Taylor 1989).

The equilibrium (1) and compatibility (3) conditions are enforced in an integral form:

$$\int_L \delta\mathbf{d}^T \left(\partial\mathbf{D} - \partial_{sc} D_{sc} - \mathbf{P}_e\right) dx + \int_L \delta\mathbf{D}^T \left(\partial\mathbf{d} - \mathbf{e}\right) dx = 0 \tag{26}$$

By integrating by parts twice the first term of (26) and substituting (5), (6), (10) and (16) into (26), after eliminating the nodal virtual displacements and forces using arbitrariness arguments, one obtains

$$\begin{bmatrix} \mathbf{0} & \mathbf{G} \\ \mathbf{G}^T & -\mathbf{F}_{bb} \end{bmatrix} \begin{bmatrix} \Delta\mathbf{q} \\ \Delta\mathbf{Q} \end{bmatrix} = \begin{bmatrix} \mathbf{Q} + \mathbf{Q}_0 \\ \mathbf{0} \end{bmatrix} - \begin{bmatrix} \mathbf{Q}_r \\ \mathbf{q}_r \end{bmatrix} \tag{27}$$

where

$$\begin{aligned} \mathbf{G} &= \int_L \left(\partial^T \mathbf{a}\, \mathbf{b} + \partial_{sc}^T \mathbf{a}_{sc}\, \mathbf{b}_{sc}\right) dx \\ \mathbf{Q}_r &= \int_L \partial^T \mathbf{a} \left(\mathbf{D}^{i-1} + \Delta\mathbf{D}_0\right) dx + \int_L \partial_{sc}^T D_{sc}^{i-1} dx \\ \mathbf{q}_r &= \int_L \left(\partial^T \mathbf{a}\, \mathbf{e}^{i-1} + \partial_{sc}^T \mathbf{a}_{sc}\, d_{sc}\right) dx + \int_L \mathbf{b}\, \mathbf{f}\, \Delta\mathbf{D}_0 dx \end{aligned} \tag{28}$$

Solving the second equation for $\Delta\mathbf{Q}$ and substituting the result into the first equation of (27), the governing equation of the element is obtained as:

$$\mathbf{K}_m \Delta\mathbf{q} = \mathbf{Q} + \mathbf{Q}_0 + \mathbf{Q}_{Rm} \tag{29}$$

where

$$\begin{aligned} \mathbf{K}_m &= \mathbf{G}\left(F_{bb}\right)^{-1}\mathbf{G}^T \\ \mathbf{Q}_{Rm} &= \mathbf{Q}_r - \mathbf{G}\left(F_{bb}\right)^{-1}\mathbf{q}_r \end{aligned} \tag{30}$$

MATERIAL MODELLING

The general constitutive laws used to represent the stress–strain characteristics of the relevant materials are described in this section. For concrete, we adopt the stress-strain curve proposed by the CEB-FIP code model. The classical theory of plasticity is adopted to write the constitutive relations for both concrete and steel. This requires identifying the analytical functions describing hardening or (and) softening in both tension and compression. This procedure is trivial for steel but quite involved for concrete.

One-dimensional hardening/softening plasticity model

The total strain splits into an elastic part ε^e and a plastic part ε^p:

$$\varepsilon = \varepsilon^e + \varepsilon^p \tag{31}$$

The stress σ is related to the elastic strain through Hooke's law:

$$\sigma = E\left(\varepsilon - \varepsilon^p\right) \tag{32}$$

The general expression of the yield function for one-dimensional problems is given by

$$f(\sigma, R) = |\sigma| - \left(\sigma_y + R\right) \leq 0 \tag{33}$$

where σ_y is the initial elastic threshold. To account for the expansion/contraction of the elastic domain, we introduce a stress-like variable R. The evolution of the elastic domain is governed by the following relationship:

$$R = h(p) \tag{34}$$

If we have hardening, then $h(p)$ is a monotonically increasing function. For concrete, this function has two branches. The flow rule is given by

$$\dot{\varepsilon}^p = \dot{\lambda}\frac{\partial f}{\partial \sigma} = \dot{\lambda}\,\mathrm{sgn}(\sigma) \quad \text{with} \quad \dot{\lambda} \geq 0 \quad \text{and} \quad \mathrm{sgn}(\sigma) = \begin{cases} +1 & \text{if } x > 0 \\ -1 & \text{if } x < 0 \end{cases} \tag{35}$$

We can deduce that $\dot{\lambda} = \left|\dot{\varepsilon}^p\right|$. The evolution of the strain-like variable p associated to R is given by:

$$-\dot{p} = \dot{\lambda}\frac{\partial f}{\partial R} = -\dot{\lambda} \tag{36}$$

The flow rule must be supplemented by the complementarity relations:

$$\dot{\lambda} \geq 0 \ , \ f(\sigma,R) \leq 0 \ , \ \dot{\lambda} f(\sigma,R) = 0 \tag{37}$$

The consistency condition is given by:

$$\dot{\lambda} \dot{f}(\sigma,R) = 0 \tag{38}$$

The above equations provide a unified format to deal with rate-independent constitutive models. For each component of the composite section, the function $R = h(p)$ must be identified in order to match the uniaxial stress-strain relations for each material. The main advantage of the above formulation is consistent time integration.

Concrete model

In compression regions, the stress-strain curve suggested by the CEB-FIB model code 1990 (CEB-FIB 1993) includes a monotonically increasing branch up to a peak value, followed by a descending part that gradually flattens to a constant value equal to zero. The initial portion of the ascending branch is linearly elastic, but at about 30% of the ultimate strength, the presence of microcracks leads to nonlinear behavior, with a reduction in tangent modulus. In the subsequent descending branch, the concrete is severely damaged with prominent cracks. In tension, the effect of the rebars is taken into account (tension-stiffening). In this paper, we suggest to transpose the CEB-FIB model into the plasticity framework where a clear distinction between the plastic strain and the total strain is made.

In tension, the initial elastic threshold is σ_y^+ and the contraction of the elastic domain is governed by the following relation

$$R_c^+(p) = f_{ct}\left(1 - \frac{1}{\left(1+\left(p/p_u\right)^2\right)}\right) \tag{39}$$

In compression, the initial elastic threshold is σ_y^- and the expansion/contraction of the elastic domain is described by the following relation

$$R_c^-(p) = \begin{cases} \left(\zeta_1 p^2 + \zeta_2 p + \zeta_3^2\right)^{\frac{1}{2}} - \zeta_4 q - \zeta_3 & \text{if } p \geq \hat{p} \\ \beta_1 p + \beta_2 + \left(\sum_{i=0}^{2} \eta_i p^i\right)^{\frac{1}{2}} \cos\left\{\frac{1}{3}\arccos\left[\left(\sum_{i=0}^{2} \eta_i p^i\right)^{\frac{3}{2}} \sum_{i=0}^{3} \mu_i p^i\right]\right\} & \text{if } p < \hat{p} \end{cases} \tag{40}$$

In the above relation, $f_{ct}, \beta_i, \zeta_i, \eta_i, \mu_i, p_u, \hat{p}$ are material parameters. The identification process is detailed in the reference (Nguyen 2008)

Steel model and connector stress-slip model

In the present study, the steel is modeled as an elastic-perfectly plastic material incorporating strain hardening. Specifically, the relationship is linearly elastic up to yielding, perfectly plastic between the elastic limit and the commencement of strain

hardening, linear hardening occurs up to the ultimate tensile stress and the stress remains constant until the tensile failure strain is reached. The initial elastic threshold is σ_y and the following function describes the evolution of the elastic domain size:

$$R_s(p) = \begin{cases} 0 & \text{if} \quad p < p_{sy} \\ H\left(p - p_{sy}\right) & \text{if} \quad p_{sy} \le p \le p_{su} \\ 0 & \text{if} \quad p > p_{su} \end{cases} \tag{41}$$

For the connector, an elastic perfectly plastic model is considered. The above relations are discretized using an implicit scheme. The procedure employed to derive the discrete relations is not described in the paper due to lack of space.

NUMERICAL EXAMPLE

In order to study the performance of the displacement-based, force-based and mixed composite beam elements presented above, a continuous composite beam illustrated in Figure 2 is considered. The beam consists of an IPE400 steel section connected to a reinforced concrete slab of 800 mm wide and 120 mm thick by the shear connectors. 152% shear connection and 1% reinforcing bars are used. The material parameters are given in Figure 2.

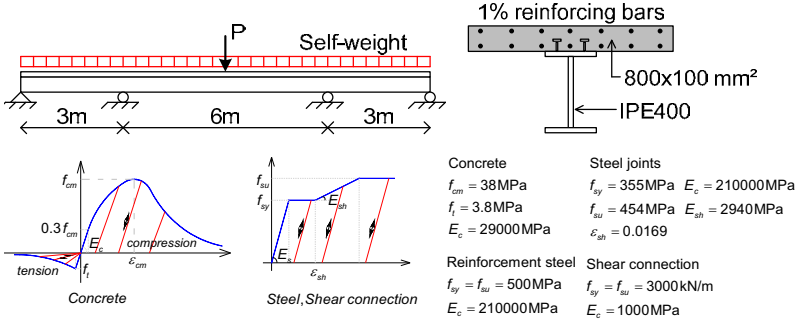


Fig. 2 – Geometrical characteristics of the investigated beam

Figure 3 provides the structural global response, where the load-deflection curves obtained by the displacement-based, force-based and mixed formulation using 8 and 24 elements, respectively, are reported. It can be noted that all three formulations give essentially identical results in the elastic range. However, in the plastic range, the three element types show different performances. From the Figure 3, it is evident that both force-based and mixed element provides practically identical results. However, the displacement-based formulation with 24 elements seems to be less accurate than the two other formulations with only 8 elements. The solution with 24 force-based elements cannot be further improved by remeshing. To obtain the load-displacement curve with the same accuracy 192 displacement-based are needed.

This is essentially because the force-based and mixed element provides a better estimation of the curvature variation in highly nonlinear response than the displacement-based element (Salari, Enrico et al. 1998).

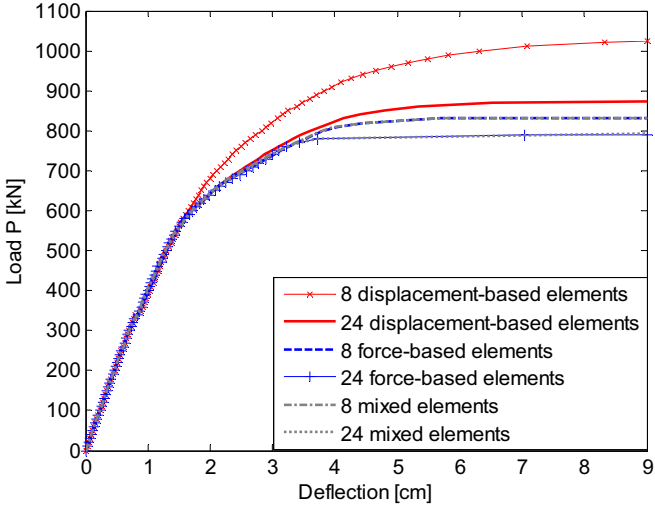


Fig. 3 Load – deflection Diagrams

Figures 4-7 show, along the beam length, the distribution of bending moment, axial force in the slab, slip and curvature, respectively, obtained by the three formulations using 8 elements. As expected, the displacement-based elements give a discontinuity of the bending moment, axial force and the curvature while the interface slip is continuous. It is understandable because in the displacement-based formulation, the equilibrium conditions are satisfied only in weak sense while the compatibility conditions are satisfied in a strict sense. On the contrary, the force-based elements give a continuity of the bending moment, axial force and a discontinuity of the interface slip because only the equilibrium conditions are satisfied in strict sense. In the mixed formulation, both equilibrium conditions and compatibility conditions of section are satisfied in weak sense, only the compatibility condition at the interface is satisfied in strict sense, this why from the figures 4-7 we can observe that the bending moment and the interface slip are continuous in the mixed elements while the axial force and curvature are discontinuous. It should be noted that because of higher degree of polynomials chosen for the connector force field, the force-based model shows a better accuracy for the internal variables (Alemdar 2001).

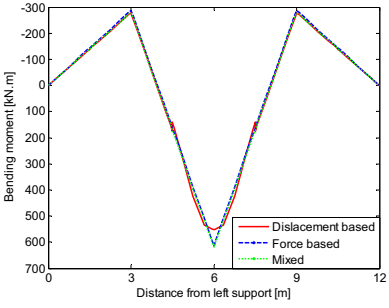


Fig. 4 Bending moment distribution

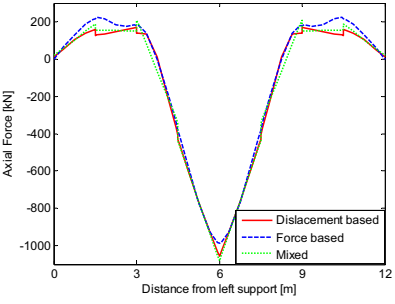


Fig. 5 Axial force distribution

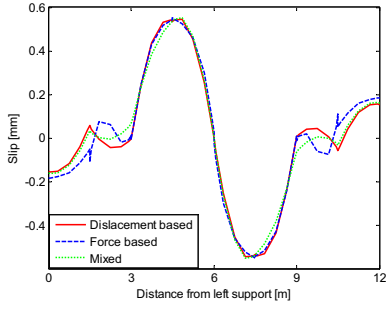


Fig. 6 Slip distribution

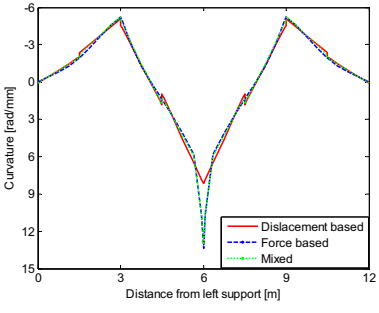


Fig. 7 Curvature distribution

CONCLUSIONS

A class of finite element models for continuous composite beam analysis is presented. This class of elements includes displacement-based, force-based and mixed formulations. The nonlinear behaviour of materials and deformable shear connectors has been formulated using the plasticity framework. In terms of global response, the forced-based and the mixed models predict essentially identical results and both elements show a better precision than the displacement-based elements. In terms of local parameters, the force-based models show greater accuracy for the internal variables (bending moment, axial force, and curvature) but their implementation in the general purpose finite element program is quite complex. The mixed model is less accurate than the forced-based model but it shows comparable results and it is easier to implement in the classical finite element program.

REFERENCES

Alemdar, B. N. (2001). Distributed plasticity analysis of steel building structural systems, Georgia Institute of Technology. **PhD**.

Aribert, J. M., Ragneau, E., et al. (1993). "Développement d'un élément fini de poutre mixte acier-béton intégrant les phénomènes de glissement et de semi-continuité avec éventuellement voilement local " Revue Construction Métallique n° 2: 31-49.

Ayoub, A. (2001). "A two-field mixed variational principle for partially connected composite beams." Finite Elements in Analysis and Design **37**(11): 929-959.

Ayoub, A. (2003). "Mixed formulation of nonlinear beam on foundation elements." Computers & Structures **81**(7): 411-421.

CEB-FIB (1993). CEB-FIP Model Code 1990: Design Code, Thomas Telford.

Daniel, B. J. and Crisinel, M. (1993). "Composite slab and strength analysis. Part I: Calculation procedure." Journal of Structural Engineering **119**(1): 16-35.

Nguyen, Q. H. (2008). Modélisation numérique du comportement des poutres mixtes acier-béton. Génie Civil. Rennes, France, Institut National des Sciences Appliquées des Rennes. **PhD**.

Salari, M. R. (1999). Modelling of bond-slip in steel-concrete composite beams and reinforcing bars. Departement of Civil, Environmental and Architectural Engineering, University of Colorado. **PhD**.

Salari, M. R., Enrico, S., et al. (1998). "Nonlinear Analysis of Composite Beams with Deformable Shear Connectors." Journal of Structural Engineering **124**(10): 1148-1158.

Spacone, E., Ciampi, V., et al. (1996). "Mixed formulation of nonlinear beam finite element." Computers and Structures **58**: 71-83.

Spacone, E., Filippou, F. C., et al. (1996). "Fiber beam-column model for nonlinear analysis of R/C frames. Part I: Formulation." Earthquake Engineering and Structure Dynamics **25**(7): 711-742.

Zienkiewicz, O. C. and Taylor, R. L. (1989). The finite element method. London, McGraw-Hill.

NUMERICAL CALCULATION OF THE DEFLECTIONS OF COMPOSITE GIRDERS

Frank Böhme
Technische Universität Darmstadt, Department of Civil Engineering and Geodesy,
Petersenstrasse 12, 64287 Darmstadt, Germany
boehme@stahlbau-tu-darmstadt.de

Jörg Lange
Technische Universität Darmstadt, Department of Civil Engineering and Geodesy,
Petersenstrasse 12, 64287 Darmstadt, Germany
lange@stahlbau-tu-darmstadt.de

ABSTRACT

To get good results in the prediction of deflections of composite girders a good mechanical model is needed. For research 3-dimensional finite elements with non-linear geometry and material laws are a very good tool. Unfortunately they generate very much effort in the modeling of the structure which reduces their applicability to special problems that have to be solved by specially trained engineers. In our paper we will show how very good results can be obtained by using a combination of simple beam and shell elements. Special emphasis is laid on the modeling of the effective width, shear lag effects in the beam and the slab, creep and shrinkage, and the non-linear behavior of the steel element due to the cambering process.

First results show very well the influence of shear lag effects for short beams with thick concrete slab as they are mainly used in experimental evaluations. Comparisons with the test results of [Rieg 2006] prove the necessity of calculating deflections with a “deflection based effective width” in contrast to the current practice of using the same width for stress and deflection analyses.

1 STATE OF THE ART

A significant number of scientific publications on the load and deformation behavior of composite girders exist.

With the exception of [Menrath 1999] the authors used 1D Beam-Elements with or without consideration of slip between concrete slab and steel profile. For the calculation the effective width has to be set by the user. [Rieg 2006] and [Amadio et al. 2004] assess the variable effective width in case of composite girders with shallow height. Rieg developed a model which considers changes of the deformation-related effective width directly in moment-curvature-relations. In [Rieg 2006] the model was developed only for simple one span systems which are statically determined. In this presentation the effect will be analyzed using a 3-dimensional Finite Element Model to verify the dimension of the practical influence. The reason is that there is an additional effect - especially in case of short beams as they are used in experiments. Because of the high inner shear forces the influence of the shear deformation cannot be neglected. The fact that both effects are not independent worsens the situation.

2 3D FINITE ELEMENT MODEL

2.1 Aim of the 3D Calculation

The knowledge of the effective width is an important point for a realistic dimensioning of composite girders. Current standards distinguish between the effective width for dimensioning of cross-section and for the calculation of inner forces / deformation. The calculation should help to clarify the question whether the calculation with a constant effective width fulfils the practical accuracy criterions. For the special case of composite girders with shallow height Rieg assessed this problem with the help of experiments and calculations with 1D Beam-Elements.

An additional aim was to clarify the question whether approximate physical non-linear calculations using the physical linear program system RFEM lead to acceptable results.

2.2 Model Geometry

Fig. 1 shows the general 3D Finite Element System in RFEM. It was necessary to use shell elements (considering longitudinal and bending effects) to include the stress distribution over the provided concrete width. Because of the fact that RFEM does not allow a direct coupling of membrane and bending effects in the constitutive matrix D, the movement of the centre of gravity was considered directly by shell eccentricity.

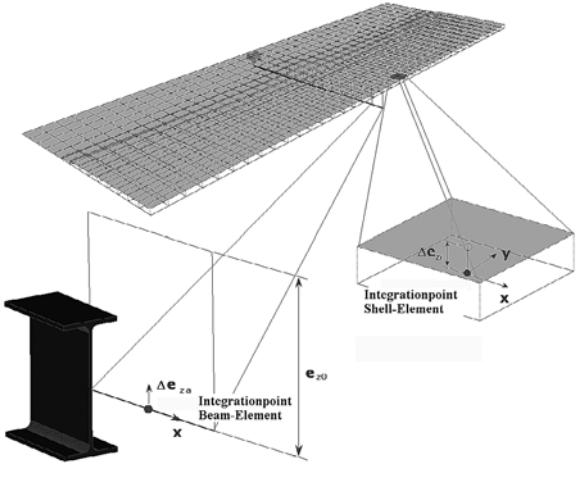


Fig. 1. Model Geometry in RFEM

The steel profile was modeled by eccentric beam-elements. The coupling between shell and beam elements was rigid. No slip between concrete slab and steel profile was considered.

2.3 External consideration of physical non-linear effects

Currently it is impossible to consider non-linear material behavior in the program system RFEM. Therefore the physical non-linear effects have to be considered in an alternative way by an external application. Important was the possibility to communicate between RFEM and the external application during the calculation. Because of these facts the application was programmed in MS Excel using the program language VBA.

The model was designed assuming that non-linear behavior of the material is decisive only in direction of the girder. Perpendicular to this linear elastic behavior is assumed. At the beginning the inner forces were calculated for the first load-increment with linear elastic material behavior. After finishing the calculation the external application reads the inner forces in the centre of the shell and beam elements. Unfortunately it is impossible to consider single FE-Elements. Because of that it was necessary to divide the concrete area in small elements (see Fig. 1). Now it was possible to change the constitutive matrix D for each of these small elements. In case of the beam elements the stiffness was influenced by changing the cross-section values (e.g. moment of inertia). As suggested in chapter 2.2 it is necessary that eccentricity could be changed for beam and shell elements. The general flow of the integration is shown in Fig. 2 and 3.

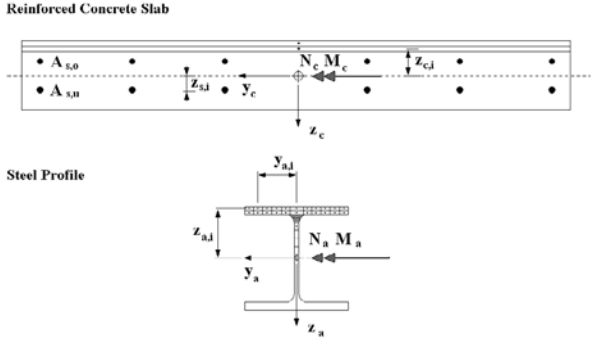


Fig. 2. Diagram of integration

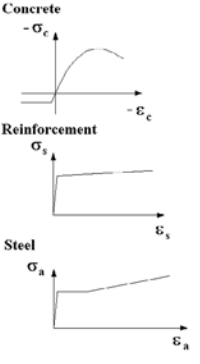


Fig. 3. Material laws

Because of the non-linear material behavior the calculation of the strain plane has to be solved with iterative methods. Due to the fast convergence close to the solution the Newton-Raphson-Method was used to find the decisive strain plane. In case of the reinforced concrete slab some modifications for better convergence were necessary. For one-axial bending with normal force the improvement of the strain vector can be calculated with equation (1).

$$\begin{vmatrix} \Delta N \\ \Delta M_y \end{vmatrix} = \begin{vmatrix} \dfrac{\delta N}{\delta \varepsilon_0} & \dfrac{\delta N}{\delta (1/r)_z} \\ \dfrac{\delta M_y}{\delta \varepsilon_0} & \dfrac{\delta M_y}{\delta (1/r)_z} \end{vmatrix} \begin{vmatrix} d\varepsilon_0 \\ d(1/r)_z \end{vmatrix} \tag{1}$$

If the residuum of the unbalanced inner forces and the change of the strain vector fall below a defined tolerance border the calculation would stop.

The single stiffness parts are calculated separately for the concrete slab and the steel profile summing over all fibers (see equation (2)-(4)).

$$EA = \sum_{i=1}^{n} EA_i \;,\; EAz = \sum_{i=1}^{n} EAz_i \;,\; EAzz = \sum_{i=1}^{n} EAzz_i \qquad (2)\text{-}(4)$$

To consider residual stresses in the steel profile it is necessary to divide the flange in y-direction too. That will lead to a double sum in equations (2)-(4). Because of the fact that interaction between longitudinal and bending effects is impossible in RFEM, the stiffness has to be recalculated in an independent form.

$$z_{cg} = EAz / EA \qquad (5)$$

The eccentricity between the concrete slab and the double symmetric steel profile can be calculated with the following equations.

$$e_{c,z} = z_{cg} \qquad (6)$$

$$e_{a,z} = \pm\left(h_c/2 + h_a/2\right) + z_{cg} \qquad (7)$$

The algebraic sign in equation (7) is positive if the steel profile is below the concrete slab and negative if the profile is above the concrete slab.

The final bending stiffness for the transfer in the finite element system RFEM has to be calculated with equation (8).

$$EI_y = EAzz - EA \cdot z_{cg}^{\,2} \qquad (8)$$

2.4 Calculation in RFEM and transfer of data

The COM-Interface allows a comfortable communication by external object-oriented program languages (e.g. Visual C++, Visual Fortran, VBA and others).

After the external application finishes the calculation of single stiffness parts, the results have to be transferred to RFEM. Results of the shell element will be recalculated directly in the single parts of the constitutive matrix D. The calculated stiffness of the steel profile has to be parted in material properties (Young's modulus) and cross-section properties (area, moment of inertia). In the introduced application the Young's modulus is set as a fixed value. The cross-section properties are calculated using the changes of stiffness.

The calculation continues for each load-increment until the change of deflections will not fall short of the defined tolerance border.

$$\Delta u_{\max,i-1} \cup \Delta u_{\max,i} \le Tol \qquad (9)$$

2.5 Recalculation of Experimental Studies

2.5.1 Description of the recalculated experiments

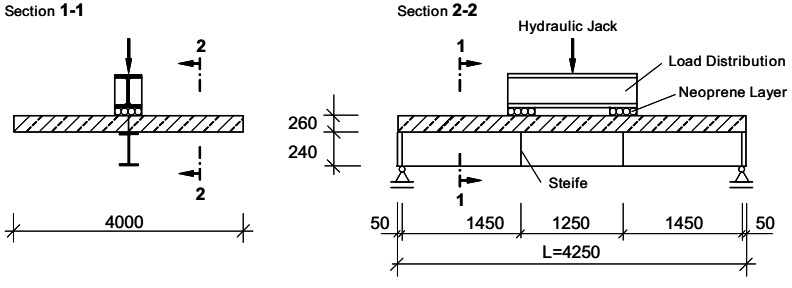


Fig. 4. Layout of experiments VT5 and VT6 from [Rieg 2006]

Fig. 4 shows the general layout of the experiments presented in [Rieg 2006]. A more detailed description of the single parts and the process of the experiments are given in [Rieg 2006].

The two tests VT5 and VT6 were recalculated with Stab2D-NL [Pfeiffer] and nonlin_rfem3 [Böhme 2007]. The precise material values are given in [Rieg 2006].

2.5.2 Analysis of the recalculated test

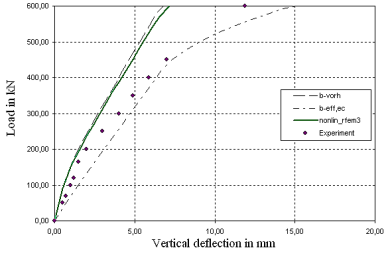


Fig. 5. Load-deflection relation VT5 shear rigid

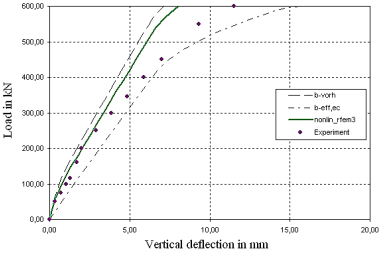


Fig. 6. Load-deflection relation VT6 shear rigid

All the experiments were calculated with a constant effective width. To get an upper limit the real width of the concrete slab was used (b_{vorh}). For the lower limit the effective width according to [ENV 1994-1-1:02.1994] was set ($b_{eff,ec}$). Residual stresses were neglected for the calculations in this publication.

The load-deflection relation calculated with [Pfeiffer] is shown in Fig. 5 and 6. In addition the experimental values are represented in the graph. Both experiments were calculated using RFEM3 and the external application nonlin_rfem3 [Böhme 2007]. It is remarkable that the results of the 3D calculation are very close to the 1D calculation if the real width is set as effective width. A consequence of this is that the specifications in the current standards (e.g. ENV 1994-1-1:02.1994 and EN 1994-1-1:2005) lead to conservative results in the calculation of deflections. Especially in case of thick concrete slabs with large contribution to the cross section stiffness the values of [ENV 1994-1-1:02.1994] seems to be too small. This was also noticed by [Rieg 2006]. In Fig. 5 and 6 the curve of the experimental data leads to the suggestion that only the bending stiffness that is reduced by cracking leads to convergence with the 1D calculation using the effective width according to [ENV 1994-1-1:02.1994]. But this is only one effect in case of short experimental girders. The shear force is not longer negligible small and this leads to an additional deflection which increases the total deformation. This raises the problem of calculating the shear stiffness of the composite girder. In some publications (e.g. [Hamme 1997, Rieg 2006]) the whole shear force was assigned to the web of the steel profile. This assumption affords an upper value of the deformation. Actually the shear stiffness is composed out of the steel profile and concrete slab contribution.

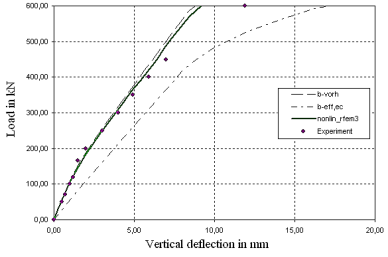


Fig. 7. Load-deflection relation VT5 shear flexible

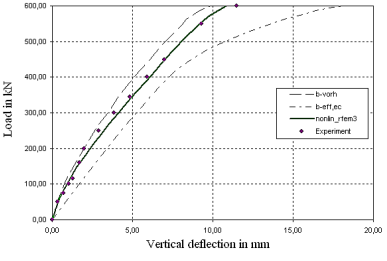


Fig. 8. Load-deflection relation VT6 shear flexible

For VT5 (Fig. 7) a simplified calculation under consideration of shear deflection is done in the way that 50 % of the shear force is assigned to the steel profile. But this does not consider that during load increasing a change of the shear stiffness will occur. It may be expected that the shear stiffness decreases while the load is increased (cracking in concrete slab). This effect was considered in recalculation of VT6 in the line of a non-constant ratio of the shear force in the steel profile. As long as the concrete is nearly un-cracked the part of the shear force in the web of the steel profile is relatively low. With beginning of the cracking a rearrangement from concrete slab to the steel profile occurs. In numerical calculations this would be considered as enhancement of the percentage part of the shear force in the steel profile (Fig. 8).

3 1D FINITE ELEMENT MODEL

3.1 Generally

One of the huge disadvantages of 3 dimensional Finite Element models is the difficulties in geometrical and physical correct input of the assessed structure. Usually a complex 3 dimensional material model for concrete, steel and reinforcement has to be considered to get realistic results. Many boundary conditions have to be defined which influence iterative solver and convergence behavior. To get realistic results detailed information of one, two and three dimensional material behavior is needed. Such information exists only in some case of experiments. Additionally the input of the geometrical model (e.g. element type, contact areas) requires a specialist in Finite Element Theory.

In case of framework models the results are better comprehensible. There is only the question if the reduction of one dimensional beam models might describe the load-deflection behavior of composite girders as detailed as necessary.

3.2 Theoretical Background

To control the more general applicability a 1D Finite Element Program for one span beams with free definable support properties was developed. The application was created using Excel XP with VBA 6.0 to generate output data in a simple and good interpretable way.

Because of the method in 3D calculation, shear deflections was considered externally. This leads to the idea to use a shear-stiff Bernoulli-Element. The kinematics was developed for consideration of geometrical and physical non-linear behavior.

3.2.1 Kinematical relations

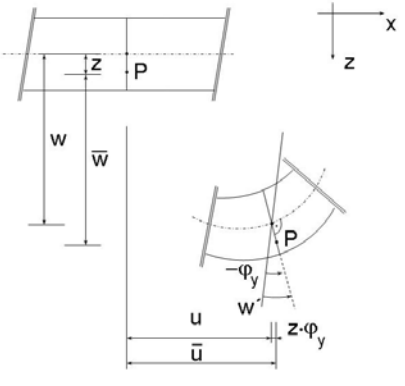


Fig. 9. Deformed beam element

With Fig. 9 the kinematical relations can be formulated.

$$\overline{w}(x,z) = w \tag{10}$$

$$\overline{u}(x,z) = u - z \cdot \varphi_y \tag{11}$$

To consider the geometrical nonlinear behavior the Green-Lagrange Strain Tensor was used. In Equation (12) the Green-Lagrange Stain Tensor is given in component form.

$$\varepsilon_{ij} = \left(u_{i,j} + u_{i,j} + u_{m,i} \cdot u_{m,i}\right) \tag{12}$$

The square term of equation (12) stands for the geometrical non-linear character of the Green-Lagrange Stain Tensor.

After solving and some mathematical transforming the strain might be written in the following form.

$$\varepsilon_x = \varepsilon_0 + z \cdot \left(\frac{1}{r}\right)_z \tag{13}$$

with

$$\varepsilon_0 = u' + \frac{1}{2} \cdot w'^2 \tag{14}$$

$$\left(\frac{1}{r}\right)_z = w'' \tag{15}$$

3.2.2 Constitutive Relation

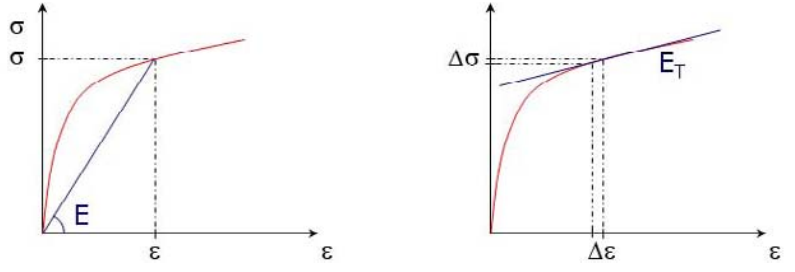


Fig. 10. Secant and Tangential Modulus of Elasticity for non-linear materials

In case of non-linear material behavior the linear relation between stress and strain is disappearing. One sequel of this is that the center of gravity is not constant for one cross-section any longer. Now the stress state influences the position directly. To avoid the recalculation of the center of gravity in each point the formulation was related to a free axis. The correlation between the strain vector **E** and the stress vector **S** is defined by the constitutive matrix **D**. For the case of one axial bending with normal force the relation is:

$$S = D \cdot E$$
$$\Delta S = D_T \cdot \Delta E \tag{16}$$

In case of the calculation of absolute stress values **S** the secant value of Young's modulus has to be used. When the stress increment **ΔS** is calculated the tangential Young's modulus has to be used.

The integration of the constitutive matrix **D** was done numerical with the fiber model shown in Fig. 11.

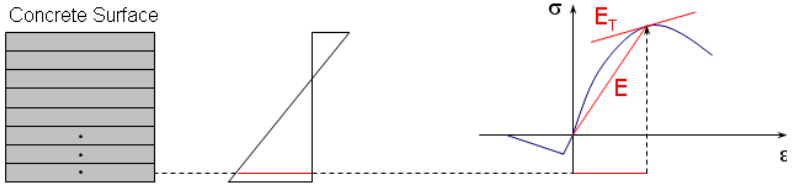


Fig. 11. Schematical representation of the integration by fiber model

3.2.3 Formulation of Equilibrium

The equilibrium was formulated with the minimum of the potential energy.

$$\pi = \pi_i + \pi_a = \frac{1}{2}\int_l E^T D\, E\, dS - \int_l u^T q\, dS \tag{17}$$

The first part characterizes the inner potential and the second integral gives the outer potential. To get a minimum of the potential it is necessary to vary it (1.Variation). This leads to the equilibrium formulation of equation (18).

$$\delta\pi = g(\delta u, u) = \int_l \delta E^T D\, E\, dS - \int_l \delta u^T q\, dS \tag{18}$$

For the Finite Element formulation it is necessary to derive the linearization of the weak form of equilibrium (18). This might be written in the following way:

$$g(\delta u^{k+1}, u^{k+1}) = g(\delta u^k, u^k) + DG(\delta u^k, u^k) \cdot \Delta u^{k+1} \tag{19}$$

The second term of equation is the second variation of equation (17) and leads directly to the solving algorithm.

$$DG(\delta u, u) \cdot \Delta u = \int_l \delta E^T \Delta S\, ds + \int_l (\Delta \delta E^T S) ds \tag{20}$$

3.2.4 Finite Element Formulation

According to the isoparametric concept, the kinematical variables (u, w) were interpolated using shape functions $N_i(\xi)$ where $\xi \in$ (-1,1). For longitudinal deformation a linear approach and for the deflection perpendicular to the element axis a cubic approach was used.

The deflections and virtual deflections can be written in the form:

$$u = N \cdot v \tag{20}$$

$$\delta u = N \cdot \delta v \tag{21}$$

For the virtual strain the equation can be written in the following way:

$$\delta\varepsilon = B \cdot \delta v$$

$$\delta\varepsilon = \left(B_L + B_{NL}\right) \cdot \delta v \tag{22}$$

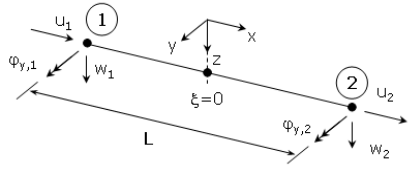


Fig. 12. Degrees of freedom of the element

Like shown in equation (22) the **B** matrix can be divided in a geometrical linear and non-linear part.

If equations (20 -22) are set in the first variation of the potential energy (equation (18)) the equilibrium formulation of inner and outer force is:

$$f_u\left(\delta u^k, u^k\right) = f_i\left(\delta u^k, u^k\right) - f_a\left(\delta u^k\right) = \delta v_L \left(\int_l B^T S \, ds - \int_l N^T q \, ds \right) \tag{23}$$

The part f_u characterizes the unbalanced part of the load, which has to be neglected. To calculate the deflection increment the second variation of the potential can be written in the form:

$$\delta v^T K_T(v) \Delta v = \delta v_L \int_l \left(B^T D \, BS + G\right) ds \, \Delta v \tag{24}$$

The integration was done in 3 Gauss points numerically. The iteration process is shown in Fig. 14.

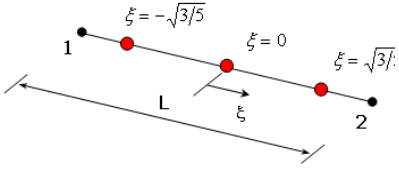


Fig. 13. Integration in 3 Gauss points of one Element

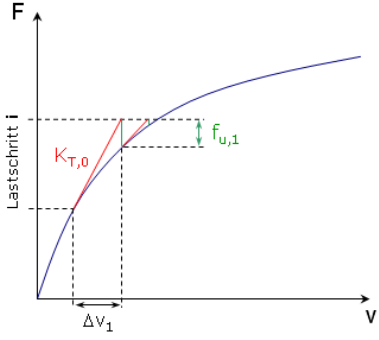


Fig. 14. Iterative solving process with Newton-Raphson Method

3.3 Variation of the Effective width

To consider the effect of a variation of the effective width for each element an analytical effective width was calculated.

As input data the linear elastic effective width for the membrane state $b_{eff,M}$ and the bending state $b_{eff,B}$ have to be defined. The values were calculated before with linear elastic 3D Model for each of the 16 elements (restriction MS Excel).

The actual used effective width was interpolated from this input data in each integration point.

$$b_{eff,calc} = \eta \cdot b_{eff,B} + (1-\eta) \cdot b_{eff,M} \tag{25}$$

The weighting factor η was calculated with the relation of the tension force in the concrete slab (reinforcement and tension stiffening) to the membrane part of the tension force of the steel profile.

$$\eta = \frac{F_{ct} + F_{s1}}{F_a + F_{ct} + F_{s1}} \tag{26}$$

In areas with tension in the concrete slab and compression in the steel profile the effective width of membrane state was used.

3.4 Recalculation of Experimental Studies

The description of the experimental data was given in chapter 2.5.1.

In addition to the analyses with a 3D model the results of a 1D model as shown in chapter 3 are given in Fig. 15 and 16 for shear flexible behavior. The additional part of the shear deflection was calculated in the same way as in the 3D Model.

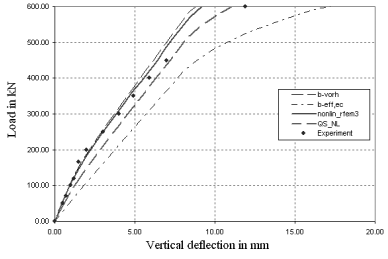


Fig. 15. Load-deflection relation VT5 shear flexible

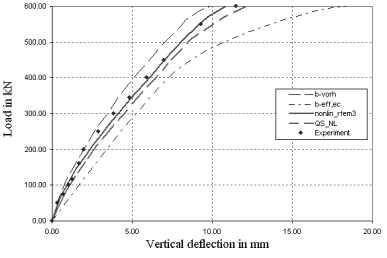


Fig. 16. Load-deflection relation VT6 shear flexible

In VT5 the calculation with the one 1D Elements leads to slightly bigger deformations than the 3 Dimensional FEM Model. It seems that the boundaries of the effective width are a bit conservative. The calculation of VT6 is very close to the 3D FEM model, confirming the approach of the developed 1D Finite Element Model.

4 SUMMARY AND ACKNOWLEDGMENT

With regard to further studies a physical non-linear 1D Model, based on a Finite Element Method will be preferred, due to the fact that physical non-linear calculation of member elements are better comprehensible and much faster than non-linear 3D FEM Models.

The approaches for realistic estimation of shear deformations seem to be an important point for the numerical recalculation of experiments on beams with short spans. This effect should be included directly in FEM concept. Furthermore the element restrictions (numbers) should be solved by external stand alone applications.

REFERENCES

Amadio et al. 2004, *Experimental evaluation of effective width in steel–concrete composite beams*, Journal of Constructional Steel Research 60, 199–220, 2004

Hamme 1997, *Zur Gebrauchstauglichkeit von Verbundträgern mit Stahltrapezprofilen*, Ph.D. Thesis, Bochum, 1997

Hannawald 2006, *Zur physikalisch nichtlinearen Analyse von Verbund-Stabtragwerken unter quasi-statischer Lastbeanspruchung*, Ph.D. Thesis, Dresden, 2006

Lukas 1999, *Theorie und Anwendung nichtlinearer Algorithmen auf Stahlverbundtragwerke*, Ph.D. Thesis, Kaiserslautern, 1999

Menrath 1999, *Numerische Simulation des nichtlinearen Tragverhaltens von Stahlverbundträger*, Ph.D. Thesis, Stuttgart, 1999

Rieg 2006, *Verformungsbezogene mittragende Breite niedriger Verbundträger*, Ph.D. Thesis, Stuttgart, 2006

Schanzenbach 1988, *Zum Einfluss von Dübelnachgiebigkeit und Unterverdübelung auf das Tragverhalten von Verbunddurchlaufträgern im Hoch- und Industriebau*, Ph.D. Thesis, Kaiserslautern, 1988

SOFTWARE

RFEM Version 3.03.1005 with RF-COM Interface, Finite Element Software, Dlubal Ingenieursoftware GmbH

Pfeiffer, Stab2D-NL and INCA2, Analysis of reinforced Concrete Structures, http://www.u-pfeiffer.de/, free for non-commercial usage

Böhme 2007, nonlin_rfem3, external application for RFEM3 to calculate composite girders under consideration of material non-linearity, Excel Application

Böhme 2008, QS_NL, 1D FEM calculation of composite girders under consideration of material and geometrical non-linearity's, Excel Application

STANDARDS

ENV 1994-1-1:02.1994, *Bemessung und Konstruktion von Verbundtragwerken aus Stahl und Beton, Teil 1-1: Allgemeine Bemessungsregeln*, Bemessungsregeln für den Hochbau, Beuth Verlag, 1994

EN 1994-1-1:2005, *Design of composite steel and concrete structures – Part 1-1: General rules and rules for buildings*, Beuth Verlag, 2005

A Mixed-Finite Element Approach for Performance-Based Design of Rectangular Concrete-Filled Steel Tube (RCFT) Frames

Cenk Tort
Staff Engineer
Skidmore, Owings, & Merrill LLP
Chicago, USA
cenk.tort@som.com

Jerome F. Hajjar
Professor
University of Illinois at Urbana-Champaign
Urbana, USA
jfhajjar@uiuc.edu

ABSTRACT

A comprehensive computational model to simulate the nonlinear seismic response of composite frames with rectangular concrete-filled steel tube (RCFT) beam-columns and steel girders and braces is presented in this work. A three-dimensional fiber-based distributed plasticity mixed finite element formulation is introduced. The finite element formulation of RCFT beam-columns was derived with separate translational degrees-of-freedoms (DOFs) defined for the concrete core and the steel tube to simulate the slip deformation that is typical for composite members. Cyclic constitutive relations were derived accounting for the interactions taking place between the steel tube and the concrete core including slip, confinement, and local buckling. A representative composite frame structure was analyzed under a suite of ground motion records and the demand imposed on the RCFT columns was quantified. A methodology based on the use of the damage function equations was proposed to evaluate the performance of RCFT members under seismic loads.

INTRODUCTION

Integrating the favorable characteristics of the steel tube and the concrete core in RCFTs provides an efficient design alternative for beam-columns in the lateral load resistance systems of low, moderate, and high rise structures. The advantages offered by RCFTs such as high strength, stiffness, ductility, and economy have long been recognized, which resulted in extensive experimental and computational research studies toward understanding their behavior and developing reliable design methods. The experimental database studies by [Aho and Leon 1997], [Tort and Hajjar 2004], [Kim 2005], and [Gourley et al. 2008] show that there exist significant experimental data in the literature that indicate the superior performance of RCFTs under static and quasi-static loading conditions. In recent experimental work on large scale multistory RCFT frames under dynamic loading, RCFT frames were found to exhibit a stable response under earthquake loading with large energy dissipation and low strength deterioration [Tsai et al. 2003], [Herrera 2005]. The information gained from this prior research on composite beam-columns resulted in the development of several new provisions in the 2005 AISC *Specification for*

Structural Steel Buildings [AISC 2005]. Leon et al. [2007] utilized the available experimental research to update the design of composite columns, where the composite interaction is taken into account more accurately through improved quantification of the concrete contribution to the flexural response. This approach helps to reduce the over-conservatism introduced by neglecting the contribution of concrete [Choi et al., 2006]. In addition, Leon et al. [2007] also recommended increasing the slenderness limit of the steel tube against local buckling. Despite the increasing number of available experimental tests and the improvement in the worldwide design specifications for non-seismic applications, guidance on earthquake resistance design of composite CFT columns still remains limited.

The quantification of seismic demand and capacity is vital in developing performance-based seismic resistant design methodologies. This is often achieved through nonlinear time-history analysis of frame structures for a range of hazard levels [Yun et al., 2002]. In this research study, a 3D beam finite element model was derived based on mixed finite element principles (building on prior research on displacement-based formulations [Schiller and Hajjar 1998]) to conduct nonlinear time history analysis of frame structures with RCFT members and steel columns. The model was calibrated and verified with respect to experimental specimens available in the literature. A representative RCFT frame was then analyzed under a suite of earthquake records and a methodology was proposed to evaluate the performance of the RCFT members utilizing the nonlinear time history analysis results.

FINITE ELEMENT FORMULATION

Mixed finite element principles were adopted to derive a 3D 18 DOF RCFT beam-column element. The 6 DOFs added to the standard 12 DOF beam formulation were defined to quantify the differential movement between the steel tube and the concrete core [Hajjar et al. 1998] A two-field form of mixed finite element methods was used, where displacements and internal element forces are interpolated independently of each other. The element stiffness and internal forces were derived by considering only the deformational DOFs. The effect of rigid body modes was included in the formulation while calculating the quantities with respect to the global coordinates. Cubic Hermitian shape functions were defined for the transverse displacements while the axial deformations were represented via quadratic shape functions. The bending moment distribution was assumed to be linear. However, the second-order moments due to the P-δ effect, which are obtained by multiplying the axial forces and transverse deformations, were added to the linear distribution of bending moments [Alemdar and White 2005]. Interpolating the element internal forces allows satisfying the element equilibrium exactly, which helps achieving good coarse mesh accuracy compared to displacement–based formulations. In addition, it alleviates the numerical problems in displacement-based formulations due to concrete cracking while ensuring element equilibrium [Schiller and Hajjar 1998]. The mixed finite element formulation also allowed quantification of slip based on the difference in the assumed axial deformation fields for the concrete core and the steel tube.

The derivation of the formulation starts by expressing the equilibrium, compatibility, and cross-section equilibrium equations in their integral forms as given in Equations 1, 2 and 3. An Updated-Lagrangian formulation was utilized, where all the variables

were defined with respect to the last converged configuration. In Equations 1 through 3, both superscripts and subscripts located to the left of a symbol refer to two configurations of interest. C1 represents the last converged state and C2 is the current state of the element body. A left superscript designates the configuration in which the quantity is measured. If a left superscript is omitted, the quantity is considered as an increment between C1 and C2 or between the current and the next C2 configuration (e.g., during an iteration process). The terms in bold represent either matrix or vector quantities while the non-bold terms represent scalar quantities. The equilibrium equation defines the balance between the work done by externally applied loads and internal forces. A distinct feature of the formulation with respect to the composite action is that the effect of slip was accounted for by adding an additional term to the equilibrium equation for the slip deformation. The compatibility equation represents the balance between cross-section strains ($\hat{\boldsymbol{d}}$, e.g., axial strain, curvature) from the interpolated deformation fields and the cross-section strains ($\boldsymbol{d}$) corresponding to the interpolated forces obtained by multiplying the inverse of the cross-section rigidity by the interpolated cross-section forces. The kinematic relations assumed in this formulation were a Green-Lagrange axial strain measure and curvatures being the second derivative of the transverse deformations. The torsional response was taken as linear. The axial strains and curvatures were defined separately for the steel tube and the concrete as part of the slip formulation. The cross-section equilibrium defines the balance between the interpolated cross-section forces ($\boldsymbol{D}$, e.g., axial forces, bending moment) and the cross-section forces ($\boldsymbol{D}_{\Sigma}$) obtained from integration of stresses of the steel and concrete material fibers over the RCFT cross-section. The cross-sectional forces defined for the RCFT members were axial forces and bending moments introduced for the steel tube and the concrete core separately.

$$\int_0^{{}^1L} \delta {}_1^2\hat{\boldsymbol{d}}^T \times {}_1^2\boldsymbol{D} \times d^1x + \int_0^{{}^1L} \delta {}_1^2\hat{\boldsymbol{d}}_{sc}^T \times {}_1^2D_{sc} \times d^1I +$$

$$\int_{{}^1V^c} {}^1\rho^c \times {}_1^2\ddot{\boldsymbol{u}}^c \times \delta {}_1^2\boldsymbol{u}^c \times d^1V^c + \int_{{}^1V^s} {}^1\rho^s \times {}_1^2\ddot{\boldsymbol{u}}^s \times \delta {}_1^2\boldsymbol{u}^s \times d^1V^s + \tag{1}$$

$$\int_{{}^1V^c} {}^1\mu^c \times {}_1^2\dot{\boldsymbol{u}}^c \times \delta {}_1^2\boldsymbol{u}^c \times d^1V^c + \int_{{}^1V^s} {}^1\mu^s \times {}_1^2\dot{\boldsymbol{u}}^s \times \delta {}_1^2\boldsymbol{u}^s \times d^1V^s - \delta {}_1^2\boldsymbol{q}^T \times {}_1^2\boldsymbol{Q}_{ext} = 0$$

$$\int_0^{{}^1L} \delta {}_1^2\boldsymbol{D}^T \times ({}_1\hat{\boldsymbol{d}} - {}_1\boldsymbol{d}) \times d^1x = 0 \tag{2}$$

$${}_1^2\boldsymbol{D}_{\Sigma} - {}_1^2\boldsymbol{D} = 0 \tag{3}$$

Linearization of Equations 1 through 3 with respect to their state variables results in the expressions for the element stiffness, mass, damping and internal forces. A non-iterative internal force calculation procedure was adopted, where the unbalances of the equilibrium and compatibility equations are eliminated through Newton-Raphson iterations conducted at the global level. The details of the formulation with the internal force calculation procedure can be found in [Tort and Hajjar 2007]. [Tort and Hajjar 2007] also developed a steel beam-column element following mixed finite element formulation to model girders in a composite frame.

MATERIAL CONSTITUTIVE RELATIONS

In the current formulation, the finite element was divided into several cross-sections along its length. Each cross-section was further subdivided into individual steel and concrete fibers, which were associated with a constitutive relation. Throughout the analysis, the nonlinearity occurring at the steel and concrete fibers was monitored and the nonlinearity was first passed to the cross-section level and then to the element level as the area and length integrations are performed, respectively while calculating the internal element forces. The fiber-based distributed plasticity approach to model nonlinearity was preferred compared to concentrated plasticity formulations since detailed information on the damage state of the structure (e.g., concrete cracking, steel yielding) can be obtained, which is important in performance-based design for defining the performance objectives.

The concrete constitutive relations were adopted from [Chang and Mander 1994]. Three different curves were introduced defining the stress-strain response as shown in Figure 1. The envelope curves represented the backbones of the hysteretic response in tension and compression. The compression envelope curve was derived based on experimental data available in the literature on axially loaded RCFT column tests. It was assumed that the concrete core in compression behaves as plain concrete until the attainment of the peak strength. A linear strength degradation region with a slope of K_c initiates once the peak strength is reached. The extent of strength degradation depends on the degree of confinement provided by the steel tube and at high strain levels, the compressive stresses do not drop below a constant value defined as f_{rc}. Therefore, the slope of the strength degradation region and the constant stress level were correlated to the slenderness parameter of the steel tube as shown Equation 4. The envelope curve in tension was taken as similar to plain concrete. The connecting curves define the relation for strain histories ranging between the envelope curves. The transition curves provide the rules to shift from one connecting to the other going in opposite direction. The model by [Chang and Mander 1994] was augmented for RCFT members by defining new rules to increase its comprehensiveness under random cyclic loading histories. For example, as shown in Figure 1, a new rule was introduced if unloading takes place between the latest unloading point and the target point on the envelope curve.

(4a) $$K_c = -332.75 \times R \times f_c^{'} + 9.60 \times f_c^{'}$$

(4b) $$\frac{f_{rc}}{f'_c} = 0.32 \times R^{-0.5}$$

where: $R = \frac{D}{t} \times \sqrt{\frac{f_y}{E_s}} \times \frac{f_c^{'}}{f_y}$

The constitutive model of the steel tube was adopted from [Mizuno et al. 1991], where the stress-strain response was traced based on evolution of loading and bounding surfaces. The loading surface defines the initiation of inelasticity while the bounding surface represents the limiting stress state attained by the material. The model accounts for typical characteristics of the steel such as Bauschinger effect, strain hardening, decreasing elastic zone etc. However, it was originally developed for hot-rolled steel. Since the focus of this research is study is on RCFT members

with cold-formed steel sections, the model by [Mizuno et al. 1991] was modified to account for typical features of cold-formed tubes and also the composite interaction between the steel tube and the concrete core. Residual strain values were calibrated for the corner and flat regions of the steel tube from coupon tests available in the literature so that the premature yielding of the cold-formed steel tube can be captured. The calibrated values of initial strains were obtained as 0.0006 and 0.0004, for the corner and flat regions, respectively. In addition, the yield strength of the steel tube was assumed to be larger in the corner regions due to the effect cold forming and the ratio of the yield strength of the steel tube in corner regions to that of the flat regions was taken as 1.1 based on the coupon test results in the literature. The strain level at initiation of local buckling (ε_{lbf}) was calibrated from axially loaded RCFT column tests. Following local buckling, a linear strength degradation was assumed until a constant stress region is attained. The slope of the strength degradation region (K_s) and the constant stress level at high strains (f_{rs}) shown in Figure 2 were also calibrated with respect to axially loaded RCFT column tests from the literature. In addition, it was assumed that local buckling also causes a reduction in the radius of the bounding surface ($\overline{\kappa}$) from its initial value ($\overline{\kappa}_o$). The rate of reduction of the radius of the bounding surface (γ_{cc}) was correlated to the plastic work done (W^p) during cyclic loading and it is calibrated to the cyclically loaded tests of RCFT members. Key equations of the steel model are given below:

(5a) $$\frac{\varepsilon_{lbf}}{\varepsilon_y} = 3.14 \times \left(\frac{D}{t}\sqrt{\frac{f_y}{E_s}}\right)^{-1.48}$$

(5b)
$$K_s = 0, \left(D/t\right) \times \left(f_y / E_s\right) \le 0.08$$
$$K_s = -644304.39 \times \left(D/t\right) \times \left(f_y / E_s\right) + 51544.35, \left(D/t\right) \times \left(f_y / E_s\right) \ge 0.08$$

(5c)
$$\frac{f_{rs}}{f_y} = 1 \text{ for } \left(D/t\right) \times \left(f_y / E_s\right) \le 0.08$$
$$\frac{f_{rs}}{f_y} = -7.31 \times \left(D/t\right) \times \left(f_y / E_s\right) + 1.58 \text{ for} \left(D/t\right) \times \left(f_y / E_s\right) \ge 0.08$$

(5d) $$\overline{\kappa} = \left(-\gamma_{cc} \times W^p + 1\right) \times \overline{\kappa}_o$$

(5d) $$\gamma_{cc} = 0.0345 \qquad (D/t) \times \sqrt{f_y / E_s} < 0.92$$

(5e) $$\gamma_{cc} = 0.196 \times (D/t) \times \sqrt{f_y / E_s} - 0.146 \quad 0.92 \le (D/t) \times \sqrt{f_y / E_s} \le 1.45$$

(5f) $$\gamma_{cc} = 0.138$$

VERIFICATION STUDIES OF THE MODEL

The finite element formulation along with constitutive relations were implemented in [OpenSees 2001]. The accuracy of the formulation and the constitutive relations were tested against numerous specimens from the literature. The RCFT beam-column specimens by [Cederwall et al. 1991] and by [Varma et al. 2002] were analyzed under eccentrically applied axial load and constant axial load and increasing bending moment, respectively. For both of the specimens, 2 elements per member with 4 integration points were defined and a displacement-controlled solution algorithm was applied. The capacity of the specimens exhibited excellent correlation with computational results as shown in Figure 3. The failure of Specimen 1 by [Cederwall et al. 1991] was governed by flexural buckling, which is accurately captured by the analysis with close agreement with the pre-peak and post-peak regions of the load-deformation response. Specimen BC32-80-40 by [Varma et al. 2002] underwent significant softening response due to the large axial load ratio and the softening behavior as a result of concrete crushing and local buckling of the steel tube, which is also captured successfully by the proposed model. The second verification study involved analysis of RCFT members under quasi-static cyclic loading, where the RCFT member, CIIS3-3 by [Tomii and Sakino 1979] and SR6A4C by [Inai et al. 2004], are tested under constant axial load and cyclic shear loading, putting the members into double curvature. The computational model and experimental results showed excellent agreement as can be seen in Figure 4. The shear and moment capacity, and the loading and unloading stiffnesses were estimated by the computational model accurately.

PERFORMANCE-BASED DESIGN METHODOLOGY

A typical 3-story RCFT structure was analyzed under a suite of far field earthquake records. The seismic response parameters were documented and a methodology to evaluate the performance of the RCFT members was presented based on the prior work by [Tort and Hajjar 2004].

The RCFT structure was assumed to be located in Los Angeles and NEHRP Site Class D soil conditions were considered. As defined in Figure 5, the structure has 4 bays of RCFT columns and steel girders [LaFore and Hajjar 2005]. The mass at each story was assumed to be lumped at the joint locations and 2% damping ratio was assumed. A total of 12 far-field ground motion records were used and they were selected to minimize the discrepancy between the spectral acceleration values at the first mode period of the structure with respect to design spectrum and the median spectrum so that large scale factors are avoided and a more accurate estimation of the nonlinear response with reduced biases can be obtained [Tort and Hajjar 2007]. The scaling of the records was done based on the first mode period of the structure.

The nonlinear time-history analysis of the structure for the selected earthquake records was conducted following the application of the factored gravity loading. Table 1 summarizes the seismic response parameters obtained from the analysis results for 2%50 hazard level. The mean (μ) and 84 percentile ($\mu+\sigma$) values of

maximum and minimum of roof drift (Δ_r) as a percentage of the height of the structure (h_r), inter-story drift ratio (IDR), and story shear (V_r) are shown. The maximum and minimum of values of IDR and V_r were found to be in the 1st story of the structure. It can be seen in Table 1 that the μ and $\mu + \sigma$ values of the seismic response parameters do not significantly deviate from each other, indicating nearly uniform demand levels over the selected earthquake records.

Tort and Hajjar [2004] proposed a deformation-based damage function ($\hat{D}$) to quantify the damage experienced by RCFT members as given in Equation 6. The value of the damage functions indicating the occurrence of local damage states (e.g., concrete cracking, concrete crushing, steel yielding, etc.) were obtained from the available experiments in the literature and equations were derived in terms of geometric and material properties of RCFT members to estimate those damage function values. Tort and Hajjar [2004] also correlated the ranges of the damage function to the performance-levels e.g., Immediate Occupancy, Life Safety etc.

(6) $$\hat{D} = \frac{d_{curr}}{d_o}$$

The time-history analysis results were utilized to quantify the deformation-based damage function values of the RCFT columns of the studied frame structure. First, static push-over analysis of the structure was conducted, where d_o of the columns were obtained from the chord rotation (R) vs. moment response extracted for each RCFT column from the push-over analysis, where R was calculated as the ratio of lateral displacement to the element length. d_o was assumed to be the R value attained when the stiffness of the RCFT column becomes 10% of its initial value. As shown In Figure 6, moment vs. R response from the static push-over analysis and time history analysis are superimposed for the windward interior column at the first story of the frame. d_{curr} was obtained from the time history analysis results as the mean maximum R experienced during the ground motions. $\hat{D}$ was calculated as the ratio of d_{curr} and d_o. It was found that mean $\hat{D}$ values ranges from 0.41 to 1.04. [Tort and Hajjar 2004] recommended that $\hat{D}$ smaller than 0.8 corresponds to the Immediate Occupancy performance level while $\hat{D}$ values from 0.8 to 1.5 represent Life Safety performance level. Therefore, the RCFT columns of the structure are either in the Life Safety or Immediate Occupancy Performance level, indicating that the RCFT columns behaved satisfactorily. Figure 7 illustrates the damage distribution over the material fibers at a typical RCFT cross-section located in the first story of the frame. The damage levels were detected based on the material constitutive relations of the steel and concrete fibers. It can be seen that the majority of the fibers experienced steel yielding and concrete cracking. However, the high damage levels of concrete crushing and local buckling were not distributed significantly over the cross-section, indicating the good performance of the RCFT frame consistent with its performance evaluations based on the associated damage function equations.

CONCLUSION

A mixed finite element formulation for RCFT beam-columns in composite frames was shown to be an efficient computational approach to simulate the nonlinear response of RCFT columns. The formulation was successful in estimating the nonlinear curvature fields with strong accuracy using a coarse mesh (one to four elements per member) as compared to more common displacement-based formulations. The constitutive relations accounted accurately for the key composite characteristics observed for RCFT members in the experiments. The mixed finite element formulation was also successfully used for performance-based design and demand assessment of composite RCFT structures.

ACKNOWLEDGEMENT

This work was supported by the National Science Foundation under Grant No. CMS-0084848 and by the University of Minnesota. Supercomputing resources were provided by the Minnesota Supercomputing Institute. The authors would like to thank Mr. Matthew Parkolap for his assistance with this research, Drs. Douglas Goode, Roberto Leon, Amit Varma, Shosuke Morino, and Jun Kawaguchi for providing experimental data, Drs. Donald White and Bulent Nedim Alemdar for providing the details of their computational studies, and Dr. Frank McKenna for his assistance with OpenSEES software development. Any opinions, findings, and conclusions or recommendations expressed in this material are those of the authors and do not necessarily reflect the views of the sponsors.

Table 1. Seismic Response Parameters

Response Parameter	μ (max)	$\mu+\sigma$ (max)	μ (min)	$\mu+\sigma$ (min)
Δ_r / h_r	1.18	1.30	-1.03	-0.90
IDR	1.06	1.19	-1.28	-1.11
V_s	3560	3818	-3841	-3624

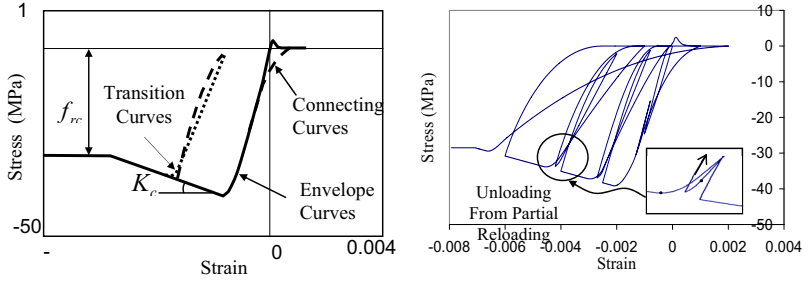


Fig. 1– Stress-Strain Response of the Concrete

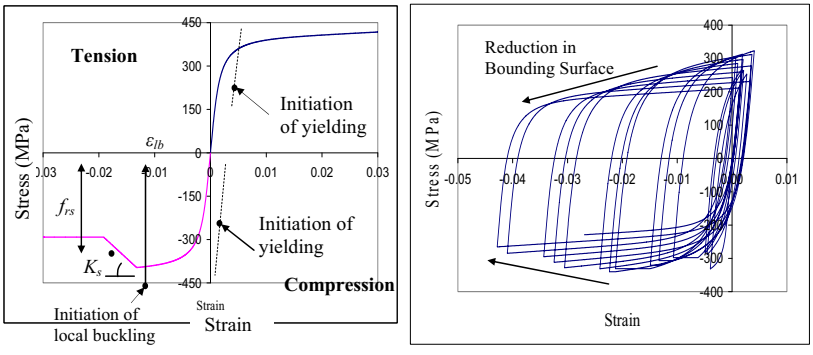


Fig. 2–Stress-Strain Response of the Steel Tube

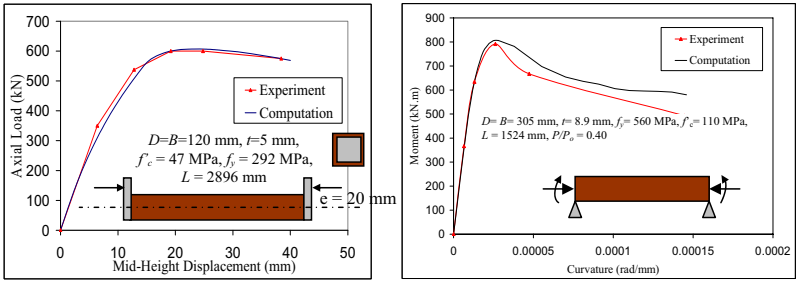


Fig. 3–Comparison of Computational and Experimental Results for RCFT Beam-Columns Specimen 1 [Cederwall et al. 1991], BC32-80-40 [Varma et al. 2002],

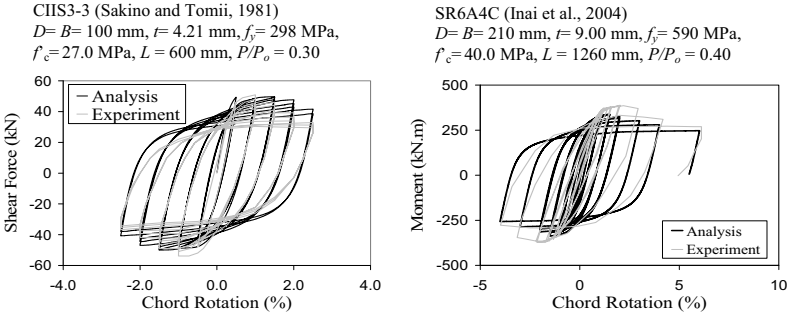


Fig. 4–Comparison of Computational and Experimental Results for Cyclically-Loaded RCFT Beam-Columns CIIS3-3 [Sakino and Tomii 1981], SR6A4C [Inai et al. 2004]

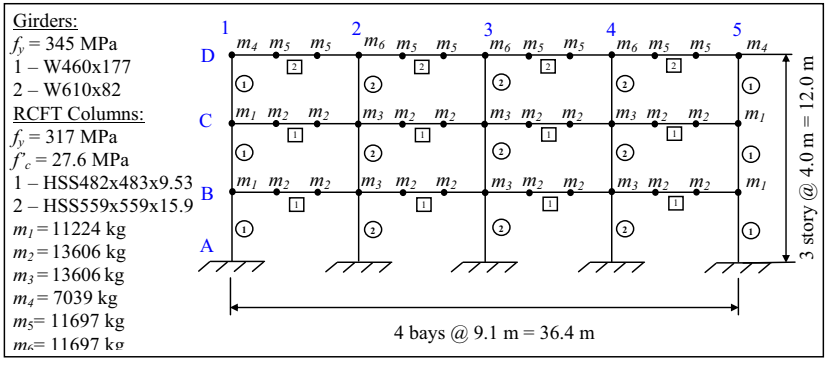


Fig. 5–RCFT Frame Configuration [LaFore and Hajjar 2005]

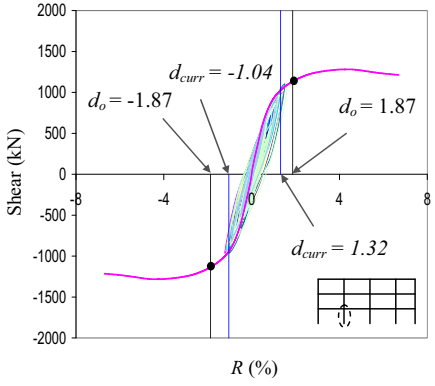


Fig. 6–Damage Function Calculation Based on Time-History Analysis

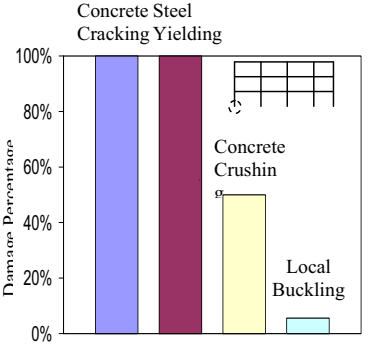


Fig. 7 – Damage Distribution at a Typical RCFT Cross-Section

NOTATION

B – width of the steel tube
$\boldsymbol{C}$ – consistent damping matrix
$\hat{\boldsymbol{d}}$ – cross-section strains from interpolation of corotational nodal displacements
$\boldsymbol{d}$ –cross-section strains corresponding to the cross-section forces
d_{curr} – the deflection of the structural member at the point in the loading history at which damage is being assessed
d_o –deflection attained when peak load is reached
$\hat{d}_{sc}$ –slip layer deformation

D –depth of the steel tube
$\hat{D}$ –deformation-based damage function
$\boldsymbol{D}$ – cross-section forces from interpolation corotational nodal forces
$\boldsymbol{D}_{\Sigma}$ – cross-section forces from numerical integration of material fiber stresses over the cross-sections
D_{sc} –force transferred between steel tube and concrete core per unit area
dx – infinitesimal length of the finite element
E_s - modulus of elasticity of the steel tube
f_y – yield strength of the steel tube
f'_c –compressive strength of concrete
f_{rc} –stress level at the constant stress region of the concrete model
f_{rs} –stress level at the constant stress region of the steel model
h_r –roof height of the building
IDR –interstory drift ratio
L – length of the RCFT member
t –thickness of the steel tube
$\boldsymbol{u}^c$ – displacement field of the concrete core
$\boldsymbol{u}^s$ –displacement field of the steel tube
$\dot{\boldsymbol{u}}^c$ – velocity field of the concrete core
$\dot{\boldsymbol{u}}^s$ – velocity field of the steel tube
$\ddot{\boldsymbol{u}}^c$ –acceleration field of the concrete core
$\ddot{\boldsymbol{u}}^s$ – acceleration field of the steel tube
$\boldsymbol{q}$ –nodal displacements
$\boldsymbol{Q}_{ext}$ –nodal forces
P – axial load
P_o – cross-section strength of RCFT cross-section
R –chord rotation
V^c – volume of the concrete core
V^s – volume of the steel tube
V_s – base shear
W^p – the plastic work done
ε_{lbf} – the strain level at initiation of local buckling
Δ_r – roof drift
ρ^c – unit weight of the concrete core
ρ^s – unit weight of the steel tube
μ – mean
μ^c – viscosity parameter of the concrete core
μ^s –viscosity parameter of the steel tube
γ_{cc} –rate of reduction of the radius of the bounding surface
$\bar{\kappa}$ – bounding surface radius
$\bar{\kappa}_o$ – initial bounding surface radius

REFERENCES

Aho, M. and Leon, R. T. (1997). “A Database for Encased and Concrete-Filled Columns,” Report No. 97-01, School of Civil and Environmental Engineering, Georgia Institute of Technology, Atlanta, Georgia.

Alemdar, B. N. and White, D. W. (2005). "Displacement, Flexibility, and Mixed Beam-Column Finite Element Formulations for Distributed Plasticity Analysis," *Journal of Structural Engineering*, ASCE, Vol. 131, No. 12, pp. 1811-1819.

American Institute of Steel Construction (AISC) (2005). *Specification for Structural Steel Buildings*, AISC, Chicago, IL.

Cederwall, K., Engstrom, B., and Grauers, M. (1990). ”High-Strength Concrete Used in Composite Columns,” Second International Symposium on Utilization of High Strength Concrete, W. T. (ed.), Berkeley, California, May 1990, pp. 195-214.

Chang, G. A. and Mander, J. B. (1994). “Seismic Energy Based Fatigue Damage Analysis of Bridge Columns: Part I – Evaluation of Seismic Capacity,” Report No. NCEER-94-0006, National Center for Earthquake Engineering Research, State University of New York, Buffalo, New York.

Choi, Y. H., Foutch, D. A., LaFave, J. M. (2006). “New Approach to AISC P–M Interaction Curve for Square Concrete Filled Tube (CFT) Beam–Columns,” *Engineering Structuures*, Vol. 28, No. 11, pp. 1586-1598.

Gourley, B. C., Tort, C., Denavit, M. D., Schiller, P. H., and Hajjar, J. F. (2008). “A Synopsis of Studies of the Monotonic and Cyclic Behavior of Concrete-Filled Steel Tube Beam-Columns,” Report No. UILU-ENG-2008-1802, Newmark Structural Laboratory Report Series (ISSN 1940-9826), Department of Civil and Environmental Engineering, University of Illinois at Urbana-Champaign, Urbana, Illinois, April.

Hajjar, J. F., Schiller, P. H., and Molodan, A. (1998). “A Distributed Plasticity Model for Concrete-Filled Steel Tube Beam-Columns with Interlayer Slip,” *Engineering Structures*, Vol. 20, No. 8, pp. 663-676.

Herrera, R. (2005). “Seismic Behavior of Concrete-Filled Tube Column-Wide Flange Beam Frames,” Ph.D. dissertation, Department of Civil and Environmental Engineering, Lehigh University, Bethlehem, Pennsylvania, September.

Inai, E., Mukai, A., Kai, M., Tokinoya, H., Fukumoto, T.,and and Mori, K. (2004). “Behavior of Concrete-Filled Tube Beam-Columns,” Journal of Structural Engineering, Vol. 130, No. 2, pp. 189-202.

Kim, D.K. (2005), “A Database for Composite Columns,” M.S. Thesis, Graduate School, The Georgia Institute of Technology, Atlanta, Georgia.

LaFore, S. and Hajjar, J. F. (2005). “Design of Concrete-Filled Steel Tube Frames for Assessment Under Seismic Loading,” Report No. ST-05-1, Department of Civil Engineering, University of Minnesota, Minneapolis, Minnesota, May.

Leon, R. T., Kim, D. K., and Hajjar, J. F. (2007), “Limit State Response of Composite Columns and Beam-Columns Part 1: Formulation of Design Provisions for the 2005 AISC Specification,” *Engineering Journal*, AISC, Vol. 44, No. 4, Fourth Quarter, pp. 341-358.

Mizuno, E., Shen, C., Tanaka, Y., and Usami, T. (1991). "A Uniaxial Stress-Strain Model for Structural Steels under Cyclic Loading," *Stability and Ductility of Steel Structures Steels under Cyclic Loading*, Fukumoto, Y. and Lee, G. C. (eds.), CRC Press, Boca Raton, Florida, pp. 37-48.

OpenSEES (2001). "Open System for Earthquake Engineering Simulation," Pacific Earthquake Engineering Research Center, University of California at Berkeley, Berkeley, California.

Sakino, K. and Tomii, M. (1981). "Hysteretic Behavior of Concrete Filled Square Steel Tubular Beam-Columns Failed in Flexure," *Transactions of the Japan Concrete Institute*, Vol. 3, pp. 439-446.

Schiller, P. H. and Hajjar, J. F. (1998). "A Distributed Plasticity Formulation for Three-Dimensional Rectangular Concrete-Filled Steel Tube Beam-Columns and Composite Frames," Report No. ST-96-5, Department of Civil Engineering, University of Minnesota, Minneapolis, Minnesota.

Tort, C. and Hajjar, J. F. (2004). "Damage Assessment of Rectangular Concrete-Filled Steel Tubes for Performance-Based Design," *Earthquake Spectra*, Vol. 20, No. 4, pp. 1317-1348.

Tort, C. and Hajjar, J. F. (2007). "Reliability-Based Performance-Based Design of Rectangular Concrete-Filled Steel Tube (RCFT) Members and Frames," Report No. ST-07-1, Department of Civil Engineering, University of Minnesota, Minneapolis, Minnesota.

Tsai, K. C., Weng, Y., Lin, M., Chen, C., Lai, J., and Hsiao, P. (2003). "Pseudo Dynamic Tests of a Full-Scale CFT/BRB Composite Frame: Displacement Based Seismic Design and Response Evaluations," International Workshop on Steel and Concrete Composite Construction (IWSCCC-2003), National Center for Research on Earthquake Engineering, Taipei, Taiwan, October 8-9, 2003, National Center for Research on Earthquake Engineering, Taipei, Taiwan, pp. 165-176.

Varma, A. H., Ricles, J. M., Sause, R., and Le-Wu, L. (2002). "Experimental Behavior of High Strength Square Concrete-Filled Steel Tube Beam-Columns," *Journal of Structural Engineering*, ASCE, Vol. 128, No. 3, pp. 309-318.

Yun, S., Hamburger, R. O., Cornell, C. A., and Foutch, D. A. (2002). "Seismic Performance Evaluation for Steel Moment Frames," *Journal of Structural Engineering*, ASCE, Vol. 128, No. 4, pp. 534-545.

MACRO-ELEMENTS FOR COMPOSITE BEAM-COLUMN CONNECTIONS

Uwe E. Dorka
University of Kassel
Kassel, Germany
uwe.dorka@uni-kassel.de

Saenboon Amorntipsakul
University of Kassel
Kassel, Germany
seanboon@uni-kassel.de

ABSTRACT

The behavior of macro-elements can be described by a set of orthogonal boundary states, each consisting of displacements and forces associated by a one-dimensional constitutive relationship. Combinations thereof are described by surface models in the force space with flow rules. Local models describing the mechanics inside the element are not restricted in detail and are needed only once to develop the constitutive relationships, surfaces models and flow rules: The problem is scaled in a mechanically consistent manner without loosing information or accuracy.

A macro-element for a plane beam-column connection has five orthogonal states: Two bending, two normal and one shear state, if linear boundary displacements are assumed. These “beam-type” boundaries enable the connection to any beam element. Thus, it can be included in regular frame analysis greatly improving its accuracy. To demonstrate this powerful scaling technique, typical component models for beam-column connections are used to develop a “beam-type” macro element.

INTRODUCTION

In modern composite frame analysis and design, beam-column connection regions play a major role. They influence the distribution of internal forces by virtue of their stiffness and often define design limits by virtue of their components’ ultimate load bearing capacity. Therefore, component models (see Figure 1) have been developed to be incorporated in the analysis and as a background to international codes like Eurocode 4 [EC4; Huber and Tschemmernegg 1997]. Unfortunately, they are rather unwieldy in applications with a multitude of parameters to be specified and changed during the design process.

Additionally, these models may not capture important local failure states with good accuracy (like weld ruptures or plastic plate buckling) or neglect complete deformation and stress states like the vertical action due to the forces and moments in the columns. To incorporate such effects, sophisticated local FE-models must be used which cannot be incorporated in a regular practical frame analysis in any reasonable fashion. To solve this dilemma and at the same time allow easy application in a practical environment, the macro-element approach is introduced in this paper for the modeling of beam-column connection regions.

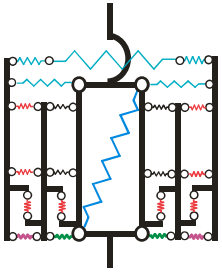


Fig. 1 – Component model for a composite beam-column joint consisting of an assemblage of nonlinear springs, modified from [Huber and Tschemmernegg, 1997]

MACRO ELEMENTS TO MODEL BEAM-COLUMN CONNECTIONS

Macro-elements, as understood in this paper, were first introduced by Dorka [Dorka 1991] and are discrete domains with their mechanical behavior described by independent orthogonal force and displacement states on their boundaries. All possible boundary forces and displacements can be represented by linear combinations of these orthogonal states. Fig.2 gives examples for a plane triangle, tetrahedron and plane quadrilateral where these states are only defined by nodal states and no assumption is required for the distribution over the boundaries.

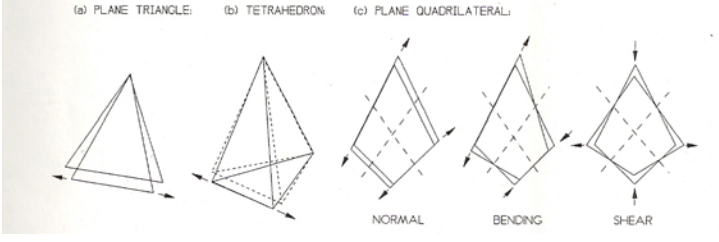


Fig. 2 – Macro stresses and strains of a plane triangle, tetrahedron and plane quadrilateral [Dorka 1991]

An orthogonal state consists of a unique and independent boundary displacement and force pattern each determined by one variable termed *macro stress* and *macro strain*. From these, the basic equations governing a discrete system can be written:

(1) $\varepsilon_k = B_k u_k$ macro strain – nodal displacement relation

(2) $\sigma_k = D_k \varepsilon_k$ macro constitutive relation

(3) $f_k = B_k^T \sigma_k$ nodal force - macro stress relation

(4) $K_k = B_k^T D_k B_k$ macro element stiffness matrix

for the kth element.

Eq. (3) and (4) can be derived from the stationarity of the potential of a discrete system by utilizing Eq. (1) and (2). The matrix B_k contains the transformations from nodal displacements to macro strains and is a geometric property of the element.

D_k contains an element constitutive law which depends on the size and internal mechanics of the element and must be described for each instant. Because of orthogonality, a macro stress does work only on its associated macro strain. Thus, each macro stress is associated to its macro strain by a one-dimensional constitutive relationship which may be non-linear (compare Figure 3).

Combinations of these orthogonal states lead to combined constitutive relationships which are best described by surface models in the macro stress space (interaction surfaces in force space) together with appropriate flow rules, similar to the approach found in multi-dimensional material laws. The dimension of these models depends on the number of orthogonal states required to represent the boundary states with the desired resolution.

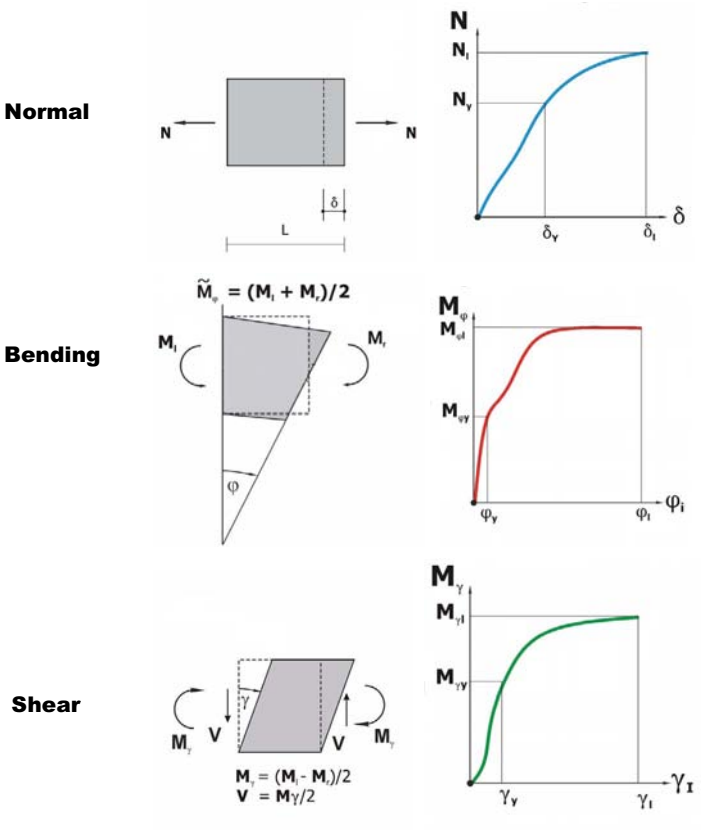


Fig. 3 – Orthogonal boundary states for a beam-type macro element with associated one-dimensional constitutive relations (illustration)

The domain of such a macro-element must be filled with a local model or its constitutive relationships may be determined through tests applying the orthogonal states alone and in combination. In modeling, there is no restriction regarding its level of detailing and no internal continuity is required. Dorka for example used a detailed FE-model and the exact solution for the stress distribution around a circular hole to present the solution for a plane triangular macro-element with a circular hole at its centre [Dorka 1991].

The local models are needed to determine the constitutive relationships, surface laws and flow rules. They are not used when the macro-element is implemented in an analysis. They may be used again after an analysis by applying selected states to analyze internal stresses or failures. Thus, the problem is scaled with considerable reduction of implementation and numerical effort on the higher scale, but without loss of accuracy and the capacity of retrieving local behavior at any point of the analysis.

In Figure 2, a linear displacement distribution is indicated for the quadrilateral leading to definitions like “normal”, “bending” and “shear” for the orthogonal states in analogy to boundary states of beams. These “beam-like” boundaries are very useful when it comes to defining macro elements for beam-column intersections, since these can be directly coupled to regular beam elements. An illustration of a beam-type macro element with its constitutive relations is given in Figure 3.

Here, the anti-metric moment and associated shear forces form the shear state and the symmetric moment the bending state. A model with yield and failure surface (two-surface model) may be useful in combination with a kinematic hardening law when it comes to non-linear cyclic loading.

The stiffness matrix for a “beam-type” macro element is given by [Dorka 1988]:

$$K \times u = k_s \times \begin{pmatrix} 1 & \frac{l}{2} & -1 & \frac{l}{2} \\ \frac{l}{2} & \left(\frac{l^2}{4}+\frac{k_b}{k_s}\right) & -\frac{l}{2} & \left(\frac{l^2}{4}-\frac{k_b}{k_s}\right) \\ -1 & -\frac{l}{2} & 1 & -\frac{l}{2} \\ \frac{l}{2} & \left(\frac{l^2}{4}-\frac{k_b}{k_s}\right) & -\frac{l}{2} & \left(\frac{l^2}{4}+\frac{k_b}{k_s}\right) \end{pmatrix} \times \begin{pmatrix} v_i \\ \phi_i \\ v_{i+1} \\ \phi_{i+1} \end{pmatrix} \tag{5}$$

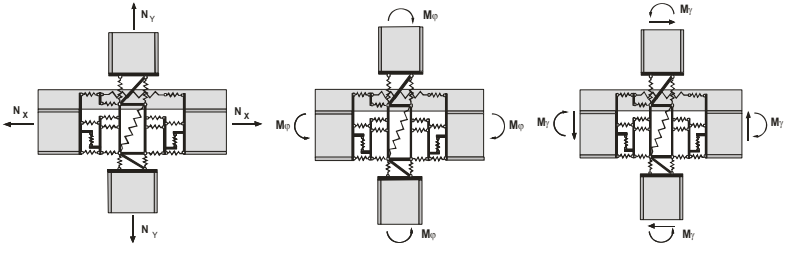


Fig. 4 – Possible modification of component model from Figure 1 to represent a plane beam-column connection as macro element with orthogonal boundary states: 2 normal, 2 bending and 1 shear state

With l - length of element and shear (k_s) and bending (k_b) stiffness are derived from the relevant macro stress – strain curves ($M_\gamma - \gamma$ and $M_\varphi - \varphi$ curves, compare Figure 3). v_i and ϕ_i are the transverse displacement and rotation of the i^{th} boundary. The normal state matrix is self evident and therefore not given here.

This macro element can be easily extended to a plane type by adding two more states: a normal and a bending state for the vertical direction. Thus, five independent states and their interactions describe the full state of a region that may represent a plane beam-column connection in a composite frame (Figure 4).

AN ILLUSTRATIVE EXAMPLE

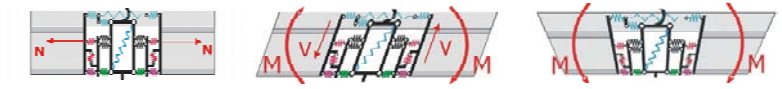


Fig. 5 – Orthogonal beam-type boundary states applied to the component model of Figure 1

To demonstrate this powerful technique, the beam-column connection model of Figure 1 is used to develop the properties of an equivalent macro model. Figure 5 shows the orthogonal states applied. Since this model does not yield any results for the vertical direction, only the horizontal states are analyzed here. Each spring has been fitted with an elasto-plastic law to include nonlinear component behavior in this illustration.

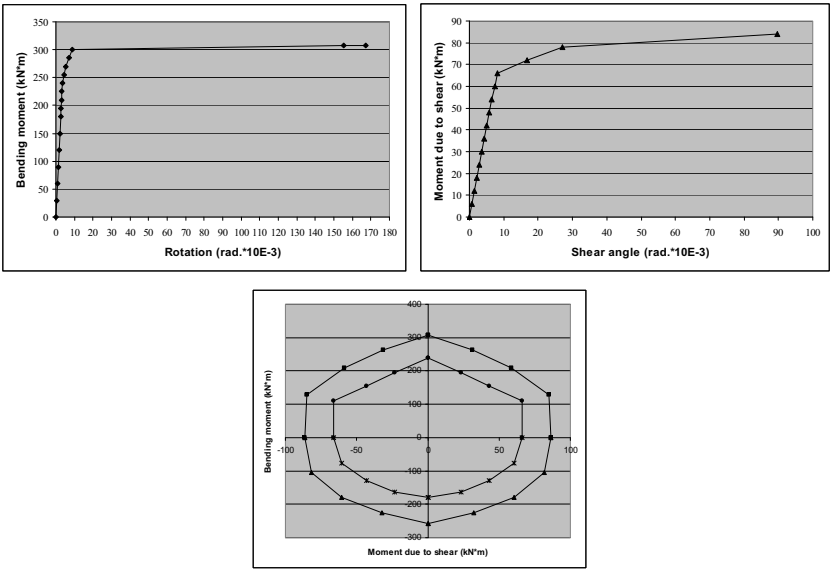


Fig. 6 – Constitutive relationship with two-surface model for macro bending and shear resulting from the analysis of the component model from Figure 1.

Figure 6 shows the resulting one-dimensional constitutive relationships for the macro bending and shear state. From these, macro bending and shear stiffness can be identified and used in the stiffness matrix (Eq. 5). Also, yield and failure levels can be identified. Analyzing combinations of macro strains in this fashion yields a two-surface representation in the force space (Figure 6).

DISCUSSION OF RESULTS

Using this macro element in a regular frame analysis will provide a good representation of the stiffness of this particular beam-column intersection and allow easy checking against yield and failure. Local yield or failure may be checked by retrieving the relevant boundary state from the frame analysis and applying it to the local model.

It should be noted here that such local models can be made “generic” to represent a certain class of beam-column intersections. In such cases, a “practical” set of parameters (like standardized materials, bolts and geometries from a CAD file etc.) can be established as input to a program that automatically calculates the constitutive relations and surfaces and sends the input to a frame analysis program that contains a “beam-type” macro element.

Of course, an extension should be made to include the vertical direction (this is straight forward for the component model as indicated in Figure 4) but since this approach poses no limit on the local model, more sophisticated FE-models should be developed to improve the quality of the input to the frame analysis and the subsequent limit state checks.

In case of cyclic loading, the analysis of the local model is more involved since a flow rule must be formulated that describes the changing of the surfaces. In general, an isotropic (change of surface size) as well as kinematic (movement of surface) rule must be established allowing not only for the representation of cyclic hardening (kinematic rule) but also of degradation (shrinkage of surfaces).

SUMMARY AND CONCLUSIONS

Using the macro element approach, the problem of including local behavior in beam-column intersections in a global analysis is scaled in a mechanically consistent manner without loss of accuracy. The approach is illustrated using a component model which was developed as a basis for Eurocode 4.

Since this model has severe limitations, more appropriate detailed FE models should be developed which can be made “generic” allowing for the use of “practical” parameter sets to describe a beam-column intersection. More sophisticated models will not increase the effort during frame analysis and design but lead to more realistic results and are open to new knowledge when it becomes available without changing the basic concept or practical application in a program.

With a set of macro-constitutive laws developed by such local models and appropriately parameterized, this will greatly simplify the modeling of composite beam-column connections in daily design practice and at the same time increase its accuracy.

The extension to cyclic behavior is straight forwards but requires a more involved analysis of the local model and the introduction of flow rules into the surface models.

REFERENCES

U.E. Dorka, 1988: “A contribution to the identification and simplified analysis of structures with hysteresis evolution” (in German), TWM Report No. 88-10, Ruhr-Universität Bochum.

U.E. Dorka, 1991: “System analysis by discrete elements” Proceedings Asian Pacific Conference on Computational Mechanics, Editors Y.K. Cheung, J.H.W. Lee, A.Y.T. Leung, Balkema, 1257-1262

EC4: Eurocode 4

G. Huber and F. Tschemmernegg, 1997: “Connections – Component method” (in German), Proceedings of the Symposium on Composite Structures, University of Kaiserslautern, Publishers H. Bode, W. Ramm, H. Wittek, H. Schmackpfeffer

GENERIC FINITE ELEMENT MODEL FOR MECHANICALLY CONSITENT SCALING OF COMPOSITE BEAM-COLUMN JOINT WITH WELDED CONNECTION

Saenboon Amorntipsakul
University of Kassel
Kassel, Germany
saenboon@uni-kassel.de

Uwe E. Dorka
University of Kassel
Kassel, Germany
uwe.dorka@uni-kassel.de

ABSTRACT

A generic finite element model for composite beam-column joints with welded connections has been developed using current state-of-the-art local modeling. Using mechanically consistent scaling, it provides the constitutive relationship for a plane rectangular macro element with beam-type boundaries that can be used in high-accuracy frame analysis. Global geometric variables allow the generation of specific FE models for each instance of a joint. Using assumptions typical for most composite frames, the constitutive relationship of the macro element can be represented by bi-linear laws for the macro bending and shear states which are then coupled by a two-surface law with yield and failure surfaces. This is demonstrated in an example.

INTRODUCTION

Economical composite connections are typically semi-rigid. This must be accounted for in the frame analysis and when designing them [EC4]. Using finite elements, intricate local geometries and non-linear local behaviour of a connection region can be modeled today with good accuracy [i.e. Ahmed, Li and Nethercot, 1996], but such local models require thousands of degrees of freedom so they cannot be used directly in practical frame analysis.

Therefore, simple component models [i.e. Huber and Tschemmernegg 1997] have been proposed and are the basis for modern codes [EC4]. With a focus on transferring the beam action through the connection region, they model the gross behavior of each component as simple non-linear spring that participates in the beam bending and shear transfer (like bolts or endplates). A detailed representation of important local states like weld strains or plastic shear buckles in the web plate is not possible. They also largely neglect the interaction with the column actions and they are very tedious to use in a practical environment.

To fully utilize the accuracy and resolution of local FE modeling in higher frame analysis, a scaling method is needed that correctly maps the performance of a detailed FE model on a macro element that represents the whole connection region during the frame analysis. If this scaling is mechanically consistent, it allows downscaling from the macro element level to the FE model to recover detailed local behavior at any time during the higher level analysis. Such scaling has been developed in general by Dorka [Dorka, 1988, 1991]. It allows not only mechanically

consistent scaling of local analytical solutions (i.e. for stress concentrations around openings), but also of highly non-linear local FE models. Recently, this has been applied to plane composite connection regions and a mechanically consistent scaling for a rectangular macro element has been formulated in this context [Dorka and Amorntipsakul 2008].

A detailed non-linear FE model for composite beam-column joints with welded connections has been developed as a possible application for this macro element and is presented in this paper. It utilizes the current state of the art in local modeling of such regions, e.g. for the steel parts and cracked concrete with reinforcement. To make it easily applicable for a range of similar joints, the FE mesh is generated automatically from macro properties such as steel cross sections for beams and columns, concrete slab thickness, reinforcement ratio, etc.

SCALING OF PLANE COMPOSITE BEAM-COLUMN JOINTS

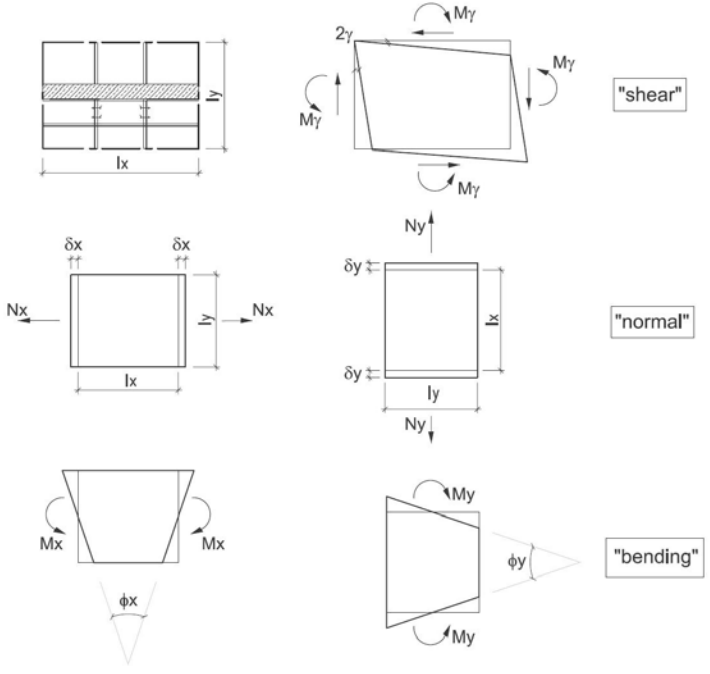


Fig. 1 – Five orthogonal beam-type boundary states of a plane rectangular macro-element that may represent a composite beam-column joint in a frame analysis

Because a rectangular macro element for mechanically consistent scaling of plane beam column joints in composite frames is discussed elsewhere [Dorka and Amorntipsakul 2008], only its main features are presented here. Mechanically consistent scaling requires the definition of a complete set of orthogonal boundary states for a macroscopic region. Each orthogonal state consists of a set of boundary

deformations and associated forces which are represented by only two variables: a deformation and a force. They are given for a plane rectangular macro element in Fig. 1 where 5 states suffice to present all possible states by linear combination. Being of *beam-type*, there are 2 *normal* states defined by δ_x-N_x and δ_y-N_y, 2 *bending* states defined by Φ_x-M_x and Φ_y-M_y and a *shear* state defined by γ-M_γ.

Orthogonality stipulates that the work done on each state is independent of the work done on the other states. Thus, single non-linear force – deformation relationships exist in general for each state (i.e. δ_x-N_x, δ_y-N_y, Φ_x-M_x, Φ_y-M_y and γ-M_γ for a plane rectangular element) with their coupling described in the force space. This type of constitutive relation can be represented by single functions for each force – displacement relationship and a surface model in the force space. Thus a five-dimensional surface law is required in general to fully describe the constitutive relationship for a plane rectangular macro element.

Certain assumptions may be made for typical beam-column connection regions leading to reduced dimensions of the surface law:

1. Normal forces in the beams may have little effect on the connection region and thus may be neglected in the law. This reduces the law to 4 dimensions.
2. The two bending states Φ_x-M_x and Φ_y-M_y hardly use the same components in the joint region for their load transfer, so we may consider them without interaction. This leads to two independent 3-dimensional laws: N_y-M_γ-M_x and N_y-M_γ-M_y.
3. We may use bi-linear approximations for the Φ_x-M_x, Φ_y-M_y and γ-M_γ relationships which gives us two-surface models for M_γ-M_x and M_γ-M_y, each with a yield and a failure surface that depends on N_y (Fig. 2).

With these assumptions, we have two 3-dimensional interactions which can be represented in plane by using the column normal force N_y as a curve parameter (Fig. 2).

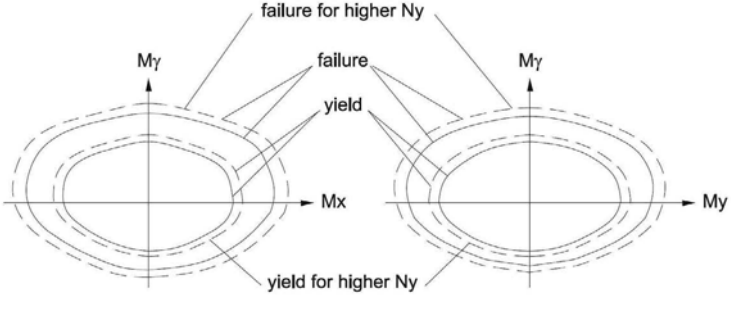


Fig. 2 – Illustration of a simplified 2-surface model for a composite beam column joint

Often, a *weak beam - strong column* concept is used so that the column remains elastic and a M_γ-M_y interaction is not required. Therefore, we concentrate on the M_γ-M_x interaction (beam bending and shear) for the local FE model in this paper.

GENERIC LOCAL MODEL FOR A WELDED COMPOSITE JOINT

The state of the art of detailed FE modeling of composite joints can be recovered for example from the work of the group around Nethercot [i.e. Ahmed, Li and Nethercot, 1996].

Leon at al. [Leon, Hajjar and Shield 1996] analyzed the failures of welds connecting the bottom flanges of steel beams to steel columns in composite joints during the Northridge earthquake with a detailed FE model. They used linear 3-dimensional brick elements in ABAQUS to model steel and concrete parts and the welds in detail. They considered the composite connection between steel beam and concrete slab to be rigid. We made the same assumption because slip is usually prevented by the column flanges.

We also used brick elements to model the steel beams, the steel columns, the concrete slab and welds. Bilinear material laws were defined for these elements representing the non-linear behavior of steel (tension and compression) and concrete (compression only). For welds, higher yield strengths are chosen to account for brittle behavior due to re-crystallization and local residual stresses after welding.

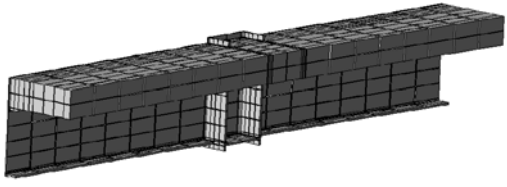


Fig. 3 – Generic FE-model for composite joints with welded connections (for reasons of symmetry, only one half is modeled)

To model cracks in the slab, bi-linear contact springs were implemented at regular intervals. These intervals were pre-determined by the prediction formulae for crack spacing in reinforced concrete proposed by Piyasena et al. [Piyasena, Loo and Fragomeni 2004]. When cracks are closed and under compression, these elements have stiffness equal to the slab. When cracks are open and under tension, the stiffness accounts for the reinforcement and tension-stiffening effect of the surrounding concrete. The parameters for this element are derived from the idealized load deformation behavior of a concrete member in tension with stabilized crack formation [Hanswille 1996]. The deformation of these springs are directly related to the strains in the reinforcement and thus to reinforcement failure.

Shear studs were not modeled here because it is assumed that slip is prevented by the column flanges. When shear springs are introduced between slab and beam, this model can accommodate them, if the need arises.

The model was implemented using the programming environment SLang [Bucher et al., 2005]. It was made generic by introducing a set of geometric parameters from which a detailed geometry is calculated. This drastically reduces the input effort for a user who should not have to develop a new FE model for each instance. The group of input parameters is shown in Table 1, i.e. geometric properties of the beam, column and concrete slab must be provided. In Figure 4, two examples of resulting FE models (one with a stocky and one with a slim geometry) are shown demonstrating a broad spectrum of application for this generic model.

Table 1 – Geometric input to generic model creating the two examples of Fig. 4

Geometric Parameters	Example 1 (mm)	Example 2 (mm)
Beam width	140	135
Beam depth	133	270
Flange thickness of beam	8.5	10.2
Web thickness of beam	5.5	6.6
Root radius of beam	12	15
Column width	160	200
Column depth	160	200
Flange thickness of column	13	15
Web thickness of column	8	9
Root radius of column	15	18
Leg size of welding	3	4
Concrete thickness	100	120
Concrete covering from top surface	25	60
Concrete covering from side surface	25	30
Effective width of slab	1500	600
Crack spacing	100	150

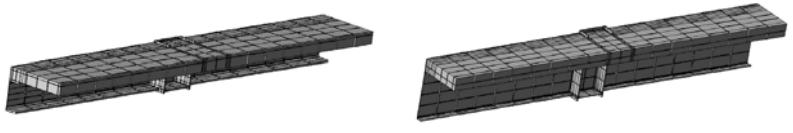


Fig. 4 – Two instances generated with the generic model: Slim on the left and stocky on the right

VALIDATION OF THE GENERIC MODEL

In detailed FE analysis, validated local models must be used in the first place. This refers to material models and components such as crack models etc. This has been done here.

The next validation step is the global model. It may be inferred that, if the local modelling is correct, the global model which only introduces different geometries may also be correct but this should be demonstrated at least for a typical case by a large scale experiment. We used a test carried out at the University of Kaiserslautern, Germany [Ramm and Elz 1996] for this purpose. Figure 5 shows the test setup.

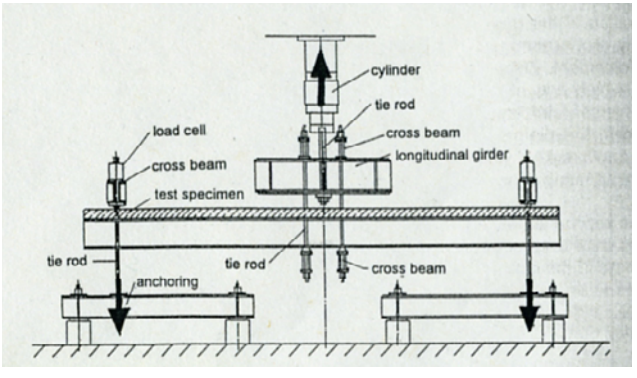


Fig. 5 – Test used for the validation of the generic model [Ramm and Elz 1996]

Figure 6 compares the moment - rotation curves generated by the model with the test results. They show that the stiffness of the connection region and the yield could be captured quite well. As expected, the initial stiffness before cracking is not captured because the crack model is based on an already stabilized crack formation.

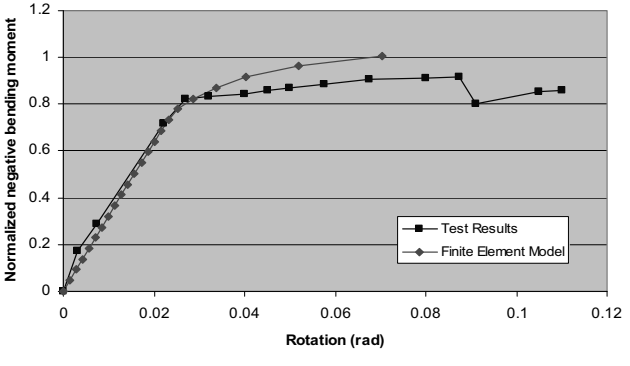


Fig. 6 – Bending moment - rotation curves of the generic model compared to test results

It was reported that the specimen failed by rupture of the reinforcement before the complete plastic state could be reached. This also occurred in the model although at a smaller rotation.

DEVELOPMENT OF CONSTITUTVE RELATION FOR A MACRO ELEMENT: AN ILLUSTRATIVE EXAMPLE

The loads corresponding to macro bending and shear and a number of their combinations were applied to a specific instance of the generic model with beam 254x102 UB25 and column 203x203 UC46. From this, Φ_x-M_x and γ-M_γ relationships (Fig.7) were obtained and evaluated for yield and rupture. Their initial and post-yield stiffness can be evaluated and used as stiffness coefficients in the respective matrix of the macro element.

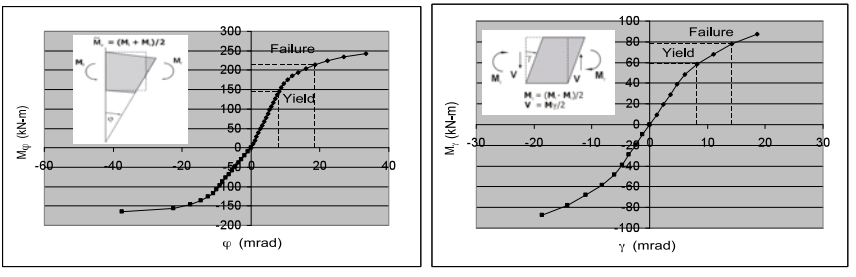


Fig. 7 – Example of derived relations for macroscopic bending and shear

The yield and rupture points are transferred for different combinations of macro bending and shear to the M_x-M_γ-diagram (Fig.8). They represent the yield and failure surfaces of the macro element which completes the derivation of its constitutive law.

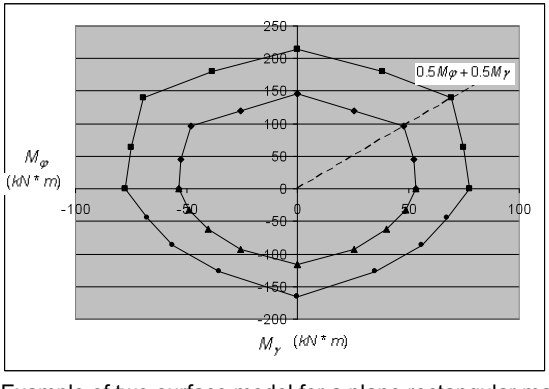


Fig. 8 – Example of two-surface model for a plane rectangular macro element representing a welded composite beam-column joint in a frame analysis

CONCLUSIONS

A generic non-linear FE model of a composite beam-column joint with welded connections has been developed using current state-of-the-art local modeling. Global geometric parameters can be used to generate a specific instance of the model, thus avoiding the creation of a new FE model by the user for every instance.

With this model, constitutive relationships are calculated for a plane rectangular macro element with beam-type boundaries that may represent this joint in a regular frame analysis. Thus, this local model is a vital step in a mechanically consistent scaling process that broadcasts local effects to the next scale and preserves accuracy without influencing numerical efficiency of the higher-scale analysis.

Similar models can be developed for other kinds of composite connections in different institutions. Once validated, they may become available to practicing engineers via the Internet to provide the required constitutive relationships for each instance of an application of a macro element in a frame analysis. If they become more and more refined as our knowledge about local behavior advances, practical analysis can directly benefit from this knowledge without any change to the higher-scale frame analysis.

REFERENCES

B. Ahmed, T.Q. Li and D.A. Nethercot 1996, “Modeling composite connection response”, Connections in Steel Structures III, Trento, Italy, Pergamon Press, pp. 259-268

C. Bucher et al., 2005: “SLang the structural language version 5.0.9”, Institute of Structural Mechanics, Bauhaus-University Weimar

U.E. Dorka, 1988: “A contribution to the identification and simplified analysis of structures with hysteresis evolution” (in German), TWM Report No. 88-10, Ruhr-Universität Bochum.

U.E. Dorka, 1991: “System analysis by discrete elements”, Proceedings of the Asian Pacific Conference on Computational Mechanics, Hong Kong, 1257-1262

U.E. Dorka, and S. Amorntipsakul, 2008: “Macro-elements for composite beam-column connections”, Composite Construction VI, Colorado, USA.

EC4: Eurocode 4

G. Hanswille, 1996: “Cracking of concrete mechanical models of the design rules in Eurocode 4”, Proceedings of an Engineering Foundation Conference Composite Construction III, Irsee, Germany, 420-433

G. Huber, F. Tschemmernegg, 1997: “Connections – Component method” (in German), Proceedings of the Symposium on Composite Structures, University of Kaiserslautern, Publishers H. Bode, W. Ramm, H. Wittek, H. Schmackpfeffer

R.T. Leon, J.F. Hajjar and C.K. Shield, 1996: “The effect of composite floor slabs on the behavior of steel moment-resisting frames in the Northridge earthquake”, Proceedings of an Engineering Foundation Conference Composite Construction III, Irsee, Germany, 738-751

R. Piyasena, Y.C. Loo and S. Fragomeni, 2004 “Factors influencing spacing and width of cracks in reinforced concrete; New prediction formulae”, Advances in Structural Engineering, Vol. 7, No. 1, 49-60

W. Ramm and S. Elz, 1996 “Behaviour and cracking of slabs as part of composite beams in regions with negative bending moments”, Proceedings of an Engineering Foundation Conference Composite Construction III, Irsee, Germany, 871-886

GEOMETRIC NON-LINEAR MODELLING OF PARTIAL INTERACTION IN COMPOSITE T-BEAMS IN FIRE

Amin Heidarpour
Centre for Infrastructure Engineering and Safety
The University of New South Wales
Sydney, Australia
a.heidarpour@unsw.edu.au

Mark A Bradford
Centre for Infrastructure Engineering and Safety
The University of New South Wales
Sydney, Australia
m.bradford@unsw.edu.au

ABSTRACT

The formulation for partial shear interaction in composite beams was developed over 50 years ago in closed form. This formulation is suitable for many cases encountered in practice, but it does not account for the geometric non-linearity produced by the "P-delta" effect. This effect is important in a compartment in a steel or composite framed building in a fire, where the initially large compressive forces which develop because of restraint against thermal expansion interact non-linearly with the large deflections of the composite floor slab, and a geometrically non-linear formulation must necessarily be invoked to capture the partial interaction behaviour of the composite floor system during a fire. This paper provides an elastic analysis of partial interaction at moderately low levels of temperature, so as to shed light on the significance of the parameters that affect the structural behaviour as well as to provide a precursor for an inelastic analysis to treat catenary action. The differential equations which quantify the problem are derived and solved numerically, and an illustrative example is worked.

INTRODUCTION

Steel and composite framed building structures nowadays account for most medium rise buildings in developed nations, comprising of floors with a concrete slab supported by a steel beam and which are connected with mechanical shear connectors. Despite their economical advantages and common usage, important questions have been posed regarding the performance of composite framed structures when subjected to extreme loading events such as fires. Because laboratory testing of full-scale structures is very expensive, recourse is needed to numerical and analytical tools to ascertain the behaviour of composite structures in a fire. Although specialised numerical models have been developed (such as those of [Bailey 1998] [Huang *et al.* 2000], [Elghazouli and Izzuddin 2000], [Iu and Chan 2004]), they do not properly account for the partial shear interaction between the slab and steel beam at elevated temperatures.

Because the performance-based design of composite frames is reliant on tensile membrane action in the slab and because of concerns regarding the ductility of the reinforcement [Gilbert and Sakka 2007], the elevated temperature strength of the

steel member and its interaction with the slab is important; this composite action can only be realised by robust shear connection during the fire. The aim of this paper, therefore, is to consider the response at elevated temperature of an isolated composite steel-concrete beam which forms a component of a compartment sub-assembly at elevated temperatures. The model allows for the geometric non-linearity arising from the "P-delta" effect because of large initial compressive forces in the restrained beam and large transverse deflections as a result of the fire, and it elucidates quantitatively the influence of several parameters on the structural behaviour. It provides a precursor for the inclusion of inelastic effects that can model catenary action.

NON-LINEAR MODEL

The composite beam is assumed to consist of a reinforced concrete slab containing (without loss of generality) one layer of reinforcement and a steel joist, joined with an elastic shear connection of stiffness k which varies with temperature (Figure 1). The curvature κ is assumed to be the same in both the steel and concrete, the load w is distributed uniformly and the member strained as a result of bilinear temperature profiles in the slab and joist. In this paper, the notation $\alpha = 1$ signifies the slab and $\alpha = 2$ the joist. Figure 2 shows the elastic end restraints assumed for semi-rigid connections, with $k_{\lambda\alpha}$ denoting a translational spring and $r_{\lambda\alpha}$ a rotational spring, with $\lambda = 0$ denoting the end $z = 0$ and $\lambda = 1$ and end $z = L$.

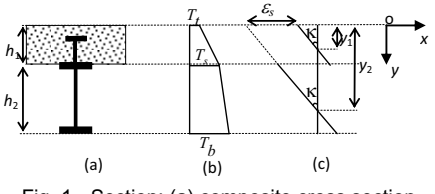


Fig. 1 - Section: (a) composite cross section (b) Thermal profile (c) Total strain diagram

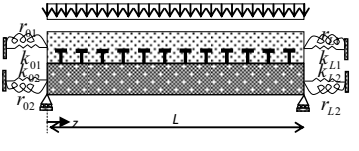


Fig. 2 - Typical steel-concrete composite beam

PARTIAL INTERACTION MODEL

Figure 1 shows the distances y_α from the assumed reference axis, so that the total strain is

(1) $$\varepsilon_{t\alpha} = (y - y_\alpha)\kappa = \varepsilon_{m\alpha} + (y - \bar{y}_\alpha)\kappa$$

where $\bar{y}_\alpha$ ($\alpha = 1, 2$) are locations of the elastic centroids below the reference axis and

(2) $$\varepsilon_{m\alpha} = u'_\alpha + \tfrac{1}{2}v'^2$$

is the non-linear membrane strain in each component needed to capture the P-delta effect, and $(\,)' \equiv \mathrm{d}(\,)/\mathrm{d}z$. The bi-linear temperature distribution assumed (Figure 1(b)) produces non-mechanical thermal strains of

(3) $$\varepsilon_{\theta\alpha} = \Phi_\alpha \left(T_t + y\nabla_\alpha - h_1 \delta_{2\alpha} \widetilde{\nabla}_\alpha \right)$$

where $\Phi_\alpha \, (\alpha = 1, 2)$ is the relevant coefficient of thermal expansion, $\nabla_1 = (T_s - T_t)/h_1$ and $\nabla_2 = (T_b - T_s)/h_2$ are the thermal gradients in the slab and joist respectively, δ_{ij} is the Kronecker delta and $\widetilde{\nabla}_\alpha = \nabla_\alpha - \nabla_1$. The mechanical strains in the steel, concrete and reinforcement (subscripted "*r*") are then

(4) $$\varepsilon_{e\alpha} = \varepsilon_{t\alpha} - \varepsilon_{\theta\alpha} = -\varepsilon_{c\alpha} - y_\alpha \kappa + y(\kappa - \Phi_\alpha \nabla_\alpha), \qquad \varepsilon_{er} = \varepsilon_{tr} - \varepsilon_{\Phi r} = -\varepsilon_{cr} - (y_1 - y_r)\kappa$$

$$\varepsilon_{c\alpha} = \Phi_\alpha \left(T_t - \widetilde{\nabla}_\alpha h_1 \delta_{2\alpha} \right) \text{ and } \varepsilon_{cr} = \Phi_2 \left(T_t + \nabla_1 y_r \right)$$

in which ε_{cr} is the thermal strain in the reinforcement. These strains then lead to stresses

(5) $$\sigma_\alpha = E_\alpha(y)\varepsilon_{e\alpha} \quad (\alpha = 1, 2) \quad \text{and} \quad \sigma_r = E_2(y)\varepsilon_{er}$$

in the concrete, steel and reinforcement respectively, where E_α is the degraded elastic modulus at elevated temperature. Using Eqs. (5), the axial forces in the concrete, steel and reinforcement are

(6) $$N_\alpha = -(\varepsilon_{c\alpha} + y_i \kappa) \cdot \overline{EA}_\alpha + (\kappa - \Phi_\alpha \nabla_\alpha) \cdot \overline{EB}_\alpha \quad \text{and} \quad N_r = -\left[\varepsilon_{cr} + (y_1 - y_r)\kappa\right] \cdot \overline{EA}_r$$

for which

(7) $$\overline{EA}_\alpha = \int_{A_\alpha} E_\alpha(y) \mathrm{d}A_\alpha, \qquad \overline{EB}_\alpha = \int_{A_\alpha} y E_\alpha(y) \mathrm{d}A_\alpha, \quad \overline{EA}_r = E_2(y_r) \cdot A_r$$

are temperature-dependent cross-sectional properties, and the axial force and internal bending moment on a cross-section are given by

(8) $$N_{int} = \sum_{\alpha=1,2} N_\alpha + N_r \quad \text{and} \quad M_{int} = \sum_{\alpha=1,2} \int_{A_\alpha} \sigma_\alpha y \, \mathrm{d}A_\alpha + N_r y_r .$$

The slip strain at the interface (Figure 1) is

(9) $$\varepsilon_{slip} = \mathrm{d}s/\mathrm{d}z = (y_1 - y_2)\kappa,$$

and substituting this into Eq. (6) and Eq. (5) into Eq. (8) leads to the curvature κ being a function of the slip strain and the internal actions in the form

(10) $$\kappa = \beta_3 \left(M_{int} + M_\Im \right) + \beta_1 \varepsilon_{slip} - \beta_2 \left(N_{int} + N_\Im \right),$$

where

(11) $$N_\Im = \sum_{\alpha=1,2} \left(\Phi_\alpha \nabla_\alpha \cdot \overline{EB}_\alpha + \varepsilon_{c\alpha} \cdot \overline{EA}_\alpha \right) \qquad M_\Im = \chi \varepsilon_{cr} \overline{EA}_r + \sum_{\alpha=1,2} \left(\varepsilon_{c\alpha} \overline{EB}_\alpha + \Phi_\alpha \nabla_\alpha \overline{EI}_\alpha \right)$$

The parameters β_1, β_2 and β_3 depend on the geometric properties of the cross-section and on the degraded elastic moduli, and are given by

(12) $$\beta_1 = \frac{\overline{EA}\,\overline{EB}_1 - \overline{EA}_1\,\overline{EB} + \chi \overline{EA}_2\,\overline{EA}_r}{\overline{EI}\,\overline{EA} - \overline{EB}^2 - \chi\left(\overline{EA}_r\,\overline{EB} - y_r\,\overline{EA}_r\,\overline{EA}\right)}$$

$$\beta_2 = \frac{\overline{EB} + \chi \overline{EA}_r}{\overline{EI}\,\overline{EA} - \overline{EB}^2 - \chi\left(\overline{EA}_r\,\overline{EB} - y_r\,\overline{EA}_r\,\overline{EA}\right)}$$

$$\beta_3 = \frac{\overline{EA}}{\overline{EI}\,\overline{EA} - \overline{EB}^2 - \chi\left(\overline{EA}_r\,\overline{EB} - y_r\,\overline{EA}_r\,\overline{EA}\right)},$$

in which

(13) $$\overline{EA} = \sum_{\alpha=1,2} \overline{EA}_\alpha\,; \quad \overline{EB} = \sum_{\alpha=1,2} \overline{EB}_\alpha\,; \quad \overline{EI} = \sum_{\alpha=1,2} \overline{EI}_\alpha\,; \quad \chi = \left(\frac{\overline{EA}}{\overline{EA} + \overline{EA}_r}\right)\left(y_r - \frac{\overline{EB}}{\overline{EA}}\right)$$

By considering a free body diagram of an infinitesimal length dz of the slab with a traction free top surface and shear connection at its bottom surface, horizontal equilibrium requires that

(14) $$\frac{\mathrm{d}\left(N_1 + N_r\right)}{\mathrm{d}z} = -ks(z),$$

where k is the modulus of the shear studs at elevated temperature [Ranzi and Bradford 2007]. Using Eqs. (8) and (10) in Eq. (14) produces the linear differential equation for the slip as

(15) $$\tilde{\beta}_1\left(\frac{\mathrm{d}^2 s}{\mathrm{d}z^2}\right) + k\,s = -\bar{\beta}_1\beta_3\left(\frac{\mathrm{d}M_{int}}{\mathrm{d}z}\right)$$

in which

(16) $$\tilde{\beta}_1 = \beta_1\bar{\beta}_1 - \overline{EA}_2\left(\frac{\overline{EA}_1 + \overline{EA}_r}{\overline{EA} + \overline{EA}_r}\right) \quad \bar{\beta}_1 = \overline{EB}_1 - \overline{EB}\left(\frac{\overline{EA}_1 + \overline{EA}_r}{\overline{EA} + \overline{EA}_r}\right) + y_r\,\overline{EA}\left(\frac{\overline{EA}_2}{\overline{EA} + \overline{EA}_r}\right).$$

The solution of Eq. (15) is

(17) $$s(z) = C_1 e^{\nu z} + C_2 e^{-\nu z} - \left(\frac{\bar{\beta}_1\beta_3}{k}\right)\frac{\mathrm{d}M_{int}}{\mathrm{d}z}$$

in which

(18) $$\nu = \sqrt{-k/\tilde{\beta}_1}$$

and C_1 and C_2 are constants of integration.

NON-LINEAR EQUILIBRIUM AND SOLUTION PROCEDURE

Using the partial interaction model developed above, the bending moment $M(z)$ at each cross-section distant z from the origin can be written as a function of the bending moment and shear force at $z = 0$ (denoted M_0 and R_0 respectively) using simple statics as

(19) $$M(z) = M_0 + R_0 z - \frac{wz^2}{2}.$$

For moment equilibrium,

(20) $$M_{int} = M + N_{int}\overline{y}$$

where

(21) $$\overline{y} = \frac{\overline{EB} + \chi\overline{EA}_r}{\overline{EA}}$$

is the temperature-dependent location of the coordinate of the neutral axis under conditions of full interaction. Integrating Eq. (10) produces the slope as

(22) $$\theta(z) = \beta_3\left[-\frac{wz^3}{6} + \frac{R_0 z^2}{2} + \left(M_0 + M_\Im - \frac{\beta_2 N_\Im}{\beta_3} + \frac{\beta_1\overline{\beta}_1 w}{k}\right)z\right] + \beta_1 C_1 e^{\nu z} + \beta_1 C_2 e^{-\nu z} + C_3$$

and integrating this again produces the deflection as

(23) $$v(z) = \beta_3\left[-\frac{wz^4}{24} + \frac{R_0 z^3}{6} + \left(M_0 + M_\Im - \frac{\beta_2 N_\Im}{\beta_3} + \frac{\beta_1\overline{\beta}_1 w}{k}\right)\frac{z^2}{2}\right] + \frac{\beta_1 C_1 e^{\nu z}}{\nu} - \frac{\beta_1 C_2 e^{-\nu z}}{\nu} + C_3 z + C_4$$

where C_3 and C_4 are additional constants of integration. From Eqs. (1) and (2), at the centroids of the slab and joist,

(24) $$u_1(z) = -\int\left[(y_1 - h_1/2)\kappa + \tfrac{1}{2}\theta^2\right]\mathrm{d}z + C_5$$

$$u_2(z) = s(z) + h\theta(z) - \int\left[(y_1 - h_1/2)\kappa + \tfrac{1}{2}\theta^2\right]\mathrm{d}z + C_5$$

in which $h = (h_1 + h_2)/2$, while at the ends of the member (Figure 2),

(25) $$N_{0\alpha} = k_{0\alpha}u_\alpha(z = 0) \quad \text{and} \quad N_{L\alpha} = -k_{L\alpha}u_\alpha(z = L) \qquad (\alpha = 1,2)$$

in which $N_{0\alpha}$ and $N_{L\alpha}$ are found by appropriate substitution of $z = 0$ and L in Eq. (6). Using Eqs. (8) and (20) and noting in the concrete slab and steel section that $\theta_1 = \theta_2$, so that $\theta_{01} = \theta_{02}$ and $\theta_{L1} = \theta_{L2}$ produces

(26) $$M_{\lambda 2} = \left[M_0 + N_{\mathrm{int}}\overline{y} - \frac{N_{\lambda 1}h_1}{2} - N_{\lambda r}y_r - N_{\lambda 2}\left(h_1 + \frac{h_2}{2}\right)\right]\left(\frac{r_{\lambda 2}}{r_{\lambda 1} + r_{\lambda 2}}\right) \qquad (\lambda = 0, L).$$

Equations (25) and (26) contain six statical boundary conditions, which when augmented with the two kinematic boundary conditions that $v(z = 0, L) = 0$ allow the vector $\{q\} = \{M_0, R_0, N_{int}, C_1, \ldots, C_5\}^{\mathrm{T}}$ to be determined from the non-linear relationship

(27) $$[A(\{q\})]\cdot\{q\} = \{b\},$$

in which $[A]$ is a matrix that depends non-linearly on $\{q\}$ and $\{b\}$ is a vector of constants. Equation (27), which is of order 8, can be solved iteratively using software such as MAPLE.

MODEL VERIFICATION

A 10 m long simply supported composite beam which was modelled by [Ranzi *et al.* 2004] using the direct stiffness method at ambient temperature and which was verified against the worked example given in [Johnson 1994] was analysed by the proposed approach in order to verify its accuracy. The concrete slab had a width of 600 mm, a depth of 300 mm and an elastic modulus E_c = 20 GPa and the steel section was chosen to be rectangular with a width of 60 mm, a depth of 300 mm and an elastic modulus E_s = 200 GPa. The load was taken as w = 35 kN/m which included its self weight, the translational stiffnesses as $k_{0\alpha} = k_{L\alpha} = \infty$ and the rotational stiffnesses as $r_{0\alpha} = r_{L\alpha} = 0$ ($\alpha = 1, 2$) to simulate pure pin ends at the beam (in deference to a roller support in simply supported beams) so that horizontal movement is restrained.

The extensive study undertaken by [Bradford and Heidarpour 2008] indicates good correlation of the slip at the interface with the solutions of [Ranzi *et al.* 2004]. However, the results in Figure 3, which shows the location of the neutral axes in the concrete slab and steel joist, are somewhat disparate with the solutions of [Ranzi *et al.* 2004]. This difference is a result of the inclusion of geometric non-linearity (the second order term v'^2 in Eq. (2)) which produces an axial force which contributes to the P-delta effect. Inclusion of this effect is necessary for modelling restrained beams subjected to fire loading, and is significantly more complex than routine solutions for partial interaction in the absence of second order effects.

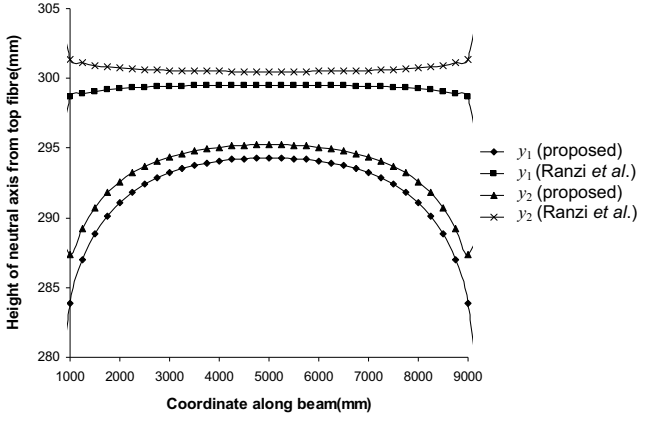


Fig. 3 - Comparison of location of neutral axes in slab and joist

PARAMETRIC STUDY

The partial interaction theory for the model depicted in Figure 2 has been used to investigate the behaviour of a steel-concrete beam parametrically at elevated temperatures. The geometric properties and loading were chosen to be the same as in the previous model validation, and the beam was restrained at its ends with elastic supports such that

(28) $$k_{0\alpha} = k_{L\alpha} = \beta_c\left(\overline{EA}_{0\alpha}/L\right) \quad , \quad r_{0\alpha} = r_{L\alpha} = \beta_c\left(\overline{EI}_{0\alpha}/L\right) \qquad (\alpha = 1, 2)$$

where β_c is an arbitrary coefficient (taken herein as $\beta_c = 0.1$). The mechanical properties of the steel and concrete were taken as $f_{sy0} = 250$ MPa, $\Phi_s = 11\times10^{-6}$ per ºC and $f_{cc0} = 40$ MPa, $f_{ct0} = 3.8$ MPa, $\Phi_c = 9.9\times10^{-6}$ per ºC respectively, and the iterative scheme was terminated when the maximum tensile or compressive stress in the steel or compressive stress in the concrete exceeded f_{sy} or $0.5f_{cc}$ under the given thermal regime. In hogging bending, the concrete cracks when its stress exceeds f_{ct} and the modulus of the concrete slab was taken as zero thereafter in the analysis. The points lengthwise at which this occurs are unknown *a priori*, but the location of the points of inflection may be converged upon after only a few iterations.

The deflections of the composite beam at elevated temperature are shown in Figure 4, and this indicates the maximum deflection, which occurs at mid-span, and the rotation of the beam ends depend significantly on the characteristics of the thermal profile and the degree of interaction between the concrete and steel components. It can be seen that the displacements increase with an increase of the difference between the thermal gradients in the steel and concrete elements or with an increase of the temperature at the extreme fibre of the steel which is due to a degradation of the mechanical properties of the material at elevated temperatures.

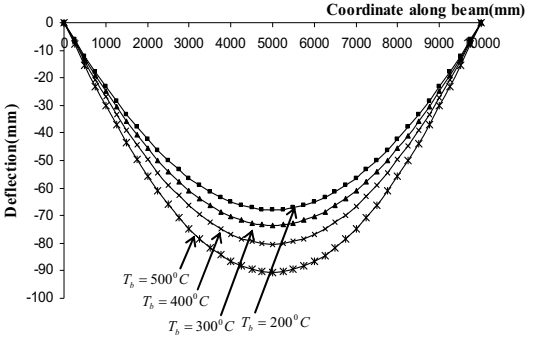


Fig. 4 - Elevated temperature deflection for $\nabla_s = 0.2\nabla_c, (vL)_0 = 10$

The location of the neutral axis in the concrete slab and steel joist are shown in Figure 5, in which it can be seen that they move away from their ambient temperature locations because of the development of axial force as the temperature increases. The distance between the two neutral axes, and their corresponding values at the ends of the beam, increase with an increase in the temperature T_b at the extreme fibre of the steel component.

Figure 6 shows the slip at the interface as a function of the temperature. The degradation of the elastic properties of the steel, concrete and shear connection as well as the large compressive forces developed at in the restrained member at elevated temperature in the early stages of a fire lead to an increase of the slip with an increase of temperature at the extreme fibre of the bottom of the steel section (T_b).

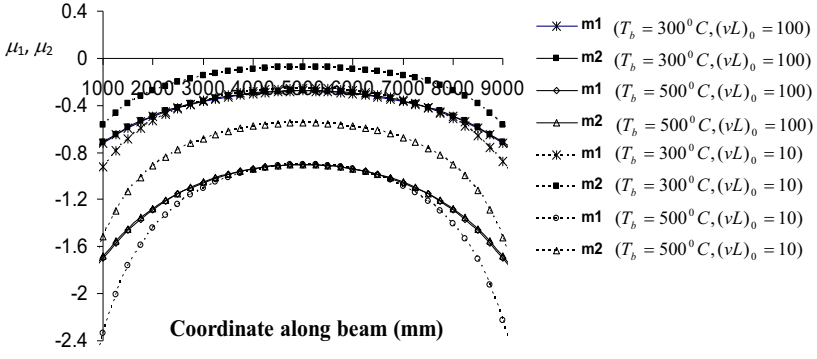


Fig. 5 - Location of neutral axes in slab and joist $\mu_\alpha = y_{\alpha,\Im} / y_{\alpha,0}$ $(\nabla_s = 0.2\nabla_c)$

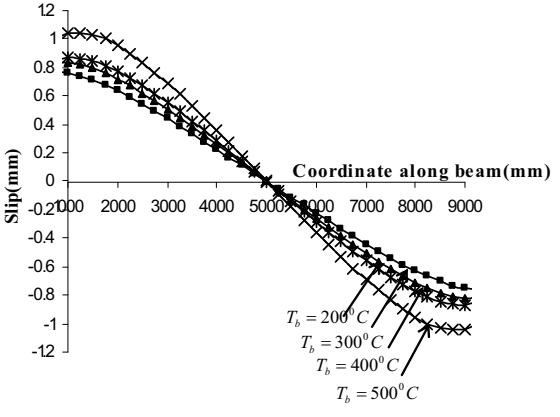


Fig. 6 - Slip along composite beam at elevated temperatures ($\nabla_s = 0.2\nabla_c, (vL)_0 = 10$)

CONCLUDING REMARKS

This paper has addressed the behaviour of an elastic steel-concrete composite beam with partial interaction within a steel or composite frame at elevated temperature using a non-linear approach that has been applied to a typical beam in a sub-assembly with translational and rotational restraints at the two ends. In a compartment fire in a composite steel frame structure, these restraints are provided by the beam-to-column connections. The formulation of the model allowed the statical and kinematic boundary conditions to be satisfied exactly, and it further allowed for the point at which first yield occurs to be identified. Because of this, the model cannot account for post-yield behaviour and its effect on producing catenary action at elevated temperature, but nevertheless it sheds considerable light on the effect of several parameters, and importantly the degree of interaction, on the structural behaviour.

The model developed and has been validated against other formulations at ambient temperature that include partial interaction, and which have been reported elsewhere. It was shown how the degradation of the material properties of the steel, concrete and shear connectors as well as the large axial compressive force developed initially in a thermal regime lead to increased slip at the steel-concrete interface, relative to that at ambient temperature. Furthermore, the location of the neutral axes in the concrete slab and steel component at elevated temperatures depends significantly on the characteristics of the thermal profile; at the initial stages of fire attack the location of these neutral axes moves away from the steel-concrete interface with an increase in temperature and an increase in distance from the support because of the development of significant thermally-induced axial forces in the steel and concrete elements. The model has potential for codification in a structural fire engineering design.

ACKNOWLEDGEMENT

The work reported in this paper was supported by the Australian Research Council through a Federation Fellowship awarded to the second author.

REFERENCES

Bailey CG (1998) Development of computer software to simulate the structural behaviour of steel framed buildings in fire. *Computers and Structures* 67: 421-438.

Bradford MA, Heidarpour A (2008) Non-linear behaviour of composite beams with partial interaction under thermal loading. 5th European Conference on Steel and Composite Structures, Graz, Austria, 1055-1060.

Elghazouli AY, Izzuddin BA (2000) Response of idealised composite beam-slab systems under fire conditions. *Journal of Constructional Steel Research* 56: 199-225.

Gilbert RI, Sakka, ZI (2007) Effect of reinforcement type on the ductility of suspended reinforced concrete slabs. *Journal of Structural Engineering, ASCE* 133: 834-843.

Huang Z, Burgess IW, Plank RJ (2000) Three dimensional analysis of composite steel framed buildings in fire. *Journal of Structural Engineering, ASCE* 126: 389-397.

Iu CK, Chan SL (2004) A simulation-based large-deflection and inelastic analysis of steel frames under fire. *Journal of Constructional Steel Research* 60: 1495-1524.

Johnson RP (1994) *Composite Structures of Steel and Concrete*. Blackwell Scientific Publishers, Oxford, UK.

Ranzi G, Bradford MA, Uy B (2004) A direct stiffness analysis of a composite beam with partial interaction. *International Journal for Numerical Methods in Engineering* 61: 657-672.

Ranzi G, Bradford MA (2007) Composite beams with both longitudinal and transverse partial interaction subjected to elevated temperatures. *Engineering Structures* 29: 2732-2750.

WHERE STEEL AND CONCRETE MEET IN THE HEAT

Rob Stark
SmitWesterman & Stark Partners
Waddinxveen & Delfgauw, The Netherlands
rstark@smitwesterman.nl

ABSTRACT
Fire resistance is one of the main arguments for using Composite Structures. Therefore it is important that reliable and accepted methods are available for the determination of the fire resistance. In the recently completed series of the Eurocodes each material dependent code has a separate part on structural fire design. For Composite Structures this is EN1994-1-2.
This Eurocode part includes rules for structural fire design of composite beams, composite columns and composite slabs. Also rules are given for constructional details.
The design rules are on three different levels of sophistication e.g.:
- Tabulated data
- Simple calculation models
- Advanced calculation models

In the paper a review is given of these methods and the opinion of a practitioner is presented on the possibilities for use of the different methods in present practice.
The presentation of the code rules is illustrated by examples of the structural fire design as used for a building in the Netherlands.
Emphasis in the paper is on practical application rather than theoretical background.

FIRE DESIGN IN THE EUROCODE
In the series of Eurocodes a special Eurocode EN 1994: Eurocode 4 is included for the design of composite structures. Part 1-1 of this Eurocode contains general rules and rules for buildings. Design rules for determination of the fire resistance of composite structures are given in a separate part EN1994-1-2. For the material properties of steel and concrete at high temperatures this part refers to the part 1-2 of EN1992 and EN1993.

CASE
The design of a composite building, build in the Netherlands, is used for illustration of the code rules. The Building is a fitness building located in a shopping center in Zoetermeer. Architect Frits van Dongen of the Architecten CIE designed an 'UFO' formed building on top of the shopping passage.



Fig. 1 - Photo fitness center above shopping passage

A composite structure is designed to obtain the round shape of the building. Due to the lightweight composite structure only three slender composite columns are able to support the whole structure. A round steel truss is the main structural component of the UFO. Three composite columns support this truss. Curved wide flange beams perpendicular to the truss divide the UFO in twelve equally pie pieces. Composite floors supported by composite beams are located between the facade and the stairways in the center.

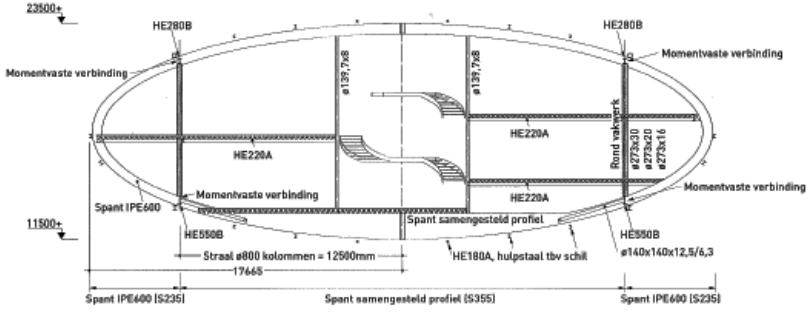


Fig. 2 - Structural section of the UFO

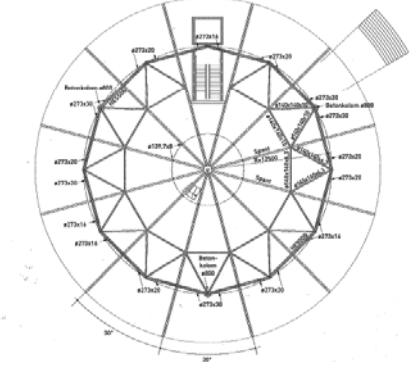


Fig 3 - Structural plan of the UFO

According the Dutch Building Regulations a fire resistance of 120 minutes for this structure is required. The total compartment is larger than 1000 m2 causing that a sprinkler installation is to be used. Due to the sprinkler installation a reduction of 30 minutes for the fire resistance is allowed. Therefore the design fire resistance of the main structural parts is 90 minutes. The composite floors in the building are not part of the main structure and therefore the design fire resistance is 30 minutes.

COMPOSITE BEAMS

During fire composite beams behave better than traditional bare steel beams.
In EN1994-1-2 the following type of beams are covered.

- Composite beams comprising steel beams with no concrete encasement.
- Composite beams comprising steel beams with partial concrete encasement.
- Steel beams with partial concrete encasement.
- Integrated steel beams having inherent fire protection.

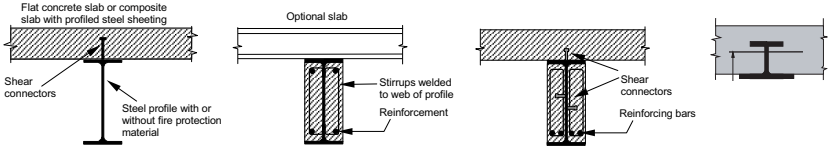


Fig. 4 - Types of beams according EN1994-1-2

In EN1994-1-2 plastic theory is used for the determination of the resistance of the beams. In addition to composite action it is possible to increase the fire resistance of the steel parts by using fire protective cladding or coating.

Steel beams with no concrete encasement

Critical temperature model

The critical temperature model is a simplified calculation model. The model is applicable within the following restrictions:

– Symmetric steel profiles with a maximum depth of 500 mm,

– A slab depth not less than 20 mm,

– Used in connection with simply supported beams exclusively subject to sagging bending moments.

Within this field of application it may be assumed that the temperature of the steel section is uniform.

The critical temperature θ_{cr} may be determined from the load level $\eta_{fi,t}$,applied on composite section and from the strength of steel at elevated temperatures according the relationship:

For R30 $$0{,}9\ \eta_{fi,t} = f_{ay,\theta cr} \big/ f_{ay} \quad (1)$$

In any other case $$1{,}0\ \eta_{fi,t} = f_{ay,\theta cr} \big/ f_{ay} \quad (2)$$

The critical temperature, belonging to the load level as mentioned above, should be compared with the steel temperature in the steel section at the desired fire safety time. To determine the steel temperature in the steel section the section factor of the lower flange may be used. For daily use the ECCS Nomogram 89 can be used (Figure 5).

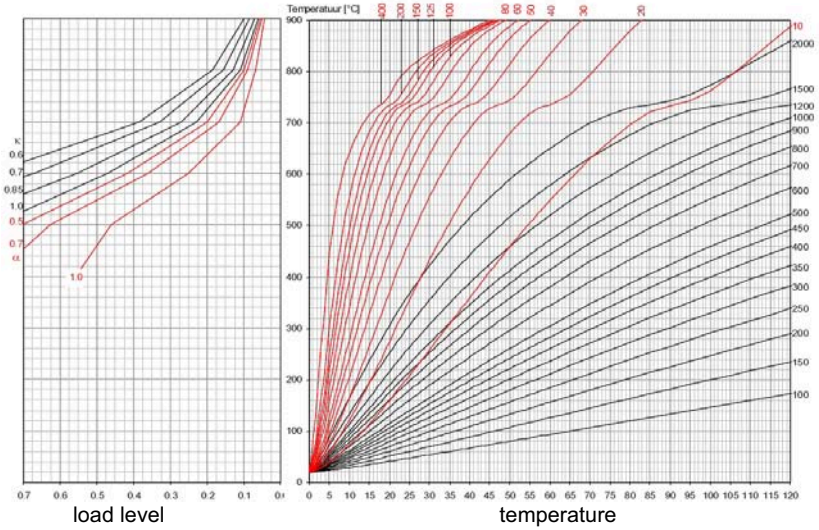


Fig. 5 - ECCS Nomogram 89.

Bending moment resistance model

The bending moment resistance model is given in the Annex E of EN1994-1-2.
Using this model the bending resistance may be calculated by plastic theory, taking in to account the variation of material properties with temperature. Plastic theory may be used for any class of cross section except for class 4 (EN1994-1-2; 4.3.4.1.2). For the hogging moment resistance the model may be used for class 1 or 2 in fire conditions. For class 3 or 4 the following simplifications are given:

- When the steel web or the lower steel flange of the composite section is of class 3 in the fire situation, its width may be reduced to an effective value determined in accordance with EN 1993-1-5.
- When the steel web or the lower steel flange of the composite section is of class 4 in the fire situation, its resistance should be neglected.

The distribution of stresses is qualitatively shown in Figure 6. The moment resistance can be determined from the balanced forces.

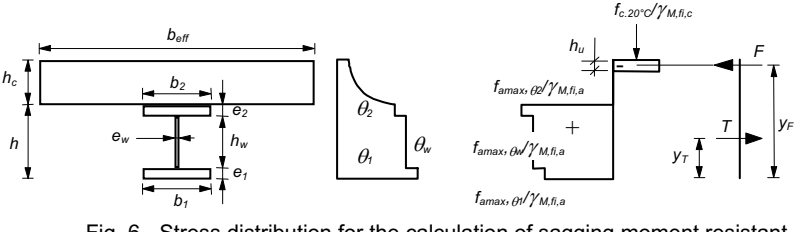


Fig. 6 - Stress distribution for the calculation of sagging moment resistant

Composite beams comprising steel beams with partial concrete encasement

Basis is fire exposure according the standard temperature-time curve. It is assumed that the profile is at three sides exposed to fire. By reducing the cross-section of the parts of the section or reducing the mechanical properties, the effect of temperature on material properties is taken in account. Plastic theory is used. EN1994-1-2 gives rules to calculate the bending resistance for different fire safety classes. For the individual parts of the section (bottom flange and web of the steel profile, reinforcement between the flanges), where the temperature range is linear or uniform, the full section and a reduced strength is taken into account. Not uniform exposed, horizontal parts of the section are assumed to have full strength. But the parts that are influenced by the exposure of the fire (concrete encasement, de lower parts of the slab and the edges of the upper flange) are neglected. (Figure 9)

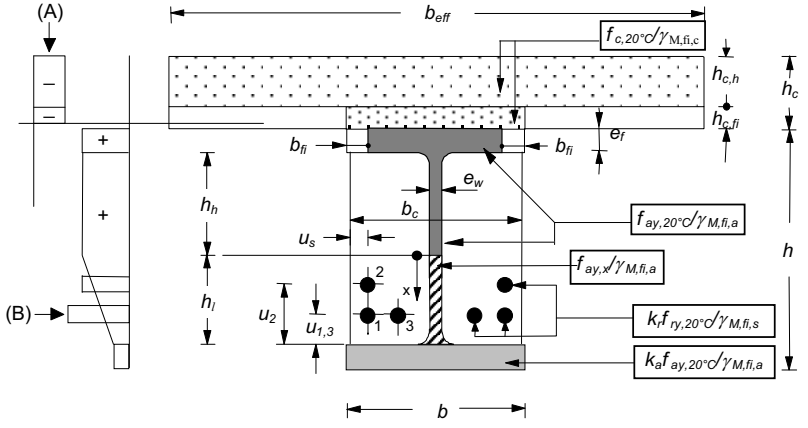


Fig. 9 - Calculation scheme for sagging bending resistance

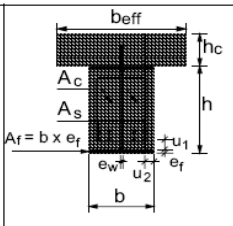
Tabulated data

The above mentioned simple calculation model can be used without any tools. However in daily practice the calculation is too laborious. It may be expected that software will be developed. As an alternative in EN1994-1-2 design tables are presented.

These design tables are available for the following types of beams:

– Composite beams comprising steel beams with partial concrete encasement.

– Composite beams comprising steel beams with full concrete cover, where the concrete is acting as fire protection.

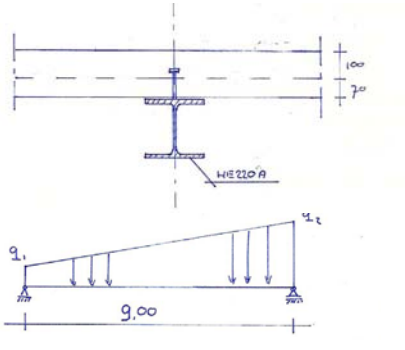


Condition for application:
slab: $h_c \geq 120$ mm
$b_{eff} \leq 5$ m
steel section: $b / e_w \geq 15$
$e_f / e_w \leq 2$
additional reinforcement area, related to total area between the flanges:
$A_s/(A_c + A_s) \leq 5\%$

		Standard Fire Resistance				
		R30	R60	R90	R120	R180
1	Minimum cross-sectional dimensions for load level $\eta_{fi,t} \leq 0,3$					
	min b [mm] and additional reinforcement A_s in relation to the area of flange A_s / A_f					
1.1	$h \geq 0,9 \times$ min b	70/0,0	100/0,0	170/0,0	200/0,0	260/0,0
1.2	$h \geq 1,5 \times$ min b	60/0,0	100/0,0	150/0,0	180/0,0	240/0,0
1.3	$h \geq 2,0 \times$ min b	60/0,0	100/0,0	150/0,0	180/0,0	240/0,0

Fig.10 - Design table for composite beams comprising steel beams with partial concrete encasement

CASE: COMPOSITE BEAM IN UFO ZOETERMEER.



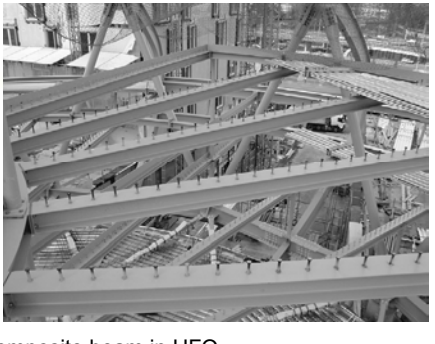


Fig. 11 - Scheme of composite beam in UFO

Steel beam: HE220A; Steel S235; $M_{pl,Rd} = 291$ kNm
Concrete: C 20/25
Composite floor: Comflor 70; $h_c = 170$ mm; $f_{yp} = 320$ N/mm^2
$G_{k,1} = 4,0$ kN/m1 $Q_{k,2} = 17,5$ kN/m1 $\psi = 0,5$
$Q_{k,1} = 5,0$ kN/m1 $\psi = 0,5$ $Q_{fi,d,1} = 4,0 + 0,5 \cdot 5,0 = 6,5$ kN/m
$G_{k,2} = 14.0$ kN/m1 $Q_{fi,d,2} = 14,0 + 0,5 \cdot 17,5 = 8,8$ kN/m
$M_{fi,Ed} = 146$kNm; $V_{fi,Ed} = 78$ kN
$\eta_{fi,t} = M_{fi,Ed} / M_{pl,Rd} = 146 / 291 = 0,5$
$k_{y,\theta cr} = 0,9 \cdot \eta_{fi,t} = 0,9 \cdot 0,5 = 0,45$
$\theta_{a,cr} = 39,19 \cdot \ln [1/(0,9674 \cdot k_{y,\theta cr}{}^{3,833}) - 1] + 482 = 585 \circ C$

Section factor of bottom flange [A/V] = 2 . (220 + 11) / (220 . 11) = 191 mm

The steel temperature after 30 minutes is more then 800 ° C see Figure 5.
Conclusion: Fire protection is necessary.

According Nomogram 89 (Figure 5) for 30 minutes fire safety => [A/V] . λ_p/d_p = 2000 => λ_p/d_p = 10,5

For a protection material with a thermal conductivity of 0,035 W/(m.K) a protection thickness during fire of 0,0033 m = 3,3 mm is necessary.

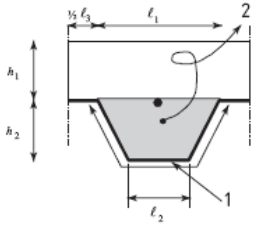
NOTE: *In the Netherlands composite beams are normally designed without concrete encasement. To achieve the necessary fire protection the beams are often protected by coating or cladding. In EN 1994-1-2 tables for composite beams without concrete encasement are not given, also software according the simple calculation models is not available for these types of composite beams.*

COMPOSITE FLOORS

For the standard fire exposure, composite slabs shall comply with the criteria load bearing (mechanical resistance R) and separating (Insulation I and Integrity E).
In EN1994-1-2 design models are given for protected and unprotected composite slabs. When these models are used for composed slabs it may be assumed that the integrity criterion is satisfied. In EN1994-1-2; annex D a model is given for the calculation of the fire resistance for unprotected slabs with regard to the criteria insulation “I” and mechanical resistance “R”.
In daily practice, same as for design at normal temperature, design tables and software delivered by manufacturers are used to verify the fire resistance of composite slabs.

Thermal insulation criterion “I”

For thermal insulation the average temperature rise, at the non-exposed side of the slab (upper side), should not exceed 140 °C and the maximum temperature rise should not exceed 180 °C. Due to the accumulation capacity of the ribs the temperature at the upper side of the slab is not uniform. Therefore both the average temperature rise as the maximum temperature rise can be determinative. The fire resistance in relation to the thermal insulation is depending on the dimension and center-to-center distance of the ribs. In EN1994-1-2; Annex D the view factor ϕ and the geometry factor, both defined by the geometry, are used. The definition of the geometry of the rib is given in figure 12.



Key
1 – Exposed surface: L_r
2 – Area: A

Fig.12 - Definition of the rib geometry

With the definition of Figure 12 the formula for the view factor is:

$$\Phi = \left(\sqrt{h_2^2 + \left(l_3 + \frac{l_1 - l_2}{2} \right)^2} - \sqrt{h_2^2 + \left(\frac{l_1 - l_2}{2} \right)^2} \right) \Big/ l_3 \qquad (3)$$

The formula for the geometry factor is:

$$\frac{A}{L_r} = \frac{h_2 \left(\frac{\ell_1 + \ell_2}{2} \right)}{\ell_2 + 2\sqrt{h_2^2 + \left(\frac{\ell_1 - \ell_2}{2} \right)^2}} \qquad (4)$$

The time when one of the two criteria is reached can now be calculated with the following formula:

$$t_i = a_0 + a_1 \cdot h_1 + a_2 \cdot \Phi + a_3 \cdot \frac{A}{L_r} + a_4 \cdot \frac{1}{\ell_3} + a_5 \cdot \frac{A}{L_r} \cdot \frac{1}{\ell_3} \quad \text{in [min]} \qquad (5)$$

The accumulation capacity and the shadow effect of the ribs on the upper flange of the steel sheet are taken in account in the formula.
The coefficients a_0 upto a_5 are given in Figure 13 for normal and lightweight concrete.

	a_0 [min]	a_1 [min/mm]	a_2 [min]	a_3 [min/mm]	a_4 [mm min]	a_5 [min]
Normal concrete	-28.8	1.55	-12.6	0.33	-735	48.0
Lightweight concrete	-79.2	2.18	-2.44	0.56	-542	52.3

Fig. 13 - Coefficients for determination of the fire resistance with respect of the thermal insulation.

Mechanical resistance criterion "R"
EN 1994-1-2;annex D gives a model for the calculation of unprotected composite slabs with or without additional reinforcement. For a simply supported slab the capacity is determined by the sagging moment capacity and for a continuous slab the capacity is determined by the sagging and hogging moment capacity.

Sagging bending resistance according EN1994-1-2;D2
The sagging bending resistance is determined by the capacity of the steel sheet and the reinforcement. To determine this capacity first the temperatures in the parts should be determined. The steel sheet is divided in three parts, the bottom flange, the rib and the upper flange. For each part a temperature is calculated. Due to the shadow effect of the rib the temperature of the upper flange will be lower than the temperature of the bottom flange. The temperature of the web will be in between the temperature of the upper- and bottom flange.
The temperatures of the steel plate can be calculated with the following formula.

$$\theta_a = b_0 + b_1 \cdot \frac{1}{\ell_3} + b_2 \cdot \frac{A}{L_r} + b_3 \cdot \Phi + b_4 \cdot \Phi^2 \qquad (6)$$

The temperature in the reinforcement depends on the position of the reinforcement and the geometry of the steel sheet.

$$\theta_s = c_0 + \left(c_1 \cdot \frac{u_3}{h_2}\right) + (c_2 \cdot z) + \left(c_3 \cdot \frac{A}{L_r}\right) + (c_4 \cdot \alpha) + \left(c_5 \cdot \frac{1}{\ell_3}\right) \quad (7)$$

The coefficients b_0 upto b_4 are given in ENV1994-1-2;table D.2 and c_0 upto c_5 are given in EN1994-1-2;table D.3. In Figure 14 and Figure 15 parts of these tables are shown.

Concrete	Fire resistance [min]	Part of the steel sheet	b_0 [°C]	b_1 [°C]. mm	b_2 [°C]. mm	b_3 [°C]	b_4 [°C]
Normal	60	Lower flange	951	-1197	-2,32	86,4	-150,7
weight		Web	661	-833	-2,96	537,7	-351,9
concrete		Upper flange	340	-3269	-2,62	1148,4	-679,8

Fig.14 - Example of coefficients to determine the temperatures in the steel sheet.

Concrete	Fire resistance [min]	c_0 [°C]	c_1 [°C]	c_2 [°C]. mm$^{0.5}$	c_3 [°C].mm	c_4 [°C/°]	c_5 [°C].mm
Normal	60	1191	-250	-240	-5,01	1,04	-925
weight	90	1342	-256	-235	-5,30	1,39	-1267
concrete	120	1387	-238	-227	-4,79	1,68	-1326

Fig.15 - Example of coefficients to determine the temperatures in the reinforcement

The z-factor, indicating the position of the reinforcement bar, is given by:

$$\frac{1}{z} = \frac{1}{\sqrt{u_1}} + \frac{1}{\sqrt{u_2}} + \frac{1}{\sqrt{u_3}} \quad (8)$$

The distances u_1, u_2 and u_3 are expressed in mm and are defined as follows (figure 16):

u_1, u_2: Shortest distance of the centre of the reinforcement bar to any point of the web of the steel sheet.

u_3: Distance of the centre of the reinforcement bar to the bottom flange of the steel sheet.

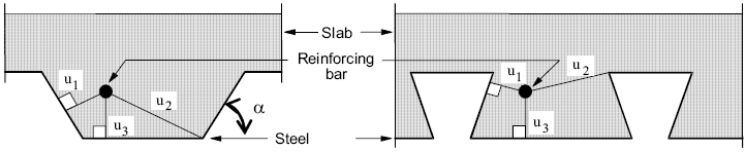


Fig.16 - Parameters for the position of the reinforcement bars

The bending resistance is determined by summation of the tension capacity of the steel sheet and the reinforcement. With this total tension force the height of the compression zone can be calculated by using the assumption that the compression stress is constant over the height of the zone, equal to $0.85f_c$, according EN 1994-1-1. The lever arm is now defined and so the sagging moment resistance can be calculated.

Hogging bending resistance according EN1994-1-2;D3

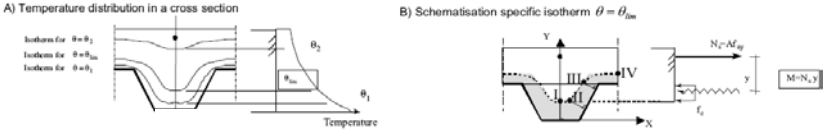


Fig. 17 - Isotherm for limited temperature

The hogging bending resistance of a slab can be calculated by using a reduced section of the slab. The parts with temperatures above the limited temperature θ_{lim} are neglected. The remaining cross section can be considered as at room temperature. As a save approximation the contribution of the steel sheet for the hogging bending resistance may be ignored. The remaining cross section is determined, on basis of the isotherm for the limited temperature (see Figure 17).

The limited temperature θ_{lim} is given by:

$$\theta_{lim} = d_0 + d_1 \cdot N_s + d_2 \cdot \frac{A}{L_r} + d_3 \cdot \Phi + d_4 \cdot \frac{1}{\ell_3} \qquad (9)$$

where:

N_s is the normal force in the hogging reinforcement [N]

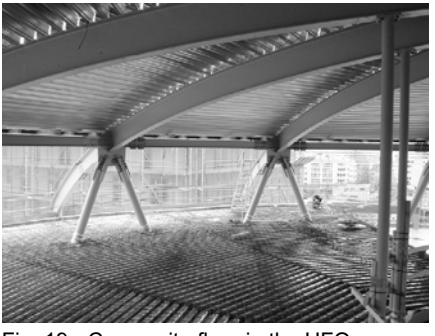
The factors d_0 upto d_4, for both normal and lightweight concrete are given in EN 1994-1-2;table D.4. In Figure 18 a condensed version is given. For intermediate values linear interpolation is allowed.

Concrete	Fire resistance [min]	d_0 [°C]	d_1 [°C] . N	d_2 [°C] . mm	d_3 [°C]	d_4 [°C] . mm
Normal	60	867	$-1{,}9\cdot10^{-4}$	-8,75	-123	-1378
weight	90	1055	$-2{,}2\cdot10^{-4}$	-9,91	-154	-1990
concrete	120	1144	$-2{,}2\cdot10^{-4}$	-9,71	-166	-2155

Fig. 18 - Condensed version of EN1994-1-2; table D.4

When the isotherm in the rib (Y_1) is higher than the depth of the steel sheet (h_2), the ribs can be neglected. For this situation a conservative approximation is given in EN 1994-1-2.

CASE: COMPOSITE FLOOR IN UFO ZOETERMEER



In the design of the Ufo a propped Comflor 70 is applied. The span of the floor is maximum 3,5 meters and the live load is 5 kN/m2. A fire resistance of 30 minutes is required.

According the design tables of the manufacturer a slab thickness of 120 mm is sufficient (figure 19). As a consequence of installations and also to satisfy vibration requirements a thickness of 170 mm is chosen.

Fig. 19 - Composite floor in the UFO

ComFlor 70 Overspanningstabellen - Grindbeton (2.400 kg/m³)

Brandwerendheid	Overspanning	Vloerdikte	Maximale overspanning [m] 0.90 mm Totale nuttige belasting [kN/m²]			1.20 mm		
[minuten]	*Staalplaat-betonvloer*	*[mm]*	3.5	5.0	10.0	3.5	5.0	10.0
30 min	Enkelvelds	120	3,60	3,60	3,20	3,60	3,60	3,20
		150	3,85	3,85	3,85	4,25	4,25	3,95
		180	3,85	3,85	3,85	4,25	4,25	4,25
	Meervelds	120	3,85	3,85	3,35	4,20	4,20	3,35
		150	3,85	3,85	3,85	4,25	4,25	4,25
		180	3,85	3,85	3,85	4,25	4,25	4,25

Figure 20: Design table Dutch Engineering

NOTE: The *tables of the manufacturers normally give sufficient information to design a composite floor for fire as well as for normal room temperature. These tables are usually based on tests and not on calculations. Therefore in special situations, when the information of the tables is not applicable, just a few manufacturers in the Netherlands are able to give more advice. That's why the advantages of composite floors are not optimally used.*

COMPOSITE COLUMNS

The calculation model given in EN1994-1-2 may only be used for columns in braced frames and exposed on all sides according the standard temperature-time curve. The calculation model for the calculation of the resistance of axial compressed columns in fire situation is split up in two separate parts:

1. Calculation of the design value of the temperature field in the composite section after a certain time of exposure to fire according a heat flow calculation mentioned in EN 1991-1-2. For the determination of this temperature field normally numerical calculations are necessary.
2. Calculation of the design value of the axial buckling load $N_{fi,Rd}$ for the temperature field as determined in step 1 .

The design value of a composite column under axial compression should be obtained from:

$$N_{fi,Rd} = \chi N_{fi,pl,Rd} \qquad (10)$$

In this expression χ is the buckling factor according buckling curve c of EN 1993-1-1;6.3.1 and depending of the relative slenderness during fire.
The relative slenderness follows from:

$$\overline{\lambda}_\theta = \sqrt{N_{fi,pl,R} / N_{fi,cr}} \qquad (11)$$

In witch the design value of the plastic resistance in fire situation can be obtained from:

$$N_{fi,pl,Rd} = \sum_j \left(A_{a,\theta}\, f_{ay,\theta}\right) / \gamma_{M,fi,a} + \sum_k \left(A_{s,\theta}\, f_{sy,\theta}\right) / \gamma_{M,fi,s} + \sum_m \left(A_{c,\theta}\, f_{c,\theta}\right) / \gamma_{M,fi,c} \qquad (12)$$

And the Euler buckling load or elastic critical load in de fire situation from:

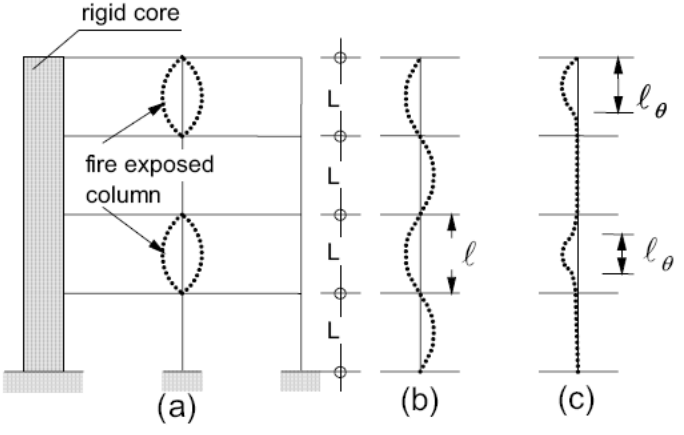
$$N_{fi,cr} = \pi^2 (EI)_{fi,eff} / \ell_\theta^2 \qquad (13)$$

For the calculation of the effective flexural stiffness de values are reduced with the factor $\varphi_{i,\theta}$ to take into account the effect of thermal stresses.

$$(EI)_{fi,eff} = \sum_j \left(\varphi_{a,\theta}\, E_{a,\theta}\, I_{a,\theta}\right) + \sum_k \left(\varphi_{s,\theta}\, E_{s,\theta}\, I_{s,\theta}\right) + \sum_m \left(\varphi_{c,\theta}\, E_{c,sec,\theta}\, I_{c,\theta}\right) \qquad (14)$$

The buckling length of the columns may be determined according Figure 21.
A column at the level under consideration, fully connected to the column above and below, may be considered as effectively restrained at such connections, provided that the resistance to fire of building elements, which separate the levels under consideration, is at least equal to the fire resistance of the column.

In EN1994 part 1-2 design tables and calculation rules are given for different kinds of composite columns. For a more exact calculation of concrete filled hollow sections the special developed software program ”Potfire” can be used.



a) section through the building
b) deformation mode at room temperature
c) deformation mode at elevated temperature

Fig. 21 - Structural behavior of columns in braced frames.

CASE: COMPOSITE COLUMN IN UFO ZOETERMEER



Circular composite column with a totally encased steel section
Concrete: diameter 700 mm (C30/35)
Steel profile HD 400 x 216 (S355)
Reinforcement 8 ∅ 25 (S500)

$L_{by} = l_{bz} = 5400$ mm

$G_k = 8762$ kN
$Q_k = 2394$ kN $\psi = 0,5$

$N_{pl,Rd} = 19.376$ kN
$N_{Rd,z} = 16.560$ kN

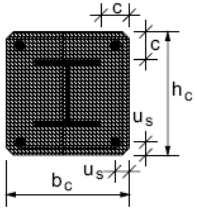
$N_{fi,d} = 8762 + 0,5 \times 2394 = 9959$ kN

$\eta = 9959 / 16.560 = 0,6$

Fig. 22 - Composite column in the UFO

To verify the column Table 4.4 (see Figure 23) of EN 1994-1-2 is used.
$u_s = 60$ mm
$c = 350 - 200x\sqrt{2} = 67$ mm
$b_c = h_c = 700$ mm

b_c and $h_c > 350$ mm \
$u_s > 30$ > so column is OK
$c > 50$ /



		Standard Fire Resistance					
		R30	R60	R90	R120	R180	R240
1.1	Minimum dimensions h_c and b_c [mm]	150	180	220	300	350	400
1.2	minimum concrete cover of steel section c [mm]	40	50	50	75	75	75
1.3	minimum axis distance of reinforcing bars u_s [mm]	20*	30	30	40	50	50
	or						
2.1	Minimum dimensions h_c and b_c [mm]	-	200	250	350	400	-
2.2	minimum concrete cover of steel section c [mm]	-	40	40	50	60	-
2.3	minimum axis distance of reinforcing bars u_s [mm]	-	20*	20*	30	40	-

NOTE: *) These values have to be checked according to 4.4.1.2 of EN 1992-1-1

Fig. 23 - Minimal cross-section dimensions, minimum concrete cover of steel section and minimum axis distance of the reinforcement bars, of composite columns made of totally encased steel sections.

NOTE: *The tables for columns given in the EN 1994-1-2 are easy to use. However for a lot of columns that are often used, tables are not given. Especially for composite columns made of concrete filled hollow sections, which are often used in the Netherlands, additional design tables and/or software are needed.*

ADVANCED CALCULATION MODELS

Advanced calculation models shall provide a realistic analysis of structures exposed to fire. Compared with tabulated data and calculation models as given in the EN 1994-1-2, advanced calculation models give an improved approximation of the actual structural behaviour under fire conditions. The thermal response model shall consider the thermal actions according EN1991-1-2. At this moment EN1991-1-2 is under discussion in the Netherlands so advanced calculation rules are not often used.

CONCLUSION

- In the Netherlands composite beams are normally designed without concrete encasement. To achieve the necessary fire protection the beams are often protected by coating or cladding. In EN 1994-1-2 tables for composite beams without concrete encasement are not given, also software according the simple calculation models is not available for these types of composite beams.
- The tables of the manufacturers normally give sufficient information to design a composite floor for fire as well as for normal room temperature. Only in special situations, when the information of the tables is not applicable, more advanced software or tables are needed.
- The tables for columns given in EN 1994-1-2 are easy to use. However for a lot of columns that are often used, tables are not given. Especially for the composite columns made of concrete filled hollow sections, which are often used in the Netherlands, additional design tables and/or software is needed.
- Advanced calculation models are not often used in the Netherlands because of a discussion about thermal actions according EN1991-1-2.

REFERENCES

[1] ENV 1994-1-2: 2005 (E); Eurocode 4 – Design of composite steel and concrete structures – part 1-2: General rules – Structural fire design.
[2] Difisek, part 2, 2005; Thermal Response by L. Twilt, TNO Bouw, The Netherlands

Predicting the Standard Fire Behavior of Composite Steel Beams

GUILLERMO A. CEDENO
School of Civil Engineering, Purdue University
West Lafayette, Indiana, United States of America
gcedeno@purdue.edu

AMIT H. VARMA
School of Civil Engineering, Purdue University
West Lafayette, Indiana, United States of America
ahvarma@purdue.edu

JAY GORE
Vincent P. Reilly Professor of Mechanical Engineering, Purdue University
West Lafayette, Indiana, United States of America
gore@purdue.edu

ABSTRACT

This paper presents the development and verification of an analytical approach based on the finite element method for modeling and predicting the standard fire behavior of composite steel beams. This approach consists of two sequentially coupled numerical analysis steps. The first step conducts nonlinear heat transfer analysis of the composite beam for the thermal loading applied using the gas furnace. The analysis was conducted using a detailed 3D finite element model of the composite beam inside the furnace. The results included the complete thermal response (nodal temperature histories) of the beam. The second step conducts nonlinear stress analysis of the composite beam for the applied structural loading and the thermal response from the first step. This analysis was conducted using two types of models: (i) detailed models using solid and shell elements, and (ii) simplified models using shell and beam elements for the concrete slab and steel beam, respectively. This two-step analytical approach was used to model and predict the standard fire behavior (thermal and structural) of ten composite beam specimens tested by other researchers. The comparisons of the experimental and analytical results are presented in this paper. These comparisons indicate that the analytical approach (using either SS or SB models) predicts the standard fire behavior of composite steel beam with reasonable accuracy. The verified approach is recommended for conducting parametric studies, and for evaluating the realistic fire behavior of composite beams with restraints.

1. INTRODUCTION

Steel building floor systems typically consist of steel beams supporting concrete slabs, where the slabs have metal decks at the bottom to serve as stay-in-place formwork. The steel beams are made composite with the concrete slabs by welding shear connectors, for example, headed shear studs to the top flanges. These *composite* steel beams are used extensively due to their economic and structural advantages. The fire performance of composite steel beams is assessed by conducting standard fire tests, and it is expressed as the design fire resistance rating (FRR) value determined from these test results. The prescriptive design approach

recommended by current building codes [IBC 2006, NFPA 2003] requires these design FRR values to determine the suitability of members and assemblies.

The ASTM E119 fire test [ASTM 2005] has been the basic and traditional standard fire test in the United States. Structural members and assemblies are tested in gas furnaces, where they are exposed to heating following the standard air time-temperature (T-t) curve [ASTM 2005]. The standard specifies the testing requirements including the minimum specimen sizes, loading conditions, and instrumentation layout for measuring temperatures inside the furnace and the specimen. The test results are used to determine the design FRR value, which is defined as period of time (expressed in hours, e.g., 1-h etc.) that the specimen withstands the fire exposure without reaching any of the specified failure criteria. The standard fire test procedures and air time-temperature (T-t) curves adopted in different countries and by the International Organization for Standardization (ISO 834) are very similar [Lie 1992]. As a result, standard fire tests conducted in different countries can be related to each other effectively [Buchanan 2002].

Standard fire tests of composite beams are costly and limited. Support conditions are difficult to reproduce in consecutive tests and in different testing furnaces. The standard fire test subjects the specimens to incident heat fluxes that may vary depending on the size of the furnace and its volume of radiating gas. Even greater differences can be identified when comparing the furnace sizes and incident heat fluxes with those corresponding to real compartment fires [Wong 2005]. The results from these standard tests include temperatures at several points within the cross-section and the vertical deflections at midspan. The ASTM fire test [ASTM 2005] does not impose any limitations on the vertical deflections of the composite beam. As a result, the comparisons of fire performance between different composite beam tests are further influenced by judgment. The standard fire test does not provide direct knowledge of the fundamental behavior, 3D stresses and strains, and failure time depending on inelastic deflections.

Currently, there is a significant need for developing analytical approaches for: (i) predicting, and (ii) modeling the fire behavior of structural components and systems. These approaches are needed to develop fundamental knowledge of the structural behavior of building components and systems under fire loading. The recent findings of the 9/11 World Trade Center (WTC) collapse investigations emphasize the need for such analytical models and approaches that can be used to develop *structural performance-based* fire resistant design guidelines in the future [Sunder et al. 2005].

Motivated by these research findings and need, this paper presents an analytical approach for modeling and predicting the complete behavior of composite steel beams subjected to standard fire tests. The approach is based on the finite element method, and it consists of two sequentially coupled numerical analysis steps: (i) The first step conducts nonlinear heat transfer analysis of the composite beam for the thermal loading applied by the gas furnace. (ii) The second step conducts nonlinear stress analysis of the composite beam for the applied mechanical loading and the thermal response from the first step.

This analytical approach was used to model and predict the standard fire behavior of ten composite beam specimens tested by other researchers. These models were developed and analyzed using ABAQUS [Hibbitt et al. 2007], which is a commercially available finite element software used extensively by structural engineers. The comparisons of the experimental results and predictions are

presented in the paper to verify the analytical models and approach. The verified models can be used by structural engineers in the future to conduct parametric studies and to model composite beams and floor systems while investigating the overall fire behavior of 3D building structures.

2. BACKGROUND

A comprehensive literature review of standard fire tests conducted on composite steel beams by different researchers from around the world is presented in Cedeno and Varma (2006). It also includes the details of various analytical models that have been developed by different researchers for predicting and modeling the fire behavior of composite steel beams. This comprehensive literature review is beyond the scope of this paper. This background section summarizes the details of some of the standard fire tests of composite beam specimens that will be modeled in this paper. It also outlines the details of the numerical models that are related to the approach presented in this paper.

Wainman and Kirby (1987) reported two standard fire tests that were conducted on simply supported unprotected composite steel beams. The tests were identified as *Fire Test 15* and *Fire Test 16*. The specimens consisted of 254 x 146 x 43 UB steel beams that were connected to flat reinforced concrete slabs using headed shear studs. The slab widths and depths were equal to $0.642m$ and $0.130m$, respectively. The slab reinforcement consisted of $0.008m$ diameter steel bars spaced $0.20m$ longitudinally and $0.10m$ transversely. Both specimens spanned $4.50m$ and were constructed similarly. They were tested with different mechanical loading. Four concentrated loads equal to $32.5kN$ were applied in *Fire Test 15* and those equal to $62.4kN$ were applied in *Fire Test 16*. The loads were centered about the midspan and were $0.25L$ apart. Local and lateral-torsional buckling were not observed in both tests, and the shear connectors performed well. Flexural failure occurred in both tests when the section plastic moment capacity was reached at elevated temperatures.

Newman and Lawson (1991) reported four tests on simply supported protected composite steel beams. The specimens consisted of 305 x 102 x 33 UB steel beams that were connected to concrete slabs using headed shear studs. The slabs were built compositely with $0.060m$ open trapezoidal steel decks, and were reinforced with A142 steel meshes. The slab widths and depths were equal to $1.125m$ and $0.125m$, respectively. The composite beam specimens spanned $L = 4.50m$, and were constructed similarly. They were subjected to similar mechanical loading consisting of four concentrated loads equal to $71.7kN$ centered about the midspan and $0.25L$ apart. The composite beam specimens had different fire protection materials. The effects of filling and not filling the voids between the protected beam and the steel deck were also investigated. In the first test the voids were filled and in the rest they were left unfilled. The experimental results indicated that the failure was due to tensile yielding of the steel beam and leaving the voids unfilled reduced the fire resistance time by up to 13%.

Zhao and Kruppa (1995) also reported four fire tests on simply supported composite steel beams as a part of a comprehensive test program. The tests were identified as *Test 1*, *2*, *3*, and *4*. The test specimens consisted of IPE300 steel beams that were connected to flat concrete slabs using headed shear studs. The slab widths were equal to $1.20m$, $1.60m$, $0.80m$, and $1.20m$, respectively, and the slab depths were

equal to $0.120m$. The composite beams spanned $L = 4.90m$. The mechanical loading level varied for the four tests. Four concentrated loads equal to $102.5kN$, $102.5kN$, $67.5kN$, $33.5kN$ were applied in *Tests 1*, *2*, *3*, and *4*, respectively. These loads were also centered about the midspan and $0.25L$ apart. The steel beams were protected with mineral wool in *Tests 1*, *2*, and *3*, and left unprotected in *Test 4*. It was reported that failure occurred due to concrete crushing for protected steel beams and due to steel plastification for the unprotected steel beam.

Huang et al. (1999) presented a 3D nonlinear procedure to model the structural behavior of composite beams under fire loading. It is important to note that this procedure does not include thermal analysis of the composite beam, which has to be conducted separately and the temperatures input to the structural analysis procedure. The steel beam is modeled with a two-node line element that allows distribution of temperatures, stresses, and strains by dividing the cross-section into segments. The concrete slab is modeled using layered flat shell elements, where each layer can have different temperatures and material properties. The reinforcing bars are modeled using smeared steel layers within the concrete slab elements. Two-node elements of zero length are used to model the shear connectors. This numerical procedure was incorporated into VULCAN, which is a special program for modeling the fire behavior (structural) of 3D steel framed buildings. The simplifications involved in this procedure prevent the modeling of steel beam local buckling, and concrete slabs with trapezoidal steel decks.

3. ANALYTICAL APPROACH AND VERIFICATION

Composite beams subjected to the standard fire test exhibit a complex response. For example, the standard fire exposure subjects the specimen volume to increasing temperatures. This leads to increasingly nonlinear thermal properties for the structural materials and the furnace air surrounding the specimen. The nonlinear rise of temperatures within the specimen volume leads to thermal expansion and degradation of strength and stiffness of the structural materials. These effects combine to produce extended plastification throughout the specimen and large deformations. Robust computational techniques are required to predict the highly nonlinear heat transfer and stress responses of composite beam specimens.

An analytical approach based on the finite element method was developed and implemented using ABAQUS [Hibbitt et al. 2007] for predicting the complete standard fire behavior of composite steel beams. It consisted of two sequentially coupled numerical analysis steps:

- The first step conducted nonlinear heat transfer analysis of the composite beam for the thermal loading (air T-t curve) applied by the gas furnace. An approximate approach that includes the size of the furnace was used to compute the heat flux over the boundary surfaces of the specimen. The analytical results included the complete thermal response (nodal T-t curves) of the composite beams.
- The second step conducted nonlinear stress analysis of the composite beam for the applied mechanical loading and the thermal responses from the first step. The analytical results included the complete structural behavior of the composite beam including the displacements and 3D stresses and strains.

Both the nonlinear heat transfer and stress analyses were conducted using two types of models: (i) detailed SS model using solid and shell elements, and (ii) simplified SB model using shell and beam elements for the concrete slab and steel

beam, respectively. Temperature-dependant thermal properties and constitutive models were used for the concrete and steel elements. The effects of nonlinear geometry and large deformations and strains were also included in the analyses. The analytical approach was used to model and predict the standard fire behavior of ten composite beam specimens. The following sub-sections 3.1 – 3.4 present the details of the analytical models, and the comparisons of the experimental and analytical results.

3.1. Step 1 - Thermal Analysis

The furnace air time-temperature (T-t) curve can be used to compute the heat flux on the boundary surfaces of the composite beam specimen. This heat flux can be approximated using Eq. (1) and (2) that are recommended by Wang (2002):

$$q = h_f \left(T_g - T_s \right) \tag{1}$$

$$h_f = h_c + h_r \tag{2}$$

Where, T_g is the temperature of the air, T_s is the temperature of the boundary surface of the structural member, h_f is the total heat transfer coefficient, h_c is the convective part, and h_r is the radiative part. Eurocode 1 Part 1.2 [CEN 2002] recommends values of h_c equal to $9 W/m^2 K$ and $25 W/m^2 K$ for surfaces in contact with ambient air and exposed to standard fire respectively. The radiative heat transfer part (h_r) was assumed to be equal to zero for surfaces in contact with ambient air.

The radiative heat transfer part for the surfaces exposed to fire were determined following the procedure proposed by Wong (2005) and Ghojel (1998). This procedure was developed to predict the temperatures of structural steel under standard or natural fires, and it explicitly includes the compartment size effect. The heated gas is assumed to be a non-grey gas mixture and the specimen is assumed to be a black body located in the compartment enclosure. Thus, the part of the heat transfer coefficient due to radiation can be computed as:

$$h_r = \varepsilon_{eq} \sigma \left(T_g^2 + T_s^2 \right) \left(T_g + T_s \right) \tag{3}$$

$$\varepsilon_{eq} = \frac{\varepsilon_g T_g^4 - \alpha_g T_s^4}{T_g^4 - T_s^4} \tag{4}$$

Where $\sigma = 5.67 \times 10^{-8} W/m^2 K^4$, ε_{eq} is an equivalent emissivity, ε_g is the total gas emissivity, α_g is the total gas absorptivity. Based on charts compiled for the radiating gases present in the mixture and using a regression technique Wong (2005) derived expressions for ε_g and α_g for practical ranges of T_g and T_s. The compartment size effect is included through the mean beam length of gases, L_m,

that is related to the volume of gas present in the fire compartment radiating to the enclosure. For rectangular fire compartments an expression to compute L_m was given as:

$$L_m = \frac{1.8hw}{h + w + \frac{hw}{L}} \tag{5}$$

Where h, w, L are the height, width, and depth of the compartment. Thus, α_g and ε_g can be computed using Equations 6 and 7:

$$\alpha_g = X_1 T_s^{X_2} T_g^{X_3} \tag{6}$$

$$\varepsilon_g = X_4 + X_5 T_g \tag{7}$$

Where X_1, X_2, X_3, X_4, and X_5 are coefficients that depend on L_m and whose values for practical dimensions of compartments up to a maximum of $500m^2$ were also given by Wong (2005).

In ABAQUS [Hibbitt et al. 2007] the convective heat flux on a surface can be computed using Equation 8, where h is a film coefficient.

$$q = h\left(T_g - T_s\right) \tag{8}$$

Considering the similarities between Equations (1) and (8), the values of h (film coefficient) for the analyses were computed using Equations (2) – (7). These equations calculate the heat flux acting on the specimen surfaces using values for h_c, T_g, T_s, L_m, and the procedure outlined above. A FILM user subroutine was developed using Equations (2) - (7) to compute and provide the film coefficient (h), and thus the heat flux acting on the boundary surfaces of the specimen.

Two 3D thermal analysis models (SS and SB) were developed using the finite element method. In the SS model, the concrete slab was modeled using eight-node continuum (DC3D8) elements, the reinforcing bars were modeled using two-node truss (DC1D2) elements, and the steel beams were modeled using four-node shell (DS4) elements for heat transfer analyses. Thermal resistance between contact surfaces was not considered, and TIE constraints were used to enforce equal temperatures for surfaces in thermal contact. TIE constraints were also used to provide temperature continuity between the reinforcing bars and the concrete nodes at the same locations. Temperature dependant density, conductivity, and specific heat were used for the concrete and steel materials according to Eurocode 4 Part 1.2 [CEN 2004]. Although migration of water vapor was not included, the latent heat of the concrete moisture was included implicitly in the specific heat of concrete. Figure 1 shows an example of the SS model for thermal analysis.

In the SB model, the concrete slab was modeled using four-node shell (DS4) elements, and the steel beam was modeled using two-node truss (DC1D2) elements. Figure 5 shows an example of an SB model for thermal analysis. The (DC1D2) truss element cannot compute the heat transfer through the steel beam section. It was used to make the thermal analysis model compatible with the corresponding SB model used for stress analysis (presented later in section 3.2). In order to make up for this limitation, a 2D model of the composite beam section depth was developed to obtain the time-temperature histories of different locations within the steel beam section. The 2D model used four-node planar (DC2D4) elements throughout the cross section. Figure 6 shows an example of the 2D model for the composite beam section.

The capabilities of the thermal analysis approach will be illustrated using comparisons of analytical results with the experimental results (measured temperatures) from one of the standard fire tests reported by Wainman and Kirby (1987). The fire test was conducted at Warrington Research Centre and was identified as *Fire Test 15*. The composite beam was unprotected and heated in a gas furnace, where the air temperature was controlled to follow the ISO 834 T-t curve. The construction details of the specimen were presented in Section 2. Temperatures were measured at five locations along the length of the bottom flange, and at four locations along the length of the web and top flange of the steel beam of the beam specimen.

The measured furnace air T-t curve was used as input for conducting the thermal analysis. The furnace dimensions used in the analysis were: $L = 4m$, $w = 3m$, and $h = 1.8m$. The calculated mean beam length L_m was equal to $1.58m$. Figure 1 shows the SS model that was developed for the composite beam specimen of *Fire Test 15*. Figures 2, 3, and 4 show comparisons of the experimentally measured and analytically predicted temperatures for the bottom flange, web, and top flange of the steel beam. The experimental temperatures correspond to the averages of the measurements along the specimen length. These comparisons show very good agreement between the measured and predicted temperatures, especially for the beam bottom flange. In Section 3.2 it will be shown that the T-t history of the bottom flange has the most significant influence on the computation of the mechanical response of composite beams. Figures 5 and 6 show an SB model and a section model for conducting similar thermal analyses. The results from these models were very similar to those shown in Figures 2-4, and are not repeated here for brevity. Similar comparisons were also obtained between the experimental results and the analytical predictions for other composite beam standard fire tests. These comparisons indicate that the thermal analysis approach is capable of predicting the temperature histories and gradients throughout the volume of the specimen subjected to the standard fire test.

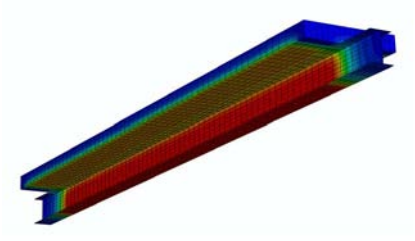


Fig. 1 - SS model for thermal analysis

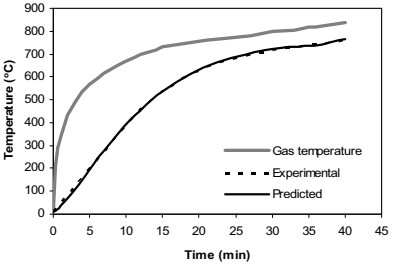


Fig. 2 - Comparison for the bottom flange

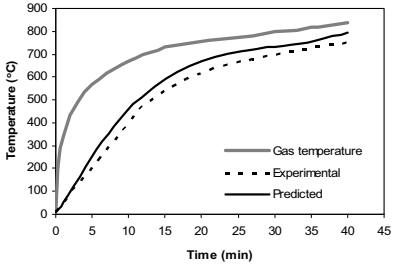


Fig. 3 - Comparison for the web

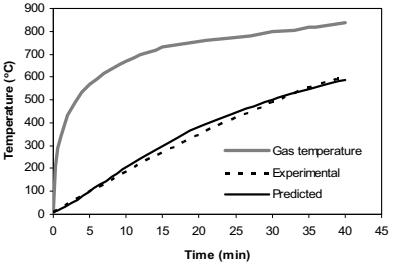


Fig. 4 - Comparison for the top flange

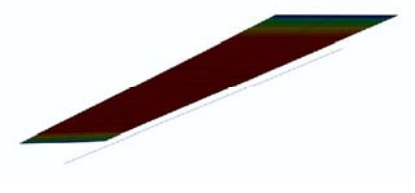


Fig. 5 - SB model for thermal analysis

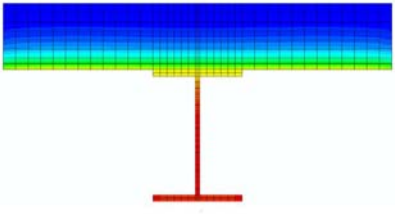


Fig. 6 - Section model for thermal analysis

3.2. Step 2 - Stress Analysis

Two 3D structural analysis models (SS and SB) were developed using the finite element method. In the SS models, the concrete slab and the steel beam and deck were modeled using eight-node continuum (C3D8R) and four-node shell elements (S4R) with reduced integration, respectively. For reinforced concrete slabs, the reinforcing steel bars were modeled by using two-node truss elements (T3D2) embedded in the concrete elements. Thus, slip was not considered between the bars and the surrounding concrete.

In the SB models, a more simplified mesh of finite elements was used. Four-node shell elements (S4R) with reduced integration were used to model the concrete slab. Longitudinal and transverse steel reinforcing bars were modeled using REBAR elements, which represent layers of reinforcing within the shell (S4R) elements. Two-node beam (B33) elements were used to model the steel beam including the cross-

section shape. In both SS and SB models, composite action between the steel beam and concrete slab was modeled using multipoint constraints. The COUPLING constraint was used for SS models and the BEAM constraint for SB models. These multipoint constraints enforce plane sections to remain plane before and after bending and heating.

The B33 beam element in the SB model requires the time-temperatures histories to be assigned directly in the stress analysis step. This is because the equivalent beam element used in the thermal analysis step was not capable of performing heat transfer analysis through the beam cross-section. The B33 beam element can accept T-t curves for five points within the cross-section. Four of these points are located at the flange tips, and the fifth is located at the web mid-height. The temperatures are interpolated linearly through the flanges and in a parabolic manner through the web. Different temperature magnitudes can be specified for the five points, but they must have the same time-amplitude curve. This is a limitation of the B33 beam element in ABAQUS [Hibbitt et al. 2007]. The time-amplitude of the T-t curve for the bottom flange was chosen to assign temperature histories for the five points through the steel beam section.

The temperature-dependent thermal expansion models and uniaxial stress-strain-temperature (σ-ε-T) models for the concrete and the steel materials were based on those reported in Eurocode 4 Part 1.2 [CEN 2004]. The isotropic multiaxial plasticity model with Von Misses yield surface, associated flow rule, and temperature dependence was used for the steel elements. The concrete damage plasticity model developed by Lee and Fenves (1998) and implemented in ABAQUS [Hibbitt et al. 2007] was used for the concrete elements. This model uses a modified hyperbolic Drucker-Prager yield surface with non-associated flow and multi-hardening in compression. It uses a linear crack surface with damage elasticity after cracking in tension. Geometric nonlinearities were included in the formulations of the finite elements and in the nonlinear stress analysis procedures.

The loads were applied in three consecutive sub steps. The self-weight was applied first, and was followed by the mechanical loads. These loads were kept constant while the thermal loading was applied in the third sub-step. The thermal loads were specified as the nodal T-t histories obtained from the results of the nonlinear heat transfer analysis conducted in Step 1.

3.3. Analytical Predictions of Composite Beam Behavior

The finite element models were used to predict the standard fire behavior of ten composite beam specimens that were tested by other researchers, namely, Wainman and Kirby (1987), Newman and Lawson (1991), and Zhao and Kruppa (1995). The details of the composite beam specimens and fire tests were presented earlier in Section 2. As mentioned earlier, both the SS and SB models were used to predict the behavior of the composite beam specimens.

Wainman and Kirby (1987) reported the results from two fire *Tests 15 and 16*. The details of these specimens were given in Section 2. The experimental results included the midspan deflection-time (δ-t) histories and the failure times for both tests. They also reported the steel and concrete material properties at ambient temperatures. The concrete compressive strength was equal to $30 MPa$; the reinforcing steel yield strength was equal to $600 MPa$; and the steel beam yield strengths in *Tests 15* and *16* were equal to $283 MPa$ and $273 MPa$, respectively. The

furnace air measured T-t curves were reported for both tests. These measured T-t curves were used for the finite element analyses instead of the standard ISO 834 T-t curve. Figures 7 and 8 show the deformed shapes of the composite beam specimen of fire *Test 15* close to failure predicted using the SS and SB models, respectively. Figure 9 and 10 show comparisons of the analytically predicted and experimentally measured midspan displacement-time (δ–t) curves for the composite beam specimens of fire Tests 15 and 16, respectively. These comparisons include predictions using both the SS and SB models.



Fig. 7 - Deformed shape of SS model for fire *Test 15*



Fig. 8 - Deformed shape of SB model for fire *Test 15*

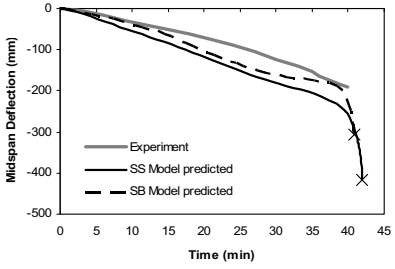


Fig. 9 - Comparisons for fire *Test 15*

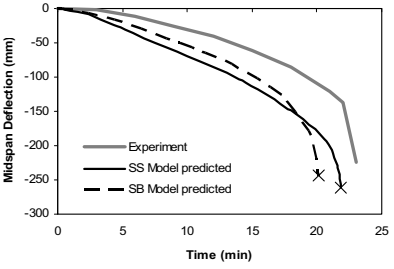


Fig. 10 - Comparisons for fire *Test 16*

Newman and Lawson (1991) reported results from four standard fire tests of composite beams. These tests will be referred as N&L 1, N&L 2, N&L 3, and N&L 4 in this paper. The specimen details were given in Section 2. The experimental results included the midspan deflection-time (δ-t) curves and the failure times for each test. Newman and Lawson (1991) also reported the steel and concrete material properties at ambient temperatures. The concrete compressive strength was equal to $45MPa$; the yield strength of the A142 reinforcing steel mesh was equal to $600MPa$; and the steel beam yield strength was equal to $295MPa$. The steel beams had fire protection in all four tests. Three different fire protection materials were used in the testing program, but their thermal properties and thicknesses (required for conducting the thermal analyses) were neither measured nor reported. The authors directly reported the measured T-t histories for the steel beams underneath the fire protection. The concrete slab temperatures were estimated analytically by conducting thermal analysis (Step-1) using the ISO-834 T-t curve for the furnace air and the measured steel beam T-t histories. The estimated and measured temperatures were used to conduct the stress analysis (Step-2) as explained earlier. Figures 11, 12, 13, and 14 show comparisons of the experimental measured and analytically predict δ-t responses for the four composite beam specimens. The comparisons include predictions using both the SS and SB models.

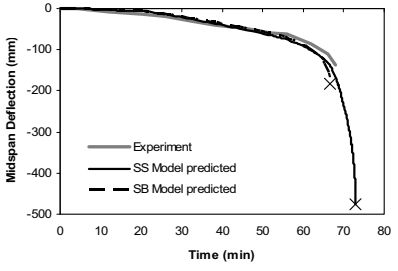


Fig. 11 - Comparisons for fire test N&L 1

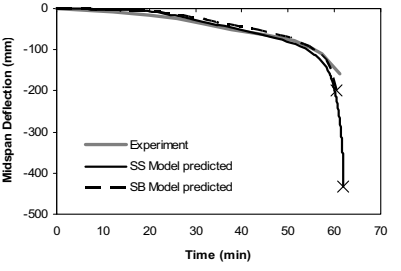


Fig. 12 - Comparisons for fire test N&L 2

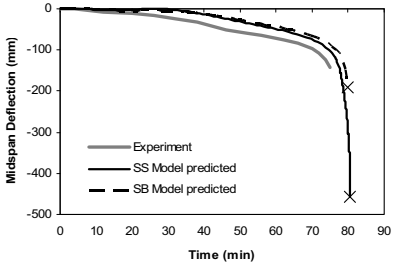


Fig. 13 - Comparisons for fire test N&L 3

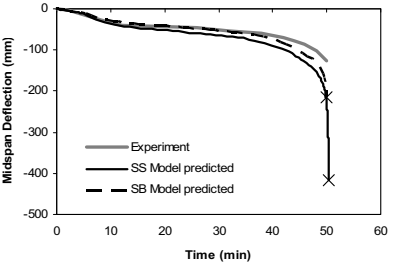


Fig. 14 - Comparisons for fire test N&L 4

Zhao and Kruppa (1995) provided detailed results from the standard fire tests of four composite beam specimens. These tests will be referred as Z&K 1, Z&K 2, Z&K 3, and Z&K 4 in this paper. The specimen details were given in Section 2. The experimental results included the midspan deflection-time (δ-t) curves for specimens Z&K 1 and Z&K 4, and the failure times for all four specimens. The authors reported the steel and concrete material properties at ambient temperatures. The concrete compressive strength was equal to $37MPa$, $37MPa$, $46MPa$, and $34MPa$ for tests 1, 2, 3, and 4, respectively. The steel beam yield strength was equal to $311MPa$ for all four tests. The steel beams had fire protection in the first three tests (Z&K 1, 2, and 3), but the steel beam in the fourth test (Z&K 4) was unprotected. The fire protection used in the first three tests was equal to 0.025 m thick mineral wool; however, its thermal properties were neither measured nor reported by the authors. Hence the following thermal properties were assumed for conducting the thermal analysis: $0.16W/mK$ for thermal conductivity, for specific heat, and $80kg/m^3$ for density of the mineral wool. The thermal analysis (Step-1) was conducted using the ISO-834 T-t curve for the furnace air and the assumed thermal properties for the mineral wool, steel, and concrete. The estimated temperature histories were used to conduct the stress analysis (Step-2) as explained earlier. Figures 15, 16, 17, and 18 show comparisons of the measured and predicted δ-t responses and failure times for the four composite beam specimens. As shown, these comparisons include predictions using both SS and SB models.

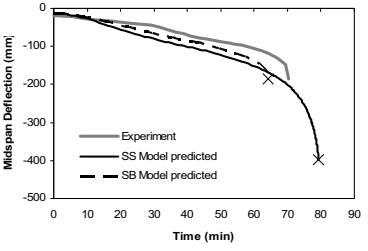


Fig. 15 - Comparisons for fire test Z&K 1

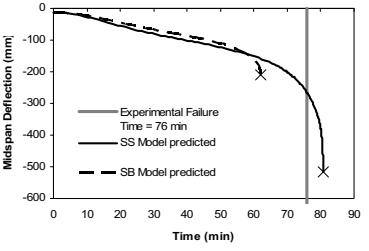


Fig. 16 - Comparisons for fire test Z&K 2

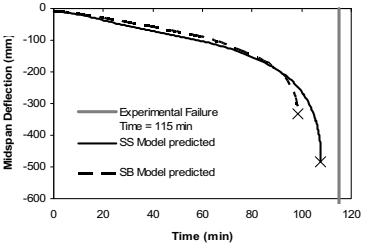


Fig. 17 - Comparisons for fire test Z&K 3

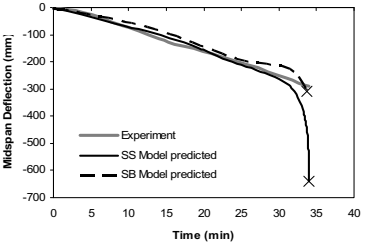


Fig. 18 - Comparisons for fire test Z&K 4

3.4. Comparison of Analytical and Experimental Results

Figures 9-18 illustrated the comparisons between analytically predicted and experimentally measured displacement-time (δ-t) curves for ten composite beam specimens subjected to standard fire tests by different researchers. These comparisons indicate that analytical models with both SS and SB models capture the salient features of composite beam behavior under standard fire loading, and compare favorably with experimental results. In some cases, the SB model shows a spurious change in the deflection rate at high temperatures. For example, this is observed in Figure 9 between the time period of 36 and 40 minutes. This occurs due to the to simplified temperature gradients and histories assumed for the B33 beam finite element in ABAQUS [Hibbitt et al. 2007]. These simplifications were described earlier in Section 3.1.

As mentioned earlier, the experimental results included the failure times ($t_{exp\text{-}f}$) for the composite beam specimens, which were established using criteria set forth by the ISO-834 standard fire test. However, these experimental failure times ($t_{exp\text{-}f}$) were influenced by judgment and practical considerations, for example, the availability and accommodation of instrumentation, sensors, and / or furnace dimensions.

Establishing the failure times from the analytical results (δ-t curves) was somewhat challenging, because the composite beam specimens failed by developing inelastic failure mechanisms producing large displacements over a period of time. This can be observed in Figures 9-18. The failure criteria set forth in BS 476: Part 20 [CEN 1987] were used to define the failure times from the analytical (δ-t) responses. Accordingly, failure was assumed to occur for either of the two following limit states:

(1) midspan deflection exceeding $L/20$, or (2) rate of deflection exceeding $L^2/9000d$ mm/min when the deflection magnitude has exceeded $L/30$. The failure times corresponding to the occurrence of limit states 1 and 2 were identified as $t_{an\text{-}f1}$ and $t_{an\text{-}f2}$, respectively. In these failure criteria, L is the clear span of the specimen expressed in mm, and d is the depth of the specimen also expressed in mm. The second limit state (corresponding to $t_{an\text{-}f2}$) was the governing limit state for all the modeled specimens, because it occurred before the first limit state ($t_{an\text{-}f1}$) in the analytical responses.

An additional failure time ($t_{an\text{-}last}$) was defined as the last point on the analytically predicted δ-t response. It corresponds to the last time a converged result was obtained from the nonlinear stress analysis before the inelastic failure mechanism prevented obtaining numerical convergence for continuing the analysis. This analytical failure time ($t_{an\text{-}last}$) is shown with a circle in Figures 9 - 18.

Table 1 summarizes the experimental and analytical failure times ($t_{exp\text{-}f}$, $t_{an\text{-}f1}$, $t_{an\text{-}f2}$, and $t_{an\text{-}last}$) for the ten composite beam specimens considered in this paper. It includes the results for both the SS and SB models. It also includes comparisons of the analytically predicted and experimentally measured failure times in terms of ratios $t_{an\text{-}f2}/t_{exp\text{-}f}$ and $t_{an\text{-}last}/t_{exp\text{-}f}$. These comparisons show consistently good agreement between the analytical predicted and experimentally measured failure times. Most of the analytical predictions are on the conservative side, i.e., the ratios $t_{an\text{-}f2}/t_{exp\text{-}f}$ and $t_{an\text{-}last}/t_{exp\text{-}f}$ are less than 1.0 with a few exceptions. In some cases, slightly better comparisons were obtained between the experimental failure time ($t_{exp\text{-}f}$) and the last converged point ($t_{an\text{-}last}$) obtained from the analysis.

Table 1 - Comparison of experimentally and analytically obtained failure times.

Fire Test	$t_{exp\text{-}f}$	Model Type	Analytical Results				
			$t_{an\text{-}f1}$	$t_{an\text{-}f2}$	$\frac{t_{an\text{-}f2}}{t_{exp\text{-}f}}$	$t_{an\text{-}last}$	$\frac{t_{an\text{-}last}}{t_{exp\text{-}f}}$
Test 15	35	SS	38	25	0.71	42	1.20
		SB	40	39	1.11	40	1.14
Test 16	22	SS	21	18	0.82	21	0.95
		SB	20	18	0.82	20	0.91
N&L 1	68	SS	69	67	0.99	73	1.07
		SB	NA	66	0.97	66	0.97
N&L 2	61	SS	60	58	0.95	62	1.02
		SB	NA	59	0.97	60	0.98
N&L 3	74	SS	79	77	1.04	80	1.08
		SB	NA	79	1.07	79	1.07
N&L 4	51	SS	49	48	0.94	50	0.98
		SB	NA	49	0.96	50	0.98
Z&K 1	70	SS	74	68	0.97	79	1.13
		SB	NA	63	0.90	64	0.91
Z&K 2	76	SS	74	69	0.91	80	1.05
		SB	NA	60	0.79	62	0.82
Z&K 3	115	SS	98	94	0.82	107	0.93
		SB	95	90	0.78	98	0.85
Z&K 4	35	SS	28	20	0.57	34	0.97
		SB	32	21	0.60	33	0.94

Based on the comparisons shown in Figures 9-18 and Table 1, the analytical approach presented in this paper is recommended for modeling and predicting the standard fire behavior of composite beams.

4. SUMMARY AND CONCLUSIONS

A two-step sequentially coupled numerical procedure based on the finite element method was developed and validated for predicting the behavior of composite beams under standard fire loading. The first step conducted thermal analysis to simulate the nonlinear heat transfer from the furnace to the surfaces of the composite beam specimen, and through its cross-section and length. The second step conducted nonlinear stress analysis to simulate the behavior of the composite beam specimen subjected to structural loads and the thermal response (nodal T-t histories) calculated in the fist step. The finite element models accounted for the nonlinear temperature-dependent thermal and structural properties of the steel and concrete materials and the effects of nonlinear geometry.

Two types of finite element models (one detailed and one simpler) were developed, and used to predict the thermal and structural behavior of ten composite beam specimens subjected to the standard fire test by different researchers from around the world. The analytical results including the: (a) surface and interior T-t curves, (b) midspan displacement-time curves, and (c) predicted failure times compared favorably with the corresponding experimental results for all composite beam specimens. Both the detailed and simple models were found to compare reasonably with each other and the experimental results.

The validated analytical approach and finite element models are recommended for modeling and predicting the standard fire behavior of composite beam specimens. They are also recommended for modeling composite beam specimens while conducting: (a) numerical parametric studies, or (b) complete floor system studies under realistic fire loading.

5. REFERENCES

ASTM (2005). *Standard Test Methods for Fire Tests of Building Construction and Materials, E119*, American Society for Testing and Materials, West Conshohocken, PA.

Buchanan, A. (2002). *Structural Design for Fire Safety*, John Wiley and Sons, Chischester, p. 109.

Cedeno, G.A. and Varma, A.H. (2006). *Behavior and Design of Composite Floor Systems under Realistic Fire Loading*, Preliminary Examination Report, School of Civil Engineering, Purdue University, West Lafayette, Indiana.

CEN (1987). BS 476-20 Fire tests on building materials and structure – Part 20: Method for determination of the fire resistance of elements of construction, European Committee for Standardization, Brussels, Belgium.

CEN (2002). Eurocode 1: Actions on structures, Part 1.2: General actions – Actions on structures exposed to fire, European Committee for Standardization, Brussels, Belgium.

CEN (2004). Eurocode 4: Design of Composite Steel and Concrete Structures, Part 1.2: General rules – Structural fire design, European Committee for Standardization, Brussels, Belgium.

Ghojel, J.I. (1998). "A New Approach to Modeling Heat Transfer in Compartment Fires," Fire Safety Journal, Vol. 31, 227-237.

Hibbitt, Karlsson, and Sorenson (2007). *ABAQUS/Standard Version 6.7*, Hibbitt, Karlsson, and Sorenson, Inc., Pawtucket, RI.

Huang, Z.H., Burgess, I.W., and Plank, R.J. (1999). "The Influence of Shear Connectors on the Behavior of Composite Steel-framed Buildings in Fire," Journal of Construction Steel Research, Vol. 51, 219-237.

IBC (2006). *International Building Code (IBC)*, International Code Council, Inc., Falls Church, VA.

Lee, J., and Fenves, G.L. (1998). "Plastic-Damage Model for Cyclic Loading of Concrete Structures," Journal of Engineering Mechanics, ASCE, Vol. 124, No. 8, 892-900.

Lie, T.T. (1992). *Structural Fire Protection*, ASCE Committee on Fire Protection, American Society of Civil Engineers, New York, p. 15.

Newman, G.M. and Lawson, R.M. (1991). "Fire Resistance of Composite Beams," The Steel Construction Institute Technical Report 109.

NFPA (2003). *Building Construction and Safety Code (NFPA 5000)*, National Fire Protection Association, Quincy, MA.

Sunder, S.S., Gann, R.G., Grosshandler, W.L., Averill, J.D., Bukowski, R.W., Cauffman, S.A., Evans, D.D., Gayle,F.W., Gross, J.L., Lawson, J.R., Lew, H.S., McAllister, T.P., Nelson. H.E., Sadek., F. (2005). "Final Report of the National Consortium Safety Team on the Collapses of the World Trade Center Towers (Draft)," NIST NCSTAR 1, NIST, U.S. Dept. of Comm., Gaithersburg, Maryland.

Wainman, D.E., and Kirby, B.R. (1987). "Compendium of UK Standard Fire Test Data, Unprotected Structural Steel – 1," British Steel Corporation Ref. No. RS/RSC/S10328/1/98/B, Swinden Laboratories, Rotherdam.

Wang, Y.C. (2002). Steel and Composite Structures – Behavior and Design for Fire Safety, Spon Press, London, p. 200.

Wong, M.B., (2005). "Size Effect on Temperatures of Structural Steel in Fire," Journal of Structural Engineering, ASCE, Vol. 131, No. 1, 16-20.

Zhao, B., and Kruppa, J. (1995). "Fire Resistance of Composite Slabs with Profiled Steel Sheet and of Composite Steel Concrete Beams, Part 2: Composite Beams," ECSC – agreement No. 7210 SA 509, CTICM, France.

New Results of Material Analysis regarding the Bauschinger- Effect on the Deflection of Composite Beams

Prof. Dr.-Ing. Jörg Lange
Darmstadt University of Technology,
Darmstadt, Germany
lange@stahlbau.tu-darmstadt.de

Dr.-Ing. Hauke Grages
Donges Stahlbau International Engineering & Construction GmbH
Darmstadt, Germany
Hauke.Grages@Donges.de

ABSTRACT

Aim of the project was to measure deflections of standard steel concrete composite beams, used in office and industrial buildings assess and analyze the reasons for those deformations and develop simple design aids for a realistic calculation of the deflections. This research was necessary, since experience has shown that results do frequently not match the deflections measured on site. This can reduce the serviceability of a structure and lead to high rectification costs. The focus was on the differences between calculations and in-situ behavior by analyzing the measured deflections of beams in structures under construction.

During the measurements it appeared that cambered beams deform more than straight beams. This effect was analyzed in tests and it was found that the reason for this behavior lies in the Bauschinger Effect, rather than in residual stresses. It will be shown when and how this effect should be considered.

INTRODUCTION

Steel concrete composite structures are common practice in today's office and industrial buildings. The combined advantages of steel and concrete lead to a very economic member for wide spanned slabs, especially in terms of high bearing capacity and small dimensions as well as time efficiency due to pre-fabrication.

Steel concrete composite structures are widely used for bridges and industrial buildings as well as for parking lots and multi storey buildings.

By prefabricating the steel substructure time for construction on site is reduced tremendously. Using composite slabs reduces the time for construction further since they replace parts of the reinforcement and are used as formwork. An alternative for composite slabs are partly or full pre-cast concrete elements that also reduce the construction time. The focus of this research project was on commonly used standard steel concrete composite beams as shown in Figure 1.

A building is designed for a special purpose. On one side the design of the bearing capacity ensures the structural integrity; on the other hand the design for serviceability ensures a proper utilization in terms of the users' demands.

To design the bearing capacity of a building theoretical loads are taken into account. They are usually larger than the real and expected loads commonly including a

safety factor. To design the buildings serviceability it is of special necessity to work with realistic loads to calculate the deflections and dynamic response close to reality.

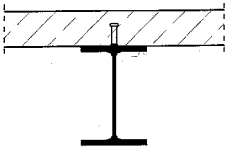


Fig. 1 - Standard section of a composite beam

Due to the trend to longer spans and the ability of composite structures to bridge those spans the design for serviceability becomes more relevant. Often the calculated deflections do not match those seen on site. The knowledge about the real deflections of composite beams can reduce high rectification costs.

In the beginning of the project buildings under construction were assessed. The deflections were measured in all relevant situations starting from the fabrication of the steel beam, via the assembly of the structure until the building was finished and major long term deflections had occurred. The focus was on the history and structural details of the building erection, e.g. whether the beams are supported during casting of the concrete or the deflections are influenced by other structural details like stiff connections. Also material uncertainties resulting from the concrete and residual stresses were taken into consideration.

STATE OF THE ART

Generally the deflection of a steel concrete composite beam is calculated for the following steps of loading with the corresponding second order moment of inertia: The dead load of the construction, i. e. the steel beam and the concrete slab under consideration of temporary propping. Secondly the superimposed dead load (cladding, finishing, mechanical services), thirdly the live load and finally long term influences of the concrete (creep and shrinkage).

Most of the commonly used calculation programs are following this pattern. When all influences are considered and calculated a camber will be assumed for the known dead load and parts of the live load, creep and shrinkage. For those assumptions the beam is assumed to be straight after its history of loading.

Reality shows, that the calculated deformations frequently do not match the real deflections. Reasons for this discrepancy can be that the assumptions made in the calculation are wrong, the theory for calculating the deflection has mistakes or further influences on the deflection behavior of the beam are not taken into account. For this reason it became necessary to compare the calculations with the deflections of composite beams in real buildings to assure that no influences are overseen.

RESULTS OF SITE MEASUREMENT

Basis for the analysis of the deflection of the beams are site measurements. In three parking lots build in composite construction the deflection of the beams were measured. The shape of the beams was measured

- after cambering the beams,
- after welding of the shear studs,
- before and after galvanising, (if the beams were galvanised)
- after erecting the steel structure,
- after concreting,
- after removing the construction supports, if the dead load shall act on the composite beam,
- frequently after finishing the structure for long term deformation.

During the measurement of the beams on site it appeared that especially the deflections of highly cambered beams were larger than calculated.

THE BAUSCHINGER EFFECT

The camber of all beams was fabricated by hydraulic presses as shown in Figure 2.

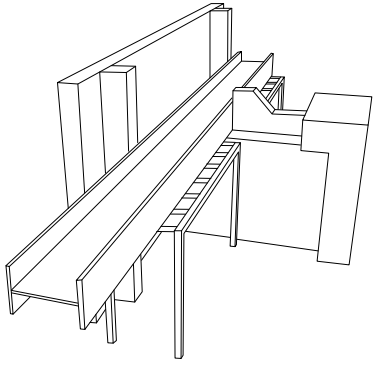


Fig. 2 - Hydraulic press

The press deforms the beam plastically in the middle of the machine's supports. After that the beam is moved about 30 – 50 cm and the beam is locally deformed again. In that manner the entire beam is cambered until it has an ideal shape according to the previously calculated deflection.

At first it was assumed, that the residual stresses implemented by cambering are responsible for the increase of deflections. Therefore tests were accomplished to measure the strains of the beam while cambering. In addition a Finite Element Analysis was performed that simulated the process of cambering. The calculated strains fitted properly to the results of the tests. In the analysis it was simulated that the beam was loaded in the opposite direction of the camber. Just before the load bearing capacity was reached, the deformations increased slightly compared to a non cambered beam. The amount of camber had no influence on the deflection of the beams.

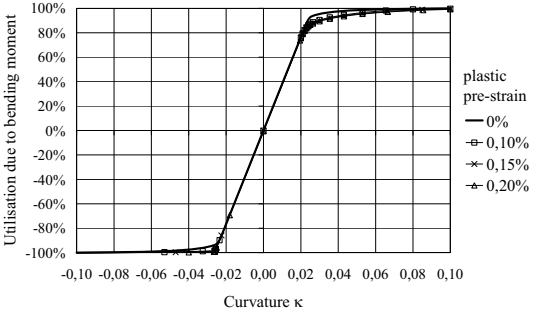


Fig. 3 - Calculated M-κ-diagram for bending beams after varied plastic pre-strain

All cambered beams showed a very similar load-deflection-behavior (Figure 3).

Still the measurements on site gave reason to the assumption that the increase of deformation was depending on the process of cambering. Since the previously described considerations and analysis did not lead to the intended results pre tests were performed to justify further investigation.

Following Hoff & Fischer (1958) tests were performed to gain more information on the influence of the Bauschinger-Effect on the deflection of beams.

Five 1 m long pieces of IPE 100 (grade S355) were loaded above the yield point. The amount of the deflection and thus the plastic deformation was varied. Afterwards the specimens were loaded against the previous deformation again until the yield point was reached (Figures 4-5).

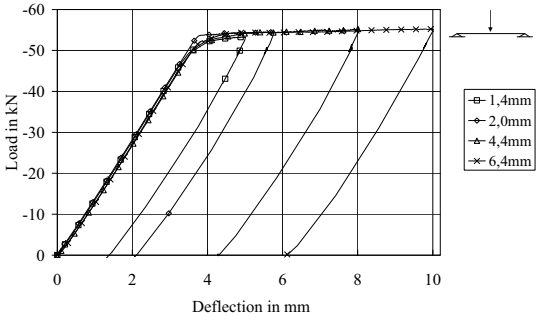


Fig. 4 - Plastic deformation - first load

While the load-deflection graphs of the first loading are nearly identical and bilinear, the course of the graphs changes tremendously when loaded in the opposite direction. Starting at a load of 30% of the bearing capacity the graphs branch out and show a deflection three times larger when reaching the bearing capacity, compared to the reference graph of a non cambered beam. The deflection increases depending on the pre-strain at small loads. The bearing capacity seems not to be influenced by the camber.

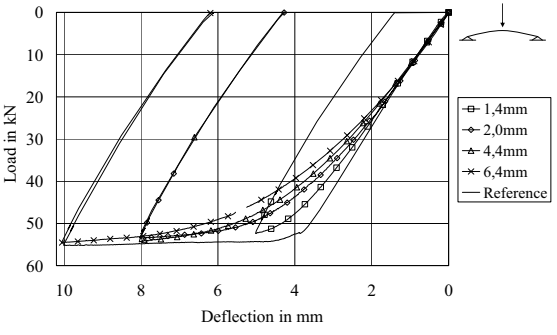


Fig. 5 - Plastic deformation - reversal load

The observed increase of deflection at the measurement on site seems to be initiated by the Bauschinger-Effect, which results form cambering the beams.

The pre-tests have shown that the Bauschinger-Effect affects also standard steel used in structural steelwork and is not limited to high alloyed steel used in mechanical engineering. Still no description could be found that describes the influence of the Bauschinger-Effect on bending beams. Thus it is essential to analyse the material behavior to simulate this effect for the bending of beams.

For the tests 18 m long IPE 220 in steel grade S355 were used. The beams were cambered with a hydraulic press by different amounts. Afterwards the beams were sawn into eight sections. The two partly non deformed sections at the ends could not be used. It was assumed that the inner six sections of 2300 mm length had equal curvature and stresses. The beams were loaded in four points and the deflections were measured (Figure 6).

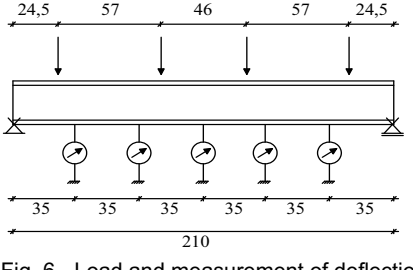


Fig. 6 - Load and measurement of deflection

Table 1 - List of specimens.

Group of specimen	Number of specimen	Average camber 1/100 mm
1	3	0
2	3	828
3	2	893

According to Table 1 three groups of beams with different camber were combined. In Figure 7 the load-deflection-graphs for the tests are shown. It is obvious that the cambered specimen deform stronger than the non cambered beams. As expected the deflection of the beams of group three are larger than those of group two due to a larger amount of cambering.

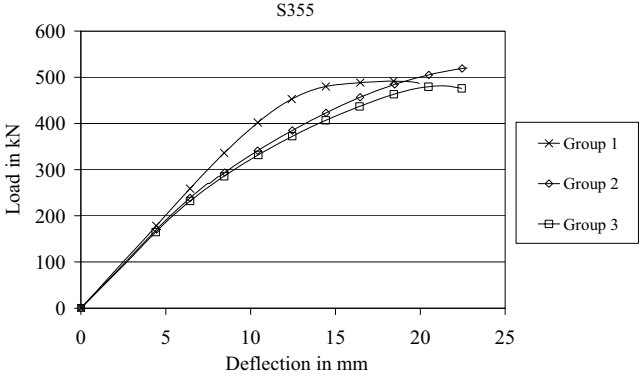


Fig. 7 - Load-deflection-diagram of cambered beams

It was previously proven that the Bauschinger-Effect is responsible for the increase of the deflection of cambered beams. To simulate this effect a material model has to be developed that can be implemented in an analysis program to calculate the resulting deflections. Therefore a material analysis is performed with the steel of the bending specimen. In order to verify the influence of the type of steel the bending beams are made of, further tests with specimen out of S235 were conducted. All tests were performed on hourglass specimen, strain controlled with pre strain of 3, 5, 10, 15 and 20 ‰. The results of the tests with S355 and S235 are shown in Figure 8 and 9.

The bold line gives the elastic-ideal-plastic material model as reference. The influence of the Bauschinger-Effect for both materials can be seen from a pre-strain of 5 ‰. At a strain of 20 ‰ for the S355 the deformations become larger already while unloading the specimen. Thus the Bauschinger-Effect affects the deformation of a cambered steel beam from the first moment of its load history.

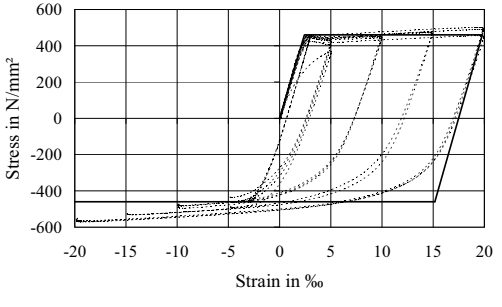


Fig. 8 - σ–ε–diagram for first and reversal loaded specimens out of S355

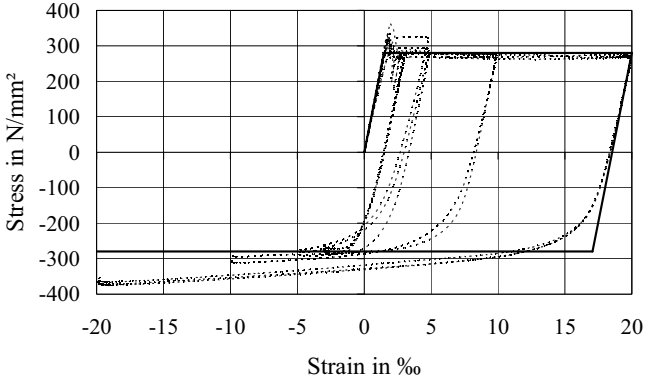


Fig. 9 - σ–ε–diagram for first and reversal loaded specimens out of S235

By comparing the test results for those two materials it appeared that the influence of the pre strain seems to be more at the S355. The curvature of the reversal loading at a pre-strain of 20‰ is higher compared to the S235. Therefore in addition to the performed tests, existing results from cyclic tests with steel S235 and S460 were analyzed.

The results of those cyclic tests for the S460 are shown in Figure 10. Obviously the influence of the Bauschinger-Effect increases with the yield strength of the steel. Especially for a pre-strain of 20 ‰ the deflection increases while unloading the specimen compared to the reference calculated with the bi-linear material law. When reaching the yield strength the deflection is three times the calculated reference.

Most of the existing attempts to find a material model that describes the Bauschinger-Effect are, according to Yamada & Tsuji (1993), oriented at the material model of Ramberg and Osgood.

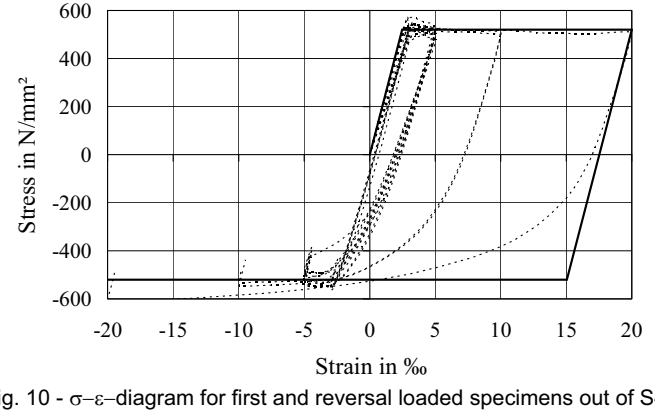


Fig. 10 - σ–ε–diagram for first and reversal loaded specimens out of S460

The shape of stress-strain-relation is usually modeled as a multilinear graph. Thus for each pre-strain a different material model must be specified. This is most inconvenient for the use in an analysis program or in an FEM simulation.

A material model has to be developed, that simulates the material behavior from the reversal point of the load depending on the previous strain. According to the existing models initially the material model from Ramberg-Osgood is used, that describes the stabilized cyclic σ–ε–curve:

(1) $$\varepsilon_a = \frac{\sigma_a}{E} + \left(\frac{\sigma_a}{K'} \right)^{1/n'}$$

Some modifications are necessary since only the first load cycle is relevant and not the stabilized cyclic curve. Due to the distinctive Lüders plateau of the tested steel the stress-strain-relation up to the reversal point is assumed to be elastic-plastic. Under consideration of the material model of Masing the material model of Ramberg-Osgood can be changed to describe the material behavior from the reversal point. Thus:

(2) $$\Delta\varepsilon = \frac{\Delta\sigma}{E} + \left(\frac{\Delta\sigma}{2^{(1-n')} K'} \right)^{1/n'}$$

With this equation a relation is given to describe the material behavior for the reversal curve in dependence of the factors n' and K'. The tests show that the shape of the reversal curve is depending on the pre-strain of the specimen. For the described material model factors for each material had to be searched for each curve so that it corresponds properly with the experimental results.

The following analysis describes the development of the material factors for the S355 as an example. To get those factors for the other Materials S235 and S460 the analysis follows the same pattern. For illustration the point of origin is defined at the reversal point of the load. Since the reversal curve is nearly identical with the elastic line in the following diagrams only the area from $\Delta\sigma$ = 440 N/mm² to $2\Delta\sigma$= 880 N/mm² is shown. In the first picture this area is shown hatched for a pre-strain ε_{pre} = 20‰. The test results are displayed as dotted lines, the calculation results as fat line and the thin line shows the elastic-ideal-plastic reference (Figure 11).

To calculate the curves the following parameters for n' and K' were chosen:

Table 2 - Parameters for n' and K'

pre-strain ε_{pre} in ‰	n'	K'
3	0,175	1650
5	0,175	1360
10	0,175	1250
20	0,175	1220

Since the solidification exponent n' is constant for this material the curvature of the reversal graph is only depending on the solidification coefficient K'. The maximal possible stress is set to the yield stress. Especially for small pre-strain the stresses would become too big otherwise.

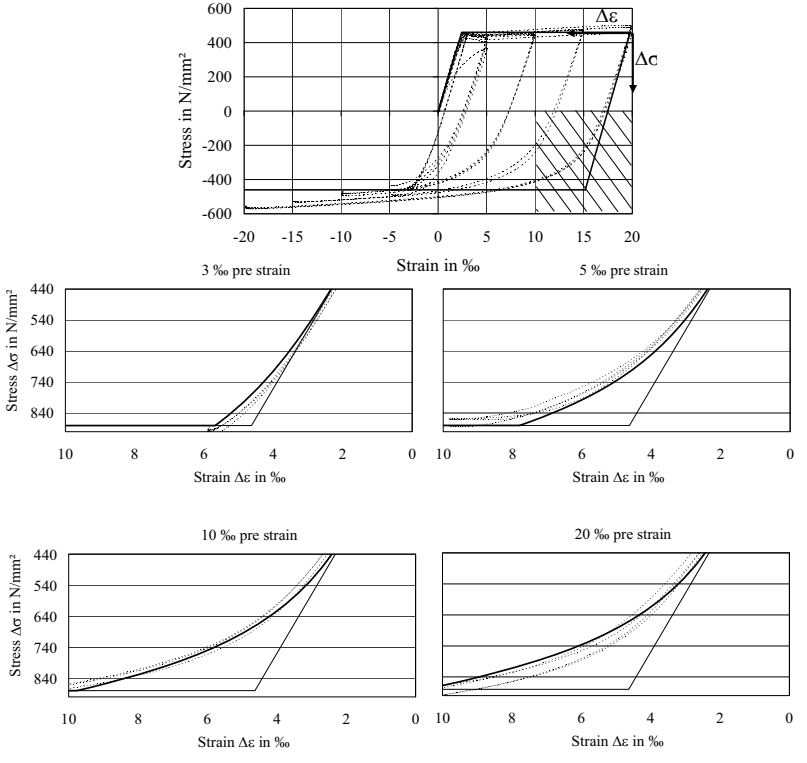


Fig. 11 - σ–ε–diagram for first and reversal loaded after plastic deformation for S355

If K' is displayed related to the pre-strain ε_{pre}, it is possible to describe this curve with the equation:

$$K' = b_1 + \frac{1}{\left(\varepsilon_{pre}\right)^{b_2}} \tag{3}$$

and the variables b_1 and b_2. The amount of pre-strain ε_{pre} must be inserted as decimal number. The parameters b_1 and b_2 are chosen similar to n' and K' until the graphs are similar. Since the Bauschinger-Effect appears only when the steel was plastically deformed the graph begins when ε_{pre} is larger than $f_{y,k}/E$ (Figure 12).

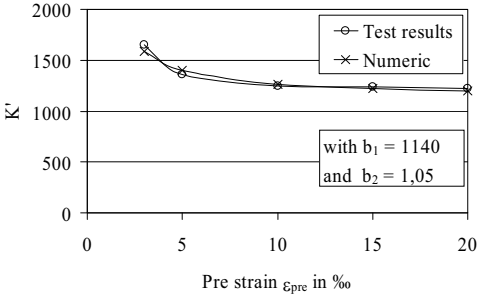


Fig.12 - K'-ε_{pre} -Diagram for reversal loaded specimen out of S355

It is now possible to describe the material behavior from the reversal point just by knowing the previous strain. From the analysis of the other materials the factors b_1 and b_2 can easily be developed following the described pattern. The results are given in Table 3. The major advantage of this material model is that it can easily be implemented into a computer program.

Table 3 – Parameters f_y, n', b_1 and b_2 for tested Materials

Steel	f_y, in N/mm²	n'	b_1	b_2
S235	284	0,17	770	0,88
S355	446	0,175	1140	1,05
S460	525	0,2	1330	1,2

A fiber model was developed to calculate the deflection of a cambered steel beam, considering the Bauschinger-Effect. At first the process of cambering the beam has to be simulated. Depending on the distance of the supports and the distance of pressure points this calculation has to be done until the entire beam is cambered. While deforming the beam with the hydraulic press the material model is elastic-ideal-plastic. While releasing the pressure the previously described material model will be activated if the deformation is plastic.

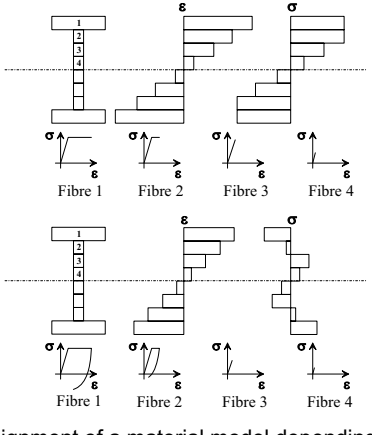


Fig. 13 - Assignment of a material model depending on the pre-strain

In the upper part of figure 13 the strains and stresses in the different fibers are shown while the beam is deformed plastically in the press. After releasing the load strains and stresses are still in the section. They were calculated with the developed material model. This procedure has to be repeated until the entire beam is cambered to the required amount. After this the pre-strain of every fiber is known as well as the residual stresses due to cambering. Thus it is clear which material model has to be chosen for every fiber when the beam is loaded in the opposite direction.

To verify the material model and the simulation by a fiber model, the results are compared with the results of the performed bending tests with the IPE 220 out of S355 already described. First the camber has to be simulated. The 18 m original beam of group 2 (Figure 7) had a camber of 475 mm. For the tests a 2100 mm long part of the beam was loaded. After simulating the camber of the 18,000 mm beam the loading of a 2,100 mm long section according to the performed tests is calculated. In figure 14 the results of the calculation are compared with the test results.

The calculation of the deflection was performed with different combinations of distance of supports and distance of pressure points, while the camber was kept constant. The dotted lines showing the calculation results are close to each other, thus independent of the chosen varieties. Obviously only the amount of camber has major influence. The calculations match the measured deflection well.

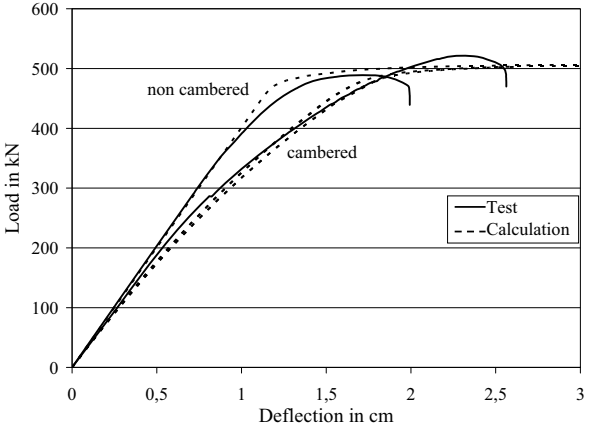


Figure 14 - Comparison of tests and numerical simulation

Thus it is possible to calculate the increase of deflection due to the Bauschinger-Effect with the presented material model. Further calculations with the other developed Material parameters lead to equally good results.

CONCLUSION

It is common practice to camber wide spanned steel beams in steel and composite construction. The process of cambering the beams with a hydraulic press has great influence on the deflection of the beams depending on the amount of camber.

Tests were performed to analyze the material behavior to gain more information about the Bauschinger-Effect. A material model was developed that is able to consider this effect depending on the amount of pre-strain in every fiber of the steel beams section. With the material data of the tests and the developed material model it is possible to calculate the increase of deformation due to the Bauschinger-Effect for commonly used steel of the grades S235, S355 and S460.

With regard to the site measurements the Bauschinger-Effect should be considered in steel and composite construction when the camber exceeds a value of L/200. This is approximately equivalent to a pre-strain of the beams flanges of 4‰ and therefore is susceptible to the Bauschinger-Effect.

REFERENCES

Bauschinger, J. 1881. Über die Veränderung der Elasticitätsgrenze und des Elasticitätsmoduls. Civiling.N.F.

Grages, H., 2007. Beitrag zur Verformungsanalyse von Verbundträgern. PhD.-Thesis, Darmstadt - Germany

Hoff, H. & Fischer, G. 1958. Beobachtungen über den Bauschinger-Effekt an weichen und mittelharten Stählen. Stahl und Eisen 78

Yamada & Tsuji. 1993. Stoffgesetze des Baustahls – Zur Traganalyse des Stahltragwerkes. Festschrift Udo Vogel

Evaluation of adhesive bonding between steel and concrete

Wolfgang Kurz, Prof. Dr.-Ing.
University of Kaiserslautern
Kaiserslautern, Germany
wkurz@rhrk.uni-kl.de

Christopher Kessler, Dipl.-Ing.
University of Kaiserslautern
Kaiserslautern, Germany
ckessler@rhrk.uni-kl.de

Paul Ludwig Geiss, Prof. Dr.-Ing.
University of Kaiserslautern
Kaiserslautern, Germany
geiss@mv.uni-kl.de

Sarunas Turcinskas, Dipl.-Ing.
University of Kaiserslautern
Kaiserslautern, Germany
turcinskas@mv.uni-kl.de

ABSTRACT

At present adhesive bonding as an alternative to mechanical connectors does not belong to the standard practice in structural applications of the building and construction industry. Therefore the scope of this study is to experimentally investigate the behaviour of adhesively bonded joints between steel and concrete. The main attention was focused on shear stressed; tension stressed and combined stressed connections.

To study the typical characteristics of adhesives in combination with steel and concrete different high-strength polyaddition curing adhesives, one polyurethane and two epoxy adhesives, were examined in this study. All tests were conducted at room temperatures. Also different aggregates for concrete such as crushed stone and round edged gravel were used. To promote a good adhesive bond cleaning and pre-treatment of the surface prior to bonding is of outmost importance. Therefore different pre-treatments for steel and concrete surfaces and their effect on the load behaviour and deformation capacity were considered. The concrete surfaces were used as grit-blasted and cut with a diamond saw. The steel adherents were grit-blasted and coated with primer prior to bonding.

INTRODUCTION

In the construction industry the requirements and specifications with respect to geometric and scheduling precision, aesthetics and long-life cycle are highly developed. Thus steel and concrete composite constructions strongly take benefit from prefabricating techniques. The established mechanical joining technologies have been further developed over the past years.

Adhesive bonding allows to create joints avoiding major stress concentrations as they occur in joints e.g. with bolts and anchors in the localized area of load transfer between concrete and steel. However in applications related to steel and concrete structures of the building and construction industry adhesive bonding has not become a commonly used technology. This is assigned to the missing of consolidated information about the load capacity of adhesive joints and their behaviour in a structural steel-concrete connection.

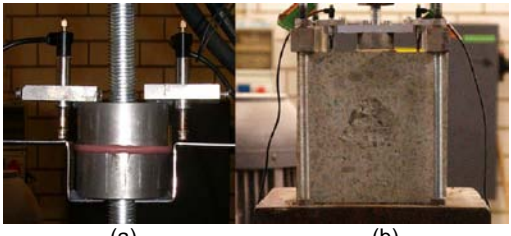
EXPERIMENTAL

Test geometries

Tension tests

To examine the behaviour in tension two different test arrangements were used depending on the examined bonding partners. In the first set up the connection between steel and steel was evaluated (Fig. 1a). Two steel cylinders were bonded together and tested in tensile mode after curing of the adhesive. Both cylinders had a diameter of 50 mm.

In the second setup a steel cylinder was bonded to the surface of a concrete cube. A special fitting supported the cube during the test (Fig. 1b) while the load of the hydraulic cylinder and the displacement close to the adhesive layer were measured. Figure 1 shows both test set-ups.



(a) (b)

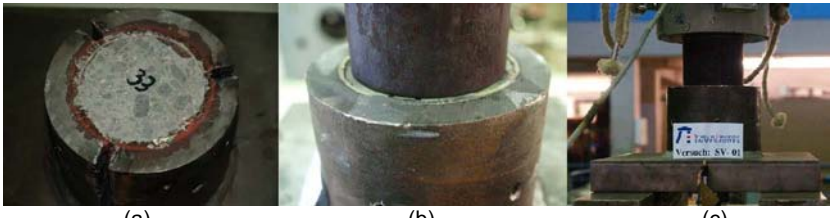
Fig. 1: Specimen and test set up for tension tests

Shear tests

For the evaluation of the shear behaviour cylindrical concrete specimens were bonded into steel tubes (Fig. 2a and 2b). Plastic spacers controlled the thickness of the adhesive layer. The thickness varied from 0.9 to 1.8 mm depending on the dimensional accuracy of the concrete cylinders. The adhesive was injected from a cartridge through the 5 mm boreholes in the walls of the steel tube filling the gap between steel and concrete.

After the curing of the adhesive between steel and concrete the joint was tested by pushing out the concrete cylinder out of the steel tube while the steel tube was supported (Fig. 2b and 2c). During the tests the displacement of the concrete cylinder and the load was measured. The displacement was measured on the lower end of the concrete cylinder versus the corresponding edge of the steel tube. The test setup is shown in Fig. 2c.

To determine the effects of the confinement condition some of the steel tubes were slotted like shown in Fig. 2a.



(a) (b) (c)

Fig. 2: Specimen and test set up for shear tests

Materials and specimen

Steel specimen

For tests only steel cylinders and tubes of the standard building and construction quality category S 235 with yield strength of 240 N/mm² were used. No effect of steel grade on the adhesive bond strength was evaluated.

The diameter of the steel cylinders for tensile tests was chosen as 50 mm. The height of the test cylinders measured 25 mm. These specifications were chosen to eliminate bending effects while loading the cylinders.

The shear tests were performed with steel tubes with an inner diameter of 104.7 mm and an outer diameter of 140.7 mm. The tubes had a wall thickness of 18 mm. The height of the tube was chosen to 100 mm. A 40 mm thick rectangular plate with a round cut out in the middle was welded on top of the tube. To examine the shear strength in absence of the confinement condition slotted tubes were also used. To enable slip between steel and concrete during the shear tests a diameter of 126 mm for the opening was chosen. For the adhesive injection the tubes were supplied with three 5 mm holes in the middle of their height. Figure 2 shows both types of shear test specimen with the on welded steel plate.

Concrete cylinders and concrete cubes

The tension tests with steel cylinders bonded on concrete cubes were accomplished on cubes with 200 mm side length. The shear tests used a concrete cylinder with 101.4 mm outer diameter. For the shear tests with slotted tubes concrete cylinders with 50 mm height were used. All other shear tests carried out used concrete cylinders of 150 mm in height.

The normal aggregate concrete had a dry density between 1.61 kg/dm³ and 2.33 kg/dm³ and a grain size of 2/16 mm. For the concrete fabrication a Portland cement (CEM I) at a strength class of 32.5 N/mm² was chosen. To study the effects of different aggregates on the bonding quality normal concrete with round edged gravel and crushed aggregates were used. Furthermore a charge (charge 4 in table1) with a high porosity caused by poor compaction was produced. This concrete was used to examine possible interlocking effects in the porous surface. Details are given in Tab. 1.

Table 1: Mechanical properties of the concrete

	1	2	3	4	5	6
1		unit	type 1	type 2	type 3	type 4
2	Cube compressive strength	N/mm²	45.70	40.61	42.51	21.23
3	Bending tensile strength	N/mm²	2.63	2.64	-	1.80
4	Splitting strength	N/mm²	3.10	2.78	4.07	1.84
5	E-Modulus	N/mm²	40789.44	29788.94	27781.06	9087.98
6	Aggregate	-	round	round	crushed	crushed
7	Dry density	kg/dm³	2.30	2.29	2.33	1.61

Adhesives

For the use of adhesives in structural applications a high strength, good durability, high deformation capacity and a good water resistance is generally required. Due to these preconditions polyaddition curing adhesives were chosen because of their corresponding characteristics. For our tests one polyurethane and two epoxy adhesives were used. The applied commercial grade adhesives were designed for the use on similar materials like steel or concrete. The following table 2 summarizes the main characteristics of the chosen adhesives.

Table 2: Characteristic mechanical properties of the tested adhesives

	1	2	3	4	5
1		unit	Adhesive 1	Adhesive 2	Adhesive 3
2	Chemical Composition	-	2 component polyurethane	2 component epoxy	2 component epoxy
3	Tensile strength	N/mm²	17.68	40.00	23.5
5	Shear strength	N/mm²	2.63		
6	E-Modulus	N/mm²	1226.02	4063.00	10000
7	Poisson Ratio	-	0.28	0.4	0.4
8	Base	-	Polyurethane	Epoxy	Epoxy

Pre-treatment of the adherent surfaces

To promote a good adhesion the pre-treatment of the surface of assembly is of major importance. The main targets of concrete pre-treatment are the cleaning of the surface, creating a certain level of roughness capable to transfer load by mechanical interlocking and allowing a good penetration of adhesives into the outer skin of the porous adherent.

Typical preparation techniques for steel surfaces to ensure a good adhesive bond are grit blasting with corundum, grinding and cleaning with isopropanol or acetone to remove lubricants and dust. These treatments affect the surface roughness and significantly increase the surface energy of the adherents and thus promote wetting by the adhesive which is considered a precondition for creating durable adhesion [1, 2].

The influence of different pre-treatments was examined in shear tests using two different concrete surfaces such as grit blasting and no treatment at all. The surfaces for the tension tests were prepared in a similar way. Additionally a third surface condition was generated by cutting with a diamond saw blade. To determine the roughness of the grit blasted surfaces the sand area test by Kaufmann [3] was used. The roughness of the other two surfaces was estimated according to comprehensive researches carried out in the 1970's and 1980's [4, 6]. The following table contains the roughness data of the concrete surfaces after different treatments.

Table 3: Surface roughness of test specimen

	1	2	3		4		5	
1		unit	no treatment		diamond saw		grit blasting	
2	aggregate	-	round	crushed	round	crushed	round	crushed
3	roughness	mm	0.1 [6]		0.085 [6]		0.43 / 0.63	0.43 / 0.75

On metal surfaces corrosion can significantly damage adhesive joints by the mechanism of bondline corrosion which can lead to complete delaminating of joints upon exposure to outside weathering [5]. Therefore all surfaces of structural steel joints need to be protected against corrosion attack by e.g. the use of corrosion inhibiting primers. Therefore the effects of commercial coatings for steel on the bonding strength were also examined.

The used primer was a chemically curing epoxy which is generally recommended for steel applications. After curing of the primer its thickness was measured and varying from 22.63 to 53.25 micrometres.

EXPERIMENTAL RESULTS AND COMPARISON WITH FEM-CALCULATIONS

Tension tests

The results of short-term tension tests showed a very high load capacity of the adhesive joint. The bonding layer thickness varied between 0.88 mm and 1.4 mm for all tension tests. For the connection steel-steel the maximum tension stress of 36.1 N/mm² could be reached with epoxy adhesive No. 2 (table 2). The examined polyurethane adhesive reached a maximum load which was 60% lower but at a higher level of deformation (5.6 times higher than for the epoxy adhesive No. 2). The load-displacement curves of these mentioned tests are shown in Fig. 3.

The fracture surfaces for all test specimens showed a cohesive failure of the adhesive in case of an uncoated surface (picture left in Fig. 4). The tests carried out with a coated steel surface were limited by the cohesion of the primer.

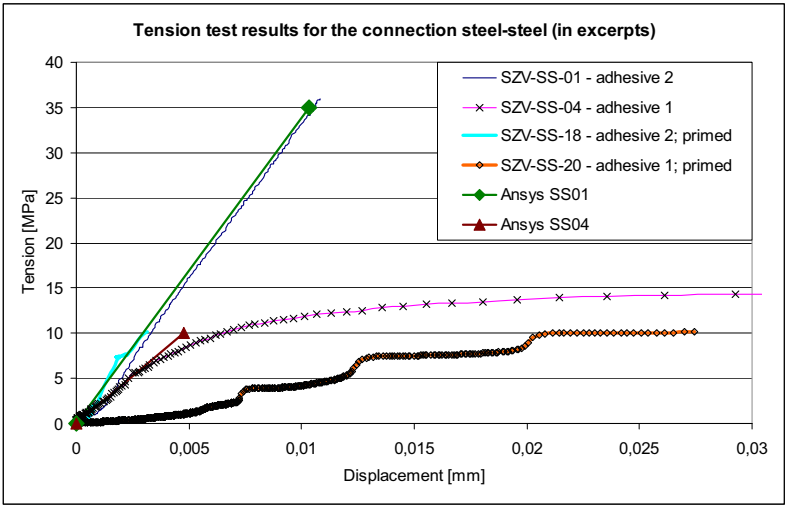
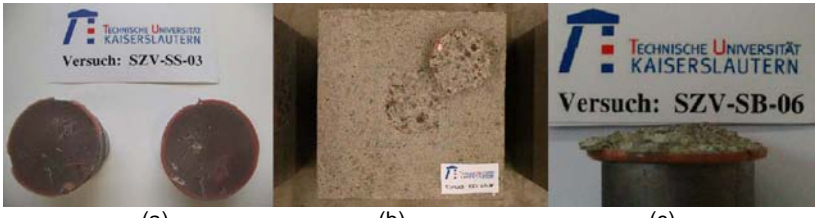


Fig. 3: Results from short term tension tests for the connection steel-steel

For the connection steel-concrete the failure load was limited by the tensile strength of concrete. Most of the fracture surfaces showed cohesive failure of the concrete (see Fig. 4) and pull-out of aggregates. The surfaces of all concrete cubes used for tests shown in figure 5 were pre-treated with grit blasting and made of round edged aggregates.

The results of all tensile tests showed no significant influence of the type of concrete aggregate. The concrete surfaces pre-treated with grit blasting led to an increased load capacity. This effect is assigned to the better penetration of adhesive and might be the reason why the concrete could be loaded above its nominal tensile strength. Surfaces that were sawed with a diamond saw had the lowest load capacity. Tests using concrete cubes with no treatment at all showed an average load capacity.

The pre-treatment of the steel surfaces by anti corrosive coating led in most of the cases to a decrease of load capacity. Only the epoxy adhesive (No. 3, table 2), being designed to harmonize with this coating, was able to increase its load capacity.



(a) (b) (c)

Fig. 4: Fracture surfaces after tension tests

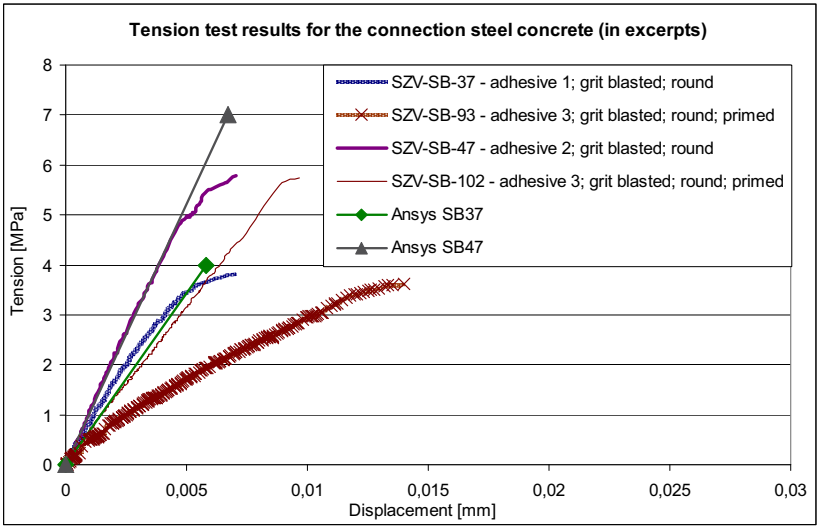


Fig. 5: Tension test results in comparison with Ansys FEM calculations

FEM-calculation of tensile tests

To compare the test results a FEM evaluation with the program Ansys was done. At first these calculations were based on linear material behaviour. For the use in Ansys the material parameters shown in table 1 and 2 were used. The Ansys model used a thickness of 1,0 mm for the adhesive layer. This adhesive layer was modelled in elements with 0.25 mm of height. The Ansys calculation results correlated very well to the test results at lower load levels. In figure 3 and 5 two of the tests carried out of each test arrangement were recalculated and correlated well to the load-deformation behaviour of the tests.

Also the distribution of stresses over the bonding layer thickness was examined. Figure 6 shows the tensile stresses of the adhesive layer in three different zones. The courses of all three graphs in figure 6 show similar stress values. The peak of stress can be observed near the middle of the cylinder. This peak is caused by the load introduction in the centre of the specimen. Also a decrease of stress can be detected near the perimeter of the cylinders. In [2] similar connections between steel and glass were examined and recalculated with Ansys. On the basis of these results the examination of different heights of steel cylinders was done. With an increase of height the stress peak in the middle of the cylinder decreased. The examined cylinder heights in [2] varied from 4 mm to 12 mm. Cylinders with a height of 12 mm showed a stress reduction of 50 % in the middle of the cylinders compared to the one with 4 mm height. Due to the thickness of the steel cylinder bending effects were minimized.

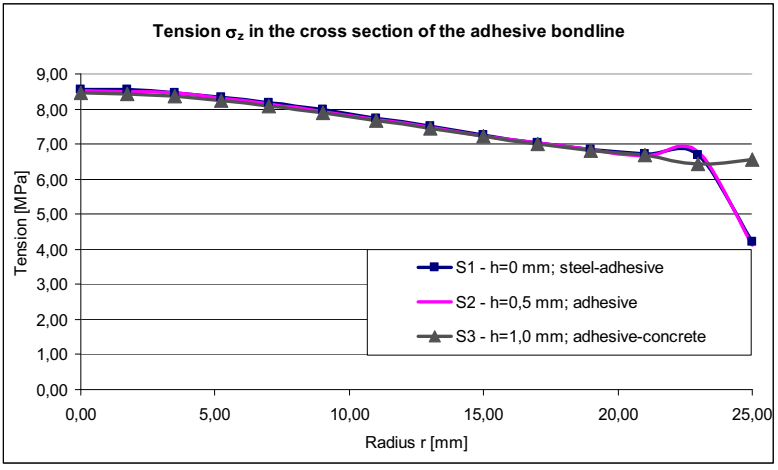


Fig. 6: Tension in bonding layer over its thickness

Shear tests

The shear tests exhibited a significantly different performance depending on the test parameters. Test specimen with grit blasted concrete surfaces achieved the highest load capacity. This is explained by a higher level of interlocking due to the surface roughness of the concrete and a resulting higher amount of friction. Compared with no treatment at all the tests using grit blasting as pre-treatment had a 40% higher load capacity in case of obstructed lateral strain (steel tube without slots).

The pre-treatment of the steel surfaces with primer lead to a decrease of load capacity. This effect is assigned to the low cohesion of the primer and can be seen on the test specimen after tests (Fig. 7). All tests showed a cohesion failure of the primer.



(a) (b)

Fig. 7: Shear test specimen with primed steel surface

The shear tests using slotted tubes had an 80% lower load capacity compared to test specimen using steel tubes without slots. These results correspond to the expectation and are caused by a change of stress distribution in the concrete. The

elimination of obstructed strain led to the reduction of pressure on the bonding layer and a decrease of load capacity (see Fig. 8).

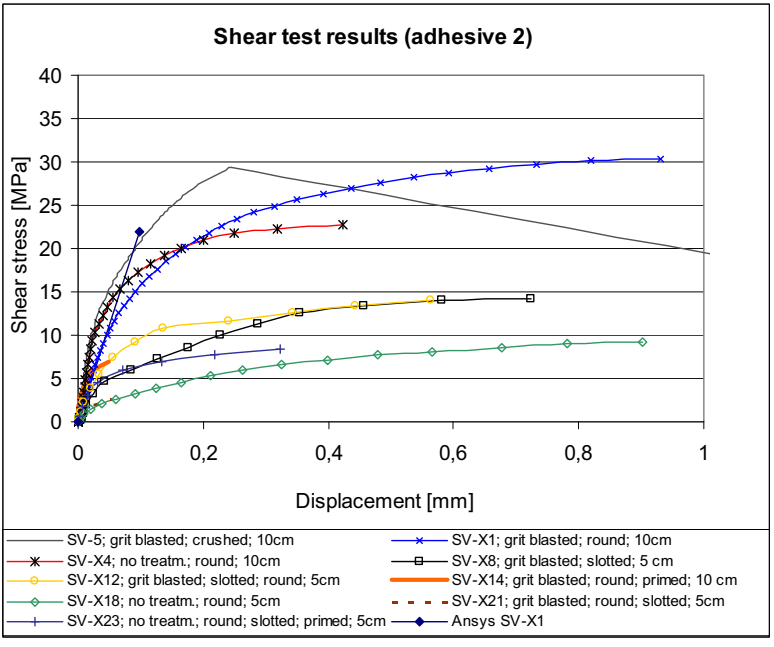


Fig. 8: Shear test results in comparison with Ansys FEM calculations

FEM-calculation of shear tests

The experimental results of these shear tests were compared to linear FEM evaluations with Ansys. The linear material properties used for the calculations are given in table 1 and 2. The geometric model of the shear test specimen was created with a bonding layer thickness of 1.6 mm. To reduce calculation time symmetry was used. Also different net densities were examined. Element width varied from 0.4 mm to 0.8 mm while the contact zones of the bonding partners were meshed similar to the meshing of the bonding layer. Figure 8 shows a good correlation to the linear characteristic of the recalculated test SV-X1 for lower load levels regarding to the load-deformation behaviour. Tests with the two other adhesives given in table 2 could be recalculated as well. The results correlated very well to the test results too.
The shear stresses over the bonding layer thickness were also examined. Therefore the shear stresses at different zones were calculated and shown in figure 9. Examined zones were the contact zone of concrete-adhesive (S1), in the middle of the adhesive (S2) and the contact zone of concrete-adhesive (S3). The graph illustrates the level of shear stresses over the cross section of the bonding layer. The constant value of shear stress calculated for test SV 5 at the load of 50 N/mm² is also included.

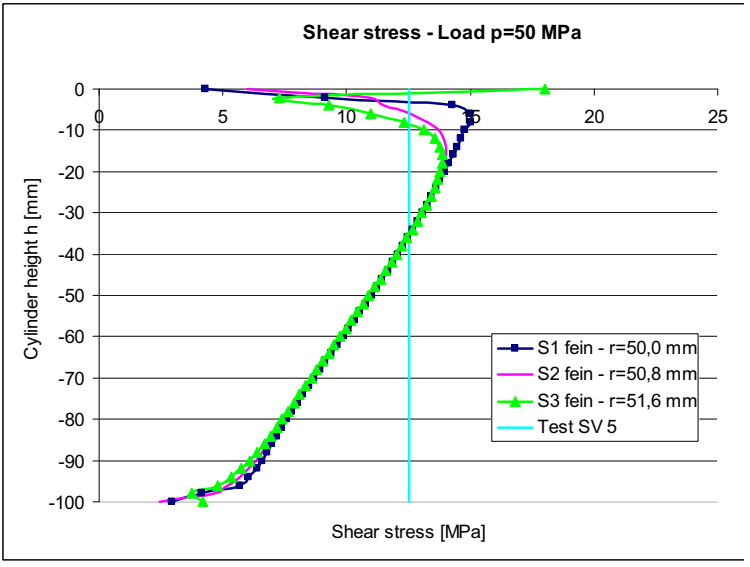
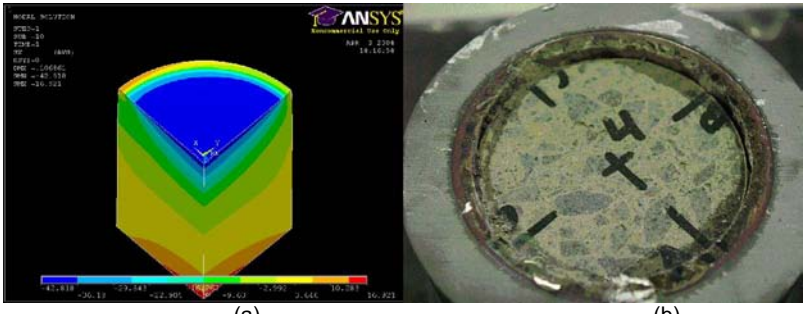


Fig. 9: Shear stresses in the cross section of the adhesive bondline

The graph shows peaks of shear stresses at the top end of the steel tube. Especially the contact zone adhesive-steel shows a stress concentration at the top of the tube. Also a decrease of shear stresses towards bottom of the bonding layer can be observed. As expected the higher deformation capacity of the concrete cylinder compared to the steel tube leads to this result.

During the progress of the shear tests a tension crack near the contact zone between concrete and adhesive could be observed (see Fig. 10). This crack was only located at the top of the tube and did not expand to the lower end. At that time the test specimen were still able to support a significant amount of load. The crack was caused by the missing obstructed lateral strain at the top of the tube. These effects could also be observed at the Ansys recalculations.



(a) (b)

Fig. 10: σ_x-stress and test specimen with cracked concrete

SUMMARY AND FUTURE PROSPECTS

To assess the load capacity of adhesive bonds between steel and concrete surfaces several tests were carried out. All tests were conducted at room temperature. The test geometries were chosen to create different types of stress and stress combinations typical for structural connections in the building and construction industry. The influence of different pre-treatments was also examined.

The results showed a high load capacity for tensile stressed, shear stressed and combined stressed connections. Most of the tests and its linear characteristics at lower load levels could be recalculated with FEM.

On the basis of further material parameters a more sophisticated non-linear recalculation will be carried out. The effects of temperature and fatigue issues need to be evaluated thoroughly in order to understand the potential of the connection. Therefore material parameters will be determined at different temperature levels from the stress-strain analysis on polymer bulk specimen. The effects of different adhesion promoting pre-treatments for steel and concrete will also be considered. Also further shear tests will be carried out equipped with strain gauges to experimentally gain insight into the localized stress distribution of the adhesively bonded joint. Being able to quantify the tangential stresses in the steel tube the increase in load capacity due to the effects of the confinement condition will be further assessed by experiments and corresponding FE-analysis. Tests on the long term behaviour of adhesive steel-concrete joints and their static load capacity including creep and relaxation are also under preparation.

REFERENCES

[1] Feldmann M., Völling B., Gessler A., Wellershoff F.,Geiss P.L., Wagner A.; „Kleben im Stahlbau", *Stahlbau*, No. 75, 2006, pp.834-846.

[2] Wißling M., „Kleben von Stahl mit Stahl und Glas mit Stahl-FE Simulationen, Anwendungen, Perspektiven", *Stahlbau*, No. 73, 2004, pp.438-440.

[3] Kaufmann N., „Das Sandflächenverfahren", *Straßenbautechnik 24,* No. 3, 1971.

[4] Rehm G., Franke L., „Kleben im Konstruktiven Betonbau", *Deutscher Ausschuss für Stahlbeton im DIN e.V. (DAfStb)*, Volume 331, Verlag Ernst & Sohn, Berlin,1982.

[5] Feldmann M., Dilger K., Geiß P.L., Pasternak H., Ummenhofer T., „Neue Konstruktionen durch Einsatz von Klebeverbindungen im Stahlbau", *1. Zwischenbericht zum laufenden AiF-Projekt Nr. 169 ZBO,* Tagungsband 6. Kolloquium „Gemeinsame Forschung in der Klebtechnik",Dechema, Frankfurt 2006.

[6] Bergmeister K., „Kleben im Betonbau", *Beton- und Stahlbetonbau 96,* 2001, Heft 10.

ULTIMATE FLEXURAL STRENGTH OF HYBRID COMPOSITE GIRDERS USING HIGH-PERFORMANCE STEEL OF HSB600 AT SAGGING BENDING

Seok-Goo Youn *
School of Civil Engineering, Seoul National University of Technology
Seoul, Korea
sgyoun@snut.ac.kr

Doobyong Bae
Department of Civil & Environmental Engineering, Kookmin University
Seoul, Korea
dbbae@kookmin.ac.kr

Young-Jin Kim
Civil Engineering Research Team
Daewoo Institute of Construction Technology, Suwon, Korea
kimyj@dwconst.co.kr

ABSTRACT

HSB600 is a high performance steel which is currently developed by a Korean steel company. HSB600 does not have an obvious yield point and yet undergoes large strains after proportional limit. Its 0.2% offset yield strength and tensile strength are over 450 MPa and 600 MPa respectively. Modern standards such as AASHTO LRFD and Eurocode 4 provide rules for determining the flexural strength of composite girders. These rules are based on the presence of a yield point in the stress-strain diagrams of steel materials. This paper presents experimental works conducted for the purpose of verifying the ultimate flexural strength of hybrid composite girders using the tension flange made of HSB600. Totally five composite girder specimens (one hybrid and a conventional composite girders (Series I), three hybrid composite girders (Series II)) have been tested. The results of the test are compared with the flexural strengths obtained by nonlinear moment-curvature analysis based on the stress-strain curves of each material and the code predictions. The test results show that, if the plastic moment is calculated with using 0.2% offset yield strength, the ultimate flexural strength is underestimated. Finally, based on the test results, some design recommendations regarding the flexural strength and the ductility requirement for hybrid composite girders with HSB600 are suggested.

INTRODUCTION

In 2004, the Korea Bridge Design & Engineering Center (KBRC) was established in order to develop new design codes and guidelines for bridge design based on limit state design concepts. The research project was supported by the Ministry of Construction & Transportation (MOCT) in Korea. As one of research projects conducted by KBRC, steel and concrete composite bridges have been investigated. Following research topics have been conducted in this project:

- Time-dependant behaviors of composite girders
- Ultimate flexural strength of conventional composite girders
- Crack width and crack spacing at hogging bending
- Ultimate flexural strength of composite girders with class 3 section at hogging bending

- Ultimate flexural strength of hybrid composite girders at sagging bending

Currently the high performance steel for bridges (HSB) has been developed by POSCO, a Korean steel company. HSB600 has higher values for tensile and yield strength, toughness, weldability, and cold formability compared to previously developed structural steels in Korea. A novel thermo mechanical control process (TMCP) rolling technology, achieves that HSB600 has the minimum yield strength (0.2% offset yield stress) of 450MPa and the minimum tensile strength of over 600MPa with varying plate thickness (Lee et al. 2007).

Different from conventional composite girder, hybrid composite girder consists of concrete slab and hybrid steel girder made of more than two steels. Hybrid composite girder using HSB represents an economical design solution for composite bridges. HSB can be used both of tension and compression flanges or tension flange only. When positive bending moments are applied, causing tension in the lower fibres of the girder, the HSB can be used only in the tension flange. This contributes most of the ultimate flexural strength to the hybrid composite girder. Similar to conventional composite girder, the ultimate flexural strength of hybrid composite girder is governed by the mechanical properties of HSB obtained from stress-strain diagram, such as yield stress, length of yield plateau, strain-hardening strain, and initial strain-hardening modulus.

Ductile girder is generally recommended for providing sufficient rotation and protecting brittle failure of composite girder (Ansourian, 1982). Ductile girders are such that strain-hardening of the lower flange occurs before the collapse moment is reached, defined by a crushing failure of the slab. It is well known that conventional steel has a yield point and sufficient length of yield plateau before strain-hardening strain. Due to the existence of yield plateau, plastic moment of conventional composite girder can be obtained when the tensile stress in the lower flange is greater than the yield stress (Wittry, 1993, Yakel et al., 2005). Different from conventional steels, HSB600 does not have an expressed yield point and yet undergoes large strains after passing the proportional limit as shown in Figure 1. Because of the non-existence of yield plateau, strain-hardening occurs just after the proportional limit and tensile stress in the lower flange increases continuously until the collapse moment is reached. The tensile strain at the 0.2% proof stress of HSB600 is very smaller than the strain-hardening strains of conventional steels. Therefore, tensile stress in the lower flange at the collapse moment is greater than the 0.2% proof stress.

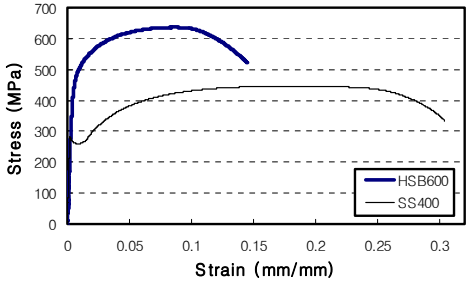


FIG 1. Stress-Strain Curves of Typical Conventional Steel SS400 and HSB600

The difference of the tensile stresses affects the location of plastic neutral axis and the ultimate flexural strength of hybrid composite girder. It also influences on the ductility parameter, which is represented as a ratio of the depth of plastic neutral axis and the total depth of hybrid composite girder.

In Korea, composite construction has achieved a high market share in bridge construction, but the rising price of steel is discouraging the application of composite construction of bridges. Currently, it is investigated to minimize the cost of composite system for highway bridges and high-speed railway bridges. Hybrid composite construction using HSB600 has been considered as an economical solution, and theoretical and experimental research works is being performed in order to develop a simple method for predicting the ultimate moment capacity.

ULTIMATE FLEXURAL STRENGTH

At sagging bending, hybrid composite girders can be classified by ductile girder or brittle girder. Ductile girder is desirable because the ultimate flexural strength always exceeds plastic moment, M_p, and sufficient rotation is occurred before failure. The ultimate flexural strength can be calculated by non-linear moment-curvature analysis considering stress-strain curves of concrete slab and each parts of steel girder. If HSB has an obvious yield point and yield plateau, the stress-strain curve of HSB can be assumed similar to the stress-strain curves of conventional steels. In this case, the data of yield strain, length of yield plateau, and initial strain-hardening strain are enough to perform non-linear moment-curvature analysis, and plastic moment can be obtained by simple plastic theory as shown in Figure 2. In case of brittle girder, because the concrete crushing occurs before strain-hardening is developed in the tension flange the ultimate flexural strength is less than the plastic moment.

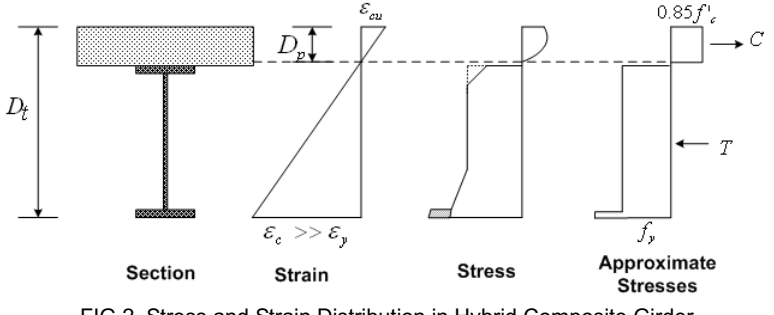


FIG 2. Stress and Strain Distribution in Hybrid Composite Girder

The ratio of D_p / D_t, called ductility parameter, is generally used for a classification factor. In the codes of AASHTO LRFD, when the ductility parameter is less than 0.1, composite girder is classified by ductile girder. If the concrete crushing strain is assumed as 0.003 mm/mm, the minimum tensile strain of tension flange will be 0.027 mm/mm. In the Eurocode 4 it is recommended that the ductility parameter, X_{pl} / h, is less than 0.15 for ductile girder and the concrete crushing strain is 0.0035 mm/mm. In this case, the minimum tensile strain of tension flange will be 0.0315 mm/mm.

When the yield stress of HSB600 is assumed as 0.2% proof stress, $f_{0.2\%,ps}$, of 450 MPa, the tensile strain at the yield stress will be less than 0.005 mm/mm. The stress at the strain of 0.027 mm/mm, $f_{2.7\%}$, is nearly 580 MPa, and it is 1.29 times higher than 0.2% proof stress, $f_{0.2\%,ps}$, of 450 MPa. In addition, the stress at the strain of 0.0315 mm/mm, $f_{3.15\%}$, is nearly 590 MPa, and it is 1.31 times higher than $f_{0.2\%,ps}$. The differences between the yield stress of $f_{0.2\%,ps}$ and the actual stresses of $f_{2.7\%}$ and $f_{3.15\%}$ are enough to change the location of plastic neutral axis, and thus, both of the distance, D_p, and the plastic moment, M_p, will be underestimated. As mentioned before, due to TMCP rolling technology, HSB600 has the minimum yield strength (0.2% proof stress) of 450MPa and the minimum tensile strength of over 600MPa with varying plate thickness. Therefore, if ductility parameter is fixed at the value of 0.1 or 0.15 for sufficient rotation capacity, the yield stress of HSB600 can be fixed as a reasonable value just for calculating plastic moment without consideration of plate thickness.

In the following the test specimens of hybrid composite beams using HSB600 are introduced and the test results of ultimate bending capacity are described. In addition, based on the comparison of test and theoretical results, a simple way for estimating the ultimate flexural strength and the ductility of hybrid composite girders is discussed.

EXPERIMENTAL WORK

SERIES I TEST

Test Beams

In order to find out the effects of HSB600 on the ultimate flexural strength at sagging bending, two composite beams of H1 and H2 were fabricated with a cross-section as shown in Figure 3. H1 is a conventional composite beam and H2 is a hybrid composite beam constructed with HSB600. H1 was designed to be a brittle girder. The cross-sectional dimensions of H2 are as same as those of H1. The details of test beams are summarized in Table1.

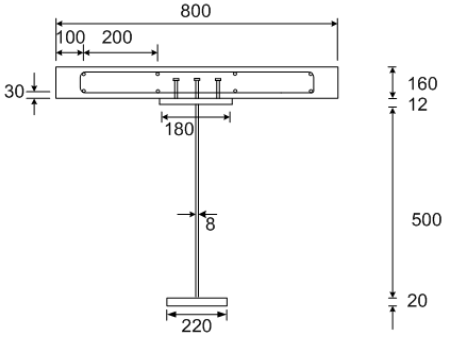


FIG 3. Cross Section of Test Beams - Series I (unit: mm)

Material properties are shown in Table 2. The initial strain-hardening modulus, E_{sh}, and strain-hardening strain, ε_{sh}, were obtained using the stress-strain curves of steels. In case of HSB600, the yield stress was assumed as 0.2% proof stress and the strain-hardening strain, ε_{sh}, was assumed to 0.00231 mm/mm, which corresponds to the cross point of the two linear lines of the initial slope line and the tangent slope line at the 2.0% strain on the stress-strain curve. The initial strain-hardening modulus, E_{sh}, represents the slope of the tangent line at the 2.0% strain. The stress-strain curve of HSB600 was simulated to bi-linear curve, and it was used for non-linear moment-curvature analysis.

Test beam	H1, H2
Slab dimensions (mm)	800 × 160
Compression flange dimensions (mm)	180 × 12
Web dimensions (mm)	500 × 8
Tension flange dimensions (mm)	220 × 20
Longitudinal bars in concrete slab	8ϕ16
Transverse bars	ϕ16 at 200
Total number of 19×100 headed studs	90
Degree of shear connection	2.05, 1.67

TABLE 1. Dimensions of Test Beams - Series I

Test beam	Series I		Series II
	H1	H2	H3, H4, H5
Concrete slab			
Average compressive strength (MPa)	35.0	35.0	45.0
Modulus of elasticity (MPa)	27,223	27,223	29,837
Lower yield stress (MPa)			
Compression flange	302.4	302.4	340.2
Web	323.9	323.9	355.9
Tension flange	261.7	451.1*	451.1*
Ultimate tensile stress (MPa)			
Compression flange	492.8	492.8	512.6
Web	451.8	451.8	516.5
Tension flange	442.9	629.1	629.1
Elastic Modulus of steel E_s (MPa)	210,000	210,000	210,000
Initial strain-hardening modulus E_{sh} (MPa)			
Compression flange	4,546	4,546	4,808
Web	3,175	3,175	4,405
Tension flange	5,468	4,455	4,455
Strain at strain-hardening ε_{sh} (mm/mm)			
Compression flange	0.014	0.014	0.0125
Web	0.021	0.021	0.0148
Tension flange	0.014	0.00231	0.00215**

Note: * 0.2% proof stress
** Proposed strain-hardening strain for Series II test

TABLE 2. Material Properties of Test Beams - Series I and Series II

Static tests were performed at a structural laboratory of the Research Institute of Industrial Science & Technology (RIST) in Korea. A single line load was applied at the center of 7.0 m simple span. Load was applied by a 10,000 kN hydraulic actuator under displacement control. The duration of a test to collapse was about 2 Hrs. During the tests, loads, deflections and strains at the mid-span cross section were measured automatically.



FIG 4. View of Before Bending Test

Test Results

The properties and behaviors of test beams are summarized in Table 3 and in Figs. 5.-7. H1 and H2 were failed by concrete crushing at the top surface of concrete slab under the longitudinal edge of loading plate. H1 was collapsed at the moment of 1,347 $kN \cdot m$, which is 8.8% greater than the plastic moment, M_p, of 1,239 $kN \cdot m$ and 15.9% greater than the nominal flexural resistance, M_n, of 1,162 $kN \cdot m$. The ultimate moment capacity of H2 was 1,865 $kN \cdot m$, which is 10.7% and 22.1% greater than the plastic moment, M_p, of 1,685 $kN \cdot m$ and the nominal flexural resistance, M_n, of 1,528 $kN \cdot m$, respectively. The ultimate moment capacities of H1 and H2 were very close to those of $M_{u,cal}$ obtained by non-linear moment-curvature analyses (see Fig. 5). In the analyses, the CEB model was used for the constitutive model of concrete and, based on the measured strains, the concrete crushing strains of H1 and H2 were assumed to 0.004 mm/mm and 0.0035 mm/mm, respectively. The ultimate moment capacity was very sensitive with varying the strain-hardening modulus, E_{sh}, of HSB600. The ultimate moment capacities $M_{u,cal}$ are 8.5% and 19.4% larger than the nominal flexural resistances M_n of H1 and H2, respectively.

Test beam	H1	H2
Test result Ultimate moment capacity, M_{ult}	1346.9	1865.4
Plastic moment, M_p $(kN \cdot m)$, D_p / D_t	1,238.5, 0.188	1,684.7, 0.233
AASHOTO LRFD Nominal flexural resistance, M_n $(kN \cdot m)$	1,162.1	1528.1
EUROCODE 4 Design resistance moment, $M_{Rd}(kN \cdot m)$,	1,085.2	1,456.6
Non-linear moment-curvature analysis Ultimate moment $M_{u,cal}$ $(kN \cdot m)$, ε_{cu}	1,261.6, 0.004	1,825.2, 0.0035
Ductility parameter, χ (Ansourian, 1982)	0.90	0.71
Deflection at ultimate load, δ_{ult} (mm), $\delta_{ult} / \delta_{mp,el}$	61.8, 3.93	53.7, 2.51
Maximum measured tensile strain (mm/mm)	0.01695	0.00973
Average measured compressive strain (mm/mm)	over 0.004	over 0.0033

TABLE 3. Test Beam Properties and Behaviors – Series I

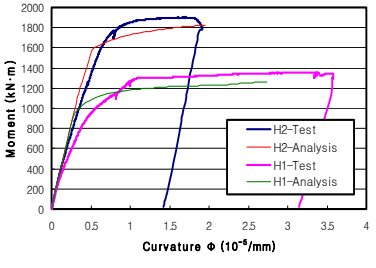


FIG. 5. Moment - Curvature Curve

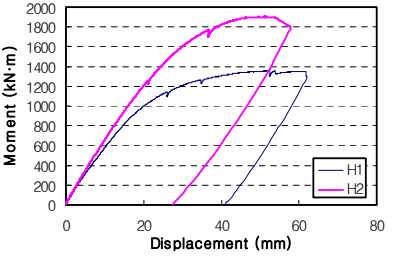


FIG. 6. Deflections at the Center

The measured deflections at the center of span are presented in Figure 6. The ratios of the ultimate deflection, δ_{ult}, and the elastic component of deflection, $\delta_{mp,el}$, calculated at M_p of H1 and H2 were 3.93 and 2.51, respectively. Those ratios of 3.93 and 2.51 are larger than 1.58 and 0.97, which are obtained using the mean regression line for ultimate deflection ratio, 3.2 χ -1.3 (Ansourian, 1982).

For H1, the maximum steel strain measured just before concrete crushing was 0.01695 mm/mm. It was larger than the strain-hardening strain, ε_{sh}, of 0.014 mm/mm. When crushing strain of concrete is assumed 0.004 mm/mm, the theoretical ultimate strain is 0.01494 mm/mm in the tension flange. In case of H2, the measured maximum steel strain was 0.00973 mm/mm, or a little higher than half of the maximum strain in H1. The theoretical ultimate strain is 0.01 mm/mm in the flange when the concrete crushing strain is assumed 0.0035 mm/mm.

Test beam	Yield stress (MPa)	M_p $(kN \cdot m)$	M_n $(kN \cdot m)$	M_{ult} / M_p	M_{ult} / M_n	$M_{u,cal} / M_n$
H1	f_y =261.7	1,238.5	1162.1	1.0875	1.159	1.085
H2	$f_{0.2\%,ps}$ = 451.8	1684.7	1528.1	1.108	1.221	1.194
	$f_{0.7\%}$ = 482	1754.7	1596.5	1.063	1.168	1.143
	$f_{1.2\%}$ = 520	1841.5	1665.1	1.013	1.120	1.096
	$f_{1.5\%}$ = 540	1887.0	1705.1	0.989	1.094	1.070
	$f_{2.0\%}$ = 560	1932.5	1784.1	0.965	1.046	1.023
	$f_{3.0\%}$ = 585	1989.3	1793.3	0.938	1.040	1.018

TABLE 4. Comparison of Test Beam Properties with the Variation of the Yield Stress.

Discussions

The test results and the theoretical analyses show that if the 0.2% proof stress, $f_{0.2\%,ps}$, is used as the yield stress of HSB600, the moment capacity is underestimated and the 0.2% proof stress, $f_{0.2\%,ps}$, is not acceptable to be the yield stress for calculating the plastic moment, M_p. The plastic moments of H2 are changed with varying the assumed yield stresses as shown in Table 4 and Figure 7. If the plastic moment, M_p, can be obtained at the ductility parameter χ = 1.4 (Ansourian, 1982), the steel strain developed at the tension flange will be 0.018 mm/mm . According to the codes of AASHTO LRFD and Eurocod 4, the corresponding steel strains are 0.027 mm/mm and 0.0315 mm/mm, respectively. Based on the test results and the theoretical analyses, it is proposed that the stress $f_{2.0\%}$ at 2.0% strain of 560 MPa is the yield stress for calculating the ductility parameter, D_p / D_t , and the plastic moment, M_p , and the strain-hardening modulus, E_{sh} , is 4,455 MPa for the non-linear moment-curvature analyses. In addition, for the safety, the stress $f_{2.0\%}$ at 2.0% strain can be reduced to 530 MPa.

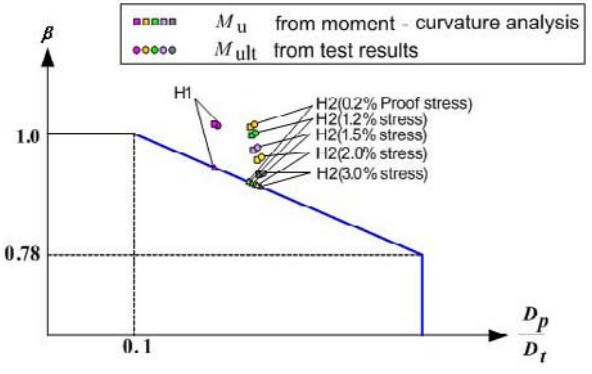


FIG. 7. Comparison of M_u / M_p and M_{ult} / M_p

SERIES II TEST

Test Beams

In order to confirm the previous proposals from the results of Series I test, three hybrid composite beams of H3, H4, and H5 were fabricated with different cross-sections as summarized in Table 5. Material properties are presented in Table 2. Static tests were performed as same as the method used for Series I test.

Series II test beam	H3	H4	H5
Slab dimensions (mm)	1000×160	800×160	600×160
Compression flange dimensions (mm)	150×12	150×12	150×12
Web dimensions (mm)	600×9	600×9	600 × 9
Tension flange dimensions (mm)	160×20	240×20	255×20
Longitudinal bars in concrete slab	8ϕ16	8ϕ16	8ϕ16
Transverse bars	ϕ16 at 200	ϕ16 at 200	ϕ16 at 200
Total number of 19×100 headed studs	90	90	90
Degree of shear connection	1.80	1.52	1.95

TABLE 5. Dimensions of Test Beams – Series II

Test Results

The ultimate bending capacities, M_{ult}, obtained by static tests are compared with the plastic moment, M_p and the nominal flexural resistance, M_n of test beams as shown in Table 6 and in Figure 8. All test beams were failed by concrete crushing at the top surface of concrete slab. When the yield stress is assumed as 0.2% proof stress $f_{0.2\%,ps}$, the ultimate bending capacities, M_{ult}, of all test beams are at least 10% greater than the nominal flexural resistance, M_n. When the yield stress is assumed as the stress at 2.0% strain, $f_{2.0\%}$, the ultimate bending capacities, M_{ult}, of all test beams are at least 1.4% greater than the nominal flexural resistance, M_n. The ductility parameters, D_p / D_t, are also increased as shown in Figure 8. In case of H5, because the plastic neutral axis is located in the web, the increase of the depth of plastic neutral axis, D_p is larger than those of the other test beams. With the proposed bi-linear curve of HSB600, the ultimate flexural strengths of all test beams are calculated by using non-linear moment-curvature analyses. The calculated strength is slightly less than the ultimate bending capacity M_{ult} of each test beam, but it can be applicable for predicting the ultimate flexural strength.

Discussions

Based on the comparison of test results and theoretical results, the proposed method is quite acceptable for estimating the ultimate flexural strength of hybrid composite girders with the tension flange made of HSB600; the stress $f_{2.0\%}$ at 2.0% strain of HSB600 shall be assumed as the yield stress for calculating the plastic moment, M_p, and the ductility parameter, D_p / D_t. In addition, it is found that the stress-strain curve of HSB600 can be simulated with the proposed bi-linear curve; which have the yield stress of 450 MPa and the modulus of strain-hardening of 4,455 MPa.

Test beam	Yield stress (MPa)	M_p $(kN \cdot m)$	M_n $(kN \cdot m)$	M_{ult} / M_p	M_{ult} / M_n
H3	$f_{0.2\%,ps}$ = 451.8	1,936	1,898	1.118	1.141
	$f_{2.0\%}$ = 531.1	2,109	2,055	1.026	1.053
H4	$f_{0.2\%,ps}$ = 451.8	2,350	2,203	1.037	1.107
	$f_{2.0\%}$ = 531.1	2,590	2,403	0.941	1.014
H5	$f_{0.2\%,ps}$ =451.1	2,330	2,142	1.018	1.108
	$f_{2.0\%}$ = 531.1	2,579	2,283	0.922	1.040

TABLE 6. Comparison of M_{ult} / M_p and M_{ult} / M_n

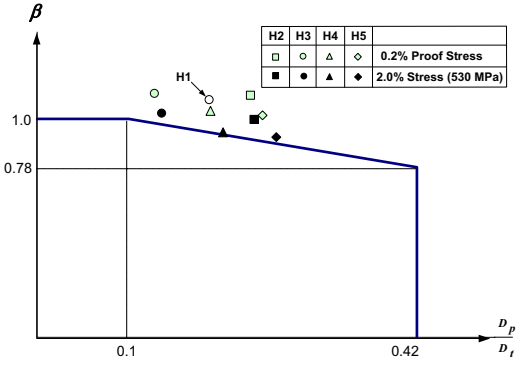


FIG. 8. Comparison of M_{ult} / M_p

CONCLUSIONS

The objective of this study is to propose a simple method for predicting the moment capacity of the hybrid composite girders constructed with the high performance steel of HSB600, which is developed in Korea. The ultimate flexural strengths of five composite beams under sagging bending are described and the test results are compared with the theoretical results obtained by non-linear moment-curvature analyses.

Due to the lack of yield plateau of HSB600, if the 0.2% proof stress is assumed as the yield stress for calculating plastic moment, the ultimate flexural strength of hybrid composite girder is underestimated. In order to obtain plastic moment in sagging bending, considerable ductility and rotation capacity are required and thus, the strain developed at the bottom surface of tension flange should be larger than the strain at the 0.2% proof stress. The stress at 2.0% strain, $f_{2.0\%}$, is proposed as the yield stress of HSB600 just for calculating the plastic moment at sagging bending. Test

results show the value of $f_{2.0\%}$ is quite reasonable for predicting plastic moment and ductility parameter. The value of $f_{2.0\%}$ is rudely selected without any sufficient consideration or calibration. However, even if the other value is selected, the difference of final results related to plastic moment or ductility parameter will be small enough to ignore.

The stress-strain curve of HSB600 is simulated with a bi-linear curve for simplifying non-linear moment-curvature analysis. The yield stress of 450 MPa and the modulus of strain-hardening of 4,455 MPa are proposed. Using the bi-linear curve, reliable bending strength of test beams can be obtained with high accuracy. In addition, concrete crushing strain is proposed 0.0035 mm/mm up to 35 MPa concrete strength, and linearly decreased from 0.0035 mm/mm to 0.0025 mm/mm until 80 MPa concrete strength.

In the ongoing research project, parametric analyses will be performed for developing new strength reduction factor for hybrid composite girders with HSB600.

ACKNOWLEDGEMENTS

The financial support for the research activity of the authors was provided by the Korea Bridge Design & Engineering Research Center (KBRC) and the assistant of Pohang Steel Corporation (POSCO) are highly acknowledged. The authors wish to thank Dr. Jong-Kwan Lee (LIST, POSCO) and Dr. Pil-Goo Lee (LIST, POSCO) for the valuable support of HSB600.

REFERENCES

American Association of State Highway Transportation Officials. (2007) *AASHTO LRFD Bridge Design Specifications, 4th Ed.,* Washington, D.C.

Ansourian, P. (1982) “Plastic Rotation of Composite Beam.” *J. Struct. Div.,* ASCE, 108(3), 643-659.

Eurocode 4. (1997) *Design of Composite Steel and Concrete Structures, Part 2. General rules and rules for bridges. ENV 1994-2:1997*.

Lee, J. K., Yoon, T. Y., Choi, J. L., and Cho, J. Y., (2007) “Development and commercialization of high performance steel for bridges(HSB600),” *Proceedings of the Korea Society of Steel Construction*, 103-107.

Yakel, A.J., and Azizinamini, A. (2005) “Improved Moment Strength Prediction of Composite Steel Plate Girders in Positive Bending,” *J. Bridge Eng.,* Jan./Feb. 28-38.

Wittry, D. M. (1993) An Analysis Study of the Ductility of Steel-Concrete Composite Sections. *MS thesis, University of Texas-Austin,* Austin, Tex.

MODERN COMPOSITE STRUCTURES MADE OF HIGH PERFORMANCE MATERIALS

Sabine Rauscher
Institute of Structural Concrete
RWTH Aachen University
Aachen, Germany
rauscher@imb.rwth-aachen.de

Josef Hegger
Institute of Structural Concrete
RWTH Aachen University
Aachen, Germany
heg@imb.rwth-aachen.de

ABSTRACT

The present paper summarizes the results of a research program involving the testing of push-out specimens and composite beams with innovative continuous shear connectors in ultra-high performance concrete. In the push-out tests the load-slip behavior of the shear connectors was evaluated and compared for various parameters. The parameters included the steel fiber content and the transverse reinforcement ratio. The test results indicate that the steel fiber reinforcement ratio has only a minor influence on the load carrying capacity whereas the transverse reinforcement ratio is more vital. The beam tests are focused on the moment carrying capacity and the transition of the shear forces across the joint between steel and concrete. Two beam tests are presented and discussed.

INTRODUCTION

The outstanding mechanical properties of ultra-high performance concrete (UHPC) in combination with high strength steel offer engineers new opportunities to design elegant and slender structures. UHPC is characterized by an extremely dense microstructure and a very high compressive strength of up to 200 MPa. Steel fibers are added to the concrete enhancing the tensile bending strength and ductility considerably. However, the challenging task with high performance materials is finding an adequate application to utilize the structural benefits. Composite structures are very appropriate due to the efficient interaction of the two components concrete and steel. Taking into account the material properties, the steel carries the tensile forces and the concrete is arranged in the compression zone. To account for the high performance and the interaction of the respective materials, the local interconnection has to be guaranteed, which calls for appropriate shear connectors capable of transferring high shear forces across the composite joint. Therefore, a series of push-out tests was carried out to determine the load carrying capacity and the ductility of the composite joint between high strength steel and ultra-high performance concrete.

The global load carrying capacity was investigated in beam tests under positive bending. Two different cross sections were tested, a conventional composite beam and a filigree beam with the shear connectors directly cut into the web of the steel profile. This way, two composite beams can be produced with one I-beam and no

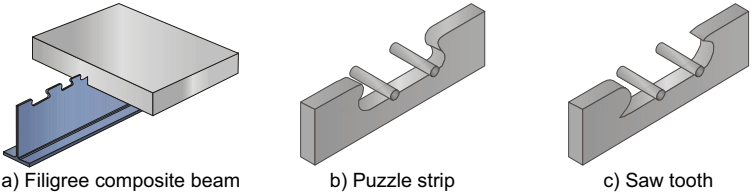
material is wasted leading to significant savings in production costs. The load carrying capacity is comparable to a conventional composite beam, since the neutral axis is in the region of the upper flange, which, therefore, does not contribute significantly to the moment carrying capacity.

RESEARCH SIGNIFICANCE

In composite construction headed studs are the predominant shear connection. Lately, continuous shear connectors are becoming more and more popular due to their high load carrying capacity and ductility [Feldmann et al. 2007]. Especially for ultra-high performance concrete this becomes evident since already in high strength concrete the shear strength of headed studs is governed by steel failure. It is obvious that using high strength materials leads to an increase in load carrying capacity of the composite structure and thus to increased stresses in the composite joint. Furthermore, the structures become more slender and therefore the stresses have to be transferred within a shorter area. Thus, the aim of the current research is to investigate the load carrying behavior of continuous shear connectors in ultra-high performance concrete and to identify the governing parameters for a shear connection that features a high initial stiffness, a high ultimate load and a sufficient ductility.

CONTINUOUS SHEAR CONNECTORS

Continuous shear connectors have been used for about 20 years. The most common one is the perfobond strip [Leonhardt et al. 1987], where the shear forces between the steel beam and the concrete slab are transferred by vertical steel plates with holes. In [Hegger et al. 2006] the so-called puzzle strip, an innovative shear connector, is introduced (Figure 1). Its main advantage is the symmetrical geometry. This way two shear connector strips can be manufactured with one cut and no material is wasted. If the cut is performed in the web of a steel I-beam, two composite beams can be produced (Figure 1a). Two different types of continuous shear connectors were investigated, the puzzle strip and the saw tooth (Figure 1b and c).



a) Filigree composite beam b) Puzzle strip c) Saw tooth

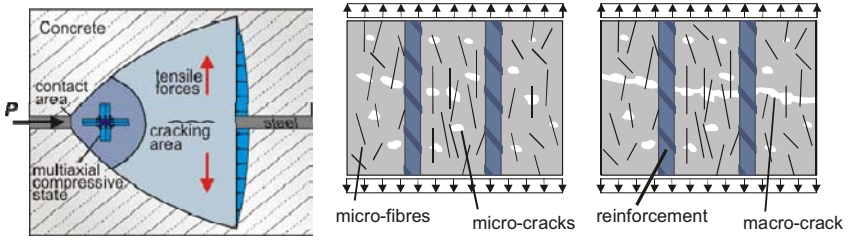
Figure 1 – Filigree composite beam and continuous shear connectors

Basically, the innovative shear connectors act as a conventional concrete dowel. So far, their load carrying behavior has been investigated by several researchers [Feldmann et al. 2007], [Wurzer 1997], [Zapfe 2001]. Four failure modes have to be considered (Figure 2), local concrete failure in front of the shear connector, concrete pry-out failure, shear failure of the concrete and steel failure due to the moment stresses acting onto the steel strip.



Figure 2 – Failure modes of continuous shear connectors

According to the model of Wurzer [1997], there are lateral tensile forces between the steel teeth resulting from the concentrated load introduction of the steel profile (Figure 3a). In the early state of testing fine micro-cracks begin to form in the concrete. The steel fibers are capable to bridge the micro-cracks and the formation of macro-cracks is deferred (Figure 3b, left). However, as the micro-cracks grow the tensile forces have to be sustained by additional reinforcement since the fibers fail due to the missing anchorage (Figure 3b, right).



a) Stresses in the concrete b) Principle of steel fiber reinforced concrete

Figure 3 – load carrying behavior

ULTRA-HIGH PERFORMANCE CONCRETE

The composition of ultra-high performance concrete differs fundamentally from conventional normal or high strength concrete (NSC and HSC). The main characteristics of UHPC are a high compressive strength (up to 200 MPa without thermal treatment) and an improved ductility. The high performance of UHPC is based on the following vital factors: a low water-cementitious material ratio (w/cm) of 0.19 and a high density which is basically achieved by a high content of cement, fine sands (mainly quartz) and silica fume. This is essential to fill the cavities between the solid particles. Furthermore, the silica fume functions as a superplasticizer. Figure 4 shows the components of the UHPC mixture, which was used in the tests.

material		M0	M1	MR
cement CEM I	[kg/m³]	650	660	666
silica fume		177	180	181
quartz powder		456	463	467
Coarse aggregates		952	966	975
steel fiber		194	70	-
steel fiber	[%]	2.5	0.9	-
w/cm	[-]	0.19	0.19	0.19

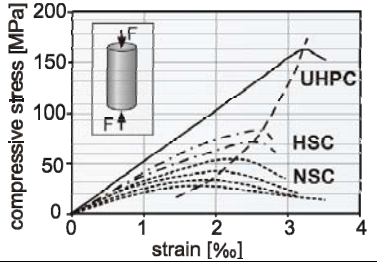


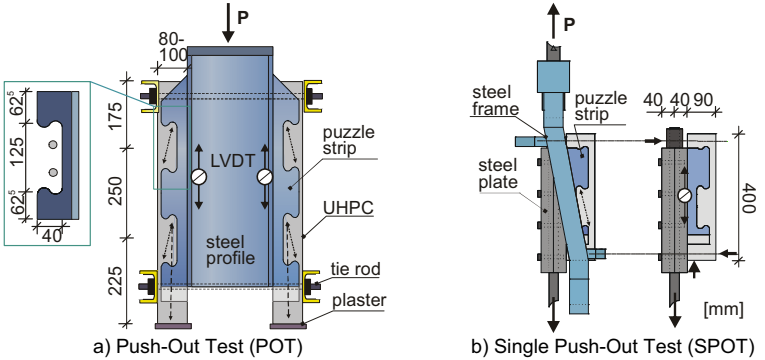
Figure 4 – Characteristics of UHPC and stress-strain diagram

To ensure a sufficient ductility thin steel fibers are added. The fiber content was varied between 0 and 2.5 % of the concrete volume. Due to the steel fibers UHPC not only features a high compressive strength but also a linear-elastic behavior until about 90 % of its compressive strength which is reached at a strain rate of about 3.2 ‰ (Figure 4, right). Conventional concrete shows a distinctive nonlinear behavior due to the micro-cracks, which develop at a stress level of about 40 % of the compressive strength. Besides the ductility the tensile strength of the UHPC is also increased, however, not to the same extend as the compressive strength.

PUSH-OUT TESTS

The test program was designed for both, concrete and steel failure. Concrete failure is mainly governed by the concrete cover between the shear connector and the concrete surface, the fiber content and the degree of transverse reinforcement. Steel failure can be controlled by the thickness of the shear connector. All these parameters were varied within an extensive research program [SPP1182 2008]. Two different continuous shear connectors were tested, the puzzle strip and the saw tooth (Figure 1). The tests were performed using two different set-ups (Figure 5), the Push-Out Test (POT) and the Single Push-Out Test (SPOT).

The POT was designed according to the push-out standard test according to [EC4 2004]. It consists of a steel I-beam with shear connectors welded on the outer side of each flange. To account for the increased material properties of UHPC the dimensions of the test specimen were adjusted and the slab thickness was reduced to 80 – 100 mm. Due to the eccentricity of the action lines of the forces the shear connectors are not only stressed by a pure shear load but by a combined shear and tensile load. To minimize this effect and to prevent an uplift between the concrete slab and the steel profile, tie rods were attached. The tensile forces in the rods were measured by strain gauges. LVDTs were applied to measure the slip between the steel profile and the concrete slab.

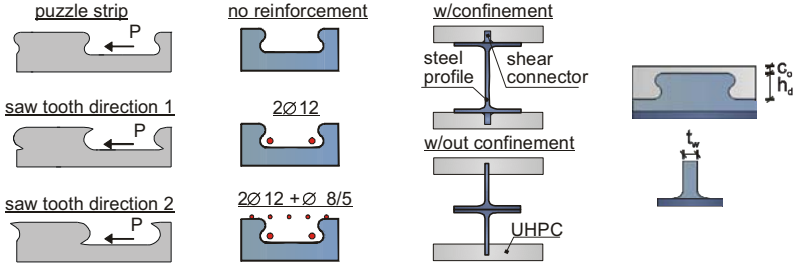


a) Push-Out Test (POT) b) Single Push-Out Test (SPOT)

Figure 5 – Test set-up

The SPOT consists of a steel frame embracing the UHPC block. Due to its compactness it is an appropriate test set-up to preselect shear connectors effectively [Feldmann et al. 2007]. In the SPOT a single shear connector is tested under nearly pure shear load.

The parameters investigated within six test series are summarized in Table 1. If not other mentioned, the thickness of the shear connector is 20 mm and the fiber content of the UHPC is 0.9 % per volume (p.v.). The first two test series were performed with the SPOT set-up (index S), the remaining three series with the POT set-up (index P). In Series SG, the puzzle strip is compared to the saw tooth. The saw tooth is not symmetrical and therefore it was tested in two directions (Figure 6a). Different thicknesses of the puzzle strip were investigated in Series ST. To determine the influence of the fiber content of the UHPC the amount of fibers in the concrete slab was varied in Series PF. The contribution of transverse reinforcement was determined in Series PR (Figure 6b). In filigree composite beams as presented in Figure 1a, there is no upper flange and, thus, there is less confinement of the concrete in this area. The tests in Series PC (Figure 6c) served as a reference for the following beam tests. Within this series different concrete strengths were tested.



a) Series SG b) Series PR c) Series PC d) Explanation

Figure 6 - Specific characteristics

For each test series the load carrying capacity was determined according to the procedure of EC 4. The concrete compressive strength for a 100 mm cube $f_{c,cube}$, the yield strength of the connector f_y, the mean maximum load $P_{max,mean}$ and the characteristic load P_{Rk} for one recess of the shear connector and corresponding slip $\delta_{uk,pl}$ are presented in Table 1. The characteristic plastic slip $\delta_{uk,pl}$ is the deformation measured in the tests during the plastic period after reaching and maintaining the characteristic load P_{Rk}.

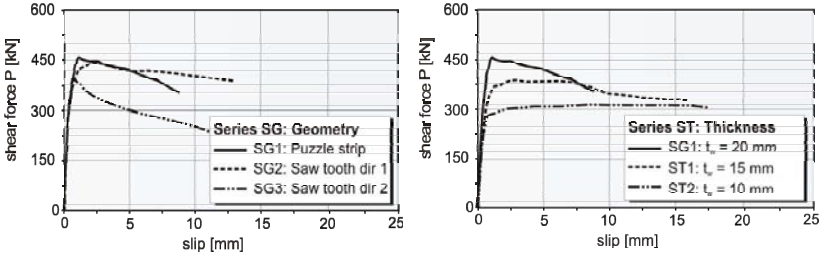
As a result of the push-out tests the load-slip diagrams are plotted for each series. In the evaluation not only the ultimate load but also the initial stiffness and the ductility were examined. For comparison reasons the diagrams are plotted for the shear force of a single shear connector. During all tests there was almost no uplift between the concrete slab and the steel profile and, therefore, almost no tensile forces were measured in the tie rods (< 1 % of the shear load). Only after failure when the maximum load was reached there was an uplift and thus tensile forces in the rods.

Table 1 - Test program

Series	No. of Tests	Description	$f_{c,cube}$	f_y	$P_{max,mean}$	P_{Rk}	$\delta_{uk,pl}$
-			N/mm²	N/mm²	kN	kN	mm
SG1	2	Puzzle, c_0 = 20 mm	179.5	499	412.6	330.6	4.6
SG2	2	Saw tooth, direction 1, c_0 = 20 mm	176.1	499	457.5	396.7	6.0
SG3	2	Saw tooth, direction 2, c_0 = 20 mm	182.6	499	418.4	354.4	1.1
ST1	2	Puzzle, c_0 = 20 mm, t_w = 15 mm	178.0	521	375.2	327.0	10.6
ST2	2	Puzzle, c_0 = 20 mm, t_w = 10 mm	182.6	441	326.2	282.1	15.1
PF1	2	Puzzle, c_0 = 10 mm, 2.5 % p.v.	191.0	499	426.0	372.5	2.0
PF2	3	Puzzle, c_0 = 10 mm, 0.9 % p.v.	177.9	499	389.1	340.7	1.3
PF3	2	Puzzle, c_0 = 10 mm, 0 % p.v.	134.2	499	268.3	200.2	0.2
PR1	2	Puzzle, c_0 = 20 mm	194.4	499	432.9	369.5	4.0
PR2	1	Puzzle, c_0 = 20 mm, 2∅12 per recess	177.9	499	492.7	443.4	4.6
PR3	2	Puzzle, c_0 = 20 mm, 2∅12 + ∅8/5	179.5	499	562.5	493.5	6.5
PC1	3	Puzzle, c_0 = 30 mm, t_w = 12 mm	179.1	472	587.0	495.0	8.4
PC2	2	Puzzle, c_0 = 30 mm, t_w = 12 mm, HSC	92.6	472	297.5	267.1	2.7

Effect of the geometry

With the saw tooth it was intended to increase the confined area in front of the shear connector and thus to improve the load carrying behavior of the shear connector. In Figure 7a, the results of the SPOT with both saw tooth directions are compared to the results with the puzzle strip. The initial stiffness was equally high independent of the load direction and geometry. The saw tooth direction 1 and the puzzle show no noticeable differences in ultimate load. However, when the saw tooth is stressed in reverse direction 2, both the load carrying capacity and the ductility were significantly reduced. In all cases concrete pry-out failure occurred. Since in most structures and especially in bridges the direction of the shear forces between the steel profile and the concrete slab changes depending on the load state, the symmetrical puzzle should be preferred and was therefore chosen for the further tests.



a) Effect of the geometry b) Effect of the shear connectors thickness

Figure 7 - Load-slip-diagram Series SG and ST

Effect of the shear connectors thickness

Depending on the thickness of the puzzle strip there is a slight difference in initial stiffness. With increased thickness of the shear connector higher ultimate loads were achieved (Figure 7b). The specimens of Series ST2 with a thickness of 10 mm failed due to yielding of the puzzle. After the test the specimens were opened and inspected for damage. The 10 mm thick puzzles were deformed noticeably. In Series

ST1 with a connector thickness of 15 mm a combined steel and concrete pry-out failure was observed. Due to the larger thickness pure concrete pry-out failure occurred in Series SG1 (same test as in Series SG) with no plastic deformation of the steel. With increasing thickness and predominating concrete failure the ductility was significantly reduced compared to pure steel failure. However, even for concrete failure the behavior is not brittle due to the steel fibers. In Figure 8 the 10 mm and the 20 mm puzzle are presented after testing. The concrete directly in front of the puzzle was compressed and in both specimens there are cracks visible in the concrete. Whereas the thick 20 mm puzzle shows no deformation at all, there is a significant offset and plastic deformation in the thin 10 mm puzzle.

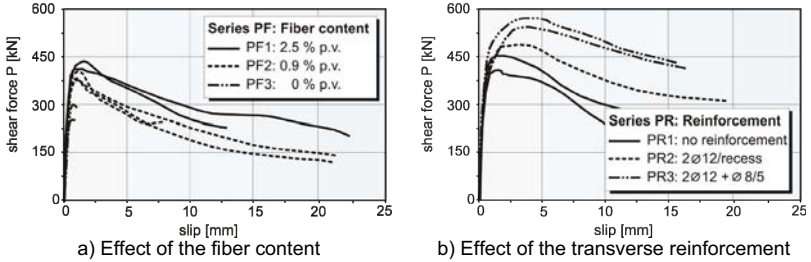


a) 10 mm puzzle b) 20 mm puzzle

Figure 8 - Puzzle strip after testing

Effect of the fiber content

The steel fibers added to the UHPC improve the ductility of the concrete, but they also contribute to the tensile stress resistance. The load-slip diagram in Figure 9a illustrates the influence of the amount of steel fibers on the load carrying behavior of shear connectors. Concerning the initial stiffness there are no differences visible. When there are no fibers added to the concrete there was a sudden failure after the ultimate load was reached. With 0.9 % p.v. steel fibers there was an increase in ultimate load of approximately 33 %. In addition, the steel fibers had a positive effect on the descending branch after reaching the maximum load. Adding 2.5 % p.v. steel fibers led to a further increase of approximately 10 %. However, an increase in the maximum load of 10 % with about 2.7 times more steel fibers cannot be recommended for practical use in terms of cost effectiveness since the steel fibers are one of the most cost-intensive factors in UHPC.



a) Effect of the fiber content b) Effect of the transverse reinforcement

Figure 9 - Load-slip-diagram Series PF and PR

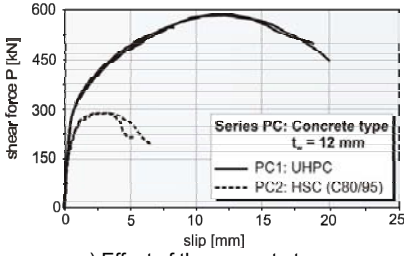
Effect of the transverse reinforcement

In Series PR the effect of transverse reinforcement in the puzzle recesses and above the shear connector was investigated (Figure 9b). The transverse reinforcement increased the confinement of the concrete in front of the puzzle and thus led to higher ultimate loads and an increase in ductility in the case of concrete failure. Therefore, transverse reinforcement is by far more effective to improve the load carrying behavior of the shear connector than the steel fiber content of the concrete.

Effect of the concrete type and confinement

The difference in load carrying behavior of the shear connectors was investigated in Series PC. In this series the shear connectors were cut directly into the 12 mm thick web of a steel profile I 600. The tests served as a reference for the beam tests with equal shear connection. All specimens in this series had transverse reinforcement consisting of 2∅12 in each recess and 6∅10/10 above the shear connection.

Due to the high compressive strength of UHPC the ultimate load of the shear connector was about twice as high as at the puzzle strip in HSC (Figure 10a). However, the load-deformation behavior was more flexible compared to the other push-out tests and the ultimate load was reached after a fairly large slip of 10 mm, which is mainly due to the cracks in the puzzle strips. For UHPC there were also some small signs of concrete pry-out failure on the outer concrete surface whereas no cracks were found on the inner surface. The specimen with HSC, however, was completely destroyed due to concrete pry-out failure and concrete crushing.



a) Effect of the concrete type

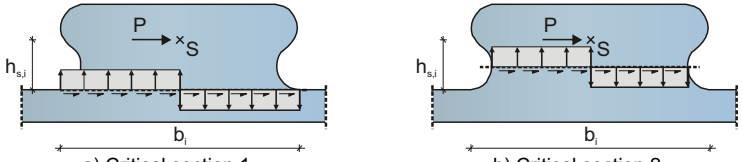


b) Crack in puzzle strip

Figure 10 - Load-slip-diagram Series PC

DESIGN CONSIDERATIONS – STEEL FAILURE

Especially for thin steel strips or for short distances between the shear connectors recesses, steel failure controls the design as it was the case for the 10 and 12 mm puzzle strips (Figure 7b and Figure 10a). The tests showed a horizontal crack in the lower region of the shear connector as it is reported in [Hegger et al. 2006] and [Hechler et al. 2007]. The theoretical model is based on the equivalent stress criterion taking into account the interaction of moment and shear stresses onto the steel strip. Two critical sections are defined, one is located at the root of the puzzle strip and the other one at the location with minimum width (Figure 11).



a) Critical section 1 b) Critical section 2

Figure 11 – Stresses acting onto the steel strip

The resistance of the puzzle strip accounting for steel failure can be determined as follows:

$$P_{sy} = \frac{f_y \cdot t_w \cdot b_i^2}{\sqrt{16 \cdot h_{s,i}^2 + 3 \cdot b_i^2}} \quad (1)$$

with:
- P_{sy} resistance accounting for steel yielding [kN]
- f_y steel yield strength of shear connector [N/mm²]
- $h_{s,i}$ distance between centroid and critical section [mm]
- b_i minimal width of shear connector [mm]
- t_w thickness of the shear connector strip [mm]

When the theoretic shear connector strength accounting for yielding of the steel is compared to the test results, a good agreement can be observed (Table 2). For all tests, critical section 2 was governing.

Table 2 – Comparison of test results with theoretical model

Test -	Description	P_{test} kN	$P_{sy,section1}$ kN	$P_{sy,section2}$ kN	P_{test} / P_{sy} -
ST2-1	Puzzle, c_0 = 20 mm, t_w = 10 mm	313.5	339.1	303.7	1.03
ST2-2		338.9			1.16
PC1-1	Puzzle, c_0 = 30 mm, t_w = 12 mm	550.0	387.6	347.2	1.58
PC1-2		588.4			1.69
PC1-3		585.7			1.69

BEAM TESTS

Under positive bending moments it has to be verified that the plastic theory is applicable, i.e. the steel profile plasticizes before the concrete compression zone fails. Using high performance materials this becomes even more vital since the high strength steel requires a higher yield strain to plasticize and for concrete the strain at failure decreases with increasing concrete strength. This effect was investigated in beam tests made of UHPC with a steel fiber content of 0.9 % p.v. and high strength steel S460. Figure 12 presents the test set-up and the cross section of the tested beam.

The tests were performed under positive four-point bending. Principally, the two beams had the same cross section. One consisted of a compact I-beam (conventional composite beam) and one of an I-beam where the puzzle strip was directly cut into the steel web (filigree composite beam). The profiles were chosen in order to achieve a comparable moment carrying capacity. Taking into account the load-slip behavior achieved in the push-out tests (Figure 10, Series PC), the beams were fully shear connected. Along the shear joint between the steel profile and the concrete slab, LVDT's were attached to measure the slip. At midspan, strain gauges were fixed across the cross section to investigate the strain distribution.

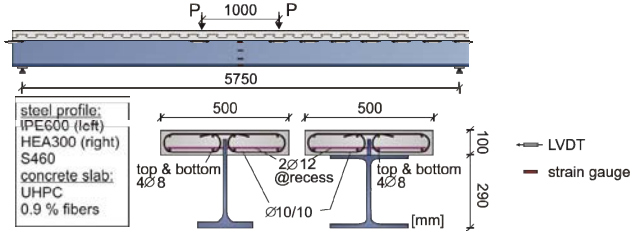


Figure 12 - Beam tests under positive bending

The characteristics of the tested beams are presented in Figure 13, left, where the concrete compressive strength $f_{c,cube}$ the medium yield strength of the steel flange $f_{y,flange}$, the ultimate moment in the tests M_{test} and the calculated plastic moment $M_{pl,calc}$ under consideration of the actual material properties (safety factors γ_i set to unity) and the ultimate concrete strain at failure $\varepsilon_{c,ult}$ are listed.

		Filigree beam	Conventional beam
$f_{c,cube}$	N/mm²	191.0	177.9
$f_{y,flange}$	N/mm²	510	537
M_{test}	KNm	1146	1026
$M_{pl,calc}$	kNm	1106	1164
$\varepsilon_{c,ult}$	‰	-3.9	-3.7
$M_{test}/M_{pl,calc}$	-	1.04	0.88

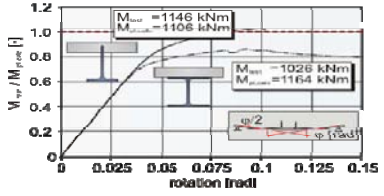


Figure 13 - Beam characteristics and moment rotation behavior of tested beams

In both tests a failure of the compression zone was observed when the ultimate strain of the concrete was exceeded. Figure 13 shows the moment-rotation curves of the tested beams. The angle φ represents the rotation of the cross section at midspan and is determined by the tangent angles of the rotation at the supports. The specific flexural capacity, which is the ratio of the experimental and the calculated plastic moment, is plotted against the rotation. The [EC 4 2004] regulation ($M_{test}/M_{pl,calc} \geq 1$) was reached for the filigree beam. The conventional composite beam, however, failed at approximately 90 % of the theoretical plastic moment. In this case, the upper flange of the HEA 300 profile, which is close to the neutral axis, does not yield in the ultimate limit state. Hence, the plastic design according to EC4 overestimates the resistance achieved by plastic stress blocks.

For full and rigid shear connection between steel and concrete there is a continuous strain distribution with no considerable slip between the two components. However, due to the flexible puzzle strip there is a step in the strain distribution in the composite joint. Figure 14 shows the strain distribution at the ultimate load level for the cross sections of the two beams at midspan. The neutral axis is in the concrete slab and the steel profile is almost completely under tension. Basically, there is hardly any difference in strain distribution between the two cross sections. However, when the areas where the steel profile does not reach the yield strength are compared for the filigree and conventional beam, it is evident, that the area is larger for the conventional beam since there is an upper flange. The error made in the plastic design increases and thus, the plastic moment carrying capacity is overestimated for the conventional composite beam.

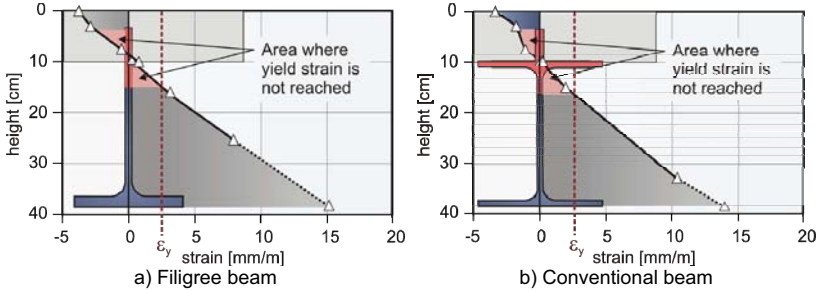


Figure 14 – Strain distribution

After testing, the concrete slabs were removed and the shear connectors in the composite joint were investigated. No cracks were found in the shear connectors or the concrete. Thus, the plastic moment was limited by the rotation capacity of the cross section rather then by the shear connection.

CONCLUSIONS

Push-out and beam tests with continuous shear connectors in ultra-high performance concrete were carried out. Two types of shear connectors made of high strength steel S460 were tested in the push-out tests, the puzzle strip and the saw tooth. The parameters were the geometry and thickness of the shear connector, the steel fiber amount as well as the transverse reinforcement. In the beam tests the moment rotation behavior was investigated. The results can be summarized as follows:

- Continuous shear connectors are capable of transferring high shear forces in UHPC. Due to its symmetry, the puzzle strip is a very appropriate shear connector.
- Depending on the thickness of the shear connector a rigid shear connection can be established with the puzzle strip.
- The influence of the amount of steel fibers added to the UHPC is of minor importance. With almost three times more steel fibers an increase of only 10 % in ultimate load could be achieved. Independent of the fiber content concrete failure occurred. Nevertheless, a minimum fiber ratio of roughly 0.9 % p.v. has to be maintained to guarantee a ductile behavior.
- Arranging transverse reinforcement in the puzzle recesses and between the shear connectors and the concrete surface leads to an increase in ultimate load of up to 30 % and an improved ductility.
- In UHPC the ultimate load of the puzzle strip is doubled compared to HSC.
- The beam tests with UHPC and high strength steel showed that the plastic design according to EC 4 is safe for the filigree beam. For the conventional composite beam the plastic design is overestimated due to the upper flange which does not yield in the ultimate limit state.

ACKNOWLEDGEMENTS

This research project is part of the SPP 1182 which is founded by the DFG (German Research Foundation). The authors acknowledge the funding through the DFG and express their thanks for the support of Arcelor Mittal, Luxembourg and Schmitt Stumpf Frühauf, Munich.

REFERENCES

Feldmann, M., Hechler, O., Hegger, J., Rauscher, S.: Untersuchungen zum Trag- und Verformungsverhalten von Verbundmitteln unter ruhender und nicht ruhender Belastung bei Verwendung hochfester Werkstoffe. FOSTA-Abschlussbericht zum AiF-Vorhaben AiF 13867, Aachen, 2007 (in german).

Hechler, O., Feldmann, M., Rauscher, S., Hegger, J.: Continuous shear connectors in high performance concrete, 2nd Symposium on connections between steel and concrete, Stuttgart, Germany, pp. 1017-1026.

Hegger, J., Feldmann, M., Rauscher, S., Hechler, O.: Load deformation behavior of shear connectors in high strength concrete subjected to static and fatigue loading. IABSE Symposium on Responding to tomorrow's challenges in structural engineering, Budapest, Hungary, 2006, pp. 438-439, full paper on CD.

Leonhardt, F., Andrä, W., Harre, W.: Neues, vorteilhaftes Verbundmittel für Stahlverbund-Tragwerke mit hoher Dauerhaftigkeit. Beton- und Stahlbetonbau 1987; 82(12): 325-331 (in german).

prEN 1994-1-1 (EC4). Design of composite steel and concrete structures, Part 1.1 – General rules and rules for buildings, Brussels, 2004.

Priority Program SPP 1182. Subproject Shear Connectors in UHPC. SPP 1182 - Sustainable building with ultra-high performance concrete (UHPC). German research foundation (DFG), 2008.

Wurzer, O.: Zur Tragfähigkeit von Betondübel, PhD thesis. Institut für Konstruktiven Ingenieurbau, Universität der Bundeswehr, München, Juni 1997 (in german).

Zapfe, C.: Trag- und Verformungsverhalten von Verbundträgern mit Betondübeln zur Übertragung der Längsschubkräfte, PhD thesis. Institut für Konstruktiven Ingenieurbau, Universität der Bundeswehr, München, Juni 2001 (in german).

NOTATION

c_o	concrete cover	$\delta_{uk,pl}$	characteristic plastic slip
$\varepsilon_{c,ult}$	ultimate concrete strani	$f_{c,cube}$	concrete strength (100 mm cube)
f_y	yield strength of shear connector	$M_{pl,calc}$	theoretical plastic moment
M_{test}	experimental Moment	$P_{max,mean}$	mean maximum load
P_{Rk}	charakteristic load	P_{sy}	resistance accounting for steel yielding
t_w	thickness of shear connector strip		

STEEL-FRP COMPOSITE STRUCTURAL SYSTEMS

Kent A. Harries
University of Pittsburgh, Civil and Environmental Engineering
Pittsburgh, PA USA
kharries@engr.pitt.edu

Sherif El-Tawil
University of Michigan, Civil and Environmental Engineering
Ann Arbor MI USA
eltawil@umich.edu

ABSTRACT

Most extant fiber reinforced polymer (FRP) applications in the structural engineering field involve concrete-FRP composite systems, where FRP components are attached to or embedded into concrete structures to improve their structural performance. A relatively small and innovative body of work focusing on steel-FRP composite structural systems is beginning to develop. A state-of-the-art review of progress in this emerging and rapidly developing area is presented. The review is divided into applications: strengthening steel structures with FRP, stabilizing (or bracing) buckling-critical steel elements with FRP and relieving fatigue or fracture-critical conditions. Discussions of concerns pertaining to joining FRP and steel as well as the potential and future of this technology are also presented.

INTRODUCTION

The use of fiber reinforced polymer (FRP) composite materials has become relatively common in infrastructure applications. Most existing applications involve concrete-FRP composite members. Nonetheless a relatively small and innovative body of work is developing focusing on steel-FRP composite structural systems. Steel-FRP composite systems are almost exclusively aimed at retrofit methods for the underlying steel material or structure. Whether strengthening, repairing fractures, relieving stress to enhance fatigue performance or enhancing local or member stability, steel-FRP systems leverage the unique material properties of each material in establishing a composite member or structure. The objective of this paper is to synthesize existing information on the use of composite FRP/steel structural systems and to establish the state-of-the-art and state-of-practice in this nascent field. Composite bridge structures comprising FRP decks on steel girders are not discussed in the present work. Such systems amount to little more than direct replacement of a concrete deck with a FRP deck and there is a significant body of work reporting this application.

FIBER REINFORCED POLYMER (FRP) COMPOSITE MATERIALS

Fiber reinforced polymer (FRP) composite materials combine high-modulus, high strength fibers in a low-modulus polymeric matrix which ensures load transfer between the fibers. The strength and stiffness of an FRP composite is largely determined by the fiber type and fiber architecture. FRP materials that are suited to

civil infrastructure and structural engineering applications typically have high fiber-volume fractions. Orientation of the fibers is controlled so that the resulting FRP is anisotropic. FRPs enable high loads to be carried safely and allow the material to be tailored to suit the local structural demands in the component to be retrofitted. The in-service performance of a composite is influenced both by the fiber and matrix material.

Carbon (CFRP) and glass (GFRP) FRP materials are ubiquitous in the field of structural retrofit. CFRP may be high strength (hsCFRP), high modulus (hmCFRP) and, most recently, ultra-high modulus (uhmCFRP). Generally an increase in CFRP stiffness is accompanied by a reduction in strength and rupture strain of the fiber. GFRP (most typically based on E-glass fibers) have a much lower modulus than CFRP and are somewhat less expensive on a unit stiffness basis. To be effective in strengthening applications, the modulus of the FRP selected for a particular application should be compatible with the substrate material. For this reason, CFRP materials have often been used with a steel substrate.

A polymeric matrix binds and protects the fibers of an FRP, transferring force into, and between, fibers through interfacial shear. The matrix also provides stability and environmental protection to the slender, delicate fibers. Epoxy resin systems are most commonly used as the matrix in hand lay-up applications and as the adhesive in plate bonding techniques. Polyester resin systems are often used as the matrix material in preformed composite materials such as those used for plate bonding applications.

In terms of ease of handling, installation and quality control, preformed CFRP plates or strips are rapidly becoming the preferred products for structural retrofit. The exception is that wet lay-up fabrics remain appropriate for applications involving retrofit forming around corners. In either case the resulting system has a steel-adhesive-FRP interface region. Table 1 provides a summary of representative basic material properties for each layer in the system. The FRP properties are given for the composite strip product rather than for the raw fibers. Hand lay-up products will typically have lower strengths and stiffnesses than those given in Table1 since the resulting fiber volume ratio is typically lower than in preformed systems.

Table 1 – Typical properties of steel-adhesive-FRP systems.

	Mild Steel	Preformed FRP Strips				Adhesive	
		hsCFRP	hmCFRP	uhmCFRP	GFRP	high modulus	low modulus
tensile modulus, GPa	200	166	207	304	42	4.5	0.4
tensile strength, MPa	276-483	3048	2896	1448	896	25	4.8
ultimate strain, %	18-25	1.8	1.4	0.5	2.2	1.0	>10
density, kg/m^3	7530	~1618	~1618	~1618	~2146	~1201	~1201
CTE, 10^{-6}/^{o}C	21.6	~0	~0	~0	8.8	162	n.r.
T_g[a], ^{o}C	-	149	149	149	resin	63	-
shear strength, MPa	-	-	-	-	-	24.8	9.0
bond strength, kPa	-	-	-	-	-	~20.7	~5.0

[a] T_g = glass transition temperature – associated with vitrification of polymer matrix

STRUCTURAL RETROFIT WITH FRP

A great deal of work has been conducted on the use of externally bonded FRP systems for structural strengthening of building and bridge systems and components. The overwhelming majority of this work has focused on the retrofit of

reinforced concrete structures. In virtually every existing application, FRP materials are used to supplement steel reinforcement. Indeed, early FRP external bonding applications were developed as an alternative to heavy and awkward steel plate bonding techniques. In some applications, the analogy to steel is appropriate; however this paradigm is restrictive and does not always result in an efficient use of the unique properties of FRP materials: their high stiffness, strength and linear behavior.

There is a variety of design guidance available for the use of externally bonded FRP materials for the retrofit and rehabilitation of concrete structures (ACI 2002 in the USA). Current research in the area has a strong emphasis on issues of the durability of the bonded FRP and the nature and behavior of the bonding mechanism itself. The bond of FRP to concrete can only be as strong as the substrate concrete and may fail through a variety of mechanisms, some associated with classical debonding mechanisms and others associated with the behavior and condition of the concrete substrate. Provided adequate quality control is executed, the behavior of externally bonded FRP will be largely governed by the substrate concrete. This will not be the case for a stronger steel substrate, allowing more conventional bond mechanics to be used to describe debonding behavior.

RETROFIT OF STEEL MEMBERS WITH FRP

There is comparatively little work investigating the use of bonded FRP materials for the retrofit of steel members. Most available research and guidance focuses on the use FRP for flexural retrofit: generally, applying FRP materials to the tensile flange of a section to increase its capacity. In Great Britain, work has been done in using externally bonded FRP to rehabilitate degraded or understrength (often due to increased load demands) cast and wrought iron structures (Moy 2001). Hollaway (2004) reported on European applications of CFRP to strengthen cast iron bridges including the first application on the Bures Bridge in Suffolk, UK and another on the Hythe Bridge, Oxford, UK. Both applications required the pre-fabrication of custom CFRP components to be fitted to the bridges to increase their load carrying capacity. Garden (2001) reports the case of a curved steel beam strengthened using a low temperature moulding hybrid carbon/glass fiber reinforced polymer composite prepreg materials with a unidirectional fiber orientation along the direction of the beam and a $0^{o}/90^{o}$ orientation employed to resist the shear and torsional loading.

Cadei *et al.* (2004) reports on thirteen applications of strengthening cast iron structures and six instances of strengthening steel structures; no applications on wrought iron are known. The selection of FRP for cast or wrought iron is largely for aesthetic purposes. It is believed that the capacity of the member can be increased using the high performance FRP materials while maintaining the architectural integrity of the member and limiting the increase in member dimension and structural weight. It is noted that while Cadei *et al.* is prepared as a guideline, the document presents design from a theoretical point of view and notes: “Experimental testing is recommended to validate the design procedures presented herein. Appropriate test programs should also be undertaken as a part of major strengthening schemes.” A lengthy list of requirements for future research and a sparse list of demonstration applications illustrate that the use of FRP to retrofit steel members is very much in its infancy. Nonetheless, the Cadei *et al.* document represents the state-of-the-art for FRP strengthening of steel structures.

STRENGTHENING OF FLEXURAL ELEMENTS

In the United States, two NCHRP-IDEA projects (IDEA-011 (Mertz and Gillespie 1996) and IDEA-051 (Mertz *et al.* 2002)) were performed at the University of Delaware in the late 1990's. These projects focused on the flexural strengthening of corroded bridge girders and addressed the use of bonded FRP materials on only the tension flange of simple girders. The rationale was that the bottom flanges of bridge girders typically see the greatest level of corrosion, largely due to debris accumulation.

In the earlier study, Mertz and Gillespie (1996) report on six small scale tests of 1525 mm long W200x15 members retrofit with the five different adhesively bonded schemes; shown in Figure 1 (the fifth scheme was similar to that shown in Fig 1(a) using a different CFRP material.) All specimens demonstrated an increase in flexural stiffness and strength compared to the un-strengthened control specimen. As might be expected, the "sandwich-reinforced" specimen (Fig. 1(b)), having the additional FRP material located a distance below the flange showed the greatest improvement in stiffness and elastic strength (although the second CFRP strip retrofit Fig 1(a) was comparable for both parameters). The "composite-wrapped" specimen (Fig. 1(c)) showed the greatest increase in ultimate capacity since the composite wrap surrounding the foam core provided better shear transfer through higher loads than the aluminum honeycomb (Although, again, the second CFRP strip method was comparable.) All specimens tested failed in a debonding mode of failure, with the CFRP peeling from the flange at its ends. The second CFRP strip specimen, and the specimen having a pultruded channel retrofit (Fig. 1(d)), did not debond until loads greater than the unstrengthened beam failure load were exceeded.

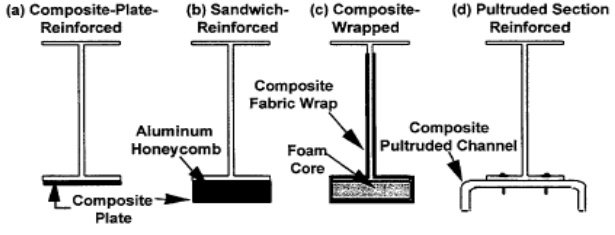


Figure 1 – Small-scale specimens tested by Mertz and Gillespie.

Two corroded 600 mm deep girders (similar to W610x125 but with tapered flanges), recovered from a 1940-era Pennsylvania bridge, were tested using a strengthening scheme similar to that shown in Fig 1(a), having CFRP strips applied to both the top and bottom of the tension flange. The CFRP strengthening was able to increase the stiffness and moment capacity of the corroded girders. The first girder had a stiffness and strength, prior to strengthening, of approximately 87% of that expected for a new, uncorroded girder. In this case, the stiffness was increased to that of the uncorroded girder and the strength was found to exceed that of the uncorroded girder. The second girder had an original condition resulting in about 62% of its uncorroded stiffness. In this case the strengthening significantly improved the behavior but was unable to restore the uncorroded stiffness or strength. The ultimate capacity of both specimens was controlled by buckling of the compression flange

which was not addressed in the strengthening scheme. Nonetheless, the tension flange did yield and no debonding of the CFRP was observed in either specimen.

Having demonstrated the viability of strengthening steel with CFRP strips, Mertz *et al.* (2002) extended their initial work with pilot studies investigating the transfer length of bonded CFRP and the fatigue performance of FRP strengthened girders. Simple steel tensile specimens having CFRP strips bonded to both faces were used to investigate the force transfer between steel and CFRP. In all specimens, regardless of load level considered, approximately 99% of the total force transfer occurred within the first 75 to 100 mm (3 to 4 in.) of the bonded reinforcement. This result is consistent with standard calculations of "effective bond length" which is considered to be a characteristic property of thin bonded FRP systems (Teng *et al.* 2002). Mertz *et al.* recognize the importance of a thin adhesive layer in allowing stress transfer between the steel substrate and CFRP. However, an efficient stress transfer exacerbates debonding stresses. Despite this, Mertz *et al.* only report debonding in one tension specimen at strains corresponding to yield of the underlying steel specimen. They attribute the lack of debonding in the other specimens to the use of adhesive having a low shear modulus and high elongation properties. Fatigue performance of CFRP bonded to the tension flange of simply supported specimens revealed little degradation of specimen stiffness or strain carried by the CFRP and no apparent debonding after several million cycles of loading.

Mertz *et al.* (2002) and Miller *et al.* (2002) report on a field installation on a single girder of a bridge carrying I-95 Southbound over Christina Creek outside Newark Delaware. This installation was a demonstration of the techniques developed in the IDEA projects. A single W610x125 girder spanning 7.5 m was retrofit with CFRP on the bottom of the tension flange. Load tests indicated a reduction in tension flange strains of 11.4% under a vehicle approximately equivalent to an AASHTO H32 loading. Chacon *et al.* (2004) report a related demonstration project involving the strengthening of two W24x100 floor beams of the Ashland Bridge carrying State Route 82 over Red Clay Creek in Delaware. In this application a decrease in tension flange strain of 5.5% was observed under service load conditions. Neither of these demonstration strengthening projects were strictly necessary – the strengthened girder and floor beams did not require strengthening. Rather, the projects are intended to serve as test beds to investigate the long term performance and durability of CFRP strengthening techniques for steel bridge girders.

Patnaik and Bauer (2004) report on an experimental program of CFRP strengthened steel beams. This study also addresses flexural strengthening by adhering CFRP strips to the tension flange. As expected, the moment capacity of the beam was increased - in this case by about 14%. Both strengthened beams are reported to have failed due to lateral torsional buckling, however the authors report a final failure involving rupture of the CFRP. This latter observation demonstrates that in this application, bond of the CFRP to the steel substrate was adequate.

A second series of tests reported by Patnaik and Bauer (2004) involved 350 mm deep beams having intentionally slender – 3 mm wide by 325 mm tall – webs intended to investigate shear strengthening with CFRP. As expected, the unstrengthened beam failed due to elastic web buckling prior to flexural yielding. The application of vertically oriented, unidirectional CFRP to both sides of the web is reported to have allowed the section to yield prior to the onset of inelastic web buckling. Furthermore, although significant debonding of the short CFRP strips was

evident, the failure is reported to have been ductile and “it was possible to sustain the load for a short time even after the initiation of web shear buckling.”

Schnerch *et al.* (2004) investigated resin and adhesive selection for wet lay-up of carbon fiber sheets and bonding of pre-cured laminate plates and their effect on the flexural behavior of a steel monopole. Resin selection for the wet lay-up process was determined through testing of double lap shear coupons using ten different resins. Test results showed a 25% increase in the elastic stiffness of the steel monopole resulting from the application of a limited number of CFRP sheets.

Other similar investigations of the use of CFRP strips attached to the tension flange of I-girders have demonstrated generally improved flexural capacity – proportional to the CFRP applied – although little improvement to girder stiffness (Sen *et al.* 2000; Tavakkolizadeh and Saadatmanesh 2003a; Lenwari *et al.* 2005). In such applications, Lenwari *et al.* (2006) demonstrated that the stress intensity at the ends of CFRP plates governs the debonding strength and that this region was critical for the initiation of debonding. Colombi and Poggi (2006a) observed similar behavior but also demonstrated a substantial increase in the post-yield stiffness provided CFRP debonding could be mitigated.

Al-Saidy *et al.* (2004) investigated the effect of CFRP plates on the behavior of composite steel-concrete beams. The investigation focused on the behavior of beams damaged intentionally at their tension flange to simulate corrosion and then repaired with CFRP plates attached to the tension area. Damage varied between no damage and a loss of 75% of the bottom flange. The test results showed that the elastic flexural stiffness of damaged beams can be partially restored (up to 50%); whereas the strength of damaged beams can be fully restored to their original, undamaged state using the particular CFRP plates investigated. Similarly, Photiou *et al.* (2006) reported a series of tests on artificially degraded flexural beams where the failure load for all specimens exceeds the plastic collapse load of the undamaged beam. Furthermore, by using U-shaped FRP applications extending up the web to the neutral axis, composite action was provided between the steel member and fiber layer leading to better performance and mitigating debonding even at failure levels.

STRENGTHENING OF TENSILE ELEMENTS

Jiao and Zhao (2004) tested 21 butt-welded very high strength (VHS) steel tubes strengthened with CFRP in axial tension. Three types of failure were reported: adhesive failure, fiber rupture and mixed failure. The authors concluded that significant strength increase was achieved using the epoxy bonded CFRP strengthening technique and proposed a theoretical model to estimate the load carrying capacity of butt-welded VHS tubes strengthened with CFRP

An experimental and numerical study was carried out by Colombi and Poggi (2006b) to verify the effectiveness of CFRP pultruded plates to reinforce steel tensile members. Three different sets of specimens were tested under uniaxial tension. In the first group, CFRP plates were used as double side reinforcement for continuous steel plates. In the second group, double lap specimens were tested to study the force transfer capability of the plates. Bolted joints were strengthened with CFRP in the final group. Force transfer and failure mechanisms were evaluated from both analytical and numerical models. The results were mixed and showed that the strengthening methods used for all three test groups lead to a mild increase in capacity for some specimens but did not realize any benefit for other cases.

RETROFIT OF STEEL CONNECTIONS

Mosallam *et al.* (1998) present a pilot study investigating the use of CFRP T-sections for strengthening steel moment connections in seismic regions. The proposed detail resembles a typical welded haunch bracket (AISC 1999) installed on both top and bottom flanges. The CFRP haunch bracket is reported to have exhibited improved rotational capacity over a comparable welded steel haunch. It is believed that the improved deformability results from the greater flexibility of both the CFRP haunch itself and the bonding adhesive which permits a more uniform force transfer than a fully welded connection.

REPAIR OF FATIGUE DAMAGE AND ENHANCING FATIGUE LIFE USING FRP MATERIALS

FRP materials, particularly CFRP, exhibit excellent performance when subject to fatigue loads. In conditions of tension fatigue where environmental effects are not affecting behavior, CFRP behavior is dominated by the strain-limited creep-rupture process. Plotted on a semi-log S-N curve, CFRP composites exhibit strength degradation due to tensile fatigue on the order of 5 to 8% per decade of logarithmic cycles (Curtis 1989). Additionally, CFRP composites do not generally exhibit a clearly defined endurance limit under conditions of tension fatigue.

Fatigue performance of FRP composites may be affected by a variety of factors (Agarwal and Broutman 1990). Fatigue performance of CFRP has been shown to be relatively unaffected by changing fiber type but the S-N response may shift significantly as the matrix composition is changed (Curtis 1989; Boller 1964). Fiber orientation relative to loading direction (Boller 1964) and laminate architecture in multi-directional FRP composites (Davis *et al.* 1964) can also significantly affect fatigue behavior. Although clearly fiber-volume ratio of an FRP composite will affect the gross section stress capacity, reduced fiber volume has been shown to result in a reduced rate of strength degradation with cycling (Tanimoto and Amijima 1975). It has also been shown that the fatigue life of CFRP bars depends on the mean stress and the stress ratio (minimum-to-maximum stress). Higher mean stress or a lower stress ratio causes a reduction in fatigue life (Rahman and Kingsley 1996; Saadatmanesh and Tannous 1999). Increased ambient temperature, even within a range typical of infrastructure applications (20^{o}C to 40^{o}C) is known to be detrimental to the fatigue performance of FRP materials, affecting the stress range although not typically the rate of degradation (Adimi *et al.* 1998; Agarwal and Broutman 1990).

Jones and Civjan (2003) used fracture specimens having CFRP applied to one or both sides to evaluate the ability of a CFRP overlay to enhance fatigue performance. Center-hole specimens with crack initiators and edge-notched specimens made of cold-rolled A36 steel having measured yield and ultimate stresses of 345 MPa and 490 MPa, respectively, were used. Increases in fatigue life were reported for all specimens tested, although the effectiveness of the FRP (and thus the fatigue life enhancement) was dominated by the adhesive behavior.

Tavakkolizadeh and Saadatmanesh (2003b) presented the results of a study on the retrofitting of notched steel beams with CFRP patches for medium cycle fatigue loading. Twenty one S127x4.5 A36 steel beams were prepared and tested under four-point bending. The number of cycles to failure, changes in the stiffness and

crack initiation and growth in the specimens were compared to unretrofitted specimens. The authors concluded that the CFRP patches not only extended the fatigue life of the notched detail more than three times, they also decreased the crack growth rate significantly.

Nozaka *et al.* (2005) report a fundamental study of the use of CFRP strips for the repair of fatigue-damaged tension flanges of steel I-girders. The focus of this study was to establish appropriate values for the effective bond length for such repairs. A variety of repair configurations were tested including providing a gap (bonded and unbonded), no gap, and fully bonded or partially bonded CFRP in the region of the existing fatigue crack. Additionally two CFRP systems and five adhesive systems were tested. The results reported the greatest increase in strength resulting from the system using both the CFRP and adhesive with the lowest moduli of elasticity of those considered.

Liu *et al.* (2006) report a study of the direct tension fatigue behavior of bonded CFRP sheets used to create "strap joints" between two steel plates. This study reported an apparent fatigue limit of 40% of the ultimate static strength of the strap joint specimens. Below this limit specimen failure and steel-CFRP bond behavior was not affected by the applied fatigue loads.

ENHANCING STABILITY OF STEEL ELEMENTS

FRP composite materials have recently been used to enhance the stability of steel members. In this application, the high stiffness and linear behavior of FRP materials are utilized to provide "bracing" that improves the buckling and post buckling behavior of steel components. Recent research has demonstrated that the application of FRP reinforcement can lead to improvements in the flange local buckling (FLB), web local buckling (WLB) and lateral torsional buckling (LTB) behavior of steel members. This application is not aimed at increasing the load carrying capacity of the steel section, *per se*; although this may certainly be accomplished if desired. Rather, the application is aimed at providing stability (in the sense of bracing) to the steel member through the addition of supplemental stiffness at strategic locations.

Ekiz *et al.* (2004) demonstrated the use of CFRP wraps to enhance the plastic hinge behavior of double-channel members modeled on chord members of a special truss moment frame. Two cases are considered, one where the entire gross cross section is wrapped, the second where only the extending flanges are wrapped; both methods exhibited improved behavior of the hinge as compared to unwrapped specimens. Ekiz *et al.* report that the presence of the CFRP wrap increased the size of the yielded plastic hinge region, inhibited the occurrence of local buckling and delayed the onset of lateral torsional buckling. These effects resulted in reduced strain demands, increased rotational capacity, and improved energy dissipation capacity in the plastic hinge region.

In a study investigating the use of CFRP to strengthen hollow structural square (HSS) columns, Shaat and Fam (2006) report on concentric axial load tests of squat HSS 88.9x88.9x3.2 sections wrapped with both longitudinal and transversely oriented CFRP sheets. Axial compression strength increases on the order of 8% to 18% and axial stiffness increases (resulting from the longitudinally oriented CFRP) of between 4% and 28% are reported. They suggested that the transverse CFRP can help restrain outward directed local buckling of the HSS walls. Similar tests on long

HSS columns did not show similar results since behavior was dominated by initial eccentricities rather than local buckling.

Accord and Earls (2006) present an analytical study wherein the effects that bonded low modulus GFRP strips have on the inelastic cross-sectional response of I-shaped sections developing plastic hinges under a moment-gradient loading is investigated. This work demonstrated that the presence of the GFRP strips enhanced the structural ductility of the cross-section as a result of providing effective bracing of the flange outstands, and thus inhibiting the formation of the local buckles in the compression flange of the cross-section. As the location of the GFRP strips was adjusted to increase their efficacy as bracing elements, a concomitant increase in structural ductility was noted; thus supporting the notion that the GFRP employed in this fashion enhances the overall performance of the steel member through the bracing that it provides against dominant plate buckling modes.

Harries et al. (2008) demonstrated the concept of strategically applying FRP material to a steel compression member in order improve global and local buckling behavior. Improvement in load-carrying capacity was found to be proportional to the increase in effective radius of gyration (r_y) affected by the presence of the FRP. For elastic buckling, the entire section is considered in which case the increase in r_y is nominal. For local (plastic) buckling, however, only the outstanding plate element (WT stem, in the cases tested) is considered in which case the proportional improvement in capacity is greater. Harries et al. showed that prior to FRP debonding, the presence of the FRP controls the plastic buckling and delays the formation of the plastic "kink". The formation of this kink affects the cyclic compressive capacity of the section upon subsequent reloading, the tensile stiffness of the section, and can lead to section fracture in relatively few loading cycles. Thus the application FRP may represent a viable option for improving the energy absorption and ultimate cyclic ductility of elements susceptible to plastic buckling in a seismic lateral force resisting system.

Ekiz and El-Tawil (2006) report on an analytical and experimental research program conducted to investigate the buckling behavior of compressive steel braces strengthened with CFRP laminates. To improve the effectiveness of the CFRP wraps, the steel member is first sandwiched within a core (comprised of mortar or PVC blocks) prior to attaching the external CFRP sheets. The authors derived expressions for requirements to prevent buckling of the steel braces from equilibrium considerations and verified the expressions with test results. Small scale tests show that significant improvements can be achieved in the inelastic axial deformation reached prior to buckling and load carrying capacity after buckling when CFRP wrapping is used. In related research, Ekiz and El-Tawil (2007) showed that the same CFRP strengthening technology can be scaled up. They demonstrated large improvements in the buckling and post-buckling response of full-scale double angle brace members subjected to reversed cyclic loading. The authors proposed that CFRP wrapping could be used to make steel braces behave in a buckling restrained manner for seismic retrofit purposes.

CHALLENGES TO THE USE OF FRP BONDED TO STEEL

Behavior of FRP-to-Steel Bond

There has been relatively little research conducted on the bond behavior of FRP-steel joints in the context of civil engineering applications. In addition to conventional modes of failure, FRP-strengthened steel members may exhibit debonding of the

FRP laminate. In considering debonding failures, the thickness of the adhesive layer plays a significant role in the failure mode (Xia and Teng 2005). Typically a thin uniform adhesive layer is desirable. Such adhesive layers of reasonable thickness (say less than 2 mm thick) will exhibit relatively ductile debonding failures within the adhesive layer. Thicker adhesive layers (as may result when the adhesive is used to make up for dimensional changes in the substrate) exhibit brittle delamination failures along the steel-adhesive interface. Additionally, Xia and Teng (2005) have shown that FRP-steel interfacial behavior is accurately modeled using relatively simple load-slip relationships. Indeed, for thin adhesive layers, a bilinear load-slip relationship approximates observed experimental behavior well. Additionally, debonding behavior in such cases is closely related to adhesive tensile properties and is relatively independent of adhesive layer thickness.

Stratford and Chen (2005) report that interfacial stress analysis to predict shear and through-thickness peel stress distributions for FRP-steel adhesive joints is easily and accurately accomplished using low-order linear elastic stress analysis such as that recommended by Cadei *et al.* (2004). Interfacial stress discontinuities occur at the termination of the adhesive layer. Based on experience gleaned from the aerospace industry, a variety of termination details may be used to reduce these discontinuities including spew, convex or concave fillets, tapers and reverse tapers, stepped FRP plates and external clamps (Stratford and Chen 2005).

Substrate Preparation

Bond to steel, regardless of the application, requires a clean and sound substrate, and practical field application requires a relatively simple procedure. The typical application (Cadei *et al.* 2004) involves abrasive (grit) blasting followed within a few hours with a primer/conditioner to ensure that corrosion product does not form and contaminate the newly exposed steel. Since epoxy adhesives will be used, the primer will typically be a (matching) silane-based product which can also serve as an "adhesion promoter". The adhesive, protective GFRP layer (see below) and CFRP are then installed. Research associated with the previously discussed NCHRP-IDEA program investigated the quality of steel-to-CFRP bonds (Bourban *et al.* 1994; McKnight *et al.* 1994; Karbhari and Shulley 1995) and recommend the use of a silane primer; although no specific mechanical surface preparation was recommended. The results from the research however are inconclusive as to whether the silane primer itself improved (promoted) bond performance. It is possible that the primer enhanced bond performance simply by inhibiting the formation of corrosion product between the time of surface preparation and that of CFRP application. Garden (2001) reports a curved I-girder completely wrapped in CFRP; in this case silica gel packs were used to protect the prepared surface from moisture and thus corrosion.

Thermoset epoxy adhesives are developed specifically to offer good adhesion to metals. They interact strongly with the adherands and promote excellent bonding. Bourban *et al.* (1994) indicates a clear benefit from curing the epoxy adhesive at elevated temperatures (around 93^{o}C) during the initial cure (10 to 20 minutes). The resulting bond is stronger, tougher and more durable when subject to adverse environments (Karbhari and Shulley 1995). Furthermore, because the epoxy cures faster, it is less likely to sag (requiring falsework) or be affected by vibrations or loading that may be present during an *in situ* application (Moy 2007). To this end,

Karamuk *et al.* (1995) have proposed the concept of using induction heating of the steel substrate to assist in the accelerated cure of the epoxy adhesive.

Environmental Exposure, Creep and Fatigue Behavior

Moisture, humidity and elevated temperature can all affect the behavior of a bonded FRP system, regardless of the substrate material to which it is applied. Some FRP materials are additionally susceptible to creep due to sustained loads and adhesive bondlines are susceptible to damage from cyclic (fatigue) loads (Harries 2005). Research efforts associated with the use of FRP materials in concrete infrastructure offer some relevant guidance as to the effect of typically experienced environmental and mechanical loading conditions. When used in conjunction with a steel substrate, some additional environmental protection may be accorded the CFRP by the presence of fireproofing materials or topcoat or finishing systems.

Galvanic Corrosion

Galvanic corrosion occurs when two different metals are electrically coupled in the presence of an electrolyte (surface moisture or condensation). The corrosion potential is "measured" by how far away on the electropotential series the two conductors are. Carbon is widely separated from steel making galvanic corrosion of the steel likely. Suitable design and detailing is sufficient to mitigate galvanic corrosion as evidenced in the aerospace industry that has been successfully joining aluminum and carbon fibers (even more widely separated than carbon and steel on the electropotential series) for many years. Although the adhesive layer itself or a coating applied to the steel substrate should be adequate to mitigate galvanic corrosion, relying on these methods is a risk in infrastructure applications where rugged handling may affect the quality of the insulating barrier. For infrastructure applications, the inclusion of a GFRP (E-glass is an insulator) layer between the steel and CFRP is suggested (Cadei *et al.* 2004; Tavakkolizadeh and Saadatmanesh 2001).

SUMMARY AND CONCLUSIONS

This paper reviews the existing state-of-the-art in the application of steel/FRP composite structures for civil infrastructure. Rehabilitation of steel members and structures using FRP materials is a relatively nascent field, building largely from the success of FRP rehabilitation methods for concrete structures. Studies have shown that strengthening steel flexural elements with FRP is viable. Improving fatigue or fracture propagation conditions have also proven successful in laboratory studies. An application unique to steel structures involving the use of FRP materials to provide stability or buckling restraint has been proposed and demonstrated by a few researchers.

As the reports reviewed in this paper suggest, the application of FRP in steel structures is currently in its infancy, much like concrete/FRP applications were in the late 1980s. Concrete/FRP technology has since burgeoned into a vibrant and rapidly growing industry. Drawing parallels from the concrete/FRP experience and the fact that steel/FRP applications show great promise, steel/FRP technology appears to be also poised for explosive growth in the near future. This growth will require extensive research to identify new applications, develop the means by which to fully realize the

potential of steel/FRP composite systems, and standardize the technology so that it can ultimately be codified and widely adopted by practicing engineers.

ACKNOWLEDGEMENTS

This paper was prepared as part of the activities of the ASCE Committee on Composite Construction (formerly chaired by the second author) Task Group on Steel-FRP Composite Structures chaired by the first author. The comments and review provided by the entire committee are gratefully acknowledged. Dr. Judy Liu of Purdue University and Mr. Ekin Ekiz, a PhD candidate at the University of Michigan working under the supervision of the second author, both contributed to the manuscript.

REFERENCES

Accord, N.B. and Earls, C.J. 2006. Use of Fiber Reinforced Polymer Composite Elements to Enhance Structural Steel Member Ductility, *ASCE J. Comp. Constr.* **10**(4), 337-344.

Adimi, R., Rahman, H., Benmokrane, B. and Kobayashi, K. 1998. Effect of Temperature and Loading Frequency on Fatigue Life of a CFRP Bar in Concrete, *Proc. 2nd Int'l Conf. Comp. in Infrastructure*, Tucson, **2**, 203-210.

Agarwal, B.D. and Broutman, L.J. 1990. *Analysis and Performance of Fiber Composites*, John Wiley and Sons,

AISC 1999. *Modification of Existing Welded Steel Moment Frame Connections for Seismic Resistance*, Steel Design Guide Series 12. AISC, 82 pp.

Al-Saidy, A.H., Klaiber, F.W., and Wipf, T.J. 2004. Repair of Steel Composite beams with carbon fiber-reinforced polymer plates, *ASCE J. Comp. Constr.* **8**(2), 163-171.

American Concrete Institute (ACI) Committee 440 2002. *ACI 440.2R-02 Guide for the Design and Construction of Externally Bonded FRP Systems for Strengthening Concrete Structures*.

Bourban, P.E., McKnight, S.H., Shulley, S.B., Karbhari, V.M. and Gillespie, J.W. 1994. Durability of Steel/Composites Bonds for Rehabilitation of Structural Components, *Infrastructure: New Materials and Methods of Repair – Proc. 3rd Mat. Eng. Conf.* 295-303.

Boller, K.H. 1964. Fatigue Characteristics of RP Laminates Subject to Axial Loading, *Modern Plastics*, **41**. 145.

Cadei, J.M.C., Stratford, T.J., Hollaway, L.C. and Duckett, W.G. 2004. Strengthening Metallic Structures Using Externally Bonded Fibre-Reinforced Polymers. *CIRIA Pub. No. C595*. 233 pp.

Chacon, A., Chajes, M., Swinehart, M., Richardson, D. and Wenczel, G. 2004. Applications of Advanced Composites to Steel Bridges: A Case Study on the Ashland Bridge. *Proc. 4th Adv. Comp. for Bridges and Structures Conf.*, Calgary.

Colombi, P., Poggi, C. 2006a. An Experimental, Analytical and Numerical Study of the Static Behavior of Steel Beams Reinforced by Pultruded CFRP Strips. *Composites Part B,* **37**. 64-73.

Colombi, P., Poggi, C. 2006b. Strengthening of Tensile Steel Members and Bolted Joints Using Adhesively Bonded CFRP Plates. *Constr. and Build. Mat.* **20**. 22-33.

Curtis, P.T. 1989. Fatigue Behavior of Fibrous Composite Materials, *J. Strain Analy.* **24**(4) 235-244.

Davis, J.W., McCarthy, J.A. and Schurb, J.N. 1964. Fatigue Resistance of Reinforced Plastics, *Mat. Design Eng.* 87-91.

Ekiz, E., El-Tawil, S. Parra-Montesinos, G. and Goel, S. 2004. Enhancing Plastic Hinge Behavior in Steel Flexural Members Using CFRP Wraps *Proc. 13th World Conf. on EQ Eng.* Vancouver.

Ekiz, E. and El-Tawil, S. 2006. Inhibiting Steel Brace Buckling Using CFRP Wraps. *Proc. 8th Nat. Conf. on EQ Eng.* San Francisco.

Garden, H.N. 2001. Use of Composites in Civil Engineering Infrastructure, *Reinf. Plastics*, **45**(7/8) 44-50.

Harries, K.A., Peck, A. and Abraham, E.J. 2008. Experimental Investigations of FRP-stabilized Steel Compression Members, *Proc. 4rd Int'l Conf. on FRP Comp. in Civ. Eng.*, Zurich.

Harries, K.A. 2005. Deterioration of FRP-to-Concrete Bond Under Fatigue Loading. *Int'l Symp. Bond Behav. of FRP in Struct.* Hong Kong.

Hollaway, L. C. 2004. Development and Review of Advanced Polymer/Fiber Composites used in the European Construction Industry, *FRP International,* **1**(1), 10-20

Jiao, H., Zhao, X.L. 2004. CFRP Strengthened Butt-Welded Very High Strength Circular Steel Tubes. *Thin-Walled Struct.*, **42**. 963-978.

Jones, S.C. and Civjan, S.A. 2003. Application of Fiber Reinforced Polymer Overlays to Extend Steel Fatigue Life, *ASCE J. Comp. in Const.* **7**(4) 331-338.

Karamuk, E., Wetzel, E.D. and Gillespie, J.W. 1995. Modeling and Design of Induction Bonding Process for Infrastructure Rehabilitation with Composite Materials, *Proc. 53rd Conf. Soc. of Plastics Eng.* Part 1, 1239-1243.

Karbhari, V.M. and Shulley, S.B. 1995. Use of Composites for Rehabilitation of Steel Structures – Determination of Bond Durability, *ASCE J. Mat. in Civ. Eng.*, **7**(4) 239-245.

Lenwari, A., Thepchatri, T., Albrecht, P. 2005. Flexural Response of Steel Beams Strengthened with Partial-Length CFRP Plates. *ASCE J. Comp. Constr.* **9**(4), 296-303.

Lenwari, A., Thepchatri, T., Albrecht, P. 2006. Debonding Strength of Steel Beams Strengthened with CFRP Plates. *ASCE J. Comp. for Constr.* **10**(1), 69-78.

Liu, H.B., Zhao, X.L. and Al-Mahaidi, R. 2006. The Effect of Fatigue Loading on Bond Strength of CFRP Bonded Steel Plate Joints, *Proc. Int'l Sym. Bond Behaviour of FRP in Struct.*, Hong Kong.

McKnight, S.H., Bourban, P.E., Gillespie, J.W. and Karbhari, V.M. 1994. Surface Preparation of Steel for Adhesive Bonding in Rehabilitation Applications, *Infrastructure: New Materials and Methods of Repair – Proc. . 3rd Mat. Eng. Conf.* 1148-1155.

Mertz, D.R., Gillespie, J.W., Chajes, M.J. and Sabol, S.A. 2002. The Rehabilitation of Steel Bridge Girders Using Advanced Composite Materials *NCHRP-IDEA Project 51*, 25 pp.

Mertz, D.R. and Gillespie, J.W. 1996. Rehabilitation of Steel Bridge Girders Through the Application of Advanced Composite Materials *NCHRP-IDEA Project 11*, 30 pp.

Miller, T.C., Chajes, M.J., Mertz, D.R. and Hastings, J.N. 2002. Strengthening of a Steel Bridge Girder Using CFRP Plates. *ASCE J. of Br. Eng.* **6(**6) 514-522.

Mosallam, A.S., Chakrabarti, P.R., and Spencer, E. 1998. Experimental Investigation on the Use of Advanced Composites & High-strength Adhesives in Repair of Steel Structures, *Proc. 43rd SAMPE Symp.*, Anaheim, **2**, 826-837.

Moy, S.S.J. (editor) 2001. *FRP composites – life extension and strengthening of metallic structures*. ICE design and practice guide, Thomas Telford, London.

Moy, S.S.J. 2007 CFRP Reinforcement of Steel Beams Adhesive Cure Under Cyclic Load. *Proc. 1st Asia-Pac. Conf. FRP in Struct.* Hong Kong, 1019-1024.

Nozaka, K., Shield, C. K., Hajjar, J. F. 2005. Effective Bond Length of Carbon-Fiber-Reinforced Polymer Strips Bonded to Fatigued Steel Bridge I-Girders. *ASCE J. of Comp. for Constr.* **9**(4) 304-312.

Patnaik, A.K. and Bauer, C.L. 2004. Strengthening of Steel Beams with Carbon FRP Laminates. *Proc. 4th Adv. Comp. Bridges and Struct. Conf.* Calgary.

Photiou, N. K., Hollaway, L. C., Chryssanthopoulos, M. K. 2006. Strengthening of an Artificially Degraded Steel Beam Utilizing a Carbon/Glass Composite System. *Constr. and Build. Mat.* **20** 11-21.

Rahman, A. H., and Kingsley, C. Y. 1996. Fatigue Behavior of a Fiber-Reinforced-Plastic Grid as Reinforcement for Concrete, *Proc. 1st Int'l Conf. on Comp. in Infrastructure*, Tucson, 427-439.

Saadatmanesh, H., and Tannous, F. E. 1999. Relaxation, Creep, and Fatigue Behavior of Carbon Fiber-Reinforced Plastic Tendons, *ACI Mat. J.* **96**(2) 143-153.

Schnerch, D., Stanford, K., Sumner, E., and Rizkalla, S. 2004. Strengthening Steel Structures and Bridges with High Modulus Carbon Fiber Reinforced Polymers: Resin Selection and Scaled Monopole Behavior, *Proc. 83rd TRB Meeting*, Washington D.C.

Sen, R. Liby, L. and Mullins, G. 2001. Strengthening Steel Bridge Sections Using CFRP Laminates, *Composite: Part B*, **32** 309-322.

Shaat, A., and Fam, A. 2006. Axial Loading Test on Short and Long Hollow Structural Steel Columns Retrofitted Using Carbon Fibre Reinforced Polymers. *Can. J. Civ. Eng.* **33**(4) 458-470.

Stratford, T.J. and Chen, J.F. 2005. Designing for Tapers and Defects in FRP-Strengthened Metallic Structures, *Proc. Int'l Symp. Bond Behaviour of FRP in Struct.*, Hong Kong.

Tanimoto, T. and Anijima, S. 1975. Progressive Nature of Fatigue Damage of Glass Reinforced Plastics, *J. of Comp. Mat.*, **9**(4) 380-390.

Tavakkolizadeh, M and Saadatmanesh, H. 2003a. Strengthening of Steel-Concrete Composite Girders using Carbon Fiber Reinforced Polymers Sheets, *ASCE J. of Struct. Eng.*, **129**(1) 30-40.

Tavakkolizadeh, M., Saadatmanesh, H. 2003b. Fatigue Strength of Steel Girders Strengthened with Carbon Fiber Reinforced Polymer Patch. *ASCE J. of Struct. Eng.,* **129(**1) 186-196.

Tavakkolizadeh, M., Saadatmanesh, H. 2001. Galvanic Corrosion of Carbon and Steel in Aggressive Environments. *ASCE J. Comp. for Constr.,* **5**(3) 200-210.

Teng, L.G., Chen, J.F., Smith, S.T. and Lam, L. 2002. *FRP-strengthened RC Structures*. Wiley.

Xia, S.H. and Teng, J.G. 2005. Behaviour of FRP-to-Steel Bonded Joints, *Proc. Int'l Symp. Bond Behaviour of FRP in Struct.*, Hong Kong.

TOWARDS A BETTER UNDERSTANDING OF BEHAVIOUR OF BRIDGES WITH INTEGRAL ABUTMENTS

Martin Nilsson, Tech. Lic.
Luleå University of Technology
Luleå, Sweden
martin.a.nilsson@ltu.se

Jörgen Eriksen, PhD Student
Luleå University of Technology
Luleå, Sweden
jorgen.eriksen@ltu.se

Milan Veljkovic, Professor
Luleå University of Technology
Luleå, Sweden
milan.veljkovic@ltu.se

ABSTRACT

One of the issues that has not been completely resolved in bridges built without expansion joints is the influence of seasonal temperature variations and soil characteristics on the maximum bridge length.

To study this problem, a 40 meter long road composite bridge over the river Leduån in the north of Sweden was built in 2005. The bridge superstructure was cast integrally with the substructure. One row of piles on each side of the bridge was constructed to support the abutment. The bridge was continuously monitored for 18 months in order to provide information on the strain level at the top of the pile as a function of the air temperature variations. The results from the measurements were compared to results obtained from 2D Finite Element Analysis. Soil characteristics were varied in the FEA to investigate its influence on the overall bridge behaviour as well as on the level of strain variations at the top of the piles.

The bridge monitoring was a part of a research project, INTAB, Economic and Durable Design of Composite Bridges with Integral Abutments, 2005-2008. The main objective of the project was to propose recommendations for rational analysis and design of bridges with integral abutments.

The total environmental impact and the life cycle costs of the integral abutment bridge were compared with a concrete bridge alternative for the same crossing.

INTRODUCTION

Integral abutment bridges are built without any expansion joints, and their benefits are the lower construction and maintenance costs. The abutments are generally supported on a single row of steel piles, to provide the required flexibility for accommodating the longitudinal bridge movements due to seasonal air temperature variations. Such movements impose cyclic displacements on the abutments, the back-fill and the steel piles. The magnitude of these cyclic displacements is a

function of the level of the temperature variation, materials used in the superstructure and the length of the bridge.

The first bridges with integral abutments were built in the 1960's in the USA. This type of bridge has in recent years gained popularity in Europe, primarily in the UK and in the Scandinavian countries. Both the maximum span length and the total bridge length have increased through the years. The longest concrete bridge is 358 m, and is located on Tennessee State Route 50 over Happy Hollow Creek. The longest steel girder integral bridge has a total length of 318 m and is located in Colorado [Hassiotis and Roman, 2005]. It is obvious that countries, such as the USA, with design requirements that are more open towards new technologies, encourage the implementation of innovative solutions even if they are not thoroughly examined. Although nationally accepted design specifications for integral bridges do not exist, each highway department is allowed to make decisions depending on their own expertise. It is interesting to note that some states in the USA allow plastic strains in the steel piles below the abutment back-walls.

The Leduån Bridge was designed for temperature range 80 ^{o}C, from -40 ^{o}C to +40 ^{o}C. This rather large temperature differences certainly decreases the length limit compared to the experience from the USA.

Only a few bridges with integral abutments have been built in Sweden since the 1980's, and the main obstacle for a wider acceptance of this type of bridge is the lack of recommendations for rational analysis and design. According to the Swedish code for bridges, BRO 2004 [Vägverket, 2004], no plastic strains are allowed at the serviceability limit state even if the critical section is at the top of a pile. Such high strains may occur due to seasonal temperature variation a few times every year, and they are limited to a very narrow region.

The first investigation focusing on development of rational design for steel piles was initiated at LTU in the late 1990's and results were published in [Pétursson, 2004], [Tlustochowicz, 2007] [Hällmark, 2007] and [Nilsson, 2008].

CONSTRUCTION OF THE BRIDGE OVER LEDUÅN RIVER

At the end of 2005, it was decided to build an integral bridge on a road with low traffic. Therefore the bridge was seen as the perfect choice to monitor influence of the temperature variations. The bridge was designed as a single span composite bridge with a span of 40 m and a concrete deck 5m wide placed on the two steel girders, Fig.1.

Six vertical end bearing circular steel piles, with nominal dimensions Ø170x10 mm, were built to support each abutment. The very flexible abutment with the single row of piles was essential to allow for the longitudinal bridge movements. The surrounding soil is mainly silty fine sand to fine sandy silt. The abutments were designed with a shelf at the bottom. This made it possible for the piles to pass rather sheltered through the crushed stone used for erosion protection. The free distance between the piles and the concrete back-wall is nominally 80 mm. Two meters of the piles below the bottom of the abutments were protected by sheltering steel pipes, Ø600 mm, filled with loose sand. The piles were also wrapped with Styrofoam sheets where they passed through the sheltering pipes, see Fig.2.



Fig. 1 – The Leduån Bridge



Fig. 2.– A part of the pile row

A conventional concrete bridge was considered as an alternative solution. Because of the construction technology this solution includes an internal support in the river. This fact greatly influenced the total bridge price. The cost estimation for the integral abutment bridge, based on Swedish prices showed that it was an economically superior solution in comparison with the concrete bridge design. This cost estimation was made without taking into account the maintenance costs, which would have made the integral abutment bridge even more competitive.

The construction of the bridge with integral abutments was made in the following sequences:

- Excavation of the soil down to level 2 m below the back-wall.
- The tolerances for driving the 12m long piles in the longitudinal direction were set to ±100 mm.
- The pile inclination and straightness were measured and approved by the bridge designer.
- Sheltering pipes, Ø600 mm, were placed around the each pile, see Fig.2. Piles were wrapped with Styrofoam sheets and loose sand filled the space between.
- The lower part of the abutments back-walls was cast together with the wing walls, which were temporarily supported during casting.
- The temporary supports below the wing walls were removed, resulting in a pile moment in the opposite direction of the moments acting on the final structure. The moment from the wing walls can bee seen as a pre-stressing of the pile.
- Steel girders were placed on temporary bearings.
- Casting the bridge deck in the desired sequence excluding the abutment back-walls and the last portions of the bridge deck equal to the back-wall width. In this manner, all dead-load slab rotations occurred prior to lock-up, and no dead-load moments were transferred to the supporting piles.
- Pouring the back-walls to full height. Since there was no back-filling at this point, the abutments were free to move without overcoming passive pressures against the back-walls.
- Pavement and rails were placed on the bridge.

MONITORING PROGRAM

To gain knowledge about the overall behaviour of the bridge, a total of 34 measurements were constantly recorded and stored, from the autumn of 2006 to the autumn 2007. Strain-gauges were welded to the bridge girders and to the piles, as shown in Fig. 3. Strains in the piles were measured at five different levels. At the upper four levels, called N1-N4 and S1-S4, the stored signal consists of the difference between two strain-gauges, to compensate for effect of the temperature variations. Signals obtained from both pairs of strain-gauges; at the fifth level, N5 and S5, were stored separately so the estimation of the axial forces in the piles was possible.

The movements of the abutments back-walls were measured with level indicators, position 6 and 7, at each side of the bridge. The level indicators were placed in a vertical plane along the centre line of the bridge at a distance of 1,5 m. The rotation and the displacement of the pile top were estimated from these measurements.

Two strain-gauges were welded on the steel girder, close to the south abutment, to get an indication of the constrained moment obtained at the bridge end. Strain-gauges were placed at the upper and lower flange, pos. 8 and 9 respectively.

Strain-gauges were also welded to the upper and lower flanges at the mid-span of the bridge, pos. 10 and 11, in order to estimate the overall bridge behaviour.

The air temperature as well as the temperatures at three positions of the bridge were measured; on the upper flange, on the lower flange and in the concrete, position 10, 11 and 12 respectively.

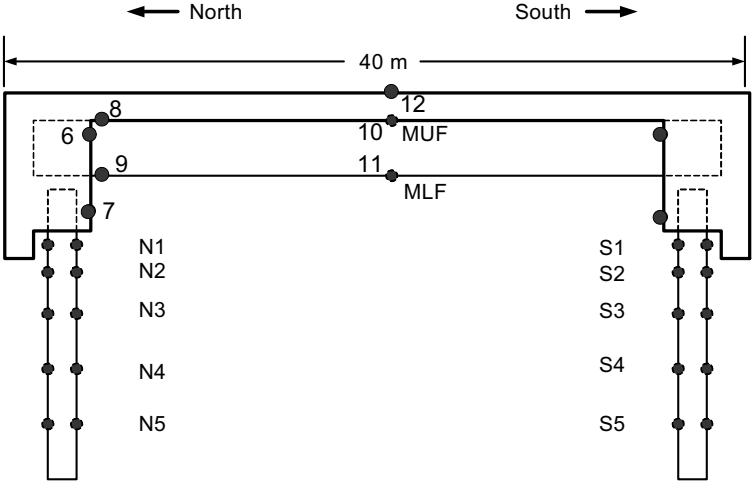


Fig. 3 – Position of long term monitoring gauges at the Leduån Bridge

FE MODEL FOR AN EVALUATION THE PILE BEHAVIOUR

FEA was used to interpret the results of the short term measurements. The short term measurements were done approximately every three months. The lorry with the maximum mass about 25t was used as the test load.

The soil characteristics was indirectly estimated calibrating results of a rather simple 2D FE model with the data measured in the short-term measurements. A limited geotechnical investigation was done in-site and used to check the credibility of FEA.

Piles were modelled using beam elements with elasto-plastic hardening material and von Mises yield criterion. The soil influence was modelled by elastic two node spring elements. The spring elements were connected to the pile nodes providing only horizontal support. Totally 69 spring-elements were used along the pile, distributed more densely at the pile top. The distance between the springs was in a range between 0.05 m to 0.15 m. Every spring had a particular property allocated to produce a reaction force equivalent to a soil layer.

Recommendations from the Swedish bridge code BRO 2004 [Vägverket, 2004] were used as the starting value for the definition of the spring stiffness, Table 1.

The spring stiffness, k , is then:

(1) $$k = k_{\mathrm{k}} A_{\mathrm{spring}} = k_{\mathrm{k}} ds$$

Where A_{spring} is the projected pile-soil contact area related to one spring, d is the pile outer diameter, and s the distance between two springs, k_{k} [MN/m^3] is the sub-grade reaction modulus at the depth z . For friction type soil the sub-grade reaction modulus is given by:

(2) $$k_{\mathrm{k}} = \frac{n_{\mathrm{h}} z}{d}$$

The constant of sub-grade reaction modulus, n_{h} [MN/m^3], can be found in tables. According to the geotechnical investigation, the soil surrounding the piles was sand with a very low consistency. Thus n_{h} was taken as:

- 2,5 MN/m^3 over the ground water level
- 1,5 MN/m^3 under the ground water level

In the considered soil model, the soil stiffness increased linearly with the depth until a maximum value of the product $k_{\mathrm{k}} d$ was reached and it then remains constant.

For sand with a very low consistency, these limits were, $(k_{\mathrm{k}} d)_{\max}$:

- 4,28 MN/m^2 over the ground water level
- 2,57 MN/m^2 under the ground water level

Calibration of FE model was done varying the characteristic of soil properties.

The ground water level was assumed to be at the top of the pile.

The depth at which the stiffness stops increasing and remains constant can be derived from $k_{\mathrm{k}} d$ and n_{h} :

(3) $$z_c = \frac{k_k d}{n_h} = \frac{4,28}{2,5} = 1,71 \text{ m}$$

and the corresponding stiffness was:

(4) $$k_c = (k_k d)_{max} s$$

Table 1 – Distribution of the soil properties along the pile, according to BRO 2004

Below ground water Level	Linear increase 0,00 – 1,71 m	$n_{hd} = 1,5 \ \frac{\text{MN}}{\text{m}^3}$
	Constant stiffness 1,71 – 6,00 m	$k_k d = 2,57 \ \frac{\text{MN}}{\text{m}^2}$

Results of FE calculations with soil properties used for design according to BRO 2004 gave lower strains than those measured in-site. FEA indicated a higher curvature that must be due to a stronger lateral support of the pile from the surrounding soil. It is important to notice that the short term test-loading was performed in January 2007 as temperatures were very close to the minimal and the soil was probably frozen. It is know from [Kerokoski, 2006] that the soil stiffness may be increased approximately by a factor 30 compared to unfrozen soil below ground water level, see Fig.4.

For the northern pile the results of FEA fit the measurements best for a soil with a constant stiffness 20 to 30 times higher than that of the unfrozen soil below the ground water down to a depth of 2 m. Below that level the characteristic soil according to BRO2004 was used. The behaviour of the southern pile was different. The soil parameters appeared to be higher only by a factor 5 to 10, see Fig.5.

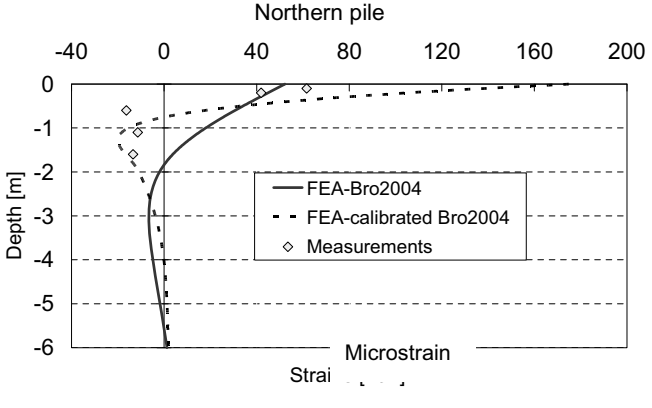


Fig. 4 – Calibration of the soil parameters by FEA

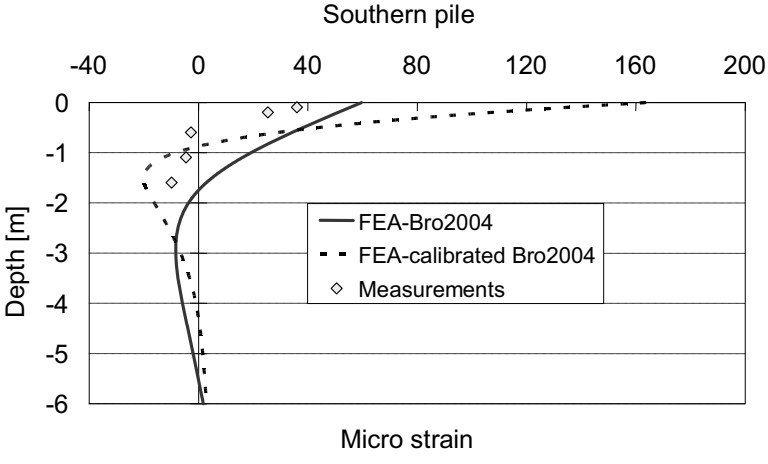


Fig. 5 – Calibration of the soil parameters by FEA

The influence of springs supporting the piles is almost negligible for the vertical displacement of the bridge measured while the empty lorry crossed the bridge, see Fig.6.

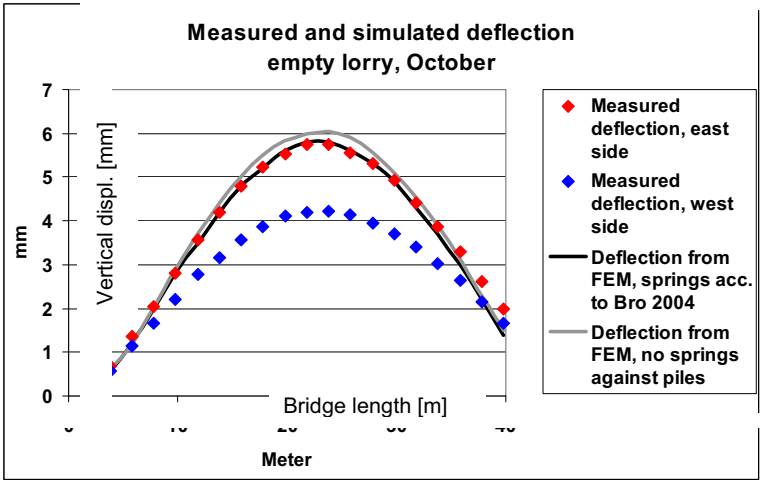


Fig. 6 – Measured deflection compared to deflection modelled by FEM the lorry mass 13,3 t

RESULTS OF LONG TERM MEASUREMENTS

In October 2007, one seasonal temperature cycle was completed.

Table 2 – Max measured movements of the end-screens, in 2007

	February 23		July 7		Total movement [mm]
North side	Upper gauge	40,7	Upper gauge	34,9	5,8
	Lower gauge	41,6	Lower gauge	34,3	7,3
South side	Upper gauge	36,3	Upper gauge	31,9	4,4
	Lower gauge	36,8	Lower gauge	31,1	5,7

Temperatures measured in the concrete in February 23 and July 7, were -17 ^{0}C and 26 ^{0}C, respectively. The total movement of the end-screen was 10,2 mm and 13 mm at the upper part and lower part, respectively. For the considered temperature difference, the theoretical movement of the bridge as the rigid body would be about 17 mm.

Measured strains at the pile's level 1, at the north side are show in Fig.7.

Strain peaks 576 microstrain and 305 microstrain were recorded in February and August, 2007, respectively. This difference led to the stress difference 185 MPa. The air temperature difference between these two datums was 37 ^{0}C compared with 80 ^{0}C which was used in design. The rate of the stress range vs. the temperature differences was $3,36\ \text{MPa}/^0\text{C}$ and $2,58\ \text{MPa}/^0\text{C}$ for the design and measured values, respectively.

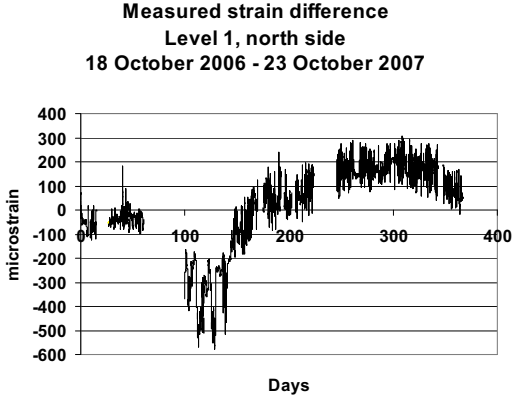


Fig. 7 – Measured strain difference at the top of the pile

LIFE CYCLE ANALYSIS

The composite bridge with integral abutment was compared with an alternative solution, a reinforced concrete bridge with two spans of 18 meters, as published in [Gervásio 2008]. The concrete bridge had the middle pier in the river and end screens at the end supports.

The comparative analysis was based on a life cycle approach taking into consideration the estimated overall performance of both bridge solutions.

The initial costs for the concrete bridge in two spans would, according to the contractor, have exceeded the initial costs for the bridge with integral abutments with more than 50%. The maintenance operations and costs were estimated and provided by the bridge inspectors at the Swedish National Road Administration, in order to create an appropriate life cycle for each bridge, see Table 3 and Table 4.

Table 3 – Maintenance plan of the composite bridge with integral abutments

Maintenance activity	Unit Cost	Start year	End year	Frequency
Inspection of the bridge	320 €	6	96	6
Painting of the steel structure	37 800 €	30	90	30
Exchange of the edge beams	51 320 €	30	90	30

Table 4 – Maintenance plan of the reinforced concrete bridge

Maintenance activity	Unit Cost	Start year	End year	Frequency
Inspection of the bridge	375 €	6	96	6
Exchange of the edge beams	60 710 €	30	90	30
Painting of bearings	1 260 €	30	90	30
Expansion joints:				
Cleaning of joint	100 €	1	99	1
Exchange of rubber band	2 625 €	10	90	10
Exchange of steel profile	11 025 €	20	80	20

The environmental Life Cycle Analysis (LCA) follows the guidelines of ISO standards for LCA [ISO14040], [ISO 14044] and it was performed according to the Eco-indicator methodology and using the SimaPro software [PRé Consultants, 2008]. The object of assessment, the functional unit, was a bridge designed for a service life of 120 years.

For each process included in the LCA, it was necessary to quantify all input flows (materials, energy, etc) and output flows (emissions to air, water, soil; waste; etc). Data for construction materials, apart from the steel, and transportation were obtained from the Ecoinvent database, which was included in SimaPro software. Data for the production of steel was obtained from the IISI database.

The normalized results of the life cycle analysis were shown in Fig.8, using three damage categories for each structural solution. In each column the results obtained for each life cycle stage were summed up. According to Fig.8, the composite bridge had a better environmental performance in every damage category.

The same results were represented in Fig.9 but according to the respective life cycle stage and for each structural solution. In each column the normalized results obtained for each damage category were summed up.

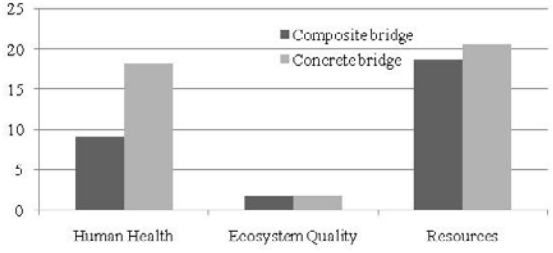


Fig. 8 – Total damage analysis per bridge solution

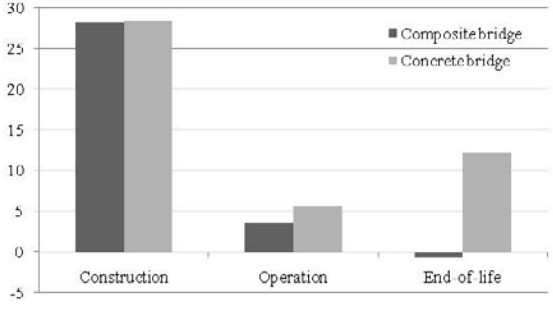


Fig. 9– Damage analysis per life cycle stage

It can also be concluded that the construction stage has a major influence on the final result of the analysis. The end-of-life stage was important, particularly in the case of recyclable materials. In this case study the operation stage was not significant as many simplifications were assumed due to lack of data.

CONCLUSIONS

The results obtained from the monitoring of the Leduån Bridge indicated that a rather simple FE model which was suitable for design practice may be used to calibrate the soil characteristics.

Results from the measurements, obtained in January 2007, showed that the stiffness of the frozen soil was 10 to 20 times stronger than the stiffness of unfrozen soil.

The measured strain range caused by the air temperature variations during the period of the monitoring was approximately 900 microstrain, which corresponds to 95 MPa on each side of the pile. Such strain amplitude due to seasonal temperature variation can not cause serviceability problems and the piles are properly designed for fatigue endurance.

Results of measurements and FEA indicated a very positive role of loose sand and styrofoam around the piles. This solution allows larger displacement of the pile which reduces the strains. In some states in the USA it is demanded to supply integral bridges with this type of solution.

A comparative analysis between the integral composite bridge and the concrete bridge with expansion joints showed that due to the minimization of maintenance operations, the integral bridge has the most economical solution, both in terms of costs for the agency and costs for the users. From the environmental perspective the composite bridge with integral abutment had advantage compared to the concrete solution, mainly due to the recycling of steel.

ACKNOWLEDGEMENTS

Financial support obtained from the Research found for Steel and Coal (RFS-PR-04120) and from Development Fund of the Swedish Construction Industry (SBUF-11708) is gratefully acknowledged. Many thanks to Prof. Peter Collin and Tech.Lic. Hans Pétursson at Ramböll, Sweden for the discussion related to the structural issues. Mrs. Helena Gervásio and Prof. Luis Simões da Silva, Coimbra University, Portugal had significantly contributed to the LCA which was much appreciated.

REFERENCES

Gervásio, G., Eriksen, J., Veljkovic, M., Simões da Silva, L., Comparative life cycle analysis of an integral abutment bridge and a concrete bridge with expansion joints, 7th International Conference on Steel Bridges, Guimarães, Portugal, 2008

Hassiotis, A.S., and Roman, E.K. Survey of current issues on the use of integral abutment bridges, Bridge Structures, Vol. 1, No. 2, June 2005, 81 – 101

Hällmark R., Low-cycle fatigue of steel piles in integral abutment bridges, Master Thesis, 2006:291 CIV, Luleå University of Technology, http://epubl.ltu.se/1402-1617/2006/291/LTU-EX-06291-SE.pdf

ISO 14040. “Environmental management – life cycle assessment – Principles and framework”, International Organization for Standardization, Switzerland, 2006

ISO 14044. “Environmental management – life cycle assessment – Requirements and guidelines”, International Organization for Standardization, Switzerland, 2006

Kerokoski, O.; Sillan ja maan yhteistoiminta: liikuntasaumattomiensiltojen laskennallinen tarkastelu. Tampereen teknillinen yliopisto, Maa- ja pohjarakenteiden laitos, tutkimusraportti 70, Tampere. 2006

Nilsson, Martin, Evaluation of in-situ measurements of composite bridge with integral abutments, Licentiate thesis (2008) , http://epubl.ltu.se/1402-1757/2008/02/LTU-LIC-0802-SE.pdf

Pétursson Hans, Broar med integrerade landfästen, Licentiate thesis, in Swedish, (2000) ISSN: 1402-1757

PRé Consultants, SimaPro 7. “Software and database manual”, Amersfoort, The Netherlands, 2008

Tlustochowicz, G., Optimized design of Integral Abutments for a Three Span Composite Bridge, Master Thesis, 2005:248 CIV, Luleå University of Technology, http://epubl.ltu.se/1402-1617/2005/248/LTU-EX-05248-SE.pdf

Vägverket, Swedish code for bridges, BRO 2004, The Swedish National Road Administration, in Swedish, http://www.vv.se/templates/page3____7900.aspx.

DEVELOPING COMPOSITE ACTION IN EXISTING NON-COMPOSITE STEEL GIRDER BRIDGES

Gunup Kwon
Department of Civil, Architectural, and Environmental Engineering
University of Texas at Austin, Austin, Texas, USA
gunup@mail.utexas.edu

Michael D. Engelhardt
Department of Civil, Architectural, and Environmental Engineering
University of Texas at Austin, Austin, Texas, USA
mde@mail.utexas.edu

Richard E. Klingner
Department of Civil, Architectural, and Environmental Engineering
University of Texas at Austin, Austin, Texas, USA
klingner@mail.utexas.edu

ABSTRACT

This paper describes the results of a study investigating methods to strengthen existing non-composite steel bridge girders using post-installed shear connectors. Four non-composite steel-concrete beams representing existing non-composite bridge girders were strengthened using three types of post-installed shear connectors. The full-scale, retrofitted partially composite beams were tested under static loading to evaluate their strength, stiffness, and ductility. One non-composite beam was also tested as a baseline specimen. Results of the study indicate that the addition of a relatively small number of post-installed shear connectors can increase the load-carrying capacity of non-composite girders by more than 50 percent. Based on the results of this study, a design approach based on partial composite action was developed for strengthening existing steel bridge girders by using post-installed shear connectors.

INTRODUCTION

Composite design for steel-concrete bridge girders is common for new construction. Many older bridges, however, were constructed with floor systems consisting of a non-composite concrete slab over steel girders. A number of these bridges have inadequate load ratings and may require replacement or strengthening. A potentially economical means of strengthening these floor systems is to connect the existing concrete slab and steel girders to permit the development of composite action.

To achieve the benefits of composite action, the existing steel girder must be connected to the existing concrete slab to transfer shear at the steel-concrete interface. For new bridges, composite action is achieved by welding shear studs to the top of the steel girder prior to casting the concrete slab. For existing bridges, however, this approach is not possible, since the slab is already in-place. Therefore, the objective of the research study described here was to identify structurally efficient and practical ways to post-install shear connectors in existing bridges, and to develop performance data and construction methods for girder strengthening using post-installed shear connectors.

This study represents the final phase of a multi-phase research program on post-installed shear connectors. In earlier phases, an extensive series of tests on various types of post-installed shear connectors were conducted under static, high-cycle fatigue, and low-cycle fatigue loads to identify connectors with advantageous structural performance characteristics (Hungerford 2004, Schaap 2004, Kayir 2006). In this final phase of the study, full-scale beam tests were performed to evaluate the system performance of beams retrofitted with post-installed shear connectors.

COMPOSITE BEAMS AND SHEAR CONNECTORS

Mechanical shear connectors are commonly used in composite construction to connect the concrete slab and steel girders to permit transfer of horizontal shear force at the steel-concrete interface. In the *AASHTO LRFD Bridge Design Specifications (2007)*, the required number of shear connectors is determined based on two criteria: static strength and fatigue strength. Shear connectors are first designed for fatigue loads due to moving vehicles and then checked for static ultimate strength. The girder is checked for static ultimate strength assuming fully composite design, that is assuming that the number of shear connectors at the steel-concrete interface is enough to transfer the shear force developed when the steel girder is fully yielded or when the concrete slab reaches its full compression capacity. In buildings, composite beams are often designed as partially composite. In bridges, however, *AASHTO LRFD Specifications* require that composite beams be designed as fully composite under static loading.

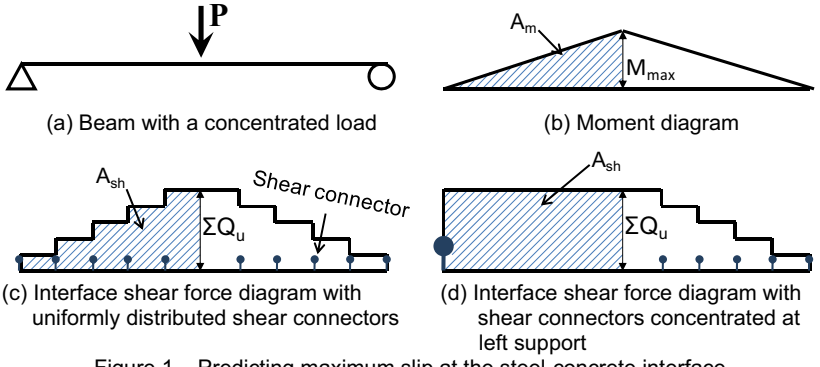
This difference in practice is important, because partially composite design is particularly useful for strengthening existing bridges. Post-installed shear connectors are expensive to install, and it is preferable to use a relatively small number of shear connectors. For a partially composite beam, the amount of shear force which can be transferred at the steel-concrete interface is limited by the strength of the shear connectors. Thus, the ultimate strength of the girder is controlled by the strength of the shear connectors. The shear connection ratio, N / N_f, can be defined as the ratio of the number of shear connectors at the steel-concrete interface, N, to the number of shear connectors required for fully composite design, N_f.

For either fully or partially composite design, slip at the steel-concrete interface is unavoidable. Slip occurs due to local crushing of the concrete around the lower shank of the shear connector and due to bending of the shear connector (Viest et al. 1997). Ollgard et al. (1971) developed Eq. 1 to predict load-slip behavior of welded shear studs. According to the equation, load in a shear connector, Q, is 99 percent of the ultimate strength, Q_u, at 5.0-mm slip.

$$Q = Q_u \left(1 - e^{-18\Delta}\right)^{2/5} \tag{1}$$

where, Δ = slip of shear connector, in.

Oehlers and Sved (1995) developed equations to predict maximum slip at the steel-concrete interface for a simply supported beam at maximum load. It is assumed in the analysis that the steel beam and concrete slab remain linear elastic and the shear connectors are plastic. A general equation to predict maximum slip at the steel-concrete interface, $s_{\max}$, is shown in Eq. 2.



(a) Beam with a concentrated load

(b) Moment diagram

(c) Interface shear force diagram with uniformly distributed shear connectors

(d) Interface shear force diagram with shear connectors concentrated at left support

Figure 1 – Predicting maximum slip at the steel-concrete interface

$$s_{\max} = A_m K_1 - A_{sh} K_2 \qquad (2)$$

where, A_m = Area under moment diagram in a shear span

A_{sh} = Area under interface shear force diagram in a shear span

$$K_1 = \frac{h_s + h_c}{(EI)_s + (EI)_c}, \quad K_2 = \frac{(h_s + h_c)^2}{(EI)_s + (EI)_c} + \frac{1}{(EA)_s} + \frac{1}{(EA)_c}$$

h_s = Distance from centroid of steel beam to the steel-concrete interface

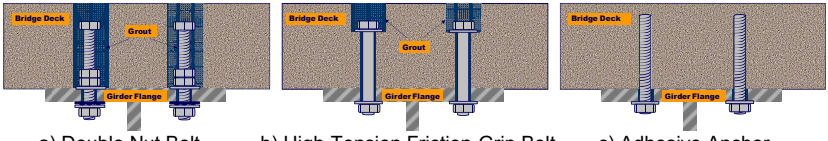
h_c = Distance from centroid of concrete slab to the steel-concrete interface

$(EI)_s$ = flexural rigidity of steel beam $(EI)_c$ = flexural rigidity of concrete slab

$(EA)_s$ = Axial rigidity of steel beam $(EA)_c$ = Axial rigidity of concrete slab

The interface shear force at a point along the beam can be obtained as the sum of the shear connector strengths from the support to the point under consideration. Note that Eq. 2 assumes fully loaded shear connectors along the span of the composite beam.

Equation 2 developed by Oehlers and Sved (1995) indicates that slip at the steel-concrete interface can be reduced if shear connectors are moved toward the supports. Figure 1 shows a simply supported beam with a concentrated load at midspan. The moment diagram is plotted in Fig. 1(b). When the shear connectors are uniformly distributed along the span, the interface shear force diagram is shown in Fig. 1(c). If all of the shear connectors are moved to the supports, the interface shear force diagram doubles in size (See Fig. 1(d)), doubling the second parameter in Eq. 2 and significantly decreasing the maximum slip at the steel-concrete interface. It is of course not possible to place all shear connectors at the support. This analysis suggests, however, that it is advantageous to locate the shear connectors closer to the supports, rather than spacing them uniformly along the length of the beam. This concept was used to advantage in this study, as described later.



a) Double Nut Bolt (DBLNB) b) High-Tension Friction-Grip Bolt (HTFGB) c) Adhesive Anchor (HASAA)

Figure 2 – Post-installed shear connectors

STUDY ON POST-INSTALLED SHEAR CONNECTORS

In the previous phases of this study, 11 types of post-installed shear connectors were developed and the performance of individual connectors was evaluated under static and fatigue loading (Hungerford 2004, Schaap 2004, Kayir 2006). After extensive tests on individual shear connectors, three types of post-installed shear connectors were selected for full-scale beam tests to evaluate the system performance of retrofitted bridges. The selected shear connectors are shown in Fig. 2 along with their designations in this study.

Kayir (2006) and Kwon (2008) proposed design equations for these shear connectors for static and fatigue loadings. For static strength, Eq. 3 was proposed to predict the ultimate strength of post-installed shear connectors, Q_u, under static loading (Kayir 2006).

$$Q_u = 0.5 A_{sc} F_u \tag{3}$$

The effective shear area, A_{sc}, of shear connectors with threads in the shear plane can be calculated as 80% of the gross area of the unthreaded connectors and F_u is the ultimate tensile strength of the connector material. Current design equations for conventional welded shear studs and concrete anchors (AASHTO 2007, ACI 2005) did not provide a conservative prediction of the ultimate strength of post-installed shear connectors measured in tests. For fatigue strength, the fatigue endurance limit of $240\,MPa$ was recommended for the DBLNB connectors (ASTM A193 B7 threaded rods), and the HTFGB connectors (ASTM A325 bolts) (Kwon 2008). The allowable range of shear force, Z_r, can be calculated using Eq. 4.

$$Z_r = 240 MPa \times A_{sc} \tag{4}$$

The HASAA connectors (ASTM A193 B7 threaded rod and ISO 898 Class 5.8 threaded rod) showed lower fatigue strength than the DBLNB and HTFGB connectors, and the relations between Z_r and the number of fatigue loads, N, before connector failure can be calculated using Eq. 5 (Kwon 2008). Note that the fatigue strength of the HASAA connectors from Eq. 5 is much higher than the fatigue strength of conventional welded shear studs.

$$Z_r = (630.9 - 74.53 \log N) MPa \times A_{sc} \tag{5}$$

TEST AND ANALYSIS PROGRAM

Test specimens

Five full-scale non-composite beams were built and tested under static loading. One reference specimen was not retrofitted, and the remaining four were retrofitted with post-installed shear connectors. All specimens were an 11.6-m long simply supported beam, with a concentrated load applied at midspan. For all specimens, the steel beam was a W30x99 section of ASTM A922 steel. The reinforced concrete slab was 2130-mm wide and 178-mm thick, with a specified concrete compressive strength of 20.7 MPa. Details are shown in Fig. 3.

Figure 4 shows the computed load-carrying capacity of the test specimens with respect to the shear connection ratio from simple plastic analysis. These beam strength values were calculated using the minimum specified concrete strength (f'_c = 20.7 MPa) and the minimum specified yield stress of the steel (F_y = 345 MPa). The contribution of the longitudinal reinforcing bars was neglected in the strength calculation. The minimum specified tensile strength of ASTM 193 B7 threaded rod for the DBLNB and HASSAA connectors and ASTM A325 high-strength bolt for the HTFGB connectors is 862 MPa and 827 MPa, respectively.

Based on these calculations, the non-composite beam has a capacity of 609 kN. As shown in Fig. 4, adding shear connectors significantly increases the computed load capacity of this beam, even with low values of shear connection ratio. Based on this analysis, it was decided to design the four partially composite beam specimens with a 30-percent shear connection ratio, resulting in a predicted increase of 48 percent in load-carrying capacity compared to the non-composite beam. To achieve a 30-percent shear connection ratio requires 16 shear connectors for each shear span (a total of 32 shear connectors for a beam). The shear connectors were 22 mm (7/8 in.) in diameter, and their static strength was predicted using Eq. 3.

The specimen designations used below begin with the connection method, followed by the shear connection ratio in percentage. “BS” stands for Beam Static test.

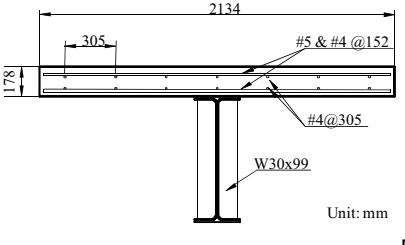


Figure 3 – Details of specimen cross section

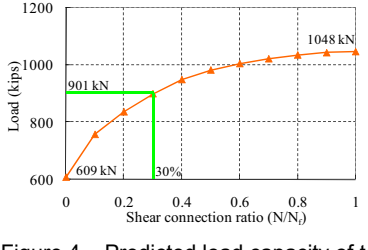


Figure 4 – Predicted load capacity of test specimens versus shear connection

Material properties

Mechanical properties of structural components used in the test specimens are shown in Table 1. Concrete for the specimens was delivered by ready-mix truck. The specified compressive strength was 20.7 MPa with 19-mm river aggregate. Five Star® Highway Patch, a fast-setting high-strength grout, was used to fill the hole in

the concrete slab after installation of the DBLNB and HTFGB connectors. Hilti HY 150 adhesive was used for the HASAA connectors.

The steel beams used for the full-scale beam tests were of ASTM A992, which has a minimum specified yield stress of 345 MPa. Steel coupons were taken from both the beam web and the flange. The Grade 60, #4 longitudinal reinforcing bars used in the specimens were also tested in tension to evaluate mechanical properties. The ultimate tensile strength of the ASTM A193 B7 threaded rod for the DBLNB and the HASAA connectors and of the ASTM A325 high-strength bolt for the HTFGB connector was determined from tension tests.

Table 1: Measured material properties (MPa)

Specimen	Beam*		Concrete**	Connector**	Grout**	Reinforcing bar*
	Flange	Web				
NON-00BS	392.6 (533.4)	419.8 (542.2)	43.12	-	-	424.9 (713.8)
DBLNB-30BS	392.6 (533.4)	419.8 (542.2)	25.38	1014	52.21	424.9 (713.8)
HTFGB-30BS	379.1 (520.6)	408.8 (536.7)	28.02	1024	62.91	435.0 (707.1)
HASAA-30BS	392.6 (533.4)	419.8 (542.2)	24.90	1014	-	397.2 (683.6)
HASAA-30BS1	379.1 (520.6)	408.8 (536.7)	22.21	1014	-	435.0 (707.1)

* Yield strength, () ultimate strength, ** ultimate strength

Installation of shear connectors

The shear connectors in the laboratory specimens were installed using the procedures described below, which were developed to be realistic for field installation. The DBLNB and HTFGB connectors require access from both the top and the bottom of the slab. The HASAA connection method, however, requires access only from the bottom of the slab.



(a) Coring concrete slab



(b) drilling beam flange



(c) Drilling/coring from bottom

Figure 5 – Installation of shear connectors

Double-Nut-Bolt (DBLNB): Installation of the DBLNB connectors requires access from both the top and the bottom of the slab. First, a 60-mm diameter hole was drilled through the top of the concrete slab using a concrete coring machine as shown in Fig 5(a). Second, a 24-mm diameter hole was drilled through the steel beam flange from the top side of the slab using a portable magnetic drill. A hollow round bar was placed inside of the cored hole in the concrete to guide the steel drill bit and to keep the inside surface of the concrete clean of cutting oil. Next, a 190-mm long ASTM A193 B7 threaded rod was placed from the top to provide a 130-mm embedment length, and the connector was tightened to a pretension of 170 kN using an impact wrench. Finally, the hole was filled with grout.

High-Tension Friction-Grip Bolt (HTFGB): Installation of the HTFGB connectors requires more steps than the DBLNB connectors. First, a 70-mm deep and 50-mm diameter hole was drilled into the concrete from the top using a rotary hammer drill. Next, a 25-mm diameter hole, concentric with the 50-mm diameter hole was drilled through the concrete slab from the top using a coring machine. After cleaning the hole thoroughly, a 24-mm diameter hole was drilled through the steel beam flange from the top side of the slab using a portable magnetic drill (Figure 5(b)). A 190-mm long ASTM A325 high-strength bolt was then inserted from the top of the slab into the hole. The connector was tightened to a pretension of 170 kN using an impact wrench. Finally, the hole was filled with grout.

Adhesive Anchor (HASAA): The same 22-mm diameter ASTM A193 B7 threaded rods used for the DBLNB connection method were also used for the HASAA shear connectors. First, a 24-mm diameter hole was drilled through the steel flange from the bottom of the slab. A portable magnetic base drill with an annular cutter was used to drill the hole (Fig. 5(c)). Second, a 130-mm deep, 24-mm diameter hole was drilled into the concrete from the bottom using a rotary hammer drill (Fig. 5(c)). Next, the hole was cleaned and partially filled with Hilti HIT HY 150 adhesive. An anchor rod was inserted in the hole. After the specified cure time of 50-min. at $68^{\circ}F$, the nut was tightened to the specified torque (125 lb-ft) using a torque wrench.

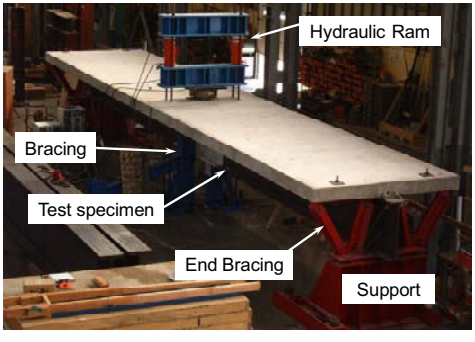


Figure 6 – Test setup

Test setup and instrumentation

The test setup is shown in Fig. 6. The test specimen was a simply supported beam, with 11.6-m long span. A concentrated load was applied at the midspan of the beam with two 100-ton capacity hydraulic rams. To prevent lateral torsional buckling of the beam during concrete casting and to provide for safety during testing of the specimen, the beam was braced laterally at midspan. Bracing was also provided at each end of the beam for safety of the specimen. These end braces were designed not to restrain longitudinal movement of the concrete slab.

During each test, measurements were made of applied load, vertical deflection, slip between the concrete slab and the steel beam flange, and longitudinal strain in the steel beam. Displacement transducers at midspan and at quarter points measured vertical deflection. Slip at the interface between the concrete slab and the steel beam was also measured at the end and quarter points of the beam. Strain gages measured longitudinal strain of the composite beam at midspan and at 152 mm from the midspan.

Finite Element Modeling of Test Specimens

In addition to the full-scale beam tests, the behavior of the strengthened beams was studied using ABAQUS (2007), a general-purpose finite-element program that addresses geometric and material nonlinearity.

To model the test specimens in ABAQUS, a 4-node conventional shell element (S4) was selected for both the steel beam and the concrete slab. ABAQUS element Type S4 is a fully integrated, finite-membrane-strain shell element. Connector elements were used to model shear connectors. Among various types of connector elements, CARTESIAN connectors were used to simulate the behavior of the shear connectors. This connector is a spring-like element defined in a local Cartesian coordinate system. Connector failure can be specified with limit values for force or relative displacement. If the specified failure criterion is reached, the connector is removed and is no longer considered effective in the model (ABAQUS 2007).

The Hognestad (1951) stress-strain relationship was used to model the concrete stress-strain curve for compression. A smeared cracking model was used to model concrete behavior in tension (ABAQUS 2007). In this model, cracking is assumed to occur when the stress reaches a failure surface. The concrete model does not track individual macro cracks. Instead, the presence of cracks affects the stress and material stiffness of the corresponding integration points (ABAQUS 2007). To model stress-strain response of the steel beams and reinforcing bars, an elastic-perfectly plastic stress-strain relationship was used. Strain hardening was not included in the material model. The load-slip relationship proposed by Ollgaard et al. (1971) was adopted for shear connector behavior. The equation by Ollgaard et al. (1971) was developed for conventional welded shear studs, not for post-installed shear studs. However, it was decided to use this equation due to limited static test data for individual post-installed shear connectors.

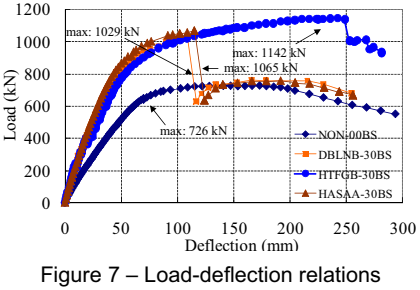


Figure 7 – Load-deflection relations



Figure 8 – Deflected specimen after typical test

TEST RESULTS

Structural behavior of test specimens

During each test, in addition to electronically recording data, the specimens were visually examined for cracks in the concrete slab, yielding and buckling in the steel beam and failure of the post-installed shear connectors. Figure 7 shows the measured load versus midspan deflection response for non-composite Specimen NON-00BS, as well as for the partially composite Specimens DBLNB-30BS, HTFGB-30BS, and HASAA-30BS. These partially composite beam specimens were provided with post-installed shear connectors that were uniformly distributed along the span at a spacing of 725 mm. All partially composite beam specimens showed significantly higher stiffness and strength than the otherwise identical non-composite beam even with a low shear connection ratio of 30 percent.

For Specimens DBLNB-30BS and HASAA-30BS, a sudden strength drop was observed at around 120-mm deflection due to the nearly simultaneous failure of multiple shear connectors. Specimen HTFGB-30BS showed better deformation capacity than the other two partially composite beams. It is believed that the oversized hole in the concrete associated with the HTFGB connectors gave them a large slip capacity, resulting in a large deformation capacity for Specimen HTFGB-30BS. It is, however, noteworthy that 120-mm deflection before shear connector failure for Specimens DBLNB-30BS and HASAA-30BS is significant and the specimens resisted significant load even after shear connector failure. Figure 8 shows the deflected test specimen at the end of the test for Specimen NON-00BS.

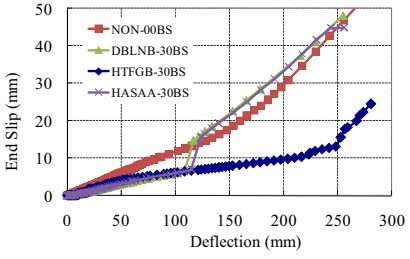


Figure 9 – Load-End slip relationships

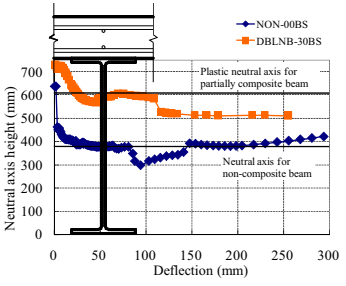


Figure 10 – Neutral axis locations of test specimens

End slip and neutral axis locations

All of the test specimens showed an increase in slip at the interface between the concrete slab and the steel beam as the deflection increased. Figure 9 shows the interface slip at the ends of partially composite beams with uniformly distributed shear connectors along with the non-composite beam specimen. The partially composite beams showed much less slip before any shear connector failure. Behaviors of Specimens DBLNB-30BS and HASAA-30BS were similar to that of Specimen NON-00BS after the multiple shear connector failures.

Specimens DBLNB-30BS and HASAA-30BS showed beam end slip values, at the point of connector failure and sudden strength loss, of 5.8 mm and 6.9 mm, respectively. For Specimen HTFGB-30BS, the first shear connector failure occurred at an end slip of 11.4 mm, much larger than for the other two partially composite beam test specimens.

Composite action in the retrofitted partially composite beams can be further evaluated by locating the neutral axis during the tests. Figure 10 shows the measured neutral axis location at mid-span of the girder throughout the tests. Neutral axis locations were obtained by interpolating strain data read from the strain gages on the beam section. For Specimen NON-00BS, the neutral axis was located near mid-height of the steel section at most load levels, as expected. At very low load levels at the start of the test, the neutral axis was located higher up in the cross-section, suggesting some degree of initial composite action, probably due to bond and/or friction between the steel and concrete. As indicated in Fig. 10, however, this composite action occurred only at very low load levels. Once the load exceeded about 10% of the girder's full capacity, the girder subsequently behaved in an almost purely non-composite manner. For Specimen DBLNB-30BS, the neutral axis stayed above mid-height of the steel section at all load levels. All of the partially composite beam specimens showed almost full composite action in the early stages of loading, likely due to friction at the steel-concrete interface. However, the neutral axis moved down as the load increased, indicating partial composite interaction between the steel beam and the concrete slab.

DEVELOPING INCREASED DEFORMATION CAPACITY

Analytical approach

The non-composite Specimen NON-00BS exhibited very high deformation capacity, as indicated in Fig. 7. Specimens DBLNB-30BS and HASAA-30BS showed less deformation capacity due to the limited slip capacity of the high-strength connectors and also due to the low shear connection ratio. Specimen HTFGB-30BS showed significantly higher deformation capacity in its overall load-deformation response due to the higher slip capacity of this connector. It is believed that high slip capacity of the HTFGB connectors enabled the shear connectors at the steel-concrete interface to redistribute interface shear among the connectors. However, the HTFGB connectors are more difficult and time-consuming to install than the HASAA and DBLNB connectors. Because of the easier installation characteristics of the HASAA and DBLNB connectors, an approach was developed to increase the deformation capacity of beams retrofitted with these connectors.

Oehlers and Sved (1995) indicate that concentrating shear connectors near zero moment regions, resulting in the increase of A_{sh} in Eq. 2, can reduce slip at the steel-concrete interface when the beam reaches its full capacity. This suggests that simply supported beams with shear connectors concentrated near the supports can likely show higher deformation capacity than beams with uniformly distributed shear connectors along the span.

Finite element analysis was used to evaluate the effect of moving shear connectors near the zero moment regions. First, the full-scale beam test specimens were modeled with ABAQUS. Figure 11 shows load-deflection relations for Specimen HASAA-30BS from the test along with the finite element analysis results. As shown

in the analysis result of Specimen HASAA-30BS, the model used in this research could not simulate the behavior after shear connector failure. However, the model is considered useful for predicting the behavior before shear connector failure and the failure of the shear connectors. Figure 12 shows the longitudinal stress distribution of Specimens HASAA-30BS from the FE analysis. As shown in the figure, neutral axis of the beam moved toward the beam top flange due to composite action between the two structural components.

Figure 11 also shows the analysis results of a partially composite beam with shear connectors concentrated near the supports. In the FE model, shear connectors were moved near the supports and were located at a 300-mm spacing. The total number of shear connectors was not changed in the model. The analysis model with concentrated shear connectors was same with the analysis model of Specimen HASAA-30BS except the shear connector locations. For Specimen HASAA-30BS, the connectors were uniformly distributed along the length of the beam, at a spacing of 725 mm. Compared to Specimen HASAA-30BS, the deformation capacity of the partially composite beam with shear connectors relocated near the supports was increased significantly. The increase of its deformation capacity can be attributed to the decrease in slip at the steel-concrete interface as shown in Fig. 13. The partially composite specimen with concentrated shear connectors near the support shows much less slip than the specimen with uniformly distributed shear connectors in ABAQUS.

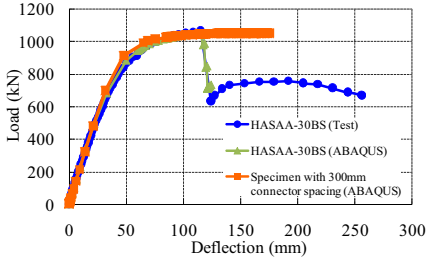


Figure 11 – Test vs. FE Analysis results

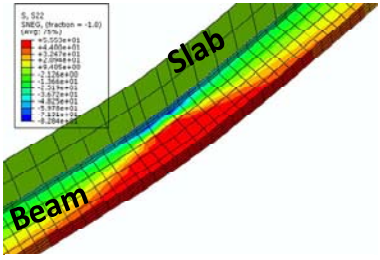


Figure 12 – Longitudinal stress distribution of a composite beam

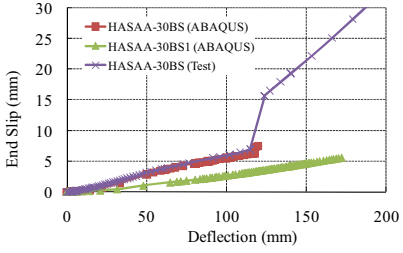


Figure 13 – Load-End slip relationships

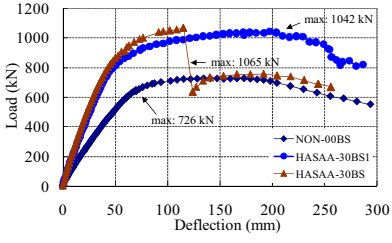


Figure 14 – Load-deflection curves for test specimens

Test Results for Partially Composite Beam with Concentrated Shear Connectors

Specimen HASAA-30BS1 was tested to verify the FE analysis results and evaluate the global behavior of partially composite beams with post-installed shear connectors concentrated near zero moment regions. Specimen HASAA-30BS1 had the same number of shear connectors as Specimen HASAA-30BS. For Specimen HASAA-30SB1, the shear connectors were moved towards the ends of the beam, and were spaced at 300 mm.

Figure 14 compares test results for Specimens HASAA-30BS1 and HASAA-30BS. The deformation capacity of Specimen HASAA-30BS1 (concentrated connectors) is much greater than that of Specimen HASAA-30BS (uniform connectors), and is comparable to that of Specimen NON-00BS. Specimen HASAA-30BS1 showed first shear connector failure at a 170-mm deflection, after which the applied load increased slightly before another shear connector failure at 210 mm. The maximum load was 1043 kN at 197-mm deflection. It appears that concentrating shear connectors near the supports not only decreases slip at the steel-concrete interface, but also helps redistribute loads among shear connectors.

Test results from Specimen HASAA-30BS1 indicate that the stiffness and strength of non-composite beams can be improved significantly by using relatively small number of post-installed shear connectors without sacrificing deformation capacity.

SUMMARY

The study reported herein was the final phase of a research project to develop methods for strengthening existing non-composite bridge girders using post-installed shear connectors. Previous phases of this study identified possible post-installed shear connectors and evaluate static and fatigue performance of those shear connectors. Based on this earlier works, three types of post-installed shear connectors were selected for full-scale beam tests.

The number of post-installed shear connectors needed to strengthen an existing bridge girder is determined based on the concept of partial composite design. Partial composite design is not normally used for new composite bridge girders, because fatigue typically controls the required number of shear connectors. Because of the superior fatigue characteristics of the post-installed shear connectors tested in this study, however, fatigue is not likely to control the required number of shear connectors, and partial composite design is therefore possible.

With partial composite design, 50 to 70 percent of the shear connectors normally needed for full composite design can be eliminated, while still achieving a 40- to 50-percent increase in load-carrying capacity in positive-moment regions of a girder. Based on the test data from single shear connector tests, overall performance of girders retrofitted with post-installed shear connectors was evaluated with a series of large-scale beam tests, supplemented with finite element analysis. The results of this study suggest that strengthening existing non-composite bridge girders using post-installed shear connectors may be an effective and economical alternative to replacement of existing bridges.

ACKNOWLEDGEMENTS

The authors gratefully acknowledge the financial support provided for this study by the Texas Department of Transportation. The authors extend a special thanks to Jon Kilgore and Clara Carbajal of the Texas Department of Transportation for their support, assistance and advice throughout the entire course of this project. The authors also gratefully acknowledge the contributions of Brad Schaap, Brent Hungerford, Hulya Kayir and Young-Kyu Ju in the earlier phases of this research study. The experiments described herein were conducted at the Phil M. Ferguson Structural Engineering Laboratory at the University of Texas at Austin.

REFERENCES

AASHTO (2007). "LRFD Bridge Design Specifications Interim Customary U.S. Units, 4th Edition." American Association of State Highway and Transportation Officials, Washington, DC.

ABAQUS (2007). "ABAQUS Analysis User's Manual (Ver. 6.7)." ABAQUS, Inc, Pawtucket, RI.

ACI (2005). "Building Code Requirements for Structural Concrete (ACI 318-05) and Commentary (ACI 318R-05)." American Concrete Institute, Farmington Hills, Michigan, 2005.

Hognestad, E (1951). "A Study of Combined Bending and Axial Load in Reinforced Concrete Members." University of Illinois Engineering Experimental Station, Bulletin Series No. 399.

Hungerford, B.E. (2004). "Methods to Develop Composite Action in Non-Composite Bridge Floor Systems: Part II." MS Thesis, Department of Civil, Architectural and Environmental Engineering, The University of Texas at Austin.

Kayir, H. (2006). "Methods to Develop Composite Action in Non-Composite Bridge Floor Systems: Fatigue Behavior of Post-Installed Shear Connectors." MS Thesis, Department of Civil, Architectural and Environmental Engineering, The University of Texas at Austin.

Kwon, G. (2008). "Strengthening Existing Steel Girder Bridges by the use of Post-Installed Shear Connectors." PhD Dissertation, Department of Civil, Architectural and Environmental Engineering, The University of Texas at Austin (expected completion in December 2008).

Lehman, H.G., Lew, H.S., and Toprac, A.A. (1965). "Fatigue Strength of 3/4 in. Studs in Lightweight Concrete." Center for Highway Research, The University of Texas at Austin.

Oehlers, D.J., and Sved, G. (1995) "Composite Beams with Limited-Slip-Capacity Shear Connectors." Journal of Structural Engineering, 121(6), 932-938.

Ollgaard, J.G., Slutter, R.G., and Fisher, J.W. (1971). "Shear Strength of Stud Shear Connectors in Lightweight and Normal-Weight Concrete." AISC Engineering Journal, 8, 55-64.

Schaap, B. A. (2004). "Methods to Develop Composite Action in Non-Composite Bridge Floor Systems: Part I." MS Thesis, Department of Civil, Architectural and Environmental Engineering, The University of Texas at Austin.

Slutter, R.G., and Fisher, J.W. (1966). "Fatigue Strength of Shear Connectors." Highway Research Record 147, 65-88.

Viest, I.M. et al. (1997). "Composite Construction: Design for Buildings." McGraw--Hill, New York, NY.

EXPERIMENTAL INVESTIGATIONS OF THE SHEAR CONNECTION BEHAVIOUR IN JOINTS OF COMPOSITE BRIDGES

Alain LACHAL
LGCGM – Structural Engineering Research Group,
INSA Rennes, France
Alain.Lachal@insa-rennes.fr

Oliver HECHLER
ArcelorMittal – Luxembourg
Oliver.Hechler@arcelormittal.com

Sao Serey KAING
LGCGM – Structural Engineering Research Group,
INSA Rennes, France
ksserey@yahoo.fr

Jean-Marie ARIBERT
LGCGM – Structural Engineering Research Group,
INSA Rennes, France
Jean-Marie.Aribert@insa-rennes.fr

ABSTRACT

Three innovative solutions of joint to restore the continuity between beams in composite bridges have been selected. Experimental specimens, representative of each innovative solution, have been designed, erected and tested under fatigue and monotonic loadings.
This paper presents the moment-rotation curves: initial stiffness, maximum moment and rotation capacity obtained for each tested joint and more particularly slip measurements at the slab – steel girder interface, insofar as one joint collapse occurred by shear failure of studs connecting the slab to the steel flange of the girders. In addition, two approaches to evaluate the fatigue damage of the shear connection are compared.
In conclusion, this paper gives useful data for a better understanding of the behaviour of shear connections between the slab and the steel girder and to propose new design methods.

INTRODUCTION

In this paper, three innovative solutions of joint to restore the continuity between beams in composite bridges are presented [Lachal A. and Aribert J.M., 2002]. In the first solution, the steel webs are connected using cover-plates and high strength preloaded bolts and the lower flanges of the girders are either connected with flange cover-plates or put directly in contact (without special treatment of the flange ends and using a special contact piece). The second solution is realized with butt-plates connected with studs to a reinforced concrete transverse deep beam. The third solution consists in two end girders completely embedded in a concrete block; the steel webs of the girders are connected by horizontal shear studs welded on the web

or by transverse bars passing through the beam web while the bottom flanges are put directly in contact. In the first solution, the joint may be located within the span or near a support while in the second and third solutions, the joint is necessarily lying on a pier. Such joints may be easily worked by any ordinary constructor provided that prefabricated beams are prepared in factory and transported on the construction site.

Three joint specimens, representative of each innovative solution, have been designed. Steel girders were fabricated in factory (ArcelorMittal - Wallerich - Differdange) at half scale and equipped with plates and welded studs. They were transported to INSA de RENNES where the reinforcement was installed and the continuity of the composite beam was completed by concreting the slab and the joint in a single shot. Finally, they have been tested under monotonic and fatigue loadings on the strong floor of the Structural Engineering Laboratory at INSA in Rennes.

The experimental results are organized as follows. Firstly the general behaviour of each tested joint expressed by its moment-rotation curve from which mean characteristics as initial rotational stiffness, maximum moment and rotation capacity are deduced. Secondly we focus on the measure of the slip at the slab – steel girder interface insofar as one shear failure of studs connecting the slab to the steel girder flange occurred in the third test. Other types of results concern the fatigue damage of the shear connection between the slab and the steel girder.

EXPERIMENTAL INVESTIGATION

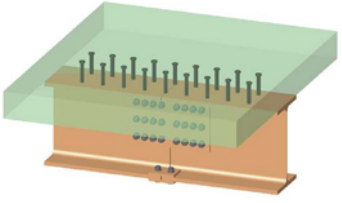
Presentation of the experimented specimens

The main characteristics of the tested specimens are presented in Table 1 and Figure 1. Locations of A1, B1, C1 joints (on the actuator 1 side) and A2, B2, C2 joints (on the actuator 2 side) are specified in Figure 3. The transfer of the tensile forces in the upper part of the joint is allowed by the shear connection and the reinforcement in the slab. Around the connected zone, over a total length of 4010 mm, the longitudinal reinforcement is composed of 2 layers of 17 ribbed bars each of diameter d = 16 mm with high bond action and in steel grade S500 – Category 3 ensuring high ductility (the percentage of longitudinal reinforcement being 2.67%). Over the same length, the slab is connected to the steel flange with 12 welded headed studs per meter (d = 22 mm and h = 125 mm). Outside the joint zone, a normal percentage of reinforcement is used for the composite beam, equal to 1.26% (composed of 2 layers of 8 ribbed bars each of diameter d=16 mm) and the number of connectors is 6 studs/meter.

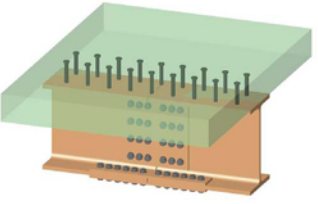
In case of joint A2, web and flange steel girders are connected with cover-plates and high strength friction bolts tightened at nominal preload. For joint A1, a new technology has been developed with a direct contact between compression bottom flanges in order to avoid flange cover-plates and so to reduce considerably the number of bolts. A contact piece in duralumin of 10 mm thickness has been used to facilitate the contact between the two flange ends. The locations of joints A1 and A2 within the test specimen are indicated in Figure 3.

Table 1 – Description of specimens

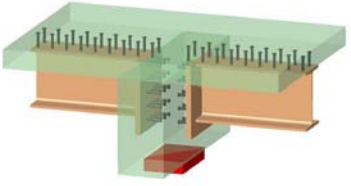
JOINT CHARACTERISTICS		COMPOSITE GIRDER CHARACTERISTICS		
TEST REFERENCE	**CONNECTION**	**STEEL BEAM SECTION (S355)**	**CONCRETE C45/55**	**REINFORCEMENT and SHEAR STUDS**
SPECIMEN A COVER-PLATE (joints in span) A1 : Contact piece A2 : Bottom flange Cover-plate	COVER-PLATES t = 14 mm f_y = 385 MPa f_u = 580 MPa BOLTS HR 10.9 ; M22	h = 490 mm b_f = 300 mm t_w = 12 mm t_f = 23 mm r = 27 mm I_a = 86 970 cm^4 $E_a = 2.10^5$ MPa γ = 1.28 f_{yw} = 450 MPa f_{uw} = 420 MPa f_{yf} = 520 MPa	SLAB DIMENSION b_{eff} = 160 cm h_c = 16 cm CONCRETE $f_{ck,28}$ = 40 MPa $f_{ck,127}$ = 48 MPa $f_{ck,211}$ = 48 MPa f_{ctm} = 3.51 MPa τ_{Rd} = 0.41 MPa E_{cm} = 35200 MPa $n_0 = E_a/E_{cm}$ = 5.68	OUTSIDE ZONE Reinforcing bars 2 layers/8×d=16 mm f_{ys} = 585 MPa $E_s = 2.10^5$ MPa Shear studs d = 22cmm h = 125 mm 2 files of 8 studs/m IN THE CONNECTION ZONE Reinforcing bars 2 layers/17×d=16 mm f_{ys} = 585 MPa $E_s = 2.10^5$ MPa Shear studs d = 22 mm h = 125 mm 2 files of 16 studs/m
SPECIMEN B BUTT-PLAT JOINTS (on support) B1 : Full penetration weld B2 : Fillet weld	BUTT-PLATE t = 45 mm M or N quality f_y = 385 MPa f_u = 580 MPa			
SPECIMEN C EMBEDDED JOINTS (on support) C1 : Web stud connectors C2 : Web transverse rebars	SHEAR STUDS 8 studs d = 22 mm h = 125 mm REBARS 8 rebars f_{ys} = 585 MPa $E_s = 2.10^5$ MPa			



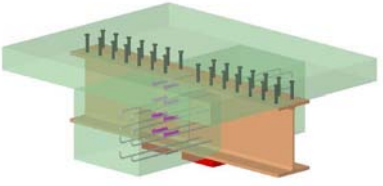
Joint A1 : Bolted joint with web cover-plates and a direct contact between bottom flanges



Joint A2 : Bolted joint with web cover-plates and bottom flange cover-plates



Joints B1 and B2 : Butt-plate joint



Joints C1 and C2 : Embedded joint

Figure 1 : Tested joints

Joints B1 and B2 are necessarily located at intermediate support. Butt plates are welded at the ends of the steel girders and connected with shear studs to a transverse concrete beam.

For joints C1 and C2 presented in Figure 1, both ends of steel span girders are embedded in a concrete block over the pier. A double support is placed over the pier where each steel beam lies directly at his end over one of the supports in order to avoid a shear force transfer through the mid-cross-section of the embedding. A direct contact (the same as the one used for joint A1) between the ends of the bottom flanges of the girders over the support ensures the transfer of the compression forces in the joint. Shear studs welded on the web and/or rebars passing through the web of the steel girders are used to connect the steel beams inside the concrete diaphragm.

Test setup and loading procedures

Figure 2 - Path of loading.

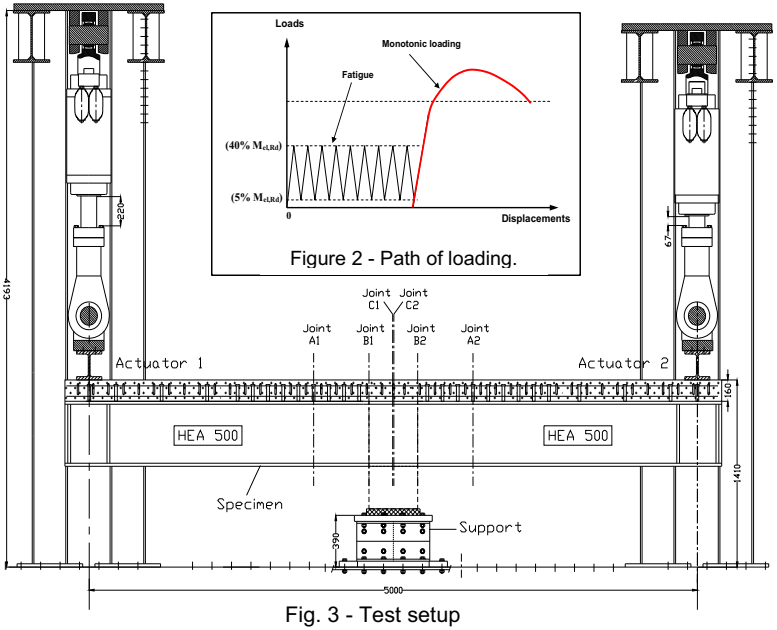


Fig. 3 - Test setup

The principle of the experimental setup is shown in Figure 3. Two vertical loads are applied at the beam end cross-sections of the specimen by mean of hydraulic servo controlled actuators.

The specimen is simply supported in its middle on a single (A and B joints) or double (C joint) neoprene plates. Two types of servo-controlled loading displacement procedure have been exerted: firstly a fatigue loading under a high range of bending moment and secondly a monotonous increase of actuator loads towards the

specimen collapse (Figure 2). The specimens were equipped with inclinometers to measure the joint rotation, linear potentiometric transducers to measure deflections along the beam in at several points and relative displacements in the joint. Furthermore one-dimensional strain gauges were used to measure the strains in at several parts of the specimen : steel beam, reinforcing bars, embedding reinforcement and shear connectors. Crack widths were measured on the top surface of the concrete slab. Figure 4 shows the arrangement of the main instrumentation and Figure 5 gives a general view of the test setup along with all tested specimens (A, B and C).

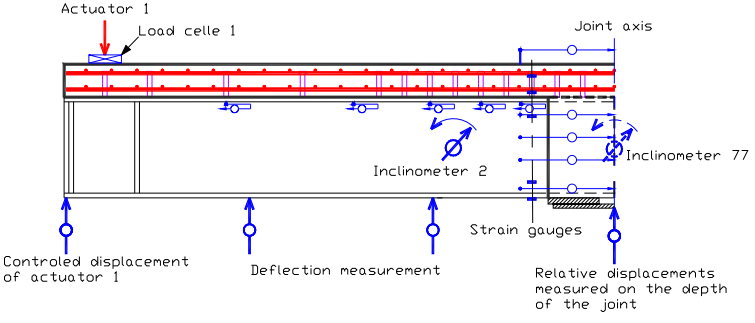


Fig. 4 – Measure arrangement.



Fig. 5 - Test setup and specimen (specimen A on the left, specimen B right top side and specimen C right bottom side)

EXPERIMENTAL RESULTS AND MAIN OBSERVATIONS

Moment-rotation curves

The moment-rotation curves of all the joints are given in Figures 6, 7 and 8. It should be pointed out that no clear collapse occurred for the joints of specimens A and B up to the maximum load capacity of the actuators. In specimen C, collapse occurred by stud failure in the shear connection of the slab close to joint C1. The rotations considered here are those defined between the cross-section at mid-joint and the beam cross-section immediately adjacent to the joint on each side. There are deduced from inclinometers, beam deflections and horizontal relative displacements measured over the whole depth of the joints (Figure 4). Moments are calculated in the connected cross-sections from the measured actuator loads multiplied by the appropriate lever arm. Main joint moment-rotation characteristics measured from the above curves are collected in Table 2.

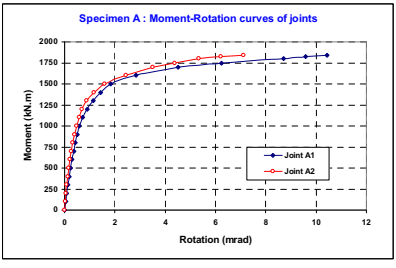


Fig. 6 – Moment-rotation curves of joints A1 and A2

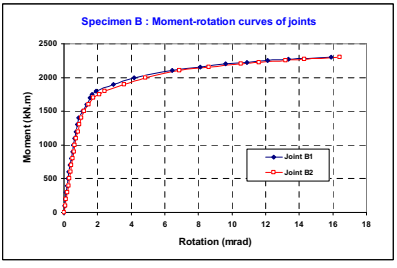


Fig. 7 – Moment-rotation curves of joints B1 and B2

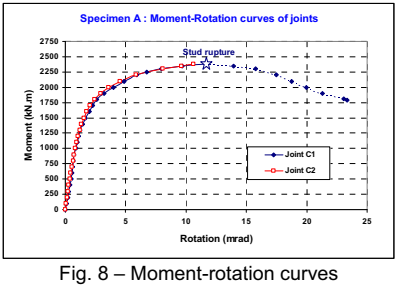


Fig. 8 – Moment-rotation curves of joints C1 and C2

Table 2 – Measured characteristics

SPECIMEN	JOINT	$S_{j,ini}^{exp}$ (kN.m/mrad)	$M_{exerted}^{max}$ (kN.m)	$\Phi_{j,max}^{exp}$ (mrad)
A	A1	1895	1845	> 7
	A2	2395	1845	> 10
B	B1	1986	2300	> 16
	B2	1986	2300	> 16
C	C1	1120	2385	11
	C2	1130	2385	>11

In order to evaluate the characteristics given in Table 2, a comparison with an equivalent composite beam section having the same length of about 250 mm (as the one used to define the joint rotation) has been undertaken. The calculated initial rotational stiffness (under flexural bending) and the elastic resistance moment of this beam segment would be:

$$S_{eq} = E\,I_2 / \ell = 210\,000 \times 140\,558 \times 10^4 / 250 = 1180 kN.m / mrad \;\; ; \;\; M_{el,b,R} = 1842 kN.m$$

Joints A1, A2, B1 and B2 appear fully efficient in stiffness and strength. Joint C may be considered acceptable in stiffness while displaying the highest resistance moment. A direct contact in joint A1 (leading to some deformations of the duralumin piece) may explain the lower stiffness than in joint A2.-

Load-slip curves at the slab-profile interface

Specimen A (Joints A1 and A2)

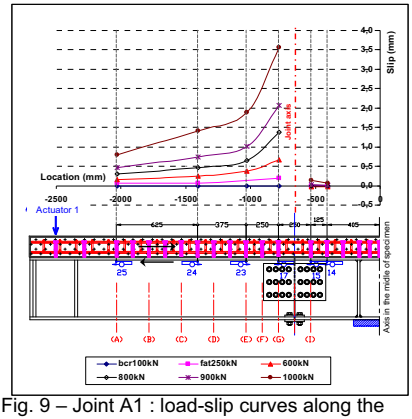


Fig. 9 – Joint A1 : load-slip curves along the slab-steel girder interface

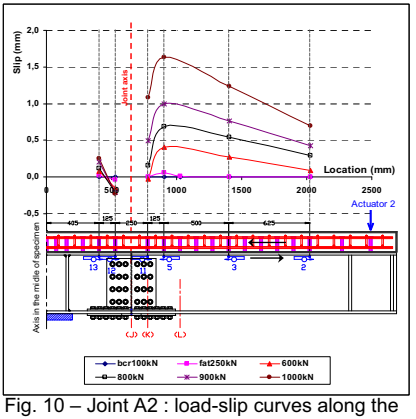


Fig. 10 – Joint A2 : load-slip curves along the slab-steel girder interface

In Figure 9 and 10 for joints A1 and A2, respectively, when the two actuators attain the highest loads (between 800 kN and 1000 kN), a plastic behaviour appears in the shear studs proved by the slip values observed in both Figures. Going from the ends of the beams towards the specimen centre, a slip increase is observed up to the connected zone where suddenly the slip curve switches to zero and stays near zero in the remaining part of the beam located between the connected zone and the centre of the specimen (even in the case of A2 joint a reversed slip direction is observed just after the connection zone). This apparent discontinuity of slip in the connected beam cross-section, seems to be confirmed by numerical finite element simulations [Guezouli S. et al, 2008].

Comparison between slip test results of joints A1 and A2 shows clearly a slip amplitude greater for joint A1 (with a direct contact) than for joint A2 (with bottom flange cover plates). This result may be interpreted as a consequence of the deformation of the duralumin contact piece comparatively to the bottom cover-plate flange connection of joint A2 which seems to be more rigid. A less rigid contact between the compression flanges leads to a less rigid joint and consequently to greater slip amplitudes at the slab-steel girder interface. This slip amplification may lead also to a significant drop of stud resistance in fatigue when cyclic loading is applied.

Considering the load of 600 kN exerted by the two actuators giving a maximum hogging bending moment near the Serviceability Limited State, the corresponding

slip shown in Figures 9 and 10 ranges between 0,15mm and 0,67mm for test A1 (with a mean value of 0.30mm) and between 0,09mm and 0,41mm for test A2 (with a mean value of 0.27mm). Starting from the tensile force of 1315 kN measured by strain gauges in the longitudinal bars of reinforcement, the average shear force of 50,5 kN in the studs of the beam can be evaluated and the corresponding slip from the load-slip relationship for a "d = 22mm, h = 125 mm" shear stud calibrated by [Hansville G., Porsch M. and Ustundag C., 2007] would be:

$$s = \left[-\frac{1}{1.22} ln\left(1 - \frac{F_{con,moy}}{P_{u,0}}\right) \right]^{1/0.59} = 0.11\,mm\,; \quad \text{with} \tag{1}$$

$$P_{u,0} = \frac{P_{Rd}}{0.68} = \frac{121.6}{0.68} = 178.8kN \quad \text{(stud failure)}$$

This calculated value is more than the half of the experimental mean slip values measured for tests A1 and A2. Nevertheless, it should be noted that the maximum longitudinal shear force may be higher that the measured one due to the tension stiffening effect of the cracked concrete not taken into account.

Specimen B (Joint B1)

In Figure 11, a more uniform slip distribution than the one obtained previously for joints A1 and A2 is observed at the slab-steel girder interface of the girder on side B1. Only a small slip increase is detected coming close to the joint. The local decreasing observed at 1000mm from the middle of the specimen is due to the lower density of the studs connecting the slab. Compared to the previous results, the slip amplitude of joint B1 is overally slightly lower than the one of test A2. The maximum slip amplitude measured close to the joint is the result of the relative displacement in the transverse beam (concrete cracking, rebar and stud elongations, local bending of the butt plates…). A mean slip value of 0.25mm may be evaluated for a load equal to 600 kN.

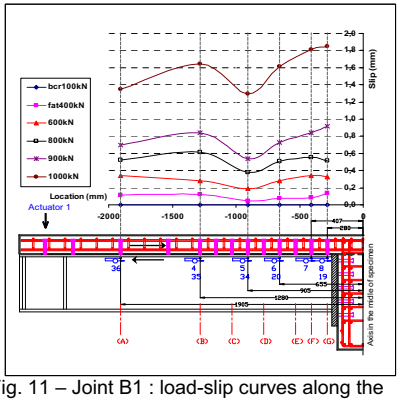


Fig. 11 – Joint B1 : load-slip curves along the slab-steel girder interface

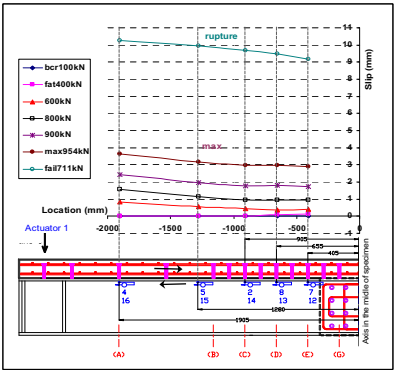


Fig. 12 – Joint C1 : load-slip curves along the slab-steel girder interface

Specimen C (Joint C1)

In case of joint CI, the slip distribution at the slab-steel girder interface shown in Figure 12 is quasi-constant all along the beam (with a mean slip value of 0.57mm), even with a slight decrease going from the beam end to the joint. The deformation of the duralumin contact piece cast between the bottom flanges has reduced the joint stiffness and lead to slip amplitudes at the slab-steel girder interface greater than the ones observed in the previous joints (even slightly greater than for the test A1).

Fatigue of the studs connecting the slab and the steel girder

Sequences of the cyclic preloading exerted at the beginning of each test are given in Table 3. No fatigue failure was observed during these first preloading phases. Only a stud failure occurred latter during the second monotonous loading phase of test C1. Therefore a deeper analysis to investigate the risks of fatigue damage of the shear studs connecting the slab and the steel girder has been carried out.

Table 3 : Sequences of fatigue preloading

Joint	-Range of loading -Tension range -Number of cycle	1	2	3	4	5	6	7
A1	F_{min}-F_{max} (kN) $\Delta F_{s,i}$ (kN) N_i	35 – 240 402 20 000	75 – 200 250 40 809	30 – 230 392 6 267	35 – 320 550 3 491	25 – 310 555 8 008	20 – 300 545 3 169	20 – 410 757 20 631
A2	F_{min}-F_{max} (kN) $\Delta F_{s,i}$ (kN) N_i	40 – 240 444 20 000	80 – 195 253 40 809	30 – 235 451 6 267	40 – 320 670 3 491	25 – 310 615 8 008	20 – 300 612 3 169	15 – 410 855 20 631
B1	F_{min}-F_{max} (kN) $\Delta F_{s,i}$ (kN) N_i	40 – 295 172 3 258	40 – 285 166 13 437	50 – 430 300 7 081	x	x	x	x
C1	F_{min}-F_{max} (kN) $\Delta F_{s,i}$ (kN) N_i	30 – 300 561 2 680	20 – 280 612 12 837	35 – 445 1012 150 174	x	x	x	x

According to EN 1994-2 [CEN, 2004], Clause 6.8.7.2, when the steel flange of the tested specimen girder to which headed stud connectors are welded is in tension, the interaction between shear stress range in the weld of stud connectors $\Delta\tau_{E,2}$ and the normal stress range $\Delta\sigma_{E,2}$ in the steel flange should be checked using the following interaction expressions (where the safety factors γ_{Ff} and γ_{Mf} are taken equal to 1 with measured data):

$$\left(\frac{\gamma_{Ff}\times\Delta\sigma_{E,2}}{\Delta\sigma_c/\gamma_{Mf}}\right)+\left(\frac{\gamma_{Ff}\times\Delta\tau_{E,2}}{\Delta\tau_c/\gamma_{Mf}}\right)\le 1.3 \text{ and } \left(\frac{\gamma_{Ff}\times\Delta\sigma_{E,2}}{\Delta\sigma_c/\gamma_{Mf}}\right)\le 1.0,\ \left(\frac{\gamma_{Ff}\times\Delta\tau_{E,2}}{\Delta\tau_c/\gamma_{Mf}}\right)\le 1.0 \quad (2)$$

$\Delta\sigma_c = 80\ MPa$; $\Delta\tau_c = 90\ MPa$;

$$\Delta\sigma_{eq}=\left(\frac{1}{N_{tot}}\sum_{i=1}^{k}\Delta\sigma_i^3 N_i\right)^{\frac{1}{3}};\ \Delta\tau_{eq}=\left(\frac{1}{N_{tot}}\sum_{i=1}^{k}\Delta\tau_i^8 N_i\right)^{\frac{1}{8}} \quad (3)$$

$$\Delta\sigma_{E,2} = \left[\frac{\Delta\sigma_{eq}^{3} \times N_{tot}}{2.10^{6}}\right]^{1/3} \quad ; \quad \Delta\tau_{E,2} = \left[\frac{\Delta\tau_{eq}^{8} \times N_{tot}}{2.10^{6}}\right]^{1/8} \tag{4}$$

$\Delta\sigma_i$ is the normal stress range calculated from the measured strain range $\Delta\varepsilon_i$ at the top flange of the steel girder at the base of the relevant stud for the loading sequence i ($\Delta\sigma_i = E.\Delta\varepsilon_i$ where E is the Young modulus). $\Delta\sigma_{eq}$ is the equivalent normal stress range for the total number of cycles N_{tot} . $\Delta\sigma_c$ is the reference value of fatigue strength given in EN1994-2, corresponding to category 80. $\Delta\tau_{i,max} = \left(\frac{\Delta F_{s,i}}{n_{con}} \frac{\Delta s_{i,max}}{\Delta s_{i,moy}}\right) \frac{4}{\pi d^2}$ is the maximum shear stress range related to the cross-sectional area of the stud shank of nominal diameter d. $\Delta F_{s,i}$ is the tension force range in the longitudinal reinforcement exactly above the investigated stud at the loading sequence i. The tension range $\Delta F_{s,i}$ is obtained from strain measurements using gauges coated on ribbed bars at several cross sections of the slab. To avoid possible singular measurements of strain gauges, an interpolation is used between the values of a smooth distribution of tension force along the beam. Due to the initial cyclic loading, the concrete slab is supposed to be totally cracked and the concrete strength in tension is neglected for the evaluation of the longitudinal shear force at the steel-concrete interface (in fact, the longitudinal shear force is slightly underestimated; but that does not question the conclusion related to Table 4). $\Delta s_{i,max}$ is the maximum slip range measured at the relevant stud and $\Delta s_{i,moy}$ is the mean value of the slip ranges measured along the beam corresponding to the same range $\Delta F_{s,i}$ (it should be noted that $\Delta s_{i,max}$ and $\Delta s_{i,moy}$ are clearly located within the linear domain of the stud behavior that justify the corrective factor used to calculate $\Delta\tau_{l,max}$). n_{con} is the total number of studs between the cross-section of the relevant stud and the beam end. $\Delta\tau_{eq}$ is the equivalent shear stress range for the total number of cycles N_{tot}.$\Delta\tau_c$ is the reference value of fatigue strength at 2 million cycles determined in accordance with Clause 6.8.3 of EN1994-2, by applying category 90. Table 4 presents the results of calculation.

Table 4 : Fatigue assessment of shear connection of slab according to EN 1994-2

Joint	Stress range (N/mm²)		$\left(\frac{\gamma_{Ff} \times \Delta\sigma_{E,2}}{\Delta\sigma_c / \gamma_{Mf}}\right) \le 1.0$	$\left(\frac{\gamma_{Ff} \times \Delta\tau_{E,2}}{\Delta\tau_c / \gamma_{Mf}}\right) \le 1.0$	$\left(\frac{\gamma_{Ff} \times \Delta\sigma_{E,2}}{\Delta\sigma_c / \gamma_{Mf}}\right) + \left(\frac{\gamma_{Ff} \times \Delta\tau_{E,2}}{\Delta\tau_c / \gamma_{Mf}}\right) \le 1.3$ (according to EN 1994-2)
	$\Delta\sigma_{E,2}$	$\Delta\tau_{E,2}$			
A1	22,88	83.99	0,286	0.927	1,199 < 1.3
A2	24,23	89,10	0,303	0,990	1,293 ≈ 1.3
B1	7,60	18,41	0,095	0,205	0,300 < 1.3
C1	34,90	69,15	0,436	0,769	1,205 <1.3

Results of Table 4 tend to prove that EC4 approach, in the case of the specimens investigated in the present research where no failure occurs during the preliminary cyclic preloading phases, is likely conservative to predict the fatigue failure of the studs connecting the slab and the steel girder. Previous researches [Feldmann M. et al., 2007] have led to the same conclusion. An explanation was proposed in the redistribution of forces along the shear joint with an increase in fatigue damage. If a shear stud is subjected to fatigue and crack propagation takes place, the stud looses

stiffness and therefore the load on the single stud drops. In the consequence the neighbouring studs have to take over more load until one of them is also damaged and looses its stiffness. Therefore fatigue damage of a shear joint is more or less characterized by a step-by-step damage of the studs. Consequently the stress range of a given stud in the shear connection is varying over time whereas its slip may stay more or less constant. On the basis of this observation [Feldmann M. and Gesella H., 2005] have derived a fatigue verification based on the determination of the crack propagation in dependency of the slip range $\Delta s = |s_{max} - s_{min}|$ and the slip amplitude in the shear joint. For the determination of the crack propagation the factors α_t and $\alpha_{t,da/dN}$ have been introduced. The crack propagation rate da/dN is given by the relationships [Feldmann M. et al., 2005]:

$$\alpha_t \Delta s \le 0.10mm : \frac{da}{dN} = 0 ; \tag{5}$$

$$\alpha_t \Delta s \ge 0.10mm : \frac{da}{dN} = \left[-1.4047 \cdot 10^{-5} + 1.4142 \times 10^{-4} \cdot \alpha_t \Delta s \right] \times \alpha_{t,da/dN}$$

Where factor α_t is equal to:

$$\alpha_t = 1 \text{ for } R_s \ge 0 \; ; \quad \alpha_t = \frac{1}{R_s}\left[1 + \frac{1}{R_s}\right]^{-1} \text{ for } R_s < 0 \qquad \text{with } R_s = \frac{s_{min}}{s_{max}} \text{(slip} \tag{6}$$

The factor α_t takes the part of the slip range into account which causes crack propagation on each side of the stud. Further the notch factor derived for the slip with $s_{min} = 0$ has to be modified when $s_{min} \neq 0$ using the factor $\alpha_{t,da/dN}$ which is a function of R_s:

$$\alpha_{t,da/dN} = \left(\left| \frac{1}{R_s} \right| \left(1 + \left| \frac{1}{R_s} \right| \right)^{-1} \right)^{-3/4} \text{ for } R_s > 0 ; \quad \alpha_{t,da/dN} = \left(1 + \frac{1}{2} \cdot R_s \right)^{-3/4} \text{ for} \tag{7}$$

The factors are experimentally validated in the range of $0 \le \alpha_t \Delta s_t < 0.25$ mm and slip ratios from $-1 \le R_s < 0.4$. If the slip amplitude is lower than 0.1 mm no crack propagation will occur.

Maximum slip s_{max}, mean slip s_{min} and the corresponding number of cycles N_i measured at the slab-steel girder interface are given in Table 5 for tests A1, A2, B1 and C1.

Table 5: Cyclic slip measurements

Loading sequences		1	2	3	4	5	6	7
Joint A1	s_{max} (mm)	0.294	0.246	0.282	0.370	0.361	0.352	0.451
	s_{min} (mm)	0.044	0.095	0.038	0.044	0.032	0.025	0.025
	N_i	20 000	40 809	6 267	3 491	8 008	3 169	20 631
Joint A2	s_{max} (mm)	0.129	0.105	0.123	0.174	0.170	0.165	0.214
	s_{min} (mm)	0.015	0.032	0.013	0.015	0.011	0.009	0.009
	N_i	20 000	40 809	6 267	3 491	8 008	3 169	20 631
Joint B1	s_{max} (mm)	0.111	0.101	0.191				
	s_{min} (mm)	0.000	0.000	0.000	x	x	x	x
	N_i	3 258	13 437	7 081				
Joint C1	s_{max} (mm)	0.394	0.371	0.552				
	s_{min} (mm)	0.040	0.027	0.047	x	x	x	x
	N_i	2 680	12 837	150 174				

Using relations (5), (6) and (7), the crack width a has been calculated for tests A1, A2, B1 and C1. Results are given in Table 6 as well as the damage factor *D* defined as the ratio between the half-moon cracked area and the whole cross-section of the stud [Oehlers D.J., 1990]. This Table allows to justify the observations of no stud failure for the fatigue loading procedures carried out in our tests.

Table 6

Joint	*a* (mm)	*D*
A1	2.50	0.06
A2	0.50	0.01
B1	0.10	0.00
C1	9.75	**0.43**



Fig. 13 : Stud failure observation

After monotonous loading (specimen C) where stud failure occurred, samples have been cored from the specimens after the test (Figure 13). It has been possible to observe the cracked area of the stud cross-section. Though the visual observation is not accurate enough to confirm the calculated values of Table 6; a slight damage (but less than 0.43) has been detected.

CONCLUSION

Experimental results presented in this paper may give useful data for the next development of continuous composite bridges of small and medium spans for which EN 1994-2 does not specify any provision to design beam-to-beam joints. It has been proved that the three types of joint under investigation may constitute efficient solutions.

About the influence of the joint design on the slip distribution at the slab – steel girder interface it appears that the less rigid the joint the more the slip amplitude is greater. An increase of the slip amplitude has generally been observed close to the joint.

Although a direct contact seems to lead to a drop of joint rigidity, the novel use of such a system between the compression beam flanges is a possible advantage insofar as an appropriate material stiffness is found for the contact piece.

EN 1994 – 2 specifications appear conservative to predict the damage and the fatigue failure of the studs connecting the slab to the steel girder. Another approach from the literature presented in this paper seems to be a possible alternative in spite of the limited number of our tests.

ACKNOWLEDGEMENTS

The authors would like to thank IREX, the "French Ministry of Ecology and Sustainable Development", ArcelorMittal-Research and SNCF-Engineering for their financial and technical support through the national project MIKTI.

REFERENCES

[CEN, 2004] EN 1994-2, Eurocode 4: Design of composite steel and concrete structures - Part 2 – General rules and rules for bridges, Brussels.

Feldmann M., Gesella H., Zur Vorhersage des Rissfortschritts bei einbetonierten Kopfbolzendübeln in Verbundträgern unter nicht ruhender Belastung, Stahlbau 74, Heft 10, S. 767-779, 2005.

Feldmann M., Hegger J., Hechler O., Rauscher S., Untersuchungen zum Trag- und Verformungsverhalten von Verbundmitteln unter ruhender und nichtruhender Belastung bei Verwendung hochfester Werkstoffe. Forschungsvorhaben P 621. FOSTA – Forschungsvereinigung Stahlanwendung e.V., 2007.

Guezouli S., Somja H., Kaing S.S. and Lachal A., Numerical modelling of composite beam-to-beam joints – Innovative solutions. Composite VI, Devil's Thumb Ranch, Colorado, 20-25 July 2008.

Hanswille G., Pörsch M and Ustundag C., Resistance of headed studs subjected to fatigue loading, Journal of constructional steel research 63, 485-493, 2007.

Lachal A.and Aribert J.M., National Research Project MIKTI, Theme 1, Design of outstanding decks in the framework of small spans, Subject 1-B : Innovative techniques to connect continuous beams, specifications. *Research report,* feb 2002.

Oehlers D.J., Deterioration in strength of stud connectors in composite bridge beams, Journal of Structural Engineering, Vol. 116, No. 12, Dec. 1990.

Inelastic Strength Behavior of Horizontally Curved Composite I-Girder Bridge Structural Systems: Fixed-End Bridge FEA Study

Se-Kwon Jung
School of Civil and Environmental Engineering
Georgia Institute of Technology
Atlanta, GA 30332-0355, USA
wavelette@dreamwiz.com

Donald W. White
School of Civil and Environmental Engineering
Georgia Institute of Technology
Atlanta, GA 30332-0355, USA
don.white@ce.gatech.edu

ABSTRACT

A representative horizontally curved composite I-girder bridge system was designed near the limits of the 2007 AASHTO bridge design specifications and tested at the Federal Highway Administration (FHWA) laboratories for its ultimate loading capacity. A synthesis of the experimental and full nonlinear FEA responses of the test bridge indicates that the component and system behavior was predominantly linear up to the AASHTO M_p-based 1/3 rule load level on the critical outside girder. Similar observations were also made for other parametric simply-supported bridges. These results indicate that simply-supported horizontally-curved composite I-girder bridges may be designed elastically using the AASHTO equation $M_u + S_x f_\ell /3 \leq \phi_f M_n$, where $\phi_f M_n$ can be as large as $\phi_f M_p$. This is a substantial gain in strength for curved I-girder bridges relative to the current curved bridge provisions, which limit $\phi_f M_n$ to a maximum of $\phi_f M_y$. Since the test bridge was simply-supported, a logical and natural extension is the consideration of continuous-span bridges. A convenient and simple way of achieving this extension is to use the base test bridge configuration but to assume that the girder ends are fully restrained. This paper presents a synthesis of the full nonlinear FEA results for this hypothetical fixed-end case.

1. Introduction

In 1992, the Federal Highway Administration initiated the Curved Steel Bridge Research Project (CSBRP) to investigate the fundamental behavior of curved steel bridge structural systems and their component members. The aim of this project was the development of more rational analysis and design procedures for horizontally curved steel bridges. The CSBRP has been conducted in three phases: an erection study, a component strength study and a composite bridge system study. The erection study addressed the deflections and stresses in representative bridge configurations during progressive erection sequences. The component strength study focused on the flexural and shear behavior and resistance of noncomposite curved I-girder components. In the third phase of the CSBRP, the major focus was on the experimental and analytical study of a representative simply-supported non-skewed horizontally-curved composite I-girder bridge designed according to the new

AASHTO (2007) Specifications. The major objective of this test was to examine the system and component responses of a representative structure under all loading stages: non-composite dead load, composite service live load and ultimate loading. The composite test bridge was designed as a representative curved structure proportioned at or above a number of maximum limits in AASHTO (2003 and 2007). Figure 1 shows the composite test bridge equipped with loading fixtures for the ultimate load test. Jung (2006a & b) describe the details of the test bridge and provide a synthesis of the experimental and full nonlinear FEA responses for this structure. The findings of this study indicate that the component and system responses of the test bridge are predominantly linear up to the M_p-based 1/3 rule load level on the outside girder, G3, or

$$M_u + \frac{1}{3} f_\ell S_x \le \phi_f M_p \tag{1}$$

where M_u is the moment calculated elastically for the targeted strength load combination, f_ℓ is the elastic flange lateral bending stress, S_x is the section modulus to the flange under consideration (the tension flange in this case), and $\phi_f M_p$ is the factored girder plastic moment resistance. Based on these results and other parametric FEA studies presented in Jung (2006a), it was concluded that simply-supported horizontally-curved composite bridges may be designed using the resistance equations for straight bridges, reduced by the flange lateral bending effects due to torsion. That is, the girder resistances in positive major-axis bending may be taken equal to $\phi_f M_n - S_x f_t / 3$ with $\phi_f M_n$ as high as $\phi_f M_p$.

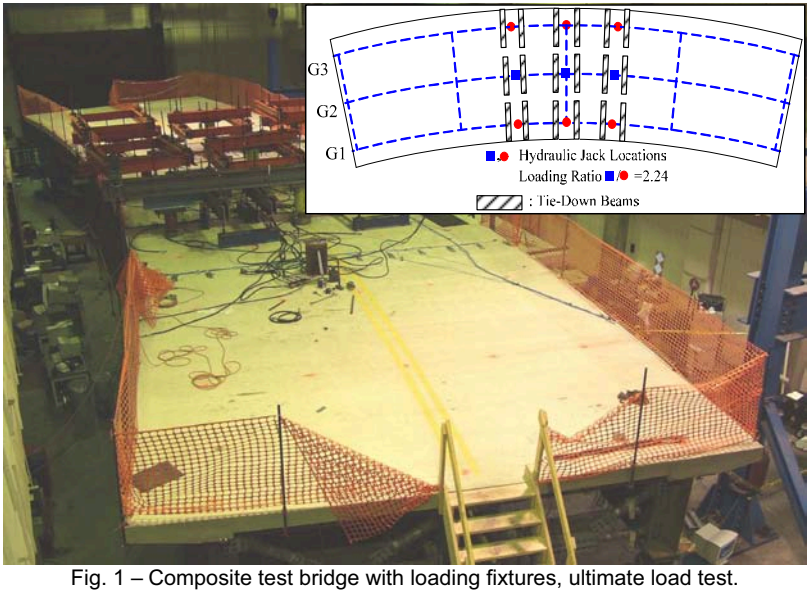


Fig. 1 – Composite test bridge with loading fixtures, ultimate load test.
(Courtesy of Federal Highway Administration)

The test bridge incorporates a number of key attributes pertaining to the requirements stipulated by the AASHTO (2007) LRFD Specifications. However, one test cannot capture all the important physical attributes that may have significant influence on the strength behavior of these types of structures. Therefore, the base test bridge was utilized as a starting point for parametric FEA investigations into the strength behavior of other horizontally curved I-girder bridge systems. Since the test bridge was simply-supported, one logical extension is the consideration of continuous-span bridges. A convenient way of achieving this extension, which limits the changes to the base test bridge configuration so that the reponses can be easily compared, is to assume that the girder ends are fully restrained. One such fixed-end bridge is considered in the following. The fixed-end bridge has the test bridge geometry, but with the unbraced length, L_b, set to 0.075R (five internal cross-frames) and a transition in the girder cross-sections to "optimize" the designs for the positive and negative moment regions. Although this case is a basic pilot study case derived from the test bridge, it allows important key attributes typical of the strength behavior of continuous-span structures to be investigated. Unless noted otherwise, the overall bridge configuration, cross-frame sizes, and material properties of the steel and concrete are taken the same as the measured values for the base composite test bridge. For the full nonlinear FEA solutions, a single monotonic loading is employed using the composite test bridge loading pattern shown in Figure 1.

The paper first contrasts the resistance equations for welded I-girders in negative bending with those discussed above for positive bending. This is followed by a description of the physical attributes and responses of the hypothetical fixed-end bridge. The paper concludes with a discussion of the current AASHTO (2007) strength equations for welded I-girders in positive and negative bending.

2.0 Background

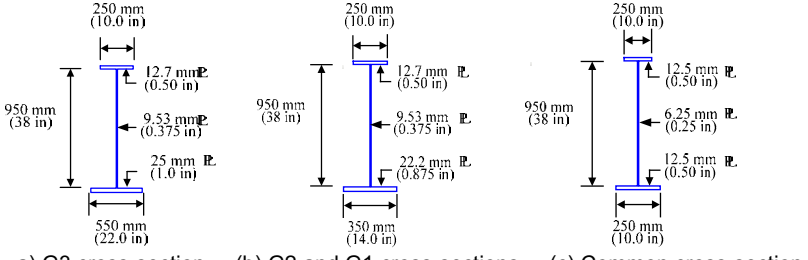
One should note that welded bridge I-girders tend to have highly noncompact or slender webs for the purpose of design economy. As such, the negative bending girder resistances can be expressed in terms of the elastically-computed stresses as

$$f_{bu} + \frac{1}{3} f_{\ell} \le \phi_f F_n \tag{2}$$

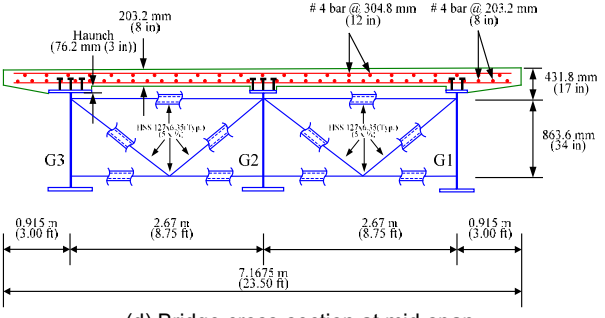
where f_{bu} is the flange major-axis bending stress and $\phi_f F_n$ is the corresponding factored flexural resistance, which is generally less than or equal to $\phi_f F_{yf}$. For typical welded I-girders in negative bending, the use of the above equation does not involve any significant economic penalty. The AASHTO (2007) Article 6.10 provisions recognize this fact by utilizing the above format for the resistance checks of composite members in negative bending. Alternative equations are provided in Appendix A of the AASHTO Specifications that give significantly higher capacities for members that have compact or nearly compact webs. Also, in the positive moment region, AASHTO (2007) provides equations that reduce to Eq. (1) in many situations for straight bridges. However a form similar to Eq. (2) is required in these regions if the bridge is horizontally curved.

3.0 Physical Attributes of the Study Bridge

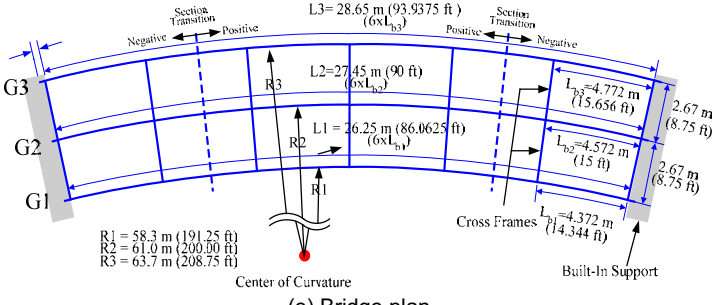
Figure 2 shows the girder profiles, the bridge plan and the girder cross-section views for the fixed-end composite bridge system. As shown in the plan view, section transitions are made at the middle of the second unbraced length from the girder ends. Both the fixed-end and mid-span unbraced lengths are designed to reach their corresponding strength limit states at the governing Strength I load level. All the girders are Grade 50 steel. The common cross-section shown in Figure 2c is used for all the girder cross-sections in the positive moment region.



a) G3 cross-section (negative bending) b) G2 and G1 cross-sections (negative bending) c) Common cross-section (positive bending)



(d) Bridge cross-section at mid-span



(e) Bridge plan

Fig. 2 – Fixed-end composite bridge with “optimized” mid-span and fixed-end girder cross-sections and $L_b/R = 0.075$.

When it comes to the design of unbraced lengths in negative bending, flange local buckling (FLB) governs the flexural resistance F_n (F_n is slightly smaller than the flange yield strength F_{yf}). The lateral-torsional buckling (LTB) resistance falls in the plateau region (i.e., $F_n = F_{yf}$) due to the moment gradient factor, C_b, which is close to 1.75 for all three girders. The design unity checks for flexure are 0.95, 0.94 and 0.98 for the G1, G2 and G3 unbraced lengths in negative bending, respectively.

The corresponding lateral bending stress limit checks, $f_l/0.6F_{yf}$, are 0.33, 0.50 and 0.40. A web thickness of 9.38 mm (0.375 in) is used for all of the girder webs to satisfy the AASHTO [2007] web bend buckling check under Service II limit state. Regarding the design of the positive bending sections, the unity checks for flexure are 0.90, 0.82 and 1.0 for G1, G2 and G3 respectively. The corresponding lateral bending stress limit checks are 0.90, 0.90 and 1.0. The web thickness is set to 6.25 mm (0.25 in) for all the girder webs in the positive moment region. It should be noted that some of the above girder dimensions are smaller than ordinarily employed in steel bridge design. In this regard, the fixed-end bridge may be considered as a scaled model of a prototype bridge structure.

4.0 FEA Modeling Considerations

The same loading used for the base composite test bridge is also used here. Also, representative residual stresses due to flame cutting and welding of the flanges to the web [ECCS 1976] are included, since they are likely to have a significant effect on the behavior of the bridge I-girders in the negative moment regions. S4R shell finite elements [HKS 2004] are utilized for the flanges to accommodate the input of the residual stresses. One percent slab reinforcing is assumed in the negative moment regions as required by AASHTO (2007) Section 6.10.1.7. The concrete tension stress-strain response is simplified such that the peak tensile stress is kept constant for strains larger than the cracking strain. This simplification is justified based on the finding that a refined representation of the tension post-peak and tension stiffening effects in the concrete strain-stress response gives essentially the same solution, but requires substantially higher computational overhead.

5.0 Full Nonlinear FEA Results

5.1 Applied Load vs. Deflection

Figure 3 gives the applied load versus the mid-span vertical deflection at the middle of G3's bottom flange for the fixed-end bridge. The full nonlinear FEA solution represented by the solid line starts to deviate from the linear elastic prediction represented by the dashed line at about 2224 kN (500 kips). This departure from the linear elastic estimate is due to the concrete cracking near the fixed-end supports and the resulting moment redistribution between the fixed-end and mid-span regions. For subsequent higher applied loads, the vertical deflection continues to increase in a nonlinear fashion up to 4106 kN (923 kips) where the deflection curve levels off showing a limit point.

Figure 4 shows the girder deformed geometries at the girder end supports when the limit point is reached at a total applied load of 4106 kN (923 kips). The connection plates and transverse stiffeners are represented by beam elements and are not shown in this image. One should note that all three girders fail essentially by a combination of the flange local buckling (FLB) and web bend buckling at their fixed

ends. Furthermore, the visual inspection of the girder deformed geometries shows that all three girders reach their strength limit states approximately at the above limit load level. As a result, there is no significant redistribution by shedding of moment from a more critical girder end section to less critical end sections.

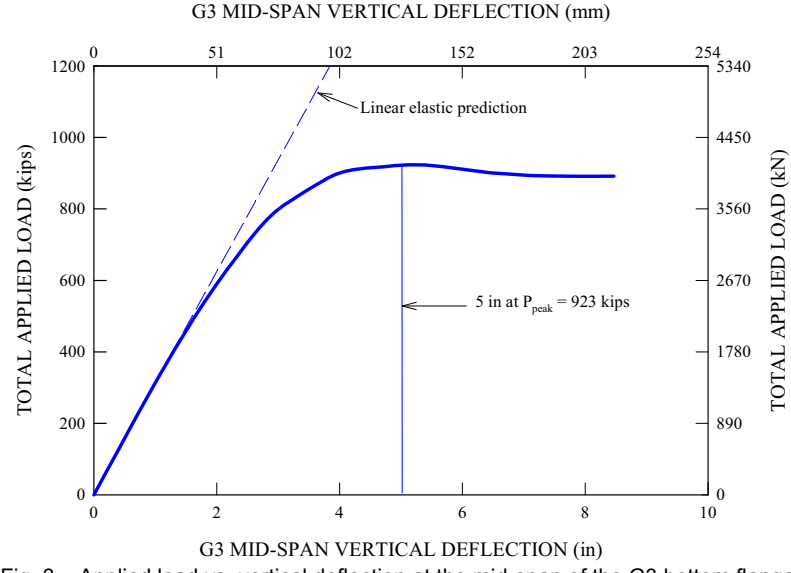


Fig. 3 – Applied load vs. vertical deflection at the mid-span of the G3 bottom flange.

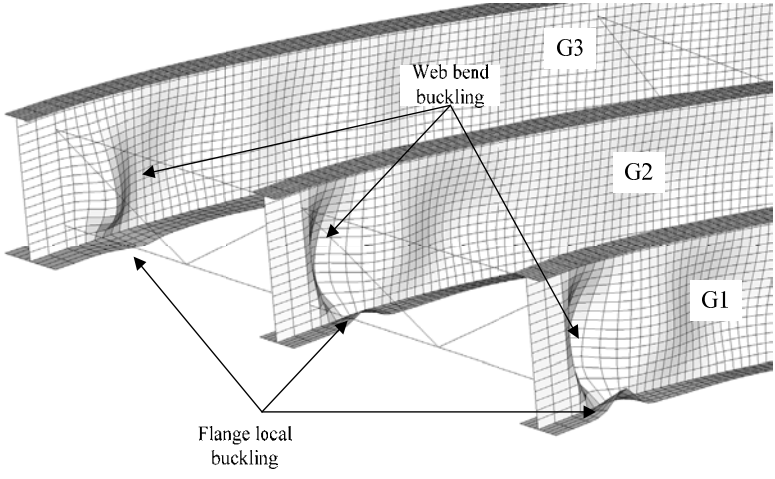


Fig. 4 – Girder deformed geometries at the fixed-end supports when limit point is reached at total applied load of 4106 kN (923 kips) (Deformation Scale Factor = 10).

Figure 5 shows the steel girder deformed geometries at mid-span with contours of the von Mises stresses at the bridge limit load. It should be noted that a large portion of the mid-span steel cross-sections are extensively yielded at this load level, indicating that the mid-span bridge cross-section is close to its ultimate capacity. As a result, the fixed-end bridge is not able to support additional applied loads at the girder end strength limits. In what follows, detailed component responses are discussed. As noted previously, the study bridge uses the average measured material properties from the physical FHWA test unless noted otherwise. The G3 web yield stress is 441 MPa (64 ksi) and F_y = 400 MPa (58 ksi) for the G3 top and bottom flanges on the study bridge.

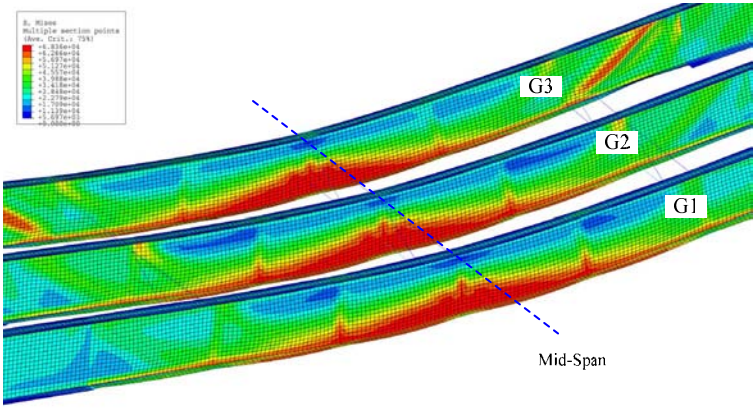


Fig. 5 – Girder deformed geometries at mid-span with contours of von Mises stresses at a total applied load 4106 kN (923 kips) (Deformation Scale Factor = 10)

5.2 Applied Load vs. Internal Moment

Figure 6 shows internal moment variations for girder G3 at the fixed-end and mid-span regions throughout the applied loading history. There are two strength limit states marked on the plots: the negative bending FLB-based and the positive bending 1.3M_y-based 1/3 rule load levels on G3. The FLB-based 1/3 rule load level on G3 relates to a total applied load of 3203 kN (720 kips) when the G3 unbraced length in negative bending starts to exhibit substantial flange local buckling (FLB) distortions. The 1.3M_y-based 1/3 rule load level on G3 relates to a total applied load of 3470 kN (780 kips). AASHTO [2007] requires that the girder base flexural capacity must be limited to 1.3M_y for straight continuous-span composite sections in positive flexure, unless special provisions are satisfied to ensure ductile inelastic moment-rotation response at the interior pier sections. For composite bridges, excessive yielding in the positive moment regions can potentially lead to significant redistribution of moments to the negative moment regions. The use of the 1.3M_y limit is intended to guard against an under-design of the negative moment regions due to this moment redistribution (by limiting the positive bending inelastic deformations). The AASHTO [2007] Section 6.10.1.5 assumption that the slab is fully effective throughout the bridge length, for the structural analysis, also tends to protect against an under-design of the negative moment region. This is discussed in more detail below.

Figure 6 shows that the girder G3 internal moments at the fixed-end and mid-span regions increase linearly until the point when the slab concrete starts to crack at the fixed-end supports. For higher applied loads, the fixed-end and mid-span moments obtained from the full nonlinear FEA simulation deviate from the corresponding linear elastic estimates indicated by the dashed lines in the figure. At the early stages of the nonlinear response, the increase in the G3 mid-span moment due to redistribution from the fixed-end regions is smaller than the redistributed fixed-end moment. This implies that some of the moment redistributed from the G3 fixed ends is not taken by the G3 mid-span cross-section, but is distributed to the other two girders. However, as the total applied load nears the limit point, this interplay between the girders starts to disappear and the redistributed moment from the mid-span is larger than that from the girder ends (indicating some shedding of load from the interior girders).

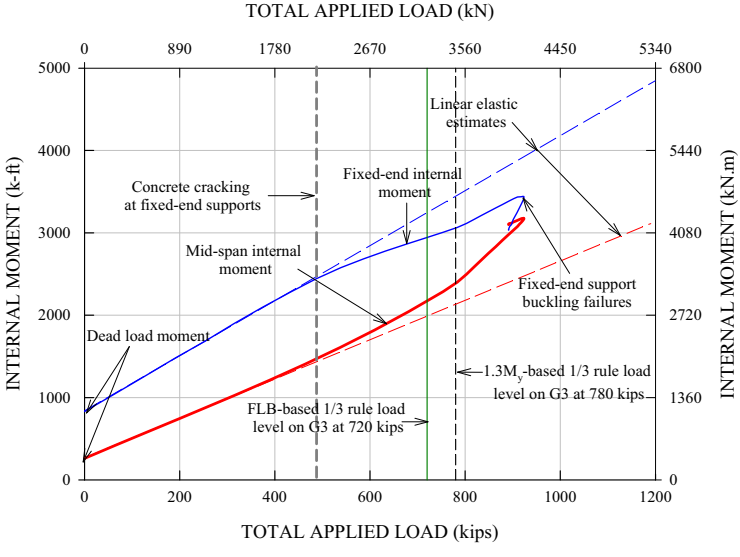


Fig. 6 – Applied load versus internal moments for the isolated G3 composite cross-section at the fixed-end and mid-span regions.

5.3 Mid-span Internal Moment vs. Curvature

Figure 7 gives the moment versus curvature for the G3 mid-span cross-section. It should be noted that the curvature is calculated approximately based on the average longitudinal normal strain at the middle of the shell element at the bottom of the web and at the comparable location at the top of the web. The difference between these strains divided by the depth between the two points gives an estimate of the curvature at a given location along the length. This calculation is termed the web strain-based curvature for purposes of discussion. Since the average strain variation through the web depth is predominantly linear for all the load levels at the bridge mid-span, the curvature based on this calculation is believed to be a reasonable estimate.

The mid-span moment increases linearly relative to the curvature until the slab cracking moment (e.g., at about 1900 kN-m (1400 k-ft) for G3). Then it starts to deviate from the linear elastic estimate represented by the dashed line. Subsequently, the curvature continues to increase in a nonlinear fashion. Interestingly, Figure 7 shows that the G3 mid-span moment levels off at a maximum internal moment of about 4204 kN-m (3100 k-ft), which is slightly larger than the section plastic moment of M_p = 3932 kN-m (2900 k-ft). With respect to the FLB-based 1/3 rule load level on G3 of 3203 kN (720 kips), the linear elastic moment estimate for the G3 mid-span region is 2720 kN-m (2000 k-ft) while the corresponding full nonlinear solution is 2992 kN-m (2200 k-ft) due to the moment redistribution from the fixed-end support. More importantly, it should be noted that the G3 nonlinear response at this load level is located well into the nonlinear portion of the moment-curvature curve. The mid-span cross-section must support a higher internal moment than the moment obtained from the linear elastic analysis due to the moment redistribution from the fixed ends. This causes early yielding at the mid-span cross-section. G1 and G2 exhibit similar moment-curvature responses. With respect to the $1.3M_y$-based 1/3 rule load level on G3 of 3470 kN (780 kips), the full nonlinear FEA solutions for the girder positive moments are larger than the corresponding linear elastic estimates by a slightly greater percentage. Also, it can be seen that the deviation of the full nonlinear FEA solutions from the linear elastic estimates is more significant. Although there is increased nonlinearity at this load level, it is important to note that the girder positive bending responses are quite ductile.

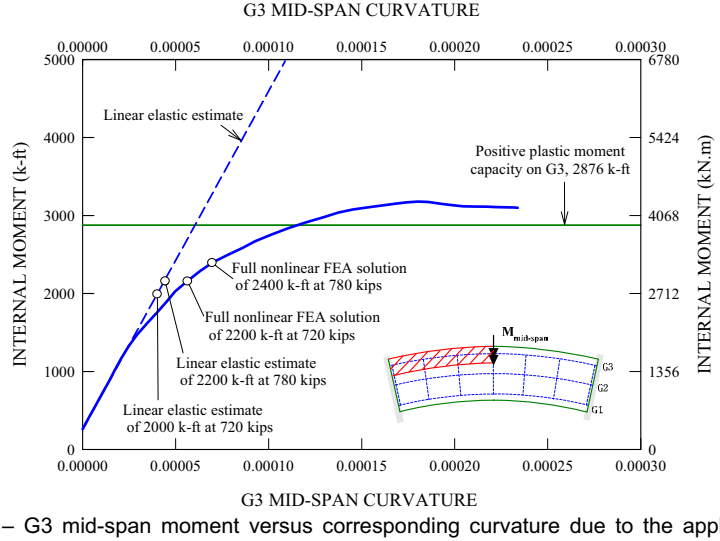


Fig. 7 – G3 mid-span moment versus corresponding curvature due to the applied loads, initial dead load moment included.

The above inelastic behavior is generally not a cause for concern. The positive and negative moment regions are designed for moments estimated based on the AASHTO [2007] Article 6.10.1.5 assumption of the slab being fully effective throughout the bridge length. The sum of all the resistances in the positive and negative bending regions is an equilibrium solution that balances with the factored

strength design loadings. Given the ductile behavior of composite I-girders in positive bending, if the positive moment regions are not sufficient to resist the calculated positive moments (because of an underestimation of these moments by the elastic analysis), redistribution to the negative moment regions will occur. This will cause the internal moments to approach the values calculated in the elastic analysis. The same cannot always be said about the negative moment regions, since a stability failure in negative bending may lead to a less ductile response.

5.4 Fixed-End Internal Moment vs. Curvature

Figure 8 presents the moment-curvature variations for the G3 fixed-end cross-section. In addition to the web strain-based curvature described earlier, one other curvature estimate is presented in this plot. This estimate is termed the nodal displacement-based curvature.

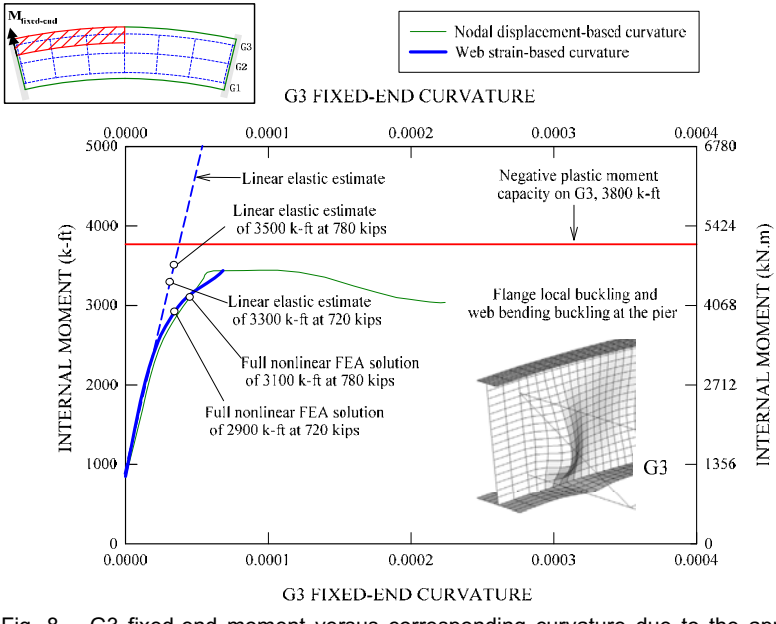


Fig. 8 – G3 fixed-end moment versus corresponding curvature due to the applied loads, initial dead load moment included.

The web strain-based curvature calculation works well as long as the web average strain distribution through the web depth is approximately linear, which is the case for the mid-span region. However, this approach generally does not work well for the fixed-end support curvature calculation once the plate buckling distortions become significant. Therefore, the web strain-based curvature calculation is only applicable prior to the buckling of the web panel at the girder ends. The curvature calculation by the web-strain based method is indicated by the thick solid line. The inset located in the lower right corner of Figure 8 shows the deformed geometry of the G3 fixed-end

support region at the end of the web-strain based curve (Deformation Scale Factor = 5.0). In order to complement the web strain-based method for calculating the post-buckling curvature, a nodal displacement-based curvature measure is calculated as follows. First, three nodes located at the web-bottom flange juncture near the fixed-end support are chosen including the fixed-end node. The two nodes other than the fixed end node are chosen such that they are as close to the fixed-end support as possible but are not located within the local buckling wavelength. Otherwise, the curvature calculation is affected significantly by the local deformed geometries resulting from the buckling distortions. The nodal displacements at these three nodes are fitted by a quadratic curve for each increment of the full nonlinear FEA solution. The second derivative of this quadratic curve, which is constant, produces an estimate for the fixed-end curvature (i.e., in essence, a representative "smoothed" curvature over the length represented by the three points). The resulting moment-curvature curve is denoted by the thin solid line. Not only does the nodal displacement-based curve closely match the web strain-based curve up to the buckling point, but also it continues to show reasonable post-buckling curvature responses.

Similar to the mid-span moment, the fixed-end moment increases predominantly in a linear fashion until the slab at the fixed-end regions starts to crack. Then, the fixed-end moments continue to increase in a nonlinear fashion, as some of the fixed-end moments predicted by the linear elastic analysis redistribute to the mid-span and between the girders. It is noteworthy in the inset of Figure 8 that the G3 fixed-end region appears to fail predominantly by a combination of flange local buckling and web bend buckling distortions. The total load level at which the calculated AASHTO FLB-1/3 rule based resistance is reached at the G3 fixed end in the linear elastic analysis is 3203 kN (720 kips). The corresponding fixed-end moment is 4488 kN-m (3300 k-ft). However, the fixed end moment in the full nonlinear FEA simulation at this load level is only 3932 kN-m (2900 k-ft). In addition, the total load level at which the mid-span cross-section of G3 reaches the $1.3M_y$-based 1/3 rule resistance is 3470 kN (780 kips). The corresponding fixed-end moment is 4760 kN-m (3500 k-ft). However, the fixed-end moment in the full nonlinear FEA simulation at this load level is only 4216 kN-m (3100 k-ft). The behavior is similar at the G2 and G1 fixed-end cross-sections. With respect to the negative moment FLB-based and the positive moment $1.3M_y$-based 1/3 rule load levels on G3, the linear elastic fixed-end moment estimates are significantly larger than the corresponding full nonlinear FEA solutions for all three girders. As a result, the total applied load necessary to induce the failure of the fixed-end region is actually much higher than the design load level predicted based on the linear elastic analysis.

6. Summary and Conclusions

In summary, the ultimate capacities for simply-supported horizontally-curved composite bridges are typically limited due to extensive yielding on the steel sections. Concrete crushing is obtained ultimately at load levels substantially higher than the strength design loadings. Thus, even for horizontally curved bridge I-girders with their webs categorized as slender elements, the section plastic moment capacity, with a reduction due to the effects of lateral bending moments, can be used for the resistance. This idealization is presently allowed in AASHTO [2007] for straight composite I-girder bridges with or without large flange lateral bending (large flange lateral bending in straight bridges can be caused by support skew). The

physical test bridge and parametric studies of simple-span bridges from Jung (2006a & b) indicate that this idealization can also be applied to simple-span horizontally-curved bridges.

In the case of typical horizontally curved continuous-span bridges with highly noncompact or slender webs, their base capacities in negative bending are typically smaller than the first yield moment since they are limited by stability-related limit states such as flange local buckling, lateral-torsional buckling and web bend buckling. In addition, linear elastic analysis assuming the concrete deck to be fully effective over the entire span length generally results in an overprediction of the negative bending moments and an underprediction of the positive bending moments. This is largely because of distributed cracking in the negative moment region of the slab prior to reaching the maximum strength levels. It is important for engineers to understand that this design practice is actually beneficial rather than problematic. That is, overestimated negative moments ensure that continuous-span bridges develop their desired strength limit states, since the positive moment region tends to behave ductily when designed according to the AASHTO [2007] criteria. The AASHTO analysis assumption leads to a slight over-design of the negative moment region and a slight under-design of the positive moment region.

Acknowledgements

This research was funded by Professional Services Industries, Inc. (PSI) and the Federal Highway Administration (FHWA). The authors gratefully acknowledge the financial support from the sponsors. The many contributions to this work from numerous individuals who have been associated with the different phases of the FHWA CSBRP, including the PSI and FHWA staff at the Turner-Fairbank Highway Research Center, are also gratefully acknowledged. The opinions, findings and conclusions expressed in this paper are the authors' and do not necessarily reflect the views of the above individuals, groups and organizations.

REFERENCES

AASHTO [2003]. *Guide Specifications for Horizontally Curved Steel Girder Highway Bridges with Design Examples for I-Girder and Box-Girder Bridges*, American Association of State and Highway Transportation Officials, Washington D.C.

AASHTO [2007]. *AASHTO LRFD Bridge Design Specifications, 4th Ed.*, American Association of State and Highway Transportation Officials, Washington D.C.

ECCS-Committee 8-Stability [1976]. "Manual on Stability of Steel Structures" 2nd Ed., European Convention for Constructional Steelwork, Publication No. 22, 328pp.

HKS [2004], *ABAQUS/Standard Version 6.4-1*, Hibbitt, Karlsson & Sorensen, Inc., Pawtucket, RI.

Jung, S.-K. [2006a]. "Inelastic Strength Behavior of Horizontally Curved Composite I-Girder Bridge Structural Systems," Ph.D. dissertation, Georgia Institute of Technology, Atlanta, GA.

Jung, S.-K. and White, D.W. [2006b]. "Strength Behavior of Horizontally Curved Composite I-Girder Bridge Structural Systems," *Proceedings*, Annual Technical Session, Structural Stability Research Council, San Antonio, TX, 143-162.

Efficient Erection Method of Cantilever Bridge Deck using Ribbed Steel Form bolted to Girder

Youn-Ju Jeong
Research Fellow/Ph.D, Hybrid Structure Research Division
Korea Institute of Construction Technology, Goyang, Republic of Korea
yjjeong@kict.re.kr

Hyun-Bon Koo
Researcher, Structure System Research Division
Korea Institute of Construction Technology, Goyang, Republic of Korea
mygoomy@kict.re.kr

Hyeong-Yeol Kim
Research Fellow/Ph.D., Hybrid Structure Research Division
Korea Institute of Construction Technology, Goyang, Republic of Korea
hykim1@kict.re.kr

ABSTRACT

In this study, in order to erect a cantilever deck without supports and formwork, the use of a steel-concrete composite cantilever deck system was explored. The cantilever deck system consists of steel plate, perfobond ribs that have been welded onto the steel plates, concrete, and reinforcing bars. In order to form a cantilever deck, the steel forms consisting of steel plate and ribs must be fabricated then, the ribs of steel form were bolted to the girder to prevent large rotation and deflection under erection loads and finally, the concrete must be cast-in-place. A total of four specimens were built and tested under erection loads. As a result of the tests, it is found that, under erection loads, the weight of the laborers, and wet concrete, the connection of the ribs to the girders has enough stiffness to satisfy in-erection deflection and the bolt connections supply sufficient force to prevent rotation. The proposed cantilever deck erection method should improve the efficiency and economy of bridge construction.

INTRODUCTION

In recent years, in order to reduce erection costs and to expand the service life of bridges, many types of bridge decks have been developed and applied. These types of bridge decks including steel plate-concrete composite decks [Kim and Jeong 2006, Nakai et al. 1998, Morino 1998], FRP(Fiber Reinforced Plastics) decks [Berg et al. 2006, Zhao 2004], half-depth [Morino 1998, Kim 2006], and full-depth [Ehmke 2006, Shim et al. 2001] prefabricated concrete decks, etc., no longer require supports and formwork during erection because they were prefabricated and designed to carry all the execution loads in addition to their service function as structural elements. However, some types of these decks, such as steel plate-concrete composite, FRP deck, and half-depth prefabricated concrete decks, were mainly focused on interior decks between girders, and the cantilever parts of the bridge deck were erected in the usual cast-in-place reinforced concrete deck method, as shown in Figure 1. Also, the some types of prefabricated decks of FRP [Berg et al. 2006, Zhao 2004] and full-

depth concrete [Ehmke 2006] can apply only straight bridge in forms of continuous deck with the interior decks, and the cantilever deck of the skew and curved bridge should be erected with cast-in-place concrete deck regardless of the deck types.

This cantilever deck erection method has a disadvantage of erection period because it requires supports and formwork for the concrete. If an erection method that does not require supports and formwork is available for the cantilever deck for these types of bridge deck, the erection of a cantilever deck would be even easier than a cast-in-place concrete deck. However, it is difficult to erect a cantilever deck without supports and formwork because it causes large rotation and deflection. In order to erect a cantilever deck without supports and formwork, the large rotation and deflection must be prevented which requires special devices to connect the cantilever deck to the girders.

In this study, in order to erect a cantilever deck without supports and formwork, an experimental study for the steel-concrete composite cantilever deck system was carried out. The cantilever deck system in this study consists of steel plates, perfobond ribs welded onto the steel plates, concrete, and reinforcing bars. In order to form a cantilever deck, the steel forms consisting of steel plate and ribs must be fabricated then, the ribs of steel form were bolted to the girder to prevent large rotation and deflection under erection loads and finally, the concrete must be cast-in-place. A total of four specimens were built for the Steel-Box girder and PSC (Prestressed Concrete) girder and tested under erection loads.



(a) Half-depth prefabricated concrete decks (b) Supports and formwork for the concrete

Fig. 1 - Conventional erection method of cantilever bridge deck

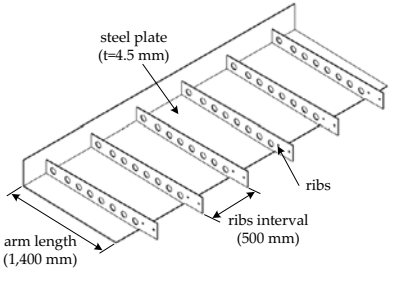
STEEL-CONCRETE COMPOSITE CANTILEVER DECK SYSTEM

Design of Cantilever Deck

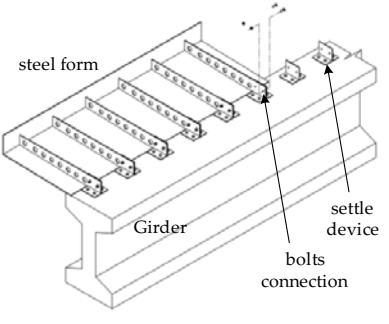
The details of cantilever deck were based on Korean bridge design specifications [MOCT 2006]. The loading conditions considered for the cantilever deck design were in-erection and in-service loads, and the details of the cantilever deck were thickness of steel plate, interval of ribs, and the bolts used to connect to the girders. The cantilever deck form must serve as the formwork and confirm the structural safety during the erection. Therefore, the erection loads of the self-weight of the cantilever deck, parapet, laborers, and of the impact of wet concrete were considered when designing the deck.

Optimal criteria for design detailing were developed [KICT 2006]. For the considered bridge, the determined values were 4 mm in thick steel plate, ribs placed at 500 mm interval, and F8T M20 bolts were used to connect the steel form to the girders. This cantilever deck, up to 1,400 mm in length, satisfies the structural safety, allowable stress and end-deflection of formwork during the erection.

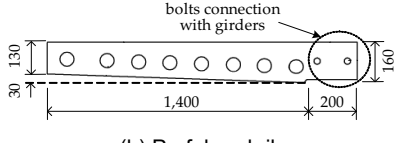
The concrete depth of 250 mm and the reinforcing bars were the same as with the reinforced-concrete deck. Therefore, after the concrete has hardened, the cantilever deck has sufficient structural performance compared to the reinforced-concrete deck, because it has additional steel forms combined with reinforced-concrete deck, under in-service loads. The details of the steel-concrete composite cantilever deck are shown in Figure 2.



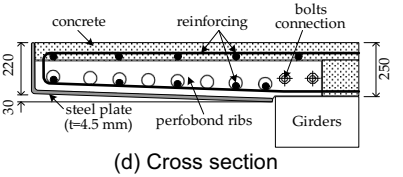
(a) Steel form



(c) Connection with girders



(b) Perfobond rib



(d) Cross section

Fig. 2 - Steel-concrete composite cantilever bridge deck

Fabrication of Specimens

In order to verify the structural safety of the cantilever deck system examined in this study, during the erection, a series of experimental studies were carried out. Four specimens were fabricated to the Steel-Box girder and PSC girder, two specimens for each girder, and each was denoted as SGF and PGF groups, respectively. The summary of the specimens is as shown in Table 1, and the procedure of specimen fabrication is illustrated in Figure 3.

First, in order to connect the steel forms of the cantilever deck to the girders, settle devices were attached to the girder. The settle devices were welded to the Steel-Box girder, as shown in Figure 3(a), and attached to the PSC girder by M12 × 110 mm

chemical anchors, as shown in Figure 4(a). Then, steel forms that were 1.0 m in width and in arm length were fabricated, in which steel forms were consisted of steel plate of 4.5 mm thickness and perfobond ribs were welded to the steel plates, as shown in Figure 3(b).

The steel forms were moved to the girders by crane, and connected to the girder with F8T M20 bolts. The connection was carried out by laborer at the top of the girder to mostly simulate real erection conditions, as shown in Figure 3(c) and Figure 4(b). After the cantilever form was connected to the girder, as shown in Figure 3(d), reinforcing bars were installed such as the reinforced-concrete deck, as shown in Figure 3(e).

Side formworks to prevent side flow of concrete, were greased and separated from the specimens to allow vertical deflection of cantilever steel form during the concrete casting. Side formworks were just contacted to specimens only by using side supports, as shown Figure 3(f). Finally, the concrete was cast. The concrete casting was performed completely from the tops of the cantilever deck to mostly simulate real erection conditions, as shown in Figure 3(f).

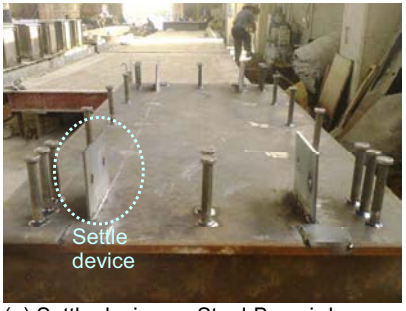
Table 1 - Summary of test specimens

Girder type	Speci-mens	Girder materials		Deck concrete (f_{ck})	Settle device on girder	Deck conn-ection with girder
		Steel (f_y)	Concrete (f_{ck})			
Steel-Box girder	SGF-1	240 MPa	-	30 MPa	Welding	Bolts (F8T M20)
	SGF-2					
PSC girder	PGF-1	-	40 MPa	30 MPa	Chemical anchor (M12 × 110)	Bolts (F8T M20)
	PGF-2					

EXPERIMENTAL STUDY

Test Program

During the concrete casting, the erection loads which consisted of laborers, wet concrete, and concrete vibrator were applied to the cantilever steel form, and the deflection and strain of the cantilever steel forms were measured. Where, cantilever deck-to-girder connection, reinforcing, and the concrete casting by laborer were performed completely from the top of the cantilever deck to mostly simulate real erection conditions. Also, wet concrete was dropped at the height of 1.0 m to simulate impact of wet concrete during the concrete casting.



(a) Settle device on Steel-Box girder



(b) Steel form



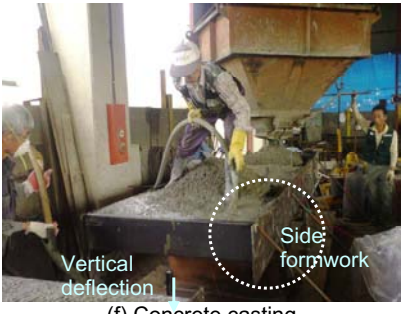
(c) Bolting steel form to settle device on girder



(d) After connection



(e) Reinforcing bars install



(f) Concrete casting

Fig. 3 - Fabrication of cantilever deck specimens

Two LVDTs were installed at the end of each arm and four strain gauges were mounted on the steel plate at the L/2 span and top reinforcing bars at the start points of each arm, respectively, as shown in Figure 5. These were measured for 30 minutes (1800 sec), from the start to finish of concrete casting, for each specimen, respectively.



(a) Settle device on PSC girder



(b) After connection

Fig. 4 - Settle device attachment on PSC girder

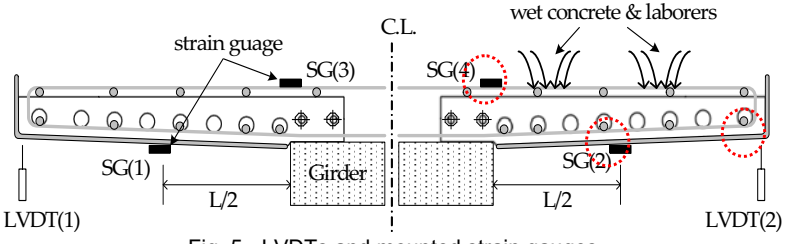


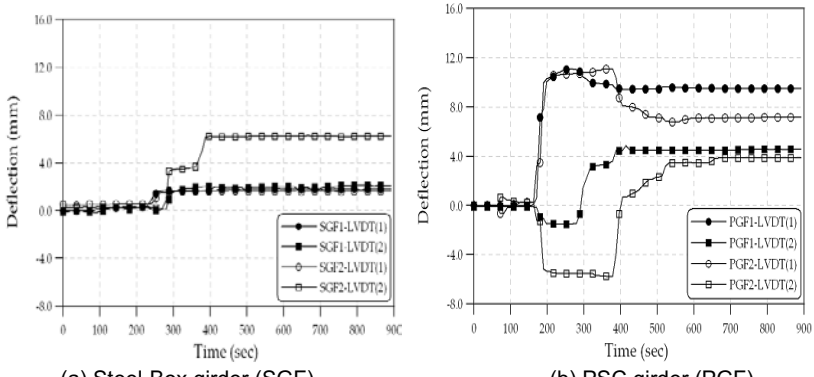
Fig. 5 - LVDTs and mounted strain gauges

Test Results

The measured deflection curves for the specimens during the erection are presented in Figure 6. The average end-deflection of the SGF specimens was measured at about 2 mm, expecting SGF-2 specimen LVDT(2) of 6 mm. The average end-deflection of the PGF specimens was measured at about 8 mm. In case of the PSC girders, the girder surface is composed of concrete and it is difficult to completely contact the ribs of the steel form with the PSC girder surface. Therefore, some gaps existed between the steel form and the girder surface after the connection which caused more deflection than the Steel-Box girder, although some gaps may have existed in the Steel-Box girders, which may have influenced the deflection.

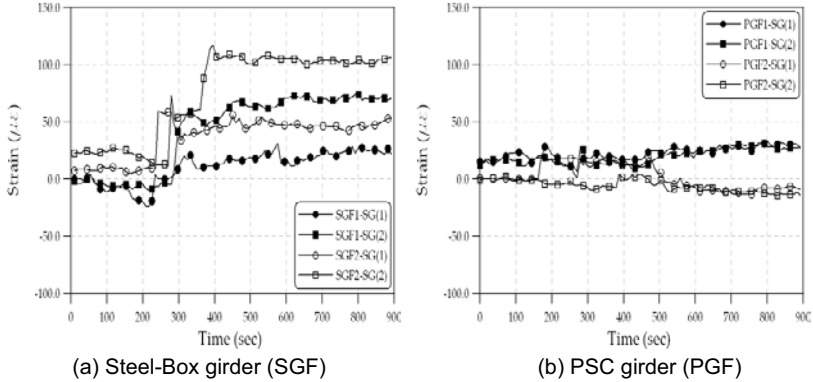
The measured strain curves for the steel plate at the L/2 arm length during the erection were presented in Figure 7. The average strain of steel plate for SGF specimen was measured at about 50 με, expecting SGF-2 specimen SG(2) of 100 με. The average strain of the steel plate for the PGF specimen was measured at about 20 με. In case of the PSC girders, larger deflection and smaller strains were recorded than those for Steel-Box girder specimens. It is resulted in free body motion due to the gap between the steel form and the girder surface.

The measured strain curves for the top reinforcing bars at the start points of cantilever arm during the erection were presented in Figure 8. The average strain of the top reinforcing bars for the SGF and PGF specimens were measured at about 75-80 με. Two specimen groups show similar values of strain at the top reinforcing bars. It is resulted in the same span length and erection loads of Steel-Box girder and PSC girder.



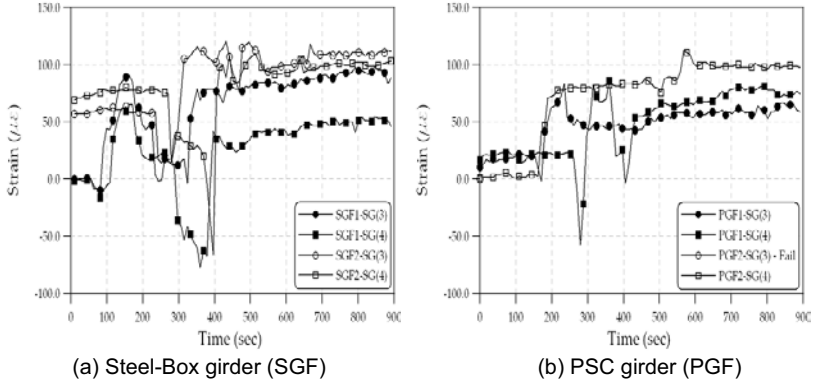
(a) Steel-Box girder (SGF) (b) PSC girder (PGF)

Fig. 6 - Deflection curves during erection



(a) Steel-Box girder (SGF) (b) PSC girder (PGF)

Fig. 7 - Strain curves of steel plate during erection



(a) Steel-Box girder (SGF) (b) PSC girder (PGF)

Fig. 8 - Strain curves of top reinforcing bars during erection

The comparison measured data with design criteria [MOCT 2006] were presented at Table 2. The design criteria are the allowable deflection, L/300, and allowable stress for the formwork of steel plate. In cases of SGF2 and PGF1, end-deflections were not satisfied allowable value of L/300. However, it may be caused by some gaps, and all recorded stresses at the steel plate were very lower level, maximum 11.3 %, than allowable stress. Judging from the test results, the steel-concrete composite cantilever deck considered in this study has a sufficient structural safety for deflection and formwork under the erection loads, laborers, wet concrete, etc.

After the concrete is hardened, the cantilever deck should have sufficient structural capacity compared to the reinforced-concrete deck under in-service loads because the concrete depth of 250 mm and the reinforcing were the same as with the reinforced-concrete deck and it has additional steel form combined with reinforced-concrete deck.

Table 2 - Comparison measured data with design criteria under erection loads

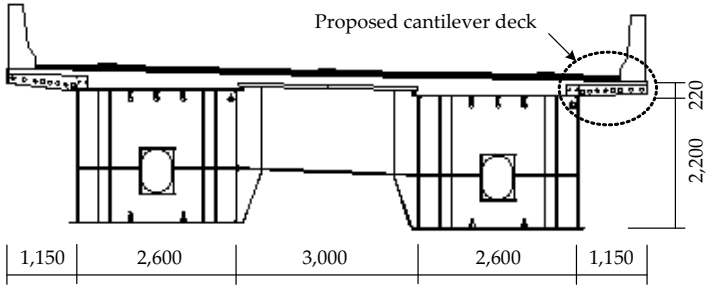
Specimens	End-deflection of formwork (mm)		Stress of steel plate (MPa)	
	Average (δ)	Allowable (δ_a, L/300)	Average (f_t)	Allowable (f_{ta})
SGF1	2.0 mm	3.33 mm	10.5 MPa(50 με)	140 MPa
SGF2	4.0 mm	3.33 mm	15.8 MPa(75 με)	140 MPa
PGF1	4.8 mm	3.33 mm	6.3 MPa(30 με)	140 MPa
PGF2	2.7 mm	3.33 mm	-2.7 MPa(-13 με)	140 MPa
* Average( ) = Average(LVDT(1), LVDT(2)) for the each specimen $f_t = E_t \cdot \varepsilon_t$ (E_t : 2.1 $\times$ 10^5 MPa, ε_t : measured strain at steel plate)				

CONSTRUCTION BENEFITS

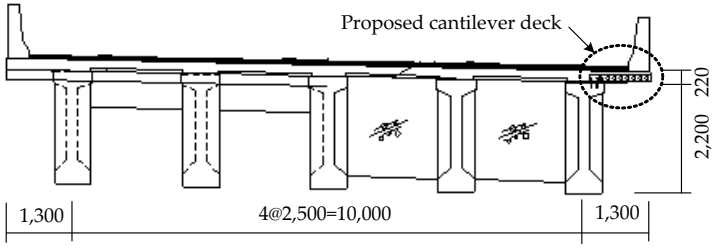
In order to evaluate the construction benefits of the steel-concrete composite cantilever deck considered in this study, the erection cost and period were evaluated for the targeted Steel-Box girder and PSC girder bridges. The dimensions of the target bridges were selected from the standard drawings of these types in Korea. The cross sections of the target bridges are presented in Figure 9, respectively. The span length and width of the target bridges are 50.0 m and 10.5 m in Steel-Box girder bridges and 35.0 m and 12.6 m in PSC girder bridges, respectively.

Erection Cost

The erection costs were drawn for the cantilever deck considered in this study and compared with the costs of reinforced-concrete deck for the target bridges. The erection costs involves only direct components related to material and laborers, excluding indirect expenses related to the duration of execution work, among others. The erection costs for the cantilever deck in this study were determined based on the test specimen fabrication costs because there is not yet a bridge of this type, on the other hand that of reinforced-concrete deck was decided based on the many erection examples.



(a) Steel-Box girder bridge



(b) PSC girder bridge

Fig. 9 - Target bridges for construction benefit evaluation

Table 3 - Erection cost details for the Steel-Box girder bridge

Cost details	Amount unit	RC deck		Proposed deck	
		Amount	Cost	Amount	Cost
Formwork	m^2	2.595	$70.7	-	-
Supports	m^3	5.101	$155.5	-	-
Steel form fabrication	m^2	-	-	3.313	$519.7
Steel form installation	m^2	-	-	3.313	$25.1
Reinforcing bars	tonf	0.094	$54.2	0.075	$43.3
Spacer	m^2	3.313	$1.6	-	-
Concrete casting	m^3	1.020	$14.8	0.708	$10.2
Concrete	m^3	1.030	$51.6	0.715	$35.8
Reinforcing bars	tonf (D>16)	0.085	$38.0	0.057	$25.5
	tonf (D=13)	0.011	$5.0	0.020	$9.0
Total cost			$391.4		$668.6
Unit cost ($ / m^2)			$118.0		$202.0

* Currency rate (2008. 07.): $1 = ₩1,000 (Korean Won)

Total cost for the unit deck module: 1.325 (width) × 2.5 m (span), Area = 3.3125 m^2

Table 4 - Erection cost details for the PSC girder bridge

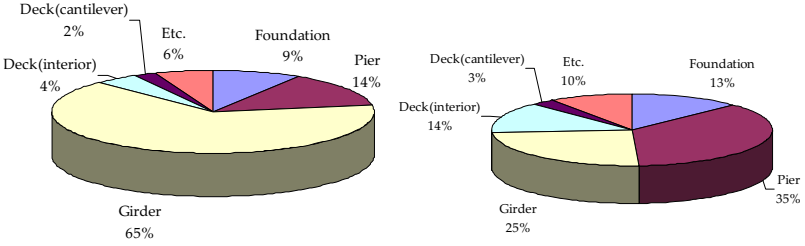
Cost details	Amount unit	RC deck		Proposed deck	
		Amount	Cost	Amount	Cost
Formwork	m^2	2.300	\$62.6	-	-
Supports	m^3	4.139	\$126.1	-	-
Steel form fabrication	m^2	-	-	3.013	\$477.1
Steel form installation	m^2	-	-	3.013	\$22.1
Reinforcing bars	tonf	0.102	\$58.9	0.064	\$36.9
Spacer	m^2	3.013	\$1.5	-	-
Concrete casting	m^3	0.723	\$10.5	0.529	\$7.7
Concrete	m^3	0.730	\$36.6	0.534	\$26.8
Reinforcing bars	tonf (D>16) tonf (D=13)	0.094 0.010	\$42.0 \$4.5	0.045 0.020	\$20.1 \$9.0
Total cost			\$342.7		\$599.7
Unit cost (\$ / m^2)			\$114.0		\$199.0

* Currency rate (2008. 07.): \$1 = ₩1,000 (Korean Won)
Total cost: for the unit deck module: 1.205 (width) × 2.5 m (span), Area = 3.0125 m^2

The erection cost details for the Steel-Box girder and PSC girder bridges were summarized in Table 3 and Table 4 [KICT 2006], respectively. As a result of the evaluation of the erection costs, as shown in Table 5, the steel-concrete composite cantilever deck has a higher erection cost than reinforced-concrete decks by 171 % in the case of Steel-Box girder bridges and by 175 % in the case of PSC girder bridges. However, considering that the erection costs of steel-concrete composite cantilever deck were drawn from the test specimen fabrication costs and the cost of the erection of a cantilever deck is a very small percentage, about 2-3 % of the total bridge construction cost, as shown in Figure 10, it is considered that the increment of erection cost of 71-75% is insignificant. If the steel forms for this cantilever deck are produced on a large scale in a factory, the cost to erect this cantilever deck should be reduced at a certain level.

Table 5 - Erection costs of cantilever deck for target bridges

Cantilever deck type	Erection cost (US dollars/m^2)	
	Steel-Box girder	PSC girder
Reinforced-concrete deck [1)]	\$118/m^2	\$114/m^2
Steel-concrete composite deck [2)]	\$202/m^2	\$199/m^2
Ratio, [2)] / [1)]	171 %	175 %



(a) Steel-Box girder bridge (b) PSC girder bridge

Fig. 10 - Distribution of erection costs for target bridges

Erection period

The most important factor that influences the construction benefit is the erection period, and the erection periods were drawn for the cantilever deck of this study and compared with that of the reinforced-concrete deck for the target bridges.

Erection period details for the target bridge were summarized in Table 6 [KICT 2006]. As a result of evaluation for the erection period, the steel-concrete composite cantilever deck has a 61 % shorter erection period than the reinforced-concrete deck, and it is estimated that the erection period would be reduced from 41 days to 25 days on the target bridges. The reduction of erection period should also reduce the construction cost, and in cases of replacing old bridge decks, it is possible to save related social costs such as a traffic blockades.

Table 6 - Erection period details for the target bridges

RC deck		Proposed deck	
Erection details	Period	Erection Details	Period
1. Formwork & supports	8 days	1. Steel form install	2 days
2. Reinforcing bars install	7 days	2. Reinforcing bars install	3 days
3. Concrete casting	4 days	3. Concrete casting	4 days
4. Curing	15 days	4. Curing	15 days
5. Un-installation	7 days	5. Un-installation	1 day
Total	41 days	Total	25 days

CONCLUSIONS

In this study, in order to erect a cantilever deck without supports and formwork, an experimental study for the steel-concrete composite cantilever deck system was carried out. The cantilever deck system consists of steel plate, perfobond ribs welded onto the steel plates, concrete, and reinforcing bars. In order to form the cantilever deck, the steel forms which consist of steel plate and ribs were fabricated then, the ribs of steel form were bolted to the girder to prevent large rotation and deflection under erection loads and finally, the concrete must be cast-in-place. A total of four specimens were built and tested under erection loads.

As a result of the tests, it was found that, under erection loads, the weight of the laborers, and wet concrete, the connection of the ribs to the girders has enough

stiffness to satisfy in-erection deflection and the bolt connections supply sufficient force to prevent rotation. As a result of the evaluation of the erection period, the steel-concrete composite cantilever deck has a 61 % shorter erection period than a reinforced-concrete deck for the target bridges. The reduction of erection period should also reduce construction cost. The proposed cantilever deck erection method should improve the efficiency and economy of bridge construction.

ACKNOWLEDGEMENT

The authors thank to Mr. Kyung-Hoon Lee, Executive Director of Hanmac Eng. Co. Ltd., and Young-Kag Shin, Executive Direct of Kyongdong Eng. Co. Ltd., for the optimal design of steel-concrete composite cantilever deck and construction benefit evaluation of this study.

REFERENCES

Kim H.Y. and Jeong Y.J. (2006) Experimental investigation on behavior of steel-concrete com-posite bridge slabs with perfobond ribs. *J. of Constructional Steel Research,* 62, No. 5, 463-471.

Nakai H., Matsui S., Yoda T. and Kurita A. (1998) Trends in steel-concrete composite bridges in Japan. *Structural Engineering International IABSE*, 1, 30-34.

Morino S. (1998) Recent developments in hybrid structures in Japan - research, design and construction. *Engineering Structures*, 20, No. 4-6, 336-346.

Berg A.C., Bank L.C., Oliva M.G. and Russell J.S. (2006) Construction and cost analysis of an FRP reinforced concrete bridge deck. *Construction and Building Materials*, 20, No. 8, 515-526.

Zhao L., Karbhari V.M., Hegemier G.A. and Seible F. (2004) Connection of concrete barrier rails to FRP bridge decks. *Composites Part B: Engineering*, 35, No. 4, 269-278.

Kim M.K. (2006) *Bridge slab construction method and lattice bar deck-shaped precast concrete plate applied thereto*. Patent Cooperation Treaty (PCT), WO 2006/ 049377.

Ehmke F.G. (2006) *Analysis of a bridge deck built on interstate highway 39/90 with full-depth, precast, prestressed concrete deck panels*. Ms.C. Thesis, University of Wisconsin-Madison.

Shim C.S., Lee P.G., Chang S.P. (2001) Design of shear connection in composite steel and concrete bridges with precast decks. *J. of Constructional Steel Research*, 57, No. 3, 203-291.

Ministry of Construction and Transportation (2006). *Design specifications for highway bridges (in Korean)*. MOCT, Korea.

Korea Institute of Construction Technology (2006). *Development of long-life deck systems for bridges: steel-concrete composite bridge deck (in Korean)*. KICT 2006-058, Korea.

This page intentionally left blank

Attendees List

Redzuan Abdullah
Universiti Teknologi Malaysia
Faculty of Civil Engineering
UTM Skudai
Skudai, Johor 81310 MALAYSIA
Phone: 6-07-5531591
Fax: 540-231-7532
Email: redzuan@utm.my

Florian Ackermann
Kaiserslautern University of Technology
Paul-Ehrlich-Straße 14
Kaiserslautern 67663 GERMANY
Phone: 49-631-205-3828
Fax: 49-631-205-3555
Email: florian.ackermann@rhrk.uni-kl.de

Doo Byong Bae
Kookmin University
College of Engineering
Jungneunggil
Seoul, Sungbuk-Gu 136-702 KOREA
Phone: 82-2-910-4697
Fax: 82-2-910-4939
Email: dbbae@kookmin.ac.kr

William Baker
Associate Partner
Skidmore, Ownings & Merrill
224 South Michigan Avenue
Chicago, IL 60604 USA
Phone: 1-312-554-9090
Fax:
Email: william.f.baker@som.com

Frank Boehme
TU Darmstadt - Fachgebiet Stahlbau
Petersenstraße 12
Darmstadt, Hessen 64287 GERMANY
Phone: 49-6151-16-3145
Fax: 49-6151-16-3245
Email: boehme@stahlbau.tu-darmstadt.de

Mark Bradford
University of New South Wales
School of Civil and Environmental Eng.
Sydney NSW 2052 AUSTRALIA
Phone: 61-2-9385-5014
Fax: 61-2-9385-9747
Email: m.bradford@unsw.edu.au

Russell Bridge
Professor
University of Western Sydney
134 Gamban Road
Gwandalan NSW 2259 AUSTRALIA
Phone: 61-2-49-761-735
Fax: 61-2-49-761-735
Email: rq.bridge@uws.edu.au

Oreste Bursi
University of Trento
Dept. Mechnical Structure Engineering
Via Mesiano 77
Trento 38100 ITALY
Phone: 39-0461-882521-2503
Fax: 39-0461-882599-2505
Email: oreste.bursi@ing.unitn.it

Antoinette Chartier
ECI Site Manager
Engineering Conferences International
6 MetroTech Center
Brooklyn, NY 11201 USA
Phone: 1-718-260-3743
Fax: 1-718-260-3754
Email: alchms@juno.com

ChulHun Chung
Dankook University
Jukjeon-dong, Suji-gu
Yonginsi, Kyunggido 448-160
KOREA
Phone: 82-31-8005-3477
Fax: 82-31-8005-3496
Email: chchung5@dankook.ac.kr

Adrian Ciutina
The Politehnica University of Timisoara
Faculty of Civil Engineering
Str. Ioan Curea
Timisoara, Timis 300224 ROMANIA
Phone: 40-256-403-932
Fax: 40-256-403-932
Email: adrian.ciutina@ct.upt.ro

Michel Crisinel
Swiss Federal Institute of Technology
Steel Structures Laboratory - ICOM
GC Building
Lausanne 1015 SWITZERLAND
Phone: 41-21-693-2427
Fax: 41-21-693-2868
Email: michel.crisinel@epfl.ch

Yao Cui
Kyoto University
Disaster Prevention Research Institute
Gokasho
Uji, Kyoto 611-0011 JAPAN
Phone: 81 774-38-4085
Fax: 81-774-38-4334
Email: snoopy.cy@steel.mbox.media.kyoto-u.ac.jp

Uwe Dorka
University of Kassel
Kurt-Wolters-Strasse 3
Kassel, Hessen 34123 GERMANY
Phone: 49-561-804-2667
Fax: 49-561-804-3275
Email: uwe.dorka@uni-kassel.de

Sam Easterling
Virginia Tech
CEE Dept - M.S. 0105
200 Patton Hall
Blacksburg, VA 24061
USA
Phone: 1-540-231-5143
Fax: 1-540-231-7532
Email: seaster@vt.edu

Michael Engelhardt
University of Texas at Austin
10100 Burnet Road
Building 177
Austin, TX 78758 USA
Phone: 1-512-471-6837
Fax: 1-512-471-1944
Email: mde@mail.utexas.edu

Fauzan Fauzan
Osaka University
2-1 Yamadaoka
Suita, Osaka 565-0871 JAPAN
Phone: 81-6-6879-7637
Fax: 81-6-6879-7637
Email: fauzan@arch.eng.osaka-u.ac.jp

Markus Feldmann
Head of Institute
RWTH Aachen
Lehrstuhl Für Stahlbau Und Leichtmetallb
Mies-van-der-Rohe-Str. 1
Aachen, NRW 52074 GERMANY
Phone: 49-241-80-25178
Fax: 49-241-22140
Email: feldmann@stb.rwth-aachen.de

Mario Fontana
Professor
ETH Zurich / IBK
Wolfgang-Pauli-Strasse 15
Zurich ZH 8093 SWITZERLAND
Phone: 41-44-633-3173
Fax: 41-44-633-1093
Email: mario.fontana@ethz.ch

Roland Friede
TU Darmstadt - Fachgebiet Stahlbau
Petersenstrasse 12
Darmstadt, Hessen 64289 GERMANY
Phone: 49-61-5116-6831
Fax: 49-61-5116-3245
Email: friede@stahlbau.tu-darmstadt.de

Marian Gizejowski
Warsaw University of Technology
Faculty of Civil Engineering
Al Armii Ludowej 16
Warsaw, Wojewodztwo Mazowieckie
00-637 POLAND
Phone: 48-660-028-154
Fax: 48-22-825-6532
Email: m.gizejowski@il.pw.edu.pl

Fernando Gonzalez
Darmstadt - Fachgebiet Stahlbau
Petersenstraße 12
Darmstadt, Hessen 64287 GERMANY
Phone: 49-61-5116-2345
Fax: 49-61-5116-3245
Email: gonzalez@stahlbau.tu-darmstadt.de

Lawrence Griffis
Walter P. Moore & Associates
3131 Eastside
2nd Floor
Houston, TX 77098 USA
Phone: 713-630-7300
Fax: 713-630-7396
Email: LGriffis@walterpmoore.com

Gabriele Guscetti
Guscetti & Tournier / EPFL
12, Rue Du Pont-Neuf
Geneva 1227 SWITZERLAND
Phone: 41-22-308-8888
Fax: 41-22-308-8899
Email: guscetti@gti.ch

Jerome Hajjar
Northeastern University
Department of Civil and
Environmental Engineering
400 Snell Engineering Center
360 Huntington Avenue
Boston, MA 02115-5000 USA
Phone: (617) 373-3242
Fax: (617) 373-4419
E-mail: jf.hajjar@neu.edu

Gerhard Hanswille
Professor
University of Wuppertal
Pauluskirchstraße 11
Wuppertal, North Rhine Westphalia
42285 GERMANY
Phone: 49-202-439-4108
Fax: 49-202-439-4208
Email: stahlbau@uni-wuppertal.de

Gunter Hauf
Universität Stuttgart
Pfaffenwaldring 7
Stuttgart 70569 GERMANY
Phone: 49-711-6856-6243
Fax: 49-711-6856-6236
Email: gunter.hauf@ke.uni-stuttgart.de

Oliver Hechler
Arcelor Commercial Sections S.A.
66 Rue De Luxembourg
Esch-sur-Alzette, Luxembourg 4221
GERMANY
Phone: 49-352-5313-2213
Fax: 49-352-5313-2299
Email: oliver.hechler@arcelormittal.com

Stefan Heyde
Technical University of Berlin
Department of Steel Structures
TIB1-B1
Berlin 13355 GERMANY
Phone: 49-30-314-72128
Fax: 49-30-314-72123
Email: stefan.heyde@tu-berlin.de

Toko Hitaka
Kyoto University
Disaster Prevention Research Institute
Gokasho
Uji, Kyoto 611-0011 JAPAN
Phone: 81-77-438-4084
Fax: 81-77-438-4334
Email: toko.h@ay2.ecs.kyoto-u.ac.jp

Mohammed Hjiaj
INSA De Rennes
20 Av Des Buttes De Coesmes
Rennes, ILLE ET VILAINE 35043
FRANCE
Phone: 33-22-323-8711
Fax: 33-22-323-8448
Email: mohammed.hjiaj@insa-rennes.fr

EunJung Hwang
Dankook University
Jukjeon-dong, Suji-gu
Yonginsi, Kyunggido 448-160 KOREA
Phone: 82-31-8005-3489
Fax: 82-31-8005-3496
Email: haiyan77@dankook.ac.kr

William Jacobs
SDL Structural Engineers
2300 Windy Ridge Parkway SE
Suite 200 South
Atlanta, GA 30339 USA
Phone: 1-770-850-1347
Fax: 1-770-850-1562
Email: rclemons@sdlal.com

Jean-Pierre Jaspart
Directeur De Recherches FNRS
Liège University
1, Chemin Des Chevreuils
Liege 4000 BELGIUM
Phone: 32-4-7850-2380
Fax: 32-4-366-9192
Email: jean-pierre.jaspart@ulg.ac.be

Youn-Ju Jeong
Korea Institute of Construction
Technology
2311, Daehwa, Ilsan
Goyang, Gyeonggi 411-712 KOREA
Phone: 82-31-9100-136
Fax: 82-31-9100-121
Email: yjjeong@kict.re.kr

Roger Johnson
University of Warwick
School of Engineering
Engineering Department
Coventry, West Midlands CV35 8EL
UNITED KINGDOM
Phone: 44-1926-624-319
Fax: 44-2476-418-922
Email: r.p.johnson@warwick.ac.uk

KwangHoe Jung
Hyundai Institute of Construction
Technology
102-4, Mabuk-dong
Giheung-gu
Youngin-si, Gyounggi-do 446-716
KOREA
Phone: 82-31-280-7217
Fax: 82-31-280-7070
Email: jkh@hdec.co.kr

DongWook Kim
Chung-Ang University
Naeri, Daeduckmyun
Anseongsi, Kyunggido 456-756 KOREA
Phone: 82-31-670-4661
Fax: 82-31-675-1387
Email: clearup7@nate.com

In Gyu Kim
Daewoo E&C
60 Songjuk-Dong
Janan-Gu
Suwon, Kyunggi 440-210 KOREA
Phone: 82-31-250-1129
Fax: 82-31-250-1131
Email: gyu@dwconst.co.kr

Young Jin Kim
Daewoo E&C
60 Songjuk-Dong
Janan-Gu
Suwon, Kyunggi 440-210 KOREA
Phone: 82-31-250-1177
Fax: 82-31-250-1177
Email: yjkim@dwconst.co.kr

Markus Knobloch
ETH Zurich / IBK
Wolfgang-Pauli-Strasse 15
Zurich ZH-8093 SWITZERLAND
Phone: 41-44-633-2787
Fax: 41-44-633-1093
Email: knobloch@ibk.baug.ethz.ch

Ulrike Kuhlmann
Professor
University of Stuttgart
Institute of Structural Design
Pfaffenwaldring 7
Stuttgart, Baden-Württemberg 70569
GERMANY
Phone: 49-711-685-6245
Fax: 49-711-685-6236
Email: Sekretariat@ke.uni-stuttgart.de

Hiroshi Kuramoto
Osaka University
Yamadaoka 2-1
Suita, Osaka 565-0871 JAPAN
Phone: 81-6-6879-7635
Fax: 81-6-6879-7637
Email: kuramoto@arch.eng.osaka-u.ac.jp

Wolfgang Kurz
Kaiserslautern University of Technology
Paul-Ehrlich-Strasse 14
Kaiserslautern 67663 GERMANY
Phone: 49-63-1205-2006
Fax: 49-63-1205-3555
Email: wkurz@rhrk.uni-kl.de

Alain Lachal
INSA, National Institute of Applied Sciences
20, Avenue Des Buttes De Cësmes
Rennes, Ille Et Vilaine 35043 FRANCE
Phone: 33-22-323-8324
Fax: 33-22-323-8448
Email: Alain.Lachal@insa-rennes.fr

Dennis Lam
University of Leeds
School of Civil Engineering
Woodhouse Lane
Leeds, West Yorkshire LS2 9JT
UNITED KINGDOM
Phone: 44-113-343-2295
Fax: 44-113-343-2265
Email: d.lam@leeds.ac.uk

Jorg Lange
TU Darmstadt - Fachgebiet Stahlbau
Petersenstrasse 12
Darmstadt, Hessen 64287 GERMANY
Phone: 49-6151-162-145
Fax: 49-6151-162-145
Email: lange@stahlbau.tu-darmstadt.de

Jean-Paul Lebet
Swiss Federal Institute of Technology
Steel Structures Laboratory - ICOM
GC Building
Lausanne 1015 SWITZERLAND
Phone: 41-21-693-2439
Fax: 41-21-693-2868
Email: jean-paul.lebet@epfl.ch

Pil Goo Lee
RIST
79-5 Youngcheon Dongtan
Hwasung, Kyonggido 445-813 KOREA
Phone: 82-31-370-9591
Fax: 82-31-370-9599
Email: pg289@rist.re.kr

Roberto Leon
Georgia Institute of Technology
Civil Engineering School
790 Atlantic Avenue
Atlanta, GA 30332-0355 USA
Phone: 1-404-894-2220
Fax: 1-404-894-2278
Email: rleon@ce.gatech.edu

Guochang Li
Visiting Professor
Georgia Institute of Technology
500 Northside Circle NW,APT# Ii6
Atlanta, GA 30309 USA
Phone: 1-404-861-9498
Fax: 1-404-894-0211
Email: liguochang0604@sina.com

Martin Lippes
University of Wuppertal
Pauluskirchstraße 11
Wuppertal, North Rhine Westphalia
42285 GERMANY
Phone: 49-202-439-4108
Fax: 49-202-439-4208
Email: stahlbau@uni-wuppertal.de

Quang Huy Nguyen
INSA of RENNES
20 Av Des Buttes De Coesmes
Rennes, Ill De Vilaine 35000 FRANCE
Phone: 33-22-323-8511
Fax: 33-22-323-8448
Email: quang-huy.nguyen@ens.insa-rennes.fr

Michael O'Rourke
Rensselaer Polytechnic Institute
Civil Engineering Dept.
4046 Jonsson Engineering Center, 4th Flr
Troy, NY 12180-3590 USA
Phone: 1-518-276-6933
Fax: 1-518-276-4833
Email: orourm@rpi.edu

Luis Pallares Rubio
University Of Illinois At Urbana-Champaign
205 N Mathews Ave
B203 Newmark Civil Engineering Lab
Urbana, IL 61801 USA
Phone: 1-217-721-2142
Fax: 1-217-265-8040
Email: luipalru@cst.upv.es

Tiziano Perea
Georgia Institute of Technology
Civil Engineering School
790 Atlantic Avenue
Atlanta, GA 30332-0355 USA
Fax: 1-404-894-2278
Email: tperea@gatech.edu

Markus Porsch
University of Wuppertal
Pauluskirchstraße 11
Wuppertal, North Rhine Westphalia
42285 GERMANY
Phone: 49-202-439-4108
Fax: 49-202-439-4208
Email: stahlbau@uni-wuppertal.de

Gian Andrea Rassati
University of Cincinnati
765 Baldwin Hall
Cincinnati, OH 45221-0071 USA
Phone: 1-513-556-3696
Fax: 1-513-556-2599
Email: gian.rassati@uc.edu

Sabine Rauscher
RWTH Aachen University
Institute of Structural Concrete
Mies-van-der-Rohe Strasse 1
Aachen, NRW 52064 GERMANY
Phone: 49-241-802-5168
Fax: 49-241-802-2335
Email: rauscher@imb.rwth-aachen.de

Elio Raveglia
ETH Zurich / IBK
Wolfgang-Pauli-Strasse 15
Zurich ZH-8093 SWITZERLAND
Phone: 41-44-633-3176
Fax: 41-44-633-1093
Email: raveglia@ibk.baug.ethz.ch

Charles Roeder
Professor
University of Washington
233B More Hall
Seattle, WA 98195-2700 USA
Phone: 1-206-543-6199
Fax: 1-206-543-1543
Email: croeder@u.washington.edu

Markus Rybinski
Universität Stuttgart
Pfaffenwaldring 7
Stuttgart 70569 GERMANY
Phone: 49-711-6856-9244
Fax: 49-711-6856-6236
Email: markus.rybinski@ke.uni-stuttgart.de

Changsu Shim
Chung-Ang University
Naeri, Daeduckmyun
Anseongsi, Kyunggido 456-756 KOREA
Phone: 82-31-670-4707
Fax: 82-31-675-1387
Email: csshim@cau.ac.kr

NaYoung Song
Dankook University
Jukjeon-dong, Suji-gu
Yonginsi, Kyunggido 448-160 KOREA
Phone: 82-31-8005-3489
Fax: 82-31-8005-3496
Email: allforny@dankook.ac.kr

Johannes Stark
Professor
TUD / Stark Partners
Molenmeesterstraat 20
Delfgauw, Zuid-Holland 2645 GW
THE NETHERLANDS
Phone: 31-15-369-3156
Fax: 31-15-369-3156
Email: janstark@planet.nl

Robert-Jan Stark
SmitWesterman Structural Engineers
PO Box 130
Nesse 34
Waddinxveen, Zuid-Holland 2740 AC
THE NETHERLANDS
Phone: 31-18-261-5655
Fax: 31-18-261-5743
Email: rstark@smitwesterman.nl

Brian Uy
University of Western Sydney
School of Engineering
Locked Bag 1797
Penrith South DC NSW 1797
AUSTRALIA
Phone: 61-2-4736-0228
Fax: 61-2-4736-0137
Email: b.uy@uws.edu.au

Amit Varma
Associate Professor
Purdue University
3363 Humboldt Street
West Lafayette, IN 47906 USA
Phone: 1-765-496-3419
Fax: 1-765-494-1105
Email: ahvarma@purdue.edu

Milan Veljkovic
Luleå University of Technology
Rengbågsalle 4
Luleå 97187 SWEDEN
Phone: 46-70-608-4731
Fax: 46-92-049-1913
Email: milan.vejkovic@ltu.se

Andrew Wheeler
University of Western Sudney
Locked Bag 1797
South Penrith DC, NSW 1797
AUSTRALIA
Phone: 61-2-4736-0139
Fax: 61-2-4736-0074
Email: a.wheeler@uws.edu.au

Donald White
Georgia Tech
11880 Devon Downs Trail
Alpharetta, GA 30005 USA
Phone: 1-678-895-5451
Fax: 1-404-894-2278
Email: dwhite@ce.gatech.edu

Riccardo Zandonini
University of Trento
Via Mesiano 77
Trento I-38100 ITALY
Phone: 39-04-6188-2530
Fax: 39-04-6188-2599
Email: Riccardo.Zandonini@unitn.it

Yan Xiao
Assistant Professor
University of Southern California
HNU-CIPRES
3620 S. Vermont Avenue
Los Angeles, CA 90089 USA
Phone: 1-213-740-6130
Fax: 1-213-744-1426
Email: yanxiao@usc.edu

Jian Zhao
University of Wisconsin, Milwaukee
3200 N Cramer Street
PO Box 784
Milwaukee, WI 53051 USA
Phone: 1-414-229-2330
Fax: 1-414-229-6958
Email: jzhao@uwm.edu

Seok Goo Youn
Seoul National University of Technology
Kongneunggil 138, Nowon-Gu
Seoul 139-743 KOREA
Phone: 82-2-970-6515
Fax: 82-2-948-0043
Email: sgyoun@snut.ac.kr

Author Index

Abdullah, Redzuan, 138
Abramski, Marcin, 102
Ackermann, Florian P., 125
Amorntipsakul, Saenboon, 604, 611
Aribert, Jean-Marie, 529, 741

Bae, Doobyong, 680
Berthellemy, Jaques, 78
Böhme, Frank, 578
Bradford, Mark A., 151, 619
Bridge, Russell Q., 225, 276
Bursi, Oreste S., 493, 506

Cedeno, Guillermo A., 642
Chen, Baisheng, 291
Chung, Chul-Hun, 92
Ciutina, Adrian Liviu, 52
Crisinel, Michel, 212
Cui, Yao, 364

Demonceau, Jean-François, 442
Dorka, Uwe E., 604, 611

Easterling, W. Samuel, 138
El-Tawil, Sherif, 703
Engelhardt, Michael D., 728
Eriksen, Jörgen, 717

Fauzan, 263
Feldmann, Markus, 39
Ferrario, Fabio, 493, 506
Fontana, Mario, 112
Fortney, Patrick J., 479
Frangi, Andrea, 112
Friede, Roland, 199
Friedrich, Thomas, 102

Geibler, Karsten, 304
Geiss, Paul Ludwig, 669
Gizejowski, Marian A., 554
González, Fernando, 419
Goode, C. Douglas, 317
Gore, Jay, 642
Goverdhan, Arvind V., 427
Grages, Hauke, 657
Guezouli, Samy, 542, 566
Guscetti, Gabriele, 212

Hajjar, Jerome F., 591
Hanswille, Gerhard, 14, 326, 391
Harries, Kent A., 703
Hauf, Gunter, 185
Hechler, Oliver, 39, 78, 741
Hegger, Josef, 39, 691
Heidarpour, Amin, 619
Heyde, Stefan, 304
Hitaka, Toko, 364, 466
Hjiaj, Mohammed, 566
Huo, Jingsi, 291

Jacobs, William P., V, 427
Jacobsen, Andres, 466
Jaspart, Jean-Pierre, 442
Jeong, Youn-Ju, 766
Johnson, Paul W., III, 479
Johnson, Roger P., 1
Jung, Se-Kwon, 754

Kaing, Sao Serey, 542, 741
Kessler, Christopher, 669
Kim, Dong-Wook, 92
Kim, Hyeong-Yeol, 766
Kim, Young-Jin, 680
Klingner, Richard E., 728
Knobloch, Markus, 112
Koo, Hyun-Bon, 766
Kuhlmann, Ulrike, 26, 185, 338
Kuramoto, Hiroshi, 263, 455
Kurz, Wolfgang, 102, 173, 377, 669
Kwon, Gunup, 728

Lachal, Alain, 529, 542, 741
Lam, Dennis, 252, 317
Lange, Jörg, 199, 377, 419, 578, 657
Lebet, Jean-Paul, 65
Lee, Pil-Goo, 92
Lehman, Dawn E., 351
Leon, Roberto T., 237, 519
Li, Guochang, 519
Lippes, M., 326
Loho, G., 529
Lorenc, Wojciech, 78

Mensinger, Martin, 112
Mirza, O., 160

Nakashima, Masayoshi, 364
Nguyen, Quang Huy, 566
Nilsson, Martin, 717

Perea, Tiziano, 237
Pi, Yong-Lin, 151
Porsch, Markus, 14
Pucinotti, Raffaele, 493, 506

Raichle, Jochen, 26
Rassati, Gian A., 479
Rauscher, Sabine, 39, 691
Raveglia, Elio, 112
Roeder, Charles W., 351
Rybinski, Markus, 338

Salah, Wael A., 554
Schnell, Jüergen, 102, 125, 173
Schwindl, Karl, 112
Seidl, Günter, 78
Shahrooz, Bahram M., 479
Shan, Jianhua, 291
Shim, Chang-Su, 92
Somja, Hugues, 542
Stark, J. W. B., 406
Stark, Rob, 628
Steinmann, Ralf, 199
Stratan, Aurel, 52
Sun, Wei, 519

Testo, Nicola, 252
Tort, Cenk, 591
Turcinskas, Sarunas, 669

Uy, Brian, 160, 566, 151

Varma, Amit H., 642
Veljkovic, Milan, 717
Viefhues, Eva, 78

Weil, Torsten, 173
Wheeler, Andrew, 225
White, Donald W., 754

Xiao, Yan, 291

Youn, Seok-Goo, 680

Zandonini, Riccardo, 493
Zheng, Qiu, 291

Subject Index

Adhesives, 669
Anchors, 338
Axial loads, 252

Beam columns, 506, 529, 542, 611
Beams, 112, 151, 466, 506, 604
Bending, 52, 138, 680, 703
Bolts, 493, 766
Bonding, 138, 669
Bridge abutments, 717
Bridge decks, 766
Bridges, 78
Bridges, composite, 65, 92, 391, 741, 754
Bridges, girder, 728, 754, 766
Buildings, 304
Buildings, high-rise, 377
Buildings, multistory, 199, 212

Cantilevers, 766
Columns, 263, 304, 317, 351, 364, 455, 519
Comparative studies, 427
Composite beams, 78, 160, 173, 212, 237, 493, 529, 542, 554, 566, 611, 619, 657
Composite columns, 237, 276, 326, 427, 493, 506, 529, 542, 604, 611
Composite materials, 102, 112, 125, 138, 151, 263, 338, 364, 442, 466, 578, 703, 717, 728
Composite structures, 14, 377, 406, 455, 628, 691, 728
Compressive strength, 291, 351
Computation, 578
Concrete, 26, 39, 276, 406, 427, 628, 669
Concrete slabs, 364
Connections, 39, 52, 65, 78, 92, 102, 160, 173, 442, 519, 604, 611, 741, 78
Construction materials, 691
Core walls, 479
Coupling, 479
Cyclic loads, 39, 52
Cyclic tests, 466

Deflection, 185, 578, 657
Design, 14, 173, 212, 225, 276, 326, 338, 391, 591, 628
Ductility, 151

Economic factors, 351
Europe, 419
Evaluation, 479
Experimentation, 741

Failure loads, 14, 317
Fatigue, 26, 39
Fiber reinforced materials, 125
Fiber reinforced polymer, 703
Fibers, 237, 276
Finite element method, 566, 591, 611, 642
Fire resistance, 628
Fires, 493, 506, 619, 642
Flexural strength, 680, 703
Floors, 1, 185, 212
Frames, 493, 591, 604

Germany, 199, 377, 391
Girders, 185, 578, 680, 703

High-strength concrete, 326
Historic sites, 304
Hollow sections, 252
Hybrid methods, 263, 479, 680, 703

Industrial facilities, 212
Inelasticity, 754
Installation, 102, 112

Japan, 364
Joints, 338, 442, 493, 506, 529, 542, 611, 741

Load bearing capacity, 304
Loading rates, 291

Material properties, 657, 691
Models, 173

Nonlinear analysis, 566
Numerical models, 225, 542, 554

Openings, 466

Parking facilities, 199
Plates, 338, 466
Predictions, 317, 642, 26
Prestressing, 102

Reinforced concrete, 138
Reinforcement, 225

Seismic effects, 263, 442, 493, 506, 519, 529, 591
Service loads, 455
Shear forces, 92, 185
Shear resistance, 1, 65
Sheets, 1
Slabs, 1, 102, 112, 125, 138, 151, 160, 173
Steel, 276, 326, 427, 628, 669, 703, 728, 766
Steel beams, 479, 642
Stiffness, 351, 519
Strain, 160
Structural behavior, 338, 717
Structural design, 252, 419
Structural elements, 604
Structural members, 442
Structural steel, 406
Structural systems, 263, 455, 754
Studs, 26, 92

Temperature effects, 291, 628
Tubes, 225, 252, 291, 317, 326, 351, 591

Walls, 466
Webs, structural, 173
Welds, 506, 611